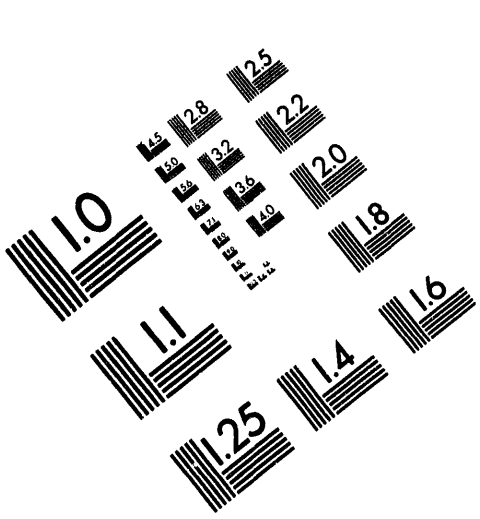
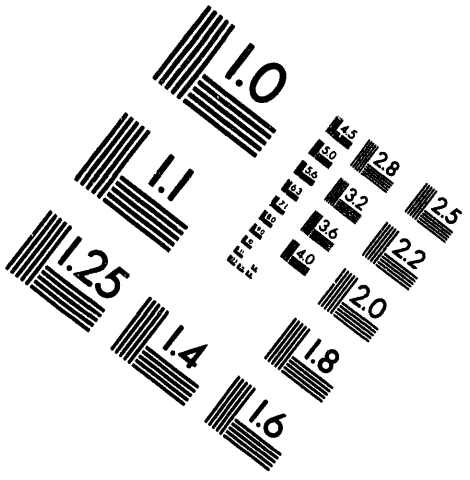
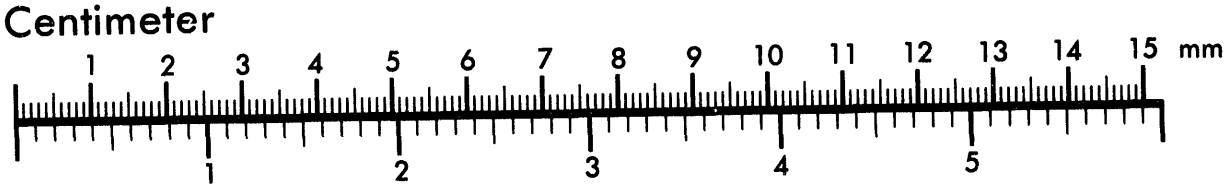
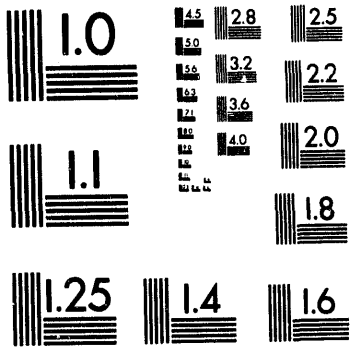
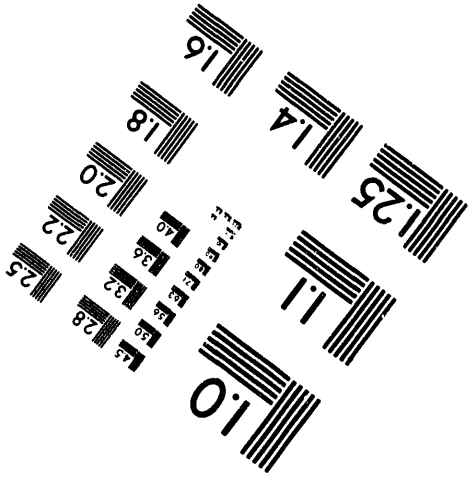


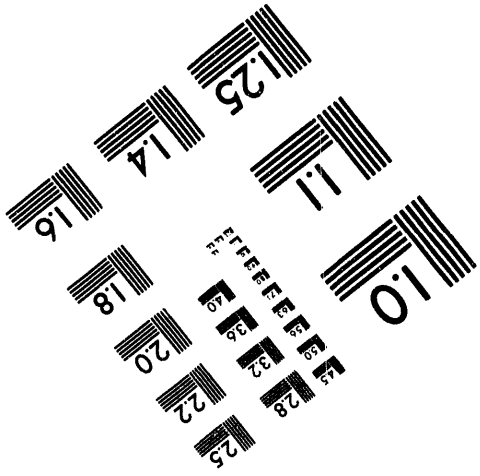
Association for Information and Image Management
1100 Wayne Avenue, Suite 1100
Silver Spring, Maryland 20910
301/587-8202











MANUFACTURED TO AIIM STANDARDS
BY APPLIED IMAGE, INC.

1 of 1

Hydrogeology, Waste Disposal, Science and Politics

Engineering Geology and Geotechnical Engineering 30th Symposium, 1994

Paul Karl Link, editor

1994 Symposium Committee

Lee Robinson
Symposium Chairman
College of Engineering
Idaho State University

Paul Link
Proceedings Editor
Department of Geology
Idaho State University

Spencer Wood
On-Site Coordinator
Department of Geosciences
Boise State University

The Engineering Geology and Geotechnical Engineering Symposium is an annual event, sponsored by:
Idaho State University
Boise State University
University of Idaho
Utah State University
University of Nevada-Reno

Copies of this volume and previous symposium volumes may be ordered from
Dr. Lee Robinson
College of Engineering
Box 8060
Idaho State University
Pocatello, Idaho 83209
Phone (208) 236-2902
FAX (208) 236-4538

Correct citation of articles in this book
in Link, P.K., editor, 1994, Hydrogeology, Waste Disposal, Science and Politics, Proceedings of the 30th Symposium on Engineering Geology and Geotechnical Engineering, College of Engineering, Idaho State University, Pocatello, Idaho.

Cover illustrations:
Front Location map of Idaho National Engineering Laboratory and Wells drilled near the Idaho Chemical Processing Plant (ICPP)
Back: Stratigraphic units beneath the ICPP
Both figures from McCurry and others, this volume

MASTER

DISTRIBUTION OF THIS DOCUMENT IS UNLIMITED

Hydrogeology, Waste Disposal, Science and Politics

1994 Symposium on Engineering Geology and Geotechnical Engineering

Compiled and edited by Paul Karl Link, Idaho State University

Table of Contents

I. Site Characterization--Pocatello Area

Hydrogeology of the Pocatello Aquifer: Implications for Wellhead Protection Strategies
J. Welhan, and C. Meehan 1

Impact of Leachable Sulfate On the Quality of Groundwater in the Pocatello Aquifer
C. Meehan and J. Welhan 19

Interpretation of Shallow Seismic Refraction Data Using Raytracing Inversion: A Simple Example from a Groundwater Resource Study in Pocatello, Idaho
J.R. Pelton, M.E. Dougherty, and J.A. Welhan 37

Frazier Hall: The Foundation Failure That Didn't
Lee Robinson 45

A Mise-A'-La-Masse Method For Landfill Contaminant Plume Evaluation
T.H. Rowley, P.R. Donaldson, J.L. Osiensky, and J.A. Welhan 83

II. Site Characterization--Boise Area

Groundwater development in granitic terrain, Bogus Basin Ski Resort, Boise, Idaho
William C.B. Gates, Craig L. Parkinson and Kevin L. Schroeder 55

A Proposed Descriptive Methodology for Environmental Geologic (Envirogeologic) Site Characterization
David L. Schwarz, and Walter S. Snyder 67

III. Site Assessment

Hotspots & Other Hidden Targets: Probability of Detection, Number, Frequency and Area
Charles L. Vita 95

The Relationship of Seismic Velocity Structure and Surface Fracture Characteristics of Basalt Outcrops to Rippability Estimates
S.E. Kay, M.E. Dougherty and J.R. Pelton 107

Geologic and Geotechnical Investigation of the Windsor Park Subdivision North Las Vegas, Nevada
Lorraine M. Linnert, James L. Werle, Alan N. Stilley, and Brad E. Olsen 121

Failure Analysis of Buried Tanks
Reynold King Watkins 137

Erosion Control Test Facilities at the Utah Water Research Lab
C. Earl Israelsen and Gilberto Urroz 147

IV. Idaho National Engineering Laboratory

Pre-anthropogenic Groundwater Evolution at the Idaho National Engineering Laboratory, Idaho
Travis L. McLing and Robert W. Smith 151

Idaho National Engineering Laboratory Integrated Field Scale Pumping and Infiltration Test
T.R. Wood, G.T. Norrell, A.W. Wylie, K.J. Dooley, G.S. Johnson and E.R. Neher 152

Mineralogy of and Depositional Sources of Sedimentary Interbeds Beneath the Idaho National Engineering Laboratory; Eastern Snake River Plain, Idaho
Michael F. Reed 154

Concentrations and Compositions of Colloidal Particles in Groundwater Near the ICPP, Idaho National Engineering Laboratory, Idaho
Mason Estes and Mike McCurry 165

Hydrostratigraphic Interpretation of the Upper Portion of the Snake River Plain Aquifer near the Idaho Chemical Processing Plant at the INEL
W. Barrash, R.H. Morin, S.H. Wood, and W. Bennecke 181

Hydrostratigraphy of the Snake River Plain Aquifer Beneath the Radioactive Waste Management Complex at the Idaho National Engineering Laboratory, A Preliminary Report
Mary J. Hegmann and Spencer H. Wood 195

IV. Idaho National Engineering Laboratory (continued)

Three-dimensional Chemical Structure of the INEL Aquifer System Near the Idaho Chemical Processing Plant
Michael McCurry, Mason Estes, Jeanne Fromm, John Welhan and Warren Barrash 207

Idaho Chemical Processing Plant (ICPP) Injection Well: Operations History and Hydrochemical Inventory of the Waste Stream
J. Fromm, J. Welhan, M. McCurry and W. Hackett 221

Straddle Packer System Design and Operation for Vertical Characterization of Open Bore Holes
James K. Olsen 238

Hydrologic Testing in Wells Near the Idaho Chemical Processing Plant at the Idaho National Engineering Laboratory
Gary S. Johnson, J. Ilhan Olsen and Dale R. Ralston 253

Vertical Variation in Groundwater Chemistry Inferred from Fluid Specific-Conductance Well Logging of the Snake River Plain Basalt Aquifer, Idaho National Engineering Laboratory, Southeastern Idaho
Spencer H. Wood and William Bennecke 267

IV. Geophysical Methods

Environmental Geophysics: Locating and Evaluating Subsurface Geology, Geologic Hazards, Groundwater Contamination, Etc.
Alvin K. Benson 285

Effects of Shale and Contaminants on (Vs/VP) Ratios in Transversely-Isotropic Geology
Alvin K. Benson 305

A Comparison of Ground Penetrating Radar Methods: Multi-Fold Data Vs. Single Fold Data
Lee M. Liberty and John R. Pelton 321

A New Geophysical Method to Measure Soil Profiles for Dynamic Analysis of Soil Embankments
Paul Michaels 331

Ground Penetrating Radar And Seismic Refraction Investigation of Fracture Patterns in the Basalt of Lucky Peak Near Boise, Idaho
M.E. Dougherty, W.K. Hudson, S.E. Kay and R.J. Vincent 345

Results of a Downhole Formation Microscanner Study in a Juro-Triassic-aged Sedimentary Deposit (Passaic Formation)
Joseph A. Fischer, Joseph J. Fischer, and Robert J. Bullwinkel 359

The Identification of Basalt Physical Features From Borehole Television Logs
William Bennecke 371

Stereological Sampling of Rock Masses for Engineering Purposes
Stanley M. Miller, Bryan D. Martin and John K. Owens 385

V. Remediation

Disposal Options for Scrap Tires
C.W. "Bill" Lovell 395

Selected Remedy at the Queen City Farms Superfund Site: A Risk Management Approach
E.F. Weber, J. Wilson and M. Kirk 413

Bioventing Feasibility Study of Low Permeability Soils for Remediation of Petroleum Contamination
Kevin M. Brackney 429

Enhanced Endogenous Biological Attenuation of Aromatic Hydrocarbons in Groundwater: A Case Study (Preliminary Results)
Christopher Lammer 445

VI. Geotechnical Engineering

Diffusion Through Statically Compacted Clay
Carlton L. Ho and Maher A.-A. Shebl 461

The Effect of Freeze-Thaw Cycles on the Hydraulic Conductivity of Compacted Clay
David Waite, Loren Anderson, Joseph Caliendo and Michael McFarland 475

From Lab to Field: Geotechnical Properties for Predicting Embankment Settlement on Lake Bonneville Deposits
Kevin C. Hoagland, Casan L. Sampaco, Loren R. Anderson, Joseph A Caliendo, Loren Rausher and Edward Keane 491

Contaminant Fluxes Through Site Containment Barriers: Performance Assessment and Illustrative Results
Charles L. Vita 505

Finite Element Analysis of A Soil Nailed Wall
Joseph A. Caliendo, Kevin C. Womack, Huey S. Nham and Loren R. Anderson 523

A Modified Cap Model Implemented in DYNA-3D
Isam G. Jardaneh, Thomas H. Fronk and Loren R. Anderson 539

Effect of Geogrid Reinforcement of Seepage through Earth-Fill Dam Cores
G.H. Gregory and S. Bang 555

Design of Flexible Pavement Subgrades with Geosynthetics
G.H. Gregory and S. Bang 569

Proposing an Alternative Landfill Liner: A Successful Example
Dale Ortman 583

VII. Hydrogeology, Northern and Western Idaho

Evaluation of the Ground Water Resources Within The Lewiston Basin
Gary R. Stevens and Dale Ralston 601

Evaluation of Ground Water Nutrient Loading to Priest Lake, Boundary Co., Idaho
K.M. Freeman and D.R. Ralston 615

Characterization of a Shallow Canyon Aquifer Contaminated by Mine Tailings and Suggestions for Constructed Wetland Treatment
John C. Houck and L.L. (Roy) Mink 621

Pages removed by authors' request just prior to printing 622

VIII. The Last Paper to Arrive (Geotechnical Engineering)

Modeling of the Pullout Characteristics of Welded Wire Mats Embedded in Sand
Casan L. Sampaco, Loren R. Anderson and Mark R. Nielsen 637

Author Index

Anderson, Loren 475, 491, 523, 539, 637
Bang, S. 555, 569
Barrash, Warren 181, 221
Bennecke William 181, 267, 371
Benson, A.K. 285, 305
Brackney, K.M. 429
Bullwinkel, R.J. 359
Caliendo, J.A. 475, 491, 523
Donaldson, P.R. 83
Dooley, K.J. 152
Dougherty, M.E. 37, 107, 345
Estes, Mason 165, 207
Fischer, J.A. 359
Fischer, J.J. 359
Freeman, K.M. 615
Fromm, Jeanne 207, 221
Fronk, T.H. 539
Gates, W.C.B. 55
Gregory, G.H. 555, 569
Hackett, W.R. 221
Hegmann, M.J. 195
Ho, C.L. 461
Hoagland, K.C. 491
Houck, J.C. 621
Hudson, W.K. 345
Israelsen, C.E. 147
Jardaneh, I.G. 539
Johnson, G.S. 152, 253
Kay , S.E. 107, 345
Keane, Edward 491
Kirk, M. 413
Lammer, Christopher 445
Liberty, L.M. 321
Linnert, L.M. 121
Lovell, C.W. 395
Martin, B.D. 385
McFarland, Michael 475
McCurry, Michael 165, 207, 221
McLing, T.L. 151
Meehan, Chris 1, 19
Michaels, Paul 331
Miller, S.M. 385
Mink, L.L. 621
Morin, R.H. 181
Neher, E.R. 152
Nham, H.S. 523
Nielsen, M.R. 637
Norrell, G..T. 152
Olsen, B.E. 121
Olsen, J.K. 238
Olsen, J.H. 253
Ortman, Dale 583
Osiensky, J.L. 83
Owens, J.K. 385
Parkinson, C.L. 55
Pelton, J.R. 37, 107, 321
Pelton, J.R. 37, 107, 321
Ralston, D.R. 253, 601, 615
Rausher, Loren 491
Reed, M.F. 154
Robinson, Lee 45
Rowley, T.H. 83
Sampaco, C.S. 491, 637
Shebl, M.A.-A 461
Schroeder, K.L. 55
Smith, R.W. 151
Snyder, W.S. 67
Stevens, G.R. 601
Stilley, A.H. 121
Urroz, Gilberto 147
Vincent, R.J. 345
Vita, C.L. 95, 505
Waite, David 475
Watkins, R.K. 137
Weber, E.F. 413
Welhan, J.A. 1, 19, 37, 83, 207, 221
Werle, J.L. 121
Wilson, J. 413
Womack, K.C. 523
Wood, S.H. 181, 195,267
Wood, T.R. 152
Wylie, A.W. 152

Hydrogeology, Waste Disposal, Science and Politics
Proceedings 30th Symposium
Engineering Geology and Geotechnical Engineering, 1994

HYDROGEOLOGY OF THE POCATELLO AQUIFER: IMPLICATIONS FOR WELLHEAD PROTECTION STRATEGIES

J. Welhan (Idaho Geological Survey)
C. Meehan (Department of Geology, Idaho State University)
both at: 325 Physical Sciences, Idaho State University,
Pocatello, ID 83209-0009 208-236-3235

ABSTRACT

A well head protection (WHP) demonstration project focusing on the Pocatello municipal water supply aquifer was initiated in 1992 to provide a preliminary characterization of the aquifer's hydrogeology and to develop a well head protection plan that could serve as a test of the State's draft WHP. Phase I of the program has focused on defining the geologic and hydrologic characteristics of the southern portion of the aquifer. Phase II is aimed at developing capture zone models for wells in the central part of the well field that are threatened by TCE contamination.

The shallow strip aquifer (1:6 width:length aspect ratio) in which the southern well field is situated comprises coarse, well-sorted fluvial gravels and is bounded laterally by low-permeability margins. It is characterized by very high transmissivities (0.1 - 10 ft^2/day) and linear velocities (6 to >60 ft/day). The effect of such high ground water flow velocities is to produce markedly elongated pumping well capture zones, with one year time-of-travel distances of the order of kilometers. Migration of contaminants laterally across the aquifer due to pumping stress should be minimized because of the rapid longitudinal nature of ground water flow along the valley, thereby facilitating interceptor well design. However, the elongated capture zones imply that special consideration will need to be given to distant up-valley land use and recharge areas.

INTRODUCTION AND SCOPE

The City of Pocatello is situated on a highly prolific, alluvial valley-fill aquifer which supplies 100% of the city's annual water demand (approximately 20 billion liters). Water demand has grown steadily with increasing population, to a present per capita demand of approximately 10^5 gallons/person/year. The aquifer is vulnerable to contamination and is currently threatened by several contamination sources, including trichloroethylene (TCE) which has closed two of the city's 20 active production wells. However, knowledge of the aquifer's water sources, dynamics, and susceptibility to present and potential contaminant threats has been limited until recently.

A program of hydrogeologic characterization of the aquifer was initiated by the Idaho Geological Survey in mid-1992, through a grant from the Idaho Water Resources Research Institute. A well head protection (WHP) demonstration project, funded by the Environmental Protection Agency (EPA), was also begun in 1992 in cooperation with the City of Pocatello and the state Division of Environmental Quality (DEQ). The goal of this work was to provide a preliminary characterization of the aquifer's hydrogeology and to develop a well head protection plan for the aquifer that could serve as a test of the state's Draft WHP Plan. In particular, the guidelines for valley fill-type aquifers in the Draft WHP Plan are being evaluated from the standpoint of general applicability in similar valley-fill aquifer situations where hydrogeological

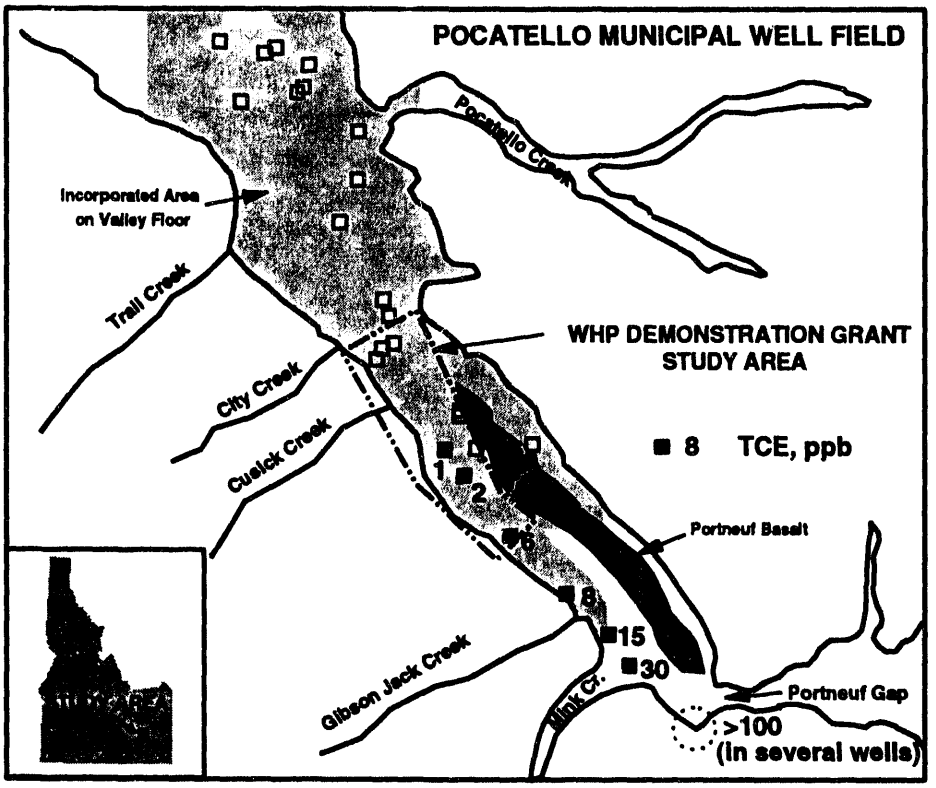


FIGURE 1 - Location of study area and concentrations of Trichloroethylene (TCE) in municipal, private and monitoring wells. Data from City of Pocatello Water Department, Idaho Department of Water Resources and Brown and Caldwell Consultants. TCE values are from various times during 1992 - 1993.

information is meager or lacking. As an example, in moderately to highly permeable, valley-fill, sedimentary aquifers characterized by high longitudinal ground water flow velocities, actual pumping well capture zones may be quite asymmetrical. In such cases, WHP zones defined on the basis of simple geometries or general guidelines may be inadequate; the definition of a realistic well head protection plan in such cases may require the collection of basic hydrogeologic information.

The municipal aquifer is considered to be vulnerable to surface-derived contaminants and directly susceptible to up-gradient contamination, in general. Of greatest concern is widespread TCE contamination along the southwest margin of the southern portion of the valley. This has forced the closure of two municipal wells in 1993 and now threatens the entire southern well field. The scope of this study was intentionally limited to the south-central portion of the municipal aquifer (Figure 1) because of the immediate need for development of a hydrogeologic framework within which to monitor and remediate existing ground water contamination in the southern portion of the aquifer system, and because of the dearth of adequate hydrogeologic information in the northern part of the well field upon which a similar WHP study could be developed at this time.

PREVIOUS WORK AND DATA SOURCES

Geologic Work

Geologic information on the area has been published by Ludlum (1943), Trimble (1976), Scott (1982), Scott et al. (1982), LaPoint (1977), Rember and Bennett (1979), Ore (1982), Link et al. (1985), Burgel et al. (1987) and Houser (1992). McDole (1969), McDole et al.(1973) and Jasmer (1987) described and mapped surficial loess deposits in the area. Several M.S. geology theses have been done in and around the Pocatello area, including Muller (1978), LeFebre (1984) and Bush (1980). A wealth of unpublished bedrock and surficial geologic data have been made available by Idaho State University's Geology Department (D.W. Rodgers, H.T. Ore and P.K. Link, pers. comm., 1992, 1993).

Figure 2 summarizes the geology of the area. The valley is defined by a half-graben Basin and Range structure, with a basin-bounding normal fault along its eastern margin dipping at 20-25° basinward and estimated to have at least 6 km of offset (D.W. Rodgers, pers. comm. 1990). Bedrock in the study area is of Late Proterozoic age, and is dominated by argillite and quartzite. Cambrian rocks, predominantly quartzite, argillite, and limestone, occur south of Cusick Creek and extend southward to Mink Creek, dipping to the east and northeast, towards the Portneuf valley and Mink Creek. Tertiary sediments and volcanics of the Starlight Formation are exposed in the southern part of the graben, as well as in outcrop to the northeast and northwest of Pocatello. The Tertiary section in the southern part of the lower Portneuf valley is dominated by sedimentary materials, characterized by poorly sorted conglomerates, alluvial and colluvial bouldery gravel and sedimentary breccia (Trimble, 1976; Ore, 1982).

The Quaternary/Holocene geology of the lower Portneuf river valley is dominated by fluvial and alluvial gravels which occur over the valley floor, in most areas blanketed by several 10's of feet of river silt and loess. Along the eastern side of the southern part of the valley, two superimposed basalt flows form a 50 foot-high tableland on the eastern side of the valley which overlooks the floor of the western half of the valley. This basalt, known as the basalt of Portneuf Valley (or Portneuf basalt, in this report), is of middle Pleistocene age (583,000 yrs BP, G.B. Dalrymple in Scott et al., 1982) and flowed into the lower Portneuf valley from vents in Gem Valley, 40 miles east, through the Portneuf Gap. As such, it predates the gravels and silts exposed on the floor of the western side of the valley which it overlooks.

The valley gravels are believed to be predominantly of fluvial origin, having been deposited within the past 15,000 years. Northwest of City Creek the Michaud Gravel, as mapped by Trimble (1976), fans out into the Snake River Plain and overlies the lake beds of American Falls Lake (72 ± 14 kyr BP). The Michaud gravels are believed to have been deposited by the flood from pluvial Lake Bonneville as it debouched onto the Snake River Plain approximately 15,000 yrs BP (Scott et al., 1982). This event was responsible for scouring the surface of the basalt and the pre-existing valley fill along the western margin of the basalt and depositing extensive well-sorted, coarse gravels and sands along the lower Portneuf River valley. Much of what is believed to be equivalent of the Michaud Gravel southeast of City Creek has been covered by a mantle of post-flood river silt and loess.

Hydrologic Work

Hydrogeologic conditions in the northwestern portion of the aquifer have been described by Mansfield (1920), Stearns et al. (1938), Crosthwaite (1957) and West and Kilburn (1963). Those

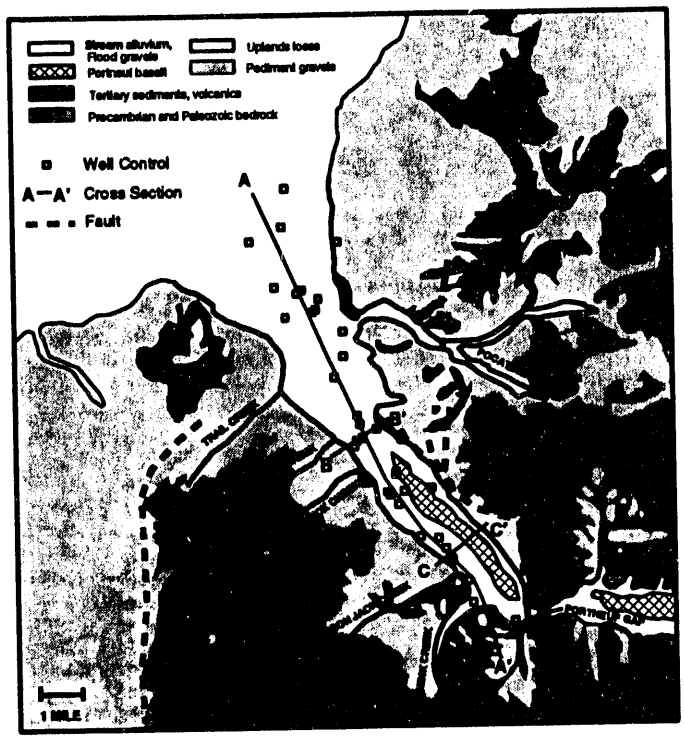


FIGURE 2 - Geology of the lower Portneuf River valley summarized from Trimble (1976) and Rodgers (unpubl. data).

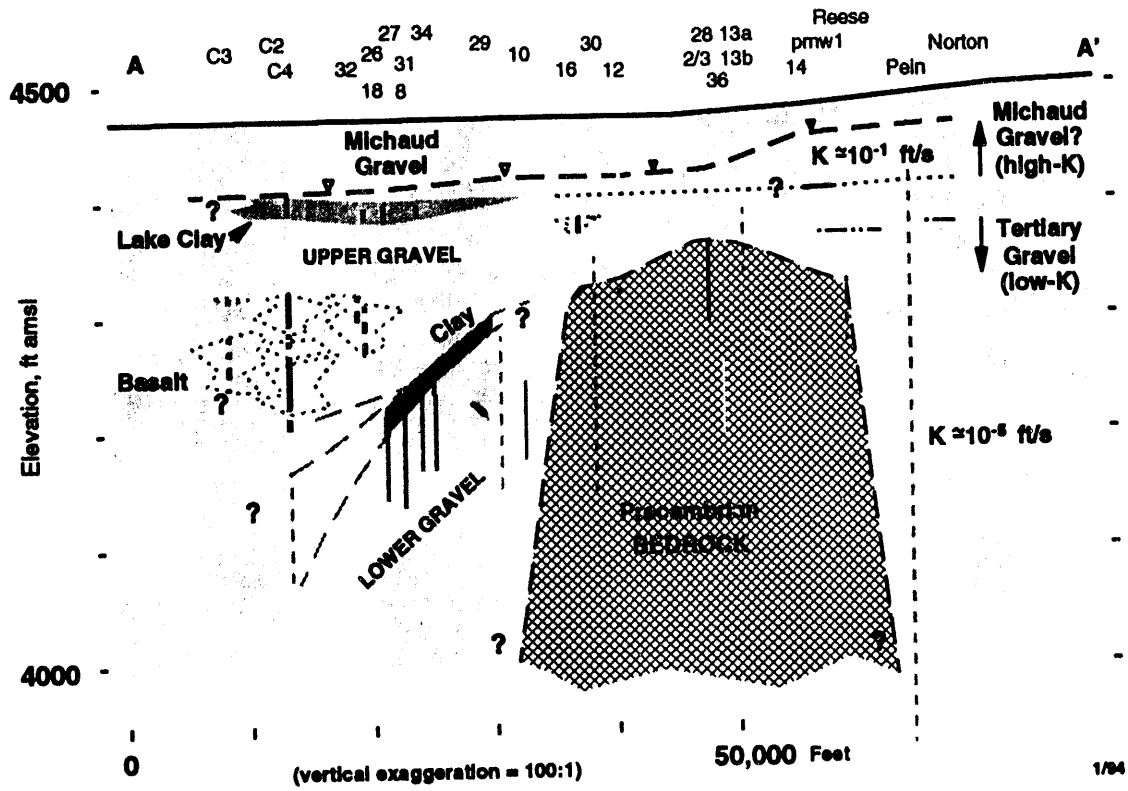


FIGURE 3 - Geologic cross section A-A' through the lower Portneuf River valley from northwest (A) to southeast (A'), showing principle correlative features and structures. Data from Pocatello and Chubbuck Municipal wells and selected private wells shown at top of section.

sources deal primarily with conditions in the Fort Hall Bottoms and Michaud Flats areas, as does work by Jacobsen (1982, 1984) and Goldstein (1981). Corbett et al. (1980) described the hydrogeology of the Tyhee area as it pertained to the geothermal resource potential of the area. The hydrogeology of a portion of the Pocatello Creek tributary drainage has been described by CH^{2}M-Hill (1992), as has the nature of inorganic salt contamination in that drainage.

To our knowledge, no published hydrogeologic information exists on the aquifer beneath the Pocatello-Chubbuck city limits or that portion southeast of Pocatello to the Portneuf Gap. Norvitch and Larson (1970) and Seitz and Norvitch (1979) published reconnaissance data on the surface and ground water of the upper Portneuf River Valley drainage basin, south of the Portneuf Gap. Kindel et al. (1991) and Brown and Caldwell (1992) presented hydrogeologic data on the mouth of Fort Hall Canyon, a tributary valley aquifer at the south end of the valley. Work by Brown and Caldwell and by CH^{2}M-Hill on hydrogeologic characterization and contamination remediation in the Fort Hall Canyon area and the southern Pocatello well field, respectively, is in progress.

Data Sources

A large amount of previously uncollated data on subsurface lithology, water level conditions and water quality has been assembled from records of the City of Pocatello's Water Department, the City of Chubbuck's public Works Department, the IDWR, and the DEQ. Meteorological data were obtained from the Department of Transportation meteorological station located at the Pocatello airport, approximately 6 miles west of the city. Data base development efforts in this study have included collection of continuous water level records to evaluate aquifer storage and responses to hydrologic events; well interference tests and conventional pumping tests to supplement transmissivity estimates obtained from specific capacity and well development data; drilling of observation wells to better define aquifer lithology and stratigraphy; and major and trace element chemical analyses and water balance calculations to identify and quantify recharge sources.

AQUIFER CHARACTERIZATION AND CONCEPTUAL MODEL

Geologic Model

Locations of wells used to constrain subsurface geology are shown in Figure 2. Interpreted geologic cross sections A-A', B-B' and C-C' are shown in Figures 3, 4 and 5. Almost all wells shown in Figure 1 are municipal wells and observation wells drilled specifically for the WHP study, although subsurface data for the area southeast of section C-C' are derived solely from selected private and county monitoring wells.

Figure 3 represents a synthesis of subsurface geology along transect A-A', from northwest to southeast, based on key units. The lack of any borehole geophysical correlative control at this stage makes this interpretation necessarily tentative. However, in creating the geologic interpretation of Figure 3, only those units that were considered to be consistently identifiable by a conscientious driller (namely: thick clay beds; basalt and basalt rubble units; and crystalline bedrock) were used for correlation purposes.

Perhaps the most striking feature of Figure 3 is the presence of a bedrock high which separates the aquifer into southern and northern portions. Henceforth, these portions of the aquifer system

will be referred to as the southern and the northern aquifers. The bedrock high may be a manifestation of the splaying of the basin-bounding fault about mid-way down the lower Portneuf valley (Figure 2) which distributed the total fault offset over numerous subsidiary faults (D.W. Rodgers, pers. comm., 1992). Similar basement highs have been mapped in other Basin and Range valleys in eastern Idaho (Link et al., 1985; Rodgers, pers. comm., 1992).

In contrast to the southern aquifer, where excellent water yields historically have been derived from coarse, clean gravels at depths less than 100-150 feet below surface, the northern aquifer's stratigraphy is characterized by much more poorly-sorted sediments (silty gravels and sands, clay) in which many more deep wells have been drilled to obtain adequate yields. Of the numerous silty and clayey zones described in various well logs, only three are considered to have been reliably described: a 5-10 ft thick clay (or mixed gravel and clay) bed at ca. 4380-4400 ft amsl elevation; a light-colored clay unit 10-20 ft thick (possibly thickening to greater than 50 feet to the northwest), at elevations of ca. 4200 - 4300 ft amsl.; and several occurrences of basalt lava and/or volcanic rubble (cinders, scoria) between 4200 and 4400 ft amsl.

Of these units, the upper clay is believed to represent the late Pleistocene American Falls Lake beds, exposed 2 miles WNW of Chubbuck wel' C4, at a maximum elevation of 4400 ft (Trimble, 1976). The extent, thickness and attitude of the deep clay unit is far more tentative, as it has been variously logged as undifferentiated clay in excess of 90 feet thick (well 32); massive hard clay intercalated over 50 feet with thin gravel seams (well 26); sticky clay (wells C4, 27, 29); sticky yellow clay and sandy yellow clay (wells 18, 34); and sticky brown clay (well 31). It is shown in Figure 3 with a fairly uniform thickness, dipping at ca. 4°, but may thicken northward and/or dip less steeply. This unit cannot be identified with any certainty in well 10 (although it may be present) since this well was logged as a series of sandy clays from 4300 ft down to 4113 ft amsl.

Correlations between the basalt occurrences identified in these wells has not been attempted. Discontinuous basalt flows intercalated with sediments in the section are a general feature of the subsurface lithology in the Snake River Plain (Corbett et al., 1980; Scott et al., 1982). It is not known whether the basalt logged in wells 16 and 30 is correlative with the other basalt occurrences identified in wells to the north.

Cross-section B-B' (Figure 4) shows the inferred subsurface lithology of the section of the aquifer above the bedrock high. This section is perhaps the most well-constrained of any in the system, being based on five boreholes (four of which define bedrock depth) and seismic refraction profiles on both margins of the valley at this location. The upper part of the section is characterized by clean, well-sorted gravels and sands (which are considered equivalent to the Michaud gravels exposed just north of this section) and capped by 5-20 feet of silt. Gravels and sands beneath 4360 ft amsl are much less well-sorted and are dominated by clay, possibly reflecting a separate stratigraphic unit.

Unlike the eastern margin of the section, which is defined by what appears to be a planar (possibly fault-derived) bedrock scarp of dense, massive Proterozoic quartzite (Caddy Canyon), the western margin's bedrock limits are unknown. Based on the location of inferred Caddy Canyon quartzite bounding the western valley margin immediately south of section B-B', the extent of the sedimentary section west of well 7 is believed to be relatively minor. Sediments encountered in four wells clustered around well 7 are dominated by clay, silt and boulders, indicating their predominantly alluvial affinity and derivation from City Creek. Based on well 7's specific capacity, the alluvial fan sediments appear to be one tenth to one hundreth as permeable as the clean gravels in the upper part of the section in the southern aquifer (see discussion of hydraulic data in a later section). The cross-sectional area available for ground

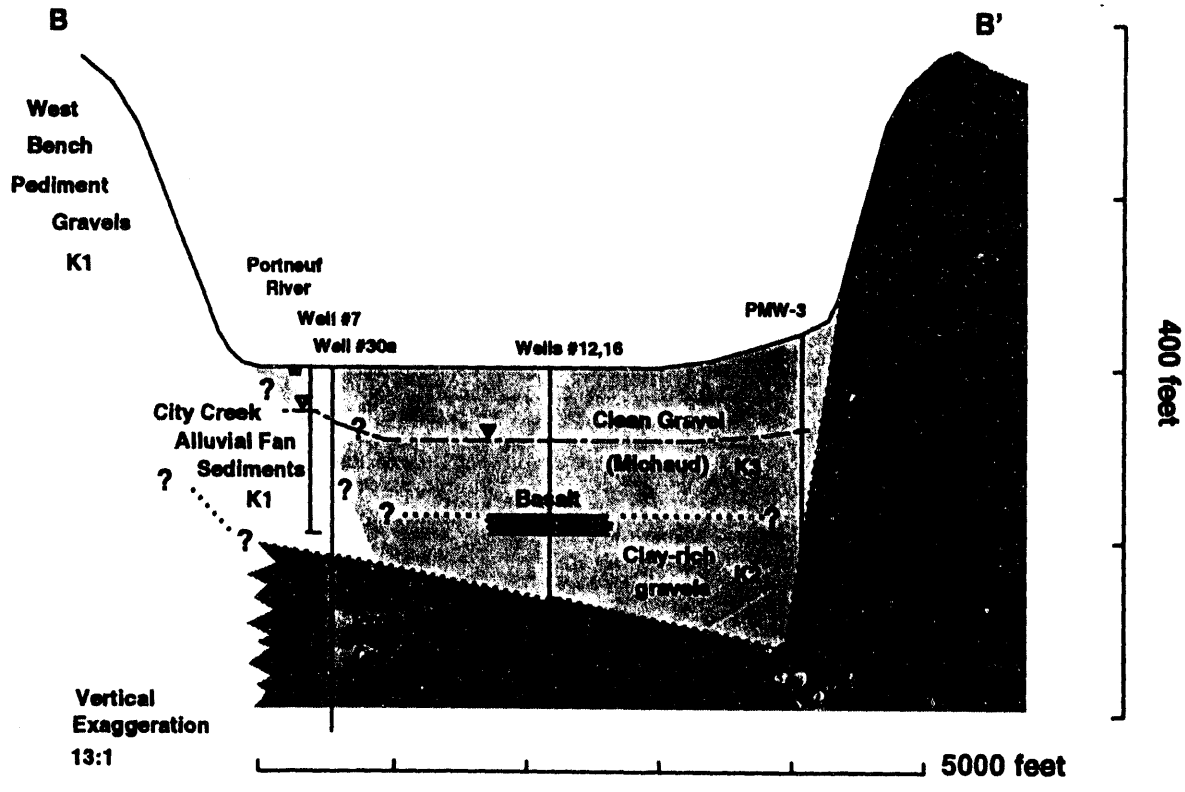


FIGURE 4 - Geologic cross section B-B' across narrowest portion of valley, over the Proterozoic bedrock high. Inferred relative hydraulic conductivities shown: K0 = impermeable; K1, K2 = low to intermediate; K3 = very high.

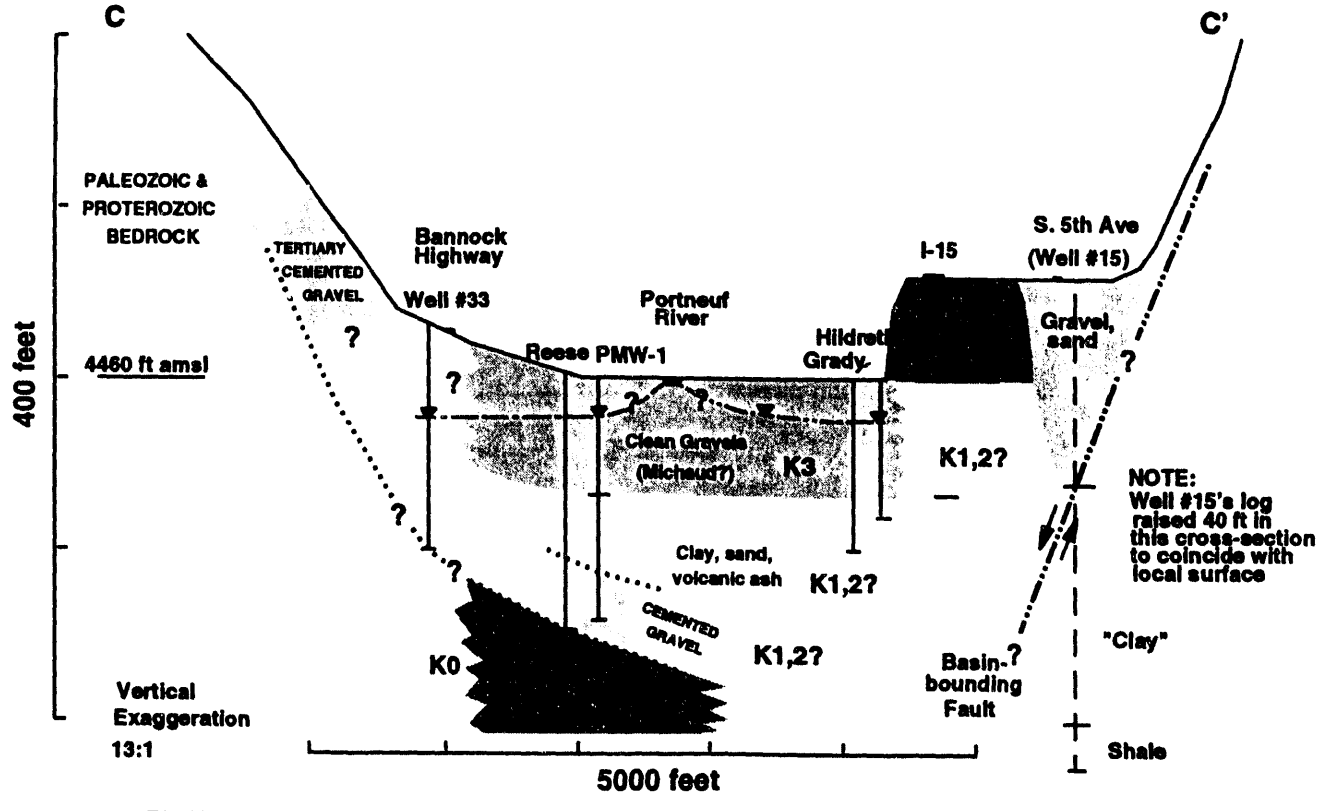


FIGURE 5 - Geologic cross section C-C' across the southern aquifer. Inferred relative permeabilities: K0 = impermeable; K1, K2 = low to intermediate; K3 = very high.

water underflow through B-B' within the saturated gravels above the basalt is 2 x 10^5 ft^2. Including the clay-rich gravels below the basalt, the total potential cross-sectional area of flow is ca. 3.5 x 10^5 ft^2.

Section C-C' (Figure 5) is perhaps the most speculative lithologic interpretation, based as it is on only one reliable observation well log (PMW-1) and several private wells whose lithologic information is, at best, only suggestive. In addition, the section has been created by rather liberally projecting available geologic data from both north and south of C-C' to arrive at a tentative synthesis of the southern aquifer's geology. The location of the basin-bounding fault represented in the cross-section was estimated based on surface mapping information, fault plane attitude and consistency with borehole lithology.

The Portneuf basalt is shown in cross-section as resting on a presumably sedimentary section which represents valley fill that predates the Bonneville flood and, hence, the uppermost (Michaud-equivalent) gravels in the western side of the valley. A deep municipal well (15), located approximately 1.5 miles north of this section provides the only reliable evidence of the subsurface lithology east of the basalt. In that well, a narrow alluvial aquifer of relatively poorly sorted bouldery gravel and coarse sand overlies a 135 ft section of dense "clay" with competent shale recorded in the bottom 10-20 feet. Since this well was drilled with a cable tool rig, it is uncertain whether the "clay" represents unindurated, soft sediment or incorrectly identified weathered shale or fault-gouge.

Observation well PMW-1 was terminated in a hard, cemented gravel which is suggested to be correlative with Tertiary (Starlight Formation) cemented gravel outcropping approximately 0.5 miles south of well 33 at the foot of the western valley margin. Since a lithologic log for well 33 is unavailable, the only other structurally meaningful data are from a recently drilled irrigation well (Reese) which bottomed in 55 feet of red quartzite (likely late Proterozoic). No other correlatable units were identified in well logs in the southern aquifer, with the exception of a hard clay or hardpan unit identified in several private wells in the vicinity of Well 13 and in Well 14 itself. Cemented gravel has been identified in several wells: PMW1, the Norton well at the mouth of Mink Creek and in monitoring wells drilled in the alluvial fan of Fort Hall Canyon (S. Howe, pers. comm., 1994). Unpublished seismic refraction data collected by Brown and Caldwell consultants over the Fort Hall Canyon alluvial fan indicates that this unit may be fairly extensive, areally, as least in localized portions of the basin.

The well-sorted gravels of the upper section shown in Figure 5 are presumed to be equivalent to the Michaud gravels exposed at the surface farther down the valley. At an elevation of ca. 4395 ft amsl (in well PMW-1), they abruptly give way to a series of partially indurated sand, silty sand and intercalated clays, a hard, grey volcanic ash or tuff and a sticky clay unit which overlies the cemented gravel. Like the abrupt lithologic change observed in wells 12 and 16 (Section B-B'), this lithologic transition may represent a separate, pre-Michaud, stratigraphic unit. The clay bed (elevation of top of bed = 4350 ft amsl) which occurs at the top of the cemented gravel may be of American Falls Lake origin (H.T. Ore, D.W. Rodgers, pers. comm., 1993); its elevation would not be expected to be strictly diagnostic in this setting, but it is within ca. 50 feet of the lake bottom's elevation on the Snake Plain. Radiometric dating of the ash unit immediately above the clay is planned to better constrain this interpretation.

A simple structure contour interpretation, based on the average dip of the basin-bounding fault on the north side of the graben and the average stratigraphic dip of the Paleozoic bedrock units on the south side, suggests that the Tertiary sedimentary section in the southern aquifer may be

as thick as 3000-4000 feet (D.W. Rodgers, 1993). The sole evidence in support of such an hypothesis is the 580 ft private well located just south of the mouth of Gibson Jack Creek (Pein well). This well was logged as a monotonous sequence of sand, silt and clayey gravel, not unlike the Tertiary Starlight section described outcropping in the Mink Creek - Gibson Jack Creek area (Trimble, 1976). A gravity survey of the southern aquifer, currently being designed for the 1994 field season, should provide additional information on the Tertiary sedimentary section in this area, as well as the basin's underlying bedrock topography.

At this point in our understanding of the basin, it is proposed that part or all of the clay-rich section underlying the presumed Michaud gravel, together with the underlying cemented gravel, is of Tertiary age and that it is of significantly lower permeability than the uppermost gravels. Well development data from the deep Pein well indicate that the bulk hydraulic conductivity of the 80-390 ft interval is several orders of magnitude lower than that of the upper, Michaud-like gravels (see Figure 3). Therefore, assuming that the lateral boundaries of this portion of the shallow aquifer are defined by low permeability bedrock on the west and pre-existing sediments of unknown permeability beneath the Portneuf basalt on the east, the area available for ground water flow through the saturated section above the Tertiary sediments could be as much as 2.5 x 10^5 ft^2. The total potential area for flow above the Tertiary cemented gravel (assuming it extends eastward) could be as much as 4.5 x 10^5 ft^2.

Hydrologic Model

Based on patterns of snowpack density, geologic structure and relative tributary valley streamflows and estimated cross-sectional areas, the principal sources of aquifer recharge are believed to be (from southeast to northwest): underflow from Marsh Valley through the Portneuf Gap, Portneuf River seepage losses (Norvitch and Larson, 1970), Mink Creek underflow, and Pocatello Creek underflow. In addition, lateral ground water inflow to the valley through the pediment gravels along the southwest margin of the valley and from small tributary streams provides an unknown amount of recharge. Of unknown significance are several wells located on the pediment gravels south of Cusick Creek, some 40-80 feet above the valley floor, which are flowing artesian. At least in one instance, the artesian head is associated with Proterozoic quartzite (Caddy Canyon?). The chemical composition of these waters is uniformly lower in TDS, Cl and other major ions. Their place in the regional hydrogeologic framework is currently unknown.

Figure 6 summarizes "static" well water level data (used here to refer to measurements taken during non-pumping periods following variable recovery times after pumping ceased) over the past 20 years in Pocatello municipal wells. Despite the noise introduced by the measurement procedure, the data reveal a fairly regular hydraulic gradient along the length of the aquifer, with the overall gradient along the valley axis of the order of 0.0015, but varying significantly from southeast to northwest. As shown clearly in Figure 3, the hydraulic gradient appears to increase abruptly in the vicinity of the bedrock high (approximately mid-way between sections B-B' and C-C ') and then to return to close to average values on either side of the bedrock high. This has been corroborated by measurements of water levels in private wells east of the Portneuf Gap to the southern City boundary and by a recently completed domestic well survey performed by CH^2M-Hill in the southern municipal well field area. As shown in Figure 6, water levels decreased by more than 5 feet between 1986 and 1991.

Figure 7 is a comparison of fluctuations in static well water levels over 22 years, with average

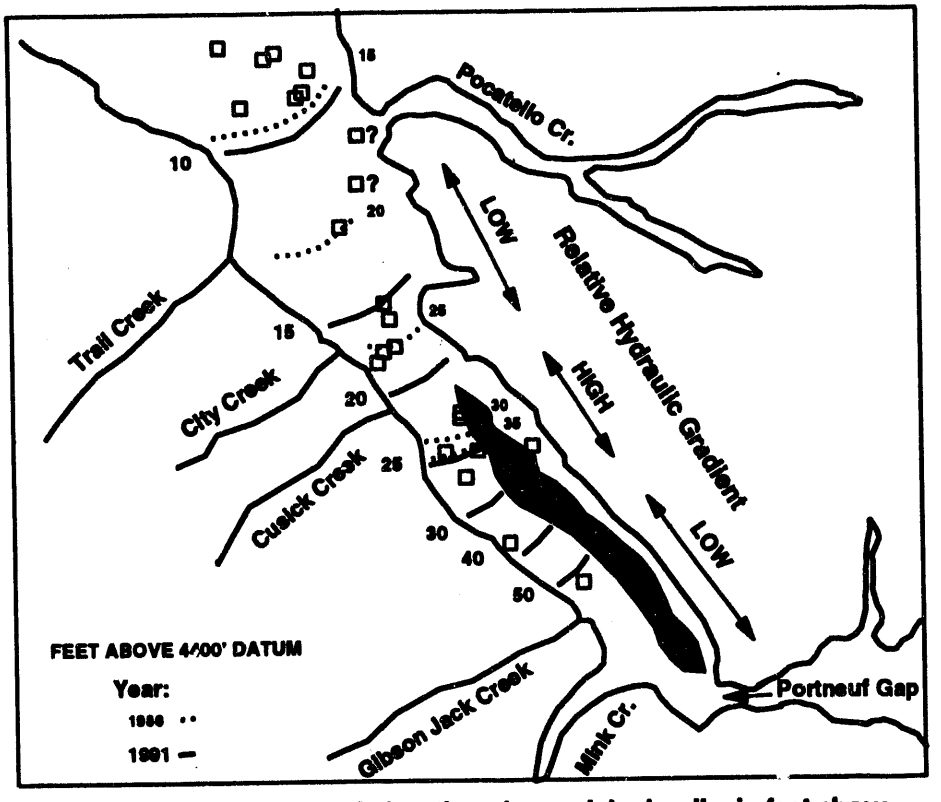


FIGURE 6 - Static water level elevations in municipal wells, in feet above 4400 ft datum, for winter, 1986 and 1991. Relative hydraulic gradients south of Gibson Jack Creek are from 1993 measurements in private wells.

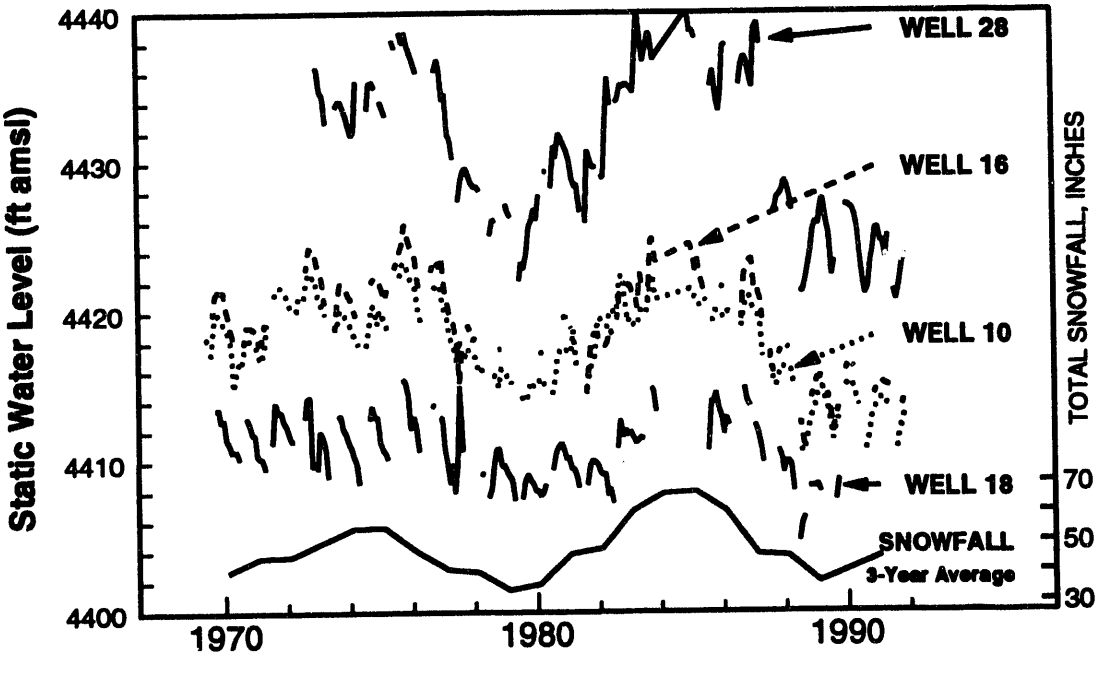


FIGURE 7 - Water level elevations in municipal wells compared to three-year moving average annual snowfall total at Pocatello airport meteorological station. All water levels shown were measured during non-pumping periods.

snowfall amounts recorded at Pocatello airport. The data reveal that the uppermost sand/gravel aquifer is strongly influenced by long-term (5-6 year) variations in precipitation and basin recharge (superimposed on seasonal water level fluctuations of the order of 2-6 feet, due to seasonal imbalance between recharge and pumping). Water levels in wells completed in the upper gravel aquifer (eg: wells 28, 16 and 10) display pronounced secular variations of 10 feet or more between periods of normal and below-normal precipitation.

Well 18 is the only well known to be completed solely in the deep gravel aquifer (located beneath the deep clay unit shown in Figure 3). As shown in Figure 7, it displays a markedly subdued long-term hydrograph amplitude in comparison with wells completed in the shallow aquifer. The lower gravel aquifer is tapped by several deep wells, but all but well 18 are perforated in multiple aquifer zones. These wells are characterized by hydrograph amplitudes which are intermediate between those of the shallow aquifer and that of Well 18, indicating their water levels represent a weighted average of upper and lower aquifer hydraulic heads. Taken together with the stratigraphic interpretation discussed in the previous section, these data support the existence of a deep aquifer in the northern well field. On the basis of well 18's water level record, the hydraulic head of this deep unit appears to be significantly lower than that of the upper unit, with a downward vertical hydraulic gradient implied. This would be surprising if the deep aquifer were considered part of the valley hydrologic system, since upward hydraulic gradients are expected in valley discharge settings. Alternatively, the observed head in the deep gravel aquifer may reflect conditions in the regional Snake River Plain aquifer.

Figure 8 shows continuous water level variations recorded in several wells located in the central and southern aquifer areas, over a portion of 1993, together with Portneuf River discharge (plotted as approximate stage, in feet). Several features are noteworthy. First, hydrographs from wells over a large area track remarkably closely, indicating aquifer storage is sensitive to upgradient recharge sources. Secondly, water levels in some wells display a pronounced diurnal oscillation, suggestive of a barometric response under confined aquifer conditions. Third and most significant, is the lack of evidence for direct forcing of aquifer storage by river seepage. This indicates that river losses may not be as significant a source of recharge in the Lower Portneuf aquifer's water budget as implied by the work of Norvitch and Larson (1970) in the upper Portneuf basin above the Portneuf Gap.

To date, transmissivity (T) estimates for the aquifer system have been derived for the most part from specific capacity data on production wells. Data were interpreted using the method of Bradbury and Rothschild (1985), with corrections for partial penetration effects. Pumping tests have been conducted in two areas, one in each of the northern and southern aquifers; a third pumping test is scheduled to occur in the southern aquifer during the Spring of 1994.

Figure 9 summarizes the statistical variation of over 50 T estimates derived from well development tests, specific capacity, and pumping tests. Figure 10 shows the spatial distribution of mean T values. Comparison of T obtained from specific capacity (not corrected for well loss) and T derived from observation well response in pump tests indicates that the effects of well loss are appreciable, as expected in perforated well casing. Transmissivities estimated from specific capacity data therefore are expected to be low, by up to one ln unit.

Analysis of drawdown responses in wells 26, 27, 31 and 34 indicates an apparent T of 2.9 (± 1.7) ft^2/sec with an apparent storativity of 0.000002-0.000009. This is consistent with the confined nature of the upper and lower water-bearing zones tapped by these wells (Figure 3). The mean T determined for these wells is approximately one ln unit higher than the mean of all available T estimates (Figure 9). Analysis of drawdown responses in wells 36, 13, 28 and PMW-

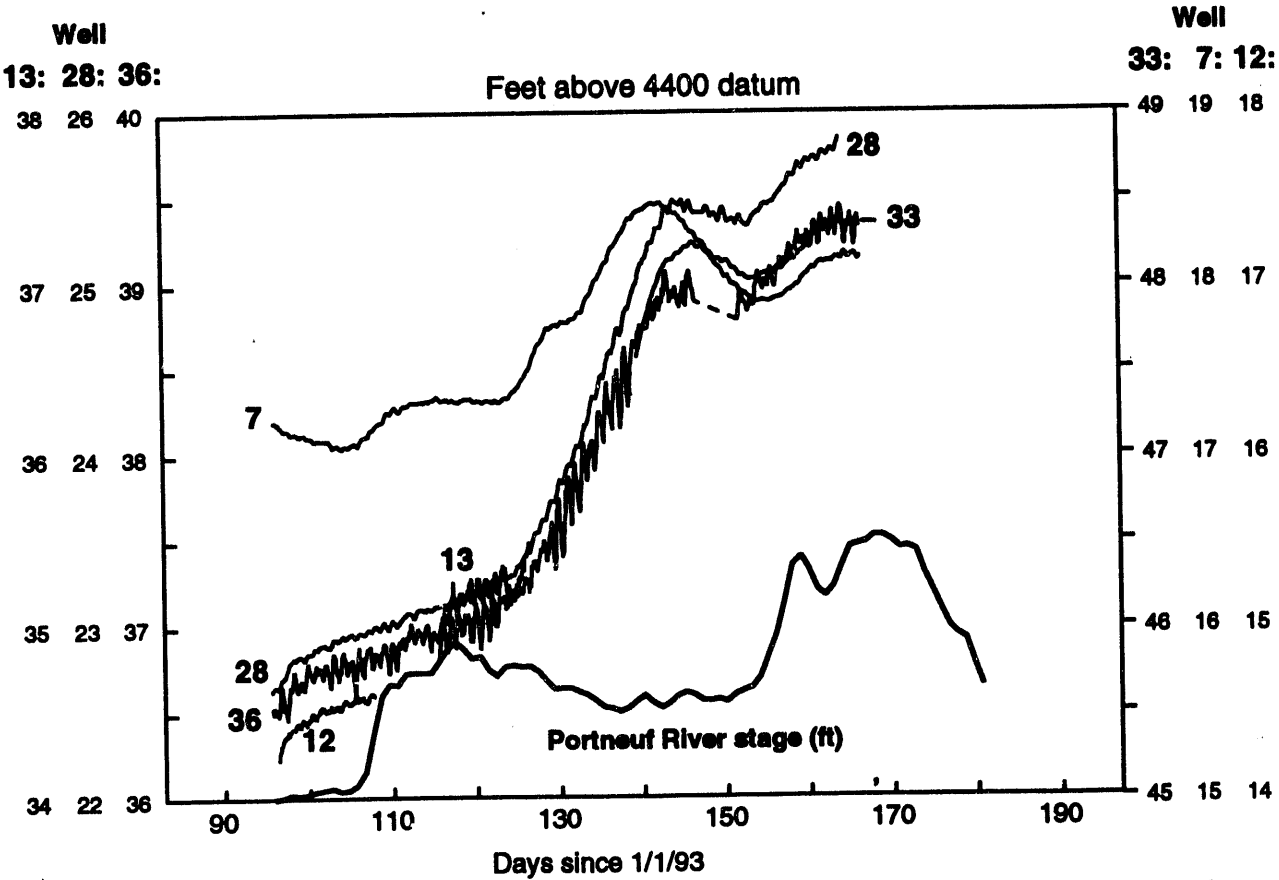


FIGURE 8 - Continuous water level measurements in wells completed in the high gravels of the southern aquifer. Portneuf River data represents total discharge (cfs) transformed to approximate stage height (feet) and plotted relative to an arbitrary datum.

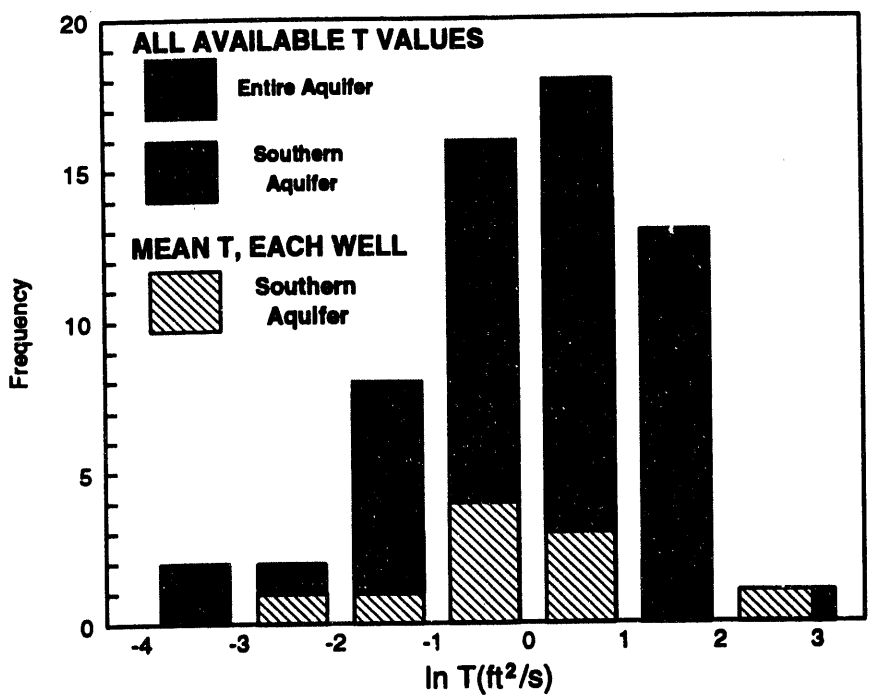


FIGURE 9 - Distribution of all available calculated transmissivity values, expressed as natural logarithm of T in ft² /sec.

1 provided the highest transmissivity estimates in the entire aquifer system, with T = 10 ft^2/sec and S = 0.005. This test also corroborated the presence of an impermeable flow boundary at a distance from the pumping well that is consistent with the presence of the inferred western bedrock margin (eg: Figure 5). Furthermore, the test indicated no direct influence of river recharge in the immediate vicinity of the pumping well (possibly because of the major channel diversions the river has experienced), corroborating the surprisingly limited influence that river levels have on aquifer storage (cf. Figure 8).

Most surprisingly, the pumping test on well 36 indicated that the aquifer in that area is confined or semi-confined, although lithologic data strongly suggest unconfined conditions. However, the well hydraulics interpretation is consistent with the apparent barometric responses observed in wells 36, 13 and, to a lesser degree, well 28 (Figure 8). Therefore, despite stratigraphic evidence that suggests otherwise, an effective confining condition apparently exists in the vicinity of well 36. This may be a reflection of the tendency of the basin to have accumulated river silt periodically over widespread areas in the area between City Creek and the Portneuf Gap. This in turn may be due to periodic flooding enhanced by the narrow neck of the valley at section B-B' and the flood plain's relatively narrow width over the entire southern portion of the valley.

Pending acquisition of more data and aquifer test results, therefore, it is tentatively suggested that the southern aquifer is effectively confined, at least in the area immediately south of section B-B'. However, it must be noted that the geologic conditions necessary to develop such an aquifer may <u>not</u> be consistent with the current interpretation of the valley's Quaternary/Holocene history. That is, if relatively thin lenses or layers of silt in the gravel section are required to explain the confined nature of the hydraulic response, depositing such layers in a Bonneville flood-based sedimentation model will be difficult. Ore (1982; pers. comm., 1993) has suggested that the upper gravel section in the southern valley may be due to braided fluvial deposition rather than a Michaud equivalent.

Utilizing a T range of 1 - 10 ft^2/sec, a hydraulic gradient of 0.0015, a mean total saturated thickness of 100 ft, and a total cross-sectional area for underflow through section B-B' of 3.5 x 10^5 ft^2, estimated ground water underflow past B-B' is 5 - 50 ft^3/sec. Assuming an effective porosity of 0.2, this is equivalent to a linear flow velocity of 6 - 60 ft/day! Comparing this flux with the current annual well field pumping rate of ca. 5 x 10^9 gallons/year (20 ft^3/sec continuous) indicates that pumping withdrawals have a major impact on the aquifer's water balance and storage potential.

Using the same T, saturated thickness and a total cross-sectional flow area of 5.5 x 10^5 ft^2 for section C-C', the hydraulic gradient at C-C' would have to be 65% of that at B-B' (on the assumption that total underflow through section C-C' equals that through section B-B'). This is almost exactly equal to the hydraulic gradient change seen in Figure 3 between the southern aquifer and the northern aquifer as ground water moves across the bedrock high. If these estimates are born out by more extensive and accurate water level map data, it would suggest that the system's lateral hydraulic boundaries and its effective thickness may be adequately defined by the geologic model proposed in this report.

IMPLICATIONS FOR WELL HEAD PROTECTION STRATEGIES

Following the development of the hydrogeological model presented above, Phase II of the well head protection demonstration study is aimed at defining pumping well capture zones and time

of travel (TOT) zones for well head protection purposes. The focus of this effort is to 1) evaluate reasonable well capture zones for selected production wells in the Pocatello municipal well field based on the hydrogeologic parameters and boundary conditions identified in Phase I; 2) compare these capture zones with simpler ones derived from application of the state's Draft WHP Plan guidelines to assess the feasibility of utilizing simpler capture zone delineation methods where the necessary hydrogeologic data are unavailable; and 3) assess the implications of capture zone geometries on the design of a rationale well head protection plan for an aquifer of this type. This report briefly summarizes work in progress along these lines.

The extremely high linear ground water velocities estimated for the southern aquifer (6 - 60 ft/day) pose a special set of problems for well head protection planning. Such high velocities are consistent with the spread of TCE contamination observed in the southern aquifer (R. Noble, pers. comm., 1994) and indicate an immediate need for development of realistic well head protection strategies.

The delineation of well capture zones can be done by mapping recharge zones contributing water to a well field or by computing capture zone shapes for individual wells with analytical or numerical methods, utilizing the equations of ground water flow. In the present approach, an analytical model was used to calculate the shape and extent of capture zones for wells 36 and 13. An idealized confined strip aquifer bounded by impermeable boundaries and with no river influence was assumed. The position of the western boundary was determined by the radius to the impermeable boundary calculated in well 36's pumping test. This coincides with bedrock position reasonably inferred from geologic data; interestingly, such a boundary coincides with the position of known flowing artesian wells. Also assumed in this modelling: a saturated thickness of 100 ft, an effective porosity of 0.1 - 0.3, and transmissivity of 1 - 10 ft^2/sec. The EPA 'WHPA v.2.0' code with the analytical GPTRAC routine was used for modelling capture zones, for wells 36 and 13 pumping concurrently at 2000 and 1000 gpm, respectively.

Figure 11 shows the nature of the calculated capture zones for the most extreme cases of low T and high porosity vs high T and low porosity. The capture zone geometries are clearly very sensitive to the aquifer transmissivity. Note that the time of travel (TOT) zones shown for the two cases are for different periods of time. In the high-T, low porosity case, a one year TOT zone for well 36 would extend more than 10 km in the up-gradient direction! Since the state Draft WHP Plan calls for the delineation and management of 2- and 5-year TOT zones, the implication is that, in such highly permeable aquifers, a well head protection plan based on such extremely distal TOT boundaries would not be feasible. In the higher porosity/lower transmissivity scenario, 5-year TOT zones would be manageable (involving up-gradient distances of the order of 4-5 km), although in well fields situated in narrow strip aquifers, the entire upgradient width of the aquifer could conceivably require WHP management out to a distance dictated by the TOT zones. This work is continuing, in order to define the range of capture zone geometries and TOT boundaries that will need to be considered in Pocatello's WHP planning strategy.

CONCLUSIONS

The hydrogeology of the Pocatello aquifer has been defined in preliminary fashion, in order to facilitate further data gathering and aquifer characterization work. Although the focus of current work is on the southern aquifer, the geology and history of the entire basin need to be integrated so as to develop the highest confidence in subsurface geologic interpretations.

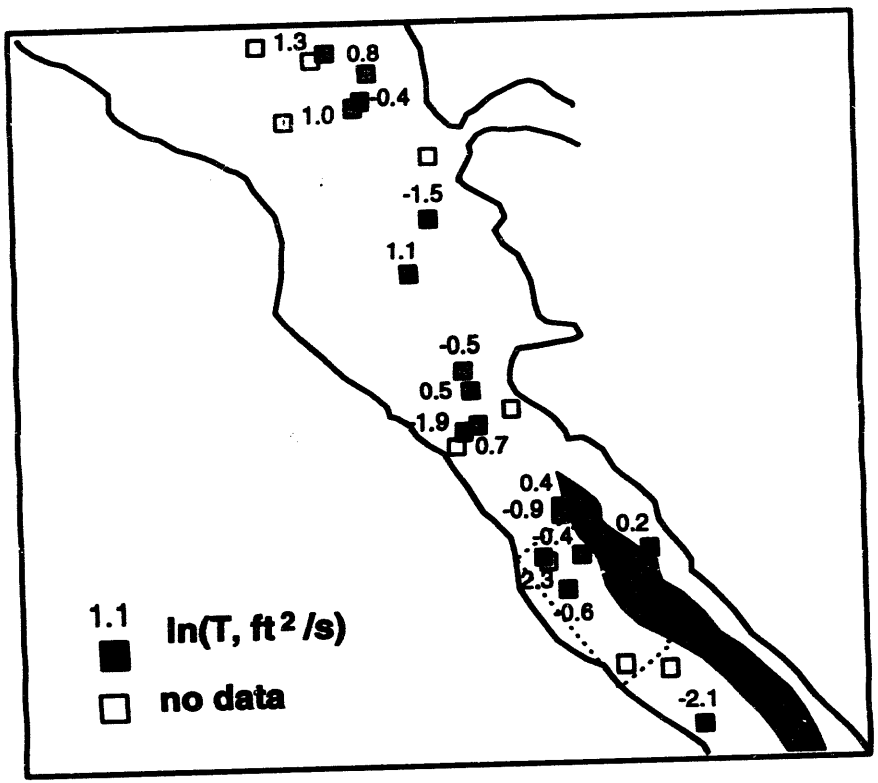


FIGURE 10 - Transmissivity map of the Pocatello aquifer. Values represent mean of available T values at each well. Dotted rectangle represents capture zone modelling area in Figure 11.

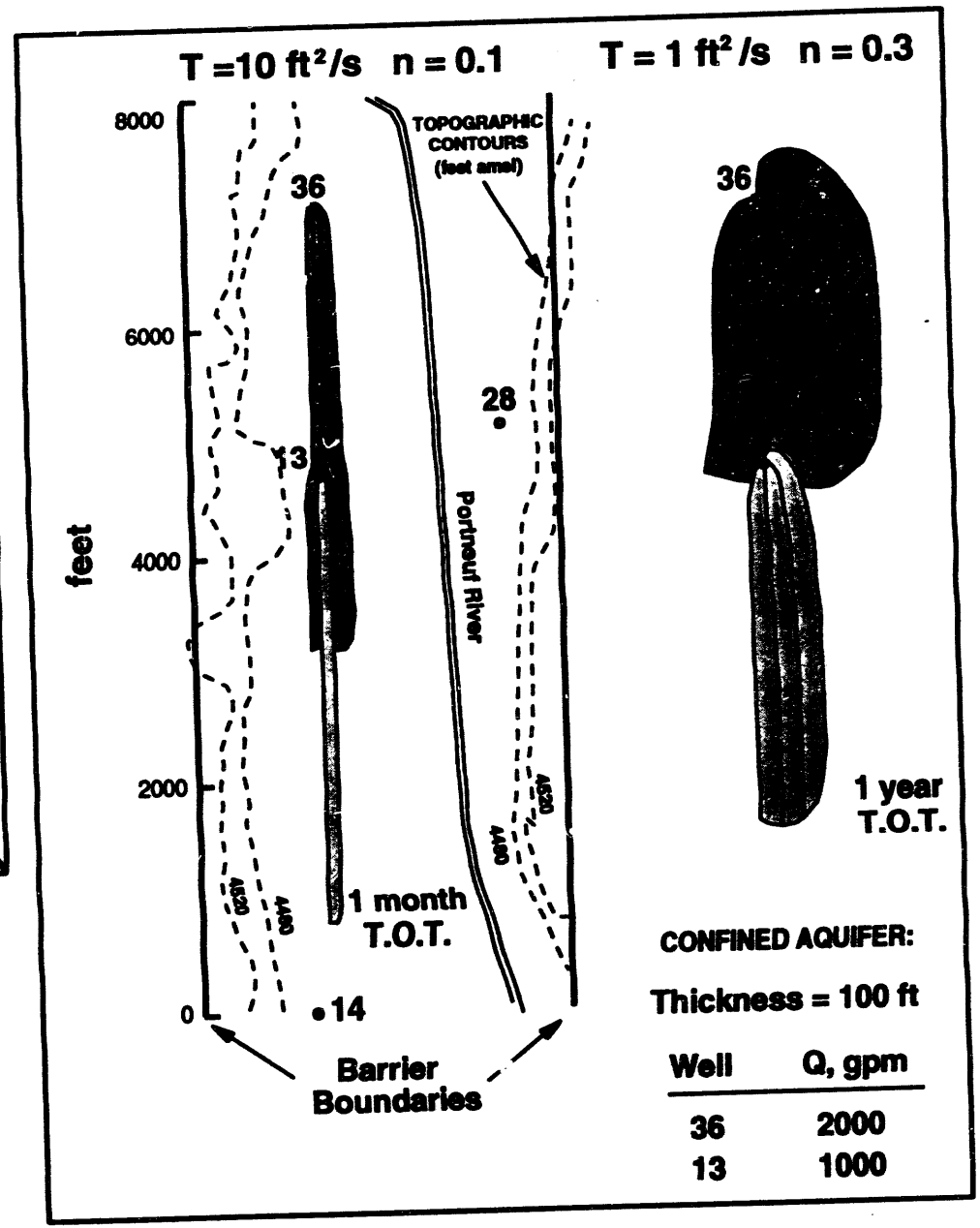


Figure 11 - Capture zones for wells 36 and 13, modelled with WHPA v.2.0 code, using analytical GPTRAC option; "n" = porosity. Note that capture zones shown are for 1 month and 1 year time of travel (TOT) periods.

Most of the interpretations of aquifer characteristics at this point in time are critically dependent on the underlying geologic model of the aquifer. Major features of the hydrogeology that have been identified in this report follow:

- the Pocatello aquifer should be regarded as an aquifer system, comprised of northern and southern subsystems which are separated by a bedrock high.
- the northern subsystem appears to consist of at least two major water-bearing zones: a shallow, confined gravel aquifer developed in late Pleistocene gravels beneath the American Falls Lake beds; and a deep confined gravel aquifer. The highly permeable Michaud gravel deposited by the Bonneville flood is, for the most part, unsaturated in this part of the system.
- the northern subsystem may grade northward into the Snake Plain aquifer. Hydraulic heads in the deep gravel aquifer are anomalously low when viewed in the context of the Portneuf valley's discharge setting, but may be reconcilable with hydraulic heads in the deep, regional Snake Plain aquifer.
- the subsurface geology of the southern aquifer system, particularly the deeper section below 100-150 ft depth, is poorly defined south of the bedrock high. Based on surface mapping, structural considerations and a single deep well, the Tertiary sedimentary section south of Gibson Jack Creek may be of considerable thickness. Its bulk hydraulic conductivity may be three or more orders of magnitude lower than the uppermost gravels in the section, which are tentatively considered to be equivalent to the Michaud gravel to the north (ie. deposited by Bonneville flood waters). Alternatively, part or all of the upper, permeable gravels in the southern aquifer may be of post-flood, braided channel fluvial origin.
- cross-sectional areas available for ground water flow through the southern aquifer and through the narrowest, bedrock-constrained "neck" of the aquifer were estimated and of the order of 5 - 50 ft^3/sec. It was shown that the difference in these cross-sectional areas could account for changes in the hydraulic gradient observed along the length of the southern aquifer.
- pumping tests conducted in both the northern and southern aquifers indicated confined conditions. This was wholly unexpected in the southern aquifer in light of available lithologic information. It is suggested that this conclusion, if corroborated, would require revision of the Bonneville flood depositional model for the upper gravels (tentatively considered as Michaud-equivalent) in the southern aquifer.
- best estimates of transmissivity (1 - 10 ft^2/sec) in the southern aquifer were used to examine pumping well capture zone geometries and time of travel zones for well head protection planning purposes. It was found that, because of the high transmissivities and the extremely high ground water velocities (6 - >60 ft/day) that are characteristic of the southern aquifer, capture zones may be drastically elongated, with a one year time of travel zone extending more than 10 km upgradient of the pumping well in the high-T case. This has serious implications for any municipality's ability to devise and adequately manage a well head protection program in such a hydrologic environment.

ACKNOWLEDGEMENTS

The authors wish to thank the City of Pocatello for its support and involvement in this and related hydrogeologic research. Fred Ostler, current Water Department Supervisor and his predecessor, Gary Thornton, have given active encouragement and support for this work.

Numerous members of the City Water Department have been extremely helpful in assembling background data and assisting in field data collection and logistics, including Larry Thomsen, Tom Dekker, Kevin Ferry and others. Mark Reid, Director of Community Development and Research, was instrumental in obtaining federal funding and managing the WHP project.

Steve Smart, City of Chubbuck Public Works Director, kindly provided well log and historical information on Chubbuck municipal wells.

We also are very grateful for the encouragement and assistance provided by Division of Environmental Quality officials in Boise and Pocatello, including Elizabeth Cody for help in obtaining the WHP grant and George Spinner and Walt Poole for providing access to water quality data.

The office of the Idaho Department of Water Resources in Idaho Falls provided domestic well logs and drilling permit assistance; we especially thank Dennis Dunn for his assistance.

REFERENCES CITED

Bradbury, K.R. and Rothschild, E.R. 1985. A computerized technique for estimating the hydraulic conductivity fo aquifers from specific capacity data; Ground Water, 23, pp. 240-246.

Brown and Caldwell 1992. Preliminary Hydrogeologic Assessment in the Vicinity of Fort Hall Canyon Landfill, Bannock County, Idaho; 20 pp.

Burgel, W.D., Rodgers, D.W. and Link, P.K. (1987). Mesozoic and Cenozoic structures of the Pocatello Region, Southeastern Idaho; in W.R. Miller (ed.), The Thrust Belt Revisited, Wyoming Geol. Assoc., 38th Field Conference Guidebook, pp. 91-100.

Bush, R.R. 1980. Gravity survey of the Tyhee area, Bannock Co., Idaho; M.S. thesis, Idaho State University, 33 pp.

CH^{2}M-Hill 1992. Phase I Site Assessment Report, Pocatello Creek Landfill Hydrogeologic Investigation, Pocatello, Idaho; 61 pp.

Corbett, M.K., Anderson, J.E. and Mitchell, J.C. 1980. An evaluation of thermal water occurrences in the Tyhee Area, Bannock County, Idaho; Idaho Department of Water Resources, Water Information Bulletin N. 30, Geothermal Investigations in Idaho, Part 10, 67 pp.

Crosthwaite, E.G. 1957. Ground water possibilities south of the Snake River between Twin Falls and Pocatello, ID; USGS Water Supply Paper 1460-C.

Goldstein, F.J. 1981. Hydrogeology and water quality of Michaud Flats, Southeast Idaho; Idaho State Univ., M.S. thesis, 80 pp.

Houser, B. (1992) Quaternary stratigraphy of an area northeast of American Falls in the eastern Snake River Plain; Geol. Soc. America Memmoir 179, pp. 269-288.

Jacobsen, N.D. 1982. Ground water conditions in the eastern part of Michaud Flats, Fort Hall Indian Reservation; USGS Open File Rept. 82-570, 35 pp.

Jacobsen, N.D. 1984. Hydrogeology of eastern Michaud Flats, Fort Hall Indian Reservation; USGS Water Resources Investigations Rept. 84-4201, 31 pp.

Jasmer, R.M. 1987. Hydrocompaction hazards due to collapsible loess in Southeastern Idaho; M.S. thesis, Idaho State University, 129 pp.

Kindel, G. and others 1991. Geological and hydrogeological characterization of the Fort Hall Canyon landfill site, Bannock County, Idaho; Proc., 27th Engineering Geology and

Geological Engineering Symp., Logan, Utah, pp. 33-1 to 33-8.

LaPoint, P.J. 1977. Preliminary photogeological map of the eastern Snake River Plain; USGS Misc. Field Studies Map MF-850, 1:250000.

LeFebre, G.B. 1984. Geology of the Chinks Peak area, Pocatello Range, Bannock County, Idaho; Idaho State Univ., M.S. thesis, 61 pp.

Link, P.K., LeFebre, G.B, Pogue, K.R. and Burgel, W.D. (1985). Structural geology between the Putnam Thrust and tghe Snake River Plain, Southeastern Idaho; in Utah Geol. Assoc. Publ. 14, Orogenic Patterns and Stratigraphy of North-Central Utah and southeastern Idaho, pp. 97-117.

Ludlum, J.C. 1943. Structure and stratigraphy of part of the Bannock Range, Idaho; Geol. Soc. America Bull. 54.

Mansfield, G.R. 1920. Geography, geology and mineral resources of the Fort Hall Indian Reservation; USGS Bull. 713.

McDole, F .E. 1969. Loess deposits adjacent to the Snake River Plain in the vicinity of Pocatello; Univ. Idaho, Ph.D. dissertation, 231 pp.

McDole, R. and others 1973. Identification of paleosols and the Fort Hall geosol in Southeast Idaho loess deposits; Soil Sci. Soc. Am. 37, 611-616.

Muller, S.C. 1978. The geology and distribution of base-metal deposits in the Fort Hall mining district, Bannock County, Idaho; M.S. thesis, Idaho State University, 194 pp.

Norvitch, R.F. and Larson, A.L. 1970. A reconnaissance of the water resources in the Portneuf River Basin; Idaho Dept. Water Resources, Water Information Bull 16, 58pp.

Ore, H.T. 1982. Tertiary and Quaternary evolution of the landscape in the Pocatello, Idaho, area; Northwest Geology 11, pp. 31-36.

Parliman, D.J. 1982. Ground water quality in east-central Idaho valleys; USGS Open File Rept. 81-1011, 55pp.

Parliman, D.J. 1987. Hydrogeology and water quality of areas with persistent ground water contamination near Blackfoot, Bingham County, Idaho; USGS Water Res. Investigations Rept. 87-4150, 102 pp.

Rember, W.C. and Bennett, E.H. 1979. Geologic map of the Pocatello quadrangle, Idaho; Idaho Bur. Mines Geology, Geologic Map Series, Pocatello 2 deg quadrangle, 1:250000.

Scott, W.E. 1982. Surficial geology map of the eastern Snake River Plain and adjacent areas; USGS Misc. Investigations Series. Map I - 1372.

Scott, W.E., Pierce, K.L., Bradbury, J.P. and Forester, R.M. 1982. Revised Quaternary stratigraphy and chronology in the American Falls Area, southeastern Idaho; in Cenozoic Geology in Idaho, B. Bonnichsen and R.M. Breckenridge, eds., Idaho Bureau of Mines and Geology Bull. 26, pp. 581-595.

Seitz, H. and Norvitch, R. 1979. Ground water quality in Bannock, Bear Lake, Caribou and part of Power Counties, Southeast Idaho; USGS Water Resources Investigations 79-14, 51 pp.

Stearns, H.T. and others 1938. Geology and water resources in the Snake River Plain in Southeast Idaho; USGS Water Supply Paper 774.

Trimble, D.E. 1976. Geology of the Michaud and Pocatello quadrangles; USGS Bull.1400, 88pp.

West, S.W. and Kilburn, C. 1963. Ground water for irrigation in part of the Fort Hall Indian Reservation; USGS Water Supply Paper 1576-D.

Hydrogeology, Waste Disposal, Science and Politics
Proceedings 30th Symposium
Engineering Geology and Geotechnical Engineering, 1994

IMPACT OF LEACHABLE SULFATE ON THE QUALITY OF GROUNDWATER IN THE POCATELLO AQUIFER

C. Meehan, Department of Geology, Idaho State University, Pocatello, Idaho 83209
J. Welhan, Idaho Geological Survey, Idaho State University, Pocatello, Idaho 83209

Abstract

During the summer of 1993, groundwaters and surface waters were found to have anomalous sulfate concentrations in the Southern Pocatello municipal aquifer in an area known as the Highway Ponds. Leach tests performed on a large pile of road aggregate stockpiled near the Highway Ponds have been identified as the most likely source for the sulfate.

Correlating trends of sulfate and chloride concentrations can be found both in the main Pocatello aquifer and in Pocatello Creek groundwaters. The chloride contamination at Pocatello Creek has previously been suggested to be derived from road salt. It is hypothesized that aggregate used in roadbed construction may be responsible for elevated sulfate in the areas groundwater.

Chemical modeling has eliminated carbonate precipitation/dissolution reactions in buffering the chemistry of sulfate-impacted groundwater. Ion-exchange with clays is hypothesized to be a more significant process and is being investigated further.

Introduction

The city of Pocatello, located in Southeast Idaho, depends entirely on groundwater for its municipal water supply. The Idaho Geological Survey and Idaho State University are working with the city of Pocatello to develop a well head protection plan for the municipal well field. Part of the initial aquifer study involves creating a water balance that utilizes the chemical signatures of the aquifer and its recharge sources in an attempt to calculate recharge fluxes to the lower Portneuf River Valley aquifer southeast of the city (Figure 1). During the summer of 1993, suites of water samples were collected and analyzed for major cation and anion concentrations. It has been well documented in chemical analyses of Pocatello's municipal well waters that chloride and sulfate concentrations are linearly correlated (City of Pocatello, Water Dept., unpublished data). This relation between chloride and sulfate suggests that their introduction to the Pocatello Aquifer may be related in some way.

In the course of the study, several surface water and groundwater samples exhibited anomalous concentrations of sulfate in the vicinity of a large borrow pit located approximately one mile south of the city limits and 2 miles upgradient of the municipal well field. Further investigation identified a large pile of road aggregate as the possible source for the anomalous waters. The Idaho State Department of Transportation has identified the substance as slag they had crushed for use as road aggregate. Because this material may represent a potential source of ionic constituents that may be important in the water balance study, further investigations were initiated to evaluate its impact on the groundwater.

In the area of Pocatello Creek, a tributary valley immediately east of Pocatello (Figure 2), chloride and sulfate also are correlated with a slope similar to that recognized in the main Pocatello Aquifer. In a study of Pocatello Creek by CH^{2}M-Hill , it was postulated that road salt used for winter de-icing was responsible for the chloride contamination in that area (CH^{2}M-Hill, 1992; Noble, 1993), but a source for the observed sulfate enrichment was not identified. With

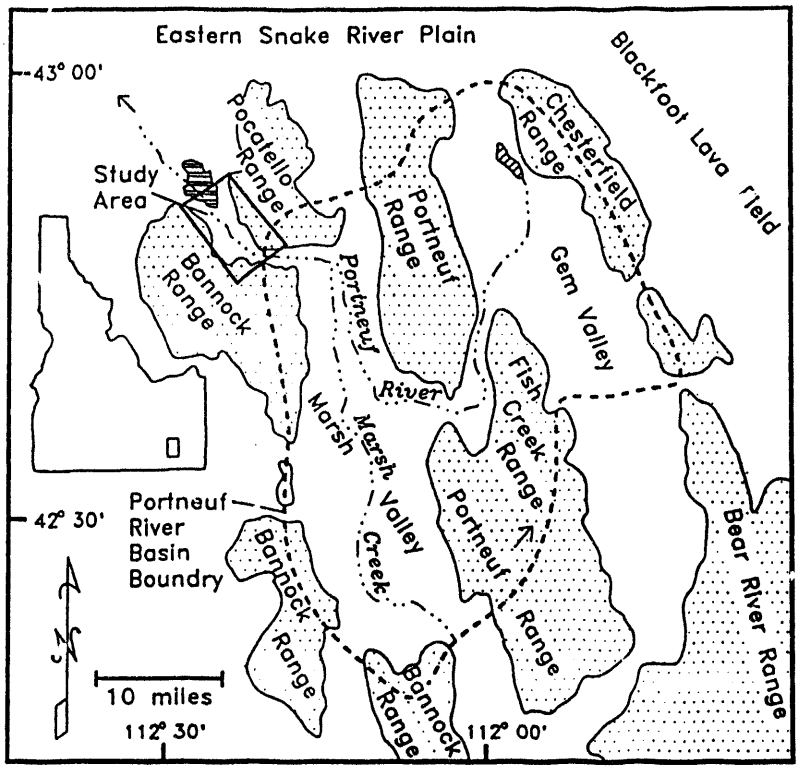


Figure 1: Location map showing Portneuf River Basin and study area for the Southern Pocatello aquifer. The Boundary for the Portneuf River Basin is denoted by the dashed line.

the discovery of the above mentioned road aggregate as a source of leachable sulfate in the borrow pit area, it was speculated that it may also be responsible for sulfate contamination at Pocatello Creek. A casual inspection of the roadbeds in Pocatello Creek revealed that similar road aggregate was used in their construction.

Further studies were conducted to see if the chloride and sulfate trends recognized at Pocatello Creek and in the main Pocatello aquifer may be related by similar processes. This paper describes the initial results of this investigation and evaluates possible chemical reaction pathways which may be influenced by aggregate-derived chemical constituents.

Geologic Setting

The city of Pocatello is situated in an alluvial valley between the Pocatello Range to the north and the Bannock Range to the south (Figure 1). These ranges consist of allocthanous upper Proterozoic and Cambrian strata of the Pocatello formation and Brigham Group that were thrust faulted during the Jurassic to Paleocene Sevier orogeny (Link et al., 1987). During the Cenozoic, south-east Idaho has extended along north trending normal faults that are characteristic of the Basin and Range Province. In the case of the Pocatello valley this process has resulted in a sediment filled half-graben structure. Pediment gravel terraces flanking the valley imply several valley sedimentary filling and downcutting episodes that are thought to be Late Tertiary to Pleistocene in age (Ore, 1982).

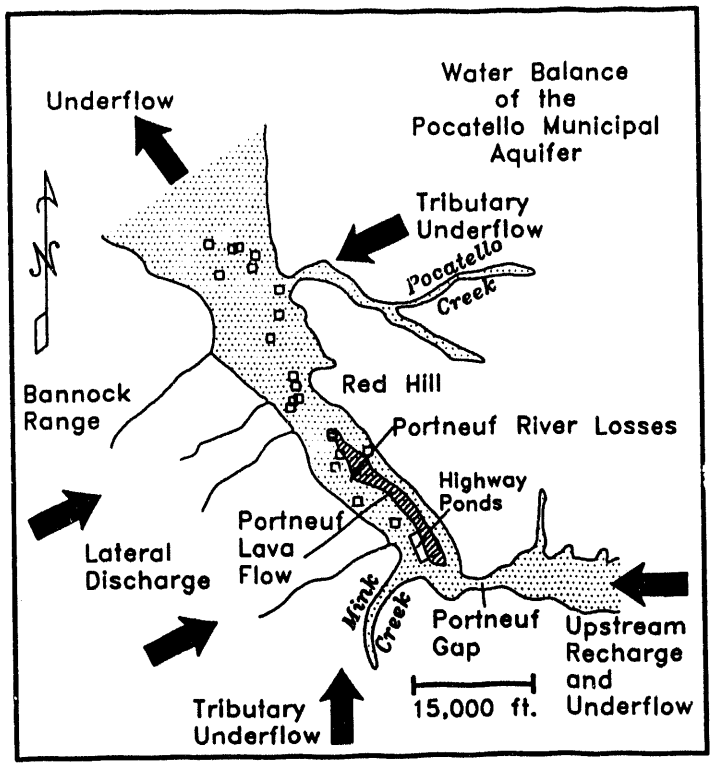


Figure 2: Pocatello Municipal Aquifer

Recharge areas to the Pocatello Municipal aquifer being used in the water balance study are designated by arrows. Also located on this map are the locations of Pocatello Creek and the Highway Ponds study area. Municipal wells are designated by open squares.

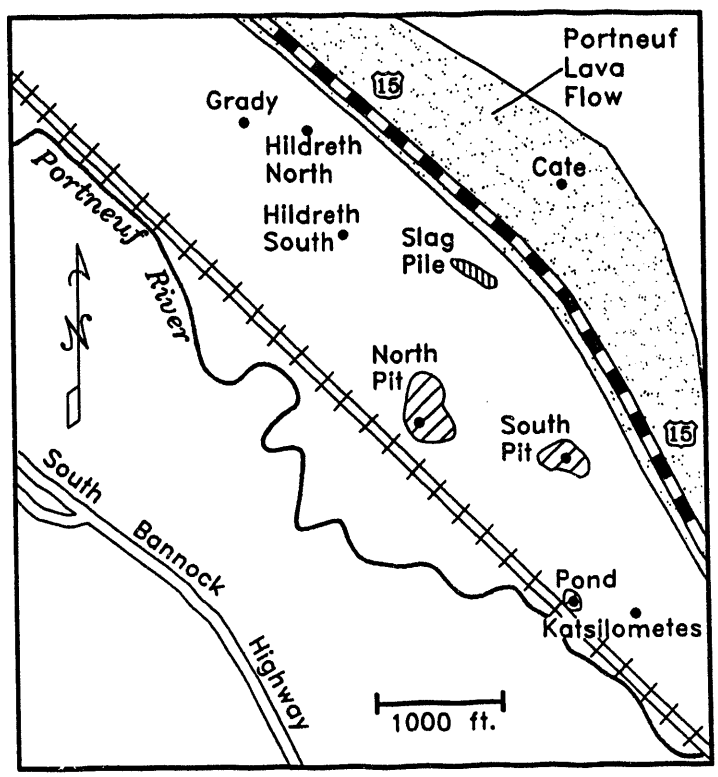


Figure 3: Location Map for Highway Ponds Study Area

Map of the Highway Ponds area where anomalous levels of high sulfate concentrations were observed in both surface waters and ground waters. Located here are the sampling points (closed circles), Portneuf River, surface waters (slanted lines), Portneuf Lava Flow (speckled), and the slag pile (vertical lines) thought to be the source of the sulfate. The Union Pacific rail line separates the Portneuf River and the Highway Ponds area.

The southern boundary of the Pocatello Valley is defined by the Portneuf Gap, sometimes called the Portneuf Narrows, where the Portneuf River cuts through the north-trending Bannock range. This narrow gap is thought to be a superposed canyon that was cut by the ancestral Bear River during the Lake Bonneville flood as it flowed into the Snake River (Link, 1982). This flood completely eroded an earlier basalt flow within the gap, but left scoured remnants within the valley near Pocatello. Drilling has shown that this flow, known as the Portneuf Lava Flow, is 50 feet thick and its base is at the same level as the valley floor (Trimble, 1976). Boulders of basalt greater than 2 meters in diameter can be found in the Bonneville flood deposits that underlie downtown Pocatello (Link, 1982).

Quaternary alluvium and flood plain silts cover most of the valley floor (Trimble, 1976). The valley strata consists of Pleistocene lacustrine and fluvial deposits related to both the ancestral American Falls Lake and the Lake Bonneville flood (See Welhan and Meehan, this volume).

Implications For Water Balance Study

The area currently being studied for water balance modeling purposes is located in a small portion of the Lower Portneuf River Basin and extends from Red Hill to the Portneuf Gap (See Figures 1 and 2). The five components of recharge to this valley aquifer that are being examined are: 1) underflow through the Portneuf Gap; 2) underflow from Mink Creek; 3) infiltration from the Portneuf River; 4) lateral underflow from the east dipping strata of the Bannock Range, west of the aquifer; 5) underflow from an adjacent alluvial aquifer east of the Portneuf lava flow.

As previously mentioned, chemical characterization of the main aquifer's groundwater and recharge sources has been undertaken. The amount of water supplied to the aquifer by each source may be calculated using the concentrations of certain constituents (i.e. sulfate, nitrate, chloride) in the various recharge sources contributing to the main aquifer. The concentrations of these constituents in the main aquifer should reflect only their amounts as delivered by the previously defined recharge sources. It is therefore important to understand the chemical impact that road aggregate may have on aquifer chemistry, if the chemical mass balance method is to properly quantify recharge fluxes.

Sampling and Analytical Methods

The results of the chemical analyses for the borrow pit area are shown in Table 1. Sampling locations are shown in Figure 3. The samples labeled North Pit, South Pit, and Pond refer to small bodies of water, known as the Highway Ponds, that lie within a large gravel pit excavated for road aggregate during the construction of Interstate Highway 15. The chemical signature of these ponds, as well as their water level elevations, indicate that they represent the surface expression of local groundwater. This is further supported by the emergence of these ponds only during periods of above-normal precipitation and high groundwater levels.

Regionally, groundwater flow in the area is along the axis of the valley, approximately from southeast to northwest. The sample designated Katsilometes refers to an irrigation well upgradient from the borrow pits and represents background aquifer water quality. The Portneuf River adjacent to the irrigation well was also sampled. Hildreth North, Hildreth South, and Grady are residential wells located downgradient of the aggregate pile. The sample designated Cate is a water well owned by a heavy equipment company. It is located in what is considered to be a separate aquifer, east of the Portneuf lava flow, which is known to be locally contaminated.

All samples were collected in one liter polyethylene containers and analyzed in the field for pH and specific conductance. Samples from residential wells were taken from household water taps in which the water was allowed to run for several minutes to ensure the sample was representative of the well water. Total alkalinity for each sample was analyzed on the day of collection by titration with standardized acid.

After filtering samples through a 0.45 micron filter, major ion analyses were performed within one week of collection. Of these, sulfate, chloride, nitrate, silica, and magnesium were analyzed with a HACH DR/2000 spectrophotometer, using standardized procedures and multiple runs to ensure the accuracy and precision were well defined. In some cases, dilution with deionized water was necessary to place a sample within the detection limits of a particular test. When this became necessary, several analyses were made at varying dilution ratios and the deionized water itself was tested to insure its integrity. Total hardness was analyzed by EDTA titration. Calcium was calculated by subtracting the magnesium concentrations determined from the spectrophotometric analyses from total hardness. Sodium and potassium were analyzed by flame atomic absorption spectroscopy. Multiple runs of analyses using the spectrophotometer have shown the relative standard deviation at the 1 sigma level is less than 4 mg/l for all elements except magnesium, which was 7 mg/l. The standard deviation at the 1 sigma level for calcium is 10 mg/l.

TABLE 1: CHEMICAL ANALYSIS FOR WATER WELLS IN THE POCATELLO AQUIFER
Concentrations of ions are all given as mg/kg of solution. Alkalinity is represented as HCO_3^- in mg/kg of solution. Specific conductance (S.C.) is in umho/cm. (Note: this table represents selected analyses only, and is not a complete listing of all background water compositions and other wells in the southern Pocatello aquifer for which data are available)

DATE	SAMPLE	Ca	Mg	Na	K	SO4	Cl	NO3	Si	Alk	pH	S.C.
Highway Pond Area and Downgradient Wells:												
06/15/93	Hildreth S	77.0	38.4	53.7	22.2	127	54.2	14.9	24.9	356	7.6	NA
12/06/93	Hildreth S	70.7	25.8	46.2	14.8	60	45	8.8	27.6	301	7.6	NA
06/04/03	Pond	78	38.4	NA	NA	90	50	1.3	17	376	7.5	NA
06/21/93	Pond	68	38.4	43.4	10.3	100	45.2	3.08	35.6	373	8.2	725
06/04/93	North Pit	74	32.4	NA	NA	42	32	7.48	22.1	333	7.2	600
06/21/93	North Pit	73	27	36.1	6.76	44	34.5	7.04	23.8	328	7.7	475
12/06/93	North Pit	93	31.1	43.5	5.8	39	41.5	7.48	24.7	341	7.64	NA
06/04/93	South Pit	66	28.8	NA	NA	42	33.5	7.04	13.8	301	8.2	575
06/21/93	South Pit	50.7	26.4	30	5.26	44	42.2	3.52	11.7	290	8.2	475
12/06/93	South Pit	85.7	28.7	44	5.73	38	33.5	7.04	22.3	296	8.14	NA
06/15/93	Hildreth N	71	30.6	45.6	6.7	53	36.5	10.5	25.7	339	7.6	NA
12/06/93	Hildreth N	77.9	23.8	38.1	6.3	43	36	8.4	25.1	305	7.5	NA
06/15/93	Grady	76	28	35.8	6.6	47	44.7	8.4	27	339	7.5	NA
12/06/93	Grady	75	22	37	5.9	37	33	8.4	25	306	7.5	NA
Background Water Quality:												
06/21/93	Portneuf	61.3	20.8	24	5.03	27	27.7	2.6	21.1	253	8.3	375
12/06/93	Portneuf	96.2	38.7	48.4	8.26	45	36	7.04	25.9	364	8.4	NA
06/15/93	Katsilomet	66.4	27.8	45.1	7.36	44	43.5	6.16	25.2	336	7.5	406
East of Portneuf Lava Flow:												
06/21/93	Cate	128	58.8	69	6.62	110	252	38.3	22.2	298	7.4	1100
12/06/93	Cate	153	53.3	80	8.38	105	207	38.2	21.4	296	7.6	NA
Aggregate Leach Test:												
3 Days	Aggregate	196	4.8	8.6	17.7	500	2.25	1.76	38.4	0.00	8.2	750

A leach test was performed on a sample of the crushed aggregate that is stockpiled near the Highway Ponds. Deionized water was placed in contact with the aggregate for three days and the resulting solution was analyzed with the above mentioned methods. The results of this test are shown in Table 1 (sample designated as aggregate). This test showed that sulfate, calcium, and potassium are major soluble components and can be leached from the aggregate pile. The analyses of the Hildreth South well, which is directly down gradient from the aggregate pile, show significant increases in sulfate and potassium levels above normal background concentrations. Calcium, however, does not show a statistically significant increase, suggesting that its concentration as a soluble component in the groundwater is being buffered by some process (e.g. precipitation, ion-exchange).

Table 2 shows trace element data for aggregate samples and Hildreth South well water which were obtained by induced neutron activation analysis (INAA) and gamma spectral analysis. Due to the lack of standards that were available at the time of these analyses and the lack of quality assurance tests, the results here are considered to be preliminary; only the largest elemental enrichments above detection are summarized in Table 2.

Table 2: INAA ANALYSES: All values are in mg/kg of solids. Solution concentrations for samples Aggregate/DI Water and Hildreth Sth. in mg/kg solution are approximately 0.00077 times the values shown, as explained in the text.

Date	Sample	Cr	As	Rb	Sr	Ba	U	Cs	Ce	Nd
	Primary Aggregate	861	435	26.3	720	650	97.2	3.15	77.6	116
	Leached Aggregate	1526	680	36	585	710	96	3.8	80	106
	Aggregate/DI Water	0.89	2	40	755	10	0.32	0.88	0.4	0.4
06/15/93	Hildreth Sth.	15	6	25	835	228	2.6	0.11	0.86	8.2

Samples labeled primary aggregate and leached aggregate represent the solid aggregate prior to, and after leaching in deionized water for three weeks. The sample designated Aggregate/DI Water represents the water which was in contact with the aggregate for three weeks. The two water samples (Aggregate DI and Hildreth S.) were filtered and evaporated to dryness so that their solid residues could be activated for INAA and gamma spectral analysis. Since the values in Table 2 for these two water samples represent mg/kg of the solid, they must be multiplied by 7.7×10^{-4} to convert them to mg/kg of solution. This conversion was obtained from the calculated total dissolved solids content (TDS) of the original waters based on their major ion analyses (TDS about 770 mg/L for each sample).

From the data in Table 2 it appears that some Sr and Rb may be leached from the aggregate. Concentrations of other analyzed elements are less than one mg/kg of solution. Since no trace element analyses were performed on upgradient well waters, it is not possible to determine if Hildreth South water shows any significant increase in other elements. More analyses are being performed to address this. The aggregate does contain significant amounts of uranium (97 ppm), which is considered a soluble, highly mobile aqueous species in this type of groundwater.

performed to address this. The aggregate does contain significant amounts of uranium (97 ppm), which is considered a soluble, highly mobile aqueous species in this type of groundwater. However, the concentration of uranium in solution for the prolonged leach test was less than 0.3 ppb. It appears that it is not readily mobilized and does not pose a threat to groundwater.

The pile of aggregate in question appears to be heterogeneous in its bulk composition. Contrary to what was expected, the leached aggregate had higher concentrations for most of the analyzed elements than the sample of unleached slag. Two other leaching tests performed by other parties on slag have shown different amounts of leachable sulfate. A leach test performed by CH^2M-Hill yielded twice as much sulfate as our test (R. Noble, personal comm., 1993), while another test performed by FMC on uncrushed slag had a sulfate concentration of less than 1 ppm (P. French, pers. comm. 1994). These results suggest that grain size may be an important factor in controlling the amount of leachable sulfate.

Interpretations of Highway Ponds Area Data

Figure 4 is a Piper diagram that depicts the relative concentrations of the major cations (calcium, magnesium, sodium and potassium) and anions (chloride, sulfate, carbonate and bicarbonate) in waters from the Highway Pond area, the Portneuf River, and wells east of the Portneuf Basalt and main municipal aquifer. The lower right hand portion of this figure depicts two trends of increasing chloride and sulfate proportions which deviate from the tight clustering of main aquifer background water. One trend observed in wells east of the Portneuf Basalt (plotted as "-" symbols), suggests that those waters are affected by chloride and sulfate addition in a proportion that differs from the main aquifer. The second trend shown in Figure 4 (as "@" symbols), reflects the addition of only sulfate in the Highway Ponds area.

Neither trend in anion compositions in Figure 4 is associated with a cation trend. Sulfate and chloride are expected to behave conservatively in these groundwaters; their concentrations change only due to additions and source dilution. In contrast the cationic constituents (including heavy metals) would not be expected to behave conservatively, since their concentrations are affected by common mineral dissolution reactions, precipitation reactions, and ion exchange on clays.

It has been brought to our attention that the Highway Department may add sulfate-containing salts to road aggregate to augment winter de-icing capabilities. However road salt used by the Highway Department contains more than 95 percent sodium chloride (P. French, pers. comm., 1994), and there has been no significant sodium or chloride observed in the leach tests on the aggregate that have been run to date. The Idaho State Department of Transportation and Bannock Paving (who provided the Department of Transportation with the crushed aggregate at the Highway Ponds) both confirmed that no additives were introduced to the stockpile in question (K. Magleby, pers. comm.,1994; L. Robson, pers. comm., 1994).

As previously mentioned, sulfate was found to be readily leachable from the aggregate source, and could explain the enrichment of sulfate observed in groundwater near the Highway Ponds. It is possible that the Highway Ponds area is connected hydrologically under the Portneuf lava flow with the eastern aquifer, which is known to be locally contaminated with chloride, sulfate, and nitrate (see Cate Well analysis, Table 1). However, our aggregate leach test produced high-sulfate, low-chloride water, which is more characteristic of the type of waters observed at the Highway Ponds. If the area east of the basalt were the source of sulfate for the Highway Ponds, then increased concentrations of chloride and nitrate would also be expected.

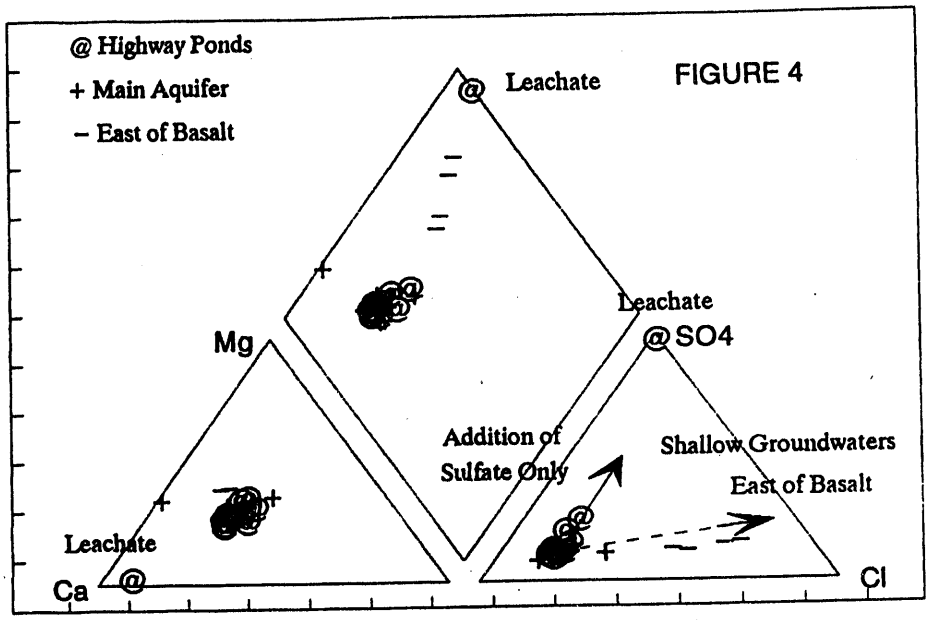


Figure 4: Piper diagram of groundwaters from the Southern Pocatello Aquifer, Highway Ponds, and area east of the Portneuf Lava Flow. This figure depicts two regional trends of increasing Cl and SO4 proportions which deviatefrom the main aquifer background water. Wells east of the Portneuf Basalt suggest Cl and SO4 addition in proportionsthat differ from the addition of only sulfate at the Highway Ponds. Leachate refers to the solution derived from the leachtest.

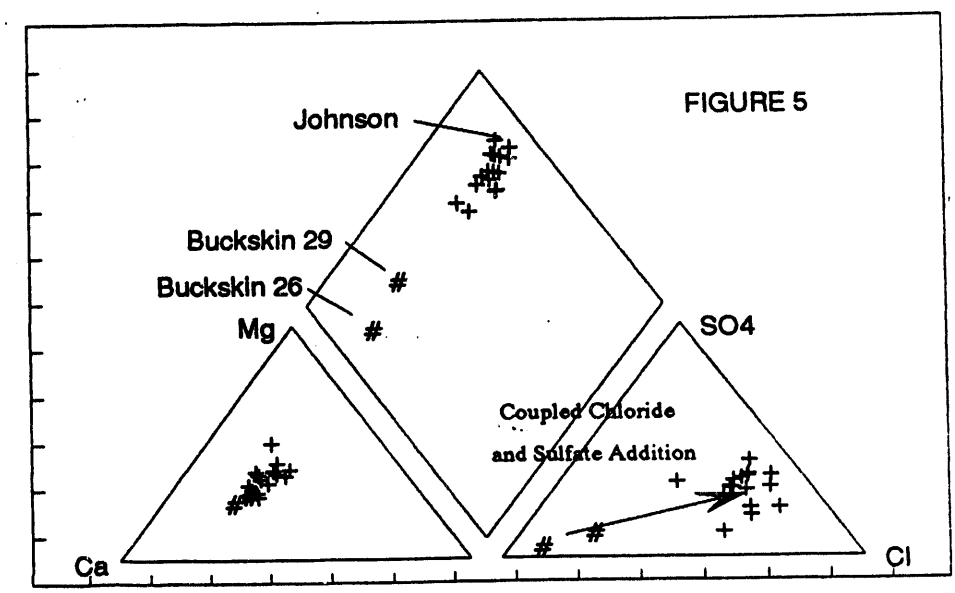


Figure 5: Piper Diagram of groundwaters from Pocatello Creek. This diagram displays the trend of sulfate and chloride enrichment in Pocatello Creek groundwaters. This trend is hypothesized to be from Cl derived from roadsalt and SO4 leached from road aggregate. Buckskin 26 and 29 are upgradient in relation to the rest of the waters in this diagram.

could explain the high sulfate levels in the pond that is directly adjacent to the Union Pacific Railroad.. Further evidence of sulfate leaching by surface waters is provided by the dramatic decrease in sulfate and potassium concentrations in the Hildreth South well between June 1993 and December 1993. Such a variation would be consistent with a surface source of sulfate that was mobilized during spring runoff. Percolation of this sulfate-rich surface water to the water table would raise local groundwater sulfate levels in spring, but by December, as the pulse of vadose zone recharge diminished, the local sulfate input to the water table would also be expected to decrease, with an ensuing decrease in groundwater sulfate levels due to normal groundwater dilution processes.

Implications of Sulfate Leaching at Pocatello Creek

Figure 5 is a Piper diagram displaying the relative concentrations of ions in groundwaters in residential wells at Pocatello Creek, analyzed by the Division of Environmental Quality and the District Health Department. This figure also displays a trend of chloride and sulfate enrichment (compare to Figure 4).

It has been hypothesized that road salt used for de-icing may be responsible for the chloride contamination in Pocatello Creek ground waters(CH^{2}M-Hill, 1992; Noble, 1993). Groundwater at Pocatello Creek shows a direct correlation between sodium and chloride, which is also observed in the Southern Pocatello main aquifer. This may suggest a similar scenario for the introduction of chloride into the Pocatello Aquifer.

It is widely accepted that material similar to the aggregate stockpiled in the Highway Pond borrow pits has been widely used in road and rail bed construction throughout Bannock County (G. Brown, pers. comm., 1993). We suggest that features constructed with this aggregate may provide a source of leachable sulfate to groundwaters. After finding similar aggregate in a casual inspection of the Pocatello Creek roadbeds, it was hypothesized that aggregate may be responsible for the high sulfate levels observed in groundwaters in that area.

Figures 6(a) and 6(b) illustrate the linear correlation between chloride and sulfate in the Southern Pocatello Aquifer and Pocatello Creek. Figure 6(a) shows the two trends displayed in the Piper diagram in Figure 4 (sulfate addition and groundwater east of the Portneuf Basalt). A third trend in Figure 6(a) shows coupled chloride-sulfate addition that is characteristic of the main Southern Pocatello aquifer. The chloride-sulfate trend in Pocatello Creek ground waters (Figure 6(b)) is almost identical to the third trend observed in the main aquifer in Figure 6(a).

On the basis of these data, it is hypothesized that chloride and sulfate enrichments observed in local groundwaters may be due to a combination of road salting and road bed leaching. Infiltration of runoff along roadbeds in the spring may introduce salt derived from winter de-icing applications; this chloride-enriched water may subsequently acquire sulfate from the dissolution of road bed material. Such a coupled mechanism for the introduction of road salt-derived chloride and road bed-derived sulfate would explain the observed correlation of elevated chloride and sulfate in area groundwaters, and would imply that road runoff may be a potentially significant point of introduction for surface-derived contaminants to the aquifer. The hypothesis for a coupled chloride-sulfate enrichment from roadbed runoff and leaching was further examined by modeling the possible chemical processes and reaction paths which may be involved in such a scenario.

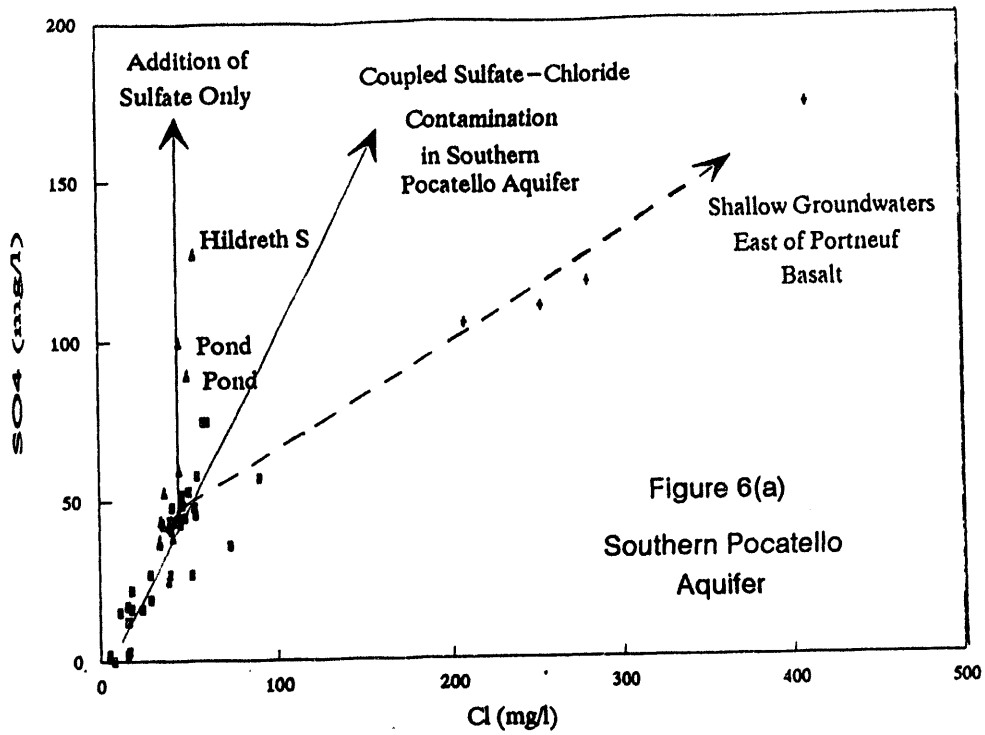


Figure 6(a)

Southern Pocatello
Aquifer

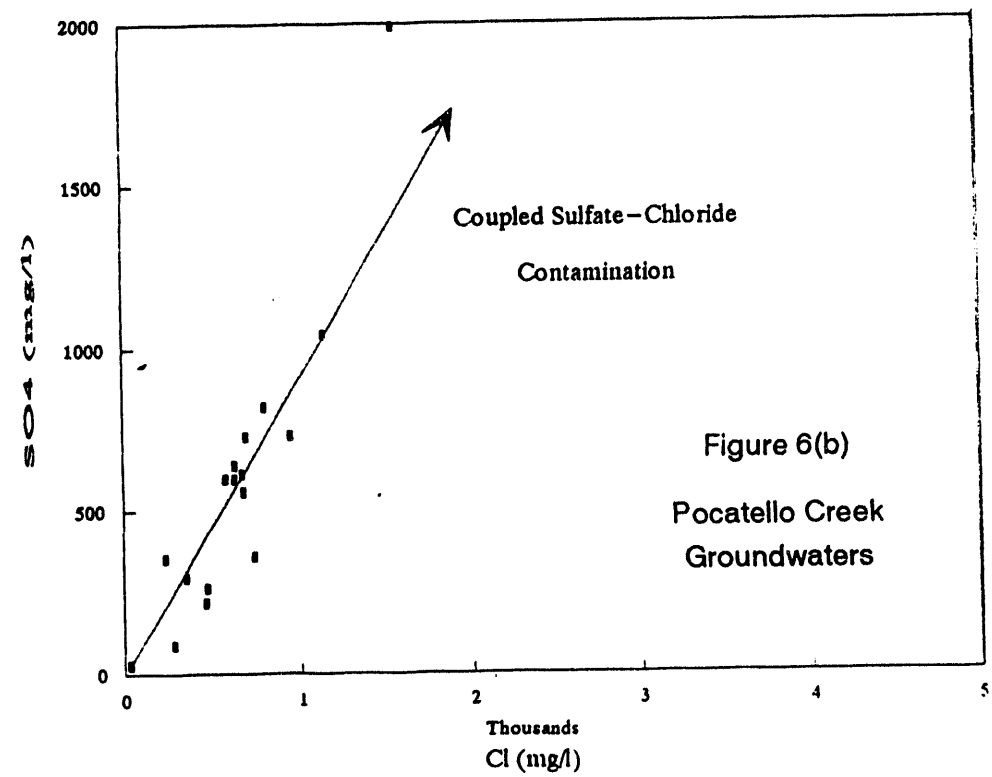


Figure 6(b)

Pocatello Creek
Groundwaters

Figure 6(a) is a plot of chloride concentrations vs sulfate concentrations in groundwaters from the main Pocatello Aquifer (squares), the Highway Ponds area (triangles), and the area east of the lava flow (diamonds). The impact of slag derived sulfate can be seen in the Highway Ponds area which deviates from other waters which have a coupled Cl–SO4 trend. Figure 6(b) shows sulfate and chloride concentrations in Pocatello Creek. The slope of the line shown in 6(b) is that observed in the main Pocatello aquifer in Figure 6(a).

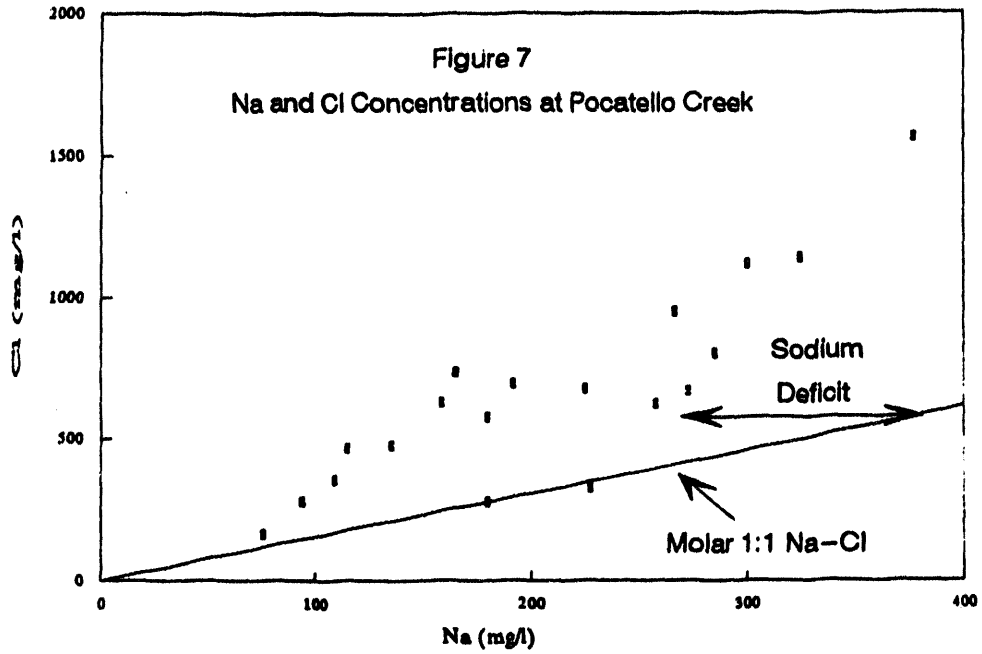


Figure 7: Correlation of sodium and chloride at Pocatello Creek. These concentrations are compared with a molar 1:1 ratio of sodium vs chloride. There appears to be a deficit of sodium, if they are mutually derived from road salt. This may be explained by ion–exchange with clays.

Reaction Path Modeling

If the change in water compositions along a hydrologic flow path between arbitrary starting and ending points is due to the effects of chemical reactions or mixing, then the reactions responsible for the change can be quantified by a chemical mass balance model (Plummer and Back, 1980). Such an approach only identifies the possible phases and/or components involved in a set of reactions. In contrast, chemical reaction path modeling is used to determine (1) the conditions under which the reactions have occurred (e.g. open vs. closed system) (2) how the water composition changes in response to perturbations in the system . The modeling of an aqueous system in this fashion is facilitated by calculations of equilibrium speciation and mass balance (Plummer et al, 1983). Two computer programs, NETPATH (Plummer and others, 1991) and MINTEQA2 (Allison and others, 1991), were used to incorporate both of these calculations.

NETPATH was used for the mass balance calculations to determine the amounts of "plausible phases" that must dissolve and/or precipitate to account for the observed water compositions. The mass balance approach consists of balancing a net chemical reaction in the form:

Initial solution composition + "Reactant Phases" =
Final solution composition + "Product Phases"

"Product Phases" represent those constituents that must physically leave the aqueous phase during the reaction, while "Reactant Phases" represent chemical constituents that must physically

"Product Phases" represent those constituents that must physically leave the aqueous phase during the reaction, while "Reactant Phases" represent chemical constituents that must physically enter the aqueous phase. The term "plausible phases" represents the reasonable choices for possible reactants and products based on the modeler's geochemical insight and as constrained by equilibrium speciation calculations (Plummer et al, 1983).

MINTEQA2 is a geochemical equilibrium speciation model for dilute aqueous systems. MINTEQA2 was used to evaluate models suggested by NETPATH and determine if they were plausible in terms of their thermodynamic requirements.

The first step was to determine the "plausible phases" that may be present and responsible for the observed chemical changes at the Highway Ponds and Pocatello Creek. Gypsum ($CaSO_4$) was used in modeling the sulfate component, since calcium and sulfate were derived from leached aggregate in a 1:1 ratio (Table 1). The addition of NaCl (road salt), was used to account for the level of chloride concentrations observed in the groundwater. Figure 7 shows concentrations of sodium and chloride in wells at Pocatello Creek compared with the trend expected for a molar 1:1 ratio of sodium and chloride. If sodium and chloride are from a single source, namely road salt, there appears to be a sodium deficiency. Ion exchange of sodium with clays may account for this deficiency. Such reactions would be of the form:

$$CaX + 2Na^{+} \rightarrow Ca^{2+} + Na_2X \qquad (1)$$

$$MgX + 2Na^{+} \rightarrow Mg^{2+} + Na_2X \qquad (2)$$

Reaction 2 could also account for the magnesium increases observed at both the Highway Ponds and Pocatello Creek (magnesium was not found to be a major constituent in the aggregate leach test). Another plausible source of magnesium may be from the dissolution of dolomite. For these reasons a calcium-sodium and a magnesium-sodium exchanger, along with dolomite, were also considered to be "plausible phases" in the modeling. Calcite and CO_2 gas were also added as phases, considering that carbonate reactions are an important chemical process for these types of ground waters and may help explain the reaction(s) buffering Calcium. A KSO_4 phase was assumed to be a component of the aggregate and was used to model the observed potassium increases.

The initial NETPATH models were run using the June 1993 analyses of Katsilometes well water as the initial background water and Hildreth South as the final endpoint. The elements carbon, sulfur, calcium, magnesium and potassium were used as constraints to fix the masses of the chosen phases that can enter or leave the aqueous solution. Initially, NaCl was not used in model runs, so sodium and chloride were not entered as constraints. NETPATH yielded nine possible models that could account for the chemical signature of the water found at Hildreth South.

Table 3 summarizes the nine possible models calculated by NETPATH. Positive values indicate dissolution of the particular phase, while negative values indicate precipitation. For the exchangers, positive values mean that reactions 1 and 2 are occurring as they are written; a negative value indicates the reaction is occurring in the reverse direction, so that sodium would be released as free ions to solution.

When NaCl was included as a plausible phase (and sodium and chloride as constraints), only models that contained exchangers were produced. Since sodium and chloride are not in a molar 1:1 ratio at the Hildreth well as they are in the phase NaCl, the exchangers provide the only other sources and or "sinks" for sodium. Table 3 indicates only one model (Model #1) in which no exchangers are required.

Table 3: NETPATH MODELS FOR HIGHWAY PONDS AREA: All values represent the amount of each phase in mmols that enters (+) or leaves (-) the solution. A (+) sign for exchangers means that reactions 1 and 2 occur as they are written above. They are reversed if they are (-).

Phase	Mod. 1	Mod. 2	Mod. 3	Mod. 4	Mod 5	Mod. 6	Mod. 7	Mod. 8	Mod. 9
Gypsum	0.4901	0.4901	0.4901	0.4901	0.4901	0.4901	0.4901	0.4901	0.4901
KSO4	0.3798	0.3798	0.3798	0.3798	0.3798	0.3798	0.3798	0.3798	0.3798
Calcite	-0.6601	-0.2252	-0.5391	0.3306	-0.7810				
CO2 (g)	0.1209	0.5558				-0.5391	0.3306	0.7810	
Dolomite	0.4349		0.4349		0.5558	.4349		-0.2252	0.1653
Ca-Exch			-0.1209	-0.5558		-0.6601	-0.2252		-0.3905
Mg-Exch		0.4349		0.4349	-0.1209		0.4349	0.6601	0.2696

MINTEQA2 can be used to test whether the precipitation/dissolution reactions proposed by NETPATH are feasible given the constraints of thermodynamic equilibrium. The mass balance method is generally an elimination process in which calculations that identify reactions that cannot occur are eliminated. Proof of a reaction is never positive with the mass balance approach, but by the process of elimination there may remain only a limited number of models that are consistent with the observed chemical data (Plummer and Back, 1980).

Initially, one may use geochemical insight to eliminate certain models in Table 3. Both the Hildreth South water and Katsilometes are saturated with respect to calcite. Thus Model 4 in Table 3 can be eliminated since it requires the dissolution of calcite. Model 8 is probably also unreasonable because it requires the precipitation of dolomite, an unrealistic process for these types of waters.

If the same processes influencing the Hildreth South well are also occurring in Pocatello Creek, their impact in the latter's setting is much greater. Groundwater analyses of residential wells by the Division of Environmental Quality and the District Health Department show concentrations of major ions one to two orders of magnitude greater than in waters at the Highway Ponds. Since the combined effects of road salt and road bed leaching seem more pronounced at Pocatello Creek, these waters were also examined to eliminate models that were not consistent with chemical equilibrium requirements.

The samples labeled Buckskin 29 and 26 in Figure 5 refer to wells that are upgradient from other wells in the diagram. Because these waters are upgradient and appear to be an end member type water on the Piper diagram, they were considered to represent the initial background water for Pocatello Creek. The sample labeled Johnson appears to be the other end-member, most heavily impacted by chloride-sulfate addition. The Buckskin 29 and Johnson wells were used as the initial and final wells respectively, for chemical modeling. The water compositions used for the modeling are given in Table 4.

NETPATH was first used without sodium and chloride as constraints, and without NaCl as a phase. This produced only one model as shown in Table 5. MINTEQA2 was then used to

gypsum and 24.12 mmols of dolomite as "finite solids." The partial pressure of CO_2 was fixed at the amount speciated in the original Buckskin water. The assumption here is that the partial pressure of CO_2 at the Buckskin well is the same in the Johnson well, i.e. the system is open with respect to CO_2.

Table 4: CHEMICAL ANALYSIS FOR WELLS USED IN CHEMICAL MODELING
All concentrations given as mg/kg of solution. Total alkalinity is given as mg/kg of HCO_3

Sample	Ca	Mg	Na	K	Cl	SO4	Tot Alk	pH	Temp
Buck 29*	49	17	20	1.1	34	27	201	7.0	15°C
Johnson	590	600	376	5.3	1563	1988	590	7.1	15°C

* Note: analysis for Buckskin 29 was obtained from U.S.G.S. Water-Resources Investigations 79-14 Open-File Report

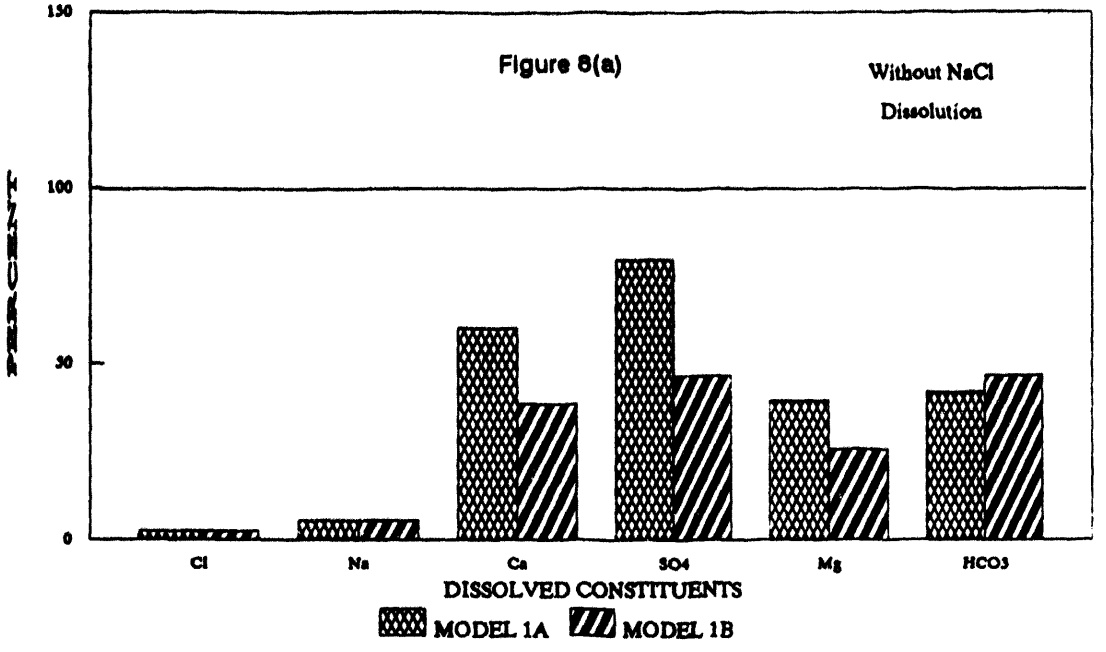
Table 5: NETPATH MODEL FOR POCATELLO CREEK (without NaCl)
All values represent the amount of each phase in mmols that enters (+) or leaves (-) the solution. A (+) sign for exchangers means that reactions 1 and 2 occur as they are written above. They are reversed if they are (-).

	Model 1
Gypsum	20.42
KSO4	0.108
Calcite	-30.96
CO2 Gas	-10.3
Dolomite	24.12

The final concentrations of ions in solution predicted by MINTEQA2 are displayed as Model 1A in Figure 8(a) as a percent of their concentrations in the Johnson well. The final equilibrium pH calculated by MINTEQA2 was 7.04 as compared to 7.1 at the Johnson well. However, figure 8(a) shows that there is a deficit in most of the ions in the model run, compared to the observed concentrations. Not enough gypsum or dolomite was able to dissolve to produce the amount of sulfate, magnesium and calcium observed in the Johnson water. In addition the alkalinity (represented by HCO_3) is much lower in the modeled water than in the Johnson water. Simply stated, this is because insufficient gypsum and dolomite were able to dissolve, as required by the NETPATH model.

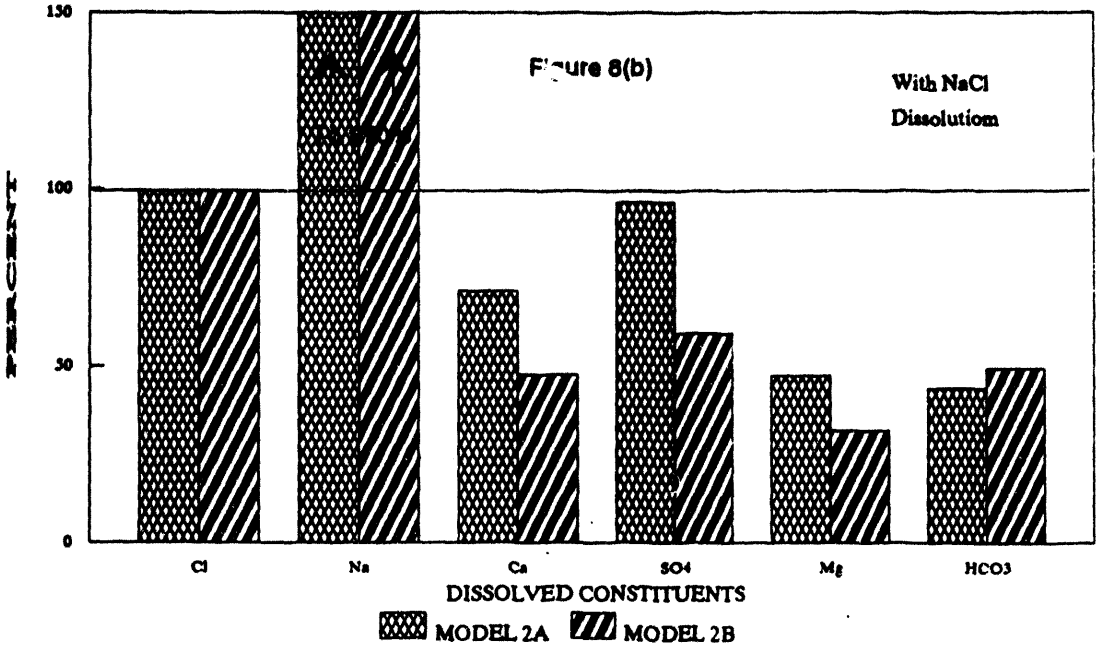
An alternative reaction path consisting of two reaction steps had similar results. Model 1B began with Buckskin water with only gypsum added as a finite solid at first. Dolomite was then added to the resultant water as step 2 and allowed to equilibrate. Even less gypsum dissolved in Model 1B as compared to 1A, because with the initial absence of dolomite dissolution, no aqueous CO_3 was added to the solution, and no calcite precipitated in the first step of the model. Therefore there was no "sink" for calcium as the gypsum dissolved. The equilibrium pH for the final model was 7.1.

Additional mass balance models were run using sodium, chloride, and NaCl as constituents. Table 6 displays the results of the NETPATH Models with chloride as the constraint for NaCl. It should be noted that Model 2 in table 6 is the same as Model 1 in Table 5, with the exception of the NaCl phase. Two equilibrium models were again constructed with MINTEQA2 using the same procedures as stated above, this time with 43.38 mmols of NaCl added as a finite solid phase. The results of the one step (Model 2A) and two step model (Model 2B) are displayed in Figure 8(b).



1A: Dissolution of Dolomite and CaSO4 in one step

2A: Dissolution of CaSO4 followde by Dolomite Stepwise



2A: Dissolution of CaSO4, Dol., and NaCl in one step

2B: Dissolution of CaSO4 + NaCl followed by Dol. stepwise

Figure 8 (a) models the dissolution of CaSO4 and dolomite only. Dissolved ion concentrations are represented as a percent of the concentrations of the same ions in the Johnson Well at Pocatello Creek. Figure 8(b) represents the same models and conditions with NaCl added as another phase.

Table 6: NETPATH MODELS FOR POCATELLO CREEK (with NaCl)
All values represent the amount of each phase in mmols that enters (+) or leaves (-) the solution. A (+) sign for exchangers means that reactions 1 and 2 occur as they are written above. They are reversed if they are (-).

Phase	Mod 2	Mod 3	Mod 4	Mod 5	Mod 6	Mod 7	Mod 8	Mod 9	Mod 10
Gypsum	20.42	20.42	20.42	20.42	20.42	20.42	20.42	20.42	20.42
KSO4	0.1081	0.1081	0.1081	0.1081	0.1081	0.1081	0.1081	0.1081	0.1081
NaCl	43.38	43.38	43.38	43.38	43.38	43.38	43.38	43.38	43.38
Calcite	-30.96	-6.84	-41.3	6.93	-20.62				
CO2 Gas	-10.3	13.77				-41.3	6.94	20.62	
Dolomite	24.12		24.12		13.78	24.12		-6.84	3.46
Ca-Exch			10.3	-13.78		-30.96	-6.84		-10.31
Mg-Exch		24.12		24.12	10.34		24.12	30.96	20.65

The results are similar to the previous models with the notable exception of a large surplus of sodium. All four reaction path models indicate that dissolution and precipitation, alone, cannot explain the chemical evolutionary trend of the water at Pocatello Creek. Thus, it is likely that other processes, such as ion-exchange reactions are important, as suggested by the original NETPATH models (Table 6). This would also explain the recognized deficit of sodium in Pocatello Creek waters relative to chloride. Future work on ion-exchange modeling with MINTEQA2 may yield more conclusive models. Laboratory tests are also in progress to empirically evaluate the cation exchange capacity of local soils.

Conclusions

Surface waters at the Highway Ponds borrow pit are the surface expression of local groundwater for that portion of the Southern Pocatello aquifer. Well and surface waters near the borrow pits have been found to have elevated levels of dissolved sulfate. The postulated source for this sulfate is a large pile of crushed slag located in the borrow pits that is used as road aggregate by the State Department of Transportation. Leach tests performed on this aggregate yielded high concentrations of calcium and sulfate in a molar 1:1 proportion, with lesser amounts of potassium. Although the aggregate contains significant amounts of uranium (97 ppm) and other trace metals, none were leached in significant quantities during a prolonged three-week-long leach test. The wide spread use of crushed aggregate in road and rail bed construction throughout Bannock County may be providing a source of readily leachable sulfate to local groundwater.

Sulfate and chloride levels in groundwaters from both the Pocatello Municipal Aquifer and Pocatello Creek are correlated in very similar proportions. The coupled sulfate-chloride enrichments observed in these waters implies a related source for both. Road salt is a likely origin for the chloride considering that sodium and chloride concentrations in these waters also show a direct correlation.

Elevated sulfate in groundwater associated with aggregate and the coupled sulfate-chloride trends may be related by a single process. It is hypothesized that infiltration of salt derived, chloride-rich water along roads in the spring and dissolution of soluble sulfate in roadbed aggregate as this water percolates to the water table is the mechanism by which the coupled chloride-sulfate enrichments originate.

Modeling of some of the possible chemical reactions which may be involved with sulfate addition from aggregate leaching revealed that dissolution/precipitation reactions alone can not

account for the observed groundwater chemistries. Ion-exchange with clays is likely to be an important process and would explain the deficit of sodium concentrations in Pocatello Creek groundwaters. Work is continuing to test the above hypotheses and to understand the nature of the chemical processes involved.

Acknowledgments

The authors gratefully acknowledge Idaho State University for laboratory space and equipment used in the analyses presented here. We would also like to thank the City of Pocatello for its support and cooperation in the ongoing hydrogeologic study of their municipal aquifer. Special thanks are due to Mr. H. Hildreth, Mr. M. Grady, Bannock County, and the many other residents of Pocatello who have allowed us to sample their well waters.

Ken Magleby and Glenn Griffith of the State Dept. of Transportation along with Larry Robson of Bannock Paving provided much useful information about the aggregate pile at the Highway Ponds.

We are also grateful to Pam French and Jim Severson from FMC for providing information about the composition and chemical characteristics of FMC slag.

References Cited

Allison, J.D., Brown, D.S., and Novo-Gradac, K.J., 1991. MINTEQA2/PRODEFA2, a geochemical assessment model for environmental systems: version 3.0 user's manual, EPA/600/3-91/021.

CH2M-Hill, 1992. Site assessment report, Phase I, Pocatello Creek Landfill Hydrogeologic Investigation.

Link, P.K., 1982. Idaho-Wyoming thrust belt: regional geology; Northwest Geology, v. 11, p. 1-12.

Link, P.K., Jansen, S.T., Halimdihardja, P., and Zahn, P., 1987. Stratigraphy of the Brigham group (late Proterozoic-Cambrian), Bannock, Portneuf, and Bear River Ranges, Southeastern Idaho; Thirty-eighth Field Conference-1987, Wyoming Geological Association Guidebook, p. 133-148.

Noble, R., 1993. Idaho State University Geology Colloquium on geotechnical and hydrogeologic results of the Pocatello Creek Landfill site investigation, Spring, 1993, Pocatello, Idaho.

Ore, H.T., 1982, Tertiary and quaternary evolution of the landscape in Pocatello, Idaho, area; Northwest Geology, v. 11, p. 31-36.

Plummer, N.L., and Back, W., 1980. The mass balance approach: application to interpreting the chemical evolution of hydrologic systems, American Journal of Science, vol. 280, p. 130-142.

Plummer, N.L., Parkhurst, D.L., and Thorstenson, D.C., 1983. Development for reaction models for groundwater systems, Geochim. Cosmochim. Acta 47, p. 665-686.

Plummer N.L., Prestemon, E.C., and Parkhurst, D.L., 1991. An interactive code (NETPATH) for modeling net geochemical reactions along a flow path, U.S. Geological Survey, Water-Resources Investigations Report 91-4078.

Trimble, D.E., 1976. Geology of the Michaud and Pocatello quadrangles, Bannock and Power Counties, Idaho: U.S. Geological Survey Bulletin 1400, 88p.

Hydrogeology, Waste Disposal, Science and Politics
Proceedings 30th Symposium
Engineering Geology and Geotechnical Engineering, 1994

Interpretation Of Shallow Seismic Refraction Data Using Raytracing Inversion: A Simple Example From A Groundwater Resource Study In Pocatello, Idaho

J. R. Pelton
M. E. Dougherty
J. A. Welhan*

Center for Geophysical Investigation of the Shallow Subsurface
Boise State University, Boise, Idaho 83725

*Idaho Geological Survey, Branch Office at Idaho State University
Pocatello, Idaho 83209

ABSTRACT

Raytracing inversion of seismic refraction data acquired on the northeast side of the Portneuf River valley at the base of Red Hill in Pocatello shows that the thickness of Quaternary and Tertiary sediments above much older quartzite bedrock is 46-53 m. This estimate, which was derived independently of any borehole data, is consistent with the lithologic log of a recently drilled monitoring well (PMW-3) drilled about 1 km northwest of the seismic line. The water table is horizontal at a depth of 22-29 m beneath a gently rising topography (20 m/km to the southeast) in the vicinity of the seismic line. The top surface of the quartzite bedrock is either horizontal or dips slightly (1.2 degrees) to the southeast. Unsaturated sediments are characterized by a strong vertical velocity gradient (13-16 s^{-1}) probably caused by compaction of the near-surface materials. Seismic P-velocities are estimated as follows: unsaturated sediments (320-780 m/s), saturated sediments (1,670 m/s), and quartzite bedrock (2,950-3,050 m/s).

INTRODUCTION

The seismic refraction method is a well-established technique used to image subsurface interfaces separating materials of strongly contrasting seismic velocity (a recent tutorial is in Lankston, 1990). Although the method has been applied to a wide variety of problems, it has made its greatest contribution in two geophysical specialties which aim to map the Earth's uppermost structure at vastly different scales: engineering or groundwater seismology (upper 0.2 km), and crustal seismology (upper 50 km). The principles and field procedures of both specialties are similar, but crustal seismologists have developed interpretation strategies which take advantage of powerful computer resources historically not available in most geotechnical or hydrogeological consulting firms. As a result, refraction studies of shallow structure rely on analyses that have the advantage of being computationally simple, but suffer from disadvantages such as the inability to use later arrivals or velocity gradients, and the lack of well-defined procedures for statistical esti-

mation of the resolution and variance of model parameters. Recent improvements in desktop computer technology have changed this situation, so that it is now appropriate to investigate the additional capabilities offered by the tools of the crustal seismologist.

We present here an example of seismic refraction interpretation of depth to bedrock using raytracing inversion based on a two-dimensional subsurface model. The inversion algorithm was developed by Zelt and Smith (1992) and is commonly used in crustal seismology. It provides estimates of the random error in model parameters that result from timing errors, and also investigates the degree to which individual parameters are free from the well-known trade-off between depth and velocity. Our data set consists of seismic travel times from a standard refraction line acquired in Pocatello, Idaho as part of a groundwater resource study. The refraction work was undertaken to define the thickness of water-bearing Quaternary and Tertiary sediments underlain by relatively impermeable Paleozoic and Precambrian bedrock. Figure 1 shows the location of the refraction line on the northeast side of the Portneuf River valley at the base of Red Hill and near the Idaho State University campus.

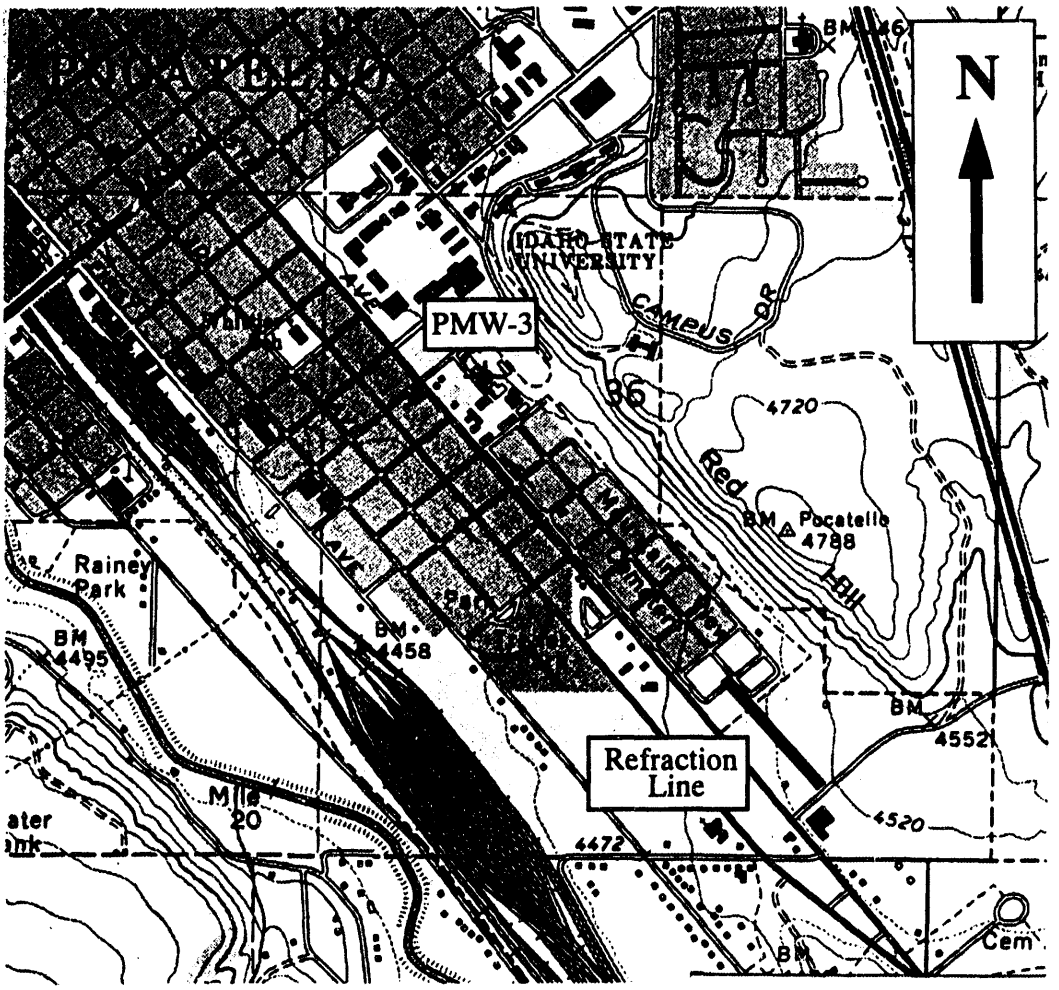


FIGURE 1. Location map showing study area. Base map is USGS Pocatello South Quadrangle (7.5 Minute Series, 1971, Photoinspected 1974). Scale given by length of section lines. Refraction line indicated by heavy black line at southeast end of Mountain View Cemetery. A nearby monitoring well (PMW-3 shown as black dot with cross) was drilled in 1993 (after the acquisition and interpretation of the refraction data) and encountered massive red quartzite at a depth below land surface of about 40 m.

DATA ACQUISITION

A standard colinear seismic refraction line was deployed with 48 geophone stations spaced at intervals of 5 m for a total receiver spread length of 235 m. Topography along the line rises gently from northwest to southeast at a rate of about 20 m/km. Two shots were fired at each end of the receiver spread (in-line end offsets of 0 m and 50 m), and one shot was fired in the middle, for a total of five shots. The seismograph was a 48-channel digital instantaneous floating point instrument (12-bit effective resolution) and geophones were 10-Hz natural frequency vertical velocity transducers. Shots were 1-lb charges of Kinestik detonated with seismic quality blasting caps in gravel-packed auger holes between 1-2 m deep. All field work was carried out over two days in late May 1993.

INTERPRETATION OF TRAVEL-TIME CURVES

First-arrival travel times picked with an interactive computerized picking program are plotted in Figure 2 as a function of receiver distance measured along the profile. The inference of earth

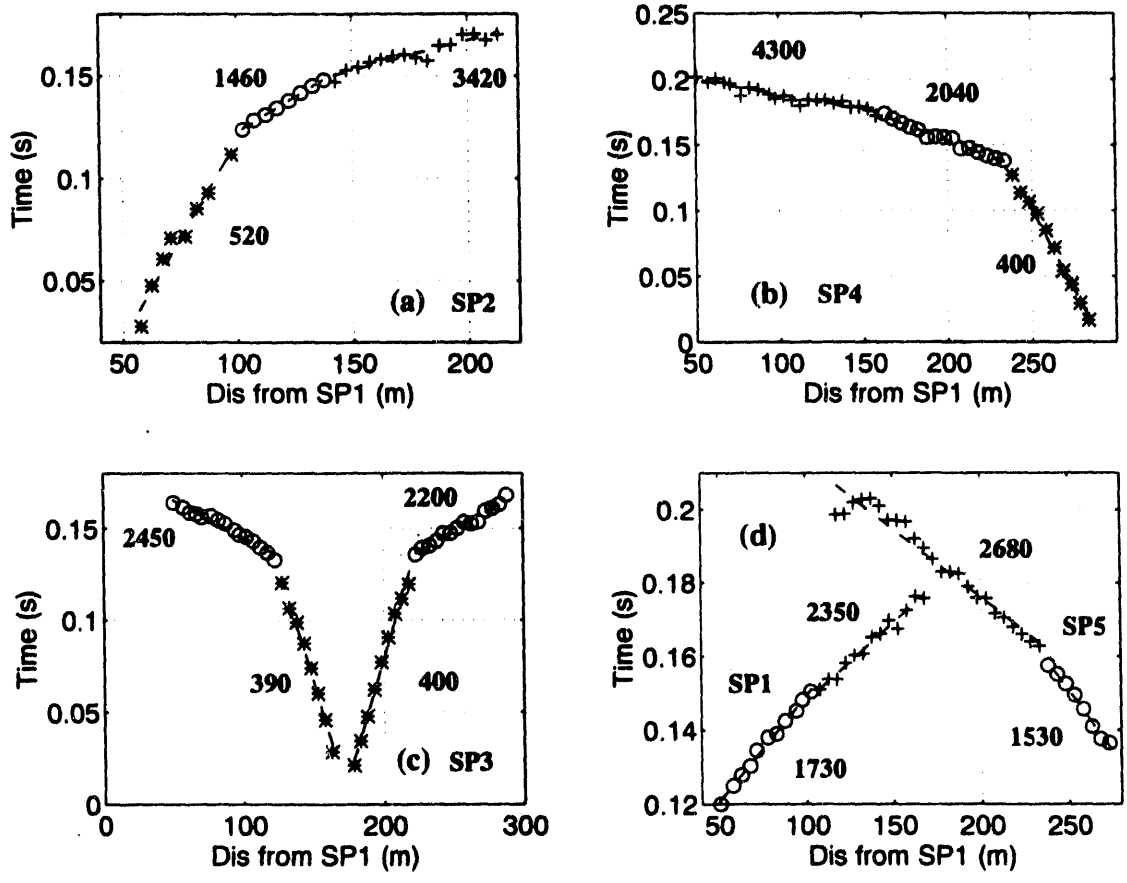


FIGURE 2. First-arrival travel-time plots for: (a) shotpoint 2 at northwest end (offset 0 m); (b) shotpoint 4 at southeast end (offset 0 m); (c) shotpoint 3 in middle of receiver spread; (d) shotpoints 1 and 5 at northwest and southeast ends, respectively (offset 50 m). Arrivals are interpreted to represent different seismic waves as follows: asterisks are turning rays in the upper layer of unsaturated sedimentary materials; open circles are head waves from the water table; crosses are head waves from the massive red quartzite encountered in monitoring well PMW-3 and also in outcrops on nearby Red Hill. Apparent velocities are in m/s and are computed by least-squares straight-line fits to the travel-time data.

structure from these data requires correlation of different branches of the travel-time curves with the arrival of different types of seismic waves. In problems characterized by sediments over bedrock, the two interfaces which usually dominate first-arrival travel times are the boundary between unsaturated and saturated sediments (i.e., the water table) and the boundary between bedrock and the overlying saturated sediments. Thus, a simple two-layer over a half-space model is suggested in which the first arrivals are (in order of increasing time and increasing distance from the seismic source): (i) the direct P-wave through the unsaturated sediments; (ii) the P-head wave from the water table; and (iii) the P-head wave from the top of the bedrock. The travel-time curves in Figure 2 support the existence of all three of these waves at reasonable apparent velocities. The discrepancies between the apparent velocities for similar arrivals on different shot records can be explained by dip, the effects of near-surface topography and velocity irregularities, timing errors, and incorrect choice of crossovers points between arrivals. In addition, slight curvature in the direct P-wave curves (difficult to see in Figure 2) suggests that the unsaturated sediments are characterized by a vertical velocity gradient (velocity increasing with depth), probably caused by compaction. A vertical velocity gradient will cause rays representing the direct P-wave to be curved and turn at a depth depending on the source-receiver distance.

RAYTRACING INVERSION

Raytracing is the computation of seismic wave paths and travel times through an earth model using Snell's law. In geophysical parlance, raytracing solves the forward problem of computing the travel time between source and receiver for a seismic wave in a defined velocity structure. Geophysical interpretation requires solution of the corresponding inverse problem, wherein the travel-time data are measured, and the objective is to infer the velocity structure from the travel times. Raytracing inversion solves the inverse problem by perturbing an initial velocity model in a systematic way until theoretical travel times (computed by raytracing) match observed times in some best-fit sense. The velocity model which provides the best fit to the seismic travel times and which also satisfies other known criteria such as geologic plausibility is considered to be the most likely interpretation.

As mentioned above, we apply here an iterative least-squares raytracing inversion algorithm developed by Zelt and Smith (1992). Although this algorithm is formulated for the interpretation of crustal refraction profiles on length scales of tens to hundreds of kilometers, it is easily adapted for use on engineering and groundwater refraction data. A "layer-stripping" method is the best way to proceed, in which one first inverts for the parameters describing the first layer (i.e., the unsaturated sediments), and then those parameters are fixed during inversion for the parameters of the second layer, and so on. In our example, we proceed as follows, using the entire data set from all five shots (180 first-arrival travel times):

- A simple starting model is formulated based on the initial interpretation of the travel-time curves (Figure 2) and raytracing tests; no inversions are performed at this stage. The velocity of the near-surface sediments is set equal to the average of the velocities computed along the slant path from each buried source to the nearest receiver (within 10 m).
- Parameters which control the velocity gradient in the unsaturated sediments are allowed to vary. The water table is constrained to be horizontal but its depth below a horizontal datum and the velocity of the unsaturated sediments just above the water table are allowed to vary.

After inversion, values on the diagonal of the resolution matrix are nearly unity, indicating that no significant averaging of the true model parameters is represented in the inverse solution (Menke, 1989). In other words, the travel-time data are sufficient to resolve the trade-off between velocity in the unsaturated sediments and their thickness.

- The velocity of the saturated sediments, assumed uniform both laterally and vertically, is allowed to vary. The top surface of the bedrock is constrained to be horizontal, but the depth to bedrock below a horizontal datum is allowed to vary. Again, the resolution matrix indicates that the travel-time data are sufficient to resolve the expected trade-off between velocity of the saturated sediments and their thickness.
- Depth to bedrock below the horizontal datum and bedrock velocity are allowed to vary. At this point in the inversion, adjustment of these parameters has little impact on the goodness of fit to the observed data.
- An additional node is inserted in the model to permit the top of the bedrock to dip either to the northwest or southeast, and the bedrock velocity is also allowed to vary. This additional complexity does result in a dipping bedrock surface and a marginal improvement in the goodness of fit, but the improvement is not statistically significant (see discussion below).

The final earth models with traced rays, observed first-arrival travel times, and calculated first-arrival travel times are shown in Figure 3 for both a horizontal and dipping upper bedrock surface.

DISCUSSION

Our interpretation indicates that the unsaturated sediments are 22-29 m thick under the refraction line and are characterized by a vertical velocity gradient of 13-16 s^{-1} which must be a result of near-surface compaction. Although P-velocities for the unsaturated materials are within normal limits (320-780 m/s), the gradient is large and needs to be checked for consistency with amplitude information for the direct arrivals. The velocity estimate for saturated sediments is a very reasonable 1,670 m/s. In another test (not described above), we inserted an additional node in the model to allow the water table to dip, but there was no tendency for the inversion process to force a non-zero dip on the water table.

The first-arrival travel-time data are consistent with both a horizontal and dipping (1.2 degrees southeast) upper bedrock surface beneath the refraction line. The fit to the observed travel times is somewhat better for the dipping bedrock model, but this improvement may be the result of random error in the travel times. To see this, a statistical model is constructed in which the discrepancy between any observed travel time and the corresponding theoretical travel time (computed by raytracing) is assumed to be a normally distributed random variable. The sum of the squared discrepancies (with each squared discrepancy normalized by its variance) is proportional to a random variable with a chi-square (χ^2) distribution. The χ^2 for the horizontal and dipping bedrock models is 16.4 and 15.6, respectively, each with 178 degrees of freedom. Using the statistical F test, we conclude that the improvement in fit (smaller χ^2) shown by the dipping model can be reasonably attributed to random error in the observed travel times. Thus, we have no compelling evidence that the bedrock is other than a horizontal interface. We note in passing that χ^2 is much greater than unity because only good quality travel-time picks have been included

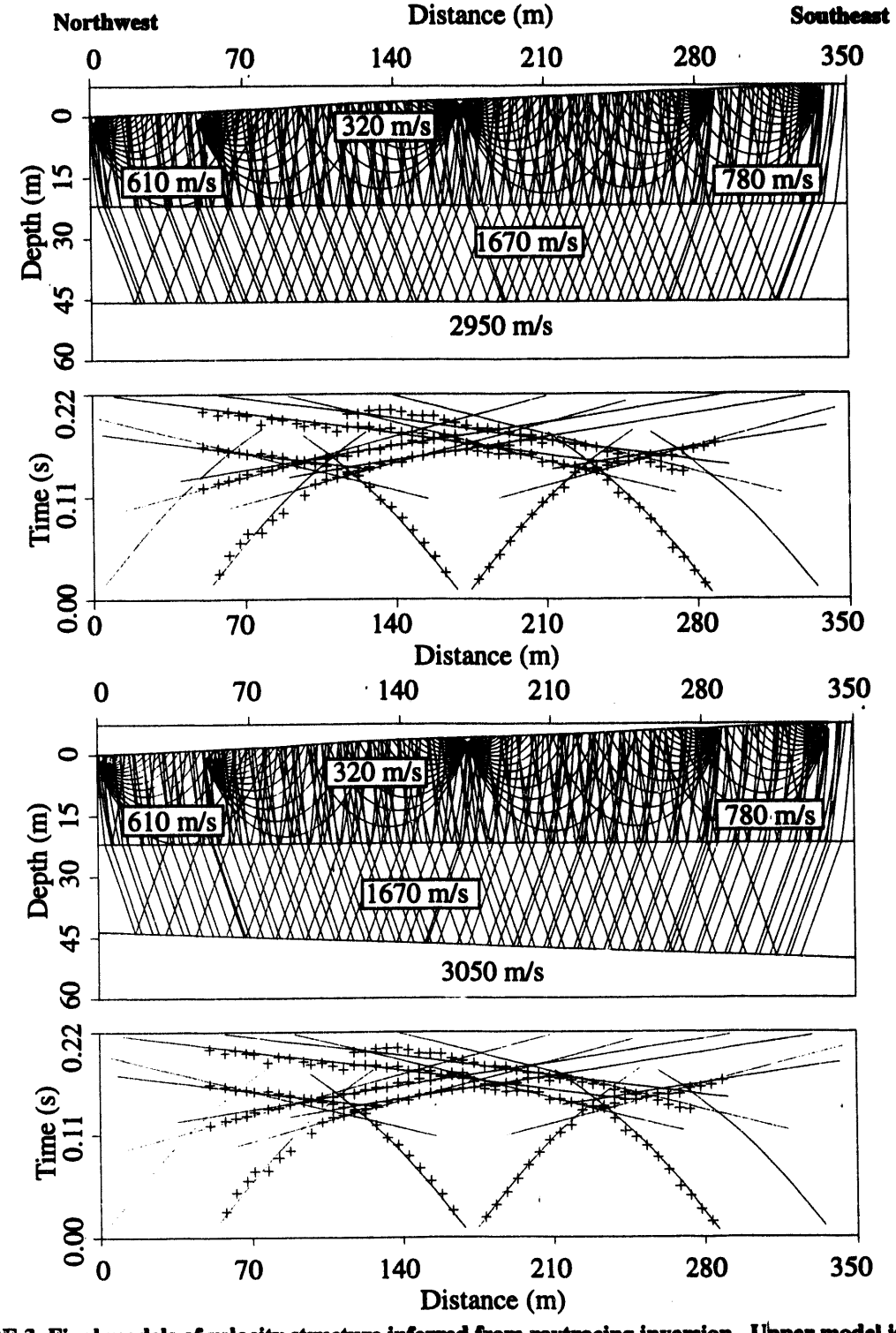


FIGURE 3. Final models of velocity structure inferred from raytracing inversion. Upper model is horizontal bedrock model, lower model is dipping bedrock model. Rays are shown as straight or curved lines emanating from shallow shotpoints. Velocities are as indicated on cross sections. Observed travel times are crosses with theoretical travel times (computed by raytracing) shown as solid lines. Vertical exaggeration is about 2.

in the inversion, and the rays are sampling more heterogeneities than have been included in the model (Zelt and Smith, 1992).

Both bedrock models (Figure 3) indicate that the bedrock is 44-46 m below the ground surface at the northwest end of the refraction line. A recently drilled monitoring well (PMW-3) located about 1 km to the northwest (Figure 1) encountered massive red quartzite at a depth of about 40 m. This suggests that we correlate the quartzite encountered in PMW-3 with the bedrock refractor; the velocity near 3,000 m/s is entirely consistent with this correlation.

Finally, we note that raytracing inversion yields advantages in the interpretation of the Pocatello refraction data when compared to standard techniques such as the reciprocal method. In particular, it enables us to characterize the unsaturated sedimentary layer with a vertical velocity gradient, it provides the means to investigate the trade-off between velocity and layer thickness, and it lends itself to statistical evaluation of the results.

ACKNOWLEDGMENTS

We are grateful to the numerous helpers who participated in the Pocatello field work, and to the caretakers of Mountain View Cemetery for their assistance. Boise State University Center for Geophysical Investigation of the Shallow Subsurface contribution 0028.

REFERENCES

Lankston, R. W., High-resolution refraction seismic data acquisition and interpretation, in *Geotechnical and Environmental Geophysics*, S. H. Ward, editor, Investigations in Geophysics No. 5, v. 1, Society of Exploration Geophysicists, Tulsa, Oklahoma, 45-73, 1990.

Menke, W., Geophysical data analysis: discrete inverse theory, International Geophysics Series, v. 45, Academic Press, San Diego, California, 289 pp., 1989.

Zelt, C. A., and R. B. Smith, Seismic traveltime inversion for 2-D crustal velocity structure, *Geophys. J. Int.*, 108, 16-34, 1992.

Hydrogeology, Waste Disposal, Science and Politics
Proceedings 30th Symposium
Engineering Geology and Geotechnical Engineering, 1994

FRAZIER HALL: THE FOUNDATION FAILURE THAT DIDN'T

by
Lee Robinson
Professor of Engineering
Idaho State University

Abstract

Frazier Hall is the oldest building on the Idaho State University campus--built before scientific foundation design was common. Its footings were clearly under designed, compared with modern practice. In fact, conventional analysis of the bearing capacity of two footings of this historic building indicate a failure condition. However, this structure is 60 years old and the foundation is still functioning. Possible reasons for the discrepancy between the analysis results and reality are posed and evaluated. This exercise gives some valuable insights into the process of foundation analysis and design.

A Historic Building

Frazier Hall was built in 1924 as the Main Building of the Idaho Technical Institute (later to become Idaho State University). The building housed a library, administrative offices, and a 5800 square-foot theater. Today, the building serves as the dramatic theater facility at I.S.U., and houses the Drama Department offices. The old library area is now a "little theater," used for small dramatic productions, and the large theater is still in use.

The building underwent remodeling in the 1940's when a balcony was added to the main theater, and again in 1993 when the south edge of the building was extended to provide handicap access with an elevator (1). Cracks were observed in walls and on-grade floor slabs early in the life of the building and have been patched several times during its tenure. The lobby floor slab was replaced during the 1940's renovation, apparently because of cracking.

In 1985 a study (2) was done to assess the structural and foundation conditions of the building to verify the feasibility of continued use with renovation. That study showed that although the concrete was weak (1410 to 1710 psi compressive strength) enough reserve capacity was designed into the structural frame that it is sound. Footing settlements on the order of 1-1/4 to 1-1/2 inches were reported. Safety of the footings with respect to bearing failure was felt to be satisfactory, since the structure had stood successfully for more than 50 years.

Predicted Failure vs. Historic Performance

The structure is of reinforced concrete construction, with a very heavy framework by modern standards supported on relatively small spread footings. This results in some very heavy foundation loads. The heaviest loads occur on two basement wall footings,

Estimated Soil Strength

Shear tests were not performed as a part of geotechnical investigations for Frazier Hall. Shear tests on similar sites on the I.S.U. campus in the author's file indicate a typical friction angle of 28 to 30 degrees for the silt soil beneath the building, and slight cohesion of about 150 psf. Conventionally, the small cohesion of the silt is neglected, on the basis that it is not permanent. Analysis with a friction angle of 32 degrees, the maximum recorded in our files for Pocatello silts, did not result in a significant increase in friction angle. However, including a cohesion of 150 psf increased the factor of safety to about 1.2, using the UBC estimated loads.

In the on-site silts, the cohesion results from very weak carbonate cementation and capillary bonds. These mechanisms act so long as the soil is not wetted to above about 90 to 95 percent saturation. Since groundwater levels are very deep at the site, the only realistically possible way the soils beneath the footings could become wet, is from over-irrigation or broken water utilities. The probability of such events wetting a significant zone beneath these deep footings is unlikely.

Boundary Conditions in Conventional Bearing Computations

To examine the effects of boundary conditions, the footings were modelled using an elastic finite element method with the computer program ANSYS (6). The elastic modulus of the soil for use in the model was computed from consolidation test data using a method proposed by McCarthy (7). This method of selecting an elastic modulus is appropriate for estimating settlements, but not for predicting failure. The settlements predicted by the finite element model (about 2 inches) compare favorably with those observed and predicted by consolidation theory (about 1-1/2 inches). The elastic model also allows the soil to experience tensile stresses, which becomes a significant error at or near failure. Within these limitations, it is still possible to draw some qualitative conclusions about the effects of boundary conditions.

The results of the finite element analysis are summarized by stress contour plots in the figures below. In comparing these plots, note that the contour interval set by the software varies from plot to plot. To make it easier to see the relatively small displacements, values 10 times the actual values are plotted. The analyses for both footings were made for a wall load of 15 kips per foot, intermediate between the actual loads to allow direct comparison of the results for the two walls.

The Central Basement Wall--The central basement wall is embedded 2.0 feet below the top of the basement floor slab. The finite element solution for this case, together with the Boussinesq case is shown in Fig. 1. The average vertical stress beneath the footing is plotted as a function of depth for these cases as lines

loaded at an estimated 4500 and 5300 psf. Conventional Terzaghi-Vesic bearing capacity analysis (3) predicts failure of each of these footings, at factors of safety of 0.76 and 0.57, respectively.

Several reasons have been suggested for the apparent contradiction between the analysis and performance. These include

(1) Estimated loads may be conservative;
(2) Redistribution of loads by the frame may have lowered the actual bearing pressure;
(3) Soil strength may have been underestimated.
(4) Boundary condition effects not considered by conventional theory may have resulted in under predicting failure capacity, such as embedment of the footings, and backfill against the west basement wall.

Each of these factors are addressed below.

Estimated Loads

The loads consist of about 70 to 76 percent dead load, and 20 to 24 percent live load estimated from Uniform Building Code (UBC) tables (4), and Idaho snow load tables (5). On the west basement wall, about 1/3 of the live load is snow load, whereas snow load is insignificant on the east wall. Based on risk levels assumed in the snow load tables, there is about a 2/3 probability that the design snow has occurred or been exceeded once during the building's existence. The remaining live load is largely from the stage of the main theater, the seating of the little theater, and audiences leaving and entering the theaters. These loads are believed to be quite conservative since performances are never scheduled simultaneously in both theaters simultaneously, and the audience cannot be in the halls and the seating at the same time. We estimate that the actual maximum live load is probably about 1/2 to 2/3 of the total predicted by UBC. This would result in at least a 16 percent under-estimate of the bearing capacity computed using UBC live load.

Load Redistribution

Several lightly loaded concrete spur walls intersect the heavily loaded walls. Observed cracks in these spur walls suggest that the intersections acted as "Tee" columns, with foundation loads redistributed perhaps 3 feet or so down the spur walls. Lightly loaded walls at the ends of the corridors act in a similar fashion. On this basis, we estimate that load redistribution has increased the effective footing area by about 20 percent, on each of the two heavily loaded walls. This would result in about a 20 percent over-estimate of the bearing capacity, for computations based on the direct bearing area.

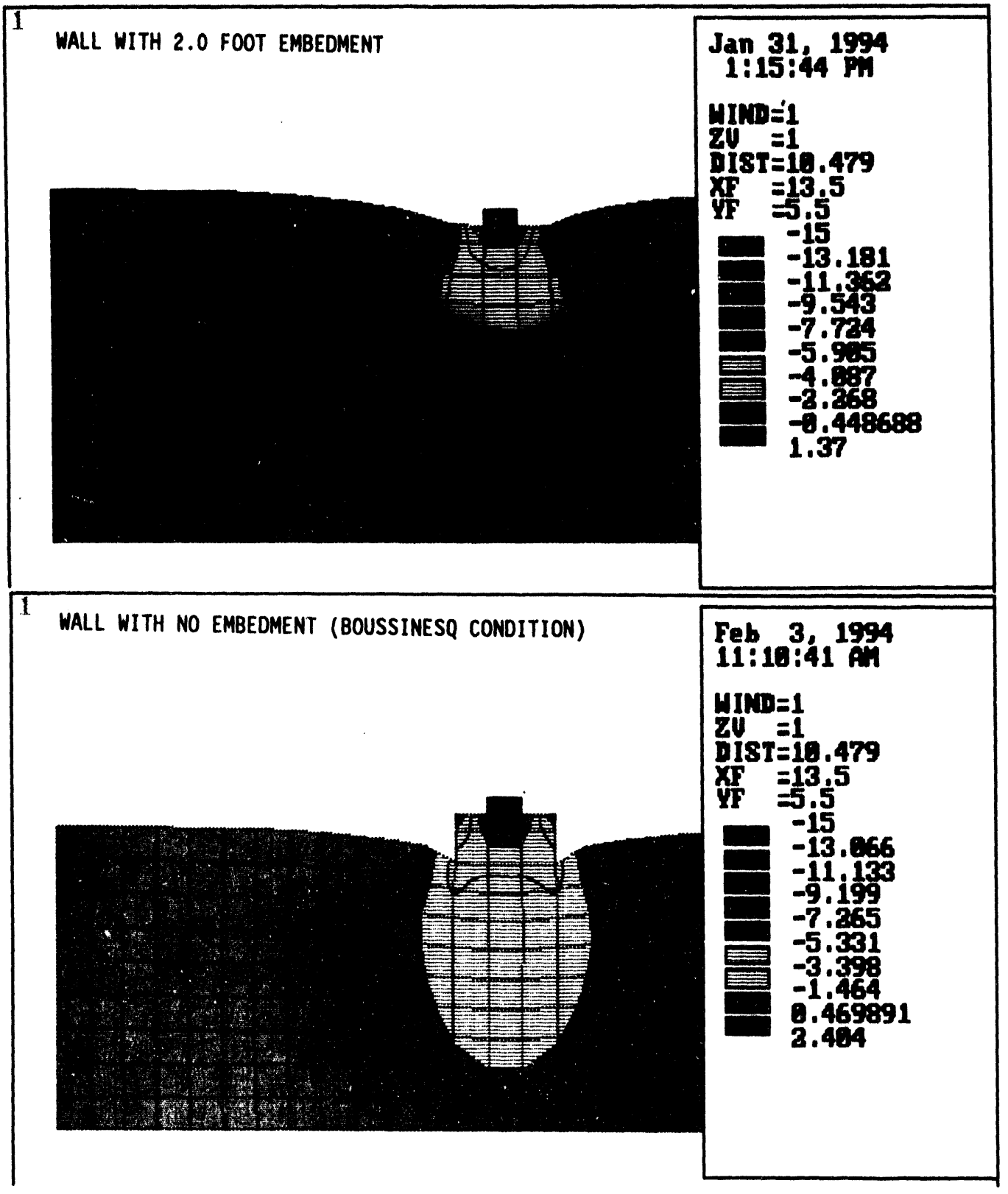


Fig. 1--Vertical stress beneath the central basement wall (embedded 2 ft) and for no embedment (Boussinseq condition). Displacements are shown multiplied by 10.

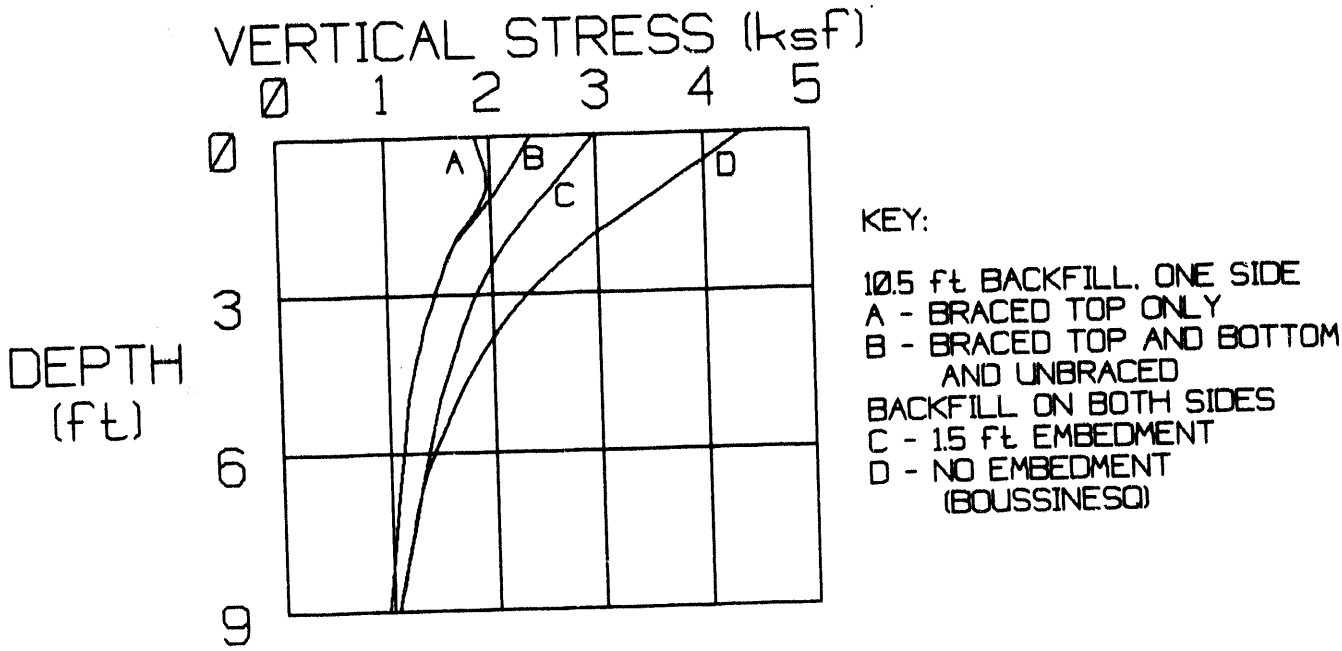


Fig. 2--Average vertical stress beneath wall footings for 15 kip/ft wall loads for various boundary conditions.

C and D on Fig. 2. Note that the bearing pressure at the base of the embedded footing is predicted to be about 67 percent that of the unembedded case. If we assume this ratio applies to the Terzaghi analysis, a depth correction factor of 1.43 results. In comparison, Vesic uses the Brinch-Hansen correction factor which computes to be 1.14. In comparison, Meyerhof's depth correction factor computes as 1.4, closely corresponding to the finite element value. On this basis, it appears that the Brinch-Hansen correction factor used in our original bearing capacity analysis appears to be somewhat conservative for this case. Use of the larger depth correction in the analysis would result in an increase in predicted bearing capacity of about 20 percent.

The West Basement Wall--The west basement wall has backfill against one side and a concrete floor on the other. If the concrete floor were strong enough and well enough bonded to the wall and footing, the two basement wall footings and the slab would act as a mat foundation. This possibility was analyzed as shown in Fig. 3. Notice the high vertical tensile stress in the floor slab at the edge of the footing--well above the tensile strength of the concrete. Thus, the slab is predicted to crack at the edge of the footing and is not expected to support any of the wall loads. Indeed, the floor slab of the actual structure has cracked at the edge of the footing as predicted.

This wall is well braced at its top and partially braced at its base by the cracked basement floor slab. We modelled the wall for the fully braced top and bottom (at-rest condition), and the

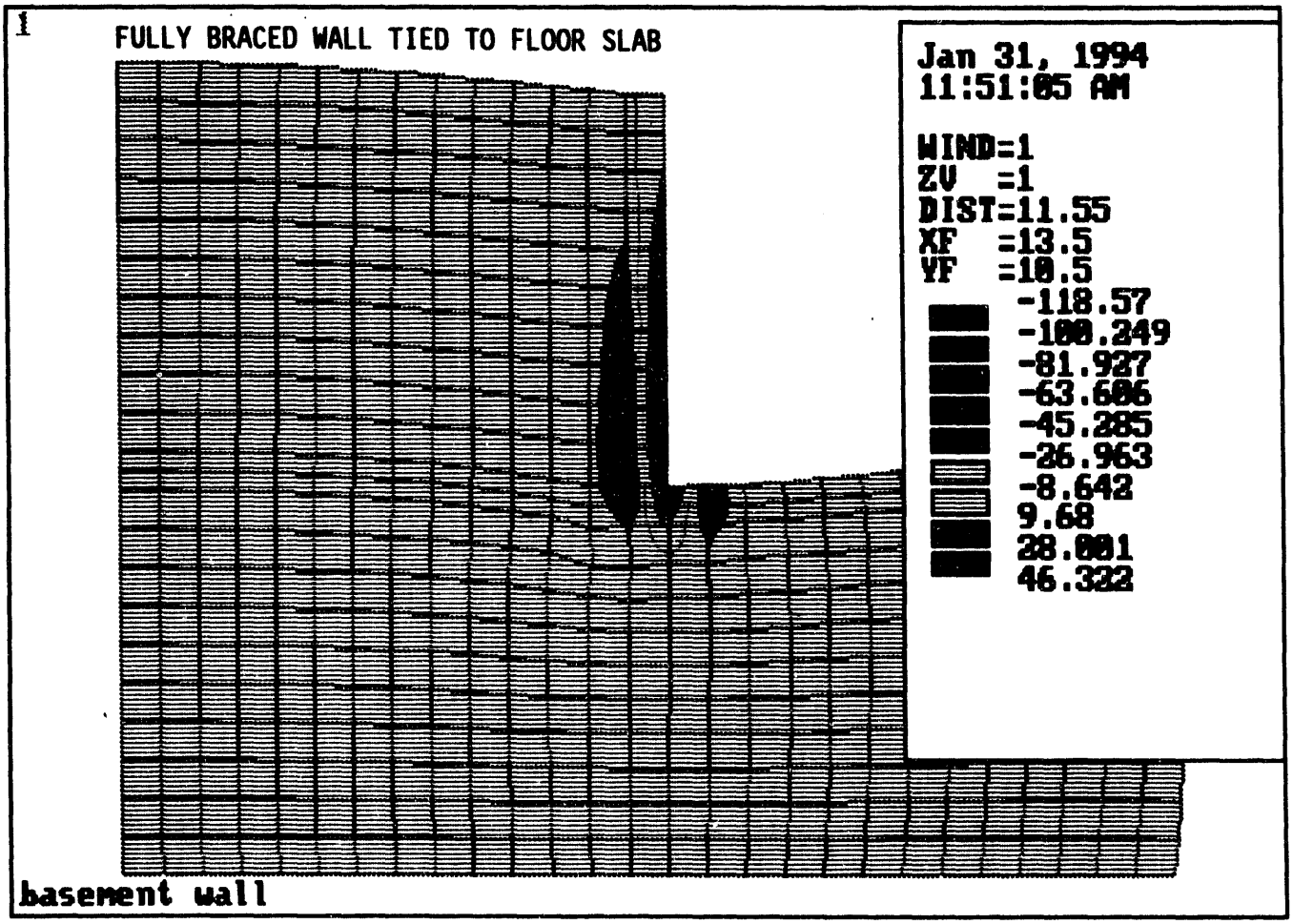


Fig. 3--West basement wall, with concrete floor acting monolithically with the footing.

fully braced at the top and unbraced at the bottom (arching condition), as shown in Fig. 4. The actual condition with partial bracing at the bottom would be expected to fall between these two limiting cases. Because of the bracing, this wall would not be expected to develop the active condition, shown for comparison in Fig. 5.

For both conditions shown in Fig. 4, some of the wall load is transferred to the backfill by friction between the wall and the backfill, which will reduce the effective vertical pressure beneath the footing. This results in an increased vertical stress to the left of the wall in comparison to the cases shown in Fig. 1, but a reduced vertical stress beneath the footing. This effect is shown in Fig. 2. on curves A and B. The fully braced and unbraced cases result in essentially the same vertical stresses beneath the footing, but the wall braced at the top has slightly lower vertical stress immediately beneath the footing.

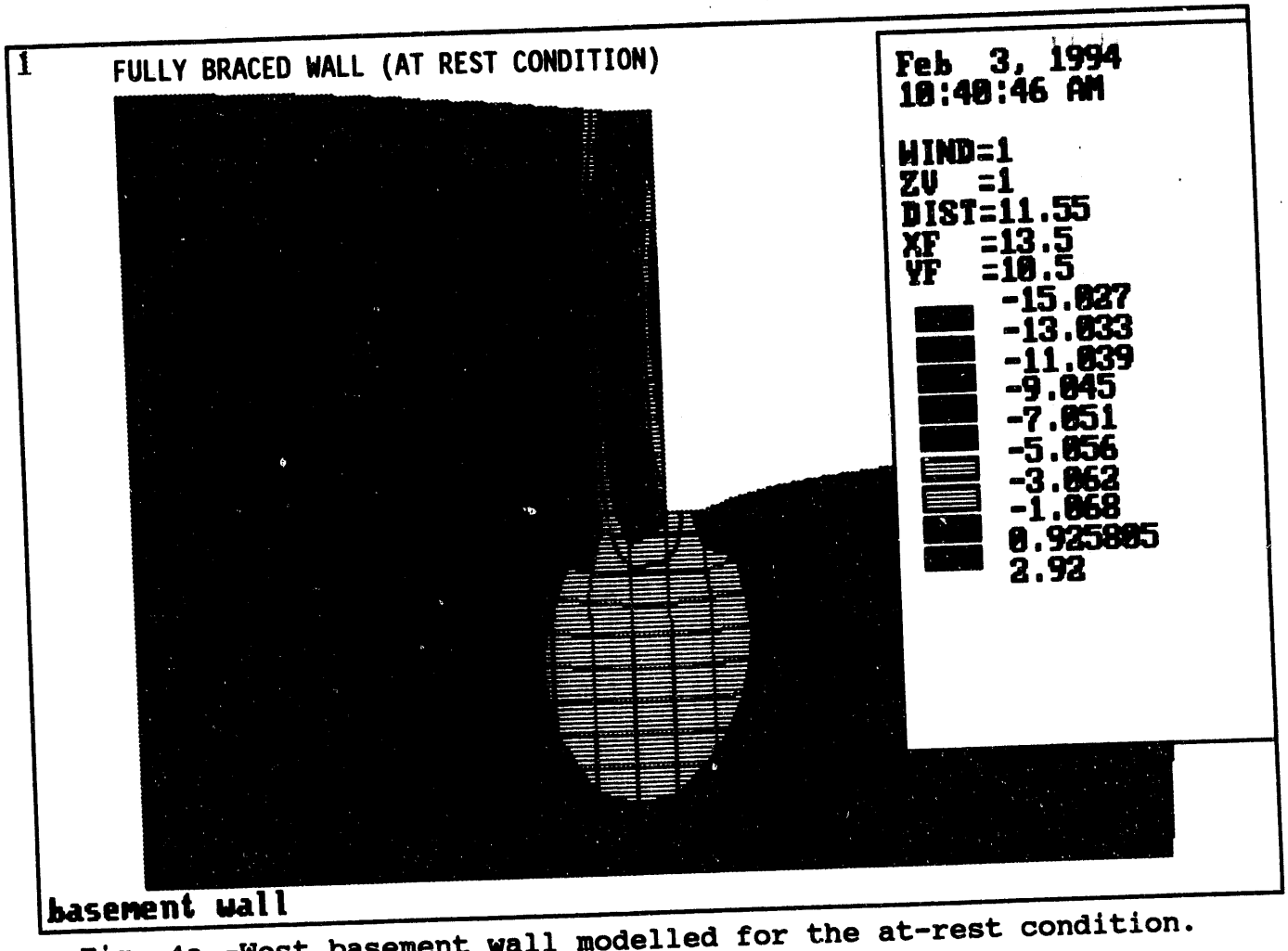


Fig. 4a--West basement wall modelled for the at-rest condition.

The cracked floor slab would be expected to allow some lateral movement. According to the finite element model, a lateral displacement of only about 0.1 inch is sufficient to reach the arching condition of Curve B. The appearance of cracking in the floor slab suggests that there has been sufficient displacement to achieve the arching condition.

The conventional application of bearing capacity theory to a wall with backfill ignores the effect of the additional backfill outside of the wall, but does reduce the bearing capacity for the lesser embedment of the two sides (2 feet, in this case). If we again assume that the relative reduction in effective bearing pressure from the finite element solution applies, an increase in bearing capacity of about 25 percent results from the backfill effect. If the effect of the conservatism of the Brinch-Hansen depth correction is included, an increase of about 55 percent results.

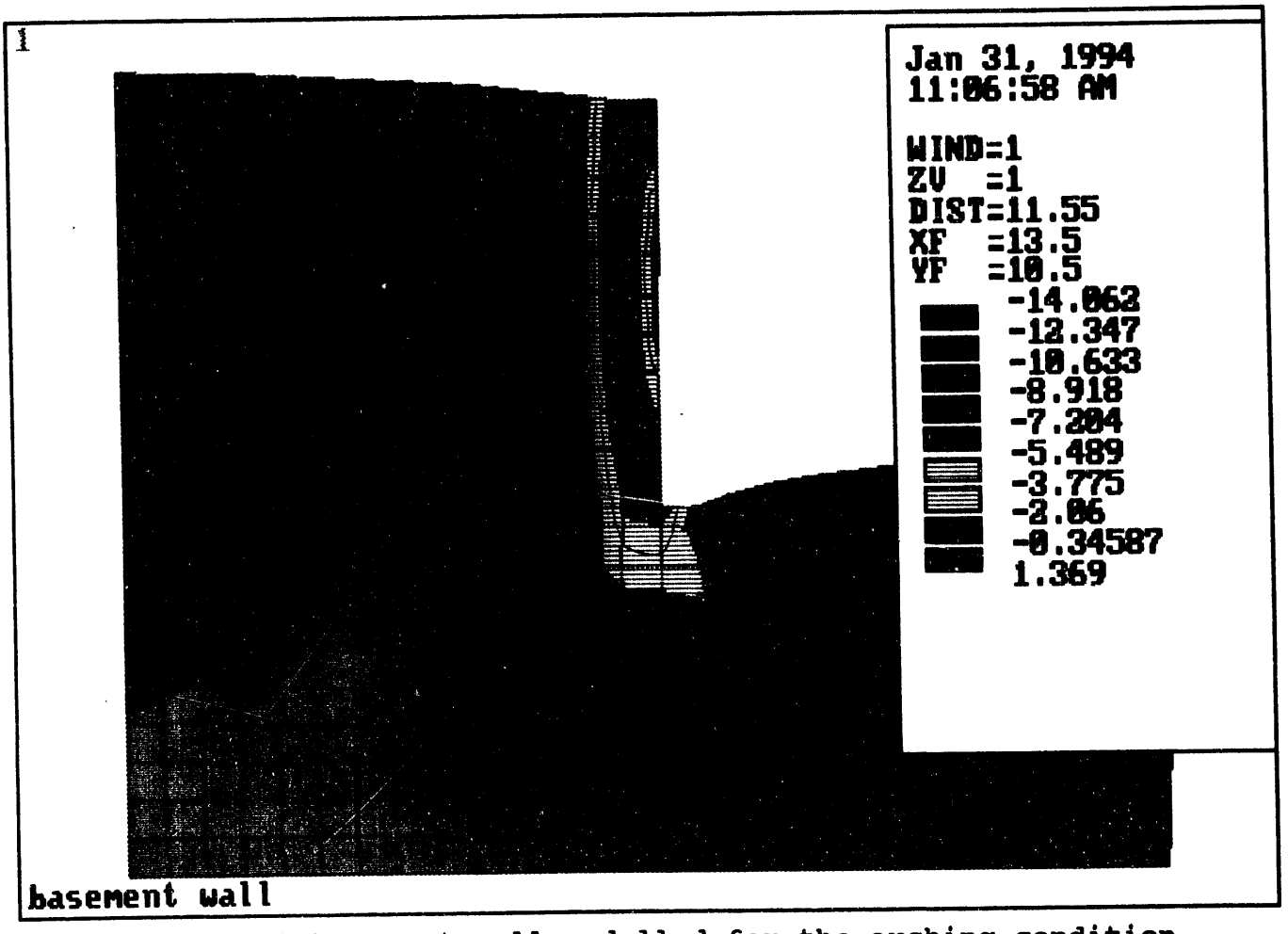


Fig. 4b--West basement wall modelled for the arching condition.

Conclusions

If the effect of soil cohesion is neglected, the combined effects of overestimated wall loads, load redistribution, and unaccounted for boundary conditions, results in the computed bearing capacity increasing to about 0.9 for the central basement wall, and to about 1.4 for the west basement wall. In short, the west wall is relatively safe, but the central wall would be in danger of failure, if the soil cohesion were lost.

If soil cohesion is included, the computed factors of safety for the respective walls increase to about 1.4 and 2.3. This means, that both walls are adequately safe, so long as the soil cohesion exists. Wetting of the subsoils beneath the footings, with subsequent loss of cohesion must be considered a relatively unlikely event, since it has not occurred during the 60 years the building has existed.

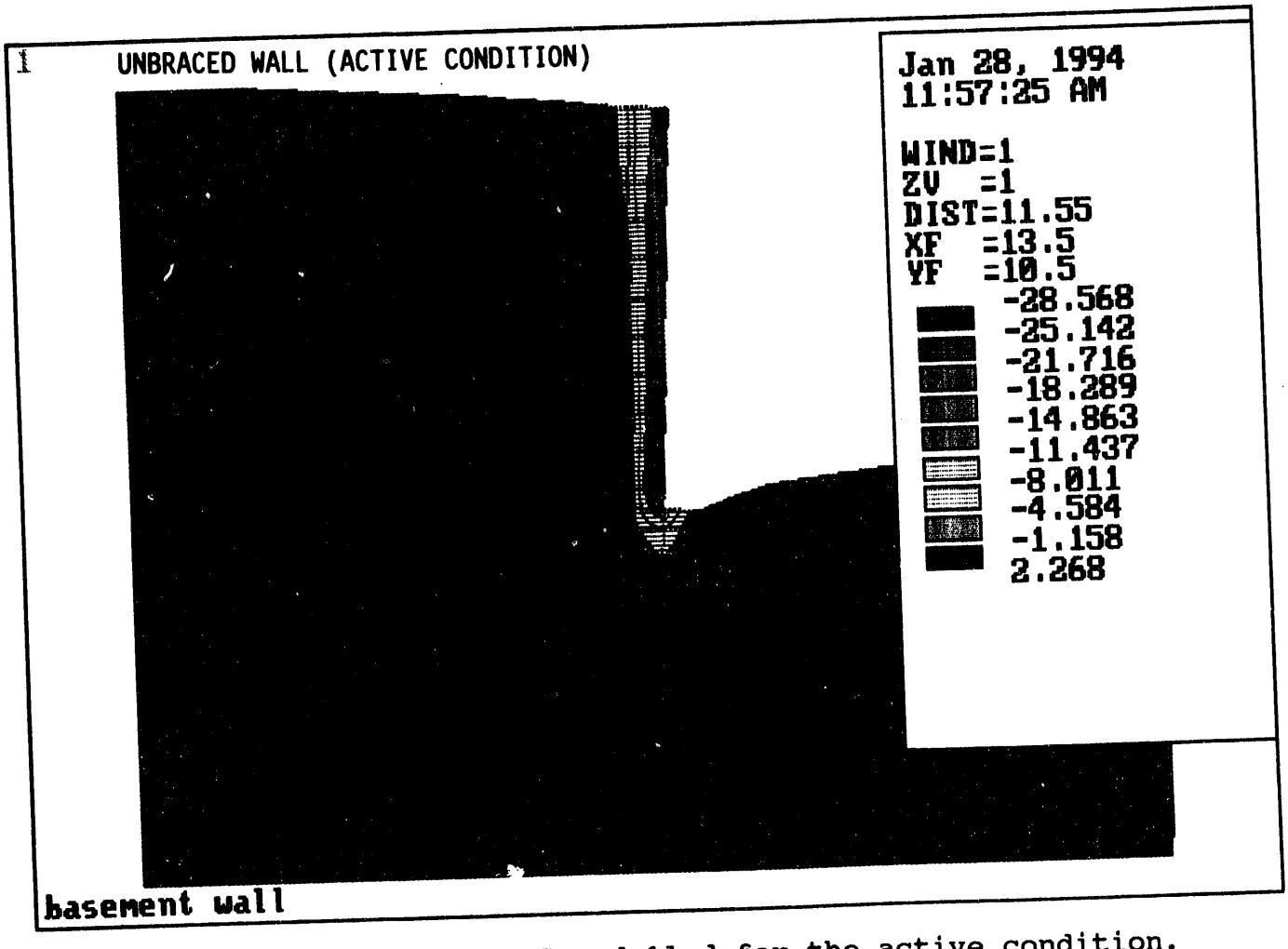


Fig. 5--West basement wall modelled for the active condition.

If Frazier Hall were being constructed today, undoubtedly larger, safer footings would be used. Based on history, however, it is evident that the existing footings are probably adequate for the remaining life of the structure.

This study illustrates that typically we as engineers tend to be conservative in estimating loads and their redistribution through the structural frame, soil strength properties, and in development of computation methods. When the combination of these conservatisms accumulate, significant error can result.

References

(1) Robinson, Lee, Geotechnical Investigation, Frazier Hall Tower Addition, Chen-Northern, Inc., Boise, ID, February 1992.

(2) Narkiewicz, S.N., Geotechnical Evaluation and Concrete Testing, Frazier Hall, ISU, Northern Engineering and Testing, Inc., Boise, ID, March 1985.

(3) Fang, H. S., Foundation Engineering Handbook, 2nd. ed., Van Nostrand Reinhold, New York, 1991. pp. 144-165.

(4) Uniform Building Code--1988 Edition, International Conference of Building Officials, Whittier, CA. 1988.

(5) Sack, R. L. and A. Sheikh-Taheri, Ground and Roof Snow Loads for Idaho, University of Idaho, Department of Civil Engineering, Moscow, ID, 1986.

(6) DeSalvo, G. J. and R. W. Gorman, ANSYS Engineering Analysis System, Revision 4.4A, Swanson Analysis Systems, Inc., Houston, PA, 1990.

(7) McCarthy, D. F., Essentials of Soil Mechanics and Foundations, 4th. ed., Regents/Prentice Hall, Inc., Englewood Cliffs, NJ, 1988, p. 427.

Hydrogeology, Waste Disposal, Science and Politics
Proceedings 30th Symposium
Engineering Geology and Geotechnical Engineering, 1994

GROUNDWATER DEVELOPMENT IN GRANITIC TERRAIN BOGUS BASIN SKI RESORT BOISE, IDAHO

By
William C.B. Gates, P.E., P.G.
Manager, Water Resources Engineering Program
Craig L. Parkinson, P.G., Hydrogeologist
Kevin L. Schroeder, Geologist
Kleinfelder, Inc.
3189 Mill Street
Reno, NV 89502

ABSTRACT

Groundwater development in the Bogus Basin Ski Area of the Idaho-Sawtooth batholith has been largely ignored because of the assumption that granitic terrain produces little groundwater.

This paper demonstrates the contrary is true. Groundwater in the Bogus Basin area is largely fracture controlled and daylights the basin headwalls as springs and seeps. Bogus Creek, Shafer Creek and Pine Creek receive their base flow from these springs.

Fracture trace analysis combined with structural mapping demonstrated a high potential for developing groundwater. The fracture trace analysis and geologic mapping of the discontinuities (fractures, joints, faults, etc.) in the bedrock show there are three major joint sets (N70°W, N20°W, and N20°E) intersecting the rock mass of Shafer Butte. Through differential erosion, Bogus Basin has opened up along one of these fracture zones. These fractures are the primary producers of groundwater in the Bogus Basin area.

Test wells targeted at the intersection of these major joint or fracture sets exhibit specific capacities ranging from 0.54 gpm/ft to 0.96 gpm/ft with estimated sustained yields of about 100 gpm. These values are acceptable for granitic terrain. The results of the hydrogeological investigation indicate Bogus Basin groundwater is primarily fracture controlled. There appears to be sufficient water resources for a small well field to support snowmaking operations. Analysis of the groundwater demonstrates the water is of excellent quality.

INTRODUCTION

Since 1942, Bogus Basin Ski Resort in Idaho has provided magnificent long slopes of natural snow to skiers. Unfortunately, mother nature doesn't always work with these winter wonderlands in producing the precise weather for these ski-filled days. Bogus Basin decided to do something about it by looking into the feasibility of developing groundwater resources for snowmaking.

Bogus Basin Ski Resort is located 16 miles north of Boise on the shoulders of Shafer Butte (Figure 1). It is the second largest night skiing resort in the pacific northwest, with five miles

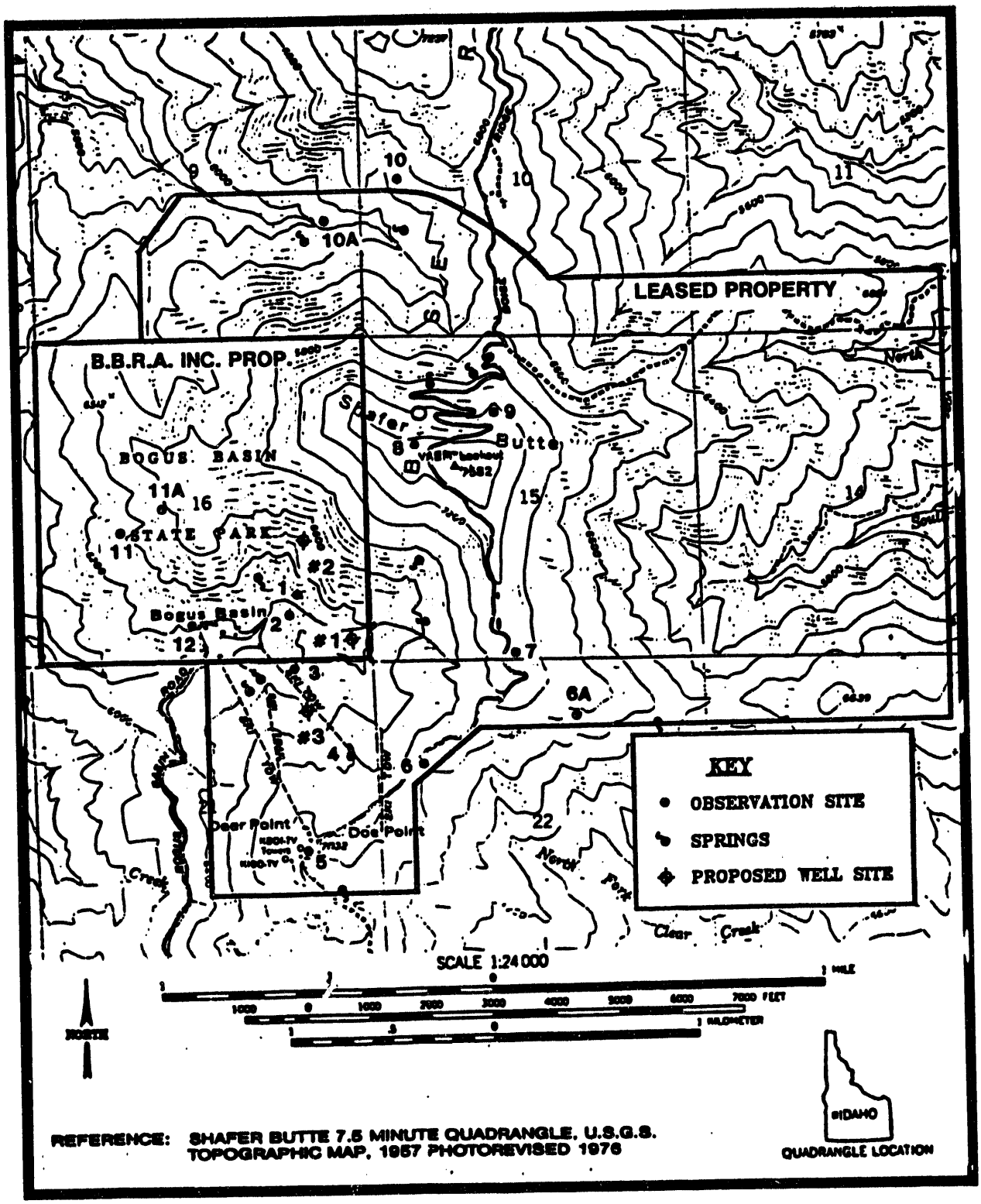


FIGURE 1: REGIONAL SITE MAP BOGUS BASIN SKI AREA

of lighted night runs, allowing the never-tired skier to ski 13 continuous hours. Bogus Basin offers 46 ski runs and over 1,800 feet of vertical drop on 2,640 acres.

Up until the 1992/93 ski season, many of the ski areas suffered with ski visits drastically reduced below normal, a reflection of past droughts throughout the western United States. During this time, Bogus Basin periodically collected surface water from the springs off the mountain to aid in their snowmaking. They currently have water rights to the surface water from November through March to provide the water for portable snowmaking fan jet guns they currently have in-place. Fortunately, they are able to impound some of the water in a 48-inch culvert for storage. The man-made snow is used to cover up some of the high volume ski areas and provide patch work at various locations on the mountain.

The bedrock geology of Bogus Basin Ski Area is composed of granites of the Idaho Batholith. Typically, granitic terrain such as this produces little groundwater, therefore, groundwater wells were never drilled in Bogus Basin.

METHODOLOGY

To conduct the groundwater resources feasibility investigation, fracture trace analysis of aerial photographs was combined with mapping of the discontinuities in the granitic outcrops exposed at the ski area. Fracture trace analysis was conducted on both color and black and white aerial photography. To verify which fracture traces were indeed fractures (joints, faults), the discontinuities in the granitic outcrops surrounding Bogus Basin were also mapped. These fracture attitudes were then plotted on "equatorial equal-area stereonets" as poles to the planes. Great circles normal to the pole clusters represent the location of major fracture sets. The location of the major fracture sets were verified by overlaying the stereonets on the aerial photographs and topographic maps. The goal was to target intersecting fracture sets for the test wells. These intersections have proven to produce high yielding wells.

GEOMORPHOLOGY

Bogus Basin Ski Resort lies completely in the northern Rocky Mountain physiographic province. Shafer Butte is the highest peak in the Bogus Basin area, attaining an elevation of 7,582 feet. The main topographic features in the region are the granitic peaks trending north to northeast, reaching elevations above 7,500 feet. Specifically, the resort occupies a portion of Boise Ridge which is part of the Atlanta section of the Idaho Batholith.

STRATIGRAPHY

The oldest rocks in the region are Cretaceous age granitic rocks of the Idaho Batholith. In the Bogus Basin area, and specifically Shafer Butte, the rocks are mainly biotite-moscovite granodiorites (Mitchell and Bennett, 1979).

Southwest of Bogus Basin, remnants of the Columbia River basalt flows cap the granites as small buttes and mesas. These are of little importance in the Bogus Basin area.

Younger (Quaternary age) unconsolidated alluvial, colluvial, and residual deposits mantle some of the larger basins such as Bogus Creek Basin and Pine Creek drainage. Depth and extent of these deposits are unclear.

STRUCTURE

Tertiary age faulting formed the dominant features of the Boise area. Boise occupies the graben basin of a downthrown block similar to the Basin and Range province to the south. The fault trace strikes northwest, approximately at the eastern edge of the city limits. Most of the faults are no longer active.

According to Lewis and Young (1982), several major north, northwest, and northeast trending fault systems have been mapped in the Boise River Basin southeast of Shafer Butte and Bogus Basin, and the Payette River Basin to the northwest. These faults appear to be high angle and have dipslip movement.

Field mapping of the Bogus Basin area indicates the granitic rock as very shattered with through-going fractures. Lineaments and fracture traces noted on the topographic map and the aerial photographs suggest three major fracture zones (Figure 2). The zones establish an average strike of N70°W, N20°W, and N20°E.

During the field mapping, 1,153 fracture attitudes at 12 stations were obtained (Figure 1). Analysis of the Schmidt net verifies there are three major steeply dipping fracture sets with associated smaller sets (Figure 3).

Fracture Set	Attitude and Dip Direction
Joint Set 1	N70°W - 60°SW
Joint Set 2	N20°W - 60°NE
Joint Set 3	N20°E - 60°NW

Some of the fracture sets appear to be parallel shear zones with small apparent offsets and slickensides. However, there are no apparent major offsets indicating major faulting. The fracture sets are more likely joints. Width between fractures ranges from 1 inch, suggesting platy cleavage, to 5 feet. The width of fractures range between <1/4 inch to 2 feet. Observation of the fractures at various stations suggest the subordinate fracture sets are actually subsets of the same dominant sets and overall system.

In some areas, quartz and basalt dikes were noted infilling the fractures. One especially prominent basalt dike (approximately 2 feet wide) strikes east-west and parallels Joint Set No. 1 near Suicide Gully (Figure 1).

The apparent joint sets compare and overlay favorably with some of the major fracture traces observed on the air photos (Figures 2 and 3).

Bogus Creek within Bogus Basin lies at the intersection of these three fracture sets. In addition, Bogus Basin opens to the west following the strike of Joint Set No. 1, after which the creek bends to the north and follows the northwest striking Joint Set No. 2. At the base of Showcase chair area and Morningstar chair area, all three joint sets appear to intersect.

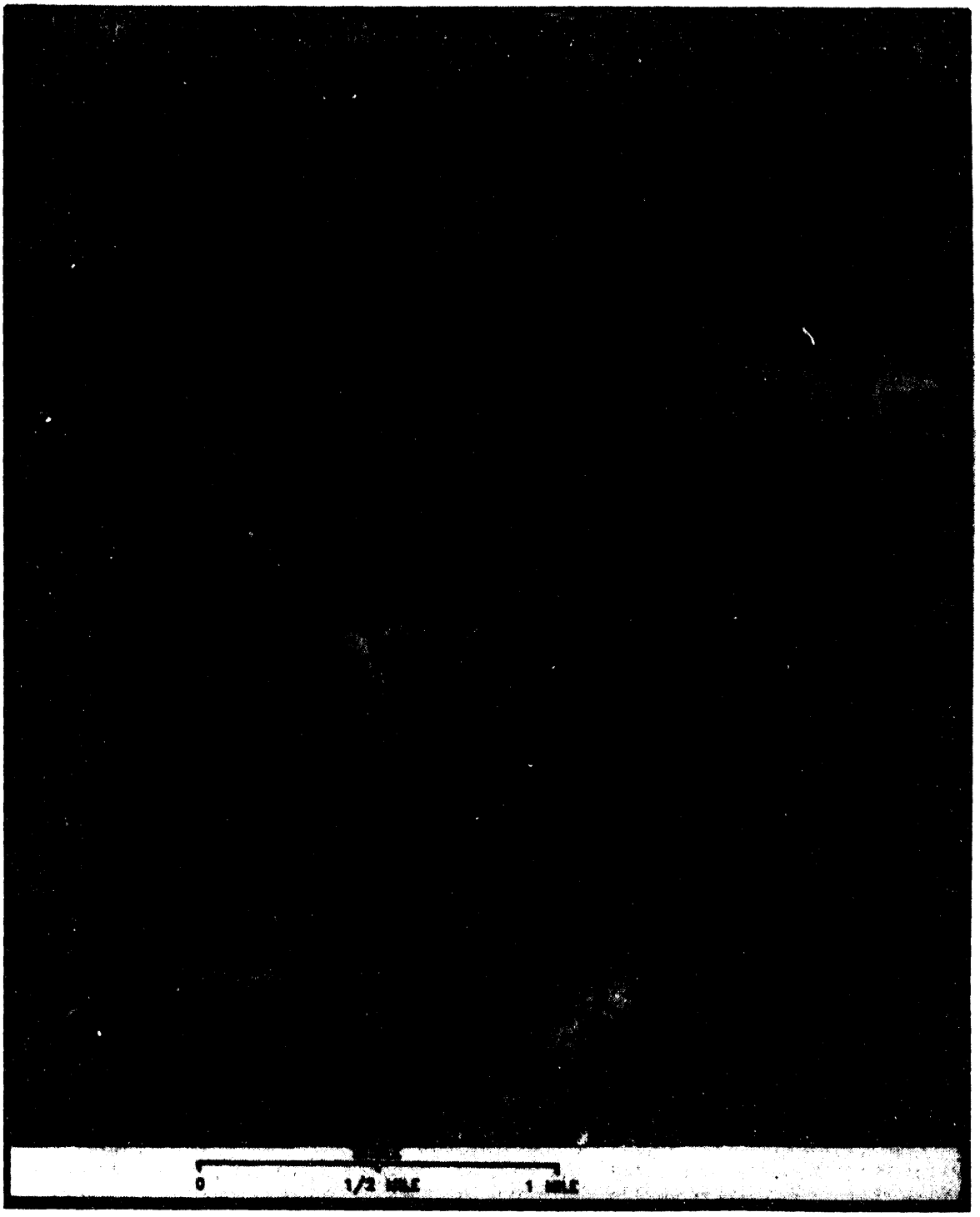
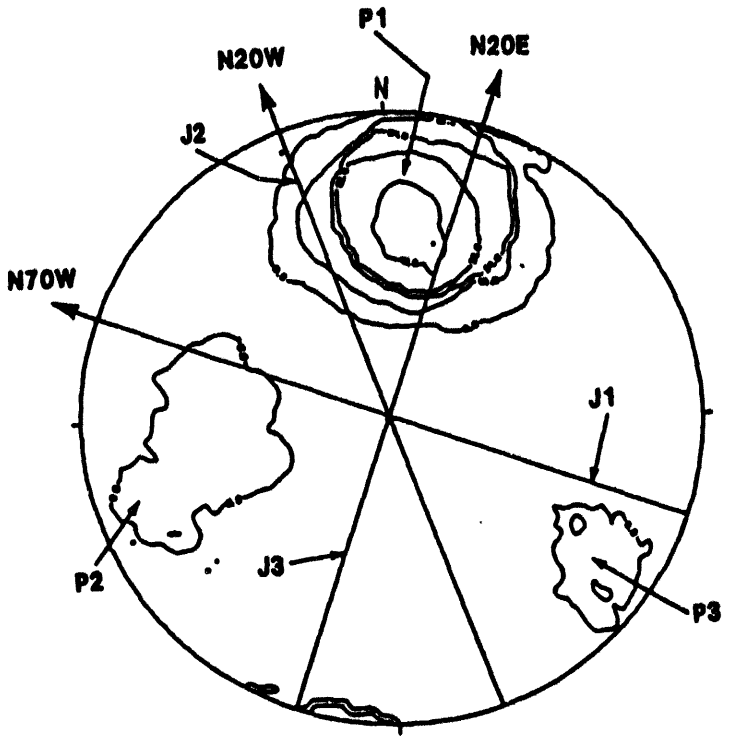


FIGURE 2 : FRACTURE TRACE ANALYSIS
BOGUS BASIN SKI AREA



FRACTURE ANALYSIS OF BOGUS BASIN SKI RESORT
Step Function Grid
Number of Sample Points 1153

LEGEND

J - INDICATES JOINT SET
P - INDICATES POLES TO JOINT SETS

FIGURE 3: SCHMIDT NET OF FRACTURE SETS IN THE GRANITIC BEDROCK BOGUS BASIN SKI AREA

HYDROGEOLOGY

During the aerial photography review, several areas with apparent springs and seeps were identified. The locations of these springs were verified during the field reconnaissance. There are at least 12 spring sites around the Shafer Butte area. These spring and seep areas characteristically have increased vegetation (mountain alder, maple, ash, etc.) around them. Many of the springs and seeps follow linear trends suggesting they are fracture controlled. All of these fracture sets have some shallow dipping planes, included as part of the set. These planes appear to intersect and daylight the slopes forming springs and seeps.

In addition, the densely fractured nature of the rock provides storage and a reservoir for groundwater. This is especially true in Bogus Creek Basin where all three sets intersect. Moreover, the surficial deposits overlying the fractured granite may provide a good reservoir.

PRIMARY AREAS FOR TEST WELLS

Three test well locations were located in the narrow valley bottom of Bogus Creek Basin (Figure 1). According to Parizek (1976), tributary valleys (such as the Bogus Creek headwaters) may be controlled or localized by differential weathering along zones of fracture concentrations revealed by fracture traces. Moreover, the results of the structural mapping verified the concentration of joint sets in this location. Therefore, vertical water wells located within narrow valley bottom settings have an increased probability of penetrating zones of fracture concentrations. These zones, because of the fractures, have a higher degree of hydraulic conductivity and porosity. Thus, they provide an excellent aquifer system. The fracture sets leading to the concentration of fractures act as "pipe conduits" for additional groundwater flowage to the area.

Test Well #1 (Showcase Chairlift)

The lithologic log for Test Well #1 indicated about 42 feet of alluvium overlies moderately to highly weathered Cretaceous granodiorite. The 6-inch test well was drilled to a total depth of 500 feet. Multiple fractures were encountered throughout the depth.

Groundwater was encountered at about 75 feet below the surface. Airlift yields started at about 3 to 4 gpm and increased when additional fractures were intersected for a total of about 45 gpm. The majority of water was encountered between 325 to 500 feet in the highly fractured and weathered zones of the granodiorite.

Test Well #2 (Morning Star Chairlift)

Test Well #2 was drilled to about 350 feet without intersecting water and, therefore, was abandoned.

Test Well #3 (Showcase Chairlift)

Test Well #3 is approximately 220 feet southeast of Test Well #1 and 26 feet higher in elevation. Therefore, the lithologic sections for these wells are quite similar, exhibiting highly fractured and weathered granodiorite.

Groundwater was first encountered at about 25 feet and yields increased with increasing fracture density, similar to Test Well #1. Total yield by airlift was about 80 gpm. The majority of the groundwater from Test Well #3 was from fractures between 220 to 400 feet.

STEP-DRAWDOWN PUMPING TEST

Step-drawdown and Recovery Test

Test Well #1 and #3 lie on the same fracture sets (Figure 2). Because of this, an extended step-drawdown pump test was conducted to evaluate the hydraulic characteristics of the fractured rock aquifer. Prior to the test, the static water levels (SWL) for Test Well #1 and #3 were 12.42 feet and 32.87 feet. Discharge rates during the step-test ranged from about 30 gpm to 200 gpm. Once the step-test was complete, the discharge rate was reduced to a sustained rate of approximately 45 gpm for the next 20.6 hours.

After the pumping test, Test Well #1 recovered to within 49.6 feet (22%) of the SWL 60 minutes after stopping the pump and recovered to within 7.7 feet (88%) of SWL at the end of the recovery test.

The test data indicated the specific capacity (rate of discharge per unit drawdown) for Test Well #3 ranged from 0.96 gpm/ft at a pumping rate of 30 gpm to 0.84 gpm/ft at a rate of 60 gpm. Calculated specific capacities ranged from approximately 0.78 gpm/ft at a theoretical pumping rate of 80 gpm to 0.54 gpm/ft at a rate of 200 gpm.

Aquifer Characteristics

To assess the aquifer transmissivity, the authors used the Jacob straight-line method. Transmissivity (T) is the rate at which an aquifer can transmit water through a unit width of an aquifer under a unit hydraulic gradient. This method is based on an approximation of the Theis equation derived by Jacob and Cooper (Driscoll, 1989). The assumptions for the Theis equation are summarized by Driscoll (1989) as follows:

1. The water-bearing formation is uniform in character and the hydraulic conductivity is the same in all directions. Highly fractured rock approximates porous media in this aspect of groundwater hydraulics.

2. The formation is uniform in thickness and infinite in areal extent.

3. The formation receives no recharge from any source.

4. The pumped well penetrates and receives water from the full thickness of the water-bearing formation.

5. The water removed from storage is discharged instantaneously when the head is lowered.

6. The pumping well is 100% efficient.

7. All water removed from the well comes from aquifer storage.

8. Laminar flow exists throughout the well and aquifer.

9. The water table or potentiometric surface has no slope.

The hydraulic characteristics of the aquifer and wells satisfy these assumptions enough to obtain reliable T values.

The Jacob straight-line method involves plotting the drawdown data versus time on a semilog scale to form a straight line. From this line, T was solved using the following equation:

$$T = \frac{264\,Q}{\Delta s}$$

Where:

T = transmissivity (gpd/ft)
Q = pumping rate (gpm)
Δs = drawdown during one log cycle (ft)

The T of the aquifer was calculated using data from the first step of the step-drawdown pumping test.

Therefore:

Test Well No. 3:

$$T = \frac{(264)(30\text{ gpm})}{16.7\text{ ft}} = 474\text{ gpd/ft or }63.4\text{ ft}^2/\text{d}$$

where:
Q = 30 gpm (pumping rate during first step of step-drawdown test)
Δs = 16.7 feet (from drawdown versus time graph)

The transmissivity of the aquifer is estimated at 474 gpd/ft (63.4 ft^2/d), which is typical for fracture flow aquifers in granitic bedrock.

Applying ideal groundwater flow equations to fracture-flow systems may lead to significant errors because flow velocities in fractures can exceed the laminar flow conditions assumed by ideal flow equations. Additionally, irregular fracture zones localize groundwater movement and deviate from the homogenous and isotropic conditions in typical sedimentary aquifers. However, if the fractures are narrow, closely-spaced, and interconnected, the fractured rock mass approximates a coarse-grained porous medium with small intergranular openings (Meiser and Earl, 1982). Taking this into consideration, the T value obtained from the Jacob method will give a general indication of the transmissive behavior of the fracture flow aquifer. Therefore, the transmissivity calculated for the aquifer gives a reliable approximation of how much water the fractures may yield.

The storativity of the aquifer penetrated by the test wells was also estimated. Storativity is the volume of water an aquifer releases from or takes into storage per unit surface area of the aquifer per unit change in head (Driscoll, 1989). We estimated the aquifer has a storativity of 0.38, which indicates the aquifer is unconfined.

Potential Yields

The potential yield for Test Well #3 was estimated using the aquifer test data and data from other wells completed in fracture aquifers. Potential yield is typically estimated using the concept of specific capacity.

Specific capacity is the pumping rate divided by the amount of drawdown at that rate and is measured as gallons per minute per foot, gpm/ft. The potential yield of a well can be

estimated by multiplying the specific capacity of the well by the available drawdown: gpm/ft x ft = gpm. However, stressing an aquifer by increasing pumping will almost always significantly increase the drawdown, thereby decreasing the specific capacity. Accordingly, using the specific capacities calculated for low test pumping rates will result in too high an estimate of potential yield.

To estimate the potential yield of a well it is necessary to calculate how much head is available for withdrawal from the well. This value is the total amount of drawdown available, which is the interval from the SWL to 20 feet above the pump intake setting. In Test Well #3, the final pump intake will likely be set about 10 feet from the bottom of the well. Therefore, the total drawdown available is from the SWL to 30 feet above the bottom of the well. The SWL is approximately 30 feet and the well is 400 feet deep, which indicates the total drawdown available is approximately 340 feet.

The step-drawdown test data was used to estimate the drawdown at higher pumping rates than those achieved during the actual pumping test. The results are then used to determine potential sustained yields. A pumping rate of 190 gpm was calculated to produce a drawdown of 340 feet, which is the total available drawdown. Therefore, the maximum potential yield of Test Well #3 is 190 gpm. However, pumping at this rate will probably dewater the well rapidly and cause cavitation of the pump. The authors recommended pumping the well at no more than 100 gpm for a period of 8 hours, followed by a 16-hour recovery period.

Impact of Wells on Groundwater and Springs

Groundwater production from Test Wells #1 and #3 is fracture controlled. These two test wells are located within the same fracture system and exhibit a strong hydraulic influence upon each other. This hydraulic connection was demonstrated during the step-drawdown test when drawdown in Test Well #1 was observed while pumping Test Well #3. However, the test wells were installed in an area which appears to be an unique flow regime based on the fracture trace analysis. Wells and springs which are not located along the same fracture system as Test Wells #1 and #3 will not be significantly affected by pumping the test wells.

CONCLUSIONS

Based on the results of the investigation, there are several potential well locations offering favorable conditions for groundwater development in the Bogus Basin area. Bedrock is highly fractured granitic rock. Groundwater is primarily by fracture flow and controlled by the major fracture sets striking N70°W, N20°W, and N20°E. The following is a summary of the hydrogeologic investigation conducted at Bogus Basin:

- Test Well #1 and #3 rely on fracture flow for groundwater production;
- Groundwater production from Test Well #3 is from discrete local fractures that do not appear to have a significant hydraulic connection with surrounding streams or springs; and
- Potential production from a completed well at Test Well #3 site appears to be approximately 100 gpm for a period of 8 hours followed by a 16-hour recovery period.

REFERENCES CITED

Alt, David D., and Hyndman, Donald W., 1989, Roadside Geology of Idaho: Mountain Press Publishing Co., Missoula, MT, 394 p.

Driscoll, Fletcher G., 1989, Groundwater and Wells: Johnson Filtration Systems, Inc., St. Paul, Minn., 1089 p.

Fetter, C. W., 1988, Applied Hydrogeology, Second Ed., Merrill Publishing Company, Columbus, OH, 592 p.

Hoek, E., and Bray, J., 1981, Rock Slope Engineering (3rd Edition): Institute of Mining and Metallurgy, London, pp. 37-63.

Kleinfelder, 1992, Phase I Groundwater Feasibility Study, Bogus Basin, Boise, Idaho.

Kleinfelder, 1993, Summary of Phase II, Hydrogeological Services, Installation and Aquifer Testing, Test Wells Nos. 1, 2, and 3, Bogus Basin Ski Resort, Boise, Idaho.

Lewis, R.E., and Young, H.W., 1980, Thermal Springs in the Payette River Basin, West-Central Idaho: U.S. Geological Survey Water Resources Investigations/Open-File Report 80-1020, 23 p.

Lewis, R.E., and Young, H.W., 1982, Thermal Springs in the Boise River Basin, South-Central Idaho: U.S. Geological Survey Water Resources Investigations 82-4006, 22 p.

Meiser & Earl, 1982, Use of Fracture Traces in Water Well Location: A Handbook: OWRT TT/82 1, US Department of Interior, Office of Water Research and Technology, Washington D.C., 55 p.

Mitchell, Victoria E., and Bennett, Earl H., 1979, Geologic Map of the Boise Quadrangle, Idaho, Scale 1:250,00, Geologic Map Series, Boise 2° Quadrangle.

Parizek, Richard R., 1976, on The Nature and Significance of Fracture Traces and Lineaments in Carbonate and Other Terranes, Yerjevich, R. ed., Karst Hydrogeology: Water Resources Publications, Fort Collins, CO., pp. 47-108.

Young, H.W., 1985, Geochemistry and Hydrogeology of Thermal Springs in the Idaho Batholith and Adjacent Areas, Central Idaho: U.S. Geological Survey Water Resources Investigations Report 85-4172, 28 p.

Hydrogeology, Waste Disposal, Science and Politics
Proceedings 30th Symposium
Engineering Geology and Geotechnical Engineering, 1994

A PROPOSED DESCRIPTIVE METHODOLOGY FOR ENVIRONMENTAL GEOLOGIC (ENVIROGEOLOGIC) SITE CHARACTERIZATION

David L. Schwarz and Walter S. Snyder, Department of Geosciences, Boise State University, 1910 University Drive, Boise Idaho, 83725

ABSTRACT

We propose a descriptive methodology for use in environmental geologic (envirogeologic) site characterization. The method uses traditional sedimentologic descriptions augmented by environmental data needs, and facies analysis. Most other environmental methodologies for soil and sediment characterization use soil engineering and engineering geology techniques that classify by texture and engineering properties. This technique is inadequate for envirogeologic characterization of sediments. In part, this inadequacy is due to differences in the grain-sizes between the Unified Soil Classification and the Udden-Wentworth scales. Use of the soil grain-size classification could easily cause confusion when attempting to relate descriptions based on this classification to our basic understanding of sedimentary depositional systems. The proposed envirogeologic method uses descriptive parameters to characterize a sediment sample, suggests specific tests on samples for adequate characterization, and provides a guideline for subsurface facies analysis, based on data retrieved from shallow boreholes, that will allow better predictive models to be developed. This methodology should allow for both a more complete site assessment, and provide sufficient data for selection of the appropriate remediation technology, including bioremediation.

INTRODUCTION

Environmental site characterization requires identification of the contaminant source(s) including the waste(s) involved, and assessment of the media impacted by the waste. The environmental geologic (envirogeologic) medias of interest are sediment (within both vadose and saturated zones) and fluids (e.g., water, air, lighter- and denser-than-water non-aqueous phase liquids). Both environmental site characterization and contaminant remediation depend on understanding the processes that control waste or chemical transport in the subsurface, with emphasis on determining the distribution of contaminants and the processes controlling their transport. Such information comes from the assessment of the impacted area. Obviously, data collection is the key to a successful site assessment. Unfortunately, some site characterizations are wholly or partly re-done because the initial study failed to supply the necessary information for adequate characterization and/or for selection of applicable remediation technologies (D.M. Miller, pers. comm., 1992). Part of this failure is caused by assumptions concerning subsurface geology. Most environmental professionals now recognize that the subsurface cannot be simplified and assumed to be a homogenous medium (e.g., Anderson, 1992). Geologic heterogeneities are the norm, and are of great interest in characterizing shallow subsurface contaminant migration.

We propose a methodology for envirogeologic site characterization of siliciclastic sediments that uses traditional sedimentologic descriptions augmented by

environmental data needs, and facies analysis. Additionally, we recommend certain field and/or laboratory analyses to aid in both defining contaminant impact and migration, and in selecting remediation technologies. A similar methodology could be used for carbonate sediments by employing a modification of the Dunham (1962) textural classification for carbonate rock. However, in this paper, we limit our discussion to methodology applicable primarily to siliciclastic sediments that are typically found in many alluvial valleys in the western United States. We discuss these envirogeologic methods in three parts: field methods, laboratory analyses, and facies analysis (Table 1).

TABLE 1 SUMMARY OF PROPOSED METHODOLOGY FOR ENVIROGEOLOGIC CHARACTERIZATION

ENVIROGEOLOGIC PARAMETER	*FIELD*	*MICROSCOPE*	*ANALYSIS*
LITHOLOGY: DESCRIPTIVE AND/OR SAMPLE			
Length of interval sample/recovered	✓		
Thickness of lithologic units	✓		
Sedimentary structures	✓		
Grain size, shape and roundness	✓s	✓	
Mineralogy	✓s	✓	
Cement and matrix	✓s	✓	
Permeability[1]	✓s	✓	✓
Moisture, odor, color	✓		
ANALYTICAL SAMPLE(S)			
Sampling for organic vapor (if applicable) and contaminant analysis	s		✓
Biologic analysis[2]	s		✓
Eh and pH	s		✓
Organic carbon content	s		✓
Cation exchange capacity	s		✓
ARCHIVE SAMPLE	✓		

NOTES:

[1] By portable air-minipermeameter in field (if available), otherwise by thin-section analysis, grain-size analysis, or other laboratory methods.

[2] Samples should be frozen for later analysis if bioremediation is selected.

Samples

Samples should be taken for: contaminants of concern; additional chemical /physical and biologic analyses; thin-section analysis; and archival purposes.

Thin-section analysis of samples (petrography) is standard procedure for most geologic outcrop studies (Boggs, 1992) and subsurface petroleum studies (Ethridge, 1992). In contrast, these petrographic techniques are rarely used in hydrogeologic studies (Younger, 1992) but would provide critical data important to solving a variety of characterization and remediation problems. We recommend that critical facies (e.g., contaminant-impacted sands) be sampled for petrographic analysis. An "undisturbed" sample from the core or split-barrel sampler can be solidified in the field with blue colored epoxy resin via a method modified from Atkins and McBride (1992). Cut the bottom out of a disposable cup and gently push the cup into the sample. Support the bottom of the sample/base of cup with a flexible spatula wrapped in aluminum foil. Pour the resin into the cup. Gently remove the foil from the spatula and form into a cover over the base of the cup. Place the cup with the resin-drenched sample into another cup. The solidified sample can be stored for later petrographic analysis, if warranted. When sample solidification is not feasible, samples of loose sediment aggregate should be carefully taken in clean, marked sample bags. These "loose" samples can be petrographically assessed under a binocular microscope for many, but not all of the features visible in thin section under a petrographic microscope.

Remaining portions of samples should be "archived" by storing in plastic bags or retaining a small amount of each defined unit or specific interval in separate compartments of a plastic rotary rock-chip storage tray. These trays allow for convenient re-examination when questions arise.

Sampling Limitations

Many envirogeologic site investigations occur in loosely consolidated alluvial sediments, such as found in the Boise Valley. These are not soils in a geologic sense, although they are sometimes refered to as such in many studies. For shallow (less than 50 meter) subsurface evaluations in such sediments, the preferred data retrieval method uses hollow-stem auger boring technology, in large part because of the ease of retrieving representative, relatively undisturbed sediment samples (U.S. EPA, 1986). The hollow stem of the auger allows the collection of samples by two methods. The "standard" sample method uses a split-barrel sampler driven 18 to 24 inches beyond the auger bit by a hammer drop system (Hackett, 1987). Sample intervals vary, but generally occur at five foot intervals or less. The second sample method uses a continuous sampling tube to retrieve a sediment core as the auger column is rotated and advanced. A continuous core is "cut" until the auger column has advanced for a specific interval, generally two and one half to five feet. The sample tube is then retrieved to the surface by a wire-line system (CME, 1987).

BACKGROUND ON FIELD DESCRIPTIVE TECHNIQUES

Geologic field descriptions of shallow borehole samples, summarize in Table 1, are developed from standard methods used to describe outcrop and hand-specimen samples of sedimentary rock; this is the realm of classic sedimentology. Techniques are well described in many texts (e.g., Boggs, 1992). In contrast, most existing

environmental sediment and soil descriptions evolved from soil engineering and engineering geology techniques (note that "soil" in the engineering sense includes soil, sediment, and unconsolidated rock fragments). These descriptive techniques typically use the American Society for Testing Materials (ASTM) standard based on the Unified Soil Classification System (USCS)(Howard, 1984). This ASTM method classifies soil by texture, along with soil engineering properties of strength, moisture content, and plasticity of fines (Table 2)(ASTM D-2487 and 2488, *in* ASTM, 1988). By itself, the USCS provides limited information pertinent to envirogeologic investigations. Additionally, the USCS grain-size scale differs from the Udden-Wentworth scale used by geologists (Table 3). For instance, the USCS coarse sand category is equal to the geologic granule gravel and a portion of the pebble gravel categories. Also, the USCS scale does not differentiate silt from clay by size: instead, degree of plasticity is used. Use of the USCS could easily cause confusion when relating descriptions based on this classification to the vast amount of sedimentology literature, particularly when interpreting the geometry of subsurface units based on our basic understanding of depositional flow regimes (e.g., Allen, 1985) and facies models (discussed below). For these reasons, we use the geologic (Udden-Wentworth) grain-size scale for clastic sediments.

TABLE 2: ASTM CHECKLIST FOR DESCRIPTION OF SOILS (ASTM D 2488 , 1984)

1. Group name (USCS)	13. Toughness: low, medium, high
2. Group symbol (USCS)	14. Color (in moist condition)
3. Percent of cobbles or boulders,	15. Odor (mention only if organic or unusual)
4. Percent of gravel, sand, or fines,	16. Moisture: dry, moist, wet
5. Particle-size range: Gravel - fine, coarse; Sand - fine, medium, coarse	17. Reaction with HCl: none, weak, strong or all three (by dry weight)
6. Particle angularity: angular, subangular,subrounded, rounded	18. Consistency (fine-grained soils only):
7. Particle shape: (if appropriate)flat, elongated, flat and elongated	19. Structure: stratified, laminated, fissured, slickensided, lensed, homogenous
8 Maximum particle size or dimension	20. Cementation: weak, moderate, strong
9. Hardness of coarse sand and larger particles	21. Local name
10. Plasticity of fines: nonplastic, low medium, high	22. Geologic interpretation
11. Dry strength: none, low, medium, high, very high	23. Additional comments.
12. Dilatancy: none, slow, rapid	

TABLE 3

Grain Size Scales for Clastic Sediments

GEOLOGIC*				USCS		
	Ø	mm	mm			
GRAVEL Boulder	−12	4096		Boulders		
			300			
Cobble	−8	256		Cobbles	GRAVEL	
			75			
Pebble	−6	64		Coarse		
			19			
			4.8	Fine		
Granule	−2	4				
				Coarse		
	−1	2	2			
Very Coarse						
	0	1		Medium	SAND	
Coarse						
	1	0.5	0.43			
Medium						
	2	0.25		Fine		
Fine						
	3	0.125				
Very Fine						
			0.08			
	4	0.062				
Coarse						
	5	0.031		Silts (nonplastic)	FINES	
MUD Medium SILT						
	6	0.016		+		
Fine						
	7	0.008				
Very Fine				Clays (plastic)		
	8	0.004				
Clay						

* Typically called the Udden–Wentworth scale (Wentworth, 1922). The Ø scale (Krumbein, 1934) was devised to facilitate statistical manipulation of grain – size data. $Ø = -\text{Log}_2 \text{mm}$.

Descriptive Parameters

Some of the parameters of Table 1 have been used to characterize environmental sites (e.g., Ball and others, 1990), though standardization is lacking. The following suggested methodology for describing split-barrel or core sediment samples is derived from standard sample logging descriptions typically used in the petroleum industry (Swanson, 1981), traditional sedimentologic outcrop descriptions (e.g., Boggs, 1992), soil descriptions for engineering purposes (ASTM D 2488), and from personal experience from envirogeologic characterization. Visual comparators can be used to help estimate many of the attributes discussed below. These can be made by photocopying published comparators (e.g., Dietrich, and others, 1982) onto transparencies. The written unit description should include all visually identifiable attributes. The written order of descriptive attributes depends on personal preferences.

Length of Interval Sampled Versus Recovered

The amount of information available will be at least partly governed by the sample interval length and the sample length recovered. Thus, these lengths should always be recorded upon retrieval and disassembly of the sampler (if required). Note that the initial few inches of sediment in the split-barrel sampler or the core tube may be drill slough. A poor recovery may dictate that all of the sample be immediately containerized for analysis of contaminant(s).

Organic Vapor Analysis and Contaminant Sampling

If the site is presumed or known to be contaminated by volatile organic compounds, then the initial effort must focus on organic vapor analysis and sampling for contaminants of concern. These samples must be quickly preserved to insure accrate analyses. First, the sample should be split lengthwise into equal halves. The core should then be subdivided into crude lithologic units based on a visual scan and easily-definable attributes such as grain size (i.e., sand vs. mud). Quickly package and label two sub-samples of each "crude" unit into appropriate containers; one container must immediately be placed into an ice-filled cooler, while the other can be allowed to warm to room temperature for vapor analysis with appropriate field instruments (e.g., flame ionization detector, Sensidyne, 1992). Detailed sample handling protocol are documented in Environmental Protection Agency (EPA) publications (e.g., EPA, 1986).

Lithologic Units: Thickness, Sedimentary Structures

Lithologic units are a fundamental characteristic of sedimentary rocks. Although seldom analyzed for enviromental studies until now (e.g., Anderson, 1992), their geometry, thickness, sedimentary structures and lithologic characteristics (e.g., grain size, grain rounding, etc.) fundamentally control subsurface fluid movement. The importance of these units is discussed later, in the section on facies analysis.

Lithologic units (facies) are typically defined by grain-size or mineralogy changes and characteristic sedimentary structures. Once these units are thus defined, the thickness of each unit should be recorded. Sedimentary structures are many times not easily discernable from samples recovered from split-barrel or core samplers.

However, they are extremely important and fundamental features. Bedding surfaces should be described as: parallel or nonparallel; even, wavy, or curved; and continuous or discontinuous. Graded bedding (gradual, distinct vertical change in grain size) should be described as normal (coarser particles at the base grading to finer at the top) or inverse (finer particles at the base grading to coarser at the top). Note that split-barrel sampling will cause distortion of structures along the wall of the sampler. Lack of any sedimentary structures should be described as massive. Uncommonly sampled features include burrows (horizontal, vertical, or both) and chaos (churned appearance caused by bioturbation or fluid escape. Note that fluid-escape structures can be created by the sampling procedure, particularly near the water table).

Grain Size, Sorting, Rounding

The grain size for each unit should be described as both the average grain size and range of grain sizes each defined unit (e.g., very fine to coarse with an average of fine). For sand sizes, use a hand lens to visually compare the sample to a grain-size comparator that is based on the Udden-Wentworth grain-size scale. Gravel size grains can be measured with a see-through ruler.

Sorting is a measure of dispersion of the size frequency of grains (note that sorting is opposite of grading in the USCS). Visually estimate by direct comparison to a sorting comparator, or by Payne's (1942) classification: Good: 90% in 1 or 2 classes; Fair: 90% in 3 or 4 classes; Poor: 90% in 5 or more classes.

Grain roundness concerns the curvature of grain corners. Visual estimates can be quickly made with a hand lens, binocular or petrographic microscope by direct comparison to a roundness comparator. Describe as very angular, angular, subangular, subrounded, rounded, or well-rounded.

Mineralogy

Some may argue that mineralogy is of little importance in environmental site characterization, and that laboratory models of glass beads can properly mimic a natural setting. However, for contaminant transport migration, mineralogy may be a major control on contaminant retardation via mineral adsorption in the absence of organic material (Anderson, 1992). Estimation of mineralogy can be done in the field with a hand lens, under a binocular microscope or by thin-section analysis with a petrographic microscope. Each method represents an increase in the accuracy of the determination.

Many alluvial sediments will consist predominantly of quartz, with lesser amounts of feldspar, rock fragments derived from volcanic or metamorphic rock, and accessory constituents such as mica (biotite, muscovite) and plant remains. Visually estimate percentage of major constituents by direct comparison to a percentage comparator. Use the major constituent to name the sediment, e.g., quartz sand with minor feldspar and rare biotite. Detailed descriptions and classifications can be derived at a later time by thin-section analysis, if appropriate.

Petrographic thin-section analysis also allows for direct measurement of grain size, pore size, and porosity (Atkins and McBride, 1992; Younger, 1992). Typically, hydraulic parameters themselves are measured (i.e., pump test), while the geologic

parameters which govern them are ignored (Younger, 1992). When pump tests are financially impossible (which they typically are), numeric modelers tend to estimate hydraulic conductivity. This should be avoided: hydraulic parameters can be successfully (and cheaply) estimated from thin-section analysis by methods outline by Younger (1992).

Cement and Matrix

Cement is deposited chemically around grains and in interstices of sediment. A common cement in arid alluvial valleys is calcite that forms duricrust (caliche). Matrix is deposited mechanically with the sediment and consists of small individual grains that fill interstices between larger grains (especially evident with gravels). Cement and matrix determination is important for understanding subsurface fluid movement

A drop of weak hydrochloric or acetic acid will cause calcite to effervesce whereas other cements are best determined in the laboratory via thin-section study. The relative induration of the sediment (a function of cement and compaction) should be estimated; typical terms are: strongly, weakly, or unconsolidated if non-cemented.

The composition of the matrix must be described (e.g., clay, silt). For gravel, describe if grains are matrix-supported (grains "floating" in matrix) or grain-supported (grains touching each other).

Permeability

Permeability can be measured rapidly on numerous samples in the field by a portable air-minipermeameter (Davis and others, in press). This instrument has been successfully used on outcrop samples (Davis and others, 1993) and similar techniques can be used for borehole samples. The air-minipermeameter can be assembled from components that cost about $1,300.00 (Davis, pers. comm., 1994). Other permeability estimates can be attained by thin-section or grain-size analysis (discussed below).

Permeability can also be estimated from thin-section analysis, but this is generally a more time consuming process. If neither the portable air-minipermeameter or thin-section method has been undertaken, then grain-size analyses can provide permeability estimates. Such permeability estimates can be produced by solving an equation derived from the intercept of a straight line fitted to a grain-size distribution curve and the difference between the average and effective grain diameters (Alyamani and Sen, 1993). However, we believe that permeability estimates derived solely from distribution curves will not correlate to *in situ* measurements because grain size analysis cannot account for the effects of mineralogy, texture, and diagenesis. For example, Hartkamp and others (1993) showed that permeability varied between topset, foreset, and bottom sets of cross-beds due to contrasts in average pore size and contrasts in mineralogic composition. Traditional, more expensive laboratory methods for permeability can also be performed, though thin-section analysis has provided good estimates that compare favorably to laboratory-derived results (Younger, 1992).

Moisture, Odor, and Color

Describe the moisture condition as dry (absence of moisture), moist (damp, but no visible water), or wet (visible free water). Before smelling any sample, screen the

sample for organic vapors with appropriate field instruments (preferably by headspace techniques). Do not smell any sediment sample that registers the presence of organic vapors greater than background levels (5 ppm). For background-registered samples, smell and describe the odor (e.g., gasoline) as strong, weak, or omit if no odor is present. Both the wet and dry color should be described (if possible). General terms such as light gray, dark brown, etc., should suffice; however, if more concise designations are required, determine the color by comparing to a soil or rock color chart (e.g., Goddard and others, 1980). Record mottles/stains (patches or lenses of one color in a matrix of another color) as to: abundance (rare, common, many) ; size; and contrast (faint, distinct, prominent).

LABORATORY ANALYSES

Sediments impacted by contaminants need additional chemical and physical analyses in order to select applicable environmental remediation technologies. As noted above, data on permeability, porosity, and grain- size are needed to determine if the sediment matrix will allow adequate movement of fluid, such as: vapors for vapor extraction; fluids containing nutrients and /or oxygen for biodegradation; or flushing solution for sediment flushing of contaminants. Application of the proposed envirogeologic methodology should supply most of this type of data via routine in house-work. However, additional anaysles using outside laboratories may be necessary to assess the effects of sediment sorption on contaminant migration and remedial removal efficiency. Additional laborartory analyses that should be performed on impacted sediment include organic carbon content, cation exchange capacity, grain density, Eh, and pH. We suggest that each facies (defined below) impacted by contamination should be characterized by a suite of such data. For a geographically small site, this would equate to only one analysis for each of the following parameters.

Eh and pH

Factors affecting contaminant sorption on sediment and soil include oxidation-reduction potential (measured by Eh) and hydrogen ion concentration (measured by pH) . Both Eh and pH partly control selectivity and competition among "contaminant" ions (particularly for trace metals) for surface sites in sediments (McComish and Ong, 1988).

Particle Density

Particle density of sediment and soil refers to the density of the solid particles collectively (Blake, 1965). Particle density is used in mathematical equations to describe aspects of contaminant transport (e.g., Feenstra and others, 1991; Bjerg and others, 1993).

Organic Carbon Content

It is assumed that sorption of contaminants on sediments results from sorption on sediment organic carbon that occur as grain coatings, organic debris, and condensed humic material (Kinniburgh and Jackson, 1981). For instance, complexation of metal ions with sediments increases at higher pH's and higher organic carbon

concentrations, and hydrophobic organic contaminants show a high affinity for association with organic macromolecules (i.e., humic material; Huling, 1989). In low organic carbon sediments, such as in the Boise Valley, sorption on mineral surfaces may be of equal or more importance (Feenstra and others, 1991). It should be noted that organic carbon content can vary considerably. In the horizontal dimension it may vary by a factor of 10 or less, while it can vary by a factor of 10 to 100 in the vertical dimension (Piwoni and Keeley, 1990).

Cation Exchange Capacity

Cation exchange capacity can provides an estimate for the total negatively-charged sites available in soil or sediment. This is important for assessing the rate of contaminant retardation through a sediment. It is determined by measuring the mass of a standard cation (usually ammonia) that displaces another cation held by the sediment. In natural conditions, these receptor sites will be occupied by cations common to flowing or percolating water (e.g., Na^{+}, Ca^{2+}). Larger organic cations and highly-charged metal ions (e.g., Cr^{3+}) can be exchanged at these sites with their normal occupants. Thus a high cation exchange capacity of a sediment would suggest that large organic cations or heavy metals would not normally be expected to move far (Piwoni and Keeley, 1990).

Biologic Analyses For Bioremediation

Recently, bioremediation has emerged as an extremely attractive alternative technology for the economical treatment of numerous contaminants. Under the right conditions, it appears that most organic compounds, and many inorganic compounds can be broken down by microbes into non-toxic compounds (Chapelle, 1993). Even highly contaminated sites have been known to harbor indigenous microbes that have become acclimated to the contaminant. To assess a site's potential for *in situ* bioremediation, specialized test(s) for microbe viability within the contaminated zone must be performed.

To test for microbe viability, an aseptic, subsurface sediment sample must be recovered for laboratory analysis. Even if sampling tools are properly sterilized, the possibility exists for recontamination by other microbe while placing the tool back down the hollow stem of the augers. Therefore, upon retrieval of the sediment sample, the outside portion of the sediment sample should be discarded (Chapelle, 1993). The remainder of the sample should be immediately placed in a sterile container such as a widemouth glass jar with tightly sealing teflon-lined screw top. The sample may need to be frozen before being transported to an appropriate microbiology laboratory for analysis of phospholipid fatty acids (PLFA). PLFA analysis defines the viable biomass, community structure, and nutritional status of microbes, information necessary to assess the potential of *in situ* bioremediation. A "standard" PLFA assay can cost $300.00 per sample. Depending on the contaminant of concern, the following additional analyses (cost in brackets) may be necessary: (1) poly beta-hydroxy alkanoate(PHA) for further refinement of community nutritional status [$50.00]; (2) steroids to further define microeukaryote community structure [$50.00]; lipopolysaccharide lipid A hydroxy fatty acids for identification of gram-negative bacteria [$250.00]; (3) diglycerides for evidence as to which communities are viable

and which ones are not [$100.00]; and (4) triglycerides to measure eukaryote nutritional status [$100.00] (summarized from information obtained from Microbial Insights, Inc., Nashville, Tennessee). Arguably, such costs (up to $850.00 per sample) are prohibitive for many site characterizations. Yet, if bioremediation becomes the only viable remediation technology for a site, the cost of retrieving subsurface samples at a later date can be even more prohibitive than an initial microbe analysis. A solution may be to routinely freeze a number of sediment cores or samples for analyses that may be needed later when the scope of the problem is fully known (suggested by D.M. Miller, Subsurface Restoration Conference, 1992).

FACIES ANALYSIS

Why Facies Analysis for Site Characterization?

Subsurface fluid migration is controlled in part by geologic features developed during sediment deposition. This deposition produces heterogeneities that complicate the prediction of fluid behavior and hence the effectiveness of proposed remediation programs for each specific site. These depositional heterogeneities are not randomly distributed, rather they occur as predicable groups of features within genetically-related sedimentary units. Facies analysis, as applied here is a descriptive methodology that allows groups of these genetically-related sediment units to be summarized into a conceptual model of a particular depositional system (e.g., Walker, 1992; Boggs, 1992). Such "facies models" allow sedimentologists to compare their detailed site-specific information against the ideal case (the facies model). In contrast, environmental geologists may be able to use the conceptual facies model to extrapolate limited field data and thereby avoid the time and expense of obtaining detailed site-specific information necessary to characterize envirogeologic heterogeneity (modified from Anderson, 1989).

History of Facies Terminology

The term facies was introduced by Gressly (1838, *fide* Selley, 1988) to define sedimentary units of rock that were characterized by similar lithologic and paleontologic attributes. Over the years, Gressley's term "facies" has been expanded to include almost all scales of everything geologic, both descriptive and interpretive. Facies scales and types range from microfacies descriptions (defined by petrographic thin-section analysis) to individual lithofacies descriptions (e.g., individual sand bed) to large-scale depositional environment interpretations (e.g., fluvial facies). The facies concept has also been applied to metamorphic rocks (Eskola, 1915, *fide* Selley, 1988), mineral assemblages (Eskola, 1922, *fide* Krumbein and Sloss, 1963); post-depositional biological effects on sedimentary deposits (ichnofacies, e.g., Seilacher, 1967); geological, technical, and economic factors connected with the formation of colliery spoil from coal mining ("geologic-technical" facies of Wiggering, 1993), and many others.

Today, there is no general agreement on the usage of the term facies. Many suggest that the term facies should be restricted to its original descriptive application (e.g., Selley, 1988; Walker, 1992), while others believe interpretive usages are acceptable if clearly defined (e.g., tidal-flat mud facies to interpret a depositional environment, or storm-generated sand-ridge facies to interpret a depositional process;

Anderton, 1985). In summary, facies remains a viable term, though one must be clear whether it is being applied descriptively or interpretively.

Application to Envirogeolgic Characterization

Facies models can be developed for envirogeologic characterization by using depositional architectural element analysis. Architectural elements are morphologic subdivisions of a particular depositional system characterized by a distinctive assemblage of facies units (Allen, 1983). These individual facies are also known as depositional elements or architectural units (Miall, 1991). Architectural element analysis provides a means of studying sedimentary deposits at scales ranging from millimeters to kilometers; its geologic significance is well documented (e.g., Allen, 1983; Miall, 1985,1991,1992; Einsele, 1992; Jordan and Pryor, 1992; Dreyer and others, 1993; Shanley and McCabe, 1993). The virtue of this method is that it reverts to the purely descriptive and frees the geologist from rigid adherence to any preconceived conceptual model. A framework for carrying out such an analysis is provided by Miall (1985).

From a purely hydrogeologic perspective, architectural element analysis defines large-scale hydrogeologic trends, hydrogeologic effective properties, and, when combined with permeability studies, provides the most comprehensive source of two- and three-dimensional information on hydrogeologic heterogeneity (e.g., Anderson, 1989; Chandler and others, 1989; Blair and others, 1991; Davis and others, 1993; Hartkamp-Baker and Donselaar, 1993). For example, architectural element analysis provided the framework to delineate dissolved pentachlorophenol movement within an aquifer at a site in California (Blair and others, 1991). At this site, detailed lithologic descriptions from 29 boreholes were augmented with rare surface outcrops to characterize aquifer heterogeneity and provide a basis for accurate modelling of the complex groundwater system.

Architectural element analysis requires data from a substantial number of boreholes along with either coeval surface exposures or outcrop analogs. Surface exposures or outcrop analogs must be studied to provide guides or models for the interpretation of subsurface data which are derived from cores, drill cuttings, and a variety of geophysical methods. Without information derived from these surface analogs, solutions to subsurface analyses are not unique. Unfortunately, most envirogeologic site investigations do not have the luxury of relevant outcrops to study or large numbers of boreholes from which continuous data can be retrieved. Despite these sampling limitations, facies analysis for predictive purposes can still be undertaken.

Envirogeologic Facies Analysis for Shallow Boreholes

The following five facies analysis guidelines follow Anderton (1985), with modifications where appropriate for hollow-stem auger sample limitations.

(1) From the short core or split-barrel sample, describe the lithology of each convenient unit. Following field description, divide the logged section by lithologies (generally) into a small number of facies. The remaining guidelines can be performed in the office.

(2) Compile a general description of the features found in the various examples of each facies from each borehole. Use proper modifiers for descriptions of features,

such as: always, usually, sometimes, and occasionally. Do not interpret - just describe.

(3) Interpret each facies in isolation from the other facies. For example, can any deductions be made about sedimentary process? Again, use appropriate modifiers, such as indicates, suggests (strongly to weakly), compatible, inconclusive, and contradicts.

(4) Look at the relationship between facies. Look for simple patterns or variations of patterns such as fining-, thickening-, or coarsening-upward sequences. Such relationships define facies associations and architectural elements. Draw cross-sections, or preferably, fence diagrams.

(5) Attempt to relate any facies associations to a simple, published conceptual model. Excellent sources of facies models include Einsele (1992) and Walker (1992). With limited borehole data, this process is very interpretive. The advantage of trying to define a model is in using its predictive power to extrapolate such limited field data. Remember to favor a simple model over a complex one: subsurface data alone does not allow unique solutions.

SUMMARY

It is becoming increasingly obvious that there is no widely used standard to analyze shallow bore hole drilling programs. ASTM descriptions of soils are good but inadequate for this task. Table 1 summarizes the proposed descriptive methodology for envirogeologic characterization of bore holes. The proposed standard cannot be universally applied to all site characterizations; for each site, the number of recommended analyses will be limited by site conditions and the project budget. Nevertheless, the proposed methodology is inexpensive and rapid; most of the techniques are part of a geologist's standard undergraduate education. During initial site characterization, it may not seem necessary to conduct such detailed assessments. This would be a mistake; the time required to make the descriptions and/or take the samples is minor compared to the possible costs associated with re-sampl;ing at a later date. In effect, using the proposed methodology may reduces overall site assessment costs.

We hope that introducing some ideas for standardization will stimulate discussion and result in the routine gathering of higher quality and larger amount of data for site characterizations.

REFERENCES

Allen, J.R.L., 1983, Studies in fluviatile sedimentation: bars, bar complexes and sandstone sheets (low-sinuosity braided streams) in the Brownstones (L. Devonian), Welsh Borders: Sedimentary Geology, v. 33, p. 237-293.

Allen, J.R.L., 1985, Principles of Physical Sedimentology: George Allen and Unwin, London, 272p.,

Alyamani, M.S., and Sen, Z., 1993, Determination of hydraulic conductivity from complete grain-size distribution curves: Ground Water, v. 31, p. 551-555.

Anderson, M.P., 1992, Basic science required for decision making: Geological setting, in: Subsurface Restoration Conference Proceedings Volume for 1992, , National Center for Ground Water Research, Rice University, Dept. of Environmental Science and Engineering,Houston, Texas, p. 5-7.

Anderson, M.P., 1989, Hydrogeologic facies models to delineate large-scale spatial trends in glacial and glaciofluvial sediments: Geological Society of America Bulletin, v. 101, no. 4, p. 501-511.

Anderton, R., 1985, Clastic facies models and facies analysis, in Brenchley, P.J., and Williams, B.P.J., eds., Sedimentology: Recent Developments and Applied Aspects: The Geological Society (London), Alden Press, Oxford, p. 31-47.

ASTM (American Society for Testing and Materials), 1988, Annual Book of ASTM Standards, Section 4, Construction, Volume 04.08, Soil and Rock, Building Stones, Geotextiles, ASTM, Philadelphia, Methods D-2487 and 2488.

Atkins, J.E., and McBride, E.., 1992, Porosity and packing of Holocene river, dune, and beach sands: American Association of Petroleum Geologists Bulletin, v. 76, p. 339-355.

Ball, W.P., Buehler, C.H., Harmon, T.C., Mackay, D.M., and Roberts, P.V., 1990, Characterization of a sandy aquifer material at the grain scale: Journal of Contaminant Hydrology, v. 5, p. 253-295.

Bjerg, P.L., and Christensen, T.H., 1993, A field experiment on cation exchange-affected multicomponent solute transport in a sandy aquifer: Journal of Contaminant Hydrology, v. 12, p. 269-290.

Blair, T.C., Baker, F.G., and Turner, J.B., 1991, Cenozoic fluvial-facies architecture and aquifer heterogeneity, Oroville, California Super Fund site and vicinity, in Miall, A.D., and Tyler, N., eds., The Three-dimensional Facies Architecture of Terrigenous Clastic Sediments and its Implications for Hydrocarbon Discovery and Recovery: SEPM (Society of Sedimentary Geology) Concepts in sedimentology and paleontology, Volume 3, p. 148-159.

Blake, G.R., 1965, Particle Density, in Black, C.A., editor-in-chief, Methods of Soil Analysis, Part 1, Physical and Mineralogic Properties, Including Statistics and Measurements of Sampling: American Society of Agronomy, Inc., Madison, Wisconsin, p. 371-373.

Boggs, S. Jr., 1992, Petrology of Sedimentary Rocks: Macmillan Publishing Company, New York, 707p.

Chandler, M.A., Kocurek, G., Goggins, D.J., and Lake, L.W., 1989, Effects of stratigraphic heterogeneity on permeability in eolian sandstone sequence, Page Sandstone, northern Arizona: American Association of Petroleum Geologists Bulletin, v. 73, p. 658-668.

Chapelle, F.H., 1993, Ground-water Microbiology and Geochemistry: John Wiley and Sons, New York, 424p.

CME (Central Mine Equipment Co.), 1987, Catalog of product literature: St. Louis, Missouri, 12p.

Davis, J.M., Wilson, J.L., and Phillips, F.M., in press, A portable air-minipermeameter for rapid in-situ field measurements: Ground Water.

Davis, J.M., Lohman, R.C., Phillips, F.M., Wilson, J.L., and Love, D.W., 1993, Architecture of the Sierra Ladrones Formation, central New Mexico: Depositional controls on the

permeability correlation structure: Geological Society of America Bulletin, v. 105, p. 998-1007.

Detriech, R.V., Dutro, J.T., Jr., and Foose, R.M. (compilers), 1982, AGI Data Sheets: for Geology in the Field, Laboratory, and Office: American Geological Institute, Falls Church, Virginia.

Dreyer, T., Falt, L.-M., Hoy, T., Knarud, R., Steel R., and Cuevas, J.-L., 1993, Sedimentary architecture of field analogues for reservoir information (SAFARI): a case study of the fluvial Escanilla Formation, Spanish Pyrenees, in Flint, S.S., and Bryant, I.D. (eds.), The Geological Modelling of Hydrocarbon Reservoirs and Outcrop Analogs, International Association of Sedimentologist Special Publication Number 15, Blackwell Scientific Publications, Oxford, p. 3-20.

Dunham, R.J., 1962, Classification of carbonate rocks according to depositional texture, in Ham, W.E., ed., Classification of carbonate rocks: American Association of Petroleum Geologists Memoir 1, p. 108-121.

Einsele, G., 1992, Sedimentary Basins, Springer-Verlag, Berlin, 628p.

Feenstra, S.D., Mackay, M., and Cherry, J.A., 1991, Presence of residual NAPL based on organic chemical concentrations in soil: Ground Water Monitoring Review, v. XI, p. 128-138.

Goddard, E.N., chairman, and five committee members, 1980, Rock-color chart: Geological Society of America, Boulder, Colorado.

Hackett, G., 1987, Drilling and constructing monitoring wells with hollow-stem augers, part I: drilling considerations: Ground Water Monitoring Review, v. 7, p. 51-2.

Hartkamp, C.A., Arribas, J., and Tortosa, A., 1993, Grain size, composition, porosity and permeability contrasts within cross-bedded sandstones in Tertiary fluvial deposits, central Spain: Sedimentology, v. 40, p. 787-799.

Hartkamp-Baker, C.A., and Donselaar, M.E., 1993, Permeability patterns in point bar deposits: Tertiary Loranca Basin, central Spain, in Flint, S.S., and Bryant, I.D. (eds.), The Geological Modelling of Hydrocarbon Reservoirs and Outcrop Analogs, International Association of Sedimentologist Special Publication Number 15, Blackwell Scientific Publications, Oxford, p. 157-168.

Howard, A.K., 1984, The revised ASTM standard on the Unified Classification System: Geotechnical Testing Journal, v. 7, p. 216-222.

Huling, S.G., 1989, Facilitated transport, EPA Superfund Groundwater Issue, Office of Solid Waste and Emergency Response, Office of Research and Development, United States Environmental Protection Agency, EPA/540/4-89/003, 5p.

Jordan, D.W., and Pryor, W.A., 1992, Hierarchical levels of heterogeneity in a Mississippi River meander belt and application to reservoir systems: American Association of Petroleum Geologists Bulletin, v. 76, p. 1601-1624.

Kinniburgh, D.G., and Jackson, M.L., 1981, Cation adsorption by hydrous metal oxides and clays, in Anderson, M.A., and Rubin, A.J., eds., Adsorption of Inorganics at Solid-Liquid Interfaces: Ann Arbor Science Publishers, Ann Arbor, Michigan, p. 91-160.

Krumbein, W.C., 1934, Size frequency distributions of sediments: Journal of Sedimentary Petrology, v. 4, p. 65-77.

Krumbein, W.C., and Sloss, L.L., 1963, Stratigraphy and Sedimentation, Second Edition: W.H. Freeman and Company, San Francisco, 660.

McComish, M.F., and Ong, J.H., 1988, Chapter 7: Trace Metals, in Bodek, I., ed., Environmental Inorganic Chemistry: Pergamon Press, New York, p 7.1-7.15-10.

Miall, A.D., 1985, Architectural-element analysis: a new method of facies analysis applied to fluvial deposits: Earth Science Reviews, v. 22, p. 261-308.

Miall, A.D., 1991, Hierarchies of architectural units in terrigenous clastic rocks, and their

relationship to sedimentation rate, in Miall, A.D., and Tyler, N., eds., The Three-dimensional Facies Architecture of Terrigenous Clastic Sediments and its Implications for Hydrocarbon Discovery and Recovery: SEPM (Society of Sedimentary Geology) Concepts in sedimentology and paleontology, Volume 3, p. 6-12.

Miall, A.D., 1992, Chapter 7, Alluvial Deposits in Walker, R.G., and James, N.D., eds., Facies Models, response to sea level change: Geological Association of Canada, St. John's, Newfoundland, p. 119-142.

Payne, T.G., 1942, Stratigraphical analysis and environmental reconstruction: American Association of Petroleum Geologists Bulletin, v. 26, p. 1697-1770.

Piwoni, M.D., and Keeley, J.W., 1990, Basic concepts of contaminant sorption at hazardous waste sites, EPA Ground Water Issue: Office of Solid Waste and Emergency Response, Office of Research and Development, United States Environmental Protection Agency, EPA/540/4-90/053, 7p.

Seilacher, A. 1967, Bathymetry of trace fossils: Marine Geology, v. 5, p. 413-428.

Selley, R.C., 1988, Applied Sedimentology: Academic Press, London, 446p.

Sensidyne, Inc., 1992, Operation Manual for portable Flame Ionization Detector (FID), Sixth Edition, Revision B, October, 1992.

Shanley, K.W., and McCabe, P.J., 1993, Alluvial architecture in a sequence stratigraphic framework: a case history from the Upper Cretaceous of southern Utah, USA, in Flint, S.S., and Bryant, I.D. (eds.), The Geological Modelling of Hydrocarbon Reservoirs and Outcrop Analogs, International Association of Sedimentologist Special Publication Number 15, Blackwell Scientific Publications, Oxford, p. 21-56.

Swanson, R.G., 1981, Sample Examination Manual: America ɔsociation of Petroleum Geologists Methods in Exploration Series, Tulsa, Oklahoma, 118p.

U.S.EPA (Environmental Protection Agency), 1986, RCRA Ground-water monitoring technical enforcement guidance document: Office of Waste Programs Enforcement, Office of Solid Waste and Emergency Response, OSWER-99501.1, United States Environmental Protection Agency, 317p.

Walker, R.G., 1992, Facies, facies models and modern stratigraphic concepts, in Walker, R.G., and James, N.P., eds., Facies Models: Response to Sea Level Change: Geological Association of Canada, p. 1-14.

Wentworth, C.K., 1922, A scale of grade and class terms for clastic sediments: Journal of Geology, v. 30, p. 377-392.

Wiggering, H., 1993, Sulfide oxidation - an environmental problem within colliery spoil dumps: Environmental Geology, v. 22, p. 99-105.

Younger, P.L., 1992, The hydrogeological use of thin sections: inexpensive estimates of groundwater flow and transport parameters: Quarterly Journal of Engineering Geology (London), v. 25, p. 159-164.

Hydrogeology, Waste Disposal, Science and Politics
Proceedings 30th Symposium
Engineering Geology and Geotechnical Engineering, 1994

A MISE-A'-LA-MASSE METHOD FOR LANDFILL CONTAMINANT PLUME EVALUATION

T.H. Rowley and Paul R. Donaldson, Department of Geosciences, Boise State University, James L. Osiensky, Hydrology Program, University of Idaho, and John A. Welham, Idaho Geological Survey, Pocatello.

ABSTRACT

A mise-a'-la-masse survey was conducted down gradient of the Bannock County Landfill, in Fort Hall Canyon, Idaho in 1993. Data collected during the survey were compared to seismic refraction data also collected at the site. The site at the mouth of Fort Hall Canyon is ideal for use of the mise-a'-la-masse method to characterize a contaminant plume under actual field conditions. A contaminant plume is believed to emanate from the Bannock County Landfill. The plume contains high concentrations of Dense Non-Aqueous Phase Liquids (DNAPLs) plus inorganic groundwater contaminants. These DNAPLs and inorganics have been detected in nearby domestic and municipal water supply wells. The field site is relatively free of cultural interference that would adversely affect electrical-potential fields.

The mise-a'-la-masse method of plume identification, first suggested by Osiensky and Donaldson (1994) has not been applied at the scale of an actual contaminant plume prior to this investigation. The method is much easier to use and the data interpretation is less subjective than other electrical methods; however, it does not yield depth information. The mise-a'-la-masse method was used successfully to identify electric-field anomalies near the Bannock County Landfill. A seismic refraction survey suggested that three large buried channels meander across an old alluvial fan beneath the site. The alluvial fan is underlain by an undulating bedrock surface. The electric-field map correlates very well with the interpretation of the seismic survey in those areas where the data sets coincide. Most electric-field highs are located above areas seismically interpreted as buried channels or basins. These features may provide preferential flow paths for the contaminated groundwater and DNAPLs.

Ongoing work involves a second phase mise-a'-la-masse survey enlarging the area of investigation to include more of the area covered by the seismic survey. These data will be correlated with existing surface geophysical data sets and with current geological studies to better understand the hydrogeology of the site.

INTRODUCTION

The Bannock County Landfill, like many pre-subtitle D landfills in Idaho, and in the United States in general, are located in sand and gravel deposits of fluvial origin. From the standpoint of ground water quality protection, these landfills are located inappropriately due to the lack of a low hydraulic-conductivity geologic unit to protect aquifers used for domestic and municipal water supplies.

Ground water monitoring in complex fluvial deposits is complicated by the fact that ground water contaminants often migrate along preferred pathways caused by lateral and vertical heterogeneity within a stratigraphic unit. Delineation of preferential flow paths historically has required the

construction of numerous ground water monitoring wells at great expense (Osiensky and others, 1984). Surface geophysics can add important information on the shape, character, and spatial distribution of heterogeneities within fluvial hydrostratigraphic units thereby reducing the uncertainty and expense in ground water monitoring programs.

Surface electrical resistivity has been used to identify subsurface lithologic variations including buried stream channels (Zhody and others, 1974; Urish, 1983; Ayers, 1989), altered and saturated zones in bedrock (Applegate and Donaldson, 1977) and other geotechnical parameters (Donaldson, 1975). Electrical resistivity has also been used by many investigators to locate variations in ground water quality and to delimit zones of ground water contamination. Recent examples of these uses include the work of Ringstad and Bugenig (1984), Weber and others (1984), and Rudy and Caoile (1984). White (1988) described a field study in New Zealand where the method of Fried (1975) was used to determine the direction of movement and velocity of a salt-water slug injected into an aquifer.

Surface electrical resistivity measurements can be manipulated to gain understanding of the geologic conditions that exist at a site. Resistivity data typically are collected using one or more electrode arrays that have been developed over the years for various geologic conditions. Examples of these electrode arrays include the Wenner array (Wenner, 1916), Schlumberger array (Compagnie Generale de Geophysic, 1955), Dipole-Dipole array (Al'pin, 1950), etc. Resistivity surveys usually include both electrical sounding and horizontal profiling. Electrical sounding is the process for performing depth investigations and horizontal profiling is the process for detecting lateral variations in resistivity (Zhody and others, 1974). According to Zhody and others (1974), the probability of correct interpretation of the resistivity data can be improved by correlating several sounding curves, making crossed soundings, sounding with different arrays, traversing the area with horizontal resistivity profiles, knowing the general geology, and identifying the electrical properties of the rocks in the studied area. The electrical resistivity arrays mentioned above are somewhat cumbersome and time consuming to use. In addition, the quality of the interpretations is dependent on the qualifications and experience of the investigators.

The mise-a'-la-masse method was first suggested by Schlumberger (1920). Information derived with this method is not as complete as with the typical resistivity array. However, the method is much easier to use and the data interpretation is less subjective. The mise-a'-la-masse method has been used successfully in the mining industry to delineate partially exposed ore bodies. Originally the method was designed to map conductive orebodies by passing an electric current into an outcrop and recording electrical potential measurements at land surface (figure 1).

The mise-a'-la-masse method has direct application to the evaluation and interpretation of inorganic (conductive) contaminant plumes that emanate from known sources (e.g., leaking

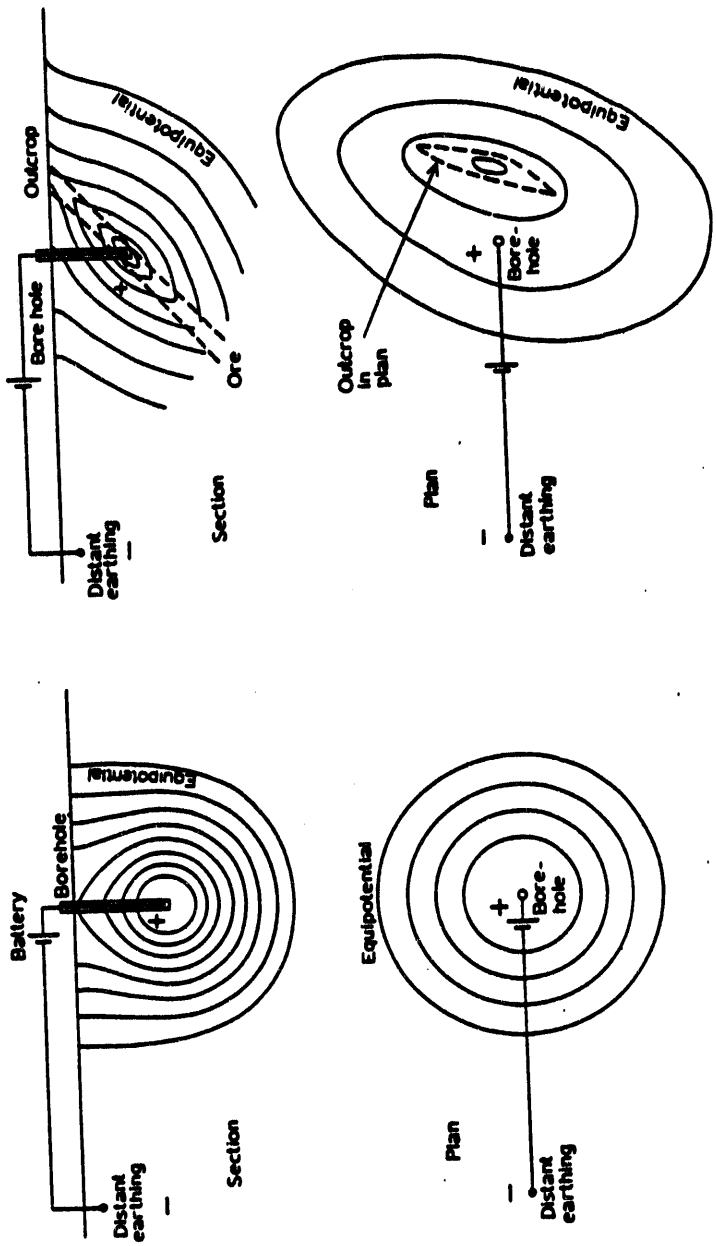


Figure 1. Principle of the mise-a'-la-masse method. Right-hand part of the figure shows the distortion of the electrical equipotential lines due to an ore body (from Parasnis, 1975).

underground tanks, landfills, etc.). If the source of contamination isn't known the contaminant plume can be electrically excited via monitoring wells. The configuration of the equipotentials derived by exciting the formation (plume) via boreholes (monitoring wells) should be nearly identical to those generated by exciting the source directly if the formation is an excellent electrical conductor (Parasnis, 1975). The resulting equipotentials may be used to help identify the contaminant source as well to help delineate extent and continuity of the contaminant plume.

The organic solvents that are denser than, and immiscible in, water such as perchloroethylene ("perc') and tetrachloroethylene (TCE) are referred to as dense nonaqueous phase liquids (DNAPLs). The unique physical and chemical properties of DNAPL chemicals often limit the effectiveness of common remediation and monitoring methods.

The resistive DNAPL chemical can exist in multiple phases (Schwille, 1988). The residual phase of DNAPL chemicals are evident in unsaturated zones after a spill has migrated to the saturated zone leaving microscopic droplets attached to soils or small grains. The gaseous phase exists as a product of evaporation of the liquid or "free" phase. The liquid phase will seek paths of least resistance along geologic structures such as dipped strata, faults and fractures without regard to saturation. The dissolved phase moves with the ground water gradient. Because it is possible for the liquid phase to move in a different direction than that of the dissolved phase, contaminant migration can be difficult to determine. The DNAPL liquid phase can pool on geological strata (i.e. clay lenses, unfractured bedrock). Thus, knowledge of the geologic and hydrologic units, if available, would assist in the development of a remediation plan.

Surface geophysical methods such as the mise-a'-la-masse method show promise for the delineation of DNAPL waste plumes by recording electrical anomalies. Currently, wells located down gradient of the Bannock County Landfill have detected high concentrations of TCE. Annan and others (1991) used surface electrical resistivity successfully to detect migration patterns of a controlled DNAPL plume.

Controlled Field Test

The following discussion is taken from Osiensky and Donaldson (1994). A field research site was developed within the floodplain of the Boise River, at Eagle Island State Park, approximately 24 kilometers west of Boise, Idaho in 1991. The site consists predominantly of coarse grained river gravels that are typical of many abandoned gravel pits which historically have been used as landfill sites. The research site was selected because of the undeveloped nature of the land (open field) and the existence of a shallow water table (less than 1.5 meters below land surface).

A backhoe trench was excavated approximately .5 meters below the water table for use as the source for the tracer experiment.

The background electrical potential field between the trench and the pumping well was measured with a "gradient array" by using the trench as a current electrode (i.e., the current electrode was driven into the bottom of the trench). The distant electrode (i.e., current sink) was driven into the edge of a swimming lake located 100 meters east of the trench. The gradient array consisted of disposable potential electrodes placed on 2 meter centers between the trench and the pumping well. Electrical potential measurements were taken one at a time at each potential electrode by completing an electrical circuit to a receiver system and a reference electrode.

The potential electrodes were placed above the zone where convergent tracer migration was being induced by ground water pumping. The electrical equipotentials were contoured for a comparative analysis through the time period of the tracer experiment (figure 2).

Electrical potentials within the test well field were measured at selected intervals during the tracer test to determine if the migration of tracer could be tracked with the modified mise-a'-la-masse method.

The controlled field test results prove that the modified mise-a'-la-masse method is very sensitive to changes in the specific-electrical-conductance of ground water. The next logical step is to apply the modified mise-a'-la-masse method to a larger field scale investigation.

FIELD APPLICATION

A field research site was surveyed within the alluvial fan below Fort Hall Canyon, Bannock County, approximately 5 miles southeast of Pocatello, Idaho. The site consists predominantly of a shallow rocky soil layer underlain by coarse grained river gravels. The research site was selected because of the undeveloped nature of the land (open fields) and the detection of high concentrations of DNAPLs in nearby water supply wells. Figure 6 shows the location of the site.

The site was surveyed using monitoring well MW3 (figure 3) as an origin for a grid of potential electrode stations every 50 meters within the test area. The current source electrode was an 8" steel well casing (T , figure 3) that extends below the water table. The distant electrode (i.e., current sink) was located approximately 1200 meters North of MW3 in Fort Hall Canyon. The electrodes were connected to the transmitter with insulated copper wire.

For this investigation, a Zonge GGT-3 transmitter and Zonge XMT-16 transmitter controller powered by a small 400-Hz generator were used for the current source. A Zonge Engineering GDP-16 receiver recorded the data. The transmitter-controller was used to ensure proper synchronization. The transmitted signal was a typical 4-second period time-domain signal. The electrical potentials were measured relative to a fixed reference electrode located north of MW3. Non-polarizing porous pots filled with approximately .2 liters of copper sulfate solution were used for the reference electrode and potential electrodes. Electrical

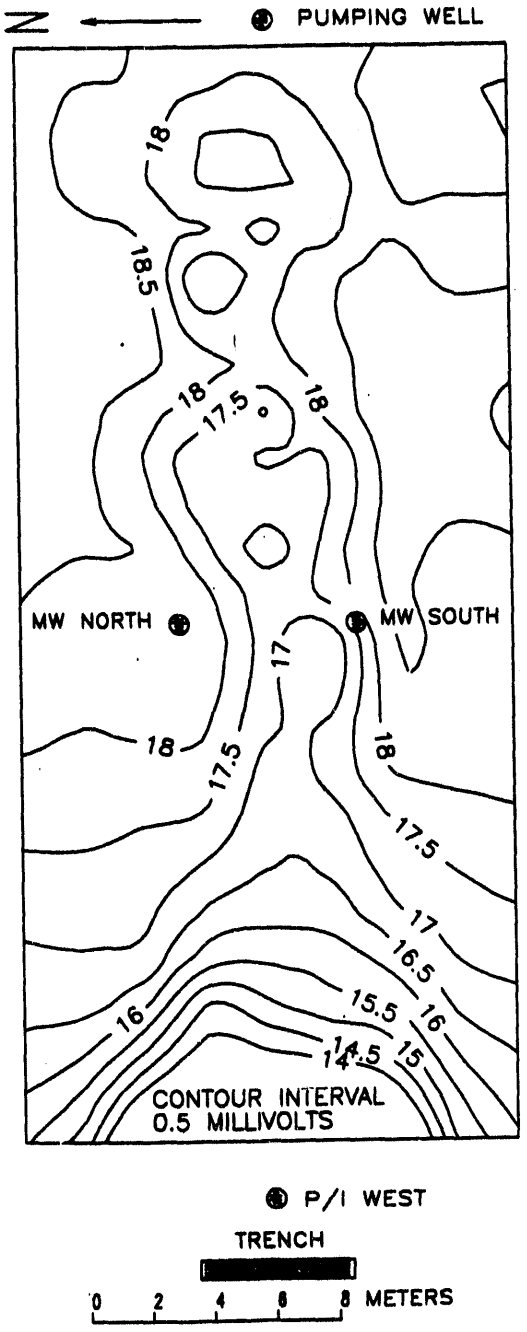


Figure 2. Electrical equipotential lines for the period 153 to 155 hours (9180 to 9300 minutes) after tracer injection. (from Osiensky and Donaldson, 1994)

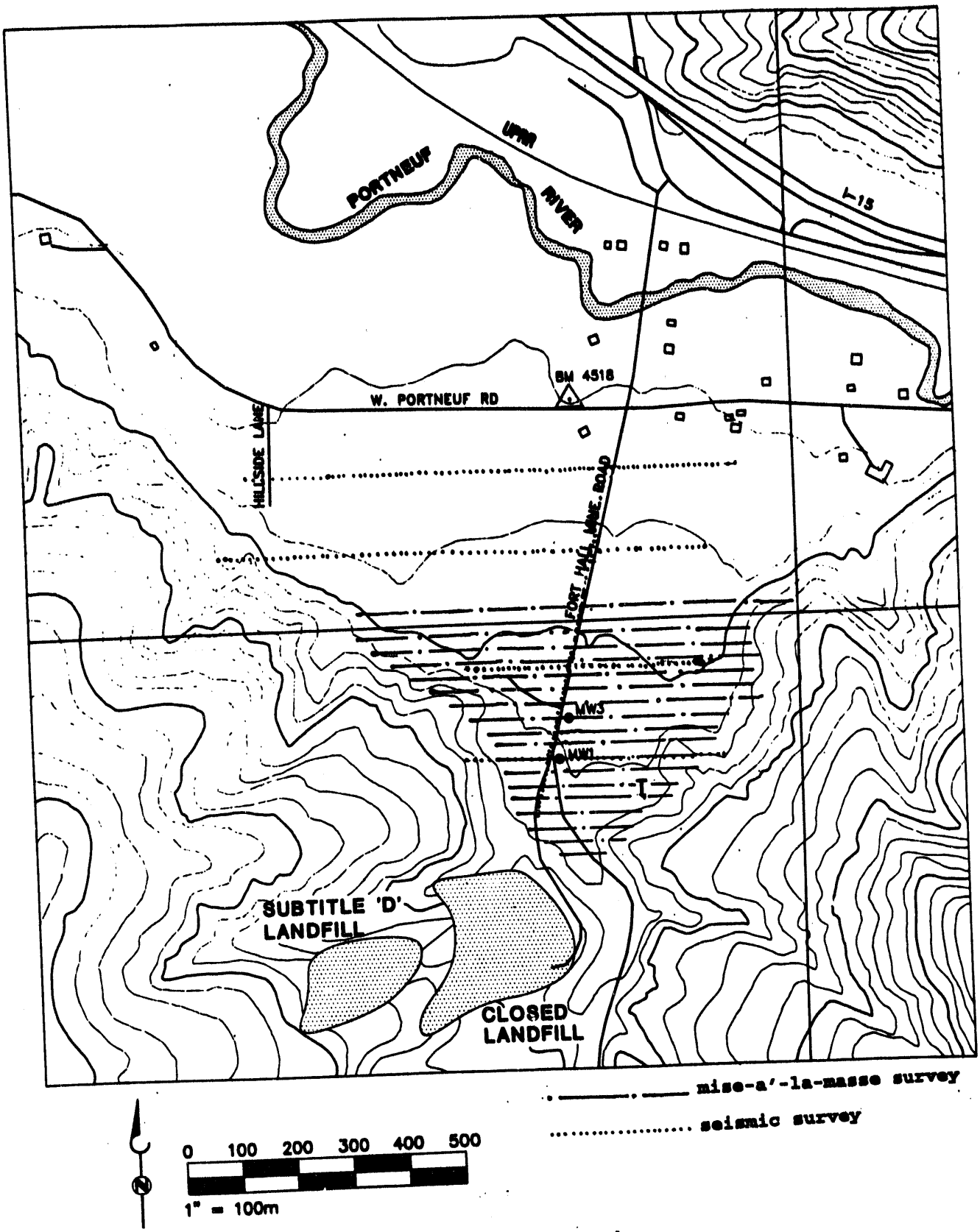


Figure 3. Map of Site

potential measurements were taken one at a time at each potential electrode by completing an electrical circuit to the reference electrode and receiver system. Data points were recorded every 25 meters East and West from the North-South baseline (see figure 3). The baseline stations were recorded every 25 meters from 300 meters South to 200 meters North from the MW3 origin. For each measurement, several cycles were recorded and averaged (stacked) to increase the signal-to-noise ratio and to allow a statistical analysis of data reliability. The recorded data were downloaded to a personal computer where they were manipulated into a gridded form. The electrical equipotentials were contoured for a comparative analysis with the interpreted seismic data provided by Bannock County.

The data points recorded at the site were downloaded to hard copies. The voltage potentials were corrected with reference point values. Figure 4 represents a contour map of the electric potentials recorded at the site.

CONCLUSIONS

The mise-a'-la-masse method was successful in delineating changes in the electric pocential field attributed to a contaminant plume emanating from Fort Hall Canyon. The contoured electric field map displays the high and low values recorded during the mise-a'-la-masse survey conducted at the Bannock County site in 1993 (figure 4). The contour pattern in figure 4 suggests that two large channels emerge from Fort Hall Canyon (below the landfill). These data correlated well with interpreted seismic data supplied by Bannock County. The seismic interpretation suggests that 3 large buried channels splay outward from the mouth of Fort Hall Canyon. The two northeasterly channels are next to each other. The third channel is directed westward. These channels possibly provide preferential flow paths for contaminant migration. The DNAPLs detected in down gradient wells confirm a pattern of relatively higher concentrations in wells located in or near the channel areas.

The relationship between the electric potential field and current density is described by Ohms Law. If current density is greater in preferential channels then the electric potential field is also greater. The higher values recorded during the survey could indicate areas of higher ground water flow, including contaminant fractions, thereby increasing the current density.

The mise-a'-la-masse survey will continue this spring. The interpreted mise-a'-la'masse data will be compared to other data provided by Bannock County.

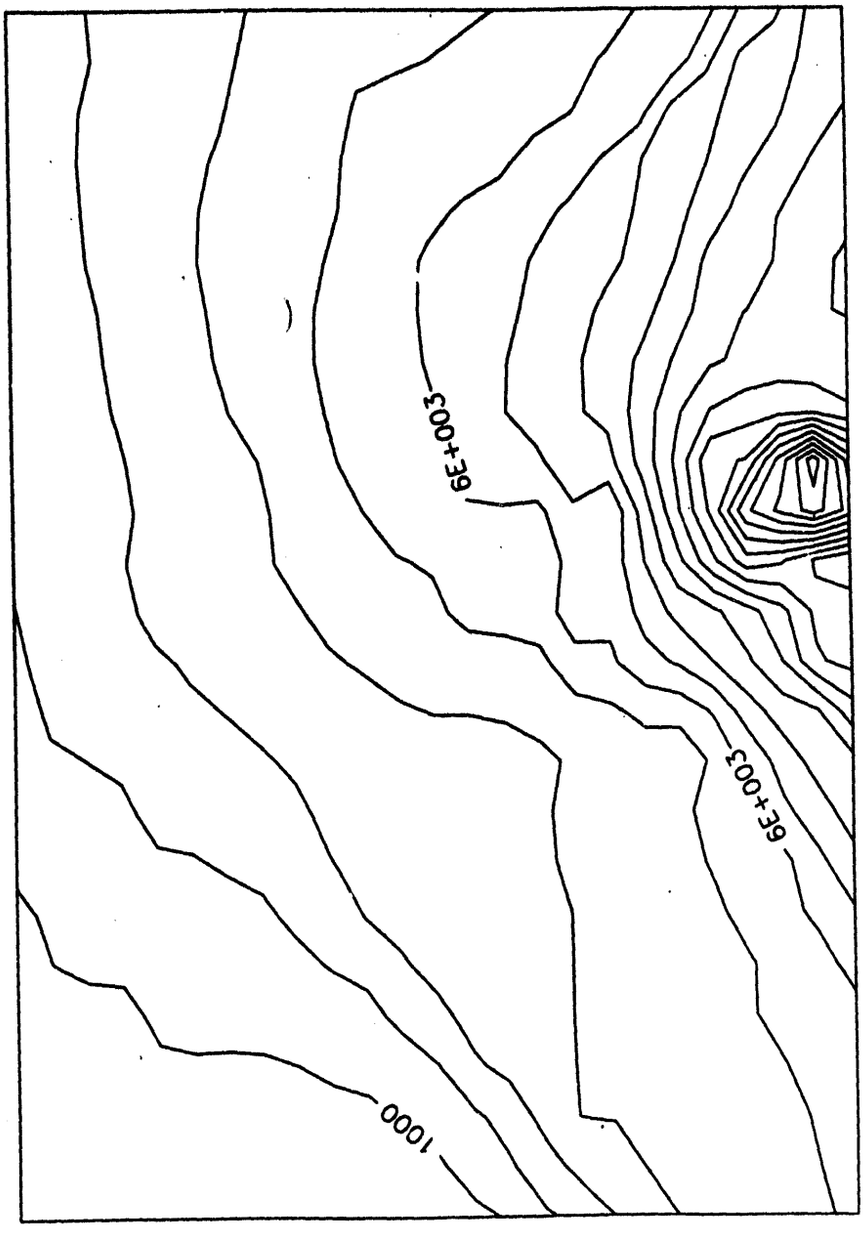
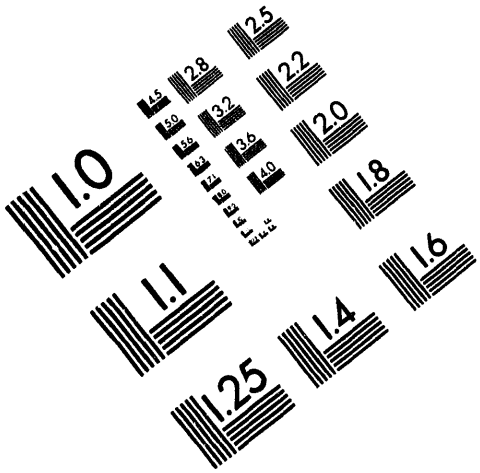
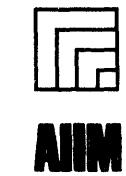
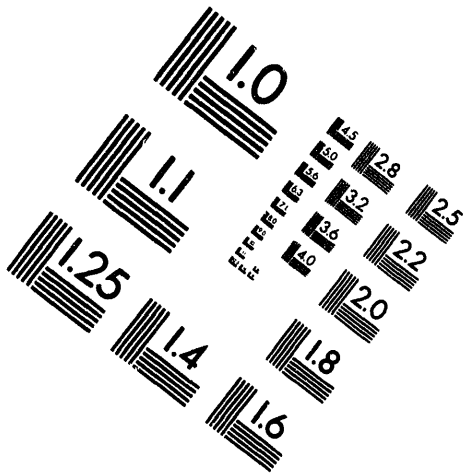


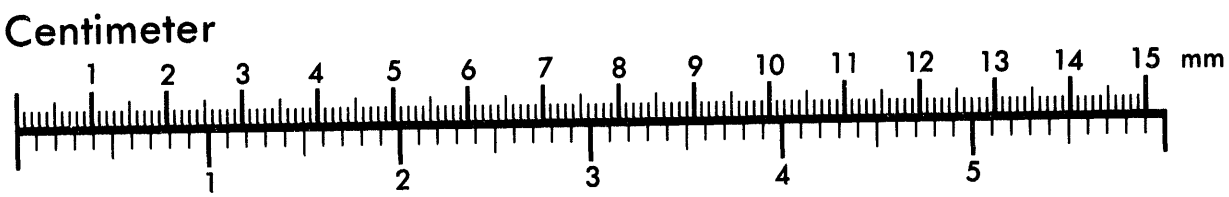
Figure 4. Electric Field Map

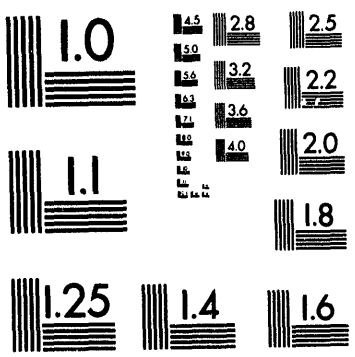


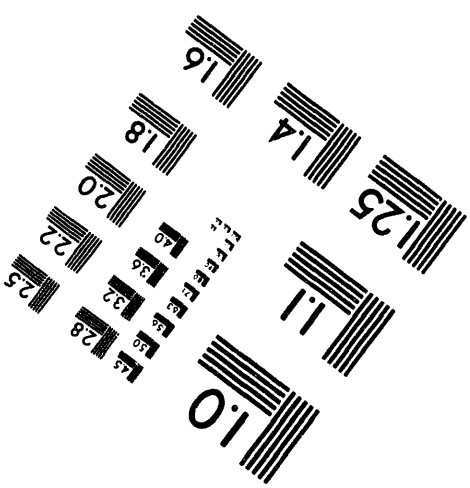


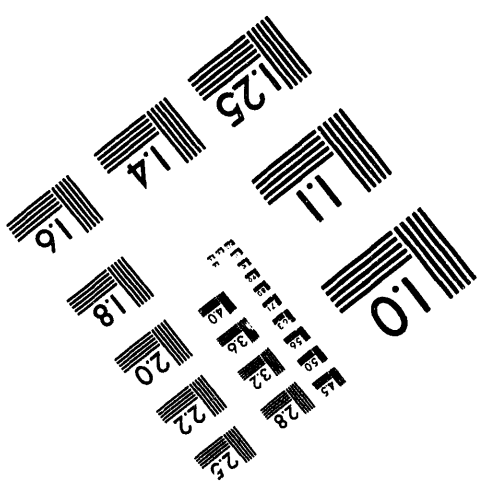
Association for Information and Image Management
1100 Wayne Avenue, Suite 1100
Silver Spring, Maryland 20910
301/587-8202











MANUFACTURED TO AIIM STANDARDS
BY APPLIED IMAGE, INC.

2 of 7

REFERENCES

Al'pin, L. M., 1950, The Theory of Dipole Sounding. Moscow, Gostoptekhizdat, 89p., (Translation in Dipole methods for measuring earth conductivity): New York, Plenum Press, 1966, p.60.

Annan, A.P., Bauman, P., Greenhouse, J.P., and Redman, J.D., 1991, Geophysics and DNAPLs, Ground Water Management No.5, Proceedings of the Fifth National Outdoor Action Conference on Aquifer Restoration, Ground Water Monitoring and Geophysical Methods, May 13-16, 1991, Las Vegas, Nevada, P. 963-977.

Applegate, J.K. and Donaldson, P.R., 1977, Geophysical Investigation of Rock Properties Near Silver Creek, Boise National Forest, Idaho, Department of Geology and Geophysics. Boise State University, Geoscience Contribution, n.107, 31p.

Ayers, J.F., 1989, Conjunctive Use of Geophysical and Geological Data in the Study of an Alluvial Aquifer, Ground Water, v.27, No. 5, pp. 625-632.

Compagnie Generale de Geophysique, 1955, Abaques de Sondage Electrique: Geophysical Prospecting, v. 3, supplement 3.

Fried, J.J., 1975, Groundwater Pollution, Theory, Methodology, Modelling and Practical rules. Elsevier, New York, p. 330.

Donaldson, P.R., 1975, Geotechnical Parameters and Their Relationship to Rock Resistivity, Proceedings of the Thirteenth Annual Engineering Geology and Soils Engineering Symposium, p.169-185.

Osiensky, J.L., Winter, G.V., and Williams, R.E., 1984, Monitoring and Mathematical Modeling of Contaminated Ground-Water Plumes in Fluvial Environments, Ground Water, v.22, p.298-306.

Osiensky, J.L., and Donaldson P.R., 1994, "The Modified Mise-A-La-Masse Method for Contaminant Plume Delineation," Ground Water, in-press.

Parasnis, D.S., 1975, Mining geophysics: methods in geochemistry and geophysics series (3), Elsevier, Amsterdam, p.395.

Ringstad, C.A., and Bugenig, D.C., 1984, Electrical Resistivity Studies to Delimit Zones of Acceptable Ground Water Quality, Ground Water Monitoring Review, v.4, n.4, p.66-69.

Rudy, R.J., and Coile, J.A., 1984, Utilization of Shallow Geophysical Sensing at Two Abandoned Municipal/Industrial Waste Landfills on the Missouri River Floodplains, Ground Water Monitoring Review, v.4, n.4, p.57-65.

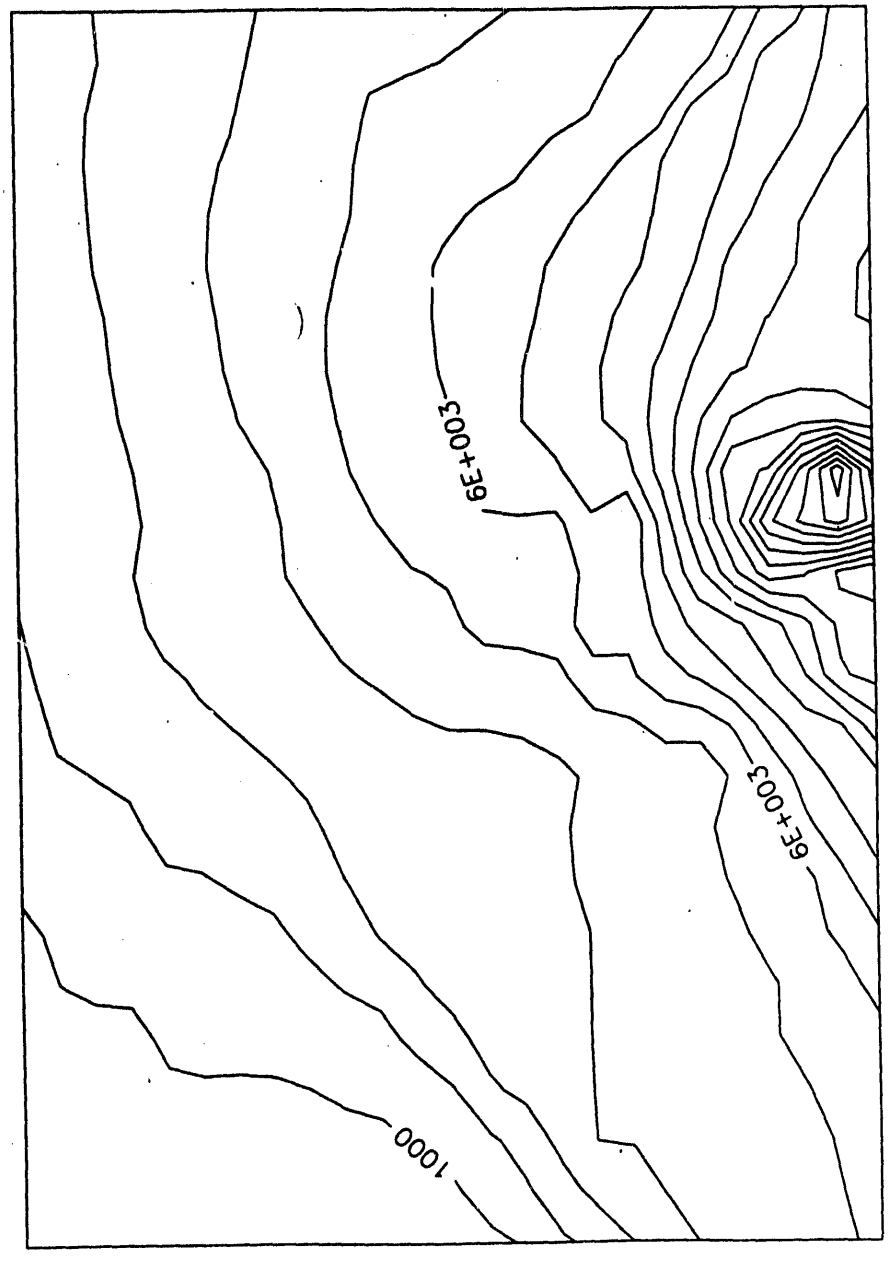


Figure 4. Electric Field Map

Schlumberger, C., 1920, Etude Sur la Prospection Electrique du Sous-sol, Gauthier-Villars, Paris, p. 94.
Schwille, F. 1988. Dense Chlorinated Solvents in Porous and Fractured Media; Model Experiments. Translated by J.F. Pankow. Lewis Publishers.

Urish, D.W., 1983, The Practical Application of Surface Electrical Resistivity to Detection of Ground-water Pollution, Groundwater, v.21, n.2, p.144-152.

Weber, D.D., Scholl, J.F., LaBrecque, D.J., Walther, E.G., and Evans, R.B., 1984, Spatial Mapping of Conductive Ground Water Contamination with Electromagnetic Induction, v.4, n.4, p.70-77.

Wenner, Frank, 1916, A Method of Measuring Earth Resistivity, U.S. Bureau of Standards Bulletin, v. 12, pp. 469-478.

White, P.A., 1988, Measurement of Ground-water parameters using salt-water injection and surface resistivity, Ground Water, v.26, no. 2, pp. 179-186.

Zhody, A.A., Eaton, G.P., and Mabey, D.R., 1974, Application of Surface Geophysics to Ground-Water Investigations, U.S. Geological Survey Techniques of Water-Resources Investigations, Book 2, Chapter D1, 116p.

Hydrogeology, Waste Disposal, Science and Politics
Proceedings 30th Symposium
Engineering Geology and Geotechnical Engineering, 1994

HOTSPOTS & OTHER HIDDEN TARGETS: Probability of Detection, Number, Frequency and Area

by

Charles L. Vita, Ph.D., P.E., G.E.
Principal Consultant
Environmental Science & Engineering, Inc. (ESE)
15444 NE 95th St., #244, Redmond, Washington 98052, 206/869-8220

ABSTRACT

Concepts and equations are presented for making probability-based estimates of the detection probability, and the number, frequency, and area of hidden targets, including hotspots, at a given site. Targets include hotspots, which are areas of extreme or particular contamination, and any object or feature that is hidden from direct visual observation--including buried objects and geologic or hydrologic details or anomalies. Being Bayesian, results are fundamentally consistent with observational methods. Results are tools for planning or interpreting exploration programs used in site investigation or characterization, remedial design, construction, or compliance monitoring, including site closure. Used skillfully and creatively, these tools can help streamline and expedite environmental restoration, reducing time and cost, making site exploration cost-effective, and providing acceptable risk at minimum cost.

INTRODUCTION

Purpose and Organization

Very simply, this paper aims to answer the question: given that hidden targets of some particular importance (such as hotspots) could exist at a site, what is the probability of detecting those targets, and what is the probable number, frequency, and area of targets? To that end, this paper presents conceptual and analytical tools for making probability-based estimates of the detection probability, number, frequency, and area of hidden targets in a given site or area of exploration. The tools are rigorous yet flexible and fundamentally consistent with observational methods and continuous improvement processes and strategies [9-14]. The purpose of these tools is to help make exploration program design, implementation, and data interpretation, efficient, rational, and technically defensible. When skillfully integrated with project requirements and conditions, these tools can help streamline and expedite environmental restoration, reducing time and cost, making site exploration cost-effective, and providing acceptable risk at minimum cost.

This paper is organized into this introductory section and five principal sections that follow. This introductory section defines targets and identifies fundamental assumptions and concepts, including statistical strata, random sampling, and probability models. The probability of target detection, Pd, is discussed second. The number of

undetected targets, U, is discussed third. Target areas are discussed fourth. General Bayesian updating is discussed fifth. The final section summarizes general conclusions.

Hotspots and Targets

Hotspots are areas of extreme or particular contamination. Targets is a more general concept that includes hotspots as a special case. That is, targets can include hotspots, as well as any object or feature that is hidden from direct visual observation--including buried objects and geologic or hydrologic details or anomalies. The tools presented in this paper apply to targets in general and hotspots in particular. Furthermore, the results presented here can be extended to quantify measures of target intensity or magnitude--for example, contaminant concentrations in hotspots.

Assumptions and Background

Estimates make three basic assumptions: (1) that the site (area being explored) has been divided into statistical strata; (2) that efficient random sampling is used; and (3) that target locations are spatially random or randomly clumped. Note that the third assumption implies that the probability, before exploration, that one or more targets exist, P_T, is not zero; if $P_T=0$, exploration is unnecessary because no targets exist, with certainty. The three basic assumptions are discussed further in the following paragraphs.

Statistical Strata

A site is divided into statistical strata (strata) [3-6] based on interpretation of available information, including project requirements. Strata reflect significant differences in target conditions, including conditions that create, or can create, targets. Strata are located so that within each stratum there are no expected significant, systematic differences in target conditions; thus, possible targets have equal probability of being anywhere in the stratum. Conversely, strata not having significant differences can be combined into one stratum. In certain situations, one stratum may cover multiple sites--thus allowing information to be transferred between sites, increasing exploration efficiency. Because strata are always defined based on available information, strata boundaries may require updating to reflect new information, as it becomes available.

Contamination targets may be distributed within a stratum in several ways: as uniformly random concentrations; as random hotspots of contamination in an otherwise clean area; or as random variations of concentration about a non-random continuous trend or "background" level of contamination. For example, absent contrary information, each of the following could be one stratum: a fuel spill soil stain; a waste pile from a single waste stream; sediment in a lagoon; a parking lot; a subsurface area of potential DNAPL pools; a transformer storage yard; an empty field; an uncontrolled landfill; a fire training area; a fuel storage yard; an aqueous-phase benzene plume; an LNAPL plume; an area of potential NAPL zones above a capillary fringe; a pipeline alignment; a section of railroad; a stream; a highway; a reach of river downstream from an outfall; a discharge zone; an air emission zone. Where significant systematic variations in contamination conditions are expected, the site is divided into multiple strata; for

example, a site consisting of product storage, waste storage, and a process area may be divided into three strata.

Because the importance and needed accuracy of information within a stratum may vary across the stratum, a stratum may be subdivided into zones requiring greater or lesser exploration to meet project requirements. And new information found during exploration may indicate, for example, that a stratum is composed of significant and systematically different target conditions, and should therefore be subdivided into strata; or vice versa, that strata are similar and can be combined. Thus, strata boundaries may change and evolve over time.

Random Sampling

Sampling within a stratum using a regular rectangular grid having a random start location provides random sampling [3-6] that is practical, efficient, uniform, and consistent with common geoscience grid sampling approaches. For given sampling density, the sampling grid used should provide uniform coverage over the stratum, to the extent practical for the site conditions. Within each grid the sampling point location $P_{(x,y)}$ is the same, but it is chosen randomly. For a uniform sample spacing of B_x in the x-direction and B_y in the y-direction, $P_{(x,y)}$ is located a distance B_xR_x and B_yR_y from the grid origin (any corner of the grid), where R_x and R_y are any two random numbers. The sampling locations will thus be regular rectangular and randomized (random sampling in three or four dimensions follows the same logic). Notice that for the common case of a square grid, the stratum sampling area, A, number of samples, N, and grid or sample spacing, B, are related by $B=Sqrt\{A/N\}$; for a one-dimensional linear grid $B=L/N$, where L is the stratum length. Because sampling density should be based on project requirements, a given stratum may be subdivided into zones requiring greater or lesser sample spacing; in each zone, sampling should provide uniform coverage to the extent practical.

Probability Models

Absent contrary information, target locations are Poisson events having an uncertain (or variable) average occurrence frequency following a gamma probability distribution function (pdf); the number of targets in a stratum thus follows a negative binomial pdf [10]. The target detection probability follows a beta pdf [10]. Each pdf is characterized by an expected value, E[ ], and coefficient of variation, CV[ ].

These probability models are consistent with the maximum-entropy principle [7]; they are therefore expected to provide robust, least-biased (maximum-entropy) estimates. The negative binomial pdf allows targets to be spatially random or randomly clumped. Assuming targets follow a negative binomial pdf is both reasonable and consistent with field observations from, and search theory used in, various geological, and biological, applications [2,8,9]. Furthermore, the models are Bayesian--making them maximally-consistent with phased-sampling and continuous updating of estimates, and combining information from multiple, independent exploration methods [1,8-14].

PROBABILITY OF TARGET DETECTION, Pd

The probability of detecting a target, Pd, given that targets could exist, depends on the probability of sampling a target, Ps, and the probability of detecting the target given that it is sampled, $Pd_{|s}$; that is:

[1] $Pd = Pd_{|s}Ps$

$Pd_{|s}$ includes uncertainty effects that depend on the sampling method. For example, $Pd_{|s}$ can reflect uncertainty from imperfect sampling and laboratory analysis [3]; uncertainty in the interpretation of site geophysical survey results; or uncertainty in the interpretation of site historical data, including airphotos. In the remainder of this paper, for brevity, Pd is tacitly understood to be conditional on $Pd_{|s}$.

Pd Based on Target Geometry

Given that targets could exist, Pd, the probability of detecting a target, depends on: target area, T_a; target geometry, T_g; and the search area, S_a. The relationship between these factors is given by Eq 2; that is:

[2] $Pd = T_g T_a S_a^{-1}$

Given any three variables, the fourth can be calculated using Eq 2. For regular rectangular grids with constant grid or sample spacing B, Eq 2 can be recast, replacing S_a with B^2 ($S_a = B^2$); that is:

[3] $Pd = T_g T_a B^{-2}$

Factor T_g depends on target geometry and the target-area to search-area ratio (T_a/S_a or T_a/B^2). Based on interpretation of [1,5,8], $T_g = 1$: for $T_a/B^2 < 0.3$, for all target geometries; for $T_a/B^2 < 0.79$, for circular targets; for $T_a/B^2 \leq 1.0$, for square targets. And for practical purposes, $T_g = 1$ for all geometries up to $T_a/B^2 = 0.50$. Eq 3 can thus be generalized and simplified to Eq 4; that is:

[4] $Pd \leq T_a B^{-2}$

Figure 1 shows the relationship between Pd and B for all target geometries up to Pd = 0.5 for selected Pd values, and selected target geometries for Pd = 1. These results suggest that $T_g = 1$ is a reasonable first approximation in most practical search situations, where grid spacing commonly exceeds 20 feet and 100 ft is not uncommon; for $T_g = 1$, Pd varies directly with the ratio of target area to grid spacing--i.e., $Pd = T_a B^{-2}$.

Implications

Eq 3 and Figure 1 imply that most practical exploration programs have a low probability of finding anything but relatively large targets. For example, there is only a

1% probability of finding a 100-ft^2 target using a grid spacing of 100 ft. Conversely, a grid spacing approaching the target size is necessary to achieve a high find probability. For example, finding a square 100-ft^2 target with 95% probability requires a grid spacing of no more than 10.3 ft; and finding 100-ft^2 targets with certainty requires a grid spacing of 10 ft or less, depending on target geometry. After exploration, no undiscovered, nearly-square targets of area exceeding B^2 exist; and no circular targets exceeding $1.57B^2$ exist; and so on.

These results indicate that small targets or hotspots are likely to go undetected in common exploration programs; and that not detecting a target or hotspot does not necessarily provide confidence that there are none. Importantly, however, other relevant site information that can be combined with grid-sampling information may be available. Combining independent information from different kinds of exploration can, in effect, increase Pd; the following section expands on this.

Pd Based On Sampling Results Or Combined Information Sources

Estimates of Pd can be based on sampling results. Imagine that an exploration program has identified D targets ($D \geq 0$) from N independent sampling points in a stratum. Assuming that Pd-estimates, $P_{Pd}[pd]$, follow a beta pdf between the limits of one and zero, $P_{Pd}[pd]$, the expected value of Pd, E[Pd], and the coefficient of variation of Pd, CV[Pd], are given by Eq 5; that is:

$$[5a] \quad P_{Pd}[pd] = (a-1)![(b-1)!(a-b-1)!]^{-1} pd^{b-1}(1-pd)^{a-b-1}$$

$$[5b] \quad E[Pd] = b/a$$

$$[5c] \quad CV[Pd] = \mathrm{Sqrt}\{(b-a)/(ab+a)\}$$

where $a=N+2$ and $b=D+1$. Parameters a and b include all actual sampling results. Because Eq 5 is Bayesian, parameters a and b may include relevant information not contained in N and D; in which case, $a=N+2+a'$ and $b=D+1+b'$, where a' and b' represent the additional information relevant to estimating Pd. In terms of target geometry, Eq 5 can be used with Eqs 2 and 3 to estimate parameters or variables, including target areas, T_a. Thus, parameters a and b may combine sampling data and target geometry information. Parameters a' and b' may also include additional information from site historical knowledge or experience with similar sites [10,11]. If a beta pdf is inappropriate, estimates of Pd can be based on any desired pdf using the total probability theorem [7].

NUMBER OF UNDETECTED TARGETS, U

Given that an exploration program over area A_e has identified D targets ($D \geq 0$) in a stratum, how many undetected targets, U ($U \geq 0$), remain? Unless $Pd=1$ (making $U=0$), U is unknown, and must be estimated. Estimates of U depend on whether Pd is known or estimated, as discussed in this section.

U, Number of Undetected Targets, Given Pd

Given that D and Pd are known, estimates of U follow a negative binomial pdf, with pdf $P_U[u]$, expected value, E[U], and coefficient of variation, CV[U], given by Eq 6; that is:

[6a] $P_U[u] = (u+D)!(u!D!)^{-1}Pd^{D+1}(1-Pd)^u$

[6b] $E[U] = (D+1)(1-Pd)Pd^{-1}$

[6c] $CV[U] = Sqrt\{(E[U]Pd)^{-1}\}$

Eq 6 has three special cases that are useful simplifications. Case 1.($U>0|D=0$): given that no targets were discovered ($D=0$), the probability that undiscovered targets remain, $P_U[u|D=0]$, and E[U] and CV[U] are given by Eq 7. Case 2.($U=0|D>0$): given that D targets have been discovered, the probability that all actual targets have been discovered, and none remain, $P_U[U=0|D>0]$, is given by Eq 8. Case 3.($U=0|D=0$): given that no targets were discovered ($D=0$), the probability that no undiscovered targets remain $P_U[U=0|D=0]$ is given by Eq 9 (which is the same as Eq 8 with $D=0$ or Eq 7a with $U=0$). That is:

[7a] $P_U[u|D=0] = Pd(1-Pd)^u$

[7b] $E[U|D=0] = (1-Pd)Pd^{-1}$

[7c] $CV[U|D=0] = Sqrt\{(1-Pd)^{-1}\}$

[8] $P_U[U=0|D>0] = Pd^{D+1}$

[9] $P_U[U=0|D=0] = Pd$

Eqs 6-9 say that the probable number of undetected targets increases as the number of detected targets increases or the probability of detection decreases. Figure 2 plots E[U] by Eq 6b for $D=0$, 1, and 10. Figure 3 plots $P_U[u|D=0]$ by Eq 7a for $u=0$ through $u=5$. Figure 4 plots $P_U[U=0]$ by Eq 8 for $D=0$, 1, 2, 3, 4 and 10. Note that D may come from one or more sampling phases in a given stratum.

Implications

Interpretation of Eqs 6-9 amplify the implications related to Pd, the target detection probability: to find all targets, or hotspots, requires a high Pd. For example, to claim a 95% probability that all targets have been found after finding no targets requires $Pd=95\%$; and if $Pd=1\%$, the expected number of remaining, undiscovered targets is 100. As another example, in terms of target areas, concluding with 95% probability that all targets have been found after finding two targets is only accurate for targets having areas greater than 98% of the sample spacing area, B^2.

Yet finding all targets or making high-confidence conclusions may or may not be necessary, depending on site conditions and project requirements. That is, exploration effectiveness should be consistent with project requirements. For example, high Pd's can be limited to areas requiring high confidence; lower Pd's can be used in areas requiring

less confidence. Exploration that is optimally consistent with project requirements is cost-effective and provides acceptable risk at minimum cost.

Target Frequency, T_f

Estimates of the total target frequency, T_f, over explored area A_e follows a gamma pdf with $P_{Tf}[t_f]$, $E[T_f]$ and $CV[T_f]$ estimated by Eq 10; that is:

[10a] $P_{Tf}[t_f] = (A_e t_f Pd)^{D+1} D!^{-1} \exp\{-A_e t_f Pd\}$

[10b] $E[T_f] = (D+1)(A_e Pd)^{-1}$

[10c] $CV[T_f] = \text{Sqrt}\{(D+1)^{-1}\}$

T_f is the sum of discovered and undiscovered target frequencies: T_{fU}, the undiscovered target frequency, being $T_f(1-Pd)$; and T_{fD}, the discovered target frequency, being $T_f Pd$. Note that T_{fD} is known ($CV[T_{fD}]=0$), whereas T_{fU} is uncertain, with $CV[T_{fU}]=CV[T_f]$.

Number of Targets in Unexplored Areas, A_u

Estimates of U_u, the number of targets in unexplored portions of a stratum, A_u, can be based on results from the explored portion A_e of that stratum. Importantly, A_u and A_e need not be contiguous or even part of the same site, provided they are from the same stratum. Estimates of U_u follow a negative binomial pdf, with $P_{Uu}[u]$, $E[U_u]$ and $CV[U_u]$ given by Eq 11; that is:

[11a] $P_{Uu}[u] = (u+D)!(u!D!)^{-1}(PdA_e)^{D+1}A_u{}^u(PdA_e+A_u)^{-D-u-1}$

[11b] $E[U_u] = (D+1)A_u(A_e Pd)^{-1}$

[11c] $CV[U_u] = \text{Sqrt}\{(D+1)^{-1} + E[U_u]^{-1}\}$

where Pd is for A_e. Note that in both explored and unexplored areas (of the same stratum) targets occur at the same frequency. Therefore, the total target frequency, T_f, can also be used to estimate $E[U_u]$; that is:

[12] $E[U_u] = A_u E[T_f]$

U, Number of Undetected Targets, With Pd Uncertain

Eqs 6-12 estimate U or U_u on the condition that Pd is known. They can also estimate U or U_u when Pd is uncertain using the total probability theorem (by summing the conditional U-estimates times the probability of each Pd value) or other estimation methods [7]. For the case of Pd following a beta pdf (Eq 5), $P_U[u]$, E[U], and CV[U] are given by Eq 13, where parameters a and b are discussed following Eq 5; that is:

[13a] $P_U[u] = (u+D)!(a-1)!(D+b)!(u+a-b-1)!\{u!D!(b-1)!(a-b-1)!(u+D+a)!\}^{-1}$

[13b] $E[U] = (D+1)(a-b)(b-1)^{-1}$

[13c] $CV[U] = Sqrt\{(a-1)(D-1)^{-1}E[U]^{-1}\}$

Eq 13, which is Bayesian, may be used to estimate targets in unexplored areas (A_u) by synthesizing estimates of parameters a, b, and D from interpretation of all available and relevant data.

TARGET AREAS, T_A

The areas of individual targets, T_a, can be estimated from Eq 3, solving for T_a: $T_a = PdT_g^{-1}B^2$. Then, $E[T_a]$ and $CV[T_a]$ can be estimated from Eq 14, where $p_{Pd,Tg}$ is the correlation coefficient between Pd and T_g (which is always negligible for $Pd < 0.5$); that is:

[14a] $E[T_a] = E[Pd]E[T_g^{-1}]B^2\ (1+p_{Pd,Tg}CV[Pd]CV[T_g])$
[14b] $CV[T_a] = Sqrt\{(CV[Pd]^2+1)(CV[T_g]^2+1)+2p_{Pd,Tg}C[Pd]CV[T_g]-1\}$

After exploration, the total area of discovered targets, T_{AD}, is the sum of the individual areas of the D discovered targets: $T_{AD} = Sum_D\{T_a\}$, with $E[T_{AD}]$ and $CV[T_{AD}]$ estimated from Eq 15; that is:

[15a] $E[T_{AD}] = E[T_a]D$
[15b] $CV[T_{AD}] = Sqrt\{CV[T_a]^2/D\}$

Similarly, the total area of undiscovered targets, T_{AU}, is the (random) sum of the individual areas of U undiscovered targets: $T_{AU} = Sum_U\{T_a\}$, with $E[T_{AU}]$ and $CV[T_{AU}]$ estimated from Eq 16; that is:

[16a] $E[T_{AU}] = E[T_a]E[U]$
[16b] $CV[T_{AU}] = Sqrt[CV[T_a]^2/E[U] + CV[U]^2\}$

The total area of targets, T_A, is the sum of discovered and undiscovered target areas: $T_A = T_{AD} + T_{AU}$. Then, $E[T_A]$ and $CV[T_A]$ can be estimated from Eq 17, where $p_{TAU,TAD}$ is the correlation coefficient between T_{AU} and T_{AD}; that is:

[17a] $E[T_A] = E[T_{AU}]+E[T_{AD}]$
[17b] $CV[T_A] = Sqrt\{[V[T_{AU}]+V[T_{AD}]+2p_{TAU,TAD}(V[T_{AU}]V[T_{AD}])^{-5}]E[T_A]^{-2}\}$

where $V[T_{AU}] = (E[T_{AU}]CV[T_{AU}])^2$ and $V[T_{AD}] = (E[T_{AD}]CV[T_{AD}])^2$ are the variances of T_{AU} and T_{AD}. Estimates of T_a, T_{AD}, T_{AU}, or T_A can also be based on simulation or other estimation techniques [7].

COMBINING ESTIMATES FROM INDEPENDENT EXPLORATION METHODS

In general, estimates of any variable (including Pd, U or U_u, and T_{AD}, T_{AU} or T_A) may be based on multiple, independent exploration methods using Bayesian updating [5,7-13]. Independent exploration methods may include information from other similar

sites or site-specific information from, for example, historical data, terrain analysis, geophysical surveys, different sample-testing methods, exploration results from other site media or strata, or information from physical or analytical modeling. By making use of all available and relevant site data, plus relevant data from others sites, Bayesian updating can reduce exploration costs and increase the accuracy of data interpretations and decisions that use those interpretations. However, skill, good judgment, imagination, knowledge and consideration of all potentially relevant data, and understanding of project requirements, are all necessary for success.

GENERAL CONCLUSIONS

The forgoing concepts and equations are tools that can be used in project planning, analysis or design--at any project stage, from initial site investigation to final site closure. A general conclusion is that finding hidden targets, or hotspots, with high confidence requires a high detection probability, Pd--which, using the tools presented here, can be maximized given available data. Yet finding all targets may be costly, and may or may not be necessary, depending on project requirements.

Exploration that is optimally consistent with project requirements is cost-effective and provides acceptable risk at minimum cost. The fundamental practical implication is that, at each project stage, field program design, implementation and interpretation, should be systematic and integrated with project requirements [11-14]. Exploration should be focused, with sampling effort concentrated where it is most needed. Therefore, site conditions and history, together with project requirements, have to be skillfully and insightfully assessed and synthesized to optimize strata definition and sampling effort. For any total level-of-effort, phased-approaches, using evolutionary, Bayesian updating and observational methods, can provide the best allocation of exploration resources. Each phase should aim to maximize Pd for the area and geometry of targets or hotspots that are important, consistent with the minimum-needed Pd--which will generally vary across a site, even within a given stratum. At each phase, exploration should be done with the least-costly appropriate detection method available; for example, geophysical surveys can help optimize sampling locations and increase Pd, and field screening methods and field labs can help expedite and focus phased-sampling efforts. Systematic exploration increases the probability of finding all important targets and controlling risk at minimum cost. The tools presented here, like all tools, can be misapplied. Yet, when appropriately used with skill, imagination, and insight, they can help streamline and expedite environmental restoration, and help control risk at minimum cost.

CITED REFERENCES

1. Baecher, G.B. 1970 *Site Exploration: A Probabilistic Approach*, Ph.D. dissertation, Dept. of Civil Engr., MIT, Cambridge, MA.
2. Elliot, J.M. 1973 *Statistical Analysis of Samples of Benthic Invertebrates*, Freshwater Biological Association, England.
3. EPA 1987 *Data Quality Objectives for Remedial Response Activities*, EPA/540/G-87/003,4.

4. EPA 1989 *Methods for Evaluating the Attainment of Cleanup Standards*, EPA/230/02-89-042
5. Gilbert, R.O. 1987 *Statistical Methods For Environmental Pollution Monitoring*, Van Nostrand Reinhold, New York, N.Y.
6. The Hazardous Waste Consultant 1992 "Soil Sampling and Analysis--Practices and Pitfalls," 10(6) 4.1-4.26, Nov/Dec., McCoy and Assoc., Lakewood, CO.
7. Harr, M.E. 1987 *Reliability-Based Design in Civil Engineering*, McGraw-Hill, New York, N.Y.
8. Koch G.S. Jr. and R.F. Link 1980 *Statistical Analysis of Geological Data*, Dover, New York, N.Y.
9. Mangel, M. 1985 *Decision and Control in Uncertain Resource Systems*, Academic Press, Orlando, FL.
10. Raiffa, H. and R. Schlaifer 1961 *Applied Statistical Decision Theory*, Harvard University Press, Cambridge, MA.
11. Vita, C.L. 1984 "Route Geotechnical Characterization and Analysis," *Journal of Geotechnical Engineering*, ASCE 110(12) 1715-34, Dec.
12. Vita, C.L. 1985 *Arctic Route Geotechnical Characterization and Analysis: A Systems Approach*, Ph.D. dissertation, Dept of Civil Engr., University of Washington, Seattle, WA.
13. Vita, C.L. 1986 "Project Geotechnical Engineering: Systems Methodology Considerations," *Civil Engineering Systems* 3(3).
14. Vita, C.L. 1987 "Risk-Based Decision Making for Hazardous Waste Sites," In *Proceedings* HMCRI 4th Nat. Conf. on Hazardous Waste & Hazardous Materials.

FIGURE 1:
PROBABILITY OF DETECTION, Pd

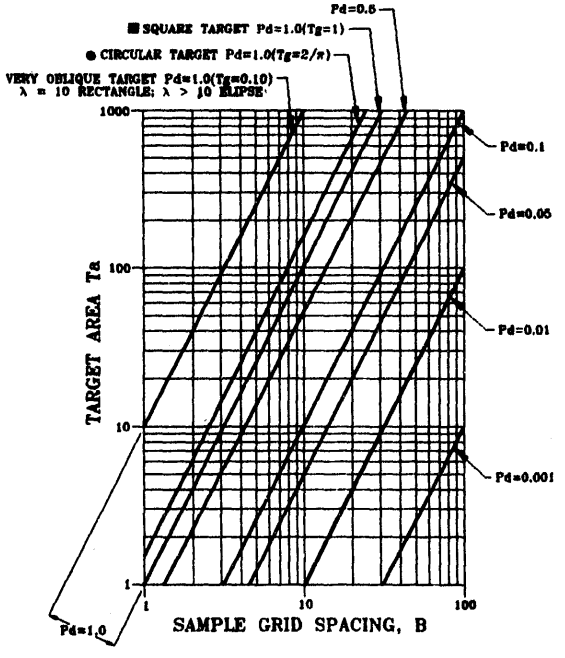


FIGURE 2:
EXPECTED NUMBER OF UNDETECTED TARGETS, E[U]

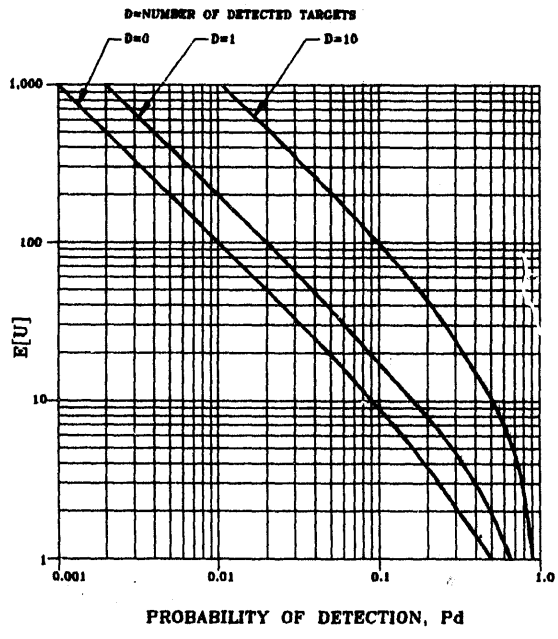


FIGURE 3:
PROBABILITY OF UNDETECTED TARGETS
GIVEN NO DETECTED TARGETS, $P_U[u|D=0]$

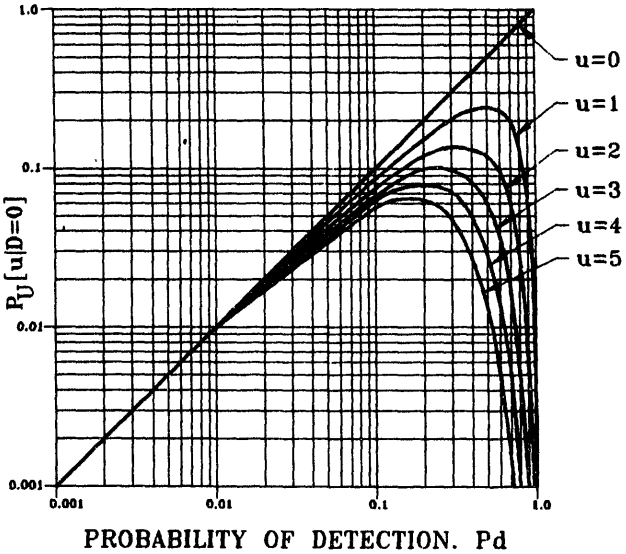
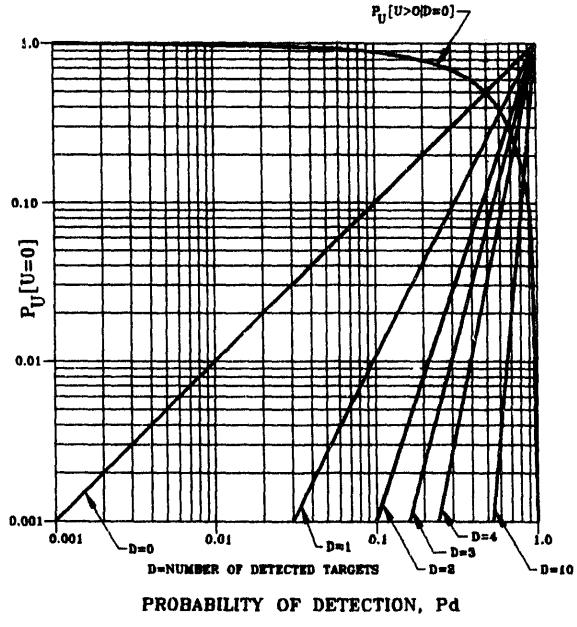


FIGURE 4:
PROBABILITY OF NO UNDETECTED TARGETS, $P_U[U=0]$



Hydrogeology, Waste Disposal, Science and Politics
Proceedings 30th Symposium
Engineering Geology and Geotechnical Engineering, 1994

THE RELATIONSHIP OF SEISMIC VELOCITY STRUCTURE AND SURFACE FRACTURE CHARACTERISTICS OF BASALT OUTCROPS TO RIPPABILITY ESTIMATES

S.E. Kay, M.E. Dougherty, and J.R. Pelton

Center for Geophysical Investigation of the Shallow Subsurface,

Boise State University, Boise, Idaho

ABSTRACT

Seismic velocity has been shown in previous engineering studies to be related to the fracture characteristics and rippability of rock outcrops. However, common methods of measuring seismic velocity in outcrops do not take into account the many possible travel paths for wave propagation and the fact that velocity zones may exist within an outcrop. Presented here are the results of using raytracing inversion of first-arrival travel-time data to map P-velocity structure in basalt outcrops, and also the investigation of the relationship of the mapped velocities to observed surface fractures and hand-sample P-velocities. It is shown that basalt outcrops commonly consist of an irregular near-surface low-velocity zone underlain by higher velocity material; that velocity gradients can exist in outcrops; that hand-sample velocity measurements are typically higher than outcrop-scale measurements; and that the characteristics of surface fractures are empirically related to near-surface P-velocity. All of these findings are relevant to the estimated rippability of rock in geotechnical engineering. The data for this study are derived from eleven sites on basalt outcrops of the Troodos Ophiolite in Cyprus. The basalt types include pillow basalts, massive flows, and a pillow breccia. A commonly available raytracing inversion program (RAYINVR) was used to produce a velocity profile of each outcrop. Different velocity zones were detailed by inverting observed travel times to produce a model of outcrop velocity structure which produces rippability profiles for each outcrop.

INTRODUCTION

The rippability of a rock or soil depends on its elastic moduli [*Konya and Walter,* 1990]. Compressional seismic velocity (which will be referred to as the seismic velocity throughout this paper) also depends on the elastic moduli of the medium. A direct correlation can be made between rippability and seismic velocity of rock (Figure 1). To some extent, the rippability of the medium depends on the equipment used for ripping. A Caterpillar D9N ripper copes with basalt of seismic velocity up to 2.3 kilometers per second, while a D11N ripper can rip up basalt with seismic velocity up to 2.6 kilometers per second.

In Cyprus, a variety of basalt outcrops were selected for detailed study. Co-ordinated seismic and geologic investigations were executed to compare the seismic characteristics of the sites and their fracture patterns. Outcrop mapping involved measuring the size and shape of lithologies; density and aspect ratios of fractures; and the evolution of fracture filling. Seismic refraction experiments were performed to understand the relationship between lithology, fracture density and seismic velocity. Since the area of study in Cyprus is an ophiolite (oceanic crust emplaced

above sea level), the primary objective of the parent study was to understand the relationship between fractures and basalt velocity in upper oceanic crust. However, results from the Cyprus study have a much broader applications, one of which is presented here. The very high quality, three component data collected can be used for engineering studies of the relationship between fractured rock and seismic velocity. Any study which discusses this relationship is applicable to considerations of rippability. Seismic exploration as a means to estimate rippability has a lot of potential, especially with the availability of 24 and 48 channel seismographs.

Rippability is directional in nature. Fractures in the rock can create planes of weakness. Basalts, in general, show preferred fault orientation while lacking preferred crack orientation. Massive flows display colonnades, which do have a preferred fracture orientation. Where fractures are oriented, one particular direction would be more susceptible to ripping than another. Other formations with fractures show slower seismic velocities perpendicular to the fracture orientation [*Stephen*, 1985], though these results are on a much larger scale than outcrops. Increased fracturing after blasting can also be detected through changes in seismic velocity [*McCann et al.*, 1986]. Other seismic parameters, such as seismic attenuation spectra, can be used to characterize

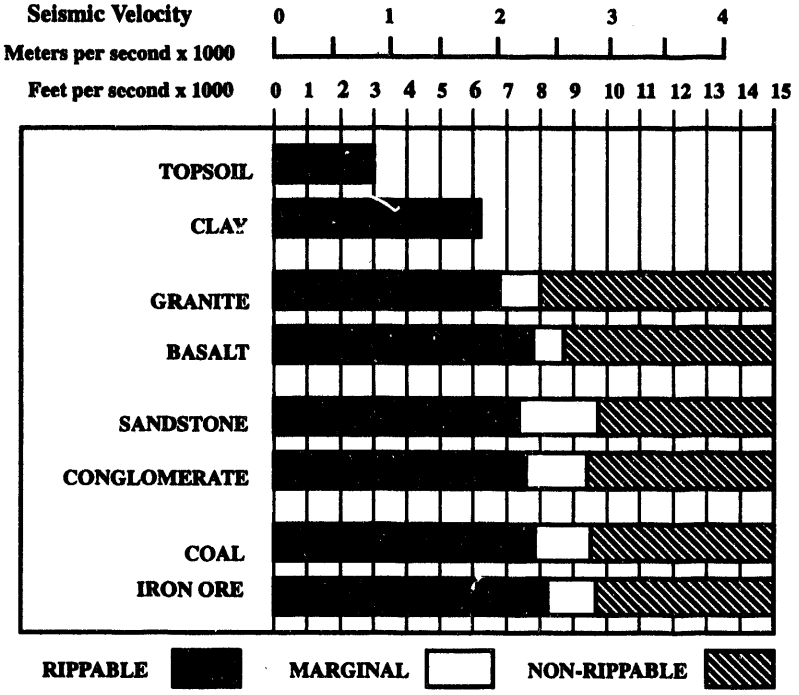


Figure 1 . The rippability of a rock may be expressed in terms of its compressional seismic velocity. For each different ripper the range of rippable velocities changes. The plot shown here is for a Caterpillar D9N ripper [from *Konya and Walter*, 1990,courtesy of Caterpillar Tractor Company]. It can only cope with basalts with velocities up to 2.3 km/s. Larger rippers can be used on outcrops with faster velocities.

rock mass [*Young and Hill*, 1986]. It is possible to investigate the best ripping direction by examining the seismic characteristics of a site. The possible volume that can be excavated, the specifications of the ripper needed, and the best direction for ripping, can be interpreted using a detailed seismic survey

Site investigations often rely on geophysical logging of selected blast holes [*Hendricks et al.*, 1992] or in simple seismic investigations using a limited number of geophones. As the use of por-

table 24 and 48 channel seismographs increases, the amount of definition that a seismic site investigation can provide will increase proportionally. Where surveys using four, eight, or twelve geophones give only an overall seismic velocity for each velocity layer, it will be shown in this paper that expanded geophone coverage combined with detailed modelling can give a much more detailed picture of subtle variations in depth and velocity.

Another important aspect of seismic velocity is the disparity of field seismic velocity measurements and laboratory measurements of velocity in hand samples. Figure 2 is one example of this relationship as seen in the Cyprus outcrops. Laboratory measurements of velocity are plotted against the velocities observed in the field refraction results. One controlling factor on seismic

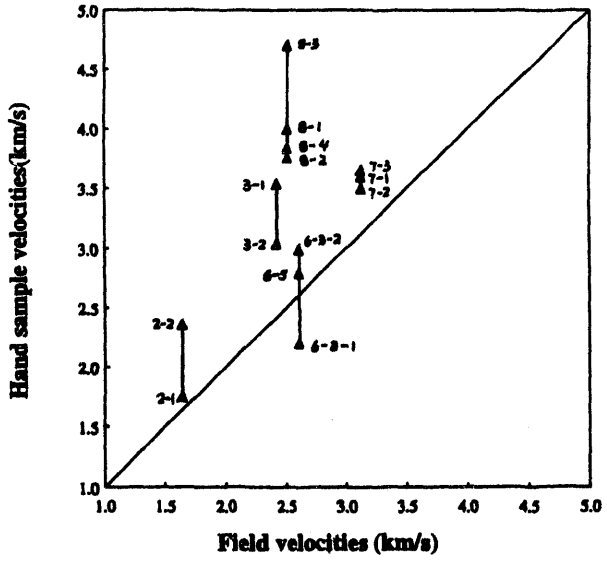


Figure 2 . Laboratory measurement of hand sample velocities compared to field measurements (under surface pressure conditions). All the laboratory measurements, except for one value for site 6, are higher than the measured field velocities. Sample velocities from each site are connected by a solid line, indicating the range of measured laboratory values. Field velocities are an average of the reciprocal velocities calculated for each site. The solid line at 45 degrees is the line along which the two velocities would line up if hand sample and field velocities agreed.

velocity is the presence of fractures in the field. Correlations can be made between lower seismic velocities and increased fracture densities [*Kuster and Toksoz*, 1974, *O'Connell and Budiansky*, 1974], and is directional in nature [*Peacock et al.*, 1994]. At the present time, however, an understanding of the exact relationship has not been reached and theoretical predictions are poor in all but ideal conditions where rock with only one set of fractures is considered.

In this paper, the variation of velocity within outcrops will be considered. It will be shown that velocities can vary within homogeneous basalt layers, and on seemingly uniform outcrops there is often a slow velocity present layer at the surface. This has a profound effect on the rippability of an outcrop. The need for good quality seismic data, along with geologic information, to produce a model in which confidence can be placed will be discussed. Outcrop seismic velocities are shown to be lower than those in measured hand samples, and to be locally variable. Variations are related to the observed fracture densities. Seismic velocities can be used to identify local changes in elastic moduli, thus giving a more detailed rippability profile of an outcrop.

GEOLOGIC SETTING

The Troodos Ophiolite Complex lies in the south western third of Cyprus. A wide variety of basalt volcanic units are present in the complex, including pillow lavas, massive and sheet flows, hyaloclastites and volcanic breccias. River canyons expose cross-sections through the volcanic sequence along the northern flank of the ophiolite. Within these canyons, volcanic units may be traced up to a few hundred meters both laterally and vertically. Sites included in this study covered the complete range of lithological types [*Dougherty et al.*, 1992a,b]. At each site, a detailed geologic study was carried out, including fracture density measurements [*Gillis et al.*, 1993].

Analysis of two sites from the Cyprus study are presented in this paper. These two sites have contrasting geology and topography. Site 6 consists of a differentiated massive flow that is greater than 10 meters thick and extends for at least 100 meters along strike. Towards the eastern end of the flow, pillow lavas begin to dominate the outcrop. Two sets of cooling fractures can be seen, vertical fractures which define the margins of the columns, and horizontal fracturing across a few of the columns. One seismic line was run near the crest of the outcrop, with an additional parallel line lower on the slope (Figure 3). In this paper, the upper line, 6u, is modelled.

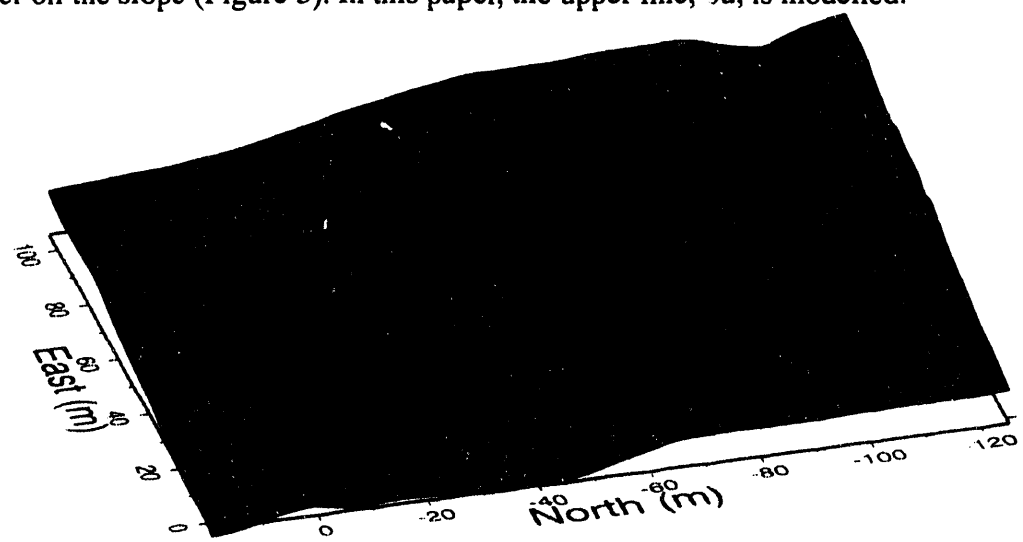


Figure 3 . Plot of site 6 showing both the upper and lower seismic lines. The geophone and shot locations are both shown as black dots. Seismic results and models of the line towards the bottom of the figure are presented below. The outcrop consisted of a ridge, with a gently dipping slope to the east. On the westerly facing edge, columnar jointing is clearly seen in outcrop, as well as the capping entablature on the exposed face of the flow

Site 8, the second site presented here, is located in an abandoned copper mine at Kampia. The line was laid out along a flat bench along the northern edge of the open pit. Hyaloclastite makes up the major part of the outcrop, with pillows, massive flows and cross cutting sheeted dikes. Sheet flows have irregular orientations with regular jointing patterns, and locally appear to flow over hyaloclastite mounds. Where dikes cross cut the hyaloclastite, it is highly competent, probably due to heating and metamorphism during emplacement. Weathering was limited at this site, and overburden had been removed in the course of mining. At the mine, two lines were laid out on adjacent benches, but in this paper only the lower line will be considered (the upper line was designated Site 9).

DATA ACQUISITION

One of the original intentions of the project was to obtain a high quality engineering seismic data set which could be applied to a variety of studies involving the relationship between fractured rock and seismic velocities. At each site, five $^1/_3$ pound dynamite shots were acquired with the seismic line laid out at 3-5 meter station spacing. Total spread lengths ranged from 48 meters to 112 meters, measuring from end shot point to end shot point. Three-component, 10-Hz geophones were used at each of 16 stations, recording a total of 48 channels for each shot record. The data were recorded on a 48-channel, digital, floating point seismograph. Hand samples were taken for laboratory measurement of rock matrix P-velocities, and fracture mapping was carried out over each outcrop by field and laboratory analyses of high-resolution photographs.

In the field, each shot record was printed to ensure that the record had been properly stored. Originally, five shots had been planned for each site, but due to misfiring, or a failure of the trigger mechanism, some lines only had four records. First arrivals were picked and some idea of velocities was obtained by taking the slope of the first picks against distance to geophone. Reciprocal velocities [*Hawkins*, 1961] at each site were calculated (Table 1). Also, the three component data for each site was isolated and velocities worked out for the transverse, longitudinal and vertical components. The vertical component was utilized for the raytracing profiles. Most field experiments are carried out using arrays of vertical component geophones, so in for most data sets only vertical velocities will be available. There is a wide range in basalt velocity measured at the different sites, from 1.64 km/s at site 2 to 3.12 km/s at site 7.

Table 1· Average P-wave velocities obtained using the reciprocal method.

1	Akaki	pillows	4	2.09
2	Akaki	pillow breccia	2	1.64
3	Akaki	pillows - west side	8	2.42
4	Akaki	pillows - low T	2	2.78
5	Eucalyptus	massive flow	2	2.48
6	Marki	weathered massive flow	6	2.61
7	Analiondas	pillows, low T	8	3.12
8-9	Kampia Mine	hyaloclastites, sheet flows, dikes	8	2.51
10	Mathiati mine	altered pillows	4	2.18
11	Delikipo	pillows	8	3.03

MODELS AND INVERSION

Model construction

Many raytracing programs are available for modelling the propagation of seismic energy through an outcrop. RAYINVR was originally designed for the modelling of deep crustal seismic data [*Zelt and Ellis*, 1987]. It is used here to model outcrops on the scale of tens of meters. The fundamental feature of RAYINVR is its simple, layered, large-block velocity model parameterization, which allows for efficient raytracing. The modeler constructs a two dimensional profile for a seismic line, consisting of distance, depth and velocity values for the layers that are expected in the model. Initially, the profile is used to forward model the arrivals that have been picked from the seismic data (Figure 4). It is important to have a clear view of how the arrival travelled, from which layer and type of seismic energy it originated. For the Cyprus sites, a detailed survey was carried out to give precise locations for the geophones and shot points. At larger sites, a grid survey was carried out so that topographic plots, such as Figure 3, could be produced.

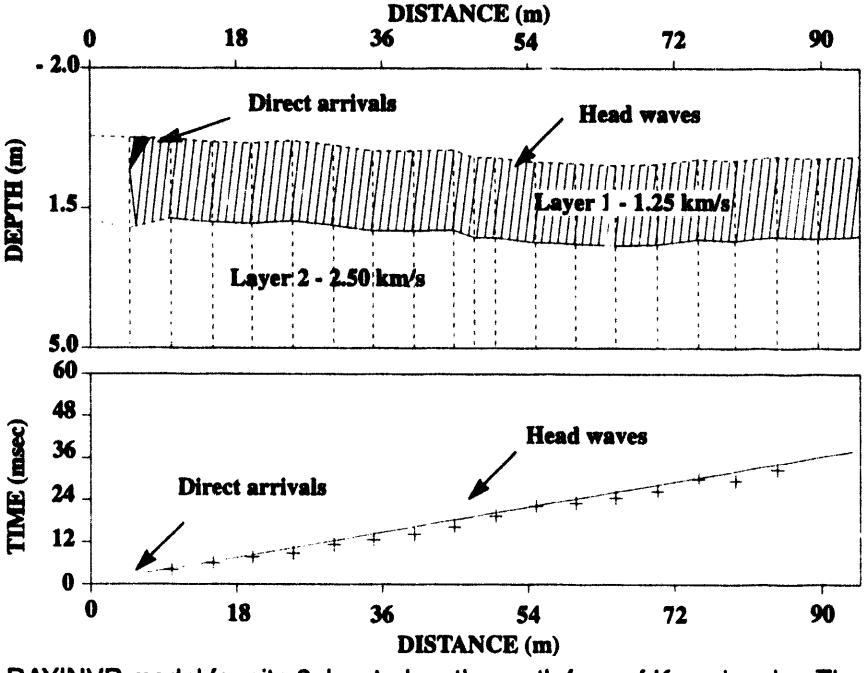


Figure 4 . RAYINVR model for site 8, located on the north face of Kampia mine.The upper portion of the diagram contains the profile model for this site, with direct arrivals and head waves from the top of the second layer plotted. Dashed lines indicate the boundaries of the blocks into which the model is divided. Velocity and depth values are entered for each corner of these blocks, and may be changed during the inversion process.The lower plot shows the actual picked arrival times as crosses with the calculated travel times as solid lines. The first layer is a uniform two meters thick for the entire line, with a uniform velocity of 1.25 km/s. Velocity of the second layer, 2.50 km/s, was taken directly from Table 1. This model fits the data fairly closely, with calculated time being slightly slower than real times. Only the ray paths for one shot are shown here, whereas in the forward modelling stage all shots are considered.

When a model has been adjusted until the root mean square residual travel time error (RMS) value is reasonably low, an inversion can be attempted. RMS error is a measure of the error between the picked arrival times and the calculated arrivals, and is calculated by summing the squared differences between real and modelled arrivals and dividing by the total number of data points. A "reasonable" value of RMS error varies from model to model, but in general, the more complicated the model, the harder it is to reduce the error. For the two following examples, Site 8 produced lower error values than Site 6, but contained one less layer. Inversions involve changes

either in the depth or the velocity of a layer (Figure 5), or both simultaneously (Figure 6). Inversions are performed after close agreement with the field data has been reached, and involve a series of damped iterations. If the forward model is too far from a reasonable representation of the site which produces the field data, the first inversion will abort.

Site 8 Results

Site 8 is located along a bench cut into the northern edge of an abandoned Kampia mine. A ledge ran parallel and below the ledge along which the seismic line was laid out, so a detailed picture of the geology underlying the line was available. The surface of the bench is flat, with little evidence of surface weathering. Initial modelling centered around one layer with velocity gradients, but the data were poorly matched by such a treatment of the site. A model then was constructed with a very thin, 25 centimeter, slow velocity or weathered layer at the surface. This proved to give a very poor fit to the data until the slow velocity layer was increased to 200 centimeters as shown in Figure 4, the RAYINVR profile which was the starting point for the inversions. From the first arrivals, a velocity of 1.25 km/s was established for the first layer, and a velocity of 2.50 km/s was established for the second layer. Real time picks are shown as crosses in the lower portion of Figure 4, with the calculated travel times shown as a solid line. Figure 4 shows the ray paths for the second shot at this site, which was offset five meters from the first geophone. Direct waves in the first layer and head waves from the top of the second layer were traced as the observed arrivals.

A series of inversions were then carried out for Site 8, using Figure 4 as the starting model. Figure 5a shows the result of an inversion which allowed the depth of the first layer to change. Considerable differences exist between the inverted and original model, chiefly being an overall increase in depth of the slow velocity layer. The ends of the seismic line show a decreased depth of the slow velocity layer. Since no actual field data are available at the end of the line, the thinning is questionable. Figure 5b shows the result of an inversion which allows only velocity in layer 2 to vary. Damping of the allowable change in velocity was greater in this inversion than for the depth inversion. Increases in velocity were observed along most of the line, with a few decreases. Calculated range of velocities in this inversion was 2.45 km/s to 2.79 km/s, with two values at 65 and 70 meters remaining at 2.50 km/s. Both inversions reduced the RMS value considerable, showing statistically a better fit to the data.

It is reasonable however to assume that both the depth and velocity values vary from the starting model. Figure 6 displays the result of an inversion allowing both parameters to vary. Rays are traced for shot point two again so the variations in the depth can be clearly seen. Variations in velocity and depth are slightly reduced. Velocities vary from 2.47 km/s to 2.72 km/s in the model. Damping was increased for this inversion, and the number of iterations increased. RMS value is lowest for this final model. Two distinct dips in the slow velocity layer can be seen, one at 10 meters and one at 50 to 60 meters.

Site 6 Results

Site 6 consists of a massive differentiated basalt flow. Originally, site 6 was modelled using rays refracted through a single continuous layer, with topography accounting for the change in slope of arrival times. It was soon obvious that it was impossible to use this model to fit the observed data without using unrealistic velocity gradients. Once a two layer model using head waves was considered, a closer fit emerged. This came close to modelling the outcrop, but observed arrivals near the end of each record were faster than calculated. At this stage, the velocity was considered as if the first arrivals from each shot were direct arrivals. This suggested the presence of a much lower velocity zone at the surface. Once this was added, an inversion was possible, as good fits could be achieved for all the time picks. The starting model contained a meter

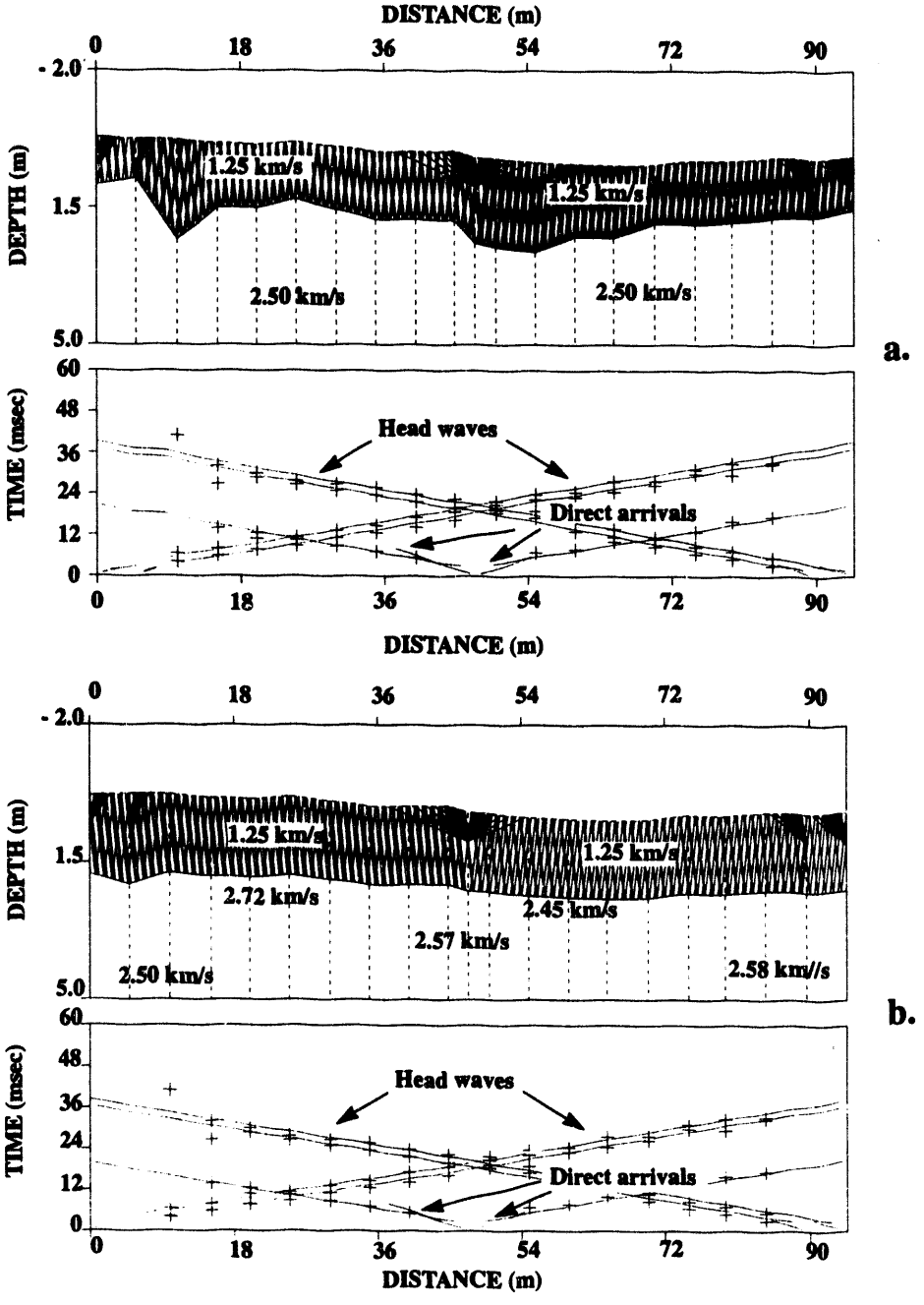


Figure 5 . Inversions, allowing depth (a) and velocity (b) to vary, for Site 8. When depth of the first layer is allowed to vary (a) two distinct areas of thickening occur and in a few areas thinning occurs allowing the calculated times to decrease and better fit the field data. In (b), the velocity of the second layer was allowed to vary, but not depth or velocity in the first layer. For the majority of the second layer, velocities are slightly increased except in the areas where in the depth inversion layer 1 was increased. For both inversions, there are two picks which RAYINVR discarded due to the fact they lay far outside the normal range expected for the arrival times for the geophones. Rays from all the shots are shown here for both inversions.

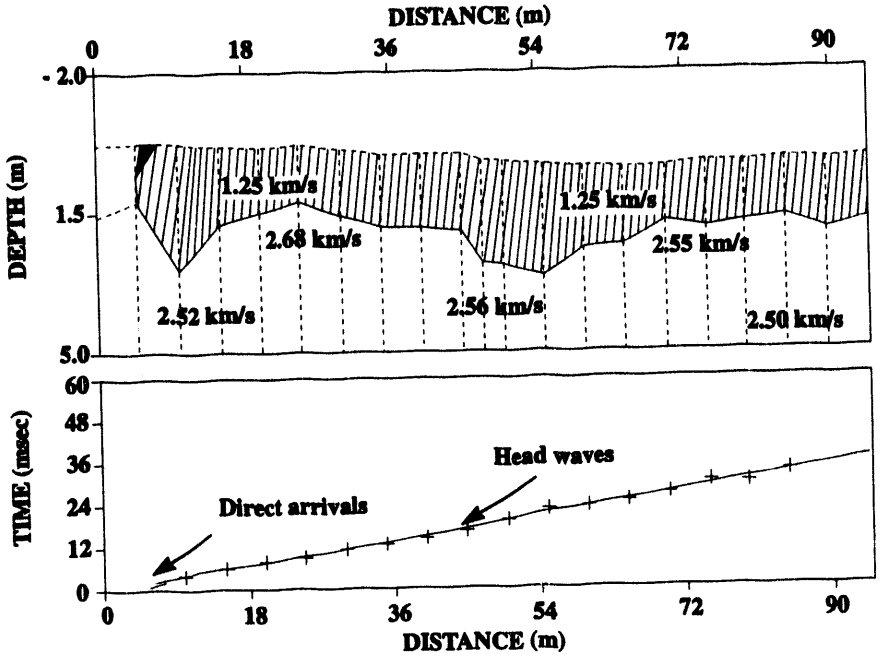


Figure 6 . Inversion for Site 8, allowing both velocity and depth to vary. The same trends seen in the previous inversions are present here. The depths of the low velocity layer vary, thickening around 10 and 48 meters, and thinning slightly, especially towards the ends of the line. Velocity variations are less than before, with most values remaining near 2.50 km/s. Ray paths for shot point two are shown here, and when compared to Figure 4, it can be seen that the agreement between the calculated and field data is much improved over the initial model.

thick slow velocity zone of 1.25 km/s, a ten to twelve meter thick intermediate velocity zone of 2.55 km/s, on top of a bottom fast zone of 3.20 km/s. Figure 7 shows this model with rays traced for the center shot. Again, crosses show the arrivals picked from the field data, and solid lines the calculated travel times. Fit between calculated and real data is poorer here than in the previous model which is in part due to the added complexity of a third layer.

As in the example for site 8, two inversions were carried out using first changes in depth, and then changes in velocity. The depth varying inversion, as seen in Figure 8a, came close to the field data, tending to increase the depth of the slow velocity layer. The inversion allowing velocity variations alone was not as successful, producing a model using unrealistic velocity gradients, as seen in Figure 8b. Finally, a combined inversion which allowed both velocity and depth to vary was carried out (see Figure 9). The overall damping was increased but the number of iterations was increased to achieve a similar RMS value as the previous depth inversion. Velocities changed slightly, but stayed within ± 0.20 km/s of their original values. There are similar changes in layer thicknesses as there was in the inversion allowing only depth to vary. For the center shot, the agreement on the lower end of the seismic line is much better than for the upper geophones. This is true throughout the data at this site, upper geophone arrivals tending to be slower in reality than those calculated.

DISCUSSION

Each one of the above models began with the surface topography, a full description of the geology, and an estimation of the thickness of slow velocity layer at the site. The starting models rely on reciprocal velocities worked out from the field refraction data. Assumptions have to be made about the depth to bedrock, the error present in picking first arrivals, even to the type of

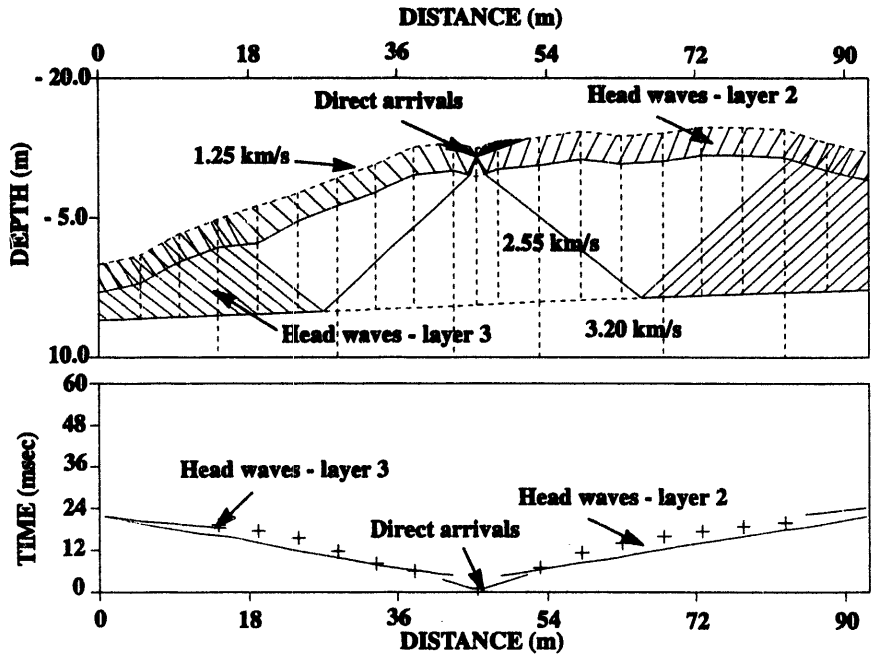


Figure 7 . The initial RAYINVR model for site 6. Three layers are included, and rays are traced for direct arrivals, head waves from the second layer and head waves from the third layer. As in the previous RAYINVR plots, actual arrival times are shown as crosses, and calculated times as solid lines. Here, layer 3 is split into fewer velocity blocks than the other layers, since it is less constrained by raypaths. For this model, all the calculated times are slower than the field data. Compared to Site 8, the starting RMS value is higher indicating greater misfit for the Site 6 model.

arrival assigned to each arrival time, whether they are refracted, reflected or head waves. However, as numerous variations are tried at each site, certain parameters become more defined.

Modelling of site 8 revealed the presence of a slow velocity layer along the surface of the outcrop. Initial modelling failed to fit the calculated rays to the data until this layer was added. Inversions of the model that showed two distinct areas of thickening occur at 10 and 50 meters. This would allow more of the outcrop to be ripped than could be judged by the starting model.Velocities from the hand samples for this site were the highest measured (Figure 2), being in the region 3.60 km/s to 4.80 km/s. Reciprocal velocities for the outcrop are much lower (Table 1), averaging only 2.51 km/s. Within the second layer, there are velocity gradients. Across the outcrop, velocities increase and decrease both horizontally and vertically (Figure 6). It was only through applying raytracing to the data, that these details emerged. Modelling produced a good fit to the data, and the combined inversion matched the observed arrival times for each shot record very closely. The velocity variation found in the second layer (Figure 6) lies outside the range of rippability seen in Figure 1. A high degree of confidence can be placed in the final inverted model for this site.

Originally, site 6 was modelled using refracted rays through a single layer. It soon became obvious that it was impossible to use this model to fit the observed data. Once a two layer model using head waves was considered, a closer fit emerged, but again this only agreed with the data to a degree. At this stage, the velocity was considered as if the first arrivals from each shot were direct arrivals. This showed the presence of a much lower velocity zone. Once this was added, an inversion was possible. It should be noted that the geologic description of site 6 includes reference to columnar jointing being present between a very weathered capping layer, and a base of minor flows and pillows. The second layer very likely represents the columnar jointed basalt, capped by an entablature. This kind of detail picked up by modelling the seismic data is very important, as it

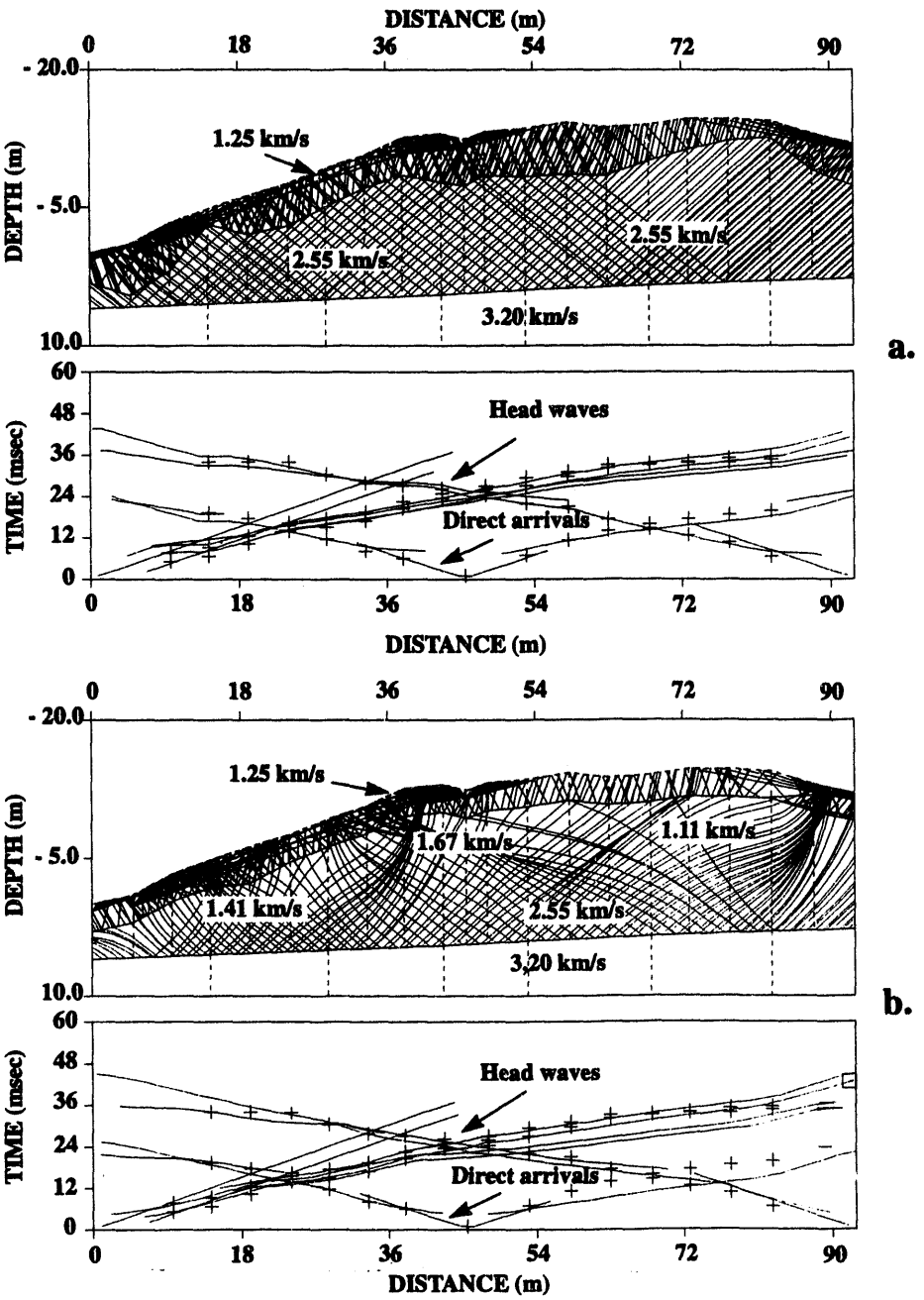


Figure 8 . Site 6, the RAYINVR inversions varying both depth (a) and velocity (b). For the depth inversion (a), the first layer was increased in thickness across the whole of the seismic line, this effect being especially pronounced at 5 meters. The overall shape of the adjusted layers fits well with geologic mapping of the site. Velocities in the second inversion (b) are unrealistically low for the top of layer two, and vary considerably more than they did in the inversion for site 8, and produce unrealistic velocity gradients.

marks the first stage of relating fracture patterns to outcrop velocities. It should be noted in Figure 2, Site 6 had the lowest hand sample velocities. These hand samples represent the weathered layer. Velocities variations for the second layer of this outcrop vary between 2.23 km/s and 2.55 km/s. From Figure 9, it can be seen that the lower section of the seismic line, between 0 and 50 meters, overlies rippable rock in layer 2 as defined in Figure 1. The upper section of the line,

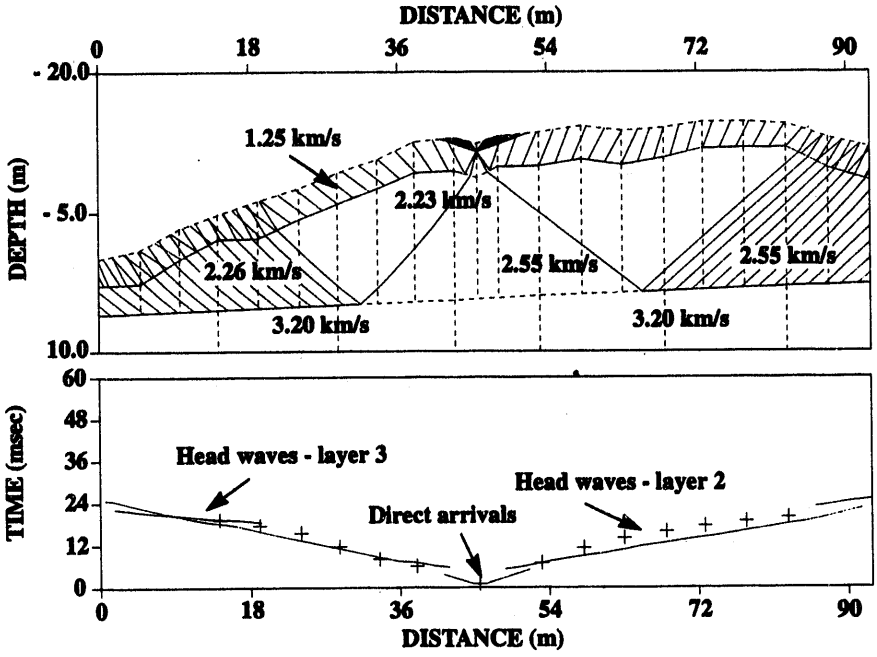


Figure 9 . Final RAYINVR model for site 6. Velocity and depth were allowed to vary in this inversion for layer 2. Damping was greater for velocities than for depths, since the velocity inversion shown in Figure 8b was relatively unrealistic. Variations in depth follow the same pattern as seen in the depth only inversion, though less extreme. It is interesting that the second layer, with velocities of near 2.45 km/s, corresponds with the columnar jointed section of the basalt flow. Lower geophone arrivals are better models than those of the upper section of the line.

between 50 and 90 meters, overlies marginally rippable to unrippable rock in layer 2. Ripping is possible for sections of the second layer at Site 6, not just in the first layer as in Site 8.

Without using detailed seismic measurements and modelling, it is unlikely that the extent and variation in the first layer shown for these two sites would ever have been realized. Only a drilling program at the sites would have firmly established the weathering along each site. At Site 6, it is questionable whether the two lower layers would have been differentiated even while drilling. By using a detailed data acquisition and modelling approach, much more information can be was uncovered. Before using these results to carry out any kind of excavation, the accuracy of the original data along with the spacing of the geophones should be considered. If detailed models are the intended result of a seismic survey, the extent of the detail should considered before any field work takes place. RAYINVR, or any similar raytracing program, can be used in the planning stages of a survey, giving estimations of the length of time to be recorded and what types of rays can be reasonable expected.

It should be made clear that inversions, and indeed forward modeling, are dependent on a good quality data set for their success. The more data available, the more confidence can be placed in a model that fits that data. For the eleven sites in the Cyprus, only averaging near 80 meters in length, 72 arrival times were used in most of the models. It is statistically unlikely, given the good fit to data obtained here for all the shot points, that a poor model of the sites has been obtained. However, at each stage of adjustment, the original mapped geology of the site was considered. As the shots were buried, five minimum values for overburden depth for each line were known. The models presented here do not violate any of the measured depths, or observed geology, for these sites.

One of the results of modelling both these sites was the realization of the importance of good quality seismic data. Reductions in the availability and quality of seismic data carry through to the modelling stage. In this study, data collection was carried out with a high degree of precision, but still, one shot which was not recorded at Site 6 resulted in a subsequent reduction of the resolution possible for this site. Site 6 is a complicated outcrop that differs from Site 8 in that three layers are present. With a smaller data set as well, it follows that it is not possible to have as much confidence in the inversion for Site 6 as in Site 8. However, clearly Site 6 is composed of three velocity layers which are quite closely approximated in Figure 9. Errors in the arrivals times for both these models are in the region of two milliseconds, so it is unreasonable to push the inversions to fit the picked times exactly.

Rippability, along with seismic velocity, is highly dependent on the fracture patterns in a rock mass. In some circumstances, prior to any excavation, it could be cost effective to conduct a detailed seismic study first. Where a simple analysis of the seismic data could lead to the conclusion that ripping is not an option, a raytracing model of the site may uncover that sufficient variation exists in the outcrop to make it worthwhile. In each of the models presented, velocities and depths vary across an outcrop, bringing sections of the outcrop into and out of the range of rippability. Planning a more effective excavation of a site may be possible with the kind of detailed seismic survey outlined here. In areas that are environmentally sensitive, a seismic survey could be used to investigate the subsurface while having minimal impact on the land. Instead of a drilling program, a detailed seismic refraction survey could obtain the same information.

CONCLUSION

It has been shown in this paper that detailed seismic data acquisition and modelling at an outcrop scale can provide a detailed velocity profile of on outcrop. On all outcrops it revealed the unsuspected presence of a slow velocity layer, even on rock outcrops with no overburden. Such a model is extremely useful when considering the rippability of a particular site, and can provide information on the best direction of ripping since seismic velocities tend to be lower perpendicular to fracture orientations. Velocities and depths have been shown to display sufficient variation in sites that the rock may vary between rippable and unrippable. The importance of good quality seismic data, with reasonable coverage for the scale of detail required can not be overstated. With the availability of 24 and 48 channel portable seismographs, seismic evaluation is a viable alternative to drilling for site assessment Such a survey can provide much more detail on subsurface conditions with far less impact on the environment.

ACKNOWLEDGEMENTS

This research was funded by the Office of Navel Research Grant #N00014-92-J-1143 to Boise State University. Boise State University Center for the Geophysical Investigation of the Shallow Subsurface contribution 0026.

REFERENCES

Curfman, J.E., Ripping of ores and overburden, *Can. Min. Metall. Bull.*, **58**, 645 - 648, 1964.

Dougherty, M.E., S.E. Kay, J.R. Pelton, and K.M. Gillis, Predictions of fine scale seismic structure of the upper oceanic crust, *Transactions, EOS*, **74**, 426, 1993.

Dougherty, M.E., K.M. Gillis, and J.R. Pelton, Heterogeneity and Permeability of the upper oceanic crust, Troodos Ophiolite Complex, Cyprus, *Center for Geophysical Investigation of the*

Shallow Subsurface Technical Report BSUCGISS #92-05, Boise State University, 72 pp, 1992a.

Dougherty, M.E., K.M. Gillis, J.R. Pelton, and K. Sapp, A geological and seismic study of the upper oceanic crust in the Troodos Ophiolite, Cyprus, *Transactions, EOS*, **73**, 355, 1992b.

Gillis, K.M., K. Sapp, and M.E. Dougherty, Distribution of porosity in the upper oceanic crust exposed in the Troodos Ophiolite, Cyprus, *Transactions, EOS*, **74**, 241, 1993.

Hawkins, L.V., The reciprocal method of routine shallow seismic refraction investigations, *Geophysics*, **26**, 806 - 819, 1961.

Hendricks, C., J. Peck, and M.J. Scoble, Machine performance monitoring in surface mines, *Min. Eng.*, **44**, 243 - 250, 1992

Konya, Calvin J., and Edward J. Walter, Surface Blast design, Prentice Hall, Englewood Cliffs, New Jersey, 303 pp, 1990.

Kuster, G.T. and M.N. Toksoz, Velocity and attenuation of seismic waves in two-phase media: Part 2 Experimental results., *Geophysics*, **39**, p 607-618, 1974.

McCann, D.M., R. Baria, P.D. Jackson, and A.S.P. Green, Application of cross-hole seismic measurements in site investigation surveys, *Geophysics*, **51**, 914 - 929, 1986.

O'Connell, R.J. and B. Budiansky, Seismic velocities in dry and saturated cracked solids, *J. Geophys. Res.*, **79**, 5412-5426, 1974.

Peacock, S., C. McCann, J. Sothcott, and T.R. Astin, Seismic velocities in fractured rocks: an experimental verification of Hudson's theory, *Geophys.Prospect.*, **42**, 27 - 80, 1994.

Savely, James P., A comparison of rippability with shear strength of a boulder conglomerate, *Proceedings of the 28th US Symposium on Rock Mechanics*, 927 - 934, 1987.

Stephen, Ralph A., Seismic anisotropy in the upper oceanic crust, *J. Geophys. Res.*, **90**, 11,383 - 11,396, 1985.

Young, R.P. and J.J. Hill, Seismic attenuation spectra in rock mass characterization; a case study in open-pit mining, *Geophysics*, **51**, 302 - 323, 1986.

Zelt, C.A. and R.M. Ellis, Practical and efficient ray tracing in two-dimensional media for rapid traveltime and amplitude forward modelling, *J. Can. Soc. Expl. Geophys.*, **24**, 16-31, 1988.

Hydrogeology, Waste Disposal, Science and Politics
Proceedings 30th Symposium
Engineering Geology and Geotechnical Engineering, 1994

GEOLOGIC AND GEOTECHNICAL INVESTIGATION OF THE WINDSOR PARK SUBDIVISION NORTH LAS VEGAS, NEVADA

Lorraine M. Linnert, James L. Werle, C.E.G., Alan N. Stilley, P.E. and Brad L. Olsen, E.I.T.

Converse Consultants Southwest, Inc., Las Vegas, Nevada

ABSTRACT

The Windsor Park subdivision in North Las Vegas, Nevada has received widespread attention for damage to the homes and infrastructure from fissures, land subsidence and adverse soil conditions. Between March and July, 1992, Converse Consultants Southwest, Inc. conducted a geologic and geotechnical investigation for the Windsor Park Revitalization Project. The purpose of the work was to investigate the probable factors contributing to the reported damage and distress in the area, evaluate the potential for future damage, and assess the feasibility of possible mitigation and repair.

The site is constructed on the juncture of at least two subsidence-related fault scarps, and earth fissures have been extensively mapped in the Windsor Park and surrounding area. A total of twenty-one trenches and fifteen borings were located within the subdivision and around the perimeter to observe subsurface geologic features and to collect samples for laboratory testing. The primary causes of damage within the development were found to be (1) earth fissuring and (2) expansive clays.

The risk of future damage to structures at the Windsor Park site was also evaluated. A high potential for fissuring was found at the site, and future structural distress in the area will likely be similar to past damage. Although engineering upgrades will reduce the risk posed by underlying expansive clays, they cannot totally eliminate the risk from fissuring.

INTRODUCTION

The Windsor Park subdivision is a residential development consisting of 246 homes in the central portion of North Las Vegas, Nevada. The homes were built between 1964 and 1965 and consist of single-story, wood-frame construction supported by either slab-on-grade foundations or perimeter footings with elevated wood floors (crawl spaces). Damage to homes and infrastructure in the area has been documented since the early 1980's, and numerous studies have been performed since 1984 to assess these problems and determine possible causes for damage and fissures in the subdivision. However, conclusions made in previous investigations were often contradictory

indicating that the problem is very complicated as multiple and possibly interrelated problems may coexist at the site.

In February, 1992, Converse Consultants Southwest, Inc. was contracted by the City of North Las Vegas to conduct a geologic and geotechnical investigation for the Windsor Park Revitalization Project. The purpose of the work was to determine the probable cause of distress to the neighborhood homes and infrastructure, evaluate the risk for future damage and provide recommendations for mitigation accordingly. The scope of work consisted of compilation and review of previous investigations and geologic literature for the area, extensive subsurface explorations, laboratory testing, and assessment of our findings.

GEOLOGIC SETTING

Geologic and Hydrologic Conditions

The Windsor Park subdivision in North Las Vegas, Nevada lies in the north-central portion of the Las Vegas Valley in the Basin and Range physiographic province. The distinctive features of the province are isolated, nearly parallel mountain ranges separated by long, wide valleys. The Valley is filled with Tertiary and Quaternary Age unconsolidated alluvial and lacustrine (playa-like) sediments derived from the surrounding mountains. It is approximately 50 miles long and 5 to 25 miles wide. Figure 1 shows the location of the site within the Valley.

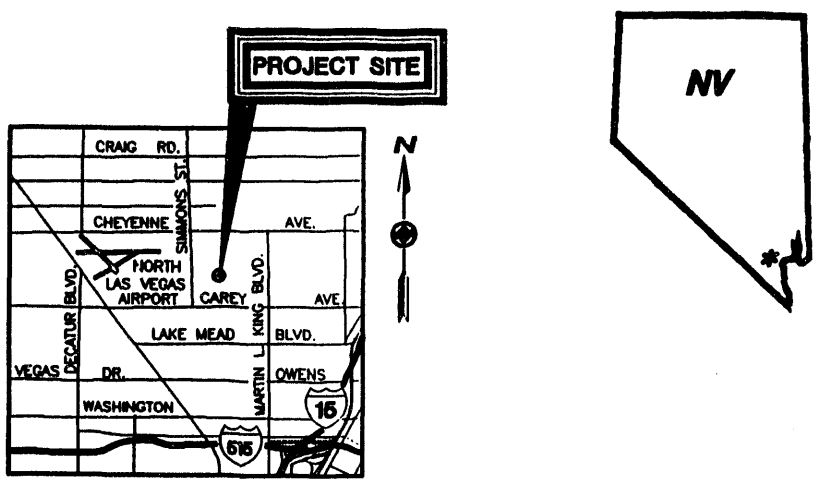


FIGURE 1: WINDSOR PARK LOCATION MAP

Two separate aquifers exist in the Las Vegas Valley: a shallow relatively unconfined aquifer and a series of deep confining water-bearing zones (Plume, 1984). Each zone typically contains granular sediments that are contained by low permeability silts and clays. The fine-grained sediments occur as lenses or layers which act as semi-confining barriers or aquitards that impede vertical flow. The majority of the groundwater withdrawn in the Valley is from the deeper aquifer zone at depths greater than 200 feet.

The aquifers are faulted as a result of differential consolidation of the interbedded fine-grained sediments. The features termed subsidence-related faults significantly affect the movement of groundwater, both laterally and between aquifers. Prior to artesian head decline as a result of heavy pumping, flowing springs were often observed along these fault scarps (Bell, 1981).

Site Conditions

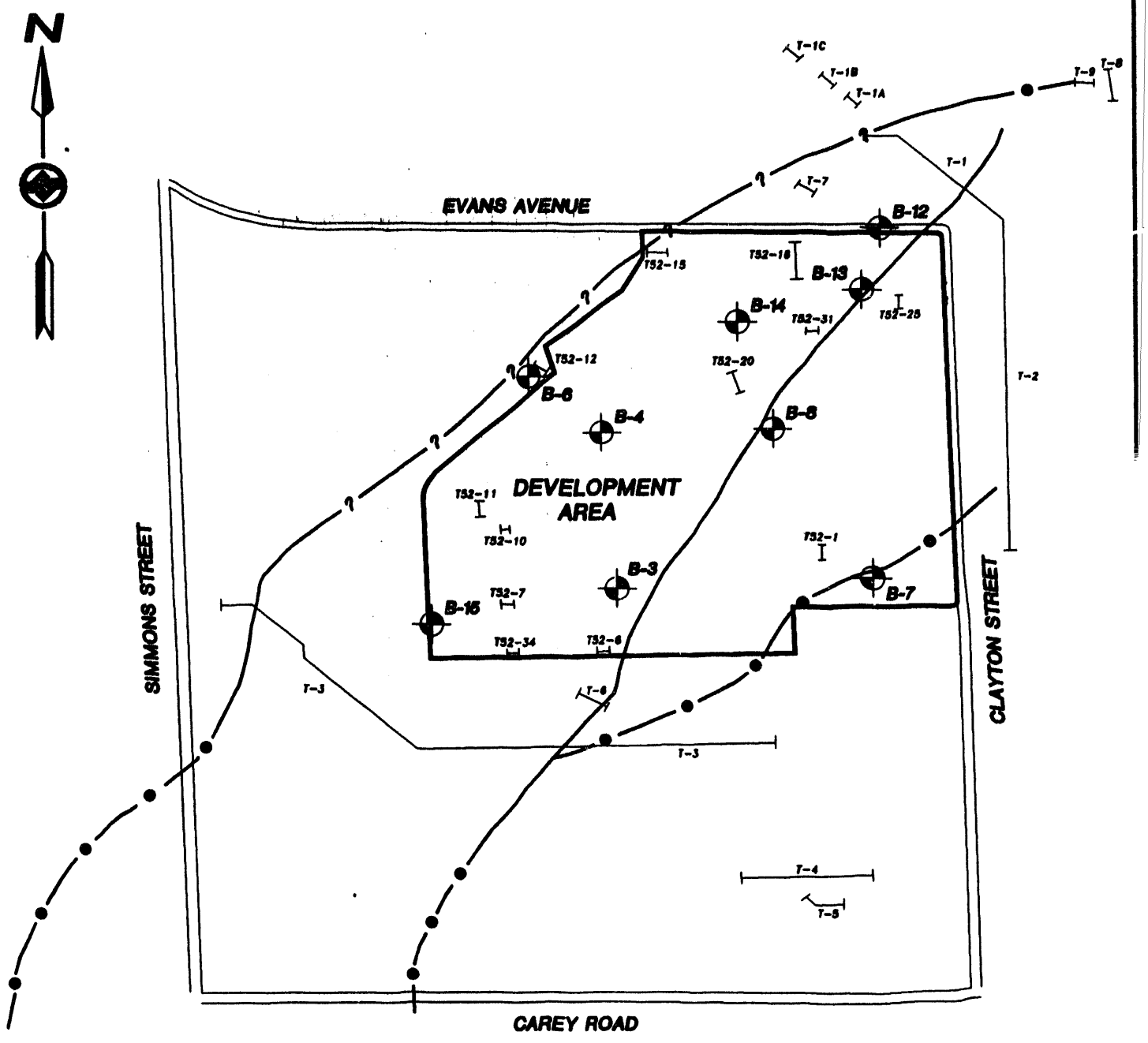
Near-surface soils at the site consisted of man-made fill and playa-like deposits including silts, clays and fine sands overlying clays, clayey sands and cemented (caliche) soils. The majority of soils contained various amounts of gypsum in the form of crystallized gypsum layers and gypsiferous clays.

Geologic Constraints

Geologic Faults

The site is constructed on the juncture of two fault scarps trending southwest-northeast across the Windsor Park Subdivision (Matti, et. al., 1987). The location of these fault scarps is shown on Figure 2. These fault scarps are generally believed to topographic expressions of subsidence-related faults that extend throughout the Las Vegas Valley. They are generally thought to be nontectonic features of Quaternary Age (Cibor, 1983). Although several authors (Bell and Price, 1991) have noted that the fault escarpments may be tectonic in origin (from faults extending up from the bedrock basement underlying the valley and capable of generating seismic events), these fault scarps are most commonly thought to be the surface expressions of prehistoric differential consolidation or compaction of alluvial and playa-like sediments having dissimilar grain-size and compressibility characteristics. Therefore, the faults are not capable of generating earthquakes although they may be partially induced by an earthquake event (Bell, 1981).

Subsidence-related faults may be historically reactivated due to differential land subsidence as a result of groundwater withdrawal. They are also associated with earth fissures, former springs and adverse geotechnical conditions.



GRAPHIC SCALE:

250 0 250 500 1000

(In feet)

1" = 500'

EXPLANATION:

- B-1 — APPROXIMATE SOIL BORING LOCATION
- —●— MAPPED SUBSIDENCE-RELATED FAULT (MATTI, 1987)
- —?— INFERRED FAULT
- —— FAULT (FIELD VERIFIED-TRENCH EVIDENCE)
- ⊢⊣ APPROXIMATE TRENCH LOCATION

FIGURE 2: LOCATION OF SUBSURFACE EXPLORATIONS AND FAULTS.

Land Subsidence

The principal cause of historical land subsidence in the Las Vegas Valley is the regional extraction of groundwater resources. The Las Vegas Valley soils contain much silt and clay sediments which are very conducive to consolidation upon fluid (water) extraction.

Evidence for land subsidence is based upon regional land level surveys conducted over years; in some areas near downtown Las Vegas, a total subsidence of more that 5 feet has been reported since land subsidence was first documented in 1940 (Bell, 1981). Elevation surveys conducted between 1963 and 1986/87 show the pattern for valley-wide subsidence as one large subsidence bowl punctuated by three secondary, localized zones. At present, the localized bowl in the northwest part of the valley is the most actively subsiding of the three and presents the greatest subsidence hazard to urbanization in the valley. The maximum surface subsidence of the northwest area is greater than 5 feet as measured between 1963 and 1986/87 (Bell and Price, 1991).

Land subsidence near the subject site is interpolated as 1½ total feet between 1963 and 1986/87 (Bell and Price, 1991). In addition, the site is directly between the northwest and downtown subsidence bowls (see Figure 4). In the period between 1978 and 1991, approximately 0.8 foot of vertical subsidence has occurred along a land level line which crosses the fault zone about 1,000 feet northeast of Windsor Park. Approximately 0.6 foot of differential subsidence between adjacent benchmarks 100 feet apart has been observed in the same period. This suggests that differential movement along the fault zones at Windsor Park is actively occurring. Fissuring (see next section) and structural damage in Windsor Park appear to be concentrated along the upthrown side of the fault roughly thought the center of the site, closest to the northwestern subsidence bowl.



Figure 3. Fissure located beneath caliche cap in trench T-5.

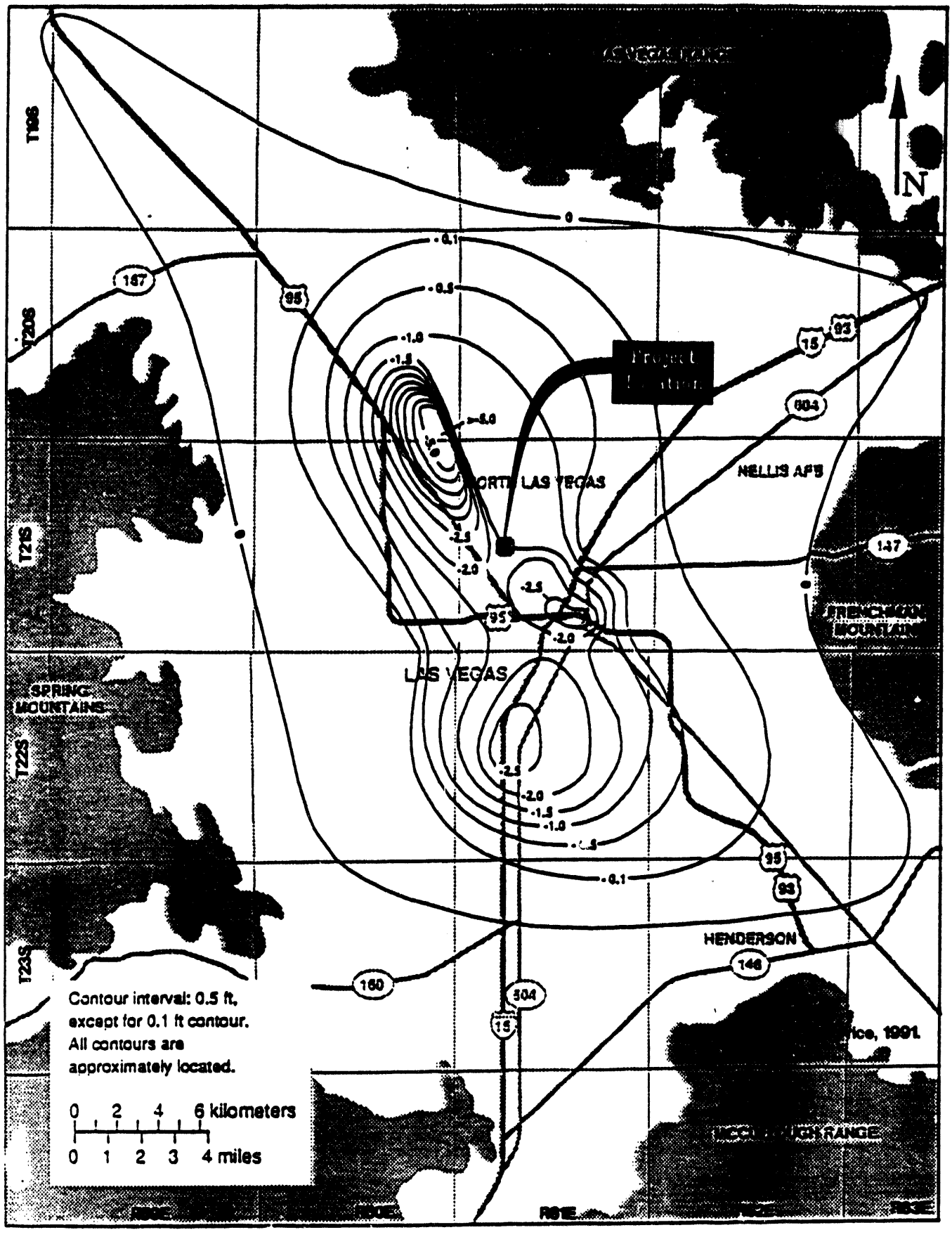


FIGURE 4: APPROXIMATE LAND SUBSIDENCE (1963-1986/87)

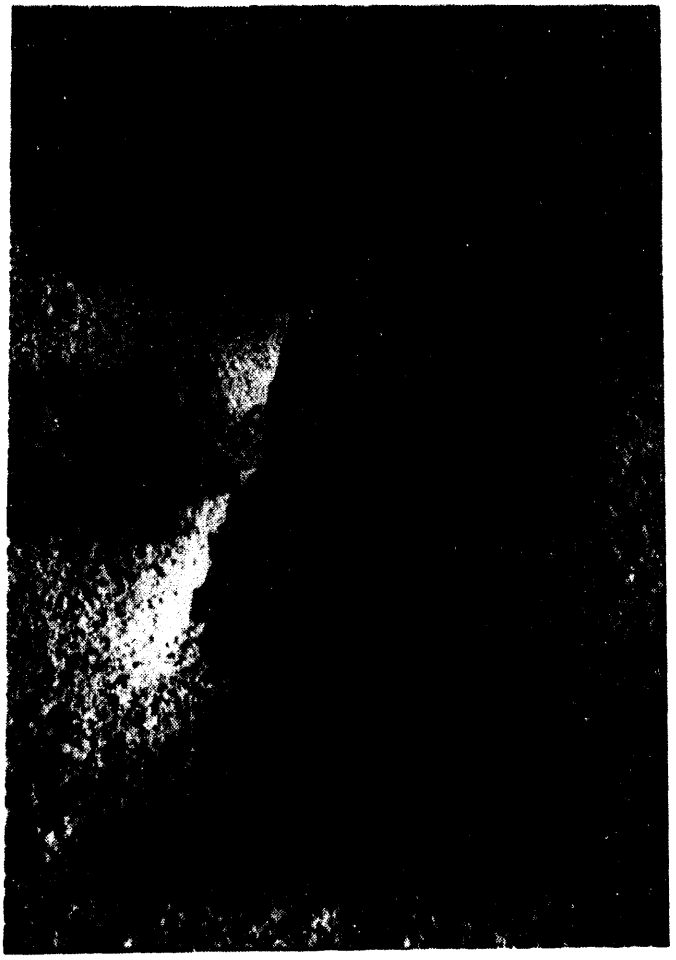


Figure 5. Fissure exposed at the surface at Trench T-9 location.

Earth Fissures

Earth fissures in the Las Vegas Valley are usually formed in the subsurface by tensional stresses associated with groundwater withdrawal (Helm, 1992). They are commonly expressed as groups of short, discontinuous, dendritic cracks or as a single, continuous, linear crack. Both types have been observed in the Windsor Park area. A fissure is believed to originate as a tensional crack approximately 1/8 to 1/4 inch wide in relatively loose sediment (Werle and Stilley, 1991). Infiltration of surface runoff widens the crack, and collapse of overlying sediments exposes the fissure to the ground surface. Surface water further erodes and enlarges the feature. Eventually the feature may be temporarily filled or obscured (Bell, 1981).

Ground fissures at the Windsor Park development were surficially mapped by Western Technologies, Inc. (1988) and Mifflin International, Inc. (1992). Nearly 3,200 linear feet of fissures were documented in the latter study. Surficial expressions were 0.1 to 3 feet wide and up to 3 feet deep. They were preferentially oriented subparallel to the surface drainage channels and subparallel to the fault scarps. In addition, fissuring in the area appeared to be active and accelerating with time as there was a significant increase in the number of new unrecorded fissures as mapped in 1991 (Mifflin, 1992).

INVESTIGATIONS

Subsurface Exploration

A total of twelve trenches within the Windsor Park subdivision and nine trenches in the area surrounding the development were excavated using a Case 580K rubber-tired

backhoe and a Case 1088 trackhoe. Excavations were logged, photographed and videotaped, and then backfilled and tamped down with a backhoe. Nine exploratory borings were drilled with a truck-mounted air-rotary drill rig equipped for soil sampling and were logged by a field geologist. (See Figure 2 for approximate trench and boring locations at the site.) Soil samples were collected from the exploratory trenches and borings for laboratory testing.

Geologic Logging

A variety of evidence for faults, fissures and spring conduits was observed in the trenches. Monoclines or gently folded stratigraphic units were encountered across fault escarpments and were interpreted to be possible indicators of a fault zone at depth. Western Technologies (1988) noted the existence of an additional fault scarp northwest of the subdivision. An inferred fault was mapped; the extent of damage to the homes in this area would support the existence of this fault near this location. Accurate positioning of these faults was critical to risk assessment for the development.

A fine-grained quartz sand was observed in two trenches south of the development. It is believed to be located in a conduit for an extinct spring east and on the downthrown side of the fault system which extends through the subdivision. This loose sand was found in lenses and nearly vertical "pipes" extending below the base of the trench. Stratigraphic soil layers were observed folding down into the spring conduit or were vertically displaced up to 1½ feet in a collapse feature. One large fissure, south of the subdivision, was located 80 feet west and paralleled the spring conduit

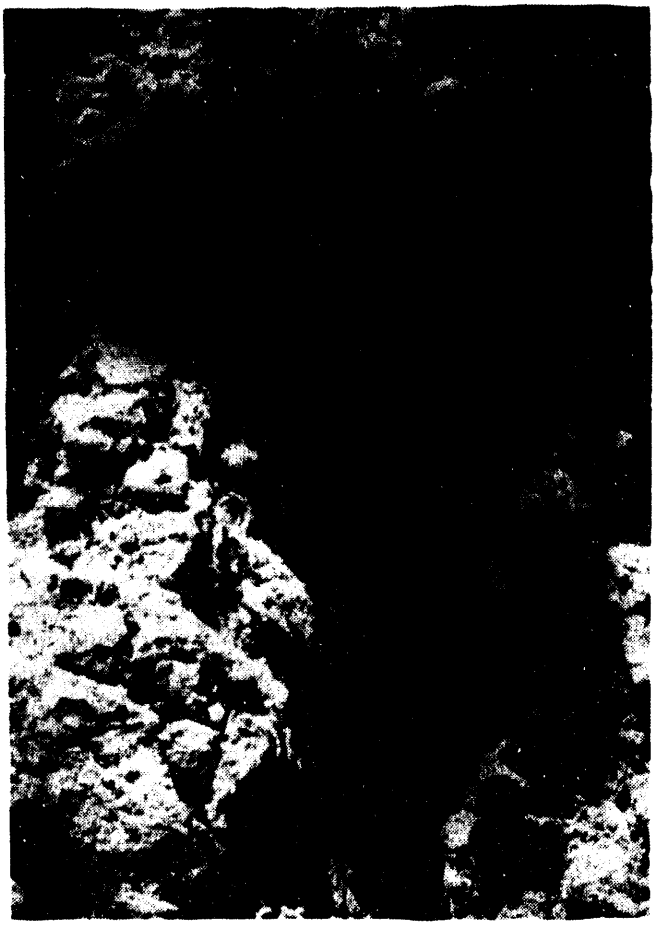


Figure 6. Subsurface expression of fissure in Trench T-9. Note the desiccation cracks.

found in Trenches T-4 and T-5. This may infer a relationship between the fissure, former spring conduit and faults mapped in the locale.

Most fissures encountered in the trenches were surficially expressed. In addition, most were encountered in association with highly desiccated clays. Highly fractured, desiccated clays were encountered in several trenches within the subdivision and in the area surrounding the site. Fissures most often were found to extend down to a highly desiccated fat clay up to 8 feet below ground surface but rarely continued below that layer. Fissures displayed a tensional or horizontal displacement; no vertical displacement was observed. Occasionally fissures were filled with soil from overlying units (Trenches T-3, T-4, T-7, TS2-12). Two fissures encountered within vacant lots in the subdivision paralleled the existing exterior footings from previous homes (Trenches TS2-20 and TS2-16). Mifflin International (1992) had postulated the presence of an extensive, subsurface fissure network in the area. Evidence could not be found to substantiate this concept.

Soils observed at the site consisted primarily of surficial silts (ML), sands (SM and SC) and clays (CL and CH) overlying clays of variable plasticity and gypsum content. Cemented soils (caliche) were encountered in many trenches. Figure 7 is a graphical representation of trench T-9. Beds were horizontal to gently dipping over most of the site area except in areas of faults and springs. In some cases, trenches were vertically exaggerated to show more detail, however, some stratigraphic features may appear exaggerated in the cross-sections.

Laboratory Testing

Laboratory test results indicate the on-site and immediate vicinity soils have (1) low to moderate dry densities, (2) a moderate to high potential for hydro-collapse (rapid settlement upon saturation), (3) a low to high degree of gypsum solubility, (4) a moderate to critical clay swell potential, (5) a low to moderate chemical (salt) heave potential and (6) contain sulfate salts in sufficient concentrations to be severely corrosive to metal and harmful to concrete. Critically expansive soils were encountered at various depths throughout the entire subdivision. Some of the laboratory swell pressures, determined from confined swell tests, were in excess of 10 feet of equivalent overburden swell pressures.

It should be noted that adverse soil conditions can be found throughout the Las Vegas Valley; however, the conditions encountered during the investigation at Windsor Park were such that nearly all adverse soils: expansive clays, hydro-collapsible and gypsiferous soils were found to be at nearly critical levels. It is highly unusual to find so many adverse soil types at one location. Table 1 provides selected laboratory test data.

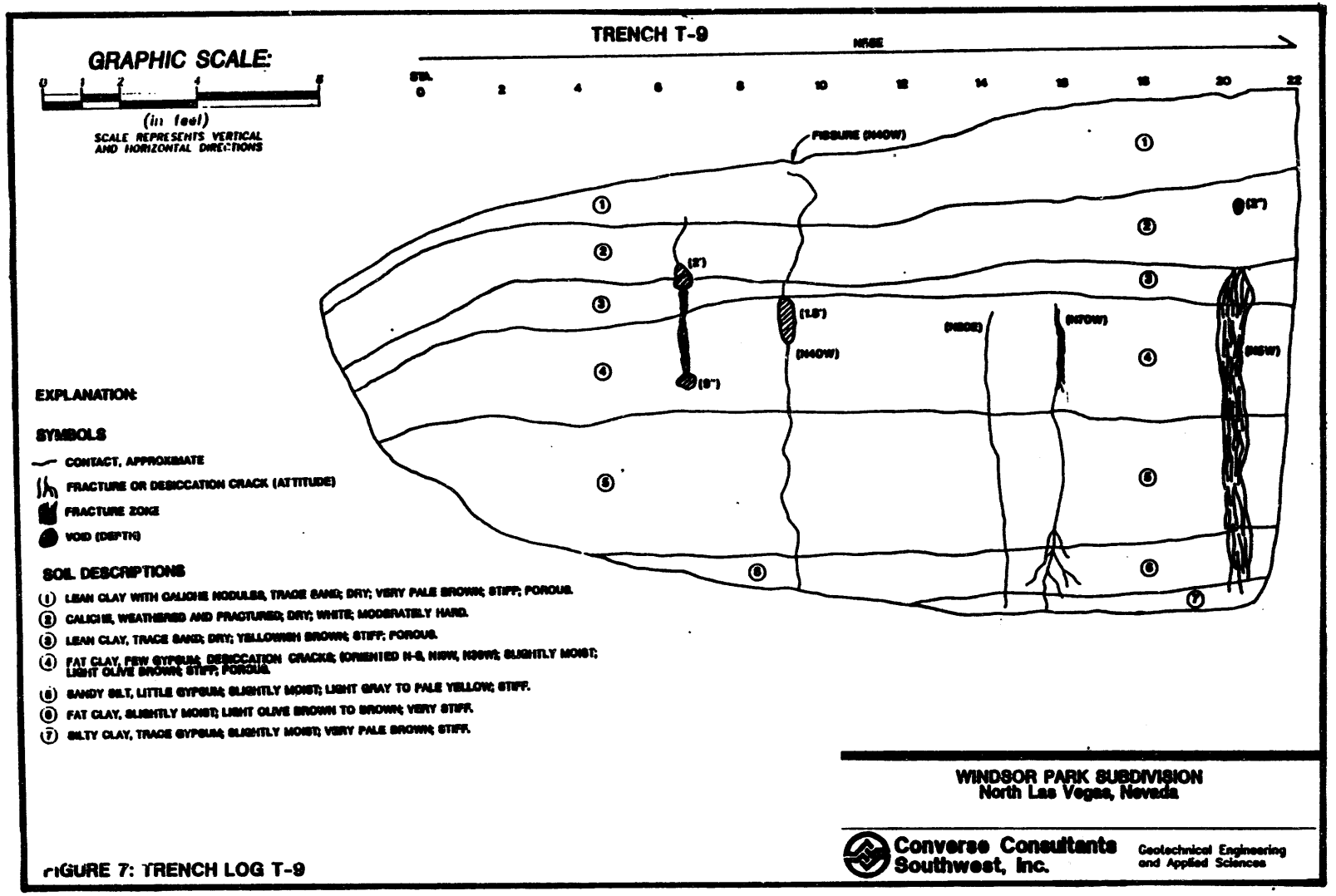


FIGURE 7: TRENCH LOG T-9

Table 1 - Selected Laboratory Testing Results

Atterberg Limits (ASTM D4318)

Exploration Location	Sample Depth, ft.	Liquid Limit, %	Plastic Limit, %	Plasticity Index	Unified Soils Classification
TS2-6, STA 20	4-6	143	47	96	CH
TS2-7, STA 0	1½-4	71	37	34	CH
TS2-7, STA 0	4-6½	247	65	182	CH
TS2-7, STA 10	8-11	83	30	53	CH
TS2-10, Pit	1½-4½	63	25	38	CH
T-1b, Pit	5-10	169	55	114	CH

Solubility*

Exploration Location	Sample Depth (feet)	Soil Description	Solubility (percent by dry weight)
TS2-1 Pit	1-2½	GYPSIFEROUS LEAN CLAY	1.5
TS2-6 STA 20	4-6	GYPSIFEROUS FAT CLAY	10.5
TS2-6 STA 20	6-8	GYPSIFEROUS FAT CLAY	3.8
TS2-7 STA 0	1½-4	GYPSIFEROUS FAT CLAY	5.8
TS2-7 STA 20	4-7	GYPSIFEROUS FAT CLAY	9.0
TS2-11 STA 15	0-4	SANDY LEAN CLAY few gyp	1.4
TS2-15 STA 25	1½-2½	GYPSUM	0.8
TS2-15 STA 25	4-5	GYPSIFEROUS LEAN CLAY	3.2

* About 2.0 liters of tap water was passed through each oven-dried sample.

Consolidation/Hydro-collapse*

Exploration Location	Sample Depth (feet)	Soil Description	Hydro-collapse (percent)
T-3 STA 1000	1-2	LEAN CLAY	1.4
T-3 STA 1010	1-2	LEAN CLAY	7.3
T-4 STA 0	½-1	CLAYEY SAND	2.8

*Sample saturated with a load of 1 kips per square foot (ksf)

Table 1 (continued)

Swell

Exploration Location		Depth (feet)	Soil Description	Moisture Content (percent) Field	Air-Dry	Final	Percent Swell
TS2-6	STA 20	4-6	GYPS. FAT CLAY	19	2	43	20
TS2-7	STA 0	1½-4	FAT CLAY	15	2	27	10
TS2-7	STA 20	4-7	GYPS. FAT CLAY	31	N/A	46	10[2]
TS2-15	STA 25	11-12	FAT CLAY	56	13	95	>25
T-1	STA 450	3-4	FAT CLAY	33	2	70	>22[3]
T-1b	Pit	5-10	FAT CLAY	27	1	67	25[3]
T-4	STA 100	0-1	GYPS. FAT CLAY	16	6	22	12*
T-6	STA 0	5-6	FAT CLAY	23	5	50	14**
T-6	STA 20	6½-10½	FAT CLAY	34	13	78	29[3]
T-9	STA 14	4½-7	FAT CLAY	15	5	46	14[3]
B-8		9-10	FAT CLAY	70	4	68	10**

Each sample was confined under a normal pressure of either 60, 120, or 500 pounds per square foot (psf)

* Undisturbed sample

** Undisturbed sample confined under a normal pressure of 120 psf.

[2] Remolded sample confined under a normal pressure of 500 psf. Some of the samples also exhibited saturated swell pressures of about 7 kips per square foot (ksf)(TS2-7) and 1.1 ksf (T-4).

[3] Remolded sample confined under a normal pressure of 120 psf.



Figure 8. Residence damaged by expansive clays. Trench TS2-7 located in front of house.

DISCUSSION

The subsurface investigation, laboratory testing and assessment revealed that the problem at the Windsor Park subdivision is indeed complex. Previous work had been centered on identifying one or two potential causes without considering the entire geologic framework, and the conclusions have been contradictory.

The primary causes of damage within the development were found to be (1) earth fissuring and (2) expansive clays. Several other causes are present at the site but they are not as significant as these two. Fissures have been extensively mapped in the Windsor Park and surrounding area. Expansive clays were encountered at various depths throughout the subdivision during our field work.

The potential for future damage at the site was assessed. The potential for fissuring at the site was considered high based on the offsite (regional) factors controlling fissure development and local factors such as soil type, proximity of faulting, drainage characteristics and the presence of existing fissures. Since underlying expansive clay was prevalent at the site, the potential for future clay expansion was also considered likely.

Future structural damage to the residences, utilities and streets from the various factors will likely be similar to the damage in the past. Without any form of mitigations whatsoever, it was believed that the damage from these factors would continue at a similar or faster rate through the next ten to fifteen years.

Engineering upgrades such as regrading of each lot and replacement with special house foundations as well as control of surface water drainage would reduce the risk posed by underlying expansive clays and other geotechnical conditions found at the site. However, they cannot totally eliminate the risk from fissuring. Engineering technology is not currently practical for solving such an extensive fissure problem as exists at Windsor Park given the nature of the development. Therefore, abandonment or alternative use of the site (i.e., park or mobile home community) was considered the best solution for eliminating all risks posed by fissuring and underlying expansive clays.

By 1992, approximately $2 million in federal and state funds were allocated for mitigation and/or relocation of the subdivision. However, the United States Department of Housing and Development (HUD), the City of North Las Vegas and the area residents needed assurance that damage would not continue after upgrades and repairs were completed. Evaluation of the data indicated fissuring and damage might continue at the site.

Since it was not economically feasible for the City of North Las Vegas to abandon or relocate all 200+ homes in the immediate future, Converse Consultants Southwest, Inc. used a statistical analysis (Bell and Price, 1991) and available data from previous damage surveys (HUD, 1988 and Mifflin, 1992) to develop 4 risk zones for City planning purposes. The intention was to relocate the homes in phases, and the residences at highest risk and with greatest damage would receive priority. Homes at

highest risk were placed in Zone 1 and those with the least risk in Zone 4. Approximately 56 percent of the fissures in the Windsor Park area were located within 400 feet of a subsidence-related fault. Zones 1 and 2 (136 lots) were positioned roughly within this 400 foot boundary, and it was believed that the potential for continued damage in these areas was extremely high. Zones 3 and 4 (110 lots) were generally located along the northwest and southeast margins of the development farther than 400 feet from the fault. Fissures and structural damage were less concentrated in these areas.

A relocation site was chosen by the City of North Las Vegas, approximately 1,000 feet east of the existing subdivision. By late 1993, relocation of homes from Windsor Park to the new site was under way.

REFERENCES

Bell, J.W., 1981, "Subsidence in Las Vegas Valley," Nevada Bureau of Mines and Geology, University of Nevada, Reno, Nevada, Bulletin 95, 84p.

Bell, J.W. and Price, J.G., 1991, "Subsidence in Las Vegas Valley, 1980-91: Final Project Report," Nevada Bureau of Mines and Geology, University of Nevada, Reno, Final Project Report to a Consortium of 11 City, County, State and Federal Agencies.

Cibor, J. M., 1983, "Geotechnical Considerations of Las Vegas Valley," Special Publication on Geological Environment and Soil Properties, ASCE Geotechnical Engineering Division, ASCE Convention, Houston, TX, October 17-21, 1983, pp. 351-373.

Helm, D. C., 1992, "Hydraulic forces that play a role in generating fissures at depth" *in* Proceedings of the Association of Engineering Geologists, Long Beach, California, October 2-9, 1992, p. 7-16.

Matti, J.C., Bachhuber, F.W., Morton, D.W. and Bell, J.W., 1987, Las Vegas NW Quadrangle, Geologic Map, Map 3Dg, Nevada Bureau of Mines & Geology, Scale 1:24,000.

Mifflin International, Inc., 1992, 1991 Inventory of Earth Fissures and Associated Damage at Windsor Park (Draft), for the City of North Las Vegas, Windsor Park Revitalization Project, February, 1992.

Plume, R.W., 1984, "Ground-water Conditions in the Las Vegas Valley, Clark County, Nevada: Part 1. Hydrogeologic Framework," U.S. Geological Survey, Open-File Report 84-130, 25p.

U.S. Department of Housing and Urban Development (HUD), 1988, "Report of Windsor Park," October, 1988, 9p.

Werle, J.L. and Stilley, A.N., 1991, "Effects of Ground Fissures on Development in the Las Vegas Valley, Nevada," *in* Proceedings of the 27th Symposium on Engineering Geology and Geotechnical Engineering, Utah State University, Logan, Utah, 15p.

Western Technologies, 1988, "Geotechnical/Geologic Evaluation, Windsor Park Development, North Las Vegas, Nevada," Project No. 4128J266, November 9, 1988, 35 pp.

Hydrogeology, Waste Disposal, Science and Politics
Proceedings 30th Symposium
Engineering Geology and Geotechnical Engineering, 1994

FAILURE ANALYSIS OF BURIED TANKS

by Reynold King Watkins, Professor Emeritus
Dept of Civil and Environmental Engineering
Utah State University, Logan, UT 84322-4110
(801) 750-2864

ABSTRACT

Failure of a buried tank can be hazardous. Failure may be a leak through which product is lost from the tank; but also through which contamination can occur. Failures are epidemic -- because buried tanks are out of sight, but also because designers of buried tanks have adopted analyses developed for pressure tanks. So why do pressure tanks fail when they are buried?

Most failures of buried tanks are really soil failures. Soil compresses, or slips, or liquefies. Soil is not only a load, it is a support without which the tank deforms. A high water table adds to the load on the tank. It also reduces the strength of the soil.

Based on tests, structural analyses are proposed for empty tanks buried in soils of various quality, with the water table at various levels, and with internal vacuum. Failure may be collapse due to vacuum in the tank, or equivalent flood level above the tank. Such collapse is a sudden, audible inversion of the cylinder when the sidefill soil slips. Failure may be flotation. Failure may be a leak. Most leaks are fractures in the welds in overlap seams at flat spots. Flat spots are caused by a hard bedding or a heavy surface wheel load. Because the tank wall is double thick at the overlap, shearing stress in the weld is increased. Other weld failures occur when an end plate shears down past a cylinder; or when the tank is supported only at its ends like a beam.

These, and other, failures can be analyzed with justifiable accuracy using basic principles of mechanics of materials.

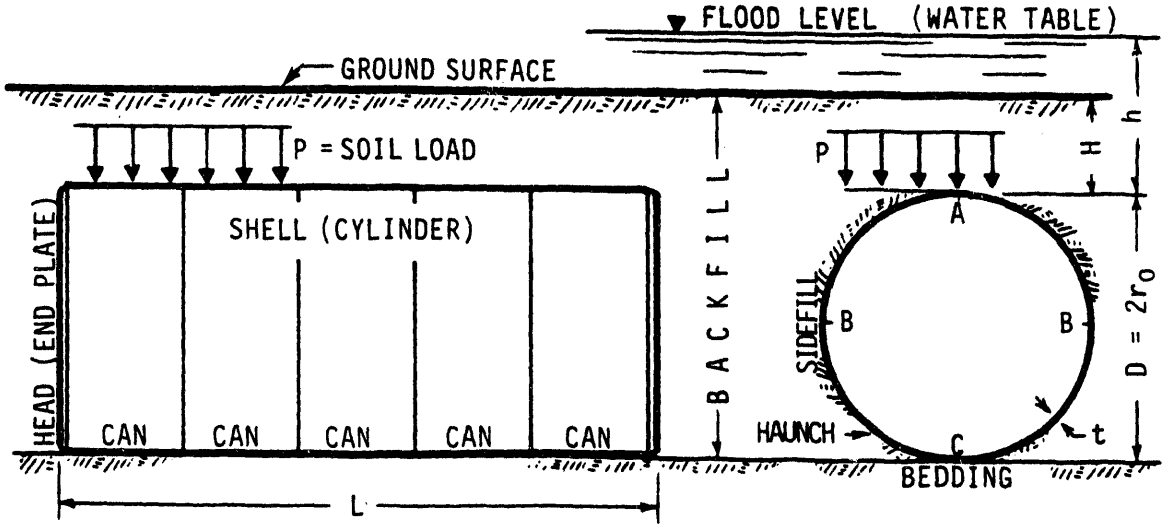


Figure 1. Some typical nomenclature for buried tanks.

INTRODUCTION

Failure of buried tanks has become a major environmental issue because of leaks that allow contents of the tank to contaminate the soil and groundwater, or allow groundwater to contaminate contents of the tank. See Nomenclature and Notation, Figure 1 and Table I.

Because the design of a tank to contain pressure is understood by tank designers and by manufacturers, rupture is infrequent -- that is, until the tank is buried. Most failures of buried tanks are really failures of the soil. Soil is complex -- not just a load on the tank, but also a support; not just a homogeneous single phase medium, but a complex three phase environment; not just a well-controlled/engineered material, but a variety of materials with deviations in properties and boundaries. Unlike the pressure tank, a buried tank is a composite, the performance of which is analyzed by soil-tank interaction mechanics.

Failure of a buried tank is a performance limit defined as any limit beyond which the tank does not perform as intended. Intended performance usually includes leak-proof containment over a design life without excessive distortion of the tank or movement of the soil. A safety factor is required for design.

Performance limits are excessive displacement or deformation.

Displacement includes unacceptable settlement of the tank or of the ground surface over the tank, and possible flotation of the tank when the water table rises.

Deformation includes excessive distortion of the tank, or rupture of the tank. Ruptures (leaks) are also deformations.

Table I. Notation

D	= mean diameter of the circular shell
L	= length of the tank
t	= thickness of the tank wall (and head?)
r	= maximum radius of the shell to the neutral surface of wall
r_o	= radius of the circular shell to the neutral surface of wall
r_x	= radius of curvature (minimum?) of the deflected ring at B
r_y	= radius of curvature (maximum) of deflected ring at A or C
x	= transition length of arc of the shell from point of maximum to point of minimum radius of curvature
w	= width of the overlap in a seam
R	= radius of curvature of the head (membrane theory)
c	= cord length for finding radius of curvature, r, of the shell
e	= mid-ordinate from cord to shell
d	= ring deflection = Δ/D
Δ	= decrease in vertical diameter of the deflected shell
P	= external pressure on the tank
P'	= critical internal pressure, or vacuum, at incipient collapse
u	= external water pressure on the shell
W	= load per unit length of tank
S	= yield strength from an axial test (compression or tension)
S_s	= shearing yield strength of the tank or weld materials
σ	= normal stress in the tank wall or weld
τ	= shearing stress in the tank wall or weld
E	= modulus of elasticity of the tank material

ANALYTICAL MODELS

In the following cases, analytical models are free-body-diagrams in static equilibrium. Performance limit is deformation. The limiting tank deformation may be a fracture at yield stress; but it may also be a flexural inversion of the cylinder ring. Inversion (collapse) is a function of ring stiffness -- not stress. For worst case collapse analysis, two models are proposed: one in unsaturated soil, and one in saturated soil with the water table at or above the ground suface. The tank is a horizontal cylinder (shell) with flat end plates (heads). The soil is cohesionless; it is placed in full contact with the tank; but it is not necessarily compacted. Soil failure is slip or liquefaction of the soil at the sides of the tank. Upon loss of support, the shell may invert. Loads on the tank include internal pressure (or vacuum) and external pressure due to soil, water table, and traffic loads.

Internal Pressure Analysis

The design of tanks to resist internal pressure applies to all tanks -- including buried tanks. External pressure of the soil and groundwater could be deducted from internal pressure at rupture. But usually the deduction is not significant or dependable, and is neglected. Figure 2 is the free-body-diagram for internal pressure analysis. The primary performance limit is a longitudinal split in the shell where circumferential stress, by the Barlow formula, is, $\sigma = P'r/t$. Rupture occurs at yield stress, S. Therefore, critical internal pressure is,

$$P' = St/r \qquad \text{RUPTURE ANALYSIS} \quad . \quad . \quad . \quad . \quad . \quad . \quad . \quad . \quad . \quad . \quad . \quad . \quad . \quad (1)$$

External Pressure Analysis

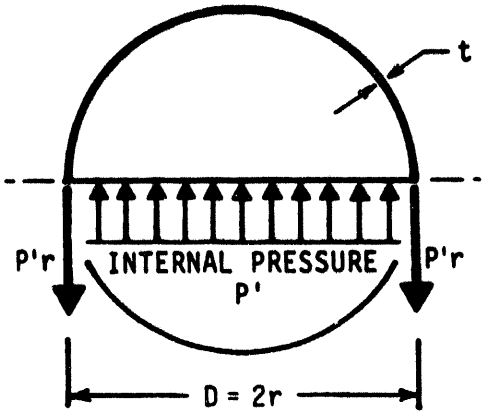
If the tank is held in circular shape by good backfill, the free-body-diagram is Figure 3a or its equivalent, 3b. At wall crushing, the critical vacuum (or flood pressure) is,

$$P = St/r \qquad \text{RING COMPRESSION ANALYSIS} \quad . \quad . \quad . \quad . \quad . \quad . \quad . \quad . \quad . \quad (2)$$

Clearly, the critical vacuum is reduced as the radius of curvature, r, is increased. The radius increases during backfilling as the ring deflects into an oval or develops flat spots -- for example, on the bottom when the tank is on a flat bedding without adequate compaction of soil under the haunches. Therefore, in Equation (2), radius r is maximum radius, usually r_y. See Figure 4.

Deformation Analysis

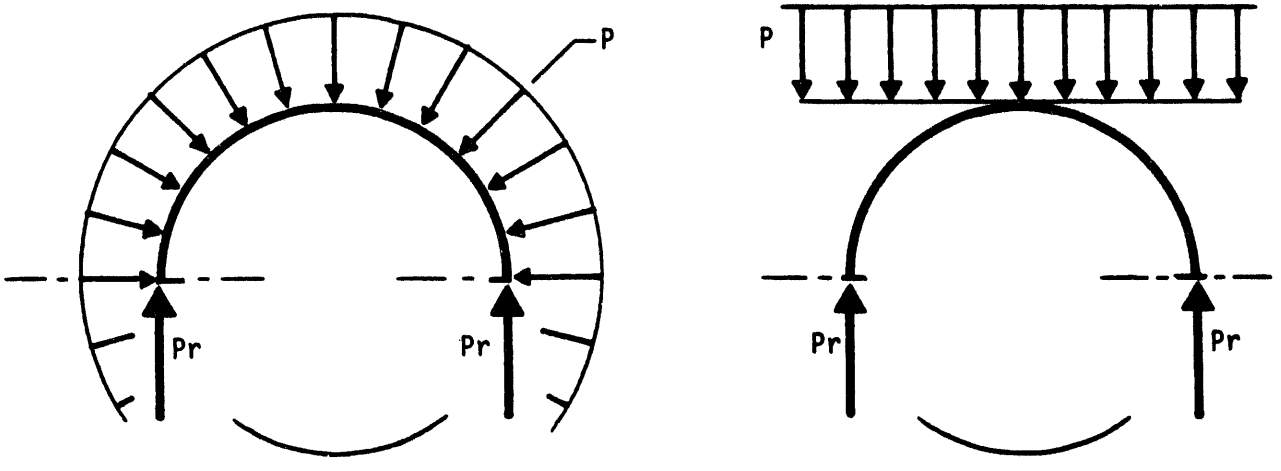
Figure 5 is the free-body-diagram for predicting stress in overlap seams where the wall thickness is doubled, but where the plates are fastened by a single circumferential weld. Due to the change in radius of curvature from r_o to r (at A, B and C for most ring deflections) the maximum normal circumferential stress on the



$\sigma = P'r/t$ = HOOP STRESS

BARLOW FORMULA

Figure 2. Free-body-diagram for internal pressure analysis of a shell (cylinder) showing the rupturing force P'D resisted by the hoop strength, $2\sigma t$ of the walls.

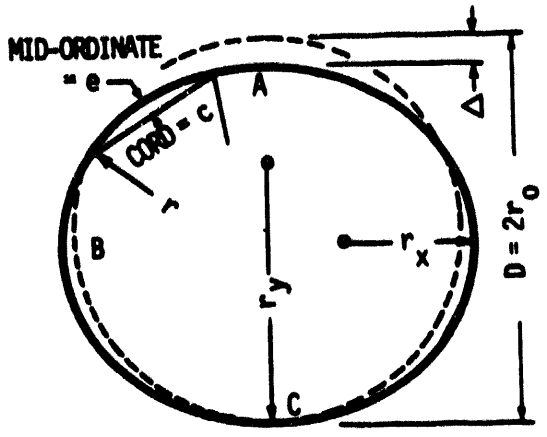


(a) RADIAL PRESSURE

(b) EQUIVALENT VERTICAL PRESSURE

$\sigma = Pr/t$ = RING COMPRESSION STRESS

Figure 3. Free-body-diagram for external pressure analysis of a shell with radial pressure P acting on it. Pressure P is resisted by ring compression, Pr, in the walls.



ELLIPSE

RING DEFLECTION, d = Δ/D

FOR ELLIPSE:

$r_x = r(1-d)^2/(1+d)$

$r_y = r(1+d)^2/(1-d)$

TO MEASURE RADIUS r,

$r = c^2/8e$

Figure 4. Tank shell ovalized during backfilling; in this case, an ellipse. Radius of curvature can be found from a mid-ordinate, e, measured from a cord of known length, c, to the cylinder. The cord may be positioned either inside or as a tangent outside the shell.

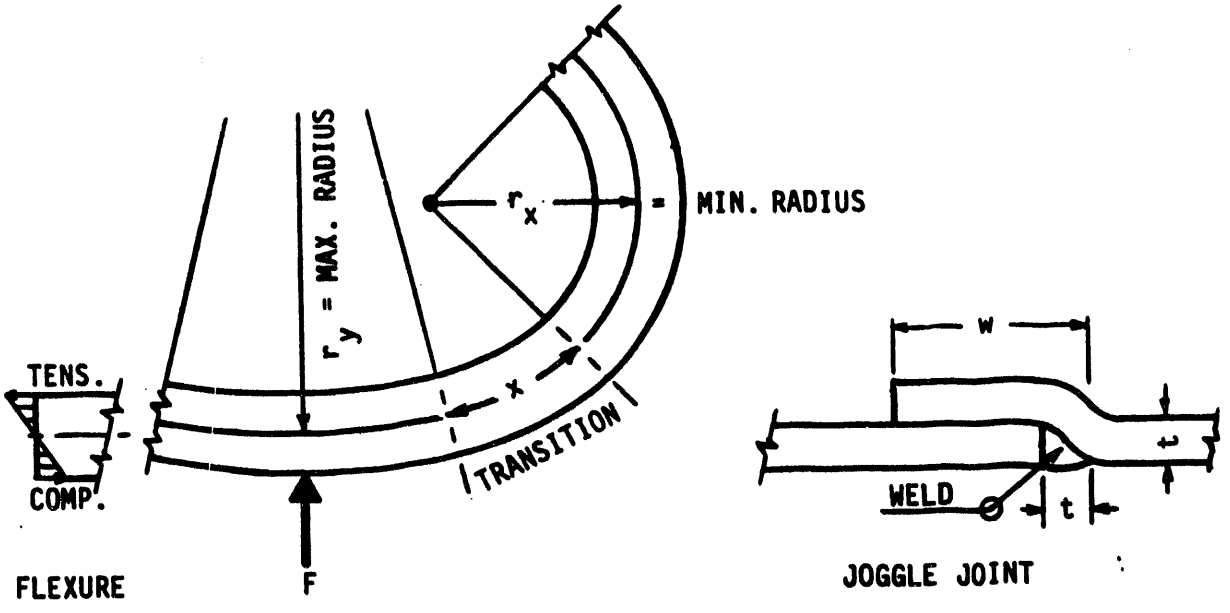


Figure 5. Change in radius of curvature in a typical overlap seam.

surfaces of the tank wall is $2\sigma = Et/r_o - Et/r$, but in the overlap (double thick) wall the stress is twice as great, i.e.,

$$\sigma = Et/r_o - Et/r \qquad \text{WALL CIRCUMFERENTIAL STRESS . . (3)}$$

Because steel can yield without fracture, normal stress is usually not a problem eventhough the deformation may be permanent.

Shearing stress is maximum at the neutral surface of the shell wall in the transition from maximum to minimum radius of curvature; e.g. at the ends of a flat spot. See Figure 5. If x is the length of transition, shearing stress in the wall is,

$$\tau = Et^2/8xr \qquad \text{WALL SHEARING STRESS . . . . . (4)}$$

Of greater concern is shearing stress in a weld at an overlap seam. See Figure 5. Shearing stress occurs throughout the length of the transition, x, (from the maximum to the minimum radius of curvature). If the shell is deflected into an ellipse, the maximum change in moment is from B to C (or A to B) over transition length $x = \pi r_o/2$. Change in moment is $M = EI(1/r_x - 1/r_y)$. From mechanics,

$$\tau = (Ewt/\pi r_o)(1/r_x - 1/r_y) \qquad \text{WELD SHEARING STRESS . . (5)}$$

In case of line load, F, on the bottom of the pipe, shearing stress in the weld of the overlap seam of Figure 5, is,

$$\tau = 3F/8xt \qquad \text{. . . . . (6)}$$

This is a significant cause of leaks in buried tanks -- especially when F is the reaction to the combined weights of: the tank, the contents, a wedge of soil on top, and a surface live load -- and more especially if the line load F is concentrated at one or two high spots in the bedding under the tank. This weld shear failure is particularly objectionable because it occurs on the bottom of the tank where the entire contents can leak out.

Another cause of leaks is shear in a circumferential weld where the stiff head shears down past the flexible shell. See Figure 6. A head picks up soil load for at least one diameter from the end of the shell. As the flange buckles, the weld is subjected to both shearing and flexural stresses.

Longitudinal Analysis

Longitudinal stresses can open cracks in circumferential welds. Due to internal pressure only, longitudinal stress is half as great as the circumferential (hoop) stress; $\sigma = P'r/2t$. But added to this may be longitudinal stresses due to temperature decrease, Poisson effect of internal pressure, and longitudinal beam bending.

But the principal cause of longitudinal stress is beam bending due to non-uniform bedding. See worst case, Figure 7. At point C, from mechanics of a simply supported beam, longitudinal stress is,

$$\sigma = W(L/r)^2/8\pi t \qquad \text{WALL LONGITUDINAL STRESS . . . (7)}$$

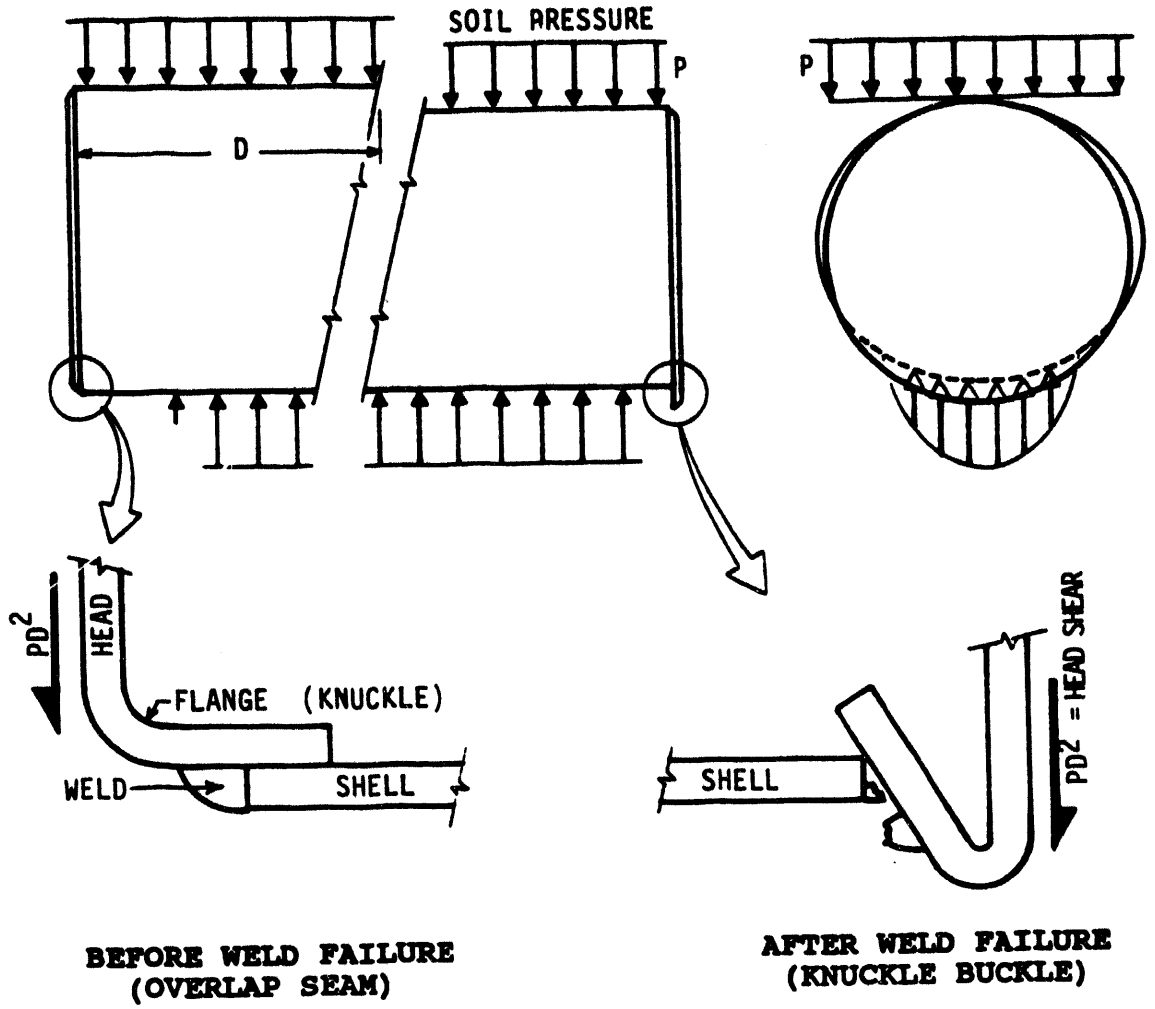


Figure 6. Mechanism for failure of a circumferential weld due to a stiff head that shears down past a flexible shell. Underwriters Laboratory code calls for a minimum 1.5 inch flange and 0.5 inch penetration into the shell.

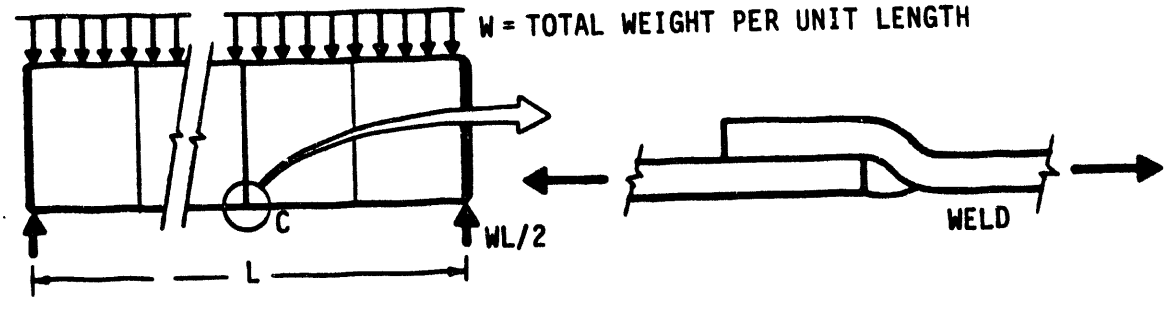


Figure 7. Typical conditions for longitudinal (tension) failure of a weld due to mounds in the bedding at the ends of the tank used to level the tank. The tank becomes a simply supported beam.

Head Analysis

Even though external pressure on the head varies from top to bottom, an assumption that pressure is uniform is accurate within two percent for typical steel tanks. A classical analysis to find maximum moment by plate theory is available, but is not justified because the ratio of thickness to diameter is small and yield stress is not failure. Membrane theory is adequate, if head analysis should be of any concern. Tension stress in the head is $\sigma = PR/2t$, where R is the radius of curvature of the pressurized spherical head and can be calculated by the strain as the head deforms from a disc to a sphere under average pressure P.

Shell Analysis -- Unsaturated Soil Envelope

With a good soil backfill, the shell is essentially circular. Few problems are encountered. Longitudinal stress is not critical except when the tank is a simply supported beam. With poor soil backfill, the ring deflects down. Ring deflection is nearly equal to settlement of sidefill soil. Soil compaction is recommended. With less than minimum soil cover, a wheel load over the top of the tank can invert the top of the shell. Live load pressure on the tank should be checked. Conditions for deformation are worstened if soil is not compacted under the haunches. At worst, for a tank with no soil support, subjected to internal vacuum, the classical analysis of collapse is plotted on Figure 8. Noteworthy is the stiffener effect of the heads in the term L/D.

Shell Analysis -- Saturated Soil Envelope

Figure 9 is the free-body-diagram for analysis of a buried tank after the water table rises. Buoyant water pressure on the bottom of the tank is critical -- not soil load on top. In fact, soil on top becomes a reaction to the buoyant tank. Analysis is equilibrium of horizontal stresses on the infinitesimal soil cube at B where pressure of the tank against soil is resisted by effective passive soil strength. It is assumed that the soil is cohesionless, placed dry, then saturated.

In case the backfill is mud -- the worst case scenario -- results of tests on 12,000 gallon service station tanks are shown in Figure 10. The worst-case soil is seventy percent fine sand and thirty percent silt. The effect of shortened tank length is offset by greater depth of the buoyant uplift water pressure.

Flotation

In saturated soil, an empty tank will not float if the soil cover is at least half of the tank diameter. However, this rule is based on the assumption that the backfill soil is cohesionless and is compacted to a density greater than 80% ASTM Method D698. Loose soil may liquefy due to earth shock waves or to soil movement. A common practice below water table is to tie the tanks down to heavy concrete foundations with straps that avoid stress concentrations.

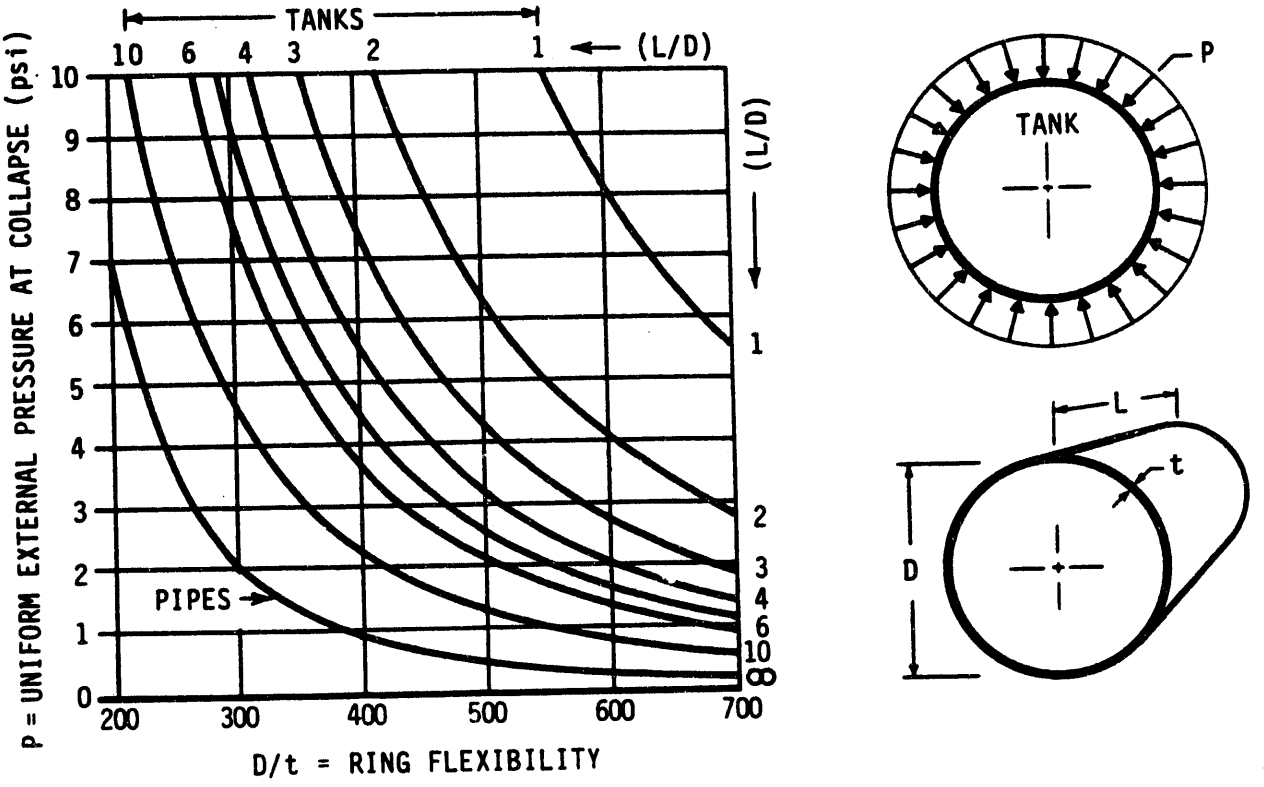


Figure 8. Uniform external pressure at collapse of steel tanks.

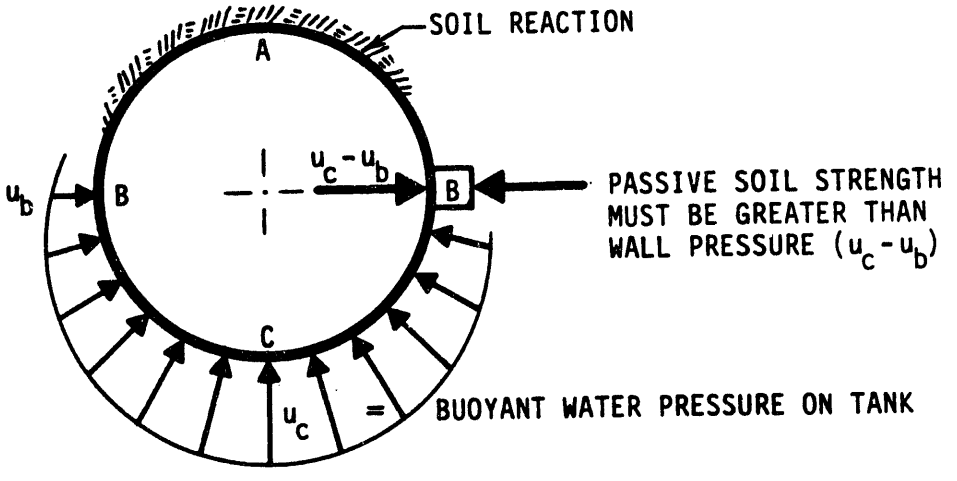


Figure 9. Free-body-diagram of an infinitesimal soil cube B for finding critical buoyant water pressure at soil slip (incipient tank collapse) by equating the horizontal stresses acting on B.

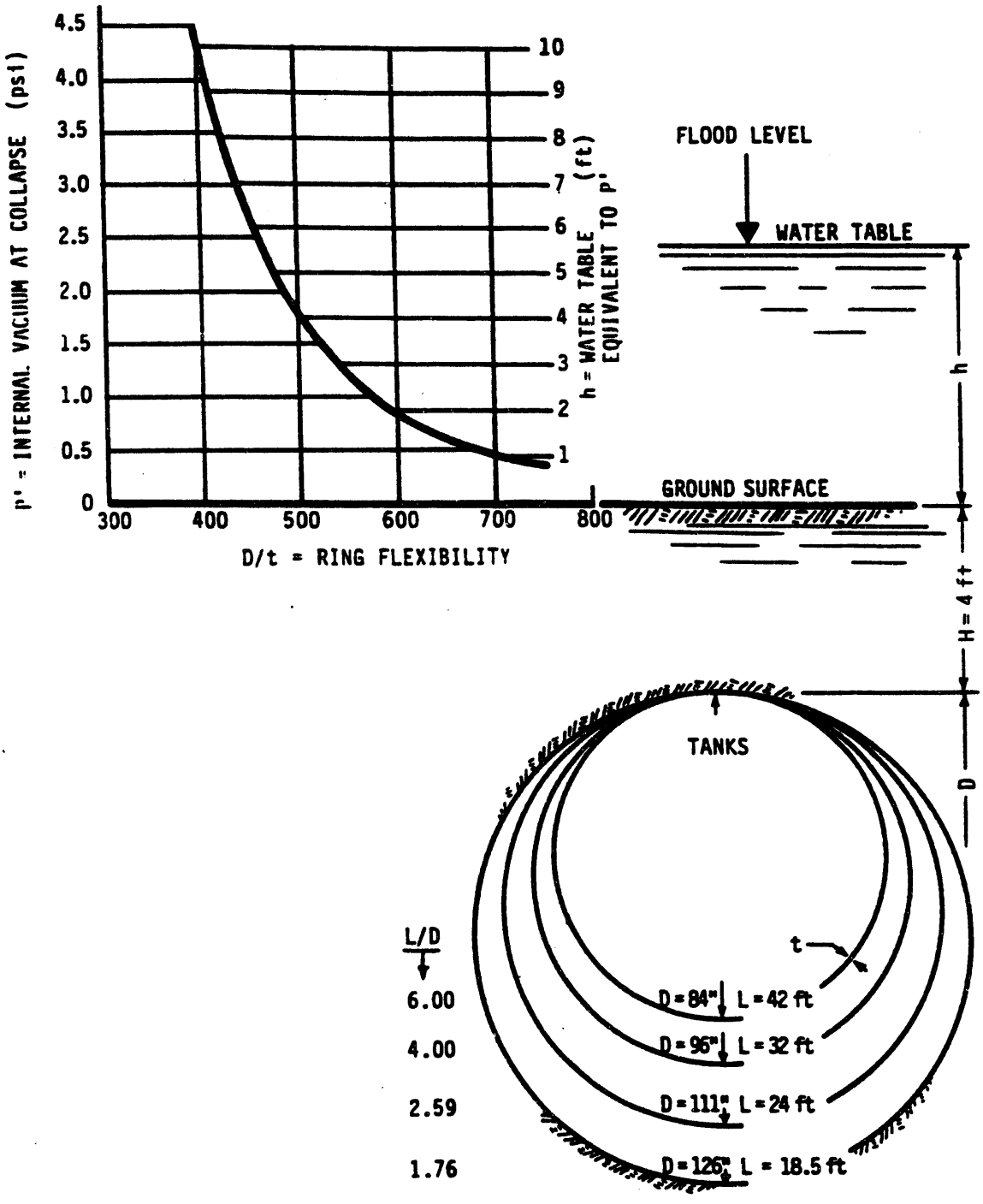


Figure 10. Results of tests at USU to find the critical vacuum at collapse of 12,000 gallon steel tanks buried in silty sand with water table at ground surface four feet above the tank; and showing both vacuum, P', at collapse and the equivalent height of a water table, h, (flood level) shown to scale.

Hydrogeology, Waste Disposal, Science and Politics
Proceedings 30th Symposium
Engineering Geology and Geotechnical Engineering, 1994

EROSION CONTROL TEST FACILITIES AT THE UTAH WATER RESEARCH LABORATORY

C. Earl Israelsen, Professor
Civil and Environmental Engineering Department
Utah State University, Logan, UT 84322

Gilberto Urroz, Assistant Professor
Civil and Environmental Engineering Department
Utah State University, Logan, UT 84322

ABSTRACT

Facilities have been developed at the Utah Water Research Laboratory in Logan, Utah, for determining the effectiveness of a variety of erosion control products including mulches, blankets, mats, rovings, chemicals, blocks, and vegetation. This paper describes in detail a rainfall simulator, a tiltable test bed, a sunlight simulator, a wind generator, twin large-scale high-velocity test channels, and a glass-walled flume for measuring shear.

INTRODUCTION

In the late 1970's, the Utah Water Research Laboratory in Logan, Utah, recognized the need for evaluating the effectiveness of a continually-increasing number of erosion control products and practices, and adapted some of its laboratory equipment to accommodate this need. Since that time, the equipment has undergone periodic upgrading and improvement until at the present time it is probably second to none in the nation. Present erosion control test facilities include a rainfall simulator and accompanying test flume, sunlight simulator, wind generator, high-velocity test flume, and a flume for measuring shear.

RAINFALL SIMULATOR

The rainfall simulator is a drip-type device in which raindrops are formed by water emitting from the ends of small-diameter brass tubes. The rate of flow is controlled by admitting water into manifold chambers through fixed orifice plates under constant hydraulic pressure. Five separate inlet orifices are used in each chamber or simulator module. The ratios of the areas of the orifices are 1:2:4:8:16. By controlling the water flow to the orifices with electrically operated solenoid valves, and the water pressure with a movable head tank, it is possible to vary rainfall rate up to approximately 25 inches per hour. Outlet from the chambers or modules is through equally spaced brass tubes on the undersides of the modules. Each module is a 24-inch square completely enclosed box about 1-inch deep and oriented so that the ends of the tubes or needles form a horizontal plane to let the water drip to test plots below. Each module has 576 needles spaced on a 1-inch square grid pattern.

The rainfall simulator consists of 100 modules that are supported adjacent to each other to make a continuous simulator 400 square feet in area. Each module can be controlled separately. The 500 electrical control switches are manually operated.

Raindrop sizes about 4 mm in diameter are representative of typical high intensity storms. The spatial distribution of rain is essentially uniform, and the control of application rates is within the accuracy requirement of most experiments.

TEST FLUME

The square test flume measures 20 feet on each side and can be tilted to any angle from horizontal up to more than a 1 1/2:1 slope. The rainfall simulator is supported over the flume so that rain falls directly onto the test plots. The plots contain a 1-foot depth of soil, supported by a metal grating which is covered with a filter cloth through which water can drain.

The flume can be divided into six 2 ft x 19.5 ft test plots, or three 4 ft x 19.5 ft test plots. The plots are separated from each other and from the side walls by 2-foot wide walkways. The rainfall simulator can be controlled to rain only on the plots and not upon the walkways.

SUNLIGHT SIMULATOR

A balance of radiant energy needed for good growth of plants is provided to the test plots by a sunlight simulator which utilizes incandescent as well as fluorescent lamps. It has the same dimensions as the tilting flume, is square, and measures 20 feet on a side. It is rolled on and off the test plots on wheels riding on horizontal rails mounted on top of the side walls of the tilting flume. When in position, it is about 3 ft above the test plot surfaces and provides illumination at a photon flux density of 216 $\mu E \cdot m^2 \cdot sec^{-1}$ (measured with a LaCor 190 S quantum sensor on a Model LI-185 quantum radiometer/photometer). The sunlight simulator is used for germinating seed and growing plants, and also to shorten the time for drying soil between runs.

WIND GENERATOR

A 24-inch diameter squirrelcage fan driven by a 15 HP, 440 VAC motor is mounted rigidly on a wall near the lower end of the testing flume. When the flume is positioned at a 2:1 slope, three 10-inch diameter metal ducts direct wind from the fan through the end of the flume onto the test plots. The wind blows upslope, parallel to the sloping surface, and impinges on the plots at approximately their midpoints. Wind enters the flume at a velocity of approximately 60 mph (88 fps), disperses to about 30 mph (44 fps) at the point of impingement, and slows to 10 mph (15 fps) at the upper ends of the plots. This uni-directional constant velocity wind does not simulate all of the conditions found in a field setting, but does enable a comparison of the performance of erosion control products under similar conditions.

HIGH VELOCITY TEST FLUME

This flume, which is 8 ft wide, 6 ft deep, and 570 ft long, is supplied with water under 35 ft of head from a nearby reservoir through a 3-ft diameter pipe. A spreader at the outlet end of the supply pipe uniformly distributes water over the 8-ft width of the channel. A plywood partition and end gates in the flume provide two test sections, each measuring 4 ft in width and 50 ft in length. A 20-ft long plywood-lined smooth approach to the test sections allow

turbulence in the high velocity water flows to subside before they reach the soil and test materials. The bottom of each channel is positioned approximately 2 ft above the floor of the concrete flume so that water can flow underneath, and so draining of the soil masses can be more quickly accomplished. The floors of the channels are slotted and covered with drainage fabric which allow water to drain through but retain the soil. Soil is compacted into the channels on top of the drainage fabric to a depth of 18 in., and the materials to be tested are installed on the soil surface. Figure 1 is a sketch of the flume and test channels.

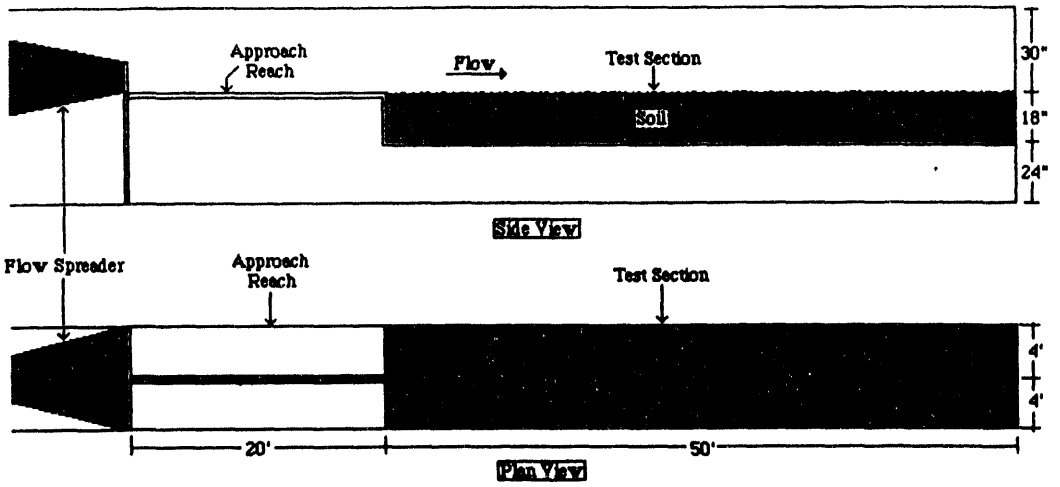


Figure 1. Elevation and plan views of test channels.

Figure 2 is a cross section of the channels showing the placement and method of anchoring the materials to be tested. Side curtains of non-woven geotextile are placed full-depth on both sides of the channels to prevent failure along channel edges due to wall effects. Figure 3 indicates how test materials are anchored in head trenches in the channels.

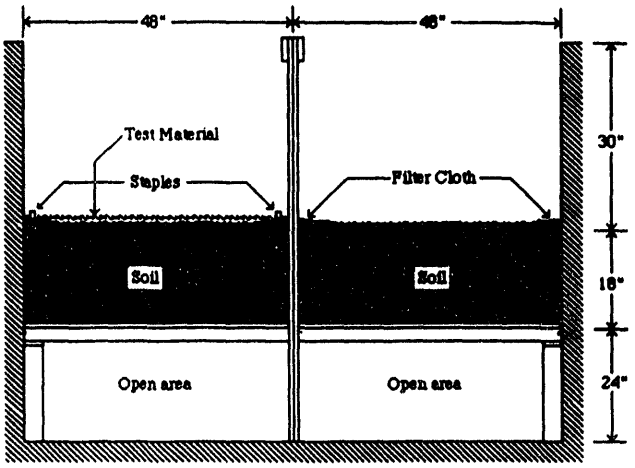


Figure 2. Placement and method of anchoring side curtains and test materials.

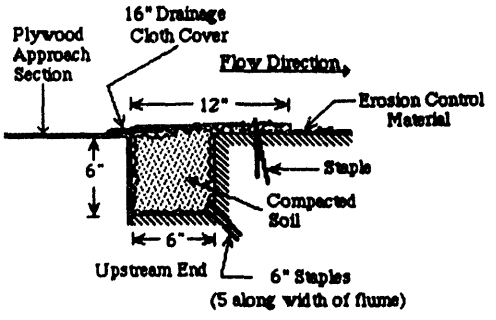


Figure 3. Test materials were anchored in head-trenches as shown.

A "test" in this unit consists of two replications of several runs, each at a different water flow amount and velocity. Normally there would be flows of 20, 32, 45, 60, and 75 cfs for 30 minutes each which translate to velocities of approximately 3, 5, 10, 15, and 20 fps. We can also run in excess of 100 cfs at approximately 25-30 fps when necessary. On durable materials, the runs may start at 10 to 15 fps and extend through 25 fps. Centerline velocity and flow-depth measurements are made of each run at stations 0, 5, 15, 30, and 45. After every run, cross-sectional measurements are made at each 1-ft width across the channels and every 5 ft along their lengths to determine erosion depths. Extended runs at any velocity and for any length of time are made when warranted.

FLUME FOR MEASURING SHEAR

Valid calculations of shear on channel linings cannot be made in erodible channels because the values change with time as well as with velocity as the soil erodes. To accommodate the many requests to determine shear values of particular lining materials, a third test facility has only recently been constructed. This consists of a 2 ft x 2 ft x 24 ft glass-walled flume supplied with water through a 10-inch diameter pipe and a spreader nozzle. In the floor of the flume is a 2 ft x 5 ft section to which materials to be tested are fastened with stainless steel staples that are anchored into the floor section at a 45 degree angle. This section rests on stainless steel ball bearings set in teflon pockets. From the underside of this section, a steel arm extends through the floor of the channel and is connected to a load cell that has a digital readout. The shear that is generated on the material by water flowing over it is imparted directly to the load cell where it is displayed as a force on the readout. These values are then recorded as force per unit area (lbs/ft^2). Even shear from the slightest flows can be detected. The shear increases as velocity increases (unless the liner fails first) up to the limit of the system which is approximately 20 ft per second, or until it reaches an equilibrium value.

The test is started at a low velocity and allowed to stabilize. The velocity is increased in incremental steps until the material fails or until the limit of the test unit is reached, whichever comes first. At each setting, the velocity and flow depth at the beginning and end of the test section are measured and recorded along with the corresponding shear.

Three replications are run of each test, and the results are averaged and plotted. Shear values at any velocity can then be read directly from the graph.

The regular utilization of these unique testing facilities can result in a continual improvement in the effectiveness of erosion control products throughout the industry.

Hydrogeology, Waste Disposal, Science and Politics
Proceedings 30th Symposium
Engineering Geology and Geotechnical Engineering, 1994

Pre-anthopogenic groundwater evolution at the Idaho National Engineering Laboratory, Idaho

MCLING, Travis L., and SMITH, Robert W., Idaho National Engineering Laboratory, P.O. Box 1625, Idaho Falls, ID 83415-2110

The Snake River Plain aquifer is the most important groundwater source in Idaho. Overlying the aquifer in eastern Idaho is the Department of Energy's Idaho National Engineering Laboratory (INEL). Activities at the INEL include reactor research, nuclear fuel reprocessing, and nuclear waste storage. Past activities at the INEL have locally affected groundwater quality. To assess the geochemical controls on water quality, water chemistries from approximately 75 US Geological Survey wells were evaluated using the MINTEQA2 and NETPATH computer codes.

Greater than 95 percent of the solute budget in the aquifer is comprised of eight ions: calcium, magnesium, sodium, potassium, silica, bicarbonate, chloride, and sulfate. Based on MINTEQA2 calculations calcite is the only significant secondary mineral precipitating in the aquifer at the INEL. Commonly occurring minerals that are under-saturated in the aquifer are plagioclase, pyroxene, and olivine. The pH in the aquifer ranges from 7.6 to 8.6 and increases with residence time, primarily due to a loss of CO_2.

The results of this study show that the aquifer chemistry is strongly controlled by groundwater mixing and minor basalt weathering. In addition, this study will aid in the establishment of a groundwater standard to be used in remediation and aid waste migration modeling activities at the INEL.

Hydrogeology, Waste Disposal, Science and Politics
Proceedings 30th Symposium
152 Engineering Geology and Geotechnical Engineering, 1994

DESIGN OF THE IDAHO NATIONAL ENGINEERING LABORATORY INTEGRATED FIELD SCALE PUMPING AND INFILTRATION TEST

T. R. Wood[1], G. T. Norrell[1], A. W. Wylie[1], K. J. Dooley[1] G. S. Johnson[2] and E. R. Neher[1]

1. Idaho National Engineering Laboratory, P. O. 1625, Idaho Falls, ID 83415
2. University of Idaho Idaho Falls, ID 83405

ABSTRACT

The high degree of heterogeneity present in the Snake River Plain subsurface precludes utilization of small or intermediate scale observation alone for hydrologic and geochemical characterization efforts. The minimum representative elemental volume for the fractured, intercalated sequence of basalt flows and sedimentary interbeds is considered to be in the 10^5 to 10^7 m^3 range. An integrated program of large scale field experiments, along with supporting laboratory investigations, has been initiated at the INEL to provide the most reliable information obtainable regarding aquifer flow and contaminant transport through the vadose zone.

An aquifer pumping test has been designed which will involve pumping the Snake River Plain aquifer (SRPA) at approximately 3000 gpm for a period of four weeks. Previous aquifer tests have been conducted at comparatively low pump rates over shorter time intervals. This increased scale is intended to allow for stressing a sufficiently large volume of the SRPA to effectively average out heterogeneities which cause wide variations in the results from smaller scale experiments. The water generated during the extended pump tests will be piped ~ two kilometers to the southwest to a seven acre infiltration basin. Conservative and reactive tracers will be added to the infiltrating water for assessing actinide and fission product surrogate retardation factors and dispersion parameters. Infiltrating water will be monitored with several overlapping systems, including ~60 wells screened at various transmissive layers within the first 200 ft depth, and geophysical techniques. Water and tracer migration will be tracked with down-hole nuclear moisture logging and gamma spectroscopy, as well as geophysically. The State of Idaho INEL Oversite Program will conduct a detailed characterization of the aquifer test observations wells using a sophisticated straddle-packer system. Additionally, the State will perform depth-discrete sampling to the base of the aquifer for stable and radiogenic isotopic analyses.

The field site was constructed (including well installation during the 1993 field season). Geological characterization has provided baseline data for predictive modeling of experimental results. The field experiments are scheduled to be performed during the 1994 field season. Results from the integrated program of field and laboratory experiments will be used to estimate projected contaminant travel times through the vadose zone to the Snake River Plain aquifer. As such, results will ultimately determine which remediation alternatives are most appropriate.

Hydrogeology, Waste Disposal, Science and Politics
Proceedings 30th Symposium
Engineering Geology and Geotechnical Engineering, 1994

MINERALOGY AND DEPOSITIONAL SOURCES OF SEDIMENTARY INTERBEDS BENEATH THE IDAHO NATIONAL ENGINEERING LABORATORY; EASTERN SNAKE RIVER PLAIN, IDAHO

Reed, M.F., Department of Geology, Idaho State University, Pocatello, Idaho 83209-8072

ABSTRACT

Idaho State University, in cooperation with the U.S. Geological Survey, and the U.S. Department of Energy, collected 57 samples of sedimentary interbeds at 19 sites at the Idaho National Engineering Laboratory (INEL) for mineralogical analysis. Previous work by the U.S. Geological Survey on surficial sediments showed that ratios detrital of quartz, total feldspars, and calcite can be used to distinguish the sedimentary mineralogy of specific stream drainages at the INEL. Semi-quantitative x-ray diffraction analyses were used to determine mineral abundances in the sedimentary interbeds. Samples were collected from wells at the New Production Reactor (NPR) area, Idaho Chemical Processing Plant (ICPP), Test Reactor Area (TRA), miscellaneous sites, Radioactive Waste Management Complex (RWMC), Naval Reactors Facility (NRF), and Test Area North (TAN). Normalized mean percentages of quartz, feldspar, and carbonate were calculated from sample data sets at each site. Percentages for quartz, feldspar, and carbonate from the NPR, ICPP, TRA, miscellaneous sites, RWMC, and NRF ranged from 37 to 59, 26 to 40, and 5 to 25, respectively. Percentages for quartz, feldspar, and carbonate from wells at Test Area North (TAN) were 24, 10, and 66, respectively.

Mineralogical data indicate that sedimentary interbed samples collected from the NPR, ICPP, TRA, miscellaneous sites, RWMC, and NRF correlate with surficial sediment samples from the present day Big Lost River. Sedimentary interbeds from TAN sites correlate with surficial sediment samples from Birch Creek. These correlations suggest that the sources for the sediments at and near the INEL have remained relatively consistent for the last 580,000 years.

INTRODUCTION

The eastern Snake River Plain (ESRP) is a northeast-trending physiographic basin approximately 200 mi long and 50-70 mi wide in southeastern Idaho (Fig. 1), within which the Idaho National Engineering Laboratory (INEL) encompasses about 890 mi^2. The INEL is underlain by a series of Miocene-Quaternary volcanic rocks and sedimentary interbeds more than 10,000 ft thick (Doherty and others, 1979; Whitehead, 1986; Rightmire and Lewis, 1987). The lower portion of the sequence contains mostly Miocene-Pliocene rhyolitic ash and tuff whereas Quaternary basalt lava flows , along with basaltic ash and cinders make up approximately 2000 ft of the uppermost part. The basaltic units of the upper sequence are interbedded with fluvial, lacustrine and eolian deposits of clay, silt, sand, and gravel. This portion of the sequence also contains the Snake River aquifer. In places the upper basaltic and sedimentary portion is intruded by rhyolite domes that are elevated by as much as 2,000 ft above the surface, e.g. Big Southern Butte.

The hydrogeologic character of the aquifer has been affected by fractures, mainly jointed lavas, and the interbedded sediments that fill many of the fractures; therefore infiltration and flow involve both fractured and porous media (Rightmire, 1984). Depth to the water table ranges from approximately 200 ft in the northern part of the INEL to approximately 1000 ft in the southwest section of the site (Barraclough and others, 1981), making the general direction of ground water flow from the northeast to the southwest.

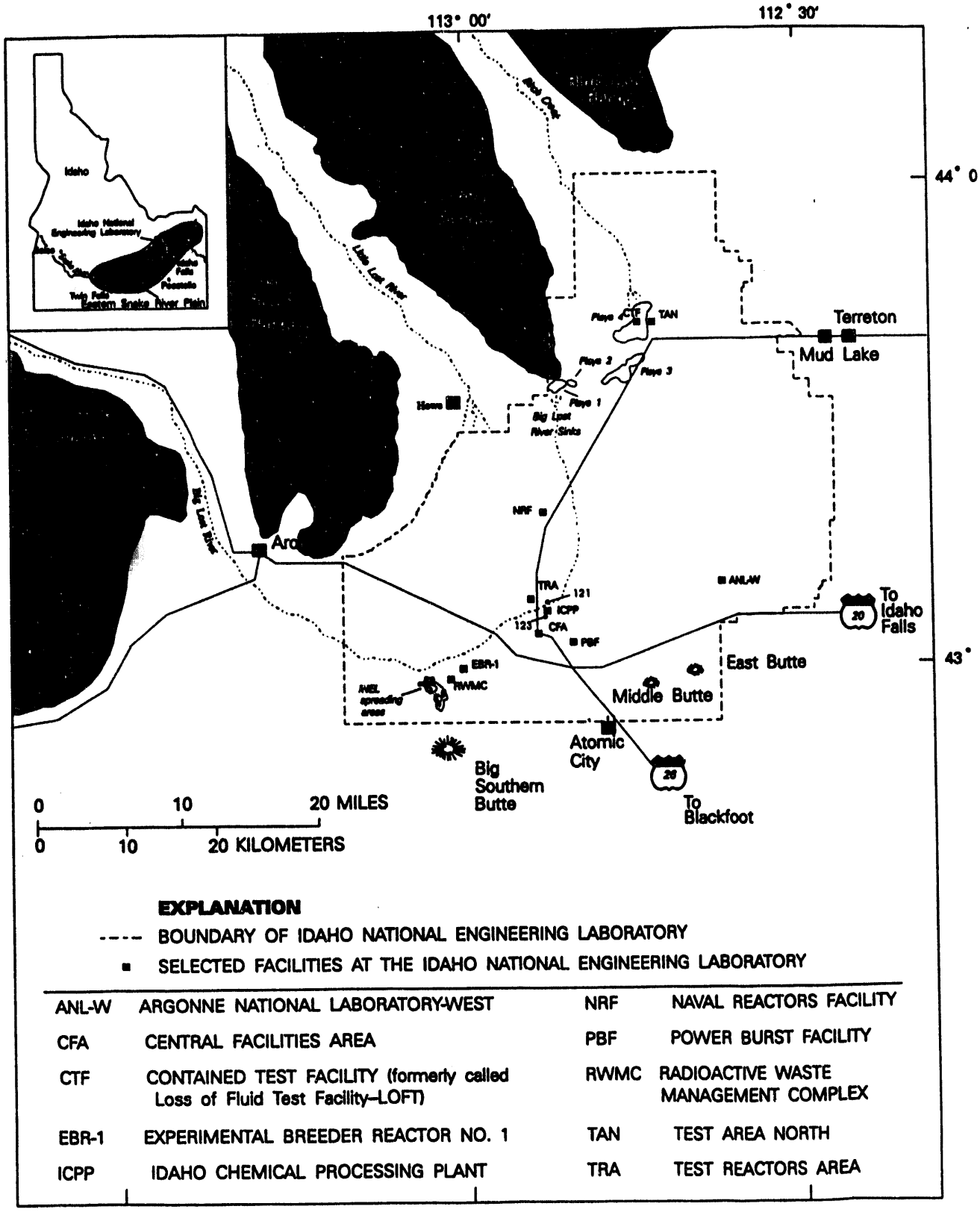


Figure 1. Locations of the Idaho National Engineering Laboratory, selected facilities, and core sample sites.

The northern part of the INEL is in a topographical closed basin that includes the Big Lost River Sinks; Little Lost River Sinks; Birch Creek Sinks, Big Lost River Playas 1, 2, and 3; and the Birch Creek Playa (Fig. 1). Big Lost River, Little Lost River, and Birch Creek terminate in the Birch Creek Playa (Robertson and others, 1974). The INEL also contains several small isolated closed basins. Surface flow from Little Lost River and Birch Creek is presently being diverted for irrigation and power generation and does not reach the playas except during years of high runoff. The majority of the surface water at the INEL is derived from flow in the Big Lost River which ultimately recharges the aquifer. Relative abundances of detrital minerals in surficial sediments from the Big Lost River drainage were presented by Bartholomay and others (1989). Mineralogical data for surficial sediments from the Little Lost River and Birch Creek drainages were presented by Bartholomay and Knobel (1989). A summary of these results by Bartholomay (1990) indicates that the three drainage systems that flow onto the INEL can be separated based on mean normalized percentages of quartz, total feldspar, and carbonate.

Previously published mineralogical data are used to correlate surficial sediments from the three different drainages with the data of sediment interbeds from this study. As in previous studies, quantitative X-ray diffraction analysis was used in this study to determine the mineralogy of all interbed sediment samples. A modification of the method described by Diebold and others (1963) and Schultz (1964) was used to obtain the relative mineral percentages.

METHODS

Sample Collection

Sediment interbeds were collected from 19 sites for mineralogical analysis from February 1993 through December 1993 (Fig. 2). Sampling sites were selected based on the availability at the USGS lithologic core library at the INEL. Sedimentary interbed samples (approximately 20 grams) were collected from 17 sites in the Big Lost River basin: 10 samples from 3 sites (DC-1, DC-4, and WO-2) at the New Production Reactor (NPR) area; 10 samples from 5 sites (PW-7, PW-11, TRA-5, TRA-8, and USGS 80) near the TRA; 13 samples from 3 sites (USGS 81, 121, and 123) near the ICPP facility; 8 samples from 2 sites (RWMC-C1A and USGS 118) near the RWMC; 5 samples from 3 sites (NRF-6P, NRF-7P, and USGS 99) near the Naval Reactor Facility (NRF); 1 sample from USGS 103; and 1 sample from USGS 104. Sedimentary interbeds from the Birch Creek basin were represented by nine samples from 2 sites (TAN CH-1, and TAN CH-2) near the Test Area North (TAN) facility. Depths of samples collected are shown on Table 1.

Sample Preparation and Analysis

X-ray diffraction analysis on the sedimentary interbeds was used to determine bulk mineralogy and clay particles less than 0.004 mm in diameter. Analyses of clay separates were made only on samples that had clay present in the bulk analysis. For bulk mineralogy a representative sample approximately 3 g of sample was ground for 8 minutes in a ball-and-mill device to reduce grain size and to homogenize the sample. The sample was subsequently ground using a mortar and pestle until all of the sample passed through a 0.062 mm sieve. The powdered sample was packed into an aluminum holder and scanned with a Philips Norelco X-ray diffractometer. The generator was operated at 35 kilovolts,

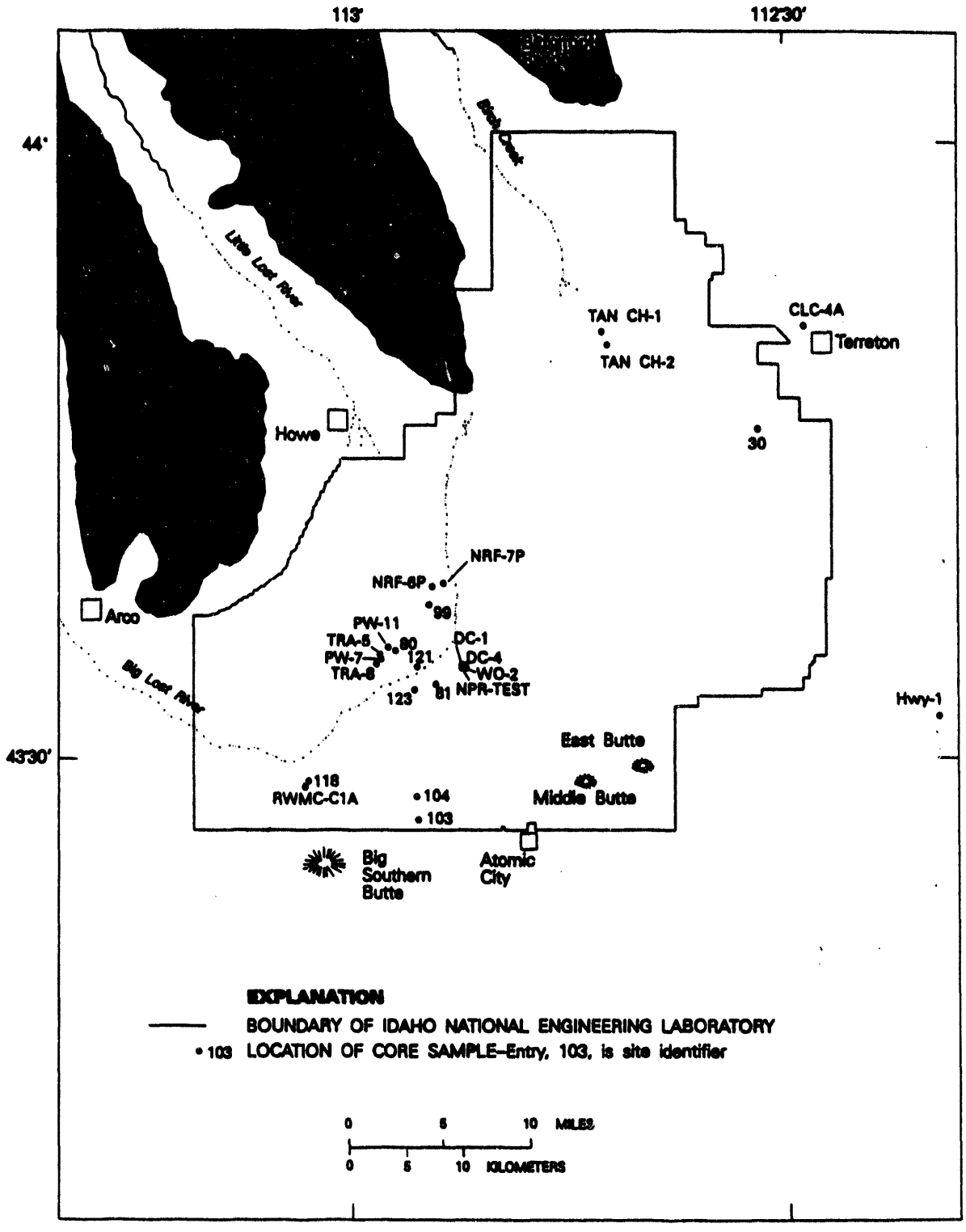


Figure 2.–Location of coreholes sampled at the Idaho National Engineering Laboratory.

and 15 milliamps. Diffractograms were prepared at a scale factor of 1, a multiplier of 0.5, and time constant of 2.

Semiquantitative analysis was used to determine the relative abundances of minerals in the samples. A modification of the method described by Diebold and others (1963) and Schultz (1964) was used to obtain the relative mineral percentages. The raw percentage of each mineral was determined by dividing the intensity of each mineral peak height by the intensity of its pure standard. The raw percentages were normalized to 100 percent. The intensities of the pure standards were calculated from standard minerals provided by the ISU Department of Geology. Schultz (1964, p.C1) reported uncertainties of $\pm$ 10 percent for minerals that make up at least 15 percent of the sample. Diebold and others (1963, table 5, p.130) calculated weight percent within $\pm$ 8 percent of the true concentrations using a 95 percent confidence interval.

For samples that had clay present in the bulk mineralogy analysis, a qualitative identification of individual clay minerals was undertaken. Clay separation followed guidelines described by Elless (1987). First the organic matter was removed by using a 30% H_2O_2 solution , then sodium hexa-metaphosphate was added to aid in dispersing clay particles. The < 45 micron fraction was then isolated by using a 325 mesh sieve. Isolation of the clay particles in the < 2 micron fraction was accomplished using the principle of Stoke's Law that predicts the finest silt-size particle settles below the top 5 cm of suspension after 3.5 hours. The suspended clay size particles were concentrated on a filter, then the filtrate was transferred to a glass slide and allowed to dry before being analyzed by X- ray diffraction.

The slides were scanned with a diffractometer using the aforementioned operating parameters with a scale factor of 1 to 0.5. The samples were glycolated and rescanned to differentiate between smectite and chlorite clays. Smectite expands from 14 to 17 Å when ethylene glycol replaces water in the crystal lattice. The expansion was achieved by exposing the clay slides to an ethylene glycol atmosphere for at least 24 hours.

The results reported by the ISU X-ray diffraction laboratory for the 43 samples analyzed for clay mineralogy (Table 2) yield qualitative estimates of the abundance of clay minerals in the samples. The estimates were based on the relative intensities of the clay mineral's 001 crystal face. Five categories were designated in order of decreasing abundance: dominant, major, minor, trace, and possibly present.

Bulk Mineralogy of Sediment Interbeds

A summary of the quantitative bulk mineralogy for the sedimentary interbeds is given in table 1. A summary of the qualitative study of the clay mineralogy is given in table 2. Statistical parameters for quantitative mineral analyses for the sedimentary interbeds (table 3) show that quartz, total feldspar, pyroxene, and total clay minerals are relatively abundant for the NPR-test, TRA, ICPP, NRF, and RWMC facilities whereas they are absence or in low abundances for the TAN facility. Interbeds from NPR-test are represented by 10 samples that have mean percentages of 34 for quartz, 30 for total feldspar, 3 for pyroxene, and 30 for total clay minerals. Interbeds from TRA are represented by 10 samples that have mean percentages of 31 for quartz, 18 for total feldspars, 10 for pyroxene, and 17 for total clay minerals. Interbeds from ICPP are represented by 13 samples that have mean percentages of 38 for quartz, 31 for total

Table 1. Semiquanitative mineralogy of bulk samples by x-ray diffraction for the sedimentary interbed intervals. Symbols: nd indicates not detected.

Sample Identifier	Interval sampled (feet below land surface)	Date collected	Bulk Analyses (in percent mineral abundance) Quartz	Plagioclas Feldspar	Potassium Feldspar	Calcite	Pyroxene	Olivine	Dolomite	Total Clays	Hematite
DC-1	238	2/24/93	44	26	5	15	nd	nd	nd	10	nd
DC-4	112.9-113.3	2/24/93	15	9	13	52	nd	nd	nd	11	nd
DC-4	241.7	2/24/93	33	23	5	15	nd	nd	nd	25	nd
Wo-2	560-564	2/24/93	62	19	19	nd	nd	nd	nd	nd	nd
Wo-2	600	2/24/93	21	15	15	6	nd	nd	nd	42	nd
Wo-2	719	2/24/93	39	13	18	3	nd	nd	1	26	nd
Wo-2	815	2/24/93	30	25	6	8	6	6	nd	20	nd
Wo-2	871	2/24/93	34	9	5	36	nd	nd	nd	16	nd
Wo-2	932.3	2/24/93	32	27	18	2	11	nd	1	8	nd
Wo-2	1001.5	2/24/93	31	20	13	1	6	nd	nd	28	nd
PW-7	219.3	6/9/93	45	17	nd	nd	nd	nd	nd	38	nd
PW-7	230	6/9/93	44	19	14	3	6	nd	nd	13	nd
PW-11	139.4	6/9/93	26	12	10	6	46	nd	nd	nd	nd
TRA-5	69	6/9/93	31	6	nd	13	6	nd	nd	43	nd
TRA-5	172-173	6/9/93	29	4	15	40	11	nd	nd	nd	nd
TRA-8	116.5	6/9/93	25	13	13	11	nd	nd	nd	38	nd
TRA-8	204.5	6/9/93	23	5	nd	33	13	nd	nd	26	nd
USGS 80	165	2/24/93	49	19	18	nd	7	nd	nd	6	nd
USGS 80	175	2/24/93	35	14	13	nd	9	nd	nd	28	nd
USGS 81	27	2/24/93	29	16	19	10	7	nd	1	17	nd
USGS 81	107	2/24/93	43	23	23	10	nd	nd	nd	nd	nd
ICPP 121	33-34.5	6/9/93	40	28	6	nd	18	nd	nd	8	nd
ICPP 121	401	6/9/93	39	23	8	nd	11	nd	nd	19	nd
ICPP 121	410.8	6/9/93	31	21	6	16	9	nd	2	15	nd
ICPP 123	10.0-12.0	6/9/93	56	15	nd	10	10	nd	nd	8	nd
ICPP 123	112.4	6/9/93	42	10	8	10	10	nd	nd	20	nd
ICPP 123	117	6/9/93	39	19	nd	15	8	nd	nd	19	nd
ICPP 123	420	5/14/93	40	27	9	nd	9	nd	nd	15	nd
ICPP 123	502	1/25/94	22	12	8	32	8	nd	nd	17	nd
ICPP 123	563.6	5/26/93	54	19	18	nd	9	nd	nd	nd	nd

Table 1 cont.

Sample Identifier	Interval sampled (feet below land surface)	Date collected	Bulk Analyses (in percent mineral abundance) Quartz	Plagioclas Feldspar	Potassium Feldspar	Calcite	Pyroxene	Olivine	Dolomite	Total Clays	Hematite
ICPP 123	690	5/14/93	20	46	18	nd	6	nd	nd	10	nd
ICPP 123	741.7	6/9/93	39	31	10	nd	nd	nd	nd	nd	20
RWMC C1A	229.7	11/30/93	42	28	17	nd	13	nd	nd	nd	nd
RWMC C1A	291.5	11/30/93	37	34	20	nd	9	nd	nd	nd	nd
RWMC C1A	332.5	11/30/93	40	16	11	9	7	nd	nd	18	nd
RWMC C1A	745.7	11/30/93	39	20	15	nd	12	nd	nd	14	nd
RWMC C1A	971	11/30/93	35	12	nd	24	nd	nd	nd	29	nd
RWMC C1A	1072.3	11/30/93	39	16	11	nd	11	nd	nd	23	nd
USGS 118	9.4	2/24/93	44	25	13	nd	4	nd	nd	14	nd
USGS 118	237.9	2/24/93	39	11	16	16	6	nd	nd	13	nd
NRF-6P	97.8	6/9/93	31	13	11	30	11	nd	3	nd	nd
NRF-6P	354	6/9/93	36	27	20	nd	16	nd	nd	nd	nd
NRF-7P	93	6/9/93	36	25	22	nd	8	nd	nd	9	nd
NRF-7P	156	6/9/93	15	9	nd	75	nd	nd	nd	nd	nd
USGS 99	25-30	2/24/93	43	19	18	6	4	nd	nd	10	nd
USGS 103	15	2/24/93	36	17	13	4	12	nd	nd	17	nd
USGS 104	142	2/24/93	64	28	nd	5	3	nd	nd	nd	nd
TAN CH-1	401	6/9/93	20	nd	nd	80	nd	nd	nd	nd	nd
TAN CH-1	411	6/9/93	11	4	4	82	nd	nd	nd	nd	nd
TAN CH-1	444.5	6/9/93	8	2	nd	81	nd	nd	nd	8	nd
TAN CH-1	446.5	6/9/93	9	8	nd	72	nd	nd	2	9	nd
TAN CH-2	245.5	6/9/93	22	3	3	58	nd	nd	nd	14	nd
TAN CH-2	449	6/9/93	44	9	nd	46	nd	nd	nd	nd	nd
TAN CH-2	471.5	6/9/93	2	nd	nd	98	nd	nd	nd	nd	nd
TAN CH-2	735	6/9/93	23	19	nd	27	13	nd	13	4	nd
TAN CH-2	977.7	6/9/93	47	13	11	10	nd	nd	nd	19	nd

Table 2. Mineralogy of the clay size particles. Symbols: dom indicates dominate, maj indicates major, min indicates minor, tr indicates trace, poss indicates possibly present, and nd indicates not indicated.

Sample	Interval sampled (feet below land surface)	Sample collected	mix layer	smectite	kaolinite	illite	Chlorite	Quartz	Feldspar	Calcite
DC-1	238	2/24/93	tr	maj	min	maj	poss	min	tr	nd
DC-4	112-113.3	2/24/93	nd	nd	tr	min	nd	min	poss	dom
DC-4	241.7	2/24/93	nd	dom	min	dom	nd	min	tr	nd
WO-2	600	2/24/93	nd	dom	min	maj	poss	min	nd	nd
WO-2	719	2/24/93	tr	dom	min	maj	tr	min	tr	nd
WO-2	815	2/24/93	tr	maj	min	maj	min	min	tr	nd
WO-2	871	2/24/93	tr	nd	tr	dom	nd	min	tr	tr
WO-2	932.3	2/24/93	nd	nd	nd	tr	nd	maj	dom	nd
WO-2	1001.5	2/24/93	min	poss	nd	dom	nd	min	poss	nd
PW-7	219.3	6/9/93	tr	dom	min	maj	poss	min	nd	tr
PW-7	230	6/9/93	tr	dom	min	maj	poss	min	poss	nd
TRA-5	69	6/9/93	tr	min	min	dom	min	maj	tr	nd
TRA-8	116.5	6/9/93	poss	dom	min	maj	nd	maj	tr	nd
TRA-8 @	204.5	6/9/93	tr	dom	min	maj	nd	min	nd	nd
USGS 80	165	2/24/93	tr	nd	nd	min	nd	maj	maj	nd
USGS 80	175	2/24/93	tr	dom	tr	maj	nd	min	nd	nd
USGS 81	27	2/24/93	tr	nd	nd	dom	nd	maj	tr	nd
ICPP 121	33-34.5	6/9/93	poss	maj	min	dom	tr	min	tr	nd
ICPP 121	401	6/9/93	nd	maj	tr	maj	poss	min	tr	nd
ICPP 121	410.8	6/9/93	nd	dom	min	min	nd	maj	tr	tr
ICPP 123	10.0-12.0	6/9/93	poss	dom	min	maj	tr	min	tr	nd
ICPP 123	112.4	6/9/93	tr	nd	nd	maj	nd	maj	maj	nd
ICPP 123	117	6/9/93	nd	nd	nd	maj	nd	dom	nd	nd
ICPP 123	420	5/14/93	min	min	nd	dom	min	maj	poss	nd
ICPP 123	502	5/14/93	tr	dom	min	min	tr	maj	poss	min
ICPP 123	690	5/14/93	poss	nd	nd	poss	nd	maj	dom	nd
RWMC-C1A	332.5	11/30/93	nd	dom	tr	tr	nd	tr	poss	nd
RWMC-C1A	745.7	11/30/93	poss	nd	nd	dom	nd	nd	nd	nd
RWMC-C1A	971	11/30/93	poss	dom	min	maj	poss	maj	tr	poss
RWMC-C1A	1072	11/30/93	poss	nd	nd	min	poss	maj	dom	nd
USGS 118	9.4	2/24/93	tr	min	min	maj	poss	maj	tr	nd
USGS 118	237.9	2/24/93	tr	dom	tr	min	nd	min	poss	nd
NRF-7P	93	6/9/93	tr	nd	nd	dom	nd	nd	nd	nd
USGS 99	25-30	2/24/93	min	min	tr	dom	nd	maj	tr	nd
USGS 103	15	2/24/93	tr	min	tr	maj	poss	maj	tr	nd
TAN CH-1	444.5	6/9/93	nd	dom	nd	nd	min	nd	nd	min
TAN CH-1	446.5	6/9/93	poss	maj	nd	tr	nd	tr	nd	dom
TAN CH-2	245.5	6/9/93	nd	dom	nd	nd	poss	min	min	nd
TAN CH-2	735	6/9/93	poss	dom	nd	tr	poss	min	tr	nd
TAN CH-2	977.7	6/9/93	tr	dom	min	maj	poss	min	tr	nd

Table 3. Summary of statistical parameters for bulk mineralogy of selected sedimentary interbeds at the National Engineering Laboratory, Idaho.

Mineral	Minimum	Maximum	Mean	Sample size
		NPR-test Facilities		
Quartz	21	62	34	10
Plagioclase	9	27	19	10
Potassium Feldspar	5	19	12	10
Total Feldspar	14	45	30	10
Calcite	0	52	14	10
Pyroxene	0	11	3	10
Dolomite	0	1	0	10
Olivine	0	6	0	10
Total Clay Minerals	8	42	19	10
		TRA Facilities		
Quartz	23	45	31	10
Plagioclase	4	19	11	10
Potassium Feldspar	0	18	9	10
Total Feldspar	5	37	18	10
Calcite	0	40	11	10
Pyroxene	0	46	10	10
Total Clay Minerals	6	43	17	10
		ICPP Facilities		
Quartz	20	56	38	13
Plagioclase	12	46	22	13
Potassium Feldspar	0	23	22	13
Total Feldspar	15	64	31	13
Calcite	0	32	8	13
Pyroxene	0	18	8	13
Dolomite	0	2	0	13
Hematite	0	20	1.5	13
Total Clay Minerals	0	20	11	13
		RWMC Facilities		
Quartz	35	44	39	8
Plagioclase	11	28	20	8
Potassium Feldspar	0	17	13	8
Total Feldspar	12	54	31	8
Calcite	0	24	6	8
Pyroxene	0	13	8	8
Total Clay Minerals	0	29	14	8
				size
		NRF Facilities		
Quartz	15	43	31	5
Plagioclase	9	27	19	5
Potassium Feldspar	11	22	14	5
Total Feldspar	9	47	33	5
Calcite	0	75	22	5
Pyroxene	0	16	8	5
Dolomite	0	3	0	5
Total Clay Minerals	0	10	4	5
		TAN Facilities		
Quartz	2	47	21	9
Plagioclase	0	19	6	9
Potassium Feldspar	0	4	2	9
Total Feldspar	0	24	8	9
Calcite	10	98	61.5	9
Pyroxene	0	13	1	9
Dolomite	0	13	2	9
Total Clay Minerals	0	19	6	9

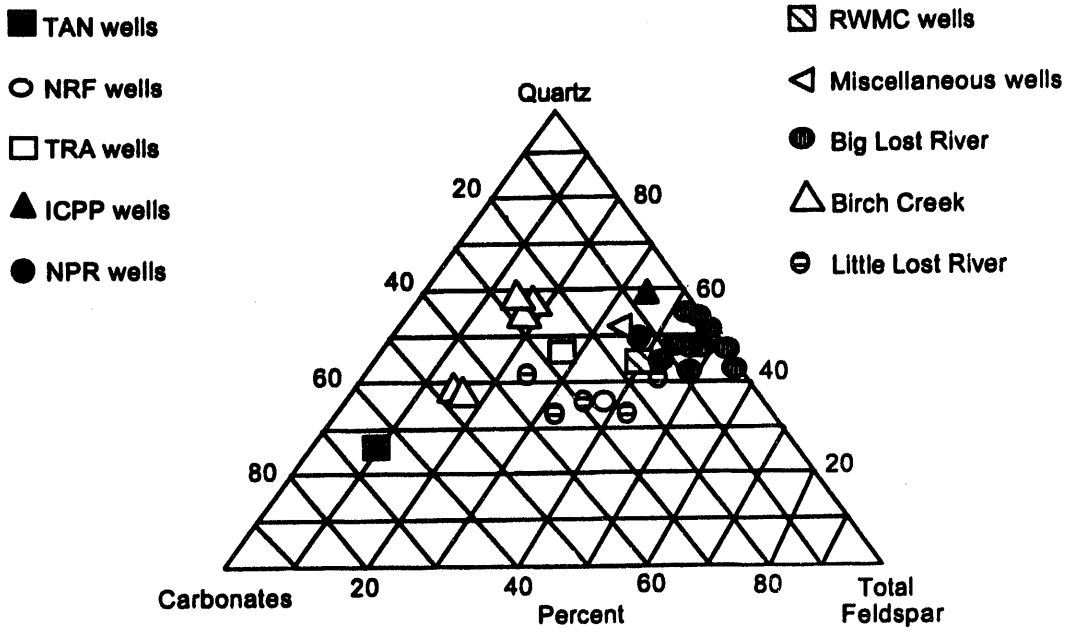


Figure 3. Normalized mean percentages for Surficial and Interbed Sediment

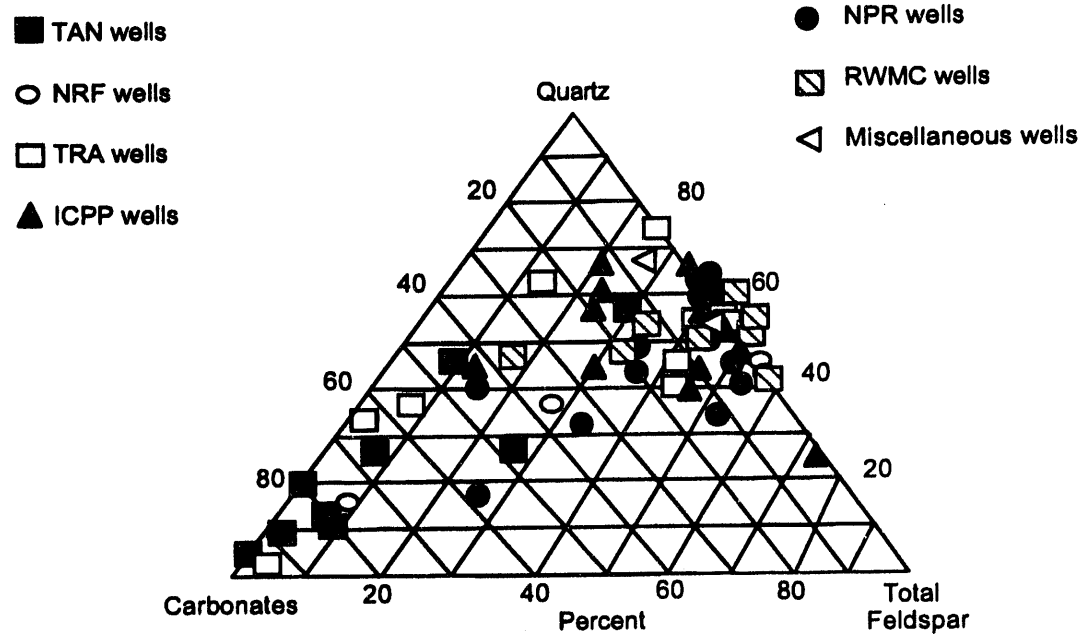


Figure 4. Normalized mean percentages for Individual Interbed Sediment Intervals

feldspar, 8 for pyroxene, and 11 for total clay minerals. Interbeds from RWMC are represented by 8 samples that have mean percentages of 39 for quartz, 31 for total feldspars, 8 for pyroxene, and 14 for total clay minerals. Interbeds from NRF are represented by 5 samples that have mean percentages of 32 for quartz, 33 for total feldspars, 8 for pyroxene, and 4 for total clay minerals. Interbeds from TAN are represented by 9 samples that have mean percentages of 21 for quartz, 8 for total feldspars, 1 for pyroxene, and 6 for total clay minerals.

Carbonates , calcite and dolomite, are not abundant in samples from interbeds at NPR-test, TRA, ICPP, NRF, and RWMC whereas are the dominate mineral phase at the TAN facility. Mean percentages for carbonates are 14, 11, 8, 6, 22, and 63.5 respectively.

CONCLUSION

Following Bartholomay (1990), semiquantitative diffraction analysis can be used to correlate the sedimentary interbeds to with the surficial sediment. The low abundance of calcite, and dolomite in the sedimentary interbeds from NPR, ICPP, TRA, RWMC, NRF, and miscellaneous well sites (Fig.2) along with the relatively high amount of feldspar and pyroxene, indicate that the sedimentary interbeds are from a source area similar to that the present day Big Lost River drainage. The large amount of calcite and dolomite combined with the relativity low amount of feldspar the absences of pyroxene in the TAN sedimentary interbeds indicate that these are similar to the surfical sediments from the Birch Creek drainage. A summary of the normalized mean percentages and normalized percentages of all the interbed from this study are shown in Figure 3a-b. This suggests that the historical drainage basin of the area contained within the INEL is similar to the present. Two anomalous intervals, TAN CH-2 at 735 and 977.7 ft, has a mineralogical signature similar to the surifical sediments from the Big Lost River. This may indicate a time interval when Birch Creek was diverted from the present day flow path, but more work on the basalt stratigraphy needs to be done to determine the validity of the argument. Age dates have been performed on basalts beneath the INEL which indicates that sedimentary interbeds are at least 580,000 years old. This along with the mineralogical data sets suggests that the historical drainage basin of the area is similar to the present day deposition basin, with the major sedimentary source being the Big Lost River.

ACKNOWLEDGMENTS

The author gratefully acknowledges the ISU Department of Geology -- Dr. David Rodgers Chairperson-- for providing X-ray diffraction equipment and laboratory. Special thanks are due to U.S. Geological Survey, Roy Bartholomay, Judith J. Kreig, Jeanne Fromm, and Dr. Scott Hughes for demonstrating the proper use of the x-ray equipment, and providing discussions on this project.

References

Barraclough, J. T., Lewis, B.D., and Jensen, R.G., 1981, Hydrologic conditions at the Idaho National Engineering Laboratory, Idaho: Emphasis: 1974-1978: U.S. Geological Survey Water-Resources Investigations Open-File Report 81-526 (IDO-22060), p.77.

Bartholomay, R.C., and Knobel, L.L., 1989, Mineralogy and grain size of the surficial sediment from the Little Lost River and Birch Creek drainages, Idaho National Engineering Laboratory, Idaho: : U.S. Geological Survey Open-File Report 89-385 (DOE/ID-22082), p.19.

Bartholomay, R.C., Knobel, L.L., and Davis, L.C., 1989, Mineralogy and grain size of the surficial sediment from the Big Lost River drainage and vicinity, with chemical and physical characteristics of geologic materials from selected sites at the Idaho National Engineering Laboratory, Idaho: : U.S. Geological Survey Open-File Report 89-384 (DOE/ID-22081), p.74.

Bartholomay, R.C., 1990, Mineralogical Correlation of Surficial Sediment from Area Drainages with Selected Sedimentary Interbeds at the Idaho National Engineering Laboratory, Idaho: U.S. Geological Survey Open-File Report 90-4147 (DOE/ID-22092), p.17.

Diebold, F.E., Lemish, J., and Hiltrop, C.L., 1963, Determination of calcite, dolomite, quartz, and clay content of carbonate rocks: Journal of Sedimentary Petrology, v. 33, p.124-139.

Doherty, D.J., McBroome, L.A., and Kuntz, M.A., 1979, Preliminary geological interpretation and lithologic log of the Exploratory Geothermal Test Well (INEL-1), Idaho National Engineering Laboratory, eastern Snake River Plain, Idaho: U.S. Geological Survey Open-File Report 79-1248, p.8.

Elless, M., 1987, Standard operating procedures for the examination of clay- sized minerals by X-ray diffraction, MS thesis, North Dakota State University.

Rightmire, C.T., 1984, Description and hydrogeologic implications of cored sedimentary material Geological Survey Water-Resources Investigations Report 87-4071 (DOE/ID-22067), p.33.

Rightmire, C.T., and Lewis, B.D.,1987, Hydrogeology and geochemistry of the unsaturated zone, Radioactive Waste Management Complex, Idaho National Engineering Laboratory, Idaho: U.S. Geological Survey Water-Resources Investigations Report 87-4198 (DOE/ID-22073), p.89.

Robertson, J.B., Schoen, R., and Barraclough, J.T., 1974, The influence of liquid waste disposal on the geochemistry of the water at the Nation Reactor Testing Station, Idaho: 1952-1970: U.S. Geological Survey Open-File Report 73-238 (IDO-22053), p.231.

Schultz, L.G. 1964, Quantitative interpretative of mineralogical composition from X-ray and chemical data for the Pierre Shale: U.S. Geological Survey Professional Paper 391-C, p.33.

Whitehead, R.L., 1986, Geohydrologic framework of the Snake River Plain, Idaho and eastern Oregon: U.S. Geological Survey Hydrologic Investigations Atlas HA-681, 3 sheets.

Hydrogeology, Waste Disposal, Science and Politics
Proceedings 30th Symposium
Engineering Geology and Geotechnical Engineering, 1994

CONCENTRATIONS AND COMPOSITIONS OF COLLOIDAL PARTICLES IN GROUNDWATER NEAR THE ICPP, IDAHO NATIONAL ENGINEERING LABORATORY, IDAHO

Mason Estes and Mike McCurry
Department of Geology
Idaho State University
Pocatello, ID 83209

SESSION: HYDROGEOLOGY, IDAHO NATIONAL ENGINEERING LABORATORY

Abstract

The presence of colloidal material is being investigated in groundwater near the ICPP to determine whether the concentrations and chemical compositions are suitable to have an impact on the transport of Sr-90. Colloids are proposed as a viable transport mechanism, and may have an influence on the chemical trends observed in three wells near the ICPP. Ultrafiltration of groundwater sarples has been performed on different intervals in USGS wells 45, 46, and Site 14, has provided filtrate samples for analyses by ICP-MS, and filters for analyses by SEM/EDS. Preliminary results indicate that concentrations of colloids are from 2.1-1.8 ppm for the >0.45 μm size fraction, and 2.3-9.8 ppm for the <0.45 μm size fractions. Compositions consist of calcite, silicic acid, ferrihydrite,clay, and possibly dolomite. Calcium was shown to have the largest contribution from both EDS and ICP-MS. Magnesium and silicon were also found to filter out in large concentrations. Iron and aluminum are minor constituents of the colloidal mass and contain concentrations of <10ppb and <1ppb, respectively.

These results indicate that if colloids are going to have a major impact on contaminant migration then the coprecipitation of Sr-90 with calcite and dolomite would have to be a sorption mechanism. Sorption onto Fe and Al colloids probably does not have a major impact because of the low concentrations. Clay colloids were noted to be relatively abundant and may also have an impact on Sr-90 migration, due to the exchange of Sr with other cations in the clay structure.

Introduction

An on going study, referred to as the Straddle Packer Project, has been administered by the State Oversight Program for the past two years and intends to quantify the

three dimensional hydrostratigraphy of the aquifer near the ICPP. The Project utilizes a straddle packer to seal predetermined intervals and extract water samples. Details on the methodology of sample collection can be found in Olsen (1994). Ultimately, sampling of monitoring wells surrounding the ICPP will provide an evaluation of how concentrations of analytes, especially I-129, Sr-90, and H-3, vary in concentration with depth. Results of the project for the wells USGS-44, 45, and 46 show a distinct chemical heterogeneity in these analytes and a decoupling of Sr-90 chemical trends with I-129 and H-3 (McCurry et.al.,1993, 1994).

We propose that the observed decoupling of Sr-90 with H-3 and I-129 is a result of differences in behavior between the different species. Strontium-90 is known to adsorb onto mineral phases such as ferrihydrite, diffuse into clays via cation exchange, and to coprecipitate with calcium carbonate (Dragun, 1989; Dozombac, 1991; McCarthy, 1993). Tritium and I-129 are conservative in nature and do not adsorb significantly. The concentration trends in the upper 42 m of the aquifer between Sr-90 and H-3/I-129 indicate that a source of contamination still exists at the ICPP.

Modeling of contaminant transport requires a thorough understanding of the mechanisms of transport. It is often assumed that contaminants are transported in the dissolved state. However, this may not always be true due to the presence of colloids smaller than the EPA cut off of 0.45 μm for dissolved versus particulate phases. Several investigators, (Degueldre et. al, 1989; Payne, 1992), have shown the potential for colloid migration. Reimus (1993) describes colloids as the dominant transport mechanism in the migration of Pu isotopes at the Los Alamos National Laboratory. The potential for colloidal transport of Sr-90 is being investigated as part of the Straddle Packer Project for two principle reasons: 1) colloids could be accelerating the transport of Sr-90 from perched zones near the ICPP injection well resulting in new inputs into the aquifer; and 2) colloids could be accelerating the migration of Sr-90 in the upper portion of the aquifer without retardation, in effect simulating the migration of conservative radionuclides such as H-3 and I-129. This paper presents the results of the first study performed at the INEL regarding colloidal particle concentration and composition. This paper covers preliminary results of experiments designed to determine colloids in the aquifer beneath the ICPP, as well as a description of the role that they may have in the transport of contaminants.

In order to substantiate this hypothesis, the concentrations and compositions of the colloids must be known. Certain compositions of colloids will have a greater impact on contaminant migration than others. For example, amorphous Fe oxyhydroxides colloids will have the greatest

adsorption capability due to the extremely large surface area to mass ratio (Dozombac, 1991).

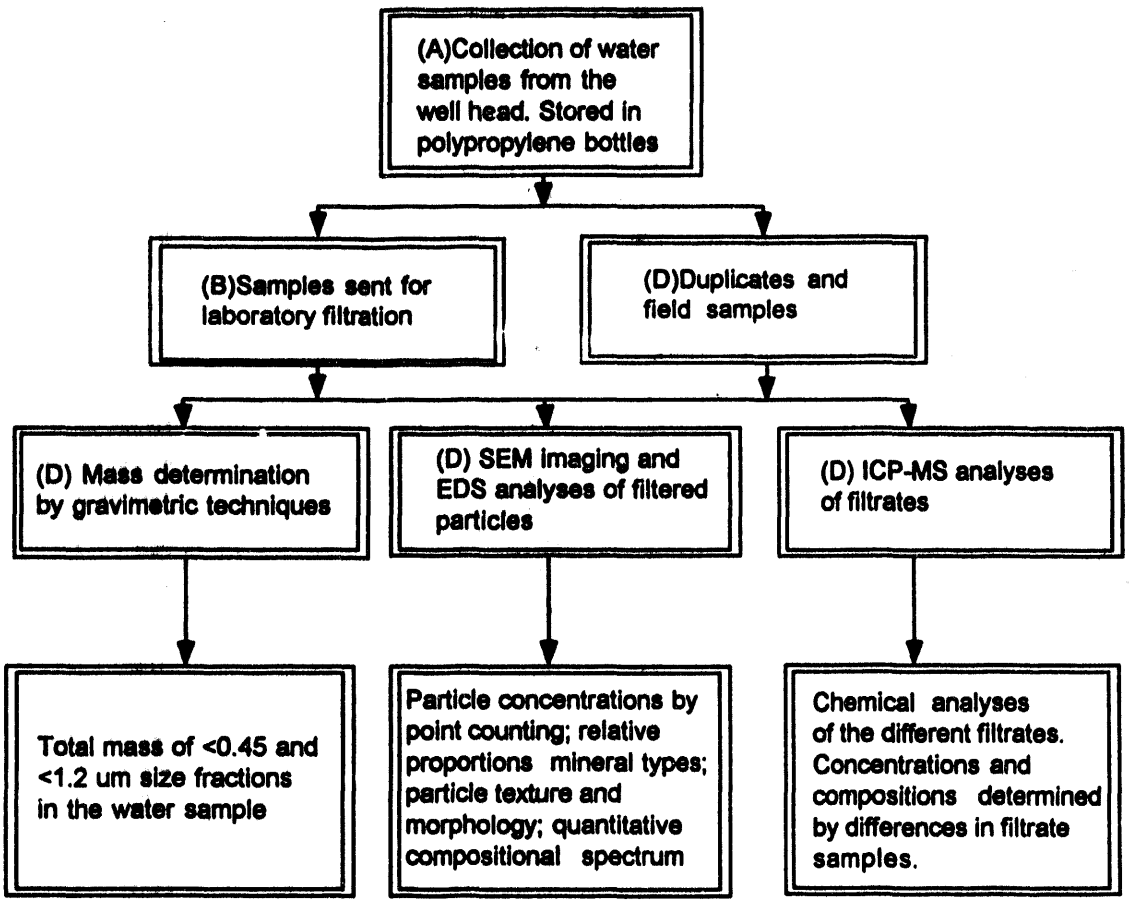
Methodology

Concentrations and compositions of colloids can be determined by two different methods. Several authors (McCarthy, 1993; Payne, 1992) have used Inductively Coupled Plasma-Mass Spectrometry (ICP-MS) analysis as the primary method of inferring colloid concentrations. These investigators utilized hollow core fiber filters which work by the tangential flow of water across the filter. This type of filtration has the benefit of allowing for efficient field filtration, but is not useful for Scanning Electron Microscopy/ Energy Dispersive X-ray Spectroscopy (SEM/EDS)work. Other investigators (Degueldre et. al, 1989) have used flat filters similar to the ones used in this study. The benefit of this approach is that it allows for the textural analysis of colloids. The concentrations and compositions of colloids using this technique involves point counting of particles and EDS to determine the elemental compositions.

This study represents an integrated approach to the study of colloids. Both analytical methods were used and will provide for a comparison of results. Figure 1.0 illustrates a flow chart of experimental procedures. Groundwater samples were taken from the well head and collected in one liter polyethylene bottles (A). Samples were taken to the ISU geochemistry laboratory for filtration (B). Two duplicate samples and one field filtration sample were collected for comparison of results in the laboratory and in the field (C). The samples were filtered with two coarse filters >0.45 μm, and were weighed before and after filtration to determine the mass of particulates extracted (D). Smaller filters consisted of 0.2, 0.1, and 0.02 μm pore sizes, and were filtered with a specially designed device. The filters produced were stored and analyzed with SEM to determine the particle concentration by point counting (D). SEM analyses allows for determination of the texture and morphology as well as the distribution of the different type of colloids. EDS analyses was performed to determine the elemental spectrum, which was used to deduce the composition of the material. Filtrate samples analyzed by ICP-MS (D)were collected, acidified, for each filtration to determine the composition of each filtrate. Each filtration produced four filtrate samples.

Samples of water were taken from the target wells at predetermined intervals. Two to three target intervals were sampled per well for filtration. Two intervals at 145.4-150 m and 157.2-161.8 m in well 45 were sampled, and three intervals at 185.4-190.6 m, 180-185.45 m, and 160.9-166.36 m were sampled in INEL-46. Samples from the deeper portions of INEL-45 were not taken because of difficulty in access. Two

Figure 1.0: Flow chart of experimental procedures



additional samples were taken at the Site-14 well at 113.36 m and 212.12 m by thief sampler. Approximately one to two liters of water were taken for each sample.

The smaller sized filters were Anotec, Al oxide filters with a surface area of 3.14 cm^2, and the 1.2 and 0.45 µm filters were constructed of cellulose nitrate. Water was initially filtered through the 1.2 µm and 0.45 µm filter using a standard Nalgene hand vacuum filtration unit. After passage through the coarser filters, the water was placed in the filtration unit and sequentially filtered with the 0.2 µm filter, followed by the 0.1 µm, and finally the 0.02µm filter.

The ultrafiltration unit devised consisted of a one liter, glass, modified separatory funnel. The filters are placed in a housing attached to the bottom of the funnel with polyethylene tubing. Argon gas was used to pressurize the chamber from 5 to 9 psi gauge pressure. The gas had an online constant pressure regulator located close to the funnel and was used to assure that during filtration a constant pressure was provided during filtration. The device was scrubbed thoroughly before each filtration and a hydrogen peroxide wash was used to kill any bacteria. A final rinse of deionized water was used to assure no residual contamination existed. The device was rinsed after filtration of each size fraction.

The concentrations of colloids can be estimated from the ICP-MS data by assuming an average diameter of colloids in each size range (r), and a specific density (ρ). Equation 1.0 shows the conversion from mass difference determined from the ICP-MS data to the number of particles/L:

(1.0) Mass Difference (in µg/l)÷(4/3πr3)ρ (in µg/particle) = Concentration in part/L

The denominator in this equation is the mass of each individual colloid and the numerator is the mass of colloids extracted. For this study colloids in the 0.45-0.2 µm range were assumed to have a average diameter of 0.3 µm, in the 0.2-0.1 µm a diameter of 0.15 µm was used, and lastly for the 0.1 -0.02 µm a average diameter of 0.07 µm was assumed. A density of 2 grams/cm3 was assumed based on recommendations of McCarthy (1993). Concentrations of colloids can also be determined with SEM analyses. By assuming an average diameter for colloids it is possible to determine the number of particles that it would take to cover the observed coverage on the filters. A series of estimation charts were developed for the estimation of percent coverage.

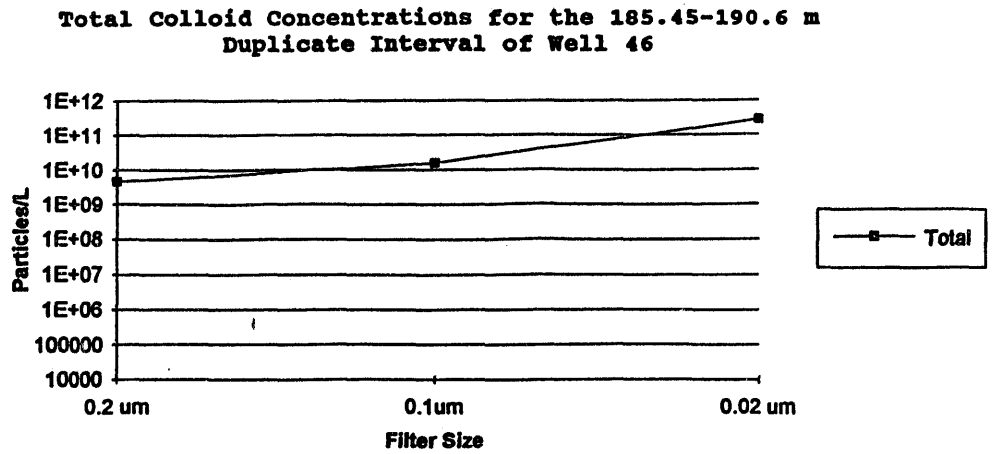
Results

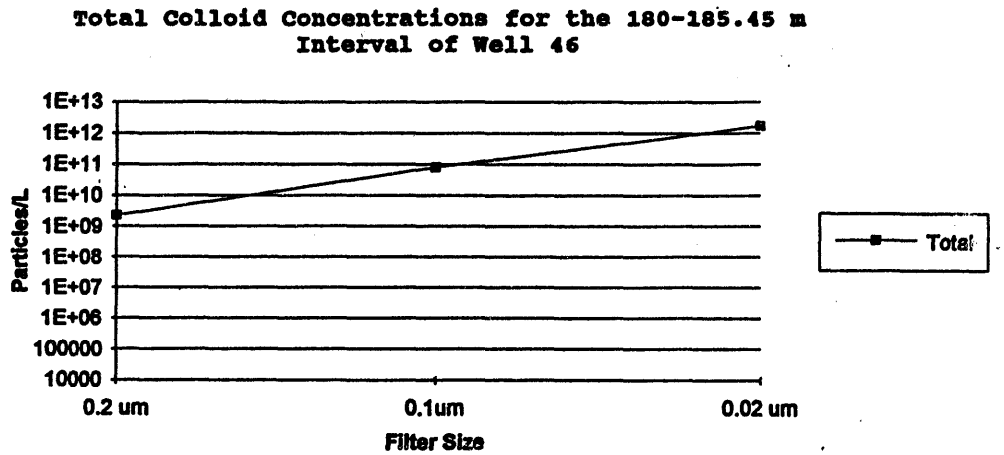
Preliminary results are given in Table 1.0 for three samples in INEL-46. Two analysis are given for the 185.4-190 m interval since a duplicate was run on this sample. Results for the 180-185.4 interval are also given. The tables provide the results of the major elements thought to form colloids. These elements consist of Mg, Si, and Ca, although Fe and Al have been shown to be important constituents of colloids. Unfortunately, the results for the latter two elements were found to be unsatisfactory using ICP-MS. The filters are constructed of Al and leaching of this element from the filter caused variable concentrations of Al in the water. ICP-MS analysis of other water samples showed that the Al concentration was consistently less than one ppb, hence the contribution of Al to the mass of colloids is probably very small. The detection limits for Fe were 10 ppb. Analysis of the colloid and groundwater samples showed that Fe was always less than this amount. Iron is still a likely constituent of colloids based on SEM/EDS analysis.

Results of the 180-185.45 ft interval show that the concentrations of colloids determined by ICP-MS, are on the order of 2.3E+09, 7.8E+10, and 1.72E+12 particles/L for the 0.2, 0.1, and 0.2 μm filters, respectively. This corresponds to a concentration of 1.0, 2.7, and 6.1 ppm for the same filter sizes. The amount of material between 1.2 and 0.45 μm was about 1.2 ppm, and that <1.2 was about 1.5 ppm. Note that Ca is the largest constituent. Results of the two 185.45-190.6 analyses show concentrations of 2.63E+09 to 4.55E+09, 1.6E+10 to 2.4E+10, and 2.7E+11 to 2.48E+11 particles/L for the 0.2, 0.1, and 0.02 μm filters, respectively. This corresponds to 940 to 1630, 450 to 670, and 710 to 790 ppb for the filter sizes. The amount of material between 1.2 and 0.45 μm was about 1.6 ppm and for the fraction <1.2 μm, 2.1 ppm was measured. Calcium was also the dominant element detected in these samples. Figure 2.0 illustrate graphically the concentrations in particles/L. Note the linear pattern on the log graph, which show that the smaller colloids consistantly have the highest concentrations.

Results of analyses using SEM are partially represented in Figure 3.0. The top photo in figure 3.0 is a SEM photo of the 0.2 μm filter surface for the intervals 140-146.3 m in USGS-46, and provides an example of three different types of colloids. Minor Fe and Ca colloids are noted by the rounded morphology, whereas the bottom jagged colloid is a clay particle. Note the pattern of the filter surface. Based on point counting, this interval contained concentrations of colloids estimated at about 750, 600, and 800 ppb for the 0.02, 0.1, and 0.2 μm filter, respectively (Table 4.0). The <1.2 μm size fraction was 2.0 ppm and the 0.45-1.2 μm

Table 1.0: Results of Duplicate Water Filtration for Well 46 at the 185.45-190.6 m interval					
46/185.45-190.6/1000/0.45-0.2D	15,200	12,970	35,520		
46/185.45-190.6/700/0.2-0.1D	14,770	12,780	34,510		
46/185.45-190.6/550/0.1-0.02D	14,670	12,700	34,240		
46/185.45-190.6/400/<0.02D	14,520	12,350	33,950		
0.2 um D	430	190	1010	1630	
0.1 um D	100	80	270	450	
0.02 um D	150	350	290	790	
0.2 um D	4.55E+09				
0.1 um D	1.61E+10				
0.02 um D	2.76E+11				
Table 1.0: Results of Water Filtration for Well 46 at the 185.45-190.6 m interval					
46/185.45-190.6/1000/0.45-0.2	15,090	12,650	33,670		
46/185.45-190.6/700/0.2-0.1	14,670	12,440	33,360		
46/185.45-190.6/550/0.1-0.02	14,720	12,170	33,110		
46/185.45-190.6/400/<0.02	14,530	12,100	32,660		
0.2 um	220	210	510	940	
0.1 um	150	270	250	670	
0.02 um	190	70	450	710	
0.2 um	2.63E+09				
0.1 um	2.39E+10				
0.02 um	2.48E+11				
Table 1.0: Results of Water Filtration for Well 46 at the 180-185.45 m interval					
46/180-185.45/750/0.45-0.2	15770	10990	56640		
46/180-185.45/450/0.2-0.1	15600	10850	55950		
46/180-185.45/300/0.1-0.2	15050	10660	53940		
46/180-185.45/200/<0.02	13870	9970	49710		
0.2 um	170	140	690	1000	
0.1 um	550	190	2010	2750	
0.2 um	1180	690	4230	6100	
0.2 um	2.32E+09				
0.1 um	7.86E+10				
0.2 um	1.72E+12				





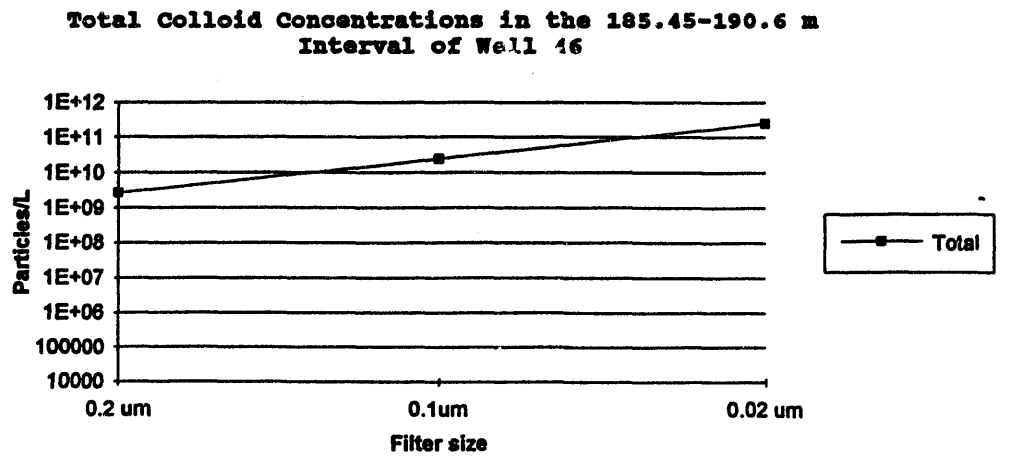


Figure 2.0: Total Concentration of Colloids in Intervals of Well 46 near the ICPP.

fraction was 1.8 ppm. The bottom photo in figure 3.0 illustrates colloids on the 0.1 μm filter for the 147.8-153.3 interval in USGS 46. Concentrations were estimated at 600, 750, 800 ppb for the 0.02, 0.1, and 0.2 μm filter,respectively. The <1.2 μm size fraction was 2.1 ppm and the 0.45-1.2 μm fraction was 1.9 ppm. The concentrations of colloids covered isolated areas of the filter, but in a few instances colloids were observed to bunch up.

Table 2.0: Results of SEM point counting of two filters

Filter Size	46/140-146.3	46/147.8-153.3
0.2 μm	750	600
0.1 μm	600	750
0.02 μm	800	800

The EDS analysis performed on random colloids on the filter surfaces showed that much of the colloidal material(~60%)was composed of Ca. When present the Ca colloids were characterized by a rounded morphology. Iron colloids were also observed and the Fe peak showed very strongly when a Fe colloid was found. These colloids also had a rounded morphology. The concentrations of Fe colloids(~5%)were much smaller than the Ca colloids. Certain colloids with a more jagged morphology showed strong peaks of Mg, Fe, Ca, Si, and Al indicating that they are possibly clays. The peak pattern for Si and Al was difficult to determine because the Al peak showed every time as a result of the Al construction of the filter. The Si peak is next to the Al peak and was often overlapped by the Al peak. However, on many of the colloids the Si peak did show up distinctly. A few of the colloids were observed to be Ti, although the concentration was less than one percent that of Ca. The Ti peak was very distinct when this type of colloid was observed.

Particulate material <0.45 μm was observed under the SEM/EDS unit. Much of the material had a rounded morphology and was composed of Fe, Ca and clay minerals. The EDS peak for Fe was very strong for many of the 0.45 μm filters indicating that a higher percentage of Fe is in the larger particulate sizes than the smaller. Distinct peaks for Al, Si, Fe, Mg, and Ca were also observed when clay minerals were encountered.

Discussion

The EPA 0.45 μm distinction between dissolved versus particulates phases is an arbitary cut off limit. This

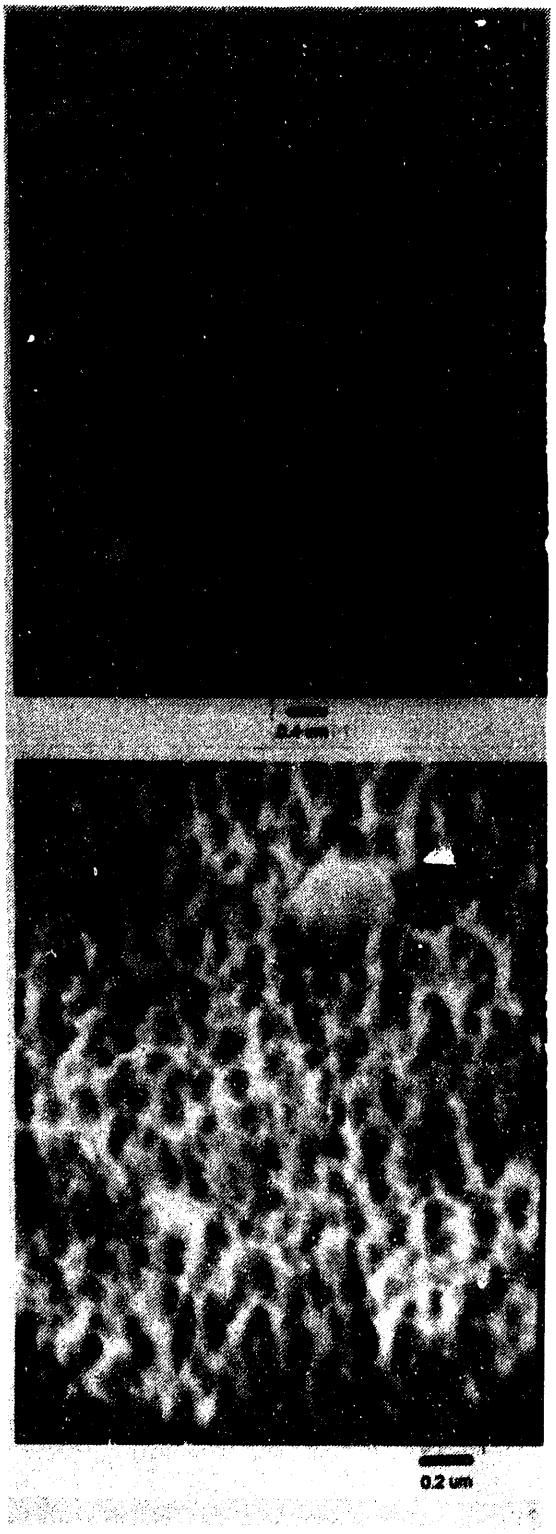


Figure 3.0: SEM photos of the 0.2 μm filter for the 139.69 - 146.3 m interval (top) and the 180-185.45 m interval (bottom). See the text for descriptions

study has shown that particulates do occur in 0.45 μm filtered water which are not dissolved. These colloids have been observed in the groundwater and consist of primarily calcite and clays. The amorphous mineral ferrihydrite has also been observed in colloidal form, but in small concentrations. Most of the ferrihydrite appears to be in the larger size fractions >0.45 μm. This has been observed in several of the samples that have been viewed under SEM/EDS. Calcite is observed as a dominant component in almost all size fractions. The presence of calcite and ferrihydrite is consistent with the equilibration, speciation modeling by the computer code MINTEQA2/PRODEFA2 (1991), which shows these minerals to be oversaturated in the waters near the ICPP. It is also consistent with XRD analysis by Fromm (per. comm.) and Reed (per. comm.) that calcite is often as much as 40 percent of the material that fills cracks and fissures in the basalts. Iron minerals have also been observed in this material.

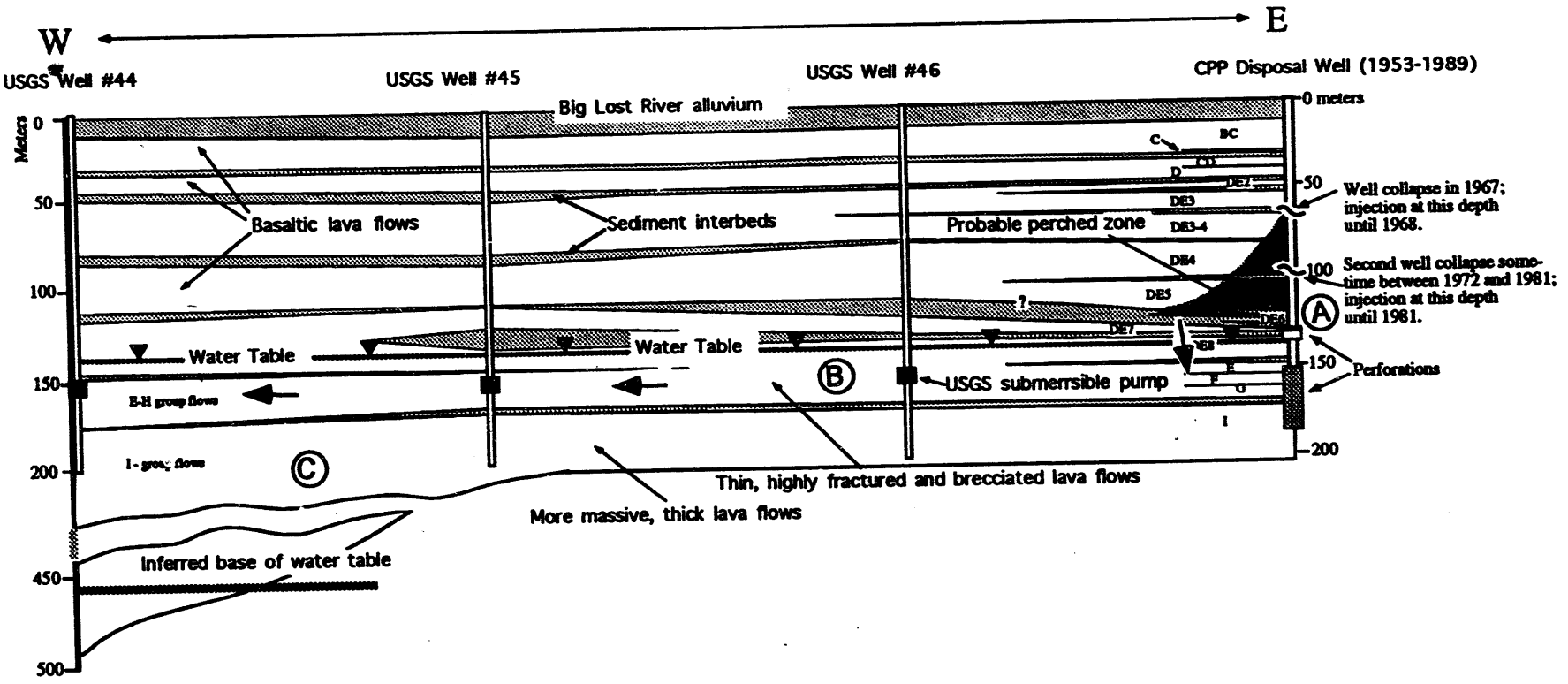
The clays that are observed have a jagged morphology and probably are detrital in origin. The source for clay particulates is likely the sedimentary interbeds as well as the Big Lost River alluvium, which covers the surface of the ICPP. Silicic acid colloids are likely responsible for part of the observed decrease in Si with filtration. Clays may be partially responsible for the drop in Mg, Si, and Ca. Although Ca-Mg smectites have not been verified specifically, smectites clays have been detected, and waters appear to be thermodynamically in equilibrium with the clay phases Mg and Ca nontronite. Dolomite colloids are also possible, and may be partially responsible for the Mg and Ca decrease. Results of the MINTEQA2 equilibration modeling also indicate that amorphous Si and dolomite are oversaturated.

Colloids do exist, but after preliminary determination of the compositions it is unlikely that ferrihydrite colloids will play a major role in the transport of Sr-90 in the saturated zone because of low concentrations. Aluminum oxyhydroxide colloids are equally as unlikely to have a major impact on contaminant migration. Ferrihydrite is in higher concentrations in the fracture filling, and is likely the primary phase for retardation of Sr-90 along the flow path (Arnett, 1993). The role that calcite colloids will play in the migration of Sr-90 is unknown. The adsorption capabilities of calcite are not as great as ferrihydrite, but it is much more abundant. It may have a significant effect as a result of coprecipitation. Strontium is capable of substituting for Ca in calcite will easily fit into the Ca site, due to the similarity in ionic radii. The presence of clays may also impact Sr-90 migration. The role that clay colloids will play is unknown, but it is possible that Sr-90 will diffuse into the clays via cation-exchange and become retarded in the basalt fractures.

The concentrations of colloids determined in this study are likely much higher than the true ambient condition. Other investigations on colloids have been conducted at the Yucca Mountain Site in Nevada and the Grimsel Site in Switzerland (Degueldre et al., 1989; Degueldre C. and Smith,1993). Geologically these sites are similar in the respect that the groundwater migrates via fractures and the water chemistries are similar. Concentrations of colloids in these areas have been determined at 500 ppb and 600 ppb, for the <0.45 μm size fractions. One of the primary problems in conducting a filtration experiment is the agitation caused by the pump. The stress imposed on the formation likely frees particulates that would normally be attached to the fracture walls. This was especially evident when sampling INEL-45. The water from this well had to be purged for more than the standard three borehole volumes because of the high concentration of large particulates, which gave the water a brownish tint. Better methods of water collection would involve slow pumping at rates of ml/min to avoid agitation (McCarthy, 1993).

We propose that the reason for the chemical trend in the upper portion of the aquifer is a result of new inputs to the system. The highest concentrations of radionuclides are found in USGS-46 which is the closest to the injection well. The trends in USGS-45 and 44 are equally close to the injection well and both have lower concentrations of radionuclides (McCurry et. al., 1994). Strontium-90 should not have the same chemical trend as H-3 of I-129, unless their was continued input into the system. Colloids could be aiding the transport of Sr-90 from the disposal well perched zone and residual injected wastes. The decoupling within the deeper, tighter zones of the wells may be a result of the adsorption onto the ferrihydrite and clays within fractures and vesicle walls.

Figure 7.0 represents an idealized cross section beneath the ICPP showing the spatial separation of Wells 45, 46, 44, and the CPP injection well. The arrows indicate potential pathways for Sr-90 migration. In this model it is assumed that the perched waters beneath the percolation ponds do not have an influence on the concentrations of Sr-90 in the target wells. This assumption is based on the location of the perched zones, which are 600 m down gradient of the wells. The most likely source for the concentrations of Sr-90, I-129, and H-3 observed in the upper intervals of the sampled wells is the inferred perched zone surrounding the ICPP injection well. This well has been documented to have collapsed several times during its operational history within the vadose zone, and subsequent effluents formed a perched zone 100 ft above the regional aquifer. Modeling performed by Robertson (1977) and Arnett (1993) both predict that Sr-90 will not migrate to the regional aquifer because of adsorption in the interbeds. However, new inputs to the aquifer appear to continue. It is likely that colloids are



* Based upon down-hole electric and TV logs and driller logs; ICPP interpretation and basalt flow unit designations based upon Anderson, 1991; injection well history work in progress by Fromm.

Figure 4.0: Idealized cross section of the subsurface beneath the ICPP showing the possible migration pathways of Sr-90. (A) Migration from the ICPP -03 perched zone. (B)Enhanced migration of Sr-90 in the upper portions of the aquifer by colloids. (C) Restricted migration in the less permeable zones causes increase H-3 and I-129. Sr-90 migration by colloids less important than in the upper zones. Sr-90 adsorbs onto the basalt matrix and secondary minerals and is taken out of the groundwater.

adsorbing Sr-90 and migrating through fracture systems without retardation and forming the new inputs to the system. Contaminants migrate downward from the perched zones and enter the regional aquifer.

List of References

Arnette R.C. and M.J. Rohe,1993, Predicted Consequences on the Snake River Plain Aquifer of Alternative Actions 1 and 2, EGG-XXX-Draft, EG&G Idaho Inc.

Degueldre C. and P.A. Smith,1993, Colloid-facilitated transport of radionuclides through fractured media, J.of Contaminant Hydrology,

Degueldre C., B.Baeyens and W. Goerlich,1989, Colloids in water from a subsurface fracture in granitic rock, Grimsel Test Site, Switzerland, Geochimica et Cosomochimica Acta, V.53, pp. 603-610.

Dragun J.,1988, The soil chemistry of hazardous materials, pub. by the Hazadous Materials Control Research Institute.

Dozombac J., 1991, Surface Complexation Modeling on Iron Oxyhydroxides, Oxford Press

McCarthy J.F. and C. Degueldre, 1993, Sampling and characterization of colloids and particles in groundwater for studying their role in contaminant transport, in Environmental Particles, Vol.2, pp. 2-31.

McCurry M., J. Welhan, J.Fromm, M.Estes,1993, Three dimensional chemical structure of the INEL aquifer near the Idaho Chemical Processing Plant(ICPP), Abstracts of AGU 1993 Meeting.

McCurry M., J. Welhan, J.Fromm, M.Estes,1994, Three dimensional chemical structure of the INEL aquifer near the Idaho Chemical Processing Plant(ICPP), this volume.

MINTEQA2/PRODEFA2 A geochemical assessment model for environmental systems: version 3.0 user's manual, EPA 600-3-91-021. 1991, A

Olsen J.,1994, Straddle packer system design and operation, this volume.

Payne T.E., R. Edis, T. Seo,1992, Radionuclide transport by groundwater colloids at the Koongarra uranium deposit, Mat. Res. Soc. Symp. Proc., V. 257pp. 481-488.

Ramsay J.D.,1988, The role of colloids in the release of radionuclides from nuclear waste, Radiochimica Acta. V. 44, pp. 167-170.

Reimus, P.W., 1993, Transport of synthetic colloids through single saturated fractures: A literature review: LANL Report 11-22, pp 1-74.

Robertson J.B.,1977, Numerical Modeling of subsurface radioactive solute transport from waste-seepage ponds at the Idaho National Engineering Laboratory, USGS open file report 76-717.

Hydrogeology, Waste Disposal, Science and Politics
Proceedings 30th Symposium
Engineering Geology and Geotechnical Engineering, 1994

HYDROSTRATIGRAPHIC INTERPRETATION OF THE UPPER PORTION OF THE SNAKE RIVER PLAIN AQUIFER NEAR THE IDAHO CHEMICAL PROCESSING PLANT AT THE INEL

W. Barrash,

Center for Geophysical Investigation of the Shallow Subsurface,

Boise State University, Boise, Idaho

R.H. Morin,

U.S. Geological Survey, Denver, Colorado

S.H. Wood and W. Bennecke,

Department of Geosciences,

Boise State University, Boise, Idaho

ABSTRACT

The Snake River Plain aquifer (SRPA) is one of the most transmissive aquifers known. At the Idaho National Engineering Laboratory (INEL), the upper portion of the SRPA consists of numerous basalt flow groups and interbedded sediments which have been tentatively traced across much of the site. Three wells about 500 to 700 ft apart have been logged through 190 ft of open interval in the SRPA near the Idaho Chemical Processing Plant (ICPP). The wells exhibit the same lithostratigraphy and intersect much of the E-H and I flow groups of Anderson (1991). Geophysical logs run in wells near the ICPP were: caliper, neutron porosity, gamma-gamma density, natural gamma activity, acoustic televiewer, television, temperature, fluid conductivity, and flowmeters.

Logging results identify two hydrostratigraphic units for the upper portion of the SRPA with contrasting borehole fluid velocities, permeabilities and lithologic characteristics. The upper hydrostratigraphic unit includes the E-H and uppermost part of the I flow groups. Intervals of high permeability are mostly confined to interflow zones. The lower hydrostratigraphic unit consists of the interior of the I group where rubbly interflow zones do not occur and permeability is low.

Borehole fluid velocity fluctuations and direction reversals occur in less than one minute in response to pumping cycles at a production well 0.5 miles away which is screened in the E-H and I flow groups, respectively. This hydraulic communication indicates lateral continuity of hydrostratigraphic units and confined aquifer conditions in the SRPA in the vicinity of the Idaho Chemical Processing Plant at the INEL. Data from wells 48 and 123 to the south indicate that the lower hydrostratigraphic unit can be correlated with a thick flow in those wells. Another flow group below the I group in wells 48 and 123 may be continuous beneath wells 44, 45 and 46 and may be a third hydrostratigraphic unit with relatively high transmissivity.

INTRODUCTION

The Snake River Plain aquifer (SRPA) consists of numerous basalt flows and sedimentary interbeds. Early investigations at the INEL recognized that the SRPA is highly transmissive overall, but heterogeneous. Reported values of transmissivity from monitoring wells in the upper part of the SRPA range over nearly six orders of magnitude (Ackerman, 1991). Also, where deep measurements have been made at the INEL (well INEL-1a) permeability decreases with depth in the SRPA (Mann, 1986). And, on a smaller scale, permeability varies with depth in any given well due to vertical changes in flow structures of the different basalt flows present.

Previous workers recognized vertical variability of head, hydrochemistry and in-hole flow (both magnitude and direction) in wells at the INEL, and at the ICPP in particular (e.g., Jones, 1961; Barraclough et al., 1967). Recent efforts to characterize contamination and evaluate remediation alternatives have increased the interest in quantifying vertical changes in hydraulic parameters and water chemistry to determine if the SRPA is well mixed or layered. This paper presents results from stratigraphic and borehole geophysical logging investigations which are part of an on-going program to understand vertical and lateral variations in hydraulic properties, hydrochemistry (including contaminant chemistry), and flow within and between wells in the SRPA at the INEL.

STUDY AREA

Three wells (44, 45 and 46) immediately west of the ICPP (Figures 1 and 2) were selected for detailed investigation because they: (a) have 190 ft of open interval to the SRPA; (b) have identical well construction; (c) are in close proximity (within 700 ft of each other); (d) have long records of water level and water chemistry measurements; (e) have similar histories of contamination with liquid wastes originating from the ICPP; and (f) are administratively available for investigation. That is, wells 44, 45 and 46 provide the opportunity to see if vertical changes occur over 190 ft of the SRPA, and if any such changes can be traced 500 to 700 ft laterally to adjacent wells.

For the interpretive purposes of this paper, the study area is extended beyond wells 44, 45 and 46 to the north and south at the ICPP to include wells CPP1, CPP2, 48 and 123. These additional four wells were not investigated in the field for this study. However, observed hydraulic interactions and detailed stratigraphic information permit tentative correlations to the north and south based on findings in wells 44, 45 and 46.

STRATIGRAPHIC FRAMEWORK

Anderson (1991) identified about 40 flows and 23 flow groups in the unsaturated zone and the upper SRPA in the ICPP area between land surface and about 750 ft below land surface (BLS). He was able to correlate flow groups in the ICPP area with equivalents in the area of the Radioactive Waste Management Complex (Anderson and Lewis, 1989; Kuntz et al., 1980) about 7 mi to the southwest of the ICPP, and with equivalents at the NPR test well 3 mi to the northeast of the ICPP (Champion et al., 1988). These correlations were based largely on natural gamma log responses (see Anderson, 1991, Fig. 8). Golder Associates (1990) report on core from well 123; Lanphere et al. (1993) add detailed flow descriptions for well 123, and place individual flow units

and flows into the regional stratigraphic nomenclature.

The three wells that were investigated in detail here (wells 44, 45 and 46,) are open to basalts and sediments of flow groups E-H, I (Anderson, 1991) and the recently recognized J flow group (S.R. Anderson, personal communication, 1994) in the saturated portions of these wells (Figure 3). Geophysical logs that were most useful for lithostratigraphic interpretation (identification and correlation of flows, flow units and flow groups) in these wells are: natural gamma, caliper and television logs.

Caliper logs showed locations of enlarged borehole diameters in the wells. These enlarged borehole diameters commonly occurred at flow tops and are abundant in the upper 120 ft of wells 44, 45 and 46. The lower 70 ft of these boreholes are smooth at the nominal drilled diameter (Figure 4). Television logs complement the natural gamma and caliper logs by providing flow structure information helpful for recognition of individual flow units or flows, and relative vertical positions within them based on flow structures (Bennecke, 1994).

From these logs and from stratigraphic interpretations by Anderson (1991), the change to smooth borehole at about 580 ft BLS (4340 ± 4 ft elevation) in 44, 45 and 46 occurs below several (two to four) relatively thin flow units or flows in the upper portion of the I flow group (Figure 3). Lanphere et al. (1993) identified two thin flow units above a 110-ft-thick flow (together forming their flow 12) in the I flow group in well 123 about 0.5 mi south of wells 44, 45 and 46 (Figure 2). Two relatively thin flows or flow units overlie a 100-ft-thick flow at comparable elevation and stratigraphic position in well 48 (Bennecke, unpublished data). The smooth borehole segments in the bottom 70 ft of wells 44, 45 and 46 appear to be the main portion of one thick flow (starting below the flow top) which is correlated here with the number 12 flow of Lanphere et al. (1993).

The thick flow in the I group is underlain by a sedimentary interbed at comparable elevations in wells 48 and 123 (Lanphere et al., 1993; Bennecke, unpublished data). This interbed marks the contact with the J basalt flow group below (S.R. Anderson, personal communication, 1994) which consists of several flows above another interbed at about 4170 ± 4 ft elevation (Figure 3).

To the north, in wells CPP1 and CPP2, the best stratigraphic information comes from natural gamma log interpretation (Anderson, 1991) and drillers' logs which: (a) locate the contact between the E-H flow groups and the I flow group about 45 ft higher than in wells 44, 45 and 46 (Figure 3); and (b) indicate that no flows occur in the I group there with thickness approaching 100 ft. Television logs are not available for wells CPP1 and CPP2. It is uncertain if individual flows (such as the thick flow in the I flow group in wells 44, 45, 46, 48 and 123) continue north to wells CPP1 and CPP2 or if flows thin northward. Also it is not clear if the elevation difference of the contact between E-H and I is due to paleotopography, structural offset or both.

HYDROSTRATIGRAPHY

Responses to geophysical logging in wells 44, 45 and 46 indicate that the basalt aquifer penetrated by these wells can be divided into two hydrostratigraphic units: an upper unit with numerous high-permeability zones and a lower unit with very low permeability throughout. The contact between these two hydrostratigraphic units occurs at about 4340 ft elevation (580 ft BLS) where the lithologic change occurs from numerous flows with enlarged borehole diameters at flow tops to the interior of the thick flow in the I flow group.

Logs most useful for characterizing hydrostratigraphy are flowmeter logs from heat-pulse and impeller tools, and the temperature log (Bennecke and Wood, 1992; Morin et al., 1992). Fluid specific conductance logging also can provide valuable information on locations of changes in hydrochemistry in open boreholes in the SRPA (e.g., Hegmann and Wood, 1994; Wood and Bennecke, 1994).

Flowmeter logging in wells 44, 45 and 46 (Bennecke and Wood, 1992; Morin et al., 1992) has demonstrated that significant in-hole flow (generally 0.9 to 8.4 gal/min) occurs in the upper hydrostratigraphic unit, and that little or no in-hole flow (<0.1 to 0.7 gal/min) occurs in the lower hydrostratigraphic unit (Table 1). Temperature logs in wells 44, 45 and 46 show approximately isothermal conditions in the upper hydrostratigraphic unit due to strong vertical in-hole flow; increase of temperature with depth in the lower hydrostratigraphic unit indicates little or no in-hole flow there (Figure 5). High in-hole flow rates and magnitudes in the upper hydrostratigraphic unit correlate with high estimates of hydraulic conductivity (generally >100 to >10,000 ft/day) from flowmeter logging while pumping (Morin et al., 1992), and from hydraulic tests with the straddle-packer system (Monks et al., 1993).

Hydraulic Indications of Hydrostratigraphic Continuity

Under "static" conditions, in-hole flow has an upward gradient in wells 44, 45 and 46 (Figure 4) including upward gradient in the lower stratigraphic unit where slight in-hole flow can be detected (Morin et al., 1992). Measurements of flow rates and directions during flow logging (Table 1, Figure 5) also demonstrate that changes occur when an ICPP production well 0.5 mi away (either CPP1 or CPP2) is turned on or off (Bennecke and Wood, 1992; Morin et al., 1992). These changes occurred in less than 30 seconds, as determined when close coordination with operations staff at the production wells provided accurate times that a production well was turned on.

The upper production zone in the E-H flow groups in CPP1 and CPP2 (screened intervals and identified producing zones from drillers' logs) and the contact of the E-H flow groups over the I flow group in CPP1 and CPP2 are at higher elevations than comparable features in wells 44, 45 and 46 (Figure 3). The lower production zone in CPP1 and CPP2 occurs in the I flow group (Anderson, 1991) at an elevation higher than the base of wells 44, 45 and 46. Also the intervening thickness between screened intervals is less than 100 ft (Figure 2). Rapid changes in head and in-hole flow rate and direction noted above that occurred in response to pumping at wells CPP1 and CPP2 0.5 mi away indicate that there is hydraulic connection to these wells and that the aquifer system is under confined conditions (Bennecke and Wood, 1992; Barrash et al., 1993). The upward gradient in wells 44, 45 and 46 is consistent with a system in hydraulic communication with higher head regions under confined conditions.

In addition, preliminary review of transient responses to pumping at CPP1 in the lower hydrostratigraphic unit in well 46 suggest hydraulic communication with a high permeability unit below the base of well 46. Head changes were recorded in the lower 10 ft of well 46 (isolated from the well above with a packer) beginning <15 seconds after pumping was started in well CPP1, but it appears that no response or a more muted or delayed response occurred in the packed-off interval above. Because the horizontal permeability in the lower hydrostratigraphic unit of well 46 is quite low (Table 1, Figure 5), such a rapid response to pumping 0.5 mi away is not likely unless the response occurs by vertical leakage communication with a high permeability zone below that is hydraulically connected to CPP1.

To explain these conditions, it has been suggested that the upper hydrostratigraphic unit in wells 44, 45 and 46 may be continuous with the upper screened producing zones in the E-H flow groups in CPP1 and CPP2, and that a higher permeability unit may exist below the bottoms of wells 44, 45 and 46 (J flow group?) that is hydraulically connected to the lower screened producing zones in the I flow group in CPP1 and CPP2 (Morin et al., 1992; Barrash et al., 1993). Tentative correlation of the thick flow (flow 12 of Lanphere et al. [1993] in well 123) in the I group with a thick flow in well 48 and with the lower region of wells 44, 45 and 46 allows us to speculate that a higher permeability unit may occur up to 25 to 35 ft below wells 44, 45 and 46 based on projection of the base of the thick flow from wells 48 and 123.

This interpretation of a three-layered hydrostratigraphy at the ICPP can be tested by investigating well 48 with geophysical logging and also with hydrologic and hydrochemical testing and sampling with the straddle-packer system described in this volume (Olsen, 1994) -- as has been employed at wells 44, 45 and 46. Such investigation has not occurred to date for logistical reasons (well 48 is inside the security area of the ICPP) and because administrative issues surrounding management of contaminated water generated by the straddle-packer system have not yet been resolved. New data on vertical variability in hydrostratigraphy in the upper portion of the Snake River Plain aquifer have significant implications for the vertical distribution of contamination in the aquifer (McCurry et al., 1993; 1994), and hence for ground water monitoring, risk assessment and modeling of aquifer flow and contaminant transport.

ACKNOWLEDGMENTS

This paper was improved by discussions with staff of the U.S. Geological Survey at the INEL, especially S.R. Anderson and R.G. Jensen, and by the reviews of G. Johnson and M. McCurry.

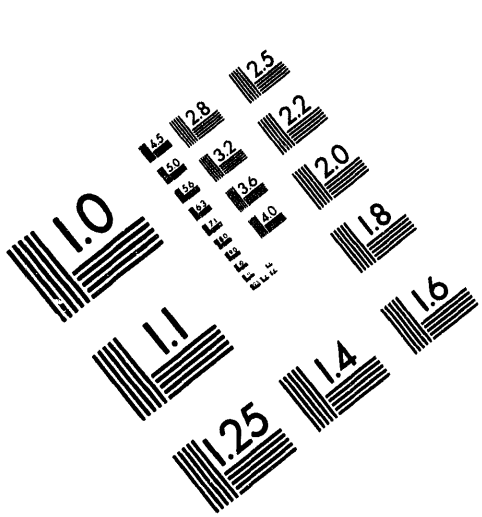
REFERENCES

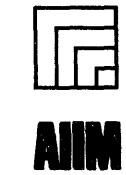
Ackerman, D.J., Transmissivity of the Snake River Plain aquifer at the Idaho National Engineering Laboratory, Idaho, *U.S. Geological Survey Water-Resources Investigations Report 91-4058*, 1991.

Anderson, S.R., Stratigraphy of the unsaturated zone and uppermost part of the Snake River Plain aquifer at the Idaho Chemical Processing Plant and Test Reactors Area, Idaho National Engineering Laboratory, Idaho, *U.S. Geological Survey Water-Resources Investigations Report 91-4010,* 1991.

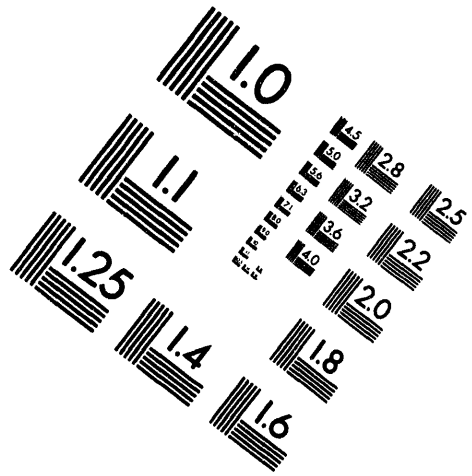
Anderson, S.R. and B.D. Lewis, Stratigraphy of the unsaturated zone at the Radioactive Waste Management Complex, Idaho National Engineering Laboratory, Idaho, *U.S. Geological Survey Water-Resources Investigations Report 89-4065,* 1989.

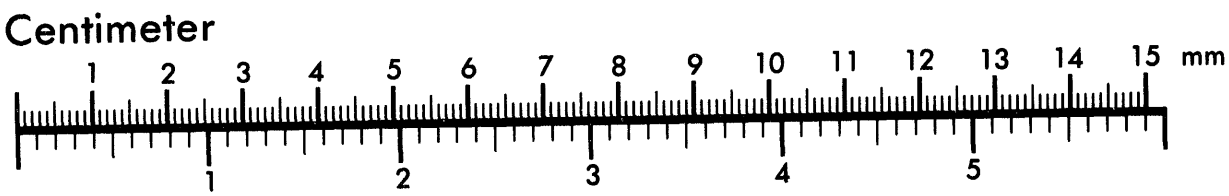
Barraclough, J.T., Teasdale, W.E. and Jensen, R.G., Hydrology of the National Reactor Testing Station, Idaho: Annual Progress Report 1965, *U.S. Geological Survey Open-File Report*, IDO-22048, 1967.

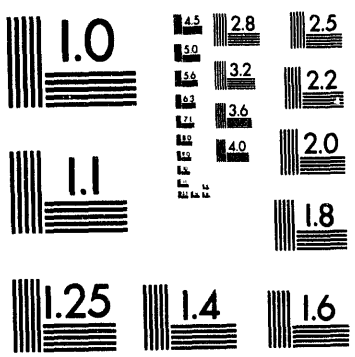


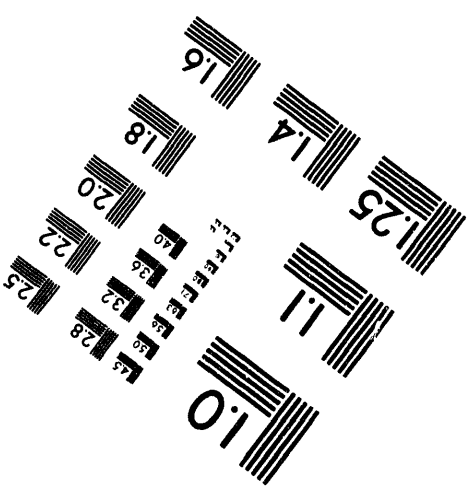


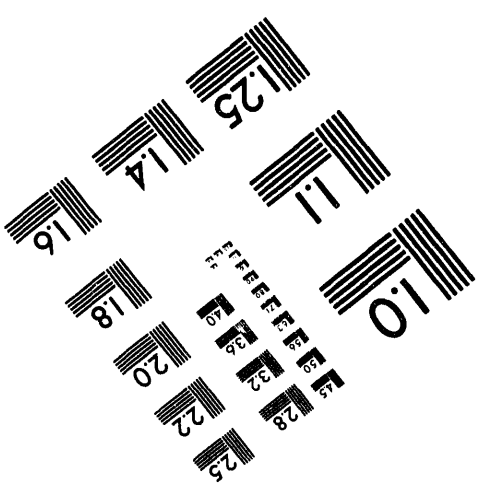
Association for Information and Image Management
1100 Wayne Avenue, Suite 1100
Silver Spring, Maryland 20910
301/587-8202











MANUFACTURED TO AIIM STANDARDS
BY APPLIED IMAGE, INC.

3 of 7

Barrash, W., R.H. Morin, S.H. Wood, S.R. Anderson, R.G. Jensen and W. Bennecke, Geophysical logging evidence for stratigraphic controls on hydrology in the Snake River Plain aquifer at the Idaho National Engineering Laboratory (INEL), southeastern Idaho, *EOS*, **74**, 283-284, 1993.

Bennecke, W.M., The identification of basalt physical features from borehole television logs, *Proceedings of the 1994 Annual Symposium on Engineering Geology and Geotechnical Engineering*, Boise, Idaho, 1994.

Bennecke, W.M. and S.H. Wood, Impeller flow-meter logging of vertical cross flow between basalt aquifers through wells at the Idaho National Engineering Laboratory, eastern Snake River Plain, Idaho, *Borehole Geophysics Research Program, Boise State University, Progress Report: June 22, 1992*, 1992.

Champion, D.E., Lanphere, M.A. and Kuntz, M.A., Evidence for a new geomagnetic reversal from lava flows in Idaho: Discussion of short polarity reversals in the Brunhes and late Matuyama polarity chrons, *Journal of Geophysical Research,* **93**, 11,667-11,680, 1988.

Golder Associates, Final well completion report for wells 121, 122 and 123 at the Idaho Chemical Processing Plant, *Report to EG&G Idaho*, Contract C86-131159, Task 6, 1990.

Hegmann, M.J. and S.H. Wood, Hydrostratigraphy of the Snake River Plain aquifer beneath the Radioactive Waste Management Complex at the Idaho National Engineering Laboratory, southeastern Idaho, *Proceedings of the 1994 Annual Symposium on Engineering Geology and Geotechnical Engineering*, Boise, Idaho, 1994.

Johnson, G.S., H. Olsen and D.R. Ralston, Hydrologic testing in wells USGS 44, 45 and 46 near the ICPP at the Idaho National Engineering Laboratory, *Proceedings of the 1994 Annual Symposium on Engineering Geology and Geotechnical Engineering*, Boise, Idaho, 1994.

Jones, P.H., Hydrology of waste disposal, National Reactor Testing Station, Idaho -- An interim report, *U.S. Geological Survey Report IDO-22042*, 1961.

Kuntz, M.A., G.B. Dalrymple, D.E. Champion and D.J. Doherty, 1908, Petrography, age and paleomagnetism of volcanic rocks at the Radioactive Waste Managemnent Complex, Idaho National Engineering Laboratory, Idaho with an evaluation of volcanic hazards, *U.S. Geological Survey Open-File Report 80-388*, 1980.

Lanphere, M.A., D.E. Champion and M.A. Kuntz, Petrography, age and paleomagnetism of basalt lava flows in coreholes Well 80, NRF 89-04, NRF 89-05 and ICPP 123, Idaho National Engineering Laboratory, *U.S. Geological Survey Open-File Report 93-327,* 1993.

Mann, L.J., Hydraulic properties of rock units and chemical quality of water for INEL-1a; 10,365 ft deep test hole drilled at the Idaho National Engineering Laboratory, Idaho, *U.S. Geological Survey Water-Resources Investigations Report 86-4020.*

McCurry, M., J. Fromm, J. Welhan and W. Barrash, Vertical profiling of aquifer hydrochemistry at the INEL, Idaho: Implications for hydrostratigraphy (abs.), *EOS*, **74**, 284, 1993.

McCurry, M., M. Estes, J. Fromm, J. Welhan and W. Barrash, Three-dimensional chemical structure of the INEL aquifer system near the Idaho Chemical Processing Plant, *Proceedings of the 1994 Annual Symposium on Engineering Geology and Geological Engineering*, Boise, Idaho, 1994.

Monks, J.I., D.R. Ralston, G.S. Johnson, J.K. Olsen and W. Barrash, Straddle-packer determination of vertical variations in aquifer properties in the Snake River Plain aquifer at the Idaho National Engineering Laboratory (abs.), *EOS*, **74**, 284, 1993.

Morin, R.H., W. Barrash, F.L. Paillet and Taylor, T.A., Geophysical logging studies in the Snake River Plain aquifer at the Idaho National Engineering Laboratory - Wells 44, 45 and 46, *U.S. Geological Survey Water-Resources Investigations Report 92-4184*, 1993.

Olsen, J.K., Straddle packer system design and operation for vertical characterization of open boreholes, *Proceedings of the 1994 Annual Symposium on Engineering Geology and Geotechnical Engineering*, Boise, Idaho, 1994.

Wood, S.H. and W. Bennecke, Vertical variation in groundwater chemistry in the Snake River Plain basalt aquifer inferrred from fluid specific-conductivity (electrical) well logging at the Idaho National Engineering Laboratory, southeastern Idaho, *Proceedings of the 1994 Annual Symposium on Engineering Geology and Geotechnical Engineering*, Boise, Idaho, 1994.

Table 1.--Thermal-flowmeter measurements in wells 44, 45, and 46

Depth (feet below land surface)	Elevation (feet above mean sea level)	Flow without pumping (gallons per minute)	Flow while pumping[1] (gallons per minute)
		WELL 44	
480	4,439	0.2 upflow	11.7 upflow
495	4,424	0.1 upflow	11.7 upflow
515	4,404	3.2 upflow	8.3 upflow
523	4,396	3.8 upflow	8.3 upflow
556	4,363	0.1 upflow	0.8 upflow
568	4,351	0.1 upflow	0.3 upflow
578	4,341	0	0
610	4,309	0	0
632	4,287	0	
		WELL 45	
475	4,445	0	12.8 upflow
504	4,416	0.5 upflow	10.6 upflow
517	4,403	0.9 upflow	10.6 upflow
531	4,389	0.9 upflow	10.6 upflow
558	4,362	0.9 upflow	10.6 upflow
574	4,346	diameter too variable - inconsistent data	
590	4,330	0.4 upflow	0
602	4,318	0.7 upflow	
617	4,303	0.7 upflow	0
632	4,288	0.7 upflow	
		WELL 46	
471	4,446	0	5.3 upflow
486	4,431	0.4 upflow	1.2 upflow
505	4,412	6.1 upflow	5.1 downflow
526	4,391	8.4 upflow	9.2 downflow
550	4,367	8.4 upflow	12.1 downflow
562	4,355	8.4 upflow	12.1 downflow
572	4,345	6.0 upflow	6.8 downflow
580	4,337	0	0
608	4,309	0	
615	4,302	0.1 upflow	0
640	4,277	0.1 upflow	

[1]The pumping rate was about 22 gallons per minute

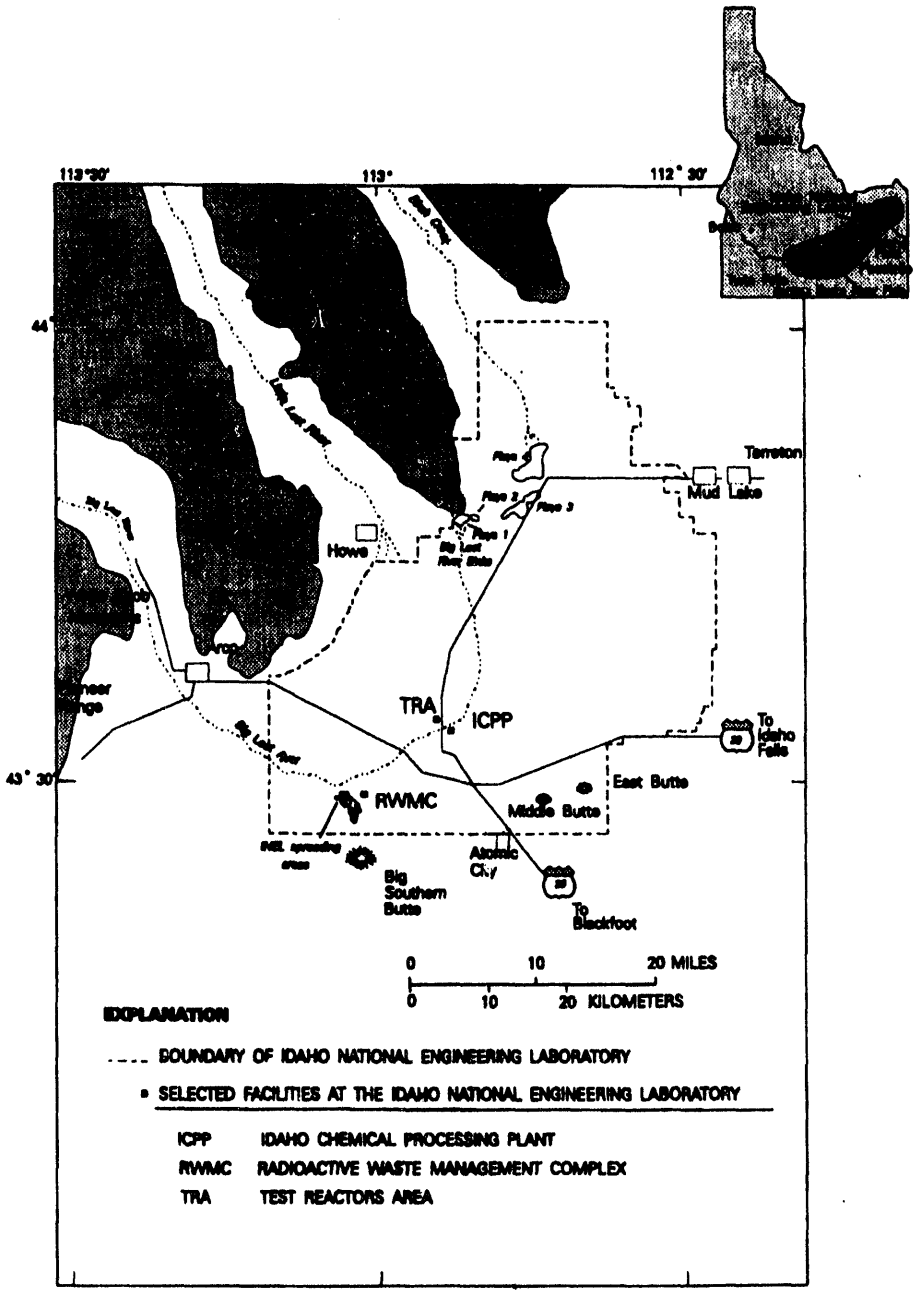


Figure 1. Location map of the Idaho National Engineering Laboratory.

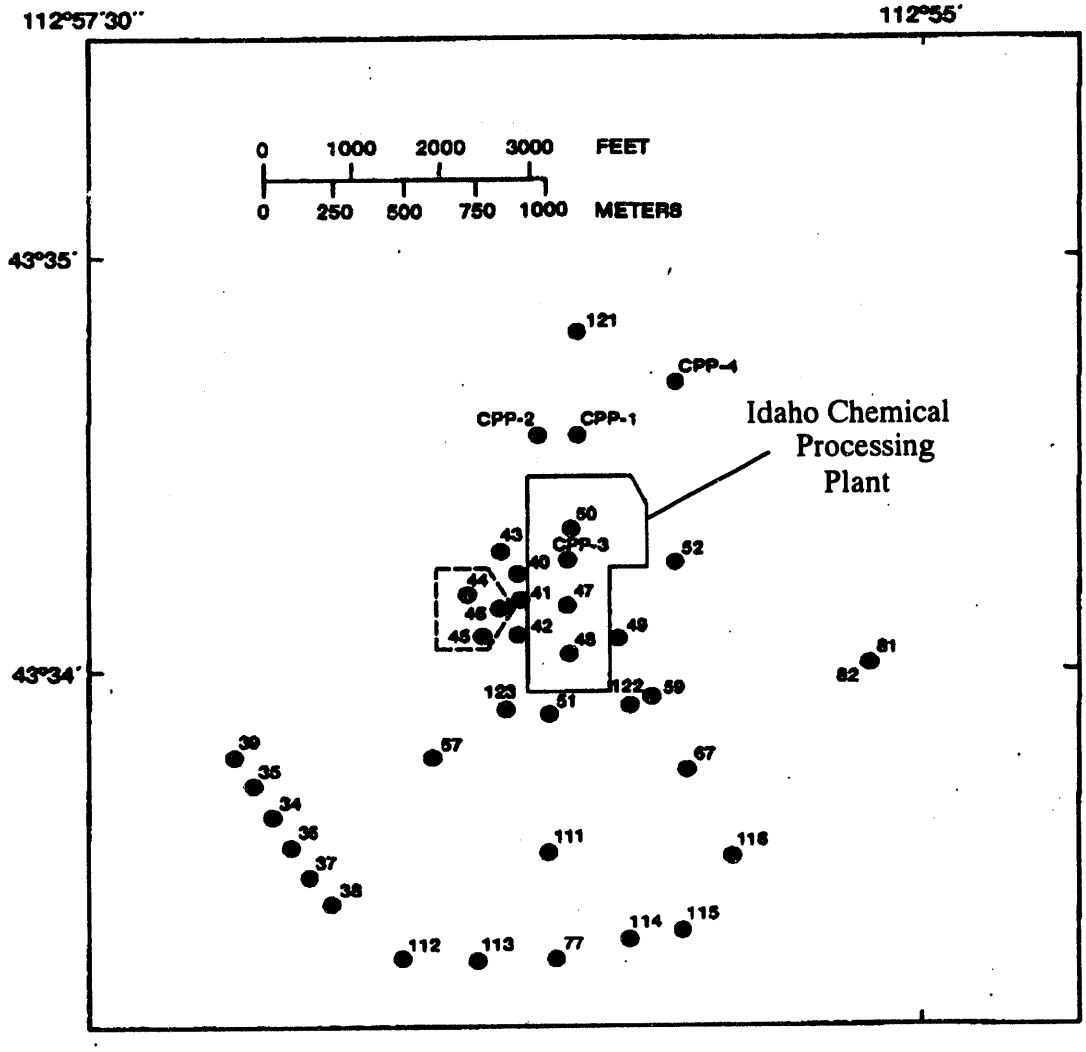


Figure 2. Location map of wells in the vicinity of the Idaho Chemical Processing Plant which penetrate the Snake River Plain aquifer. Wells CPP1 and CPP2 are production wells.

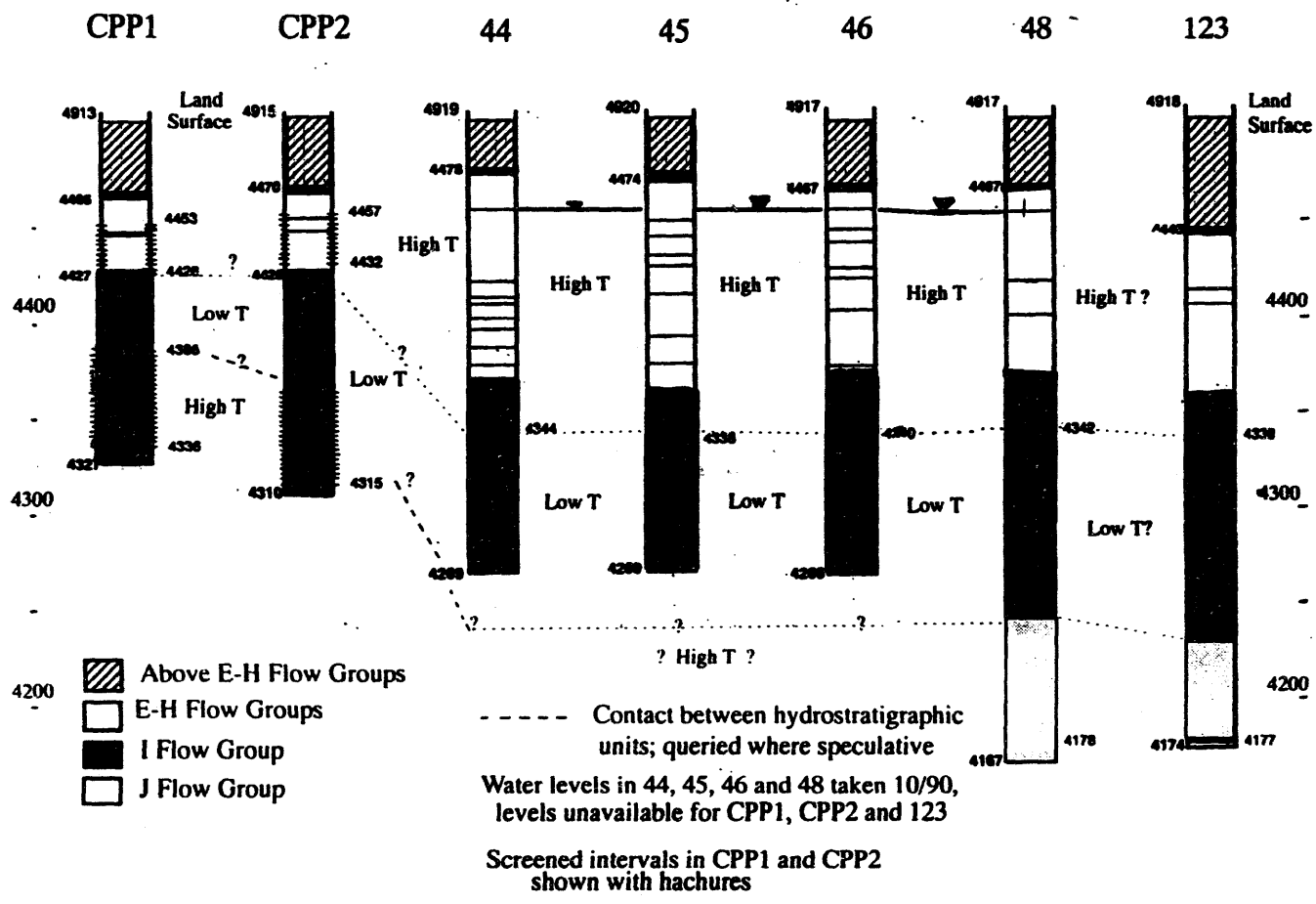


Figure 3. Interpreted lithostratigraphic and hydrostratigraphic cross section in the upper portion of the Snake River Plain aquifer in the ICPP area.

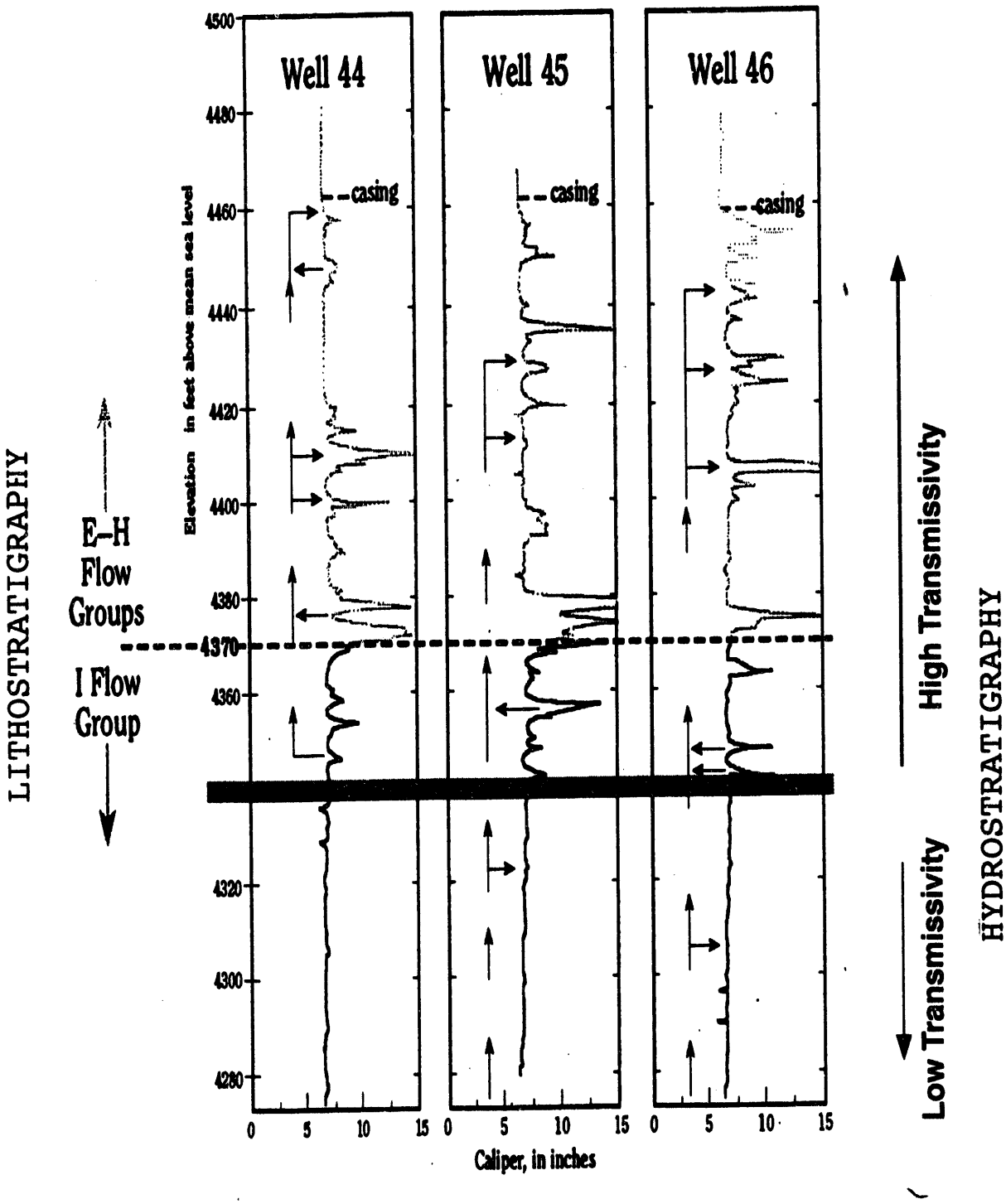


Figure 4. Sketches of fluid circulation patterns in wells 44, 45 and 46 based on heat-pulse flowmeter measurements. In-hole flow direction indicated by arrows. Upward gradient was present when production wells were off. (After Morin et al., 1992)

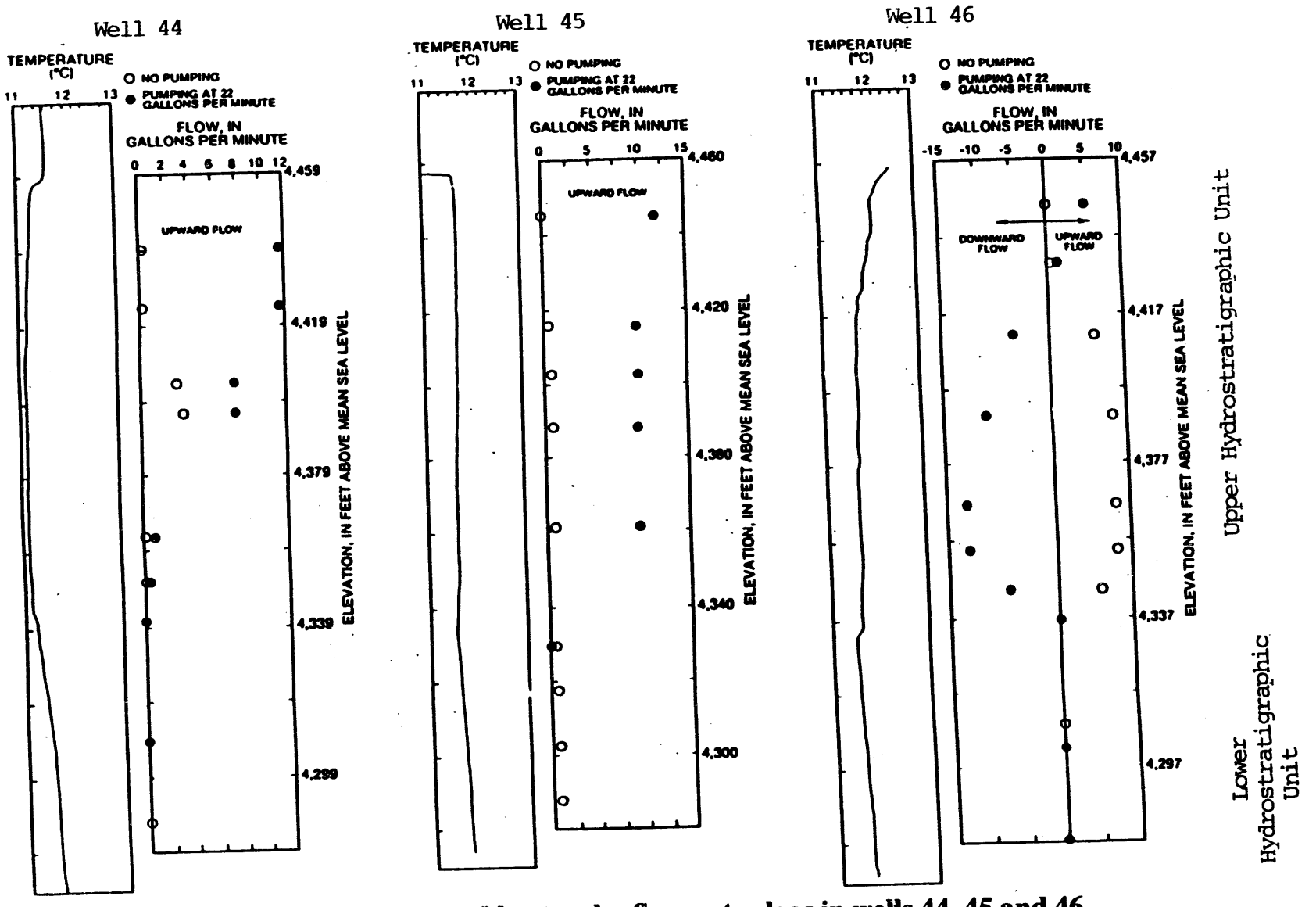


Figure 5. Temperature and heat-pulse flowmeter logs in wells 44, 45 and 46 showing flow regime changes at about 4340 ft elevation (hydrostratigraphic contact). (After Morin et al., 1992)

Hydrogeology, Waste Disposal, Science and Politics
Proceedings 30th Symposium
Engineering Geology and Geotechnical Engineering, 1994

HYDROSTRATIGRAPHY OF THE SNAKE RIVER PLAIN AQUIFER BENEATH THE RADIOACTIVE WASTE MANAGEMENT COMPLEX AT THE IDAHO NATIONAL ENGINEERING LABORATORY: A PRELIMINARY REPORT

Mary J. Hegmann and Spencer H. Wood
Geoscience Department
Boise State University
Boise, ID 83725

ABSTRACT

Geophysical logs for 6 wells which penetrate the Snake River Plain aquifer at the Radioactive Waste Management Complex (RWMC) were analyzed for preliminary information on the hydrostratigraphy. Using stratigraphic correlation of flow groups worked out by Anderson and Lewis (1989), and by Anderson (pers.comm., 1994), as well as gamma signatures of flows within these flow groups, correlation of individual flows is attempted. Within these flows, probable permeable zones, suggested by density and caliper logs, are identified, and zones of hydraulic connection are tentatively correlated. In order to understand the response of density and neutron logs in basalt, the geological characteristics are quantified for the 150-ft section of the well C1A core, from depth 550 to 710 ft.

INTRODUCTION

The Radioactive Waste Management Complex (RWMC) is located in the southwest corner of the Idaho National Engineering Lab (INEL) in eastern Idaho (Fig. 1). The RWMC was established in 1952 as a disposal site for solid radioactive waste and is situated approximately 600 ft above the Snake River Plain aquifer. The site is underlain by a complex series of basalt flows and sedimentary interbeds, and horizontal movement through the aquifer is believed to occur chiefly through interflow zones (Ackerman, 1991). The groundwater generally flows from northeast to southwest, and its velocity is estimated at between 5 and 20 ft/d (Robertson and others, 1974). Because of the potential for migration of contaminants through the aquifer, it is important to identify zones in the aquifer which are likely to be permeable.

APPROACH

Six of the deeper wells located at the RWMC were chosen for a hydrogeologic cross-section beneath the water table (Fig. 1). Using primarily gamma logs, as well as core descriptions, geomagnetic properties, K-Ar age dates, and location and thickness of sedimentary interbeds, Anderson and Lewis (1989) have correlated stratigraphic units in 2 of these wells (RWMC-Prod. and 120) to five wells previously described by Kuntz and others (1980).

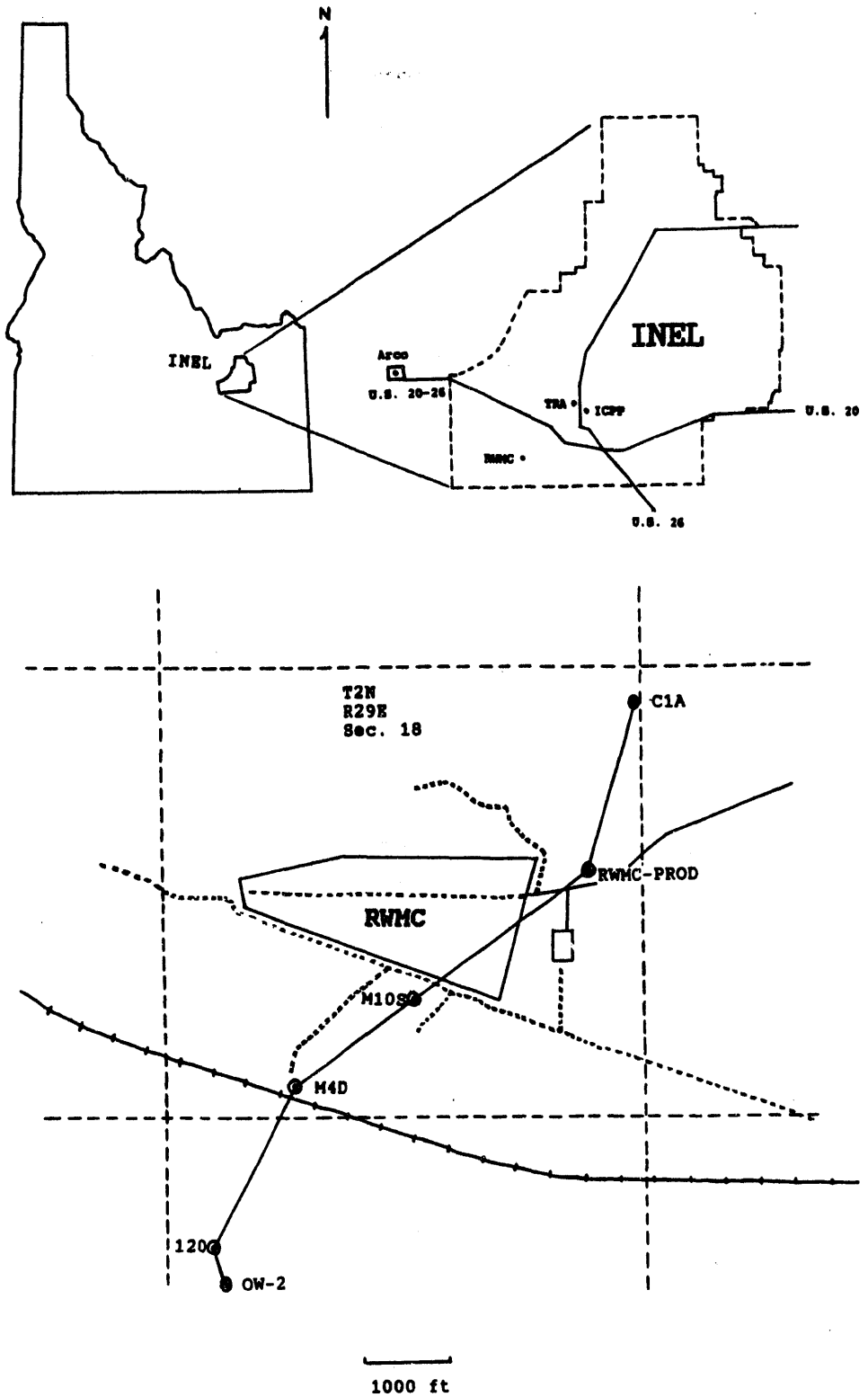


Fig. 1. Location of the Radioactive Waste Management Complex and hydrogeologic cross-section through 6 wells.

Anderson has since correlated stratigraphic units in the 4 remaining wells in this cross-section (OW-2, M4D, M10S, and C1A). These stratigraphic units are termed "flow groups", originally defined as petrographically similar flows extruded from the same source during eruptive events of less than 200 years (Kuntz and others, 1980).

For this study, gamma, caliper, and density logs were examined to identify possible permeable zones and individual flows within Anderson's time-equivalent flow groups. Gamma logs were studied to identify gamma signatures. By comparing signatures of individual flows, correlation between wells of some of these flows was hypothesized. Density logs and caliper logs were studied to identify zones of low density and caved zones, which may indicate permeability. The core of well C1A, the only core available within the cross-section, was inspected and compared to its density and neutron logs to identify the characteristics which cause deflections on density and neutron logs.

LOG INTERPRETATION

Gamma Logs

By identifying sedimentary interbeds and by examining gamma signatures, Anderson and Lewis (1989), and Anderson (pers.comm., 1994) correlated sequences of basalt flows in wells OW-2, 120, M4D, M10S, RWMC-Prod., and C1A, to other wells in the area. These time-equivalent sequences were termed "flow groups", and the alphabetical naming convention for these groups, originated by Kuntz and others (1980), is retained for this report.

Natural gamma logs were used in this study in an attempt to correlate individual basalt flows within Anderson's flow groups. An analysis of eastern Snake River plain basalts of Pleistocene age demonstrated that flows vary from 0.26% to 2.71% K_2O (Kuntz and others, 1992), and this is thought to be responsible for variations in natural gamma response (Anderson, pers. commun., 1994). Gamma emissions are believed to be uniform in related flows of similar age and source at the site (Anderson and Lewis, 1989; Anderson, pers.comm., 1994).

Natural gamma logs were inspected, and signatures were tentatively identified. These signatures were used to divide Anderson's original flow groups into "gamma units", or sequences of basalt flows believed to have erupted from the same source. Each gamma unit retains its original group name, but because gamma signatures within some of Anderson's groups varied significantly, they were identified as separate gamma units.

For example, Anderson believes that flow group H in well M4D probably correlates with flow group H in other wells. But because group H in M4D contains three distinctly different gamma signatures, it may contain flows of 3 different sources (Anderson, pers.comm., 1994). These 3 gamma units were named H_1, H_2, and H_3 because they are the first, second, and third gamma units (counted from the surface) to occur in this well, within what Anderson and Lewis (1989) originally called group H. Note that subscripts are

used only to order gamma units stratigraphically within a group in an individual well; the same subscript does not imply correlation of units across wells. Also, to simplify correlation, it was decided that gamma units could contain more than a single flow, but could not contain interbeds. An accumulation of sediment would tend to indicate a long period of time passed between flows and would make it unlikely that the flows were part of the same event.

Because the base of flow group F is known with certainty, and it is uniquely characterized by reversed polarity and high gamma emission (Anderson and Lewis, 1989; Anderson, pers. comm., 1994), its gamma signature was utilized as the basis for correlating individual flows beneath it.

Figure 2 illustrates the manner in which gamma signatures were identified and correlated. For example, because Anderson has tentatively correlated all G groups with respect to time, the similarity of gamma units G_1 in OW-2, G_1 in 120, and G_2 in M4D may indicate correlation of individual flows within the gamma unit. Density and caliper logs indicate there may be 2 flows within G_1 of 120, and 2 flows within G_2 of M4D. It might be hypothesized then that the 2 flows in G_1 of 120 correlate to the 2 flows in G_2 of M4D. It is important to note that this was a loose, qualitative comparison, because some of the wells were logged with uncalibrated tools, and caving of sediments, drilling fluid, and well construction can each affect the gamma log.

Caliper Logs

Caved zones as expressed on caliper logs were used to identify possible flow tops within gamma units. Flow tops are likely to be permeable zones because they are usually very vesicular and sometimes rubbly (Whitehead, 1992). Caved zones are also caused by the presence of unconsolidated sedimentary interbeds, which may or may not be permeable. These major interbeds were previously identified by Anderson and Lewis (1989), and Anderson (pers.comm., 1994). Several zones where minor interbeds might exist, such as at elevations 4325 ft and 4383 ft in well M4D, were identified by examining natural gamma logs. It is important to note that these excursions on the gamma log are not as strong as those of known interbeds, and they may be due to conditions other than the presence of sediment.

Caved zones within a gamma unit may also be caused by zones of fracture. Unfortunately, it appears they cannot be positively distinguished from flow tops except by examining cores, which are rarely collected, or by examining the borehole with a televiewer. Caved zones which did not appear to contain interbeds, and which occurred within a gamma unit, were assumed to be flow tops. For example, caved zones occur at elevation 4410 ft in RWMC-Prod., and between elevations 4288 and 4268 ft in OW-2.; natural gamma logs do not indicate sediment. In logging OW-2 with spinner-flowmeter, Wood and Bennecke (this volume) have determined that flow is occuring in this caved zone. Such zones were assumed to be permeable as long as the density log did not indicate otherwise.

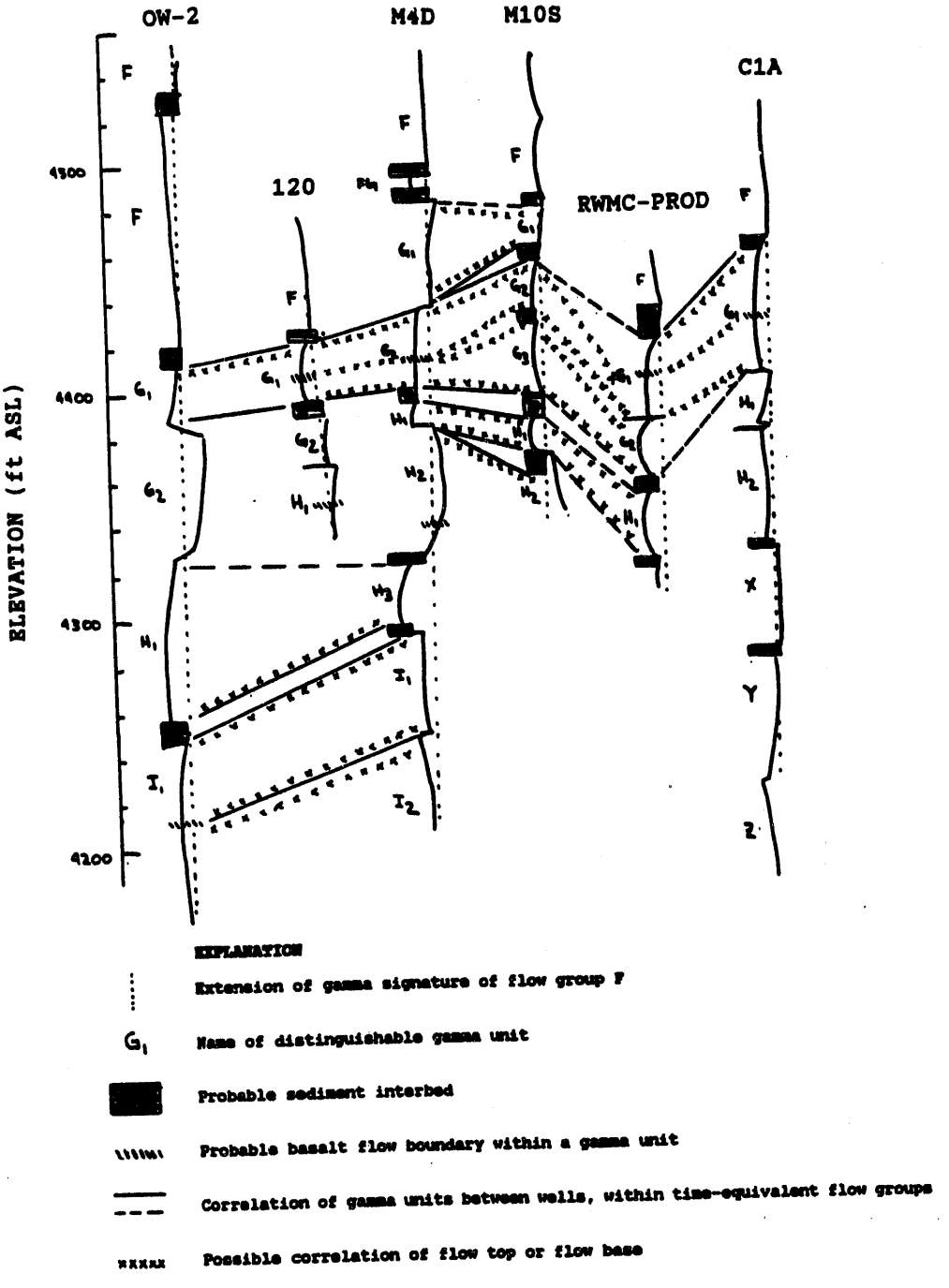


Fig. 2. Sketch shows division of flow groups into identifiable gamma units, and comparison of relative intensity of gamma units to that displayed by group F. Intensity increases to the right. Subscript indicates change in gamma signature within Anderson's original flow group (Anderson, pers.comm., 1994). Note that units below H in well C1A are referred to as X, Y, and Z only within this report--Anderson has not been able to correlate them.

Density Logs

The gamma-gamma or density log is used as a measure of bulk density or porosity (Keys and MacCary, 1971). The excursions on the gamma-gamma logs displayed in this report are not directly proportional to formation density as explained in the appendix. In this study the density log was used in a qualitative manner to identify permeable zones such as fracture zones and flow tops, which sometimes are not expressed on the caliper log. Zones of low density in the absence of caving were interpreted as a flow top and adjacent flow base. For example, at elevations 4414 ft and 4356 ft in well 120, the density log displays marked drops in density, but the caliper log does not show caving. These zones were interpreted as vesicular flow tops, although it is possible they may be fracture zones within an individual flow. Marked drops in density, especially in combination with a caved zone, were tentatively identified as flow tops.

C1A Core and Logs

In comparing the sketch of a 150-ft section from depth 550 ft to 710 ft of the C1A core to the density and neutron logs, it can be seen that certain characteristics of the core cause deflections on both logs (Fig. 3). For example, the neutron log shows a zone of very low porosity, and the density log displays high density between elevations 4456 and 4444 ft. An examination of the core in this zone revealed it to be very dense and practically unfractured.

Between elevations 4433 and 4430 ft, the neutron log displays a marked deflection to the left, indicating high water-filled porosity; the density log shows a gradual, then very sharp drop in density. The core was poorly recovered in this zone, but no sediment is indicated on the gamma log. The caliper indicates a caved zone. This was interpreted as a rubble zone between flows, within a single gamma unit, mostly because of the gradual character of the density log, but it is possible that the zone is highly fractured flow basalt.

In studying the remainder of the core between elevations 4470 and 4320 ft, it is seen that features such as vesicularity, degree of fracturing, and presence of sedimentary interbeds produce distinct deflections on both logs. The rock quality designation (RQD), which is a modified core-recovery percentage (Bieniawski, 1989), and roughly estimated porosity also appear to be at least crude indications of the relative degree of density and porosity. For example, the RQD shows a high degree of core recovery, nearly 100 percent, between elevations 4454 and 4442 ft (Fig. 3). The density log displays a zone of high density, and the neutron log indicates low saturated porosity. Estimated porosity tends to drop in zones where the density log indicates high density, between elevations 4402 and 4385 ft for example.

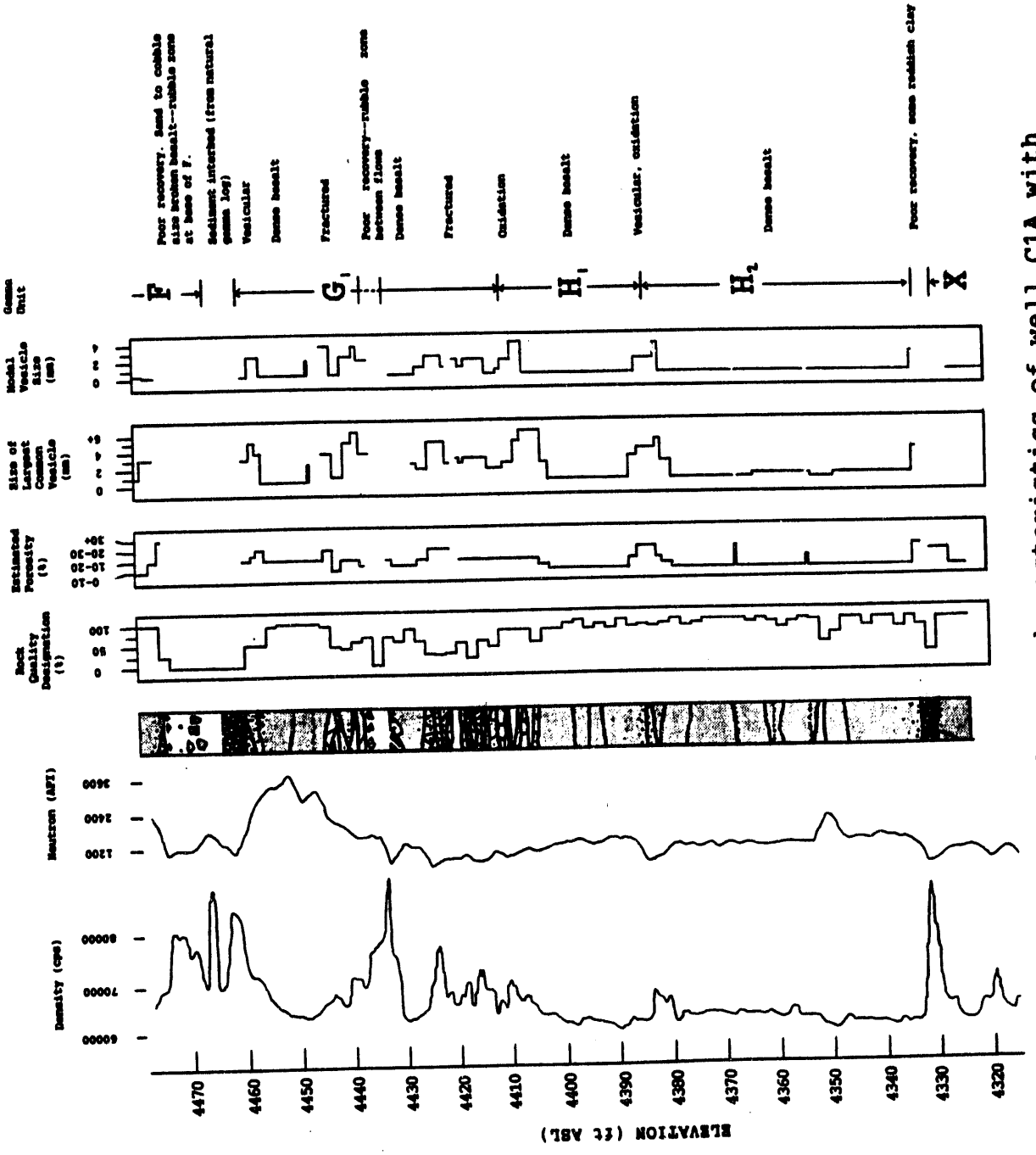


Fig. 3. Comparison of core characteristics of well C1A with density and neutron logs, from depth 550 to 710 ft.

HYDROGEOLOGIC CROSS-SECTION

Groundwater flows vertically through fractures, faults, and joints in basalts. Horizontal movement occurs through interflow zones, which are zones of fractured, vesicular basalt and cinders between adjacent lava flows (Whitehead, 1992). Assuming that individual lava flows may be correlated between wells in the manner suggested above, then one may speculate that the permeable zones within these flows, especially flow tops and rubble zones, may be correlated. It should be noted, however, that not all flow tops will be permeable, nor is it expected that permeable zones be continuous over the area. Figure 4 displays possible hydraulic connections between wells, based on stratigraphic correlation methodology described above.

The hydrogeologic cross-section displays likely zones of permeability as inferred from low-density zones on density logs, and caved zones on caliper logs. Flows are labeled according to their original flow group designation as F, G, H, and I (Anderson and Lewis, 1989; Anderson, pers.comm., 1994). Units below H in well C1A are referred to as X, Y, and Z only for the purpose of this report. Anderson has not been able to correlate these units.

CONCLUSION

Caliper and density logs appear to be useful for identification of possible zones of groundwater flow in wells at the RWMC. It is possible to speculate on the correlation of individual basalt flows. It appears to be very difficult to positively identify hydraulic connections between wells using only caliper, density, and gamma logs. Nevertheless, the hydrogeologic section of this report presents a framework for more detailed investigations, including re-logging of existing wells with borehole TV, flowmeter, and temperature logs to verify permeable zones.

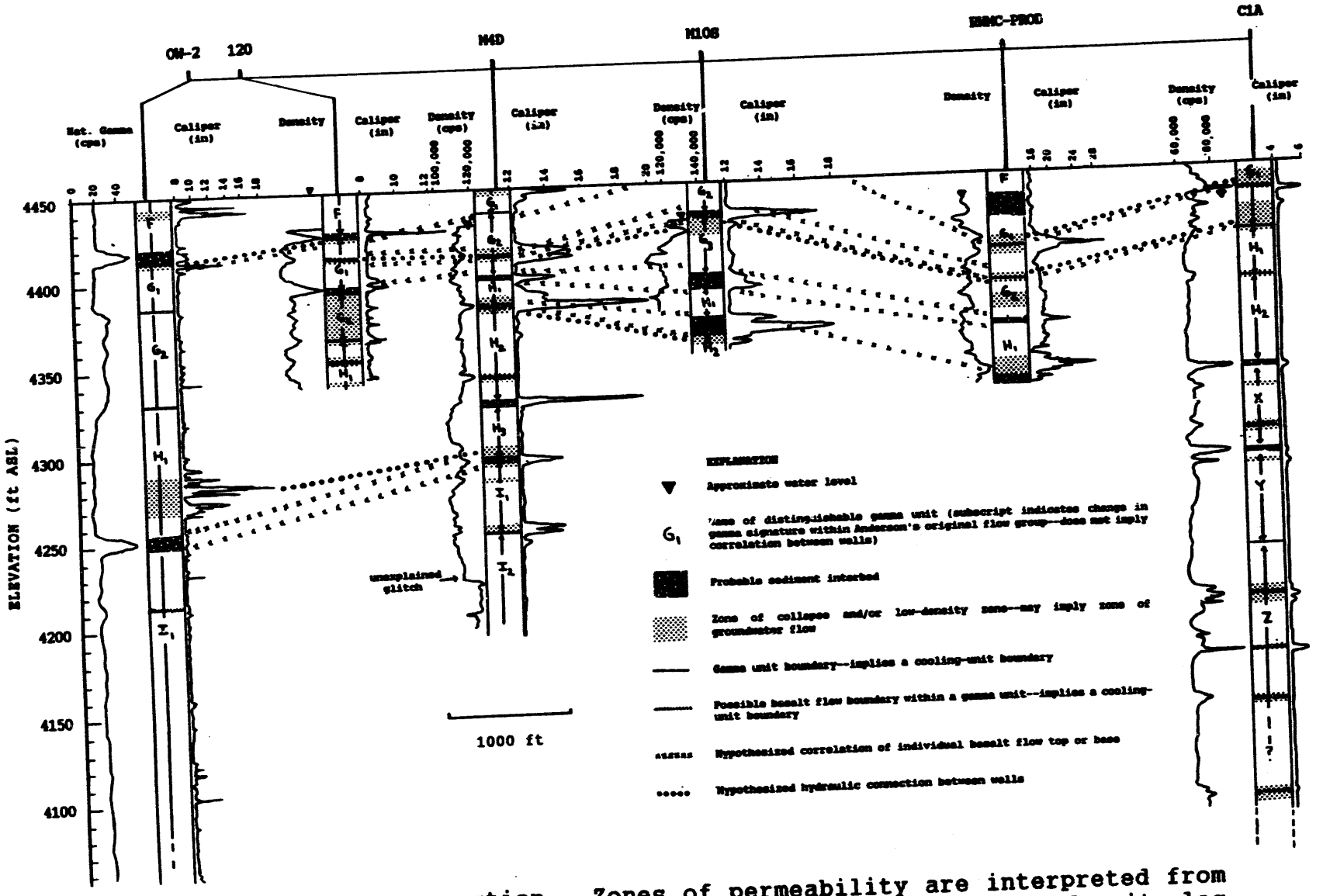


Fig. 4. Hydrogeologic cross-section. Zones of permeability are interpreted from density and caliper logs. Natural gamma log is shown for OW-2, density log was unavailable. Speculative stratigraphic correlation of flow tops and bases is based upon gamma signatures. Groundwater flow between wells is hypothesized by connecting permeable zones within correlated lava flows.

REFERENCES CITED

Ackerman, D. J., 1991, Transmissivity of the Snake River plain aquifer at the Idaho National Engineering Laboratory, Idaho: U.S. Geological Survey Water-Resources Investigations Report 91-4058, 35 p.

Anderson, S. R., and Lewis, B. D., 1989, Stratigraphy of the unsaturated zone at the Radioactive Waste Management Complex, Idaho National Engineering Laboratory, Idaho: U.S. Geological Survey Water-Resources Investigations Report 89-4065, 54 p.

Bieniawski, Z. T., Engineering rock mass classifications, 1989: John Wiley & Sons, Inc., 251 p.

Keys, W. S., and MacCary, L. M., 1971, Application of borehole geophysics to water-resources investigations: Techniques of Water-Resources Investigations of the U.S. Geological Survey, Book 2, ch. E1, 126 p.

Kuntz, M. A., Dalrymple, G. B., Champion, D. E., and Doherty, D. J., 1980, Petrography, age and paleomagnetism of volcanic rocks at the Radioactive Waste Management Complex, Idaho National Engineering Laboratory, Idaho, with an evaluation of potential volcanic hazards: U.S. Geological Survey Open-File Report 80-388, 63 p.

Kuntz, M. A., Covington, H. R., and Schorr, L. J., 1992, An overview of basaltic volcanism of the eastern Snake River Plain, Idaho, in Link, P. K., Kuntz, M. A., and Platt, L. B., eds., Regional Geology of Eastern Idaho and Western Wyoming: Geological Society of America Memoir 179.

Robertson, J. B., Schoen, R. N., and Barraclough, J. T., The influence of liquid waste disposal on the geochemistry of water at the national reactor testing station, Idaho--1952-1970: U.S. Geological Survey Open-File Report (IDO-22053), 231 p.

Whitehead, R. L., 1992, Geohydrologic framework of the Snake River Plain regional aquifer system, Idaho and eastern Oregon: U.S. Geological Survey Professional Paper 1408-B, 32p.

Serra, O., 1984, Fundamentals of well-log interpretation (v. 1), the acquisition of logging data: Pau, France, Elf-Acquataine; or Amsterdam, Elsevier, 423 p.

APPENDIX

Formation density is <u>not</u> directly proportional to counts per second (I) recorded by the gamma-gamma density logs shown in this report. Rather, density is proportional to the logarithm of the counts per second. The equation used as a basis for calibration of tool response is give by Serra (1984, p. 196):

$$I = I_o \exp[-\mu\sigma_e L]$$

where I = tool response in counts per second
I_o = intensity of gamma-ray source (usually a ^{137}Cs source, of about 20 mCi).
σ_e = electron density of formation (i.e. no. of electrons per unit volume: for most rock forming minerals and water, electron density is approximately proportional to bulk density, σ_b, so that we can express bulk density as $\sigma_b = b\sigma_e$, where b varies from about 0.9 to 1.0 for most minerals and water, but varies somewhat as indicated in Serra (1984, p. 197).
μ = a number characteristic of the source and detector (tool specific) which is determined empirically when calibrating tool response to blocks of known density.
L = source-detector spacing.

Taking the natural logarithm of the above equation and substituting for μ_e, $\sigma_b = b\sigma_e$, one obtains the following equation used as a basis for calibrating density tools:

$$\sigma_b = -[b/\mu L] \cdot \ln[I] + [b/\mu L] \cdot \ln [I_o]$$

which is of the form $\sigma = A \ln I + B$, where A is the slope, and B is the intercept value for σ_b vs. I plotted on semi-logarithmic paper. In practice one is not concerned with values of b, μ, L, and I_o, since they are just components of constants determined empirically.

Hydrogeology, Waste Disposal, Science and Politics
Proceedings 30th Symposium
Engineering Geology and Geotechnical Engineering, 1994

THREE-DIMENSIONAL CHEMICAL STRUCTURE OF THE INEL AQUIFER SYSTEM NEAR THE IDAHO CHEMICAL PROCESSING PLANT

M. McCurry, M. Estes and J. Fromm
Department of Geology, Idaho State University, Pocatello, ID 83209
J. Welhan
Idaho Geological Survey, Idaho State University, Pocatello, ID 83209
Warren Barrash
Center for Geophysical Investigation of the Shallow Subsurface
Boise State University, Boise, ID 83725

Sampling and analysis from the Snake River Plain aquifer using a stainless-steel and teflon constructed straddle-packer system has established detailed vertical profiles of aquifer chemistry from three wells near a major source of low-level waste injection at the Idaho Chemical Processing Plant. Multiple intervals, varying from 4.6 to 6.1 m in length, were sampled between the water table (140.5 mbls - meters below land surface), and approximately 200 mbls to obtain a wide spectrum of metals, anions, radiological and organic components analyses. Measurements were also made at the well sites of important transient parameters (T, Eh, Fe^{3+}, Fe^{2+}, DO and SC). The principal purpose of this ongoing work is to improve our understanding of the third (i.e. vertical) dimension of aquifer chemistry at the INEL as a basis for critically evaluating site-wide monitoring procedures, and, ultimately, for improving fate and transport models for aquifer contaminants within basalt-hosted aquifers.

Chemical and radiological data indicates that substantial systematic vertical and lateral variations occur in the aquifer hydrochemistry - in particular for conservative radiological nuclide concentrations. Radiological data define a three-layered zonation. Ground water within upper and lower zones contain up to 10 times higher concentrations of H-3 and I-129 than in the middle zone. Sr-90 activity is decoupled from H-3 and I-129—relatively high activity was detected within the upper zone nearest the ICPP, but activities elsewhere are very low. Concentrations of radiological constituents within the upper two zones decrease systematically away from the ICPP whereas there is no systematic decline within the lower zone. Other probable contaminants, including Na, Cl and NO_3, exhibit similar systematic behaviors.

Vertical and spatial variations in upper zone chemistry suggests an ongoing input to the aquifer from within the ICPP of H-3 and Sr-90, perhaps from perched zones or from percolation ponds at that site. The origin of anomalously high H-3 and I-129 at the base of the wells is more ambiguous, and may be related to any of the following: 1. inputs from other sites (e.g. TRA or NRF); 2. relicts of past, larger plumes which have been preferentially retained within porous but relatively impermeable basalt strata; or 3. upward leakage from a deeper contaminated aquifer zone below the level penetrated by the monitoring wells. Decoupling of Sr-90 from H-3 and I-129 can be accounted for by their differing sorbtive behaviors. However, the inferred flux of Sr-90 is higher than expected and may indicate a significant role for colloidal transport for that (and possibly other) sorbtive metals (Estes and McCurry, 1994). Our preliminary data suggest that no better than order-of-magnitude results can be expected from fixed-depth, open-hole sampling methods for radiological constituents at the INEL.

Introduction:

Statement of Problem:

The ICPP was a localized source of low-level radioactive waste disposal for over 30 years. Between 1953 and 1989 over 10^4 Ci of waste, mostly as H-3, but also including a wide variety of other radionuclides, were disposed of to the aquifer via an injection well (Figure 1). Additional waste was disposed of to the vadose zone in a ~5 meter deep hole (CPP603) and percolation ponds. Over much of this time aquifer plumes associated with disposal at this and other sites

Location and Geologic Sketch Map of the INEL and Surroundings

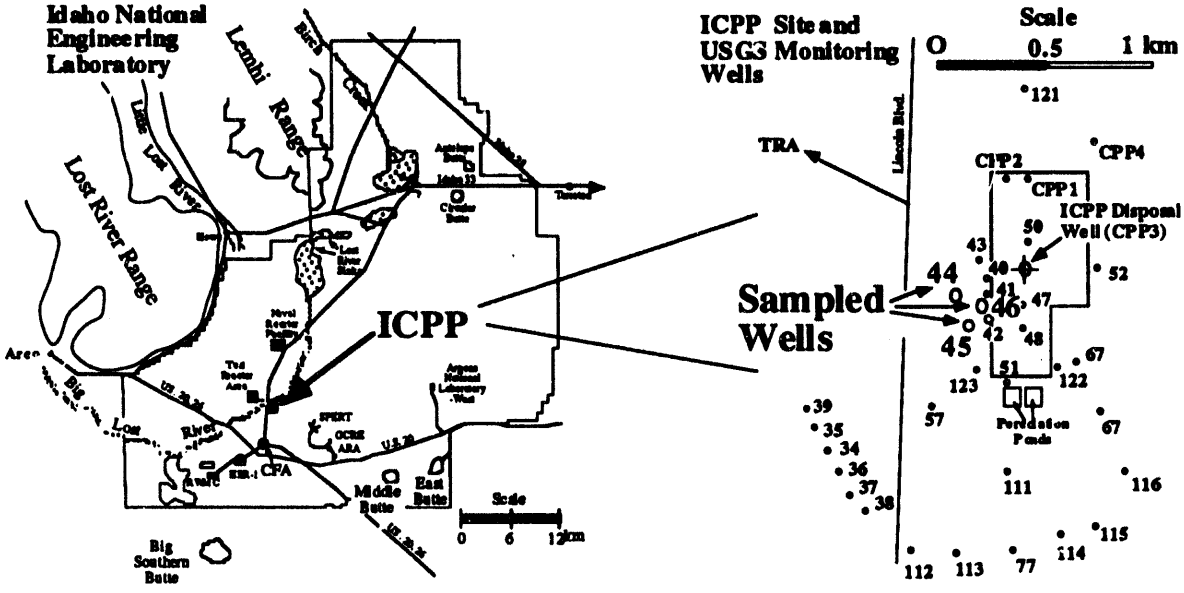


Figure 1. Sketch maps of the INEL illustrating outline of the site and surrounding geographic features (left); ICPP and nearby monitoring wells, including wells sampled for this study (# 44, 45 and 46).

have been monitored via a network of wells, principally by the USGS (e.g., Mann and Cecil, 1990; Lewis and Jensen, 1984). Almost all of the sampling has been from open holes by thief sampler or submersible pumps at fixed depths near the top of the aquifer.

Part of the rational for this sampling strategy is that qualitative and semiquantitative tracer and hydrologic studies suggest that effluent is generally confined to upper parts of the aquifer (e.g., Schmalz, 1959), and that there is a general upward gradient of vertical flow in the aquifer (Mann, 1986). However, tracer studies conducted to date have been qualitative, and could be misleading because of cross-mixing from the existing monitoring well system, which probably attenuated chemical stratification near the ICPP monitoring wells ((Jones, 1961)). In addition, previous thief sampling and hydrologic vertical profiling of wells near the ICPP indicate complex smaller scale upward and downward movements of water and radioactive effluent (e.g., (Barraclough et al., 1966); (Robertson et al., 1974)), which along with the heterogeneous, fractured nature of the host rocks suggest that injected solutes may have pathways to even deeper parts of the aquifer. Significant reversal of the usual upward hydraulic gradient may have been induced near the CPP injection well during periods of high discharge (Mann, personal communication, 1993). There is therefore considerable uncertainty as to the vertical distribution and transport of contaminants within the aquifer system.

The principal purpose of this ongoing study is to employ state-of-the-art sampling and analysis methods from a network of wells surrounding the ICPP, that are open through large intervals, to establish for the first time a detailed three-dimensional chemical and isotopic characterization of plume geometry in that area. This work will ultimately form the basis for making recommendations, as needed, for changes in modeling and sampling practices, reconstruction of existing wells, and/or location and construction of additional wells to improve the regional aquifer monitoring system. In this paper we present preliminary results of radiological and major anion and cations analyses from sampling of three wells (INEL #44, 45 and 46) located west of the ICPP (Figure 1).

Previous Work, Geologic and Hydrologic Setting:

Idaho National Engineering Laboratory (INEL) is located on the eastern Snake River Plain, approximately 60 km west of Idaho Falls. The reader is referred to excellent recent summaries emphasizing the volcanic geology and stratigraphy of the INEL area by Hackett and Smith, 1992 (1992) and Kuntz et al., 1992 (1992). Additional general geologic, physiographic, and meteorological surveys of the INEL are provided by Nace et al. (1972; 1975). The overall stratigraphic framework for the INEL, to a depth of 200-300 meters has been established by Anderson (1991), based primarily upon detailed examination of numerous geophysical well logs (Figure 2).

The study area is underlain by approximately 1-km of interlayered, nearly flat-lying, thin Quarternary basalt and polygenetic clastic sedimentary rocks, and minor amounts of silicic tuff. These in turn overlie several kilometers of late Tertiary silicic ignimbrites associated with the Yellowstone volcanic track (Pierce and Morgan, 1992). The basalt-sediment sequence is intruded in some areas by silicic domes and laccoliths, some of which may be buried beneath the INEL (Anderson, personal communication, 1992). It may also be intruded by numerous NNW trending basalt dikes (cf. Rodgers et al., 1990), although none are exposed at the surface. Few, if any major faults cross the SRP, in contrast to fault bounded ranges on either side (Rodgers et al., 1990).

The sample wells penetrate the upper portion of an aquifer hosted within a stratigraphically complex assemblage of 1 to 10-meter-thick, lobate, highly fractured basaltic lava flows and minor, thin sediment interbeds (Figure 2) (Chase, et al., 1964; Morin et al., 1993; (Bartholomay, 1990). Fractures within the flows are commonly choked with fine-grained sediment similar to and probably elutriated from sediment interbeds. Most flows are separated by vesicular breccia zones which are the primary conductive zones within the aquifer (Barrash et al., 1994).

Alteration and authigenic mineralization of the basalts within the upper 100 meters of the aquifer is minimal. Authigenic calcite is common, though volumetrically minor, particularly along tops and bottoms of flows in fractures and vesicles. Additional authigenic minerals include hematite(?), goethite and quartz. Clays are common, but with the possible exception of colloidal clays, are apparently allogenic (cf. Estes and McCurry, 1994).

The base of the wells penetrate into a sequence of unusually thick and massive flows defined by Anderson as the I-flow group (Figure 2). Based on downhole televiewer log thick parts of this group contain few fractures, and are dense-looking. However, they contain prominent horizontal and vertical vesicular zones which are apparently not associated with flow contacts. In addition, based upon examination of correlative parts of the I-group exposed in core from Well #123, the dense appearing parts of the flow group have zones of high intergranular (i.e. diktytaxitic) porosity. Knutson, et al., 1990, have documented porosities as high as 15% in similar rocks elsewhere at the INEL; therefore these apparently "massive" basalts may have significant water-bearing capacity, and conductivity.

Major hydrologic and water chemistry features of the region are described by Wood and Low (1986), and more specifically for the INEL area by Robertson (1974), Mann (1989), Olmsted (1962) and Lewis and Goldstein (1982). Site-wide background (i.e. natural) concentrations for a variety of radiological and chemical constituents are documented by Orr, et al. (1991) and McLing (ISU M.S. Thesis, in progress, 1994), and specifically for the ICPP area by Fromm (ISU M.S. Thesis, in progress, 1994). Estimates for selected solutes are listed in Figure 3.

Major features of the background major-solute hydrochemistry are consistent with derivation from ranges bordering the northwest and north part of the INEL, and recharge zones concentrated along the Big Lost River, Little Lost River, Birch Creek and Mud Lake (Busenberg et al. 1993; Orr and Cecil, 1991; Rogers, et al., 1974). Spatial variations, based upon reconnaissance two-dimensional modeling of the aquifer, are documented by Olmsted (1962) and McLing (ISU M.S. Thesis, in progress, 1994), and are better explained by mixing of waters from

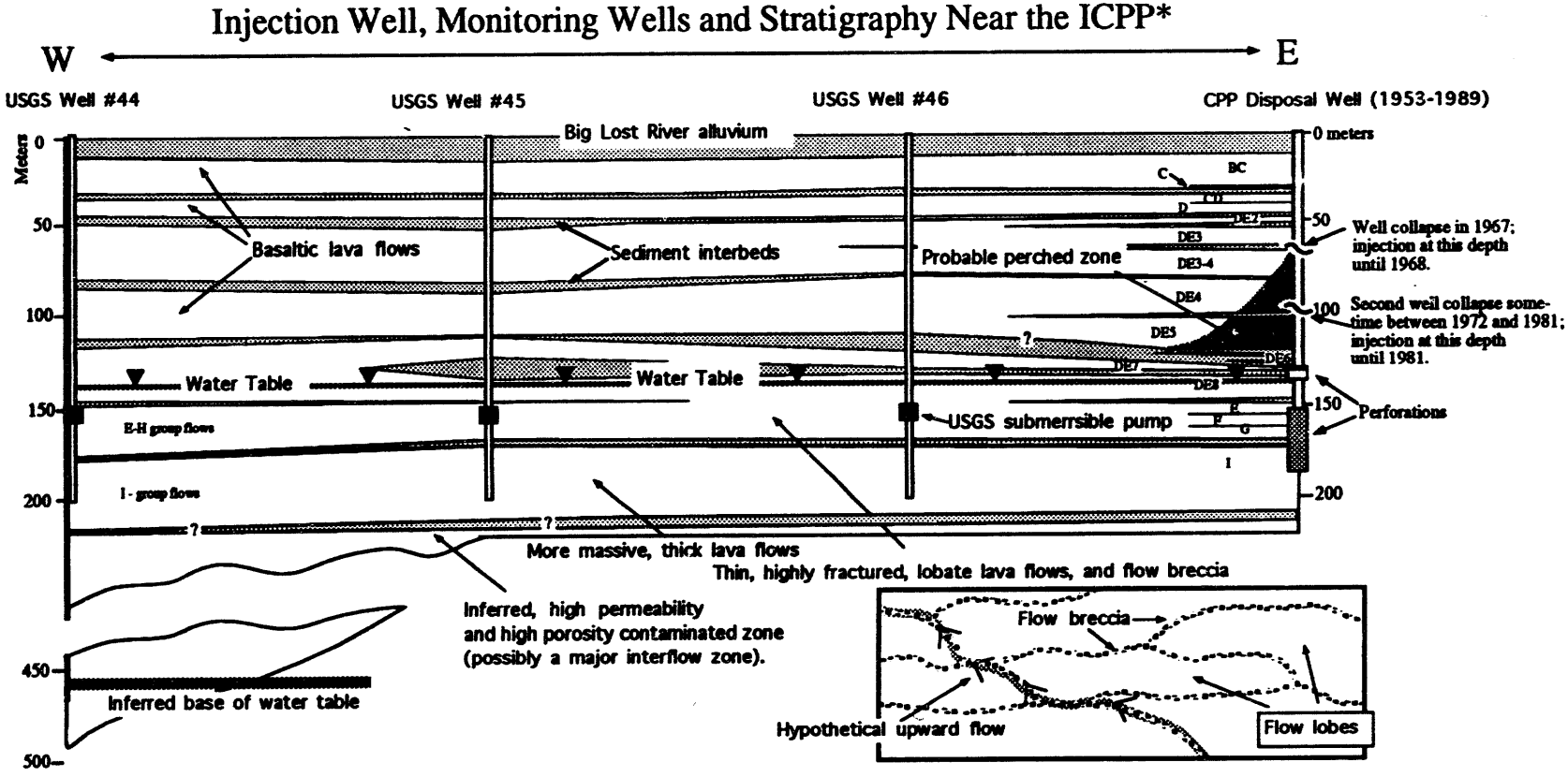


Figure 2. A simplified representation of stratigraphy west of the ICPP based upon down-hole electric and TV logs and driller logs; ICPP interpretation and basalt flow unit designations based upon Anderson, 1991; injection well history work in progress by Fromm (and Fromm, et al., 1994). Inset figure schematically illustrates the lobate nature of lava flows, and shows a possible vertical flow path for ground water along highly transmissive breccia zones at flow contacts—vertical flow is possible through such zones, even if fracture-flow is impeded by infiltration of silt and clay. Wells are projected along an E-W line through the ICPP and are space approximately to scale.

different recharge zones and deep basin water than from water-rock interactions (cf. Wood and Low, 1986, 1988).

Busenberg et al. (1993) used CFC-dating methods to suggest a range in groundwater residence times of from 4 to >50 years, with relatively young recharging water being the dominant type sampled by the INEL monitoring well system—consistent with other evidence for relative innertness of the aquifer for major solutes. Their data also are interpreted to indicate that the younger water has not equilibrated with deep vadose zone gas, but has retained signatures inherited from water-vapor equilibration with near-surface soil zone.

Barrash, et al. (1994) and Monks, et al. (1993) recently characterized the hydrostratigraphy of wells 44 through 46 as having a two-layer zonation: 1. a highly conductive upper zone consisting of numerous, highly permeable zones (conductivities of about 3000 meters/day); 2. a lower zone of much lower conductivity (conductivities of about 0.03 meters/day). Contact between the zones occurs at a depth of ~177 meters and correlates with a lithologic transition from thinly layered to more massive flows of the I-group. Vertical flow is stagnant in the lower zone and upward in the upper zone in all the wells. Barrash, et al. (1994) also infer that a third, highly permeable zone exists below the depth penetrated by wells 44-46.

Methodology:

Sampling was undertaken during June-August 1982 (wells 44) and July-October 1983 (wells 45, 46) using a specially designed stainless-steel and teflon constructed straddle-packer system (Olsen, 1994). Duplicate samples were taken of selected intervals by thief sampler and in-situ U.S. Geological Survey submersible pumps, for comparison of open-hole sampling techniques with the packer samples. Sampled intervals were selected on the basis of several criteria: 1. ground water producing zones; 2. packer seal integrity; 3. risk to packer (e.g., the lower parts of well #45 were not sampled because of excessive risk of losing the packer from debris in and tortuosity of the well); 3. complete well coverage. They are illustrated in Figure 3.

Standard operational procedures were established for sampling, filtering, preservation and sample storage, and are outlined in the project QA/QC report. Field measurements were obtained for transient parameters including water temperature, pH, Eh, dissolved oxygen (DO), specific conductance (SC), alkalinity, total filtered and unfiltered ferric and ferrous iron. Measurements of parameters sensitive to exposure to air (T, pH, Eh, SC and DO) were made using electrodes inserted into an enclosed flow cell. Alkalinity and DO (duplicate) were determined with titration procedures.

All samples were taken directly at the well-head though a teflon valve off the stainless steel riser pipe (Olsen, 1994). Subsamples were prepared for the following analyses: 1. major cations and silica; 2. trace elements (by ICP-MS); 3. major anions and nutrients; 4. VOC's; 5. BNA's; 6. radiologicals (H-3, Sr-90, I-129, Cl-36, U-235; Pu-239/40; Pu-238; Co-60; Cs-137; gross a, b, g); 7. stable isotopes (O-18, H-2, C-13). No significant activities were found in the sampled wells for a variety of these constituents (e.g., Cl-36, U-235; Pu-239/40; Pu-238; Co-60; Cs-137, VOC's and BNA's). This report focus' on the major solute, H-3, I-129 and Sr-90 hydrochemistry of the target wells.

An important assumption made in the following discussion regarding comparisons of water samples from well 44, with those of wells 45 and 46, is that the aquifer chemistry has not varied substantially during the one year gap in time between sampling. There is no simple way of evaluating this problem: previous work based upon open-hole sampling methods are not reliable for this purpose for reasons stated later in this report. However, the highly conductive nature of parts of the aquifer indicate it would respond rapidly to fluctuations in input, etc. This is an open question which we believe should resolved by a dedicated straddle-packer-based sampling program.

TABLE 1. Water quality analyses (µg/L; pCi/L)*

Method	DP	DP	DP	TS	TS	TS	UP	P	P	P	P	P	P	P	DP	TS
Location	INEL44	INEL45	INEL46	INEL44	INEL45	INEL46	INEL44	INEL44	INEL44	INEL44	INEL44	INEL44	INEL44	INEL44	INEL45	INEL45
Year*	1992	1992	1992	1992	1992	1992	1992	1992	1992	1992	1992	1992	1992	1992	1993	1993
Depth (feet)	499	503	502	500	500	500	499	467-482	495-515	519-534	535-555	557-577	580-600	580-base*	499	500
Ca	58,000	58,500	60,500	60,000	61,000	61,000	59,500	62,000	60,000	58,700	60,167	59,000	49,333	52,000	56,000	55,000
Cr	6.4	6.5	6.7	6.3	6.3	6.0	5.4	5.9	5.7	6.0	6.2	5.8	5.6	5.2	5.5	6.0
Mg	14,900	15,800	16,300	15,000	15,500	16,000	15,000	15,000	15,000	15,000	15,100	15,750	16,000	16,000	14,300	14,600
K	2,480	2,800	2,750	2,400	2,600	2,500	2,100	2,300	2,250	2,270	2,380	2,700	3,200	3,300	2.6	2.4
SiO_2	21,400	23,500	21,400	-	22,000	21,000	21,100	20,600	21,200	21,000	21,300	21,400	25,200	24,400	22400	23,000
Na	10,100	10,000	12,000	10,000	10,000	15,000	10,000	9,900	10,500	11,000	10,300	9,750	15,300	15,000	11,500	10,300
Sr	295	315	290	290	310	280	305	300	305	303	310	315	293	290	240	340
Cl^-	18,000	20,000	23,000	-	21,000	29,000	19,000	20,000	18,000	20,000	20,000	20,000	27,500	25,000	19,400	19,000
F^-	200	200	200	-	200	200	300	200	190	200	240	230	300	300	160	160
$SO_4(2-)$	24,600	25,000	27,800	-	26,300	28,200	28,000	28,000	26,500	29,000	24,000	26,000	24,500	25,000	27,000	23,500
Alk. (SL)	279,000	276,000	279,000	-	272,000	266,000	279,000	280,000	276,000	278,000	279,000	284,000	251,000	261,000	264,000	267,000
Alk. (field)	-	-	-	-	-	-	220,600	250,100	232,000	-	183,000	262,000	214,000	256,000	-	-
Nit.	1,250	1,300	2,930	1,260	1,290	5,150	1,255	1,240	1,090	1,290	1,085	1,310	2,100	2,025	1,200	1,230
Phos.	70	45	45	80	170	70	65	30	30	<50	56	20	20	20	80	60
H-3 (pCi/L)	400	1,100	3,100	1,100	800	4,000	950	1300	500	750	400	300	7,250	6,500	1,600	1,700
I-129	-	-	-	-	-	-	-	0.23	0.21	0.26	0.20	0.13	0.97	0.87	-	-
Sr-90	4.1	16.9	17.8	3.2	1.0	13.1	7.9	9.8	8.8	8.5	5.5	4.9	4.3	6.1	3.7	-
Method	P	P	P	P	P	TS	P	P	P	P	P	P	P	P	P	
Location	INEL45	INEL45	INEL45	INEL45	INEL45	INEL 44	INEL46	INEL46	INEL46	INEL46	INEL46	INEL46	INEL46	INEL46	INEL46	
Year	1993	1993	1993	1993	1993	1993	1993	1993	1993	1993	1993	1993	1993	1993	1993	
Depth (feet)	462-477	480-495	500-515	519-534	538-553	505	464-483	488-506	507-525	531-549	553-571	575-593	594-612	595-613	612-629	
Ca	51,200	52,500	51,300	53,000	55,000	55,200	58,600	60,000	57,500	56,200	58,300	58,900	56,700	34,500	34,800	
Cr	6.9	5.8	6.9	5.3	5.7	6.9	6.9	6.4	8.4	8.5	7.9	8.5	9.8	3.4	5.2	
Mg	14,500	14,400	15,000	14,600	15,000	14,700	15,700	15,600	15,100	15,400	15,900	16,300	15,700	15,330	15,300	
K	2,520	2,500	2,640	2,600	2,400	2,050	2,240	2,150	2,160	2,230	2,200	2,320	2,010	2,250	2,340	
SiO_2	24,500	23,500	24,000	24,000	22,800	23,000	21,000	20,000	20,000	21,000	22,000	23,000	23,400	27,100	27,400	
Na	11,500	11,500	10,800	11,800	10,200	8,590	14,700	13,200	10,200	9,850	9,480	8,640	8,590	8,230	8,020	
Sr	310	305	310	360	390	290	290	310	320	305	305	312	305	210	210	
Cl^-	23,800	21,500	20,400	21,000	23,000	15,800	27,700	24,500	19,300	19,000	19,300	19,300	19,100	13,400	13,900	
F^-	205	170	210	210	160	-	200	135	150	140	110	120	-	-	-	
$SO_4(2-)$	22,200	24,500	23,800	25,000	25,000	-	23,000	29,000	29,000	-	25,500	27,000	-	-	-	
Alk. (SL)	256,000	266,000	259,000	266,000	272,000	-	271,000	276,000	280,000	-	290,000	287,000	-	272,000	-	
Alk. (field)	-	-	-	-	-	-	-	-	-	-	-	-	-	-	-	
Nit.*	1,560	1,290	1,220	1,290	1,240	-	4,830	3,270	1,630	1,350	1,470	1,300	-	-	-	
Phos.*	110	245	360	260	120	-	80	<50	<50	80	90	50	-	-	-	
H-3 (pCi/L)	4,500	3,000	2,700	3,200	1,700	-	8,000	5,000	2,500	3,200	2,000	1,300	1,300	900	4,930	
I-129	-	-	-	-	-	-	-	-	-	-	-	-	-	-	-	
Sr-90	3.7	2.7	2.4	3.5	4.9	5.2	22.0	16.5	8.6	6.5	8.9	4.9	7.5	-	2.8	

* All concentrations in µg/L; radiological activities are in pCi/L. Symbols: P - straddle-packer; UP - uninflated packer; TS - thief sampler; DP - 8.5U.S. Geological Survey submersible pump. Year is indicated to indicate times samples were taken (1992: July - August; 1993: June - November). Alkalinities (as HCO_3) are listed as d16300etermined by field titration (Alk. (field)) and by a contract laboratory (Alk. (SL)); discordances between field and lab data are not well understood at this time. Depths are in feet below lan2320d surface. 580-base: indicates upper packer was inflated, lower packer was uninflated (samples interval from 580 to base of well—640 feet). Hyphens indicate no data was obtained. Total nitrogen (Nit.) and phosphorus (Phos.) are as N and P, respectively. Accuracy and precision of the data, based upon duplicate analyses and laboratory data, is estimated at < 10% RSD (excluding alkalinity).

Aquifer Chemistry:

Metals and Anions:

Metal and anion hydrochemistry of ground waters from wells 44 through 46 exhibit a variety of systematic variations. Data are listed in Table 1 and a representative group of solutes are illustrated in Figure 3. Two prominent patterns emerge from these data: 1. there is a distinctive three-layered pattern to the data for many solutes, in particular Na, Cl and NO3 (expressed in the Figures and Table as N), while other solutes exhibit little or no systematic vertical variation. These are defined from top to bottom, respectively, as Zone 1, Zone 2 and Zone 3. 2. The same solutes exhibit a systematic decline in concentration away from the ICPP

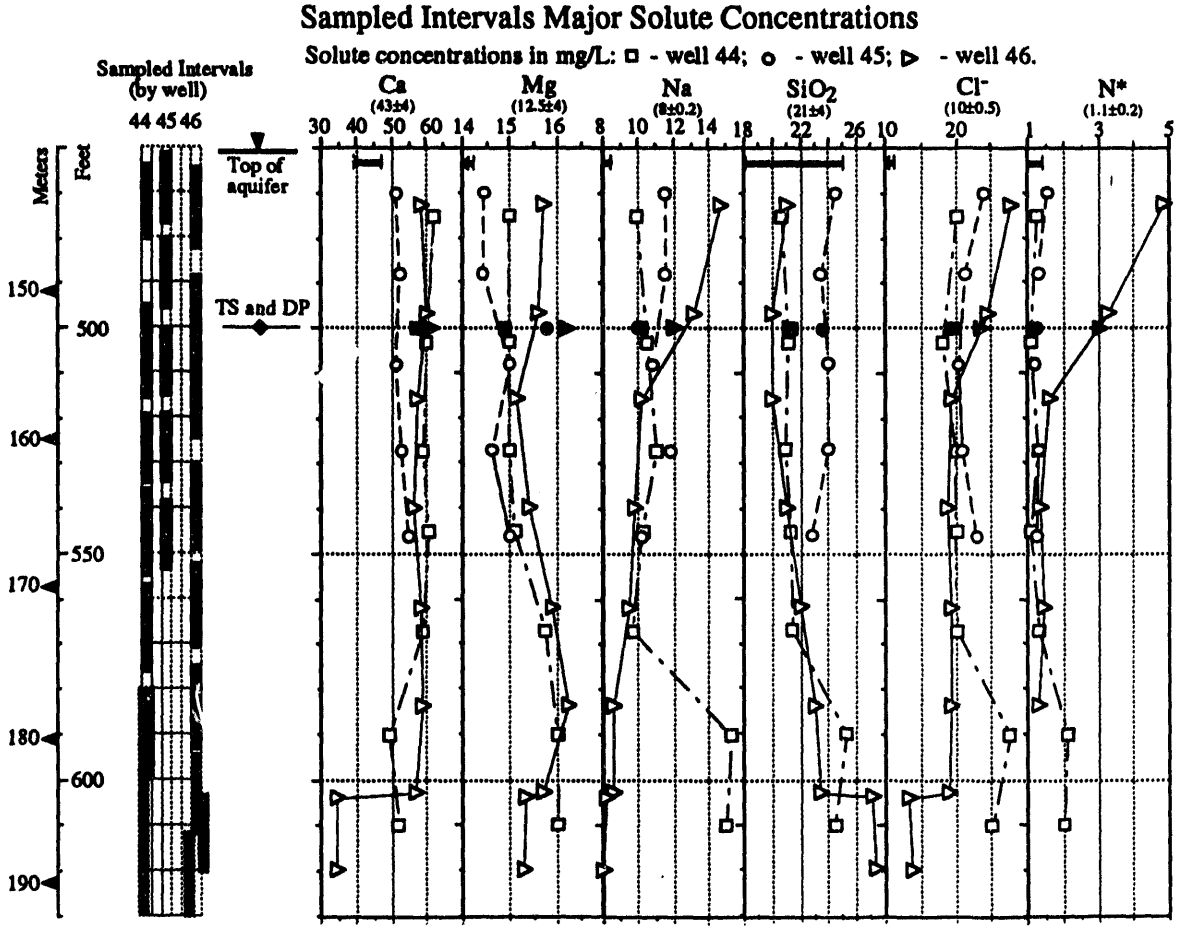


Figure 3. Selected major solutes are plotted against depth sampled by the straddle-packer system. Solute concentrations are in mg/L; total phosphorous is plotted as P; total nitrogen as N. Sampled intervals are shown with solid bars. Estimates of natural (background) solute concentrations are shown in parentheses and with range bars at the top of each plot. Thief and USGS pump samples (500') are illustrated with filled symbols for the respective wells.

within the upper zone, but exhibit no systematic variation in concentrations with respect to the ICPP in the lower two zones. Zone 2 has the greatest consistency among the wells and is described first.

Zone 2, from 158 to 175 mbls (meters below land surface), is characterized by essentially flat vertical gradients in solute components. Concentrations are near inferred background (BK) for some (e.g., SiO2 and NO3). Significant exceptions include Ca (10-50% above BK), Mg (20-30% above BK), Na (20% above BK) and Cl (100% above BK). Although uncertainties for our

inferred background values have not been rigorously quantified we believe these deviations are significant and assume therefore that direct or indirect anthropogenic processes have played a role in elevating their values.

Several constituents (e.g., SiO_2 and Mg) exhibit vertical variations greater than would be expected from analytical uncertainties. Although trends are subtle, concentrations of both increase slightly with depth.

Zone 1, from 140 to 158 mbls, is distinguished by steep upward gradients in Na, Cl and NO_3. The upward gradients decrease systematically to the west (in projection) from the ICPP, from wells 46 to 44. These variations are shown in Table 2 as concentration ratios. Nearest the ICPP (well 46) NO_3 increases by nearly a factor of 3.6, while Na and Cl increase upward by about 50%. These gradient decrease by about half at well 45, and are essentially flat at well 44. Little variation is exhibited by other constituents.

Zone1 concentration ratios

Component	Well 44	Well 45	Well 46
Na	0.90	1.1	1.5
Cl	1.00	1.2	1.5
N	0.96	1.3	3.6

Table 2. This table lists ratios of concentrations of Na, Cl and NO_2 + NO_3 as N between the top of Zone 1 and top of Zone 2 for INEL Wells 44-46.

Zone 3, from 175 to base in well #44 and from 180 to base in well #46, is distinguished by step-wise increases and decreases in solution concentrations, and by a lack of correlation in concentrations with distance to the ICPP. Several constituents exhibit systematic patterns of variation, e.g., Ca decreases downward by 15% and 40% in wells 44 and 46; SiO_2 increases downward by 20% in both wells. Nitrate also increases downward in well 44, but no analyses are yet available for comparison with the other wells.

However, discordant variations occur among other solutes. For example, Na decreases downward by about 20% in well 46 (to inferred background concentration), while it increases downward by 75% in well 44.

Comparisons are made between data gathered by the packer with analyses obtained sampling from the open-borehole with the U.S. Geological Survey dedicated submersible pump, and thief sampler. As illustrated in Figure 3, samples taken from the same depth (160 meters) are comparable for many solutes, particularly those most likely to consist partially of waste products (i.e. Na, Cl and NO_3). Note, however, that those concentrations are not reflective of the complex aquifer formation (i.e. host rock) hydrochemistry, particularly near the ICPP.

Thief samples were taken at widely separated time intervals (~1 year) from wells 44 and 45, to evaluate possible temporal variations in aquifer chemistry (Table 1). Although most data are similar within uncertainties associated with analytical and sampling errors, some significant differences were observed: 1. Na and Cl decrease by ~15% in well 44 (but not in well 45); 2. 2. H-3 activity increases by ~200% in well 45. Interpretation of these data is complicated because we now have clear indications of vertical variations in aquifer chemistry which exceed these ranges. Variations in vertical flow rates (e.g., in response to production pumping cycles at the ICPP) could induce changes in borehole water chemistry at any particular depth by mixing from various levels, producing a possible artifact of the type observed. This is a serious limitation of open-borehole sampling methods near the ICPP.

Radiological Activities:

Patterns among radiological constituents are similar to those of the major solutes, and even better define the proposed three-layer zonation in hydrochemistry. Only three radionuclides were detected, in decreasing order of activity: H-3 >> Sr-90 > I-129. Data are listed in Table 1, along with major solutes concentrations, and are plotted in Figure 4. Zone boundaries occur at the same depths as previously described for the major solutes.

Zone 2 is characterized by flat gradients in radiological concentrations. However, in contrast to the major solutes, there is a systematic decline in activities of H-3, and possibly Sr-90, away from the ICPP (I-129 is not included because no analyses are available from either of wells 45 or 46). The pattern is best demonstrated by H-3; concentrations decline from about 2500 pCi/L in well 46 to approximately 500 pCi/L in well 44.

Strontium-90 may also decrease slightly away from the ICPP. The Sr-90 data are complicated by a cross-over of well 44 and 45 data near the top of Zone 2. However, we interpret this as a result of disturbance of the well rather than reflecting changes in formation chemistry. Note that thief and dedicated pump (U.S. Geological Survey) samples taken shortly before installing the packer into the well, are much lower than those obtained by the packer. We tentatively suggest that the "anomalously" high Sr-90 data from the packer samples is a result of detachment of particles from near the borehole (because of disturbance to the formation by pumping from the confined interval), which had adsorbed Sr-90 during peak periods of plume activity, effectively doubling the actual aquifer Sr-90 activity.

Zone 1 is characterized by steep upward increasing gradients in H-3 and Sr-90 concentrations. The break in activity occurs at the same depth as described above for some major solutes. They also exhibit a decline in gradient in westward projection from the ICPP, to the flat "background" of Zone 2. Maximum H-3 concentrations decrease from 8000 pCi/L (well 46), to 4500 pCi/L (well 45), to 1300 pCi/L (well 44). Maximum Sr-90 concentrations decrease from 22 pCi/L (well 46) to ~4 pCi/L (well 45). Sr-90 concentrations is Zone 1 from well 44 are complicated for the same reasons stated above for Zone 2. However, thief and U.S. Geological Survey pump data suggest that it is approximately the same as for well 45.

Curiously, there is no increase in I-129 through Zone 1, at least at well 44. H-3 increases by about a factor of two, resulting in a decrease in I-129/H-3 activity ratio from ~4 to $2x10^{-3}$. Variations in I-129 activities are within analytical uncertainties. I-129 and H-3 should have nearly identical, nonreactive (i.e. conservative) behaviors during transport. Both occur at above background levels. The decoupling of their concentration patterns in Zone 1 would therefore seem to require a nearby mixing source of contaminants characterized by a very high H-3/I-129 ratio (Fromm, ISU M.S. Thesis, in progress, 1994).

In contrast to Zone 1, Zone 3 is distinguished by a prominent step-wise increase in both H-3 and I-129. The increases are by about a factor of 10 in H-3 activity for well 44, and are more modest (~5X) for well 46. I-129/H-3 activity ratios decrease downward from Zone 2 to Zone 3 from ~4 to $1.3x10^{-3}$—similar to the transition to Zone 1. Sr-90 exhibits no change from Zone 2. Two salient aspects of these preliminary data are that: 1. the vertical patterns of nonconservative (Sr-90) and conservative (H-3, I-129) radionuclides activities are decoupled; 2. there is not a decline in radionuclides activities away westward from the ICPP (H-3 activities are about 15% higher in well 44 than in well 46).

Summary and Discussion:

Vertical and horizontal patterns in ground water hydrochemistry define a three-fold zonation of the aquifer west of the ICPP: 1. an upper zone (Zone 1), extending approximately 15 meters downward from the water table; 2. a middle zone approximately 15 meters thick; 3. a lower zone extending from a depth of ~171 meters to the base of the wells (~200 meters).

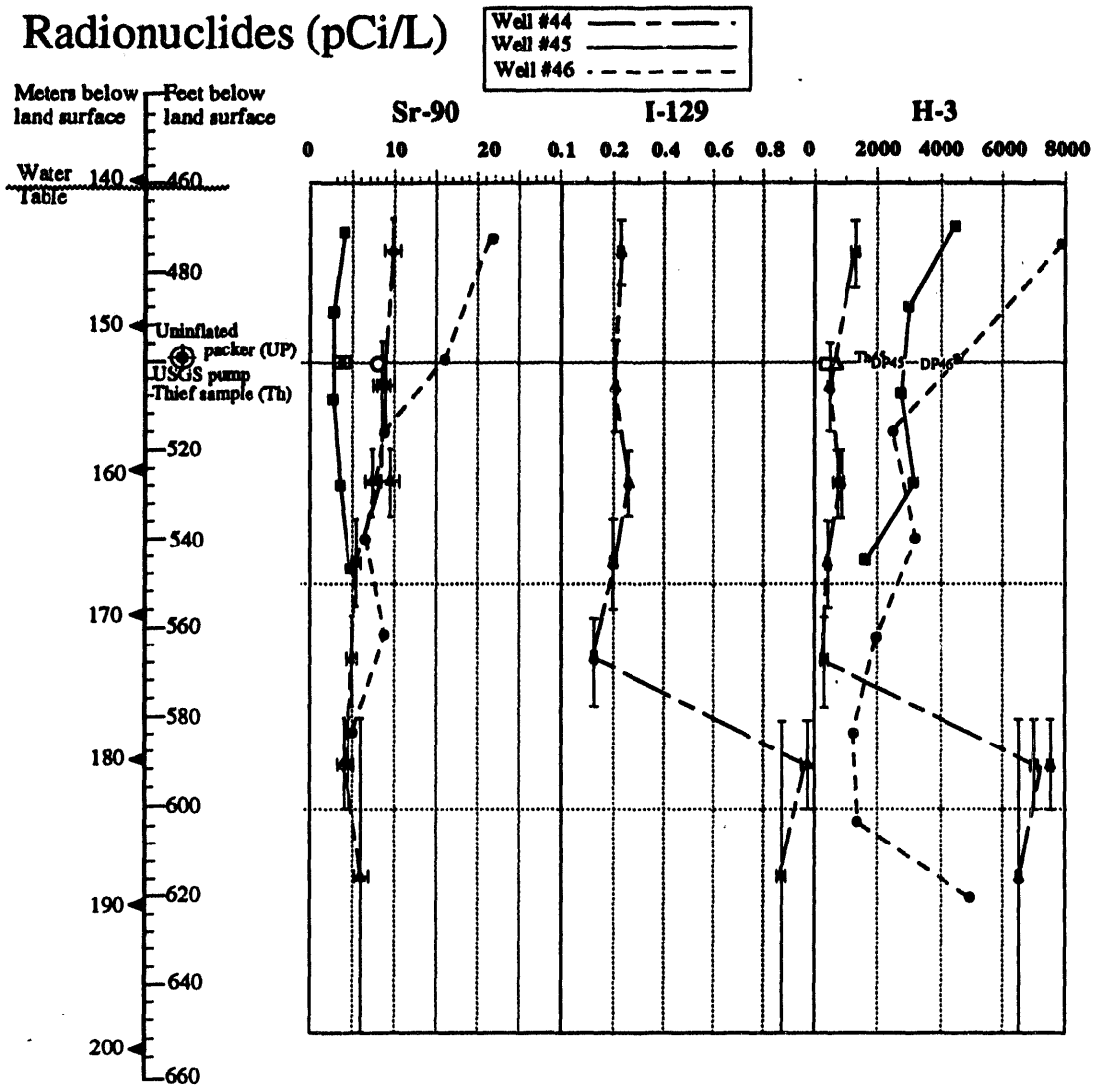


Figure 4. Plots of H-3, I-129 and Sr-90 vrs. depth for wells 44 through 46. Units are in pCi/L. Thief (TS) and U.S. Geological Survey open-hole submersible pumps sample (DP) analyses also plotted for comparison as follows: Open square, circle and triangle - USGS pump, uninflated packer and thief sampler, respectively for Well #44; Th45 and DP45, DP46 - thief and dedicated pump analyses for wells 45 and 46 (analyses plot at center of symbols).

Zone 1 is characterized by steep upward gradients in H-3 and Sr-90 (and possibly I-129) activities and by increases in Na, Cl and NO3. All of these constituents are principal components of the ICPP waste stream (Fromm, ISU M.S. Thesis, in progress, 1994). They also exhibit a systematic horizontal decline away from the ICPP.

A constraint on the of the source of contamination can be obtained by analyzing ratios of contaminants, and is described in this volume by Fromm et al., 1994. In addition, steep concentration gradients, extending to the top of the water table, suggest that the source is from the vadose zone (i.e. perched zones or percolation ponds within the ICPP) rather than from the injection well (CPP3 was deactivated in 1989).

Although infiltration from known perched zones and from percolation ponds is qualitatively consistent with much of our data there are significant anomalies. Fromm et al. (1994) describe several. In addition, it is curious that significant Sr-90 is still present in the upper part of the

aquifer; past Sr-90 plumes were related to injection of low levels of Sr-90 directly into the aquifer from the CPP3 injection well. Sr-90 is strongly adsorbed to mineral surfaces; preliminary modeling suggests that little if any should reach the aquifer from the inferred surface sources. This suggests the interesting possibility that Sr-90 may have either another source or, a different transport mechanism (such as via colloidal particles, Estes and McCurry, 1994).

Zone 2 is characterized by flat gradients in concentrations and activities. H-3 activity drops systematically away from the ICPP, suggesting that waste from that site has at least some influence on the chemistry of the zone. However, in contrast to the upper zone, no other constituents exhibit systematic spatial variations. Flat concentration gradients within Zone 2 may be a result of strong vertical flow and cross-mixing over that interval.

The most intriguing patterns in aquifer hydrochemistry occur in Zone 3. This zone is characterized by a step-wise change in a wide variety of solute concentrations and activities, several of which are of opposite direction between wells, and none of which appear to correlate with distance to the ICPP. Conservative radiological constituents (H-3 and I-129) exhibit concordant order-of-magnitude downward increases. In well 44 these correlate with increases in Na, Cl and NO_3. This pattern is similar to increase observed in Zone 1. Prominent exceptions are the lack of increase in Sr-90, and proportionate increases in I-129 and H-3 activities.

Samples from well 46 are distinguished from well 44 by significant downward decreases in Na and Cl. Na and Cl concentrations generally correlate closely with radiological activities in ICPP waste plumes. Such correlations are to be expected because of the relatively conservative nature of the solutes, and composition of the waste stream from the ICPP (Fromm, ISU M.S. Thesis in progress, 1994). The inverse correlation within Zone 3 of well 46 is therefore surprising, and cannot be accounted for by any simple mixing or sorbtion mechanisms.

The boundary between Zones 2 and 3 correlates with a significant change in host rock lithology. Above the contact the host rocks are dominantly, thin, highly fractured basalts and basalt breccia: hydraulic conductivites are up to 3000 m/day. Below the contact the basalts are much more massive (although no necessarily dense, as previously described); conductivity is ~0.03 m/day (Barrash, et al., 1994). These features would suggest a much greater residence time for possible intergranular water (i.e. in diktytaxitic cavities), and water-rock reaction may account for the increase in SiO_2 observed at this depth.

Three possible mechanisms have been examined for the anomalous features of Zone 3: 1. inputs of contaminants from distant sources (e.g., TRA or NRF); 2. residual contaminants trapped in porous but relatively impermeable basalt during higher periods of plume activities; 3. inputs from a possible porous and transmissive zone located below the level penetrated by the monitoring wells. Preliminary analyses of these mechanisms suggests that none are adequate for explaining all aspects of Zone 3 three hydrochemistry. However, many aspects of the chemistry could be accounted for most simply by inputs from a relatively highly contaminated, highly transmissive zone (scenario 3). The existence of such a zone has been proposed on the basis of independent hydrological information (e.g., Barrash et al., 1994). However, additional work is needed to better define extent and magnitudes of anomalies which are not accounted for by this model, and to verify that this inferred zone does in fact exist.

Conclusions:

Significant vertical heterogenities, on the scale of 10-20 meters, occur in major components and radiological concentrations within the aquifer system. Steep vertical concentration gradients occur within the aquifer despite cross-mixing through the monitoring wells and general upward convective flow within the system. These indicate continued input of low-level waste to the top of the aquifer from the ICPP, and hint at the existence of a more contaminated zone at depth. Decoupling of Sr-90 from H-3 and I-129 near the base of the wells, and relatively high Sr-90 activities near the top of the aquifer suggests a possible nonaqueous transport mechanism for that solute.

Straddle-packer data suggest that open-hole measuring techniques could be expected to yield no better than order of magnitude estimates of radionuclide concentrations for aquifer plumes.

Acknowledgments:

We acknowledge funding from the State of Idaho, Dept. of Health and Welfare, INEL Oversight Program; J. Fromm acknowledges funding from a DOE EPSCoR Apprenticeship Program. We gratefully acknowledge Dr.Bill Hackett and Dr. Dick Smith, EG&G, Idaho, for their assistance in obtaining samples of well core, and for their interaction and guidance in attacking the problem of basalt alteration.

List of References:

Anderson, S. R., 1991, Stratigraphy of the unsaturated zone and uppermost part of the Snake River Plain aquifer at the Idaho Chemical Processing Plant and Test Reactors Area, Idaho National Engineering Laboratory, Idaho: U.S. Geological Survey, 91-4010.

Barraclough, J. T., Teasdale, W. E., Robertson, J. B., and Jensen, 1966, Hydrology of the National Reactor Testing Station, Idaho, 1966, IDO-22049-03.

Barrash, W., Morin, R. H., Wood, S. H., Bennecke, W., Anderson, S. R., and Jensen, R. G., 1994, Hydrostratigraphic interpretation of the upper portion of the Snake River Plain aquifer near the Idaho Chemical Processing Plant at the INEL, Proceedings of the 1994 Annual Symposium on Engineering Geology and Geotechnical Engineering.

Bartholomay, R. C., 1990, Mineralogical correlation of surficial sediment from area drainages with selected sedimentary interbeds at the Idaho National Engineering Laboratory, U.S. Geological Survey Water-Resources Investigations Report 90-4147, 18 p.

Busenberg, E., Weeks, E. P., Plummer, L. N., and Bartholomay, R. C., 1983, Age dating ground water by use of chlorofluorocarbons (CCl3F + CCl2F2), and distribution of chlorofluorocarbons in the unsaturated zone, Snake River Plain aquifer, Idaho National Engineering Laobratory, Idaho, U.S. Geological Survey Water-Resources Investigations Report 93-4054, 47 p.

Estes, M., and McCurry, M., 1994, Concentrations and compositions of colloidal particles in groundwater, near the ICPP, Idaho National Engineering Laboratory, Idaho, Proceedings of the 1994 Annual Symposium on Engineering Geology and Geotechnical Engineering.

Fromm, J., McCurry, M., Hackett, W. R., and Welhan, J., Idaho Chemical Processing Plant (ICPP) injection well: Operation, history and hydrochemical inventory of the waste stream, Proceedings of the 1994 Annual Symposium on Engineering Geology and Geotechnical Engineering.

Hackett, W. R., and Smith, R. P., 1992, Quaternary volcanism, tectonics, and sedimentation in the Idaho National Engineering Laboratory arera, *in* Wilson, J. R., eds., Field Guide to Geologic Excursions in Utah and Adjacent Areas of Nevada, Idaho, and Wyoming: Salt Lake City, Utah Geological Survey, p. 1-18.

Jones, P. H., 1961, Hydrology of waste disposal National Reactor Testing Station Idaho: Prepared on behalf of the U. S. Atomic Energy Commission, Idaho Operations Office, Idaho Falls, Idaho, IDO-22042-USGS.

Knutson, C. F., McCormick, K. A., Smith, R. P., Hackett, W. R., O'Brien, J. P., Crocker, J. C., 1990, FY 89 report RWMC vadose zone basalt characterization, Informal Report EGG-WM-8949 prepared by EG&G, Idaho, for the U.S. Department of Energy, 126 p.

Kuntz, M. A., Covington, H. R., and Schorr, L. J., 1992, An overview of basaltic volcanism of the eastern Snake River Plain, Idaho, *in* Link, P. K., Kuntz, M. A., and Platt, L., eds., Regional geology of eastern Idaho and western Wyoming, Geological Society of America Memoir, p. 227-267.

Lewis, B. D., and Goldstein, F. G., Evaluation of a predictive ground-water solute-transport model at the Idaho National Engineering Laboratory, Idaho, U.S. Geological Survey Water Resources Investigations 82-25 (IDO-22062), 71 p.

Lewis, B. D., and Jensen, R. G., Hydrologic conditions at the Idaho National Engineering Laboratory, Idaho: 1979-1981 update, U.S. Geological Survey Open-File Report 84-1981.

Mann, L. J., 1986, Hydraulic properties of rock units and chemical quality of water for INEL-1 - A 10,365-foot deep test hole drilled at the Idaho National Engineering Laboratory, Idaho, U.S. Geological Survey Water-Resources Investigations Report 86-4020, 23 p.

Monks, J. I., Ralston, D. R., Johnson, G. S., Olsen, J. K., and Barrash, W., 1993, Straddle-packer determination of vertical variations in aquifer properties in the Snake River Plain aquifer at the Idaho Naional Engineering Laboratory (abs.), EOS, 74, 284.

Morin, R. H., Barrash, W., Paillet, F. L., and Taylor, T. A., 1993, Geophysical logging studies in the Snake River Plain aquifer at the Idaho National Engineering Laboratory - Wells 44, 45, and 46: U. S. Geological Survey, 92-4184.

Nace, R. L., Deutsch, M., Voegeli, P. T., and Subitsky, S., 1972, Physical environment of the National Reactor Testing Station, Idaho—A summary: Washington, D.C., U.S. Geological Survey Professional Paper, 38 p.

Nace, R. L., Voegell, P. T., Jones, J. R., and Deutsch, M., 1975, Generalized geologic framework of the National Reactor Testing Station, Idaho: Washington, D.C., U.S. Geological Survey Professional Paper, 49 p.

Olsen, J. K., 1994, Straddle packer system design and operation for vertical characterization of open boreholes, Proceedings of the 32nd Annual Symposium on Engineering Geology and Geotechnical Engineering.

Olmsted, F. H., 1962, Chemical and physical character of ground water in the National Reactor Testing Station, Idaho, U.S. Atomic Energy Commission, Idaho Operations Office Publication, IDO-22043-USGS, 142 p.

Orr, B. R., and Cecil, D., 1991, Hydrologic conditions and distributions of selected chemical constituents in water, Snake River Plain aquifer, Idaho National Engineering Laboratory, Idaho, 1986-1988, U.S. Geological Survey Water-Resources Investigations Report 91-4047.

Orr, B. R., Cecil, L. D., and Knobel, L. L., 1991, Background concentrations of selected radionuclides, organic components, and chemical constituents in ground water in the vicinity of the Idaho National Engineering Laboratory, U.S. Geological Survey Water-Resources Investigations Report 91-4015, 53 p.

Pierce, K. L., and Morgan, L. A., 1992, The track of the Yellowstone hot spot: Volcanism, faulting, and uplift, Geological Society of America Memoir 179: Boulder, Geological Society of America, p. 1-53.

Robertson, J. B., Schoen, R., and Barraclough, J. T., 1974, The influence of liquid waste disposal on the geochemistry of water at the National Reactor Testing Station, Idaho: 1952-70: U. S. Geological Survey, IDO-22053.

Rodgers, D. R., Hackett, W. R., and Ore, H. T., 1990, Extension of the Yellowstone plateau, eastern Snake River Plain, and Owyhee plateau: Geology, v. 18, p. 1138-1141.

Schmalz, B. L., 1959, Interim report of liquid waste disposal in the vicinity of the Idaho Chemical Processing Plant (ICPP): U. S. Geological Survey, ID-12011.

Wood, W. W., and Low, W. H., 1986, Aqueous geochemistry and diagenesis in the eastern Snake River Plain aquifer system, Idaho, Geological Society of America Bulletin, 97, 1456-1466.

Hydrogeology, Waste Disposal, Science and Politics
Proceedings 30th Symposium
Engineering Geology and Geotechnical Engineering, 1994

IDAHO CHEMICAL PROCESSING PLANT (ICPP) INJECTION WELL: OPERATIONS HISTORY AND HYDROCHEMICAL INVENTORY OF THE WASTE STREAM

By: Jeanne Fromm[1], John Welhan[2], Mike McCurry[1], and William Hackett[1]

1. **Department of Geology, Box 8072, (208)-236-3365**
Idaho State University
Pocatello, ID 83209

2. **Idaho Geological Survey, (208)-236-4254**
Idaho State University
Pocatello, ID 83209

ABSTRACT

Department of Energy (DOE), United States Geological Survey (USGS), and Idaho Chemical Processing Plant (ICPP) documents were searched for information regarding service disposal operations, and the chemical characteristics and volumes of the service waste emplaced in, and above, the Eastern Snake River Plain aquifer (ESRP) from 1953-1992. A summary database has been developed which synthesizes available, but dispersed, information. This assembled data records spatial, volumetric and chemical input patterns which will help establish the initial contaminant water characteristics required in computer modeling, aid in interpreting the monitoring well network hydrochemical information, and contribute to a better understanding of contaminant transport in the aquifer near the ICPP. Gaps and uncertainties in the input record are also identified with respect to time and type.

Concentration (μg/L, pCi/L) ratios of average annual H-3, I-129, Cr, N, SO_4, F^- : Cl^- inputs are developed at the disposal source for the available years of record. These input ratios are compared to similar ratios observed in water samples obtained from six aquifer intervals, isolated by straddle packer sampling in monitoring well USGS-44. These straddled intervals can be grouped into an upper (467-577' BLS),very transmissive zone; and a lower (580-600' BLS), much less transmissive zone, and are demarcated by a step-like concentration change of selected contaminant components. The ratios observed at the observation well were adjusted for natural, aquifer background concentration. Preliminary interpretations suggest USGS-44 waters, especially in the deep zone, resemble disposal well-emplaced service waste more closely than percolation pond waters in the Cl:H-3, I-129, and F ratios. Upper intervals' Cl:SO_4 and Cl:Cr ratios in USGS-44 are enriched in SO_4 and Cr when compared to ICPP service waste waters. These results suggest that waters in the aquifer, at the location of USGS-44, are being influenced by other contaminated waters from upgradient facilities, possibly from deep disposal methods. Hydrochemical effects related to vertical infiltration of waters from the percolation ponds, or from river water, was not obvious at USGS-44.

INTRODUCTION

The purpose of this paper is to briefly describe the operating history of the Idaho Chemical Processing Plant (ICPP) service waste disposal system; to characterize the waste chemistry, amounts, and depths of emplacement from 1953-92; and to develop a preliminary interpretation of the source(s) of waste observed in a downgradient monitoring well, USGS-44. In the summer of 1992, water samples were obtained from different aquifer intervals by sampling with a straddle packer system. Aquifer hydrochemistry, in

the USGS-44 location, changes with depth and aquifer transmissivity. Straddled interval hydrochemistry is compared to the input waste chemistry to further understand contaminant transport in this portion of the ESRP.

Geographic Location

The ICPP is a nuclear fuel reprocessing facility located on the Idaho National Engineering Laboratory (INEL). The INEL is a Department of Energy (DOE) research facility, established in 1949, and primarily dedicated to the development of nuclear reactors for power production. The INEL, occupying 890 mi^2, is located on northern margin of the eastern Snake River Plain (ESRP), near the southern margins of the Big Lost, Lemhi, and Beaverhead Mountains, Fig. 1, inset map. The flat surface of the ESRP supports a cool desert shrub biome, at an average elevation of 4900'. Beneath the semi-arid surface, lodged in basalt flows and sedimentary interbeds, is an extremely productive and pure body of water that supports local agricultural and commercial fish farming industries.

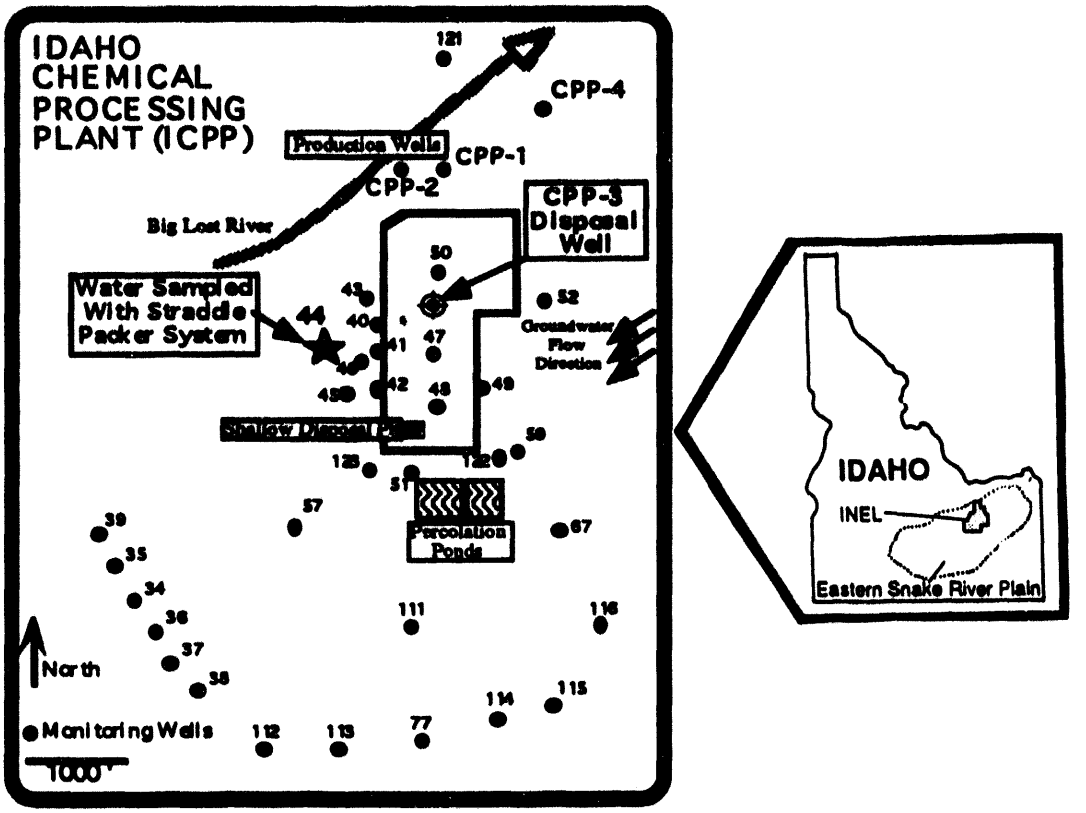


Figure 1. Location map of the Idaho Chemical Processing Plant showing production wells, disposal well, and percolation ponds. USGS-50 is due north of the disposal well and the shallow disposal pit is in the SW facility corner. USGS monitoring well network and USGS-44, the straddle-packer sampled well, are also depicted. Regional aquifer flow direction is to the southwest.

Hydrogeologic Setting

The ESRP, a structural and topographic basin, is a part of an intraplate bimodal-volcanic province extending from Yellowstone to the Owyhee Plateau. The subsiding structural basin is bounded on the north and south by the seismically active Basin-and-Range mountains and the volcanically active Yellowstone plateau to the east. The basin is filled with rhyolitic ash flow tuffs, erupted from a series of calderas younging to the northeast, capped with ≈ 1 km of late Tertiary and Quaternary age basalt (Hackett and Smith 1992). INEL basalt stratigraphy, in the ICPP area, consists of a 2,000' package of at least 40

separate flows, that has accumulated in the last 640,000 years (Anderson 1991). Flows are separated by long periods of time, during which thin deposits of fluvial, lacustrine, and eolian sediments can accumulate. Basalt flows emanate from rift zones that are (1) subparallel to the range bounding faults of the adjacent Basin-and-Range province, (2) located in the axial volcanic zone. The axial volcanic zone is a topographic high aligned with the long axis of the ESRP (Hackett and Smith 1992).

The Big Lost River, Little Lost River, and Camas Creek are surface drainages that flow into the INEL area. These drainages sink into the closed basin created by the axial volcanic zone high. The Big Lost River provides most of the local recharge to the aquifer (Robertson, 1974). The water table of this anisotropic, non homogeneous, and mostly unconfined aquifer is between 200-900 ' BLS on the INEL. The upper aquifer lies above 800-1500' BLS (Mann, 1986) and is the most productive zone. Horizontal hydraulic conductivities are much higher than vertical conductivities and the general flow direction is to the southwest, moving at 5-20 feet per day (Robertson, 1974). Hydraulic properties are variable but average values for storativity (0.1) and transmissivity (1.6 ft^2/day) were made by Robertson (1974).

Anderson's (1991) work on the basalt stratigraphy in the ICPP area suggests that the disposal well and USGS-44 penetrate the same suite of basalt flows and interbeds. Both wells bottom out in the I flow group, a relatively thick flow issuing from AEC Butte and underlying much of the ICPP area.

ICPP Background

The ICPP is located in the southwest area of the INEL on 201 acres of surface alluvium. The alluvium is about 40' deep and consists sandy gravels deposited by the Big Lost River. The plant's primary purpose has been to recover fissile uranium-235 from various types of spent nuclear fuel rods, and to store radioactive materials . Incoming fuel rods are held in water-filled basins before processing. Process-related, radioactive liquids are stored in stainless steel tanks prior to calcining. The calcine storage bins house the fission product radioisotopes, in the spent fuel rods, processed into a dry, granular form. Fuel dissolution and waste calcining results in abundant aqueous wastes which are handled by the plant's service waste system. Plant water is provided by production wells CPP-1 and -2. Service waste was disposed of, at the water table depth (450' BLS), by CPP-3 from 1953 until 1986. Surface percolation ponds went into service in 1984 (Cecil, Orr et al., 1991) and are still in use, Figure 1. The Shallow Disposal Pit, Fig. 1, received radioactive wastes from the fuel rod storage basin and cutting facility until 1971 (Amberson, 1971).

ICPP service waste is a mixture of steam condensate, cooling water, demineralizer and boiler blowdown wastes, and the distilled/condensed fraction of radioactive process wastes (Swanson 1990). Service waste is warm and contains dilute concentrations of various chemicals and radionuclides, but the most abundant waste constituents have been, Na^+, Cl^-, NO_3, SO_4, PO_4, H-3, Sr-90, Cs-137, Ce-144, Ru-106, and I-129 (Swanson, 1990). Service waste is metered for flow rate/volume, scanned for gross radioactivity, and sampled for analysis, prior to disposal to CPP-3 or the percolation ponds.

Methodology

Service waste disposed of by CPP-3 and percolation ponds is characterized by compiling data from ≈ 225 USGS reports, ICPP contractor documents, and DOE databases. USGS Open-file reports, ICPP Service Waste Division monthly reports and other documents, the Industrial Waste Management Information System (IWMIS), and the Radioactive Waste Management Information System (RWMIS) comprise the bulk of the references. ICPP personnel, particularly Frank Ward, greatly assisted in this compilation.

Data describing service waste average annual chemical composition and volumes is entered into a spreadsheet program. Concentration ratios of selected conservative components from the waste stream are developed from the spreadsheets. Details of disposal well behavior, changes in service waste handling, monitoring, and recording; record gaps; and data uncertainties were indicated after synthesis of the obtained reports.

The authors were members of the research team that vertically sampled the waters of USGS-44 with a straddle packer system. A written report of this work is in the review stages and contains the hydrochemical information used in this report. Specific methodologies (Johnson, Olsen et al. 1993) and some results (McCurry, Estes et al. 1993) are presented at this meeting.

SERVICE WASTE DISPOSAL TIMELINE

This section is a brief chronological presentation of CPP-3's operating history and those events at the ICPP that influenced the chemical nature and/or volumes of service waste released to CPP-3. It includes the documented, atypical releases to the well, planned ICPP process changes, and modifications to service waste monitoring methods and record keeping.

1951	Disposal well, CPP-3, is installed and completed.
1953	ICPP begins operation and CPP-3 is disposing plant service waste. Waste is monitored for gross β–γ activity and discharge volume (King, 1956).
1956	There are several perched water bodies in the vadose zone below the ICPP and they are encountered during monitoring well installation (Robertson, Schoen et al., 1974) in late 1950's and early 1960's.
1958	Largest annual tritium release (3,504 Ci) in this year 1967; (Mann and Cecil 1990). Plant process changes release less I-131 and more long-lived isotopes to service waste. Fluorescein dye and salt slug tracer test at CPP-3. 29 Ci accidentally released and registers in monitoring wells (Schmalz, 1959). Salt and gross beta activity plumes mapped for ICPP.
1959	First instance of fission products (Ru-106) in ICPP production well water (Horan and Others 1960). Line to CPP-3 has disintegrated and is replaced (Ayers and Burn 1960). Second largest annual H-3 release in this year (2,565 Ci) (Mann and Cecil 1990).
1960	Tritium is discovered in ICPP service waste (Hawkins and Schmalz, 1965). Na^+ concentration map of aquifer around ICPP contoured (Horan and Others 1960)
1961	Monitoring service waste for H-3 begins (Barraclough, Teasdale et al., 1967). 209 Ci released in December (Horan and Others 1962). Tritium (Horan and Others, 1962) and Na^+ (Jones, 1961) isoconcentration lines drawn around ICPP.
1962	More activity released to ICPP disposal pit than CPP-3 (Robertson, Schoen et al., 1974). Tritium plume mapped.
1963	Clinoptilolite ion exchange column installed at ICPP to remove cationic radioisotopes (Sr-90, Cs-137, Ce-144) (Robertson, Schoen et al., 1974). Large tritium release in June (Barraclough, Teasdale et al., 1967). Tritium plume mapped.
1965	Tritium plume mapped (Barraclough, Teasdale et al., 1967).
1967	High levels of H-3 and Cl- in ICPP production wells (Hawkins, 1968). CPP-3 fails in this year or 1968 (Robertson, Schoen et al., 1974). 20% error in volume estimates (Schmalz, 1968).
1968	Water levels, and tritium concentrations, in USGS-50 rise abruptly (Hawkins, 1968).
1969	19 Ci tritium inadvertently released to CPP-3 in September.
1970	New ion exchange column (Amberlite-200 resin) installed at ICPP to remove cationic radioisotopes (Amberson, 1970). CPP-3 is found to have collapsed and filled to 225' BLS (Gildersleeve, 1971). Well repair begins.

1971	Disposal well repair completed (Barraclough 1981). Releases to disposal pit end (Amberson 1971). Industrial Waste Management Information System (IWMIS) commences (AEC 1974). Monitoring well USGS-50 used as a temporary disposal point while CPP-3 is repaired (Amberson, 1971).
1972	Raw water usage substituted for treated water at ICPP and salt usage/disposal declines (Amberson, 1972). Sodium, chloride, specific conductance, H-3, Sr-90 plumes mapped for ICPP (Barraclough and Jensen, 1976)
1973	Service waste diversion system begins operation, designed to shunt service waste with high activity levels to a holding tank (Amberson, 1972). Nitrate concentration in service waste reported.
1978	H-3, Sr-90, I-129, specific conductance, sodium, chloride, & nitrate plumes mapped for the ICPP (Barraclough and Lewis, 1981).
1974	Plant switched back to treated water (Amberson, 1975). Pu-238, 239/40 service waste monitoring begins (Barraclough and Lewis, 1981).
1975	Pu isotopes detected in an ICPP monitoring well (Barraclough and Lewis, 1981).
1980	EPA Resource Recovery and Conservation Act and Underground Injection Control programs are phasing in. ICPP service waste system is responding and needs to reduce Sr-90, I-129, Hg, and nitrate levels (Miskimin, 1980). Service waste monitored for As, Ba, Cd, Cr, Pb, Hg, Se, & Ag . Service waste ion exchange system reactivated.
1981	Mercury released as mercuric nitrate in March (Willbanks, 1990). CPP-3 PVC lining beginning to fail. ICPP waste plumes are H-3, Sr-90, I-129, specific conductance, sodium, chloride, and nitrate (Lewis and Jensen 1984). First Cs-137 detected in an ICPP monitoring well (Lewis and Jensen, 1984). Naval Reactor Facility is included in the specific conductance and chloride plumes.
1982	Subsurface service waste line to CPP-3 replaced. CPP-3 completion has deteriorated further and is repaired by November. Some service waste is diverted to a surface disposal area during repairs.
1984	CPP-3 taken out of routine use and service waste diverted to a percolation pond (#1) on the surface, south of plant (Cecil, Orr et al., 1991).
1985	Second ICPP percolation pond is in service (Cecil, Orr et al., 1991).
1986	Last year CPP-3 receives any service waste (850 gal).
1989	CPP-3 plugged with concrete from surface to 475' BLS. Plant process activities are minimal (1989-91) and very low levels of radioisotopes released in service waste.

SERVICE WASTE EMPLACEMENT PATTERNS

Over time, where in the subsurface was the ICPP service waste actually released by the disposal well? This is an important consideration because it influences rates of contaminant transport and the type of geochemical interactions likely to influence contaminant movement. An input pattern has been developed by examining USGS reports, ICPP service waste documents, and letter reports in ICPP Service Waste files.

CPP-3 was intended to release service waste at, and below, the water table. In 1953, a 24" diameter hole was cable-tooled to 598' BLS and extended ≈150' below the water table, Figure 3A (Jones and Jones, 1952). A 16" carbon steel casing was perforated at 412-52' and 489-592' BLS. The annular space was filled with gravel. The first pump test indicated that CPP-3 did not take water readily. Following 40 hours of redevelopment to remove silt and sand, a recharge test indicated that CPP-3 received 800 gpm for 15.5 hours with a net buildup of 0.2' (Stewart, 1951). Peckham (1959) noted that static water level inside the

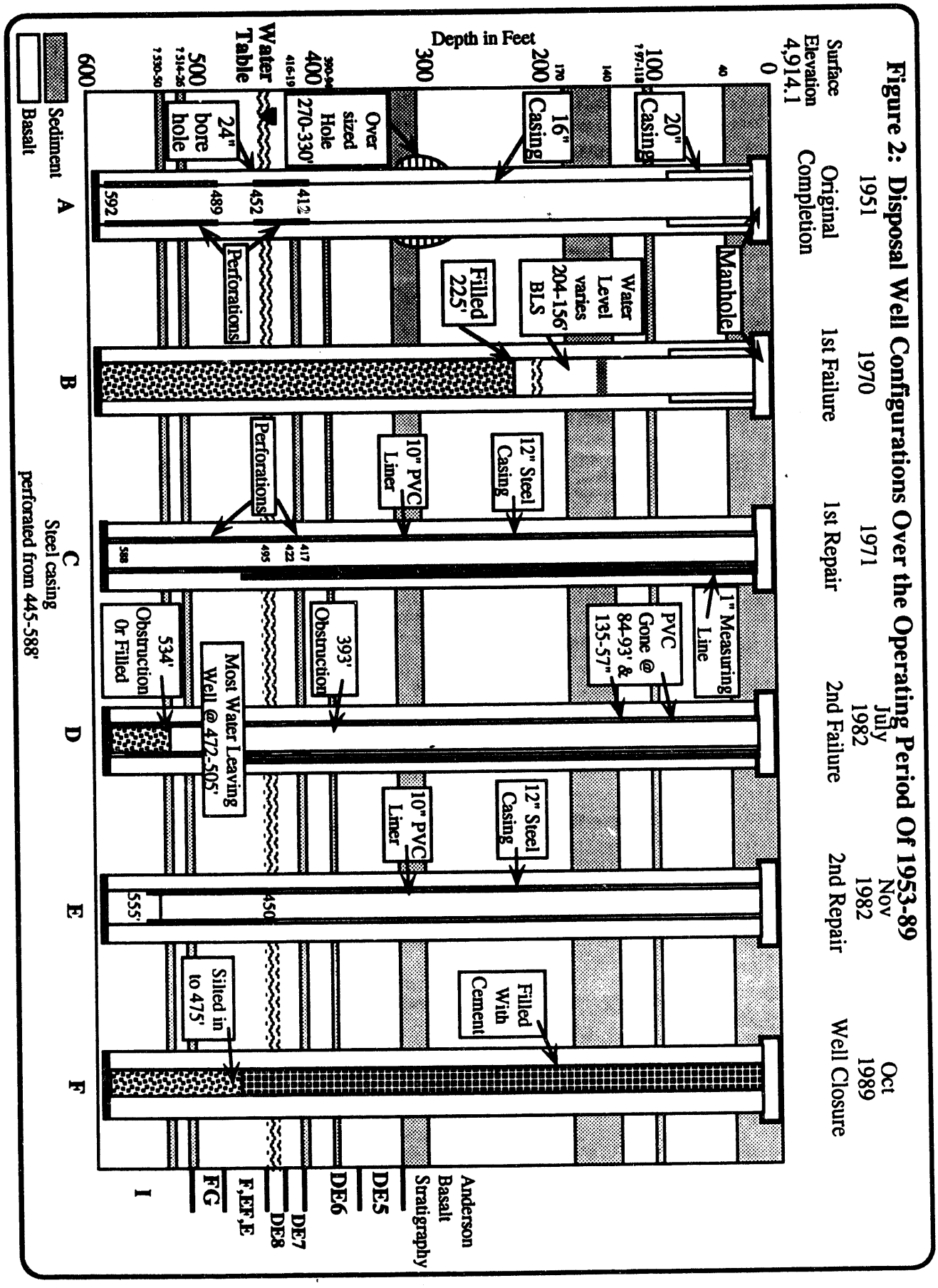


Figure 2: Disposal Well Configurations Over the Operating Period Of 1953-89

well was 18' above the water table but the elevation of the recharge mound outside the well was 0.6 feet. Water level measurements were made by the USGS until 1959 and occurred mostly at 450', but levels increased to 419' in 1959.

The first failure of CPP-3 was recognized in 1970 when the well was found to be filled to 225' BLS (Gildersleeve, 1971), and had a water level that fluctuated between 204-156' BLS. The well received water up to, and after, the failure was discovered. Workers estimated that CPP-3's steel casing had a service life of only 3-5 years because of the salty, aerated characteristics of service waste. The casing slowly dissolved away, developing numerous water table and vadose zone "perforations", which allowed the gravel pack to drain from the annular space into the well bore and slowly filled the borehole up. Sometime in 1967-8, the casing became so eroded that a discrete break occurred and the well rapidly filled to the 225' level. A large perched water body was created by this event and eventually contaminated the production wells, CPP-1 and -2, with H-3 and Cl^-.

The first repair of CPP-3, Fig. 3C, was a long and frustrating affair. In 1971, a 12" steel casing was finally in place and lined with 10" PVC pipe. USGS-50 disposed of service waste for about one month while well repairs were made and this practice maintained the perched water body created by disposal well failure.

When the well completion began to disintegrate a second time, in 1981, a flow meter was lowered through the borehole until it met an obstruction, or the fill level, at 534' BLS (Barraclough, 1982). The log indicated that most of the waste was leaving the well at 472-505' BLS. Once again, the well had continued to dispose of the service waste influx as its casings and linings deteriorated. The well configuration, after the second repair was finished in 1982, was similar to the first repair completion- a 10" PVC liner inside a 12" steel casing, except that the liner was perforated to a shallower depth, Fig. 3E. A temporary surface disposal area, to the east of the well, received ≈ 7 million gallons of service waste while well is repaired.

By 1985, most service waste was released to the percolation ponds. Pump tests performed in 1986 indicated that the CPP-3's specific capacity declined to the values it had before redevelopment (Ackerman, 1991). When the well is plugged with concrete, in 1989, it was noted that the borehole has silted in to 475' BLS.

Observations and tests suggest that CPP-3 emplaced service waste at approximately the 450-505' BLS for most of its service life. Intervals of vadose zone emplacement occurred in 1967?-71, and 1982. Surface release commenced in 1984. Releases to the shallow disposal pit , Fig. 1, were a source of vadose zone water and contaminants until 1971. The 24 " line to CPP-3 was occasionally a source of shallow leaks and contaminants, and it was replaced twice during the 1953-84 period. While the disposal well was operating, basalt flow groups DE7, DE8, F, EF, E, FG, and possibly the top of I group received the majority of ICPP service waste. The I flow received less waste over time because the well failures tended to block the bottom portions of the well, and the well perforation zone became shallower with time.

DISPOSAL VOLUMES

King (1956) gives a description of the ICPP system that (1) measures service waste volume, (2) monitors flow-by activity level, and (3) obtains aliquot samples for subsequent chemical analysis. This system is in place when the plant begins to operate in 1954. Production well flow meters are installed in 1959 (Robertson, Schoen et al., 1974). The record, Figure 3, indicates that total service waste volume, disposed of by CPP-3 over its operating life, is 10,623,470,765 gallons, for an average of 331,981,904 gallons per year. Disposal rates ranged from 356 to 1,135 gpm and averaged 632 gpm. These volume values must be qualified, however. Their accuracies are at least ± 10%, could be ±30%, and are commonly treated as ±15%. Percolation pond annual releases are similar to disposal well releases.

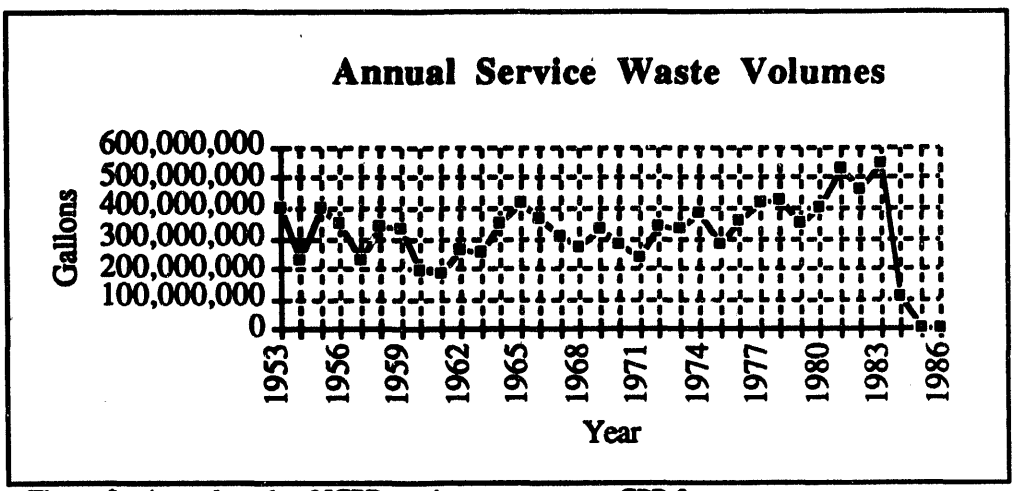


Figure 3: Annual totals of ICPP service waste sent to CPP-3

SERVICE WASTE CHEMICAL COMPONENT RECORD

The identity and amounts of the anthropogenic components in the service waste stream were determined by analysis of the composite sample. Gross β and γ were analyzed daily and the composite sample was analyzed monthly. Total mass additions are determined by multiplying concentration values with measured service waste volume. The uncertainty associated with the volume measurements will also influence the amounts of mass addition. Records of monthly salt, sulfuric acid, and other chemicals usage have been kept by various ICPP divisions from 1954 to present, but the record is incomplete. Tables 2 and 3 illustrate the type of chemical input records available for the radioactive and nonradioactive components of service waste. The record becomes more complete with time and is expanded dramatically with the advent of the Resource Conservation and Recovery Act in 1980. Anthropogenic additions to the service waste stream occur as pulses of varying frequency and magnitude. Tritium, which accounts for $\approx$ 95% of the radioisotopes in the ICPP aqueous wastes, is not monitored until 1961. Annual tritium additions have been estimated for the pre-1961 period by calculations based upon kilograms of fuel rod uranium processed.

USGS-44 HYDROCHEMICAL ZONES

Figure 4 shows the concentration of selected analytes in water samples obtained from straddled intervals in USGS-44. Sampling intervals were chosen because they were regions of active borehole flow. These intervals were isolated with inflatable packers and sampled after purging the standing borehole water within the isolated interval. The intervals above 577' were located in very transmissive, actively flowing parts of the aquifer. These upper straddled intervals occurred in flow groups E-H, and the top of the I group. The 580-600' interval was located in the least transmissive portion of the aquifer sampled and occurs in the I flow group. The deepest sampled interval contains water with the highest concentration levels of H-3, I-129, NO_3^- + NO_2^- as N, and Cl^-. F^-, SO_4, and Cr show more uniform concentration-with-depth behavior, but Cr concentrations are 2-2.5 times background concentration throughout. SiO_2, Mg, Na, and K are not shown, but their concentrations are also highest in the 580-600' interval. Sr-90, and Ca concentrations are highest in the 467-82' interval.

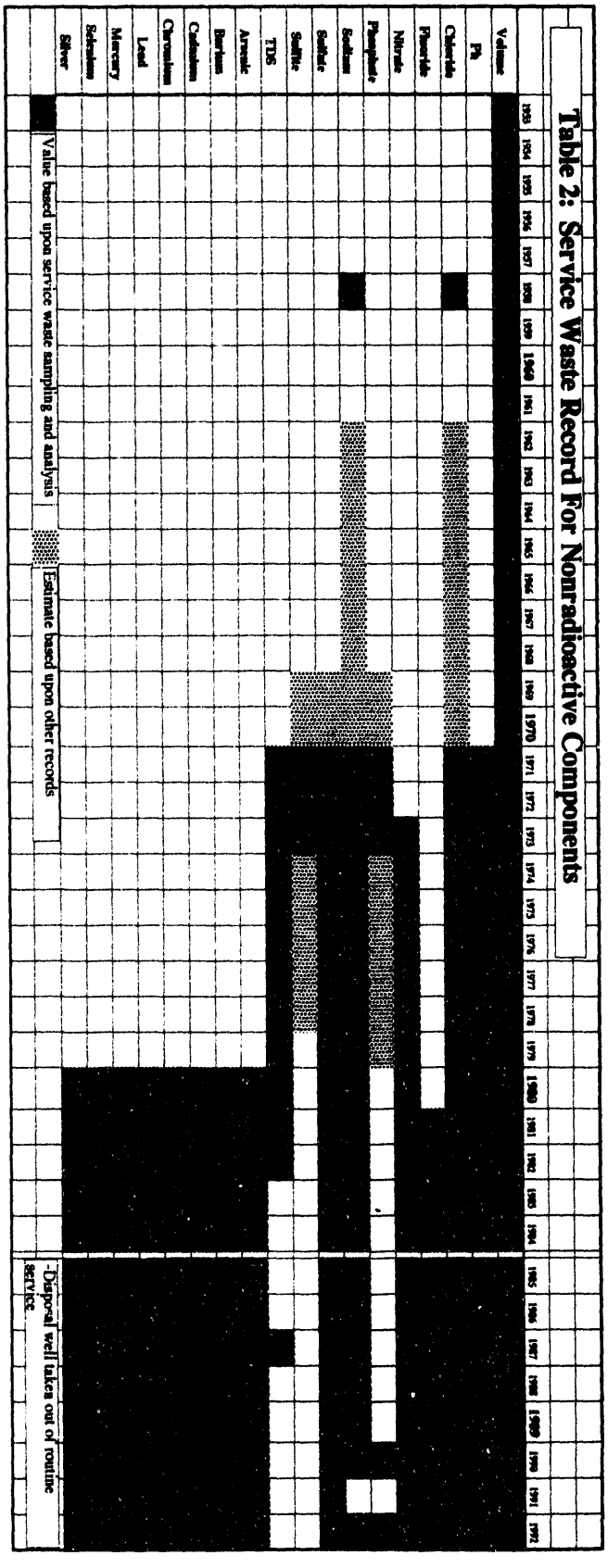
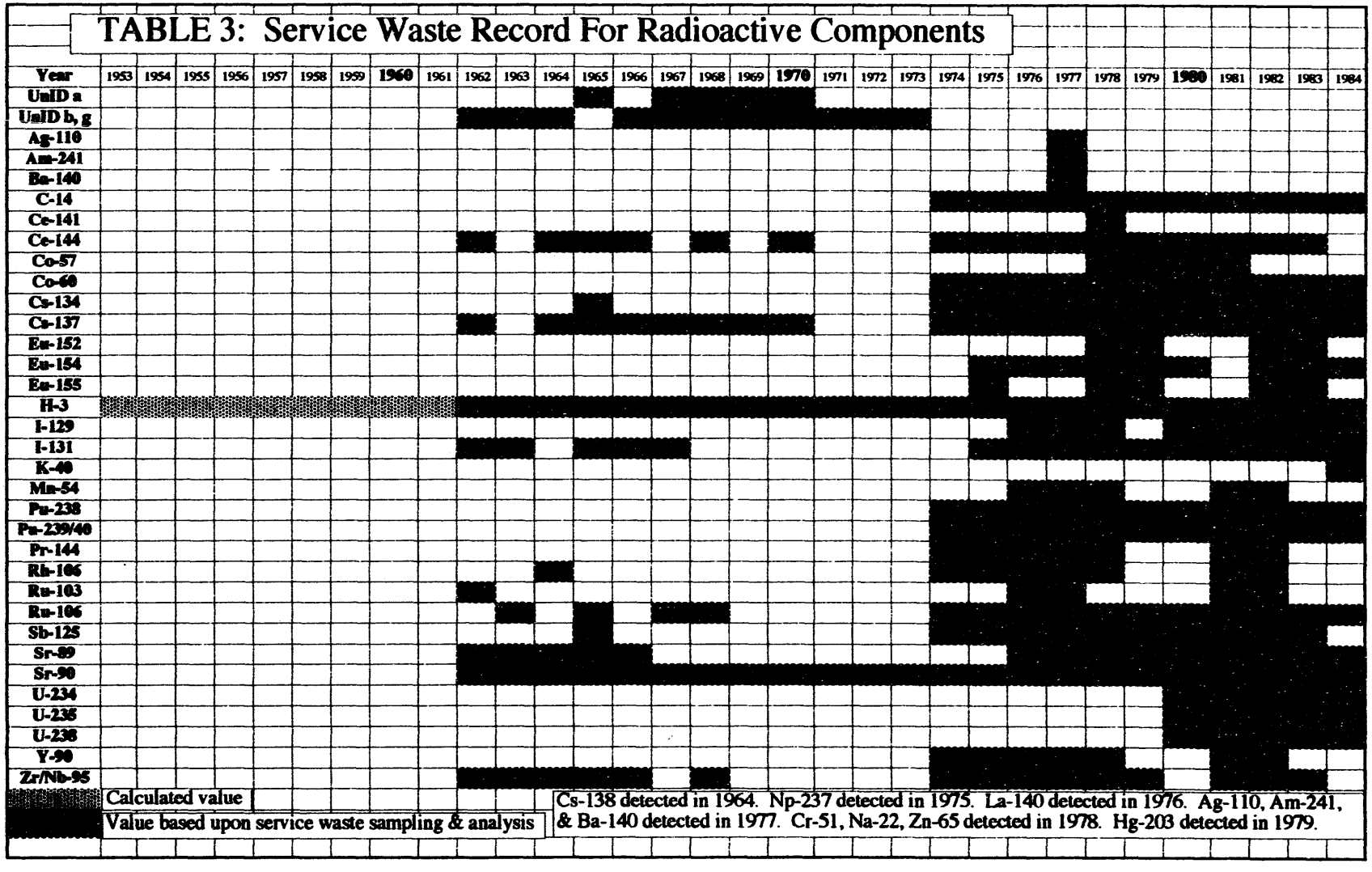


Table 1: Natural Background Water Chemistry in the Aquifer Near ICPP	
T in °C	12.5
pH	8
SiO2, ppm	21
Dissolved Fe, ppm	0.07
Ca, ppm	43.5
Mg, ppm	12.5
Na, ppm	8
K, ppm	3
HCO3, ppm	174
SO4, ppm	21
Cl-, ppm	10
F-, ppm	0.2
NO3, ppm	1.1
Noncarbonate hardness	17
Hardness as CaCO3	160
TDS, ppm	206
Spec. Cond, μmhos @ 25°C	360
As, μg/L	2.5
Ba, μg/L	54
Cd, μg/L	<1
Cr, μg/L	2.5
Pb, μg/L	1.6
Hg, μg/L	<0.1
Se, μg/L	<1
Mn, μg/L	<0.1
Ag, μg/L	<1
H-3, pCi/L	42
Cs-137, pCi/L	0
Co-60, pCi/L	0
Sr-90, pCi/L	0
I-129, pCi/L	0
Total U, μg/L	3.1

TABLE 3: Service Waste Record For Radioactive Components



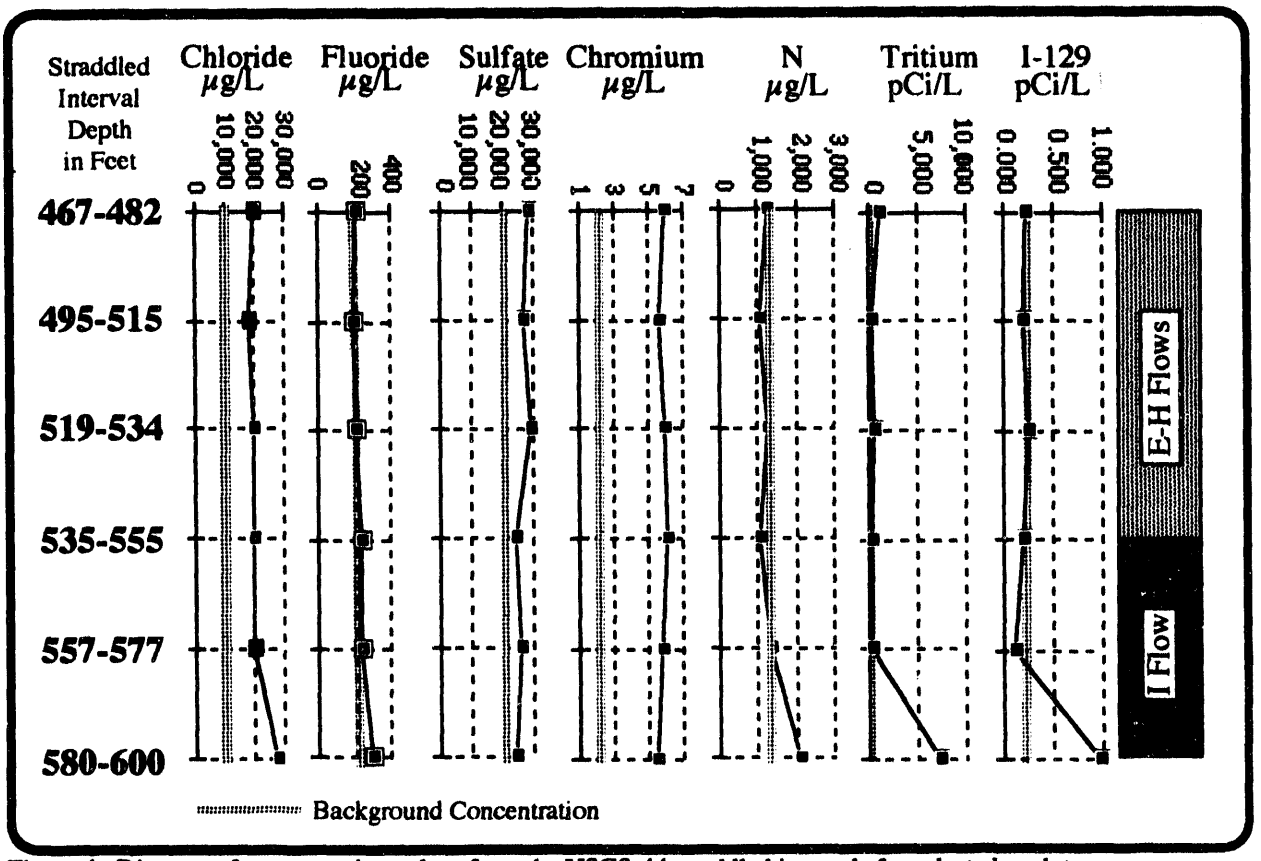


Figure 4. Diagram of concentration values from the USGS-44 straddled intervals for selected analytes. Depth, in feet, of the straddled interval is given on the left and basalt flow group designations are indicated on the right of figure. Background concentration zone shown with stippled band.

The waters from the tight interval in the I group (580-600') have a contaminant signature that is different from the more transmissive portions of the aquifer. The lowest straddled interval contains higher concentrations of anthropogenic additions to the aquifer, except for Cr and SO_4. These waters may be remnant from a previous time interval when the entire upper aquifer had similar contaminant chemistry derived from a common source. The active zones may have been flushed of contaminants preferentially over the less permeable zone. Alternatively, the water in the tight I flow may have received contaminants from a contaminant source other than CPP-3.

The analytes selected for inclusion in Figure 4 will be compared to Cl^-, on a concentration basis. These components, except for Cr, were selected because they are anionic, elevated with respect to natural background concentration at some well interval, and are known components of the ICPP service waste stream.

COMPARISON OF CONSERVATIVE COMPONENT RATIOS IN USGS-44 INTERVALS AND ICPP SERVICE WASTE STREAM

The ICPP disposal well and/or percolation pond historically has always been considered to be the primary source of the contaminant chemistry in USGS-44. When USGS-44 was installed in 1957, it was expected to be a sensitive indicator of aquifer contaminant levels. It was placed directly downgradient of USGS-40, a well that contained high concentrations of anthropogenic chemicals and responded quickly to inadvertent releases of high contaminant levels to the service waste system. Historically, USGS-44 does show the

Table 5: Conservative Component Ratios

ICPP Service Waste						
	Cl:H-3	**Cl:I-129**	**Cl:SO4**	**Cl:N**	**Cl:F**	**Cl:Cr**
1958	1	14,087				
1959						
1960						
1961						
1962	3	10,169				
1963	1	6,989				
1964	1	10,252				
1965	14	15,089				
1966	4	11,437				
1967	1	9,842				
1968	2	10,549				
1969	6	10,891				
1970	14	15,354				
1971	13	12,127	7.3			24,679
1972	2	10,277	6.5			20,914
1973	7	4,041	2.3	7		8,224
1974	1	8,485	3.6	24		17,267
1975	13	11,069	7.9	35		22,525
1976	16	31,967		34		27,973
1977	1	12,352	5.8	14		25,136
1978	2	2,360	4.8	11		33,621
1979	2	7,505	5.3	9		27,186
1980	6	21,721	5.7	11		7,415
1981	3	14,127	6.8	19	211	20,820
1982	3	20,028	4.1	12	246	16,705
1983	1	8,441			135	14,684
1984	42		4.0	16	267	
pre-'85 ave	**7**	**12,137**	**5.3**	**17**	**215**	**20,550**
1985	1		2.7	15	335	
1986	3		8.7	23	547	
1987	3	67,837	4.5	40	427	32,738
1988	8		4.3	36	639	
1989	1102		3.8	57	271	
1990	1476	261,990	7.5	140	1,315	
1991	267	261,350	9.9	111	1,633	
post-84 ave	**409**	**197,059**	**6**	**60**	**738**	**32,738**

USGS-44 Straddled Intervals and Background Ratios

Intervals						
467-82	8	43,478	1.4	71		2,941
495-515	18	37,735	1.5			2,540
519-534	14	38,910	1.3	53		2,898
535-55	28	50,000	3.3		250	2,717
557-77	39	75,758	2.0	48	333	3,030
Upper Zone Ave	**21**	**49176**	**2**	**57**	**292**	**2825**
580-600	2	18,041	5.0	18	175	5,738
Background	238		0.5		50	4,000

effects of waste disposal, but it has been relatively "clean", in spite of its proximity to the disposal well and USGS-40.

As a preliminary effort to understand more about the relationship between the input function at the disposal point and the contaminant concentrations in the sampled intervals in USGS-44, ratios of conservative components were developed for the straddled intervals in USGS-44 and service waste over time. These two sets of ratios are compared for similar, or disparate patterns, and the ratio values are listed in Table 5.

The concentration ratios in the monitoring well are adjusted for background (pre-anthropogenic) concentrations in the aquifer. Background aquifer hydrochemistry is estimated, Table 1, by comparing values reported from several sources. The ICPP production (CPP-1, -2) and disposal wells were sampled after completion and development, but before the ICPP facility began to operate. These common ion analyses are listed in reports by the United States Geological Survey (USGS) (Nace, Jones et al., 1951) (Bagby, White et al., 1985). In addition, raw water analyses, from five years during the late 1960s and early 1970s, and taken from CPP-1 and -2, are also available. Background values for radioisotopes and trace metals are taken from recent USGS reports (Orr, Cecil et al., 1991) (Knobel, Orr et al., 1992).

The set of ratios for conservative components in the service waste are based on annual average concentration values recorded in waste monitoring records. The effect of an annual average will be to "smooth" the considerable monthly variability in the input function, especially for the radioisotopic components. What is observed, at a point in time, in the USGS-44 straddled intervals may be the pulsed, not the averaged, signal from the disposal source. The annual tritium concentrations have been reduced from their initial input levels to "decayed" 1992 concentrations, because tritium has a short half-life (12.3 years). The H-3 and I-129: Cl ratios are in pCi/L:µg/L units. The blank positions in the USGS-44 interval ratios table are the result of negative values in the N and F^- concentrations after background concentrations are subtracted. Background concentration values are higher than measured concentrations in these intervals.

Table 5 shows that there is a great deal of variability in the input concentration ratios and there are significant gaps in the service waste record. For purposes of comparison, the component ratios for service waste disposed of to the well and the percolation ponds have been grouped and averaged. Grouping and averaging has been performed on the monitoring well component ratios also- the lower, tight interval (580-600') is separated from the more transmissive, upper (>577') intervals. These averages are plotted in Figure 5. The larger the ratio values, the more enriched the service waste stream is in H-3, I-129, N, SO_4, F, and Cr components.

Preliminary interpretations of this approach suggest that Cl: H-3, I-129, F and N ratios, in USGS-44 lower interval water, most closely resemble disposal well water (<1984). Cl: H-3, I-129, and F ratios from upper interval waters in USGS-44 plot closer to service waste disposal well ratios than percolation pond ratios, but they are more intermediary than the deep zone waters. The N:Cl ratio in USGS-44 upper intervals is similar to the service waste percolation pond ratio. The monitoring well Cl:Cr ratio does not resemble the Cl:Cr ratio in the ICPP service waste, from either the disposal well or pond disposal periods. Cl:SO_4 ratios for service waste are higher than the ratios calculated for USGS-44. F concentrations in the upper three intervals in USGS-44 are close to background in concentration. Nitrogen concentrations are also close to background in two intervals from the upper, permeable intervals in USGS-44.

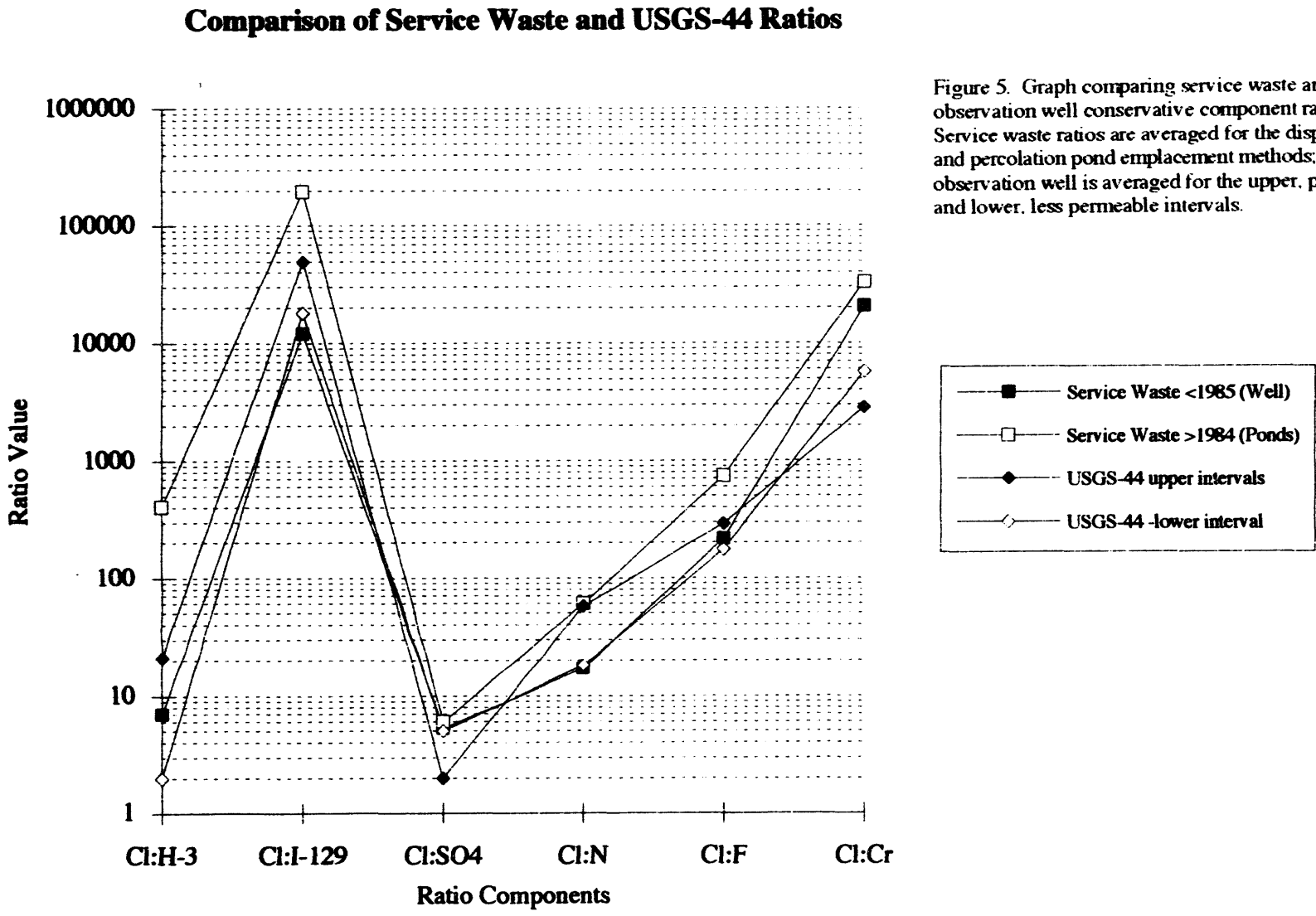


Figure 5. Graph comparing service waste and observation well conservative component ratios. Service waste ratios are averaged for the disposal well and percolation pond emplacement methods; and observation well is averaged for the upper, permeable and lower, less permeable intervals.

CONCLUSIONS

The ICPP has added anthropogenic chemicals to a complex, anisotropic, non homogenous aquifer in a manner that has changed over time in many respects. Plant processes affect the chemical content of service waste and radioisotopic releases vary considerably in concentration, and content, over time. Method of service waste disposal has changed from mostly water table to percolation pond releases. Disposal well disintegration and line/valve leaks have created perched water bodies in the vicinity of the disposal well. ICPP service waste records contain data on volumes released and chemical content, but they are incomplete and of uncertain accuracy over some of the time intervals. Local, preanthropogenic aquifer water chemistry can be estimated for the ICPP area from various sources.

Straddle packer sampling techniques were applied to a nearby monitoring well, USGS-44, in the summer of 1992, to characterize the aquifer hydrochemistry. Aquifer is hydrochemically stratified with respect to depth. Less transmissive and/or deeper zones contain higher concentrations of certain contaminants (H-3, I-129, N, F, Cl, Na). There are interesting exceptions to this trend (Cr, SO_4, Sr-90). Ratios of conservative components observed in the observation well and in the ICPP service waste stream were calculated and compared. These ratios were adjusted for natural, background aquifer concentration. Preliminary interpretations suggest USGS-44 waters, especially in the deep zone, resemble disposal well-emplaced service waste more closely than percolation pond waters in the Cl:H-3, I-129, and F ratios. The upper intervals' Cl:SO_4 and Cl:Cr ratios in USGS-44 are enriched in SO_4 and Cr when compared to ICPP service waste waters. These results suggest that waters in the aquifer, at the location of USGS-44, are being influenced by waters containing Cr and SO_4, perhaps from upgradient facilities, or possibly from deep disposal methods. Based on the same comparison of component ratios, hydrochemical effects related to vertical infiltration of waters from the percolation ponds, or from river water, cannot be identified in USGS-44.

Acknowledgments:

This work has been supported by the DOE-EPSCoR Program and the State of Idaho INEL Oversight Management Program. Idaho Chemical Processing Plant documents and databases were provided by Frank Ward, LeRoy Lewis, and Tim McKenna. Their technical expertise and cooperation have contributed immensely to this work. Dr. Bill Hackett and Dr. Dick Smith have served as DOE-EPSCoR mentors. Steve Anderson and Larry Mann, USGS, have helped with basalt stratigraphy and supplied practical, comprehensive knowledge about the INEL and the ESRP aquifer.

REFERENCES

Ackerman, D. J. (1991). Transmissivity of the Snake River Plain Aquifer at the Idaho National Engineering Laboratory, Idaho. United States Geological Survey. 35.

AEC (1974). NRTS Waste Management Information System. Atomic Energy Commission.

Amberson, C. B. (1970). CPP Production Monthly Report. ICPP.

Amberson, C. B. (1971). ICPP Operations Branch Monthly Report. ICPP.

Amberson, C. B. (1972). ICP Operations Branch Monthly Report. ICPP.

Amberson, C. B. (1975). ICPP Production Monthly Report. ICPP.

Anderson, S. R. (1991). Stratigraphy of the Unsaturated Zone and Uppermost Part of the Snake River Plain Aquifer at the Idaho Chemical Processing Plant and Test Reactors Area, Idaho National Engineering Laboratory, Idaho. United States Geological Survey.

Ayers, A. L. and P. Burn (1960). Waste Management At The Idaho Chemical Processing Plant. Phillips Petroleum Company.

Bagby, J. C., L. J. White, et al. (1985). Water-Quality Data For Selected Wells On or Near the Idaho National Engineering Laboratory, 1949 Through 1982. United States Geological Survey. 799.

Barraclough, J. (1981). ICPP Disposal Well--current conditions and proposed future modifications. USGS.

Barraclough, J. (1982). ICPP Disposal Well-Deterioration of the 10-inch PVC liner. USGS.

Barraclough, J. T. and R. G. Jensen (1976). Hydrologic Data For The Idaho National Engineering Laboratory Site, Idaho: 1971 to 1973. United States Geological Survey.

Barraclough, J. T. and B. D. Lewis (1981). Hydrologic Conditions at the Idaho National Engineering Laboratory, Idaho Emphasis: 1974-1978. United States Geological Survey. 77.

Barraclough, J. T., W. E. Teasdale, et al. (1967). Hydrology Of The National Reactor Testing Station Area, Idaho: Annual Progress Report 1965. United States Geological Survey. 107.

Barraclough, J. T., W. E. Teasdale, et al. (1967). Hydrology of the National Reactor Testing Station, Idaho, 1966. USGS.

Cecil, L. D., B. R. Orr, et al. (1991). Formation of Perched Ground-water Zones and Concentrations of Selected Chemical Constituents in Water, Idaho National Engineering Laboratory, Idaho, 1986-88. United States Geological Survey.

Gildersleeve, R. P. M. (1971). Repair of CPP Disposal Well: Problem Analysis. ICPP.

Hackett, W. R. and R. P. Smith (1992). Quaternary Volcanism, Tectonics, and Sedimentation in the Idaho National Engineering Laboratory Area. Field Guide To Geologic Excursions In Utah and Adjacent Areas Of Nevada, Idaho, and Wyoming. Boulder, Geological Society of America. 1-18.

Hawkins, D. B. and B. L. Schmalz (1965). Environmental Tritium At The National Reactor Testing Station. Health and Safety Division, AEC. 38.

Hawkins, M. (1968). Situation Report- Tritium in ICPP Production Wells. AEC.

Horan, J. R. and Others (1960). Annual Report of the Health and Safety Division, 1959. Health and Safety Division, Atomic Energy Commission. 152.

Horan, J. R. and Others (1962). Health and Safety Division Annual Report, 1961. Health and Safety Division, Atomic Energy Commission.

Jones, J. R. and S. L. Jones (1952). Logs of Water Wells, Reactor Testing Station, Idaho. United States Geological Survey, Water Resources Division. 38.

Jones, P. H. (1961). Hydrology Of Radioactive Waste Disposal At The Idaho Chemical Processing Plant National Reactor Testing Station, Idaho. United States Geological Survey, Water Resources Division, Ground Water Branch. 8.

King, W. C. (1956). Monitoring The Liquid Wastes Discharged From The Idaho Chemical Processing Plant. Atomic Energy Commission (AEC) Research and Development Report Prepared by Phillips Petroleum Company, Atomic Energy Division. 29.

Knobel, L., B. R. Orr, et al. (1992). "Summary of Background Concentrations of Selected Radiochemical and Chemical Constituents in Groundwater From the Eastern Snake River Plain Aquifer, Idaho: Estimated From An Analysis of Previously Published Data." Journal of the Idaho Academy of Science **28**(1): 48-59.

Lewis, B. D. and R. G. Jensen (1984). Hydrologic Conditions at the Idaho National Engineering Laboratory, Idaho: 1979-1981 Update. United States Geological Survey. 61.

Mann, L. (1986). Hydraulic Properties of Rock Units and Chemical Quality of Water for INEL-1: A 10,365-foot Deep Test Hole Drilled at the Idaho National Engineering Laboratory, Idaho. United States Geological Survey. 23.

Mann, L. and D. Cecil (1990). Tritium in Groundwater at the Idaho National Engineering Laboratory, Idaho. United States Geological Survey. 35.

Miskimin, P. A. (1980). RCRA and UIC Programs. ICPP.

Nace, R. L., J. R. Jones, et al. (1951). Geology and Groundwater in the Central Construction Area, Reactor Testing Station, Idaho. United States Geological Survey, Water Resources Division, Ground Water Branch.

Orr, B. R., L. D. Cecil, et al. (1991). Background Concentrations of Selected Radionuclides, Organic Compounds, and Chemical Constituents In Ground Water In the Vicinity of the Idaho National Engineering Laboratory. United States Geological Survey. 51.

Robertson, J. B. (1974). Digital Modeling of Radioactive and Chemical Waste Transport in the Snake River Plain Aquifer at the National Reactor Testing Station, Idaho. United States Geological Survey. 41.

Robertson, J. B., R. Schoen, et al. (1974). The Influence of Liquid Waste Disposal on the Geochemistry of Water at the National Reactor Testing Station, Idaho: 1952-1970. Prepared by the United States Geological Survey, Water Resources Division, for the U.S. Atomic Energy Commission. 231.

Schmalz, B. L. (1959). Interim Report of Liquid Waste Disposal in the Vicinity of Idaho Chemical Processing Plant (ICPP). Analytical Branch of the Health and Safety Division of the Idaho Operations Office-Atomic Energy Commission.

Schmalz, B. L. (1968). Liquid Waste At The National Reactor Testing Station, Idaho. Health Services Laboratory, Atomic Energy Commission.

Stewart, J. W. (1951). Results Of Tests On Wells At Sites 3 and 7, Reactor Testing Station, Idaho. United States Geological Survey, Water Resources Division, Ground Water Branch. 28 plus charts.

Swanson, D. S. (1990). ICPP Plant Safety Document: Aqueous Liquid Waste Management. WINCO.

Willbanks, J. (1990). Closure Plan For LDU CPP-23 Injection Well (MAH-FE-304). Westinghouse Idaho Nuclear Company, Inc. 63.

Hydrogeology, Waste Disposal, Science and Politics
Proceedings 30th Symposium
Engineering Geology and Geotechnical Engineering, 1994

STRADDLE PACKER SYSTEM DESIGN AND OPERATION FOR VERTICAL CHARACTERIZATION OF OPEN BORE HOLES

by
James K. Olsen, Idaho Department of Health and Welfare, INEL Oversight Program, 900 North Skyline, Idaho Falls, Idaho 83402

ABSTRACT

Bore holes open to large intervals provide groundwater samples and test results which represent an unknown integration of properties throughout the depth of the hole.

The State of Idaho's INEL Oversight Program is utilizing a custom straddle-packer system to develop a vertical characterization of water chemistry and hydrology in selected open bore holes at the Idaho National Engineering Laboratory. This report describes the design and operation for bore hole zone isolation, water sampling, and hydrologic testing. To reduce potential influences on in situ water chemistry, the system utilizes chemically inert components to the extent possible.

Straddle packer systems are effective in producing representative water samples from isolated formations. Hydrologic testing is limited by the ability to produce a measurable stress on the aquifer in individual formations, and head measurement sensitivity.

INTRODUCTION

The State of Idaho, INEL Oversight Program, is conducting hydrologic studies in wells open through large intervals to the Snake River Plain Aquifer at the Idaho National Engineering Laboratory. The project is now beginning the third year field season.

The project is a joint effort between the Idaho Department of Health and Welfare, U.S. Department of Energy, Idaho Geologic Survey, U.S. Geologic Survey, Idaho State University, Boise State University and the University of Idaho. The project purpose is to investigate chemical and hydrologic properties of the Snake River Plain Aquifer through existing monitoring wells open over large intervals. The primary tool for data gathering is a straddle packer system capable of isolating individual zones in the open bore holes. Water samples can be taken for chemical analyses, and hydrologic testing can be accomplished with remote pressure sensing transducers, a submersible pump and remotely controlled valves.

A complete system was engineered and built for purchase from Baski Water Instruments, Inc., Denver, Colorado, in the spring of 1992. Design changes were added to the original system as problems developed.

Primarily constructed of stainless steel, viton coated rubber, and teflon, the system is chemically inert as reasonably possible considering cost and engineering constraints.

The system is remotely controlled by five pneumatic lines, and two electrical cables. A tracer injection line also provides for limited gas bail pumping. The control and injection lines are housed and deployed from a wire line bus. The bus also serves as an office for data gathering, and chem lab for tracer preparation. The control lines are secured to the outside of the riser pipe when the system is deployed.

The system is constructed with protective housings providing the structural strength required to penetrate bore holes to 1,000 feet. A minimum of 2 inch, schedule-80 type 304 stainless steel pipe is used throughout the system and riser string. American Petroleum Institute (API) non-upset tubing threads and a galling resistant alloy coupling are used to preserve the strength and useable life of the pipe. Any drilling or pump rig capable of hoisting the maximum system weight of 7,500 pounds can be used for deployment. However, hole drag from deviation or caving would require a larger capacity rig to retrieve the system.

Summary of Packer System Capabilities:

I. Zone Isolation:
From 13 to approx. 30 feet (requires reconfiguration outside test well) in 6 to 8 or 8 to 10 inch smooth bore-holes (requires reconfiguration).
Total depth approx. 1020 feet.
Maximum submergence of transducers 900 feet.

II. Sampling by:
Pumping at approx. 2 to 20 gpm.
Bailing at 1 or 3 liter per bail.
Gas bailing at <2 gpm.

III. Purging by:
Pumping at approx 2 to 20 gpm.
Bailing at 1 or 3 liters per bail.
Gas surging at 5 to 10 gal per surge.

IV. Injection:
Approx. 1 gpm up to 70 psi over static head.
Full circulation at approx. 20 gpm, top to bottom of isolated zone or top of zone to total depth (requires reconfiguration).
Partial circulation at 0 to 15 gpm while discharging at 15 to 0 gpm.

V. Hydraulic testing:
Slug tests, both positive (increased head) and negative (depressed head) to the vertical limits of the system and well.
Pumping tests to capacity of pump (20 gpm max).
Relative static head measurements to ± 0.005 feet.
Absolute static head measurements to ± 0.05 feet.

PRINCIPLES OF OPERATION

Description of Components:

The straddle packer system described in this report consists of component parts which work together as a system. Without a thorough understanding of each component and how the system functions as a unit, the operation of the system is not possible.

Following figure one below from top to bottom, each component part and it's functions are described.

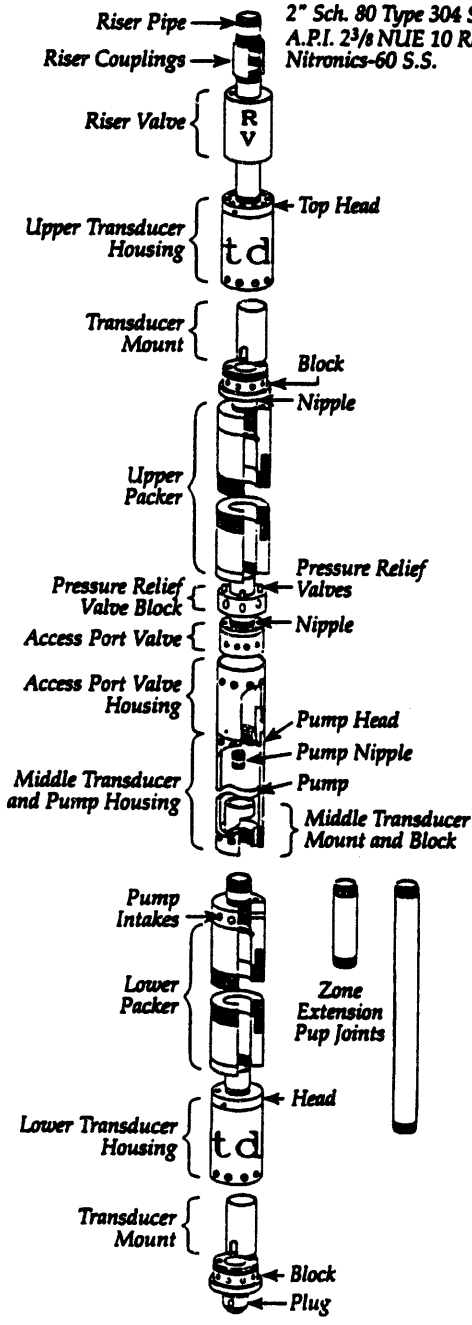


Figure 1. Straddle Packer Assembly

(not to scale)

Riser Pipe and Couplings:

The primary functions of the riser string are to suspend the system in the well and to provide a conduit for purge water and samples to the surface.

The riser pipe is constructed of 2 inch, schedule-80 type 304 stainless steel pipe connected with API 2-3/8 inch NUE 10 round tubing thread couplings. The API round thread form greatly increases the connection strength over standard National Pipe Threads by reducing the depth of the root and stress concentration from a sharp V. The couplings are made from Armco Nitronics-60 stainless steel to decrease metallic galling. The connections are lubricated and sealed with a teflon based compound or antisieze grease.

The maximum safe working load for the riser string is approximately 31,000 lbs. Pulling over this weight could cause permanent damage to the riser string. The riser string is handled with either elevators or a lifting sub screwed into the top coupling. The coupling is then set on the well casing or drill rig with either another elevator, or a slip plate.

A 3/4 inch piece of steel plate with a 2-3/8 inch machined slot in it is used to secure the pipe to the casing. Keys welded to the plate prevent the collar from slipping during torquing of connections.

Riser Valve:

The riser valve shuts off any flow through the riser pipe by inflating a small rubber packer between a 4 inch casing and a solid base pipe. The valve is actuated with compressed nitrogen through an 1,100 foot long 3/16 inch tube. The valve is capable of forming a competent seal even when subjected to silt or sand, and is used as a backup valve under those conditions. Because of the time required to inflate or deflate the bladder through the single control line, the valve operates too sluggishly for effective timing, and has limited capability for slug testing. In addition the bladder causes pulsations in water flow when partially inflated. The valve is useful for holding a full riser column while circulating water through the access port valve.

Upper Transducer Housing:

The transducer housings provide a mechanical link through the system, protect the pressure transducers and allow a sealed connection to the annuls. A five inch Sch-80 casing is connected between two opposing fittings labeled the "top head and block" on figure one. The heads and blocks are o-ring sealed to the casing and secured with non tapered round threads or cross bolts.

The top head serves as the means for the control lines to pass from the annulus to inside the riser column. All lines entering at the top head are sealed with o-rings in fittings designed so the lines can slide through.

The Bottom Block, shown in figure two, also serves as a base for mounting the pressure transducer, and a sealed pressure sensing port. The port system consists of 1/16 inch oil filled tubing, and connects from the port of the transducer to the

annulus through a 1/2 inch hole drilled through the block. A plug seals the hole at the bottom and a 1/16 inch tubing to 1/4 inch NPT fitting seals the top. The tube passes through the fitting, and terminates about 3/4 of the way down the hole. A 1/16 inch hole drilled through the block directly below the fitting aligns with a 1/4 inch hole through the housing to provide a water connection to the annulus.

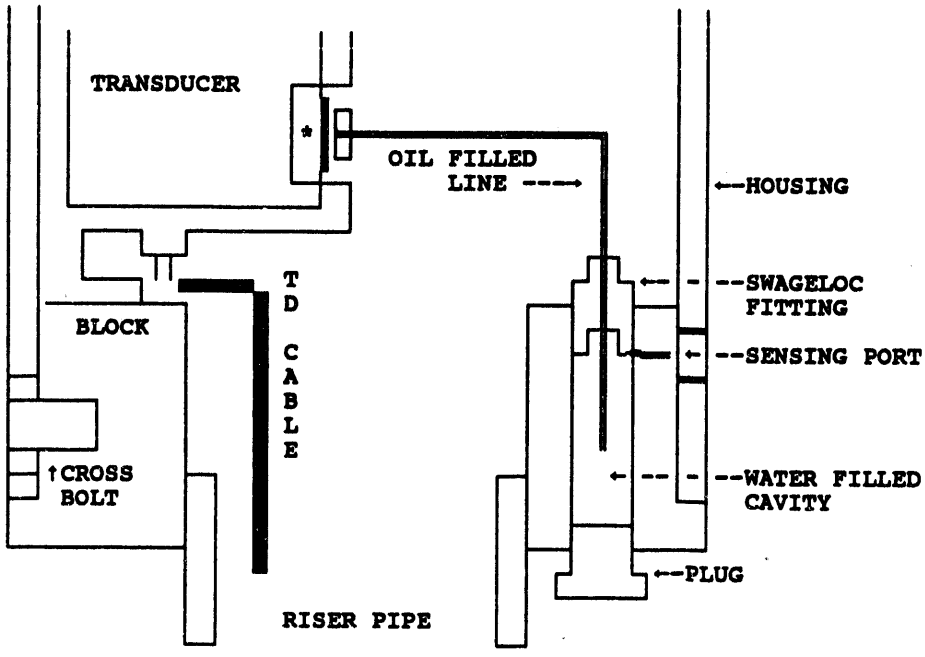


Figure Two: Transducer Housing Bottom Block Showing Pressure Sensing System

This system provides a simple bubble free pressure connection from the transducer to the annulus. All the air in the tubing and transducer port is expelled by silicone oil with a syringe. Then the block cavity is filled with deionized and degassed water by the same method.

Control Lines:

Eight 1100 foot flexible control lines accompany the riser string from the surface to the packer system. There are five type 304 stainless steel pneumatic lines: two 1/4 inch lines for packer inflation, a 3/16 line for riser valve inflation, and two 3/16 inch lines for the access port valve opening and closing. In addition a 1/2 inch Tefzel line for tracer injection, a four conductor transducer cable, and a four wire 14 gauge power cable for the pump. To reduce the volume of control lines within the housings and riser at the top head, the power cable converts to 3 wires by dropping the ground, and the injection line reduces to 1/4 inch. Quick connector couplings are provided to attach the pneumatic lines to a regulated nitrogen supply, transducer cable to computer hardware, and power to the pump cable.

Cable Control System:

The flexible control lines are contained and transported on spools mounted in the wire line bus. The spools are mounted on adjustable stands with an adjustable break. The lines are fed out the rear of the bus to a guide suspended over the well from the rig. The guide evolved from an extra wooden spool, to a heavy steel spool, to a piece of 12 inch PVC pipe with u-bolt guides for the lines.

The spool breaks provide a slight drag on the cables when going into the hole, and need only to be watched for snags. When coming out of the hole the spools have to be turned by hand to retrieve the lines.

Upper Packer:

Packers provide the seal in the bore hole to isolate specific zones. They must be set on smooth bore hole sections of appropriate diameter in order to form an effective seal. Both packers are similar in design. Inflatable steel cable reinforced rubber bladders are secured at the top but allowed to slide at the bottom. A base pipe provides the physical connection and riser conduit for the system. Length measurements should not be referenced to the bottom ends of the packers since that point moves relative to the system, but should be noted to determine approximate packer seats. The packers can be inflated separately by two lines or together with one line splitting above the top head.

Sliding end packers should be run with the sliding end down. This prevents debris from damaging the o-ring seals in the sliding end. When the packers are inflated they produce a downward pull on the entire system, as the bladders secure to the bore hole walls and continue to pull at the bladder ends. Because the lower end is free to slide but the upper end is not, the reinforcing cables pull the upper end of the packer down. During testing in 6 inch holes at of a depth of 500 feet, with an inflation pressure of 400 psi, the downward pull has averaged 0.04 feet. This change in depth must be accounted for during hydrologic testing.

In addition, a safety factor must be considered. Assuming a spring constant for the pipe based on a yield strength of 30,000 psi producing 0.02% elongation, the amount of pull can be calculated by the ratio of the actual elongation to the theoretical yield strength elongation, times the yield strength, times the mean cross-sectional area of the pipe.

$0.04'/0.10' \times 30{,}000$ psi $\times$ 1.59 in^2 = 19,800 lbs. This is important to note if the packer system is being hung from a hoist while inflating. The approximate 20,000 lbs must be added to the existing string weight to obtain the total string weight after inflation. If the hoist is not capable of safely holding the added pull the riser string must be secured to the well casing or the ground. Another method for securing the packers during inflation is to hang them in the hole with friction by slacking off the hoist about 0.04' as the packers inflate.

Pressure Relief Valve System:

When an isolated zone within a well is incapable of producing the full flow rate of the pump, flow can be throttled with a surface valve. However, sufficient flow must be maintained to adequately cool the pump motor. To throttle the discharge below the minimum pump flow, a pressure relief valve allows circulation bypass of the water back to the pump by way of the annulus. The valves are Swageloc adjustable relief valves, which are available in a variety of pressure ranges. The valves are mounted in a cross drilled block, with tubing threads connecting to the riser system through the center.

Static tests performed in a test tank provide the data illustrated in **figure three**. The unmodified pump curve follows the upper line, from A to C. The curve modified by the pressure relief valve follows the lower line from B to D. As the head pressure rises and discharge flow decreases from A to B both curves are the same. At point B (16 gpm, 300 psi) the pressure relief curve begins to diverge from the pump curve. From points B to D the circulated volume increases as the discharged volume decreases. At any point E along the modified curve the discharge rate is the value of X. The total flow, discharge plus circulation, is the value of X along the unmodified curve adjacent to point E of equal value Y, point F. The circulation rate is the difference between the total and discharge.

A pressure gauge and discharge flow meter are used to regulate the circulation and discharge flow. The gauge and meter can also identify washed-out or plugged pressure valves, system leaks, and pump performance. The pressure relief system allows continual mixing of the isolated zone during purging.

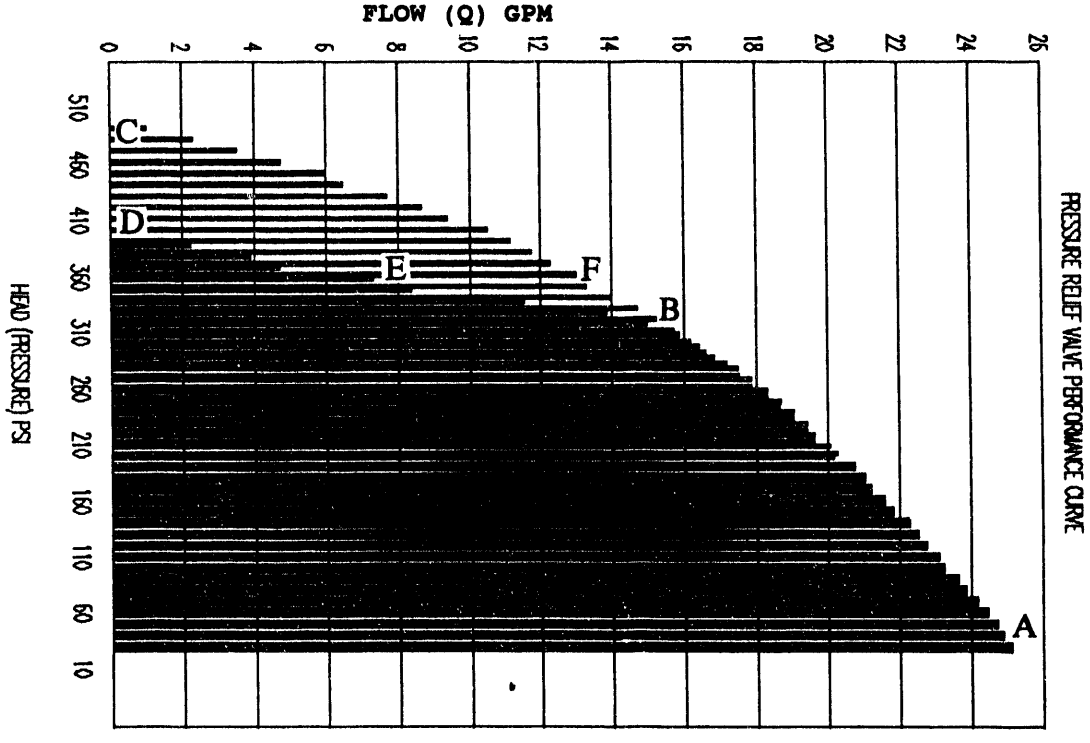


FIGURE THREE:
PRESSURE RELIEF VALVE PERFORMANCE CURVE

Access Port Valve and Housing:

The access port valve (APV) provides open circulation between the riser pipe and the annulus of the isolated zone. It is used for rapid mixing of tracer in the isolated zone before purging, and in combination with the pump check valve for slug tests. In operation the valve acts very quickly after a predictable delay. The valve is actuated with two pneumatic lines, which act on opposite sides of a vertical piston. The piston seals the riser from the annulus with o-ring seals against the valve body. The o-rings are subject to leakage, damage, and failure from sand and pebbles. Care should be taken to clear the valve of sediment before closing. The valve is very compact, helping to reduce the minimum length of the isolated zone. The access port valve is contained in a separate 5-1/2 inch sch-80 housing to provide the required mechanical link and riser seal. Sealed with o-rings and secured by threads to the pump head and cross bolts to the valve body. The top of the access port valve attaches to the pressure relief valve by a tubing nipple. The access port valve housing is the main connection where the packer system breaks into the upper and lower half. The original housing was increased in length from 12 inches to 18 inches to ease assembly of the control line connections also contained there.

Pump and Middle Transducer Housing:

The pump housing, directly below the APV housing is 5-1/2 inch sch-80 stainless steel pipe. The pump is hung from the pump head within the housing by a 1-1/4 inch NPT nipple. The housing attaches to the head with cross-bolts and o-ring seals. Cables and tubing pass through the pump head and are sealed by fittings with o-rings. The bottom block serves as the mount for the middle transducer similar to the upper transducer.

Pump and Check Valve:

A Grunfoss 16 gpm 5 hp pump with a 3-ph 460v Franklin motor is used for purging and sampling. Because the system was designed to operate at 1000 foot depths, a pump with adequate lift capacities was chosen. A 3-ph 460v motor was chosen to allow smaller gauge power cable to be used, (14 ga). However, a variety of 4 inch pumps could fit in the housing with the proper fittings. Custom stabilizers were installed on the pump to maintain alignment and reduce stress on the pump nipple when the unit is laid down.

The pump check valve supplied with the pump is essential when holding a column of water for slug testing, and beginning pumping tests with a constant discharge. The check valve is subject to leakage when clogged with sand, and care must be taken to flush pump and valve clean before depending on a seal.

Extension Zone Pup Joints:

The isolated zone between packers can be adjusted by substituting various length pup joints between the pump housing and the lower packer. The connecting threads are the same as the riser string so joints are interchangeable throughout the system. The transducer cable extensions continue through the joints,

while the lower inflation line runs to the outside. There is no limit to the length of the isolated zone, up to the limits of the system, however, 13 feet is the minimum length, and 25 feet has been the maximum length used to date.

Lower Packer:

The lower packer is similar to the upper packer except that pump intake holes are provided in the upper (fixed) end. Placing the intake holes in the packer head reduces the minimum length of the isolated zone. The intake holes in the packer head at the bottom of the zone insure through mixing when water is circulated through the access port valve or pressure relief valve. A replacement packer was modified from the original design to increase the base pipe from Sch-80 to Shc-160. The first packer base pipe suffered some crushing damage from a wrench.

Lower Transducer Housing:

The lower transducer housing is interchangeable with the upper housing except for the top head. A solid plug seals the block from the bore hole. Pipe lengths could be used instead of the plug to extend the pump intake into smaller hole diameters than could be accessed with the entire system. In that case the pump intakes in the lower packer would be plugged.

Pressure Transducers:

Three Paroscientific, Inc. "Digiquartz" RS-232 depth sensors provide temperature and temperature compensated pressure readings for the packer system. The temperature sensor is internal to the transducer and is used primarily for temperature compensation of the pressure reading. Although temperature readings are relatively slow to respond, water temperature data can be obtained if enough time is allowed for equilibration.

The transducers have a pressure range of 0 to 400 psi with an over pressure rating of 1.2 times full scale. The repeatability and hysteresis are both listed at ± 0.005% full scale, or approximately ± 0.046 feet of head. The resolution or sensitivity can be controlled by adjusting the integration time between the internal counter and the oscillators monitoring temperature and pressure. The integration time is adjustable in 0.003 second steps up to 45 seconds. Resolution is increased with integration time, but maximum sampling speed is reduced. For most tests a default setting of 0.7 seconds per reading is adequate and provides resolution of one part per million. The temperature compensated pressure is then calculated with a microprocessor that loads the data onto the RS-232 bus. The transducers are fully programmable and data is recorded with basic programs to a data file on a portable computer. In tests to date background noise has limited the useful resolution to approximately 0.005 feet. The transducers are linked with a single transmission cable in a serial loop. As many as four transducers have been run together with the fourth used at the surface for a barometer.

Electrical Power supplies:

Power for the submersible pump is supplied by a portable generator. Minimum requirements are 15 Kw, 3-ph, 480 volts, KVA code K. 480 volts are generally run to compensate for line resistance and deliver 460v at the pump. Because of the generator configuration, when the 3-ph power is regulated to 480v, the single phase 120v system rises to about 147v. This voltage is not acceptable to the regulated power supply used for large computers. Reducing the pump voltage would cause damage to the pump motor. As a result a smaller generator is used when running sensitive computer equipment with the power supply.

Power for lap top computers can be supplied through an invertor from the bus batteries, or a the small generator through a power converter. Power for the transducers is supplied directly from two large batteries hooked in parallel in the bus. The batteries are capable of running five day tests with a lap top computer.

Injection System:

The injection system consists of 1100 feet of 1/2" Tefzel tubing, and 1/4" SS tubing, a shut in valve and pump. The line terminates directly below the access port valve. A small teflon gear pump injects the tracer into the Tefzel tubing inside the bus. There is a shut-off valve at the end in the bus, with the down hole end open. The injection line is also used for purging the riser pipe by nitrogen injection, and gas bail pumping by displacement. For gas bailing, the riser pipe is pressurized from the surface, which forces water back up the injection line. Enough pressure must be used to overcome the head from the water table to the surface and fluid friction in the injection line. 300 psi provides a good flow of sample at 200 psi of head. Due to the volume of the confining pipe, extreme caution must be taken when pressurizing the riser pipe because of the possibility of explosion. Should the pipe rupture, serious injury or damage could result. Excessive pressure would be vented through the pressure relief valve providing it is operational and adjusted properly.

Surface Control Valves:

The well head stack diagramed in figure four controls flow and pressure for well discharge, circulation, and sampling. The construction is schedule-80 type stainless steel and will safely contain 500 psi, the shut in pressure of the pump. The stack is assembled with unions to be easily portable. The double tee fittings at the base allow in-line access to the riser pipe for water level and sounding measurements, and a convenient place for a temperature probe. The 1 inch sampling branch can be regulated for sample collection and flow cell supply by the combination of the control valve and sampling valves. The 2 inch ball valve is used for rapid release of pressure such as during a depressed head slug test. Above the 2 inch valve is a 1 inch high pressure control valve. This valve is the primary way of regulating discharge and circulation through the pressure relief valve. The pressure gauges and a flow meter in the discharge plumbing are

both used to adjust the valve. A flow regulator installed just past the 1 inch valve can also be used. However, the available pressure may exceed the range of the regulator. In that case, decreasing the available pressure with the control valve may cause cavitation, affecting the stability of the regulator. Another tee is included to allow injection of nitrogen into the riser pipe. The nitrogen is used for depressing the head for slug tests, or gas bail pumping through the injection line.

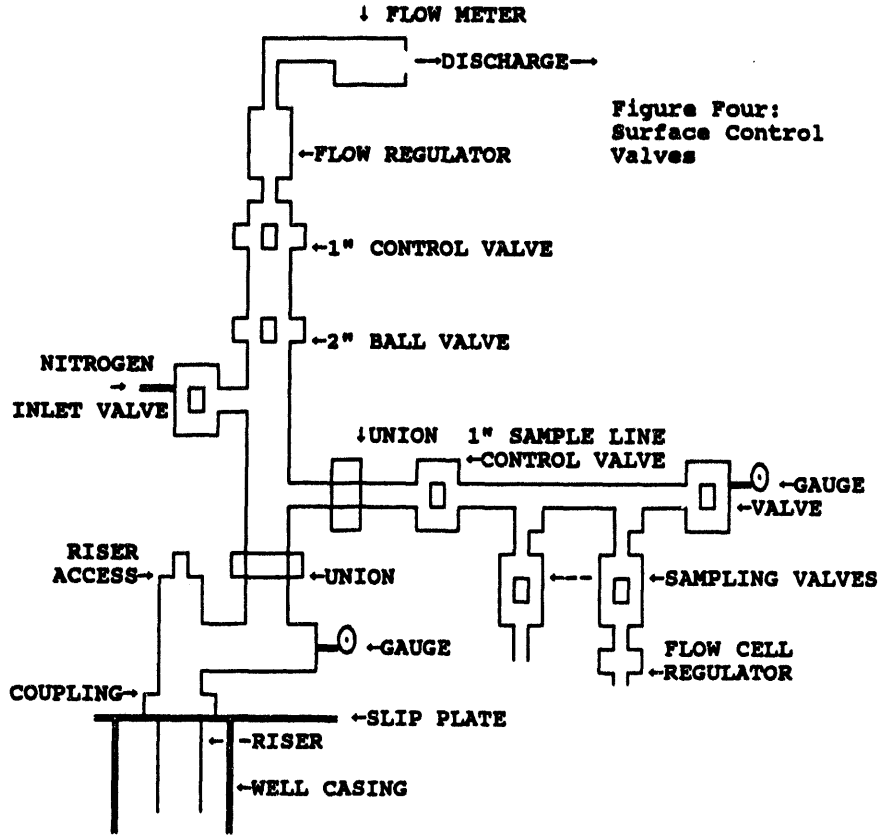


Figure Four: Surface Control Valves

HYDROLOGIC TESTING

Static Head Profiling:

Although the Paroscientific pressure transducers employed in the Idaho packer system are potentially capable of tremendous sensitivity to less than 0.001 foot, the accuracy of the system is limited to ± 0.05 feet. Sensitivity, precision or relative measurement is not the same as accuracy, repeatability or absolute measurement. Testing to date in the Snake River Plain Aquifer at the INEL has detected vertical head profiles in the order of ± 0.01 feet. While that range is within the capacity of the system to detect relative changes, there are many factors which contribute background noise of over 0.1 feet. The result is that absolute head measurements are not possible to the accuracy required, and relative head measurements are also limited. Listed below in order of magnitude are the principal

factors affecting absolute accuracy and relative precision which have been documented in actual field tests.

I Regional aquifer changes over months ± 1 foot
II Calibration drift over months ± 0.5 feet
III Barometric effects over days ± 0.1 to 0.3 feet
IV Production well pumping over hours ± 0.01 to 0.1 feet
V Physical movement on packer inflation/deflation ± 0.03 to 0.05 feet
VI Vertical bore hole flow restriction head loss around packers in small diameter (6 inch) holes ± 0.01 to 0.1 feet
VII Physical measurement errors of system depth ± 0.01 to 0.5 feet

Because complete testing and sampling of wells, near the Idaho Chemical Processing Plant has typically taken one to two months each, accurate absolute head measurements have not been possible. The calibration drift combined with regional aquifer changes has contributed the greatest error. Barometric effects can be accounted for if the barometric efficiency of the interval can be measured. However, only with monitoring over days can barometric efficiency be determined by comparing atmospheric changes with interval head. The production wells at the ICPP produce 3300 gpm and cycle throughout the day. The result is that static conditions in the nearby monitoring wells within one mile are never achieved, and draw down and recovery are not consistent throughout the saturated interval being tested.

An alternative method to measure relative head gradients is proposed and will be tested on wells far enough away to not be directly affected by the production pumping. Should the method is perfected it will be applied in future tests near the production wells at the ICPP.

Before the packers are inflated, static heads will be monitored and the calibration of the transducers checked by the physical length between sensing ports. Transducers are calibrated to a barometric reference in the bore hole before going under water. A steel tape and sounding weight will be used to measure from the surface to a measuring point at the top of the riser valve. Transducer sensing ports are also referenced to the same point. With the access port valve open to allow free flow to the riser, an electrical tape will be used to measure the static head level of the open bore-hole. The measuring tapes will then be left in the riser and static head monitored with the transducers while the packers are inflated. The actual head change of the isolated interval, relative to the open bore hole, is the change recorded by the e-tape. The physical movement of the packers will be the change in head on the middle transducer minus the e-tape change. For a check, the relative head change can also be obtained by directly measuring the change in depth on inflation with the steel tape and sounder, then subtracting that value from the change on the middle transducer. A map of head profiles relative to the open bore hole can then be plotted for the intervals tested. The assumption on which the method is

based is that the head profile will be constant over the length of testing, approximately one month. That assumption is reasonable provided there are no major changes in the regional aquifer water table, there is no detectable production well influence, and barometric efficiency is fairly consistent throughout the saturated interval. It would also be helpful if a head gradient of sufficient magnitude to measure actually exists. The finished profile could be further checked by comparing to flow logs for the well, or to near by nested wells completed at discrete intervals, provided they exist.

Slug Tests:

Slug tests for determining aquifer transmissivity can be accomplished by one of two methods, either by releasing a stabilized depressed head or instantaneously inducing an increased head. However, the effectiveness of the test depends on the ability of the testing system to produce a measurable stress on the aquifer being tested. If the aquifer being tested can accept water at a rate much higher than can be delivered, a measurable response may not be possible. In tests with the Idaho system, a 460 foot induced head will produce a maximum flow rate through the APV of approximately 200 gpm. That range limits effective slug testing to approximately half of the formations tested at the INEL. Fluid friction in the 2 inch riser pipe over 500 feet has been determined to be the most limiting factor. In addition, the upper section of the packer system contains control lines in the riser which increases restriction. With the restrictions in mind, slug testing has been an effective tool for measuring medium to low conductivities by the following methods. A single Basic test program with variable sampling rates can be run to monitor the transducer readings throughout the entire sequence. Being able to slow down sample rates at times when fast readings are not needed allows you to reduce the size of the resulting data file to a more manageable size, while preserving a large enough time span to recognize any antecedent trends.

First a rough estimate of conductivity can be made by inflating the packers at a desired test zone and observing the pressure change on the three transducers as during the first test for static head relative measurements. If the zone isolated increases dramatically over the other two on packer inflation, the approximate draw down at 20 gpm will be 150 times the pressure spike minus the pull down of 0.04 feet. Because using excessive head for a slug test can cause damage to the well and equipment, and can waste time waiting for conditions to stabilize an estimate of the size of slug needed is valuable.

An example would be, if on inflation the center transducer rises 0.15 feet then stabilizes within a minute, the expected draw down from the zone would be about 16.5 feet. This method is very imprecise and could actually be 10 to 50 feet. However it serves the purpose to design the magnitude of the test. A 500 foot slug would be much too much and would probably take hours to accomplish stable conditions. A slug of about 50 feet would be much more reasonable. Under such conditions the packers should

be deflated to reduce draw down when the pump is used to fill the riser, or when the head is depressed.

Induced Head Slug Test:

The riser pipe can be filled with the submersible pump. The access port valve must be closed and the riser valve open to do this. The pump is turned off when the water level reaches the predetermined mark. By using an e-tape, the induced head can be accurately measured above the static head of the zone, or approximated by timing the pump rate. Continue monitoring the water level in the pipe to make sure the pump check valve or access port valve are not leaking as they might if the water contains much silt or sand. If no leakage occurs, the riser valve can be ignored. If leakage does occur, close the riser valve.

Inflate the packers and monitor the transducers until conditions stabilize to a pre-test state. The slug test can then begin by opening the riser valve (if used) and then open the access port valve. A standard test timing sequence and pressure settings was developed during field testing. Remember the riser valve must be fully open before the APV opens or it will cause wild oscillation and unusable data.

At time 0 open riser valve, release pressure.
At time 25 seconds release pressure from APV close side.
At time 45 seconds pressurize APV open side.
At time 60 seconds riser valve is fully open.
At time 70 seconds APV opens instantly test begins.

The slug height can be checked again prior to the test with the e-tape if desired, or read directly on the PC as the APV opens. When the APV opens the slug is delivered to the isolated zone usually within one second. By monitoring the transducers until the head returns to the pre-test state the test is completed, and the data can be examined.

Depressed Head Slug Tests:

Depressed head slug tests can be used as long as the zone being tested has sufficient head to depress. The following method has proven successful in field testing. The riser valve cannot be used effectively in this case because it opens too sluggishly and cause wild oscillations in head measurements. Instead of the riser valve the 2 inch ball valve on the stack is used to control the test. All fittings above the 2 inch valve should be removed to allow full volume flow when the head is released.

With the packers deflated and the APV open, depress the head in the riser by injecting nitrogen through the stack (figure four). Monitor the pressure directly by the gauge on the stack until the desired head is reached. The supply regulator can be set to provide a constant head should leaks occur, or the stack shut in completely if leaks are not a problem. The packers can then be inflated and transducers monitored until conditions stabilize again. An e-tape measurement of the depressed head

cannot be made at this time because the stack is sealed, however e-tape readings should be made prior and after a test as a check. The head magnitude will be recorded within a second or two after the 2 inch surface is opened. Continue monitoring until heads recover. The data can then be analyzed.

Pumping Tests:

Pumping tests require a constant discharge rate throughout the test to produce accurate results. A reasonable pumping rate should be estimated from the inflation test to prevent excessive draw down in tight formations. Set up the test with the packers deflated, APV closed and riser valve open. Start pumping and adjust the flow to the desired level with the surface control valves and regulators. Note if any excessive draw down occurs on the transducers. If draw down occurs in the whole well or central zone with the packers deflated, the pump must be stopped after setting the discharge and the head allow to recover. If the pump is turned off and leakage occurs through the check valve or APV the test will be compromised. The riser valve can be used as a back up but must be completely deflated before starting the pump or oscillations will occur. Should the check hold and APV hold the full column without leaking, the pump can be started as soon as conditions stabilize. If no draw down occurs the packers can be inflated with the pump running and the test begun. The pull down of 0.04 feet on all three transducers must be subtracted from the test readings. The variable rate sampling program allows slowing the readings after the initial draw down during long tests.

Tracer Injecting, mixing:

Tracers are injected directly into the pump stream below the APV and mixed throughout the isolated zone back to the pump intakes (figure one). The tracer should be injected and mixed with the APV open and pump circulating. The riser valve can be used if a full column constant discharge is desired for pumping tests or other reasons until mixing is completed. Then the pump must be shut off while the APV is closed first then the riser valve opened. Purging the zone at the predetermined discharge rate can then began with the pump. Allowing some circulation through the pressure relief valve while purging eliminates dead spots in the isolated zone. The tracer is monitored in the surface discharge stream with either ion specific or specific conductance instrumentation until background levels are approached or reached. Background levels can be determined when pre-setting the discharge rate.

Hydrogeology, Waste Disposal, Science and Politics
Proceedings 30th Symposium
Engineering Geology and Geotechnical Engineering, 1994

HYDROLOGIC TESTING IN WELLS NEAR THE IDAHO CHEMICAL PROCESSING PLANT AT THE IDAHO NATIONAL ENGINEERING LABORATORY

by
Gary S. Johnson
J. Khan Olsen
Dale R. Ralston

University of Idaho, Geology and Geologic Engr. Dept.
Idaho Department of Health and Welfare, INEL Oversight Program

ABSTRACT

The Snake River Plain aquifer beneath the INEL is often viewed as a 2-dimensional system, but may actually possess 3-dimensional properties of concern. A straddle-packer system is being used by the State's INEL Oversight Program to isolate specific aquifer intervals and define the 3-dimensional chemical and hydrologic characteristics of the aquifer. The hydrologic test results from wells USGS 44, 45, and 46 near the Idaho Chemical Processing Plant indicate that: 1) Vertical variation in static head is less than 0.3 feet, 2) barometric efficiencies are between 25 and 55 percent, and 3) the system responds to distant pumping as a multi-layered, but interconnected system.

INTRODUCTION

The State of Idaho INEL Oversight Program is evaluating the ground-water monitoring system at the Idaho National Engineering Laboratory (INEL). The project includes use of a straddle-packer system to isolate, sample, and hydraulically test discrete intervals of the Snake River Plain aquifer. The program will ultimately improve knowledge of the three-dimensional characteristics of the aquifer system and the efficacy of current sampling programs in wells open to the aquifer over large intervals.

The straddle-packer apparatus has been used to test three wells in the vicinity of the Idaho Chemical Processing Plant (ICPP) at the INEL. Wells USGS 44, 45, and 46 were selected for straddle-packer testing based on location, well diameter, open interval, and long history of water quality data. All three wells are open from the water table, at about 460 feet below land surface (bls) to the bottom of the well at about 650 feet bls. The wells are located in about a 400 foot radius, just west of the ICPP (figure 1).

The straddle-packer isolates specific intervals of the aquifer by closing-off the open borehole with inflatable rubber packers. The system components of interest to this paper are, from top to bottom: a) an upper pressure transducer, b) the upper packer, c) the middle transducer, d) the lower packer, and e) the lower transducer. A pump is also located between the two packers. The system components are described in detail in Olsen (1994).

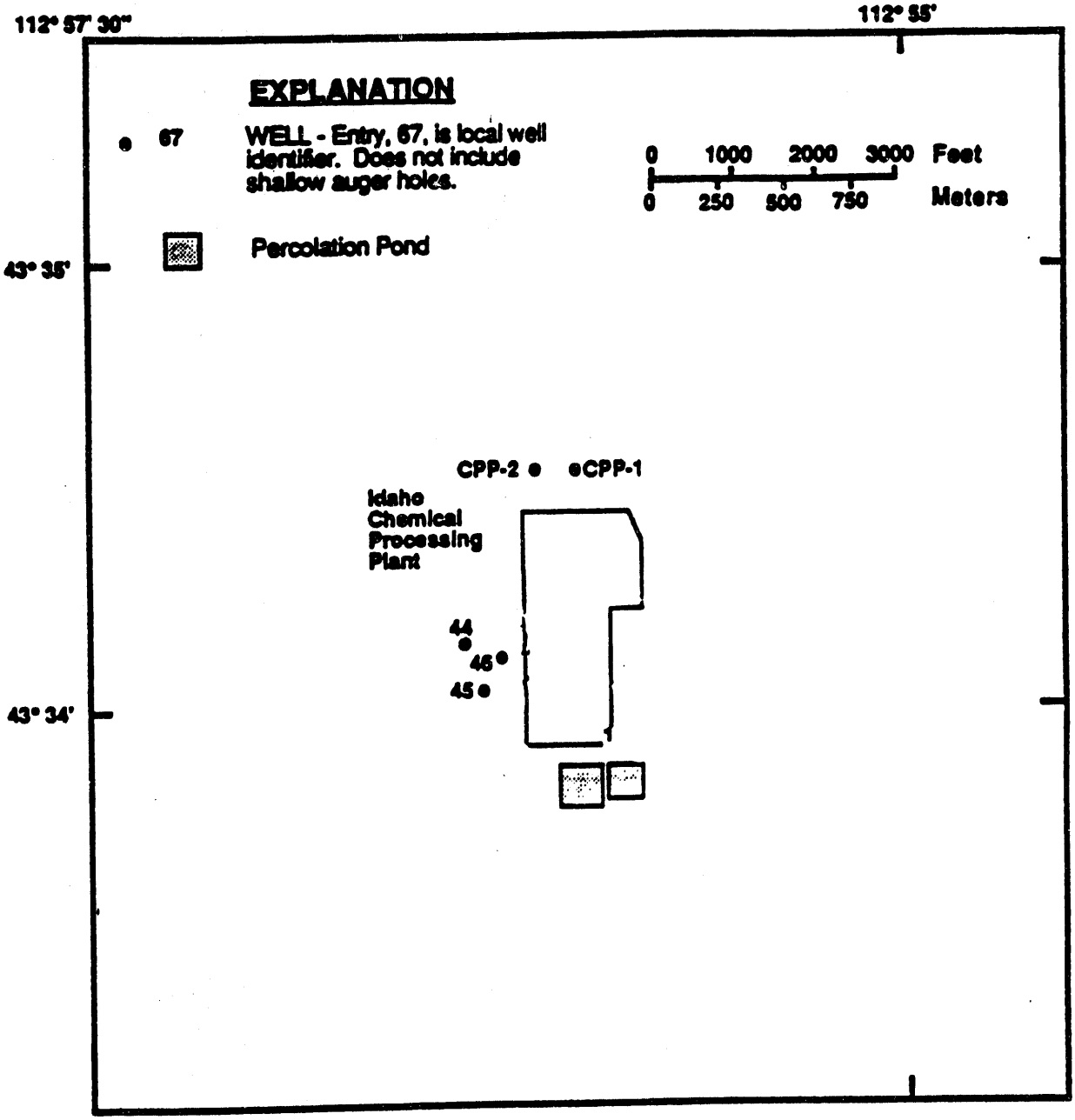


Figure 1. Location of wells CPP-1, CPP-2, USGS 44, 45, and 46 Relative to the Idaho Chemical Processing Plant (after Anderson, 1991).

PURPOSE AND OBJECTIVES

The purpose of this paper is to describe the results and interpretation of selected hydrologic tests conducted with the straddle-packer system in three wells near the ICPP. The test results will ultimately be used in concert with chemical and tracer testing to develop improved concepts of the three-dimensional characteristics of the ground-water flow system near the ICPP.

The specific objectives of the hydrologic testing are:

1) To determine the vertical variation in static head in the aquifer system,
2) To determine the hydraulic head response of specific intervals to changes in barometric pressure,
3) To evaluate water level response in the selected wells to production well pumping at the ICPP, and
4) To determine relative variation of hydraulic conductivity of isolated individual aquifer intervals.

The first three objectives are addressed in this paper. Vertical variations in hydraulic conductivity will be described in subsequent publications.

HYDROGEOLOGIC SETTING

The Snake River Plain aquifer occurs in tertiary and quaternary age basalts and interbedded sediments underlying the Snake River Plain at the INEL and most of eastern Idaho. In the upper 700 feet of deposits near the ICPP a sequence of 23 basalt flow groups and 15 to 20 sedimentary interbeds have been identified (Anderson, 1991). The 23 flow groups consist of about 40 separate basalt flows (Anderson, 1991) normally ranging in thickness from 20 to 50 feet and of limited areal extent.

The Snake River Plain aquifer at the INEL is generally considered as unconfined, but may act confined in short duration pumping situations. Transmissivity of the aquifer at the INEL is highly variable, ranging from 1 ft^2/day to 760,000 ft^2/day (Ackerman, 1991). Hydraulic conductivity varies greatly with depth. Rubbly basalt flow tops are generally highly productive, with lower hydraulic conductivity associated with the more dense flow interiors. Sediment interbeds may have high or low hydraulic conductivities depending on the texture of the deposits.

RESULTS

Hydrologic data are collected by three high-precision, pressure transducers positioned: 1) above the upper packer, 2) between packers, and 3) beneath the lower packer. The transducers have an accuracy (repeatability) of 0.05 feet of water (0.02 psi) with a maximum pressure of over 900 feet of water (400 psi). The precision of sequential measurements, relating to the ability to measure drawdown, is about 0.005 feet, depending upon the frequency of observation.

The packer system is used to collect hydrologic data in isolated aquifer intervals for estimation of static head and aquifer properties of hydraulic conductivity and storativity. This paper describes results and interpretation of vertical profiles of:

1) Static head data,
2) Barometric pressure response, and
3) Response to the ICPP production wells about 0.5 miles away.

Straddle-packer testing was conducted on multiple intervals in wells USGS 44, 45, 46. Table 1 provides a list of tested intervals discussed in this paper.

Table 1. Straddle-Packer Tested Intervals.

USGS 44	USGS 45	USGS 46
(depth, in feet below land surface)		
467-482	462-477	465-483
480-495	480-495	507-525
495-515	500-515	531-549
500-515	519-534	553-571
519-534		575-593
580-600		594-612
600-620		612-629

Well USGS 45 was not tested below 534 feet due to borehole deviation which prevented access with the packer system.

Temporal Variation in Water Levels

True static conditions are non-existent in the Snake River Plain aquifer near the ICPP. Hydraulic head is continuously changing as a result of production well pumping at the ICPP and changing barometric pressure. Conditions appear static if short-term variations in head are less than the resolution of the measuring device. The continuously variable nature of "static" head is apparent in observations with the straddle-packer system due to the high transducer resolution. Examples of variations in hydraulic pressure with time are shown in figures 2 and 3 for the water table to 483 foot interval and 553 to 571 foot interval (bls) in well USGS 46. The graphs show the response of the three submerged transducers and variations in barometric pressure with time. The transducer observations have been adjusted for elevation and an average barometric pressure, but are not compensated for instantaneous barometric pressure. Only two transducers are plotted in figure 2 because the upper transducer was above the water table.

Production well pumping at the ICPP results in about an 11 hour cyclic response in the graphs of figures 2 and 3. The duration of the pumping cycle varies somewhat with the operation of the facility. All three transducers show response of generally less than 0.1 feet of drawdown to ICPP pumping. The response appears more attenuated in the upper transducers, and is affected by superimposed barometric effects. The initial transducer response generally occurs 10 to 15 seconds after the ICPP well begins pumping, some 2400 to 3100 feet away. A relationship is also apparent between aquifer head and barometric pressure in figures 2 and 3. Aquifer response to ICPP pumping and barometric

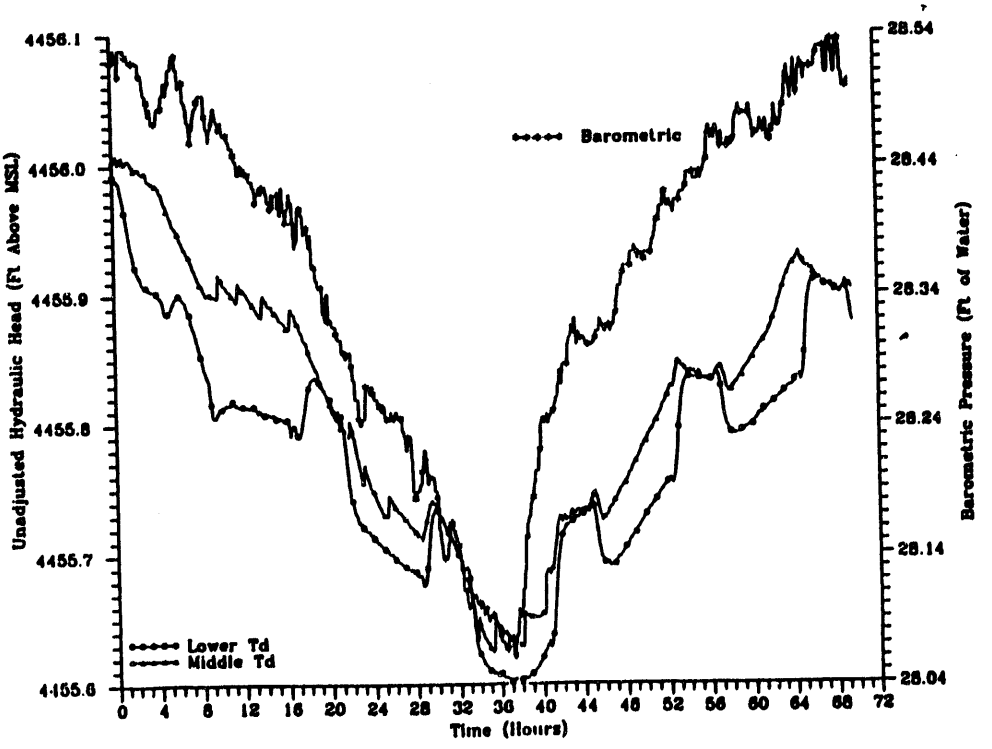


Figure 2. Transducer and Barometric Pressure Variation in Well 46, 465 to 483 feet bls Interval.

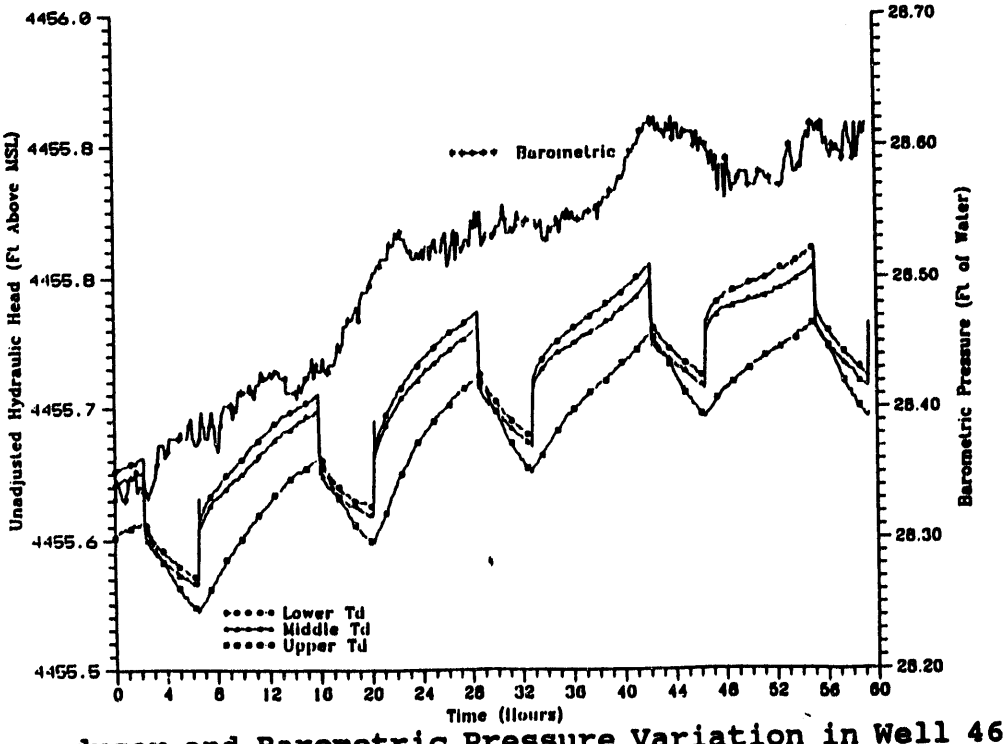


Figure 3. Transducer and Barometric Pressure Variation in Well 46, 553 to 571 feet bls Interval.

pressure are discussed in the following sections.

Barometric Pressure Relationships

Water levels in confined or semi-confined aquifers often exhibit an inverse relationship to changes in barometric pressure. The relationship also exists when aquifer hydraulic pressure is monitored using pressure transducers, although the relationship varies, depending on whether absolute or relative transducers are used. The absolute transducers of the straddle-packer system register a direct relationship between aquifer pressure and barometric pressure. That is, increases in barometric pressure result in increases in aquifer pressure. The sensed aquifer pressure is converted to head or water level by the following relationship:

$$WL = TR + Z - Pa \qquad (1)$$

where:

WL = aquifer water level (feet of water),
TR = transducer pressure reading (feet of water),
Z = altitude of transducer (feet above sea level), and
Pa = barometric pressure (feet of water, adjusted for depth to the water table).

The subtraction of actual barometric pressure from the transducer reading in equation (1) converts the direct relationship of aquifer and barometric pressure into an inverse relationship between water level and barometric pressure. Graphs illustrating the relationship between barometric pressure and aquifer water levels in wells USGS 44, 45, and 46 are presented in figures 4 through 6.

The relationship between barometric pressure and aquifer water level is apparent for most of the intervals tested with the straddle-packer system in well USGS 44, 45, and 46. In intervals where barometric pressure changed by less than about 0.3 feet of water, however, barometric pressure variation was insufficient to produce a reliable estimate of the relationship between barometric pressure and aquifer water level. Linear regression between barometric pressure and aquifer water level (as determined by equation (1)) for each interval yielded coefficients which represent the slope of the lines presented in figures 4 through 6, and the negative barometric efficiency of the interval. The regression coefficients, coefficients of determination, and resulting barometric efficiency are presented in table 2. Tests in which barometric pressure variation was less than 0.3 feet were omitted from table 2 due to insufficient range of data.

The calculated barometric efficiencies of individual intervals ranges from 26 to 54 percent (table 2). Some of the variation in barometric efficiency between intervals is likely error resulting from insufficient data and noise from ICPP pumping response. It is difficult to justify a low barometric efficiency near the bottom of well 46 (612-629 interval), with higher barometric efficiencies in overlying intervals. Low barometric efficiencies are possible near the water table, since well casing often terminates above the water table and provides a conduit for barometric pressure change to the aquifer. Longer duration testing on individual intervals is necessary to conclusively determine barometric efficiency.

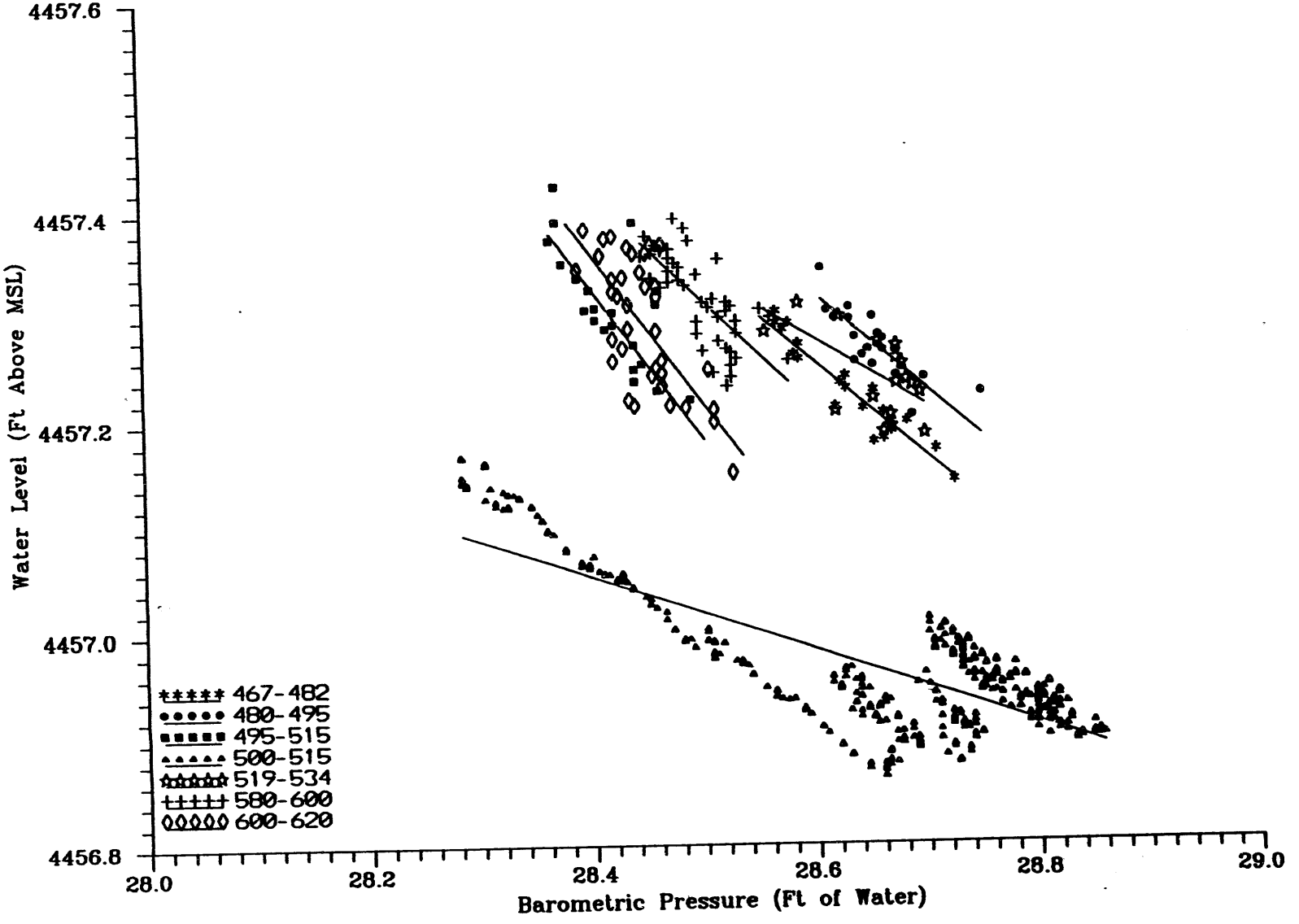


Figure 4. Aquifer Water Level Relationship to Barometric Pressure for Intervals in Well 44.

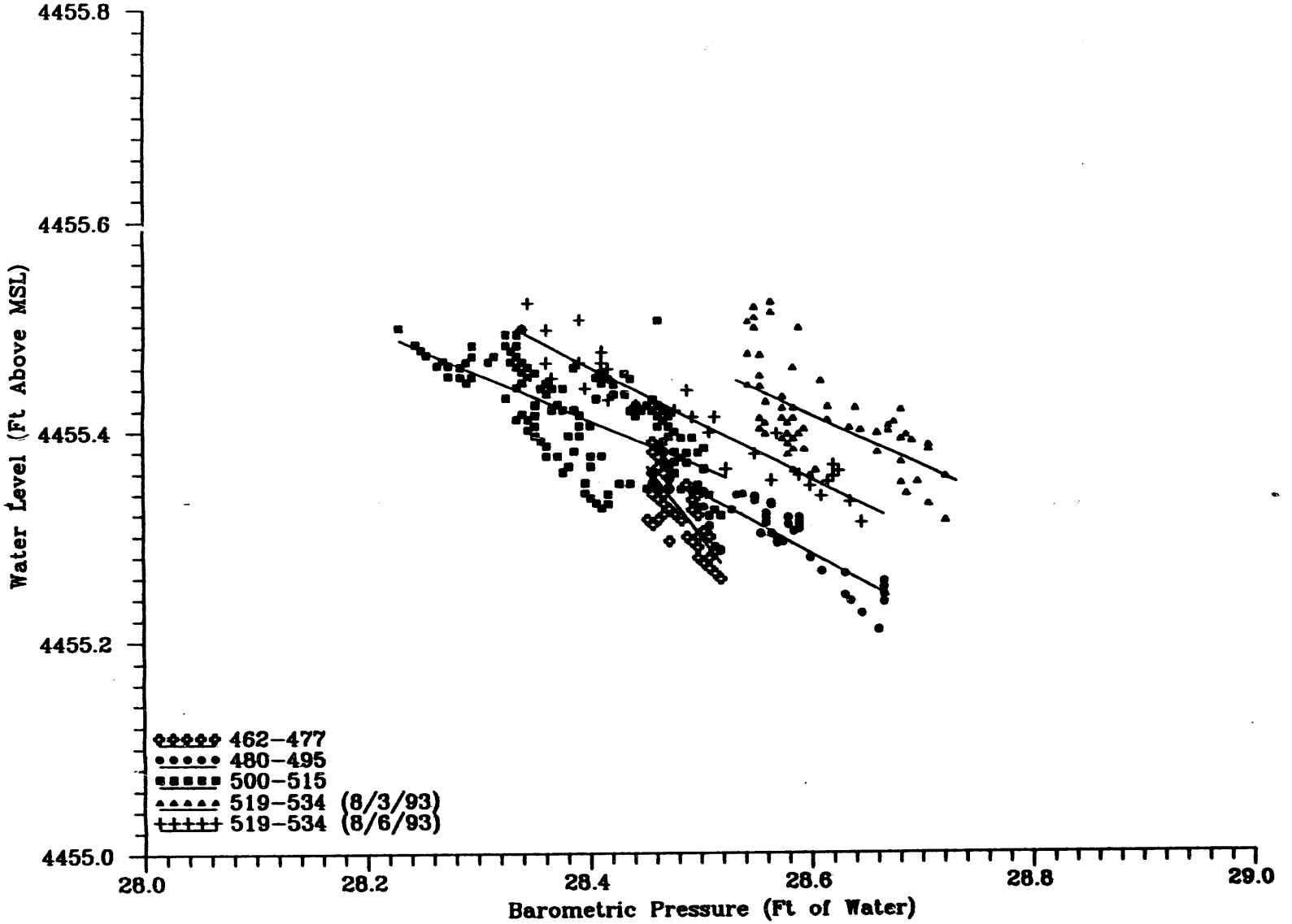


Figure 5. Aquifer Water Level Relationship to Barometric Pressure for Intervals in Well 45.

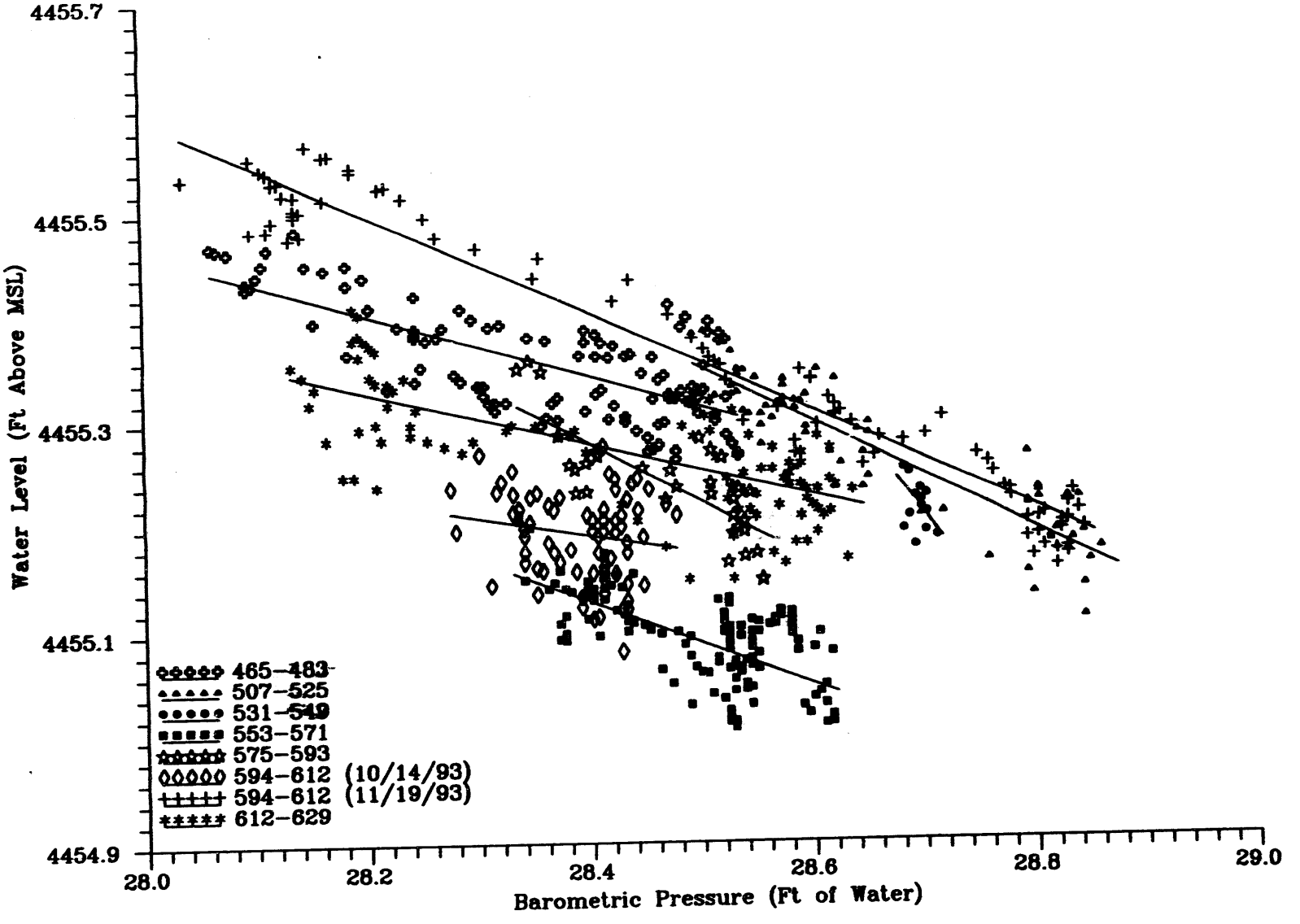


Figure 6. Aquifer Water Level Relationships to Barometric Pressure for Intervals in Well 46.

Table 2. Results of Linear Regression of Barometric Pressure and Aquifer Water Level.

Well	Interval	Regression Coefficient	R^2	Barometric Efficiency (%)
44	500-515	-0.35	0.65	35
45	519-534	-0.54	0.90	54
46	465-483	-0.30	0.53	30
46	507-525	-0.52	0.81	52
46	553-571	-0.40	0.45	40
46	594-612	-0.47	0.96	47
46	612-629	-0.26	0.52	26

Vertical Variations in Static Head

Little variation of hydraulic head with depth is apparent in wells USGS 44, 45, and 46. The relatively small degree of difference in water level between intervals is shown by the small vertical offset of the interval data sets presented in figures 4 through 6. The calculated head difference between intervals within a well ranges between 0.15 to 0.3 feet. The vertical offset is not considered to be representative of head difference between intervals due to inconsistency when compared to pressure differences among the three transducers during simultaneous readings. The offset is thought to be the cumulative result of a) inaccuracy in transducer readings, b) inaccuracy in measurement of system depth, and c) seasonal variations in aquifer water levels. The data indicate only that vertical head variation in the 170 feet of submerged, open borehole is less than 0.3 feet.

ICPP Pumping Response

Water levels in wells USGS 44, 45, and 46 respond to pumping in the ICPP production wells about 0.5 mile to the northeast. The two production wells, CPP-1 and CPP-2, provide water for the facility at a rate of about 3000 gpm. The two wells are rotated into production on a monthly basis and currently cycle on and off about every 11 hours. Both of the wells are completed in two intervals in the aquifer, at depths ranging from 460 to 600 feet below land surface. The completion zones correspond to two basalt flow groups: 1) the E through H group, and 2) the I flow group, according to the stratigraphy defined by Anderson (1991). Anderson (1991) determined that these same basalt flow groups intersect wells 44, 45, and 46 at the depths listed in Table 3.

The drawdown in wells USGS 44, 45, and 46 from pumping at the ICPP production wells ranges from 0.02 to 0.10 feet, depending on the well and interval. The drawdown is apparent from cyclic response of the graphs of figures 2 and 3. The magnitude of the drawdown in specific packer intervals can be used as a qualitative measure of the degree of hydrologic connection between the interval and the pumping zones of the ICPP well.

Table 3. Depth of Basalt Flow Groups Intersecting the Saturated Portion of Wells USGS 44, 45, and 46 (after Anderson, 1991).

	Well		
Flow Group	44	45	46
E through H	------(feet below land surface)------		
Top	441	446	450
Bottom	550	550	547
I Flow			
Top	440	550	550
Bottom	>650	>651	>648

ICPP production well drawdown varies with depth in wells USGS 44, 45, and 46 (figure 7). The drawdown is determined graphically as the amplitude of the drawdown cycle in figures 2 and 3 and similar graphs for other intervals. Small vertical variations in drawdown are apparent in the lower transducer, with the general trend indicating the minimum response near the water table. The response of the middle and upper transducers varies significantly with depth. The trend is toward maximum response near the bottom of the wells, generally within the I flow group defined by Anderson (1991).

The relative difference between upper, middle, and lower transducer response in figure 7 is more meaningful than the absolute magnitudes of the drawdown. Drawdown is consistently lowest in the upper transducer (above the upper packer) compared to the middle and lower transducers, separated by inflated packers. The consistently low relative readings of the upper transducer may be the result of either of two conditions: a) the upper transducer may be representing unconfined conditions, and b) the upper saturated intervals are not as well connected to the ICPP production wells. In most intervals, the drawdown in the middle transducer is also less than or equal to drawdown in the lower transducer, reflecting diminishing drawdown nearer the water table.

The relative differences in drawdown among the three transducers varies with depth of the isolated interval. Figure 7 shows that there is little difference in drawdown from the ICPP well in the middle and lower transducers for intervals near the bottom of the wells. This indicates that the wells may be divided into two units based on their hydrologic response to ICPP pumping. In well 44, the middle and lower transducer register approximately the same magnitude of drawdown in all intervals below 515 feet below land surface. In intervals above 515 feet the response of the middle transducer is attenuated relative to the lower unit, implying that the lower portion of the well is hydrologically more strongly connected with the ICPP wells. Wells 45 and 46 show similar conditions, with the transition zones at depths of 500 and 550 feet below land surface, respectively.

The qualitative grouping of drawdown response may define two flow systems with differing degrees of connection to the ICPP

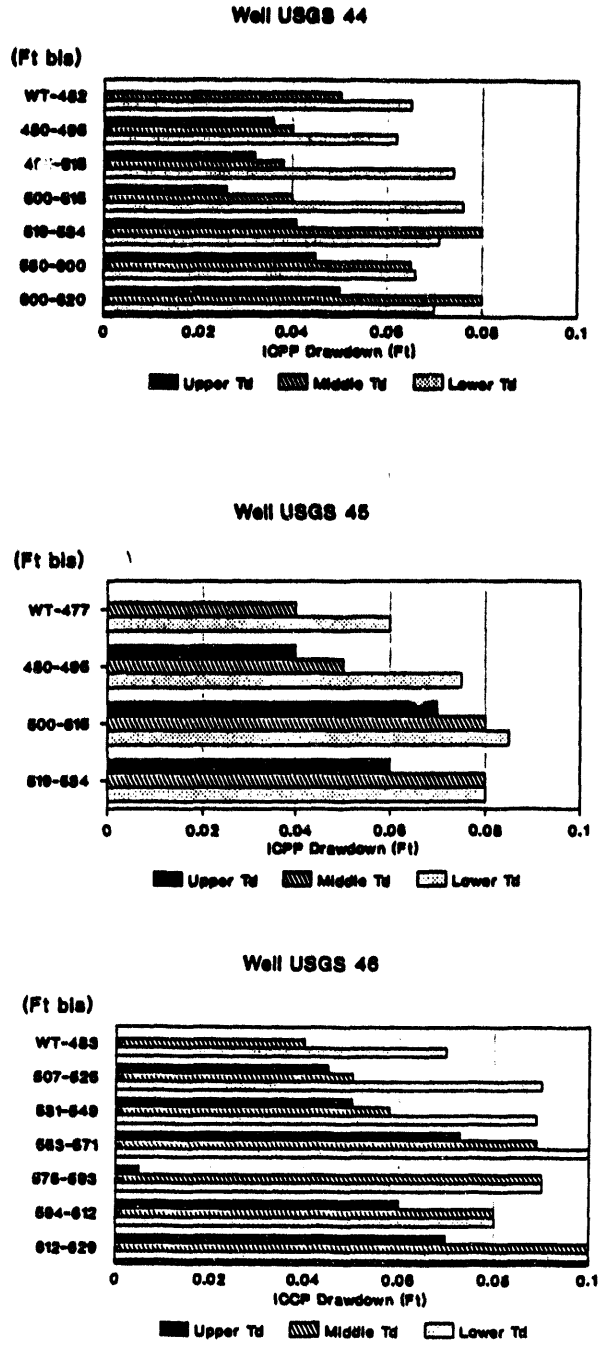


Figure 7. Interval Specific Drawdown at Wells USGS 44, 45, and 46 in Response to Pumping at CPP-1 and CPP-2.

production wells. A layer of lower vertical permeability could conceivably separate the two units. In well USGS 46 the transition approximately corresponds to the sediment interbed at the lithostratigraphic contact between basalt flow groups E-H and I as determined by Anderson (1991). In wells USGS 44 and 45 the transition appears at a higher lithostratigraphic point in the profile, somewhere within the E-H basalt flow group. Within the I flow group, and within the lower depths of the E-H flow group in wells 44 and 45, a nearly homogeneous response is observed to production well pumping for the ICPP.

SUMMARY

The straddle-packer system is effective for determining vertical variations in hydrologic characteristics of the Snake River Plain aquifer within certain limitations. It has been determined that: 1) Vertical variation of static head within the upper 170 feet of aquifer near the ICPP is less than 0.3 feet, 2) the tested wells respond as semi-confined with a barometric efficiency ranging between 0.25 and 0.55, and 3) response to ICPP production wells indicates a multi-layer hydrologic system with a hydraulic interconnection of the two layers. These results will be confirmed and expanded as testing progresses into additional wells near the ICPP and as hydrologic, geochemical, and geophysical information are pieced together as components of the conceptual flow system puzzle.

REFERENCES

Ackerman, D.J., 1991, Transmissivity of the Snake River Plain aquifer at the Idaho National Engineering Laboratory, Idaho: U.S. Geological Survey Water Resources Investigations Report 91-4058, 35 p.

Anderson, S.R., 1991, Stratigraphy of the Unsaturated Zone and Uppermost Part of the Snake River Plain aquifer at the Idaho Chemical Processing Plant and Test Reactors Area, Idaho National Engineering Laboratory, Idaho: U.S. Geological Survey Water Resources Investigation 91-4010, 71 p.

Olsen, James K., 1994, Straddle-Packer Design and Operation for Vertical Characterization of Open Bore Holes: 1994 Symposium on Engineering Geology and Geotechnical Engineering, Boise, Idaho.

Hydrogeology, Waste Disposal, Science and Politics
Proceedings 30th Symposium
Engineering Geology and Geotechnical Engineering, 1994

VERTICAL VARIATION IN GROUNDWATER CHEMISTRY INFERRED FROM FLUID SPECIFIC-CONDUCTANCE WELL LOGGING OF THE SNAKE RIVER PLAIN BASALT AQUIFER, IDAHO NATIONAL ENGINEERING LABORATORY, SOUTHEASTERN IDAHO

Spencer H. Wood and William Bennecke
Department of Geosciences
Boise State University
Boise, Idaho 83725

ABSTRACT

Well logging of electrical fluid specific conductance (C_s) shows that permeable zones yielding ground water to intrawell flows and the water columns in some wells at INEL have highly different chemistry, with as much as a two-fold variation in C_s. This suggests that dedicated-pump sampling of ground water in the aquifer may not be representative of the chemistry of the waste plumes migrating southwest of the nuclear facilities. Natural background C_s in basalt-aquifer ground water of this part of the Snake River Plain aquifer is less than 325µS/cm (microSiemans/cm), and total dissolved solids in mg/L units, (TDS) ≈ $0.6C_s$. This relationship underestimates TDS for waters with chemical waste, when C_s is above 800 µS/cm.

At well 59 near the ICPP water of 1115 µS/cm (≈670+ mg/L TDS) enters the well from a permeable zone between 521 and 537 ft depth; the zone being 60 ft below the water level and water of 550 µS/cm. At the time of logging (9/14/93) the 1115µS/cm water was flowing down the well, mixing with less concentrated waters and exiting at 600 or 624-ft depth. Waste water disposed of down the injection well at ICPP until 1984 was estimated to have a C_s of 1140 µS/cm, identical to the water detected in logging.

At well OW2, the highest C_s water (760µS/cm) is in the upper 30 feet of the water column: water from two flow zones below have different chemistry with lower values of C_s. The Site 14 well and USGS 83 show uniform values throughout the water column. The water column in Site 14 is dominated by a downward flow of 50 gal/min probably entering between 475 and 500 ft depth and exiting near the bottom of the well at 700 ft depth.

Impeller flowmeter and precision temperature logging are used to define and quantify temperature variations and intrawell flows. At well 59 (depth=657 ft) and OW2 (depth=996 ft), are downward decreasing temperatures in the bottom zones of no flow, suggesting that major flow zones lie beneath the deepest parts of these wells.

INTRODUCTION

Fluid temperature, electrical specific conductance, and spinner-flowmeter logs were run in four wells within the saturated zone of the eastern Snake River Plain basalt aquifer (Figures 1

and 2). This reconnaissance logging was done to identify wells in which to deploy packer systems to hydraulically test and sample ground water from the aquifer - a project of the State of Idaho Oversight Program of U.S. Government nuclear facilities at the Idaho National Engineering Laboratory. Identification of the major permeable conduits in the stack of Quaternary lavas, sediments and basalt bodies that make up the aquifer is a major goal of the project. Knowledge of the major permeable zones, and determining the position of waste water in the aquifer is important to monitoring plumes of waste water, and to design a strategy for diverting plumes or recovering and reprocessing waste waters should that become necessary or feasible in the future.

Thickness of the Quaternary basalt section exceeds 2,500 ft (760 m) beneath parts of the Idaho National Engineering Laboratory (Figure 3). A K-Ar age of 820 Ma is obtained from basalt at 2321-ft (708 m) deep in well NRF 89-04, and ages of 200-650 Ma are common for the sequence (Lanphere and others, 1993. The lava sequence that comprises the saturated aquifer contains several thin but very transmissive zones which we believe to be mostly lava-flow tops - although not all flow tops are highly permeable. Well tests of the upper 150 to 500 ft (45 to 150 m) of the aquifer show very small drawdowns for large flows, from which are derived some of the highest transmissivity values known in the world, ranging up to 2,400,000 ft^2/day (220,000 m^2/day) (Garabedian, 1992, p. F12). Typical value is 60,000 ft^2/day (5580 m^2/day) (Ackerman, 1991). We do not yet know the typical thickness of the highly transmissive zones, but we suspect that several zones of only a few meters of fractured or rubbly flow-top basalt may dominate the response of the wells to pumping. Much of the eastern Snake River Plain basalt is near-vent and tube-fed pahoehoe lava (Kuntz and others, 1992). We have been impressed by the apparent permeability of coarse rubble and sequences of shelly pahoehoe in the upper few meters of flows with partings typically spaced a few centimeters. Downgradient ground water velocities are estimated at 4 to 20 ft/day at a gradient of 10 ft/mile (0.0019) (Robertson and others, 1974).

The wells are situated on the Quaternary basalt fields of the eastern plain and were drilled for various groundwater monitoring and experimental programs associated with nuclear facilities at the Idaho National Engineering Laboratory (INEL). The Site 14 well is upgradient of injection wells, disposal ponds and waste ponds that have introduced low-level waste radionuclides and other constituents into the southwest migrating ground water. Well 59 is within a plume of waste constituents attributed mostly to the injection well at the Idaho Chemical Processing Plant (ICCP), a disposal-well practice that was discontinued in 1984. Well 83 is down gradient, within the track of the waste water plume area, but shows low Tritium (0.1±0.3 pCi/mL)in contrast to surrounding wells which are above 2 pCi/mL (Knobel and Mann, 1988). [(note that 1 pCi/mL ≈ 312 TU = 2.25 ^{3}H-disintegrations/min/mL), where 1 TU = isotope ratio $^3H/^2H$ of 10^{-18} = = 0.0032 pCi/mL (Rhodehamel and others, 1971, p. 4), and that values of less than 5 TU are considered natural, pre-atmospheric testing of thermonuclear devices in the period 1953-69 (Freeze and Cherry, 1979)]. Well OW-2 was drilled in 1993 south of the Radioactive Waste Management Complex (RWMC) for the purpose of monitoring the saturated zone during a large scale infiltration experiment (Norell and Wood, 1993).

METHODS

Well logging was conducted with Boise State University's Series 3000 Mount Sopris Instruments Company 4-conductor wireline unit with data acquisition using the ACQUIRE

software and interface electronics. We used the bi-directional Halliburton (formerly Gearhart-Owen, Mineral Logging Service) 1 7/16-inch-(36.5 mm)-diameter impeller flowmeter with a low-density plastic impeller spinning on jewelled pivots (Figure 4). The impeller has an embedded magnet that allows the electronics in the sonde to sense the direction of spin and change polarity of the pulses according to spin direction. The impeller has a stall speed of about 11 ft/minute for down-wash flow, and about 8 ft/minute of up-wash flow. In order to detect small flows the tool is trolled at speeds of 15 to 25 feet/minute. The least noisy signal is obtained on down trolled runs (up-wash). Noise level is about 2 to 3 feet per minute (Figures 6 to 9) on account of the somewhat jerky nature of the revolutions of the impeller. Calibration is obtained by trolling at various speeds in casing. Counts per second [cps] response have a linear relationship to troll speed in the range 15 ft/min to 25 ft/min. For uptroll (downwash): ft/min = 8.00·[cps] + 11.00, and for downtroll (upwash): ft/min = 6.06·[cps] + 6.80.

Intrawell flows detected by flowmeter, in terms of ft/min can be converted to volumetric flow, by multiplying by the cross-sectional area of the borehole, which for a 6-inch well is 0.20 ft^2, and for an 8-inch well is 0.35 ft^2 to give flow in terms of ft^3/min. One cubic foot is 7.5 gallons, so that for a 6-inch well, 1 ft/min = 1.5 gal/min; and for an 8-inch well, 1 ft/min = 2.6 gal/min. A uniform volumetric flow fluctuates with borehole diameter, so that in break-out intervals or constrictions seen on caliper logs, the flow will vary on account of borehole size.

Fluid electrical resistivity and temperature are recorded simultaneously by logging with the Mount Sopris Instruments MLP-4280 probe. Temperature and fluid resistivity response of the tool is calibrated by immersing the sonde in 6-gallon buckets of waters for which the temperature and resistivity have been determined using a Prestotech Corp. meter previously calibrated to an ASTM thermometer to an accuracy of ± 0.1 °C and to standard solutions so that absolute resistivity is ± 2.0 ohm-meters. When fluid resistivity is converted to specific conductance (C_s), the absolute values are accurate to ± 20 µS/cm (microSiemans/cm) over the range 100 to 1300 µS/cm.

The logged values of fluid resistivity are corrected for temperature to the standard 25°C using the Arps' equation (Serra, 1984, p. 9): $R_w(T_1) = R_w(T_2)\cdot[(T_1 + 21.5)/(T_2 + 21.5)]$, where temperature ($T_2$) and resistance $R_w(T_2)$ are the pair of logged values. Units on the formula are degrees centigrade, and resistivity is in ohm-meters. The resulting $R_w(T_1)$ is converted to specific conductance (C_s) in µS/cm units by the formula: $C_s = 10{,}000/R_w$). These calculations are most simply done for the entire log by importing the ASCII-format well-log files into a spread-sheet program.

The reported temperatures on the log are accurate to ± 0.2°C, and the values of C_s to ± 20 µS/cm, and relative changes of 0.02°C and 10µS/cm are reproducible on repeated logging runs. As discussed later, C_s is about 1.6 x (total dissolved solids expressed in mg/L). This implies that relative changes in electrolyte concentrations of about 10 mg/L are detectable with the calculated C_s log from the MLP logging tool.

TEMPERATURE PROFILES

Temperature gradients observed in wells at INEL are of three types. The simplest is one in which the temperature increases with depth as is expected for solid conduction of the heat of the earth vertically outward to the surface. Variations in gradients of this type can occur in a

steady-state heat-flow situation where the lithology changes are associated with a significant change in thermal conductivity of the rocks. This type of gradient is observed below 200 m in INEL GT-1, where the deep geothermal gradient is 40°C/km, and heat flow is calculated to be 109 W/m^{2}s (2.6μcal/cm^{2}s) (Brott and others, 1981; Blackwell, 1989). Thermal conductivity for the deep rhyolite section ranges from 1.9 to 2.76 W/m°K, and for the stratified basalt and sediment section, thermal conductivity is 1.4 to 1.6 W/m°K. Lower geothermal gradients indicate that some of the deep heat flow has been conducted away by groundwater flow (Brott and others, 1981), and low gradients are indeed observed in most wells in the basalt aquifer at INEL.

A common feature of wells in the basalt aquifer are isothermal intervals caused by water flowing vertically in a well, having entered at one permeable zone, and exiting at another permeable zone of lower head.

Many wells at INEL show a geothermal gradient that decreases downward (negative gradient). This situation occurs where a major zone of groundwater flow lies beneath the interval penetrated by the well. Such gradients are indicators of zones of colder-water flow beneath the bottom of the well.

FLUID SPECIFIC CONDUCTIVITY

The fluid specific electrical conductivity (C_s) is due to concentrations of ions dissolved in the ground water. The conductivity contribution of each ion depends upon the product of its valence, mobility, and concentration, so that double valence, high mobility ions have a large contribution. Conductivity of dilute electrolyte solutions can be calculated from the following formula from Daniels and Alberty (1961):

$$C = F[z_1u_1c_1/M_1 + z_2u_2c_2/M_2 + \cdots\cdots + z_iu_ic_i/M_i]$$

where
- C = electrical conductance in S/cm
- F = 96,493 coulombs/equiv (Faraday constant)
- z_i = valence of ion
- u_i = ion mobility, @ 25°C, cm^2/V·s units
- c^i = ion concentration in mg/L units
- M^i = molecular weight of ion in mg/mmole units

The major contributors to electrical conductivity of natural ground waters at INEL are HCO_3^-, Ca^{2+}, Mg^{2+}, and Na^+, because they dominate the concentration of dissolved solutes, expressed in terms of milliequivalents/liter. Contribution of each ion to specific conductance can be readily calculated from concentration in mg/L using the factors Fz_iu_i/M_i given in Table 1. The contributions to conductivity of concentrations of Ca and Mg are disproportionately large relative to other ions on account of their +2 valence.

Specific conductance of water from basalt aquifers at INEL can be used to approximate total dissolved solids (TDS in mg/L), in the range 220 to 800 μS/cm, by the relationship (Robinson and others, 1974):

$$TDS\ (mg/L) \approx 0.6\ C_s\ (\mu S/cm)$$

At higher values of C_s, (>800 µs/cm) which are in most cases influenced by waste water, the above equation underestimates TDS by as much as 200 mg/L.

Table 1. Contribution to specific conductance (C_s) of major solutes in ground water.

solute species	z_i	M	$u_i \times 10^5$	$F z_i u_i / M$
	mequiv per mmole	mg per mmole	ion mobility @ 25°C in $cm^2/V \cdot s$ [1]	contribution to conductance(µS/cm) per mg/L concentration
HCO_3^{-1}	1	61.0	46	0.73
SO_4^{-2}	2	96.0	82.7	1.66
Cl^-	1	35.5	79.0	2.15
Ca^{+2}	2	40.1	61.6	2.96
Na^{+1}	1	23.0	52.0	2.18
K^{+1}	1	39.1	76.2	1.88
Mg^{+2}	2	24.3	55	4.37
$^*SiO_2$	-		-	0.0*

[1]from Maron and Lando (1974, p. 516)

F = Faraday constant = 96,493 coulombs/equiv

*SiO_2 is not significantly ionized for pH below 8.5. At low pH SiO_2 is entirely as undisassociated $H_4SiO_4°$. From equations in Krauskopf (1979, p. 133) it can be shown that at 25°C, the pH dependency of the mole ratio of ionized silica to non-ionized silica is expressed as: $\{H_3SiO_4^{-1}\}/\{H_4SiO_4°\} = 10^{[pH - 9.9]}$. The highest pH for basalt aquifer waters at INEL is pH=8.3, so that the ratio of ionized to non-ionized silica is 1/40.

VARIATIONS IN WATER CHEMISTRY

Spatial variation in groundwater chemistry at INEL was systematically mapped by Robert Schoen in the study by Robertson and others (1974). He speculated that the recharge water from the northwest mountains is enriched in Ca, Mg, and HCO_3 on account of being derived from mountains underlain by Paleozoic carbonate rocks, whereas recharge water from the northeast is enriched in Na, F, and SiO_2. These waters appear to mix along a northeast-striking zone through central INEL. Recharge water from the Mud Lake area has high dissolved solids (300 to 500 + mg/L) on account of evaporation of irrigation water, being particularly high in Ca, Mg, K, Na, Cl, SO_4, and NO_3 as shown by concentration lobes extending from Mud Lake to about well no. 21.

Schoen (in Robertson and others, 1974, p. 74-76) was aware that significant changes in water chemistry occur vertically in the aquifer in some wells. He recognized in some wells, a body of relatively fresh water (C_s of 100 to 200 µS/cm) at the top of the water table, as much as 50 feet thick , though usually much thinner, underlain by normal groundwater with a C_s of

300 to 400 µS/cm. It was initially thought to be direct recharge from on-site percolation, but it was later noticed that the zone only occurred in cased wells, and then only above the level of perforations. He surmised that it may be a layer of condensed water from the humid air within cold steel casing, but was not satisfied with either explanation.

Significantly different water was obtained from well 7 for the interval 214 -698 ft, than from 212 - 1200 ft with the deeper water exhibiting an eightfold increase in F, a doubling of SiO_2, together with small reductions in Ca, Mg, and HCO_3, and a ninefold increase in NO_3 (Robertson and others, 1974). The deeper water was attributed to silicic volcanic rocks at depth. The INEL-1 well (completed in 1979) penetrated silicic volcanic rocks at depth of 2435 ft, and waters from those rocks have greater than 900 mg/l TDS, and F above 12 mg/L. In the section from 1511 ft to 2206 ft, and in the nearby water-supply well drawing from 395-595 ft, TDS is less than 390 mg/L, and F less than 1.1 mg/L (Mann, 1986).

Waste water with industrial or chemical and radioactive wastes has been disposed to the Snake River Plain aquifer by various means since 1952. The greatest volumes have been injected in disposal wells at the Test Reactor Area (TRA) and the Idaho Chemical Processing Plant (ICCP). These and other facilities (notably the National Reactor Facility (NRF), Test Area North (TAN), Central Facilities Area (CFA), Special Power Excursion Reactor Test (SPERT), Experimental Breeder Reactor II (EBR) have also disposed of lesser volumes of waste through various seepage ponds, sewage lagoons, drainage ditches, and septic tanks (see Table XIII in Robertson and others, 1974, p. 142). Major dissolved inorganic waste products are NaCl, H_2SO_4, NaOH, and smaller amounts of sodium sulphates, sodium phosphates, and hexavalent chromium (Robertson and others, 1974). South and southwest-oriented plumes of waste water are detected by mapping the groundwater concentrations of Cl, Na, and ^3H, as well as specific conductance, and appear to emanate mostly from the ICCP, NTF, and the TRA areas. By 1985 the ^3H 0.5pCi/ml value had reached the INEL south border, a distance of 14 km south of the ICCP, and by 1988, it had retreated north somewhat on account of radioactive decay, dilution, and curtailment of injection (Pittman and others, 1988; Mann and Cecil, 1990). A chlorine plume defined by values over 20 mg/L had reached a point 9 miles south of the ICCP by 1994, as had the specific conductance plume defined by values within the 325 µS/cm isopleth (Pittman and others, 1988). Beasley and others (1993) have reported that detectable ^{36}Cl from nuclear-fuel reprocessing facilities occurs in ground water sampled from well 108, on the south border of INEL, 14 km south of ICCP, as of 1992.

Specific conductance of waste effluent injected into the disposal well at the ICCP has been estimated at 960 to 1140 µS/cm by Robertson and others (1974, p. 159). They considered natural background to be 300 to 325 µS/cm and show that specific conductance is a fairly sensitive waste parameter. They map the plumes of anomalous C_s for the years 1962, 1966, 1968, and 1970. Pittman and others (1988) contoured values for the October, 1985 set of samples from monitor wells and show a maximum value of 700 µS/cm at the head of the plume at the NRF, and a maximum value of 500 µS/cm at the head of the plume at ICCP.

Pittman and others (1988) report large fluctuations of C_s from wells 87,88, 89, and 90 near the RWMC. Values ranged from 240 to 290 µS/cm . In well 88 the values ranged from 330 to 669 µS/cm, and high values correlate with high water levels. In the case of well 88, C_s which had formerly been 522 µS/cm jumped to 1650 µS/cm after cement grouting casing down to 587 ft below land surface (8/20/72). It is also documented that C_s changed again after rising water table levels began in June, 1983, when C_s jumped from a June value of 350 µS/cm to a July value of 550 µS/cm, accompanying a water level rise from 590 to

580 feet below land surface. Over the next 2 years water level rose to 520 feet and then dropped to 550 feet, and the specific conductance has remained above 500 µS/cm. They attributed the high value in 1972 to effects of the cement chemistry, but allowed that some of the chemical fluctuation may be the result of waste material buried at the Radioactive Waste Management Complex that migrated to the water table as a result of local flooding of the area in 1982.

INTRAWELL FLOWS

It has been established that many wells at INEL have significant intrawell flows, up to 20 feet/minute (and up to 60 gallons/minute) between vertically separated permeable zones with small head differences (Morris and others,1963; Morris and others, 1964; Barraclough and others, 1965; Bennecke and Wood, 1992, Bennecke and others, 1993; Morin and others, 1993; Barrash and others, 1993). The flows enter and exit in intervals that are permeable zones less than 20 feet thick, and in some cases the intervals are less than the 1-foot depth resolution of the impeller flowmeter.

In the vicinity of the large production well at ICPP (≈3,000 gallon/minute) intrawell flows reverse direction of flow and establish a constant flow magnitude within tens of seconds of the pump turning on or turning off (Bennecke and others, 1993). Away from large pumping wells the intrawell flows are thought to be steady, and possibly due to natural vertical-head gradients within the aquifer system, but we have not studied the intrawell flows extensively at these distant sites for more than a few hours.

Where these ambient intrawell flows are present, the flowmeter logs clearly identify permeable zones within a well. One also pump the well to induce flow, and troll the impeller flowmeter to identify permeable zones. It is tempting to try to derive hydraulic conductivity or transmissivity over narrow intervals using a flowmeter, and measuring pumpage (Moltz and others, 1989; Morin and others, 1993); however, one does not know the vertical head profile in the well - and the assumption of a uniformly distributed head drop throughout the well bore may not be always be appropriate. Nevertheless, the flowmeter is a useful tool to locate and determine relative permeability of zones.

SITE 14 WELL

The Site 14 well was cable-tool drilled to 717 ft in 1956. Well construction is important to interpreting the logs run in the afternoon of 9/13/93 (Figure 5b). Water flows into the well at the top of an 8-inch-casing riser at 315 ft and flows down the casing and down the open interval at a rate of 20 ft/min (50 gal/min) and exits into an enlarged diameter zone 701 to 717 ft (exceeding 35 inches diameter as shown on the caliper log [a 1960 caliper log is published by Bartholomay, 1990, p. 331]. A slight shift in the temperature of 0.1°C in the zone 475 to 500 ft suggests that water enters at that point and flows upward in the annulus between the 8-inch casing and the borehole wall.

The temperature log shows an abrupt increase downward starting at 652 feet and a small peak at 670 ft, and then increases in the lower part of the hole about 2°C to 18.4°C (Figure 5a). There is a slight increase in downward flow at 685 ft, which is apparently warmer water entering at that point and mixing with the downward flow. The downward flow exits abruptly at 702 ft. Water appears to be stagnant below 702 feet to the total depth logged of 716 feet.

The C_s log shows a uniform 365 µS/cm throughout the hole (Figure 5a). The ≈ 16.3° water presumed to enter at 475 to 500 ft appears to be the same C_s as the 18.4° water at the bottom of the hole. In this well, the dedicated pump sample from below 315 ft would appear to be representative of the flow zone at about 475-500 ft.

The logged values compare closely to water from a thief sample taken at 275 ft on 2/20/62, from which a temperature of 16.7° and C_s of 322 µS/cm are reported (Robertson and others, 1974). The temperatures are among the highest reported for the INEL area. Robertson and others (1974) show a belt of relatively high temperature > 14°C, about 5 km wide, trending from Atomic City north-northeast to between TAN and the east border of INEL. The belt is approximately parallel to ground water flow lines inferred from the slope of the piezometric surface. Robertson and others (1974) thought the warm waters were the result of sun-warmed summer irrigation water in the Mud Lake area that recharged the aquifer. However, the belt does not parallel the group wells showing a trend of high total dissolved solids and nitrates emanating from Mud Lake, a trend thought to be related to evaporation of irrigation water prior to recharge. If this is not warm irrigation water it may be geothermal water from depth flowing laterally in a permeable intraflow zone. Neither explanation is totally satisfying at this point in our examination of the data.

WELL USGS 59 (IDAHO CHEMICAL PROCESSING PLANT AREA)

The USGS 59 well was cable-tool drilled near the southeast corner of the ICCP in 1960 to a depth of 657 feet. Eight-inch steel casing extends from the surface to 464 ft below which is 6-inch open hole. Water level when logged on the afternoon of 9/14/93 was 461 feet.

The flowmeter log shows stagnant water from 461 to 521 feet (Figure 6). Flowing water enters the hole from a 16-ft thick zone from 521 to 537 feet. The water flows down the hole at a rate of 7 ft/min (10 gal/min). At 570 feet more flowing water enters the hole and boosts the downward flow to 11 ft/min (16 gal/min). At 600 ft all of the downward flow exits, and water below 600 feet appears to be stagnant on the flowmeter log.

The temperature log confirms that the upper water from 460 to 521 is relatively stagnant, and that colder water (13.9°C) enters at 521 and flows downward (Figure 6). Additional water entering at 570 is slightly cooler and mixes, and apparently flows down. There is discrepancy between the two logging runs, for the T-C_s log indicates flow exits at 624, whereas the previously run flowmeter indicated the downgoing flow abruptly exited at 600 ft. Because logs were run an hour apart, there could have been a flow regime change caused by the pump cycle at the ICPP production wells, but the discrepancy remains unexplained at this point. Below 624 ft the water appears to be stagnant; however the temperature profile shows a decreasing downward gradient the significance of which is discussed below.

Most remarkable is the specific conductance log which shows a value of 550 µS/cm in the upper 30 ft of the stagnant zone (from 461 to 491 ft), and an increase to 1115 µS/cm caused by the inflow from the zone 521 to 537 ft (Figure 6). This is among the highest values of C_s for INEL ground water , and is the same at that reported for the original waste water pumped down the ICPP disposal well (Robertson and others, 1970, p. 159). This downflowing water of high-C_s apparently mixes with water of lower C_s entering at 575 ft, which dilutes the downflowing water in the well to about 850 µS/cm. This downflowing water mixes with water from lower down the well of high C_s over a zone from 610 to 624 ft

and then exits at 624 feet. The lower stagnant water in the well has a high C_s of 1020 µS/cm.

This profile of C_s dramatically shows major vertical variations in chemistry in the water in this well that would not be correctly sampled by a dedicated pump set 50 feet below the water level. In fact, monthly samples from this well would not detect the high values of dissolved solids that occurs in the most dynamic part of the aquifer.

In other wells we have logged in the vicinity of ICPP and those logged by Morin and others (1992) the temperature profiles show increasing temperature downward in the lower parts of wells (generally below the permeable zone at the top of the "I" group of flows - using stratigraphy of Anderson (1991). In this well, the lower 28 feet, from 624 to 652 shows decreasing temperature suggesting that a flow zone of cooler water lies below 652 feet (Figure 6). This supports the speculation of Barrash and others (this volume) that an important flow zone lies below the level of most monitor wells in the ICCP area, one that was probably penetrated by well 123 and well 48.

WELL USGS 83

Well USGS 83 was cable-tool drilled to 752 feet in 1962. The well has 6-inch steel casing from the surface to 516-foot depth, below which it is open hole. When logged on 79/23/93 water level was at 503, and the well was obstructed below 720.

No major flow was detected by flowmeter logging (Figure 7). There is a slight shift in the temperature log 645 to 650 ft (≈0.03°C) which corresponds to a shift to slight downward flow on the flowmeter, but the flow measurement is within the noise level of the impeller flowmeter, and it has questionable significance. The C_s log does not show significant vertical variations suggesting water in the well bore may be of uniform major-ion chemistry. The temperature log shows an increasing gradient downward of 0.3°C/100 ft (10°C/km) typical of a well that does not intersect major flow zones.

The saturated zone from 503 to 720 feet appears from these logs to be relatively impermeable, explaining perhaps why the water samples from this well have traditionally shown low ^3H (0.1±0.3 pCi/mL)in contrast to surrounding wells which show above 2 pCi/mL (Knobel and Mann, 1988). This may be an area of low permeability, and the waste plum has flowed around without affecting the water in the vicinity of well USGS 83.

WELL OW-2 (RADIOACTIVE WASTE MANAGEMENT COMPLEX AREA)

Well OW-2 was air-rotary drilled in September and October, 1993, to a depth of 996 ft, about 2 weeks prior to logging on 10/19/93. The well is a monitoring well for the large-scale infiltration and pump test to be conducted about 1 mile (1.6 km) south of the RWMC, and about 500 ft southeast of well USGS 120. At time of logging the well was an open 8-inch-diameter hole from 50 feet to total depth, and the water level stood at 619 ft.

The flowmeter log indicates no flow in the upper 70 feet of the well, the interval from 619 to 690 ft (Figure 8). At 692 ft a small flow enters and by 700 ft the downward flow is about 2 to 3 ft/min. Small fluctuations in detected flow from 700 to 768 ft are due to borehole diameter variation in the enlarged-diameter interval from 744 to 772 ft where the caliper log shows excursions up to 18 inches (see caliper log in paper by Hegmann and Wood, this volume). The large excursion at 768 ft is produced by two opposing flows exiting

at that point in the well. Below 768 is an upward flow of 3 ft/min, which enters the hole gradually over the interval 805 to 790 ft. Below 805 feet the water appears stagnant. Thus flows set up by a lower head in the 768-ft zone are coming from 805-790, and from 692-700 ft.

The temperature log shows that the water entering at 692 is 10.7°C, and the water entering at 790 ft is 10.6°C, a small but detectable difference (Figure 8). Below 790 ft the well shows a negative geothermal gradient profile with inflections possibly related to small flows at 835 and at 895 ft. Temperature of the bottom of the hole is 9.2°C

The specific conductance log shows that the relatively stagnant water in the top interval from the water level down to about 650 ft has a high value, up to 760 µS/cm, at the water level (Figure 8). Water entering and flowing down from the 692-700 ft interval has a lower value of 520 µS/cm, and water entering at 805 and flowing up has a still smaller value of 430 µS/cm. Below 805 ft, the water has the same uniform value of 430 µS/cm. All of these values are above the value of 300 to 325 µS/cm considered background by Robertson and others (1974). The vertical variations in C_s show that a dedicated pump sampling program in this well would not obtain a sample representative of the aquifer, because three intervals have different chemistry.

The negative temperature gradient from 805 to the bottom of the hole at 996 ft suggests that a major flow zone lies beneath 996 ft (Figure 8). It has been suggested that the negative geothermal gradient may be an artifact of drilling; however, water introduced into the well during drilling in September and October would most likely have been warmer that the ground water, and would have warmed the lower part of the hole, rather than cooled the lower hole, as the temperature log shows.

CONCLUSIONS

Flowmeter, temperature, and specific conductance logging of borehole fluid show that the chemistry of ground waters varies vertically from flow zone to flow zone in many wells the penetrate 300 feet or less into the Snake River Plain aquifer beneath INEL. Monitoring the aquifer with dedicated pump samples is only meaningful if one knows the permeable flow zone from which the water actually entered the well. In wells 59 and OW-2 the value of specific conductance varies vertically by a factor of 2. This would suggest that historic sampling and mapping of the waste plumes may not be showing the maximum waste level in certain zones of the aquifer.

The Site 14 borehole fluid is entirely fluid entering from one zone and flowing down the well. Well 83 appears to be in a relatively less permeable section and does not show significant flow zones or variations in specific conductance.

Profiles of downward decreasing temperatures are observed at the bottom of wells 59 and OW-2 suggesting that a major flow zone lies beneath the bottoms of these wells.

It is recommended that flowmeter, temperature, specific conductance logs combined with previously obtained caliper, natural gamma, and calibrated- density logs be used to design a monitoring program using a downhole wireline thief sampler to obtain ground water for analysis from specific flow zones encountered by wells. Fluid specific conductance logs give an indication of chemical variation, but the actual constituents need to be analyzed from water samples taken by thief sampler or from zones isolated by packers.

ACKNOWLEDGEMENTS

We wish to thank W. Barrash, J. Olsen, S.R. Anderson, and R. Jensen for providing data, discussions, and advice which contributed to this study. Niel Smith and Curtis Baker of Mt. Sopris Instruments have helped us improve our logging instrumentation over the years and we are most appreciative of their efforts.

REFERENCES

Ackerman, D.J., 1991, Transmissivity of the Snake River Plain aquifer at the Idaho National Engineering Laboratory, Idaho: U. S. Geological Survey Water-Resources Investigations Report 91-4058, 35 p.

Anderson, S.R., 1991, Stratigraphy of the unsaturated zone and uppermost part of the Snake River Plain aquifer at the Idaho Chemical Processing Plant and test area, Idaho National Engineering Laboratory, Idaho: U.S. Geological Survey, Water-Resources Investigations Report 91-.

Bartholomay, R.C., 1990, Digitized geophysical logs for selected wells on or near the Idaho National Engineering Laboratory, Idaho: U. S. Geological Survey Open-File Report 90-366, 347 p.

Barrash, W., Morin, R.H., Wood, S.H., and Bennecke, W., 1994, Hydrostratigraphic interpretation of the upper portion of the Snake River Plain aquifer near the Idaho Chemical Processing Plant at the idaho National Engineering Laboratory (this volume).

Barrash, W., Morin, R.H., Wood, S.H.,Anderson, S.R., Jensen, R.G., and Bennecke, W., 1993, Geophysical logging evidence for stratigraphic control of hydrology in the Snake River Plain aquifer at the Idaho National Engineering Laboratory (INEL), southeastern Idaho: EOS, v. 74, No. 43, p. 283-284.

Beasley, T.M., Cecil, L.D., Sharma, P., Kubik, P.W., Fehn, U., Mann, L.J., and Gove, H.E., 1993, Chlorine-36 in the Snake River Plain aquifer at the Idaho National Engineering Laboratory: origin and implications: Ground Water, 31, p. 302-310.

Bennecke, W., Wood, S.H., 1992, Impeller flow-meter logging of vertical cross flow between basalt aquifers through wells at the Idaho National Engineering Laboratory, eastern Snake River Plain, Idaho: a progress report: Borehole geophysics research program, Department of Geosciences, Boise State University, 23 p.

Bennecke, W., Wood, S.H., Olsen, J., and Barrash, W., 1993, Vertical cross-flows induced in observation wells by distant pumping of the Snake River basalt aquifer, eastern Idaho: Geological Society of American Abstracts with Programs, v. 25. no.5 (Reno, Nevada, May 1992).

Brott, C.A., Blackwell, D.D., and Ziagos, J.P., 1981, Thermal and tectonic implications of heat flow in the eastern Snake River Plain, Idaho: Journal of Geophysical Research, 86, 11,709-11,734.

Blackwell, D.D., 1989, Regional implications of heat flow in the Snake River Plain, northwestern United States: Tectonophysics, v. 164, p. 323-343.

Daniels, F. and Alberty, R., 1961, Physical Chemistry (2nd Edition): New York, John Wiley and Sons, 744 p.

Freeze, R.A., and Cherry, J.A., 1979, Groundwater: Englewood Cliffs, New Jersey, Prentice-Hall, Inc., 604 p.

Garabedian, S.P., 1992, Hydrology and digital simulation of the regional aquifer system, eastern Snake River Plain, Idaho: U.S. Geological Survey Professional Paper 1408-F, 102 p.

Hegmann, M., and Wood, S.H., 1994, Hydrostratigraphy of the Snake River Plain aquifer beneath the Radioactive Waste Management Complex at the Idaho National Engineering Laboratory: a preliminary report: (this volume).

Knobel, L.L., and Mann, L.J., 1988, Radionuclides in ground water at the Idaho National Engineering Laboratory, Idaho: U. S. Geological Survey Open-file Report 88-731, 37 p.

Krauskopf, K.B., 1979, Introduction to Geochemistry (2nd Edition): New York, McGraw-Hill Book Co., 617 p.

Kuntz, M.A., Covington, H.R., and Schorr, L.J., 1992, An overview of basaltic volcanism of the eastern Snake River Plain, Idaho: in Link, P.K., Kuntz, M.A., and Platt, L.B. eds., Regional Geology of Eastern Idaho and Western Wyoming: Geological Society of America Memoir 179, p. 1-53.

Lanphere, M.A., Champion, D.E., and Kuntz, M.A., 1993, Petrography, age, and paleomagnetism of basalt flows in coreholes Well 80, NRF 89-04, NRF 89-05, and ICPP 123, Idaho National Engineering Laboratory: ;U. S. Geological Survey Open-File Report 93-327, 40 p.

Mann, L.J., 1986, Hydraulic properties of rock units and chemical quality of water for INEL-1 - a 10,356-foot deep test hole drilled at the Idaho National Engineering Laboratory, Idaho: U. S. Geological Survey Water-Resources Investigations Report 86-4020, 23 p.

Mann, L.J., and Cecil, L.D., 1990, Tritium in ground water at the Idaho National Engineering Laboratory, Idaho: U. S. Geological Survey Water-Resources Investigations Report 90-4090, 35 p.

Maron, S.H. and Lando, J.B., Fundamentals of Physical Chemistry: New York, MacMillan Publishing Co., 853 p.

Moltz, F.J., Morin, R.H., Hess, A.E., Melville, J.G., Güven, O., 1989, The impeller meter for measuring aquifer permeability variations: evaluation and comparison with other tests: Water Resources Research, v. 25, p. 1677-1683.

Morin, R.H., Barrash, W., Paillet, F.A., and Taylor, T.A., 1993, Geophysical logging studies in the Snake River Plain aquifer at the Idaho National Engineering Laboratory - wells 44, 45, and 46: U. S. Geological Survey Water-Resources Investigations Report 92-4184, 44 p.

Norrell, G.T., Wood, T.R., Porro, I. Wylie, A.H., Dunnivant, F.M., Newman, M.E.,and Dooley, K.J., 1993, The Idaho National Engineering Laboratory integrated field scale pumping and infiltration tests: EOS, v.74, no. 43, (October 26, 1993), p. 240.

Pittman, J.R., Jensen, R.G., and Fischer, 1988, Hydrologic conditions at the Idaho National Engineering Laboratory 1982-1985. U.S. Geological Survey Water-Resources Investigations Report 89-4008, 73 p.

Robertson, J.B., Schoen, R., and Barraclough, J.T., 1974, The influence of liquid waste disposal on the geochemistry of water at the National Reactor Testing Station, Idaho: U.S. Geological Survey Open-File Report IDO-22054, 231 p.

Serra, O., 1986, Fundamentals of well-log interpretation (v. 1), the acquisition of logging data: Pau, France, Elf-Acquitaine; or Amsterdam, Elsevier, 423 p.

REFERENCES ADDENDUM

Rhodehamel, E.C., Kron, V.B., and Dougherty, V.M., 1971, Bibliography of tritium studies related to hydrology: U. S. Geological Survey Water-Supply Paper 1900, 174 p.

Whitehead, R.L., 1992, Geohydrologic framework of the Snake River Plain regional aquifer system: U.S. Geological Survey Professional Paper 1408-b, 32 p.

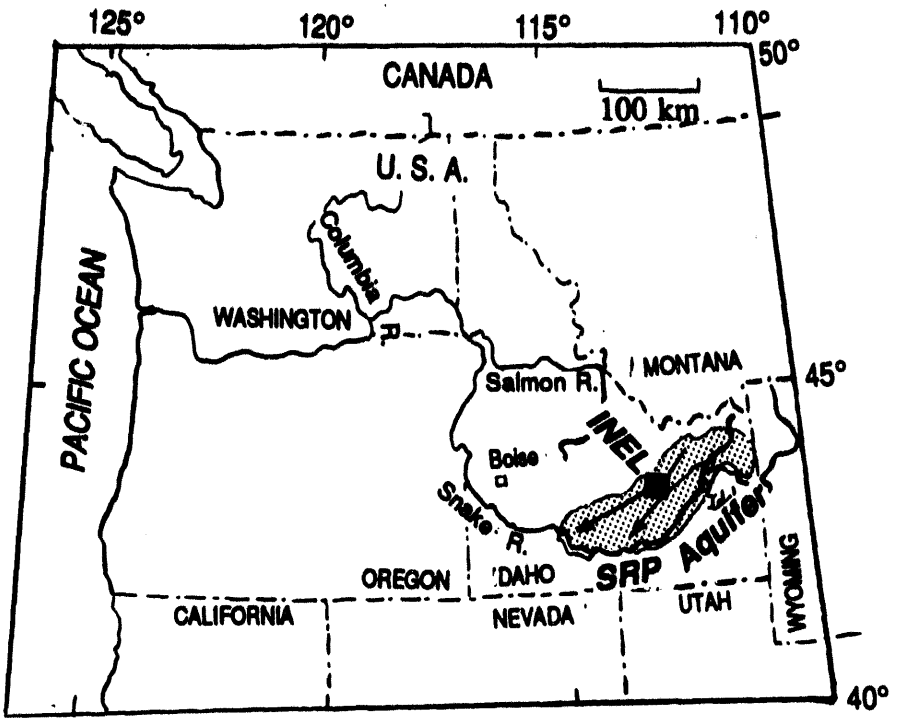


Figure 1. Map showing location of the eastern Snake River Plain basalt aquifer system and the Idaho National Engineering Laboratory.

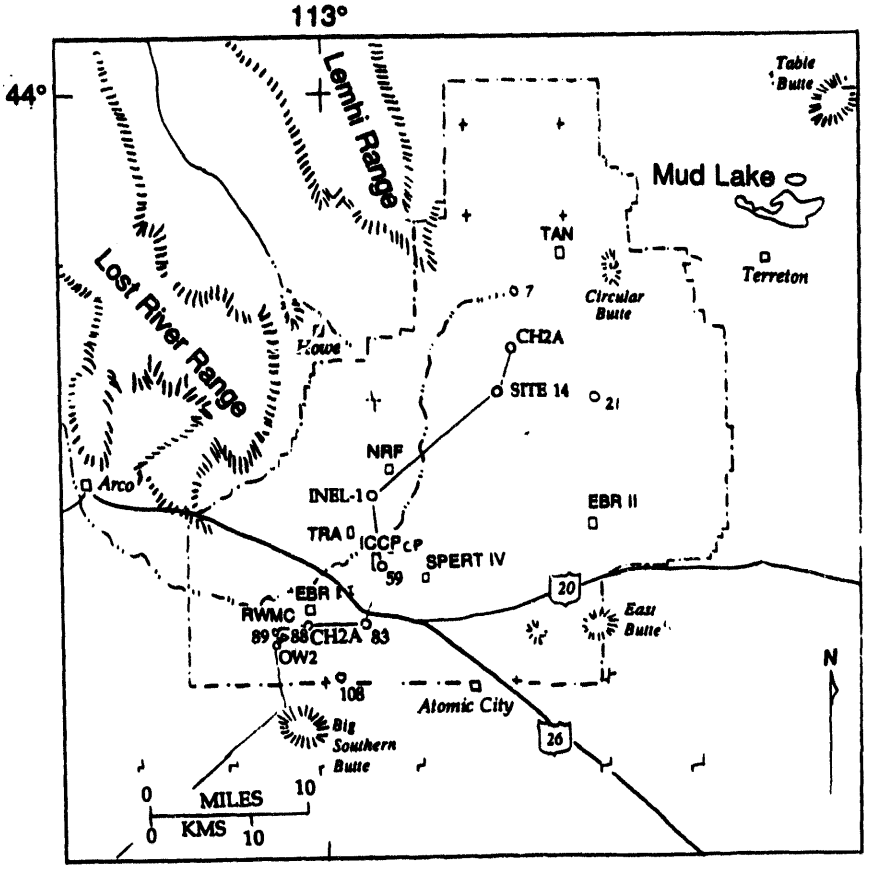


Figure 2. Map showing location of cross section (Figure 3) and wells discussed in this report, and boundaries of the Idaho National Engineering Laboratory.

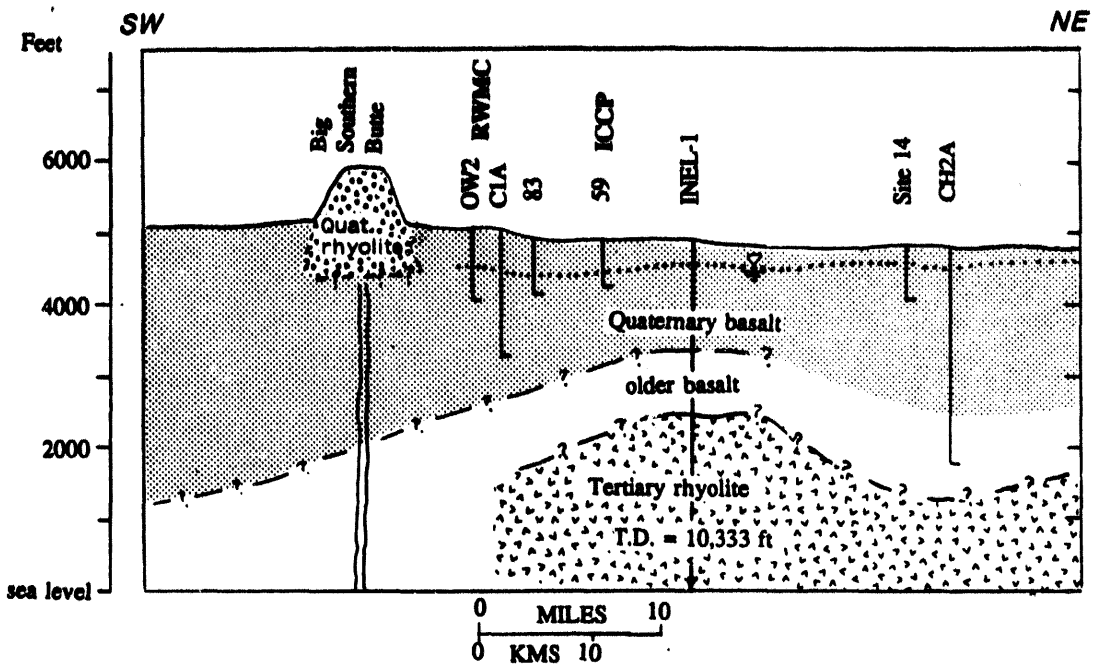
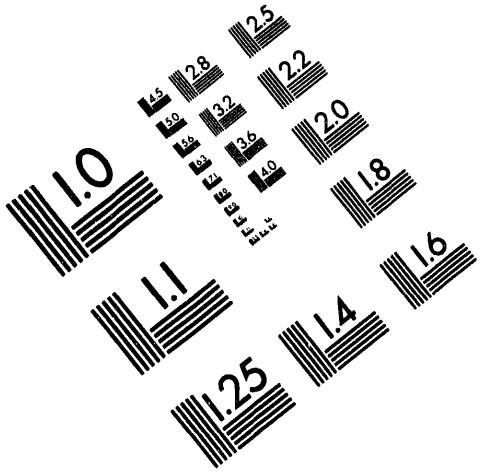


Figure 3. Generalized geologic cross section of selected wells at INEL (exaggerated vertical scale). Water level in wells indicated by dotted line (depth of basalt south of Big Southern Butte is from resistivity soundings reported by Whitehead (1992).

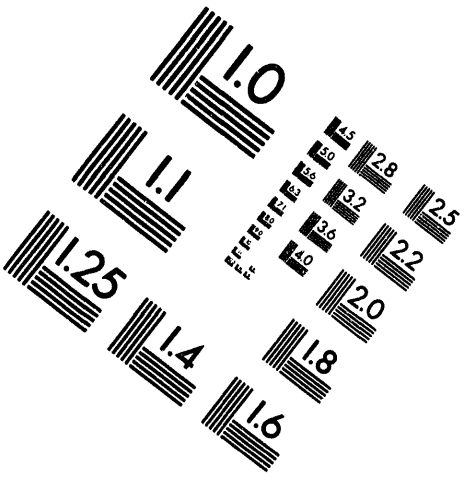


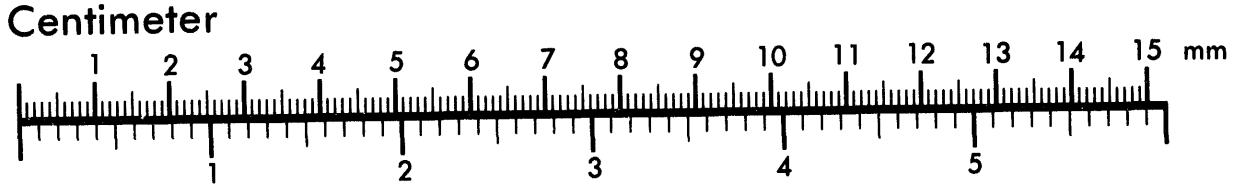
Figure 4. Photograph of Halliburton (Gearhart-Owen) bi-directional impeller flowmeter (36.5 mm diameter), and the thermistor-housing end of the Mt. Sopris combination fluid-resisitivity and temperature logging tool (51 mm diameter).

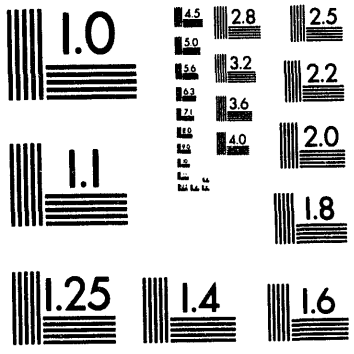


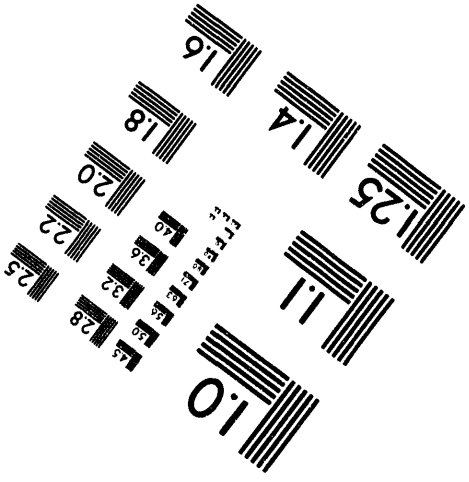


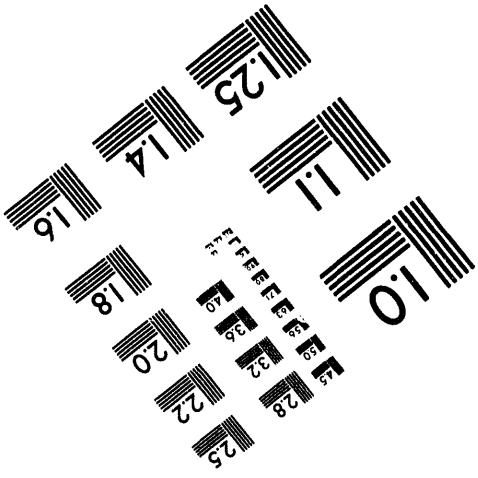
Association for Information and Image Management
1100 Wayne Avenue, Suite 1100
Silver Spring, Maryland 20910
301/587-8202











MANUFACTURED TO AIIM STANDARDS
BY APPLIED IMAGE, INC.

4 of 7

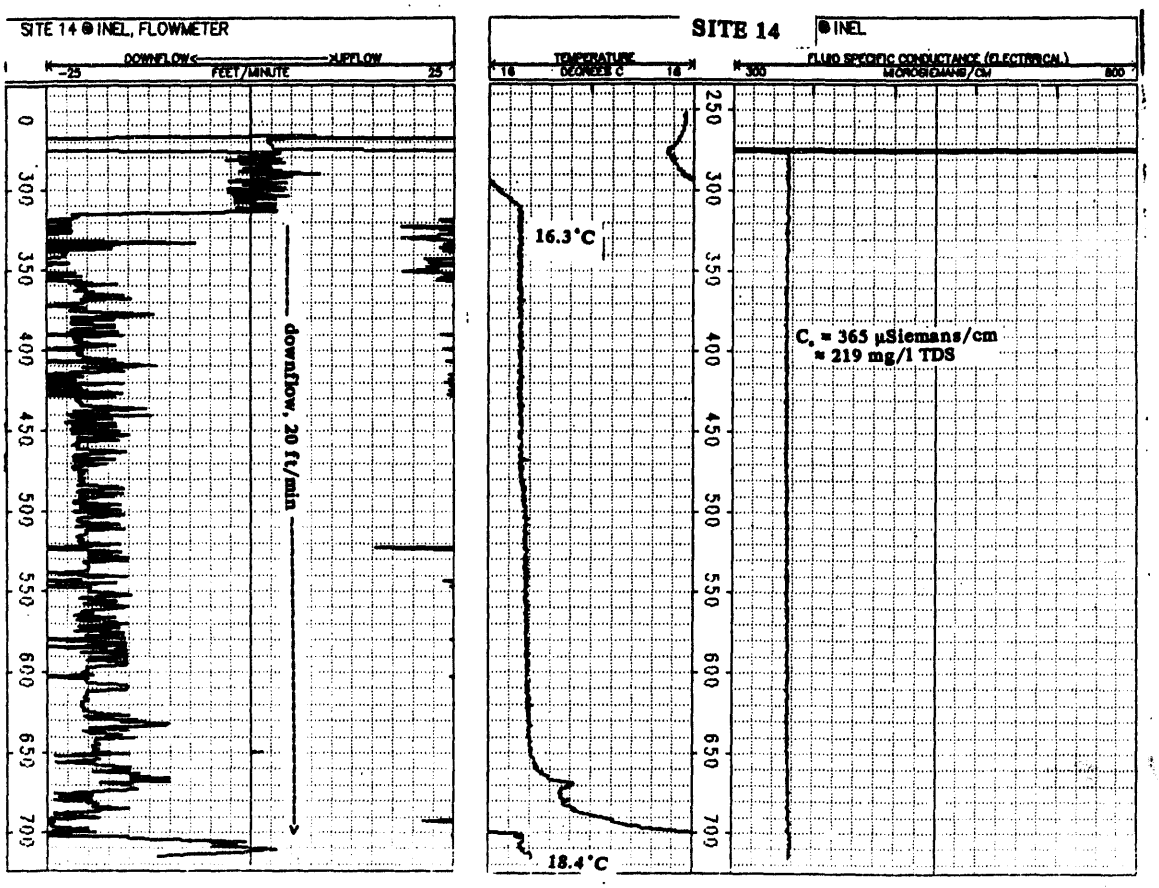


Figure 5a. Site 14 impeller flowmeter, temperature, and specific conductance logs. Flowmeter shows downward flow of 20 ft/min (50 gal/min) from top of 8-inch riser pipe at 315 feet exiting near bottom of well at 702 feet.

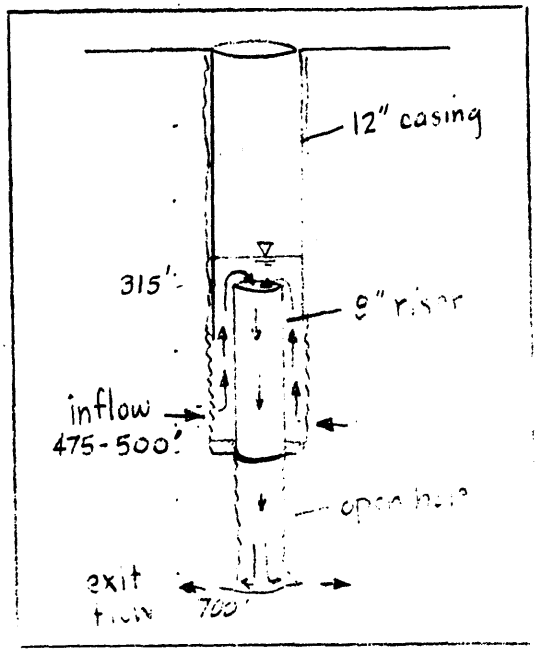


Figure 5b. Sketch of well construction and interpretation of flow at Site 14.

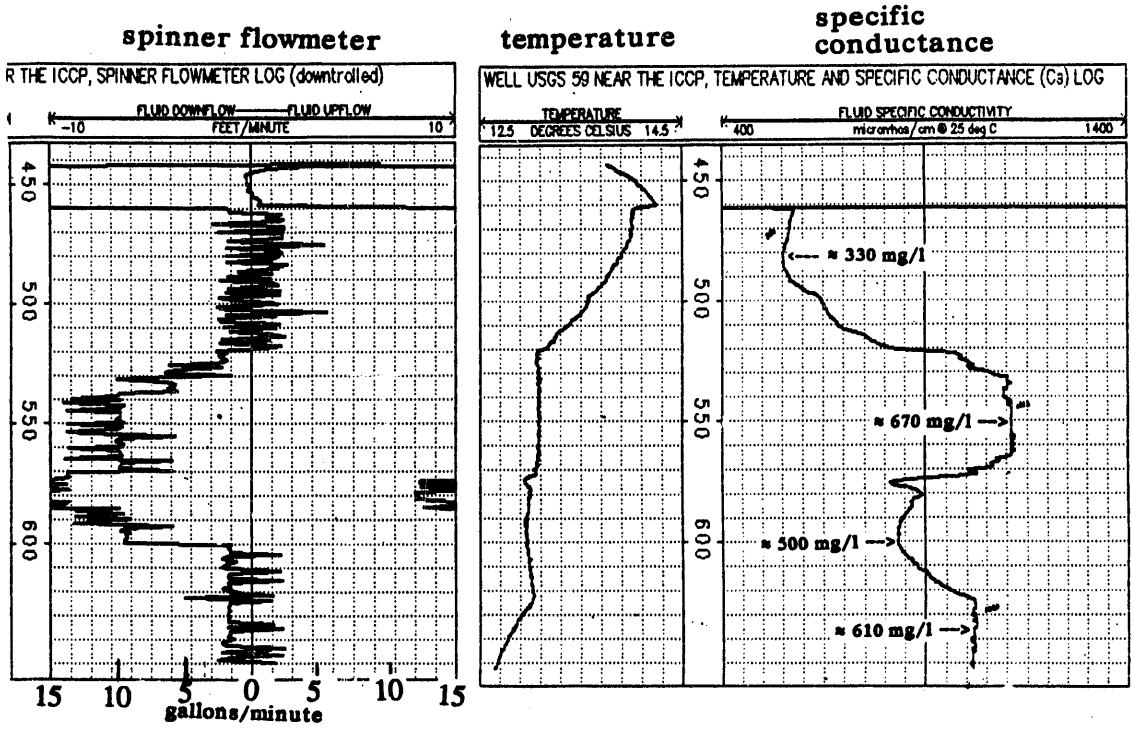


Figure 6. Well 59 impeller flowmeter, temperature and specific conductance logs showing major differences in water chemistry in the water column. Flowmeter shows downward flow of water with a C_s of 1115 µS/cm mixing and diluted by additional downward flow entering at 570-ft depth. Flow appears to exit at 600 or 624 ft.

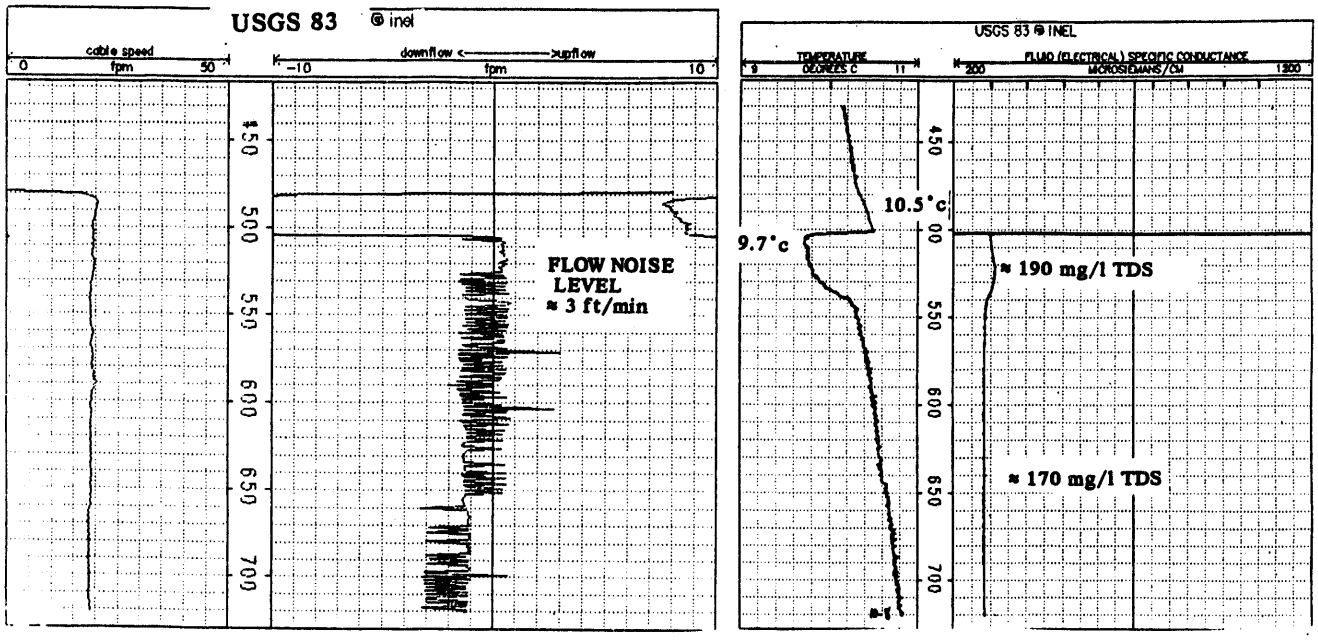


Figure 7. Well 83 impeller flowmeter, temperature, and specific conductance logs showing no significant flow, a positive temperature gradient, and uniform specific conductance of 280 µS/cm.

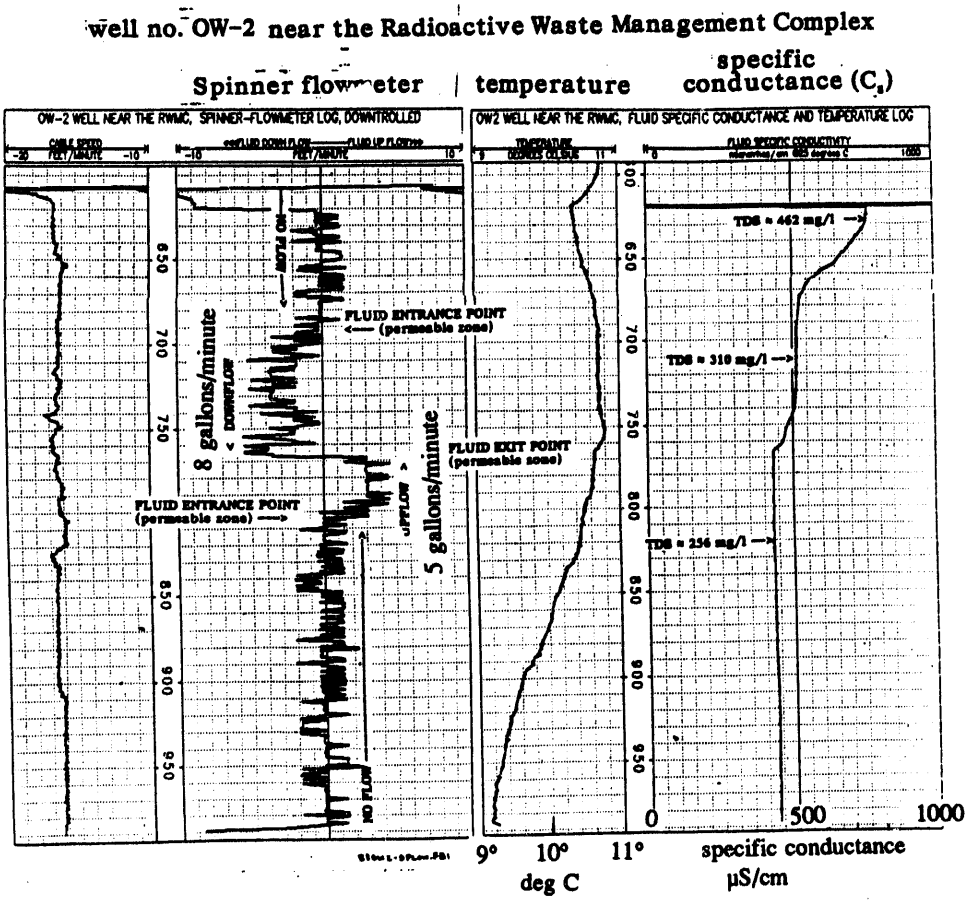


Figure 8. Well OW2 spinner flowmeter, temperature, and specific conductance logs. Opposing intrawell flows exit at 768-depth. Water of three different chemistries are apparent from the specific conductance log, with the highest value at the top of the water column. The negative temperature gradient suggests a major flow zone lies beneath the bottom of the well (996 ft deep)

Hydrogeology, Waste Disposal, Science and Politics
Proceedings 30th Symposium
Engineering Geology and Geotechnical Engineering, 1994

ENVIRONMENTAL GEOPHYSICS: LOCATING AND EVALUATING SUBSURFACE GEOLOGY, GEOLOGIC HAZARDS, GROUNDWATER CONTAMINATION, ETC.

Alvin K. Benson
Department of Geology, Brigham Young University
Provo, UT 84602

ABSTRACT

Geophysical surveys can be used to help delineate and map subsurface geology, including potential geologic hazards, the water table, boundaries of contaminant plumes, etc. The depth to the water table can be determined using seismic and ground penetrating radar (GPR) methods, and hydrogeologic and geologic cross sections of shallow alluvial aquifers can be constructed from these data. Electrical resistivity and GPR data are especially sensitive to the quality of the water and other fluids in a porous medium, and these surveys help to identify the stratigraphy, the approximate boundaries of contaminant plumes, and the source and amount of contamination in the plumes. Seismic, GPR, electromagnetic (VLF), gravity, and magnetic data help identify and delineate shallow, concealed faulting, cavities, and other subsurface hazards. Integration of these geophysical data sets can help pinpoint sources of subsurface contamination, identify potential geological hazards, and optimize the location of borings, monitoring wells, foundations for building, dams, etc. Case studies from a variety of locations will illustrate these points.

INTRODUCTION

Geophysical methods can play a very important role in environmental and engineering applications that involve shallow subsurface mapping studies. These methods are applicable to the study of groundwater contamination, underground cavities (natural or man-made), subsurface faulting, buried pipes, cables, barrels, etc., all of which pose potentially dangerous geological hazards (Benson, 1993). Geophysical exploration is a nondestructive, cost effective way to help locate and characterize these hazards.

In addition to helping locate the water table, characterization of subsurface contamination produced by hazardous materials has become an important application of geophysical methods. The objectives of subsurface investigations at sites containing contamination caused by hazardous materials include: (a) the location of buried material; (b) the determination of the presence of contaminant plumes, their source(s), and geometry; and (c) the assessment of associated hydrogeologic conditions. The purpose for locating buried

hazardous materials is typically for site assessment and some kind of remedial action, usually involving excavation and safe disposal of the hazardous materials with minimal damage to the environment.

Geophysical surveys can play an important role in defining the subsurface geology and the associated parameters which govern the movement of contaminant plumes (Foster et al. 1987); Benson & Mustoe (1991); Beres and Haeni (1991); Benson, (1992, 1993)). Analysis of these data sets can help produce a more cost effective program in locating monitoring wells. Understanding the hydrogeologic setting is essential in defining potential contaminant migration pathways and assessing the fate of contaminant movement along the pathways. This understanding comes from data detailing the three-dimensional distribution of the surficial soils and fill material, the geologic strata and structure, and the groundwater conditions, such as hydraulic and chemical properties of the soils and ground water.

Through early use of geophysical methods, such as seismic refraction, electrical resistivity, ground penetrating radar (GPR), very low frequency electromagnetic (VLF), and/or magnetic, many subsurface problems can be detected, and the sooner they are detected and evaluated, the quicker a strategic clean-up program can be implemented to minimize any further damage to the environment. Electrical resistivity and GPR surveys can be very helpful and cost effective in : (a) locating strategic monitoring wells to sample subsurface soils and fluids; (b) determining hydrogeologic gradients; and (c) monitoring the clean-up process. Case studies from central Utah will illustrate some of these applications.

Geophysical surveys, including seismic refraction, gravity, GPR, VLF, and magnetic, also have the capability of mapping underground discontinuities, such as faults, concrete walls, boulders, pipes, etc., in the shallow subsurface. Planning and development along the Wasatch front in central Utah and at many other locations must compensate for the geological hazards associated with faulting. Studies by Gori and Hays (1987, 1988) show that future ruptures will probably occur along already existing zones of weakness. Although some faults can be detected by surficial geological mapping, others have no visible expression and can only be located by subsurface investigation. Geophysical surveys can be integrated with geotechnical engineering methods, such as drilling and trenching, to obtain a better understanding of potential subsurface geological hazards at a specific site.

Geophysical data collected near Rock Canyon in eastern Provo, Utah show subsurface faulting from which estimates were made of the magnitude and direction of throw on the fault. This area was later trenched by the Utah Geological and Mineral Survey (UGMS), which enabled a direct comparison with the geophysical data. The characteristics of the subsurface deformation were analyzed to gain a better understanding of the potential for surface rupture at the site, and thereby, to plan future site development as well as devise remedial measures for mitigating the effects of potential earthquakes in populated areas.

GPR data are very helpful in locating air-filled cavities and voids, whether natural or manmade. These caverns could include mines, tunnels, ancient burial chambers, structures within buried cities, caves, lava vents, etc. Determining their location and geometry has diverse applications, including; (a) safe construction of buildings, roadways, and airports; (b)

archaeological excavations; and (c) mineral investigations.

A case study to determine the location of an underground laboratory at Brigham Young University will be examined. Good contrast exists between the dielectric constants for the overlying soil, the concrete ceiling, floors, and walls, and the large air-filled cavity. Consequently, GPR was successful in outlining this underground cavity. In addition, a magnetic survey was successful in locating underground piping at Brigham Young University.

CONTAMINATED GROUNDWATER STUDIES

Fresh, clean groundwater is becoming an increasingly valuable resource around the world. In some area, supplies have been greatly decreased by careless management and/or disposal of hazardous materials. Hydrogeologists require methods to map the soil stratigraphy at sites where contaminants are in the subsurface.

The first site of investigation is associated with leaking fuel tanks at a site in Utah County, near Provo, Utah. The general layout of this site is shown in Figure 1. The underground storage tanks leaked hydrocarbons (gasoline and diesel fuel) into the groundwater which flowed to the southwest following the water-table gradient of about 1.1 meters/100 meters. Based upon maps by Hintze (1988) and our well and GPR data, the geology at this site was determined to consist of three main layers: (1) an asphalt/sand layer (0.9 to 1.3 meters thick); (2) a layer of silty-clay and sand (1.7-2.4 meters thick); (3) a sand and gravel layer (1.1-1.8 meters thick); and (4) a water-bearing, sandy-gravel layer. The water table at monitoring wells 1 and 2 was 3.2 and 3.6. meters, respectively.

This site is currently undergoing bioremediation to recover the contaminated soil and ground water. Contaminated ground water is being pumped out of the subsurface and then reinjected after it is combined with nitrate and phosphate nutrients from commercial fertilizers, as well as with hydrogen peroxide, to help the microorganisms (bacteria) digest the groundwater contamination in situ. The nutrients add nitrate (NO_3^-) and Phosphate (PO_4^-) ions to the subsurface, and the degradation of the hydrocarbons adds carbonate (CO_3^{2-}), sulfate (SO_4^-), and chlorine (Cl^-) ions. Although hydrocarbon plumes might typically be mapped as resistivity highs, these additional ions could decrease the electrical resistivity and outline the contaminant plume as a resistivity low.

Electrical resistivity data were collected at the site using a Bison Offset Sounding System (BOSS) in a Wenner array configuration. In Particular, the sounding centered near MW-1 will be analyzed (Figure 1). These data are plotted in Figure 2 as a function of electrode spacing. The data were modeled for subsurface structure using the BOSSIX software from Interpex. Initial layer thicknesses and internal resistivities were constrained by the geological data from MW-1. Table 1 shows the initial model and the final computed model after two iterations. The first layer (.91 meters thick) corresponds to the asphalt/sand layer, the second (1.44 meters thick) to the silty-clay, sand layer, the third (1.08 meters thick) to a sand, gravel/cobble layer, and the fourth to a layer of water-saturated sediments. This correlates with the stratigraphic data cited above from MW-1. Adding up the thicknesses of the upper three

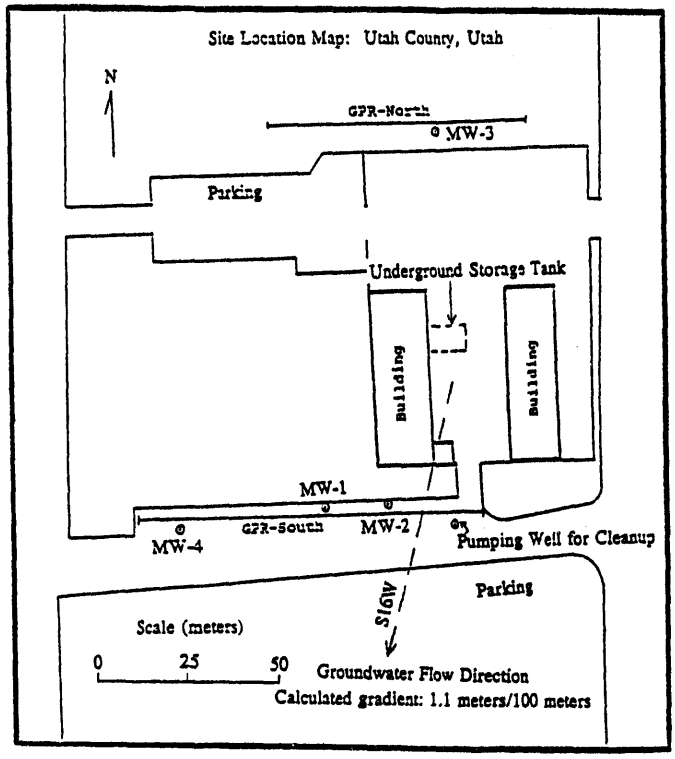


Figure 1 Underground storage tanks at central Utah site.

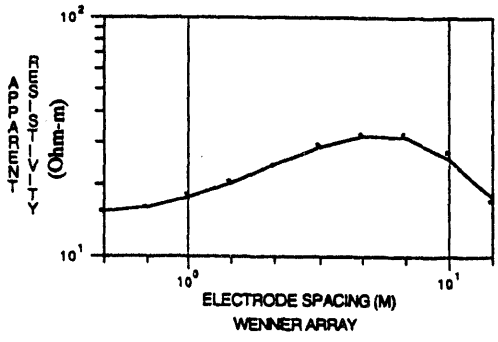


Figure 2 Electrical resistivity sounding data near MW-1.

Wenner Array
Initial Model

Layer No.	Thickness (m)	Resistivity (ohm*m)
1	1.000	14.500
2	1.000	30.500
3	1.000	186.300
4	Infinite	10.000

Computed Model
2 Iterations

Layer No.	Thickness (m)	Resistivity (ohm*m)
1	0.912	14.937
2	1.439	30.465
3	1.080	186.301
4	Infinite	6.653

Computed Values
RMS Error: 2.285

Electrode Spacing	Field A. Resistivity	Model A. Resistivity
0.464	15.400	15.412
0.681	16.000	16.183
1.000	18.100	17.812
1.468	20.500	20.632
2.154	24.000	24.606
3.162	29.000	29.031
4.642	32.000	32.131
6.813	32.000	31.445
10.000	27.000	25.917
14.678	17.000	17.803

Table 1 Field and modelled resistivity data near MW-1.

layers gives a depth to the water table of 3.4 meters, as compared with 3.3 meters measured directly in the well. Seismic refraction data also indicate that the water table is about 3.4 meters deep. Due to the added ions cited above, and also possibly due to leaching of salts from the soils by the hydrocarbons, the contaminant plume at this site is outlined by lower resistivities relative to the surrounding geology.

GPR data were also collected across two traverses at this site. These lines are shown in Figure 1 as GPR-South and GPR-North. GPR-South is about 45 meters down-gradient from the leaking tank and runs across the contaminated area. GPR-North is approximately 60 meters north of the tank in an uncontaminated, up-gradient area.

The GPR-North section (Figure 3) shows relatively "clean," continuous subsurface strata. The stronger reflection at about 3.3 to 3.5 meters in depth is interpreted as the water table. Reflections below the water table tend to dim and fade out, characteristic of some water-saturated sediments. Indications of rocks and gravel can be seen in the reflectors above the water table.

On the GPR-South profile shown in Figure 4, the water table is interpreted to be the reflectors between 3.4 and 3.7 meters. Between the surface locations of 40 to 90 meters, the water table is "smeared out" by reflections interpreted to come from hydrocarbon contamination. This was later confirmed by well groundwater sample data. Due to ions added by the nutrients and biodegradation, these dispersed hydrocarbons are less conductive than water, and therefore enhance the radar reflectivity in this part of the profile. From the GPR data, it appears that some of the hydrocarbons may be floating on the water table. In addition, some of the radar peaks between 1.2 and 3.0 meters in depth seem indicative of larger rocks and gravel, which is also in agreement with the monitoring well data in the area.

Groundwater samples taken from monitoring wells 1,2,3, and 4 (Figure 1) were analyzed by an independent laboratory for hydrocarbon content. For MW-3, which is near the "uncontaminated" GPR-North line, the TPH value was about 1.2 ppm, whereas for MW-1 and MW-3 which are near the "contaminated " GPR-South line, TPH values were about 44 ppm and 51 ppm, respectively. At MW-4, the TPH value was about 1.8 ppm, which is comparable to the value in MW-3 to the north. These values are in good agreement with the interpreted electrical resistivity and GPR data. Based upon the interpretations of the resistivity and GPR data, other strategically located wells have or will be installed to accelerate the clean up.

LOCATING CONCEALED FAULTS

The Wasatch fault zone shown in Figure 5 lies along the western edge of the middle Rocky Mountain and Colorado Plateau regions and the eastern edge of the Basin and Range region in north-central Utah. The fault zone is distinguished by extensive Late Quaternary fault scarps, truncated bedrock spurs, sag ponds, and springs (Hintze 1988). Several strands of the fault zone have surface expression, but geophysical and trenching data show that many others are concealed (Benson & Baer 1987; Benson & Mustoe 1989; Benson, 1993). Since ninety percent of Utah's population lives near or within this active fault zone, large-magnitude

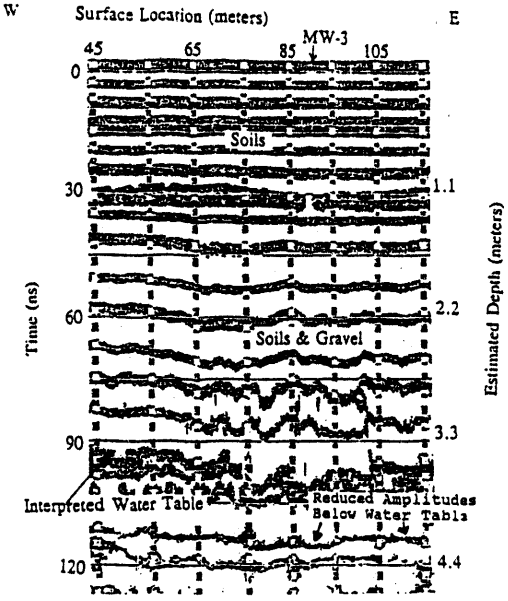


Figure 3 GPR data recorded along traverse GPR-North located up-gradient from the leaking fuel tanks. (Surface distances are consistent with those along the GPR-South line.)

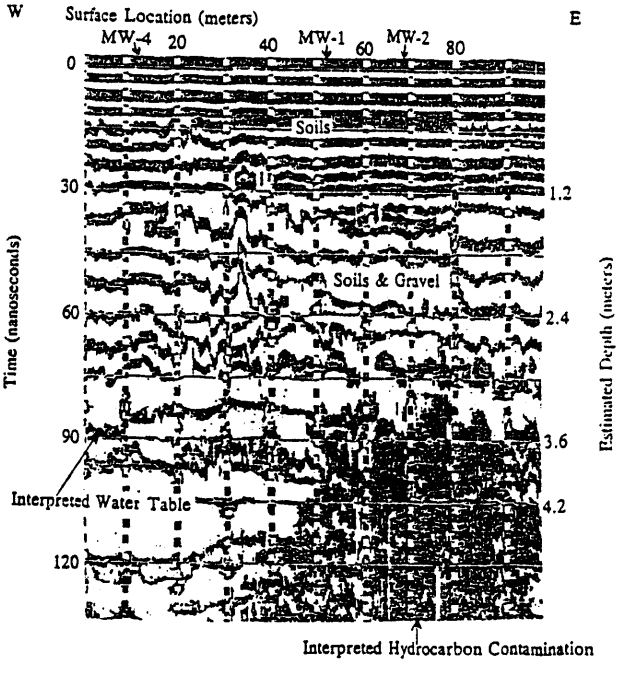


Figure 4 GPR data recorded along traverse GPR-South located down-gradient from the leaking fuel tanks.

earthquakes would have a significant impact (Gori & Hays 1987, 1988). To mitigate the effects of possible earthquakes, the location and characteristics of individual fault strands need to be determined as accurately as possible in order to establish and implement building codes and zoning ordinances.

In the past, a number of surficial studies have focused on the shallow structure and history of movement of the fault zone. These studies include large scale aerial surveys and small-scale trenching along the fault zone (Cluff, Brogan & Glass 1973). To delineate shallow discontinuities associated with the Wasatch Fault shown in Figures 5 and 6, a populated area northeast of Provo, Utah, near Rock Canyon was selected.

The geology at the Rock Canyon site is taken from maps and reports by Hintze (1978) and Machette (1989). The surficial sediments in the area are predominantly Holocene to Late Pleistocene alluvial deposits (Machette 1989), deposited primarily by debris flows and low-to-high-energy intermittent streams. Bedrock in the Wasatch Range at Rock Canyon consist of Paleozoic and Proterozoic sedimentary rock, including tillite, quartzites, limestones, dolomites and shales. These rocks were folded and thrust-faulted during the Sevier Orogeny (20-30 million years ago) and subsequently cut by numerous normal faults during Basin and Range extensions (10-20 million years ago). The Wasatch Fault separates the bedrock of the mountains form the alluvial and lake deposits in Utah Valley to the west. Older sediments within the valley are of alluvial, fluvial, and lacustrine origin. Thicknesses of sediment fill varies form less than a meter near the margins to over 4000 meters near the center (Hintze 1988).

Gravity data, VLF data, and a GPR profile were acquired along the GPR line by Rock Canyon Road, as illustrated in Figure 7. Fault scarp expressions at the surface have been culturally removed along the road, but some scarp remnants have been found a few meters north and south of the road. Such remnants exist both to the north and the south of the GPR traverse.

The residual Bouguer anomaly profile (Figure 8) has a prominent fault signature between 378 and 408 meters. Initial Parameters for gravity modelling were determined from field observations and characteristic curves (Grant and West, 1965). By changing estimates of depth, dip angle, and density contrasts, a final model (Figure 9) was obtained after three iterations with the Talwani and Ewing (1960) method. The final model indicates a fault offset of approximately 3.4 meters, a dip angle of 78° W, a density contrast between alluvium and a limestone\quartzite layer of 0.7 g/cc, and a bed thickness of 2.9 meters.

VLF data were also acquired over the same traverse along Rock Canyon Road using a WADI System manufactured by ABEM (Figure 10a). The primary VLF field transmitted by a military radio transmitter induces a secondary electromagnetic VLF field from localized resistivity contrasts in the subsurface. The in-phase (real) and out-of-phase (termed imaginary) components of the total VLF field are recorded and compared. The raw VLF data (Figure 10b) were filtered with a Karous-Hjelt Filter (1983) in order to correctly position the anomalies with respect to their subsurface source(s) (Figure 8a). These data show the characteristic "lazy S" fault signature at almost the same location as the gravity data, and both data sets agree very

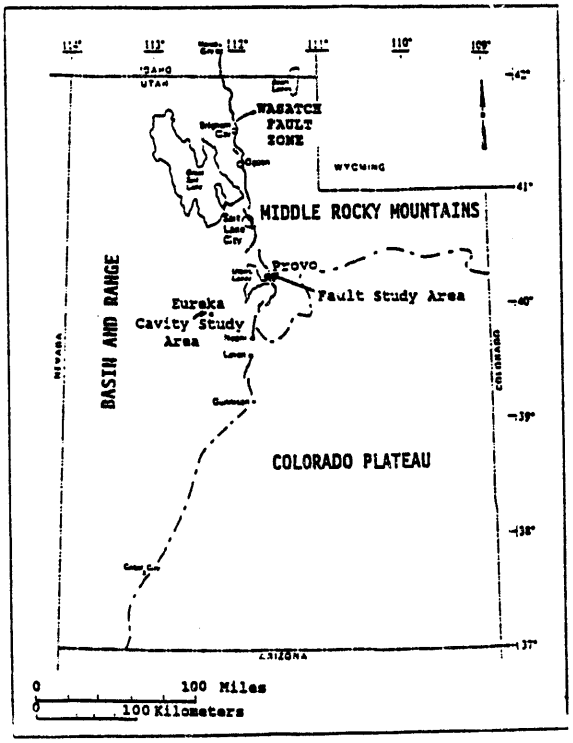


Figure 5 Regional location map showing the Wasatch Fault and physiographic provinces (after Hintze (1988), p.80).

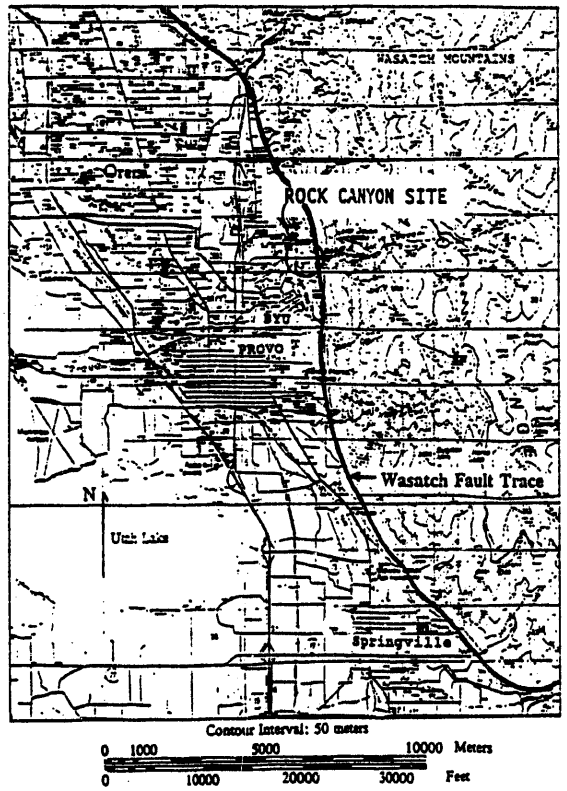


Figure 6 Map of the Provo, Utah area showing the trace of the Wasatch Fault and the Rock Canyon site (from U.S. Geological Survey 30x60 minute metric topographic map of Provo, Utah, 1986).

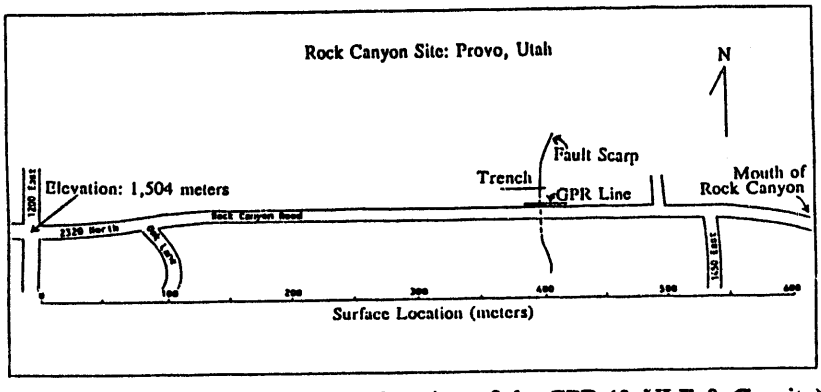


Figure 7 Map of Rock Canyon Road showing location of the GPR (& VLF & Gravity) traverse, observed fault scarp trace, and the UGMS trench. The dashed section of the fault scarp indicates that much of it has been culturally removed across Rock Canyon Road.

well with the fault scarp location observed in the field.

The GPR profile over the same traverse (Figure 11) also suggests a high-angle normal fault in the subsurface, whose surface exposure is probably the exarp to the north and south of the roadway. Some of its surface expression was probably removed when Rock Canyon Road was built. The upper layers in the GPR profile are interpreted to be road fill, soils, rocks, and gravel. Some of the rocks and gravel are probably from post-fault debris flow out of the canyon. Using an average dielectric constant of 2.5 for dry soils and rocks near Rock Canyon, the fault offset is estimated to be 3.3 meters, and the dip angle of the interpreted fault is estimated to be 75° W. Above the fault plane between surface locations 385-395 meters, a radar reflection is seen which we interpret to come from the colluvial wedge of materials associated with the faulting.

After the geophysical work was completed, the Utah Geological and Mineral survey (UGMS) dug a 30-meter long trench across the fault scarp approximately 5 meters due north of our GPR line. In going north form the GPR traverse to the trench location, the north side of Rock Canyon Road slopes down a gradient of about 1.5 meters, and most of this material appears to be road fill and gravel base, with some rock debris from Rock Canyon.

A schematic diagram of the trench is shown in Figure 12 (W.R. Lund, UGMS, personal communication, 1991). The trench indicates a single-event rupture with 3.5 meters of throw, dipping at 76° W beneath the scarp. Comparing the GPR data (Figure 11) with the trench cross-section suggests that the fault reflections are probably coming from the rock layer between the upper and middle soil horizons. Examination of natural exposures in the trench showed competent rock between these two horizons, consisting of fractured limestone and quartzite, as well as some debris-flow deposits from the canyon. The gravity, VLF and GPR data are all in good agreement with the geology of this subsurface faulting.

OUTLINING UNDERGROUND CAVITIES

The effectiveness of GPR in locating and outlining the boundaries of an underground cavity was tested by running some traverses over an underground physics laboratory located on the campus of Brigham Young University, Provo, Utah. The surveys were conducted and interpretations made knowing only the general area where the lab was located. To avoid bias, comparisons with lab blueprints were not made until the geophysical work was completed. An E-W cross section of the lab taken from the blueprints is sketched in Figure 13a, and a schematic of the experimental setup is shown in Figure 13b.

The air cavity and floor of the lab can be clearly seen on the GPR profile in Figure 14. This traverse was taken over the central portion of the lab ceiling. The overlying soil, concrete ceiling, and associated multiple reflections are in the upper 40 nanoseconds of this profile. Since the relative dielectric constant of air is 1 and from Figure 14 the time interval between the interpreted ceiling and floor is 60 nanoseconds, the average depth form the ceiling to the floor is 9.1 meters. This is the same value as found on the blueprints for the lab. Between the surface positions at 6 and 9 meters, the larger amplitudes along the floor of the lab

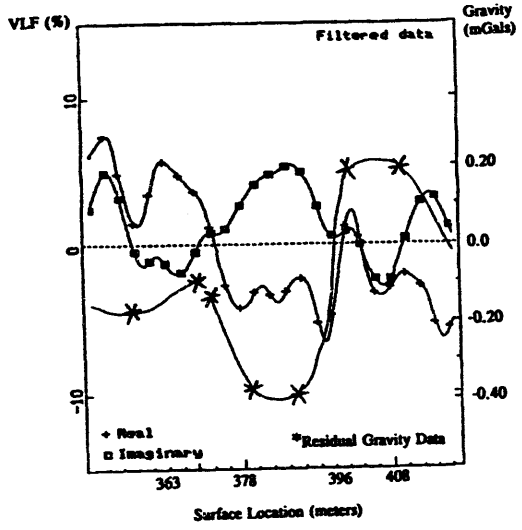


Figure 8 Residual gravity data and filtered VLF data along the GPR traverse shown in Figure 7.

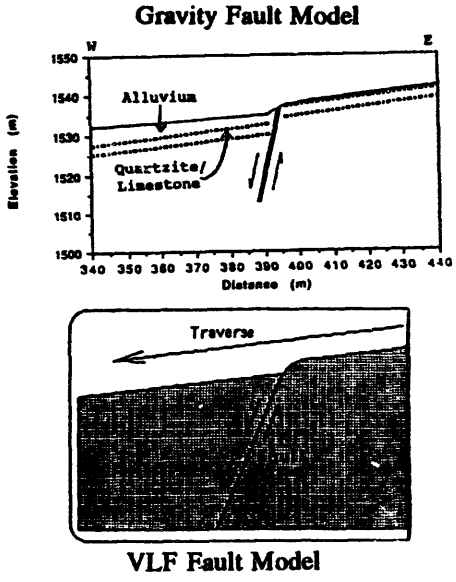


Figure 9 Fault models constructed from gravity and VLF data shown in Figure 8.

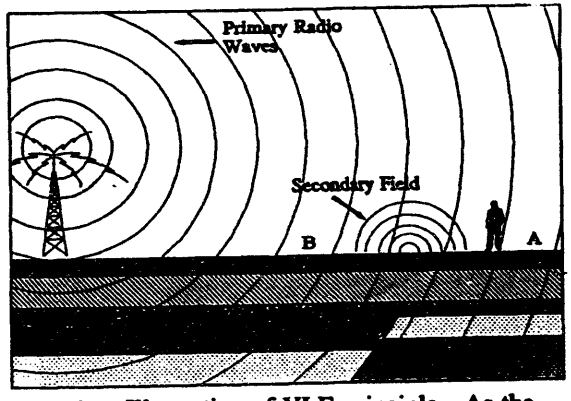


Figure 10a Illustration of VLF principle. As the operator walks along traverse A-B, the WADI VLF system detects the phase lag between the primary and secondary waves.

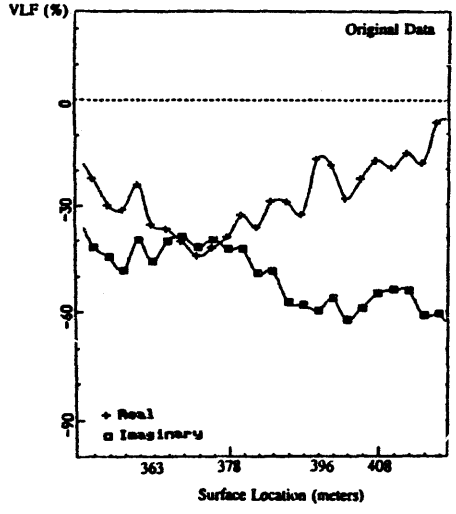


Figure 10b Original VLF field data acquired along the GPR line shown in Figure 7.

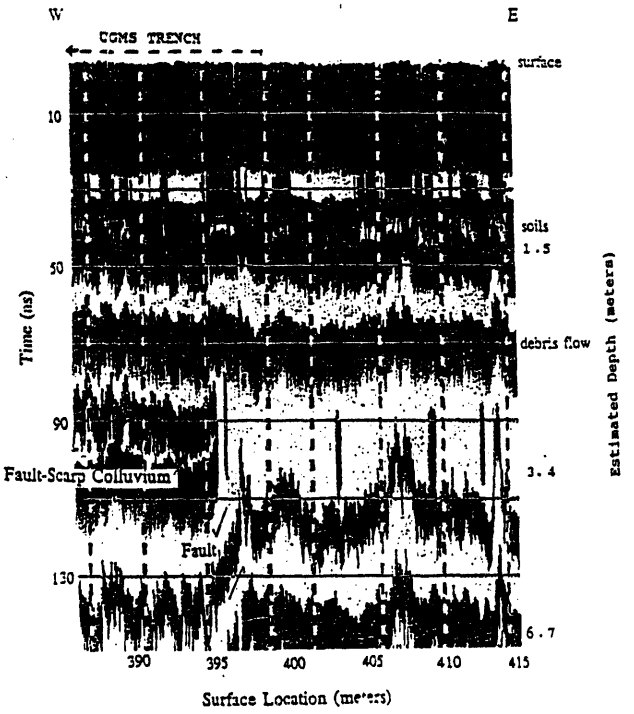


Figure 11 GPR profile along Rock Canyon Road. Vertical dashed lines represent a distance of about 3 meters. Horizontal lines are 20 nanoseconds apart. The main fault is clearly visible.

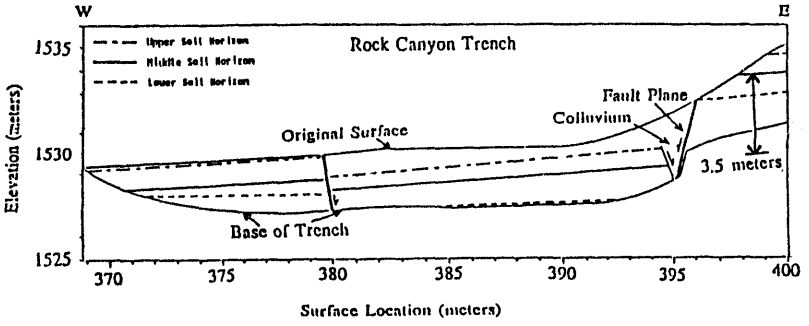


Figure 12 Schematic diagram of the stratigraphy in the UGMS trench along Rock Canyon Road. Three mapped soil horizons are shown. Heavy black lines represent faults; arrows show directions of relative movement. The upper soil horizon is on a debris flow, the middle soil horizon is on a matrix-supported debris flow, and the lower soil horizon is on a high-energy fluvial deposit.

are interpreted to be the approximate location of a Van de Graaff generator housed in the lab. This location was later confirmed by inspecting the blueprints and the lab itself.

Another GPR traverse was recorded across U.S. Highway 6 near the Eureka, Utah location shown in Figure 5. Eureka is an old mining town dating back to the 1890's having numerous mine shafts and tunnels under the town and surrounding areas. Locations of many of the older underground excavations are unknown since they were never recorded on any maps. Most of the mines are in Cambrian and Ordovician limestone, and the area is rich in ores of gold, silver, copper, iron, and other metals. Tertiary intrusions have brought in ore-bearing solutions which have solidified in the cracks, vugs, and fissures in the limestone. In many places the ground is cracked or collapsed from the mining activity, and some mines are now just cone-shaped cave-ins (Chronic, 1990).

Two areas of apparent subsidence in the upper strata can be seen in Figure 15. Any surface expressions of this slumping were most likely filled in many years ago when the highway was resurfaced. Some nearby cracking and warping in the highway may be clues that some subsurface movement is still occurring. Almost directly below each area of subsidence is a hyperbolic diffraction pattern that is characteristic of reflections from localized objects or cavities in the subsurface. The hyperbolae in Figure 15 most likely originate from man-made cavities, such as a mine shaft or a tunnel, but could also arise from sinkholes carved out in the limestone. Cavity diameters appear to be on the order of 2-4 meters.

Whatever the source of the apparent subsurface cavities and possible associated subsidence, the important point is that GPR can often be successful in locating these potential hazards. This information is very useful in planning and site development. Early detection of such cavities or the mechanism causing subsidence can result in substantial savings in time and money.

UNDERGROUND PIPING

Magnetic exploration can be used to locate and characterize subsurface features that differ in magnetic susceptibility from the surrounding material. Some examples include buried iron objects, ore bodies, and rock units containing magnetic minerals. A magnetic survey was conducted on the Brigham Young University (BYU) campus to determine the location and depth to some underground high-temperature water pipes. The experimental setup is illustrated in Figure 16a.

The residual magnetic values measured with a proton-precession magnetometer are plotted in Figure 16b. The maximum magnetic field intensity correlates with the location of the subsurface pipe.

The depth to the center of a hollow cylinder (Telford et al., 1984) can be approximated by solving the following equation for r:

$$F_a = 2kF_e\pi Dt / r^2 \quad , \tag{1}$$

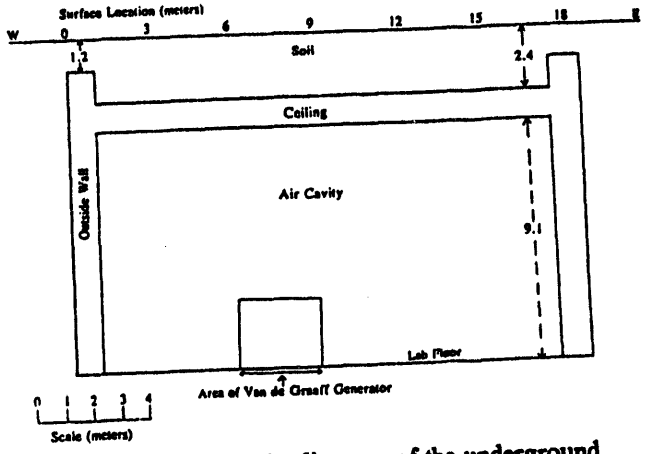


Figure 13a Schematic diagram of the underground physics laboratory on the campus of Brigham Young University, Provo, Utah.

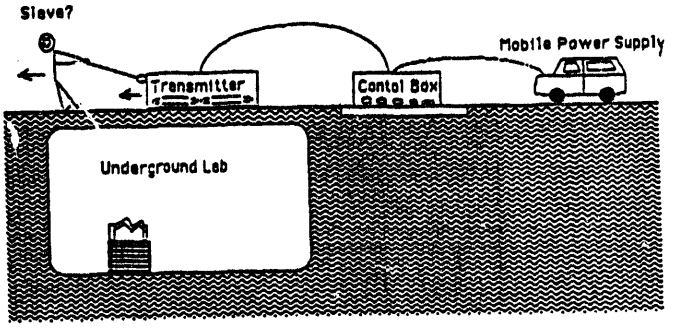


Figure 13b Illustration of the GPR exploration setup.

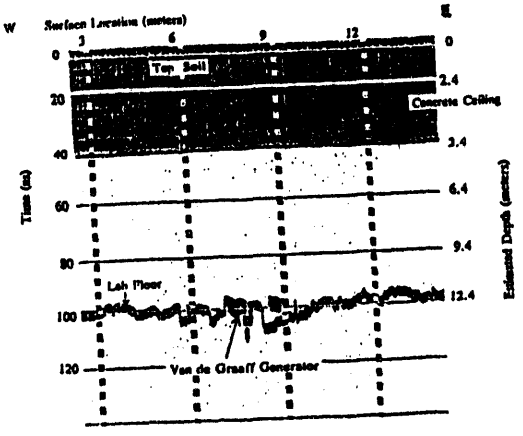


Figure 14 East-west GPR profile over the center of the BYU lab. The underground air cavity and floor are clearly detectable.

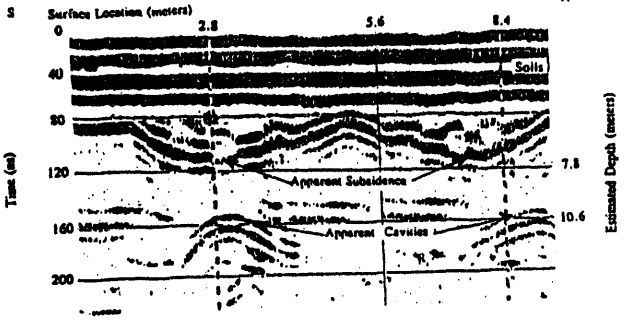


Figure 15 GPR profile across U.S. Highway 6, near Eureka, Juab County, Utah.

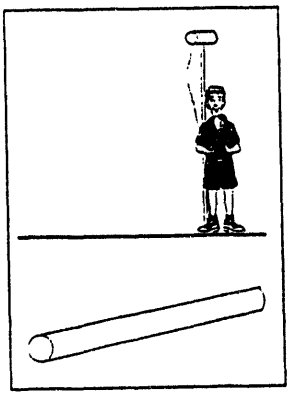


Figure 16a Illustration of magnetic exploration setup.

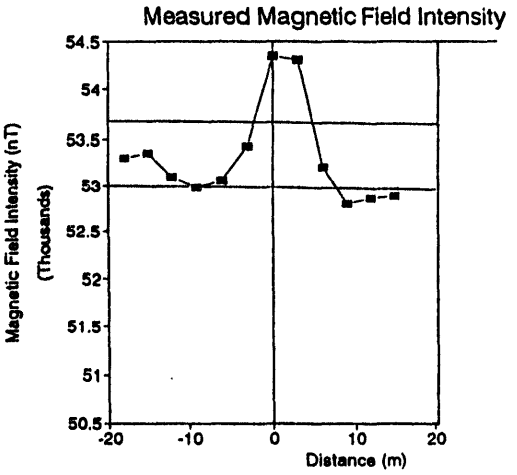


Figure 16b Reduced magnetic filed data collected over underground piping on Brigham Young University campus.

X (m)	Field Strength Measured	Calculated	Fa
-18	53305	305	2.38
-15	53360	360	3.43
-12	53098	98	5.35
-9	52980	-20	9.48
-6	53058	58	21.15
-3	53430	430	80.75
0	54350	1350	1339.06
3	54318	1318	80.75
6	53205	205	21.15
9	52796	-204	9.48
12	52865	-135	5.35
15	52888	-112	3.43
18	52695	-305	2.38
21	52496	-504	1.75
24	52542	-458	1.34
27	52430	-570	1.06
30	52065	-935	0.86
33	51610	-1390	0.71
36	50806	-2194	0.60

Diameter (m)	0.254
Thickness (m)	0.009144
r (m)	0.76
k	1
Fe (nT)	53000

Table 2 Modelled magnetic data over a hollow pipe.

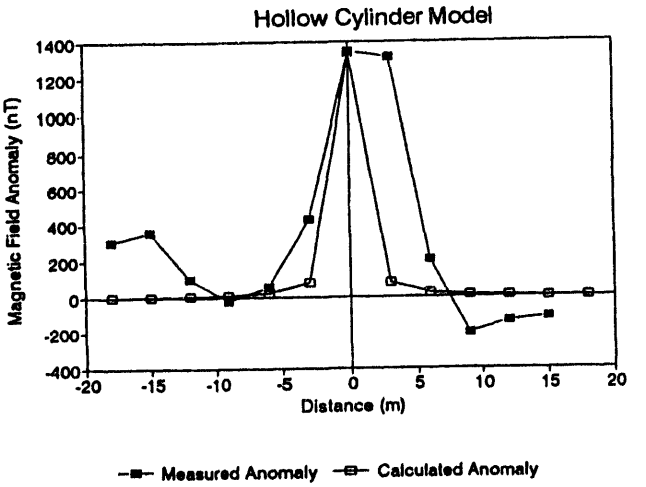


Figure 17 Modelled magnetic data superimposed on the reduced magnetic field data.

where F_a is the anomaly value, k is the magnetic susceptibility contrast, F_e is the strength of the earth's magnetic field (53,000 nanoTeslas at this site), D is the diameter of the pipe, t is the pipe thickness, and r is the depth to the center of the pipe. Since the BYU utilities department told us that the piping used was 10 inches in diameter and 0.36 inches thick, and since k for this steel is about 1, the depth to the center of the pipe is estimated from equation (1) to be 0.76 m, which was later confirmed by BYU utilities. Table 2 shows the calculated anomaly values over the pipe using the above equation. These modelled values are compared with the measured anomaly values in Figure 17. Since the steel pipe is quite shallow, one would expect a narrow anomalous peak as shown by the modelled data. However, due to a nearby underground cable and steel supports for the piping, the measured anomaly is broadened. These effects were not accounted for in the magnetic modelling, but very good results were still obtained for locating and estimating the depth to this subsurface piping.

CONCLUSIONS

Depending on the geological setting, geophysical surveys are reliable, rapid, and economical for mapping shallow subsurface sediments and assessing hydrogeologic conditions. The thickness of the sediments, the depth to the water table, the presence of groundwater contamination, the location of subsurface faults, underground cavities, and subsurface piping can all be reliably mapped at field sites where subsurface geometries are not too complex and where sufficient contrasts exist in the physical properties being measured. The surface geophysical methods for general investigation of the shallow subsurface are summarized in Table 3 and the common borehole geophysical methods are summarized in Table 4. More specifically, the surface geophysical methods effective for locating and mapping buried wastes and utilities are summarized in Table 5, with detailed specifications for mapping contaminant plumes summarized in Table 6.

In particular, electrical resistivity and GPR data from sites in central Utah have been helpful in mapping groundwater contamination produced by leaking underground fuel tanks. Based upon the estimated depths to the areas of subsurface contamination from the resistivity and GPR data, the lateral extent of the contaminant plumes are outlined and monitoring wells installed at strategic locations at the sites. Analysis of the monitoring well data shows that estimated water table depths and qualitative assessments of contamination location and concentrations inferred from the resistivity and GPR data are in good agreement with the depths and contamination levels found in the wells.

Gravity, VLF, and GPR data collected in east Provo, Utah demonstrate the reliable detection of shallow concealed faulting in appropriate geologic settings. Interpretations of these geophysical data sets coincide with many features observed in a recently opened nearby trench. The net offset and dip of the fault correlate quite well. Determining the characteristics and distribution of subsurface faulting and folding can provide useful information for establishing and implementing building codes and zoning ordinances in the Provo area.

Cavity detection is another challenging exploration problem that requires good

Table 3 Common surface/subsurface geophysical methods (after Melvin, 1993).

SURVEY METHOD	APPLICATIONS
Magnetic	Locate buried metallic objects and utilities, map buried channels and depth to bedrock if magnetic minerals are present and locate faults and fractures.
Electromagnetic (EM)	Locate contaminant plumes, boundaries of landfills, buried metallic objects or utilities and locate fractures and faults.
Electrical Resistivity	Locate contaminant plumes, the water table and locate fractures and faults.
Gravity	Determine overburden thickness, map bedrock topography and locate fractures and faults.
Seismic (Reflection and Refraction)	Determine overburden thickness, locate the water table, lithologic boundaries, fractures and faults.
Ground Penetrating Radar (GPR)	Locate buried objects whether metallic or structures or boundaries of landfills and can assist in locating contaminant plumes, fractures, faults and karst topography.

Table 4 Common borehole geophysical methods (after Melvin, 1993).

SURVEY METHOD	APPLICATIONS
Caliper Logs	Determine lithologic and stratigraphic correlations, fractures and solution openings and the construction of existing wells.
Electric (Resistivity and Spontaneous Potential) Logs	Determine lithologic and stratigraphic correlations, grain size and effective porosity and locate water level and saturated zones.
Natural Gamma	Determine depth and concentration of clay or shale.
Gamma-Gamma	Determine total porosity or bulk density, locate water level and saturated zones and the construction of existing wells.
Neutron	Determine total porosity or bulk density, specific yields of unconfined aquifers, moisture content, infiltration, and to locate water level and saturated zones.

Table 5 **Surface Geophysical Methods for Location and Mapping of Buried Wastes and Utilities.[a]** (after R. Benson, 1991)

Method	Bulk Wastes w/o Metals	Bulk Wastes w/Metals	55 Gal. Drums	Pipes and Tanks
Radar	Very good if soil conditions are appropriate; Sometimes effective to obtain shallow boundaries in poor soil conditions	Very good if soil conditions are appropriate; Sometimes effective to obtain shallow boundaries in poor soil conditions	Good if soil conditions are appropriate (may provide depth)	Very good for metal and non-metal if soil conditions are appropriate (may provide depth)
EM	Excellent to depths less than 20 feet	Excellent to depths less than 20 feet	Very good (Single drum to 6–8 feet)	Very good for metal tanks
Resistivity	Good (sounding may provide depth)	Good (sounding may provide depth)	—NA—	—NA—
Seismic Refraction	Fair (may provide depth)	Fair (may provide depth)	—NA—	—NA—
Micro Gravity	Fair (may provide depth)	Fair (may provide depth)	—NA—	—NA—
Metal Detector	—NA—	Very good (shallow)	Very good (shallow)	Very good (shallow)
Magnetometer	—NA—	Very good (ferrous only; deeper than metal detector)	Very good (ferrous only; deeper than metal detector)	Very good (ferrous only; deeper than metal detector)

[a]Applications and comments should only be used as guidelines. In some applications, an alternate method may provide better results.

Table 6 **Surface Geophysical Methods for Mapping of Contaminant Plumes.[a]**

Mapping Permeable Pathways, Bedrock Channels, etc.
The fundamental approach to evaluating the direction of groundwater flow and the possible extent of a contaminant plume is by determining the hydrogeologic characteristics of the site.

Mapping of Inorganics or Mixed Inorganics and Organics
When inorganics are present in sufficient concentrations above background or organics are part of such a inorganic plume, they can be mapped by the electrical methods and sometimes radar. The higher specific conductance of the pore fluids acts as a tracer by which the plume can be mapped.

Mapping of Hydrocarbons
When sufficient hydrocarbons have been present in the soil or floating on a shallow water table, for a sufficient period of time they may sometimes be mapped by the electrical methods or by radar. Because of their low conductivities (high resistivity) they may sometimes be detected by the electrical methods. Due to changes in dielectric constant or suppression of the capillary zone they may sometimes be mapped by radar (in some situations where degradation of hydrocarbons is occurring, conductivity may increase). These applications are limited and should be treated with caution. A more reliable approach is to map natural permeable pathways.

Radar • Limited applications—may sometimes be used to detect shallow floaters (0 to 20 feet) to map hydrocarbons in soil. May detect thickness in some cases.

EM • May be applicable to detect low conductivity at some sites.

Resistivity • May be applicable to detect high resistivity at some sites.

[a]Applications and comments should only be used as guidelines. In some applications, an alternate method may provide better results.

(after R. Benson, 1991)

resolution and good depth penetration. GPR can be successful in detecting near-surface cavities when the host rock has a relatively low electromagnetic wave attenuation factor. The geometrical features of an underground laboratory at Brigham Young University were successfully outlined and specified in depth using GPR surveys. Interpretations of the ceiling, floor, and air cavity are in good agreement with the blueprints of the laboratory. GPR data also provided useful information about the location and approximate depths for two apparent cavities and associated areas of subsidence under U.S. Highway 6 near Eureka, Utah.

Magnetic exploration is a primary method for locating subsurface pipes, cables, ore bodies, archaeological artifacts, and metal objects in general. The location and depth to underground high-temperature water pipes at Brigham Young University were delineated using a proton-precession magnetometer. Likewise, this method can locate buried barrels and old well casings that pose significant contamination hazards, as well as map the metal objects in a buried landfill.

In summary, in appropriate geology, geophysical surveys can provide useful, cost-effective data which can help assess potentially dangerous geological hazards, including groundwater contamination, concealed faulting, underground cavities and piping. Planning and remedial measures based upon these data can then be implemented to help protect human life and produce minimal threat to the environment.

REFERENCES

Benson, A.K., 1993. Case Studies Using Ground Penetrating Radar to Help Assess Groundwater Contamination, Shallow Faulting, and Cavities: Proceedings of the 29th Symposium on Engineering Geology and Geotechnical Engineering, 63-89.

Benson, A.K., 1992. Integrating Seismic, Resistivity, and Ground Penetrating Radar Data to Delineate the Water Table and Groundwater Contamination: in Water-Rock Interaction, Vol. 1, Low Temperature Environments, A.A. Balkema, Rotterdam, 359-366.

Benson, A.K. and Mustoe, N.B., 1991. Ground Penetrating Radar, Electrical Resistivity, and Water Quality Studies Integrated to Determine the Source(s) and Geometry of Hydrocarbon Contamination at a Site in North-central Arizona: Proceedings of the 27th Symposium on Engineering Geology and Geotechnical Engineering, 38.1-38.18.

Benson, A.K. and Mustoe, N.B., 1989. Seismic and Gravity Surveys as Tools in Delineating Subsurface Geology and Assessing Some Geologic Hazards: Proceeding of the 25th Symposium on Engineering Geology and Geotechnical engineering, 25-30.

Benson, A.K. & Baer, J.L., 1987. Close Order Gravity Surveys: A Means of Fault Delineation in Valley Fill Sediments: Proceedings of the 23rd Symposium on Engineering Geology and Soils Engineering, 219-240.

Benson, R.C., 1991. Remote Sensing and Geophysical Methods for Evaluation of Subsurface Conditions: in Practical Handbook of Ground-Water Monitoring, D.M. Nielsen, ed., Lewis Publishers, Chelsea, Michigan, 143-194.

Beres, M. and Haeni, F.P., 1991. Application of Ground-Penetrating-Radar Methods to Hydrogeologic Studies: Ground Water, 29, 375-386.

Chronic, H., 1990. Roadside Geology of Utah: Mountain Press Publishing Company, Missoula, Montana, 336 p.

Cluff, L.S., Brogan, G.E. & Glass, C.E., 1973. Wasatch Fault, Southern Portion: Woodward-Lundgren and Associates, Oakland, California. Report prepared for Utah Geological and Mineral Survey, Salt Lake City, Utah.

Foster, A.R., Veatch, M.D., and Baird, S.L., 1987. Hazardous Waste Geophysics: Geophysics, The Leading Edge, 6, 8-13.

Gori, P.L. and Hays, W.W. (eds.), 1987. Earthquake Hazards Along the Wasatch Front, Utah: U.S. Geological Survey Open File Report 87-154.

Gori, P.L. and Hays, W.W. (eds.), 1988. Assessment of Regional Earthquake Hazards and Risk Along the Wasatch Front, Utah, Volume III: U.S. Geological Survey Open File Report 88-680.

Grant, F.S. and West, G.F., 1965. Interpretation Theory in Applied Geophysics: McGraw-Hill, New York, 282-287.

Hintze, L.F., 1988. Geologic History of Utah: Brigham Young University Geology Studies. Special Publication 7, 7-10, 29-32, 77-89.

Hintze, L.F., 1978. Geologic Map of the Y Mountain Area, East of Provo, Utah and Cross Sections of the Y Mountain: Brigham Young University Geology Studies, Special Publication 5. Map scale is 1:24,000.

Karous, M. and Hjelt, S.E., 1983. Linear Filtering of VLF dip-angle measurements: Geophysical Prospecting, 31, 782-794.

Machette, M.N., 1989. Preliminary Surficial Geologic Map of the Wasatch Fault Zone, Eastern Part of Utah Valley, Utah Country, and Parts of Salt Lake and Juab Countries, Utah: USGS Misc. Field Studies Map and Pamphlet MF-2109. Map scale is 1:50,000.

Melvin, R.J., 1993. Geologic Skills Used in the Site Characterization of Environmental/Hazardous Waste Projects: The Professional Geologist, September, 12-15.

Talwani, M. and Ewing, M., 1960. Rapid Computation of Gravitational Attraction of Three-Dimensional Bodies of Arbitrary Shape: Geophysics, 25, 203-225.

Telford, W.M., Geldart, L.P., Keys, D.A., and Sheriff, R.E., 1984. Applied Geophysics: Cambridge University Press, New York, New York, 161-162.

Hydrogeology, Waste Disposal, Science and Politics
Proceedings 30th Symposium
Engineering Geology and Geotechnical Engineering, 1994

EFFECTS OF SHALE AND CONTAMINANTS ON (V_S/V_P) RATIOS IN TRANSVERSELY - ISOTROPIC GEOLOGY

ALVIN K. BENSON

Department of Geology, Brigham Young University, Provo, Ut 84602

ABSTRACT

The mechanical properties of rocks and soils can be calculated from the shear-wave velocity, V_S, the compressional-wave velocity, V_P, and the density, or from (V_S/V_P) ratios and the density. Therefore, determination of (V_S/V_P) ratios is an important tool to assist with lithological identification and many associated applications.

In most geologic settings, mixtures of different materials are quite common, and it is important to understand the effect of thin laminations on measured (V_S/V_P) ratios. An equation is derived for (V_S/V_P) in transversely-isotropic materials. It is found that even small amounts of a second component, such as 10% shale, can change (V_S/V_P) ratios significantly from that of a pure end member, such as sandstone. Case studies will illustrate some practical applications.

INTRODUCTION

For an elastic earth model, one can predict the occurrence of two distinct body-wave types: (1) a compressional wave with particle motion in line with the direction of propagation and (2) a shear wave with particle motion perpendicular to the direction of propagation. At each boundary of the model, any incident body wave is transmitted and reflected as both wave types. The Zoeppritz equations (Telford et al., 1976) predict the amplitude and wavefront direction of the resulting P- and S- wave signals as a function of the angle of incidence for an incident P- or S- wave at each boundary.

It is possible to generate and receive polarized versions of these elastic signals by confining the ground motion at the source to emphasize a certain polarization and by using a sensor that is sensitive to particle motion in only one direction (Garotta, 1983). In addition to compressional sources, seveal shear wave sources have been developed. Conoco developed a S- wave vibrator along with the P- wave vibrator in the 1950's. In a later development, Compagnie Generale de Geophysique (CGG) developed a transverse hammer source called SEISLAP^R. With SEISLAP, CCG demonstrated how explosive sources could be combined with transverse receivers for reception of horizontally polarized shear-wave signals. Still later, Prakla-Seismos developed a technique which uses two 180° out-of phase P-wave vibrators placed side-by side and perpendicular to the seismic line, known as SHOVER.^{TM} (See Waters 1987; Danbom and Domenico, 1987).

Two uses of shear-wave data have beome readily apparent (Danbom and Domenico, 1987). First, since shear waves are not propagating under the influence of the fluid in the pore space of the rock, measured properties of shear waves having gone through or reflected from rocks with anomalous pore fluids will be different when compared with the response of compressional waves. Secondly, by measuring the velocity ratio V_S/V_P for a sequence in the stratigraphic column, some of the physical characteristics of that zone can be described. In addition, Poisson's ratio can be directly calculated from V_S/V_P. Indeed, if one uses either Gardner's equation (Gardner et al., 1974) with the variable V_P, or the relationship established by Ludwig et al. (1970) with Poisson's ratio as the variable, the density of the formation can be empirically estimated. With the availability of V_P, V_S, density and Poisson's ratio, the remaining elastic constants, namely Young's modulus, bulk modulus, and shear modulus can be calculated. In other words, compressional and shear wave data together form a synergistic system. Some applications of compressional plus shear wave data have been discussed by Polškov, et al. (1980), Meissner and Hegazy (1981), Helbig and Mesdag (1982), Neidell (1985), and Ahmed (1989).

Gregory (1976a) showed a relationship between the pore filler and the V_S/V_P ratio for porous sedimentary rocks. Pickett (1963) and Domenico (1983, 1984) showed a separation of lithology as a function of the V_S/V_P ratio. Tatham and Stoffa (1976) and Tatham (1982) discussed V_S/V_P ratios as possible lithology and hydrocarbon indicators, and Tatham and Goolsbee (1983) extended these ideas to the marine environment. Brown et al. (1989) described usage of V_S/V_P ratios for finding oil and gas. Most of these are empirical relationships which should be used subject to the conditions established by the original author(s), since universal application of empirical formulae can be inaccurate. This paper considers the effect of thin layers of shale or contaminants, such as hydrocarbons, on (V_S/V_P) ratios in otherwise pure sedimentary rocks, such as sandstone or limestone.

VELOCITIES IN TRANSVERSELY-ISOTROPIC MEDIA

Thinly laminated materials are quite common in most geological settings, with many sedimentary sections consisting of thin layers of contrasting properties. Hence, it is an important problem to understand the effect that thin laminations have on physical properties, such as measured (V_S/V_P) ratios. Laminated materials consist of a number of isotropic components in layers parallel to a horizontal plane, with variable thicknesses, such as layers of shale in sandstone or in limestone, or layers of sandstone or limestone contaminated with hydrocarbons in other layers of sandstone or limestone.

In order for the layered material to approximate a homogeneous medium, its average properties must be the same throughout any elementary volume in the medium. An elementary volume must have its largest dimensions small in comparison to the shortest probing wavelength of seismic energy. Therefore, the layers need not be identical for each elementary element, but the average properties must be the same. This implies that the fractional concentration of the various components (N_1, N_2, N_3,...) are the same for each elementary

element, where the numbers refer to different geological constituents.

By symmetry, it can be shown that a laminated material should behave as a transversely - isotropic medium with the vertical axis being the unique axis. Hence, as shown by White (1965), the P- and S-wave (horizontal-shear) velocities are expressed as

$$V_S = \{(N \sin^2 \Upsilon_z + L \cos^2 \Upsilon_z)/\rho\}^{1/2} \quad \text{and}$$

$$V_P = \{(A \sin^2 \Upsilon_z + C \cos^2 \Upsilon_z + L + D)/2\rho\}^{1/2}, \tag{1}$$

where

$$D = (G + H)^{1/2},$$

$$G = \{(A-L) \sin^2 (\gamma_z) - (C - L) \cos^2 (\gamma_z)\}^2,$$

$$H = 4 (F + L) \sin^2 (\gamma_z) \cos^2 (\gamma_z),$$

A,C,F,L,N are dependent on the properties of the transversely-isotropic medium, and Υ_z is the angle between the direction of wave propagation and the vertical Z-axis. White shows that for a laminated material with N components that C,F,L,N,A, and ρ are given by the following expressions:

$$A = R + (T^2/W),$$

$$C = (1/W),$$

$$F = (T/W),$$

$$R = \sum_{i=1}^{N} [4 \mu_i n_i (\lambda_i + \mu_i)] / (\lambda_i + 2\mu_i),$$

$$W = \sum_{i=1}^{N} (n_i) / (\lambda_i + 2\mu_i),$$

$$T = \sum_{i=1}^{N} (n_i \lambda_i) / (\lambda_i + 2\mu_i),$$

$$L = \left(\sum_{i=1}^{N} (n_i/\mu_i)\right)^{-1},$$

$$N = \sum_{i=1}^{N} n_i \mu_i,$$

$$\rho = \sum_{i=1}^{N} n_i \rho_i, \qquad (2)$$

where n_i, ρ_i, λ_i, μ_i are the fractional concentration, density, and Lame's constants, respectively, for the i^{th} constituent of the laminated medium. The density of each component is

$$\rho_i = \rho_s (1-\phi) + \phi\rho_f, \qquad (3)$$

where ρ_s is the density of the matrix grains, ρ_f is the density of pore fluids, and ϕ is the porosity.

COMPOSITE (V_S/V_P) DERIVATION

Since (V_S/V_P) data from vertical seismic profiles, checkshots, and CDP stacked seismic sections essentially simulate wave propagation in the vertical direction, let's take $\Upsilon_z = 0$. Hence, the expressions for V_S and V_P in equation (1) simplify to

$$V_S = (L/\rho)^{1/2} \text{ and } V_P = (C/\rho)^{1/2}. \qquad (4)$$

Consequently, the (V_S/VP_P) ratio for a transversely-isotropic (composite) material is given by equation (4) as

$$(V_S/V_P)_{\text{composite}} = (L/C)^{1/2}, \qquad (5)$$

as in White (1965), Levin (1979), and Melia and Carlson (1984). For a two-component system, L is the geometric mean of the shear moduli,

$$L = \{(n_1/\mu_1) + (n_2/\mu_2)\}^{-1} \qquad \text{and}$$

$$C = \{(n_1/(\lambda_1 + 2\mu_1) + n_2/(\lambda_2 + 2\mu_2)\}^{-1}, \qquad (6)$$

where n_1, μ_1, λ_1 and n_2, μ_2, λ_2 are the fractional concentrations and elastic parameters for the two components, respectively. After some extensive algebra, equations (5) and (6) yield

$$(V_S/V_P)_{\text{composite}} = (\mu_1/(\lambda_1 + 2\mu_1))^{1/2} (\mu_2/(\lambda_2 + 2\mu_2))^{1/2} Y^{1/2}, \qquad (7)$$

where $Y = (n_1(\lambda_2 + 2\mu_2) + n_2 (\lambda_1 + 2\mu_1)/(n_1\mu_2 + n_2\mu_1)$.

However, from equations (2) and (4) for a one-component system,

$$V_{S1} = (\mu_1/\rho_1)^{1/2},$$

and

$$V_{P1} = ((\lambda_1 + 2\mu_1)/\rho_1)^{1/2}$$

for the first component, and

$$V_{S2} = (\mu_2/\rho_2)^{1/2},$$

and

$$V_{P2} = ((\lambda_2 + 2\mu_2)/\rho_2)^{1/2} \quad (8)$$

for the second component. Combining the results of equations (7) and (8),

$$(V_S/V_P)_{composite} = (V_{S1}/V_{P1})\,(V_{S2}/V_{P2})\,Z^{1/2}, \quad (9)$$

where $Z = (n_1\,\rho_2\,V^2_{P2} + n_2\,\rho_1\,V^2_{P1})/(n_1\,\rho_2\,V^2_{S2} + n_2\,\rho_1\,V^2_{S1})$,

which is the equation for the (V_S/V_P) ratio for a transversely-isotropic, two-component system. Using the bulk and shear moduli of the rock components, this can also be written as

$$(V_S/V_P)_{composite} = (V_{S1}/V_{P1})\,(V_{S2}/V_{P2})\,Q^{1/2}, \quad (10)$$

where $Q = (n_1(k_2 + (4/3)\,\mu_2) + n_2\,(k_1 + (4/3)\,\mu_1))/(n_1\,\mu_2 + n_2\,\mu_1)$,

where k is the bulk modulus (or incompressibility), and μ is the shear modulus. Thus, the composite (V_S/V_P) ratio is the product of the (V_S/V_P) ratios of the individual components multiplied by a factor involving the percentages of individual components and the shear and bulk moduli. Note that equation (9) is a function of the square root of the shale content, as is an empirical relationship determined by Eberhart-Phillips et al. (1989) using lab data from 64 different water-saturated sandstones, including clean quarry sandstones, other well-consolidated sandstones from quarries and boreholes, tight-gas sands, and samples (some poorly consolidated) from offshore wells in the Gulf of Mexico.

CASE STUDY EXAMPLES

Using equation (9) or equation (10), the effect of thin shale laminations on the (V_S/V_P) ratio in limestones and sandstones can be estimated. First, let's consider some vertical seismic profile data tabulated by Omnes (1980) for the Paris Basin, approximately 50 miles southwest of Paris, France. Both compressional and shear wave events were recorded. Table 1 shows parameters selected from the Kimmeridgian shales and the Lusitanian limestones, which are adjoining strata at about 1000 meters deep. Figure 1 shows a plot of the composite (V_S/V_P) data calculated from equation (9) and shown in Table 1. Note the rapid change from the value of the (V_S/V_P) ratio for Lusitanian limestones when they are contaminated with rather small amounts of laminated shale. For example, for the shaley limestone, only 10% shale gives a composite (V_S/V_P) of .529, whereas the Lusitanian limestone has a V_S/V_P of .550, and 20% shale drops the ratio to .515, which is a change of 6.4%. Thus, the composite (V_S/V_P) ratio may be a good indicator of shale as the Kimmeridgian shales grade into the Lusitanian limestones.

As a second case, let's apply equation (9) to some Gulf Coast well log data compiled by Gregory (1976b). Parameters selected for some brine-saturated Gulf Coast sands and shales at a depth of 5,182 meters are shown in Table 2. The average sandstone porosity at this depth is 17.8%, while for the shales it is 15.3%. These porosities are kept fixed as the shale content varies, and the resulting composite (V_S/V_P) data in Table 2 are plotted in Figure 2. Again, significant changes occur in the (V_S/V_P) ratio of clean, saturated sands as they grade into laminated shaley, sands. These results agree favorably with lab findings of Mann and Fatt (1960). These changes are a good indication of content and are probably important estimators to help correctly determine the subsurface lithology. Of course, this could be very critical in hydrocarbon reservoir evaluation or in soil and groundwater contamination evaluation. If field data and lab results are good quality, then combined with the geology and experience in a given area, the data can be modeled and correlated to point out regions where hydrocarbons and contaminants most likely exist.

A third example is the basin hinge-line model of Tatham et al. (1977). They consider shale grading into shaley lime then into limestone at about 1100 meters deep. Parameters taken from their compressional and shear wave models are shown in Table 3. The effect of the facies change can be seen directly from the nonlinear drop in the composite (V_S/V_P) ratio as shaliness increases. Similar results to those shown in Figures 1-3 are also found from equation (9) for Berea sandstone data (Porosity - 10.3%) compiled by Winkler (1985) and for Ottawa sandstone data (Porosity - 37.74%) compiled by Domenico (1976) by letting the shale content vary from 0% to 100%.

As another example, let's consider a shallow, transversely-isotropic medium consisting of a sand partially saturated with a contaminating fluid, such as leaking oil, layered with a dry sand. What happens to the (V_S/V_P) ratio as the amount of contaminated sand increases? The parameters selected for the two sands are taken from data reported by McLamore et al. (1978), and are shown in Table 4. The composite (V_S/V_P) ratio decreases rapidly as the amount of contaminated sand increases (Figure 4). The same phenomena occurs as the amount of clay

Paris Basin

Lusitanian Limestone	Kimmeridgian shale
V_p = 4,745 m/sec	V_p = 3,195 m/sec
V_s = 2,610 m/sec	V_s = 1,502 m/sec
V_s/V_p = .550	V_s/V_p = .470
Density = 2.60 g/cc	Density = 2.32 g/cc

Fractional Shale Concentration	(V_s/V_p) composite
0.0	.550
0.1	.529
0.2	.515
0.3	.504
0.4	.496
0.5	.489
0.6	.484
0.7	.480
0.8	.476
0.9	.473
1.0	.470

Table 1 Parameters and calculation of (V_s/V_p) composite for shaly limestones in the Paris Basin. The depth considered is approximately 1,000 meters.

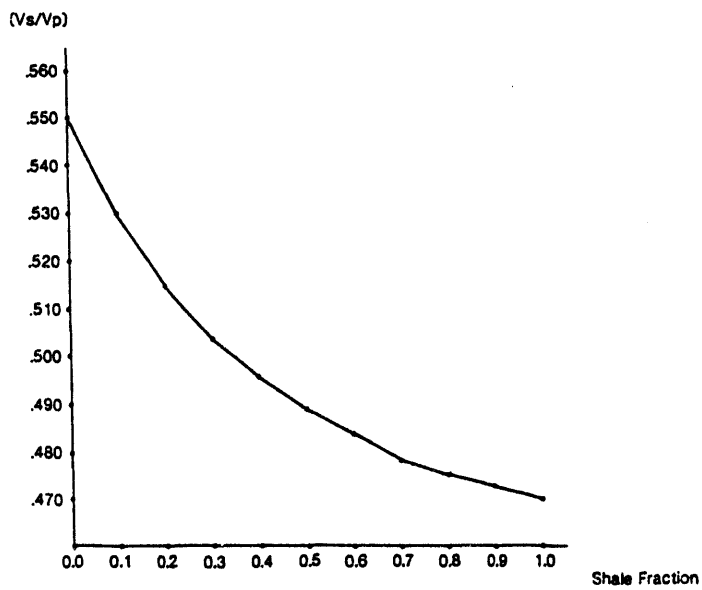


Figure 1 (V_s/V_p) composite as a function of fractional shale concentration for limestones in the Paris Basin.

Gulf Coast

Sandstone (brine-saturated)	Shale (brine-saturated)
V_p = 3,962 m/sec	V_p = 3,703 m/sec
V_s = 2,426 m/sec	V_s = 1,963 m/sec
V_s/V_p = .612	V_s/V_p = .530
Density = 2.35 g/cc	Density = 2.43 g/cc

Fractional Shale concentration	(V_s/V_p) Composite
0.0	.612
0.1	.601
0.2	.591
0.3	.582
0.4	.573
0.5	.565
0.6	.557
0.7	.550
0.8	.543
0.9	.536
1.0	.530

Table 2 Parameters and calculation of (V_s/V_p) composite for shaly sandstones in the Gulf Coast. The depth considered is approximately 5,182 meters.

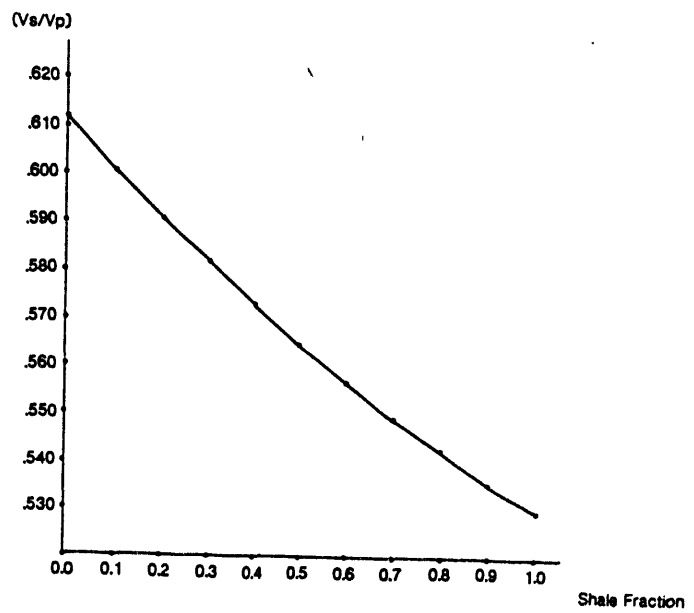


Figure 2 (V_s/V_p) composite as a function of fractional shale concentration for Gulf Coast sands.

Basin - Hinge Line Model

Limestone	Shale
V_p = 3,475 m/sec	V_p = 2,743 m/sec
V_s = 1,917 m/sec	VS = 1,382 m/sec
V_s/V_p = .552	V_s/V_p = .504
Density = 2.37 g/cc	Density = 2.25 g/cc
Fractional Shale Concentration	(V_s/V_p) Composite
0.0	.552
0.1	.543
0.2	.536
0.3	.530
0.4	.525
0.5	.520
0.6	.516
0.7	.513
0.8	.509
0.9	.506
1.0	.504

Table 3 Parameters and Calculation of (V_s/V_p) composite for shaly limestones in a basin-hinge line model. The approximate depth is 1,100 meters.

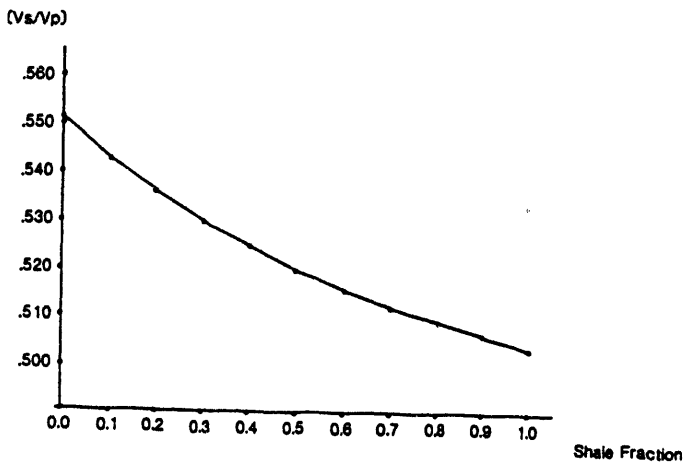


Figure 3 (V_s/V_p) composite as a function of fractional shale concentration for limestones in a basin hinge line model.

Contaminated Sand in a Dry Sand

Dry Sand	Oil-Saturated Sand
V_p = 530 m/sec	V_p = 2,210 m/sec
V_s = 300 m/sec	V_s = 540 m/sec
V_s/V_p = .5660	V_s/V_p = .2443
Density = 1.76 g/cc	Density = 2.03 g/cc
Contaminated Fraction	**(V_s/V_p) composite**
0.0	.566
0.1	.559
0.2	.551
0.3	.542
0.4	.530
0.5	.515
0.6	.496
0.7	.469
0.8	.431
0.9	.369
1.0	.244

Table 4 Parameters and calculation of (V_s/V_p) composite for sandstones contaminated with hydrocarbons at shallow depths.

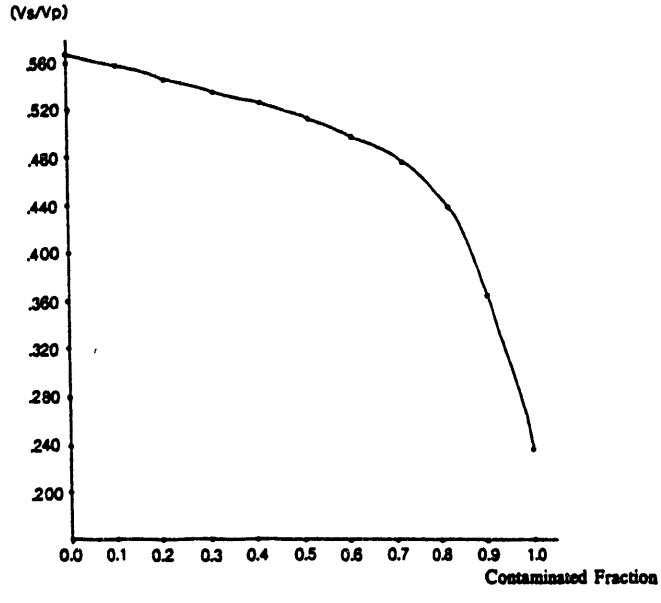


Figure 4 **(V_s/V_p) composite as a function of the amount of oil-saturated sand in a dry sand.**

contaminated with leaking oil is increased in a dry, clean sand (Table 5, Figure 5). However, when the amount of oil-saturated clay is increased in a brine-saturated sand there is a much smaller decrease in the composite (V_S/V_P) ratio (Table 6, Figure 6). The decrease in the composite (V_S/V_P) ratio is almost linear for this case, and it would take very high quality compressional and shear data to detect the contamination from the composite (V_S/V_P) ratio.

Notice that for each of the three cases of hydrocarbon contaminated layers that the composite (V_S/V_P) ratio decreases as a convex-shaped curve, whereas for the previous three cases of shale contaminating a pure sandstone or limestone that the composite (V_S/V_P) ratio decreases as a concave-shaped curve. Thus, for some cases, this shape difference might be used as an indicator of hydrocarbon contaminated layers versus shale contaminated layers. In addition, since the first three examples were for deeper, consolidated sediments and the latter two were for shallow, unconsolidated sediments, this shape difference might be an indicator of depth and type of sediments involved.

The accuracy of equation (9) was tested by using lab data from Kowallis et al. (1984) for sandstone cores obtained from three Gulf wells drilled in the West Delta Block, Plaque-Mines County, Louisiana. The sandstone at 3863.9 meters contains 11% clay, mostly kaolinite, and has a porosity of 21.7%. At a confining pressure of 48.3 MPa, lab measurements on the wet sandstone core yielded V_P = 3,630 m/sec and V_S = 2,080 m/sec, so that the composite (V_S/V_P) = .573. From Tatham et al., the average Gulf Coast sandstone density at this depth is 2.27 g/cc, V_P = 3,551 m/sec, and V_S = 2,109 m/sec, and for shale, V_P = 3,414 m/sec and V_S = 1,809 m/sec. The average density of kaolinite from well logs is 2.42 g/cc (Doveton, 1986). Using this data in equation (9), the composite (V_S/V_P) = .583, a difference of 1.7% with the measured value of .573. Obviously, other factors also need to be considered, such as degree and type of cementation, how the shale is distributed, porosity changes, fluid saturations, pressure gradients, etc., but it is obvious that shale content is a first-order effect in the determination of (V_S/V_P) and that equation (9) appears to model this variable reasonably well.

CONCLUSIONS

The (V_S/V_P) ratio is a very useful parameter to help identify rock matrix type and fluid saturation. A relationship was derived for transversely-isotropic media showing the effect of thin laminations (stringers) of contaminants on the (V_S/V_P) ratio of clean sedimentary rocks. This relationship estimates variations in (V_S/V_P) ratios for shaley sandstones, shaley limestones, limey sandstones, sandy limestones, limey shales, oily sandstones, etc.

Several case studies using published data were examined showing the effect of shale and hydrocarbon content on (V_S/V_P) ratios in sandstones and limestones. Small amounts of shale can change this ratio significantly. The composite (V_S/V_P) ratio is a function of the square root of the clay content, bulk moduli, and shear moduli, and of the (V_S/V_P) ratios of the individual clean lithologies making up the rock. This relationship yields reasonably accurate (V_S/V_P) ratios when compared with lab values for shaley sandstone cores. With good quality field data, combined with the geology of the area and available lab results, the derived expressions in

Contaminated Clay in a Dry Sand

Dry Sand	Oil-Saturated Clay
V_p = 530 m/sec	V_p = 1,700 m/sec
V_s = 300 m/sec	V_s = 390 m/sec
V_s/V_p = .5660	V_s/V_p = .2294
Density = 1.76 g/cc	Density = 1.99 g/cc
Contaminated Fraction	**(V_s/V_p) composite**
0.0	.566
0.1	.553
0.2	.538
0.3	.521
0.4	.501
0.5	.478
0.6	.450
0.7	.416
0.8	.373
0.9	.315
1.0	.229

Table 5 Parameters and calculation of (V_s/V_p) composite for dry sandstones containing clays contaminated with hydrocarbons at shallow depths.

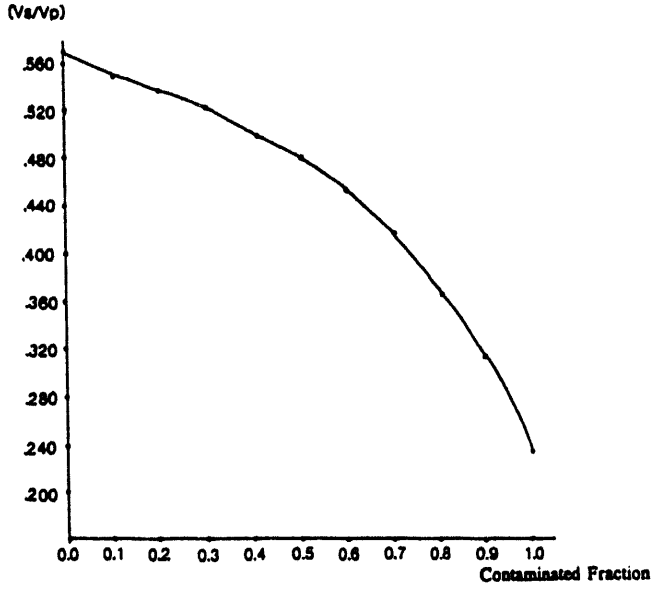


Figure 5 (V_s/V_p) composite as a function of the amount of oil-saturated clay in a dry sand.

Contaminated Clay in a Brine-Saturated Sand

Brine-Saturated Sand	Oil-Saturated Clay
V_p = 2,210 m/sec	V_p = 1,700 m/sec
V_s = 540 m/sec	V_s = 390 m/sec
V_s/V_p = .2443	V_s/V_p = .2294
Density = 2.03 g/cc	Density = 1.99 g/cc

Contaminated Fraction	(V_s/V_p) composite
0.0	.244
0.1	.242
0.2	.240
0.3	.238
0.4	.236
0.5	.235
0.6	.233
0.7	.232
0.8	.231
0.9	.230
1.0	.229

Table 6 Parameters and calculation of (V_s/V_p) composite for brine-saturated sandstones containing clays contaminated with hydrocarbons at shallow depths.

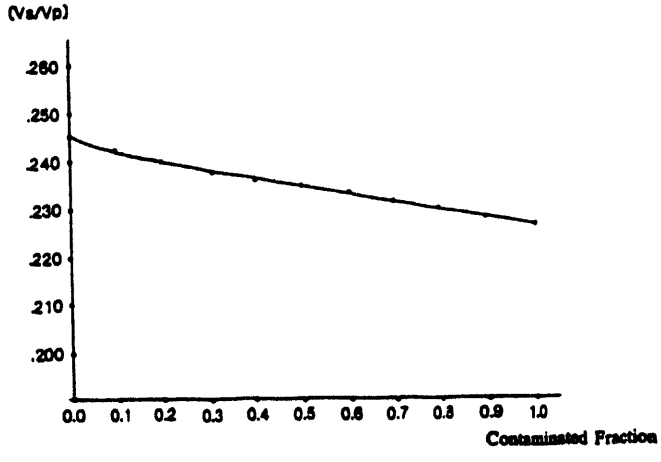


Figure 6 (V_s/V_p) composite as a function of the amount of oil-saturated clay in a brine-saturated sand.

equation (9) or equation (10) can be used to help model the data to point out regions where hydrocarbons, geothermal reservoirs, ground water, soil and groundwater contamination, etc. might best be located.

REFERENCES

Ahmed, H. 1989, Application of mode-converted shear waves to rock-property estimation from vertical seismic profiling data. Geophysics 54, 478-485.

Brown, R.L., Cook, R.N., and Lynn, D. 1989. How useful is Poisson's ratio for finding oil/gas? World Oil 209, 99-106.

Danbom, S. and Domenico, S.N. 1987. Shear Wave Exploration. SEG, Tulsa, OK.

Domenico, S.N. 1976. Effect of Brine-Gas Mixture on Velocity in an Unconsolidated Sand Reservoir. Geophysics 41, 882-894.

Domenico, S.N. 1983. Sandstone and Limestone Porosity Determinations from Shear- and Compressional-Wave Velocity. 53rd SEG meeting, Las Vegas, Nevada.

Domenico, S.N. 1984. Rock lithology and porosity determination from shear and compressional wave velocity. Geophysics 49, 1188-1195.

Doveton, J.H. 1986. Log Analysis of Subsurface Geology. John Wiley & Sons, New York, N.Y.

Eberhart-Phillips, D., Han, D.H., and Zoback, M.D. 1989. Empirical relationships among seismic velocity, effective pressure, porosity, and clay content in sandstone. Geophysics 54, 82-89.

Gardner, G.H.F., Gardner, L.W., and Gregory, A.R. 1974. Formation Velocity and Density--The Diagnostic Basis for Stratigraphic Trust. Geophysics 39, 770-780.

Garotta, R. 1983. Comparisons Between P, SH, SV, and Converted Waves. Compaganie Générale de Géophysique, Technical Series No. 521.82.08, Massy, France.

Gregory, A.R. 1976a. Fluid Saturation Effects on Dynamic Elastic Properties of Sedimentary Rocks. Geophysics, 41, 895-921.

Gregory, A.R. 1976b. Some Aspects of Rock Physics from Laboratory and Log Data that are Important to Seismic Interpretation. Notes distributed at AAPG-SEG School on Stratigraphic Interpretation of Seismic Data, September 20-25, 1976, Houston, Texas.

Helbig, K. and Mesdag, C.S. 1982. The Potential of Shear-Wave Observations. Geophysical Prospecting 30, 413-431.

Kowallis, B.H., Jones, L.E.A., and Wang, H.F. 1984. Velocity-Porosity-Clay Content Systematics of Poorly consolidated Sandstones. Journal of Geophysical Research 89, 10,355-10,364.

Levin, F.K. 1979. Seismic Velocities in Transversely Isotropic Media. Geophysics 44, 918-936.

Ludwig, W.J., Nafe, J.E., Drake, C.L. 1970. Seismic Refraction in The Sea, Vol. 4, Part I, pp. 53-84, A.E. Maxwell (ed). John Wiley and Sons, N.Y.

Mann, R.L. and Fatt, I. 1960. Effect of Pore Fluids on the Elastic Properties of Sandstone.

Geophysics 25, 433-444.

McLamore, V.R., Anderson, D.G., and Espansa, C. 1978. Crosshole Testing Using explosive and Mechanical Energy Sources. Dynamic Geotechnical Testing, ASTM STP 654: ASTM, 30-50.

Melia, P.J. and Carlson, R.L. 1984. An Experimental Test of P-Wave Anisotropy in Stratified Media. Geophysics 49, 374.

Meissner, R. and Hegazy, M.A. 1981. The Ratio of the PP- to the SS- Reflection Coefficient as a Possible Future Method to estimate Oil and Gas Reservoirs. Geophysical Prospecting 29, 533-540.

Neidell, N.S. 1985. Land applications of shear waves. The Leading Edge, November, 1985, 32-44.

Omnes, G. 1980. Logs From P and S Vertical Seismic Profiles. Journal of Petroleum Technology, 1843-1849.

Pickett, G.R. 1963. Acoustic character Logs and Their Applications in Formation Evaluation. Journal Petroleum Technology, 659-667.

Polškov, M.K., Brodov, L. Ju., Mironova, L.V., Michon, D., Garotta, R., Layotte, P.C., and Coppens, F. 1980. Utilisation Combinée Des Ondes Lognitudinales et Transversales en Sismique Reflexion. Geophysical Prospecting 28, 185-207.

Tatham, R.H. and Stoffa, P.L. 1976. V_P/V_S--A Potential Hydrocarbon Indicator. Geophysics, 41, 837-849.

Tatham, R.H., Danbom, S.H., Tyce, R.C., and Omnes, G. 1977. Seismic Parameters and Their Estimation: Progress in Estimation and Determination. Notes distributed at SEG Continuing Education Symposium, November 27-28, 1977, Houston, Texas.

Tatham, R.H. 1982. V_P/V_S and lithology. Geophysics 47, 336-344.

Tatham, R.H. and Goolsbee, D.V. 1983. Separation of Shear-Wave and P-Wave Reflections Offshore Western Florida. 53rd SEG Meeting, Las Vegas, Nevada.

Telford, W.M., Sheriff, R.E., Geldardt, L.P., and Keys, D.A. 1976. Applied Geophysics. Cambridge University Press, London.

Waters, K.H. 1987. Reflection Seismology. John Wiley & Sons, New York, N.Y.

White, J.E. 1965. Seismic Waves: Radiation, Transmission, and Attenuation. McGraw-Hill, New York, N.Y.

Winkler, K.W. 1985. Dispersion Analysis of Velocity and Attentuation in Berea Sandstone. Journal of Geophysical Research 90, 6793-6800.

Hydrogeology, Waste Disposal, Science and Politics
Proceedings 30th Symposium
Engineering Geology and Geotechnical Engineering, 1994

A COMPARISON OF GROUND PENETRATING RADAR METHODS: MULTI-FOLD DATA VS. SINGLE FOLD DATA

Lee M. Liberty and John R. Pelton
Center for Geophysical Investigation of the Shallow Subsurface (CGISS)
Boise State University, Boise, ID 83725

ABSTRACT

Ground penetrating radar (GPR) data has been used since the 1970's in geotechnical and engineering problems to image the soil and bedrock strata of the near surface. GPR data has traditionally been acquired as analog, single-fold, fixed source/receiver offset data. The reasons for this included quick, simple acquisition and processing of the data to arrive at an interpretation in the field for the client, and the limitations of digitally recording high frequency data (>100 MHz). In the 1980's, significant advances were made with personal computers and GPR systems. Real time digitizing became possible, resulting in enhanced processing of the data. Optimization of acquisition parameters, including the source/receiver offset and field stacking, also improved the results. Now, enhanced acquisition and processing steps are becoming more common, using standard techniques developed by the oil industry for seismic reflection data. With detached radar source and receiver antennas now readily available for GPR systems, common mid-point (CMP) experiments are possible.

A comparison of the single fold method vs. the multifold method for acquisition and processing of GPR data is presented. Data are shown from an old lumber mill site on a river flood plain which has undergone excavation and backfilling. Results show an improved image can be attained by compensating for the problems related to complex geology, a complex wavefield and cultural noise. The results also show that in regions with a complex near-surface, multi-fold radar sections are the preferred method over single fold coverage. Steeply dipping horizons are placed in a correct spatial position and reflections are better imaged in the section by reducing coherent noise. Additional time and computing resources are needed for acquisition and processing of the data, but the costs are justified by an improved and more accurate radar section.

INTRODUCTION

Acquisition and processing of GPR data has recently evolved in much the same way as seismic reflection techniques evolved since the 1960's. Technological advancements have allowed digitization at faster sample rates to keep up with the high frequencies used in radar (20-500 MHZ). Also, GPR designs have improved, now allowing for the separation of the source and receiver antennas as a standard feature. The CMP method for data collection was patented in 1956 by Henry Mayne, who recognized the benefits of collecting seismic reflection data at variable offsets. With this technique, a better understanding of the wavefield and a more improved image of the subsurface was possible and, in return, more complex structures were imaged. The technique was adopted by the oil industry in the 1960's and is still standard practice today. The CMP method in radar is just now gaining in popularity, but multi-offset data acquisition has been used in the

past with analog systems. Separating source and receiver antennas have been used to determine velocity models (Annan and Davis, 1976), analyze lateral waves (Clough, 1976), and study dispersion of electromagnetic waves (Arcone, 1984). Only recently has the implementation of seismic reflection processing techniques been used to study digital radar data (Fisher and others, 1992, where common receiver gathers were used).

ACQUISITION OF RADAR DATA

Single Channel Radar (SCR)

The traditional SCR method for data acquisition involves moving the source and receiver antennas along the ground at fixed intervals (Figure 1A). The selection of antenna frequency, sta-

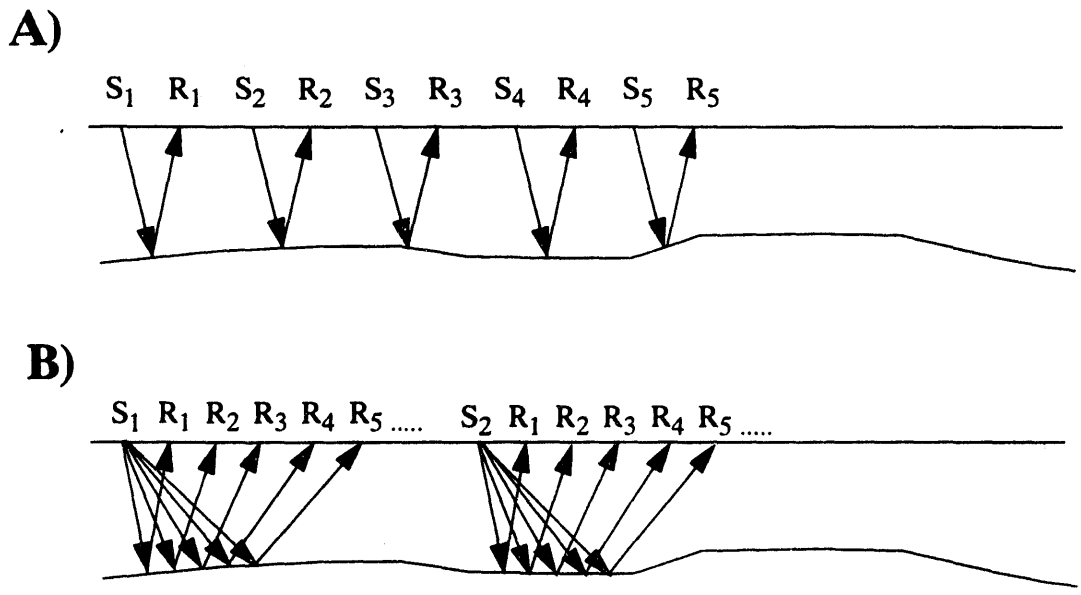


Figure 1. (A) Traditional SCR acquisition style, source and receiver move in fixed intervals along the profile. (B) CSRG acquisition, where one source location is used for many receiver locations. Once all receivers are collected, the source is moved to the next station location.

tion spacing and sample interval are all important to ensure the target is not spatially or temporally aliased. Other parameters that affect the data quality include antenna separation, field stacking and the time window. Commonly, many parameters are fine tuned by performing CMP gather tests to estimate velocity and depth for a given target. Once CMP's have been collected at a few stations, appropriate SCR parameters are chosen and data are collected.

Radar data are typically summed and stacked at the same location within the field computer to increase the signal to noise ratio. Commonly, 64 traces are averaged to attenuate random noise by a factor of 8 ($\sqrt{n}$, where n=64 in this case). The field stacking can be performed in a few seconds for each source/receiver location.

The source/receiver antenna separation is important because reflection amplitudes are inci-

dent angle-dependent and the amplitudes are greatest at the critical angle. The antenna separation at the critical angle can be calculated by estimating a target depth for a given reflection and relative permittivity (or velocity) for the overlying material:

$$AntennaSeparation = \frac{2Depth}{\sqrt{(K-1)}} \quad (1)$$

$$K = \left(\frac{c}{Velocity}\right)^2 \quad (2)$$

(from Annan and Cosway, 1992, where K is the relative permittivity and c=velocity of light in free space = 0.3 m/ns)

The antenna separation in (1) will yield the optimum amplitude for a reflector, although the results will be less than ideal if the target of interest is not flat lying or unknown, or if many targets are of interest.

Multichannel Radar

Acquisition of common source radar gathers (CSRG) is similar to the SCR method, only the source remains fixed while many receiver offsets are collected (Figure 1B and Figure 2). The data are still summed at each source/receiver location, as with SCR data, but the station spacing need not be tuned for a particular target depth or relative permittivity, because a wide range of values are used. This technique is better than selected CMP field gathers (used with SCR data) in that it provides the same source coupling with the ground for each trace within a gather (as opposed to both source and receiver moving) and velocity information for each station is available along the profile.

As already mentioned, amplitudes do vary with offset. Figure 3A shows a large amplitude reflection from 60-90 ns. Many other reflections are also seen in the unprocessed record. At offsets 3 m - 8 m, the relative amplitude of the 60-90 ns reflection is largest, but other reflected arrivals do not peak in amplitude at these offsets (for example, reflectors at 45 ns, 150 ns and 200 ns). This demonstrates the effectiveness of differing the source/receiver offsets for a range of depths and velocities compared to the SCR method which tunes the antenna separation for a single horizon.

The fold, or redundancy at different offsets, at a particular station can vary, but should be at least 6-12 fold for significant noise reduction through CMP stacking (see below). This design would require 24 to 48 receiver locations for each source location, moving the source every other station. The station interval at our test site (an old lumber mill site) was 0.2 m, and the source antenna moved up every 0.4 m. With a 48-receiver CSRG experiment, we covered roughly 100 m/day (on backhoe scraped ground) with a crew of 2 people. SCR acquisition at the same site averaged 700-800 m/day at a 0.2 m station interval and 2 m antenna spacing with a crew of 3-4 people. This provided 12 fold data (compared to 1 fold SCR data) and half the station spacing for the midpoints (0.1 m instead of 0.2 m) or 24 times the total SCR data. Thus, surveys undertaken with the CSRG technique may take several times longer to acquire, but a more complete subsurface coverage will result.

Noise Attenuation and Muting

CSRG data have the advantage of separating out many different arrivals on a radargram, giving information not attainable from SCR acquisition (Figure 2). There are three kinds of signal

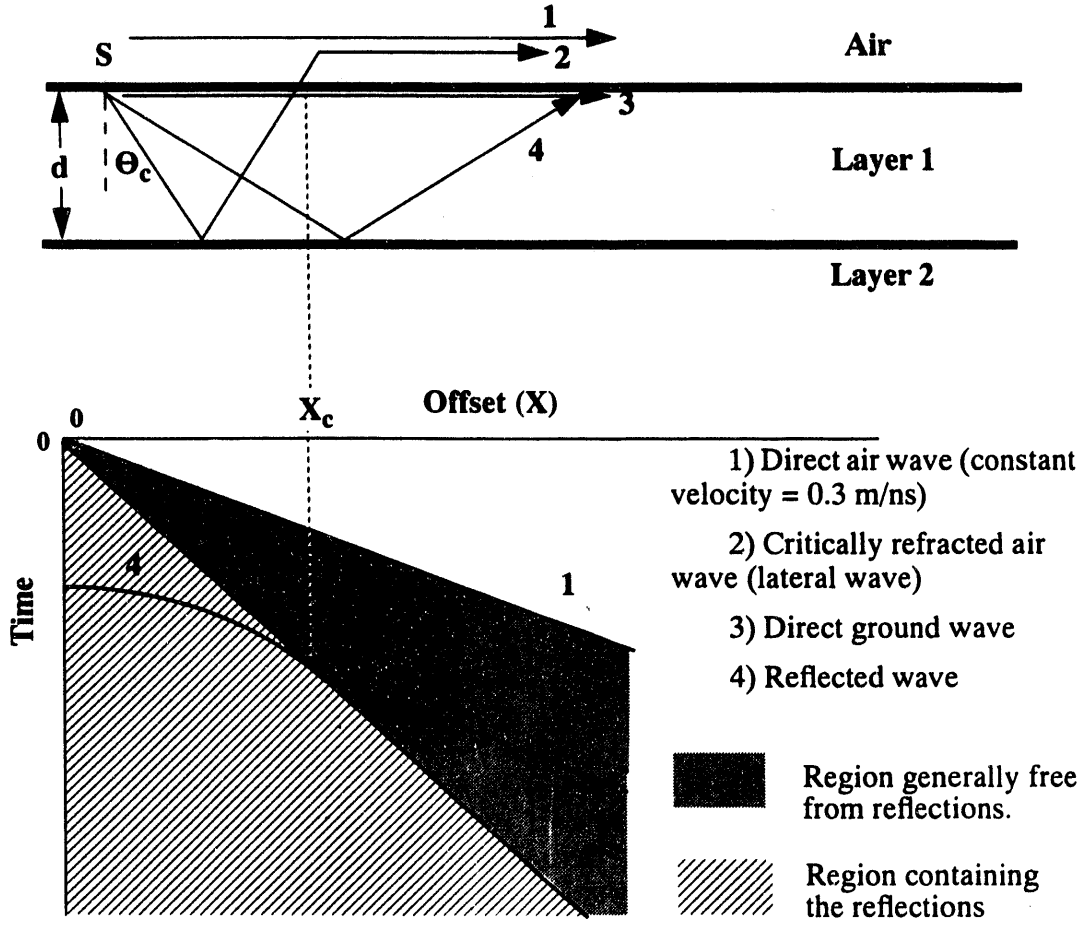


Figure 2. Raypaths and arrival times for a flat, two-layer model (modified from Annan and Cosway, 1992). Four arrivals are shown. The first arrival in a radar section will always be the air wave (event 1). The arrival time will equal distance/c, where c=0.3 m/ns. Arrival 2 is a critically refracted air wave or lateral wave, observed past the critical distance for a reflection. This arrival also travels at 0.3 m/s and is caused by the inverse velocity relationship between the air/ground interface. The direct ground wave (event 3) travels through the near-surface directly from source to receiver and event 4 represents a reflection. The reflection has hyperbolic moveout and asymptotically approaching the direct wave arrival. Since velocities tend to decrease with increasing depth, reflections usually do not cross the ground wave arrival.

that can be recorded with a digital system: random noise, coherent noise and desired signal (or reflections, in this case).

Random noise is energy which does not exhibit correlation between distinct receiver chan-

nels (Sheriff, 1984). Random noise can be attenuated by averaging traces in the field at the same source/receiver location, as is done for both single channel and multichannel methods. Multichannel processing allows additional attenuation of the random noise by adding more traces to average and allowing different averaging techniques (weights) during processing to remove specific noise (for example, removing noise bursts by averaging traces without the maximum and minimum amplitudes for a given time). Random noise can appear at any frequency and a bandpass filter may aid in attenuating the noise and boosting the signal. If random noise still persists in a trace after filtering and/or averaging techniques have been tested, traces can be completely removed from the processing flow. With 12-fold data, the removal of a few bad traces may greatly increase the quality of a final stack.

Coherent noise appears as laterally continuous arrivals that are not reflections across the multichannel records. These arrivals can be generated from the radar source or from other cultural sources and are hard to distinguish from reflections on SCR records. Standard processing techniques allow attenuation or complete removal of the coherent noise on multi-offset radargrams. There is no way to conclusively separate reflections from coherent noise with SCR data because apparent velocity information is not available. Undesired coherent noise includes the direct air wave, ground waves, lateral waves, multiples and out of plane energy (Figures 2 and 3A). These events are of no interest when plotting a final stack of the data, but contain information regarding the site and subsequent processing steps.

The air wave is beneficial in radar data because the velocity is a known physical constant. CSRG data can be aligned to the air wave because the arrival will always be first on the radargrams with a constant linear velocity of 0.3 m/ns (Figures 2 and 3). This provides the initial system statics, allowing the data to be lined up in the case of system errors (possibly related to fiber optic cable problems). The system static shift can also be performed on SCR data with a known source/receiver offset.

The direct ground wave travels through the near surface directly from the source antenna to the receiver antenna (Figure 2). This arrival can appear very strong on the section or can be masked by different arrivals (compare Figure 3A with Figure 3B). With SCR data, the ground wave may be misinterpreted as a reflector in the radargram, depending on the complexity of the near surface. If the near-surface conditions change drastically across the line, the ground wave may also appear to have topography across the radargram with SCR data. The apparent topography is caused by changes in the near-surface velocity (or permittivity). With CSRG data, the ground wave arrival is usually easily distinguished, even if masked by other arrivals. With simple filtering techniques, the ground wave can be enhanced, allowing direct measurement of the near-surface velocity (Figure 3B). The ground wave is beneficial if near-surface statics are to be applied to the data. Although it is possible to perform a few CMP tests along a single channel line to acquire the ground wave velocity, this arrival may still interfere with reflected arrivals in the section and near-surface velocities may also change between CMP locations.

Generally, the zone of reflections appears below the ground wave (Figure 2). The area above the ground wave is free from reflections, provided velocities decrease with depth, as is common for electromagnetic waves (because the dielectric permittivity generally increases with depth in soil and in bedrock). Above the ground wave on a CSRG lies critically refracted arrivals often travelling through air after a critical distance (Figure 2), due to the inverse velocity relationship between the air and the ground. Processing to remove the refracted arrivals and direct arrivals includes muting the region between the air wave and the ground wave. In a SCR section, if the source/receiver antenna separation is tuned to image deeper arrivals (wide aperture), arrivals

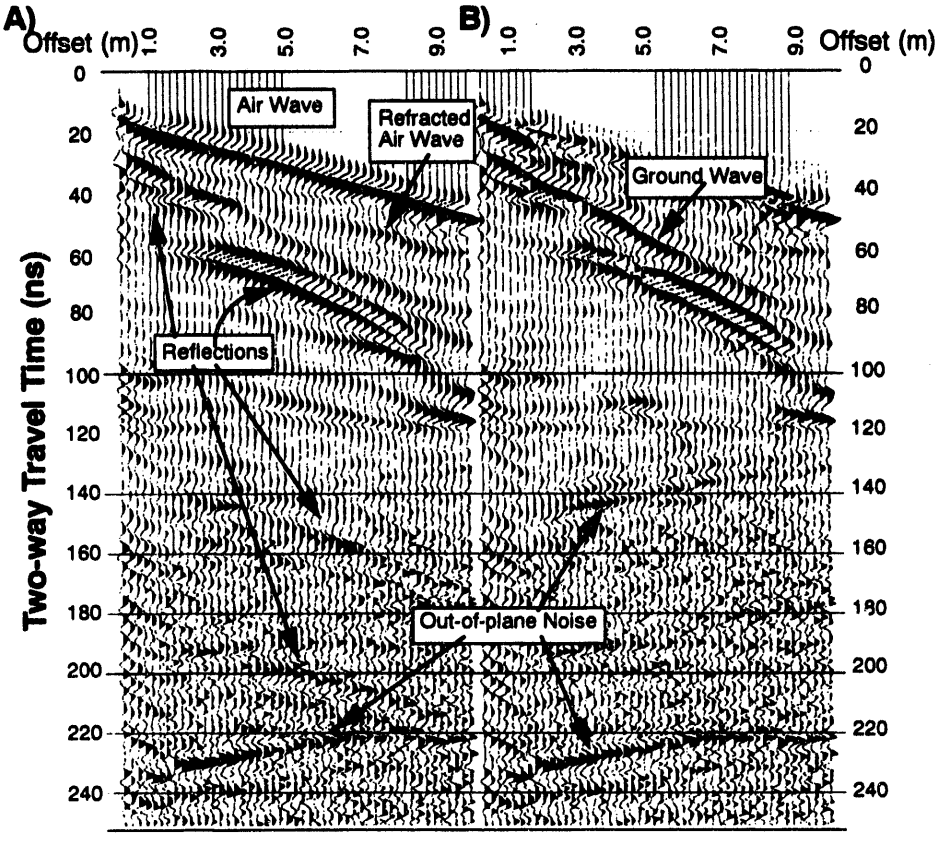


Figure 3. A) CSRG from the lumber mill test site. The gather has system and datum statics applied and an automatic gain control (AGC) window of 80 ns. Note the change in amplitudes for the different reflections with respect to offset. B) The same gather with a filter to remove coherent energy at the air wave velocity. The filter has the effect of highlighting the ground wave arrival (0.15 m/ns) and other coherent energy. The noise in the lower section is energy from out-of-plane arrivals. The energy is out-of-plane because of the anomalous apparent velocities of the arrivals (<-0.4 m/s or greater than the (negative) air wave velocity).

above the tuned depth will appear at anomalously fast times, and all amplitude information will be lost because the refracted air wave energy appears instead of the reflection.

Other undesired coherent arrivals that appear in a radargram include out-of-plane noise and multiples. Figure 3A shows a strong arrival at 220-230 ns that has a negative apparent velocity. This arrival is anomalous and its source is from out of the plane. On a single channel radar gather, the arrival could be not easily be distinguished from a reflection. Coherent noise that is in the plane of the radar line can usually be identified as noise if travelling through air (will appear at the air wave velocity on SCR data), but out-of-plane noise can have any apparent velocity, making it harder to conclude coherent noise is present. With multi-offset data, out-of-plane noise be noticed and attenuated through processing.

Multiples are another common source of coherent noise, especially where large impedance contrasts are found. The only way to determine if multiples are a problem in radar data is to record the velocity information and measure travel paths. Multiples will appear at an anomalous velocity due to their repeated reflected raypaths. These arrivals may be hard to separate from primary arrivals, but their presence can be noted in the stacked section.

Statics

System statics have already been mentioned as a necessary tool to ensure that data are collected and processed properly. Datum (or elevation) statics can also benefit from the CSRG method of data acquisition. Datum statics involve shifting the data to a common datum (or elevation) to account for topography of the surface and near-surface lateral velocity changes. Since elevation statics are velocity dependent (3), this information is only possible by calculating the velocity of the direct arrival and applying this velocity to the static calculations. If the velocity is

$$TotalStatic = SourceStatic + ReceiverStatic = \frac{(Es - Ed)}{Vs} + \frac{(Er - Ed)}{Vr} \qquad (3)$$

where:

Es=elevation of the source

Er=elevation of the receiver

Ed=datum elevation

Vs=near-surface velocity at the source

Vr=near-surface velocity at the receiver antenna.

nearly constant across the section, a constant velocity can be assumed for both Vs and Vr. Also, if the topography is flat, no static correction may be necessary.

Velocity Measurements and Corrections

If the subsurface changes across the section, velocities should be measured every 10-20 stations. This is necessary to place the reflectors at their proper two-way travel time and for depth calculations. A useful and easy way to perform velocity analyses is to stack CSRG data at different constant velocities and display them side by side (figure 4). When the reflection appears flat, the best root mean square (RMS) velocity is attained for a given time and this is the proper normal moveout (NMO) velocity for the arrival. By analyzing gathers with this method, it is easy to notice out-of-plane events and multiples. These events often attain the greatest RMS stacking velocity at anomalously high or low velocities.

Anomalous velocity measurements may also occur if there are steeply dipping reflections in the section. Dip moveout (DMO) is essential in the case of steeply dipping events (see Hale, 1984). DMO is a change in the arrival time for a reflection because of the dip of the reflector (Sheriff, 1984). The DMO correction migrates the dipping reflector to a zero offset reflector for a given velocity. DMO makes the stacking velocities become independent of dip, enabling events with conflicting dips to be properly imaged. The velocity model used with DMO should be estimated by a generalized velocity model from the original velocity tests. The data can then be reanalyzed to attain a higher degree of accuracy in picking proper velocities.

Sorting and Stacking

CMP sorting is the process of moving traces with the same midpoint locations into one gather, and is performed before velocity analyses. Once the velocity analyses and corrections are complete, the traces for each mid-point can be averaged at each station and stacked. Stacking traces with different offsets will attenuate coherent events not associated with reflections, reduce random noise, and highlight the reflections pinpointed in the velocity analyses. Figure 5 shows a comparison between SRG and CSRG stacks for the same profile. Note the strong reflection in fig-

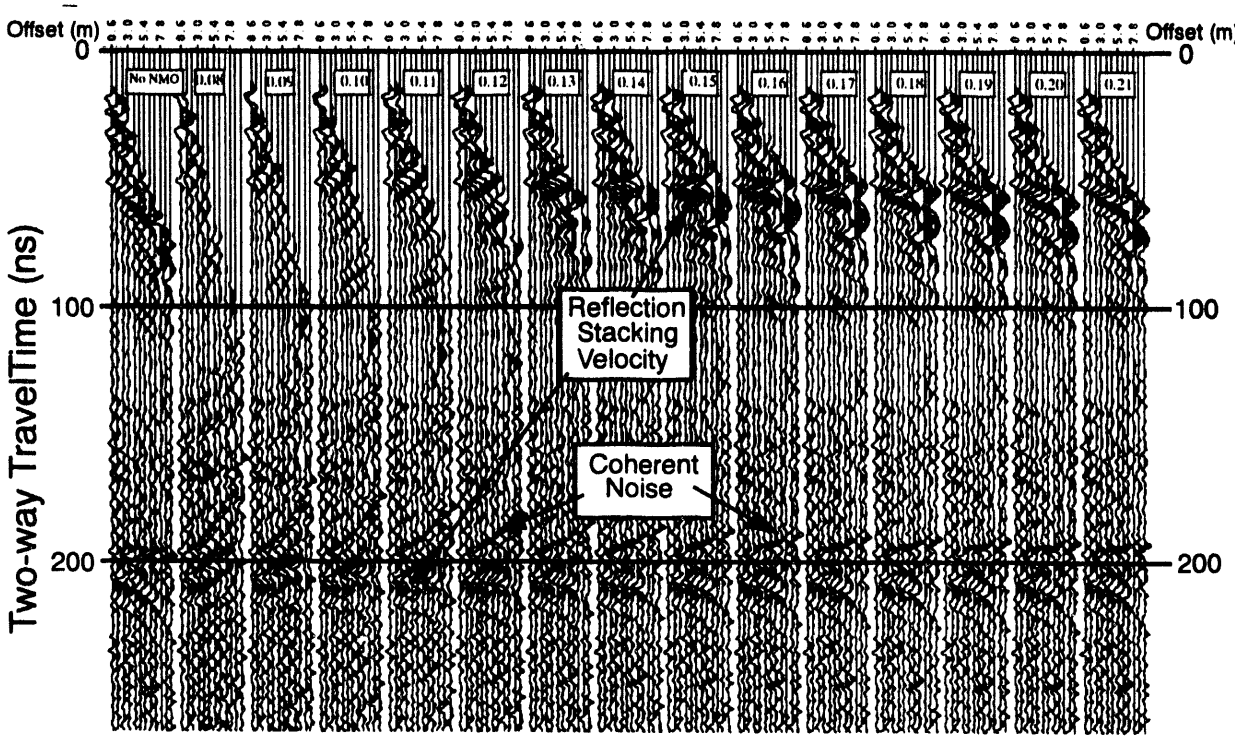


Figure 4. Constant velocity stacks for a CMP gather from the lumber mill site. The RMS velocity can be found by finding the flat arrivals (shown at the tops of the gathers in m/ns). If the velocity is too slow, the arrival will be overcorrected (sloping up), when the velocity is too fast, the arrival is undercorrected (sloping down). Note the general decrease in velocity with depth and the anomalous stacking velocity for the coherent noise.

ure 5B at 50 ns does not clearly appear in the SCR stack (Figure 5A). This is because the antenna separation is not tuned for this depth. With a 2 m antenna separation for the SCR data and an estimated near-surface velocity of 0.15 m/ns, the tuned depth is 1.7 m (from equation 1) and this reflector depth is estimated at 3.75 m (assuming a constant velocity of 0.15 m/s). Even reflected arrivals above 50 ns in the CSRG stack appear more coherent than the SCR stack because there is less interference from coherent noise in the section. Also note the presence of diffractions below 100 ns on the SCRG stack. These arrivals are much less coherent on the SCR stack (Figure 5A) where background noise begins to dominate the radargram below 140 ns.

CONCLUSIONS

The CSRG technique involves collecting GPR data at different source/receiver offsets to separate the different components of the wavefield, to look at the velocity structure at each location, to increase the signal to noise ratio, to account for steeply dipping structures, and to remove anomalous arrivals from the radargrams. The increase in data collected and processed compared to single channel acquisition allows a significant increase in resolution and confidence in interpretation of the profile in complex regions, but at a cost of additional time. Although fewer field hands are needed (commonly 1-2 people for CMP collection, instead of 3-4 people for fixed offset collection), one should expect 2-3 times longer in the field for the same surface coverage. This increased coverage and repetition may only be needed if the subsurface is complex or if the objec-

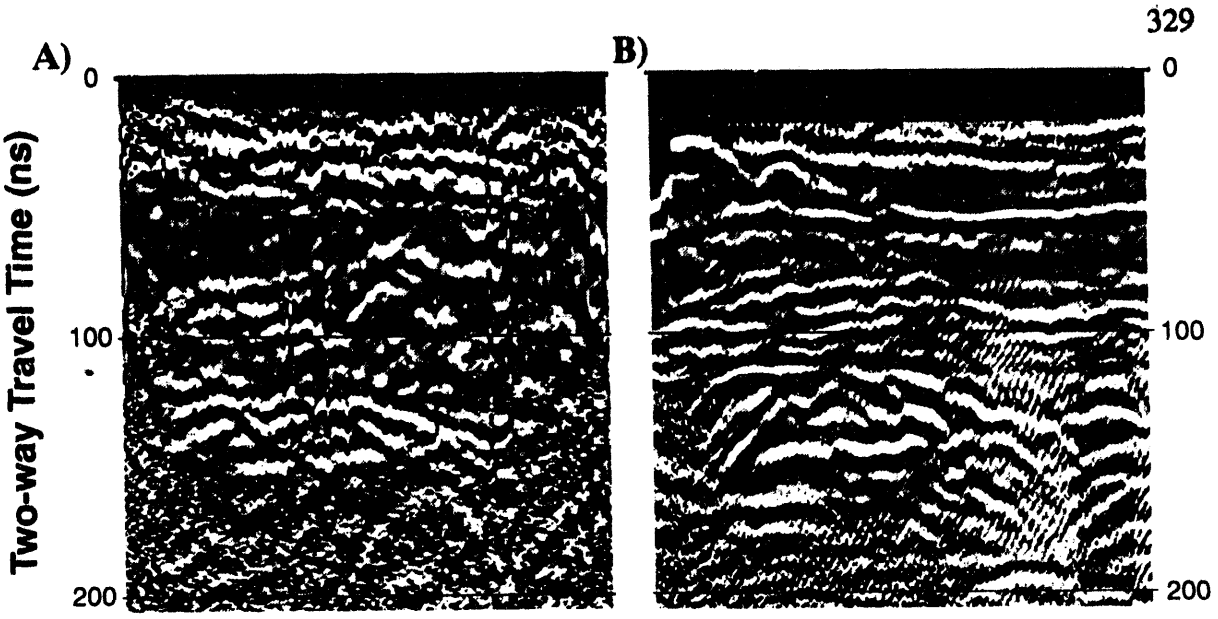


Figure 5. (A) SCR stack from the lumber mill test site. Processing included system and datum statics (assuming a near-surface velocity of 0.13 m/ns) and subtraction of a mean trace across the section to remove laterally coherent arrivals, like the air wave (applied before datum statics). Also, an 80 ns AGC window was used. (B) CSRG stack for the same profile as.A. Note the strong, laterally continuous reflections in the upper 50 ns compared to A and the increase in coherent energy down to 200 ns. The lower section contains diffractions, possibly from large cobbles in the river channel sequence. Processing is summarized in the text with an 80 ns AGC applied after stacking.

tive includes more than one reflector. If a single horizon with little topography is known to be the target, SCR acquisition may suffice.

Interpreting a single fold GPR line as a cross section of the earth must be done with caution. Often, ground waves, multiples and out-of-plane events appear in the section. These noise trains can cause a misinterpretation of the data. In regions of a complex near surface (e.g. disturbed zones and river channels), steeply dipping arrivals and diffractions may appear. A complex region may also contain dramatic lateral and vertical velocity changes. All of these problems can be addressed by collecting multi-fold CSRG data. Processing steps, including muting, trace editing, velocity analyses, dip filtering, dip-moveout, sorting and stacking are all available to increase theclarity of the radar section.

Acknowledgments

The authors are grateful to Mark Petteys for help with the CSRG field work and Envirosearch International for permission to collect and publish the data. CGISS contribution 25.

References

Annan, A.P. and Cosway, S.W., 1992, Ground penetrating radar survey design: SAGEEP Annual Meeting, **2**, 329-351.

Annan, A.P. and Davis J.L., 1976, Impulse radar sounding in permafrost, Radio Science, **11**, 383-394.

Arcone, S.A., 1984, Field observations of electromagnetic pulse propagation in dielectric slabs: Geophysics, **49**, 1763-1773.

Clough, J.W., Electromagnetic lateral waves observed by earth-sounding radars: Geophysics, **41**, 1126-1132.

Fisher, E., McMechan, G.A., and Annan, P., 1992, Acquisition and processing of wide-aperture ground penetrating radar data: Geophysics, **57**, 495-504.

Hale, D., 1984, Dip-moveout by fourier transform: Geophysics, **49**, 741-757.

Mayne, W.H., 1962, Common reflection point horizontal data stacking techniques: Geophysics, **27**, 927-938.

Sheriff, R.E., 1984, Encyclopedic dictionary of exploration geophysicists, 2nd ed., Society of Exploration Geophysicists, Tulsa, Ok., 323 p.

Hydrogeology, Waste Disposal, Science and Politics
Proceedings 30th Symposium
Engineering Geology and Geotechnical Engineering, 1994

A New Geophysical Method to Measure Soil Profiles for Dynamic Analysis of Soil Embankments

Paul Michaels
Center for Geophysical Investigation of the Shallow Subsurface
Boise State University
Boise, Idaho 83725

ABSTRACT

Following the February 9th, 1971 San Fernando earthquake (and near collapse of the San Fernando Dams), there has been an increased awareness for the need to evaluate dam safety in the engineering community. Part of that evaluation is the dynamic analysis of the soil embankment structure. This analysis requires a soil profile.

A problem with alluvium embankments has been the measurement of soil profiles. Traditional blow count methods often produce scattered results due to the very localized nature of the measurement. This paper describes an alternative geophysical approach to measuring the soil profile.

The method is to acquire shear-wave borehole data following blow count measurements. Measurements of the shear wave amplitudes and velocity dispersion are jointly inverted to produce a soil profile of the elastic and inelastic properties needed for dynamic analysis by computer programs such as SHAKE or DESRA-2. Since the measured profiles correspond exactly to the parameters needed by the computer programs, improved dynamic evaluations can be made without employing conversion charts or empirical formulae. The resulting profiles will be valid over a broad range of frequencies, since the correct differential equation is used in place of simpler constant Q models. Furthermore, since geophysical measurements probe a larger volume of soil, less scatter can be expected in the measured soil profiles.

INTRODUCTION

The evaluation of embankment dam safety includes an assessment of the dam's dynamic behavior when exposed to an earthquake hazard. Such a dynamic analysis can be performed using currently available software. However, the quality of the computer analysis depends significantly on the quality of the soil profile.

What is needed is a profile of the elastic and inelastic properties of the soil. Geophysical measurement of these properties by seismic methods is highly desirable when the final objective is to evaluate the seismic response of the embankment. However, it has become apparent that seismic measurements made in the limited frequency band of engineering seismology may not accurately predict the seismic behavior in the broader frequency band of naturally occurring earthquakes.

This issue was recently raised by Jongmans and Campillo (1993). In their work, they demonstrated that measurements of the inelastic properties of soils at high frequencies were in conflict with a low frequency measurements extracted from surface waves.

Specifically, they examined the apparent frequency variation in quality factor, Q.

In my view, the apparent contradiction is caused by assumptions made in the analysis of the seismic observations. Specifically, the spectral ratio method should not be interpreted in terms of the constant Q model. Rather, the spectral ratio should be interpreted in terms of a model consistent with the differential equation used by the dynamic analysis software.

A computer program such as DESRA-2 (Lee and Finn, 1982) presupposes that Q is not constant with respect to frequency. This observation follows from the matrix form of the differential equation that is used in DESRA-2. Since the stiffness and dampening matrices are invariant with respect to frequency, it is Q that will have to vary predictably with frequency.

This paper presents an alternative to the traditional constant Q analysis. I will show how it is possible to interpret engineering seismograms in a manner consistent with the eventual use of the soil profile. Two key advantages of this approach are:

1). The solution is for soil parameters that are exactly those parameters needed by the dynamic analysis software. Thus, no empirical or other corrections need be made.

2). The solution is appropriate for a broad range of frequencies since it honors the differential equation currently accepted by engineering practice.

METHOD

Geophysical Data Acquisition

There are a number of ways to acquire geophysical measurements suitable for determination of soil profiles. Because the intended application is primarily for evaluation of soil embankments, I will present the method in the context of borehole measurements.

Figure 1 shows a classic borehole experiment as described by Kudo and Shima (1970). A shallow reference geophone is planted in hole A where it remains fixed. A sounding geophone is clamped at different levels in the deeper borehole, B. The seismic source consists of a wooden plate struck on edge to produce vertically propagating SH-waves which are then recorded by both geophones. The shallow reference geophone is critical, since it provides a way to monitor any variations in the seismic source that may occur during the course of the experiment.

The elastic and inelastic properties of the soil are determined by comparing seismogram waveforms recorded at the different depths in borehole B. The details of how waveform variations are converted to a soil profile follows next.

The Inelastic Model

The key to the method is to use the same differential equation in both the analysis of the geophysical data and the dynamic analysis of the embankment. Figure 2 shows how the soil dynamics are modeled in a program such as SHAKE or DESRA-2. The soil is modeled as a Voigt solid (spring and dashpot in parallel). In the limit of continuous

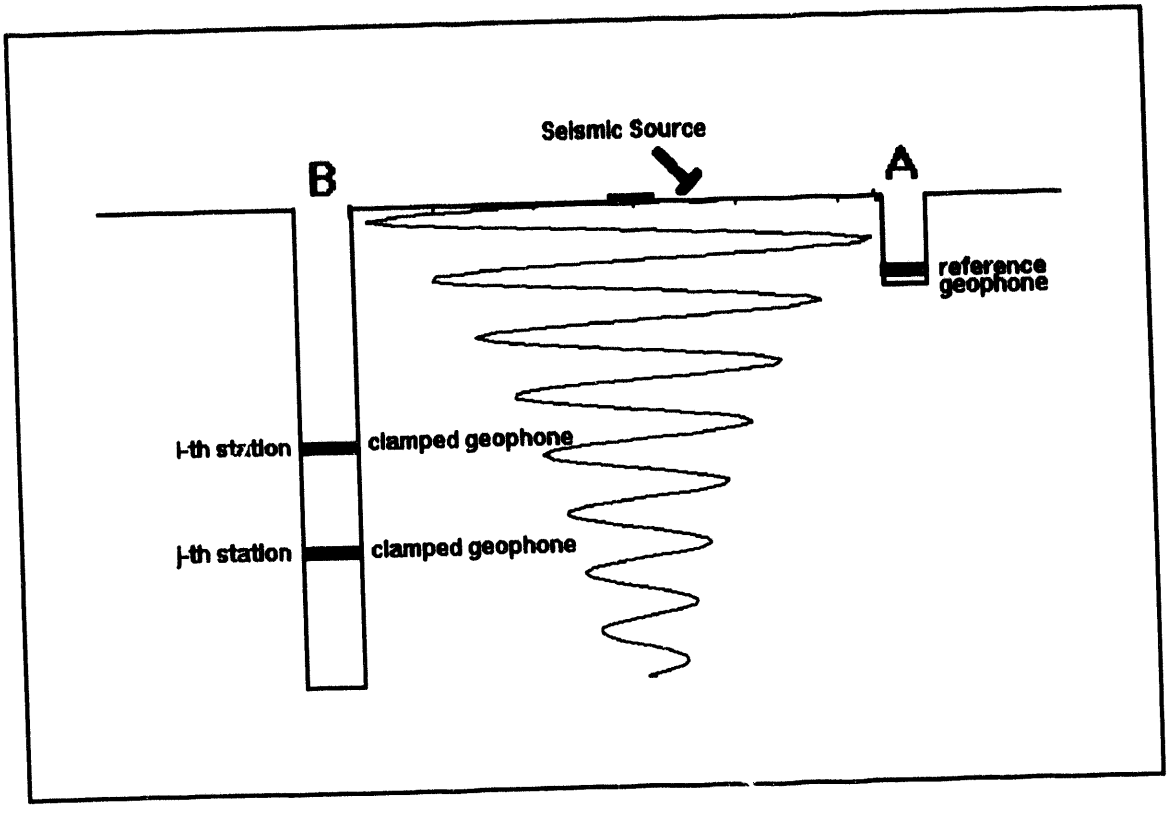


Figure 1: Geophysical experiment to measure a soil profile. A reference geophone is kept fixed in shallow hole A. The clamping geophone is lowered to different depths in the deeper hole, B. Each time the seismic source is energized, a seismogram is recorded at both hole A and B. Changes in the seismic waveform can be used to determine the soil profile at the different depths probed by hole B.

theory, this corresponds to the following differential equation:

$$\frac{\partial^2 u}{\partial t^2} = C_1 \frac{\partial^2 u}{\partial x^2} + C_2 \frac{\partial^3 u}{\partial x^2 \partial t} \qquad (1)$$

This equation describes soil particle motion, u, within any homogeneous region of the embankment as a function of time, t, and space, x. The two constants are:

$$C1 = Elastic\ Constant\ \ (the\ spring)$$
$$C2 = Inelastic\ Dampening\ Constant\ \ (the\ dashpot) \qquad (2)$$

The above constants are properties of the soil and constitute the soil profile when plotted as a function of depth. They are also the constants that correspond to the stiffness and dampening matrices of software like DESRA-2.

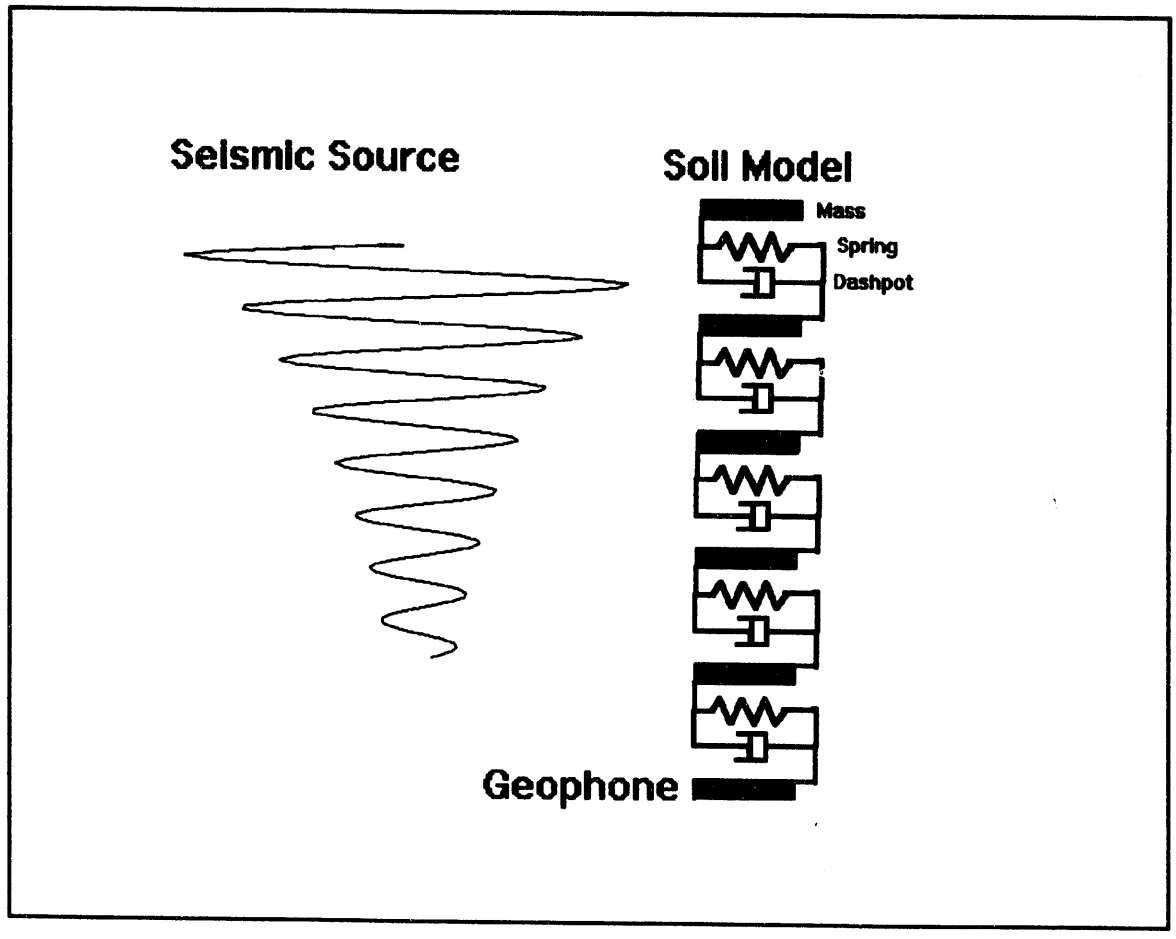


Figure 2: The model used to describe the elastic behavior of soil. The wave propagates by transferring energy from one mass to the next via the spring/dashpot connection. In the continuous limit, the dynamics of this model (a Voigt solid) are described by the differential equation (1) in the text. This is the same kind of model used by SHAKE and DESRA-2.

The elastic constant, C1 is actually equivalent to the square of the S-wave velocity for an elastic case,

$$C_1 = \frac{G}{\rho} = \frac{shear\ modulus}{density} \qquad (3)$$

The dampening term, C2, corresponds to the frictional resistance of the dashpot and can significantly alter the resonant characteristics of a soil embankment. A single value of C2 is sufficient to describe both the frequency variation in S-wave velocity and the amplitude attenuation.

For example, if a solution of the form

$$u(x,t) = \exp(-\alpha x) \cdot \cos\left(\omega\left(\frac{x}{v} - t\right)\right) \qquad (4)$$

is substituted into equation (1), then we may solve for C1 and C2 in terms of amplitude decay, α, and phase velocity, v. The result is

$$C_1 = \frac{\left[\left(\frac{\omega}{v}\right)^2 - \alpha^2\right] \cdot \omega^2}{\left[\alpha^2 + \left(\frac{\omega}{v}\right)^2\right]}, \qquad C_2 = \frac{\left[\frac{2\alpha\omega^2}{v}\right]}{\left[\alpha^2 + \left(\frac{\omega}{v}\right)^2\right]} \qquad (5)$$

Note that α and v are both functions of angular frequency, ω. However, they vary in such a way that both C1 and C2 are constant over all frequencies. By specifying constant values for C1 and C2, the frequency dependent behavior of the soil in a given region is completely described by equation (5).

The connection to loss factor, Q, is as follows:

$$Q = \frac{\omega}{2 \cdot \alpha \cdot v} \qquad (6)$$

Thus, Q also is a function of frequency because of its dependence on decay and phase velocity.

A typical situation can be visualized by examining Figure 3. Here, equations (5) have been inverted to show the frequency behavior for α, v, and Q for a region whose soil constants are C1=12000 m^2/sec^2 and C2=10 m^2/sec. The increase in phase velocity with frequency is due to the increased frictional resistance to motion of the soil at higher frequencies. This increase in friction causes the soil to appear stiffer, resulting in faster wave propagation.

The increase in decay constant, α, with increasing frequency shown in Figure 3 is a consequence of the decrease in wavelength at high frequencies. Since the energy lost per wavelength is constant, propagation losses accumulate faster with shorter wavelengths. This causes a loss of higher frequencies as the wave propagates.

The spectral effects predicted by equation (1) and illustrated in Figure 3 are measurable in the borehole experiment. These effects cause a propagating wave to change amplitude and shape (see Figure 4). That change in shape can be easily quantified in the frequency domain (see Figure 5). The next section shows how the changing amplitude and shape of the seismic wave can be used to compute the soil profile.

Computing the Soil Profile

The method begins with the traditional spectral ratio method. The recorded signal at the ith station in the borehole, B, can be expressed as a product of transfer functions in the frequency domain:

$$B_i(\omega) = S_i(\omega) \cdot H_{bi}(\omega) \cdot C_b(\omega) \cdot G_{bi}(\omega) \qquad (7)$$

where ω is angular frequency and the other terms are as follows:

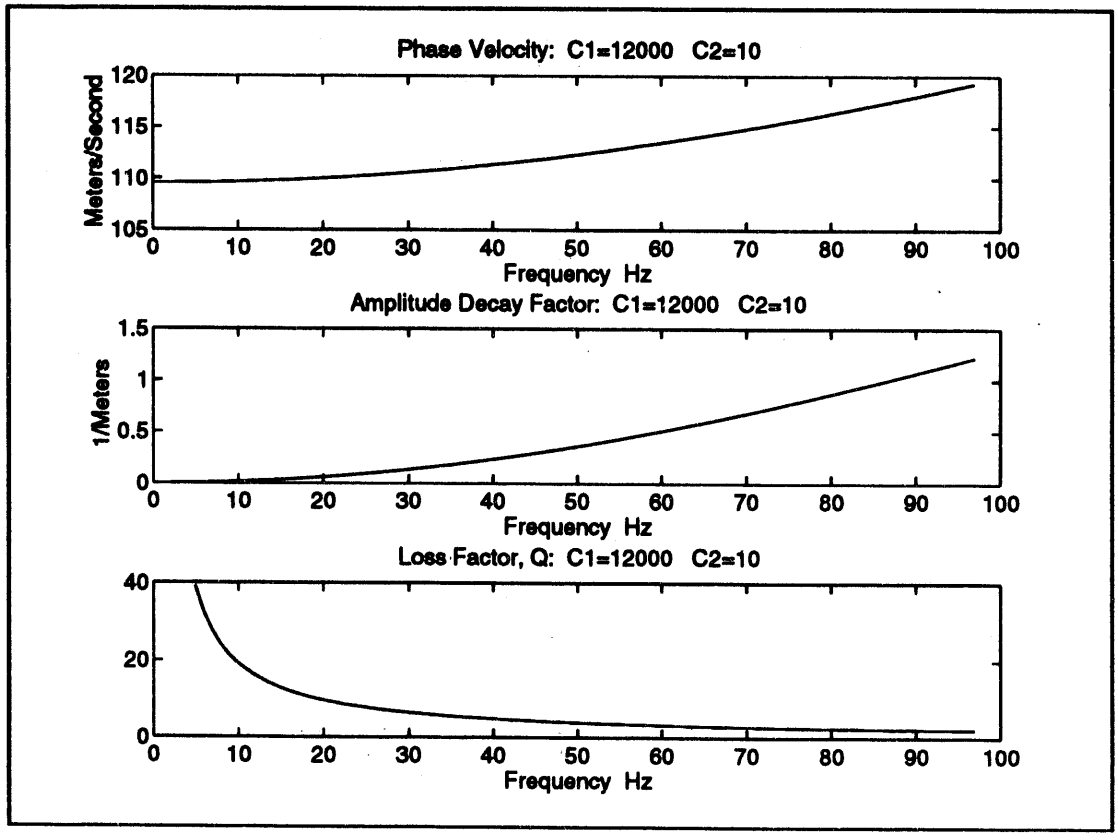


Figure 3: The variation in phase velocity, amplitude decay, and loss factor Q as a function of frequency. These plots are for a soil with C1=12000 m^2/sec^2 and C1=10 m^2/sec. These curves were obtained by inverting equations (5) in the text. They predict the changes in a propagating seismic wave over a wide range of frequencies. By measuring the phase velocity and amplitude decay from recorded seismograms, we may determine the soil profile, C1 and C2 between geophone stations in the borehole.

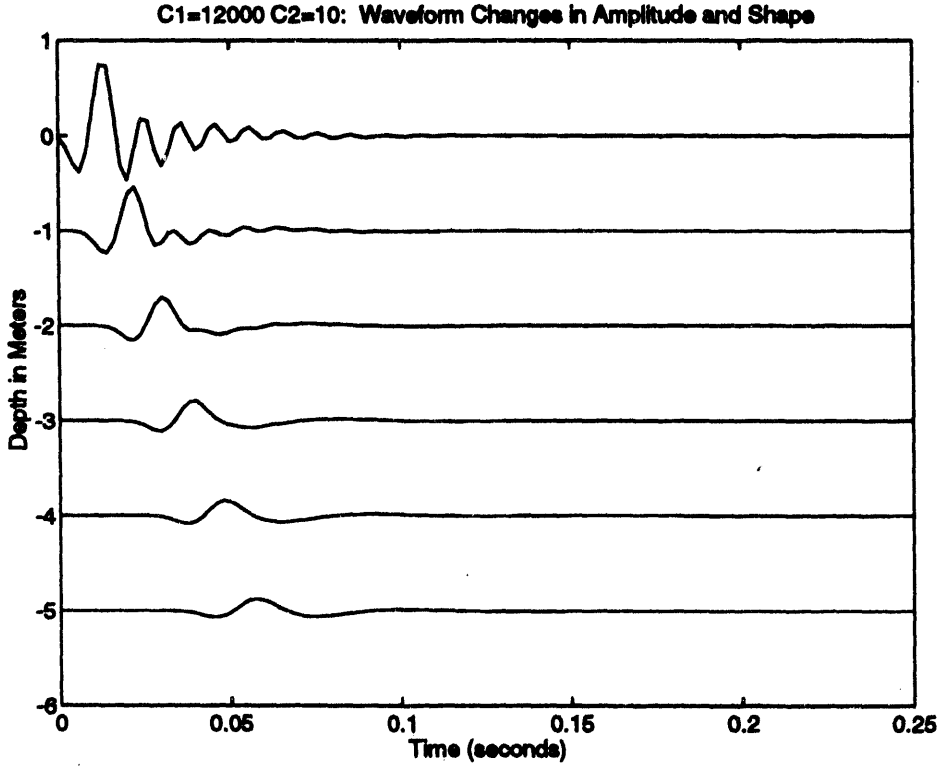


Figure 4: Synthetic data showing the change in waveform and amplitude predicted by the inelastic wave equation (1). In this example, the signals correspond to receivers spaced at 1 meter intervals. The amplitude decay and waveform changes can be inverted to obtain the wave equation coefficients. When plotted as a function of depth, these coefficients are the soil profile parameters needed to construct the stiffness and dampening matrices in DESRA-2 or SHAKE.

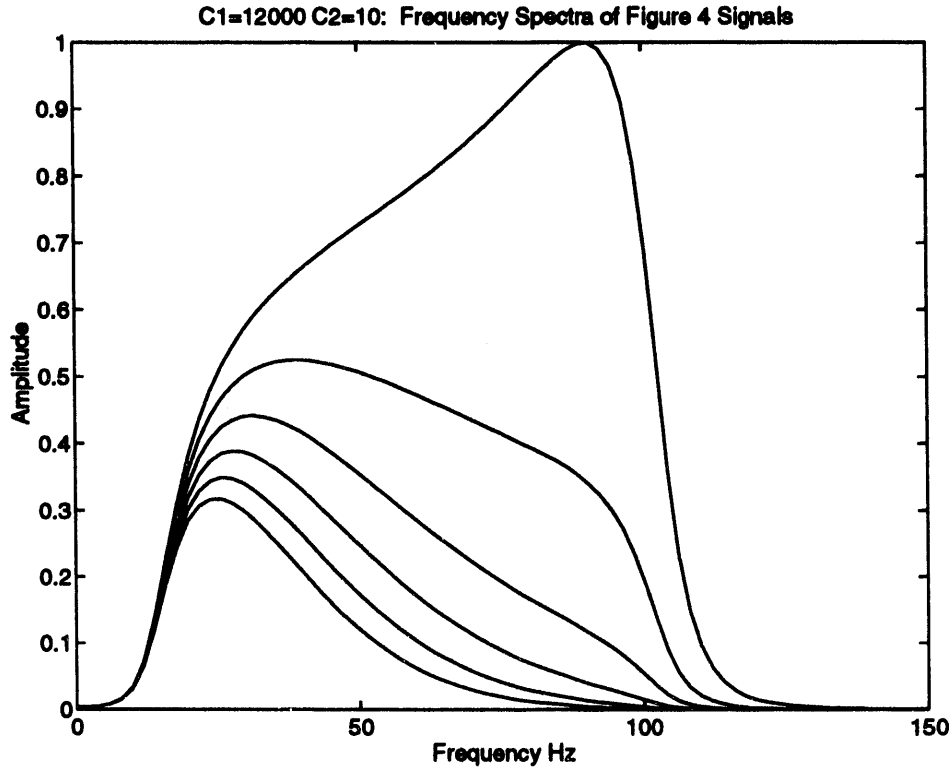


Figure 5: Amplitude spectrum of waveforms in Figure 4. The near receiver spectrum has been normalized to unity. As the source to receiver separation increases, the peak amplitude of the spectrum decreases. In addition, the shape of the spectrum changes due to bodywave dispersion. Both the change in amplitude, and the change in spectral shape can be measured between any two receiver depths. The soil profile can be computed from these spectral measures (see text).

$B_i(\omega)$ = Seismogram Spectrum
$S_i(\omega)$ = Source Spectrum
$H_{bi}(\omega)$ = Soil Transfer Function (source to station "i")
$C_b(\omega)$ = Instrument Transfer Function
$G_{bi}(\omega)$ = Geometric Spreading (beam divergence)

Similarly, the seismogram obtained from the reference geophone for the ith source effort is given by:

$$A_1(\omega) = S_1(\omega) \cdot H_a(\omega) \cdot C_a(\omega) \cdot G_a(\omega) \qquad (8)$$

Since the reference phone is fixed, the medium and geometric spreading terms are constant for all "i".

The traditional method of spectral ratios can be used to determine the amplitude decay rate, α, between the ith and jth stations in hole B. In this method, one computes the ratio of the amplitude spectra for the ith and jth seismograms. Variations in the source spectrum are corrected for by solving (8) for $S(\omega)$ and substituting into the spectral ratio. The result is:

$$\frac{B_i(\omega)}{B_j(\omega)} = \frac{H_{bi}(\omega)}{H_{bj}(\omega)} \cdot \left[\frac{A_i(\omega)}{A_j(\omega)} \cdot \frac{G_{bi}(\omega)}{G_{bj}(\omega)} \right] \qquad (9)$$

To obtain the spatial amplitude decay rate, we begin by solving (9) for the ratio of the soil transfer functions in terms of the measured spectra,

$$\frac{H_{bj}(\omega)}{H_{bi}(\omega)} = \frac{B_{bj}(\omega)}{B_{bi}(\omega)} \cdot \left[\frac{A_i(\omega)}{A_j(\omega)} \cdot \frac{G_{bi}(\omega)}{G_{bj}(\omega)} \right] \qquad (10)$$

The spatial amplitude decay is given as an exponential decay (see equation (4)). Thus the final step is to take the natural logarithm of the spectral ratio of the soil transfer functions in (10) and divide by the distance separating the ith and jth station,

$$\alpha(\omega) = \frac{\log_e \left[\frac{H_{bj}(\omega)}{H_{bi}(\omega)} \right]}{(x_i - x_j)} \qquad (11)$$

Departure from Traditional Practice

It is at this point that my method deviates from traditional practice. Under the constant Q assumption, traditional analysis would be to assume that $\alpha(\omega)$ is a linear function of frequency, ω. This would be true if the phase velocity were constant (nondispersive). Recall equation (6) and solve for spatial amplitude decay,

$$\alpha(\omega) = \left(\frac{1}{2 \cdot V \cdot Q} \right) \cdot \omega \qquad (12)$$

As long as phase velocity, V, and loss factor, Q, are constant, linearity is expected. Thus

traditional analysis has been to fit a straight line to the results obtained in (11) by a
340 method such as least squares.

This linearity is in conflict with the inelastic wave equation (1). The SH-wave should be dispersive. Thus, both V and Q will also vary with frequency (see Figure 3 for example). My method is to least square fit equation (11) results with a nonlinear curve of the shape shown in Figure 3. Furthermore, since phase velocity is also a function of frequency, $V(\omega)$ may also be measured and used to further constrain the solution in a way consistent with the inelastic wave equation.

The Forward Problem

The solution for $\alpha(\omega)$ can be found by taking the ratio of equations (5) and using that to eliminate phase velocity from the C2 equation. The result is as follows:

$$\alpha = \frac{4\sqrt{B}\cdot\omega^2\cdot C2}{[(2\cdot\omega\cdot C2)^2+B^2]} \qquad (13)$$

$$\text{where} \quad B = 2\cdot C1+2\sqrt{C1^2+\omega^2\cdot C2^2}$$

Solving equation (13) at any given frequency yields the spatial amplitude decay at that frequency.

The ratio of equations (5) can also yield an expression for the phase velocity dispersion,

$$V = \frac{2\cdot\omega^2\cdot C2}{B\cdot\alpha} \qquad (14)$$

Once $\alpha(\omega)$ has been determined at a desired frequency by (13), then that result can be used in (14) to compute phase velocity, $V(\omega)$.

The Inverse Problem

The procedure is to start with an initial guess at C1 and C2. Based on the difference between the observed and computed $\alpha(\omega)$ and $V(\omega)$, sensible corrections to C1 and C2 are made. The nonlinear nature of the problem can be overcome by the use of Taylor's series expansion, retaining only the first order terms. For each frequency for which a measurement of $\alpha(\omega_i)$ and $V(\omega_i)$ can be made, we have two equations. At the ith frequency we have,

$$\frac{\partial V(\omega_i)}{\partial C1}\cdot\Delta C1 + \frac{\partial V(\omega_i)}{\partial C2}\cdot\Delta C2 = \Delta V(\omega_i) \qquad (16)$$

$$\frac{\partial \alpha(\omega_i)}{\partial C1}\cdot\Delta C1 + \frac{\partial \alpha(\omega_i)}{\partial C2}\cdot\Delta C2 = \Delta \alpha(\omega_i) \qquad (15)$$

Here, ΔC1 and ΔC2 are the changes in C1 and C2 which will reduce the difference between the observed and calculated $\alpha(\omega)$ and $V(\omega)$. That is,

$$\Delta\alpha(\omega_i) = \alpha(\omega_i)_{observed} - \alpha(\omega_i)_{calculated} \tag{17}$$

$$\Delta V(\omega_i) = V(\omega_i)_{observed} - V(\omega_i)_{calculated} \tag{18}$$

If there are measures of $\alpha(\omega)$ and $V(\omega)$ at N frequencies, the above can be written as an N x 2 matrix equation. The least squares solution for this system is well known (Menke, 1984 for example) and is given by

$$G_{LSQ}^{-1} = (G^T \cdot G)^{-1} \cdot G^T \tag{19}$$

where

$$G = \begin{bmatrix} \vdots & \vdots \\ \dfrac{\partial\,\alpha(\omega_i)}{\partial\,C1} & \dfrac{\partial\,\alpha(\omega_i)}{\partial\,C2} \\ \vdots & \vdots \\ \dfrac{\partial\,V(\omega_i)}{\partial\,C1} & \dfrac{\partial\,V(\omega_i)}{\partial\,C2} \\ \vdots & \vdots \end{bmatrix} \tag{20}$$

The derivatives in matrix G can be computed numerically or analytically. I was able to derive the derivatives using the symbolic processing software known as MAPLE. The resulting formula are quite long, but can be easily implemented in a computer program.

Practical Considerations

Although the computational procedure is straight forward, there are a number of practical matters to be considered:

1). The separation between stations must be large enough to permit an accurate measurement of the phase velocity dispersion.

2). The separation between the source and the stations must be small enough so that the loss of high frequencies is not so large as to adversely reduce the useable bandwidth.

If the station separation is too small, there will not be a significant difference in arrival time between different frequencies. Fortunately, shear waves are some of the slowest traveling seismic waves. This permits one to work at a finer resolution than with P-waves. A good experimental design will insure that a measurable dispersion curve is possible. However, it is not absolutely required. As long as the sampled spectrum captures enough curvature in the spatial decay measurement (spectral ratio), a solution is possible.

The desirability of large station spacings in the dispersion measurement is tempered by the need to retain as much bandwidth as possible. If too much of the high frequency energy is lost, one will not be able to measure either the spatial decay or velocity dispersion over a sufficient bandwidth. Thus it becomes a compromise between measurement precision and retention of bandwidth.

CONCLUSIONS

The proposed new method to measure soil profiles is designed to overcome a significant inconsistency between engineering and geophysical practice. By making the geophysical analysis subject to the same differential equation as is used in engineering practice, this inconsistency is overcome. Furthermore, two major advantages are realized:

1). The soil profiles produced consist of the same parameters that will be later used in the dynamic analysis of an embankment or foundation site.

2). The resulting soil profiles should better predict soil dynamics beyond the spectral bandwidth of the geophysical measurements. The realization of this last point will be subject to measuring a sufficient bandwidth for determining the nonlinear spatial decay factor, $\alpha(\omega)$, or velocity dispersion, $V(\omega)$.

REFERENCES

Futterman, W.I. (1962). Dispersive Body Waves, Jour. of Geophysical Research, Vol 67, No. 13, pp5279-5291.

Hardin, B.O., and V.P. Drnevich (1972a). Shear modulus and damping in soils: measurement and parameter effects, *J. Soil Mech. Foundations Div.* ASCE 98, pp603-624.

Hardin, B.O., and V.P. Drnevich (1972b). Shear modulus and damping in soils: design equations and curves, *J. Soil Mech. Foundations Div.* ASCE 98, pp667-692.

Jongmans D., and M. Campillo (1993). The determination of soil attenuation by geophysical prospecting and the validity of measured Q values for numerical simulations, *Soil Dynamics and Earthquake Eng.*, 12, pp. 149-157.

Kudo, K., and E. Shima (1970). Attenuation of shear waves in soil, *Bull. Earthquake Research Institute,* v. 48, p.145-158.

Lee, M.K.W. and W.D.L. Finn (1982). Dynamic effective stress response analysis of soil deposits with energy transmitting boundary including assessment of liquefaction potential, Rev., Dept. of Civil Eng., Soil Mechanics Series, No. 38, Univ. of British Columbia, Vancouver, Canada.

Menke, W. (1984). Geophysical data analysis, discrete inverse theory, Academic Press, San Diego.

Michaels, P. and R.B. Smith (1992). Recurrent neural network representation of the inelastic wave equation and full-waveform inversion without local minima, *SEG Annual Meeting Expanded Abstracts, New Orleans,* AI1.7, pp22-25.

Seed, H.B., and I.M. Idriss (1970). Soil moduli and damping factors for dynamic response analyses, Report EERC 70-10, Earthquake Engineering Research Centre, University of California, Berkeley.

Seed, H.B, K.L. Lee, and F.I. Makdisi (1973). Analysis of the slides in the San Fernando dams during the earthquake of Feb. 9, 1971, Report No. EERC 73-2, University of California, Berkeley.

Tonn, R. (1991). The determination of the seismic quality factor from VSP data: A comparison of different computational methods. Geophys. Prospecting, 1991, vol. 39, 1-29.

ACKNOWLEDGEMENTS

I would like to acknowledge Phillip Sirles at the Bureau of Reclamation who brought the work of Jongmanns and Campillo to this author's attention. This paper is CGISS contribution 29.

Hydrogeology, Waste Disposal, Science and Politics
Proceedings 30th Symposium
Engineering Geology and Geotechnical Engineering, 1994

GROUND PENETRATING RADAR AND SEISMIC REFRACTION INVESTIGATION OF FRACTURE PATTERNS IN THE BASALT OF LUCKY PEAK NEAR BOISE, IDAHO

M.E. Dougherty, W.K. Hudson, S.E. Kay, and R.J. Vincent

Center for Geophysical Investigation of the Shallow Subsurface,

Boise State University, Boise, Idaho

ABSTRACT

In hard rock environments, fluid flow and basement integrity are often controlled by the degree and connectivity of fracturing on an outcrop scale, rather than strictly by laboratory values of the permeability and competence of the matrix rock. Therefore, in many cases it is important to have a subsurface image of fracture characteristics of rock units in addition to an image of gross rock type. Fortunately, within a single rock type, many physical properties on outcrop scale are greatly influenced by fracturing, and changes in these physical properties should be detectable through the innovative use of geophysical methods. Work presented here is an attempt to use surface geophysical methods to delineate areas within a basalt flow which display different fracture characteristics and which have different electrical and seismic properties.

The Basalt of Lucky Peak is an intracanyon basalt flow exposed in cliffs around Lucky Peak Reservoir and in a terrace downstream from Lucky Peak Dam near Boise, Idaho. Visible in the face of the terrace below Lucky Peak Dam are the colonnade and entablature structures characteristic of differential cooling rates within basalt flows. Exposure of structural units within the cliff face is used to ground truth results from ground penetrating radar (GPR) and seismic refraction data collected along a line running perpendicular and away from the top edge of the cliff.

GPR data were collected using 25, 50, and 100 MHz antennas with the best results obtained with the 25 and 50 MHz antennas. Very little, if any information is contained in the 100 MHz GPR records from the 35-40 m thick basalt flow. One seismic refraction line with seven sledge hammer shotpoints was run along the same line as the GPR data collection line. In general, there is excellent agreement between the results obtained with the two methods. Two overburden layers and three basalt layers can be identified in the results. Arrivals from the bottom of the flow were not successfully obtained due to attenuation of the GPR signal and insufficient line length of the seismic refraction line. Results from this simple study warrant further research into the simultaneous use of electrical and seismic methods to image fracture systems in terrestrial basalts.

INTRODUCTION

Non-invasive characterization of the shallow subsurface is becoming an invaluable aspect of many hydrogeologic and geological engineering studies. In hard rock environments, fluid flow and basement integrity are often controlled by the degree and connectivity of fracturing on an outcrop scale, rather than strictly by laboratory values of the permeability and competence of the matrix rock. Therefore, in many cases it is important to have a subsurface image of fracture characteristics of rock units in addition to an image of gross rock type. Fortunately, within a single rock type, many physical properties on outcrop scale are greatly influenced by fracturing, and changes in these physical properties should be detectable through the innovative use of geophysical methods.

 Ultimately, individual geophysical methods measure only a limited set of physical properties. Ground penetrating radar (GPR) is most sensitive to changes in the electromagnetic properties of a medium (particularly the electrical properties of conductivity and permittivity at the frequencies used in most GPR surveys), while seismic techniques respond only to contrasts in the elastic parameters of density, bulk modulus, and shear modulus. Either of these techniques can individually provide a wealth of subsurface information given proper environmental conditions. If a change in geologic structure, such as porosity or fracture pattern, results in a perturbation of both electrical and elastic properties, then independent verification of this structure can be obtained by each of the two techniques. Previous work suggests that fracture characteristics may indeed affect high frequency electrical properties through scattering [*Olhoeft*, 1990] and also that cooling zones within a basalt flow exhibit unique petrographic textures [*Long and Wood*, 1986] which may affect electrical properties. Seismic velocities are known to be fairly sensitive to fracture density as well as porosity [*Kuster and Toksöz*, 1974; *Cheng and Toksöz*, 1982; *O'Connell and Budiansky*, 1974].

Work presented here is an attempt to use surface geophysical methods to delineate areas within a basalt flow which display different fracture characteristics and which presumably have different electrical and seismic properties. Imaging of the top and bottom of the flow is an additional goal of this work. The basalt of Lucky Peak is exposed in a canyon along the Boise River just east of Boise, Idaho and displays zones of entablature and upper and lower colonnades (see Figure 1). Relative abundances of these zones vary spatially along the canyon walls. We present here the results of a ground penetrating radar and seismic refraction study of a small portion of the Lucky Peak basalt flow in a area where three distinct zones of upper colonnade, entablature, and lower colonnade are exposed in the canyon wall. GPR and seismic lines were run on the relatively smooth upper surface of the flow above the cliff face. Profiles were run perpendicular to the cliff and ended at the cliff face for absolute ground-truth of at least one end of the line.

GEOLOGIC SETTING

The basalt of Lucky Peak is exposed as a single flow unit, approximately 40 meters thick, forming terraces downstream from the Lucky Peak Dam (see Figure 2). This flow is one of a series of intra-canyon basalt flows erupted along the Boise River and its tributaries over the past 2 million years [*Howard, et al.*, 1982]. Flow age is estimated between 0.572 Ma and 0.730 Ma [*Mankinen and Dalrymple*, 1979; *Berggren, et al.*, 1985]. Buried beneath the flow are two former surfaces consisting of relatively unweathered alluvial gravel deposits: (1) the active flood plain at the time of eruption, and (2) a secondary terrace approximately 18.5 meters (60 feet) above the floodplain [*Othberg and Burnham*, 1990]. Alluvial fan deposits cover the surface of the flow. Sand and granule gravels eroded from the granite of the Idaho batholith are the major constituents of the alluvium in this area. Loess 1-2 meters thick discontinuously covers the alluvial fans. Soils have formed in both the thin loess and in the upper part of the fan gravel. The soils have clayey and calcic B horizons [*Collett*, 1980].

The basalt of Lucky Peak is a Type III basalt flow as defined by *Long and Wood* [1986], displaying a distinct upper colonnade, entablature, and lower colonnade (see Figure 1). Below the point of the experiment, the upper colonnade is approximately 10 meters thick. Below this, the hackly jointed entablature is approximately 14 meters thick. A lower colonnade is exposed for 10 meters at the base of the flow. A talus pile obscures the absolute base of the flow in the study area. Boundaries and thicknesses of these zones shift in both directions away from the study area. In some places, the entablature disappears completely and the lower colonnade extends to the top of



Figure 1. Photo of Lucky Peak basalt outcrop showing typical basalt flow fracture patterns. This site contains an upper and lower colonnade surrounding a large central entablature zone. Note also that the columns are less regular in the upper colonnade than in the lower colonnade. Maximum thickness of the basalt exposure is approximately 34 m, with exposure thicknesses of 10, 14, and 10 m for the upper colonnade, entablature, and lower colonnade, respectively. GPR and seismic refraction data were collected along a line which started at the top of the cliff approximately in the center of this photo and ran perpendicular to the cliff on the top of the flow.

the flow.

Wells drilled in the area confirm the depth of the flow and also seem to define its extent to the north, away from the cliff. The log of a well drilled within 200 meters due west of the GPR line records hard basalt between 9.5 and 37.5 meters (31-122 feet) depth, then 7 meters (23 feet) of gravels. Two other wells which lay in an east-west line within 100 meters north of the GPR line encounter no basalt within 40.6 meters (132 feet) of the surface.

GROUND PENETRATING RADAR

Field Acquisition Parameters - GPR

GPR data were collected along a 100 m long line which started approximately 5 m from the cliff face and ran at an azimuth of approximately N10°W (see Figure 2b). A Sensors and Software pulseEKKO IV GPR unit was used with 25, 50, and 100 MHz antennas to collect the data. The relatively brush free ground surface provided excellent antenna/ground coupling. Any excess brush was removed before collection of the GPR data.

Data were collected using a constant offset, single channel geometry with the first midpoint located at a range of one half of the antenna spacing. Antenna spacings of 20, 20, and 4 m were used for the 25, 50, and 100 MHz lines, respectively. Station spacings of 1.0, 0.5, and 0.25 m were used for the 25, 50, and 100 MHz lines, respectively. Each sample trace was composed of a stack of 64 source pings of 1250 points in length. The sampling interval used was 0.8 ns for a total trace time of 1000 ns.

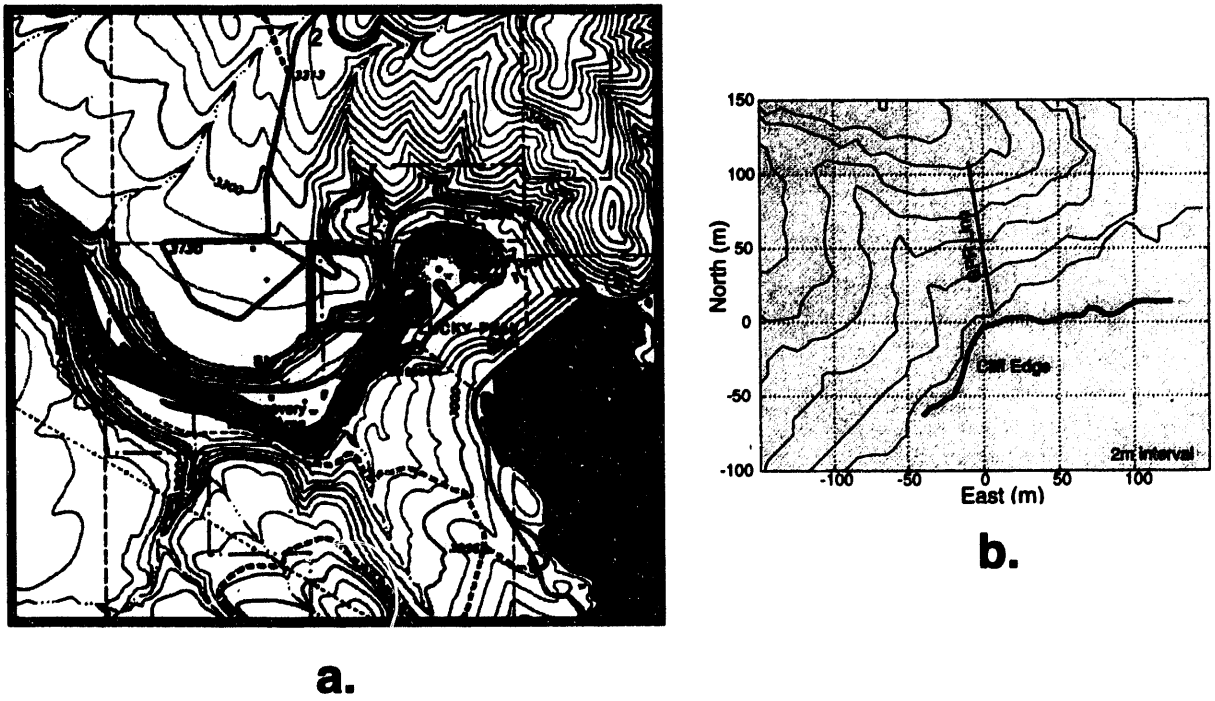


Figure 2. (a) Location of Lucky Peak Basalt GPR and seismic refraction study near Boise, Idaho. Lucky Peak Reservoir and the Boise River are shown by the shaded regions. Inset (b) shows location of GPR/seismic line relative to cliff face. Zero point of line is on the south end of the line near cliff face. Contour interval in (b) is 2 m with the elevation of the upper cliff edge at approximately 3080 m.

Data - GPR

Processed 25, 50, and 100 MHz data from the GPR line are presented in Figure 3. While raw data taken directly from the pulseEKKO system can usually provide a fairly complete initial view of the subsurface, additional post-processing is often necessary to take full advantage of the collected data [*Gerlitz, et al.*, 1993; *Fisher, et al.*, 1992; *Dougherty, et al.*, 1994, *Liberty and Pelton*, 1994]. This is particularly true for these Lucky Peak basalt data which have relatively low amplitude reflected arrivals. While a thorough explanation and display of the inherent trade-offs in processing is beyond the scope of the paper, a brief description of final processing steps used with these data is presented below.

A DC shift of each trace for all records in Figure 3 exists and is due to recording offsets of an unknown origin. The magnitude of the DC shift seems to drift somewhat from trace to trace and is more dramatic in the 25 and 50 MHz data than in the 100 MHz data. Removal of the DC shift is carried out as the first processing step and is a straight forward subtraction of the mean value of each trace for times before arrival of the direct wave. All traces in each record section are next bandpass filtered with a Butterworth filter in order to remove any residual low-frequency 'WOW' effects [*Gerlitz, et al.*, 1993] and random high frequency noise. Bandpass cutoffs were set at 5-50 MHz, 10-100 MHz, and 10-200 MHz for the 25, 50, and 100 MHz data, respectively. 'WOW' effects are manifested by a time-varying DC shift in the data following the direct air wave and are due to swamping of the system by the high amplitude direct wave. These effects are most prevalent when using small-offset geometries and were not a major problem with the 20 m offsets used while collecting the 25 and 50 MHz data. Some 'WOW' can be seen in the 100 MHz data, but

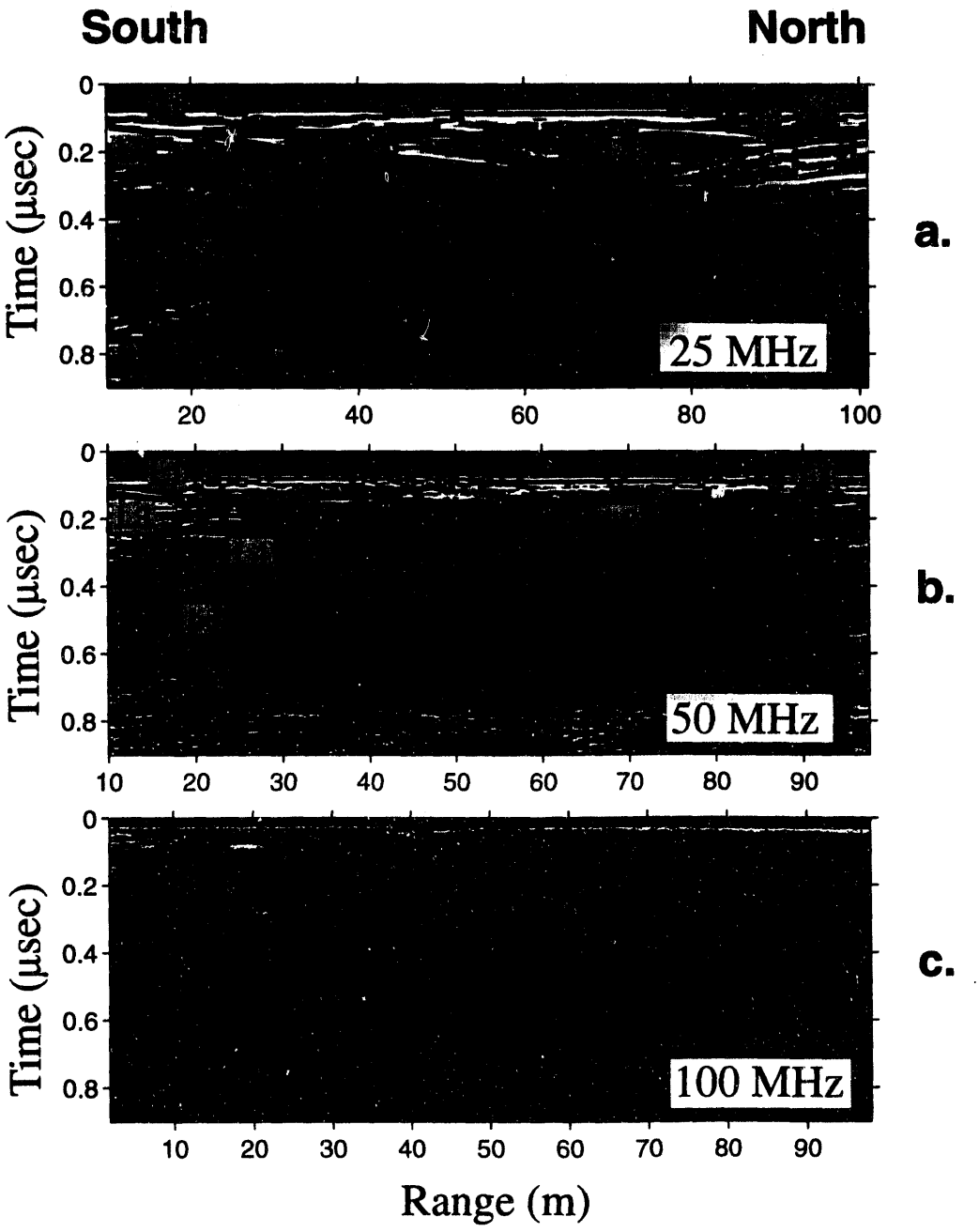


Figure 3. Images of GPR data collected over the Lucky Peak basalt. Receiver antennas with central frequencies of 25 MHz (a) 50 MHz (b) and 100 MHz (c) are shown. Data have not been corrected for elevation. Layers of loess, clayey overburden, upper basalt colonnade, basalt entablature, and lower basalt entablature are marked L1, L2, L3, L4, and L5, respectively.

since not much geologic information was found in that record section, great care was not taken to completely remove these effects.

Perhaps the most important processing step when dealing with shallow GPR data collected in the single offset geometry is removal of the direct air wave. This strong arrival travels directly from source to receiver antenna through the air and is always the first signal recorded on each

trace. Fortunately, since the arrival is traveling a constant distance through a relatively homogeneous medium (air), its arrival time and waveform are relatively invariant. Reflections from very shallow strata may interfere with the latter part of this waveform, but generally this does not affect the main lobes of the arrival. Various methods have been proposed to dampen the affects of this arrival and we have found that the subtraction of a normalized 'average' trace is sufficient to prevent this arrival from dominating the record sections. The 'average' trace is calculated by first aligning all traces by first arrival (to correct for instrument timing errors) then summing all of the traces in a record section. This has the effect of cancelling out most geological arrivals (except continuous horizontal arrivals) and enhancing the direct wavelet. Finally, the 'average' trace is normalized in amplitude to the maximum amplitude of the direct arrival in each individual trace and subtracted from each trace. After subtraction of the air wave arrival, the data are scaled linearly with time (depth) to recover the effects of spherical spreading of the wavefronts.

Arrivals seen in the GPR data include signal returned from geological features, instrument interference, and signal returned from cultural features. In general, because of the presence of the cliff, clayey overburden, and field vehicles, there is a fair amount of cultural and geologic noise in the record sections. The most obvious non-geological arrivals are large diffractions which extend over the entire range of the 25 and 50 MHz data lines and have their peaks beyond the northern end of the line. Velocities of the branches of these diffracted arrivals indicate an origin of air wave reflections from field vehicles parked approximately 30 meters from the northern end of the line. Diffractions with peaks on the southern (cliff) end of the line originate by scattering off the cliff face itself. Other diffractions in the center of the line are most likely due to scattering from the rough basalt surface and thus can be considered to contain some geologic information. Diffractions are often collapsed in seismic data through a migration process. However, migration was not carried out here because of the mix of geological diffractions and out-of-plane surface air wave diffractions which have widely different velocities, and hence make the migration process difficult. Coherent horizontal noise which is prevalent after about 600 ns in the 25 and 50 MHz data is most likely background instrument noise which has been increased in amplitude through the linear gain function used to correct for spherical spreading.

Once the origins of noise in the GPR records are realized and understood, a number of geologically relevant arrivals and layers can be identified. Rather than label individual arrivals in the GPR data plots, layers have been labeled and assigned geological significance based on details seen in the cliff exposure (see Figure 3) and well log results from nearby wells. In order of increasing depth, these layers are: L1, thin surface loess layer which thins below resolution of the wide aperture collection geometry near the center of the line; L2, clayey overburden which generally increases in thickness with range; L3, upper colonnade portion of exposed Lucky Peak basalt; L4, entablature portion of exposed basalt flow; and L5, lower colonnade of exposed basalt flow. These same layers can be seen in both the 25 and 50 MHz GPR records and are slightly more obvious in the 25 MHz record section. Very little, if any, useful information can be obtained from the 100 MHz line. There is a slight hint of scattering off the top of the flow at ranges where the overburden is not thick (ranges less than 40 meters). The 100 MHz section also suffers from low frequency 'WOW' effects directly following the direct wave as described above.

Data images in Figure 3 are plotted with respect to two-way travel time instead of depth because of poor constraints on subsurface electromagnetic velocity. A few common midpoint (CMP) experiments were run unsuccessfully near the center of the line in order to obtain accurate velocity information. However, using an estimated velocity of 0.13 m/ns within the basalts and a 20 m antenna spacing would put the upper colonnade/entablature contact at approximately 9-10 meters depth and the entablature/lower colonnade contact at approximately 24-25 meters depth at the cliff face. These depths correspond very closely (within measuring error) to the depths of

those contacts seen in the cliff exposure. Also, because of insufficient velocity information, the record sections in Figure 3 are not corrected for static shifts (elevation) due to increasing overburden thickness. The true ground surface elevation of the profiles slopes upwards at a slope of approximately 6° from south to north. This would make the upper surface of the basalt flow approximately level in agreement with the approximate elevation of the top of the flow seen in cross-sections of the flow in the cliff exposure. True dips are, however, used below for the seismic modeling.

SEISMIC REFRACTION

Field Acquisition Parameters - Seismic Refraction

Data from a seismic refraction line were collected over the same line as the GPR survey (see Figure 2b and Figure 4) on December 29, 1993. Data recording was carried out with a Bison 9000 Series Seismograph. A low cut acquisition filter was set at 4 Hz in the field. The high cut filter was inoperative during the experiment due to the cold weather. A total of 48, 10 Hz geophones was used with a station spacing of approximately 2 meters along the line. Seven shots were recorded, each composed of a stack of five sledge hammer blows on a metal plate. Three shots were located on both ends of the line (offsets of zero, five, and eight meters) with an additional shot located between geophones 24 and 25 (Figure 4).

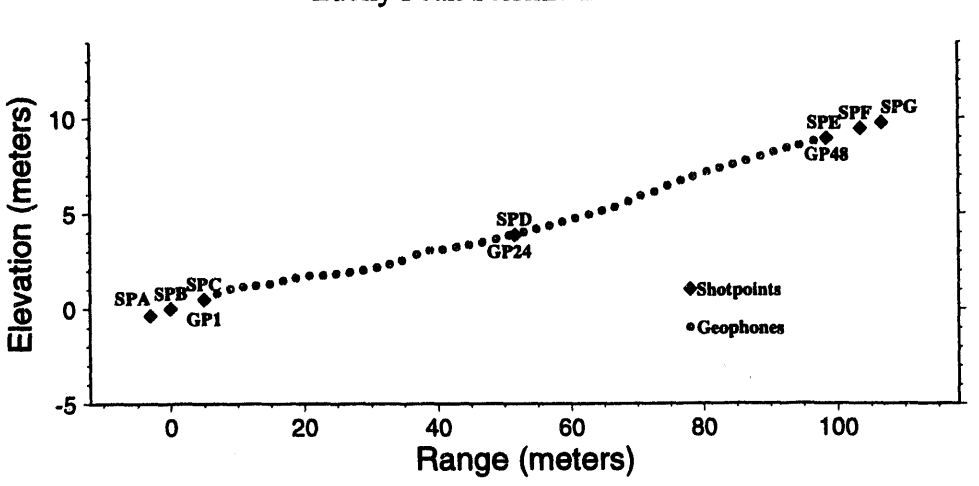


Figure 4. Elevation plot of refraction shot and geophone locations. Ranges are relative to the zero point of the GPR line as seen in Figure 3. Shotpoints A-G are marked with triangles and labeled as SPA-SPG. Geophones are marked with circles with the locations of geophones 1, 24, and 48 labeled as GP1, GP24, and GP48

Air temperature on the day of the seismic refraction experiment ranged from the high 20°'s in the morning to the mid 30°'s in the afternoon. The ground surface was partially frozen, making planting of the geophones difficult. Most geophones had only the first 3.75-5.0 cm of the spike penetrating the ground, leaving 2.5-3.75 cm of the spike exposed. We do not believe that this lack of complete planting caused any data recording problems as the plants were quite firm. Also, we do not believe that the frozen ground surface extended to any significant depth.

Data - Seismic Refraction

Final record sections from the seven refraction shots are shown in Figure 5. Within each record, the channels are individually gained using a linear gain function. Signal to noise ratio in

each of the records becomes fairly low beyond ranges of approximately 50-60 m. Confidence in picks beyond those ranges is given a low value in subsequent analyses. In an effort to facilitate picking first arrivals, the data are filtered with a 50-150 Hz band pass Butterworth filter. This has the effect of removing some of the low frequency noise and all of the high frequency noise. After filtering, it is possible to pick first arrivals for a few more channels in each record, but the confidence in these picks is low.

Four main refraction branches can be seen in the final seismic data. While data from only one shotpoint (shotpoint C, see Figures 4 and 5) show all of the refraction branches, individual record sections show various combinations of the four arrivals. These branches were picked according to crossovers in the first arrival curves and labeled based on similar slopes (reciprocal velocities). Slopes were roughly corrected for dip of refractors based on a simple layered model and the reciprocal method [*Hawkins*, 1961; *Burger*, 1992] before assigning labels. Arrivals R1, R2, R3, and R4 correspond to a direct wave through the thin loess layer, and head waves along the tops of layers of clayey soil, upper basalt colonnade, and basalt entablature, respectively, as seen in the GPR data and in the cliff exposure for the basalt contacts.

Models - Seismic Refraction

Forward and inverse raytracing models were constructed in order to confirm interpretation of the seismic refraction results. Construction of the models was also aided by preliminary interpretation of the GPR data. RAYINVR, a seismic raytracing inversion program, was used for all of the model development and inversions [*Zelt and Ellis*, 1988]. Inputs to the RAYINVR models include seismic velocities (compressional and shear, if desired), surface elevation, shot locations, and subsurface layer structure. Once seismic field data are available, arrival times with uncertainties and arrival type can also be entered for inversion of the field data. A preliminary model based on GPR results and expected seismic velocities was calculated before the seismic refraction experiment. Results from this model were used to determine the resolution of the refraction method and also as an aid in laying out the seismic line.

After acquisition of the refraction data, a refined starting model was developed based on the GPR results and preliminary velocities obtained by using the reciprocal method [*Hawkins*, 1961]. As seen in Figure 6a, this model contains many of the geologic features as seen in the GPR results (Figure 3) including two overburden layers and two basalt layers. Figure 6 is an example of the output of the RAYINVR modeling program. The upper portion of both Figures 6a and 6b are plots of the model geometry and rays traced through the model. Layer boundaries are shown with dashed lines and seismic rays are shown by the solid lines. Ground surface elevations were obtained from a survey of the seismic line and shot locations. Subsurface information was inferred form the GPR results and reciprocal method reduction of the refraction data. Depths and ranges are relative to zero being at the edge of the cliff face in these diagrams. The lower portion of the plots in Figures 6a and 6b are plots of the seismic arrival times for both the model and field results. Solid lines indicate model travel time results and crosses indicate actual arrival times observed in the field.

Figure 6a shows results of the starting model compared to field data from shotpoint B of the refraction line. In general, agreement between the model and the field data is quite good, indicating that the model is a good fit to the actual field conditions (within the constraints of non-uniqueness). Arrivals from layers 2, 3, and 4 are found in the data, as seen in Figure 5b. Although preliminary model-data comparisons are only shown here for shotpoint B, comparisons for all of the shotpoints were calculated and all show a high degree of agreement.

Once general agreement is made between the preliminary RAYINVR forward model and field data, inversions of the field data can be carried out with the program. This technique is useful

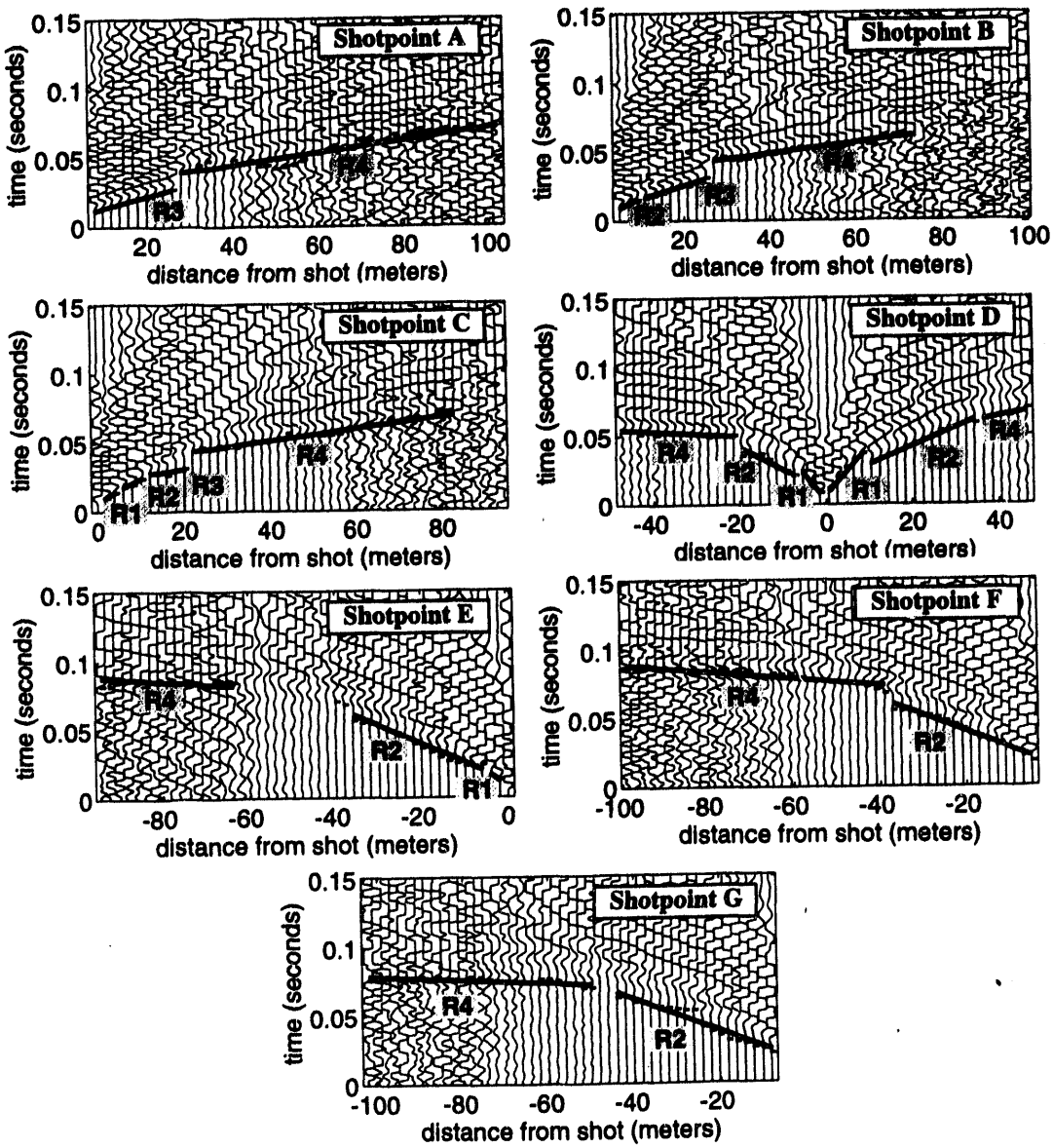


Figure 5. Seismic data from all shots of the Lucky Peak basalt refraction line. Arrivals from similar refractors are labelled on each plot. See Figure 4 for location of shotpoints.

for investigations of the trade-off between depth to layers and their velocity. Inversions were carried out on the Lucky Peak basalt refraction data by using arrival time picks from all of the shotpoints simultaneously. This overconstrains the inversion calculation given the number of free variables (grid node locations and/or velocity values) used in these models (node locations given by crossing dashed lines in model geometry plots of Figure 6).

Three separate inversions were obtained from the refraction data, each allowed different sets of variables to vary. In general, travel time variations can be caused by variations in layer velocities or thicknesses. Inversions with varying layer depths, velocities, and a combination of varying velocities and depths were calculated. Results from the inversion which allowed both velocities

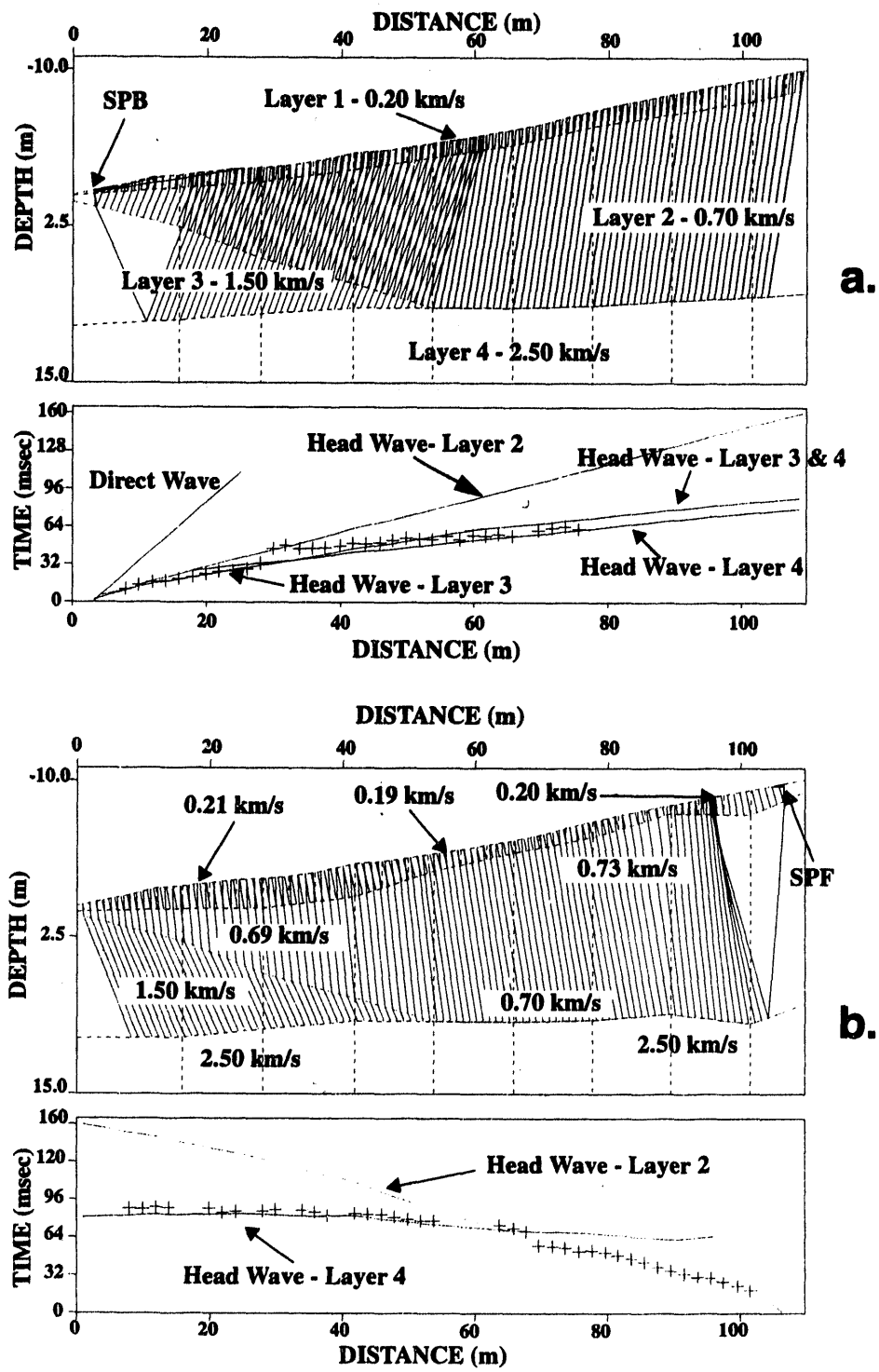


Figure 6. (a) Starting RAYINVR model derived from the interpreted GPR records showing rays traced from shotpoint B (SPB) of the Lucky Peak basalt refraction experiment. Model grid boundaries (dashed lines) and traced rays (solid lines) shown in the upper portion of the plot. Observed (crosses) and calculated (solid line) arrivals shown in the lower portion of the plot. (b) Final inverted RAYINVR model showing rays traced from shotpoint F (SPF) of the Lucky Peak basalt refraction experiment. Velocities and depths to layers have been allowed to vary for this inversion. Although only rays and arrival times from shotpoint F are shown for clarity, all shots and arrivals were used for calculation of the inversions.

and depths to vary are shown in Figure 6b. This final model incorporates most of the features seen in the inversions with only one variable parameter. As can be seen in Figures 6a and 6b, since the starting model produces arrival times that are relatively close to the observed data, very little change in the model is seen upon three iterations of inversion. The main features that change are the thickness of the loess layer and some very slight velocity variations within layers 1 and 2 (loess and clayey overburden, respectively). Variable thickness of the loess layer in the seismic model corresponds well with the general characteristics of that layer as seen in the GPR data.

DISCUSSION

Although the ground penetrating radar results exhibit a relatively low signal to noise ratio, most of the important geological features can still be identified in the GPR images (Figure 3). Depths to the boundaries between internal flow structures (entablature and colonnades) agree closely to the corresponding boundaries seen in the cliff exposure. We believe that attenuation due to the presence of clayey overburden limits the ability of the GPR to see into the basalts except where the overburden is relatively thin on the cliff end of the line. Scattering from fractures contributes additional propagation losses once the signal has entered the basalts. These loss mechanisms prevent the bottom of the flow from being imaged at this site.

The seismic refraction line was originally proposed as a mechanism to constrain overburden thickness. Results presented here contain the added information of internal structural layering within the basalt flow. Velocity variations within the basalt flow could be due to weathering and/or differing degrees of fracturing in the different structural units. Since the upper colonnade is relatively less fractured than the entablature, one would expect its seismic velocity to be relatively faster based on fracture density/velocity relationships. However, compressional velocities of approximately 1.5 km/s indicate that the upper colonnade probably has experienced greater weathering than the rest of the flow. A velocity difference between the entablature and lower colonnade could not be resolved within the constraints of the experiment geometry used for this refraction line. A longer line oriented perpendicular to the refraction line presented here would possibly be more effective at resolving all layering within the basalt flow.

It is clear in data from both geophysical methods presented above that layering exists within the Lucky Peak basalt flow as seen in the cliff exposure, and that this layering is detectable using surface geophysical methods. A thinning of the upper colonnade is typical for these types of basalt flows [*Long and Wood,* 1986] as the cooling structures are often not laterally continuous over any great distance. This can be seen in lateral cross-sections of the Lucky Peak basalt cliff exposure as well. Differential weathering throughout the flow with a higher degree of weathering towards the top of the flow is to be expected as well and can account for the relatively low seismic velocities seen in the refraction data [*Dougherty, et al.*, 1992; 1993]. It is not clear, however, why distinct seismic arrivals are not seen for the entablature and lower colonnade layers. One factor is that the length of the line and source strength may not have been sufficient to resolve these two layers.

Interpretation of data from GPR in combination with that from seismic techniques is a powerful tool and allows for a high degree of confidence in the final model presented above. While GPR collected in the single offset geometry used here can give a quick first look at the geological environment, seismic refraction can add additional depth constraints to the model. Also, since the two techniques essentially measure different physical properties, independent confirmation of the geologic structure is obtained by the two methods. This assumes, of course, that the respective physical properties measured by the two techniques are unique in different geologic structures. Also, it

suggests that joint inversion of data collected by these two techniques should provide a well constrained model of fracture structure within basalts.

Data presented here are the result of two days of opportunistic fieldwork carried out in time windows when geophysical equipment was available. A limited amount of planning and reconnaissance time was available prior to days when it was necessary to carry out the fieldwork. Given the success of these initial results, we feel that this study could benefit greatly by additional data collection from other portions of the Lucky Peak basalt. Specifically, areas where less overburden is present and where longer lines could be run at a greater distance from the cliff face are available in close proximity to the line used for this study.

CONCLUSIONS

We have presented here the results from a geophysical investigation of the Lucky Peak basalt flow using ground penetrating radar and seismic refraction techniques. In general, agreement of the results between the two techniques and between the geophysical models and structure seen in the adjacent outcrop exposure is excellent. Structures within the overburden as well as from within the basalt flow itself can be distinguished with both methods. However, attenuation of the GPR signal due to absorption in clayey sediments and scattering from cracks in the basalt, as well as insufficient seismic source strength and line length, prevent the base of the flow from being imaged by either geophysical method used here. Results from this study warrant further research into the simultaneous use of electrical and seismic methods to image fracture systems in terrestrial basalts.

ACKNOWLEDGEMENTS

This work was supported by the Idaho State Board of Education and the Office of Naval Research Grant #N00014-92-J-1143. Boise State University Center for Geophysical Investigation of the Shallow Subsurface contribution #0027.

REFERENCES

Burger, R.H, *Exploration Geophysics of the Shallow Subsurface*, Prentice Hall, Englewood Cliffs, NJ, 489 p., 1992.

Berggren, W. A., D.V. Kent, J.J. Flynn, and J.A. Van Couvering, Cenozoic geochronology, *Geol. Soc. Am. Bull.*, **96**, 1407-1418, 1985.

Cheng, C.H., and M.N. Toksöz, Elastic wave propagation in a fluid-filled borehole and synthetic acoustic logs, *Geophysics*, **46**, 1042-1053, 1981.

Collett, R. A., *Soil survey of Ada County area, Idaho*, U.S. Department of Agriculture, Soil Conservation Service, 1980.

Dougherty, M.E., Gillis, K.M., Pelton, J.R., and Sapp, K., A geological and seismic study of the upper oceanic crust in the Troodos Ophiolite, Cyprus, *Transactions, EOS*, **73**, 355, 1992.

Dougherty, M.E., Kay, S.E., Pelton, J.R., and Gillis, K.M., Predictions of fine scale seismic structure of the upper oceanic crust, *Transactions, EOS*, **74**, 426, 1993.

Dougherty, M.E., Enhancement of ground penetrating radar data through signal processing, *submitted to the Proceedings of the Symposium on the Application of Geophysics to Engineering and Environmental Problems*, SAGEEP '94, 1994.

Fisher, E., G.A. McMechan and A.P. Annan, Acquisition and processing of wide-aperture ground-penetrating radar data, *Geophysics*, **57**, 495-504, 1992.

Gerlitz, K., M.D. Knoll, G.M. Cross, R.D. Luzitano and R. Knight, Processing ground penetrating radar data to improve resolution of near-surface targets, *Proceedings of the Symposium on the Application of Geophysics to Engineering and Environmental Problems*, SAGEEP '93, **2**, 561-574, 1993.

Hawkins, L.V., The reciprocal method of routine shallow seismic refraction investigations, *Geophysics*, **26**, 806-819, 1961.

Howard, K.A., J.W. Shervais, and E.H. McKee, Canyon-filling lavas and lava dams on the Boise River, Idaho, and their significance for evaluating downcutting during the last two million years, in Bill Bonnichsen and R.M. Breckenridge, editors, *Cenozoic Geology of Idaho*, Idaho Bureau of Mines and Geology Bulletin, **26**, 629-641, 1982.

Kuster, G.T., and M.N. Toksöz, Velocity and attenuation of seismic waves in two-phase media, I. Theoretical formulations, *Geophysics*, **39**, 607-618, 1974.

Liberty, L.M., and J.R. Pelton, A comparison of ground penetrating radar: Multi-fold data vs. single fold data, *this volume*, 1994.

Long, P. E., and B.J. Wood, Structures, textures, and cooling histories of Columbia River basalt flows, *Geol. Soc. Am. Bull.*, **97**, 1144-1155, 1986.

Mankinen, E.A., and G.B. Dalrymple, Revised geomagnetic time scale for the interval 0-5 m.y. B.P., *J. Geophys. Res.*, **84**, 615-626, 1979.

Olhoeft, G.R., Tutorial: High frequency electrical properties, *United States Geological Survey Open File Report OFR-90-0414*, 48, 1990.

O'Connell, R.J. and B. Budiansky, Seismic velocities in dry and saturated cracked solids, *J. Geophys. Res.*, **79**, 5412-5426, 1974.

Othberg, K. L., and W. L. Burnham, Geologic map of the Lucky Peak quadrangle, Ada County, Idaho, *Idaho Geological Survey Technical Report 90-4*, 1990.

Zelt, C.Z., and R.M. Ellis, Practical and efficient ray tracing in two-dimensional media for rapid traveltime and amplitude forward modelling, *Canadian Journal of Exploration Geophysics*, **24**, 16-31, 1988.

Hydrogeology, Waste Disposal, Science and Politics
Proceedings 30th Symposium
Engineering Geology and Geotechnical Engineering, 1994

RESULTS OF A DOWNHOLE FORMATION MICROSCANNER[1] STUDY IN A JURO-TRIASSIC-AGED SEDIMENTARY DEPOSIT (PASSAIC FORMATION)

by
Joseph A. Fischer, Geoscience Services
Joseph J. Fischer, Geoscience Services
Robert J. Bullwinkel, Schlumberger Wireline & Testing Services

ABSTRACT

Studies to determine the structural and geohydrological properties of the Passaic Formation were performed at two sites. Both sites are located in northeastern New Jersey, within the Juro-Triassic-aged Newark Basin. The Passaic Formation rocks are described in the literature as a reddish brown, thin to massively bedded, sedimentary deposit with lithology ranging from claystone through conglomerate. A fractured "layer cake" model has been proposed (and is generally accepted) to describe the prevailing geohydrological conditions.

The Formation MicroScanner tool was used in four wells drilled for these projects (two at each site). In addition to this microresistivity tool, a suite of other oil field geophysical tools (Gamma, Induction, Dipmeter, Temperature, and Neutron probes) were also utilized. The data collected with the Formation MicroScanner were correlated with detailed logs and the continuous core retrieved from three of the wells. Pump test data was also obtained at both sites. The geophysical data obtained at both sites allowed the direct identification of fractures and their orientation in relation to bedding. Fracture and bedding aperture size and orientation were measured. The results, as presented in this paper, show a high degree of inhomogeneity at both sites rather than the conventional layer cake model. For appropriate site analyses it was necessary to significantly refine the previously assumed Passaic Formation geohydrological and structural model.

INTRODUCTION

The role of geophysical instrumentation in various geotechnical disciplines is well accepted. While many geophysical tools are extremely useful, they have often been oversold or misapplied. While recognizing this concern, the authors would like to describe the use of the Formation MicroScanner tool in Passaic Formation rocks at two sites in New Jersey.

The Passaic Formation underlies some 3000 square miles of New Jersey. Similar rocks are found in all the Juro-Triassic-aged basins of the eastern United States. Bordered by major northeast trending faults along the western margin, the Newark Basin of New Jersey is filled with thick, clastic sediments transported from the west. Igneous events have resulted in dikes, extrusive units, sills and plutons.

As a result of its' extent in New Jersey, the Newark Basin is a source of potable water as well as a repository for hazardous waste. Many large structures are built upon and within the basin and many more are planned for the future. Hence, a thorough understanding of its physical characteristics is necessary whether one wishes to 1) locate a potable water supply, 2) cleanup a hazardous waste site, or 3) build upon or within it.

---

[1]Trademark of Schlumberger Well Services

At the two sites described herein, both the structural and hydrogeological properties of the Passaic Formation were of significance. Traditional field techniques (high-quality coring, detailed logs and pump test data) were used to characterize the formation. In addition, a new oil field geophysical tool, a downhole microresistivity (MR) tool was employed in four borings ranging in depth from 105 to 500 feet below the ground surface. The available geologic information for each site was expanded and enhanced by correlating FMS data with the results of continuous and careful coring and logging in three boreholes at these two sites.

FORMATION MICROSCANNER TOOL

The MR tool images the borehole wall by utilizing a four pad array of sixteen microconductivity electrodes each. The electrodes examine 0.1 inch vertical increments laterally around the borehole wall as the tool is pulled uphole. A triaxial accelerometer and three magnetometers are used to determine tool orientation and subsequently, attitudes of bedding planes.

Variations in currents for each of the electrode buttons are recorded in a series of traces. These variations in microresistivity can be caused by changes in porosity, grain-size, mineralogy, cementation, and fluid type. The resistivity traces are converted to a sixteen channel white, black or gray image with white denoting the highest resistivity and black the lowest resistivity.

Data processing is required to correct for variations in tool movement, voltage output and button contact. The image is converted from gray shades to a 256 channel color image, on a specially designed workstation, in order to improve analysis capabilities.

Figures 1 and 2 show typical black and white copies of workstation displays taken from the two sites discussed. Bed thickness can be identified to an order of 1 mm. Bedding planes and fluid-filled fractures are readily seen and can be selected for true dip and strike calculations. A three dimensional display aids the interpreter in visualizing in situ characteristics at varying orientations. Stratigraphic patterns can be measured and described with an unusual degree of confidence. Lithological features such as grain-size, porosity and mineralogy can be identified to a relative degree. With the use of a calibrated resistivity curve and borehole fluid salinity measurements, the fracture aperture can be measured within a fraction of an inch.

PASSAIC FORMATION - NEW JERSEY

The Newark Basin shows two fundamental depositional patterns (Schlisse and Olsen, 1990). The first is fluvial, formed in a hydrologically open basin and characterized by 1) basinwide channel systems; 2) lenticular bedding; 3) conglomerate intervals; 4) paleocurrent patterns that are often axial or trend in one direction across the basin (indicating extensive subsurface drainage); and 5) the lack of evidence of large lakes, although some pond or paludal deposits have been noted. The second is a lacustrine pattern that would be consistent with a hydrologically closed basin model. These criteria include (from Smoot, 1985): 1) increases in grain-size toward the basin boundaries; 2) paleocurrent patterns away from the basin borders; 3) local coarse-grained strata near the basin margins; 4) evaporites or evaporite crystal clasts; and 5) cyclicity of fine-grained sedimentary rocks in the central basin. Cyclically deposited lacustrine beds extend over large areas (Olsen, in press), and the basin margins show significant deposits of lake-margin fluvial and deltaic sequences, as well as alluvial fans. Within the basin, these two generalized depositional systems are very

persistent through time and are the largest stratigraphic elements of the Newark Basin, although igneous extrusive and intrusive flows are common, particularly near the border fault.

From a structural standpoint, the Newark Basin may be considered a half-graben bounded by northeast trending, southeasterly dipping faults (the Ramapo border fault system) to the west and gently westward dipping strata to the east. Numerous faults, both synthetic and antithetic to the border fault in nature, are recognized throughout the basin. Numerous, generally northwest trending thrust features have been mapped across the border fault and would probably be found within the basin itself if further investigation were undertaken.

The available literature did not indicate any faulting in the vicinity of either site discussed herein, although shear zones and/or jointing could be expected anywhere as a result of the major movements that have taken place in this rift basin.

The current in situ stress system is believed to be generally consistent with that of much of the northern Atlantic coastline. The minor principal stress is vertical, with the major and intermediate principal stresses of a compressive nature. Thus, the in situ stress system would tend to open any uncemented sub-horizontal bedding planes. With the major principal stress oriented to the northeast, one would also expect that shallowly dipping fracture zones oriented in a northwest/southeast direction would be those most susceptible to movement.

PASSAIC FORMATION - SITE SPECIFIC

General

In the literature (New Jersey Geological Survey Atlas Sheets and Summaries, and Monteverde, in press), the structure and lithology of the two sites in question (although separated by some 10 miles) are relatively similar. Site A had two wells logged with the Formation MicroScanner tool, with one well cored with a triple-tube, wireline, split barrel. Site B had two wells cored with a triple-tube, wireline, conventional barrel and were logged in a similar manner. The Passaic Formation (formerly known as the Brunswick Formation or Brunswick Shale) was believed to be relatively thinly-bedded and presumed to be a primarily sandy section at Site A, while at Site B, the section was presumed to be more silty. Bedding was reported to dip about 15° northwest with a N±30°E strike at Site A and dip at about 8° to 10° northwest with a N±40°E strike at Site B.

Table 1, below, prepared from as yet unpublished (New Jersey Geological Survey) information, summarizes the range of hydrogeologic characteristics measured in various tests within the Passaic at a number of locations throughout the Newark Basin. As may be seen from Table 1, the large variations in properties from the many sites would seem to indicate the non-uniformity of the formation, perhaps indicating the typical, current assumption of uniform anisotropy is, at best, a local condition.

TABLE 1

HYDROGEOLOGIC ESTIMATES - PASSAIC FORMATION

Transmissivity = 400 to 88,200 gpd/ft

Storativity = 1x10-6 to 4.5x10-6

Hydraulic Conductivity = 0.15 to 90 ft/day

From a structural standpoint, the rocks can be considered to be relatively weak, brittle sediments, sometimes with open bedding planes and joints. Although not necessarily noted in the literature, fractures are often closed with secondary mineralization. Soft rock tunneling machines generally would be appropriate for controlled excavation. Ordinarily, blasting is necessary for conventional excavation below some ±10 feet beneath the varying depth weathered zone. Excavation in fault zones has proceeded, easily, to the maximum reach of the available equipment.

Hydrogeologically, a series of papers have described the Passaic sediments somewhat differently, but perhaps in a more definitive manner with time and increased information. The earlier papers on the subject, by a number of geologists in New Jersey (e.g., Vecchioli, 1965, and Vecchioli, et al, 1969), discussed the non-homogeneity of the aquifer system in the Passaic. These earlier studies and evaluations were a cooperative effort of the USGS and the forerunner of the NJGS. It was generally accepted by these investigators that drawdown along strike was greater than drawdown parallel to strike.

In the Vecchioli, 1965 paper, transmissivities were reported at sites in Kenilworth, Linden, New Brunswick, Wyckoff, and Flemington. T values ranged from about 400 to 88,200 gallons/day/foot (gpd/ft) apparently using Theis, 1935 assumptions to analyze the test results. "Always, cross-strike T's were less than along strike T's". The 1969 Vecchioli, et al paper concluded that the Passaic had "anisotropic hydraulic properties everywhere. The degree of anisotropy varies from place to place. In some areas it is considerably less; in fact, it may even approach isotropy. Where mildly anisotropic conditions exist, one could conclude that discrete producing zones do not occur, but that the formation is thoroughly dissected by interconnecting fractures resulting in hydraulic continuity in all directions. Nonetheless, drawdown is always greatest along strike".

In a later paper, Michalski (1990) concluded: "Ground water flow in the Passaic appears to be influenced primarily by partings along bedding and by the contrast in degree of fracturing between beds. A lingering belief that near vertical fractures oriented parallel to the strike of the beds dominates the flow is not supported by field data.

"On a scale typical of most ground water contamination studies, the Passaic hosts a multiunit, leaky ground water system in which individual water bearing units are relatively thin and parallel to the bedding. A large scale anisotropic flow pattern results from the inherent heterogeneity of the multiunit system. Along strike flow direction is favored within the saturated reaches of individual water-bearing units, and vertical flow across intervening aquitards is produced by head differences in the water bearing units".

Boyle's (1991) study of a well field in Pennington had a number of interesting conclusions, as follows:

1. There was a "general trend of increasing water level depth with increases in well depth".
2. The hydrogeologic analysis in the paper supported an earlier theorization of a fault fracture system "complicity" in measured well interference effects.

Rather than the more conventional Theis analysis, Boyle utilized (apparently successfully) the Jenkins and Prentice, 1982 analyses which presumes a dominant fracture system as the major influence on water movement.

If one were to attempt to summarize the literature available in 1993 for the Passaic Formation, both sites would be presumed to be geohydrologically similar, as follows:

A multi-layered aquifer system with low primary porosity and rela-

tively high secondary porosity. Water could be found under both confined and unconfined conditions. Secondary porosity would be primarily composed of major bedding plane partings and near-vertical joints. If existing at a site, faults or fracture zones could also influence water movement. However, in the absence of faulting a "uniform anisotropy" could be presumed in evaluating test data.

Site A

Figure 3 shows 20 feet of core run taken from the 311 foot deep well at Site A (correlative with the MR log, Figure 1). The recovered core is consistent with the generic description of the Passaic Formation except, perhaps, for the relatively interbedded nature of the rocks encountered in this borehole which, in effect, results in massively- rather than a thinly-bedded nature. Additionally, far fewer sandstone layers were encountered throughout the borehole than might be assumed from the available local information. The interbedded nature of the formation at this location is quite evident on both Figures 1 and 3. Fractures, bedding plane partings and mineralization were noted on the core logs throughout the full depth of the borehole.

Our interpretation of the MR log of this hole was completely consistent with the core log in relation to type and thickness of the various beds and major fracture locations. In addition, the MR log indicated that structural dip generally ranged from 10° to 12° to the west-northwest (although some dips as high as 20° were measured). The log also indicated uncorrected depositional flow to the west-northwest. Porosity was estimated to be in the 6% to 10% range in the shales and 16% to 21% in the sandstones and conglomerate zones.

In general, fracture aperture was small (<0.1 mm) and dipped at an angle of 60° to 80°. Partial healing was apparent in most fractures. Fracture orientation was predominantly east and southeast in the deep well and random in the shallow (105 foot) well. Some indication of bedding displacement is visible in both boreholes. This could have resulted from nearby faulting. However, any fault orientation is not readily identifiable from the MR images.

A pump test on the deep well yielded a transmissivity value of about 0.0005 ft^2/min (5 gpd/ft) using the "confined leaky" assumptions described in Hantush, 1956. The shallower well had a measured transmissivity of 0.016 ft^2/min (170 gpd/ft) in the same multi-well pump test with the same Hantush, 1956 aquifer assumptions. Other wells at the site had T values as high as 0.19 ft^2/ min (2,000 gpd/ft). One high T well was only 150 feet from the 311 foot deep, low T well. Thus, there is no evidence of any homogeneity or uniform anisotropy from the multi-well pump test performed at the site.

Site B

Two deep (500 foot) holes were cored at this site using a triple-tube, wireline, split core-barrel. The core log for the 481 to 489 foot depth in one of the boreholes is provided as Figure 4 (see also the MR log of this interval on Figure 2). In general, the logs show thinly- to massively-bedded shales, siltstones and sandstones. Porosity ranged from about 10% in the shales to 16% to 18% in the siltstones and sandstones. Calcareous fracture fillings were noted throughout both the core and the photoelectric factor (PEF) curve.

Bedding planes dipped 10° to 15° to the northwest, with again, an apparent (uncorrected) northwest sediment transport direction. Fracture aperture ranges from about 0.1 mm to 1.0 mm. Many fractures are healed. Fracture orientation was predominantly to the southeast at about 90° to the structural trend. Additional fractures were detected in a west-northwest direction dipping at about 20° to 30°, which would be consistent with the present regional stress regime.

Using the structural information for the two borings at this site (spaced some 700 feet apart) a N±30°E striking fault, dipping ±45° to the southeast can be postulated. As interpreted, this fault would pass quite close to the northerly well.

A pump test in the more southerly well yielded transmissivity values of 0.05 ft^2/min (500 gpd/ft) with the "confined" aquifer assumptions of Theis, 1935 and similar, but slightly lower values with the Moench, 1984 fractured rock aquifer assumptions.

ENGINEERING GEOLOGY ASSESSMENT

From an engineering geology standpoint, several concerns were quite evident from the investigations at these two sites. First and perhaps most important is the extreme variability of the Passaic Formation over relatively short vertical and horizontal distances. Even in relatively close boreholes (essentially on-strike at Site B), all with full core recovery and a suite of geophysical logs, lithologic correlation was impossible. The borings are fully representative of the lithology described in the literature and often seen in outcrop, but definitive, continuous marker beds are rare and geophysical signatures are probably the most suitable (albeit questionable) means of correlating between borings. In fact, the attempts to draw a cross section at Site B were finally predicated upon bedding plane dip variations, uranium-thorium measurements and volumetric analyses rather than upon conventional lithology or gamma ray signatures.

This variability probably results in the need to make conservative simplifications in subsurface assumptions in designing structures on or through the Passaic. Additionally, fracture zones, which will certainly influence supporting capacity, slope stability, as well as tunnelling procedures and lining, are probably quite common. Obviously, investigations, planning, design, and construction must consider the likelihood of major or minor fractures through the brittle rocks of the Newark Basin. Perhaps even more important in subsurface construction is that these fractures will be the primary conduits for water or contaminant movement.

HYDROGEOLOGIC ASSESSMENT

The results of the various evaluations at these two sites indicate that studies performed within Passaic Formation rocks must be conducted with care and with the knowledge that the hydrogeologic characteristics of the formation may vary rapidly over short horizontal distances. At both locations, determining the strike and dip of the bedding would have been difficult (if not impossible), even with oriented core, because of the lack of obvious marker beds.

Bedding plane openings (size and frequency) were extremely variable from location to location, and even from well to well at Site A. Thus, the pervasiveness of bedding plane openings that might be presumed to exist from some of the available literature was not found at these sites. It is important to note that only the MR logs could show the nature of the bedding planes in situ, i.e., tightness, aperture size and filling.

The estimates of porosity made from the MR logs are also unique to these procedures. Alternate methods of measuring porosity would likely require laboratory testing.

The MR logs also provided a much better understanding of the fracture systems at each site than could have been obtained in any other manner, even with oriented core.

SUMMARY AND CONCLUSION

The quality of the subsurface data developed in these projects is a result of the use of old fashioned, good drilling and core logging combined with sophisticated, high-resolution geophysical technology. The combination of techniques allowed a far better understanding of the physical properties of the Passaic Formation than was available in the past. It was recognized in the past that the Passaic (Brunswick) was not homogeneous (e.g., Vecchioli, 1965), but neither can it be accurately described as a simple(?) uniform anisotropy model (e.g., Michalski, 1990), except perhaps in localized areas.

While the Formation MicroScanner log provided information not available from conventional drilling techniques, modern core barrels and careful core logging, the authors wish to emphasize that it does not replace conventional procedures, but we do believe that it is an invaluable complementary tool.

By combining conventional and geophysical techniques at the two sites described herein, a somewhat different subsurface picture than commonly presumed was defined at both sites. Of the extensive geohydrological literature available on the Passaic Formation of the Newark Basin, Boyle's (1991) conclusions appear closest to those actual sampled at Sites A and B.

BIBLIOGRAPHY

Boyle, J., 1991. **A Case Study of Well Interference at Pennington, New Jersey**, draft NJGS Tech. Memo. 91-?.

Hantush, M.S., 1956. **Analysis of Data from Pumping Tests in Leaky Aquifers**, Amer. Geophys. Union Trans., v. 37.

Jenkins, D.N. and J.K. Prentice, 1982. **Theory of Aquifer Test Analysis in Fractured Rocks Under Linear (Nonradial) Flow Conditions**, Ground Water, v. 20, no. 1.

Michalski, A., 1990. **Hydrogeology of the Brunswick (Passaic) Formation and Implications for Ground Water Monitoring Practice**, Ground Water Monitoring Rev., Fall, 1990.

Moench, A.F., 1984. **Double-Porosity Models for a Fissured Groundwater Reservoir With Fracture Skin**, Water Resources Res., v. 20, no. 7.

Monteverde, D., in press. **Bedrock Mapping in the Weehawken Quadrangle**, NJGS.

New Jersey Dept. of Conservation and Economic Development, 1957. **Topographic Series Sheet 28 with Geologic Overlay**, NJGS.

New Jersey Geological Survey, in press. **Tables of Hydrologic Properties of Selected Formations**.

Olsen, P.E., in press. **Tectonic, Climatic, and Biotic Modulation of Lacustrine Ecosystems - Examples from Newark Supergroup of North America**, Lamont-Doherty Geol. Obs.

Schlisse, R.W. and P.E. Olsen, 1990. **Quantitative Filling Model for Continental Extensional Basins With Applications to Early Mesozoic Rifts of Eastern North America**, J. of Geology, v. 98.

Smoot, J.P., 1985. **The Closed Basin Hypothesis and the Use of Working Models in Facies Analysis of the Newark Supergroup**, Proc. of the 2nd USGS Workshop on the Early Mesozoic Basins of the Eastern U.S., USGS circ. 946.

Theis, C.V., 1935. **The Relation Between the Lowering of the Piezometric Surface and the Rate and Duration of Discharge of a Well Using Groundwater Storage**, Am. Geophys. Union Trans., v. 16.

Vecchioli, J., 1965. **Directional Hydraulic Behavior of a Fractured-Shale Aquifer in New Jersey**, Proc. of Symp. of Dubrovnik, Int. Assoc. of Scientific Hydrology.

Vecchioli, J., L.D. Carswell, and H.F. Kasabach, 1969. **Occurrence and Movement of Ground Water in the Brunswick Shale at a Site Near Trenton, New Jersey**, USGS Prof. Paper 650-B.

Downhole Formation Microscanner Study, Passaic Formation

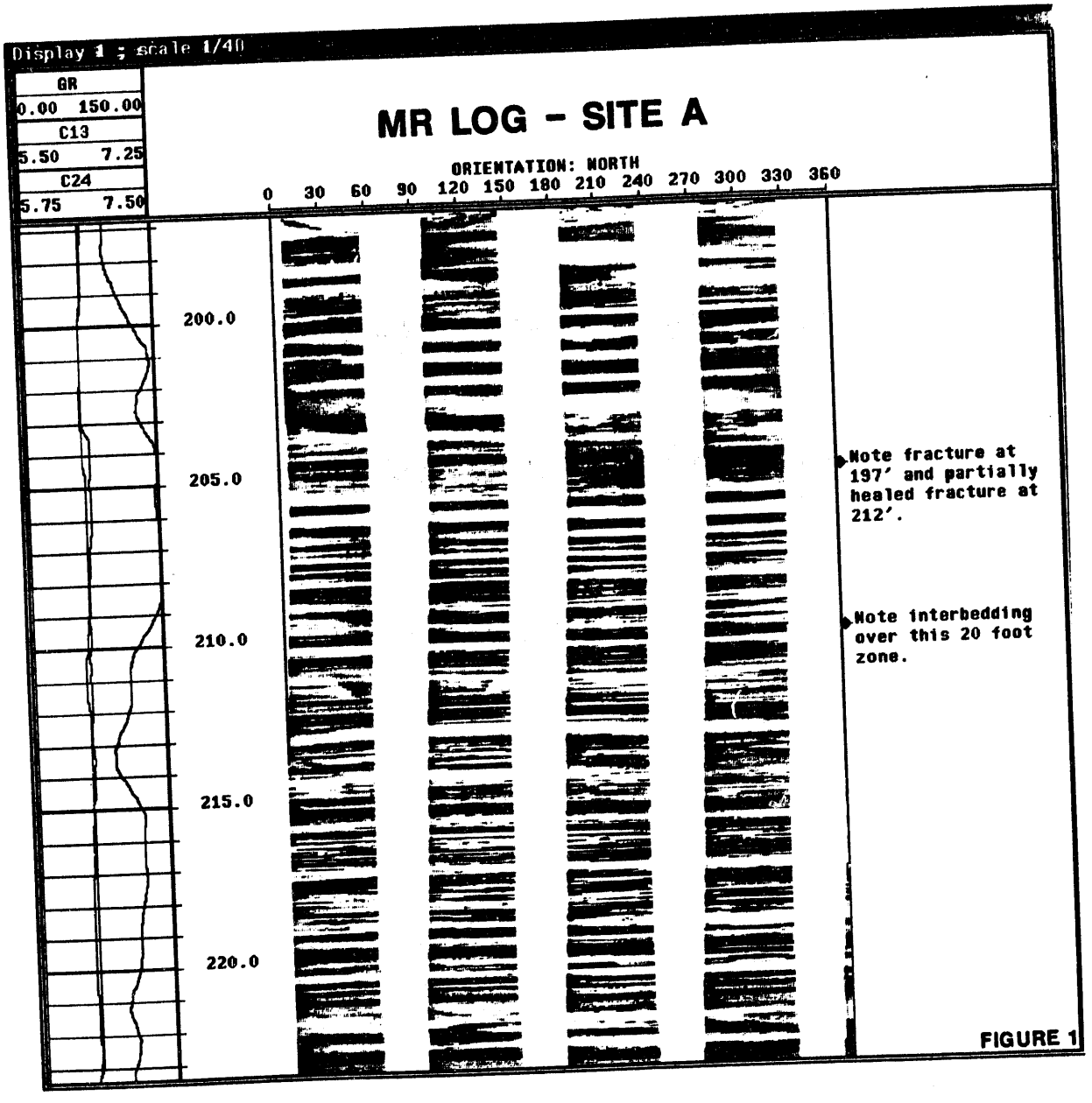


FIGURE 1

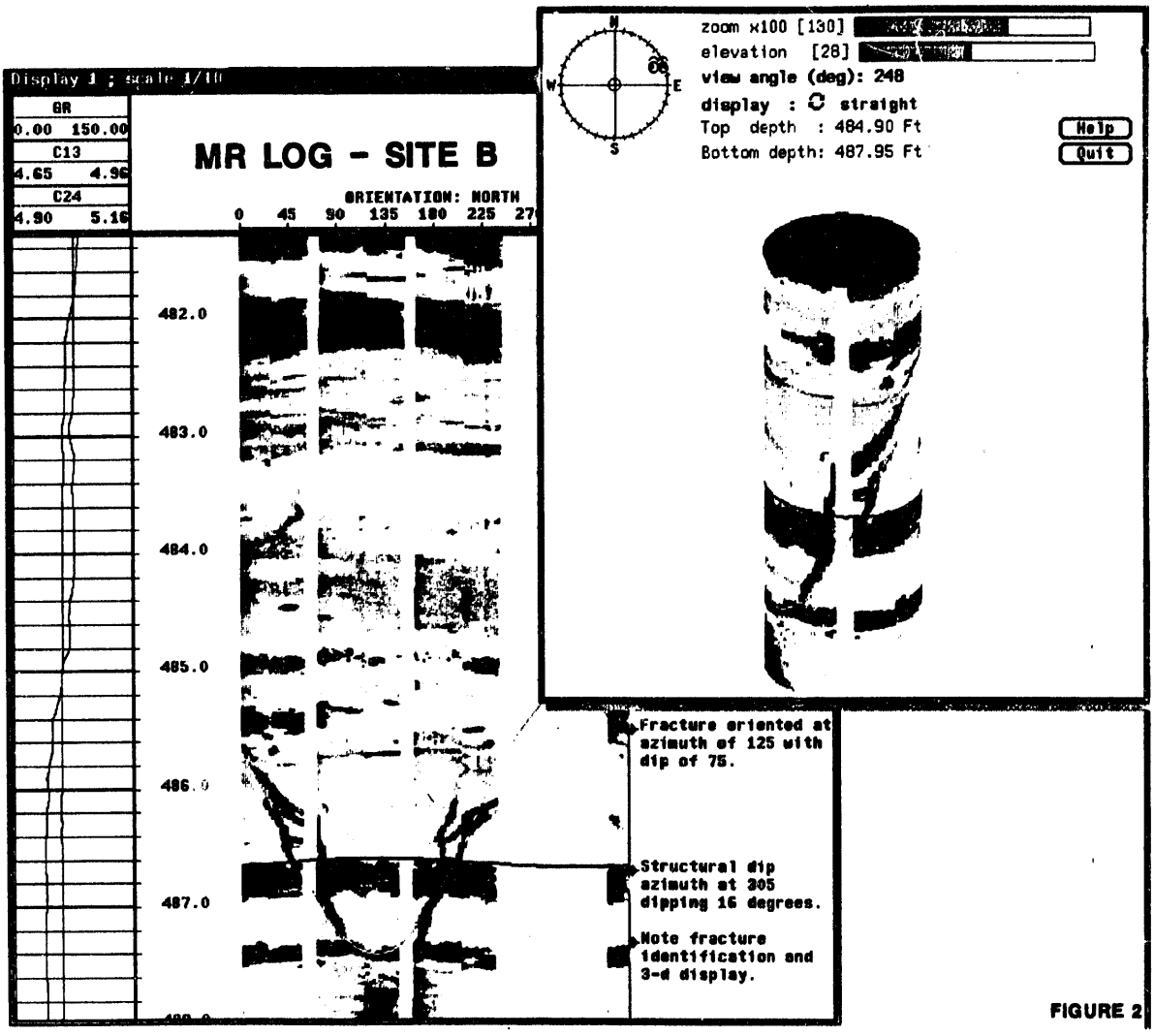

Display 1 ; scale 1/10
GR
0.00 150.00
C13
4.65 4.96
C24
4.90 5.16
MR LOG - SITE B
ORIENTATION: NORTH
0 45 90 135 180 225 27
482.0
483.0
484.0
485.0
486.0
487.0
N
E
S
W
zoom x100 [130]
elevation [28]
view angle (deg): 248
display : straight
Top depth : 484.90 Ft
Bottom depth: 487.95 Ft
Help
Quit
Fracture oriented at azimuth of 125 with dip of 75.
Structural dip azimuth at 305 dipping 16 degrees.
Note fracture identification and 3-d display.

FIGURE 2

CORE LOG - SITE A

DEPTH IN FEET	SAMPLE	STANDARD PENETRATION RESISTANCE	SYMBOL	DESCRIPTION	CORE RECOVERY	RQD	JOINT FREQUENCY
195				Brown shale grading to grayish red med sandstone (195' - 196.2')		196.2' Run 19	
				Lt red, fresh, competent, med sandstone, unweathered partings at 3" - 2.5'(196.2' - 201.2')			
200				Mineralized joint plane at 70° to 75° (197')	97.5%	83%	0
				Brown shale (201.2' - 202.5')			
				Lt red, med sandstone w/ vertical mineral-filled veins (202.5' - 204.5)			
205				Brown shale grading to med, red/brown sandstone, open, mineralized fractures (204.5' - 207.5')		206.2' Run 20	205.0 to 206.2 at 80°
				Micaceous brown shale, silt stringers, mineral filled partings at 4" - 6" (207.5' - 210.2)			
210				Interbedded shale, siltstone, sandstone, graded, sediment deformation (210.2' - 211.5)	100%	90%	
				Competent pinkish red to gray/red, laminated sandstone, partings at shaley laminations, fresh (211.5' - 215.2')			
215				Turbidites of sand to shale, partings at <1" - 8", fresh (215.2' - 217.5')		216.2' Run 21	223.5 to 224.2 at 80°
				Fairly competent interbedded, grayish red sandstone, brown/red siltstone, & stringers of brown & gray shale, partings at 6" - 15" - 18", usually at shale stringers, some of which are mineralized (217.5' - 226.2')	99%	89%	
220							

FIGURE 3

CORE LOG - SITE B

DRILLING LOG	HOLE NO: B	SHEET: OF	PROJECT: SITE B

ELEV. (FT)	DEPTH (FT)	LEGEND	DESCRIPTION	REC. (%)	SAMPLE NO.	SAMPLE TYPE	REMARKS	DRILL TIME
-485.0	481.0		SANDSTONE soft, permeable Munsell 10R 3/4 (dk reddish brown)	104.5% 61%	RUN 39		10° - 30° jointing Ø>α Crushed & shattered from 476.15' to 480.5' w/ vertical and horizontal jointing Fractured w/ vertical jointing from 480.5' to 484.2'.	2 20
-486.0	482.0							3 20
-487.0	483.0		SANDSTONE medium soft, fine, silty Munsell 10R 4/6 (moderate reddish brown).					6 20
-488.0	484.0						Ie = 196 PSI @ 483.9'.	6 35
-489.0	485.0		SANDSTONE medium soft, fine, silty Munsell 10R 4/6 (moderate reddish brown).				10° - 30° jointing Ø>α	9 25
-490.0	486.0		SANDSTONE soft, permeable Munsell 10R 3/4 (dk reddish brown)					4 45
-491.0	487.0		SANDSTONE medium soft, fine, silty Munsell 10R 4/6 (moderate reddish brown).				80° joint @ 487.5', Ø<α	4 35
-492.0	488.0		SHALE medium soft. Munsell 10R 3/4 (dk reddish brown).					6 00
	489.0		SANDSTONE medium soft. Munsell 10R 3/4 (dk reddish brown).					
			SANDSTONE soft, permeable. Munsell 10R 3/4 (dk reddish brown).					
			SANDSTONE medium soft. Munsell 10R 3/4 (dk reddish brown).					

FIGURE 4

Hydrogeology, Waste Disposal, Science and Politics
Proceedings 30th Symposium
Engineering Geology and Geotechnical Engineering, 1994

THE IDENTIFICATION OF BASALT FLOW FEATURES FROM BOREHOLE TELEVISION LOGS

William Bennecke, Boise State University, Boise Idaho

ABSTRACT

This study investigated whether basalt flow features found in outcrops and cores could be identified in open borehole walls by the use of the borehole television camera. To answer this question detailed outcrop surveys were carried out in several locations in the Snake River Plain, Idaho. A similar type of survey was also done on several cores from the Idaho National Engineering Laboratory, southeast Idaho. Borehole television logs were viewed to find similar basalt features that were noted in cores and outcrops. From these studies it was found that basalt features can be identified in open borehole walls by the borehole television camera. The basalt flows can be divided into four zones: an upper vesicular zone; a columnar zone; a central zone; and a lower vesicular zone. The upper vesicular zone can be further subdivided into four subzones: an upper vesicular subzone; a transitional subzone; a lower vesicular subzone; and a bubble train subzone. Some specific features found in the borehole TV logs were: bubble-trains, vesicle plumes, borehole extensions, and pipe vesicles.

The overall distinctions for the zones were based on their vesicularity. An overall pattern of vesicles was found to be a progression of small numerous vesicles at the top of a flow which increase in size, but decrease in number, towards the center of the flow. The opposite is true starting at the bottom of the basalt flow where small vesicles are numerous, but increase in size while decreasing in number towards the center part of the flow.

INTRODUCTION

Borehole television cameras have been used to inspect the inside of pipes, tubing, and boreholes which could not otherwise be satisfactorily observed (LeRoy, et al., 1977). A typical borehole TV camera is made of a long pipe housing a TV camera with its own source of illumination in the form of an internal lamp; operation of the tool is accomplished by lowering the camera down the borehole. The speed at which the camera is lowered, the lamps' intensity, camera scanning, focusing power, iris adjustments, and sensitivity are all controlled by equipment on the surface. As the camera is lowered information gathered by the TV camera is recorded simultaneously by a video-cassette-recorder (VCR) onto a video tape. Real-time viewing of what the borehole camera images can be seen by the operator on a TV monitor. Underwater viewing as well as open air records can be made in the borehole.

Borehole television logs were obtained from more than thirty wells by the U. S. Geological Survey at the Idaho National Engineering Laboratory (INEL). The INEL is located in the eastern Snake River Plain (ESRP), Idaho. Basaltic and sedimentary sequences underlie the INEL and are then underlain by rhyolitic lava flows, ignimbrites, and pyroclastic deposits. Basalts found in the ESRP are chiefly olivine tholeiite basalts that show little evidence of differentiation or contamination consisting of normative olivine and hypersthene, a single clinopyroxene, plagioclase, titanomagnetite, ilmenite, and brown glass (Kuntz, et al., 1992). Basalt rocks in the TV logs are of Quaternary age from the Snake River Group and Idaho Group (Malde, 1987 and Whitehead, 1992). The details of

the basaltic features found in these rocks can be observed in the borehole television logs, cores from the area, and outcrops.

METHOD

A number of outcrops were examined in the Snake River Plain area. Examination entailed measurements and observations of fractures, vesicles, color, and other physical features observed at outcrops. A similar type of examination was carried out on cores from the INEL. Following these two types of examinations, borehole television logs were inspected from the boreholes that have cores and from other boreholes throughout the INEL area.

Table 1: TV Logs and Cores at the INEL

BORE HOLE NAME	CORE	TV LOG	BORE HOLE NAME	CORE	TV LOG	BORE HOLE NAME	CORE	TV LOG
VVE-1		X	USGS 57		X	DD-33		X
VVE-3		X	USGS 70		X	DC-1		X
VVE-10		X	USGS 80	X	X	DC-2	X	X
USGS 41		X	USGS 81	X	X	DC-3	X	X
USGS 42		X	123	X	X	DC-4	X	X
USGS 43		X	ID-8		X	SI-13	X	X
USGS 44		X	ID-9		X	SI-14	X	X
USGS 45		X	ID-11		X	SI-16	X	X
USGS 46		X	DD-22		X	IC-5	X	X
USGS 47		X	DD-23		X	IC-7	X	X
USGS 48		X	DD-24		X	IC-10		X
USGS 50		X	DD-25		X	IC-12	X	X

Borehole TV logs are watched on a television from a VCR; the view recorded by the camera is one looking down the borehole with a fish-eye view that is distorted from a perpendicular view of the borehole wall. Still photographs are usually taken from TV logs, which are also distorted. Relative corrections can be made knowing how much distortion occurs to a reference unit as recorded on the picture. Two measuring devices (a 7 cm by 2.5 cm rod with 5 cm taped increments and a 61 m by 6 mm steel tape with taped 2 cm sections) were used as standards and were lowered down a 15 centimeter diameter casing. They were then recorded by a borehole TV camera on a VHS tape. This tape was then processed into a photograph and the relative distortion was measured (Plate 1).

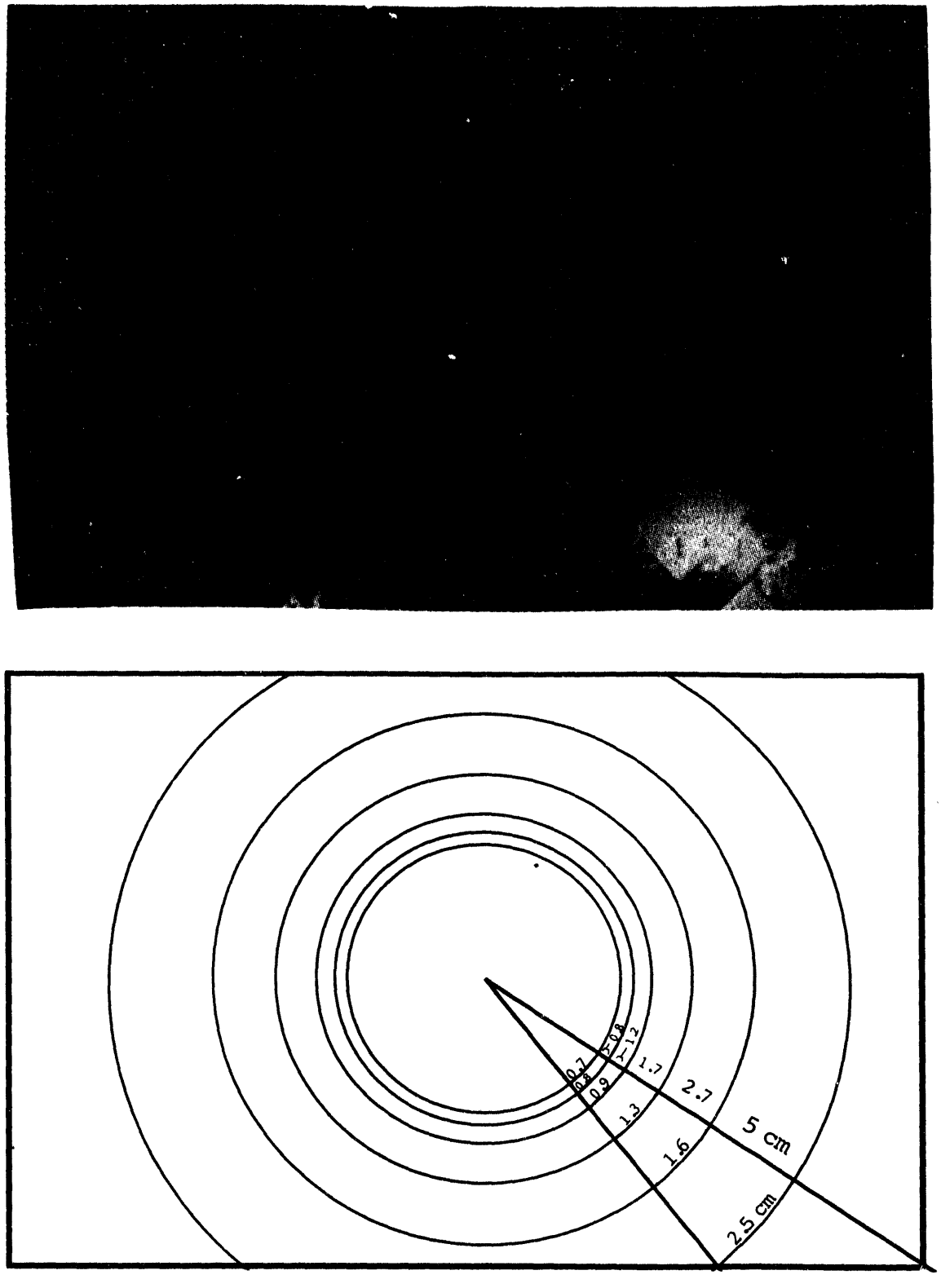


Plate 1. Calibration picture showing standard of reference and sketch.

Based on the measured changes in lengths and widths of the measuring devices a distortion factor was calculated by taking the slope of a best fit line on a graph of the change in length and width versus its position on the standard (Figures 1 and 2).

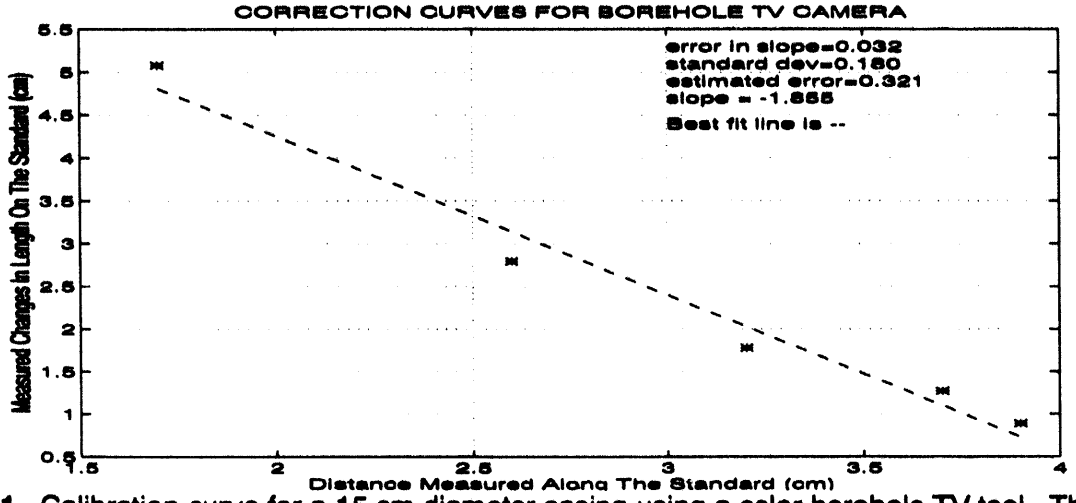


Figure 1. Calibration curve for a 15 cm diameter casing using a color borehole TV tool. The change in a standards length was measured in a borehole TV picture for each increment along the standard. These changes in length are plotted for each increment. The solid line shows a nonlinear relationship. A best fit line (dashed) has been plotted in the data and the accompanying slope calculated for a scale factor for a borehole photograph. This approximation can be used to calculate how much distortion has taken place to an object measured from photographs from a borehole TV log. Distortion factor: -1.855.

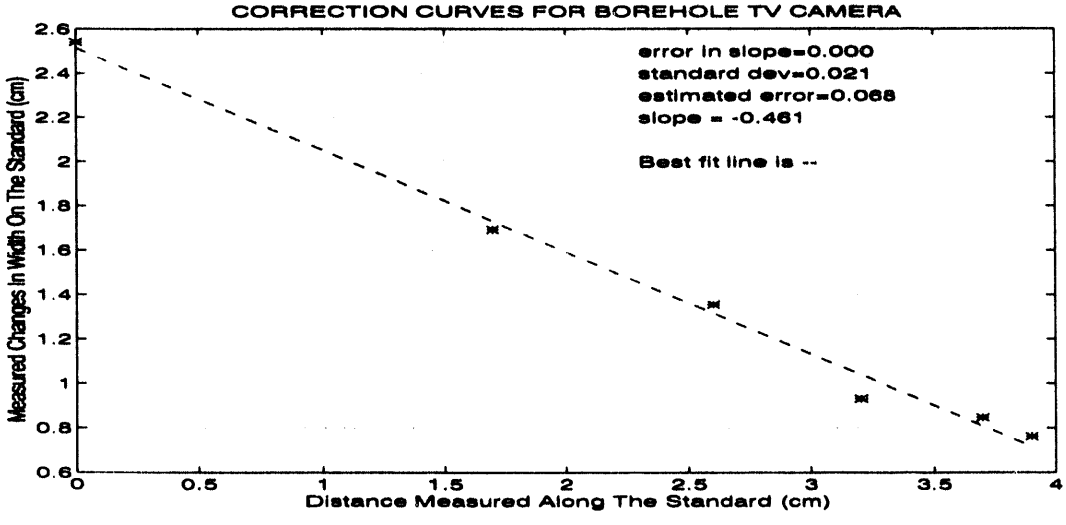


Figure 2. Calibration curve for a 15 cm diameter casing using a color borehole TV tool. The change in a standards width for each increment along it was measured in a borehole TV picture. This change in width was then plotted followed by a dashed best fit line. The slope of the dashed line was calculated for a distortion factor that can be used to determine how much an objects width will change when it is measured anywhere on the picture. Distortion factor: -0.46.

A distortion factor of -1.855 for the change in the length and -0.46 factor in the change in width of an object was calculated. To obtain the correct dimensions of an object simply measure its dimensions on the photograph, multiply by the distortion factor, then take the original measured value and subtract from it the value multiplied by the distortion value.

The distortion factor is accurate only for the 15 centimeter diameter portion of the boreholes and can not be used for other wells of different diameters. Fifteen centimeter casing is very common in the INEL and the distortion factor for it can be used with minor loss of accuracy when looking at diameters from 12.7 cm to 15.24 cm.

A dark circle can usually be seen in the middle of the photograph taking from a borehole TV camera; this object is not a feature found on the basalt borehole wall. It is a 5.4 cm diameter metal cap for the lighting unit that is positioned under the camera.

Nomenclature

Based on observations of borehole TV logs a model of what a typical basalt flow would look like was generated for reference (Figure 3).

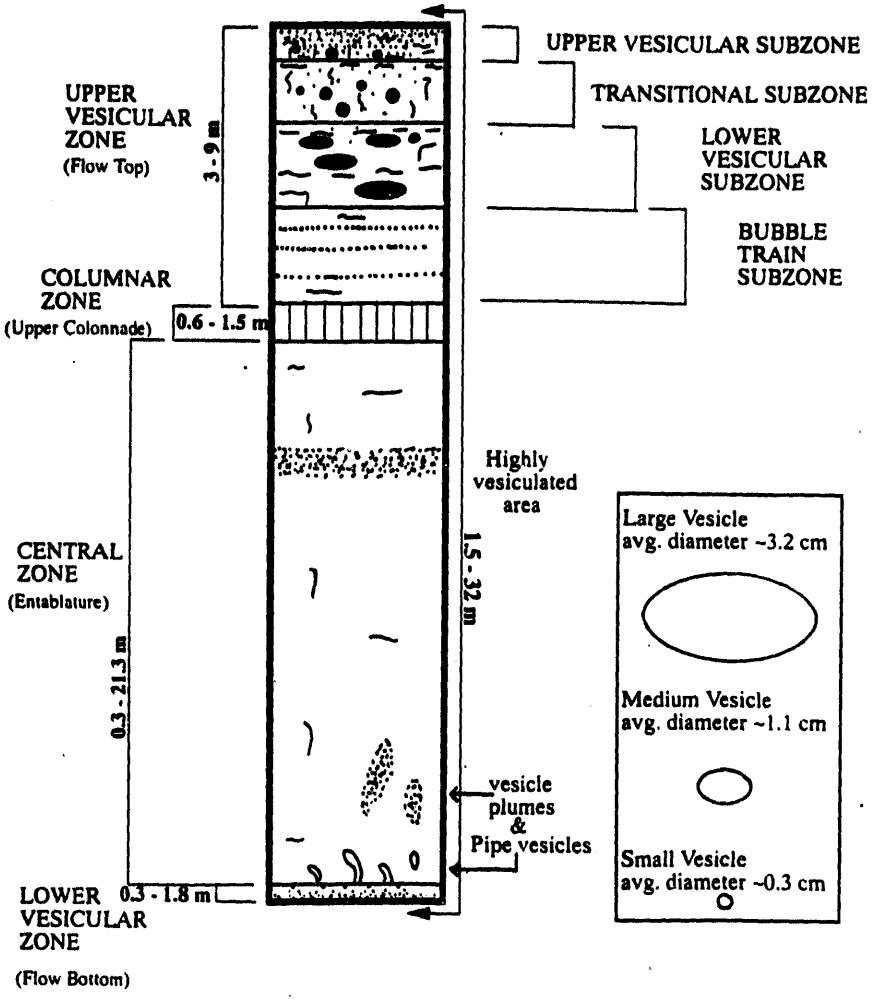
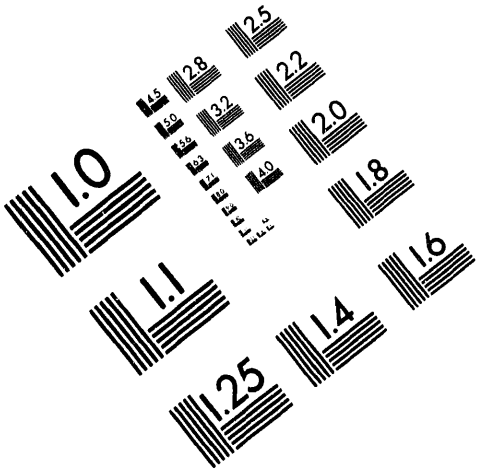
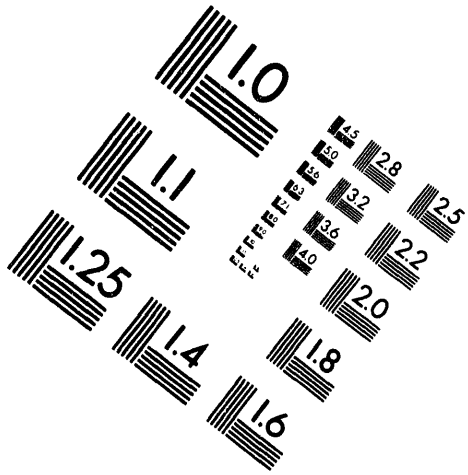


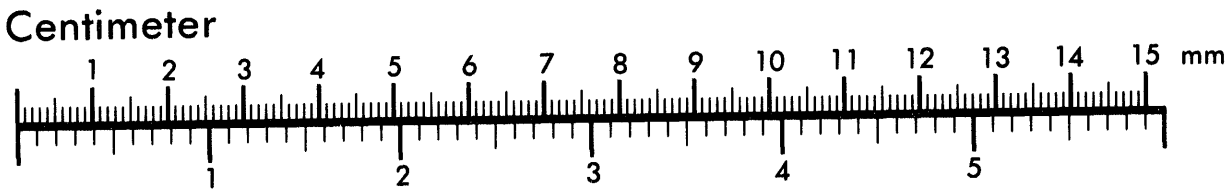
Figure 3. Schematic diagram of an ideal basalt flow in the eastern Snake River Plain, based on TV camera logs. Average diameters for large, medium and small vesicles and general shape are also shown.

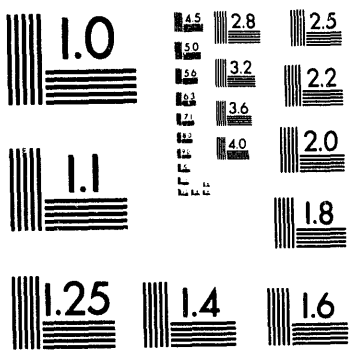


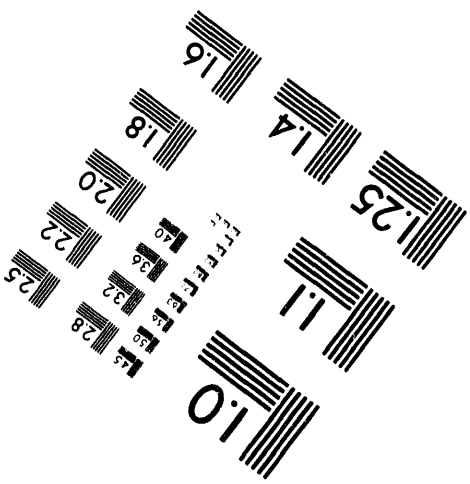


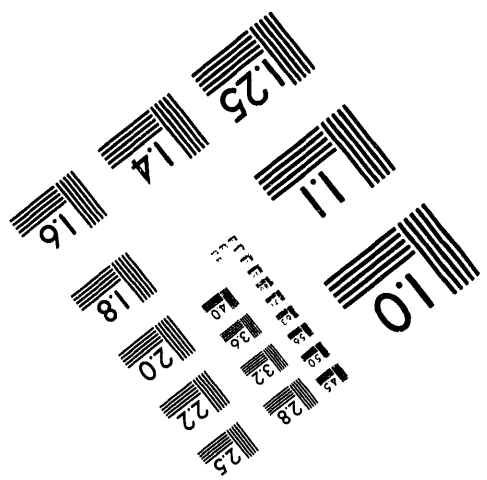
Association for Information and Image Management
1100 Wayne Avenue, Suite 1100
Silver Spring, Maryland 20910
301/587-8202











MANUFACTURED TO AIIM STANDARDS
BY APPLIED IMAGE, INC.

5 of 7

The model is based on the work of George Faust in the Watchung Basalt Flows (Faust, 1978). An upper vesicular zone, columnar zone, central zone, and lower vesicular zone make up an idealized basalt flow. The upper zone is further subdivided by four subzones an upper vesicular subzone, transitional subzone, lower vesicular subzone, and bubble train subzone. Entablature is a term used for the central massive zone while the upper and lower vesicular zones can be labeled colonnades. These zones may be absent in a given basalt flow.

Typically the entablature occupies the interior one-third to upper one-half of a flow (Long, et al., 1986) and maybe the thickest portion of the lava flow. A basalt flow also may have colonnades; either an upper or lower, or both may be present. Colonnades typically occur in the lower or upper third of a flow with the entablature between the two colonnades (Long, et al., 1986). Well spaced, near-vertical columnar jointing is very common in colonnades and this differentiates them from the entablature.

UPPER VESICULAR ZONE

Upper Vesicular Subzone

The upper vesicular subzone makes up the smallest portion of the upper vesicular zone and has the greatest vesicularity. The size of the vesicles are very small (average diameter 0.3 cm), but they are nearly perfectly spherical in shape (Plate 2).

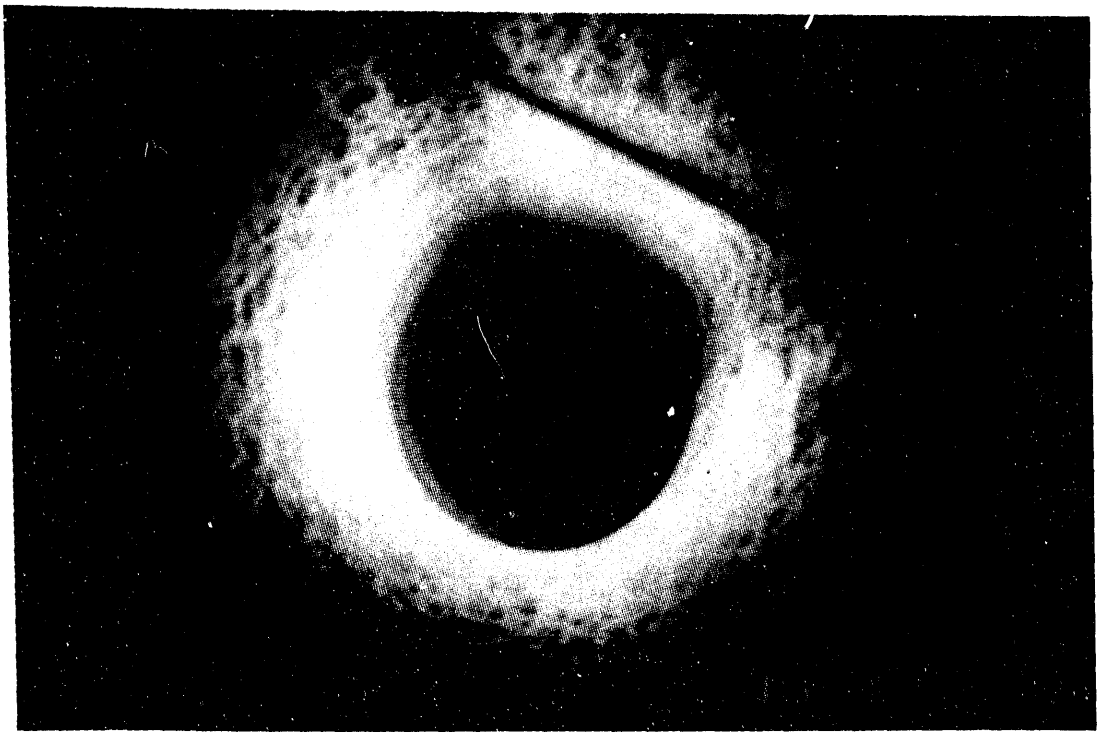


Plate 2. Borehole TV picture of the upper vesicular subzone. Notice the many vesicles present (Picture from borehole TV log of well VVE-3 RWMC, INEL).

Vesicles are small round cavities in the basalt and are the result of gasses being exsolved from cooling lava. Numerous fractures found in this subzone have a characteristic light colored material filling them. Based on observations from the TV logs at the INEL this subzone commonly ranges from 15 cm to one meter in thickness. In the upper subzone of the upper vesiculation zone red colored basalt with white coating of vesicles and fractures are very contrasting to the center part of a basalt flow. Most of the white color comes from alteration of the basalt in the form of calcite with zeolites possibly from water transport through the fractures and vesicles in the rock (Lanphere, et al., 1993) and secondary mineral precipitation. Red discoloration is most likely the result of oxidation of the rock during the initial deposition of the lava flow and possibly baking from an overlying flow (Lanphere, et al., 1993).

Transitional Subzone

The most prominent features found in the borehole TV logs in the transitional subzone of the upper vesicular zone are vesicles. Both the size and number of the vesicles are changing towards the center of a flow. The overall vesicularity or density of vesicles is intermediate between the upper vesicular subzone and the lower vesicular subzone. Large and small vesicles can be found there but medium sized vesicles are the predominate types (average diameter 1.1 cm); large and medium vesicles outnumber smaller ones. The medium sized vesicles tend to occur towards the center of the flow and above the larger vesicles in the lower vesicular subzone. Medium vesicle shapes are oblate spheroids, and are more spherical in shape than the larger vesicles. This subzone is usually thicker than the upper vesicular subzone but thinner than the lower vesicular subzone and the bubble train subzone below.

Lower Vesicular Subzone

Vesiculation is less in the lower vesicular subzone than in the upper vesicular subzone and the transitional subzone. These vesicles are larger (average diameter 3.2 cm), but small and medium vesicles can also be present (Plate 3).



Plate 3. Borehole TV picture of large vesicles making up the lower vesicular subzone. Notice the oblate spheroidal shape of the vesicles (Picture from borehole TV log of well VVE-3 RWMC, INEL).

Large vesicles are the result of coalescing of many smaller vesicles (Walker, 1989). Diktytaxitic textures might puncture the walls of forming bubbles, aiding in the coalescence process. The term diktytaxitic was applied by Dickinson and Vigrass (1965) to a distinctive texture, found in some basalts, that is characterized by the presence of numerous angular voids interstitial to the crystals. These voids are due to a volume decrease that accompanies crystallization of the liquid or by the late-stage release of gasses by crystallization (Walker, 1989). The irregular shape of these vesicles and their larger size suggest that they maybe the result of diktytaxitic interactions with coalescing bubbles; although in the TV logs diktytaxitic textures can not be seen. Cores studied from the INEL indicated that the midflow portions were commonly diktytaxitic. Fewer larger vesicles can be found further into the center of the flow with the vesicles at the bottom of the lower subzone being the largest. Not only is the size of the vesicles different, but the overall shape of the vesicles is also changed in that they are more oblate spheroids. Some vesicles may have secondary crystalline material filling the inside of the void space from circulating ground water making them amygdules (Macdonald, 1967). These can usually be seen by the borehole camera as a reflecting substance appearing as the camera passes the vesicle.

Bubble Train Subzone

The bubble train subzone is the lowermost and thickest (around 2 meters) subzone making up the upper vesicular zone. Bubble trains are thin (ranging from 0.1 to 2 cm thick) tabular laminae of small vesicles that are parallel to the top of a flow (Plate 4).

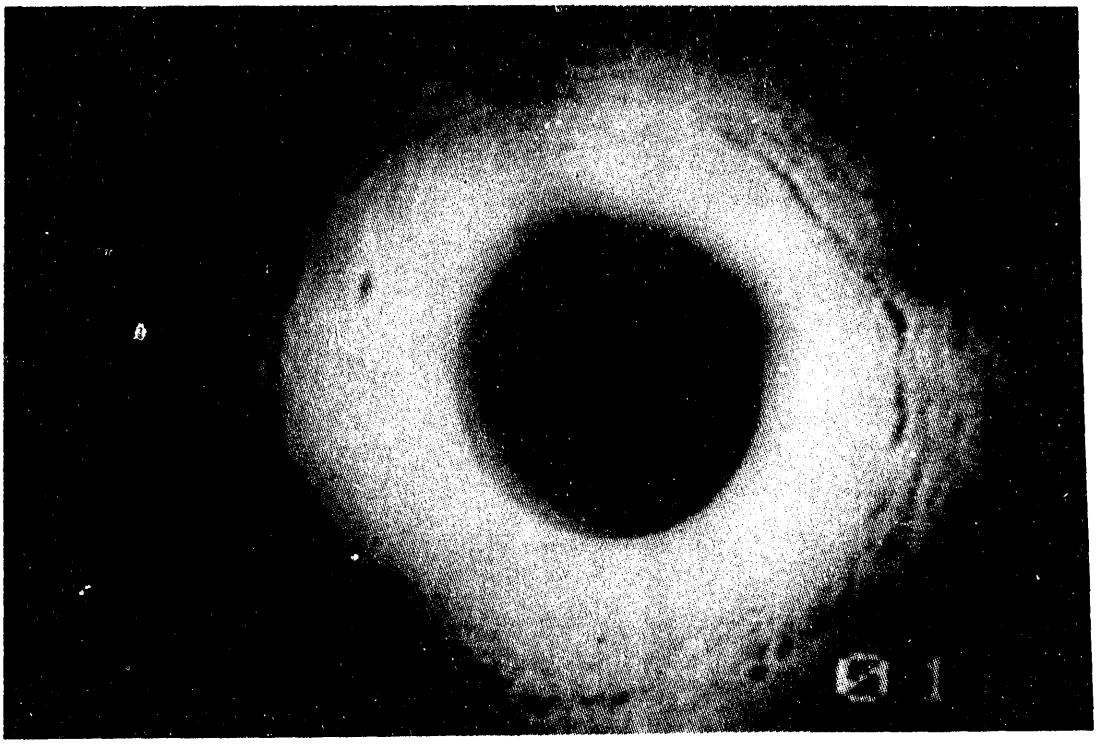


Plate 4. Borehole TV picture showing a bubble train in the bubble train subzone (Picture from borehole TV log of well VVE-3 RWMC, INEL).

Termed "micro-vesicular lamina" or "vesicle sheets" by McMillan, et al. (1987) represent vesiculation in melt within the crystal framework of the rock or they might be the result of the liberation of gases from residual crystals at the point of solidification. In outcrop these vesicle rich laminae form a crude line across a basalt surface which can be easily seen. These trains occur within an area of diktytaxitic texture; furthermore, they crosscut large vesicles meaning that they formed after the larger vesicles. The trains are very common in the upper portion of this subzone; however, the number of trains decreases towards the center of the flow becoming very rare in the dense central zone. Spacing between trains varies greatly from 3 cm to 3 m or more. In outcrop the bubble trains may be traced along the entire length of the flow.

COLUMNAR ZONE

The thickness of the columnar zone can vary greatly and usually makes up only a small portion of the flow. The relative location of this zone within a basalt flow is also highly variable; it commonly occurs in the colonnades just under the flow tops or occasionally at flow bottoms. In some basalt flows it is completely absent. The zone is more

common in ponded basalt flows and can attain great thickness. Columnar joints form five or six sided polygonal columns with five sided pentagons being most common (Beard, 1959). These columns can range from 40 cm in diameter to 19 m in height (Beard, 1959). The origin of these features has well been studied and their formation has been attributed to contraction due to cooling which has overcome the tensile strength of the cooling rocks (James, 1920).

Boreholes have problems as due cores with their smaller diameters not being able to sample the larger polygons; however, evidence for their presence are found in TV logs. What can be distinguished is a regular jointing seen in the borehole wall and a jutting step-like pattern which is reminiscent of columns in outcrops. In some TV logs, hexagonal-like blocks with vertical fractures make up the sides of the borehole (Plate 5). Large cavernous areas are also common in these places which could be the result of the drilling of the columns.

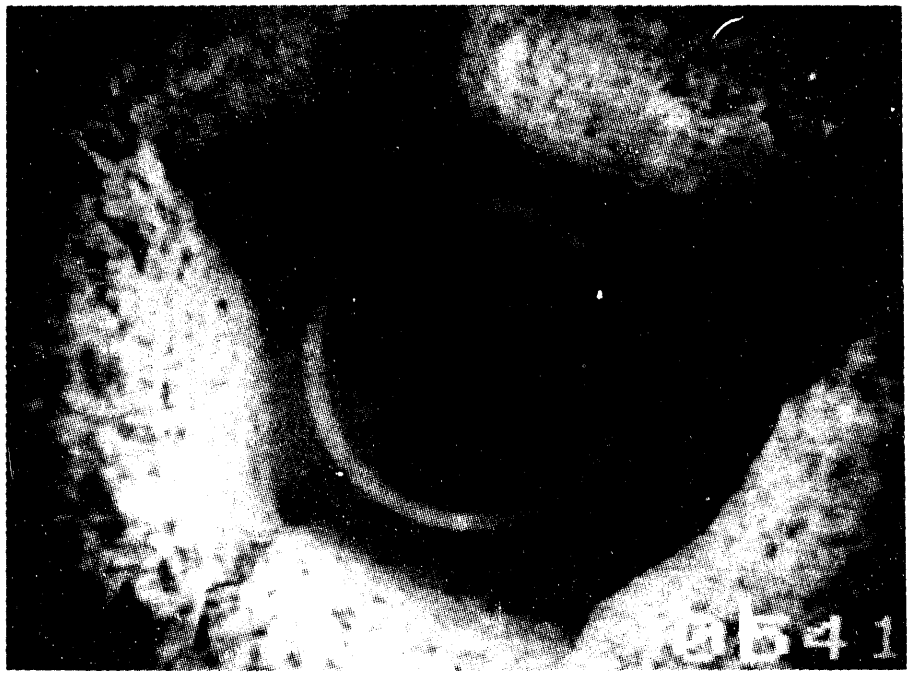


Plate 5. Borehole TV picture of the columns in the columnar zone. Jointing distinguishes the columns (Picture from borehole TV log of USGS well 44 ICPP, INEL).

CENTRAL MASSIVE ZONE

The central massive zone makes up the thickest portion of the basalt flow. These zones are easily identifiable both in cores, outcrops and in the TV logs as a very smooth textured surface lacking vesicles or many fractures. The thickest zone identified by me in the TV logs of wells at the INEL is 21 meters. Occasionally a very pronounced area of vesicles is encountered in this zone; these areas can range up to 0.3 meters in thickness. Above and below these areas vesicles commonly are absent throughout the central massive zone. More rare are areas of extreme vesiculation called vesicle plumes or "vesicle cylinders" by McMillan et al., (1987). Plume is a more accurate term in that their shapes are very irregular. Such as irregular amoebid-like shapes with long linear vesicu-

lar arms coming out of the general mass. Unlike the trains, the plumes are not very long, with the longest being approximately 1.8 m (while the trains can go the entire length of a lava flow). The origin of these vesicles plumes is unknown. They are found more commonly in the lower part of the flow and thus could be the result of a lava flowing over a body of water.

Fractures and Borehole Extensions

Borehole extensions are areas where the borehole wall extends outward (maximum diameter measured by calipers is 53 cm) from the normal diameter. Fracture zones and borehole extensions can be found throughout a basalt flow. Fractures are most numerous in the upper vesicular zone, but longer fractures are found in the central zone. These extensions contain numerous fractures and rubble material. Extensions have very regular fractures to jumbled blocks in appearance. Many possible mechanisms can generate these fractures and extensions; blasting, the drilling process, tectonic adjustments, lava tubes, shelly pahoehoe flow tops, and others could be the cause of these features. In outcrops certain pockets of abundantly fractured rock occur that are not very large (only several meters) or deep into the rock itself; these pockets are very angular and broken up, yet lack any other indication that they are special to the surrounding rock. These features could be borehole extensions.

LOWER VESICULAR ZONE

Vesicles

Vesicles in the lower vesicular zone have an opposite arrangement when compared to the upper vesicular zone. The vesicle size decreases closer to the bottom of the flow as compared to the increase in size of the vesicles towards the center of the flow. Overall size of the vesicles is smaller than in the upper vesicular zones, and most of the vesicles are irregular in shape compared to those near the top of the flow. Vesicularity increases towards the bottom of the lower vesicular zone opposite to the upper vesicular zone where the vesicularity is the greatest at the top and decreases towards the bottom. At the bottom of this zone many small vesicle are present, yet the relative number is fewer than the vesicles found at the flow top. Ranging from 0.3 to 1.8 meters thick this is usually the thinnest zone that can be found in a basalt flow; only the columnar zone can possibly be smaller. The overall color of this zone is also different in that it is usually a darker color than the rest of the basalt flow.

Pipe Vesicles

Pipe vesicles are usually found just at the lowest point of the central massive zone or at the top of the lower vesicular zone; typically they range in size from 3 to 8 mm wide and are in the shape of hollow tubes. These tubes exhibit a rounded top and a tapered bottom. Pipe vesicles differ from vesicle plumes because they are hollow compared to the plumes which are just areas in the basalt made up of vesicles. Magmatic gas exsolved from the lava as it crystallizes is one possible source for the generation of the pipes vesicles rather than trapped air or steam generated beneath the lava (Walker, 1987).

SUMMARY

Upon completing an outcrop and core analysis of basalt rocks common to the INEL a further study was carried out on over thirty six borehole TV logs of boreholes at the INEL.

A distortion factor was determined for a 15 cm diameter borehole so accurate measurements of basalt features could be made from the TV logs. From the study of the TV logs a generic section for a basalt flow was put forward as a model. This generic section was subdivided into separate zones with the upper zone further subdivided into four subzones. The marked change in shape and changes in vesicularity are the main criteria that distinguishes the four subzones from each other and is used as one of the main bases for breaking the column into separate zones. Vesicles, fractures, and borehole extensions were easily identified by the use of the borehole TV camera. The detail of the logs enabled direct measurements of these features. These same features also are directly comparable to outcrops and cores. A great potential exists for this tool to better our understanding of subsurface geology.

REFERENCES CITED

Beard, N. C., 1959, Quantitative study of columnar jointing: The Geological Society of America Bulletin, vol. 70, p. 379-382.

Dickinson, W. R., and Vigrass, L. W., 1965, Geology of the Suplee-Izee area, Crook, Grant and Harney Counties, Oregon: Oregon Department of Geological Mineral Resources Bulletin, vol. 46, p. 69-94.

Faust, G., 1978, Joint Systems in the Watchung Basalt Flows, New Jersey: U. S. Geological Survey Professional Paper, 864-B, p.1-45.

James, A. V. G., 1920, Factors producing columnar structure in lavas and its occurrence near Melbourne, Australia: Journal of Geology, vol. 28, p. 458-469.

Kuntz, M. A., Covington, H. R., and Schorr, L. J., 1992, An overview of basaltic volcanism of the eastern Snake Rive Plain, Idaho: Geological Society of America Memoir 179, p. 227-267.

Lanphere, M. A., Champion, D. E., and Kuntz, M. A., 1993, Petrography, age and paleomagnetism of basalt lava flows in coreholes Well 80, NRF 89-04, NRF 89-05, and ICPP 123, Idaho National Engineering Laboratory: U. S. Geological Survey, Open-File Report 93-327, p. 2-40.

LeRoy, L. W., LeRoy, D. O., and Raese, J. W., 1977, Subsurface Geology: 4th ed., Colorado School of Mines, Golden, Colorado.

Long, P. E., and Wood, B. J., 1986, Structures, textures, and cooling histories of Columbia River basalt flows: Geological Society of America Bulletin, vol. 97, p. 1144-1155.

Macdonald, G. A., 1967, Forms and structures of extrusive basaltic rocks. In The Poldervaart Treatise on rocks of basaltic composition, H. H., Hess and A. Poldervaart (eds.): vol. 1, Interscience, New York, p. 1-61.

Malde, H. E., 1987, A guide to the Quaternary geology and physiographic history of the Snake River Birds of Prey area, Idaho, in Field Trip Guidebook: American Association of Petroleum Geology & Society of Economic Mineralogists and Paleontologist, Rocky Mountain Section, Meeting, September 10-18, 1987, Boise Idaho, p. 234-246.

McMillan, K., Cross, R. W., and Long, P. E., 1987, Two-stage vesiculation in the Cohassett flow of the Grande Ronde Basalt, south-central Washington: Geology, vol. 15, p. 809-812.

Walker, G. P. L., 1987, Pipe vesicles in Hawaiian basaltic lavas: their origin and potential as paleoslope indicators: Geology, 15, p. 84-87.

Walker, G. P. L., 1989, Spongy pahoehoe in Hawaii: a study of vesicle-distribution patterns in basalt and their significance: Bulletin of Volcanology, vol. 51, p. 199-209.

Whitehead, R. L., 1992, Geohydrologic framework of the Snake River Plain Regional Aquifer system, Idaho and eastern Oregon: U. S. Geological Survey Professional Paper 1408-B, p. 1-32.

Hydrogeology, Waste Disposal, Science and Politics
Proceedings 30th Symposium
Engineering Geology and Geotechnical Engineering, 1994

STEREOLOGICAL SAMPLING OF ROCK MASSES FOR ENGINEERING PURPOSES

Stanley M. Miller
Bryan D. Martin
Department of Geology and Geological Engineering
University of Idaho, Moscow, Idaho 83844

John K. Owens
U.S. Bureau of Mines Spokane Research Center
Spokane, Washington 99207

ABSTRACT

Stereological analysis of observations made in drill holes or along the walls of underground excavations can provide two- and three-dimensional measures that help characterize discontinuous rock masses for engineering and hydrogeologic purposes. The approach is based on sampling methods developed previously in stereology for the analysis of microstructures in the fields of biology and materials science.

Input information for a stereological analysis of a rock mass is best obtained by scanning (imaging) the walls of clean drill holes using a borescope or other video device. Two classes of features are investigated: 1) lithologic types that comprise the overall rock mass, and 2) structural discontinuities (e.g., joints, foliation, bedding planes) within a given lithologic unit. For the former case, the volume fraction of a given lithologic entity in regards to the entire rock mass can be estimated. For the latter case, the intact-block size distribution, the mean intercept length between adjacent structures, and the surface area density (say, area in m^2 per unit volume in m^3) of the geologic structures can be estimated.

Example samplings and computations are presented for several situations based on drill holes associated with underground mining activity. Extensions of the methodology are proposed for larger diameter borings or tunnels and for exposed rock faces.

INTRODUCTION

The origins of stereology can be traced to petrological applications proposed by the French geologist, Delesse, in the mid 1800's [3], but recent developments and applications have been primarily in the fields of biology and materials science [2, 10, 11]. Stereology provides a mathematical protocol for relating simple measurements made along test probes (or on planar sections) to three-dimensional geometric properties of the body being sampled.

Although stereological principles have been applied rarely to the engineering study of discontinuous rock masses [7], they have been used to assess large-scale fracturing on the earth's surface [5, 6] and to analyse the crack geometry in stressed concrete [4, 9]. The primary difficulty in obtaining representative stereological samples for site-specific engineering work is that continuous, linear probes of the rock mass are possible only in competent rock where drill-core recovery is effectively 100 percent. Planar, two-dimensional sections for sampling rock exposures also are rare in nature; consequently, such faces must be blasted and cleaned to allow for stereological measurement of its structural features. This extensive effort probably will not be justified at the exploration and site investigation stages of most projects.

However, recent technological developments in miniature video equipment and fiber-optics now make it possible to record video images of the inside walls of drill holes in the rock mass, regardless of whether any drill core was recovered. Of course, the holes must be clean enough to observe discontinuities and any changes in rock type or physical characteristics, such as zones of dike material, breccia, fault gouge, or alteration/weathering. By obtaining fundamental stereological measurements from such images, we can derive useful information to help characterize discontinuous rock masses for engineering purposes.

STEREOLOGICAL RELATIONSHIPS

When line probes are used to sample the structures within a three-dimensional body for stereological purposes, care must be taken to assure that the probes are chosen randomly from a uniform and isotropic population of all such probes in the sampling space. This implies that the line probes must sample all positions and orientations uniformly. An important advantage of having line probes along the walls of a cylindrical hole (in our case, a drill hole) is that the cylindrical surface of the hole automatically samples uniformly all orientations about the axis of the hole [1].

Practical guidelines for such sampling include the following [1]:

1. Sample uniformly; draw observations that are uniformly distributed in position;
2. It is better to sample the entire population lightly, rather than concentrate on detailed samples at only a few locations;
3. A systematic sampling plan can reduce the statistical variance of observations and, thus, increase the precision of stereological estimates, provided a random starting point is used for the plan layout.

For stereological measurements, the braces <...> around an attribute denote the "expected value" or mean of that attribute. In this sense, the stereological attributes are considered random variables, and each sample mean is assumed a reasonable estimate of the population mean. The following attributes can be measured from line probes and are relevant to our study of rock masses:

$<P_P>$ Point Fraction -- The ratio of n_i to n, where n = total number of points on a counting grid that covers the sampling image and n_i = the number of points contained in the i-th constituent of the rock mass as counted along the sampling grid.

$<L_L>$ Line Fraction -- The ratio of L_i to L, where L = total length of a sampling line that covers the sampling image and L_i = the summed length of segments of the sampling line contained in the i-th constituent of the rock mass.

$<P_L>$ Line Intercept Count -- The ratio of n_{ij} to L, where L = total length of a sampling line that covers the sampling image and n_{ij} = the number of interfaces (boundaries) between constituents i and j in the rock mass as counted along the sampling line.

The point fraction and the line fraction essentially provide the same measure, because as the point grid spacing is reduced to zero, the ratio $n_i : n$ will approach the limit $L_i : L$. Deciding which parameter to measure depends on the selected sampling procedures and on the available equipment used for sampling and analysis.

The point fraction and the line fraction both provide unbiased estimates of the **volume fraction** V_V, which represents the fraction (similarly, the percentage) of the total volume sampled that consists of the specified constituent [10, 11]:

$$<P_P> = <L_L> = V_V \qquad (1)$$

The line intercept count for a specified type of interface or boundary is related to the **surface area density** S_V of that type contained in the sampled volume, as expressed in units of area per unit volume (say, m^2/m^3) [10,11]:

$$\langle P_L \rangle = (1/2)\, S_V \tag{2}$$

These are but a few of the fundamental stereological parameters and relationships that have been applied in the fields of biology, medicine, and materials science. Basic point counts or line measurements often are performed automatically by computerized imaging systems or semi-automatically using some type of human delineation of features [8].

STEREOLOGICAL SAMPLING IN DRILL HOLES

The stereological parameters reported above are the most applicable ones for characterizing fractured rock masses, particularly when using drill holes as the sampling probes. However, some modifications and orientation corrections are needed when the drill holes are parallel to each other and constitute a set of directed line probes. Such is the case when using rock-bolt holes drilled in the roof of an underground mine.

The line intercept count obtained from such parallel sampling lines provides an unbiased estimate of the **total projected area** A_V of the specified interface type onto a plane perpendicular to the sampling lines [2, 10]. The corresponding stereological relationship is [1]:

$$\langle P_L \rangle_{ori} = A_V \tag{3}$$

where $\langle P_L \rangle_{ori}$ is the line intercept count obtained from parallel, oriented sampling lines.

The cosine of the angle ϕ between the sampling-line direction and the normal to an intersected surface (interface) relates the actual surface area to the projected area of the surface. That is, for the i-th interface encountered:

$$A_{Vi} = (\cos \phi_i)\, S_{Vi} \tag{4}$$

Thus, by averaging all such cosines of angles for all surfaces (interfaces) encountered, we obtain the following:

$$A_V = (\cos_{avg}\phi)\, S_V = \langle P_L \rangle_{ori} \tag{5}$$

$$S_V = \langle P_L \rangle_{ori} / (\cos_{avg}\phi) \tag{6}$$

The **mean intercept length** of a specified constituent in the rock mass as measured in the reference direction of the sampling lines is given as [1]:

$$\langle \lambda \rangle_{ori} = 2V_V / A_V = 2V_V / \langle P_L \rangle_{ori} \tag{7}$$

It is important to note that when sampling to estimate the volume fraction of a constituent (feature), such a volume does not possess an orientation as do line or surface features. Thus, sampling to obtain the point fraction and line fraction does not require an isotropic array of sampling lines to yield unbiased estimates of the volume fraction [1]. Consequently, such stereological sampling from parallel drill holes will suffice in this regard.

EXAMPLES

Estimating Volume Fractions

Estimating the volume fraction of a given constituent in a discontinuous rock mass can be helpful in assessing its engineering performance, especially if the constituent is a structurally weak component of the overall rock mass. Also, if ore dilution was a concern in a proposed mining operation, knowledge of the volume fraction of non-ore materials would yield the expected amount of such dilution when mining through a specified volume of rock.

For example, consider a situation where mudstone layers and lenses in a sedimentary formation overlying a coal seam could cause potential stability problems in mining excavations. To estimate the volume fraction of mudstone, 12 rock-bolt holes (each 2.5-m long) in the mine roof have been imaged by a videoscope, and pertinent measurements collected regarding the line intercept lengths of mudstone encountered (Table 1).

Table 1. Line intercept measurements for mudstone example.

Hole Number	Sum of Mudstone Intercept Lengths (L_i), m	Line Fraction (L_L), m/m
1	0.62	0.248
2	1.00	0.400
3	1.25	0.500
4	0.43	0.172
5	1.18	0.472
6	0.00	0.000
7	1.37	0.548
8	1.09	0.436
9	1.12	0.448
10	1.76	0.704
11	1.45	0.580
12	2.14	0.856
		Mean = 0.45
n = 12		SD = 0.23

Given the mean and standard deviation (SD) for the line fraction, we now can calculate the volume fraction of mudstone according to Equation 1, as well as define a 0.95 confidence interval (CI) for the estimate.

Volume fraction of mudstone, $V_V = < L_L > = 0.45$, or 45%

95% CI for the mean volume fraction: $0.45 \pm t_{.025,\,11}(SD/\sqrt{n}) = 0.45 \pm 2.201(.066)$

$= 0.45 \pm 0.15$

where $t_{.025,\,11}$ = value of appropriate Student's-t statistic = 2.201.

As a second example, consider a crystalline rock mass with localized, highly fractured zones (that is, shatter zones), from which it is practically impossible to recover core during diamond drilling. In fact, because considerable intervals of core are lost, we are uncertain as to what actually is present in the insitu rock mass at those locations. A videoscope inserted into such drill holes can provide valuable information about the character of those shatter zones, as well as provide stereological data for estimating their volume fraction. The data presented in Table 2 represent a stereological sampling of the rock mass using five drill holes, ranging in length from 8.8 to 18 m.

Table 2. Line intercept measurements for shatter zones in crystalline rock example.

Hole Number and Length, m		Sum of Shatter Zone Intercept Lengths (L_i), m	Line Fraction (L_L), m/m
1	12.5	0.8	0.064
2	15.2	2.2	0.145
3	8.8	1.1	0.125
4	18.0	2.2	0.133
5	13.6	1.6	0.118
			Mean = 0.12
n = 5			SD = 0.03

Given the mean and standard deviation (SD) for the line fraction, we now can calculate the volume fraction of shatter zones according to Equation 1, as well as define a 0.95 confidence interval for the estimate.

Volume fraction of shatter zones, $V_V = < L_L > = 0.12$, or 12%

95% CI for the mean volume fraction: $0.12 \pm t_{.025,4}(SD/\sqrt{n}) = 0.12 \pm 2.776(.013)$

$= 0.12 \pm 0.04$

where $t_{.025,4}$ = value of appropriate Student's-t statistic = 2.776.

Estimating Surface Density of Fracture Classes

Estimating the surface area density of fractures in a rock mass can be helpful in assessing potential rock failure mechanisms and in the subsequent design of rock support systems. Of particular interest to underground excavations might be an evaluation of the surface area density of flat or nearly flat structures that could be intersected and supported via rock bolts or cable bolts. A portion of the roof with a surface area density of 1.0 m^2/m^3 for flat-lying structures should be treated much differently than a portion with a surface area density of 5.0 m^2/m^3 for similar structures.

For example, consider a situation where fractures observed in the roof of an excavation can be separated into two classes: 1) flat-lying (dips are less than 45°), and 2) steep-lying

(dips exceed 45°). To estimate the surface area density of the two fracture classes, 10 vertical rock-bolt holes (each 4-m long) in the roof have been imaged by a videoscope, and pertinent measurements collected regarding line intercept counts (Table 3).

Table 3. Line intercept counts for two fracture classes.

Hole Number	No. of Fractures Observed Flat (≤45°)	Steep (>45°)	$< P_L >_{ori}$ Flat	Steep
1	9	2	2.25	0.50
2	11	3	2.75	0.75
3	8	1	2.00	0.25
4	12	4	3.00	1.00
5	10	2	2.50	0.50
6	13	2	3.25	0.50
7	11	0	2.75	0.00
8	9	1	2.25	0.25
9	8	3	2.00	0.75
10	9	4	2.25	1.00
			Mean = 2.50	0.55
n = 10	$\cos_{avg}\phi = 0.887$	0.462	SD = 0.425	0.329

Given the mean and standard deviation (SD) for the oriented line intercept counts, we now can calculate the surface area density for each fracture class according to Equation 6, as well as define a 0.95 confidence interval for each estimate.

Flat fractures: $S_V = <P_L>_{ori} / (\cos_{avg}\phi) = 2.50 / 0.887 = 2.82\ m^2/m^3$

$S_{VSD} = 0.425 / 0.887 = 0.479\ m^2/m^3$

95% CI for the surface area density: $2.82 \pm t_{.025,9}(SD/\sqrt{n})$

$= 2.82 \pm 2.262(0.479 / 3.162) = 2.82 \pm 0.34\ m^2/m^3$

where $t_{.025,9}$ = value of appropriate Student's-t statistic = 2.262.

Steep fractures: $S_V = <P_L>_{ori} / (\cos_{avg}\phi) = 0.55 / 0.462 = 1.19\ m^2/m^3$

$S_{VSD} = 0.329 / 0.462 = 0.712\ m^2/m^3$

95% CI for the surface area density: $1.19 \pm t_{.025,9}(SD/\sqrt{n})$

$= 1.19 \pm 2.262(0.712 / 3.162) = 1.19 \pm 0.51\ m^2/m^3$

This example illustrates how the orientation (directional) bias that causes undersampling of steep fractures in vertical holes is taken care of automatically in the stereological calculations used to estimate the surface area density of such structures. The averaged line intercept count $\langle P_L \rangle_{ori}$ for the steep fractures was approximately one-fifth of that for the flat fractures, yet the resulting surface area density for the steep fractures was about half of that for the flat fractures. For this particular stereological procedure, the cosine term contained in Equation 6 appropriately corrects for the undersampling of steep structures in vertically oriented drill holes.

If the stereological sampling for this example also included the point fraction or line fraction (to estimate V_V), then Equation 7 could be used to calculate the mean vertical intercept length as measured between adjacent flat fractures or adjacent steep fractures. This term would be equivalent to the mean fracture spacing between adjacent flat fractures or adjacent steep fractures.

Estimating Intact-Block Size Distributions

In some engineering projects, estimates of core-piece size distributions are useful for predicting fragmentation and for characterizing overall rock-mass deformation under loading. If certain geometrical conditions reasonably can be assumed for intact block shapes, then a core-piece size distribution can be converted to a volumetric, intact-block-size distribution using stereological methods.

When measuring line intercept distances from one fracture to the next in a borehole, we are, in fact, measuring the core-piece lengths that would be observed in drill core if it had been recovered from the hole. The cumulative relative frequency plot of these lengths provides an estimate of the core-piece length probability distribution. However, if we were interested in relating such data to the entire rock mass volume, we could divide the length intercepts into size categories and then use the L_L for each category to estimate the volume fraction V_V for each of the intact-block size categories. The information presented in Table 4 illustrates this procedure for a set of 20 drill holes (each approximately 60 inches long) in the siltstone roof of an underground coal mine, covering an area of approximately 6 by 18 meters (108 sq. m).

Table 4. Intercept lengths for intact siltstone and corresponding volume fractions for selected size categories (total length of sampling lines was 1220 in.).

Intact Rock Size Category, in.	Sum of Intact Rock Intercept Lengths (L_i), in.	Line Fraction (L_L) = Vol. Fraction (V_V)
0 - 4	192	0.16
4 - 8	305	0.25
8 - 12	312	0.26
12 - 16	283	0.23
16 - 23	129	0.10

To determine whether the position of the sampling line in drill holes affects the stereological results, a chi-squared statistical procedure (5 x 2 contingency tables) was used on

this data set to compare the volume fractions predicted by two sampling line positions located on opposite sides of the drill holes. The results indicated that the two sets of volume fractions thus obtained did not differ significantly. Consequently, the positioning of the scanning device in drill holes probably is not critical when conducting line scans for most stereological studies.

Another statistical comparison (chi-squared goodness of fit) was conducted for this siltstone data set to estimate the minimum number of drill holes required to provide repeatable results in regard to intercept length distributions. Subsets of 6 randomly selected drill holes from the original 20 were compared to one another using the chi-square test; this was repeated for randomly selected subsets of 5 holes, 4 holes, and 3 holes. Significant differences in the predicted size distributions began to show up with 4 holes and were common with 3 holes. Thus, intact-rock size distribution repeatability becomes questionable when less than 4 drill holes are used. This implies that as long as geologic conditions do not vary significantly, a minimum of 4 roof-bolt holes per 100 square meters of roof need to be sampled to provide representative stereological results in regards to intercept length measurements.

In situations where the fractures in a rock mass divide it into fairly equidimensional intact blocks (i.e., blocks shaped more like spheres than plates or columns), stereological procedures can be used to adjust size distributions of intact-rock intercept lengths to volumetric size distributions of three-dimensional blocks [8]. The method we developed to accomplish this transformation is based on three steps:

1) Describe the cumulative relative frequency distribution (crf) of the measured intercept lengths;
2) Convert this crf to one describing the distribution of the diameters of corresponding spherical particle sizes (i.e., spherical blocks pierced by the drill hole);
3) Convert the derived crf of spherical particles to one describing the distribution of corresponding polyhedral shapes (such as dodecahedra or icosahedra) using a ratio of 1.08 for their mean tangent diameter to that of a sphere of equal volume [8].

Output from an example set of computations for intercept lengths (core-piece lengths) measured in three exploration drill holes (each approximately 60 m long) in a rhyolite formation are given in Figure 1. The measured intercept length distribution is skewed right and probably can be modeled by a lognormal probability distribution. The resultant cumulative distribution of polyhedral mean tangent diameters is less skewed and covers a wider range of sizes. It is worthy to note that this latter distribution is a volumetric particle size distribution, rather than a weight-percent particle size distribution as is commonly reported for soils and crushed rock.

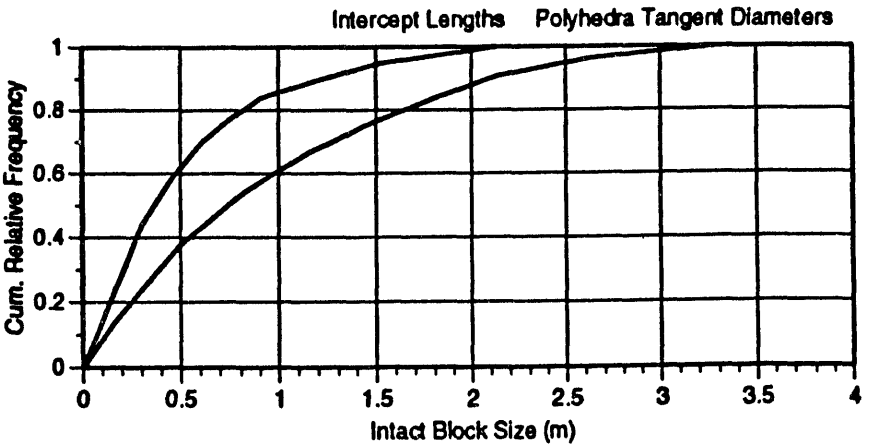


Figure 1. Intact rock size distributions estimated from three drill holes in rhyolite.

CONCLUSIONS

With recent advances in hardware development for imaging drill holes, applications of stereology to rock mass sampling and characterization are feasible. More comprehensive three-dimensional characterizations of rock masses are now possible, ones that include volume fractions of various lithologic constituents (of rock engineering interest, these might include altered or weathered zones, veins, shatter zones, fault breccia and gouge), surface area densities of fractures (particularly of interest are those with orientations critical to rock engineering projects), and intact-rock volumetric size distributions. Such measures provide an enhanced understanding of a rock mass over such descriptors as RQD and fracture density.

Stereological sampling lines can be used on tunnel walls or on exposed rock faces. Care must be taken to avoid aligning such probes in the same plane, because our experience has shown that many more sampling lines are needed to produce representative and repeatable stereological results for this case. If sampling into the rock mass is desired, then relatively short holes can be drilled economically with percussion drilling equipment.

Additional field work is needed in discontinuous rock masses to investigate relationships between traditional rock engineering descriptors and stereological descriptors. One clear advantage of stereology is that recovered drill core is not required, provided that a borehole video imaging system is available.

ACKNOWLEDGMENTS

Much of the funding for this research work was provided by the U.S. Bureau of Mines, Spokane Research Center. The authors also express their appreciation to the engineering personnel at the Center who shared technical information and field data during the course of this investigation.

REFERENCES

1. DeHoff, R.T., 1993, Use of Bolt Holes as Stereological Sampling Probes; unpubl. report to U.S. Bureau of Mines, Spokane Research Center, Spokane, WA.
2. DeHoff, R.T. and Rhines F.N., 1968, *Quantitative Microscopy*; McGraw-Hill, New York.
3. Delesse, A., 1848, Pour Determiner la Composition des Roches; Ann. des Mines, v. 13, Fourth Series, p. 379.
4. Hong, T., 1991, Quantitative Characterization of Crack Geometry in Concrete Compressed Uniaxially at High Strain Rate; unpubl. M.S. thesis, Dept. of Matl. Sci. and Engrg., Univ. of Florida, Gainesville, FL.
5. Karcz, I., 1977, Rapid Determination of Lineament and Joint Densities; *Tectonophysics*, **44**, p. T29-T33.
6. Karcz, I. and Dickman, S.R., 1979, Determination of Fracture Intensity; *Tectonophysics*, **56**, p. T1-T7.
7. Kanatani, K., 1985, Measurement of Crack Distribution in a Rock Mass from Observation of its Surfaces; *Soils and Foundations* (Japanese Soc. Soil Mech.), **25** (1), p. 77-83.
8. Russ, J.C., 1986, *Practical Stereology*; Plenum Press, New York.
9. Stroeven, P., 1976, Application of Various Strereological Methods to the Study of the Grain and the Crack Structure of Concrete; *Proc. of 4th Intl. Congress for Stereology*, Natl. Bureau of Standards Special Publ. 431, p. 281-286.
10. Underwood, E.E., 1970, *Quantitative Stereology*; Addsion Wesley, Reading, MA.
11. Weibel, E.R., 1979-80, *Stereological Methods, Vol. I and II*; Academic Press, New York.

Hydrogeology, Waste Disposal, Science and Politics
Proceedings 30th Symposium
Engineering Geology and Geotechnical Engineering, 1994

DISPOSAL OPTIONS FOR SCRAP TIRES

by C. W. "Bill" Lovell, Research Engineer
School of Civil Engineering
Purdue University
W. Lafayette, IN 47907-1284

ABSTRACT

Scrap tires have been a high profile waste because of improper disposal in the past.

They have been mandated for use in crumb form in asphaltic pavements by Federal ISTEA legislation. In addition, useful disposal options have been developed for shreds as a lightweight geomaterial for embankments or backfills. In these later cases, problems of excessive deformability may be countered by mixing with sand.

Tires may also be reduced to basic constituents in a process known as pyrolysis. A principal byproduct of this process is an impure form of carbon black, which may be useful as a filler in asphaltic concrete. There are limited applications for whole tires in restraining structures, and for linkages of tire beads or tire sidewalls as reinforcing elements in soils. In addition, tires yield a high BTU return when burned.

The paper summarizes research experiences of the author in research on scrap tires, and recommends future uses of these materials, particularly in highway applications. In a number of instances, use of the scrap rubber produces performance superior to or more economical than that for conventional materials.

INTRODUCTION

Solid wastes produced in the U.S. in decreasing order of quantity are: (1) agricultural (most); (2) mining; (3) industrial; and (4) domestic (least). Scrap tires are considered a part of the domestic waste, and therefore are exceeded in quantity by a number of others. Yet, scrap tire disposal has received as much or more national attention than any solid waste. Why is this so?

Careless and uncontrolled storage and disposal seems the obvious answer. Outdoor tire dumps have the following unfavorable features: unsightly; fire hazard; and breeding ground for rodents and insects.

Many states prohibit the outdoor storage of whole tires. The disposal of whole tires in solid waste landfills is also usually forbidden.

Used tires are accumulated in small quantities by tire dealers, who pay tire haulers (recyclers) to periodically truck them away. The recycler will have an indoor

storage/sorting/ processing facility. Useable tires are retrieved and sold to primarily Asian markets. The other tires are either cut or shredded for market or disposal. The latter option involves hauling, tipping fees, and wasting of a potentially valuable engineering material. However, present markets are very limited and in great need of expansion.

Some of the rubber may be mechanically ground or cryogenically reduced to crumb size. As such it has a variety of uses including incorporation into asphaltic mixes. The experiences of state highway agencies with these mixes varies widely. Many conclude that such mixes almost double the cost without significant improvement in the performance of the paving.

Another market exists as fuel in the generation of power. Indeed, the tires produce more BTU's than coal. However, special combustion features are needed and air emissions also require extraordinary attention.

Reduction of the tire to basic components of oil, gas, steel and "carbon black" in the pyrolysis process is quite promising. A major obstacle to success of this recovery process is finding a market for the rather impure carbon black accumulated from it.

Tire shredding through mechanical cutting and tearing actions may be accomplished by a variety of fixed or mobile devices...some commercial, others "homemade". Successive passes through the shredding operation produce smaller sizes, and pieces which are more nearly equal in length/width dimensions.

Tire shreds have a much higher bulk unit weight than whole tires and hence are much more convenient to store or haul. The product is referred to as "shreds" or "chips" of a maximum length or width dimension. There seem to be a variety of potential civil engineering uses for such materials, including fills, backfills and drainage media. They may be used alone or in mixtures with soil.

BACKGROUND

Scrap tires are generated in the U.S. at the rate of about a tire/person/year (EPA, 1991). This quantity of about a quarter billion tires per year is added to an estimated prior accumulation of about 2 billion tires. The high visibility of this waste (and associated hazards cited earlier) has caused national and state legislative bodies to mandate studies or applications of various reuse options.

Fortunately, tire rubber is an excellent civil engineering material, being both strong and durable. Environmental constraints seem to be minimal for certain usage, e.g., shred/chip forms, although applications are being pursued with appropriate caution.

Figure 1 (Ahmed, 1993b) shows the scrap tire generation cycle. The recycling portion is followed on Figure 2 (Ahmed, 1993b). Note that a variety of options exist for (a) whole tires or tire sidewalls, (b) shredded tires, and crumb rubber.

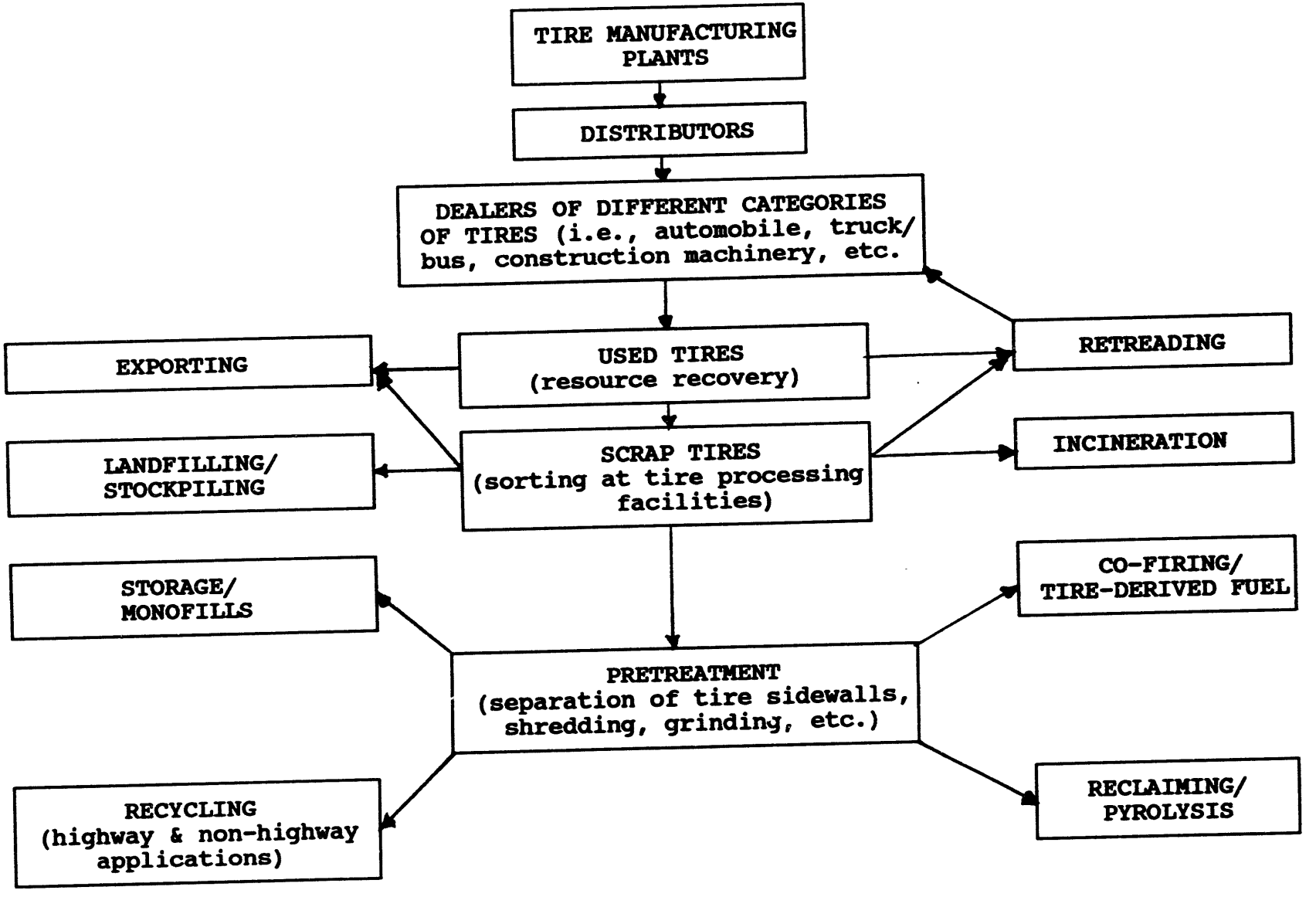


Figure 1 Tire manufacturing, retreading, and discards (Ahmed, 1993b)

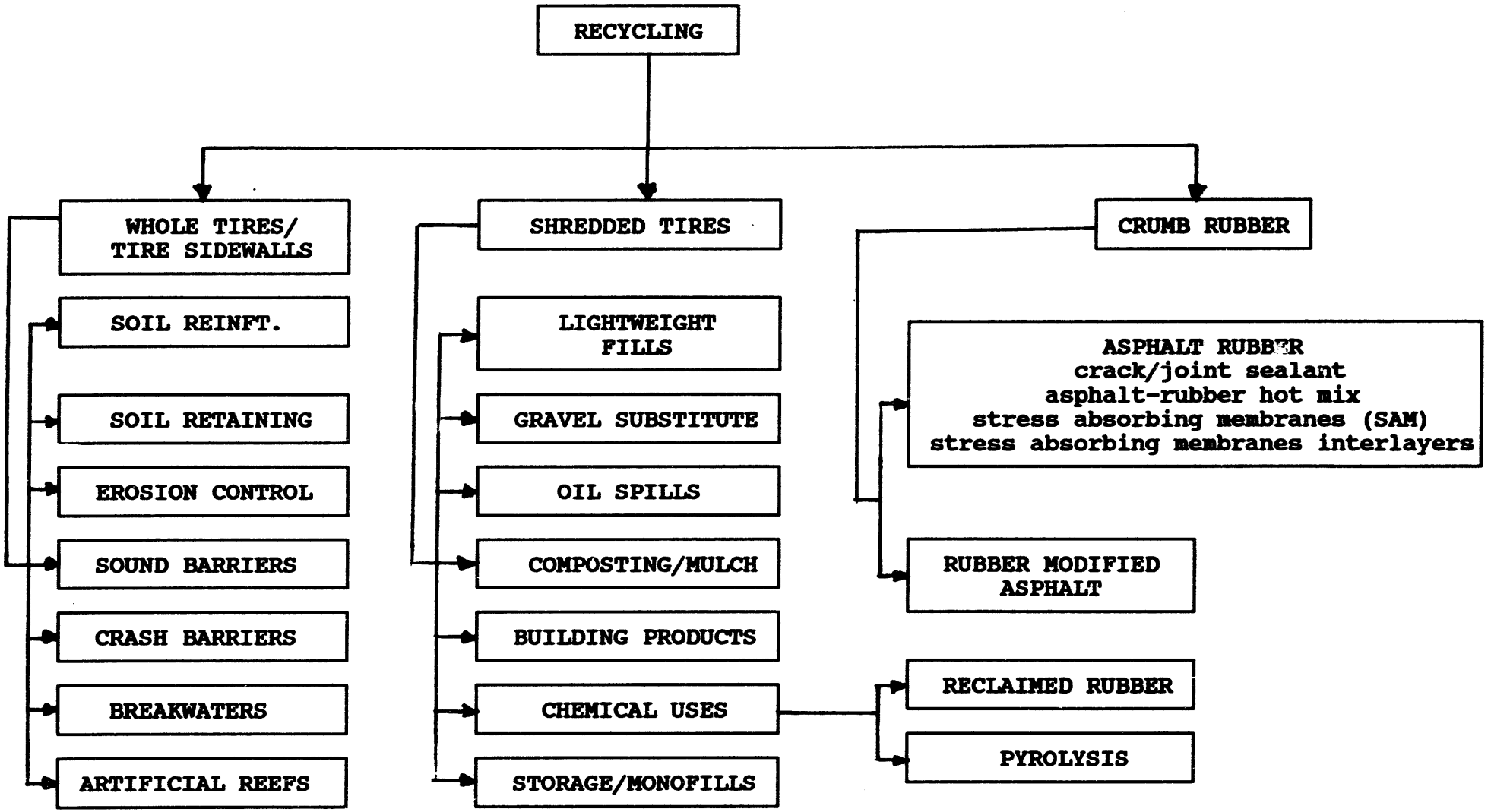


Figure 2 A summary of recycling options for scrap tires (Ahmed, 1993b)

Whole tires are bulky and expensive to transport, but may require no processing prior to use. Some applications are not uncommon, such as retaining structures and crash barriers, but have intrinsic limitations. Use to form artificial reefs (fish holding structure) requires only linking and weighting, but source and market are often geographically separated.

The inner rim of the tire contains a wire hoop (the bead) which may be cut out and has potential usage. The same is true for the tire sidewalls. When linked into mats, the beads or the sidewalls form a layer of high tensile strength which can be used to reinforce soil masses (very low tensile strength). Fabrication of the mats, as well as transportation and placement of them, involves significant cost.

Shredding is a relatively inexpensive operation and may simply constitute a conditioning which allows the rubber to be used as a raw material for other purposes, e.g., pyrolysis. In other cases, the shred or chip is directly used as a fill, backfill or drainage layer. Because of minimal preparation and extra construction costs, this option is attractive. This paper provides additional details on the use of shreds as a lightweight geomaterial.

Production of crumb rubber as an additive to asphalt is expensive. Such additive has produced best success in crack/joint sealants and in stress absorbing membranes. When used as an additive to asphaltic mixes, the experience is mixed. In Indiana for example, the benefits do not seem to warrant the added costs.

Reduction of the tire to basic ingredients in the pyrolysis process (oil, gas, steel, carbon black) is promising, but depends upon identifying a market for the pyrolyzed carbon black. While pure carbon black may be useful in asphalt mixes, the pyrolyzed product is sufficiently impure to cause doubts. Research to identify the effects of pyrolyzed carbon black on asphaltic binders and in asphaltic mixes is currently under way in Indiana.

LIGHTWEIGHT GEOMATERIALS

A number of studies have indicated the potential benefits of using tire shreds as lightweight geomaterial (Ahmed, 1992; Ahmed, 1993a; Ahmed and Lovell, 1993). When such materials are used, settlements are reduced and stability is increased. A variety of materials may be used for the above purpose, and these are summarized in Table 1.

Manufactured products tend to be relatively expensive, while waste products are essentially free at the source. This is because the recycler thus avoids disposal costs. Thus, only transportation costs must be borne by the user.

Qualification of a waste material for routine use in a highway system would ideally involve the following steps:

(1) chemical/mineralogical characterization;

(2) physical/mechanical characterization in the laboratory;

Material	Unit weight (pcf)	Comments
Bark (Pine & Fir)	35-64	Waste material used relatively rarely as it is difficult to compact. The risk of leachates can be reduced by using material initially stored in water and then allowed to air dry for some months. The compacted/loose volume ratio is in the order of 50%. Long term settlement may be around 10% of compacted thickness.
Sawdust (Pine & Fir)	50-64	Waste material commonly used below permanent groundwater level but occasionally employed for embankments with asphalt or geotextile sealed side slopes.
Peat: Air dried Milled Baled Horticultural Compressed bales	 19-32 13 51-64	Found particularly useful in Ireland for repairing existing roads by replacing gravel fill with baled peat.
Fuel ash, slag, cinder, etc.	64-100	Waste materials such as pulverized fuel ash (PFA) are generally placed at least 1 ft above maximum flood level. Such materials may have cementing properties producing a significant increase of strength with time. Some may absorb water (e.g. furnace slag) and increase in density.
Scrap cellular concrete	64	Significant volume decrease during compaction. Excessive compaction reduces material to powder.
Expanded clay or shale (lightweight aggregate)	20-64	Physical properties such as density, resistance and compressibility are appropriate for use as a lightweight fill, although properties are affected by manufacturing process. The material is relatively expensive. A 20 in. soil cover on the slopes and 2 ft. road base thickness are minimal requirements for embankment construction.
Shell (oyster, clam, etc.)	70	Commercially mined or dredged shells are available on Gulf and Atlantic coasts. Size: 0.5 to 3 in. When loosely dumped, shells possess low density and high bearing capacity due to interlock.
Expanded Polystyrene	1.3-6	Superlight material used in Norway, Sweden, U.S.A. and Canada with satisfactory performance and increasing popularity. Thickness varies between 0.5 and 1 m, depending on traffic loads. Very expensive but attractive due to its very low density.
Low-density cellular concrete, Elastizell: Class I Class II Class III Class IV Class V Class VI	 24 30 36 42 50 80	Manufactured with Portland cement, water and a foaming agent ("Elastizell EF"). Six different categories (I to VI) of engineered fill are produced with varying compressive strengths of 10, 40, 80, 120, 160, 300 psi and bearing capacities of 0.7, 2.9, 5.8, 8.6, 11.5 and 21.6 tsf, respectively. The material is cast in-situ and has been used in highway embankments, bridge approaches, foundations, etc. (Elastizell Corp. of America, Ann Arbor, Michigan, 1992)
Tire chips	20-45	Has been widely used in the U.S.A. Benefits include: reduced weight of fill, free draining medium, inexpensive, and recycling of tires. Potential problems include metal and hydrocarbon leachate, high compressibility and fire hazard. Recommended in unsaturated zones of embankments. Requires top and side cap against fire and for confinement (Authors).

Table 1 Lightweight embankment fill materials (adapted from Holtz, 1989; OECD, 1979; Merdes, 1992; Elastizell, 1992; and other sources)

(3) preparation of guidelines/standards/specifications for demonstration projects, including monitoring as needed;

(4) construction of demonstration projects, short term observation of behavior;

(5) modification of guidelines/standards/specifications for routine use, and observation of longer term behavior.

Following this procedure, the Indiana Department of Transportation (INDOT) has reached step (4) for fills of tire shred or tire shred/soil mixes. Other states already have demonstration projects in place, including Minnesota (Lamb, 1992), Oregon (Read et al, 1991), Wisconsin (Bosscher et al, 1992), and others. While the laboratory studies preceding these projects was limited, performance of them has been good. The Minnesota work incorporates tire shreds above the water table, but wood chips below, as a guard against unknown long-term effects on the ground water. Other studies have indicated that the low resilient modulus of tire shreds (Ahmed, 1993b) makes it desirable to interpose 3-5 feet of conventional materials between the rubber and the pavement surface. Side slopes must be covered with soil to protect against combustion of the rubber.

As reported in subsequent sections of this paper, properties of a tire shred fill may be improved by mixing the shreds with sand.

GEOTECHNICAL CHARACTERIZATION OF TIRE SHREDS AND SHRED/SOIL MIXTURES

The characterization reported herein results from laboratory study by Ahmed (1993b). The shred gradations used are shown on Figure 3. Limitation to 2 in. sizes was dictated by the usual requirement that $\frac{\text{min. } \textit{sample size}}{\text{max. } \textit{particle size}} \geq 6$. The soils used in shred/soil mixes are shown in Table 2.

Both vibration and Proctor type compaction techniques were tried in the laboratory. Compaction had only minor effects on unit weight of shreds only as shown in Figure 4. Note the range in unit weights of about 24-36 pcf.

Compressibility of the tire shreds can be predicted to be a problem. Accordingly, mixtures of shreds and both sandy and clayey soils were studied. As more soil is added, the unit weight increases, for example as shown in Figure 5 for clayey soil. A mixture of about 40% by weight of chips seems to be one where the soil effectively fills the inter shred spaces. Vibration was the most effective compactive mode for sands and shred-sand combinations, whereas Proctor type compaction was somewhat more effective for clays, clay-shred mixtures, and shreds alone.

Compressibility testing was accomplished with large sized equipment. As expected, 1-D vertical strains of the tire shreds alone were quite high, e.g., Figure 6 shows about 14% at a loading of 10 psi and about 21% at a loading of 20 psi. On the other hand, a mix of

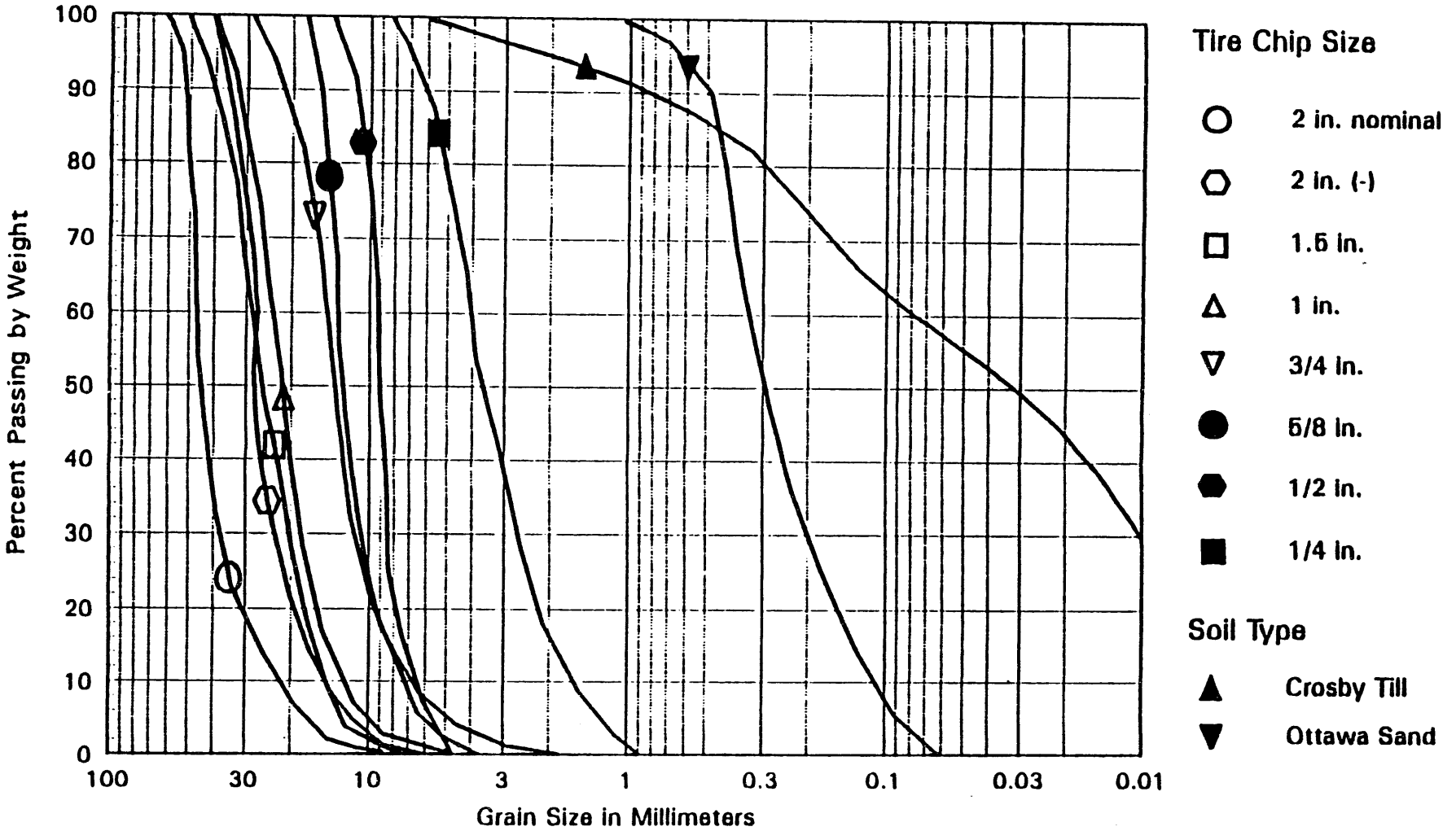


Figure 3 Gradation of tire shreds (chips) and test soils

Physical Properties	Crosby Till	Ottawa Sand
Liquid Limit (%)	19.8	-
Plastic Limit (%)	15.5	NP
Plasticity Index (%)	4.3	NP
Maximum Dry Density:	-	-
Modified Proctor (pcf)	130.25	-
Standard Proctor (pcf)	124.1	-
Vibration Method (pcf)	-	118.75
Optimum Water Content:	-	-
Modified Proctor (%)	9.3	-
Standard Proctor (%)	10.6	-
Soil Classification:		
Unified Soil Classification	CL-ML (Sandy Silty Clay)	SP (Poorly Graded Sand)
AASHTO Soil Classification	A-4(0)	A-3(0)

Table 2 Index values for test soils (Ahmed, 1993b)

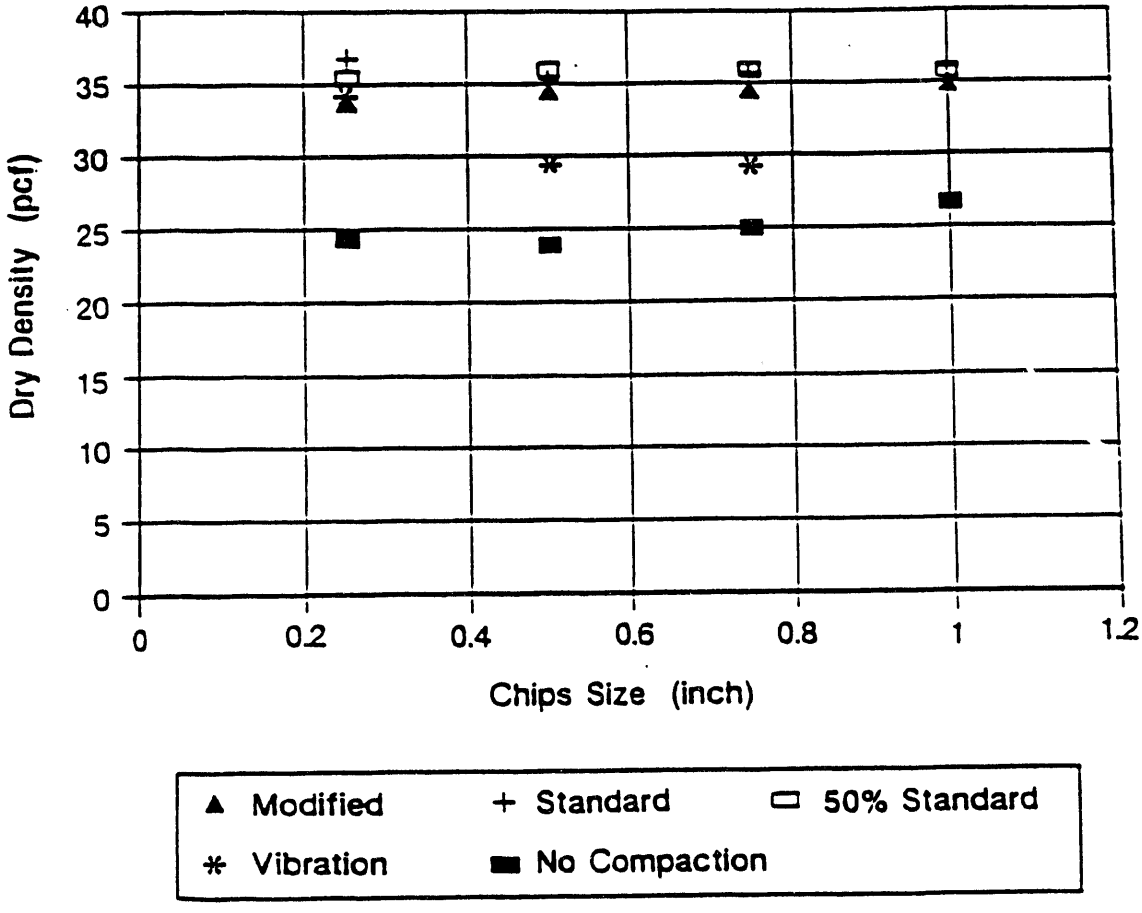


Figure 4 Minor effects of compaction on tire shreds (chips) (Ahmed 1993b)

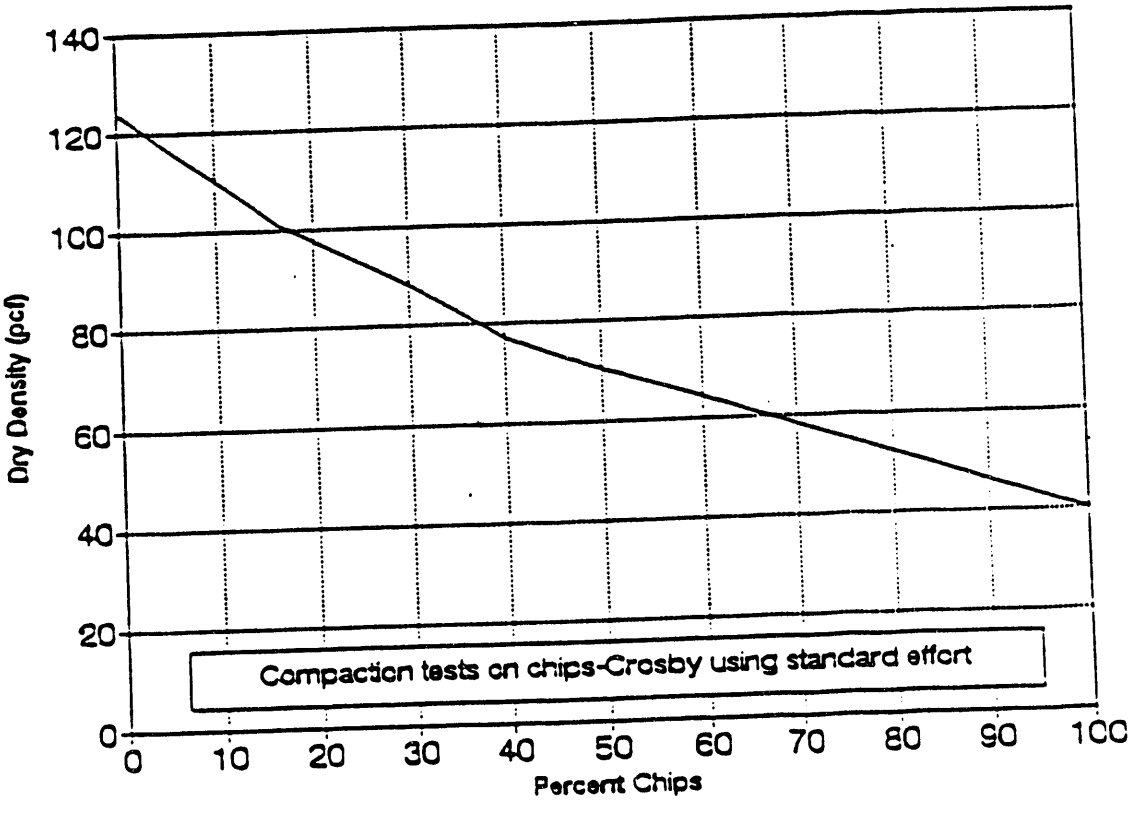


Figure 5 Compacted density with variation in % shreds (chips) (Ahmed 1993b)

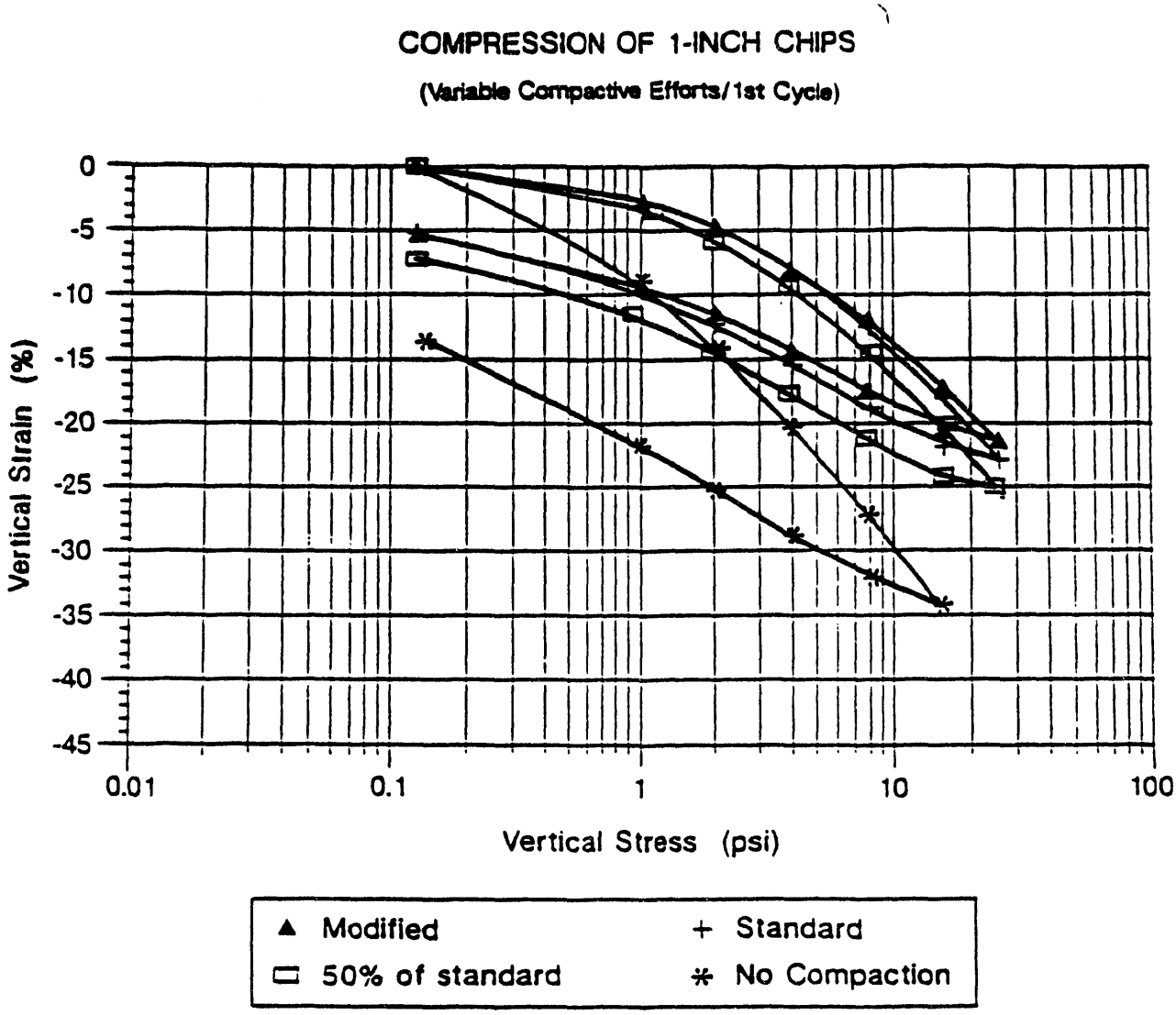


Figure 6 Compression of shreds (chips) for various compactive efforts (Ahmed 1993b)

sand +37% shreds by weight produced only 3% strain at 10 psi and 4% strain at 20 psi. Similar data were produced for shred/clay mixtures, where a mix of clay +40% shreds produced 4% strain at 10 psi and 6% at 20 psi.

Obviously, the problems of excessive settlements can be offset by the mixture approach. The lightweight feature is still present in the mixtures trending from a 2/3's reduction in weight with shreds only, to a 1/3 reduction with a proper mix of shreds and soil.

Shear testing also required large triaxial cells with special features. Samples of shreds only did not demonstrate any definite shear failure, and required that strength parameters be selected for a limiting strain of 20%. As shown in Table 3, values of the strength intercept c = 4.8 psi and the strength angle $\phi = 25°$ might be expected. A mixture of sand and 39% shreds by weight would yield values of c = 5.2 psi and $\phi = 38°$. Thus at lower confinements (4 to 5 psi), the shreds increase strength with respect to sand only. This is well illustrated in Figure 7. The shreds produce a reinforcing effect in the sand that can be quite beneficial.

Table 3 also shows that shred collections have a high hydraulic conductivity. Mixing sand with rubber shreds is seen to moderately increase the conductivity with respect to sand alone. Mixing rubber shreds and clay produces a major increase in the conductivity with respect to clay only.

Resilient modulus testing revealed significantly lower values of the modulus for even rubber soil mixtures compared to natural subgrade soils (Ahmed, 1993b). Accordingly, tire shreds alone or mixed with soils should probably not be used in highway pavement courses or even in the subgrade layer. A separation of 3 to 5 ft from the surface of the pavement is likely advisable.

SUMMARY AND CONCLUSIONS

Disposal options for scrap tires are numerous. One particular promising use is that of a lightweight geomaterial involving tire shreds or tire shred-soil mixtures.

Use of these materials in fill or backfills is recommended based upon the experimental evidence reported in this paper. Such use can eliminate landfill disposal for very large numbers of discarded tires.

Some states have reached the demonstration or implementation stage for such lightweight geomaterial applications. It is likely that many additional states will follow this lead in the very near future.

ACKNOWLEDGEMENTS

The author is grateful to his graduate researcher, Dr. Imtiaz Ahmed, for the dedicated experimental effort reported herein. He also thanks the Indiana Department of

Material	Dry Density (pcf)	Strength Intercept c (psi)	ϕ (°)	Hydraulic Conductivity (cm/s)	Compressibility	Reference
Poorly graded clean sand, sand-gravel mix (SP)	100-120	-	37	10-100	-	Hunt (1986)
Medium sand, angular: Loose Dense	- -	- -	32-34 44-46	10^{-1}-10^{-2}	-	Leonards (1962)
Inorganic silt and clay, compacted (CL-ML)	100-120	9.4	32	10^{-4}-10^{-6}	-	Peck et al. (1974)
2-in. tire chips in 6-in. diam. triaxial compression test	38	3.75	21	6-15	-	Bressette (1984)
1-in. chips, Std. Proctor	40			0.6		Authors
Strain = 10%		3.2	14.6		CR=0.169	
Strain = 15%		4.0	20.3		RR=0.139	
Strain = 20%		4.8	25.3		SR=0.108	
Ottawa Sand	115	-	41.4	1.6×10^{-4}	CR=0.005 RR=0.003 SR=0.003	Authors
1-in. chips 39%, sand 61%	89			8.7×10^{-5}		
Strain = 5%		7.3	25.5		CR=0.029	
Strain = 10%		6.3	34.6		RR=0.019	
Strain = 15%		5.2	38.1		SR=0.021	
Crosby till, strain = 10%	119	10.7	29.4	8.8×10^{-7}	CR=0.030 RR=0.007 SR=0.003	Authors
1-in. chips 40%, till 60%	81			8.8×10^{-5}		
Strain = 5%		5.6	12.7		CR=0.096	
Strain = 10%		8.2	21.1		RR=0.056	
Strain = 15%		9.4	27.0		SR=0.045	

Notes: 1. Compressibility parameters were determined for samples prepared using Standard Proctor compactive effort.
CR = Compression ratio, average slope of ϵ_v vs $\log(\sigma_v)$ in virgin compression zone (σ_v between 4 and 10 psi)
RR = Recompression ratio, average slope of recompression part of curve (σ_v between 4 and 10 psi)
SR = Swelling ratio, slope of rebound of curve (σ_v between 10 and 1 psi)

Table 3 Engineering values for soils, shreds (chips) and mixtures

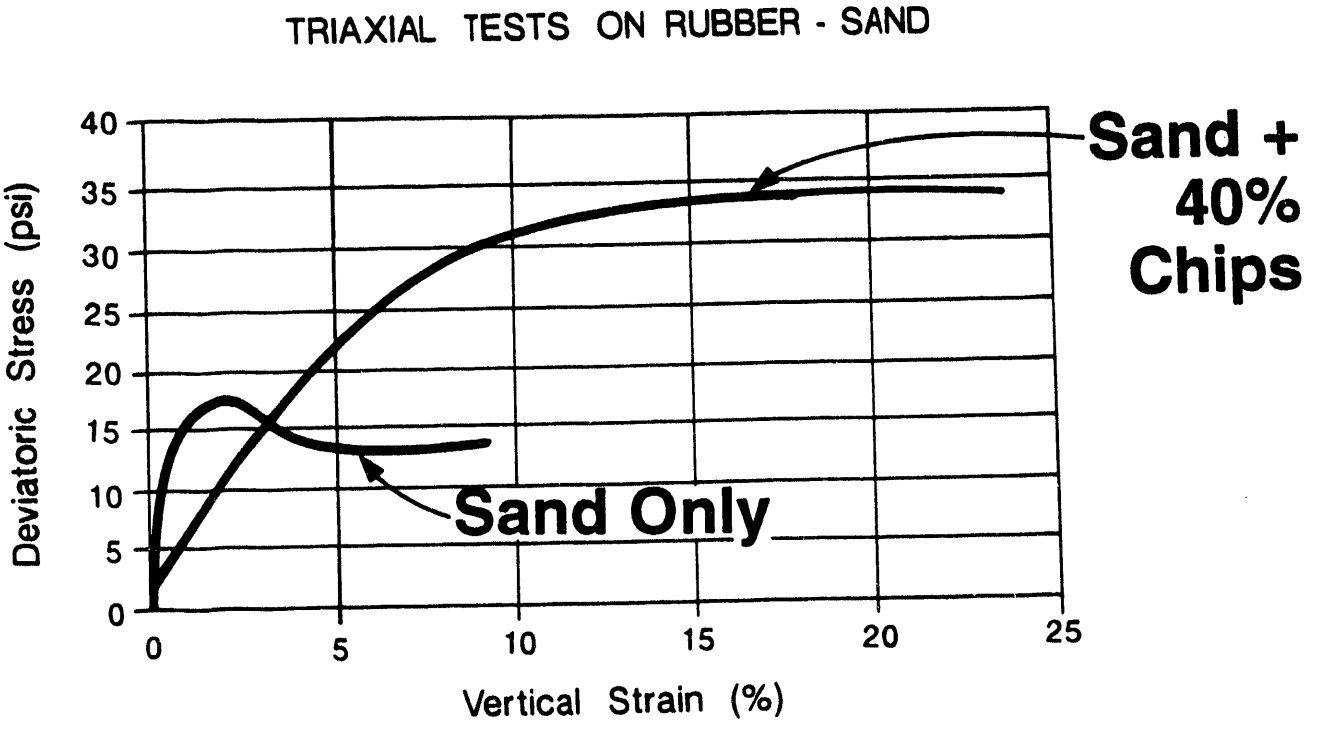


Figure 7 Increased strength of sands with shreds (chips); confining pressures of 4-5 psi

Transportation and the Federal Highway Administration who provided financial support through the Joint Highway Research Project, School of Civil Engineering, Purdue University.

REFERENCES

Ahmed, I. (1992), "Laboratory Study on Properties of Rubber Soils -Interim Report", Report No. FHWA/IN/JHRP-92/11, School of Civil Engineering, Purdue University, West Lafayette, Indiana, 145 pp.

Ahmed, I. (1993a), "Use of Waste Materials in Highway Construction", 1st Ed., Noyes Data Corporation (ndc), Park Ridge, New Jersey, 114 pp.

Ahmed, I. (1993b), "Laboratory Study on Properties of Rubber-Soils", FHWA/IN/JHRP-93/4, School of Civil Engineering, Purdue University, W. Lafayette, Indiana, 348 pp.

Ahmed, I. and C. W. Lovell (1993), "Rubber-Soils as Lightweight Geomaterials", Preprint for January 1993 Transportation Research Board Meeting, TRB, Washington, D.C., 22 pp.

Bosscher, P. J., Edil, T. B., Eldin, N. N. (1992), "Construction and Performance of a Shredded Waste-Tire Embankment", Department of Civil and Environmental Engineering, University of Wisconsin-Madison, Wisconsin, 17 pp.

Bressette, T. (1984), "Used Tire Material as an Alternative Permeable Aggregate", Report No. FHWA/CA/TL-84/07, Office of Transportation Laboratory, California Department of Transportation, Sacramento, California, 23 pp.

Elastizell (1992), "Engineering and Research Reports on Elastizell Engineered Fill", Sales Literature, Elastizell Corporation of America, Ann Arbor, Michigan.

EPA (1991), "Markets for Scrap Tires", Report No. EPA/530-SW-90-074A, United States Environmental Protection Agency, Office of Solid Waste, Washington, D.C. 115 pp.

Holtz, R. D. (1989), "Treatment of Problem Foundations for Highway Embankments", NCHRP Synthesis of Highway Practice No. 147, National Research Council, Washington, D.C. 72 pp.

Hunt, R. H. (1986), "Geotechnical Engineering Techniques and Practices", McGraw-Hill, Inc., New York, 729 pp.

Lamb, R. (1992), "Using Shredded Tires as Lightweight Fill Material for Road Subgrades", Draft Report Dated April 28, 1992, Materials and Research Laboratory, Minnesota DOT, Maplewood, Minnesota, 18 pp.

Leonards, G. A. (1962), "Engineering Properties of Soil", in Foundation Engineering, G. A. Leonards, ed., McGraw-Hill Book Company, New York, pp. 66-240.

Merdes, R. S. (1992a), Personal Communication, Dated March 15, 1992.

OECD (1979), "Construction of Roads in Compressible Soils", Organization for Economic Cooperation and Development, Paris, France, 148 pp.

Peck, R. B., Hanson, W. E. and Thornburn, T. H. (1974), Foundation Engineering, 2nd Ed., John Wiley & Sons, Inc., New York, 514 pp.

Read, J., Dodson, T., and Thomas, J. (1991), "Use of Shredded Tires for Lightweight Fill", Report No. DTFH-71-90-501-OR-11, Oregon DOT, Highway Division, Road Section, Salem, OR, 13 pp.

Hydrogeology, Waste Disposal, Science and Politics
Proceedings 30th Symposium
Engineering Geology and Geotechnical Engineering, 1994

SELECTED REMEDY AT THE QUEEN CITY FARMS SUPERFUND SITE: A RISK MANAGEMENT APPROACH

Weber, E.F., J. Wilson, and M. Kirk
Landau Associates, Inc., Edmonds, Washington
Tochko, S., The Boeing Company, Seattle, Washington

ABSTRACT

A risk management approach at a former industrial waste disposal site in western Washington resulted in a selected remedy that is cost-effective and that meets the CERCLA threshold criterion of protecting human health and the environment. The proposed remedy, which addresses contamination in soil and groundwater, does not require an ARARs waiver and received state and community acceptance. By analyzing the current and potential risk at the site, a proposed remedy was chosen that would control the source and naturally attenuate the groundwater plume. Source control will include removal and treatment of some light nonaqueous phase liquid (LNAPL) and some soil, followed by isolation of the remaining soil and LNAPL within a slurry wall and beneath a multilayer cap. A contingent groundwater extraction and treatment system was included to address uncertainty in the risk characterization.

Implementing source control is predicted to result in a steady decline in volatile organic compound levels in the drinking water aquifer through adsorption, degradation, and dispersion. Exposure to groundwater during the period of natural attenuation will be controlled by monitoring, institutional controls, and a thorough characterization of the plume and receptors.

INTRODUCTION

A selected remedy for groundwater and soil contamination is being implemented at the Queen City Farms (QCF) Superfund site in western Washington by the Potentially Responsible Parties (PRPs), in accordance with the requirements of the Comprehensive Environmental Response and Claims Liability Act (CERCLA). The scope of the remedy is the result of a decision making process by EPA documented in the Record of Decision (ROD) and based on the results of a Remedial Investigation (RI), Baseline Risk Assessment (BRA), and Feasibility Study (FS) conducted by the PRPs.

Three small ponds on the property received industrial wastes from the mid-1950s to 1968. The QCF site was entered on the National Priorities List (NPL) in 1984. Initial Remedial Measures (IRM) were completed in 1986, following a focused remedial investigation by the PRPs. One purpose of the IRM was to remediate and isolate the original waste ponds. The IRM actions, including a multilayer cap that covered the former ponds, are an integral part of the selected remedy.

A site-wide RI (including BRA) and FS, initiated in 1988 and completed in 1992, was intended to characterize the risk to human health and the environment and to provide a basis for evaluating and formulating a remedial response. The FS and ROD issued by the EPA in December 1992 are the result of a risk management approach used to evaluate and select a remedy. The risk management approach provided a context for balanced decision making based on multiple factors, including: the results of the baseline risk assessment and its inherent uncertainty; site characteristics and likely future land use; statutory requirements; and economic, social, and political factors. Site waste disposal and environmental regulatory actions are summarized in Table 1.

SITE CHARACTERISTICS (REMEDIAL INVESTIGATION)

The QCF site is a 320-acre parcel located in a rural setting directly east of the Seattle-Tacoma metropolitan area. The RI at QCF provided a thorough characterization of the site that is relevant to environmental decision making. Elements of this characterization are as follows: a history of the site, including hazardous waste disposal activities; a description of site features; a conceptual model of the site hydrology and hydrogeology; a characterization of the nature and extent of contamination; and a conceptual model of contaminant migration.

The QCF site has been used for a variety of activities, including: a pig farm, an industrial waste disposal site (at former ponds 1,2 and 3), an airstrip, a gravel mine (beginning in the mid-1970s), and recently a yard waste composting facility. The extent of these activities at the site is delineated on a plan view (Figure 1). Also shown on Figure 1 is the approximate location of the IRM multilayer cap, which was placed over the industrial waste

TABLE 1
SITE HISTORY

- Industrial waste disposal from mid-1950s to 1968 into three ponds
- Site placed on NPL list in 1984
- Initial Remedial Measures (IRM) in 1986 - removal of residual wastes, sludges, and contaminated water from ponds; and covering pond area with a multilayer cap
- Remedial Investigation, Baseline Risk Assessment, and Feasibility Study conducted from 1988 to 1992
- ROD issued in 1992
- Consent Decree for Remedial Design/Remedial Action to be signed in early 1994.

ponds after liquids, sludge, and surface soils were removed for treatment and disposal in 1986 as part of an interim measure.

Much of the geology at the site is the result of depositional and erosional processes at a glacial ice margin. These processes resulted in extensive commercial gravel deposits at the site, as well as complex geology that was difficult to characterize.

Three aquifers were identified at the site. Aquifer 1 is a small (less than 15 acres) perched aquifer in the glacial gravel deposits. Aquifers 2 and 3 are regional (used for drinking water) aquifers consisting of relatively low-permeability, interglacial silty sands of fluvial lacustrine origin. Aquifer 3 is separated from Aquifer 2 by a silt aquitard. Aquifer 1 discharges to surface springs and as groundwater directly to Aquifer 2. The relationship of these three aquifers is summarized on a conceptual hydrogeologic cross section on Figure 2.

Contamination at the site is separated into four remedial units. The IRM area remedial unit consists of residual soil contamination, LNAPL, and associated Aquifer 1 groundwater contamination. Because of a natural groundwater divide, only a small portion of Aquifer 1, beneath the IRM, shows appreciable contamination. The portion of Aquifer 1 outside the IRM, along with associated surface springs, has low levels of contamination and represents a second remedial unit. The Buried Drum Area (BDA) remedial unit represents near surface soil contamination and associated debris near the IRM. These three remedial units are delineated on Figure 3. An impacted area of Aquifer 2 represents the fourth remedial unit which is approximately delineated by the extent of detected Trichloroethene (TCE) contamination (Figure 4).

Volatile and semi-volatile organic constituents, PCBs, and metals are associated with the IRM and BDA remedial units. The mobility of most of these constituents is limited by natural fate and transport processes in combination with physical characteristics of the site. Consequently, only low levels of volatile organic compounds (VOCs) principally TCE, are associated with the Aquifer 1 (outside the IRM vicinity) and Aquifer 2 remedial units. The nature and extent of impacted media is summarized in Table 2.

Concentrations of constituents in groundwater have not changed appreciably since the beginning of a long-term monitoring program initiated in 1987. Significantly, concentrations of VOCs have not increased and the plume does not appear to have expanded in Aquifer 2, a consequence of natural processes of adsorption,

Figure 1

SITE PLAN

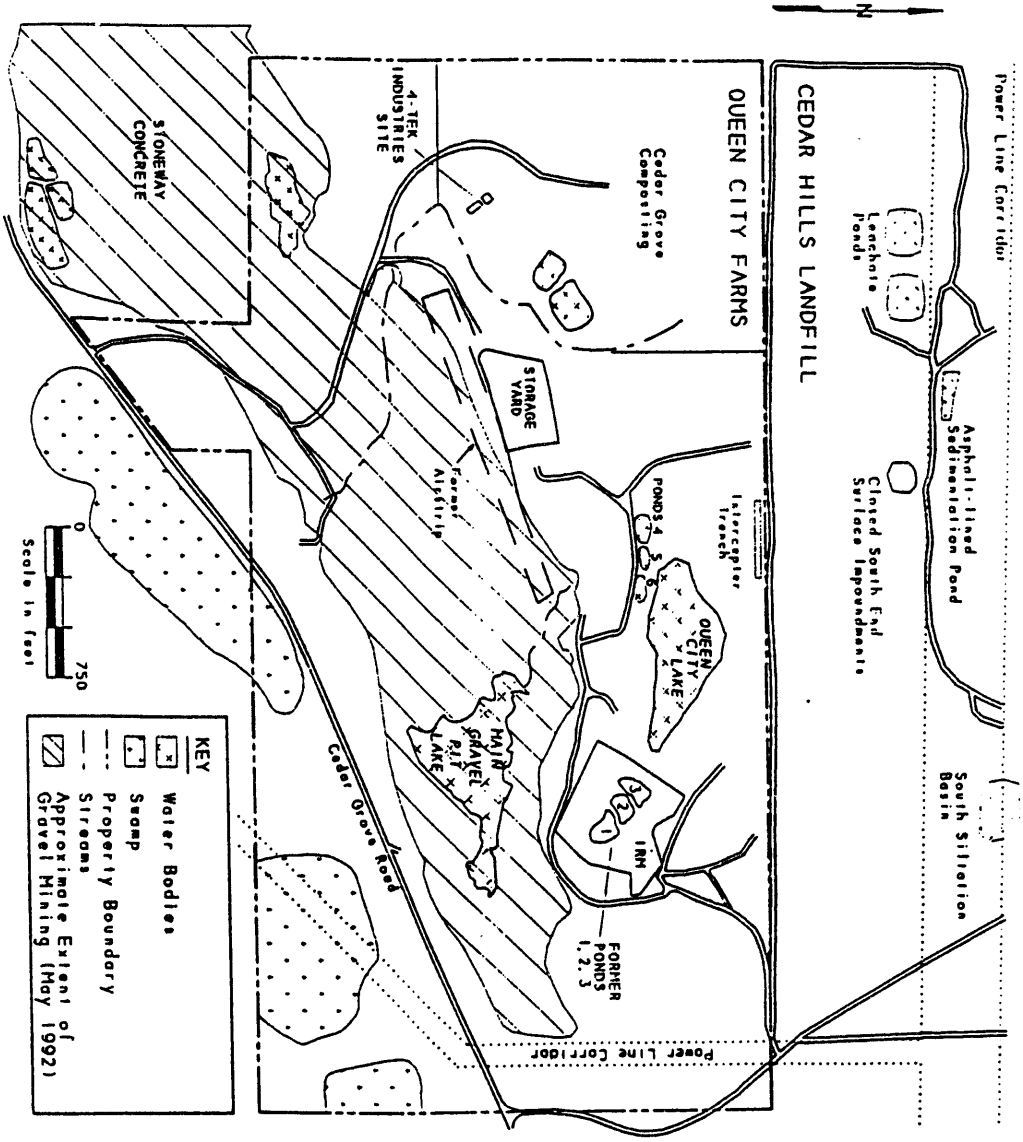


Figure 2

CONCEPTUAL HYDROGEOLOGIC CROSS SECTION

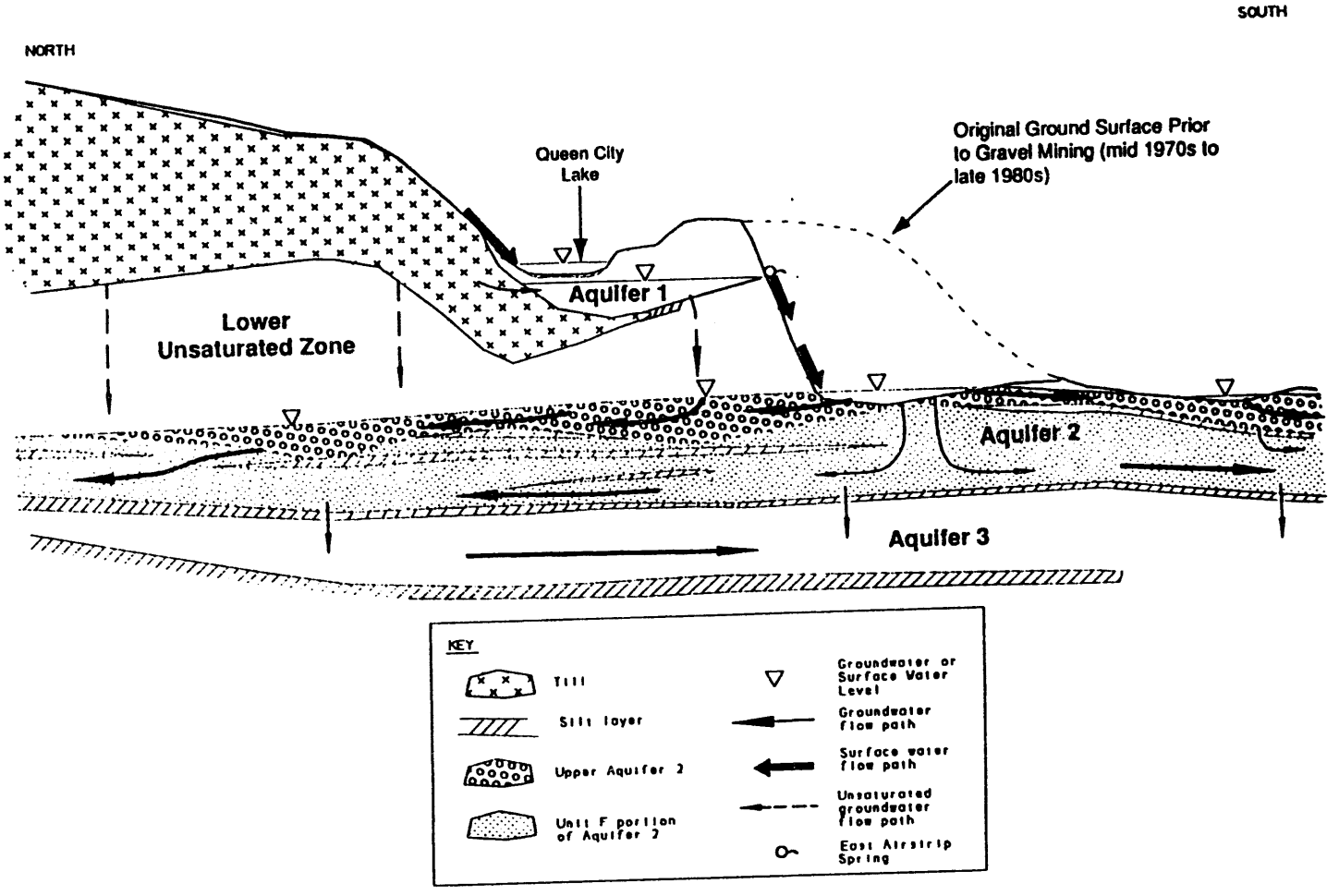


Figure 3
AQUIFER 1, IRM, AND BURIED DRUM AREA

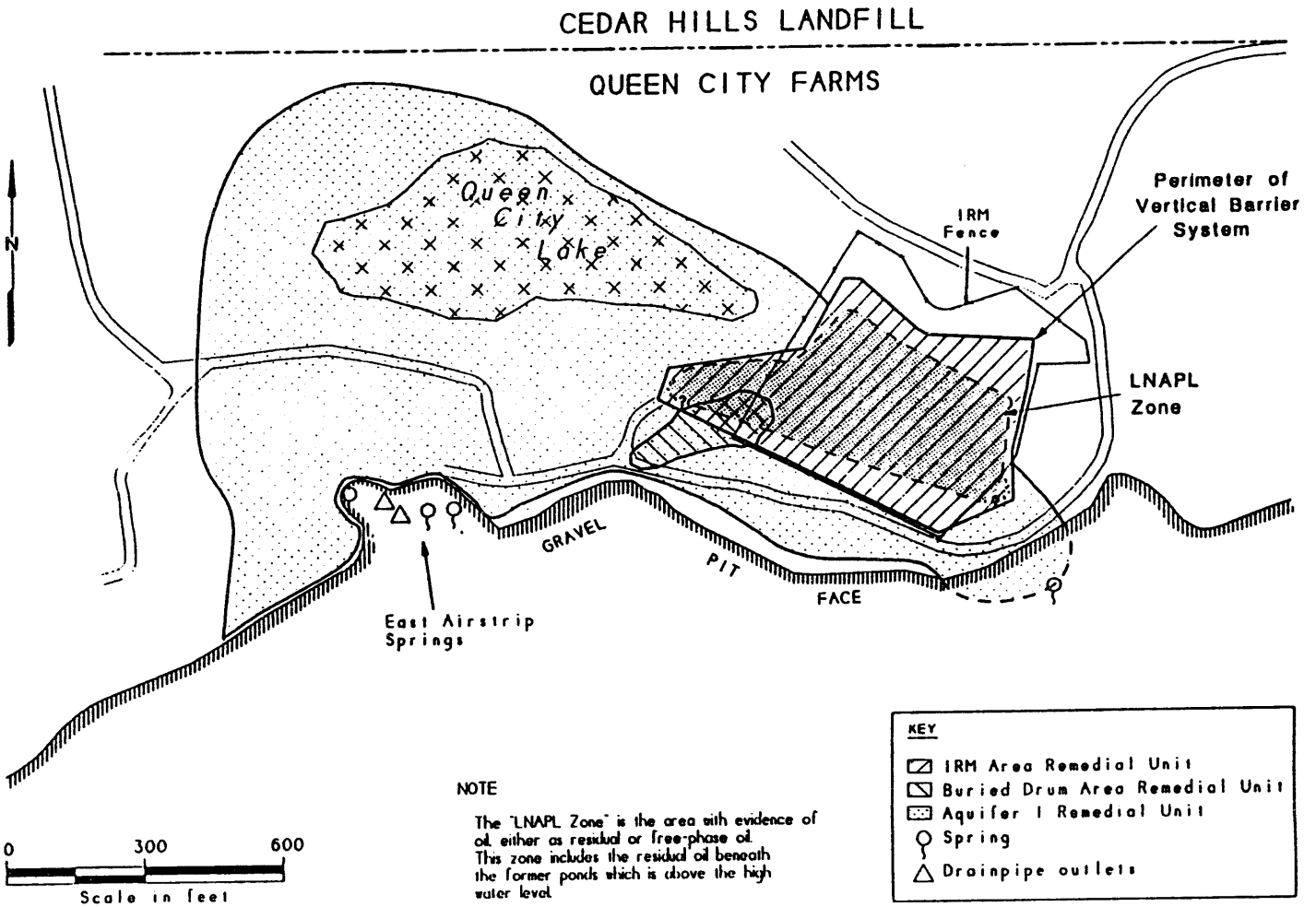


Figure 4

DISTRIBUTION OF TCE IN AQUIFER 2

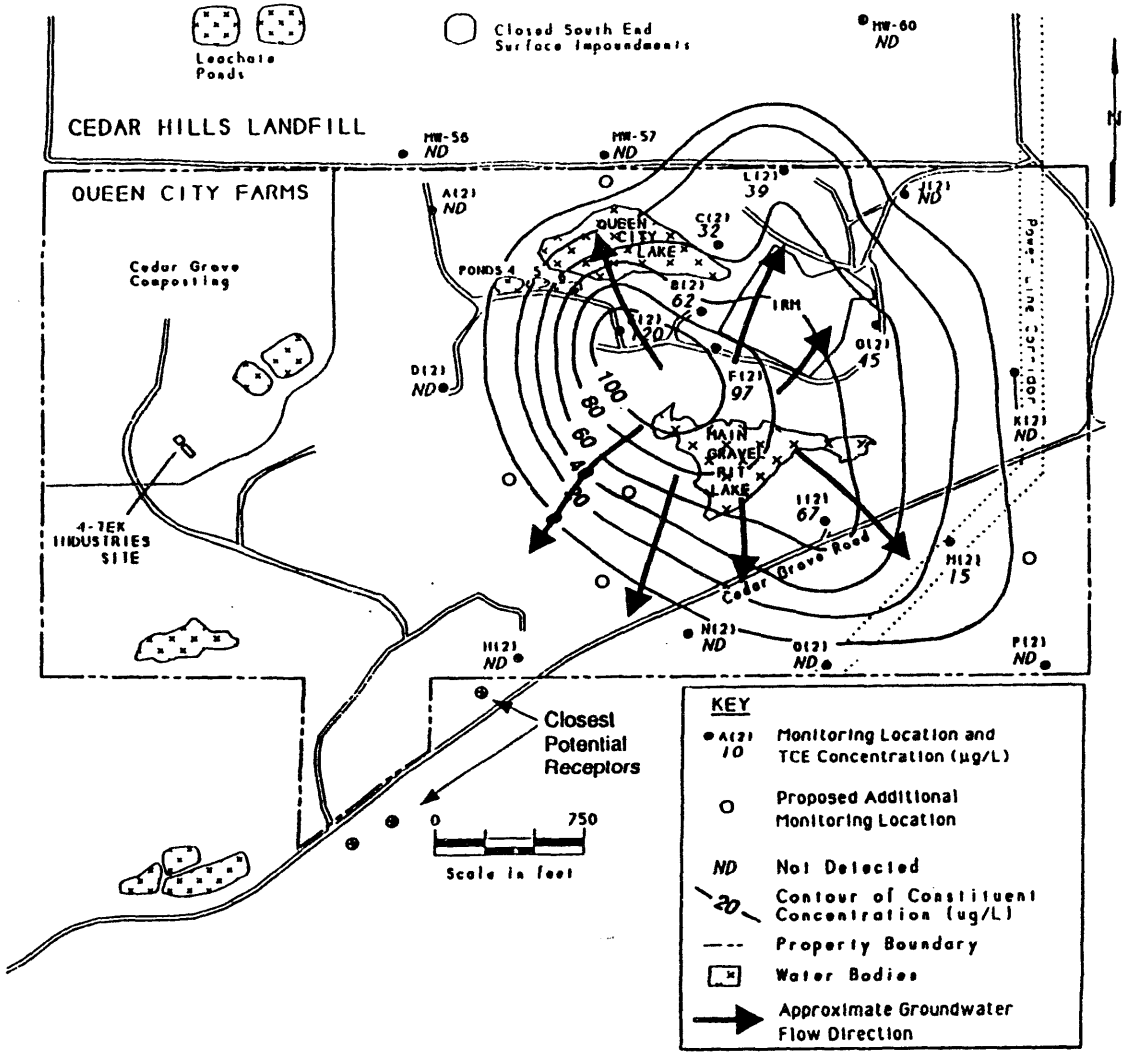


Table 2
IMPACTED MEDIA

Media	*Source of Contamination*	*Extent*	*Constituents of Concern*
IRM Area Soils (IRM Remedial Unit)	• Original disposal ponds that were remediated in 1986 • Existing LNAPL layer in Aquifer 1	• Area beneath the IRM cap extending down to the Aquifer 1 aquitard	• Volatile and semivolatile organic compounds • Metals • PCBs
Buried Drum Area (BDA) Soils (BDA Remedial Unit)	• Buried drums and associated soils	• Near surface soils beneath the BDA	• Volatile and semivolatile organic compounds • Metals • PCBs
Aquifer 1 Groundwater in the Vicinity of the IRM (IRM Remedial Unit)	• Residual soil contamination • LNAPL layer	• Limited extent of Aquifer 1 in the direct vicinity of the IRM	• Volatile and semivolatile organic compounds • Metals • PCBs
Aquifer 1 Groundwater Outside the Vicinity of the IRM (Aquifer 1 Remedial Unit)	• Aquifer 1 groundwater in the vicinity of the IRM	• All of Aquifer 1 outside the vicinity of the IRM, which includes the majority of the aquifer	• Chlorinated volatile organic compounds
Surface Water Springs (Aquifer 1 Remedial Unit)	• Aquifer 1 groundwater	• Two spring discharge areas limited in areal extent	• Chlorinated volatile organic compounds
Aquifer 2 Groundwater (Aquifer 2 Remedial Unit)	• Aquifer 1 groundwater	• Plume extending radially from groundwater mound located in Aquifer 2 beneath Aquifer 1 and the Main Gravel Pit Lake	• Chlorinated volatile organic compounds

degradation, and dispersion, and the effect of the IRM source control in 1986.

SITE RISKS (BASELINE RISK ASSESSMENT)

The BRA conducted by the PRPs formed a basis for remedy selection. The BRA consisted of four stages of analysis: hazard assessment, toxicity assessment, exposure evaluation, and risk characterization. Risk characterization represents the synthesis of the preceding three analyses into a conclusion as to the baseline risk to humans at the site. A summary of the BRA process performed at QCF is presented in Table 3. Estimated site cancer and non-cancer risks are summarized in Figures 5 and 6.

The results of risk characterization indicate that relatively few constituents and exposure pathways were found to contribute to the majority of estimated human health risk. Most estimated site cancer and non-cancer risk is due to Aquifer 1 groundwater directly beneath the IRM, along with BDA surface and subsurface soils. Consequently, the selected remedy focused most resources on the IRM and BDA remedial units. Remedial actions being implemented include treatment and containment technologies. Estimated site cancer and non-cancer risk is limited due to exposure to Aquifer 1 groundwater outside the IRM and associated surface water springs, as well as Aquifer 2. Consequently, institutional controls and natural attenuation were deemed appropriate response actions for the Aquifer 1 and Aquifer 2 remedial units.

SELECTED REMEDY

The selected remedy in its simplest form consists of source control and aquifer restoration. The BDA and IRM areas are the source areas for groundwater contamination. Implementation of source control measures in these areas is predicted to result in a steady decline in VOC concentrations in Aquifer 1 and Aquifer 2 by natural processes of dispersion, degradation, and adsorption.

The application of source control at QCF will consist of the following approach:

- Remove and treat sludges, soils and LNAPL exhibiting high levels of contamination
- Leave soils with low levels of contamination in place
- Apply containment options to prevent exposure to and migration of soil contaminants
- Apply institutional controls to protect containment options and limit exposure to soils left in place.

The majority of remedial resources will be applied to source control treatment and containment actions, which included extending the multilayer cap to cover part of the BDA, as well as installation of a slurry wall that, when completed, surrounds the IRM and part of the BDA remedial units to the bottom of Aquifer 1. Extension of the cap and installation of the slurry wall will result in dewatering the most contaminated portion of the aquifer.

The application of aquifer restoration at QCF will consist of the following approach:

- Remove and isolate the potential sources of groundwater contamination (IRM and BDA soils)
- Achieve long-term restoration of groundwater through natural remedial processes of degradation, adsorption, and dispersion

Table 3
SUMMARY OF BASELINE RISK ASSESSMENT PROCESS AT QCF

Hazard Assessment

Metals and organic compounds were found to be present in soil, groundwater, and surface water springs as a result of onsite waste disposal.

Exposure Assessment

Three exposure scenarios were evaluated:
- Onsite occupational
- Onsite residential
- Onsite recreational

Exposure Pathway Evaluated:

- Dermal contact with and incidental ingestion of soil
- Use of groundwater as a potable water source (dermal contact, inhalation of vapors, and ingestion)
- Ingestion of food crops grown onsite
- Soil particulate inhalation
- Ingestion of surface water

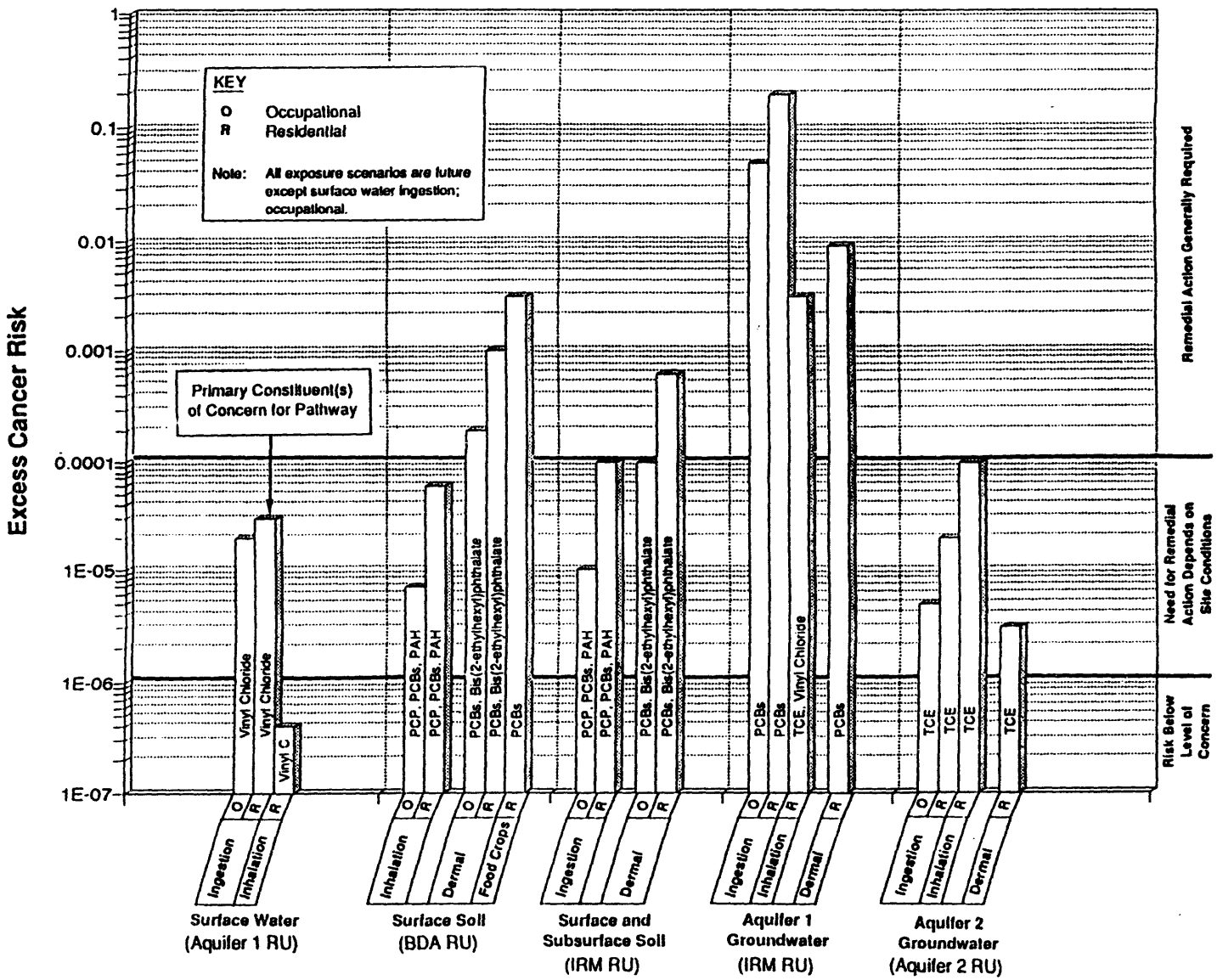
Toxicity Assessment

EPA-derived toxicity criteria were used.

Risk Characterization

Relatively few constituents and exposure pathways were found to contribute to the majority of estimated human health risk.

Figure 5
Total Cancer Risks at QCF Site



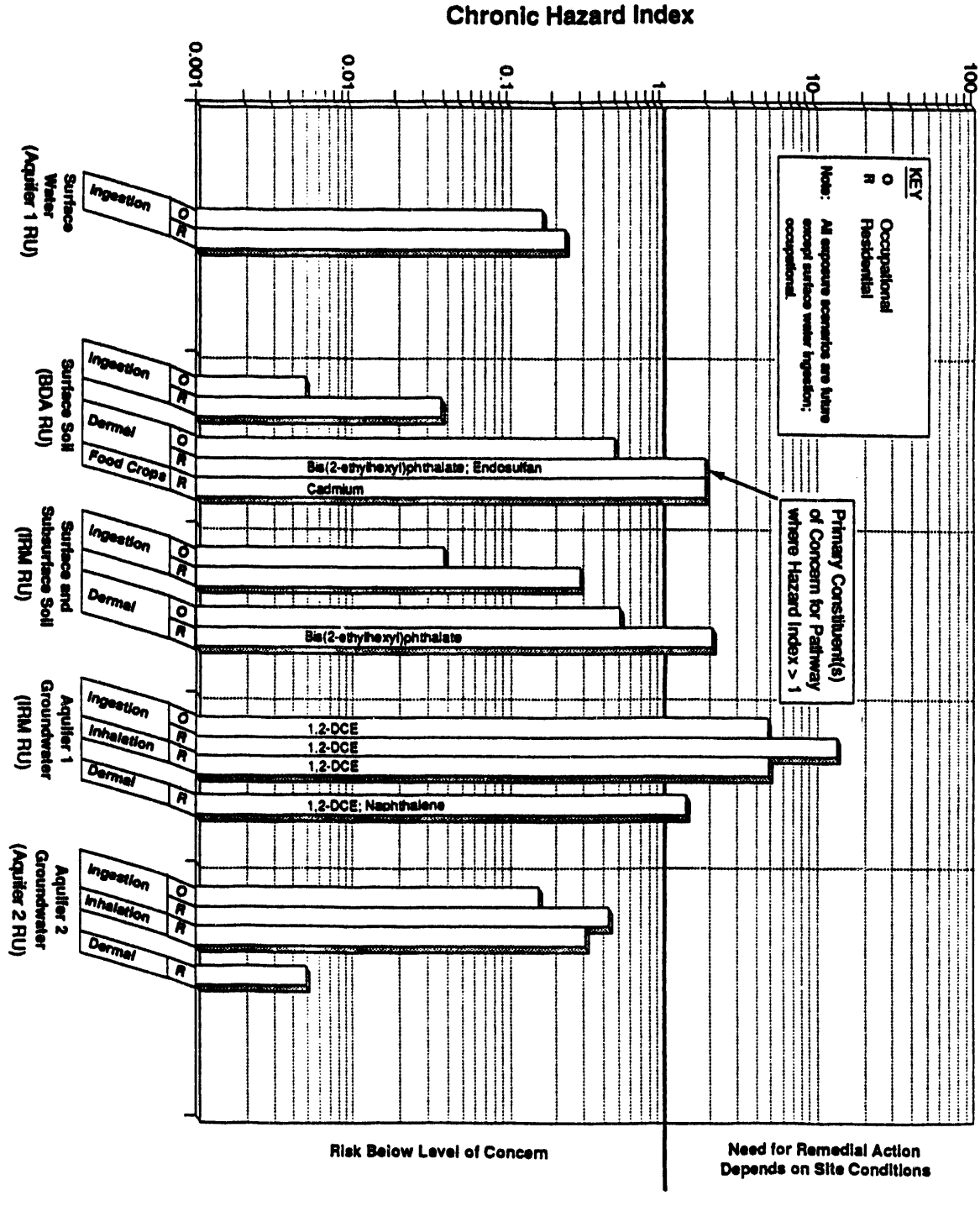


Figure 6
Total Non-Cancer Risks at QCF Site

- Evaluate the effectiveness of natural attenuation through statistical trend analyses of groundwater monitoring data
- Control short-term exposure to contaminated groundwater through institutional controls, groundwater monitoring, and possible use of remedial contingencies.

Because of uncertainties in predicting the rate and effectiveness of natural attenuation processes, contingent extraction (pumping) and treatment systems were included in the remedy, as was a contingent alternative water supply for private drinking water wells. The contingent remedy may be triggered based on an interim evaluation of the effectiveness of natural attenuation. Aquifer 1 is targeted to meet risk-based cleanup goals in 5 years and Aquifer 2 to meet maximum contaminant levels (MCLs) within 10 years.

RISK MANAGEMENT APPLICATIONS IN THE SITE REMEDY

Risk management is the process of regulatory decision making once a problem has been identified through risk assessment. At the QCF site this process involved balanced application of CERCLA decision making criteria in the FS and ROD. Risk management uses the results of the risk assessment and other information, including statutory, economic, and political considerations. The result is a balanced remedy that is cost-effective, protective of human health, consistent with applicable laws and statutory preferences, and received community acceptance. The risk management process at QCF involved eight elements. A summary of the risk management process and its application at the QCF site is presented in Figure 7.

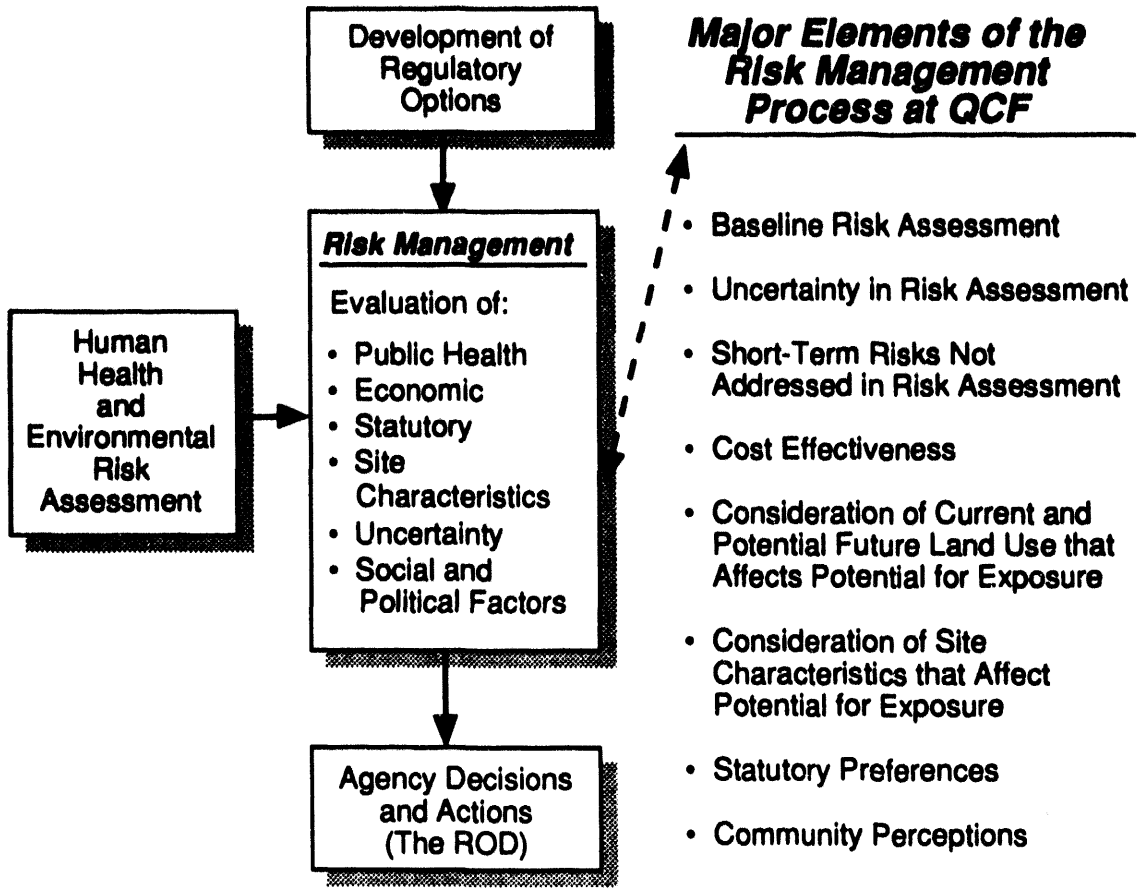
The BRA established site risks at QCF based on standardized procedures. This element of the risk management process established the extent and scope of the problem. The BRA is a quantitative and qualitative assessment based on a data base that is incomplete, which leads to potential uncertainty in the following areas:

- Accuracy and representativeness of sampling data
- Accuracy and representativeness of exposure scenarios
- Accuracy and representativeness of toxicological data.

Where uncertainty was identified to be relatively high, the BRA approach was to apply conservative (protective) assumptions that tend to overestimate risk. This approach invariably leads to the selection of a remedy that is also conservative. A goal of the RI was to reduce uncertainty where possible. For example, the uncertainty associated with the accuracy and representativeness of sampling data was considered to be fairly small due to thorough characterization of contaminant migration pathways and rigorous QA/QC program. A goal of the FS and ROD was to identify and account for areas where conservative risk assumptions were applied. For example, exposure to Aquifer 1 and Aquifer 2 is based in part on future residential use. Aquifer 1 residential use is very unlikely, due to its limited ability to supply potable water to a household year-round. This limitation supported the use of a natural attenuation remedy that might take longer than an extraction and treatment remedy. Scenarios involving long-term exposure to soil are probably conservative because exposure

Figure 7

SUMMARY OF THE RISK MANAGEMENT PROCESS AT QCF



concentrations are based on hot-spot sampling, thereby supporting the effectiveness of containment and isolation of some soils in place. The uncertainty associated with the natural variability in hydrogeology makes it difficult to completely characterize physical, chemical, and biological parameters that control contaminant fate and transport. Consequently, there is some uncertainty associated with the effectiveness of natural attenuation, uncertainty that was addressed by implementation of long-term monitoring and the specification of contingent remedial actions.

Remedy selection at QCF considered short-term risks associated with the remedy. Complete excavation and treatment of all contaminated soil at the site was eliminated as a consideration, in part because of the associated health risk to workers and the community.

A cornerstone of the risk management approach is the realization that typically, only finite resources are available to address risk. Therefore, the decision maker is concerned about the cost-effectiveness of the selected remedy. At QCF, more resources were allocated to media and pathways that represented higher risks in order to achieve the most risk reduction for a given cost.

Consideration of current and future land use was also a part of the remedy selection process. The location of a landfill along the site's northern boundary, for example, makes future residential exposure to Aquifer 2 unlikely, supporting natural attenuation. Future residential exposure was also considered less likely because of the existing gravel mine and composting facility.

In addition, site characteristics influenced remedy selection. For example, it was determined that Aquifer 2 recharge and discharge patterns and low permeability limit the likelihood of future offsite exposure and favor natural attenuation processes. These characteristics were a factor in selecting natural attenuation as part of the remedy.

Finally, effective risk management should also include the consideration of legal, social and political factors. Accordingly, elements of the QCF site remedy specifically address statutory preferences. LNAPL and soil removal and treatment address the preference for treatment. A passive soil venting pilot test addresses the preference for innovative technologies. And based on the mandate and guidelines for community involvement, local landowners were informed about the risks and the remedial alternatives and accepted the selected remedy.

SUMMARY

Balanced application of remedy evaluation and selection criteria in the FS and ROD results in a risk management approach to remedy selection. This approach, as applied at the QCF site, results in the following:

- A remedy that is consistent with the NCP
- A context for balanced decision making
- More efficient and consistent risk reduction policies
- Efficient allocation of resources to address site risks
- A more effective and implementable remedy
- Consideration of the concerns of all affected parties within the constraints of threshold criteria.

Hydrogeology, Waste Disposal, Science and Politics
Proceedings 30th Symposium
Engineering Geology and Geotechnical Engineering, 1994

BIOVENTING FEASIBILITY STUDY OF LOW PERMEABILITY SOILS FOR REMEDIATION OF PETROLEUM CONTAMINATION

Kevin M. Brackney, M.S., P.G.
University of Idaho Center for Hazardous Waste Remediation Research
Moscow, ID 83844-1052

ABSTRACT

A site characterization of leaking underground gasoline and diesel storage tanks at the University of Idaho, West Farm Operations Center, identified approximately 800 cubic yards of petroleum-contaminated soil exceeding regulatory action limits of 100 ppm TPH. Bioventing, a combination of in situ soil vapor extraction and microbial degradation, was selected as a remedial alternative on the basis of the presumably unsaturated paleo-soil with a 45-foot depth to groundwater, and a microbial study which concluded that indigenous petroleum-degrading microorganisms existed throughout the contamination. Soil vapor extraction tests were conducted by applying a 60-inch water column vacuum to a soil vapor extraction well and monitoring pneumatic pressure drawdown in 12 adjacent pneumatic piezometers and vertically distributed piezometer clusters. Pressure drawdown vs time data plots indicated that air permeability is inadequate everywhere at the site except at 20 feet below ground surface. Low soil permeability creates conditions for a perched water table that was documented during the investigation, resulting in unsatisfactory conditions for in situ bioventing.

SITE INVESTIGATION

Two 1500-gallon gasoline and diesel underground storage tanks (USTs) were excavated at the University of Idaho (UI) West Farm Operations Center in December of 1990. The tanks had been abandoned a decade earlier when water began contaminating the fuel. When the two USTs were excavated at the UI West Farm site, several four-inch-diameter holes were observed in the tanks. Strong odors were noticed, and concentrations exceeding 2000 parts per million (ppm) were determined with a hand-held photo ionization detector (PID) (Chen-Northern, 1991).

A site investigation was conducted by drilling 17 hollow-stem auger boreholes (Fig. 1) which were sampled by drilling 3 feet, then driving a split-spoon sampler lined with brass sleeves into the soil for 2 feet. Drilling and sampling continued to an average 25-foot depth for each borehole. One six-inch core from each sample was analyzed by the UI Analytical Laboratory for total petroleum hydrocarbons (TPH)-gas and TPH-diesel by EPA Method 8020, volatile organics by EPA Method 8260, and total lead by EPA Method 3050. A hand held PID calibrated to isobutylene was used to assist in field contaminant characterization. Geologic cross-sections were constructed in the field and plotted with PID concentrations to guide the investigation. The boreholes were terminated where geologic evidence suggested the limits of contamination had been reached and PID readings were <100 ppm.

Approximately 800 yd^3 of petroleum-contaminated soil exceeding regulatory action limits of 100 ppm TPH as gasoline or 1000 ppm TPH as diesel were identified in an area approximately $35 \times 50 \times 20$ feet deep (Fig. 1.) (Ralston et al. 1992.) Interestingly, the highest contamination was not found under the tank but offset $\approx$40 feet downhill, suggesting a component of lateral

subsurface flow. Sample values of up to 2,900 ppm TPH-gas and 54,000 ppm TPH-diesel were collected from 10-20 feet below ground surface in borehole WF-6 in this area. No volumetric estimate of leaked fuel is available, since inventory control records were not maintained.

Mean lead concentration at the site was 20 ppm with background lead concentrations of ≈10 ppm. One borehole immediately adjacent to the regular gasoline tank location (WF-3) had 15 feet of gasoline contaminated soil averaging 226 ppm total lead, a concentration considered high enough to fail the toxicity leaching control procedure (TCLP) for lead, thereby potentially characterizing the soil as hazardous waste, *if excavated.* This lead-contaminated borehole was later twinned by drilling a second borehole (WF-16) 1.5 feet south which contained a mean lead concentration of 28 ppm total lead and <3.5 ppm leachable lead based on TCLP results.

General Geologic/Hydrologic Setting

At the West Farm site, surface geology consists of silt and clay of the Palouse formation, mostly wind-derived sediments (loess.) Soils have been mapped by the University of Idaho Agricultural Experiment Station as Palouse Series soils consisting of silt loam and grading into silty clay loam at 52 inches. The Palouse soils are characterized as being very deep, well drained soils on upland positions with 7% to 12% slopes. Depth to water is >6 feet. The available water-holding capacity of the soil is high (0.19-0.21 in/in) with a permeability of 0.6 to 2.0 inches per hour. Of potential significance is the tendency of the soil to develop severe piping characteristics defined as the formation of tunnels or pipe-like cavities by moving water. The soil texture is blocky to prismatic with many very fine to medium-fine tubular pores. Some soil horizons have up to 20% old vertical worm channels (McDole and Peterson, 1989). Locally, erosion has exposed flows of the underlying Columbia River Basalt Group.

A downward groundwater gradient exists within the Moscow area. Shallow wells (<20 feet) located at the University of Idaho Groundwater Research Site (located 1000 feet north of the UST site) have static water levels 5-10 feet below land surface. Deeper wells (80-150 feet) completed in the basalt have depth-to-water values in the range of 10 to 20 feet. Nearby city and university water supply wells draw water from depths of 600 to 1,200 feet and have static depth-to-water values of 250-300 feet. Based on available information, the estimated depth to the shallowest groundwater underlying the UST site is >45 feet (Ralston, et al, 1992.)

Site Stratigraphy

Although the fine-grained silty clay loess soils at the site were difficult to characterize, relative soil density was one of the more significant stratigraphic characteristics. Total blow counts to pound a 2-foot split-spoon sampler with a 140 pound safety hammer at approximate ≈5-foot intervals in each borehole indicate relative soil density. A mean value was calculated for each 5-foot interval, representing the relative density for that interval over the site. The relative soil density at 5 feet below ground surface (bgs) was 43 blows. A dense silty clay from 10-20 feet bgs averaged 73 blows, with maximum values of >100 blows. In contrast, the mean blow count to penetrate 2 feet at 25 feet bgs was 37 blows. This dense silty clay present from about 10-20 feet represents a paleo-"B" soil horizon that may have formed during the Pleistocene. Two buried lenticular paleo-stream channels consisting of quartz feldspar sand and gravel were intercepted at 30 feet bgs. These paleo-stream channels were surrounded on at least three sides by loess. The

deeper of the two (WF-2) was not fully penetrated, while the shallower lenticular sand was underlain by loess. When borehole WF-2, which bottomed in gravel at 30 feet bgs, stood open overnight; no water was present in the borehole the following morning. Two other boreholes had minor water seeps that appeared to be entering the holes on top of the dense clay horizon.

Basaltic bedrock or boulders were intercepted in two boreholes at the site. Depth to the basalt at the UST site increases from 14 feet bgs in VE-1 southwest of the site (Fig. 2), to 27.5 feet on the northeast side of the contamination (WF-17), to >31 feet on the north end of the site. This deepening of basalt intercepts is believed to reflect basalt ledges buried by loess stair stepping down to the valley of Paradise Creek located about 1000 feet north of the site.

SOIL VAPOR EXTRACTION/BIOVENTING FEASIBILITY STUDY

A literature review of possible remediation methods covered landfarming, low-temperature thermal desorbtion, and soil vapor extraction/bioventing. The advantages of treating the petroleum contaminated soil by in situ bioventing are potentially lower cost, avoidance of "generating" hazardous waste (e.g. lead) by excavation, and ability to remediate under buildings, roads, utility conduits, etc. Some of the disadvantages of excavating contaminated soil are that additional non-agricultural land is needed for landfarming, and landfarmed soils are only suitable for construction backfill or disposal as solid waste.

In situ soil vapor extraction/bioventing seeks to take advantage of two processes:

1. The removal of volatile phase hydrocarbons from the soil by establishing a pressure gradient and venting the effluent to the surface for subsequent disposal.
2. Supplying oxygen and nutrients to petroleum-degrading microbes.

The combination of these two processes is very effective for landfarming petroleum contaminated soils where oxygen, nutrients, and microbes can be manipulated to enhance volatilization and microbial degradation. In situ soil vapor extraction/bioventing utilizes these same processes, but control of the critical variables is more difficult in subsurface geologic materials that must be accessed from the surface via wells and trenches. The main distinction between bioventing and soil vapor extraction (SVE) is that bioventing attempts to degrade contaminants in situ by minimizing the amount of volatiles extracted, while soil vapor extraction attempts to maximize the mass transport aspects of remediation. Essentially, they are end members of the same process.

In sandy soils with high air permeability there are many well documented examples of soil venting of volatile organic fluids (e.g. gasoline) (Hutzler et al, 1989). However, organic molecules larger than C_{10} do not readily volatilize and are logical targets for microbial degradation (Johnson, 1990.)

The diesel- and gasoline-contaminated West Farm site soils consist of silt loam to silt clay loam. Although soils of this size fraction are less amenable to bioventing due to low air permeability values, the presence of soil macropores suggested that natural permeability might be sufficient for effective bioventing. The possibilities for permeability enhancements by utilizing vapor extraction trenches to increase surface contact of the vacuum with the soil and the potential for hydraulically or pneumatically fracturing the sediments further supported possible bioventing at this site. Johnson (1990) identified the need for a well-documented case history of soil vapor extraction in low-permeability soil. These combined factors led to the university's conclusion that the advantages of bioventing at the West Farm site outweighed the disadvantages of the low

permeability soil. With the encouragement of the Idaho Department of Environmental Quality, we began evaluating the in situ soil air permeability and potential for microbial degradation.

Pneumatic Well Field Design and Installation

A pneumatic well field and piezometer cluster network was designed to characterize the vertical and horizontal distribution of air permeability within a 10 foot radius around a vapor extraction well (Fig. 2.) Proposed testing included a constant pumping test and monitoring change in pneumatic pressure and soil gas concentrations (TPH, O_2) with respect to time at varying radial distances and depths from a pumping or vapor extraction well. Oxygen content of extracted soil gas from the contaminant zone was to be compared with a background well to determine if oxygen uptake (an indication of microbial respiration) was occurring.

During the vapor extraction well drilling it was observed that significant formation damage occurred with the buildup of a clay wall cake on the borehole wall. Removal of the clay wall cake was considered necessary since it would inhibit the characterization of the natural soil air permeability. Two methods of open borehole well development were attempted, utilizing compressed air and oversize borehole reaming. The compressed air seemed to have the highest likelihood of success but the results were erratic and difficult to control. Lack of visibility down the borehole, combined with either ineffective removal or significant erosion of the borehole wall, prevented consistent removal of the wall cake. Oversize reaming with a short piece of 6 inch diameter steel casing studded with sharpened bolts was moderately effective at tearing the clay wall cake off without smearing the clay.

To complete the vapor extraction wells, we used groundwater monitor well construction techniques, including 20 slot (0.020 inch spacing) well screen, a pea gravel filter pack surrounding the screen, and a minimum of 4 feet of non-shrink construction grout to form an impermeable seal from the surface to prevent short-circuiting of the well to the atmosphere. Piezometer clusters were constructed similarly except that 5 one-inch PVC standpipes were installed in a single borehole from 5-25 feet. Each 0.5-foot screened interval had an individual gravel pack and was sealed from adjacent piezometers with 3 feet of non-shrink construction grout. The wells and piezometers were then sealed and plumbed with hose barbs, narrow flexible tubing, and valves to allow the measurement of soil air pressure with Dwyer differential air pressure gages.

Well and piezometer installations appeared to be very effective at isolating zones from each other and the atmosphere. Indeed, both positive and negative differential pressures were measured under ambient (non-pumping) conditions in a single borehole at variable depths. This decouplement of soil air pressure from atmospheric air pressure was later determined to be some of the more significant data used to characterize the air permeability at the site.

Soil Vapor Extraction Tests

The extraction test was conducted using an explosion-proof Rotron regenerative blower (Model DR 505) capable of producing a maximum of 60-inch water column (wc) vacuum, air-water separator tank, Dwyer differential air pressure gages ranging from 2- to 80-inch wc, pieto tube and gage to measure exhaust air velocity, and a recording microbarograph to correct differential soil pressures to actual pressure.

Four vapor extraction tests were conducted with limited success. Test 1 pumped well VE-2 (Fig. 2) and was abandoned after 6 hours because short circuiting was occurring and all extracted air was being withdrawn from a 0.25 inch sand layer correlated with one of the previously described sand channels. This short circuiting of air was determined when pressure drawdown was occurring only at the 20-foot pneumatic piezometer level at a radial distance of 5 feet from the extraction well. The vapor extraction blower was then moved to well VE-4. Test 2 pumping well VE-4 was abandoned because of technical difficulties. Test 3 pumping well VE-4 collected the most useful data (see below). Test 4 repeated Test 3 but an impermeable soil cover and the substitution of the totalizing gas flow meter for the pieto tube. Very low flow velocities from the extraction well were below the design tolerances for the pieto tube. Because the recording microbarograph operated by the State Climatologist at UI failed during Test 4, the interpretation of data is seriously inhibited by lack of barometric data.

Soil Vapor Extraction Data Analysis (Test 3)

Vapor extraction test 3 operated for about 5.6 days at a 60 inch wc vacuum that produced a flow of 0.17 standard cubic feet of air per minute (SCFM). Passage of an atmospheric front through the Moscow area during the test complicated the interpretation of the data. A review of the soil pressure drawdown vs time data from the two piezometer clusters at 5-and 10-foot radial distances from the pumping well (clusters VE-5 and VE-6, respectively) illustrates the horizontal and vertical heterogeneities of air permeability at the West Farm site (Fig. 2.) At the 5, 10, and 15 foot depths in both piezometer clusters soil air pressures generally exceeded atmospheric pressures (Figs. 3-8.) Negative differential soil air pressures (i.e., less than atmospheric pressure) were only seen at 20-foot depths in both clusters (Figs. 9 and 10) Soil air pressure in VE-5 at 25 foot depth exceeded atmospheric pressure at most time increments (Fig. 11), while the highest positive differential pressures observed on the site occurred in VE-6 at 25 ft (Fig. 12).

The highest permeabilities at the site were found at the 20-foot soil depth, repeating the pressure response observed in Test 1. This increased permeability may be correlated with an erosional period and lateral deposition of stream channels from ancestral Paradise Creek. The very dense paleo-"B" soil horizon does not appear to have sufficient natural air permeability to support bioventing.

A limitation of the above data set is that insufficient ambient soil pressure monitoring (non-pumping) data was collected. This would have been useful in an attempt to calculate the barometric efficiency of the individual pneumatic piezometers. Preliminary data suggests that barometric efficiency ranges from 50 to 100%. However, it is not clear that the relationship is linear, and factors other than air permeability may be significant.

Microbial Degradation

Zhou (1993) investigated the microbiology of the West Farm site and conducted microbial degradation experiments on petroleum contaminated soils collected during the site investigation. Figure 13 shows the results of biodegradation experiments in a microcosm at various levels of petroleum contamination at a constant temperature (25°C). He concluded that *(1)* Indigenous petroleum-degrading microorganisms existed throughout the contaminated area, and *(2)* soil microbial populations were affected by contamination level, oxygen availability, and nutrient

availability. If these environmental factors could be appropriately manipulated through bioventing, the microbial communities could be adapted to the contaminated environment and degrade the hazardous contaminants.

Soil Gas Monitoring

The background vapor extraction well VE-1 was completed in a previously unidentified water-saturated loess and was useless for collecting background soil air quality data. The well was maintained as a groundwater piezometer and is discussed below.

TPH and oxygen were monitored during Test 4, with the results probably comparable to those of Test 3. Over the 24-day testing period, continuous vapor extraction from well VE-4 produced 6,600 SCFM of air, a volume representing ≈ 1 contaminated soil pore volume, assuming 30% porosity. Zhou reported (personal communication) that gas chromatographic analysis of 15 samples of soil vapor extraction off-gas showed that total petroleum hydrocarbons in air ranged from 20 to 470 ppm. Oxygen content of the off-gas ranged from 3 to 7%, with no discernible trend from the beginning to the end of the test. Kittel et al. (1993) report that typical hydrocarbon content of soil gas beneath a contaminated site is <100 ppm, while oxygen content is usually 0 to 2%. Oxygen content of soil gas at uncontaminated sites is typically 15 to 20%.

Perched Water Table

Piezometers VE-5 at 10 ft, and VE-5 at 15 ft bgs became saturated with groundwater during test 3 or 4. With the exception of well VE-1 all other piezometers and wells remained unsaturated during the testing; no water or condensing water vapor was produced from the vapor extraction well or the air water separator tank. A drive point piezometer (VE-7, Fig. 2) was installed in the petroleum tank excavation to monitor what was interpreted to be rainwater filling the sand-backfilled excavation. It was assumed that groundwater had been drawn in laterally by the 60-inch water column vacuum induced by the vapor extraction well. Later, an additional groundwater piezometer cluster (VE-9) was installed upgradient from the site and the presence of a perched water table was documented and monitored throughout the following year.

Groundwater monitor well hydrographs are shown in Figure 14. The monitor wells are arranged in the legend from south to north through the site. The hydrographs show a distinct decline in hydrostatic head with increasing depth, indicative of a groundwater recharge zone. For example, in early July, 1993, the groundwater elevation of piezometer cluster VE-6 at 5 ft was 2588 feet, at VE-6 at 10 ft it was 2587 ft, and at VE-6 at 15 ft it was 2577 ft. Interestingly, VE-6 at 15 ft had previously been unsaturated (dry), and the groundwater elevation rose 6 feet over the next 3 months. These hydrographs appear to be documenting groundwater recharge occurring in the vadose zone. However, it should be remembered that the piezometers at 20 and 25 feet were unsaturated during this same period.

The hydrographs document the effectiveness of the impermeable soil cover placed over the site before the start of test 4 during the fall of 1992. VE-6 at 5 ft is on the uncovered edge of a plastic cover. Before February 1993, the piezometer was unsaturated until the wet spring of 1993. However, VE-5 at 5 ft was under plastic during this same period and remained unsaturated throughout the measurement period. This observation underscores the need to address both groundwater inflow and surface water infiltration in any attempt to dewater the remediation site.

Capillary Pressure

Soil capillary pressures within the vadose zone have a significant role in understanding the relationship between soil vapor pressure and soil water movement. Corey (1990) describes capillary pressure (Pc) as equal to the pressure of the non-wetting phase (Pnw) minus pressure of the wetting phase (Pw); that is, Pc = Pnw - Pw. He states (1990, p. 13.)

> In a system in contact with the atmosphere, such as soil, either the wetting phase (water) or the non-wetting phase (air) will normally be at atmospheric pressure. If the soil is sufficiently desaturated for an interconnected air phase to exist, the air will be at atmospheric pressure and the liquid will be at less than atmospheric pressure. This is the reason that soil scientists refer to water as being under 'suction' or 'tension.' . . . In a water-gas system, water tends to be preferentially adsorbed by the solid surfaces and the gas is compressed if it is entirely surrounded by water. The gas pressure is higher than the water. In an water-oil-gas system, the gas will usually be the highest pressure, the oil at the next highest and water at the lowest pressure when equilibrium exists.

The presence of groundwater in piezometers VE-5 and VE-6 provides a partial explanation for the air pressures above atmospheric pressure in these wells. Air trapped beneath a perched water table would become compressed. Air contained in an enclosed piezometer column above the water table would also become compressed as water levels increased. This does not provide an explanation for the positive soil air pressures observed in the unsaturated wells. Obviously, the vertical air conductivity of the sediments is a limiting factor. It may be that soil air pressures exceeding atmospheric pressure are related to a lag time phenomenon created by the passage of an atmospheric pressure front. It may also be related to the high vapor pressures of the volatile organics. Headspace analysis of contaminated soil sample occasionally exceeded 2000 ppm TPH so that physical measurement of soil pressures exceeding atmospheric pressures may be partly attributable to petroleum contaminants.

One commonly reported result of negative capillary forces applied to soil during soil vapor extraction is that water is raised by reducing the pressure of the air, a phenomenon believed to have occurred at the West Farm site. Water in piezometer VE-5 was first identified during soil gas sampling with a vacuum pump. The relatively high vacuum is believed to have drawn water in laterally from the adjacent rain saturated sand backfill from the petroleum tank excavation. The first two water level measurement in VF-5 at 10 ft drop nearly 2 feet after the sampling induced vacuum dissipates (Fig. 14.) Piezometer cluster VE-6 was 10 feet further downgradient from the backfilled tank basin and remained unsaturated at all levels untill the following year.

Applying a vacuum to soils with high soil matric suction such as silty clays has the tendency to pull moisture out from the soil and artificially raise the water table further reducing the already limited pore space available for air flow. However, capillary forces could also be reduced by increasing the soil air pressure and driving water out of the soil. This has important implications, since dry soil has the highest air permeability.

CONCLUSIONS AND RECOMMENDATIONS

The combination of low-permeability silty clay soils and groundwater inflow creating perched water table conditions at the West Farm site are not conducive to soil vapor extraction without significant engineering modifications. The most important of these would be the diversion of groundwater flow around the site by the construction of a groundwater interception trench. This trench would need to be about 15 feet deep to intercept the observed groundwater inflow. An impermeable or low permeability cover is also necessary to prevent precipitation from infiltrating and reducing air permeability.

Applying a positive pressure head instead of a vacuum to supply oxygen would be an appropriate application of bioventing technology. This has the benefit of forcing water out of the soil, omitting costly off-gas treatment if excessive volatiles are produced. At the West Farm site there are no sensitive subsurface receptors such as basements or utility conduits that would be impacted by volatile organics. If this were a concern, vapor interception trenches or positive pressure barriers could be installed to protect sensitive receptors. An additional caution is that enhanced groundwater recharge by pressurizing the vadose zone might also increase the vulnerability of groundwater from impacts by dissolved organics such as benzene.

The dense paleo-"B" soil horizon would need to be artificially fractured to increase the very low permeability of this zone. This dense horizon is a logical candidate for hydraulic or pneumatic soil fracturing. These and other engineering solutions are quite expensive relative to excavation and conventional landfarming. In certain situations, the expense of bioventing silty clay soils would be justified. If the entire West Farm site had permeabilities similar to those experienced at the 20 foot depth without the perched water, the situation would be significantly enhanced. As a prudent manager, I would not recommend bioventing in this situation if saving money is an objective. However, Kittel et al. (1993) reported that in the US Air Force bioventing initiative, out of over 100 fuel-contaminated sites evaluated for bioventing only 3 were found to have unacceptable air permeabilities. The West Farm site has an unfortunate combination of factors working against successful bioremediation.

REFERENCES

Chen-Northern, Inc. 1991. Limited environmental site assessments for tank closures. North Idaho Tank Closure Project. University of Idaho, unpublished report prepared for Idaho Department of Public Works, 36 p.

Cory, A. T. 1990. Mechanics of immiscible fluids in porous media. Water Resources Publications, Littleton, Colorado, 255 p.

Hutzler N. J., B. E. Murphy, and J. S. Gierke. 1989. State of technology review, soil vapor extraction systems. U.S. EPA, CR 814319-01-1, EPA/600/2-89/024.

Johnson P.C., C .C. Stanley, M. W. Kemblowski, D. L. Byers, and J.D. Colthart. 1990 A practical approach to the design, operation, and monitoring of in situ soil venting systems. Ground Water Monitoring Review, Spring 1990.

Kittel, J. A., R. E. Hinchee, R. M. Miller, C. V. Vogel, and R. Hoeppel. 1993,. In situ respiration testing: A field treatability test for bioventing, *in* Proceedings of the 1993 Petroleum Hydrocarbons and Organic Chemicals in Groundwater: Prevention, Detection, and

Restoration, November 10-12, 1993, Houston Texas. American Petroleum Institute and National Groundwater Association.

McDole, R. E., and P. N. Peterson. 1989. Soil Survey of the University of Idaho Agricultural Experiment Station and Campus, Moscow, Idaho. Bulletin no. 698, Agricultural Experiment Station, University of Idaho, College of Agriculture, 52 p.

Ralston D., J. Kaufman, and K. Brackney. 1991. Site assessment report, West Farms underground storage tank (UST) site. University of Idaho, Site Assessment Consent Order 39-108.

Zhou, E. 1993. Physical, chemical, and microbiological factors affecting bioremediation of a petroleum hydrocarbon contaminated soil. M.S. Thesis, University of Idaho, Moscow, Idaho.

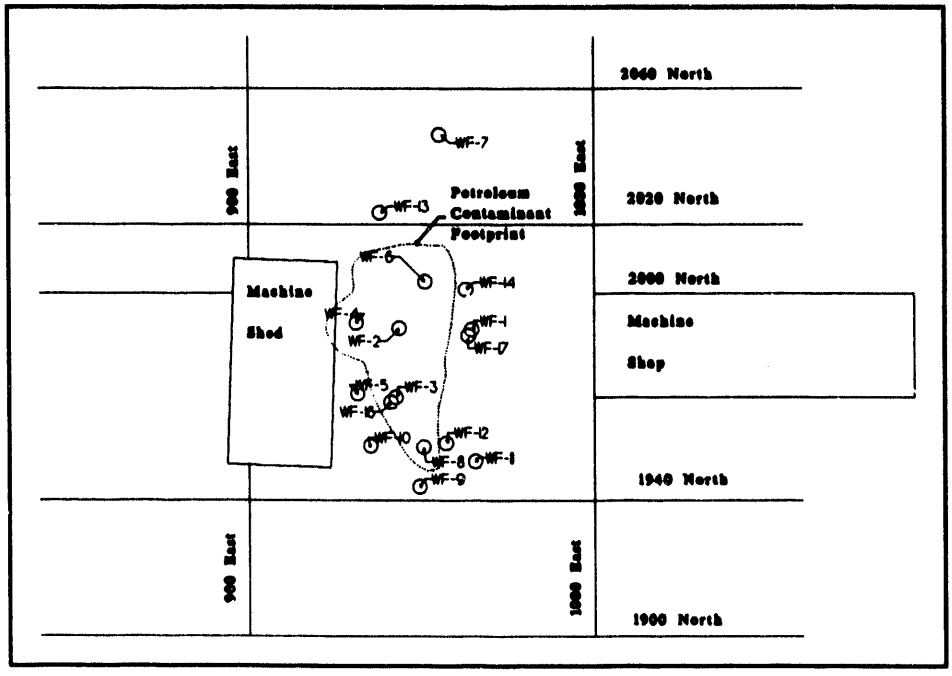


Figure 1. West Farm UST site, University of Idaho, Moscow, Idaho. Location map showing boreholes. Plan view projection of petroleum contaminated soil. X-Y coordinates shown for scale.

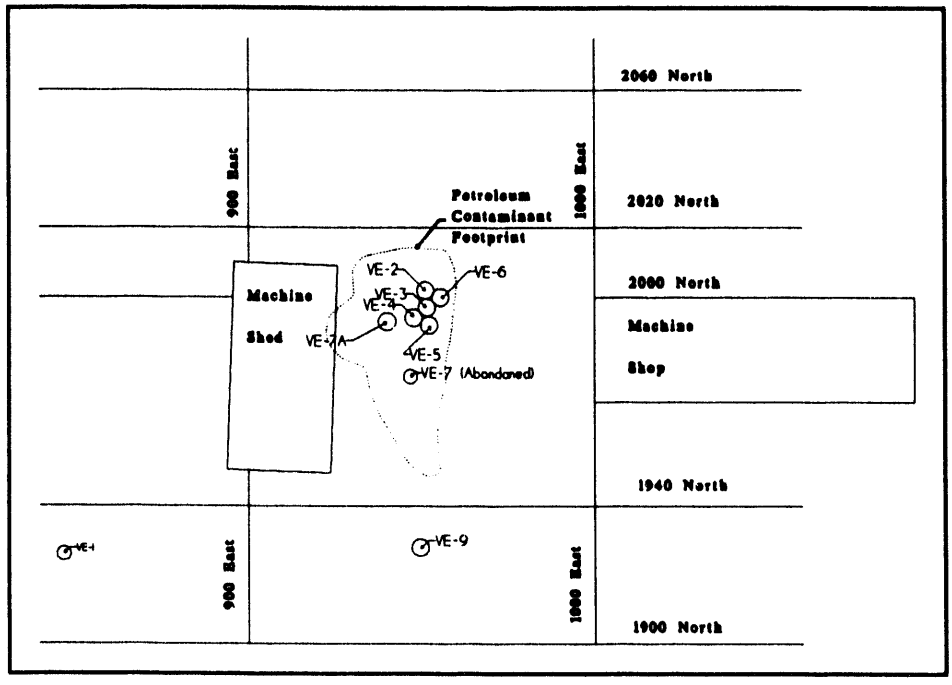


Figure 2. West Farm UST site. Location map showing groundwater and pneumatic piezometers.

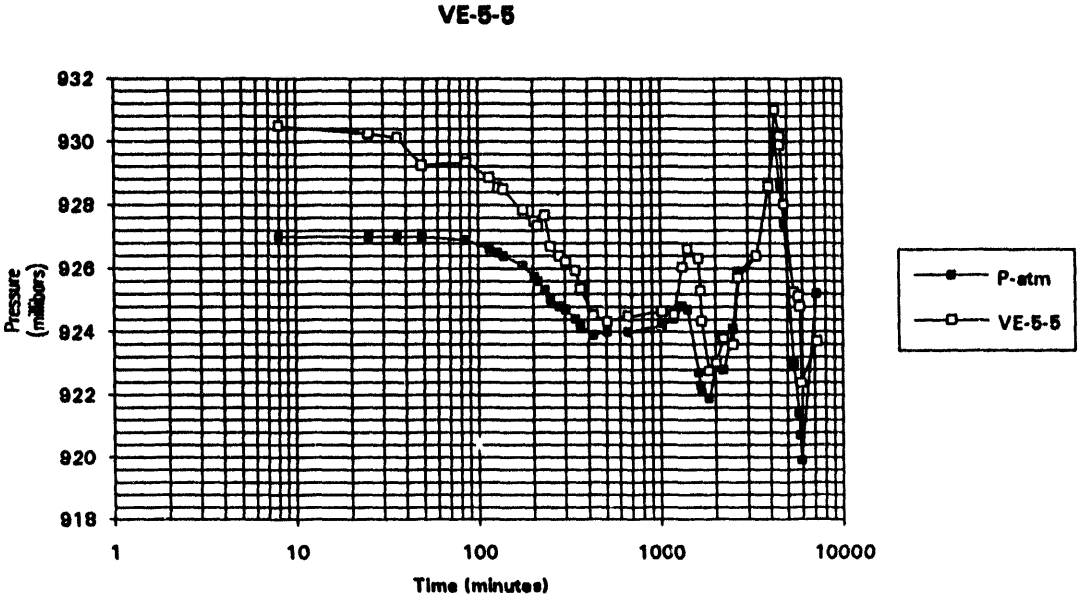


Figure 3. Piezometer VE-5 at 5 feet bgs. Radius from pumping well equals 5 feet.

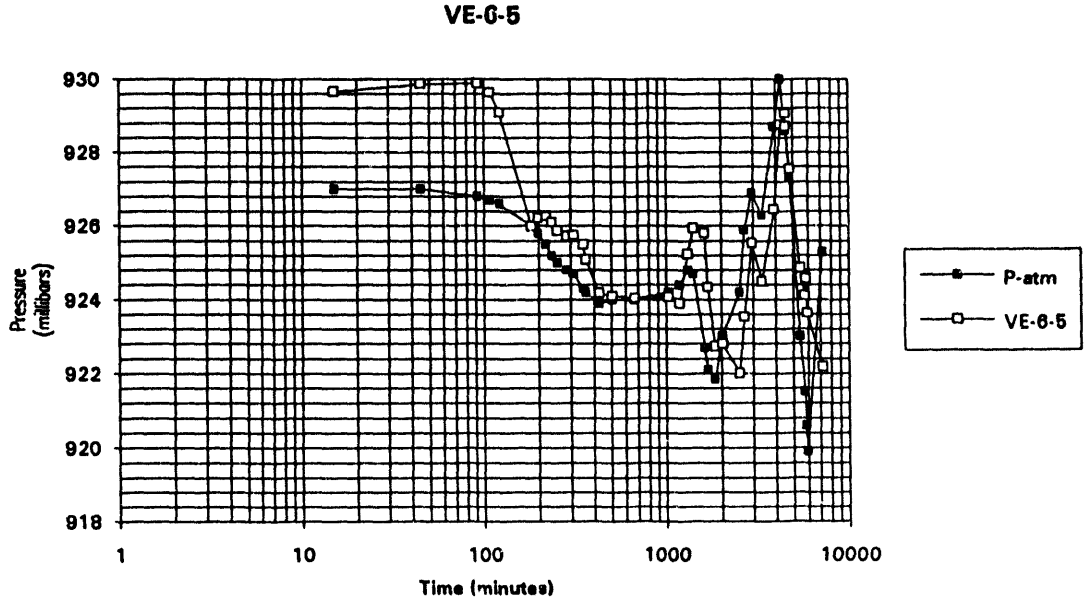


Figure 4. Piezometer VE-6 at 5 feet bgs. Radius from pumping well equals 10 feet.

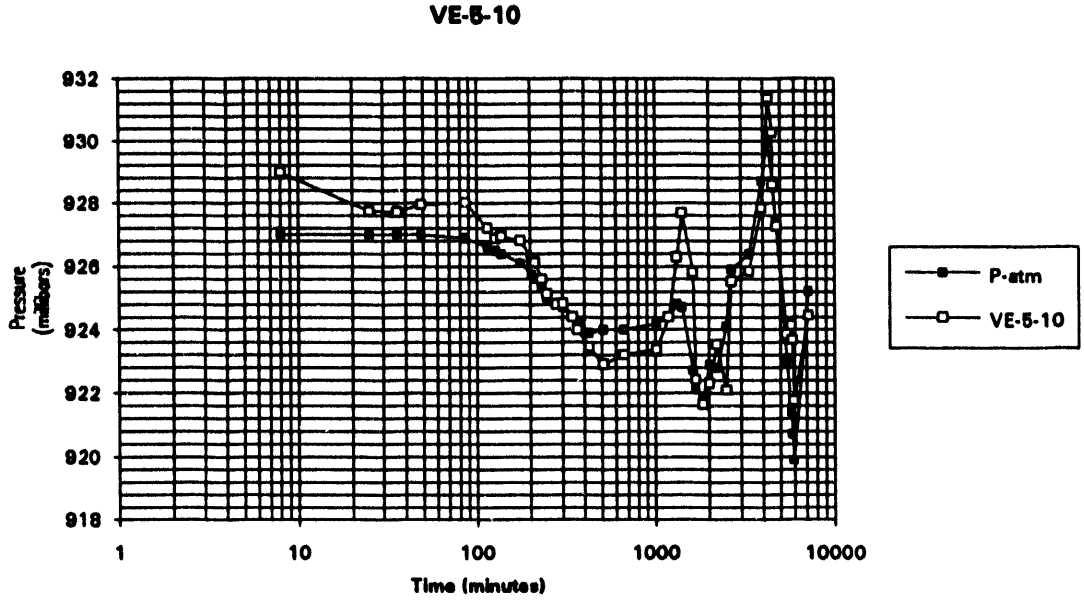


Figure 5. Piezometer VE-5 at 10 feet bgs. Radius from pumping well equals 5 feet.

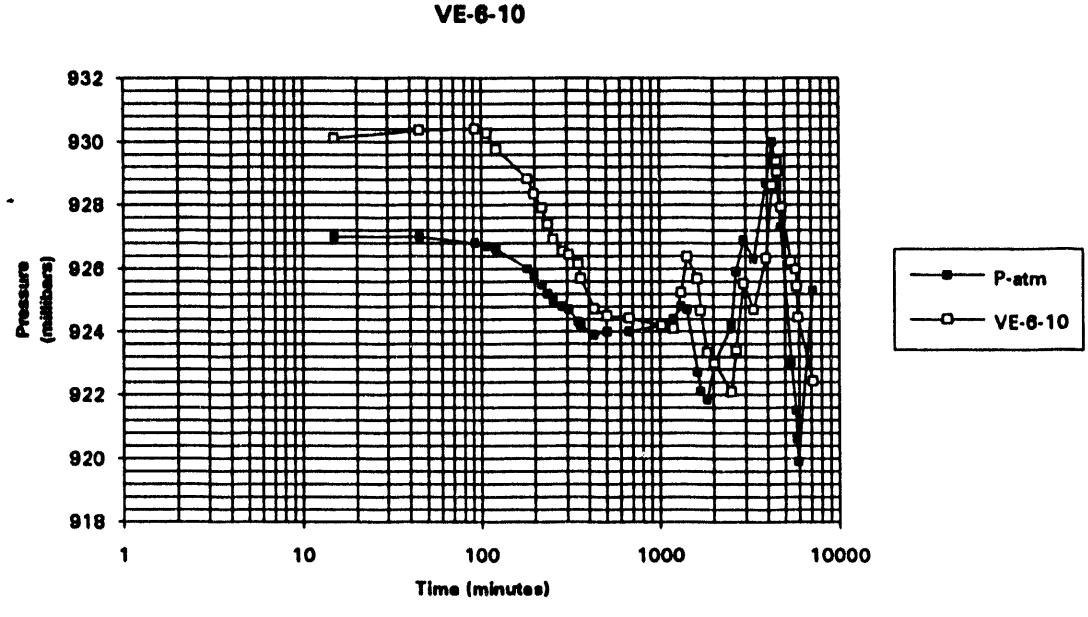


Figure 6. Piezometer VE-6 at 10 feet bgs. Radius from pumping well equals 10 feet.

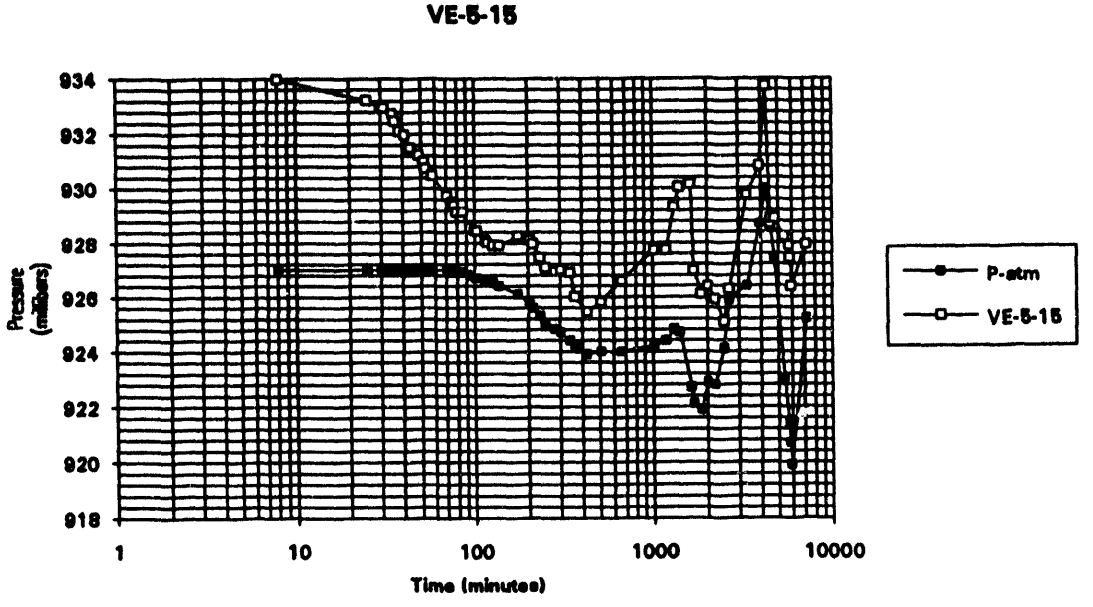


Figure 7. Piezometer VE-5 at 15 feet bgs. Radius from pumping well equals 5 feet.

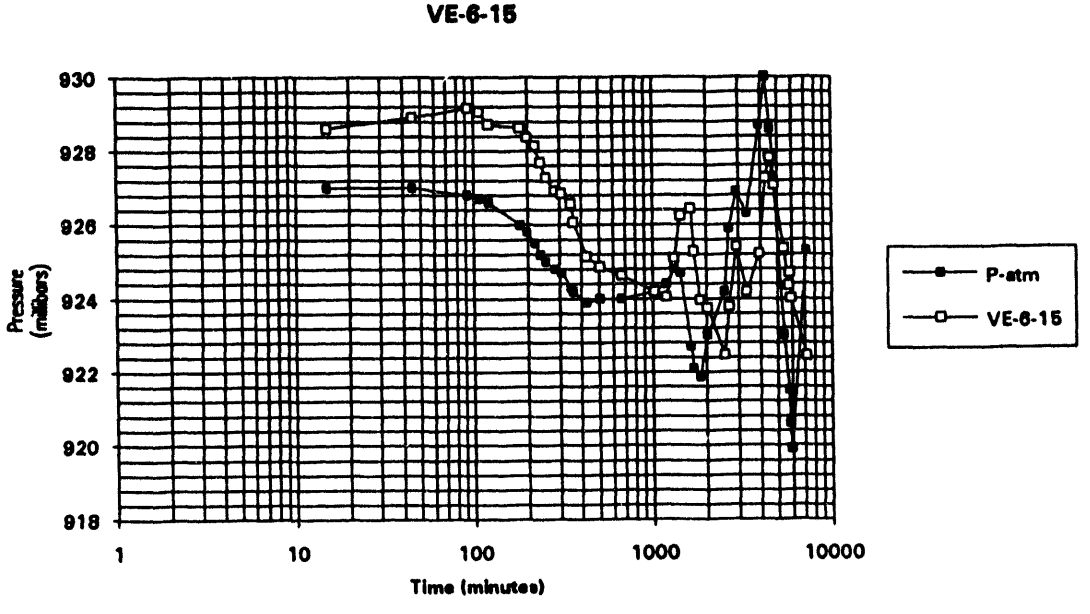


Figure 8. Piezometer VE-6 at 15 feet bgs. Radius from pumping well equals 10 feet.

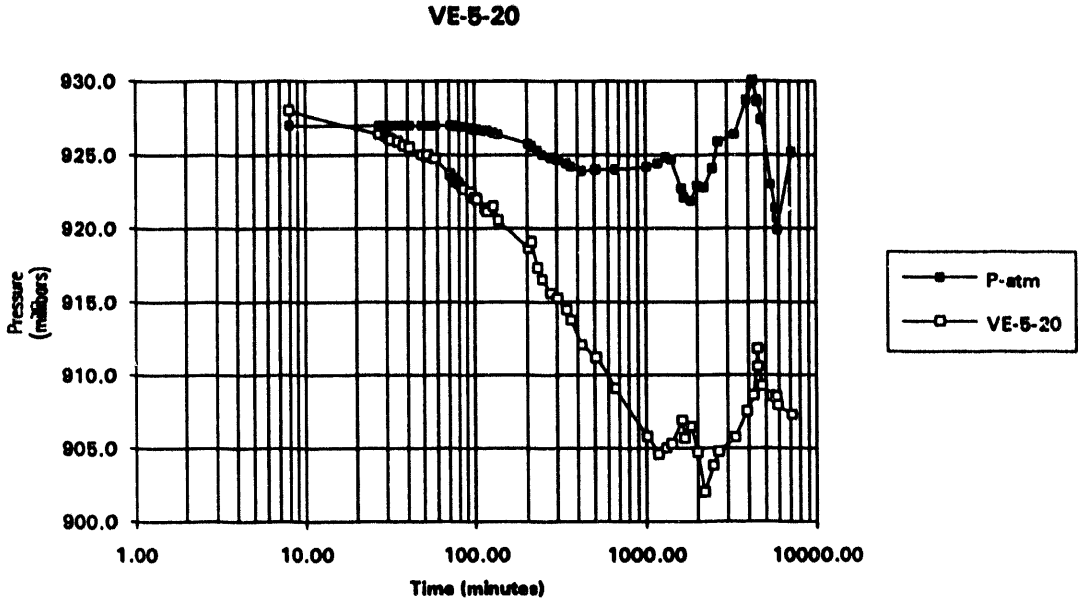


Figure 9. Piezometer VE-5 at 20 feet bgs. Radius from pumping well equals 5 feet.

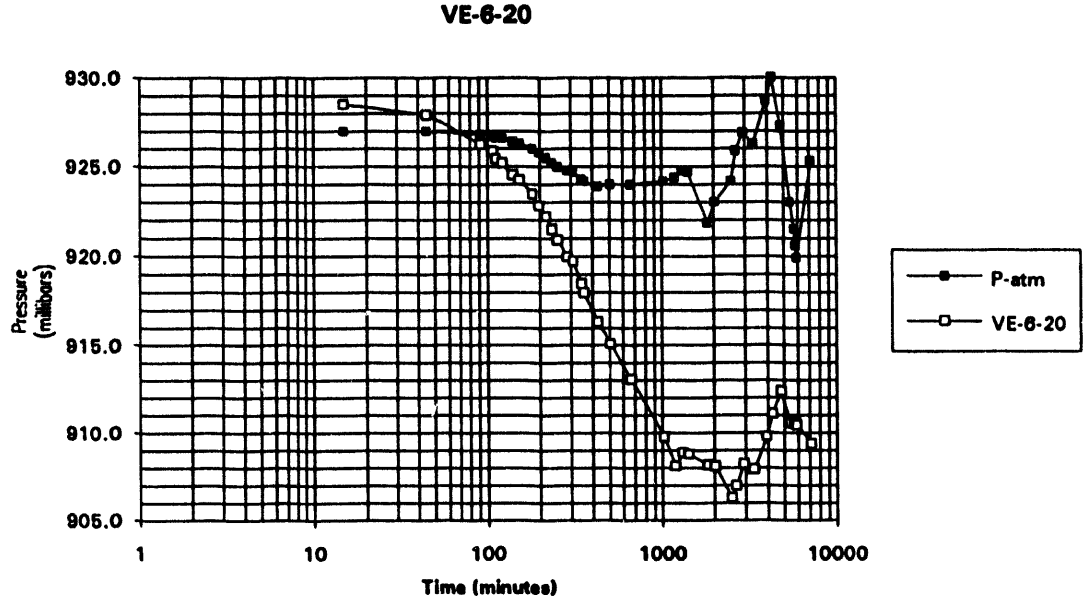


Figure 10. Piezometer VE-6 at 20 feet bgs. Radius from pumping well equals 10 feet.

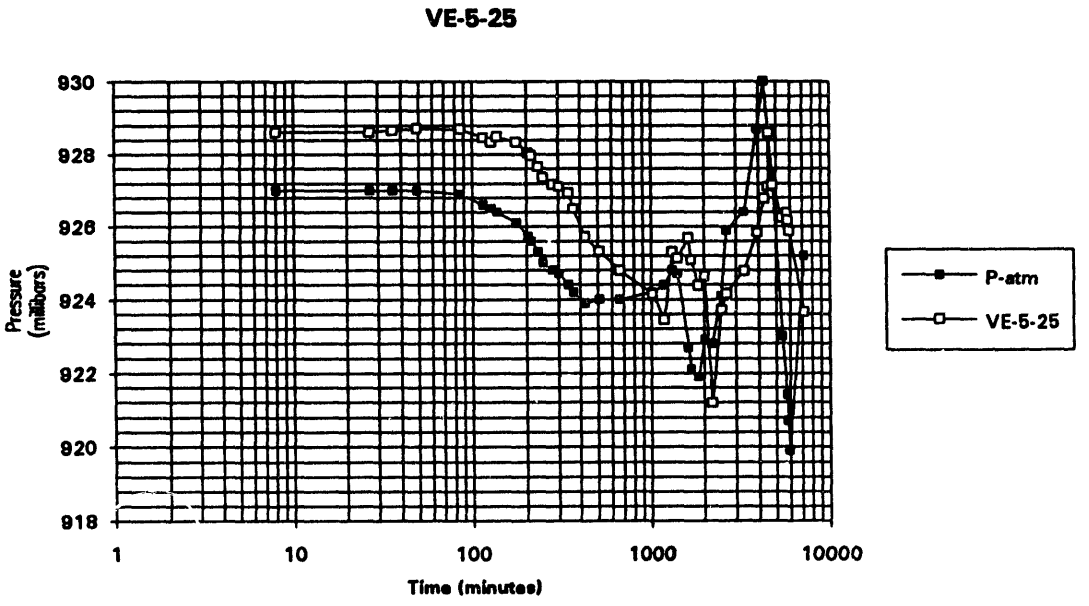


Figure 11. Piezometer VE-5 at 25 feet bgs. Radius from pumping well equals 5 feet.

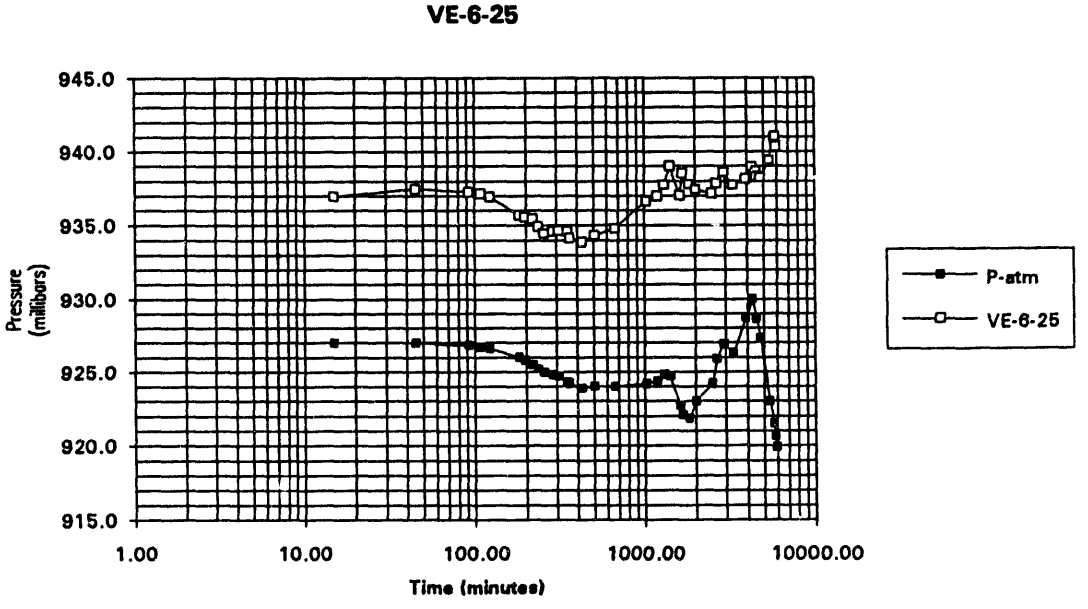


Figure 12. Piezometer VE-6 at 25 feet bgs. Radius from pumping well equals 10 feet.

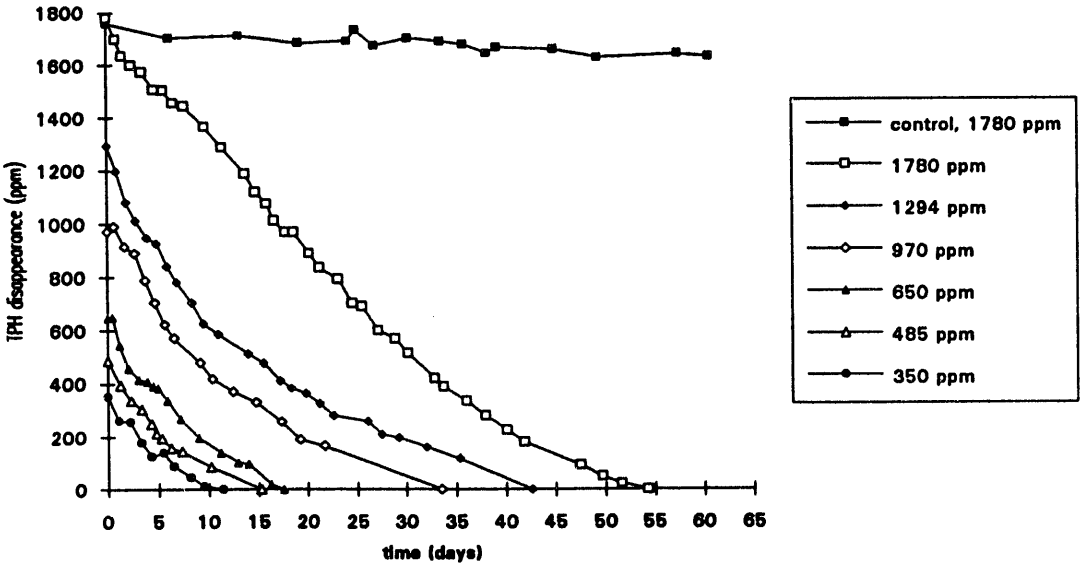


Figure 13. Biodegradation of total petroleum hydrocarbon by microorganisms in a microcosm for sample S3-1 at various initial levels of petroleum contamination while other conditions were kept constant (25°C.) Adapted from Zhou (1993.)

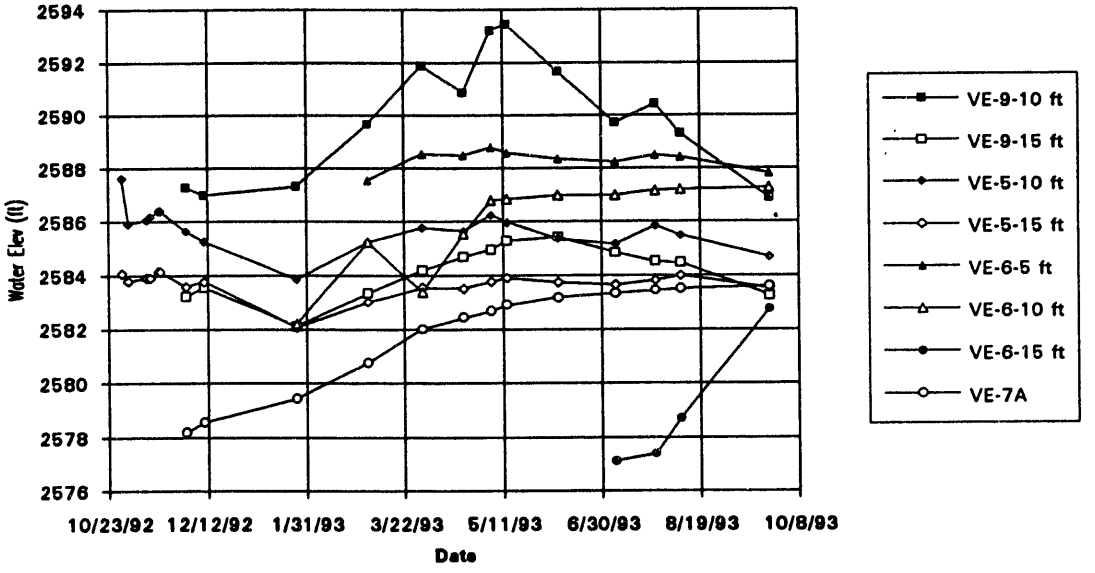


Figure 14. West Farm site monitor well hydrographs for a perched water table. Water level elevations show a distinct declining head with depth indicative of a ground water recharge zone. Piezometer VE-6-5 ft is located outside the perimeter of an impermeable soil cover; piezometer VE-5-5 ft (located 10 ft away from VE-6-5) was under the impermeable soil cover and remained unsaturated during the same period. Piezometers VE-5 and VE-6 at 20 and 25 ft were also unsaturated during the period. VE-7A is a soil vapor extraction trench.

Hydrogeology, Waste Disposal, Science and Politics
Proceedings 30th Symposium
Engineering Geology and Geotechnical Engineering, 1994

ENHANCED ENDOGENOUS BIOLOGICAL ATTENUATION OF AROMATIC HYDROCARBONS IN GROUNDWATER: A CASE STUDY
(Preliminary Results)

Christopher Lammer, P.E.
EnviroSearch International
1605 N. 13th Street
Boise, Idaho 83702

ABSTRACT

EnviroSearch International has designed and is currently operating a groundwater treatment system to address a release of petroleum hydrocarbons at a site in Meridian, Idaho. Among these hydrocarbons, the principal compound of concern, benzene, was reported at concentrations of up to 4.0 mg/ℓ prior to system operation. The system is designed to reduce hydrocarbon concentrations in groundwater and saturated soil through enhancement of naturally occurring aerobic microbial activity.

An *in situ* treatment system was selected in order to simultaneously address hydrocarbons dissolved in groundwater and adsorbed to the saturated soil matrix. Petroleum-utilizing bacteria were identified in groundwater samples collected from the project site. The *in situ* system was designed to create conditions more conducive to aerobic microbial activity by increasing the initially low concentrations of dissolved oxygen and the nutrients nitrogen and phosphorus.

Operation of the *in situ* treatment system was initiated in August 1993. A significant decline in concentrations of the aromatic hydrocarbons benzene, toluene, ethylbenzene, and xylenes was observed over the first seventeen weeks of system operation; concentrations of these compounds were reported as less than or equal to drinking water maximum contaminant limits in November 1993. These preliminary results suggest that *in situ* biological treatment is a practical approach to shallow aquifer petroleum contamination in the Treasure Valley.

INTRODUCTION

Biological degradation of petroleum hydrocarbons, particularly benzene, has been a recognized phenomenon documented in the literature over recent years (Delfino, 1985 and Urano, 1986). Application of this process to *in situ* treatment of soil and groundwater impacted by petroleum hydrocarbon releases has also been documented at a variety of sites (Wilson, 1989 and USEPA, 1993). EnviroSearch International has applied this technology to an industrial facility in Meridian, Idaho to address impacts to groundwater from a hydrocarbon release at this location.

Biological groundwater treatment utilizes indigenous bacteria and other microbes to degrade hydrocarbons. These hydrocarbons, which can provide a substrate (i.e., energy source) for certain microorganisms, are metabolized into harmless compounds such as carbon dioxide and water. This type of hydrocarbon degradation often occurs naturally at contaminated sites, but can be severely limited by a lack of oxygen and

nutrients. The *in situ* groundwater treatment system was designed to accelerate this natural biological process by providing these potentially rate-limiting compounds.

Traditional "pump and treat" approaches to groundwater treatment are often limited in their ability to remove hydrocarbons adsorbed to saturated soil, often leading to long treatment times (McCarty, 1988). An *in situ* treatment system was selected in order to simultaneously address hydrocarbons dissolved in groundwater and adsorbed in the saturated soil matrix. Petroleum-utilizing bacteria were identified in groundwater samples collected from the project site, indicating that conditions were favorable for biological treatment. The *in situ* system was designed to create conditions more conducive to aerobic microbial activity by increasing the initially low concentrations of dissolved oxygen and the nutrients nitrogen and phosphorus.

The *in situ* treatment system operates by pumping groundwater from a shallow well upgradient of the impacted area. This water is then augmented with hydrogen peroxide, nitrogen, and phosphorus and injected in the impacted area. Hydrogen peroxide reacts with groundwater to increase the dissolved oxygen concentration (Huling, 1990) The increased availability of oxygen and nutrients then leads to increased microbial activity. The resulting increased population of petroleum-utilizing microorganisms was expected to reduce the concentration of hydrocarbons, both those dissolved in groundwater and adsorbed in the soil matrix.

SITE HISTORY

The project site is an industrial facility in Meridian, Idaho (Figure 1). Petroleum hydrocarbons were released from leaking underground storage tanks (USTs) removed from the site in 1991. These tanks were used to store both diesel fuel and regular gasoline; the quantities of each fuel released are unknown. EnviroSearch International conducted a UST closure investigation and subsequent hydrogeologic assessment at the facility in early 1992. Though most of the unsaturated soil impacted by the release was removed with the USTs, dissolved hydrocarbons were detected in groundwater samples collected from monitoring wells downgradient of the former UST location. Among these hydrocarbons benzene was reported at concentrations up to 4,000 $\mu g/\ell$. Site cleanup was complicated by aqueous transport of dissolved hydrocarbons under a large building adjacent to the former UST location, limiting access to the contaminated area.

HYDROGEOLOGY

The project site is located within the Boise River Valley. The valley's landforms consist of six terrace levels of alluvial gravel deposits. The Project site is located on the second terrace above the current channel of the Boise River. The shallow subsurface contains 100 to 500 ft of Quaternary alluvium that consists of interfingered and interlayered sands, silts, clays, and gravels (Othberg, 1992). This shallow alluvium unconformably overlays the Quaternary-Tertiary age Idaho group deposits which consist of several thousand feet of moderately to poorly consolidated clastic sediments and basaltic volcanics. The Idaho Group sediments consists of sands, silts, and clays of variable thickness and lateral extent (Malde, 1962).

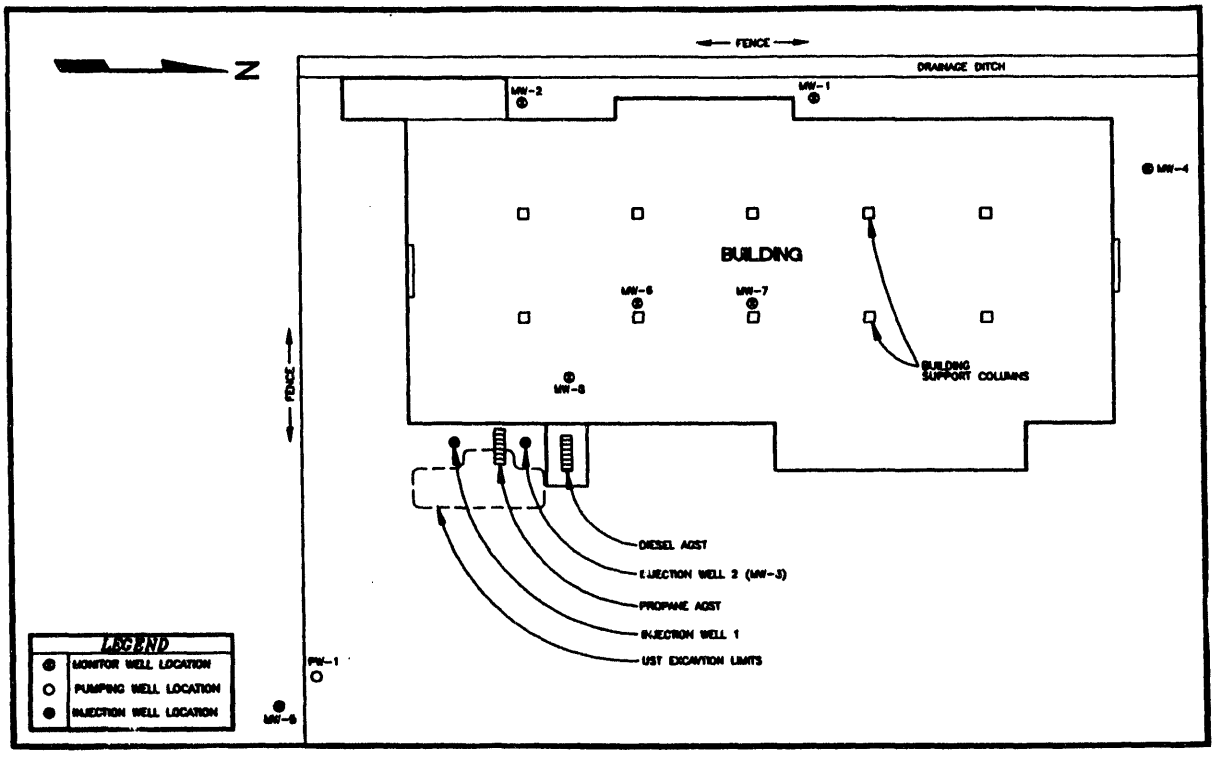


Figure 1 - Site Plan

Two aquifers are known to exist in the area. Throughout much of the valley, an unconfined water table aquifer is found within the shallow alluvium, normally at a depth of less than 15 ft. Slug testing of monitoring wells at the project site indicates a hydraulic conductivity in the vicinity of 2 ft/day. Groundwater elevations in monitoring wells at the project site have ranged from 6.7 to 13.5 ft below ground surface since our initial measurements in January 1992 (Figure 2). In the immediate area of the site groundwater in the shallow, unconfined aquifer generally flows to the northwest toward the Boise River (approximately 4.5 miles away). Seepage losses from the Ninemile Drainage lateral canal (less than 500 ft to the north of the site) creates seasonal fluctuations in local groundwater flow directions. Potentiometric surface diagrams from the period prior to system startup are presented as Figures 3 and 4. These show a generally consistent north to northwesterly groundwater gradient over the 18 months prior to the mid 1993 system startup.

At a depth of approximately 300 to 500 ft below ground surface, the region's principal water supply aquifer is contained within the Upper Idaho Group strata. Toward the northwestern end of the Boise River Valley several hundred feet of silts and clays separate the water supply and water table aquifers, thereby reducing the potential for flow between the aquifer. However, subsurface data recently compiled by Squires *et al* (1992) suggest that the boundaries between aquifer units and hydrogeologic settings are gradational, and flow may exist across the system. This appears to be most evident through pump test data obtained from the east Boise area (Squires *et al*, 1992). Due to an incomplete data base, an adequate hydrogeologic

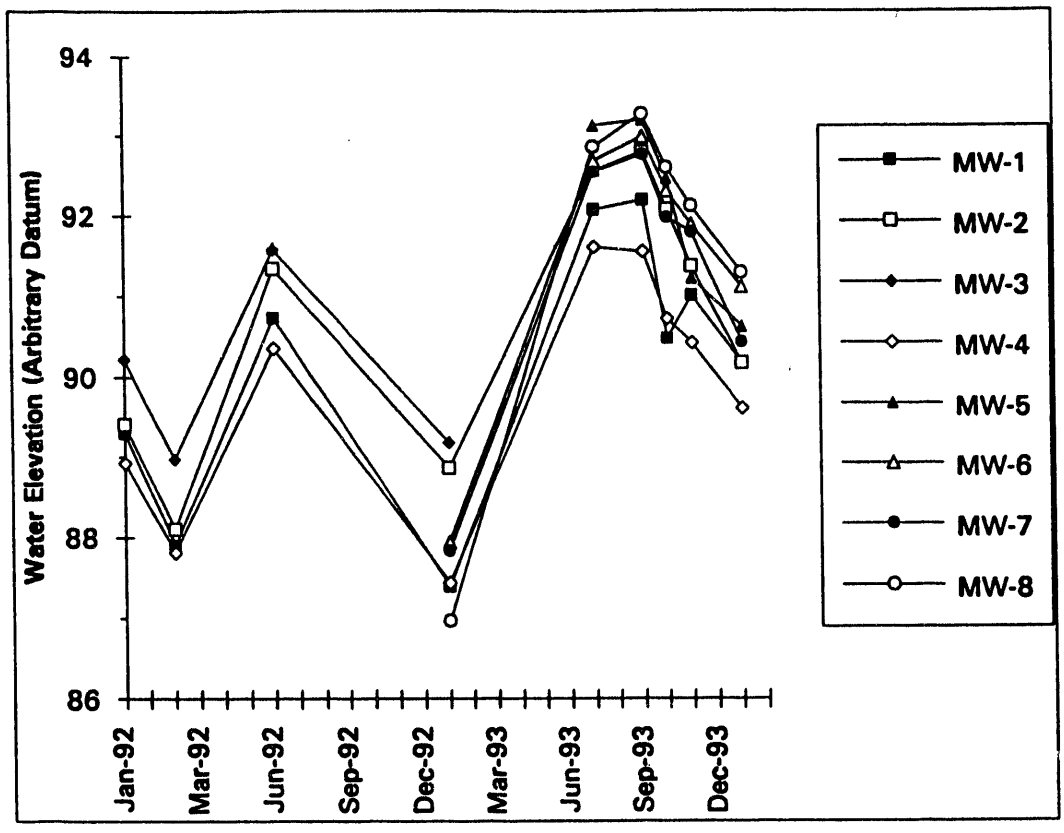


Figure 2 - Groundwater Elevations

model describing the nature and extent of the hydraulic continuity between the shallow and deep aquifers has not yet been developed.

IN SITU GROUNDWATER TREATMENT SYSTEM

The *in situ* groundwater treatment system was designed to accelerate natural biological hydrocarbon degradation processes in order to provide cost effective removal of hydrocarbons in the saturated zone within a reasonable time frame. This accelerated degradation rate was achieved by increasing the concentration of the potentially rate limiting components oxygen, nitrogen, and phosphorus. Oxygen was supplied to the saturated zone by injecting a dilute solution of hydrogen peroxide, which dissociates into oxygen and water. The nutrients nitrogen and phosphorus were provided by a dilute fertilizer mixture. These amendments were mixed with groundwater pumped from an upgradient well at a rate of 4.8 gpm (18 *ℓ*/min) and injected through two shallow injection wells in the former UST area. A process flow diagram is shown in Figure 5, locations of the groundwater extraction, injection, and monitoring wells are shown in Figure 1.

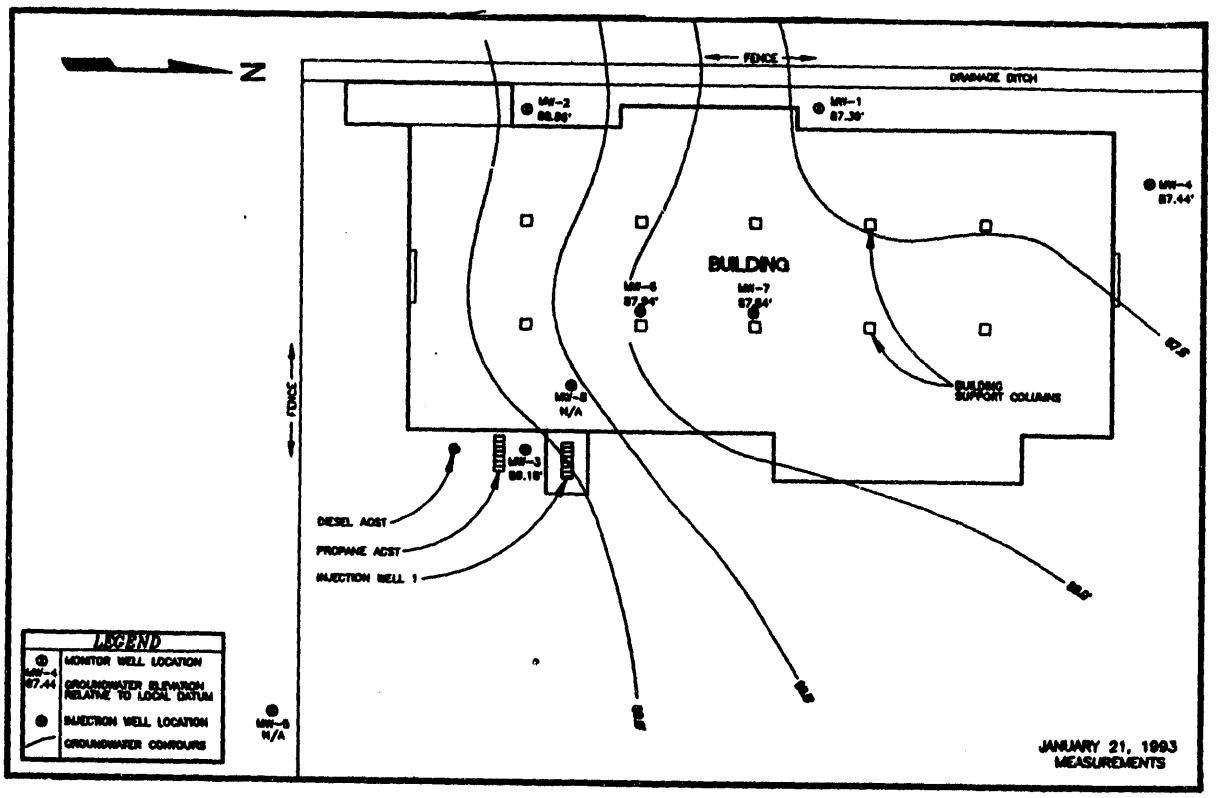


Figure 3 - Groundwater Contours, January 1993

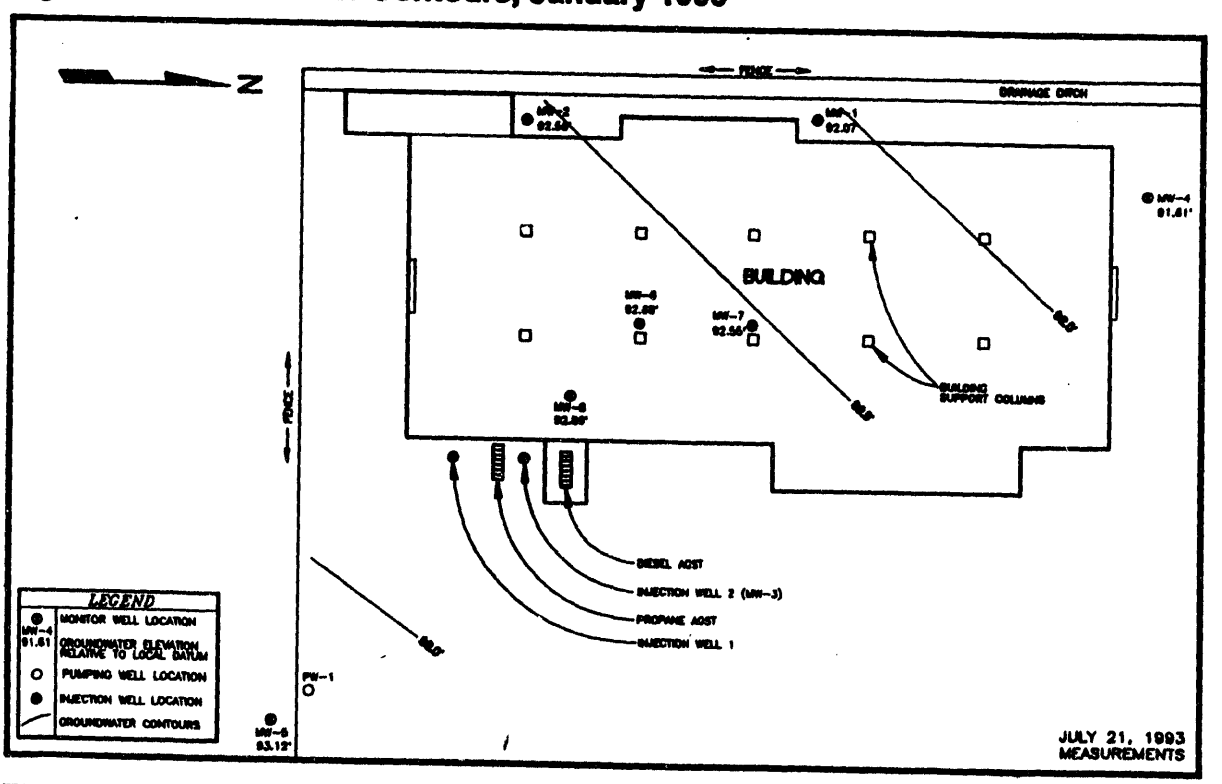


Figure 4 - Groundwater Contours, July 1993

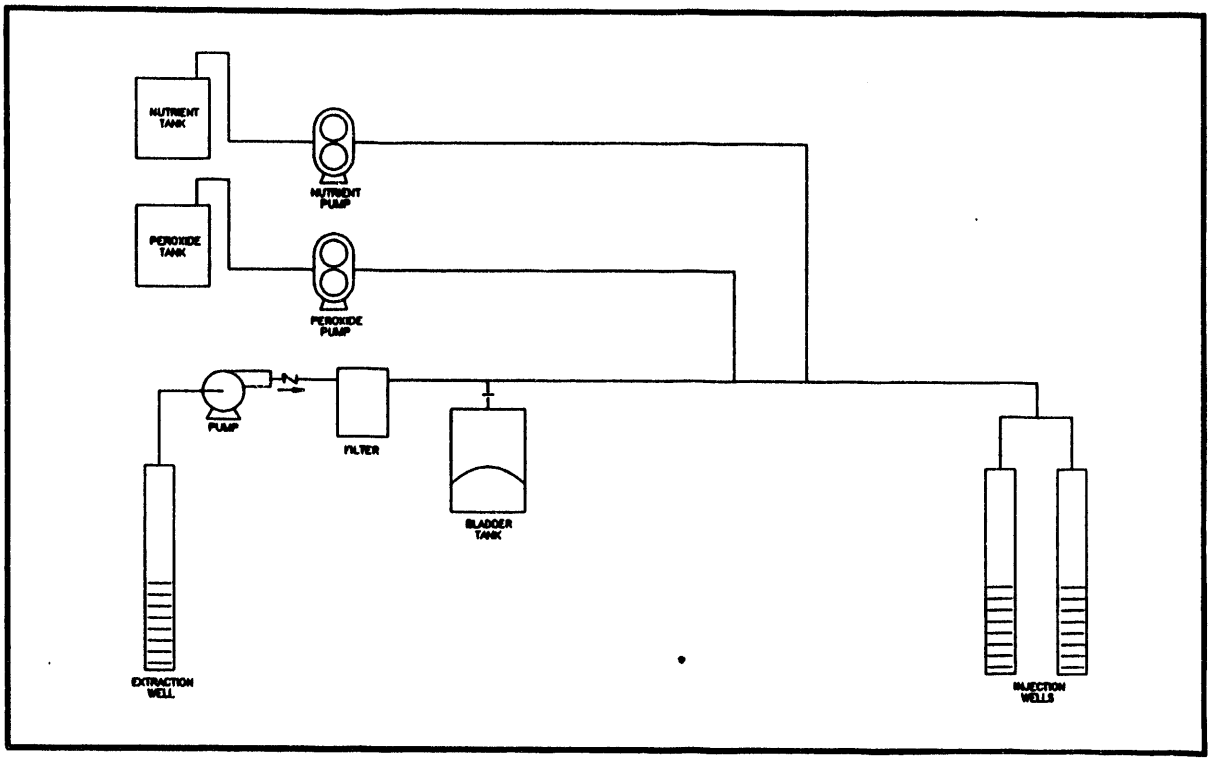


Figure 5 - Process Flow Diagram

Subsurface monitoring was conducted in the seven monitoring wells at the project site to allow evaluation of system performance. Baseline data was collected prior to the system startup. No monitoring was conducted during the first seven weeks of system operation, since it was considered unlikely that effects from system operation would reach the subsurface monitoring wells during this early period of system operation. After this initial hiatus, system performance was monitored on a monthly basis. Parameters tracked in these monthly monitoring events included water levels, dissolved oxygen concentrations, microbial populations, and nutrient concentrations. Concentrations of the petroleum hydrocarbons benzene, toluene, ethylbenzene, and xylenes (BTEX) were measured on a quarterly basis.

All parameters tracked as part of system performance monitoring were measured prior to system startup in order to provide baseline data. In addition to baseline measurements made in July 1993, water levels and petroleum hydrocarbon concentrations were periodically measured over the previous eighteen months as part of site assessment activities. These data, included as Figures 3 and 4, provide information regarding conditions prior to operation of the treatment system. These show a generally consistent north to northwesterly groundwater gradient prior to system startup.

Baseline concentrations of hydrocarbons, dissolved oxygen, nutrients, and microbial populations are included with operational data in Figures 10 through 14. Hydrocarbon concentrations were followed for 19 months prior to system startup to

allow for potential seasonal effects. Concentrations less than method detection limits are reported as the detection limit in the figures.

Performance Monitoring Results

Operation of the *in situ* treatment system was initiated on August 2, 1993; the system has operated continuously since that time. The first performance monitoring event was completed on September 21, 1993, seven weeks after system startup. This monitoring included field measurements of water levels and dissolved oxygen concentrations and collection of samples for laboratory measurement of microbial populations and nutrient concentrations. This routine monitoring was then repeated on a monthly basis. On November 26, 1993, seventeen weeks after system startup, groundwater samples were collected for laboratory analysis of BTEX compounds by GC/MS. Dissolved oxygen, microbial populations, nutrient concentrations, and water levels were also measured as in the previous monitoring events.

Groundwater Elevations

Potentiometric surface diagrams measured at approximately 5 week intervals during system operation are presented as Figures 6 through 9. Static water level elevations in monitoring wells at the project site over 22 months are shown in Figure 2. These water levels show seasonal variations typical of the Boise valley; groundwater elevations in the second half of 1993 have been slightly higher than those measured previously. The most recent potentiometric surface diagram (January 20, 1994) shows some influence from the injection wells on water levels in nearby monitoring wells. This mounding suggests that groundwater and injected constituents may be migrating in a more westerly direction near the southern extent of the building. The gradient through the remainder of the impacted area continues to be northwesterly as was typical prior to startup of the treatment system.

Hydrocarbon Concentrations

The November 26, 1993, sampling event provided the first BTEX concentration data after system startup. Water samples were collected from all seven monitoring wells at the project site and analyzed for BTEX by EPA Method 624. Among these compounds benzene was of primary concern due to the low 5 µg/ℓ drinking water maximum contaminant limit (MCL). The maximum benzene concentration reported among the November samples was 5 µg/ℓ in well MW-4; all other benzene concentrations were reported as below method detection limits (Figures 10 and 11). This detection limit for benzene was 1 µg/ℓ in all wells except for MW-6, which was set at 10 µg/ℓ. The detection limit for MW-6 was elevated due to potential interference from xylene isomers, reported at 238 µg/ℓ in this sample.

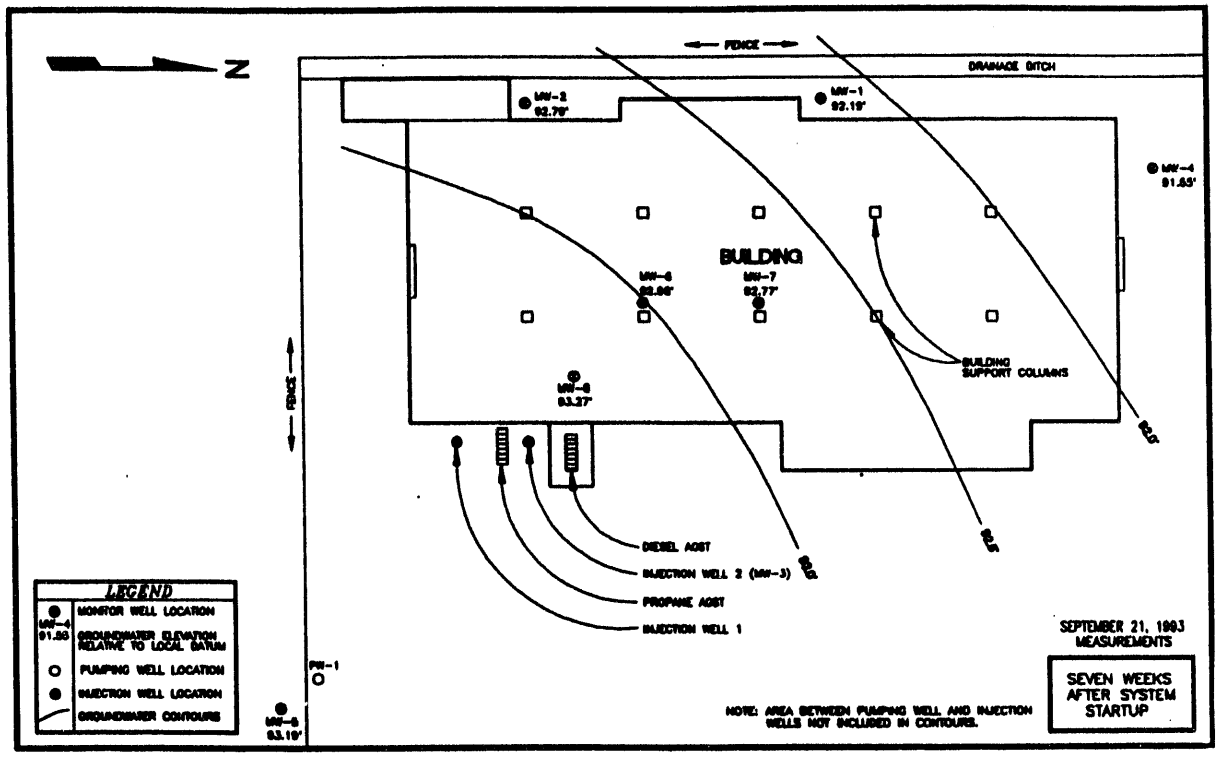


Figure 6 - Groundwater Contours, September 1993 (Seven Weeks After System Startup)

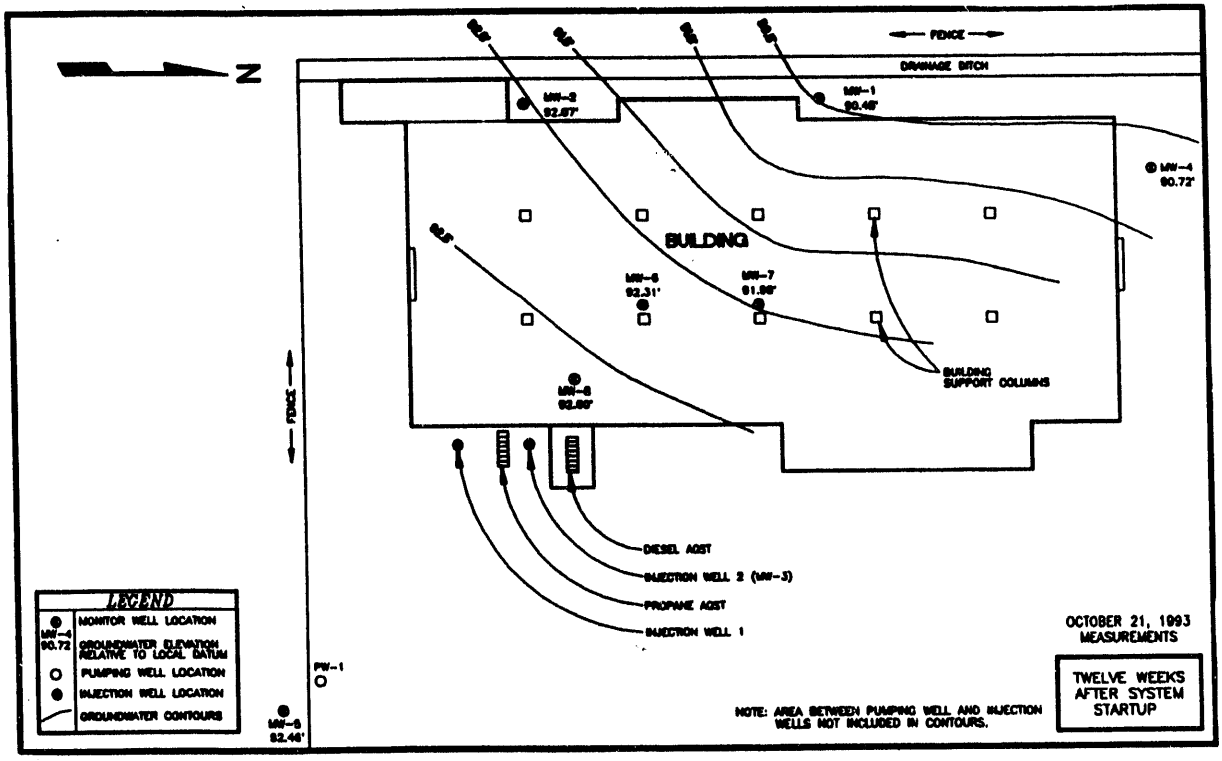


Figure 7 - Groundwater Contours, October 1993 (Twelve Weeks After System Startup)

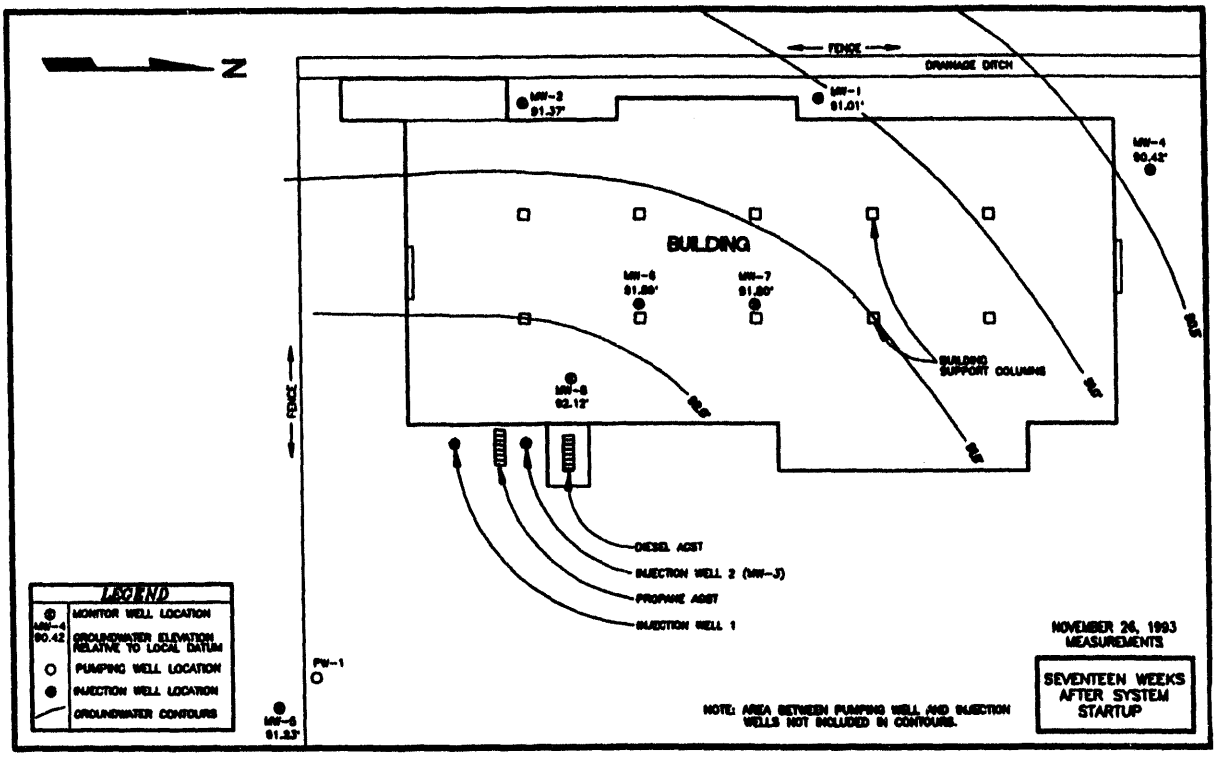


Figure 8 - Groundwater Contours, November 1993 (Seventeen Weeks After System Startup)

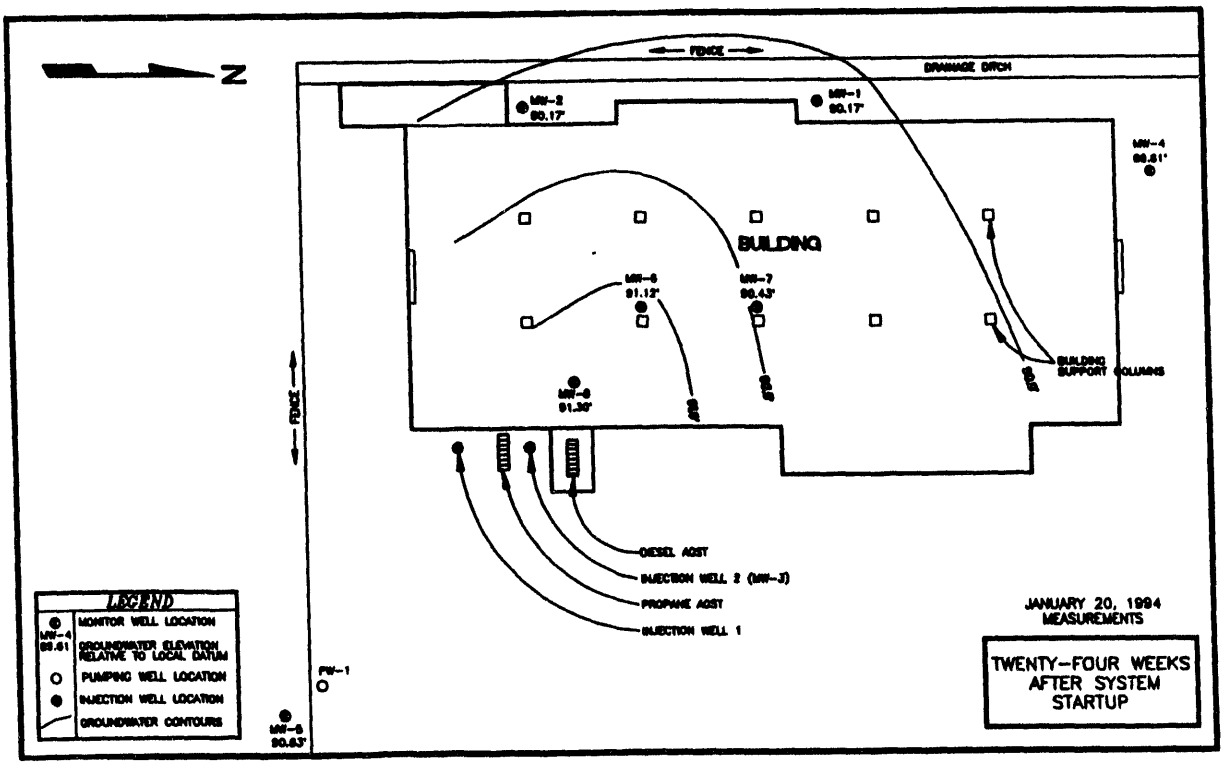


Figure 9 - Groundwater Contours, January 1994 (Twenty-four Weeks After System Startup)

BTEX concentrations in samples collected from all wells other than MW-4 and MW-6 were reported as below analytical method detection limits. These reported concentrations are significantly lower than the July 1993 baseline BTEX measurements, where benzene concentrations were reported to be as high as 2,800 µg/ℓ (in well MW-8). The increase in reported BTEX concentrations in well MW-4 may be due to some down gradient transport of hydrocarbons due to hydraulic effects of the water injected in the former UST area (Figure 11). Although detectable concentrations of some BTEX compounds remain in both wells MW-4 and MW-6, concentrations of these compounds are not above drinking water MCLs. The two wells located to the west of the injection wells, MW-1 and MW-2, continue to be free of detectable concentrations of BTEX compounds as in the baseline analytical results.

Microbial Populations

Populations of heterotrophic bacteria have been measured in samples collected on a monthly basis (Figure 12). In the first of these performance monitoring sampling events, conducted in September 1993, populations were higher than those reported in baseline samples collected in June 1992, prior to system startup. Microbial populations generally decreased in all wells from September through the November sampling event. The January 1994 sample results yielded mixed results.

Some variations may be due to the lack of precision of the laboratory analysis used to measure microbial populations. Variations in reported microbial populations between blind duplicate samples submitted to the same laboratory were 150% and 156% in the two instances that duplicates were submitted.

Dissolved Oxygen

The primary purpose of equipment installed as part of the *in situ* groundwater treatment system was to increase the amount of oxygen available for use by aerobic microorganisms in the impacted area. These microorganisms were expected in turn to degrade petroleum hydrocarbons at an increased rate due to the increased availability of oxygen. However, the expense of the hydrogen peroxide used as an oxygen source comprises the majority of system operating costs. Therefore, the hydrogen peroxide injection rate was set at a level expected to foster robust microbial populations while minimizing any excess released from the treatment area.

Dissolved oxygen concentrations were measured in monitoring wells on a monthly basis (Figure 13). Oxygen concentrations in the three wells located closest to the impacted area (MW-6, MW-7, and MW-8) have consistently been lower than concentrations measured in outlying wells. The oxygen concentration in well MW-4, located downgradient of the former UST area, declined rapidly over the first 17 weeks of system operation and has remained at a very low level since the November sampling event.

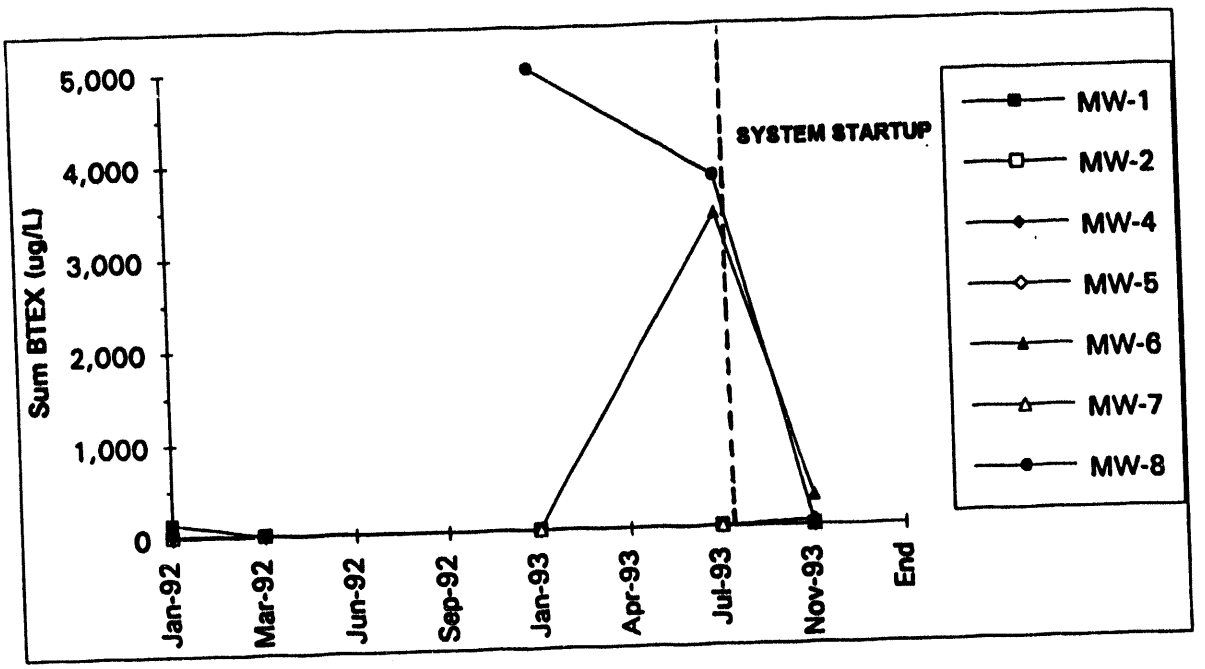


Figure 10 - Total BTEX Concentrations in Groundwater

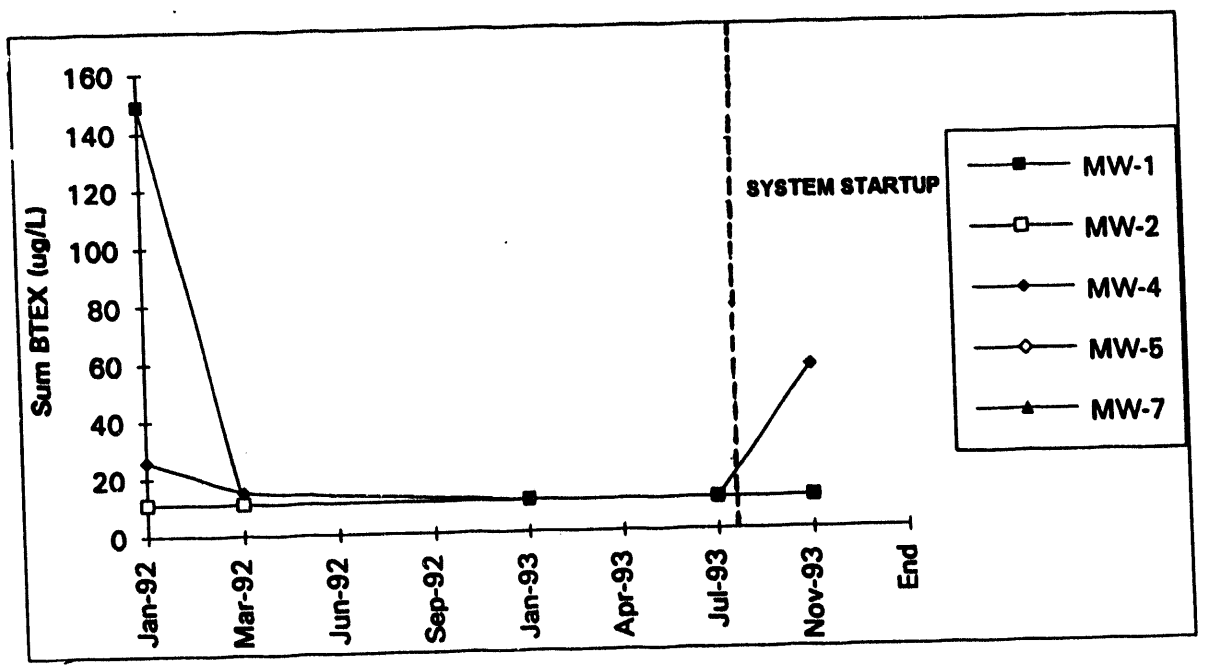


Figure 11 - Total BTEX Concentrations in Groundwater (Excluding Wells MW-6 and MW-8)

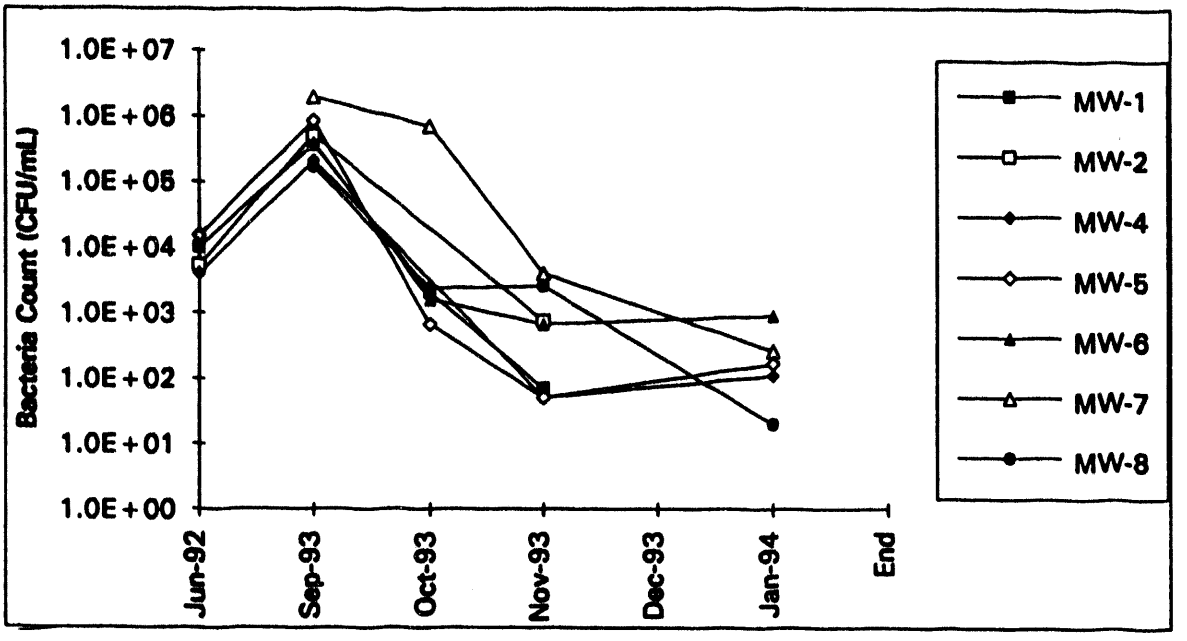


Figure 12 - Microbial Populations in Groundwater

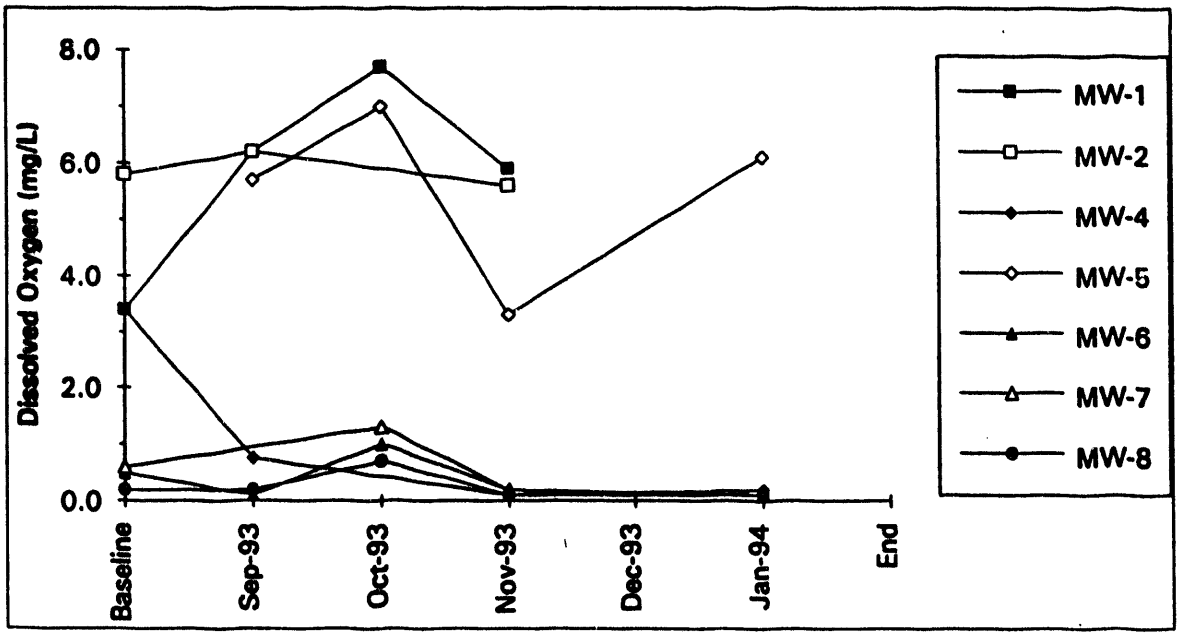


Figure 13 - Dissolved Oxygen Concentrations in Groundwater

Despite continuous injection of hydrogen peroxide solution from August through October only a slight increase in oxygen concentrations was observed in wells MW-6, MW-7, and MW-8. This slight increase was reversed in the November measurements, which were even lower than baseline concentrations.

Nutrients

Over the course of system operation concentrations of both nitrogen and phosphorus have been gradually increasing in MW-8, the monitoring well closest to the injection wells. Nitrogen (as nitrate) concentration trends are presented in Figure 14. Nutrient concentrations in these wells have consistently been lower than those reported for the outlying wells MW-1, MW-2, and MW-5. Nutrients in MW-4 fell during system operation in a trend similar to that discussed above regarding dissolved oxygen.

Nitrogen concentrations in the outlying wells MW-1, MW-2, and MW-5 have been significantly higher than those reported in the wells closer to the former UST area. Baseline concentrations in these wells were near the 10 mg/ℓ MCL, the nitrate concentration in well MW-2 was reported as 32 mg/ℓ in the September 1993 sampling event. It is not likely that these high nitrate levels are a result of nutrients applied as part of this project as the nitrogen concentration in the nutrient-amended injected groundwater is only 8 mg/ℓ. Also, concentrations in wells closer to the injection wells have consistently been reported as less than 2 mg/ℓ.

CONCLUSIONS

A significant decline in BTEX concentrations was observed over the first seventeen weeks of system operation. Immediately prior to system startup benzene concentrations were as high as 2,800 µg/ℓ (MW-8, July 1993). Results of the November sampling event indicate that benzene concentrations are at or below the drinking water MCL of 5 µg/ℓ in all wells at the project site. The method detection limit for benzene in MW-6 was 10 µg/ℓ because the presence of 240 µg/ℓ xylenes necessitated sample dilution for BTEX analysis. Therefore, though no benzene was reported in this sample, it is possible that up to 10 µg/ℓ benzene was present. Except for this detection limit issue, it appears that Idaho Division of Environmental Quality (DEQ) water quality guidelines have been satisfied at the project site.

Residual concentrations of xylenes in wells MW-4 and MW-6 were higher than those of benzene, toluene, and ethylbenzene. The maximum reported concentration of xylene isomers was 240 µg/ℓ in well MW-6. It is common for xylene isomers to be more resistant to biological degradation than benzene, toluene, and ethylbenzene (Tabak, 1991). Although xylenes were reported at detectable concentrations in these two wells, these concentrations were well below the maximum contaminant limit of 10,000 µg/ℓ.

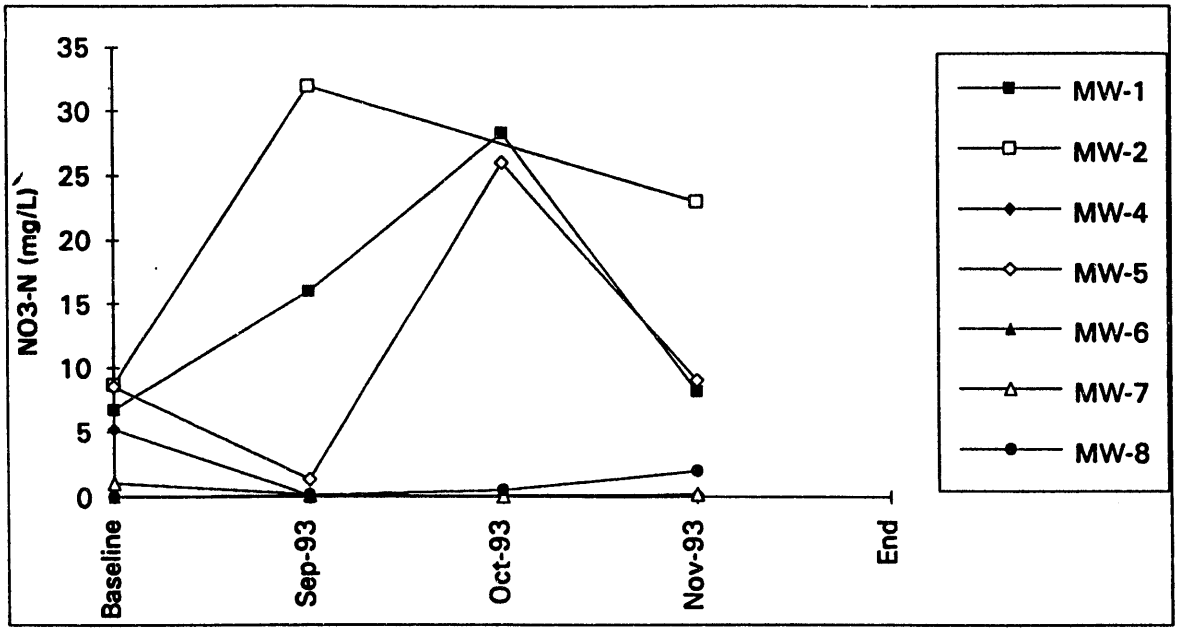


Figure 14 - Nitrogen (as Nitrate) Concentrations in Groundwater

The concentration of both benzene and xylenes increased in well MW-4 over the first seventeen weeks of system operation. The benzene concentration in this well increased from below the 1 µg/ℓ method detection limit to 5 µg/ℓ. Well MW-4 is located downgradient of the injection wells and former UST location. Elevated benzene concentrations as high as 16 µg/ℓ had previously been measured in samples collected from this well in both January 1992 and March 1992. Benzene concentrations in subsequent samples collected from this well in January 1993 and July 1993 were below method detection limits. The recent increase in benzene concentration could be the result of hydraulic transport from the impacted area and/or natural seasonal variations, as suggested by earlier variations in reported concentrations. A sharp decline in both dissolved oxygen and nutrient concentrations in this well suggest that hydraulic transport of oxygen- and nutrient-depleted water from the impacted area is taking place and, therefore, is likely responsible for at least some of the observed increase in benzene and xylene concentrations. Since reported concentrations of these compounds are not above drinking water MCLs, and the shallow water table is not used as a drinking water supply, this potential for some hydraulic transport is not considered a major concern. Two wells located west of the impacted area, MW-1 and MW-2, remain free of detectable concentrations of BTEX compounds, indicating these hydrocarbons are not being transported off-site in this direction.

Microbial populations declined in all wells from September to November. Since this effect is common to all of the monitoring wells, including the upgradient well MW-5,

it appears to be a regional trend rather than the result of system operation. This apparent regional trend could be due to decreased intrusion of surface water during the winter months. Populations in MW-6, MW-7, and MW-8, the three monitoring wells located closest to the injection wells, either increased slightly or decreased at a slower rate than the other, more distant, monitoring wells. This suggests that operation of the *in situ* groundwater treatment system was having a positive effect on microbial populations in contrast to a regional decline. Microbial counts in samples collected in January, 1994, remained low, with some wells showing minor declines while samples from other wells contained slightly higher populations than in earlier samples. Because there were significant variations between microbial counts for duplicate samples, microbial population measurements must be interpreted as only a rough indicator of actual microbial populations.

Despite low microbial populations, decreasing BTEX concentrations indicate that an active microbial population is present. These apparently conflicting data could be an indication that the microbial community is largely held in the soil matrix in the area between the injection wells and the monitoring wells.

Despite continuous injection of hydrogen peroxide solution from August through October only a slight increase in oxygen concentrations was observed in the three monitoring wells located closest to the injection wells (MW-6, MW-7, and MW-8). This slight increase was reversed in subsequent measurements, which were even lower than baseline concentrations. Dissolved oxygen concentrations in these three wells have consistently been lower than those measured in outlying wells. This is most likely due to oxygen demand exhibited by aerobic microorganisms in the presence of an ample carbon substrate (*i.e.*, hydrocarbon compounds) as is available in the contaminated area.

The microbial community is apparently increasing in population as rapidly as oxygen becomes available (i.e., the oxygen supply is limiting the microbial population and therefore the rate of hydrocarbon degradation). The slight rise in oxygen concentrations measured in October followed by the very low values measured in November may have been caused by a lag in the microbial population catching up with the increasing availability of dissolved oxygen.

Nutrient concentrations have been gradually increasing in the monitoring wells located closest to the injection wells. This indicates that nutrients have been supplied at a rate slightly in excess of the demand imposed by the microbial population.

FUTURE ACTIVITIES

Except for MW-6, where the 10 µg/ℓ detection limit for benzene was higher than the 5 µg/ℓ drinking water MCL, it appears that DEQ water quality guidelines have been satisfied at the project site. If BTEX concentrations continue to be reported as below drinking water MCLs, system operation be terminated. If ongoing groundwater quality monitoring supports the promising results of the initial BTEX analyses presented in this report, *in situ* biological treatment may offer a relatively rapid and cost effective

treatment alternative for additional petroleum release sites in the Treasure Valley region.

LITERATURE CITED

Delfino, J.J. and Miles, C.J. "Aerobic and anaerobic degradation of organic contaminants in Florida groundwater" *Soil and Crop Science Society of Florida, Proceedings* 44 (1985): 9-14

Dion, N.P. "Some effects of land use changes on the shallow groundwater system in the Boise-Nampa area, Idaho" *Idaho Department of water Administration, Water Information Bulletin No. 26* (1972): 47

Huling, S.G., Bledsoe, B.E., and White, M.V. "Enhanced bioremediation utilizing hydrogen peroxide as a supplemental source of oxygen: a laboratory and field study" *U.S. Environmental Protection Agency Report* EPA/600/2-90/006 (1990)

Malde, H.E. and Powers, H.A. "Upper Cenozoic stratigraphy of Western Snake River Plain" *Idaho: Geological Society of America Bulletin* 73 (1962): 1197-1220.

McCarty, P.L. "Bioengineering issues relating to in situ remediation of contaminated soils and groundwater" Environmental Biotechnology (1988): 153-156

Othberg, K.L. and Stanford, L.R. "Geologic Maps of the Boise Valley and adjoining areas, Western Snake River Plain, Idaho, Scale 1:100,000" *Idaho Geologic Survey Map Series* (1992)

Squires, E., Wood, S.H., and Osiensky, J.L. "Hydrologic framework of the Boise aquifer system, Ada County, Idaho" *Idaho Water Resources Research Institute, Research Technical Completion Report* 14-08-0001-G1559-06 (1992): 109

Tabak, H.H., Desai, S., and Govind, R. "Development and application of a multilevel respirometric protocol to determine biodegradability and biodegradation kinetics of toxic organic pollutant compounds" *On-Site Bioreclamation.* Ed. Hinchee, R.E., and Olfenbuttel, R.F. Butterworth-Heinemann, Stoneham, Massachusetts, 1991. 325-39.

United States. Environmental Protection Agency. Bioremediation in the field. EPA/540/N-93/001, 8 (1993)

Urano, K. and Kato, Z. "Evaluation of biodegradation ranks of priority organic compounds" *Journal of Hazardous Materials* 13 (1986): 147-159

Wilson, J.T., et al. "In situ bioremediation of spills from underground storage tanks: new approaches for site characterization, project design, & evaluation of performance" *U.S. Environmental Protection Agency Report* EPA/600/2-89/042 (1989)

Hydrogeology, Waste Disposal, Science and Politics
Proceedings 30th Symposium
Engineering Geology and Geotechnical Engineering, 1994

DIFFUSION THROUGH STATICALLY COMPACTED CLAY

by Carlton L. Ho, M. ASCE[1] and Maher A.-A. Shebl, S.M. ASCE[2]

ABSTRACT :

This paper presents experimental work on the effect of compaction on contaminant flow through clay liners. The experimental program included evaluation of soil properties, compaction, permeability and solute diffusion. A permeameter was built of non reactive materials to test samples compacted at different water contents and compactive efforts. The flow of a permeating solute, LiCl, was monitored. Effluent samples were collected for solute concentration measurements. The concentrations were measured by performing atomic adsorption tests. The analyzed results showed different diffusion characteristics when compaction conditions changed. At each compactive effort, permeability decreased as molding water content increased. Consequently, transit time (measured at relative concentration 50%) increased and diffusivity decreased. As compactive effort increased for soils compacted dry of optimum, permeability and diffusion decreased. On the other hand, as compactive effort increased for soils compacted wet of optimum, permeability and diffusivity increased. Tortuosity factor was indirectly measured from the diffusion and retardation rate. Tortuosity factor also decreased as placement water content was increased from dry of optimum to wet of optimum. These decreases were more pronounced for low compactive effort tests.

Keywords: clay, clay liner, compaction, diffusion, laboratory, solute transport.

INTRODUCTION

Clay is commonly used as a liner material for hazardous wastes containment. These clay liners are used to contain the wastes and to minimize contamination of the groundwater. Clay is chosen because of its low permeability and stability. In order to use clay as a liner, the clay must be compacted in place. The method of compaction influences the properties of the clay. This study is intended to emphasize the effect of compaction on clay as well as to emphasize the effect of compaction on contaminant flow properties.

Compaction produces volumetric and structural changes in the clay soil. Dry of optimum compaction reduces the voids between the clay particles (Lambe, 1958a, 1958b; Seed and Chan, 1959), which can be expressed as a volumetric change. Compaction wet of optimum rearranges the clay particles into a parallel structure (Lambe, 1958a, 1958b), which can be expressed as structural changes. Permeability is dependent upon soil structure (Mesri and Olsen, 1971), and the pore size (Garcia-Bengochea, et al., 1979). When the soil is compacted wet of optimum or at a high compactive effort, the permeability decreases. Also, permeability depends on the properties of the permeating fluid (Kozeny, 1972; Carman, 1937, 1941).

Since flowing contaminants consist mostly of water and salt solutions, the flow must be expressed as a coupled movement (Greenberg, et al., 1973). It is therefore important to understand the mechanisms that control the flow of water and solute through clay. Water flow

[1] Asst. Prof., Dept. of Civ. and Env. Engrg., Wash. St. Univ., Pullman, WA 99164-2910.

[2] Res. Asst., Dept. of Civ. and Env. Engrg., Wash. St. Univ., Pullman, WA 99164-2910.

is controlled by the soil properties. Solute transport mechanisms (diffusion, advection, dispersion, and adsorption) are controlled by soil properties as well as by the fluid properties and species properties. For low permeability of clays subjected to low gradient, the diffusion appears to be the most dominant contaminant transport mechanism (Goodall and Quigley, 1977; Dessaulinier, et al., 1981; Crook and Quigley, 1984; Folkes, 1982; Barone, et al., 1989; Barone, et al., 1990). So the analysis of the obtained experimental data will show the significance of compaction variables on the transport mechanisms. Also, it will show the effect of compaction variables on diffusion.

This paper presents an experimental study on the effect of compaction method on solute transport through clay. The solute chosen for this study was of LiCl, with an initial concentration of 500 mg/l. LiCl was used because, Li^+ has a low potential to be adsorbed to the negatively charged clay particles. This allows for easier evaluation of diffusion. This study investigated the effect of compactive effort and molding water content on permeability and diffusivity (Shebl, 1990).

MODEL AND ASSUMPTIONS

The three-dimensional constitutive model used in this work is composed of a solid phase with an open void domain. The solid phase consists of soil particles. The open domain consists of the void space which can contain liquid and gas phases. For fully saturated soils, the open domain is completely occupied by liquid. The concept of conservation of mass was applied to derive the governing differential equation for the continuum model. The model was built on the following assumptions:

- Homogeneous medium
- Isotropic medium.
- Saturated medium.
- Steady state flow
- Darcy's law is valid.
- No biological transformations.
- No radioactive reactions.
- Isothermal conditions.
- The coefficient of diffusion assumed to be constant over the migration profile.
- Solute of single species (no chemical reaction between different species).
- Sufficiently diluted solute.
- Conservation of mass.
- Conservation of energy.

No chemical reaction between different species into the medium was assumed. The measured diffusion differ from field conditions. The diffusion coefficient obtained from a leachate model is typically lower than that obtained from a single salt model (Barone, et al., 1989).

The one-dimensional dispersion differential equation can be expressed as,

$$D_x \frac{\partial^2 C}{\partial x^2} - (V_s)_x \frac{\partial C}{\partial x} = \frac{\partial C}{\partial t} \qquad (1)$$

where D_x equals the coefficient of hydrodynamic dispersion in the x direction, C equals the concentration of the solute, and $(V_s)_x$ equals the seepage velocity in the x direction.

Ogata (1961) obtained the solution for the differential equation of the model used under the following boundary and initial conditions,

$C(x,0) = 0 \qquad x > 0$

$C(0,t) = C_o \qquad t \geq 0$

$C(\infty,t) = 0 \qquad t \geq 0$

The solution of the differential equation is documented by Crooks and Quigley (1984). Although the boundary condition at $x=\infty$ is not perfectly compatible with the actual boundary condition at the effluent end of a 1-D test, it was felt that the solution was reasonable. The solution is in the form,

$$\frac{C}{C_o} = \frac{1}{2}\left[erfc\left(\frac{x - V_s\, t}{2\sqrt{D_x\, t}}\right) + \exp\left(\frac{V_s\, x}{D_x}\right) erfc\left(\frac{x - V_s\, t}{2\sqrt{D_x\, t}}\right)\right] \qquad (2)$$

The adsorption effect must also be included. Adsorption causes a time delay of the solute flow. This delay is expressed by the retardation factor, R_t, the ratio of the measured resident time to the calculated resident time. The measured resident time is the time for reaching $C/C_0 = 0.5$ taken from breakthrough curve. The calculated resident time is the actual time for the solute front to reach the effluent end if there was no adsorption.

This governing equation is used to determine the migration profile and change in the diffusion variables. If V_s is sufficiently low, the dispersion coefficient will have no contribution from the hydrodynamic dispersion, and will be equal to the coefficient of diffusion (Rowe, 1987).

EXPERIMENTAL METHODOLOGY

Representative samples of 85% commercial Kaolinite and 15% Ottawa sand were tested. The testing program consisted of four parts: soil properties, soil compaction, soil saturation and permeability, and sampling and concentration measurements. Each portion of the test program was used to characterize changes in diffusion as a function of changes in compaction conditions.

Soil Properties And Compaction

The soil properties testing consisted of specific gravity (ASTM D854), liquid and plastic limits (ASTM D4318), and consolidation tests (ASTM D2435). These tests provided the soil parameters needed for the analysis. The moisture-unit weight relationships were obtained by performing the compaction tests. Compaction was performed at different compactive efforts: standard proctor test (ASTM D698) and Modified proctor test (ASTM D1557). The results were plotted in terms of water contents verses dry unit weight (Fig. 1). Two sets of three samples were prepared. One set was prepared at 90 % relative compaction of Standard Proctor maximum dry density. A second set was prepared at 90 % relative compaction of Modified Proctor maximum dry density. The three samples of each set were prepared at different water contents. For each set one sample was prepared dry of optimum water content, one prepared at the wet of optimum water content, and one at the line of optimum water content (Fig. 1).

Compaction for the Solute Transport Samples

Solute transport samples were formed using static compaction in a plexiglass cylindrical mold. The mold has an inside diameter of 7.11 cm, a height of 50.8 cm, and a wall thickness of 1.91 cm. It consists of two separable half cylinders connected with screws along the sides. Also,

it had a 0.64 cm thick rubber disk and a 0.64 cm thick aluminum plate with diameters the same as the inside diameter of the cylinder.

The soil was prepared for compaction in the following manner. The soil specimens dimensions were approximately 1.27 cm tall and 7.11 cm in diameter. Since the dry density and the volume of the specimen were predetermined, the mass of soil solids required for each specimen could be calculated. This mass of soil solids and water were mixed to the predetermined water contents required for each test. Each batch of soil sat overnight in a sealed container to allow for even hydration. Then, the soil was placed in the mold for compaction. The sample was covered with the rubber disk and the aluminum disk. A steel loading rod (55.9 cm tall and 6.91 cm diameter) was placed at the top of the aluminum plate. The mold and its contents were placed between compression plates and compacted under continuous pressure.

The soil was compressed between the loading plates until the desired thickness was obtained. At that point, the load on the sample remains for about 1/2 hour to limit any soil swelling of the sample upon removal from the mold. Zero swell was confirmed by measuring the thickness of the specimen with a dial gage.

Falling Head Permeameter Design

The permeameter consists of a sample confining chamber, flow reservoirs and control panel (Fig. 2). The arrows in Fig. 2 indicate the fluid flow during the solute transport phase of the test. A triaxial cell is used as a confining chamber. There are three stainless steel 2 liter reservoirs. The first cylinder is used as an influent water reservoir. The second cylinder is an influent solution reservoir. The third cylinder is an effluent water reservoir. A 6 mm diameter effluent sampling septum is placed near the bottom platen T-valve, between the T-valve and the effluent reservoir. This T-valve controls the flow to the septum, and allows for change of the septum when necessary.

Two pressure regulators are mounted on a control panel. One regulator controls fluid back pressure. A second regulator controls confining pressure. One differential pressure transducer measures effective confining stress. A second differential pressure transducer is used to measure volume changes. The transducer measures the pressure difference between the top and bottom of a standard volume change burette. Changes in the transducer output relate to changes in fluid volume.

Fittings and tubes were selected to minimize any chemical reactions. All fittings, connectors and valves were made of stainless steel. 0.635 cm i.d. TEFLON tubes were used for the pressure lines. 0.318 cm i.d. TEFLON tubes were used for the flow lines.

Sample preparation and permeability testing

The soil specimen was placed between two glass filter papers and two fretted glass porous plates. This combination was placed between the two stainless steel platens and confined with a latex membrane. The membrane was sealed to each platen with two O-rings. The triaxial cell was closed and filled with water to approximately 2.0 cm above the top of the upper platen to provide a hydrostatic isotropic pressure. Confining pressure and back pressure were incrementally increased to 345 kPa and 276 kPa respectively in increments of 34.5 kPa. This provided a net effective stress of 69 kPa. Back pressure is necessary to saturate the sample. $\bar{B}$ ($= \Delta u/\Delta\sigma_3$) was greater than or equal to 0.96. After the saturation, the inflow and outflow valves were closed in preparation for the permeation stage.

At the beginning of the permeation stage the effluent valve was opened for about 6 hours to allow for stabilization of the pore water flow. Once the flow rate stabilized, the solution was then allowed to flow through the soil column. The flow direction was from the top to the bottom of the soil column. This simulated actual field situation. The flow driving head was the difference between the elevated solution tank head and the volume change burette head. The head difference was kept at 290 mm ± 5 mm during most of the test period. Volume change readings were taken every 3 to 6 hours during the test period (2 to 4 weeks). The soil permeability was calculated using these readings. The entire test was conducted in a temperature controlled room at 20° C. Replicate tests were conducted to confirm reliability of results.

Sampling and Samples Concentration Measurements

Samples of the effluent were taken at 3 hour intervals up to 12 hours, then at 12 hour intervals thereafter. A 1.0 ml syringe was used to extract the effluent solution through the sampling septum. As the effluent solution was extracted, the volume change burette head decreased. 1.0 to 2.0 ml of the solution were extracted until the head difference between the influent reservoir and the volume change burette was the same as at the beginning of the test. This was to keep the head constant. The samples were stored in sealed vials and kept at 4° C until the solute concentrations could be analyzed.

The solute concentrations were determined by atomic adsorption tests. For the tests presented in this paper, two atomic adsorption spectrophotometers were used, a Perkin-Elmer 303 and a Varian SpectrA-A300. Sample concentrations were determined by comparison of the sample reading with standard concentration calibration curve.

DATA ANALYSIS

The test soil was a mixture of 85% kaolinite and 15% Ottawa sand. Fig. 1 shows the Standard Proctor and Modified Proctor compaction curves. Identified on the curves are the points chosen for the permeability testing samples. Three points were for the low compactive effort (γ_d of 14.4kN/m^3): A (at dry of optimum), B (at optimum) and C (at wet of optimum). These were compacted at water contents of 10.4, 24.8 and 28.8% respectively. Another three points were for the high compactive effort (γ_d of 15.1 kN/m^3): D (at dry of optimum), E (at optimum) and F (at wet of optimum). These were compacted at water contents of 9.4, 23.0 and 26.7% respectively. Although it is known that a liner should always be compacted wet of optimum (Reades, et al., 1987), the entire range of water contents (from dry of optimum to wet of optimum) was considered because there is always the possibility of placement error resulting in a dry of optimum, or optimum water content.

The results obtained from the permeability and atomic adsorption tests appear in Table 1. The table presents the following data: coefficient of permeability; seepage velocity; retardation factor; coefficient of diffusion; and tortuosity. Fig. 3 shows the coefficient of permeability at different water contents. For both high compactive effort and low compactive effort, coefficient of permeability decreased with an increase in water content. This phenomenon was observed by others (Lambe, 1958b; Mitchell et al., 1965). This variation in coefficient of permeability is attributed to the dependency of soil structure on the placement water content. Soils compacted dry of optimum tend to exhibit a more flocculated structure. Soils compacted wet of optimum tend to exhibit a more dispersed structure (Lambe, 1958b). It is important to note that γ_d for each compactive effort series was constant. Hence, porosity was also constant. Therefore, the variation in permeability is a function of the orientation of the soil particles and size of macropores

Table 1 Flow parameters for samples at different water contents and different compactive efforts.

Test conditions	Water content (%)	Coeff. of permeability (cm/day)	Seepage velocity (cm/day)	Retention factor (C/C_0=0.5)	Coeff. of diffusion (cm^2/day)	Tortu-osity
(1)	(2)	(3)	(4)	(5)	(6)	(7)
Low compactive effor (Std. Proctor)						
Dry of Optimum (pt. A)	10.4	0.01760	0.767	1.21	0.0920	0.125
Optimum (pt. B)	24.8	0.00461	0.195	1.46	0.0224	0.037
Wet of optimum (pt. C)	28.2	0.00455	0.196	1.60	0.0223	0.040
High compactive effort (Mod. Proctor)						
Dry of Optimum (pt. D)	9.4	0.00712	0.329	1.40	1.40	0.059
Optimum (pt. E)	23.0	0.00616	0.282	1.41	1.41	0.051
Wet of Optimum (pt. F)	27.0	0.00529	0.239	1.50	1.50	0.046

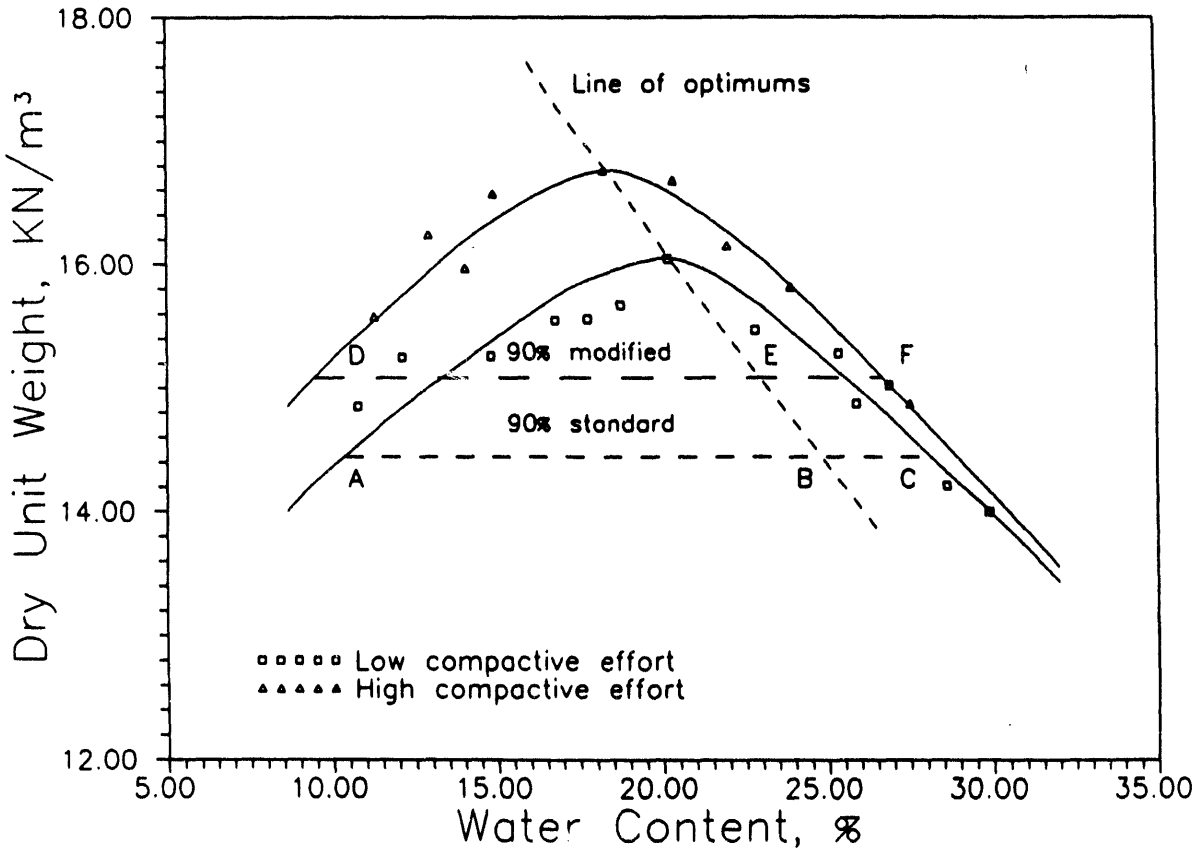


Fig. 1. Compaction curves for standard and modified proctor tests.

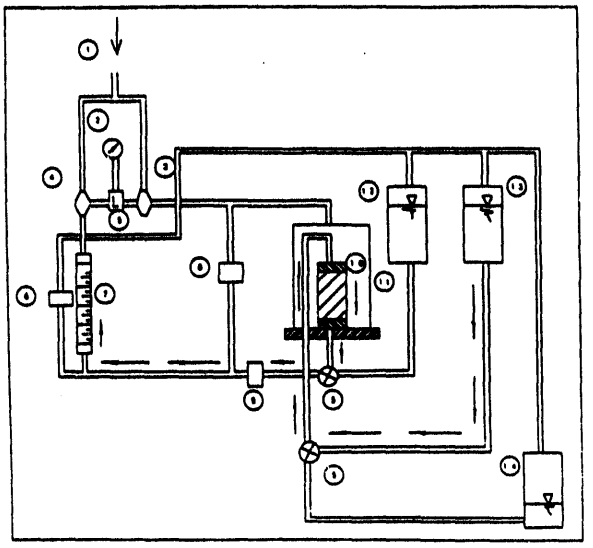


Fig. 2. Schematic of diffusimeter/permeameter: 1) compressed air: 2) Pressure gauge; 3) confining pressure regulator; 4) back pressure regulator; 5) T-valve; 6) volume change pressure transducer; 7) volume change burette; 8)effective stress pressure transducer; 9) sampling septum; 10) sample confined in membrane; 11) confining chamber; 12) influent water reservoir; 13) influent solute water reservoir; 14) effluent water reservoir.

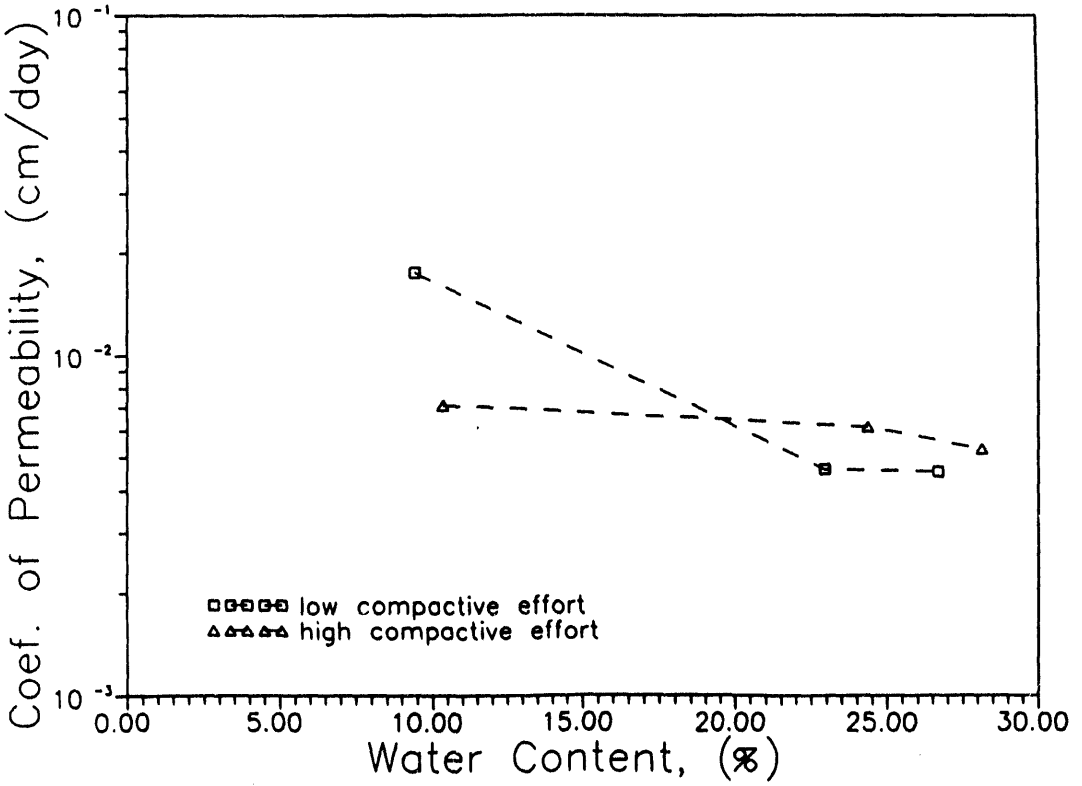


Fig. 3. Effect of changes in water content at different compactive efforts on the coefficient of permeability.

between original precompacted soil lumps (Mitchell and Madisen, 1987; Quigley, et al., 1988).

The coefficient of permeability decreased with an increase in compactive effort for soils compacted dry of optimum (tests A and D). This is as expected. The soil compacted with a greater compactive effort had lower porosity. Hence, that soil should have a lower permeability.

To the contrary, the coefficient of permeability increased slightly with an increase in compactive effort for soils compacted wet of optimum (tests C and F). One would expect that an increase in compactive effort would decrease permeability. This is an indication that particle orientation must have a significant influence on permeability. Also, the particle orientation has a greater influence on the coefficient of permeability than porosity.

Fig. 4 and 5 show the fitted break-through curves. They are shown for dry of optimum, at optimum, and wet of optimum, and are plotted for both high and low compactive efforts. The influent concentration of the Li^+ (C_o) was 500 mg/l. The normalized effluent concentration of Li^+ (C/C_o) were plotted as a function of transit time. These plots show the effect of water content on effluent concentration variation with time. The transit time at C/C_o=0.5 increases as the water content increases. This transit time increase results from a consistent reduction in the seepage velocity. Transit time variation with respect to compactive effort is greater for dry of optimum conditions than for wet of optimum conditions. This most likely results from a greater variation in the coefficient of permeability. Also, there is a large time difference between samples prepared dry and wet of optimum at low compactive effort. To the contrary, there is a much smaller difference between the transit times of the solute through samples compacted dry and wet of optimum at high compactive effort. This results from larger variations in the particle orientation at low compactive effort.

The data shows a small decrease in the transit time from low to high compactive effort. This reduction occurs at optimum and wet of optimum but not at dry of optimum conditions. This was not expected. It is possible that the soil structure is more dispersed at low compaction and higher water content. This is most unlikely. Another possible explanation is that adsorption reduces the solute transport. Variations in particle orientation may affect the adsorption of the solute. The effect may have been more apparent in wetter soil.

The low permeability of the soil allowed diffusion to be the dominant transport mechanism. Fig. 6 shows the relationship between the coefficient of diffusion and the water content. At low compactive effort, the calculated coefficient of diffusion (at $C/C_o = 0.5$) decreases as the water content increases. This implies that the diffusion coefficient is a function of water content, which was observed by Shakelford (1989). Also, at high compactive effort the coefficient of diffusion decreases when the water content increases. Table 2 and 3 present these changes. There is a consistent decrease of the coefficient of diffusion with respect to an increase in water content at both compactive efforts. That was expected because of the increase in the dispersivity of clay. As water content increases, dispersivity increased. This occurs when the water content increases from dry of optimum to optimum and from optimum to wet of optimum.

One measure of the openness of the structure of the soil is the tortuosity. The tortuosity, τ, is defined as follows (Bear, 1972):

$$\tau = \left(\frac{L}{L_0}\right)^2 \tag{3}$$

where L equals the distance between two points in the sample, L_0 equals the length of the flow

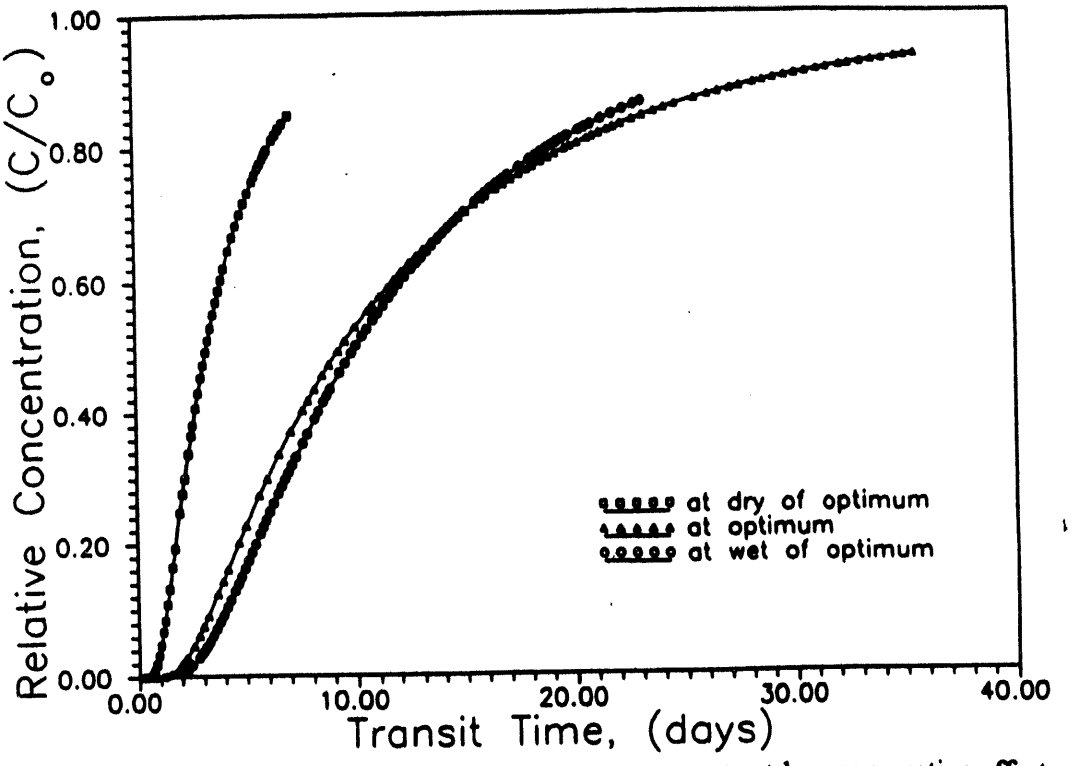


Fig. 4. Break-through curves for Li^+ at different water contents at low compactive effort.

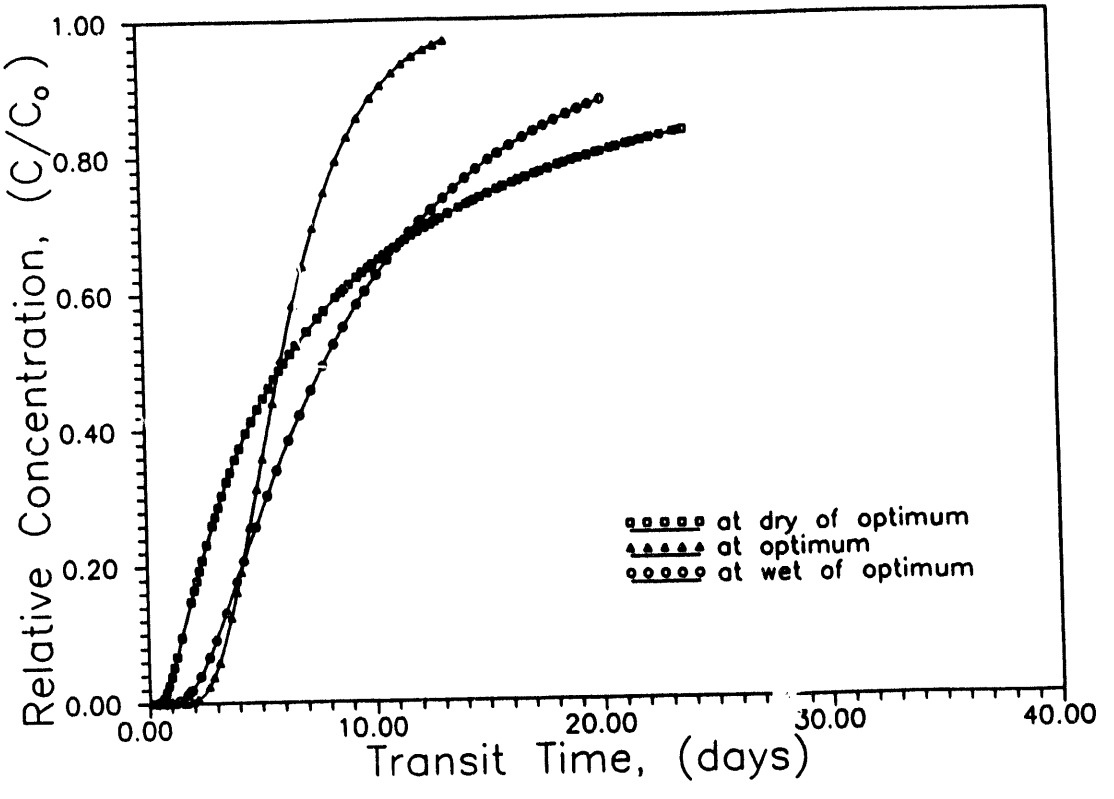


Fig. 5. Break-through curves for Li^+ at different water contents at high compactive effort.

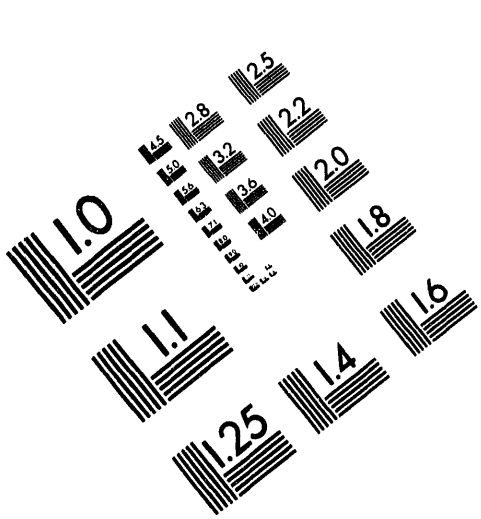
Table 2 Results of nonlinear least square regression analysis for the diffusion coefficient from the observed concentration data.

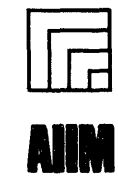
Test conditions	NO	IDCV (cm^2/day)	R-square	T-value	LB for 95% confidence	UB for 95% confidence
(1)	(2)	(3)	(4)	(5)	(6)	(7)
Low compactive effort (Std. Proctor)						
Dry of Optimum (pt. A)	49	0.326	0.987	14.50	0.281	0.371
Optimum (pt. B)	90	0.121	0.969	12.20	0.101	0.141
Wet of optimum (pt. C)	87	0.082	0.972	14.90	0.071	0.093
High compactive effort (Mod. Proctor)						
Dry of Optimum (pt. D)	90	0.657	0.957	7.73	0.488	0.825
Optimum (pt. E)	53	0.058	0.985	12.40	0.049	0.068
Wet of Optimum (pt. F)	45	0.114	0.992	16.40	0.100	0.129

Table 3 Results of nonlinear least square regression analysis for the retention factor from the observed concentration data.

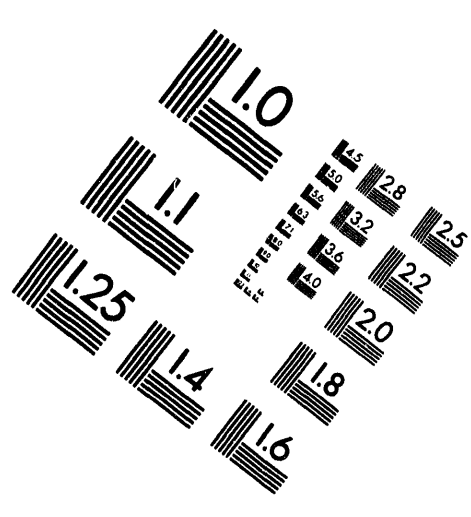
Test conditions	NO	IRFV	R-square	T-value	LB for 95% confidence	UB for 95% confidence
(1)	(2)	(3)	(4)	(5)	(6)	(7)
Low compactive effort (Std. Proctor)						
Dry of Optimum (pt. A)	49	2.60	0.987	54.4	2.50	2.70
Optimum (pt. B)	90	2.13	0.969	42.6	2.03	2.22
Wet of optimum (pt. C)	87	2.03	0.972	52.5	1.95	1.10
High compactive effort (Mod. Proctor)						
Dry of Optimum (pt. D)	90	4.00	0.957	14.4	3.45	4.55
Optimum (pt. E)	53	1.66	0.985	66.8	1.61	1.71
Wet of Optimum (pt. F)	45	2.05	0.992	60.8	1.98	1.12

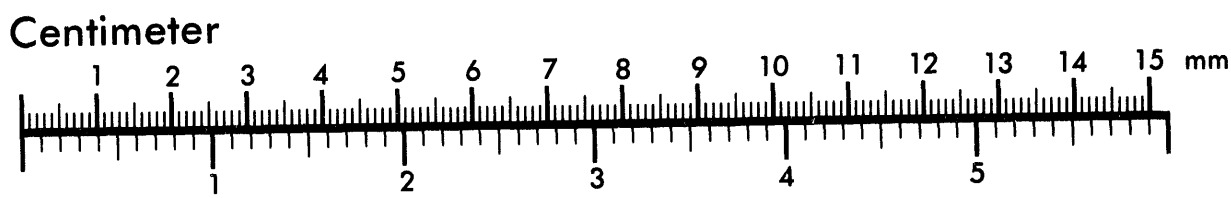
(NO) Number of observations.
(IDCV) Interpolated diffusion coeffecient value.
(IRFV) Interpolated retention factor value.
(LB) Lower bound.
(UB) Upper bound.

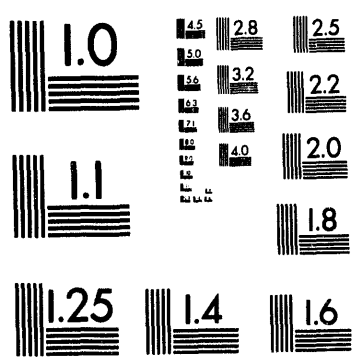


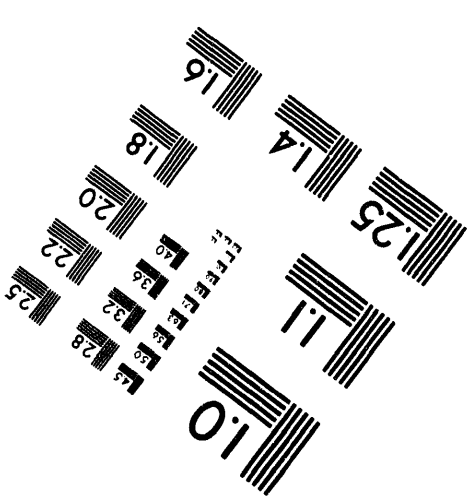


Association for Information and Image Management
1100 Wayne Avenue, Suite 1100
Silver Spring, Maryland 20910
301/587-8202

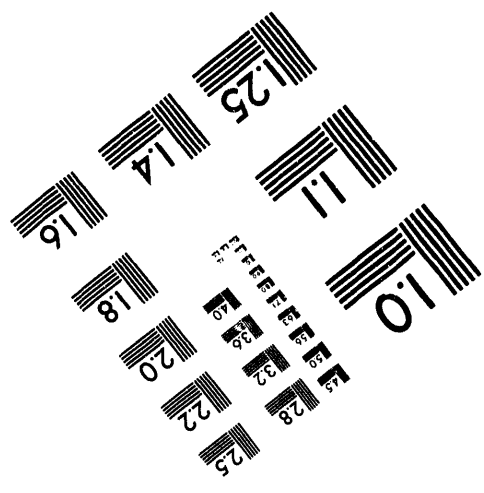








MANUFACTURED TO AIIM STANDARDS
BY APPLIED IMAGE, INC.



6 of 7

Evaluation of the tortuosity indicated that there is a variation in soil structure with respect to placement water content. Soils placed dry of optimum have a higher tortuosity (less tortuous flow path) than soils placed at optimum or wet of optimum. That variation is less significant for soils placed with high compactive effort.

These conclusions are based upon experimentation with one type of soil at two typical compactive efforts. The trends inferred from the test data indicate the dependence of solute transport mechanisms upon the method of compaction. Other soil types may have more or less dependence than the Kaolinite and Ottawa sand mixture used in the experimentation described in this paper.

ACKNOWLEDGMENTS

The authors would like to express their appreciation for the technical advice given by Dr. Richard Fragaszy, Dr. Yavuz Corapcioglu, Dr. David Mulla and Dr. David Yonge. The authors also thank the Office of Graduate and Research Development and the Department of Civil and Environmental Engineering at Washington State University for their financial support of this research.

REFERENCES

Barone, F. S., Rowe, R. K., and Quigley, R. M. (1990), "Laboratory determination of chloride diffusion coefficient in an intact shale," *Can. Geotech. J.*, **27**, pp. 177-184.

Barone, F. S., Yanful, E. K., Quigley, R. M., and Rowe, R. K. (1989), "Effect of multiple contaminant migration on diffusion and adsorption of some domestic waste contaminants in a natural clayey soil," *Can. Geotech. J.*, **26**, pp. 189-198.

Bear, J. (1972), *Dynamics of Fluids in Porous Media*, American Elsevier, New York.

Carman, P.C. (1937), "Fluid flow through a granular bed," *Trans. Inst. Chem. Engrg.*, London, **15**, 150-156.

Carman, P.C. (1941), "Capillary size and capillary movement of moisture in fine sands," *Soil Sc.*, **52**, 1-14.

Crooks, V.E. and Quigley, R.M. (1984), " Saline leachate migration through clay: a comparative laboratory and field investigation," *Can. Geotech. J.*, **21**, 349-362.

Dessaulinier, D.E., Cherry, J.A. and Fritz, P. (1981), "Origin, age and movement of pore water in argillaceous quaternary deposits at four sites in southwestern Ontario," *J. of Hydrology*, 231-257.

Folkes, J.d. (1982), "Control of contaminant migration by the use of liners," Fifth Can. Geotech. Colloquium, *Can. Geotech. J.*, **19**, 320-344.

Garcia-Bengochea, J., Lovell, C.W. and Altschaeffl, A.G. (1979), "Pore distribution and permeability of silty clays," *J. Geotech. Engrg. Div.*, ASCE, **105**(7), 839-856.

Gilham, R. W., Robin, M. J. L., and Dytynyshyn, D. J. (1984), "Diffusion of non-reactive and reactive solutes through fine grained barrier material," *Can. Geotech. J.*, **21**, pp. 541-550.

Goodall, D.C. and Quigley (1977), "Pollutant Migration from Two Sanitary Landfill Sites Near Sarina, Ontario", Can. Geotech. J., **14**(27), 223-236.

Greenberg, J.A., Mitchell, J.K. and Witherspoon, P.A. (1973), "Coupled salt and water flows in a groundwater basin," *J. Geophys. Res.*, **78**(27), 6341-6353.

Kozeny, J. (1927), "Über kapillar leitung des wassers im boden," Akad. Wiss. Wiener, Abt. **IIa**, 136, 271-306.

Lambe, T.W. (1958a), "Compacted clay: engineering behavior," *J. of the Soil Mech. and Found. Div.*, ASCE, Paper 1655, May, 1958.

Lambe, T.W. (1958b), "Compacted clay; structure," *J. of the Soil Mech. and Found. Div.*, ASCE, Paper 1654.

Mesri, G. and Olson, R.E. (1971), "Mechanisms controlling the permeability of clays," *Clays and Clay Minerals*, **19**, Pergamon Press, Great Britain, 151-158.

Mitchell, J. K., Hooper, D. R., and Campanella, R. G. (1965), "Permeability of compacted clay," *J. Soil Mech. and Foundations Div.*, ASCE, **92**(7), pp. 41-65.

Mitchell, J. K., and Madisen, F. T. (1987), "Chemical effect on clay hydraulic conductivity," *Proc. ASCE Spec. Conf. Geotech. Aspects of Waste Disposal*, Ann Arbor, pp. 87-116.

Ogata, A. and Banks, R. B. (1961), "A solution of the differential equation of longitudinal dispersion in porous media," U.S.G.S. Prof. Paper 411-A, 7 pp.

Parker, J.C. and Van Genuchten, M. Th. (1984), "Determining transport parameters from laboratory and field tracer experiments," *Virginia Agr. Exper. Stn.*, Bulletin 84-3.

Quigley, R. M., Fernandez, F., and Rowe, R. K. (1988), "Clayey barrier assessment for impoundment of domestic waste leachate (southern Ontario) including clay--leachate compatibility by hydraulic conductivity testing," *Can. Geotech. J.*, **25**, pp. 574-581.

Reades, D. W., Poland, R. J., Kelly, G., and King, S. (1987), disc. (of "Hydraulic conductivity of two prototype clay liners," *J. Geotech. Engrg.*, **111**(8), pp. 957-970), *J. Geotech. Engrg.*, **113**(7), pp. 809-813.

Robinson, R. A. and Stokes, R. H. (1959), *Electrolyte Solutions*, 2nd ed., Butterworth's Scientific Publications, London, 559 pp.

Rowe, R. K. (1987), "Pollutant transport through barriers," *Proc. ASCE Spec. Conf. Geotech. Aspects of Waste Disposal*, Ann Arbor, pp. 159-181.

Seed, H.B. and Chan C.K. (1959), "Structure and strength characteristics of compacted clays," ASCE, *J. of the Soil Mech. and Foundation Engrg. Div.*, **85**(5), Paper 2216.

Shakelford, C. D. (1989), "Diffusion of contaminants through waste contaminant barriers," *Trans. Res. Rec.*, **1219**, pp. 169-182.

Shebl, M.A. (1990), "Effect of compaction technique on the diffusion characteristics in clay liners," M.S. Civ. Engrg. thesis, Wash. St. Univ., Pullman, WA, 83 pp.

Hydrogeology, Waste Disposal, Science and Politics
Proceedings 30th Symposium
Engineering Geology and Geotechnical Engineering, 1994

THE EFFECT OF FREEZE-THAW CYCLES ON THE HYDRAULIC CONDUCTIVITY OF COMPACTED CLAY

David Waite
Bingham Environmental, Salt Lake City, Utah
Loren Anderson, Joseph Caliendo, and Michael McFarland
Department of Civil and Environmental Engineering,
Utah State University, Logan, Utah

ABSTRACT: A study was conducted to investigate the detrimental effects of freeze-thaw on the hydraulic conductivity of compacted clay. The purpose of this study was to determine the effect that molding water content has on the hydraulic conductivity of a compacted clay soil that is subjected to freeze-thaw cycles, and to determine the relationship between the number of freeze-thaw cycles and the hydraulic conductivity of the compacted clay soil. Clay soils compacted and frozen wet of optimum experienced an increase in hydraulic conductivity of approximately 140 fold. The hydraulic conductivity of clay compacted dry of optimum increased ten fold. These results are consistent with recent research which suggests that clay compacted wet of optimum experiences large increases in hydraulic conductivity while the hydraulic conductivity of clay compacted dry of optimum increases to a lesser extent.

INTRODUCTION

Solid and hazardous waste containment is a major environmental problem that only promises to escalate. In light of this dilemma, long-term integrity of the liners and covers that contain these wastes is of paramount importance to Engineers. Landfill covers are expected to isolate municipal and hazardous waste from the surrounding environment by promoting runoff and minimizing infiltration of surface water into the waste materials (Landreth, 1990). Landfill covers are commonly constructed of low-permeability compacted clay which is susceptible to many long-term problems such as; effects of freeze-thaw, differential settlement, and desiccation. One of the primary reasons for landfill cover failure in northern climates is cracking of the cover due to freeze-thaw (Miller, 1992). If hydraulic conductivity increases significantly the cover will not perform the intended function. Review of current literature shows that the hydraulic conductivity of fine-grained soils subjected to freeze-thaw increases dramatically (Chamberlain, 1990) (Kim, 1992) (Zimmie, 1992). Thus an understanding of the effects that freeze-thaw has on hydraulic conductivity is crucial in the design of waste containment systems.

Taber (1930) was one of the first to observe the increase in hydraulic conductivity of clay due to freeze-thaw. Subsequent researchers have observed an increase of 2 to 300 fold in the hydraulic conductivity of clay that has been exposed to freeze-thaw (Chamberlain, 1990), (Kim, 1992), (Zimmie, 1992). Soil conditions that promote or negate the detrimental effects of freeze-thaw have not been precisely identified or quantified. But it is clear that water content and

number of freeze-thaw cycles that the clay is exposed to, influences the hydraulic conductivity of compacted clay.

A study was conducted to investigate the detrimental effects of freeze-thaw on the hydraulic conductivity of compacted clay. The purpose of this study was to:

- determine the effect that molding water content has on the hydraulic conductivity of a compacted clay soil that is subjected to freeze-thaw cycles
- determine the relationship between the number of freeze-thaw cycles and the hydraulic conductivity of the compacted clay soil

Compacted clay samples were frozen and thawed at various water contents and varying numbers of cycles. Falling head permeability tests were performed on a set of clay samples prior to freezing, then on other sets of samples that had been subjected to freeze-thaw cycles. Water content and the number of freeze-thaw cycles were varied to ascertain the importance of these factors. All other parameters were held constant.

Because of the small size of the clay samples used in this test, predicting field hydraulic conductivities from this data would be inappropriate. However, the *relative* increase in hydraulic conductivity with respect to water content and number of freeze-thaw cycles is important. This will help identify the factors that influence this phenomenon and may lead to design and construction techniques that will help mitigate the effects of freeze-thaw. Mitchell (1990), states that clay liners/covers should always be protected from freezing. With frost penetration reaching a depth of 6 feet in northern climates, the economic ramifications of burying a compacted clay cover under this depth of soil can be significant (Kim, 1992). Factors that influence the increase in hydraulic conductivity, and solutions that are economically feasible, must be identified.

PREVIOUS RESEARCH

General

Chamberlain (1990) states that all engineering properties of soils containing a significant amount of clay particles are affected by the process of freeze-thaw: structure, strength, compressibility, and hydraulic conductivity are all influenced. Taber (1930) was one of the first to recognize there was a correlation between freeze-thaw cycles and a corresponding increase in the hydraulic conductivity of clay. This increase in hydraulic conductivity has been attributed to macrofractures that develop in the soil structure, which then function as conduits for liquid to readily pass through the soil matrix (Chamberlain, 1990). A drawing of the macrofracture pattern is shown in Figure 1.

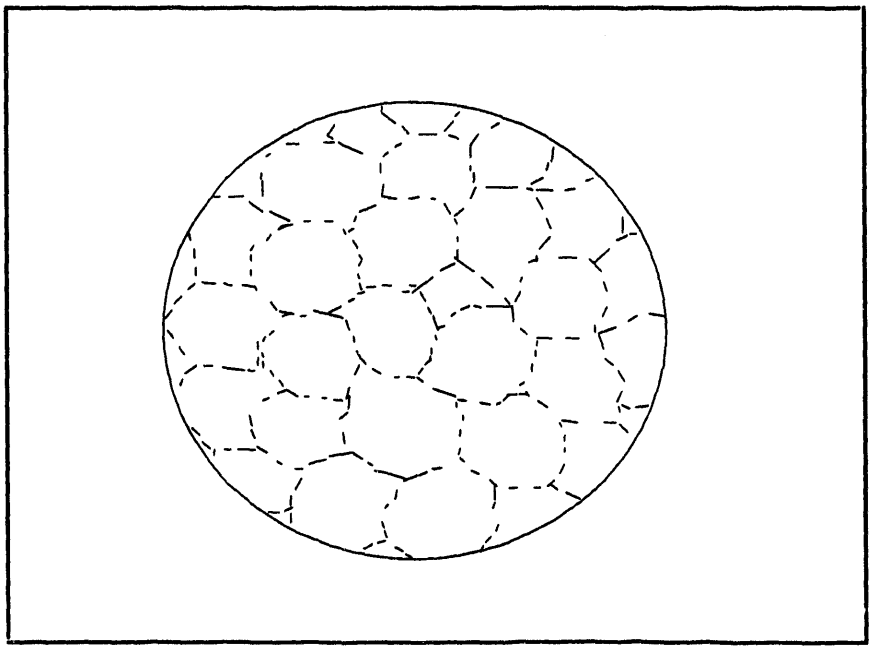


Figure 1. Sketch of Crack Pattern Resulting From Freeze/Thaw (After Kim, 1992)

While the hydraulic conductivity of the material bounded by macrofractures may be relatively low, secondary features can increase the actual hydraulic conductivity of the clay by several orders of magnitude. This can be equated to fractured rock in which the material of the matrix is relatively impermeable, but the apparent hydraulic conductivity is relatively high due to these fractures. These cracks are thought to be formed because of high soil suctions that develop in the freezing zone (Trautwein, 1990). Chamberlain (1990) reports that this suction causes a large increase in the effective stress directly below the freezing front which, in fine-grained soils, causes shrinkage of soil structure and the formation of cracks.

Factors That Affect The Tendency of Clay Subjected To Freeze-Thaw To Increase In Hydraulic Conductivity

Molding water content

Molding water content is known to significantly influence the hydraulic conductivity of unfrozen compacted clay. Daniel (1990) reports that acceptable molding water content for liners and covers varies with the soil type, but is typically zero to four points wet of optimum. A graph of hydraulic conductivity and dry density versus molding water content for a typical clay soil is shown in Figure 2. Optimum water content is 20% for the clay soil.

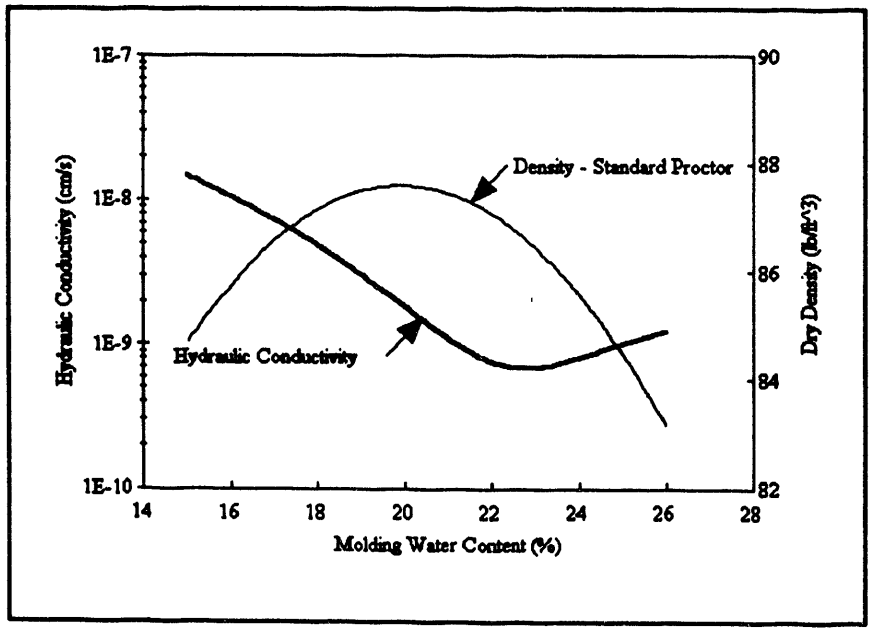


Figure 2. Variation of Hydraulic Conductivity And Dry Density With Molding Water Content

While it is well known what the effect of molding water content on the hydraulic conductivity of unfrozen compacted clay is, how molding water content effects the hydraulic conductivity of clay that has been exposed to freeze-thaw is inconclusive. Zimmie (1992) reports that there is no significant difference in hydraulic conductivity increase, due to freeze-thaw, between clay samples compacted dry of optimum and wet of optimum clay samples. Chamberlain (1990) studied four clays that were frozen after being compacted at typical landfill cover molding water content and compactive effort. The increase in hydraulic conductivity, after freeze-thaw, ranged from a ratio of 35 to 300. Kim (1992) tested clay samples at varying moisture contents and determined that wet of optimum specimens realize an increase in hydraulic conductivity of 70 to 300 fold, while the hydraulic conductivity of dry of optimum samples increased in hydraulic conductivity by a factor of 2 to 6. Kim concluded that molding water content was the single most important variable that affected the tendency of compacted clay to undergo an increase in hydraulic conductivity when subjected to freeze-thaw. Kim's data is shown in Figure 3; optimum water content is 15% and the clay was compacted at 100% of standard proctor.

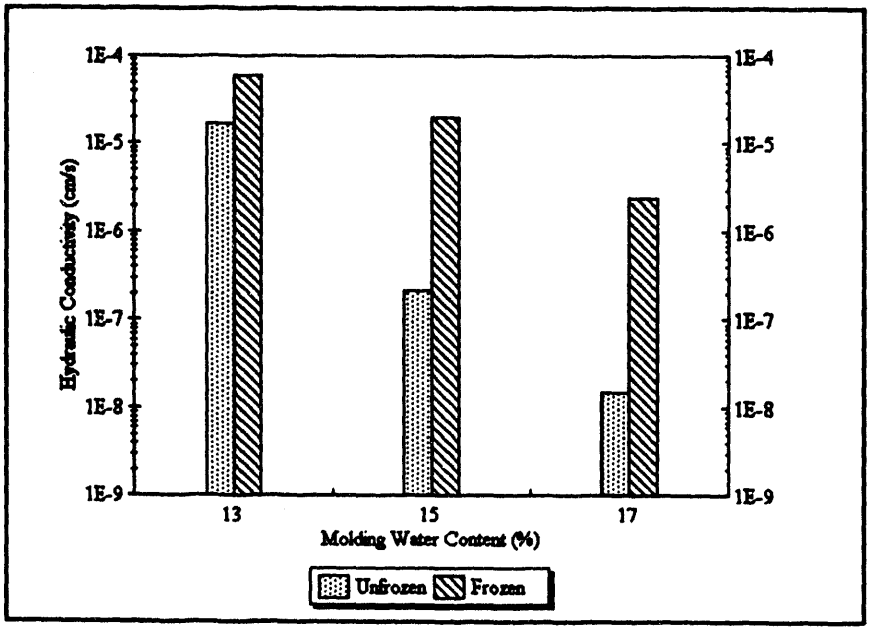


Figure 3. Effect of Molding Water Content On The Hydraulic Conductivity of Compacted Clay Subjected To Freeze-Thaw (After Kim, 1992)

As demonstrated in Figure 3, Kim's results indicate that the hydraulic conductivity of clay compacted at a molding water content optimum or wet of optimum increases dramatically as a result of exposure to freeze-thaw.

Number of freeze-thaw cycles

The hydraulic conductivity of compacted clay appears to rise with an increasing number of freeze-thaw cycles, with the largest increases corresponding to the first few cycles. Zimmie (1992) reports that the hydraulic conductivity of clay rapidly increases during the first few freeze-thaw cycles and after five cycles appears to taper off. Chamberlain (1990) tested four compacted soils and observed that hydraulic conductivity rapidly increased with the first few cycles and started to taper off after eight to ten cycles. Chamberlains data is shown below in Figure 4.

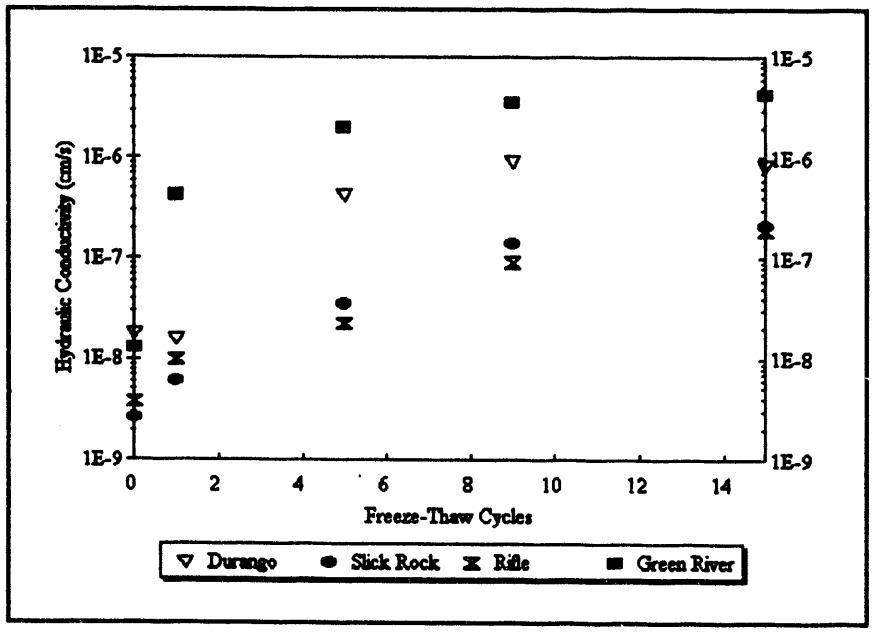


Figure 4. Hydraulic Conductivity Increase As A Function of The Number of Freeze-Thaw Cycles (After Chamberlain, 1990)

It is believed that the first few cycles start fracturing the soil and hydraulic conductivity increases quite rapidly. After the clay is fissured significantly, further fracturing is less likely as water can freely move through the soil and large suction forces do not readily develop.

Other Factors

Macrofractures that develop because of freeze-thaw are closed under large effective stresses. Zimmie (1992) reports that the change in hydraulic conductivity due to freeze-thaw is a function of effective stress. At a low effective stress, typical of a landfill cover, the maximum change in hydraulic conductivity was about two orders of magnitude. At higher effective stresses, representative of a liner, the increase was approximately one order of magnitude. Boynton and Daniel (1985) found similar results and concluded that confining stress greater than about 10 psi closed cracks and moderated the detrimental effects of freeze-thaw.

Density that is typically specified for covers/liners is 95% of the maximum dry density obtained from a standard proctor test, or 90% of modified proctor (Daniel, 1990). For practical compactive effort, compaction has been shown to be insignificant in influencing the change in hydraulic conductivity due to freeze-thaw. Kim (1992) investigated how varying levels of compactive effort effected the increase in hydraulic conductivity due to freeze-thaw and determined that compactive effort had no consistent influence on the effects of freeze-thaw. Kim concluded that compactive effort was a far less significant variable than water content.

Zimmie (1992) demonstrated that allowing the clay samples access to free water during freeze-thaw does not significantly effect the increase in hydraulic conductivity due to freeze-thaw.

One dimensional freezing duplicates field conditions as freezing temperatures advance downward from the top of the cover. Three dimensional freezing is more easily accomplished

in the lab though, and for this reason there has been testing to determine if there is a significant difference between one dimensional and three dimensional freeze-thaw effects in hydraulic conductivity. Zimmie (1990) investigated this factor and found the same rate of increase in hydraulic conductivity for fine-grained soil exposed to one dimensional freezing and three dimensional freezing.

MATERIALS AND METHODS

Approach

Where possible, conditions typical of a landfill cover were used while compacting, freezing, and performing falling head permeability tests on the clay samples. These conditions include;

- an overburden that is comparable to the overburden that a landfill cover would be subjected to
- no access to free water during freeze-thaw as the cover typically will not be saturated
- densities and compaction methods that would be typical of that which would be used in the construction of a landfill cover

The variables in the freeze-thaw tests were molding water content, and the number of freeze-thaw cycles. The molding water content of the samples in the test was $\pm$ 3 percent of optimum, which resulted in molding water contents of 23.5% and 29.5%. The clay samples were frozen in groups of 0, 1, 3, 5, and 10 cycles. A minimum of three tests were performed for each combination of molding water content and number of freeze-thaw cycles. The clay samples were compacted and frozen in consolidometers which were also used as the permeameters for the falling head permeability test.

Soil Properties and Preparation

The soil used in this test was acquired from the Utah State University Drainage Farm and is Lake Bonneville lacustrine deposits. The soil is a inorganic silt-highly plastic clay and is classified a MH-CH, according to the Unified Soil Classification System. Soil properties are provided in Table 1.

TABLE 1
SOIL PROPERTIES

Plastic Limit	30%
Liquid Limit	51%
Plasticity Index	21%
Specific Gravity	2.63
Optimum Water Content	26.5%
Maximum Dry Density	93.5 lb/ft^3

Proctor tests were performed to determine the optimum moisture content of the soil used in the testing. Results from the standard proctor tests are shown in Figure 5.

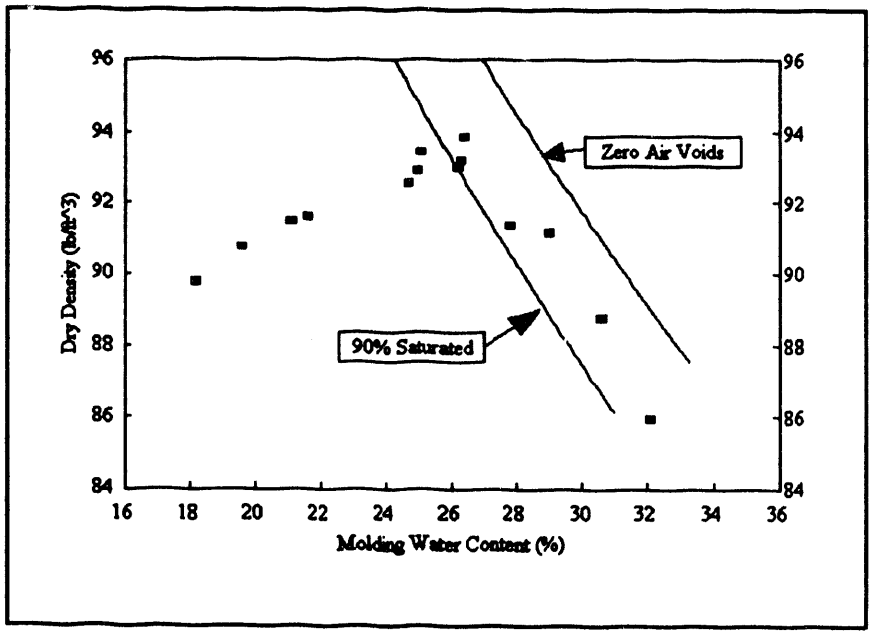


Figure 5. Results From Standard Proctor Tests

In preparation for testing, the soil was brought into the lab and allowed to air-dry for two days. After the soil was air-dried, the clods in the soil were broken down and the soil was passed through a #4 sieve. Soil passing the #4 sieve was thoroughly mixed and quartered to get smaller samples that were representative of the soil. The air-dried clay was slowly mixed with water to achieve the desired water content. The sample was then allowed to stabilize for 24 hours, enough time for all the soil particles to hydrate.

After the soil moisture had stabilized it was compacted into the consolidometer. The clay was compacted in three lifts, with 3 blows per layer. The hammer constructed for compaction of the samples had a weight of 0.6178 lbs, and a drop of six inches. The volume of the clay

sample was 0.00284 ft^3. This procedure gave a compactive effort of 12,400 ft-lb/ft^3 which is equivalent to the compactive effort of a standard proctor. Care was taken to compact close to the sides of the consolidometer to minimize the potential for piping. Clods that had formed due to the addition of water, and were larger then the openings in the # 4 sieve, were broken down before compaction. Compacted clay properties are shown in Table 2.

TABLE 2
PROPERTIES OF COMPACTED SOIL

PROPERTY	MOLDING WATER CONTENT 23.5%	26.5%	29.5%
Dry Density (pcf)	92.5	93.5	89.9
Moist Density (pcf)	114.2	118.3	116.4
Void Ratio	0.77	0.76	0.83
Percent Saturation	79.9	92.3	94.0

Freeze-Thaw Procedures

Conditions

The goal of laboratory freeze-thaw testing was to simulate field conditions. Of course laboratory conditions are, at best, only an approximation of actual field conditions. Many of the conditions of freeze-thaw that an actual cover would be subjected to are reproducible in the laboratory though.

An overburden stress of 2.4 psi was placed on the compacted clay and remained there during freeze-thaw. This was believed to best simulate field conditions where the clay would be subjected to a relatively constant overburden. Municipal waste landfill covers are often subjected to an overburden stress that ranges from 2 to 3 psi. This is based on a topsoil cover depth of approximately two feet and a one foot sand drainage layer.

While the landfill cover would generally be frozen under one dimensional conditions, from the top down, studies have shown that freezing samples in a three dimensional manner produces the same results as freezing one dimensional (Zimmie, 1992). For this reason the clay samples were frozen three-dimensionally as freezing all-around is more readily performed in the laboratory.

The consolidometers were wrapped in aluminum foil to prevent any drying during freeze-thaw. Samples in this test were frozen at molding water content with no access to water.

Procedure

The clay samples were frozen in a large chest freezer, then the freezer compressor was turned off and the samples were thawed. After the samples were frozen, the compressor was shut off and a timer turned on heat lamps that had been placed in the freezer. The freezer used

in the testing advanced from room temperature to -25°C in approximately 1½ hours, and then the samples were subjected to -25°C for 1½ hours to insure the sample was totally frozen. After the freezer ran for three hours the compressor was turned off and the sun lamps were turned on for one hour, which brought the temperature up to approximately 38°C. The samples thawed at this temperature in approximately two hours. The clay specimens were held at 38°C for 2½ hours to assure complete thawing of the samples. To run a complete freeze-thaw cycle took approximately six hours as outlined in Figure 6.

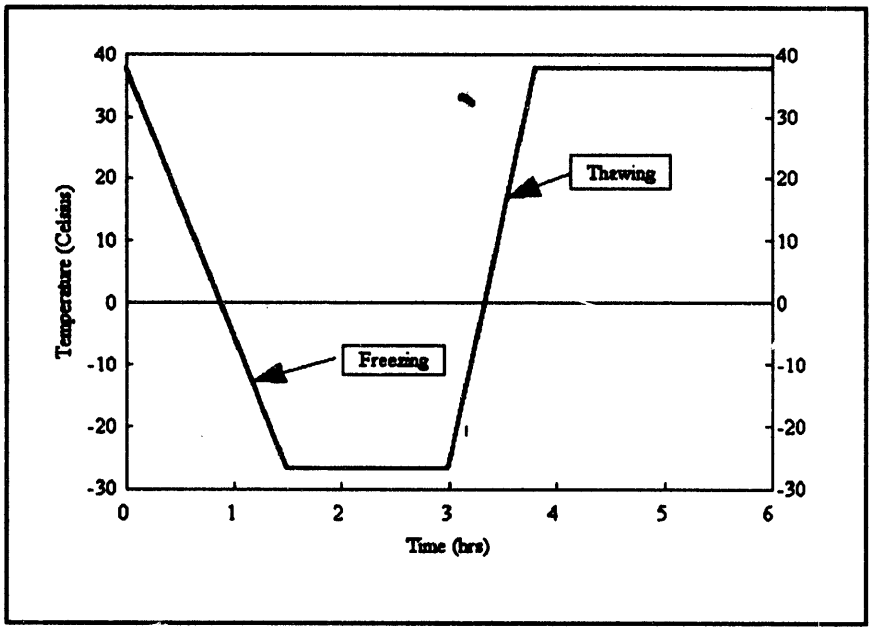


Figure 6. Graph Depicting Temp. Versus Time For One Freeze-Thaw Cycle

Measurement of Hydraulic Conductivity

The saturated hydraulic conductivity of the compacted clay specimens was measured utilizing the falling head permeability test. Falling head permeability tests are commonly used to measure the vertical hydraulic conductivity of fine-grained soils.

After the clay samples were frozen the correct number of cycles, the sample was brought to room temperature. The soil was then saturated by filling the top of the consolidometer with water and subjecting the bottom of the consolidometer, through the petcock, to a vacuum for approximately 15 minutes. Having the sample saturated before the start of the test shortened the length of time that it took for the hydraulic conductivity readings to reach steady state conditions. Porous stones were placed within the consolidimeter on the top and bottom of the clay sample while the falling head permeability test was being performed.

After saturation the clay was subjected to an overburden stress utilizing the consolidation frame. The overburden pressure placed on the samples was 2.4 psi. Kim (1992) placed an overburden of five psi on the clay while performing the falling head permeability test, while Zimmie (1992) placed 10 psi on the samples.

The burette was then filled with deaired water to the initial desired height. The burette was filled to 30 inches above the top of the sample, giving a initial gradient of 30. Steady-state

conditions were usually reached after the gradient had fallen to around 20. For the dry of optimum tests gradients this large would generally not be needed to perform the test in a reasonable length of time, as the clay would transmit water readily. Similar gradients were used throughout the test though to insure that all the conditions of the test were as similar as possible for all samples regardless of molding water content and number of freeze-thaw cycles. A minimum of three readings were taken past the point were the falling head permeability test had reached steady state conditions.

TEST RESULTS

Summary

Falling head permeability tests were performed on 7 unfrozen compacted clay samples and 26 frozen samples that had been subjected to freeze-thaw cycles. The hydraulic conductivity of wet of optimum clay increased dramatically with smaller increases in hydraulic conductivity for the clay frozen 3% dry of optimum.

Wet of Optimum

As seen in Figure 7, the increase in hydraulic conductivity of clay compacted wet of optimum was approximately 140 times. The hydraulic conductivity of the clay prior to freezing was 1.6E-8 cm/s while the hydraulic conductivity of clay subjected to 10 freeze-thaw cycles was 2.2E-6 cm/s. Polygonal fracturing, as seen by Kim (1992), was not seen. Some random fracturing was observed, but the amount of visible cracks was minimal. Some of the samples experienced piping, however, these readings were not used to calculate the average hydraulic conductivity.

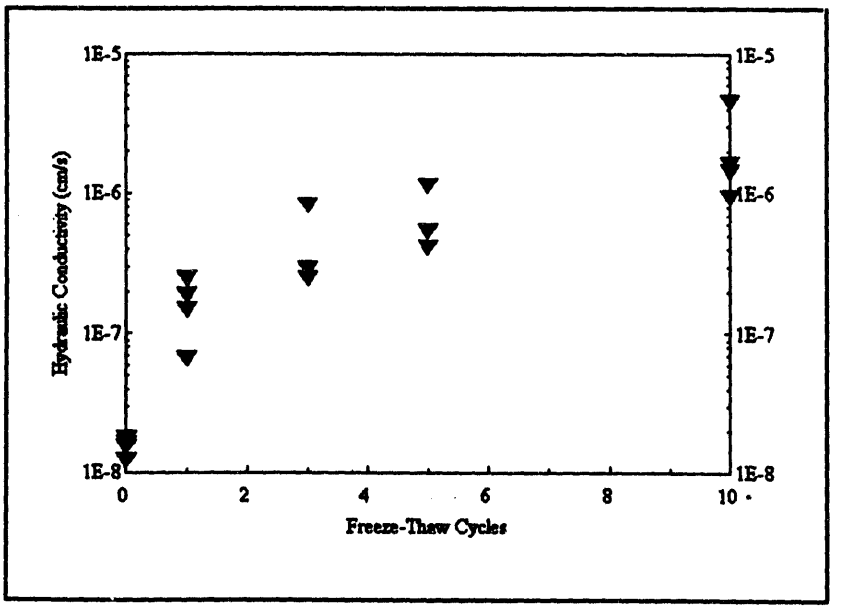


Figure 7. Results From Falling Head Permeability Tests For Clay Compacted At 29.5% Water Content.

Dry of Optimum

The hydraulic conductivity of dry of optimum clay increased by a ratio of 11 after 10 freeze-thaw cycles as shown in Figure 8.

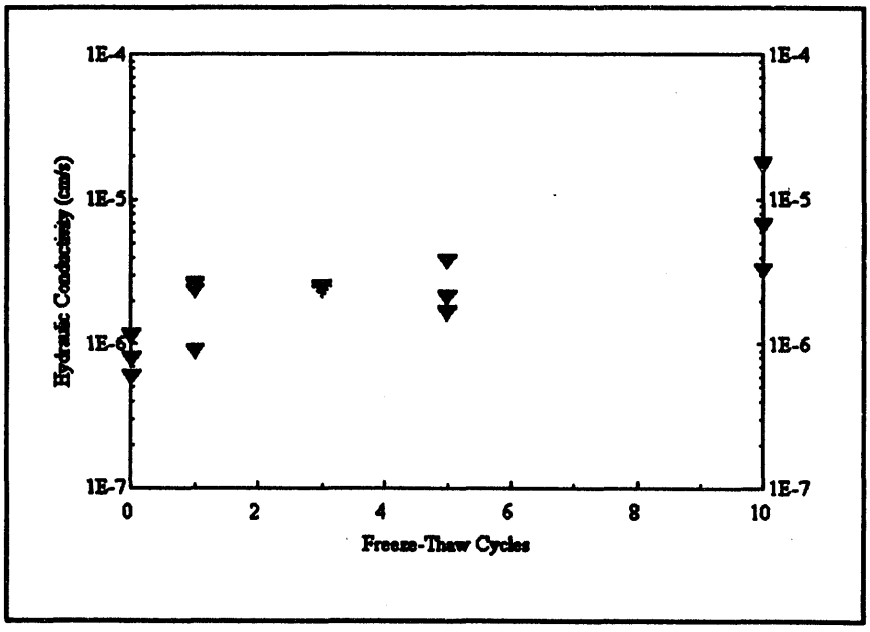


Figure 8. Results From Falling Head Permeability Tests For Clay Compacted At 23.5% Water Content.

The hydraulic conductivity of the clay prior to freezing was 8.3E-7 cm/s and the hydraulic conductivity of clay subjected to 10 freeze-thaw cycles was 9.1E-6 cm/s. Polygonal fracturing, as with the wet of optimum samples, was not seen. Some random fracturing was observed, but the amount of visible cracks was minimal. Some of the samples experienced piping, however, these readings were not used to calculate the average hydraulic conductivity. A minimum of three samples, with no testing anomalies, was recorded for each freeze-thaw cycle.

Number of Cycles

As seen in Figure 9, increases in hydraulic conductivity tapered off with increasing numbers of freeze-thaw cycles. However, the hydraulic conductivity was still increasing after 10 freeze-thaw cycles.

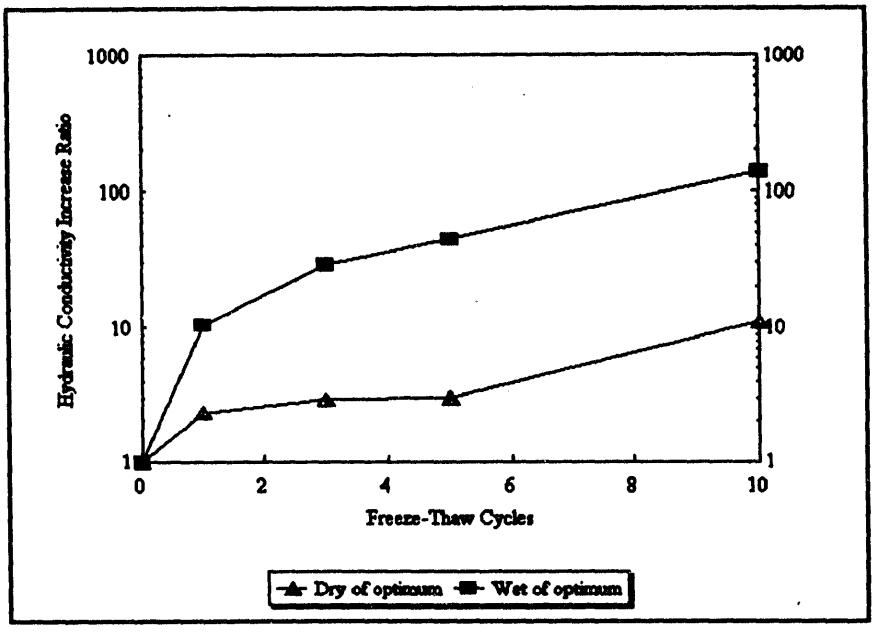


Figure 9. Ratio of Hydraulic Conductivity Increase

ANALYSIS/CONCLUSIONS

Molding Water Content

Hydraulic conductivity of clay compacted wet of optimum increased greatly as a result of freeze-thaw. Clay samples compacted dry of optimum also experienced an increase in hydraulic conductivity but to a lesser extent. Possible reasons for this difference are:

- Wet of optimum samples were frozen at 94% of saturation while dry of optimum samples were frozen at 80% of saturation.

- The initial hydraulic conductivity of wet of optimum clay was much lower then dry of opt clay which could lead to higher suction forces in front of the freezing front in wet of optimum clay, due to the diminished freedom of movement of the free water.

Wet of optimum samples in this experiment experienced an increase in hydraulic conductivity of approximately a factor of 140, after 10 cycles. This leads to the conclusion that clay compacted wet of optimum, and exposed to a least 10 freeze-thaw cycles, will increase in hydraulic conductivity by a factor of roughly two orders of magnitude. Results from this test were comparable to the findings of other researchers. Kim's (1992) tests suggested an increase in hydraulic conductivity in wet of optimum clay of approximately a factor of 110 after 5 freeze-thaw cycles. Chamberlain (1990) tested four clays at typical landfill design molding water contents and observed that the ratio of increase in hydraulic conductivity, after 9 cycles, ranged from 24 to 269 with an average of 100.

Clay compacted dry of optimum did not increase in hydraulic conductivity as much as clay

compacted wet of optimum. Clay compacted 3% dry of optimum in this experiment increased in hydraulic conductivity by a factor of 11, after ten freeze-thaw cycles. The increase in hydraulic conductivity after five cycles was threefold, which is similar to the results of Kim (1992). Kim tested clay compacted at various moisture contents and determined that clay compacted dry of optimum experienced an increase in hydraulic conductivity, after 5 freeze-thaw cycles, of a factor of four.

Number of freeze-thaw cycles

Hydraulic conductivity increases dramatically with the first two to three freeze-thaw cycles, with a rapid tapering off with increasing numbers of freeze-thaw cycles. The possible reasons for this are:

- Conduits are opened in the soil matrix allowing for the permeant to flow freely. After several freeze-thaw cycles the soil would be so fractured that large suction forces could not develop and there would be no significant additional fracturing.

- Voids develop in the soil which act as pockets for the release of the suction forces that develop.

The tapering off of hydraulic conductivity increases is well documented in previous research. The results from this investigation, which demonstrate the decrease in the effects of freeze-thaw with an increase in the number of cycles, agree well with results from Chamberlain (1990), Kim (1992), and Zimmie (1992).

Conclusions

Molding water content and the number of freeze-thaw cycles that a fine-grained soil is exposed to, significantly affect the hydraulic conductivity of the soil used in this test. Results from this investigation clearly demonstrate the sensitivity of compacted clay to these factors.

The hydraulic conductivity of compacted clay increased when exposed to freeze-thaw. Clay compacted wet of optimum was effected significantly by freeze-thaw and experienced large increases in hydraulic conductivity. Clay compacted dry of optimum experienced increases in hydraulic conductivity, but to a lesser extent. The largest increases in hydraulic conductivity were seen in the first few freeze-thaw cycles that the soil was exposed to. A summary of the results is outlined below:

- Molding water content affects the tendency of a fine-grained soil to experience increases in hydraulic conductivity, due to freeze-thaw.

- Landfill covers typically must be compacted at a molding water content optimum or wet of optimum to achieve the required hydraulic conductivity. It appears that clays compacted at these water contents are most susceptible to freeze-thaw

- Molding water content is the single most important variable influencing the effects of freeze-thaw on the hydraulic conductivity of compacted clay.

- The hydraulic conductivity of a fine-grained soil increases with the number of freeze-thaw cycles. The increase in hydraulic conductivity tapers of rapidly with an increase in the number of cycles.

- Landfill covers must be protected from the effects of freeze-thaw if the low hydraulic conductivity of the cover is to be maintained.

Results of this test support the conclusions of previous research which suggests that landfill covers are susceptible to the effects of freeze-thaw. Once the factors that effect the hydraulic conductivity increase due to freeze-thaw are identified, solutions to the problem can be identified.

REFERENCES

Boynton, S. S., and Daniel, D. E. (1985). "*Hydraulic Conductivity Tests on Compacted Clay*," J. Geotech. Engrg., ASCE, 111(4), 465-478

Chamberlain, E., Iskander, I., and Hunsicker S. E. (1990). "*Effect of Freeze-Thaw Cycles On The Permeability And Macrostructure of Soils*," Proc., Int. Symp. on Frozen Soil Impacts on Agric., Range, and Forest Lands, CRREL Special Report 90-1, U.S. Army Corps of Engineers, Cold Regions Research & Engineering Laboratory, Hanover, N.H., 145-155.

Daniel, D. E., and Benson, C. H. (1990). "*Water Content-Density Criteria For Compacted Soil Liners*," J. Geotech. Engrg., ASCE, 116(12), 1811-1830

Day, S. R., and Daniel D. E. (1985). "*Hydraulic Conductivity of Two Prototype Clay Liners*," J. Geotech. Engrg., ASCE, 111(8), 957-970

Kim, Woon-Hyung, and Daniel D. E. (1992). "*Effects of Freezing On Hydraulic Conductivity of Compacted Clay*," J. Geotech. Engrg., ASCE, 118(7), 1083-1097

Landreth, R. E. (1990). "*Landfill Containment Systems Regulations*," Waste Containment Systems: Construction, Regulation, and Performance, R. Bonaparte (ed.), ASCE Geotech. Spec. Pub. No. 26.

Miller, C. J., and Lee J. Y. (1992). "*Effects of Freeze-Thaw on Clay Cover Liner Performance*," Environmental Geotechnology, Usmen and Acar (ed.), Proceedings of the Mediterranean Conference on Environmental Geotechnology /CSME/Turkey/May 25-27 1992, 205-211

Mitchell, J. K. and Jaber, M. (1990). "*Factors Controlling the Long-Term Properties of Clay Liners*," Waste Containment Systems: Construction, Regulation, and Performance, R. Bonaparte (ed.), ASCE Geotech. Spec. Pub. No. 26.

Taber, S. (1930). "*The Mechanics of Frost Heaving*," J. Geology (38), 303-317

Trautwein, S. J. and Williams, C. E. (1990). "*Performance Evaluation of Earthen Liners*," Waste Containment Systems: Construction, Regulation, and Performance, R. Bonaparte (ed.), ASCE Geotech. Spec. Pub. No. 26.

Zimmie, T. F., LaPlante C. M., and Bronson, D. (1992). "*The Effects of Freezing And Thawing On The Permeability of Compacted Clay Landfill Covers And Liners*," Environmental Geotechnology, Usmen and Acar (ed.), Proceedings of the Mediterranean Conference on Environmental Geotechnology /CSME/Turkey/May 25-27, 1992, 213-217

Zimmie, T. F. and LaPlante, C. M. (1990). "*The Effects of Freeze-Thaw Cycles on the Permeability of a Fine-Grained Soil*," Proc., 22nd Mid-Atlantic Industrial Waste Conf., Drexel Univ., Philadelphia, Pa., 580-593

Hydrogeology, Waste Disposal, Science and Politics
Proceedings 30th Symposium
Engineering Geology and Geotechnical Engineering, 1994

FROM LAB TO FIELD: GEOTECHNICAL PROPERTIES FOR PREDICTING EMBANKMENT SETTLEMENT ON LAKE BONNEVILLE DEPOSITS

Kevin C. Hoagland, Graduate Student
Casan L. Sampaco, Graduate Research & Teaching Assistant
Loren R. Anderson, Department Head & Professor
Joseph A. Caliendo, Assistant Professor
Civil and Environmental Engineering
Utah State University, Logan Utah 84322
Loren Rausher and Edward Keane
Geotechnical Engineers, Utah Department of Transportation
Salt Lake City, Utah 84119

ABSTRACT

The results of a laboratory analysis, to determine geotechnical properties of lacustrine Lake Bonneville deposits, within the I-15 corridor of Salt Lake City, Utah, is presented. Laboratory vertical and horizontal consolidation coefficients are compared with those back-calculated from observed, field settlement data and linear relationships established. The results are used to select vertical and horizontal field coefficients and predict settlement rate of an existing embankment, scheduled for enlargement.

INTRODUCTION

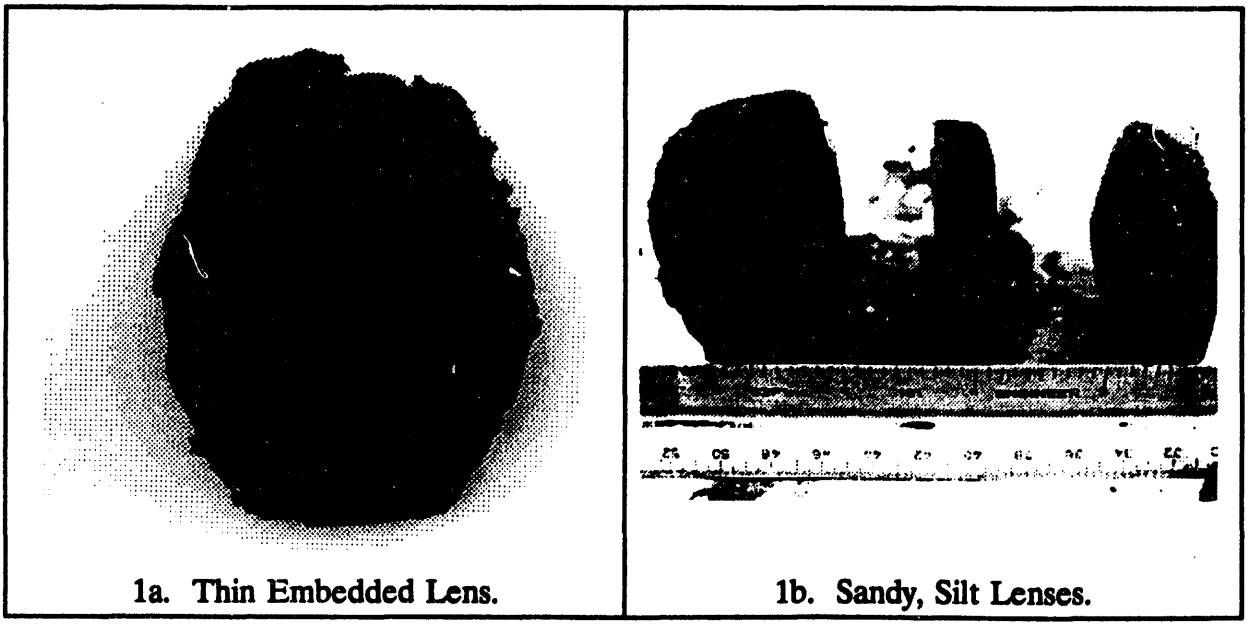
Geotechnical engineering of earth embankments, requires accurately predicting slope and foundation stability, and magnitude and rate of settlement, for proper design and construction scheduling. In the 13th Rankine Lecture, Lambe (1973) referred to the geotechnical engineer, as the "master predictor." He points out, that predictions are often based on insufficient, inaccurate and varying data, due to the complexity of natural deposits, limitations in the theories used to make predictions, and that sound engineering judgement is essential, if predictions are to be useful. He further suggests, the need for simple techniques to make type A predictions, i.e., before the events occur.

The Utah Department of Transportation (UDOT) proposes widening the existing highway embankments, within the I-15 corridor of Salt Lake City, Utah, to accommodate additional travel lanes. Settlement rate predictions are required in order to coordinate embankment construction and paving, to avoid differential settlement in the new surface.

This paper presents the results of a laboratory analysis on five soil samples supplied by UDOT. The samples ranged in depth from twenty-seven to sixty-two feet and are typical of the stratified, lacustrine Lake Bonneville deposits. Consolidation coefficients from one-dimensional consolidation tests, on vertically and horizontally trimmed specimens, are compared with those back-calculated from observed settlement data. Linear relationships were developed between the vertical and horizontal consolidation coefficients, obtained from the laboratory and the field data. The linear equations are used to determine field consolidation coefficients, from those acquired in the laboratory. A settlement prediction is made for an embankment scheduled for enlargement, using one-dimensional theory. The use of vertical drains is considered.

GEOLOGY

The existing embankments, of I-15 through Salt Lake City, Utah, rest on soft, compressible, lacustrine Lake Bonneville deposits. These Pleistocene deposits typically show alternating, light and dark laminae, with intermittent, thin sandy, silt lenses. If continuous over a large enough area, these lenses would shorten the vertical drainage distance and allow excess pore water pressure to dissipate more rapidly. As a result, primary consolidation would be accelerated. Figure 1a shows a typical cross-section of a sample retrieved from twenty-eight feet, containing a thin, embedded, sandy, silt lens. Figure 1b shows sandy, silt lenses with thickness varying between 0.5 and 1.0 inch.



1a. Thin Embedded Lens. 1b. Sandy, Silt Lenses.

Figure 1. Possible Drainage Paths.

LABORATORY ANALYSIS

Geotechnical Properties

The laboratory analysis was conducted on five soil samples supplied by UDOT and varied in depth between twenty-seven and sixty-two feet. The samples were retrieved from borings along I-15, from 1st North to 24th South. The laboratory testing was performed in accordance with, the American Standards for Testing and Materials (ASTM) or, the American Association of State Highway and Transportation Officials (AASHTO) testing standards, as described by Bowles (1992).

Figure 2 shows the variation with depth of the Atterberg Limits, consisting of the Liquid Limit (LL), Plastic Limit (PL) and Plasticity Index (PI). Also shown in Figure 2, is the water content (w), the dry unit weight (γ_d), and percent saturation (S).

The samples had been stored for one year from the time of retrieval until testing. This causes a time dependent increase in disturbance and allows the samples to loose moisture (Olsen, 1986). The low saturation values in Figure 2, reflect this.

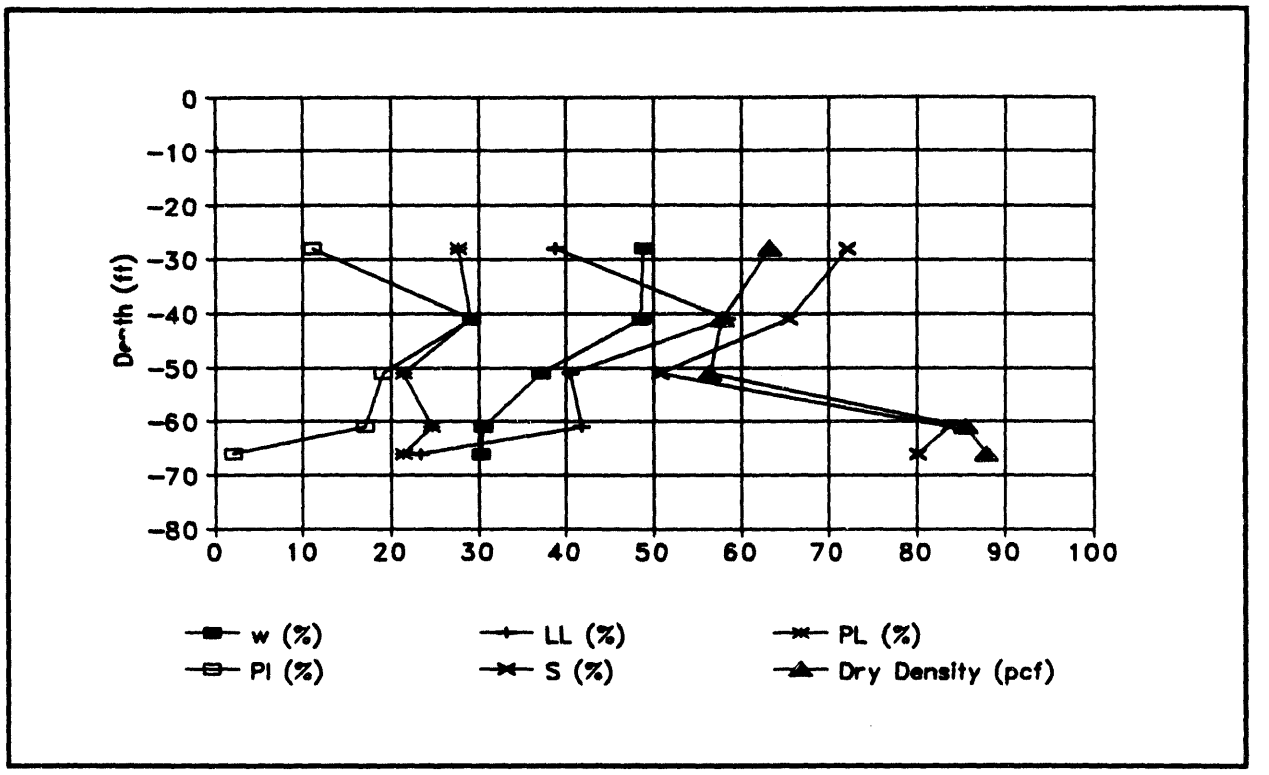
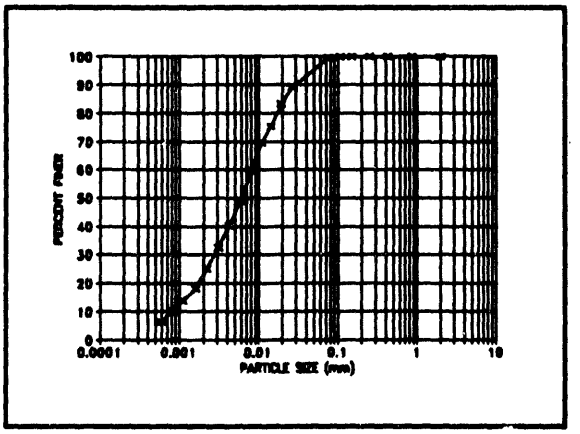
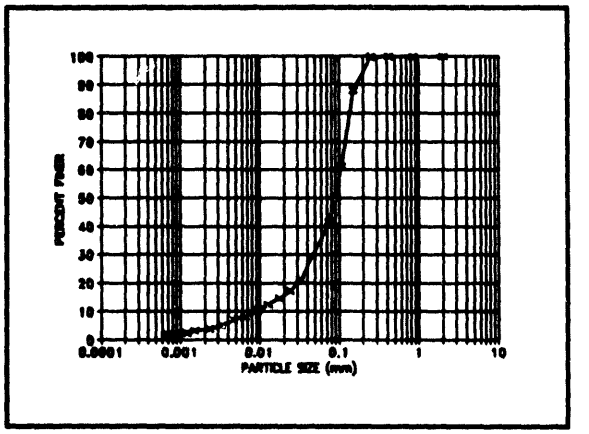


Figure 2. Variation with Depth of Laboratory Geotechnical Properties.

Mechanical and hydrometer particle size analyses were conducted on each of the five samples and the sandy, silt lenses shown in Figure 1b, in accordance with ASTM D 421 and ASTM D 422. Figure 3 shows the particle-size distributions for a typical clay sample and the sandy, silt lenses of Figure 1b.



3a. Typical Clay.



3b. Sandy, Silt Lenses.

Figure 3. Particle-Size Distributions.

Consolidation Parameters

Seven consolidation tests were conducted to determine the laboratory values for the vertical consolidation coefficient ($c_{v\ lab}$), in accordance with ASTM D-2435-90. To determine the laboratory horizontal consolidation coefficients ($c_{h\ lab}$), eight samples were rotated ninety degrees from their in-situ orientation, trimmed into rings and consolidated.

Determining $c_{h\ lab}$ in this manner correctly models the direction of flow but, the application of the load is incorrect and consequently so is the deformation characteristics of the sample (Olsen, 1986). However, good results have been reported by Bergado et al. (1992) and Leminen et al. (1983) using this technique. Rowe (1959) reports the values of $c_{h\ lab}$ are greatly affected by the sample size. He found that with increasing sample thickness, the coefficient also increased.

Taylor's (1948) square root of time fitting method, was chosen over Casagrande's (1938) logarithmic time method, in determining the consolidation coefficients because the square root method consistently produced more usable data.

The value of $c_{v\ lab}$ varied between 0.00132 and 0.07270 square inches per minute, with a mean of 0.01592. The value of $c_{h\ lab}$ varied between 0.00205 and 0.09490 square inches per minute, with a mean of 0.02949. The ratio of $c_{h\ lab}$ to $c_{v\ lab}$ ranged from 1.1 to 4.1, with a mean of 2.0.

Figure 4 shows the initial void ratio (e), the compression ratio (C_c'), the recompression ratio (C_r'), the over-consolidation ratio (OCR) and the ratio, $c_{h\ lab}$ to $c_{v\ lab}$. Also shown in Figure 4, are averaged estimates of the un-drained shear strength (S_u).

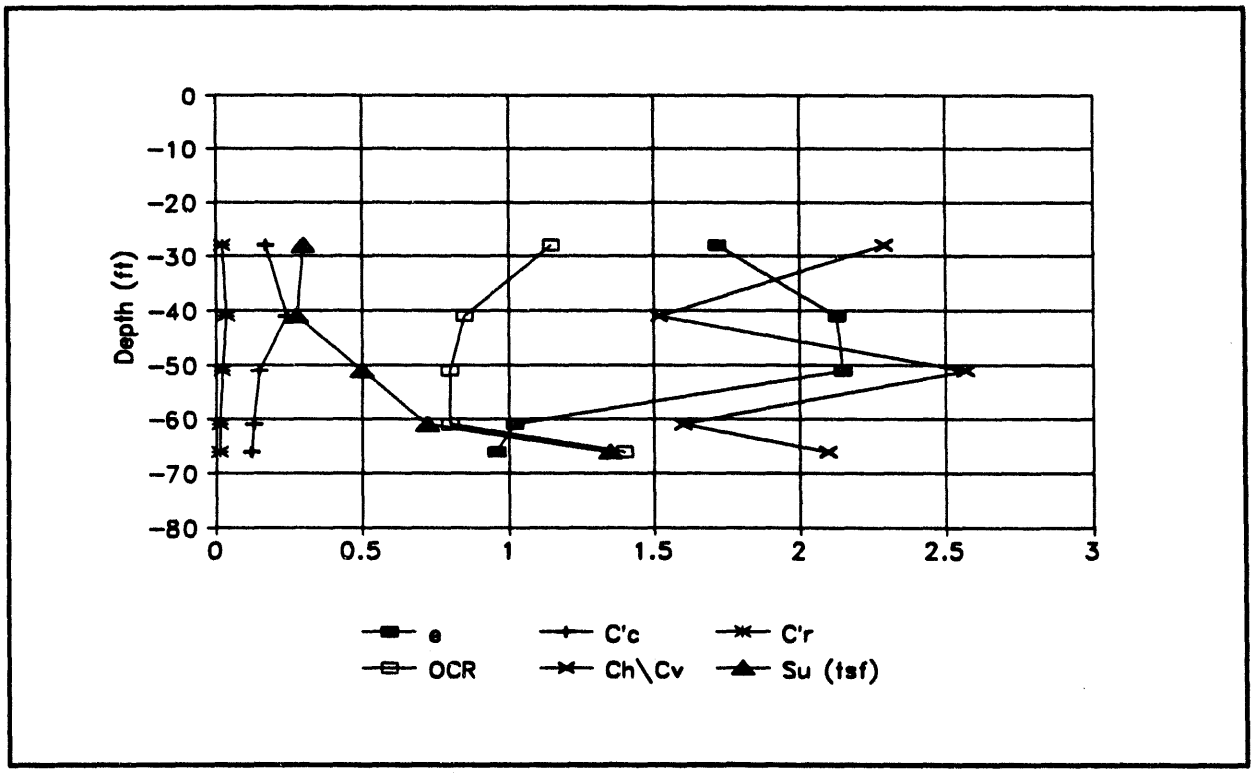


Figure 4. Variation with Depth of Laboratory Consolidation Parameters.

To develop a relationship between the laboratory horizontal and vertical coefficients of consolidation, the values of $c_{h\ lab}$ were plotted against $c_{v\ lab}$, for each identical loading increment. Figure 5 shows the results of this comparison. A linear regression analysis of the data produces Equation 1 where, $c_{v\ lab}$ and $c_{h\ lab}$ are in square inches per minute. The regression yields a value for R^2 equal to 0.81, a standard error of the constant (Y) equal to 0.004 and a standard error of the coefficient (X) equal to 0.133.

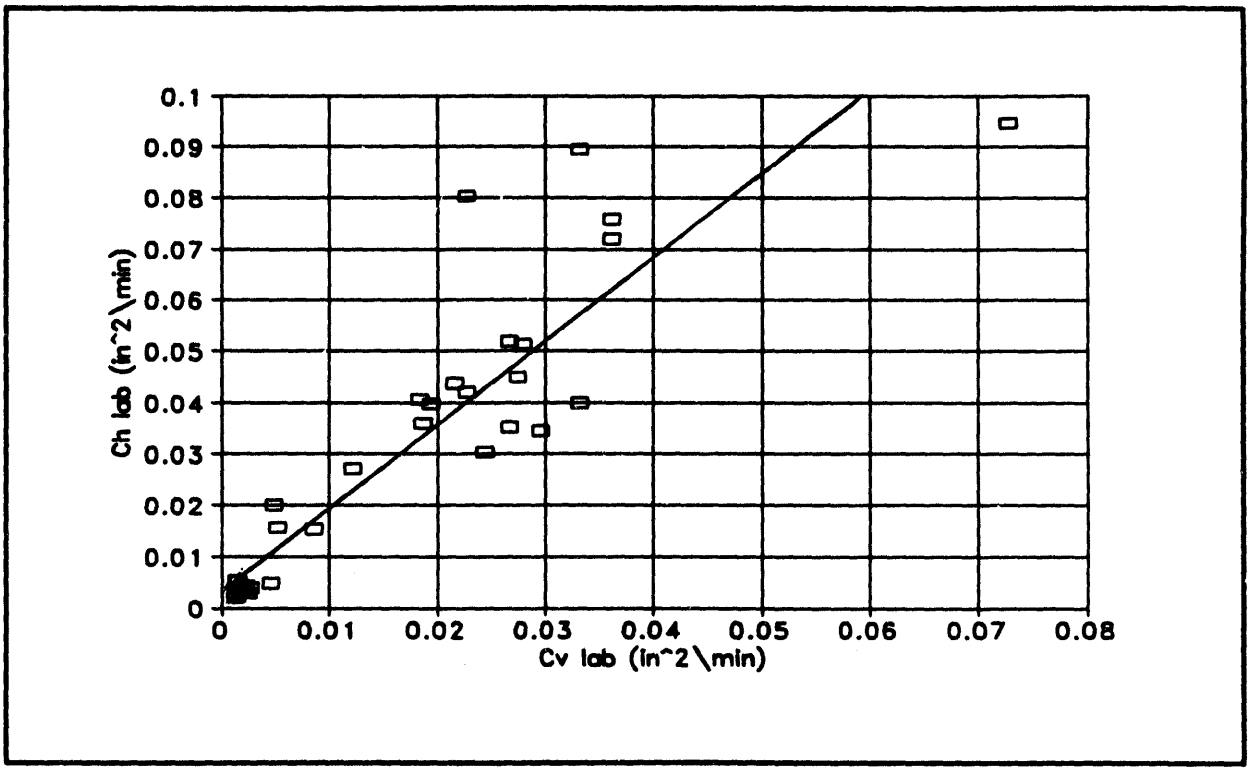


Figure 5. Relationship Between $c_{v\ lab}$ and $c_{h\ lab}$.

$$c_{h_{lab}} = .004 + 1.58(c_{v_{lab}}) \qquad (1)$$

OBSERVED FIELD SETTLEMENT

Embankment Settlement Data from I-15

Observed settlement data of embankments constructed in 1959, from 5th North to 24th South along I-15 was obtained from Su (1966). The embankments were constructed with and without vertical sand drains, in close proximity to each other, presenting an opportunity to back-calculate the coefficients of consolidation for a given site.

Back-Calculating Consolidation Parameters.

The observational method of Asaoka (1978), as described by Magnan et al. (1983) and Holtz et al. (1991), was used to back-calculate values of the coefficients of consolidation, $c_{v\ field}$ and $c_{h\ field}$. The method consists of conveniently dividing the settlement versus time curves into equal time intervals (Δt). The corresponding settlement (s_n) is then determined for each time increment (t_n) and the Cartesian coordinates, (s_n-1, s_n) are plotted. The slope (β) of the straight line formed by the points (s_n-1, s_n) is used in Equation 2, to determine $c_{v\ field}$, from embankments without vertical drains or Equation 3 to determine $c_{h\ field}$, from embankments with vertical drains,

$$c_v = -\frac{4(H_{DP})^2(\ln\beta)}{\pi^2(\Delta t)} \qquad (2)$$

$$c_h = -\frac{(d_e)^2(F(n))(\ln\beta)}{8(\Delta t)} \qquad (3)$$

where, in Equation 2, c_v is the vertical coefficient of consolidation and H_{DP} is the height of the drainage path. In Equation 3, c_h is the horizontal coefficient of consolidation, d_e is the diameter of an equivalent soil cylinder and F(n) is a drain spacing factor.

The intersection of the line with slope β and a line formed at 45°, represents the magnitude of primary consolidation for that loading increment. Equation 2 is based on Terzaghi's (1923) theory for vertical flow and Equation 3 in based on Barron's (1948) theory for horizontal flow. The value of F(n) is shown in Equation 4 (Hansbo, 1979),

$$F(n) = \ln\left(\frac{d_e}{d_w}\right) - \frac{3}{4} \qquad (4)$$

where, d_w is the equivalent diameter of a vertical drain.

Good results have been reported by Bergado et al. (1992) and Magnan et al (1981) using Asaoka's method to back-calculate field consolidation coefficients.

Gilani (1993) back-calculated the average drainage distance, under double-drained conditions, from observed settlement data of embankments in the vicinity and estimates values between 1.5 and 5 feet. A value of 3 feet was selected for back-calculating $c_{v\ field}$ and represents the mean of the values determined by Gilani. A triangular drain spacing pattern was assumed for calculating d_e and is equal to 1.05 times the drain spacing.

The value of $c_{v\ field}$ varied between 0.00110 and 0.01410 square inches per minute, with a mean of 0.00695. Notice the mean $c_{v\ lab}$ is 2.29 times greater than the mean $c_{v\ field}$. The value of $c_{h\ field}$ varied between 0.00594 and 0.29200 square inches per minute, with a mean of 0.05084. The ratio of $c_{h\ field}$ to $c_{v\ field}$ ranged from 2.2 to 22.2, with a mean of 9.0.

Similarly to the laboratory results, the back-calculated values of $c_{h\ field}$ and $c_{v\ field}$ were plotted, as shown in Figure 6. The linear regression analysis of the data in Figure 6, yields Equation 5 where, $c_{v\ field}$ and $c_{h\ field}$ are in square inches per minute. The regression generated a value for R^2 equal to 0.89, a standard error of the constant (Y) equal to 0.022 and a standard error of the coefficient (X) equal to 0.545.

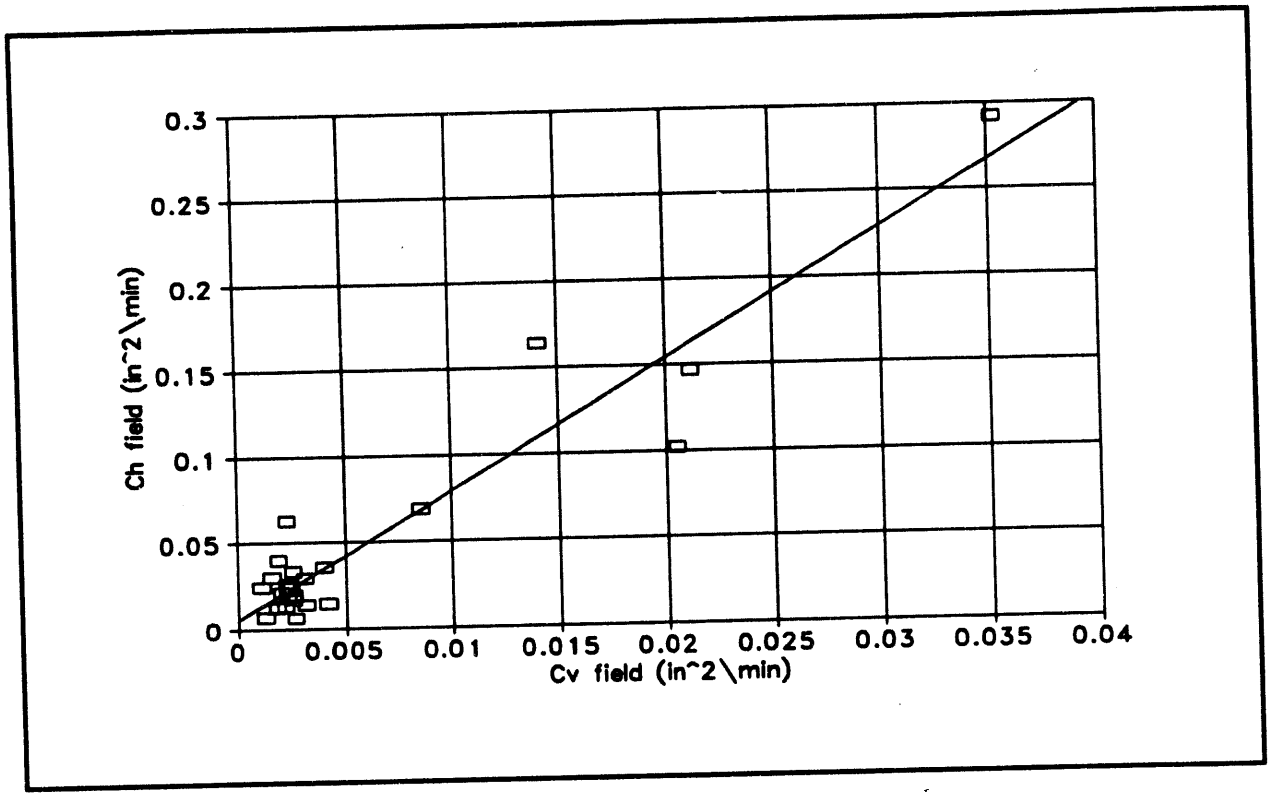


Figure 6. Relationship Between $c_{v\ field}$ and $c_{h\ field}$.

$$c_{h_{field}} = 0.006 + 7.44\,(c_{v_{field}}) \qquad (5)$$

Equation 5 would be useful in determining the value of $c_{h\ field}$ if, the assumption that $c_{v\ lab}$ was equal to $c_{v\ field}$ was valid. However, it appears that the laboratory values overestimate the field values, as previously noted. This is an unusual situation because the opposite is generally true for disturbed samples (Olsen, 1986). The back-calculated values of $c_{v\ field}$ compare well with those determined by UDOT, from one-dimensional consolidation tests, on samples near those tested in this study. It seems reasonable that the relationship of Equation 5 is satisfactory and could be used to determine $c_{h\ field}$.

An attempt was made to correlate the laboratory and field vertical coefficients of consolidation. The results are shown in Figure 7 and the regression results in Equation 6 where, the coefficients are in square inches per minute. The regression analysis of the data in Figure 7 was not nearly as convincing as that of Figures 5 and 6. This is probably due to the low number of data points. Notice in Figure 7, there does not appear to be a convincing linear relationship between the horizontal coefficients.

It now seems possible to use Equation 6 to determine the field coefficient of consolidation ($c_{v\ field}$) from the laboratory coefficient of consolidation ($c_{v\ lab}$), knowing the laboratory value was obtained from disturbed samples. Combining the results of Equation 6 with Equation 5, the value of horizontal field coefficient of consolidation ($c_{h\ field}$) can be obtained.

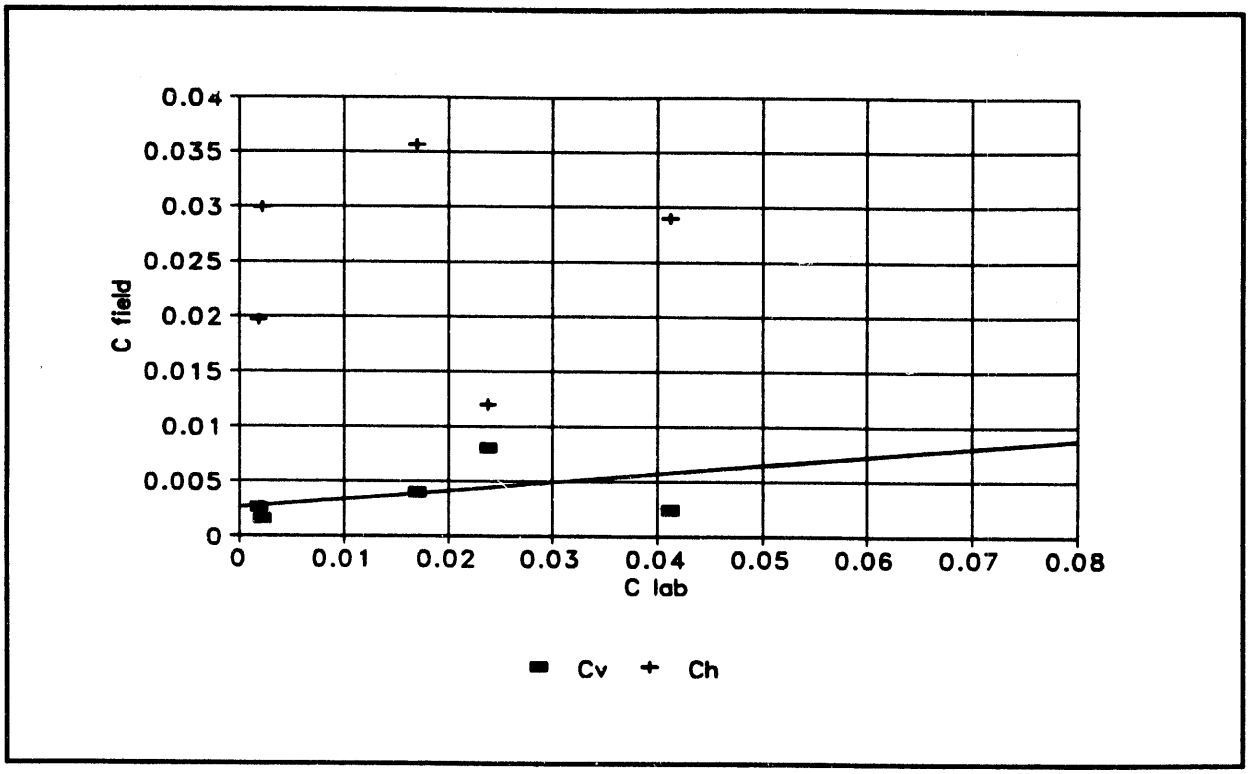


Figure 7. Relationship Between $c_{v\ lab}$ and $c_{v\ field}$.

$$c_{vfield}=0.003+0.04\,(c_{vlab}) \qquad (6)$$

EMBANKMENT SETTLEMENT PREDICTION

Settlement Magnitude

To illustrate the use of the previously described relationships, a settlement prediction was made for an embankment addition at the Junction of I-15\I-80 East. Using the one-dimensional method proposed by Karl Terzaghi (1925), the settlement magnitude was calculated according to Equation 7 for the normally consolidated deposit,

$$\Delta H=\sum (H_o)\,(C_c')\log\left(\frac{\bar{\sigma}_o+\Delta\bar{\sigma}}{\bar{\sigma}_o}\right) \qquad (7)$$

where, H_o is the depth of the compressible layers or each subdivision, C_c' is the compression ratio and represents the slope of the virgin compression portion of the log of pressure versus strain curve, $\bar{\sigma}_o$ is the initial vertical effective stress and $\Delta\bar{\sigma}_o$ is the increase in vertical effective stress due to the embankment enlargement.

The compressible layer was determined to be sixty feet in depth and was subdivided into six layers. The value of C_c' was chosen to be 0.152, and represents the

mean value determined from consolidation tests, on samples from the site. The values of $\overline{\sigma}_o$ and $\Delta\overline{\sigma}_o$ were determined at the center of each subdivision using Osterberg's (1957) integration of the Boussinesq (1885) equations, for an infinitely long embankment. Overburden stresses were calculated assuming the water table was located at 3.0 feet and the dry unit weight (γ_d) of the soil was 110 pounds per cubic foot. The unit weight of the embankment was assumed to be 125 pounds per cubic foot.

Gilani (1993) concluded that this method provides reasonably accurate results and compares favorably with solutions by other methods, for embankments constructed locally. The effective stresses and corresponding settlement were calculated for various location below the embankment. The settlement results are shown in Figure 8.

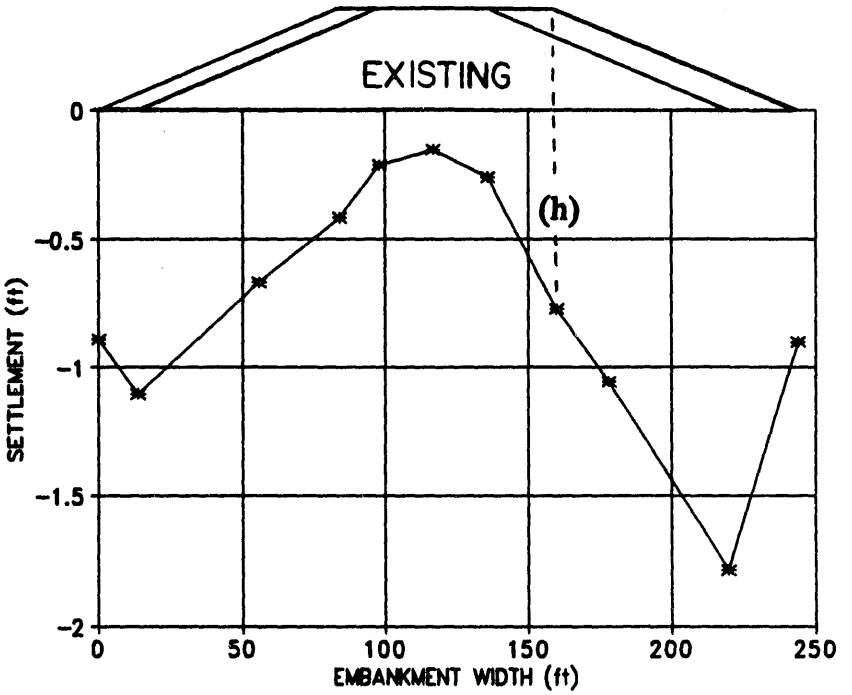


Figure 8. Predicted Settlement Magnitude Below Embankment.

Settlement Rate

Terzaghi's (1923) differential equation describing the time rate of one-dimensional consolidation is given in Equation 8, in terms of the excess pore water pressure,

$$c_v \frac{\partial^2 u}{\partial z^2} = \frac{\partial u}{\partial t} \qquad (8)$$

where, c_v is the coefficient of consolidation due to vertical flow, u the excess pore water pressure at any time t and z the depth from the top of the compressible layer to a point within the layer under consideration. The solution to the differential equation is presented in terms of the average degree of consolidation ($\bar{U}_v$) and the time factor (T_v) shown in Equation 9.

$$T_v = \frac{c_v(t)}{H_{DP}^2} \tag{9}$$

To predicted settlement rate, Equation 9 is solved for the time (t) required for 100 percent consolidation to occur (T_v=1). Equation 9 is then solved successively for the time (t), corresponding to each of the well known time factors (T_v), that are related to the average degree of vertical consolidation ($\bar{U}_v$), from ten to ninety percent. The settlement (S) at time (t) is expressed as follows in Equation 10,

$$S = (\bar{U}_v)\ (\Delta H) \tag{10}$$

where, ΔH is the magnitude of settlement from Equation 7.

A settlement rate comparison was made under the shoulder of the enlarged embankment as shown by position (h) in Figure 8. The magnitude of settlement at this location was 0.7 feet. The average value of $c_{v\ lab}$, for the range of effective stresses the embankment will undergo due to loading, was 0.0165 square inches per minute. Using the linear relationship of Equation 6, $c_{v\ field}$ is equal to 0.00366 square inches per minute.

Figure 9 shows the time-rate of settlement, in months, for two double drained conditions, to 90 percent consolidation. They are, case (1), H_{DP} equal to 30 feet, assuming the lenses are ineffective and case (2) H_{DP} equal 3 feet, as determined by Gilani (1993), and the sandy, silt lenses are effective. The time required to ninety percent consolidation for case (1) is 20850 days, about 57 years or 695 months and for case (2), 209 days or about 7 months.

Accounting for the sandy, silt lenses, primary consolidation will occur 100 times faster. This can easily be shown by the selection of H_{DP} in Equation 9, going from 30 feet in case (1), to 3 feet in case (2), or one-tenth the drainage path length squared, which is one, one-hundredth the time for case (1). This solution is simplified and assumes evenly distributed sandy, silt lenses at six foot intervals or averaged values. More complex strata require the use of computer programs.

Often the error associated with underestimating settlement rate predictions is attributed to the value selected for the coefficient of consolidation. Attempts are made to correct the laboratory coefficient by multiplying it by some factor, assuming this will result in an accurate field value for the consolidation coefficient. This approach may be in error, when in fact, the problem may be in the selection of the drainage path length.

Concluding that primary settlement will occur in 209, days the embankment could be enlarged one season and surfaced the following. However, if complete construction was required in one season, the use of vertical drains should be considered as one alternative to accelerate primary consolidation. An estimate was made that primary consolidation would need to take place in 100 days to complete construction in one season.

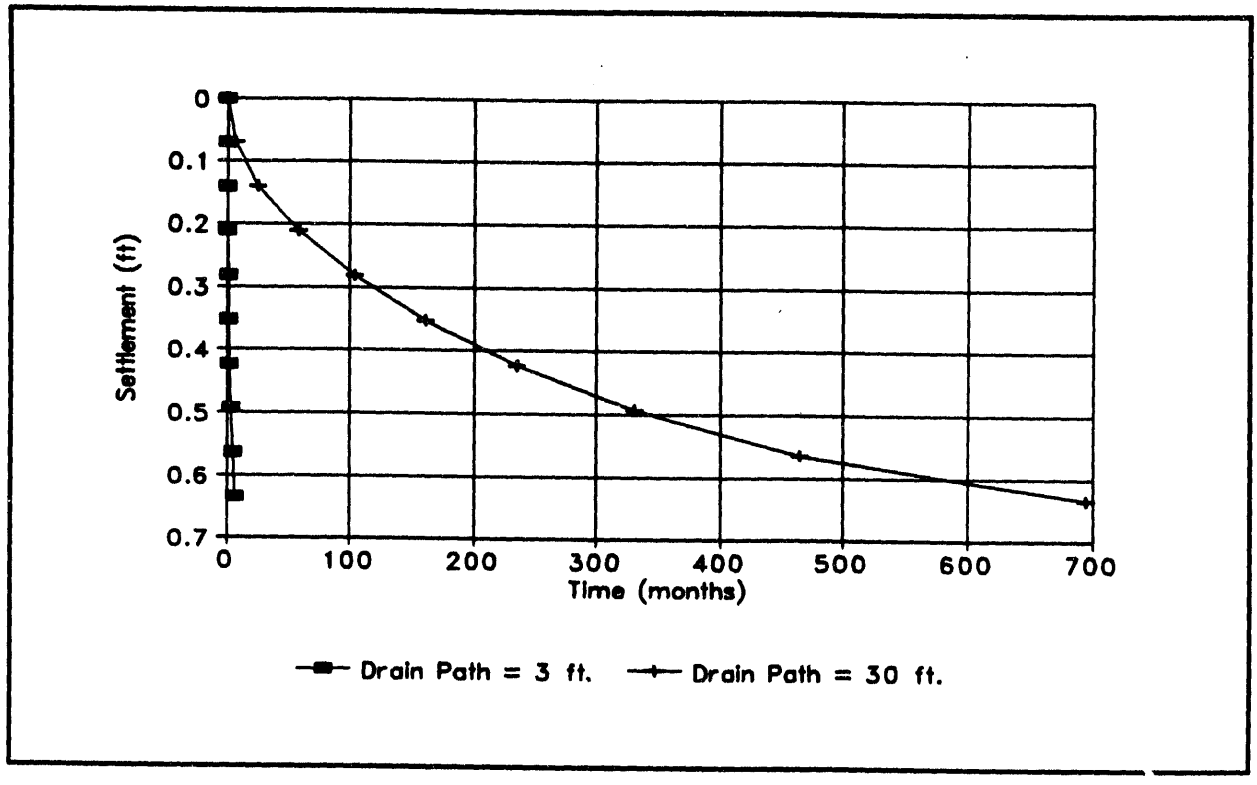


Figure 9. Predicted Settlement Rate.

Barrón (1948) derived the differential equation describing pure radial flow to sand drains as shown in Equation 11,

$$\frac{\partial u}{\partial t} = c_h \left(\frac{1}{r} \frac{\partial u}{\partial r} + \frac{\partial^2 u}{\partial r^2} \right) \qquad (11)$$

where, c_h is the coefficient of consolidation due to horizontal flow, u the excess pore water pressure at any time t and r the radius of the drained soil cylinder.

Carrillo (1942) developed the relationship for the combined, average degree of consolidation, due to vertical and radial flow as shown in Equation 12,

$$\bar{U} = 1 - (1 - \bar{U}_h)(1 - \bar{U}_v) \qquad (12)$$

where, $\bar{U}$ is the combined average degree on consolidation, $\bar{U}_h$ is the average degree of consolidation due to horizontal flow and is expressed in Equation 13 and $\bar{U}_v$ is the average degree of consolidation due to vertical flow, as previously described. The time factor for horizontal flow (T_h) is shown in Equation 14.

$$\bar{U}_h = 1 - \exp\left(\frac{-8 T_h}{F(n)} \right) \qquad (13)$$

$$T_h = \frac{(c_h)\,(t)}{(d_e)^2} \tag{14}$$

In order to determine the required drain spacing that will allow consolidation to occur in 100 days, accounting for vertical and horizontal flow, T_v is solved for in Equation 9, with t equal 100 days. H_{DP} and $c_{v\ field}$ have been previously determined. The value of $\bar{U}_v$, corresponding to the resulting T_v, equals 0.407, is approximately 70 percent. Equation 12 is then solved for in terms of the required average degree of consolidation due to horizontal flow ($\bar{U}_h$) and designing for the combined, average degree of consolidation ($\bar{U}$), equal to 90 percent. The result is $\bar{U}_h$ approximately 70 percent.

Finally, we combine Equations 13, 14 and 4 and solve for time (t). The result is shown in Equation 15 and represents the ideal case, that is, the effects of smear and drain resistance are not accounted for.

$$t = \frac{(d_e)^2}{8c_h}\left[\ln\left(\frac{d_e}{d_w}\right) - \frac{3}{4}\right]\left[\ln\left(\frac{1}{(1-\bar{U}_h)}\right)\right] \tag{15}$$

Solving Equation 15, with t equal to 100 days, by trail and error for d_e, which is approximately the drain spacing and considering d_w equal to 0.16 feet, which represents a common prefabricated vertical drain size, results in the desired drain spacing. The value of $c_{h\ field}$, using Equations 6 and 5 is 0.0332 square inches per minute. The result is a drain spacing of 8.5 feet after converting units. More detailed information on the use of vertical drains can be found in the U.S. Department of Transportation's manual on prefabricated vertical drains (Rixner et. al, 1986) and in Holtz et al. (1991).

CONCLUSIONS

In the 27th Karl Terzaghi Lecture, Duncan (1993) discusses the difficulties associated with estimating settlement magnitude and rate. Among those discussed, are the selection of consolidation coefficients and the effects of internal drainage by embedded sand layers. He states, "the prime prerequisite for any analysis is a good definition of soil properties that reflect the behavior of the undisturbed clay in situ." The use of back-calculated field parameters might assist in accomplishing this prerequisite. The use of disturbed samples will not.

The use of linear relationships appear to provide a mechanism, for obtaining field consolidation coefficients, from the laboratory coefficients. This technique may contribute to simplifying settlement predictions, as suggested by Lambe (1973) in the introduction of this paper.

The following conclusions are drawn from the results of this study on lacustrine Lake Bonneville deposits and may be useful in correlating consolidation parameters for similar deposits, when making settlement predictions.

1) The use of undisturbed soil samples is imperative if geotechnical properties are to be determined accurately in the laboratory.

2) Not accounting for the thin sandy, silt lenses will lead to inaccurate settlement rate predictions.
3) The one-dimensional consolidation tests, conducted on vertically and horizontally trimmed specimens, suggest a linear relationship exists between the laboratory consolidation coefficients.
4) Asaoka's method was useful in back-calculating field consolidation coefficients from observed field settlement data.
5) Linear relationship appear to exist between the back-calculated, vertical and horizontal consolidation coefficients, obtained from field settlement data.
6) If linear relationship can be established between the consolidation coefficients from laboratory and field data, they may be useful in determining a reasonably accurate consolidation coefficient, on which to base settlement rate predictions.

REFERENCES

Asaoka, A. 1978. Observational Procedure of Settlement Prediction. Japanese Society of Soil Mechanics and Foundation Engineering. 18 (4):87-101.

Barron, R. A. 1948. Consolidation of Fine-Grained Soils by Drain Wells. American Society of Civil Engineers Transactions. 113:718-754.

Bergado, D. T., Enriquez, A. S., Sampaco, C. L., Alfaro, M. C. and Balasubramaniam, A. S. 1992. Inverse Analyses of Geotechnical Parameters on Improved Soft Bangkok Clay. Journal of Geotechnical Engineering. 118 (7):1012-1030.

Boussinesq, J. 1885. Application des Potentiels à L'Ètude de L'Èquilibre et due Mouvement des Solides Èlastiques, Gauthier-Vallars, Paris. (referenced in, Dunn, Anderson and Kiefer, 1980).

Bowles, J. E. 1992. Engineering Properties of Soils and their Measurement. 4th ed. McGraw-Hill, Inc., Hightstown, New Jersey. 241 p.

Carrillo, N. 1942. Simple Two and Three Dimensional Cases in the Theory of Consolidation of Soils. Journal of Math and Physics. 21:1-5.

Casagrande, A. 1936. The Determination of the Pre-Consolidation Load and Its Practical Significance. Proceedings, First International Conference of Soil Mechanics and Foundation Engineering. Cambridge. Vol. III. p. 60-64. (referenced in, Holtz and Kovacs, 1981).

Casagrande, A. 1938. Notes on Soil Mechanics-First Semester. Harvard University (unpublished). 129 p. (referenced in, Holtz and Kovacs, 1981).

Duncan, M. J. 1993. Limitations of Conventional Analysis of Consolidation Settlement. 27th Terzaghi Lecture, Journal of Geotechnical Engineering. 119 (9):1332-1359.

Dunn, I. S., Anderson L. R. and Kiefer, F. W. 1980. Fundamentals of Geotechnical

Analysis. John Wiley and Sons, New York. 414 p.
Gilani, S. H. 1993. Observed and Predicted Settlements of Highway Embankments on Soft Lacustrine Deposits. Report, Utah State University, Logan, Utah. 80 p.
Hansbo, S. 1979. Consolidation of Clay by Band-Shaped Prefabricated Drains. Ground Engineering. (12) 5:16-25.
Holtz, R. D., Jamiolkowski, M. B., Lancellotta, R. and Pedroni, R. 1991. Prefabricated Vertical Drains: Design and Performance. Butterworth-Heinemann, Ltd., Jordan Hill, Oxford. 130 p.
Holtz, R. D. and Kovacs, W. D. 1981. An Introduction to Geotechnical Engineering. Prentice-Hall, Inc., Englewood Cliffs, New Jersey. 733 p.
Lambe, T. W. 1973. Predictions in Soil Engineering. Géotechnique 23 (21):155-205.
Leminen, K. and Rathmayer, H. 1983. Experience on Horizontal Oedometer Tests to Determine the Parameter c_h. Proceedings, of the 8th European Conference on Soil Mechanics and Foundation Engineering. Helsinki, Vol. 2. p. 647-651.
Magnan, J. P. 1981. An Inverse Problem Approach to Settlement Prediction. Discussion, Japanese Society of Soil Mechanics and Foundation Engineering. (21) 4:117-120.
Magnan, J. P., Pilot, G. and Queyroi, D. 1983. Back Analysis of Soil Consolidation Around Vertical Drains. Proceedings, 8th European Conference on Soil Mechanics and Foundation Engineering. Helsinki, Vol. 2. p. 653-658.
Olsen, R. E. 1986. State of the Art: Consolidation Testing. in, Consolidation of Soils: Testing and Evaluation, ASTM STP 892. Yong, R. N. and Townsend, F. C., Eds. American Society For Testing And Materials. Philadelphia, Pennsylvania. p. 7-68.
Osterberg, J. O. 1957. Influence Values for Vertical Stresses in a Semi-Infinite Mass Due to an Embankment Loading. Proceeding of the Fourth International Conference on Soil Mechanics and Foundation Engineering. London. Vol. I p. 393-394. (referenced in, Holtz and Kovacs, 1981).
Rixner, J. J., Kraemer, S. R. and Smith, A. D. 1986. Prefabricated Vertical Drains. U. S. Department of Transportation, Federal Highway Administration, McLean, Virginia. No. FHWA/RD-86/168, 107 p.
Rowe, P. W. 1959. Measurement of the Coefficient of Consolidation of Lacustrine Clay. Géotechnique 7 (3):107-119.
Su, T. R. 1966. The Investigation of Sand Drain Installation in Interstate Highway Construction in Salt Lake and Box Elder Counties, Utah. Thesis, University of Utah, Salt Lake City, Utah. 82 p.
Taylor, D. W. 1948. Fundamentals of Soil Mechanics. John Wiley and Sons, New York. 700 p.
Terzaghi, K. 1923. Die Berechnung der Durchlässigkeitsziffer des Tones aus dem Verlauf der Hydrodynamischen Spannungserscheinungen. Akademie der Wissenschaften in Wien. Sitzungsberichte. Mathematisch-naurwissenschaftliche Klasse 132 (3/4):125-138. (reprinted in Terzaghi, 1960).
Terzaghi, K. 1925. Erdbaumechanik auf Bodenphysikalischer Grundlage. Franz Deuticke, Leipzig und Wein. 399 p. (referenced in, Dunn, Anderson and Kiefer, 1980).
Terzaghi, K. 1960. From Theory to Practice in Soil Mechanics, Selections from the Writings of Karl Terzaghi. Bjerrum, L., Casagrande, A., Peck, R. B. and Skempton, A. W., contributors. John Wiley and Sons, Inc., New York. 425 p.

Hydrogeology, Waste Disposal, Science and Politics
Proceedings 30th Symposium
Engineering Geology and Geotechnical Engineering, 1994

CONTAMINANT FLUXES THROUGH SITE CONTAINMENT BARRIERS: Performance Assessment and Illustrative Results

by

Charles L. Vita, Ph.D., P.E., G.E.
Principal Consultant
Environmental Science & Engineering, Inc., (ESE)
15444 NE 95th St. #244, Redmond, Washington 98052, 206/869-8220

ABSTRACT

Contaminant mass flux by advective and diffusive transport is predicted for five containment barriers that use one or more clay liners, flexible membrane liners (FMLs), or liquid collection and removal systems (LCRS)s. Barriers are engineered systems intended to contain and isolate site contaminants from the environment. Barriers include liners, caps, and cutoff walls. Barriers may be used in contaminated-site cleanups (including CERCLA and RCRA), RCRA landfills, or other RCRA TSDFs. Concepts are provided for barrier performance assessment, including analysis and optimization, for meeting performance requirements and controlling risk at minimum cost. Concepts and results can help in planning, designing or evaluating, and communicating, the use or effectiveness of proposed or existing barriers for site cleanups or waste containment.

INTRODUCTION

Purpose and Organization

Very simply, this paper aims to help answer the question: given an existing or proposed barrier, what is the contaminant flux out the barrier, and how can risks be controlled at minimum cost? To that end, this paper: (1) introduces methodology for barrier performance assessment, including analysis and optimization, for meeting performance requirements and controlling risk at minimum cost; and (2) provides illustrative results on the relative flux performance of five different barrier systems. These concepts and results can help in planning, designing or evaluating, and communicating, the use or effectiveness of proposed or existing barriers for site cleanups or waste containment. Furthermore, these efforts can fit within a systems approach [11,12] to environmental protection or restoration, including streamlined and innovative approaches to site cleanup.

The paper is organized into three main sections and one appendix. First, is a brief background discussion on barriers and contaminant transport through barriers. Second, barrier performance assessment methodology is summarized. Third, flux results for five selected barriers are presented and discussed. Appendix 1 provides modeling details on advective transport through FMLs and composite liners.

Site Containment Barriers

Site containment barriers are engineered structures used to isolate waste bodies or contain contaminated media, including groundwater or NAPL plumes, and limit contaminant migration into the environment. Contaminated media typically include solids (soil, sediments, stabilized material, or debris), liquids (NAPLs, groundwater, or leachate), or both.

Barriers include liners, caps, and cutoff walls that may be used in contaminated-site cleanups (including CERCLA remedial actions and RCRA corrective actions), RCRA landfills, or other RCRA TSDFs [6,7]. Barriers may provide total containment, as for RCRA landfills, or partial containment, as for vertical cutoff walls.

Barriers are composed of one or more components that may include clay liners (using natural or geosynthetic clays); FMLs (flexible membrane liners) or geomembranes; composite liners (an FML placed directly on an underlying clay liner); sheet pile walls, made of steel or plastic; or pavement liners (typically asphalt or portland cement concrete). Barrier designs may also include injected grout curtains, auger-cast walls, frozen ground curtains, or other containment technologies.

Barriers may also provide for liquid control using (1) covers, (2) pumping, or (3) LCRSs (liquid collection and removal systems). Covers use surface water control, LCRSs, and liners to limit infiltration and percolation into waste bodies or affected media, thereby limiting leachate creation and hydraulic heads that drive advective contaminant migration. Groundwater or leachate pumping can create an inward hydraulic gradient through contaminant barriers that limits or prevents contaminant migration through the barrier. Depending on needs, LCRSs can be designed to collect and remove surface water, percolation, leachate, NAPL, or groundwater. Barriers may also include soil or landfill gas control, typically using gas extraction wells, passive vents, interceptor trenches, or collection blankets.

Advective and Diffusive Contaminant Transport Through Barriers

Commonly, contaminant transport through barriers is due to advection and diffusion, which occurs to the extent contaminants contact the barrier. Advective transport is due to contaminated liquid flow through the barrier, and in the direction of decreasing hydraulic head. Diffusive transport is due to molecular diffusion of contaminants through the barrier, and occurs in the direction of decreasing contaminant concentration. Diffusion through barriers is outward. Advection is outward when head decreases through the barrier, and inward when head increases, as when groundwater or leachate is pumped from within the barrier enclosure. Inward advection counteracts diffusion; high inward advection can overcome diffusion, creating a zero-flux condition.

Effective Diffusion Coefficient and Hydraulic Conductivity

A barrier's effective coefficient of diffusion (D) and hydraulic conductivity (K) directly influence the diffusive and advective transport through the barrier. D and K values are generally variable and depend on: barrier design, including materials and thicknesses; barrier construction, including construction QA/QC (CQA/QC);

contaminant chemistry, including barrier-contaminant and co-contaminant chemical effects; temperature, thermal and frost effects; and barrier structural integrity.

Saturated K-values for high-quality liners generally range from 1E-7 to 1E-9 cm/sec. Lower-quality liners have higher K-values; high-quality geosynthetic clay or pavement liners may have lower K-values. Intact FMLs have negligible K [5] for practical purposes.

K-values can change over time. K-values can increase from loss of barrier integrity. Barrier rupture, fractures, or cracks can come from site instability or ground movement (including earthquake effects), frost effects, weathering or aging effects, adjacent construction, flooding, or other hazards. K-values can also change from various chemical or physical barrier-contaminant effects, including sorption [3,8,10].

Saturated D-values for soils generally range from 1E-5 to 1E-8 cm^2/sec, or less, depending on contaminants and sorption effects [5,8]. Results presented by Lord et al. [9], imply D-values of approximately 1E-8 to 2E-8 cm^2/sec for an HDPE FML. D values for common chlorinated solvents and HDPE composite liners could range from 1E-6 to 1E-7 cm^2/sec. Co-contaminant effects can increase D in both soils and FMLs.

Barrier systems with partially saturated components will have decreased K and D relative to fully saturated systems. For example, well-functioning LCRSs that remain dry or nearly dry can greatly decrease K and D.

Advection (Leakage) Through FMLs

Advection through FMLs occurs by leakage through FML holes (any kind of macroscopic discontinuity). Most FML holes occur in field seams. For RCRA (HSWA Subtitle C) landfills, EPA [5] recommends an FML "standard hole" area and frequency of 1 cm^2 per acre for design calculations and liner leakage analysis. EPA's "standard hole" covers all FML defect types (including those from operations) and requires high-quality design and construction, including intensive CQA/QC. Leakage through FML holes strongly depends on the FML-subgrade contact compliance and subgrade K [13,14]. Advection through intact FMLs is negligible.

BARRIER PERFORMANCE ASSESSMENT METHODOLOGY

Precise barrier contaminant-containment performance is uncertain, even with high-quality design and construction. This section provides analytical and conceptual tools for dealing with that uncertainty and the risk it creates--including reliability/risk-based barrier design that controls risk at minimum cost.

Contaminant Flux Estimates: q(t)

Barrier performance is inversely proportional to q(t), where q(t) is the predicted contaminant mass flux through the barrier system and into the external environment (per unit area and time). Low q(t) means high performance, and vice versa. q(t) is estimated using the one-dimensional advection-dispersion equation with dispersion due to molecular diffusion only [1,2]; that is, q(t), is calculated from Eqs 1 and 2:

[1] $q(t) = n (CV - D\, dC/dx)$ $[M/L^2/t]$

[2] $dC/dt = V/r\, dC/dx + D/r\, d^2C/dx^2 - zC$

Eqs 1 and 2 apply throughout the barrier, where: C is the contaminant concentration, a function of time and location; V is the effective average (uniform) advective flow; D is the effective average coefficient of diffusion; n is effective average porosity; r is the effective average retardation factor for the contaminant; and z is a contaminant decay-rate factor that accounts for chemical or biological degradation (if any) of the contaminant as it passes through the barrier. Because each parameter (V,D,r,z) and variable (q(t) and C) is spatially variable, each represents spatial averages; parameters V, D, r and z also represent temporal averages. Eq 1 is evaluated at the exterior face of the barrier.

The initial and boundary conditions for Eqs 1 and 2 assume that time, t, is measured from the beginning of contaminant contact with the barrier interior face; that $C=0$ throughout the barrier system at $t=0$; and that for $t \geq 0$, the contaminant is in continuous barrier contact at a constant concentration of C_i at the barrier interior face, and C_e at the barrier exterior face. Because q(t) is linear with C_i (e.g., doubling C_i doubles q(t)), effects of time-varying C_i can be estimated by summing independent solutions of Eqs 1 and 2 using (positive or negative) increments of $C_i(t)$ appropriately time-lagged to account for the contact-time variation.

Eq 1. says q(t) is proportional to n, V, D, and C and dC/dx at the exterior barrier face. Since barrier performance increases as q(t) decreases, Eqs 1 and 2 predict that barrier performance (1) decreases with time, until reaching steady state, q(ss), and (2) increases with either decreased n, V, D, or C_i, increased C_e, or increased barrier thickness. Through its inverse, Eq 1 also predicts the time to any level of flux, including breakthrough.

Barrier Advective Flow Velocity, V

Advective flow through the barrier, V, is conservatively assumed uniform, neglecting the time required to achieve the steady state hydraulic gradient. Estimates of V depend on barrier design, as summarized in Appendix 1. For most common barriers, V can be reasonably approximated by Eq 3; that is:

[3] $V = L K i / n$ $[L/t]$

where: K is average barrier hydraulic conductivity for the contaminant of concern; i is average hydraulic gradient through the barrier (total head loss through barrier divided by total barrier thickness); and L is the barrier FML/LCRS factor ($0 \leq L \leq 1$). Estimates of L, K, and n, can be calculated using the relationships in Appendix 1.

FML/LCRS-factor L measures FML and LCRS effectiveness as the ratio of barrier leakage to leakage through the same barrier without FMLs or LCRSs (i.e., a clay-only barrier). As developed in Appendix 1, L depends principally on the number, size, and flow effects of FML holes, as well as barrier LCRS performance.

Barrier Effective Diffusion Coefficient, D

For multiple-component barriers, the average effective diffusion coefficient can be estimated using Eq 4 [9]; that is:

$$[4] \qquad D = SUM[T_i] / SUM[(T/D)_i] \qquad [L^2/t]$$

The T_i and D_i are the thickness and diffusion coefficient for each barrier component (natural or synthetic). The D_i are contaminant-dependent.

Performance Uncertainty, Risk, Reliability & Optimization

q(t) estimates the actual flux through the barrier, which is unknown. As with all predictions and estimates, q(t) is uncertain to the extent available information and its interpretation is imperfect. Risk is created by this uncertainty and the potential consequences of q(t), recognizing that project-specific risk covers many issues [11,12], including costs, regulatory requirements, community relations, and possible adverse affects on human health or the environment.

Optimization meets performance requirements and controls risk at minimum cost. That is, the optimum barrier meets performance reliability criteria using the most cost-effective design, as discussed in the following paragraphs.

Uncertainty in q(t)

Total uncertainty in q(t) consists of parameter uncertainty and model uncertainty. Parameter uncertainty stems from the impracticability of precisely predicting V(L,K,i,n), D, r and z. Model uncertainty comes from the assumptions and approximations, explicit and implicit, in the formulation and solution of Eqs 1-4--including possible contaminant transport effects not represented in the advective-diffusion equation [1-3].

Uncertainty is modeled using engineering probability and reliability [11-13]. Parameter uncertainty is modelled with each parameter, as well as q(t), lognormally distributed, characterized by an expected value, E[], and coefficient of variation, CV[]. Model uncertainty (including bias-effects) is included implicitly, by appropriately adjusting parameter uncertainty, and explicitly, using multiplicative or additive factors or general Bayesian methods [13].

Unnecessary complexity and analysis costs can be eliminated by allowing a parameter, modeling detail, or effect, to be uncertain, and modeled probabilistically, within the bounds of available information and resources, even though it could be determined more accurately with greater effort or cost. Conversely, "conservative assumptions" can be avoided by probabilistically modeling the uncertainty related to the assumption. As in all aspects of the performance assessment process, skill and judgment are necessary for effective modeling.

This approach to uncertainty is practical, flexible, and defensible--provided it is based on available site-specific, design-specific information and project requirements. Used systematically, important assumptions, hypothesizes, and their effects, are made explicit and documented, open to appropriate interpretation and negotiation, with

analysis, design and performance criteria updated as needed to reflect new information, including evolving or changing project requirements [11,12].

Performance Probabilities and Reliabilities

The lognormal distribution of q(t) is used to calculate the barrier performance measures $P_N[q(t)]$ and $R[q_L(t)]$. $P_N[q(t)]$ is the q(t) value having non-exceedance probability N--i.e., the value of q(t) having a probability of "N" of not being exceeded by the actual (and unknown) flux. For example, $P_{90}[q(t)]$ is the q(t) value having 90% probability of not being exceeded by the actual flux at time t.

$R[q_L(t)]$ is the probability that q(t) is below $q_L(t)$, a specified flux limit (e.g., 1.0 $mg/m^2/yr$). $R[q_L(t)]$ thus estimates the probability, R, that the actual flux will not exceed $q_L(t)$. $R[q_L(t)]$ and $P_N[q(t)]$ are identical if $N=R$ and $P_N[q(t)]=q_L(t)$. For example, if $R[q_L(t)]=N$, then $P_N[q(t)]=q_L(t)$, and vice versa. And because higher barrier performance means lower q(t), as performance increases: $P_N[q(t)]$ decreases and $R[q_L(t)]$ increases, for given N and $q_L(t)$.

Proposed or existing barriers are evaluated based on $P_N[q(t)]$ or $R[q_L(t)]$. Criteria for acceptable barrier performance requires (1) a specified flux limit, $q_L(t)$, and (2) a corresponding acceptable reliability level, R_a, or non-exceedance probability, N_a (where $N_a=R_a$). This performance acceptance criteria is called R-criteria, to emphasize the reliability interpretation of the criteria. An example R-criteria is that barrier performance, to be acceptable, must have a maximum contaminant flux of 1.0 $mg/m^2/yr$ at steady state (flux limit) with 90% reliability (Ra). Therefore, acceptable barrier performance means that the performance reliability is at or above an acceptable level for the specified flux limit: $R[q_L(t)]>R_a$; or equivalently, that $P_{Na}[q(t)]<q_L(t)$, where $N_a=R_a$.

R-criteria equate with acceptable risk. That is, the flux limit and reliability level should be set (in combination) to meet the acceptable risk. For example, if possible health effects drive the R-criteria, the flux limit and acceptable reliability level should be consistent with the acceptable health risk to downgradient receptors from flux through the barrier.

In practice, project-specific R-criteria may involve multiple issues and opposing viewpoints or goals. To build consensus, good communication is essential, with pragmatic tradeoffs and compromises likely. Provided time and resources are available, an open, honest, evolutionary process of communication, understanding, and negotiation, which includes all active stakeholders, can build consensus and achieve agreeable criteria. Any strategy to reach consensus in a contentious environment must be flexible.

Optimization: Required Performance at Minimum Cost

The optimum barrier achieves required performance at minimum cost using a creative design/analysis/evaluation process consistent with project-specific requirements [11,12]. Required performance means the barrier meets project-specific R-criteria: the predicted flux is below a specified flux limit at a given reliability level. Minimum cost means the design meets the R-criteria and is the most cost-effective available alternative. A design is cost-effective when each design variable affecting cost and reliability has equal marginal cost-reliability. The optimum barrier for a given project, consistent with

practical constraints, (1) meets the R-criteria and (2) is the most cost-effective available alternative. Equivalently, the optimum barrier meets R-criteria at least cost. That barrier controls risk at minimum cost.

BARRIER PERFORMANCE ANALYSIS RESULTS

Performance analysis results of five high-quality contaminant-containment barriers using the methodology discussed in this paper are presented in Tables 1 through 5 and Figures 1 through 6. Analysis inputs are illustrative of data interpretations that are practicable for a given design--recognizing that any project-specific interpretation, analysis, design or decision must be consistent with project-specific conditions, data, and goals.

The analyses use a contaminant (or group of contaminants) with (total) concentration at the interior barrier face (C_i) of 1 mg/L. Although $C_i = 1$ mg/L has no specific representation, because q(t) is linear with C_i, the q(t) results do correctly indicate relative barrier performance. Furthermore, the q(t) results can be transformed to any specific C_i (or C_i distribution) simply by multiplying q(t) and C_i (normalized for units). The analyses also use a zero contaminant concentration at the exterior face ($C_e = 0$); and a retardation factor of one ($r = 1.0$) and contaminant decay-rate of zero ($z = 0$), which are representative of mobile, stable compounds--e.g., halogenated solvents.

Representative Barrier Systems

Each barrier assumes: high-quality design and construction on stable sites; consistency with EPA recommendations for FMLs [5]; clays of continuous, uniformly very-low, hydraulic conductivity, K; barrier constructability and structural integrity. The five barriers are summarized as follows.

Case 1.--Single Clay-Liner Or Cutoff-Wall Barrier: 91-cm [3-ft] clay liner. This barrier represents a cutoff wall design for contaminated site cleanup or TSDF site containment. Case 1(a) is a low-gradient (low-head) situation, potentially representative of operating conditions where groundwater pumping is not used to create an inward gradient. Case 1(a) could also represent an operating or closed landfill having limited head on the liner system--because of an effective landfill cover, liner LCRS (with or without pumping), or both. Case 1(b) represents a potential uncontrolled (high-head) condition where the cutoff wall (or landfill) has created a site "bathtub effect" with a relatively-high outward gradient through the barrier. Case 1(c) simulates groundwater being pumped within the cutoff wall (or landfill), creating a continuous and relatively-high inward gradient through the barrier. Inputs and results are presented in Table 1; q(t) results are plotted in Figure 1.

Case 2.--Single Composite-Liner Or Cutoff-Wall Barrier: 1 composite FML/91-cm [3-ft] clay liner. This barrier could be used as a cutoff wall or other barrier system for site containment. It also represents a common design for current RCRA/HSWA Subtitle D (MSW) landfills. Cases 2(a), 2(b) and 2(c) are similar to Cases 1(a), 1(b) and 1(c). For landfills, Case 2(b) potentially represents long-term (high-head) conditions after post-closure; it assumes cover leakage and non-functioning LCRSs. Case 2(c) simulates groundwater being pumped to create a continuous inward gradient through the

barrier, assuming the FML is on the exterior of the barrier. Inputs and results are presented in Table 2; q(t) results are plotted in Figure 2.

Case 3.--Double Composite-Liner Barrier: 2 composite FML/91-cm [3-ft] clay liners separated by a 30-cm [1-ft] LCRS. This barrier represents a common design for current RCRA Subtitle C (hazardous waste) landfills. Cases 3(a) and 3(b) are similar to Cases 2(a) and 2(b). Case 3(a) assumes well-functioning LCRSs. Case 3(b), representing potential long-term (high-head) conditions after post-closure, assumes non-functioning LCRSs and a leaking cover. Case 3(b1) represents possible (extreme) long-term FML degradation; it is the same as Case 3(b) except the number of FML holes has been increased 1,000% and D includes no benefit from the FMLs. Inputs and results are presented in Table 3; q(t) results are plotted in Figure 3.

Case 4.--Single FML or Cutoff-Wall Barrier: 1 FML over relatively high-permeability soils. This barrier could be used as a cutoff wall or other barrier system for site containment. It also represents a possible single-FML design for landfills. Cases 4(a), 4(b) and 4(c) are similar to Cases 2(a), 2(b) and 2(c). Case 4(c) simulates groundwater being pumped to create a continuous negative gradient on the FML, effecting an inward gradient on FML holes (advection through an intact FML being essentially zero). Inputs and results are presented in Table 4; q(t) results are plotted in Figure 4.

Case 5.--Single Geosynthetic Composite-Liner Or Cutoff-Wall Barrier: 1 composite FML/10-cm [0.3-ft] geosynthetic-clay liner. This barrier could be used for site containment or landfills. Cases 5(a), 5(b), and 5(c) are similar to Cases 2(a), 2(b), and 2(c). Inputs and results are presented in Table 5; q(t) results are plotted in Figure 5.

Results and Implications

Results presented for each case analyzed include: the expected values and coefficients of variation for the FML/LCRS factor, L, barrier advective velocity, V, and steady state contaminant flux, q(ss); E[q(t)], the expected values of the (unknown) flux; $P_{90}[q(t)]$, the 90% non-exceedance fluxes, q(t) values having an estimated 90% probability of not being exceeded by the actual flux; and $R[q_L(ss)]$, the steady state barrier performance reliabilities, the estimated probabilities that the actual steady state flux would not exceed specified $q_L(ss)$ values of 1, 5 and 10 $mg/m^2/yr$.

The analytical results suggest several implications to barrier selection, design, or operation. How these implications are interpreted and applied in practice would depend on project-specific conditions and requirements.

Performance

One potentially important implication is that composite liners generally provide the highest performance barriers, particularly for uncontrolled (high-head) situations. Tables 1 through 5 show this general superiority in terms of E[q(t)], $P_{90}[q(t)]$, and $R[q_L(ss)]$. Figure 6a illustrate relative barrier performance for operating (low-head) conditions, based on Case (a) results for each barrier. Figure 6b illustrates relative barrier performance for long-term, uncontrolled (high-head) conditions, based on Case (b) results for each barrier.

In particular is the superior performance of the double composite-liner barrier, both for operating and uncontrolled, post-operating conditions. The double composite-liner barrier has the lowest flux for all times, including steady state; and it has the longest breakthrough time, for any level of breakthrough. It has the lowest average flux, E[q(t)]. It has the lowest $P_{90}[q(t)]$; and it would have the lowest $P_N[q(t)]$ for any N. It has the highest reliability, $R[q_L(ss)]$, for each $q_L(ss)$; and it would have the highest reliability for any $q_L(ss)$ or any $q_L(t)$. Furthermore, the high performance is maintained even under extreme FML degradation.

The high performance of composite liners occurs because FMLs and clay liners complement each other. Advection decreases substantially when FMLs are underlain by high-quality clay liners--based on comparison of V-results for Cases 2(a) and 2(b) vs. Cases 4(a) and 4(b). The FML limits advective transport, particularly under high heads. Diffusive transport is controlled by the clay components (and not FMLs--as comparison of Case 4(c) and Case 1(a) results suggest)--provided the clay is not too thin, as indicated by comparison of Cases 2(a) and 2(b) vs. Cases 5(a) Case 5(b).

There are important exceptions to the generality that composite liners make the most effective barriers. One exception is that a thick clay-only barrier, of uniformly low-K, may be more effective under low heads than a thin composite liner. That is, there is increased diffusive transport through thin composite liners relative to thick clay liners--as a comparison of Case 1(a) and Case 5(a) results suggest. Greater contaminant transport occurs through the thin composite liner even though there is more leakage and advective transport through the thicker clay-only liner.

However, as a comparison of Case 1(b) and Case 5(b) suggests, the decreased-diffusion advantage of thicker clay is swamped under high heads--because of increased advection through the clay-only liner. Higher clay K leads to the same conclusion. Of course, a clay-only barrier of adequate thickness, with low-enough K, could be constructed to also control high heads.

Under high inward hydraulic gradients, clay-only barrier performance can exceed composite-liner barrier performance. The inward advection counteracts the outward diffusion. The high inward advection of clay-only barriers counteracts more diffusion than composite liners, which have reduced advection because of the FML. This effect can be seen by comparing Case 1(c) and Case 2(c). Thus, with an adequate inward gradient, clay-only barriers are more effective than composite-liner barriers. If high enough, the inward advection can prevent diffusion, creating a zero-flux condition, with total contaminant containment.

Cost

Potential cost-effectiveness and cost-minimization implications are also apparent, as the following simple examples suggest. A single composite-liner design can perform as well as a double-composite liner that meets R-criteria by adequately increasing T (clay thickness); and if less costly, it would be a more cost-effective alternative. Similarly with a clay-only barrier, T and K could be adjusted and balanced to achieve R-criteria with equal marginal cost-reliability, to make the design cost-effective; and if it were also the least-costly barrier alternative, it would be the optimum barrier, controlling risk at minimum cost. And at the hypothetical extreme of a site with continuous, uniformly

very-low permeability soil (e.g., unfractured clay), a relatively low-performance barrier may meet R-criteria; if the design was cost-effective and the least-costly barrier alternative, it would be the optimum barrier for that situation. For a given project, cost is minimized by that design meeting R-criteria most cost-effectively--using composite liners, clay liners, FMLs, or other barrier technology, singly or in combination, and with or without LCRSs, pumping, or covers. The value of insightful, creative design and rigorous analysis to cost and risk control is evident.

Conclusion

To conclude, recall that, because q(t) assumes $C_i = 1$ mg/L and risk is project-specific, conclusions are limited to relative barrier performance. However, to help evaluate potential barrier performance, it is enlightening to gain some perspective on possible health-risk implications or perceptions of flux rates. Therefore, imagine a barrier having a total area of 10,000 m^2 and an average contaminant flux of 10 $mg/m^2/yr$. The resulting flux could yearly contaminate 100 million liters of groundwater to an average concentration of 1 ug/L. If the contaminant was PCE, that groundwater could have a worst-case potential to expose more than 100,000 people to a cancer risk exceeding 1E-6, based on maximum exposure assumptions in EPA health risk assessments. This implies that, in actual situations and to the extent practicable: barrier performance should be rigorously assessed--with siting, design, operation, and communication, used to control the risks and costs involved. This paper has introduced tools to help achieve that end.

SITED REFERENCES

1. Bear, J. 1972 *Dynamics of Fluids in Porous Media*, American Elsevier, New York, N.Y.
2. Bear, J. and A. Verruijt 1987, *Modeling Groundwater Flow and Pollution*, D.Reidel, Holland.
3. Cherry, J.A., R.W. Gillham and J.F. Barker 1984 "Contaminants in Groundwater: Chemical Processes," *Groundwater Contamination*, National Academy Press, Washington, D.C.
4. Daniel, D.E., C.D. Shackelford, and W-P. Liao 1988 "Transport of Inorganic Compounds Through Compacted Clay Soil," *IN* EPA/600/9-98/021.
5. EPA 1987 *Background Document on Bottom Liner Performance in Double-Lined Landfills and Surface Impoundments*, EPA/530-SW-013.
6. EPA 1989 *Requirements for Hazardous Waste Landfill Design, Construction, and Closure*, EPA/625/4-89/022.
7. EPA 1990 *Design and Construction of RCRA/CERCLA Final Covers*, EPA/625/4-91/025.
8. Johnson, R.L., J.A. Cherry, and J.F. Pankow 1989 "Diffusive Contaminant Transport in Natural Clay..." *ES&T* 23, 340-349.
9. Lord, A.E., R.M. Koerner, and R.H. Swan 1988 "Chemical Mass Transport Measurements to Determine Flexible Membrane Liner Lifetimes," *Geotechnical Testing Journal*, 11(2) 83-91.

10. Roy, W.R. and R.A. Griffin 1985 "Mobility of Organic Solvents in Water-Saturated Soil Materials," *Envir Geol Water Sci*, 7(4) 241-247, Springer-Verlag, New York,N.Y.
11. Vita, C.L. 1986 "Project Geotechnical Engineering: Systems Methodology Considerations," *Civil Engineering Systems* 3(3).
12. Vita, C.L. 1987 "Risk-Based Decision Making for Hazardous Waste Sites," *Proceedings* HMCRI 4th Nat. Conf. on Hazardous Waste & Hazardous Materials.
13. Vita, C.L. and K. Haskel 1987 "Flexible Membrane Liner Reliability Analysis Methodology," 4 vols., U.S. EPA Contract No. 68-03-4040.
14. Vita, C.L. 1988 "Reliability-Based Design of Secure Landfills," *Proceedings* Symposium on Reliability-Based Design in Civil Engineering, Lausanne,Switzerland.
15. Vita, C.L. 1989 "Secure Landfills: Reliability-Based Analysis and Design," *Proceedings* 5th International Conference on Structural Safety and Reliability, ASCE, New York, N.Y.

APPENDIX 1: Advection Through Composite-Liner Barriers

A general approximation for flow (leakage) through a barrier system, Qb, consisting of multiple FMLs, soil layers, and LCRSs can be developed assuming steady-state flow continuity through the barrier; that is, for a barrier system having b FMLs (b>1) and c soil layers (c>1):

[A1a] $$Qb = (fNSFKh)_{fml\text{-}1} = (fKh/T)_{soil\text{-}1} = (fNSFKh)_{fml\text{-}2} = (fKh/T)_{soil\text{-}2} = \ldots = (NSFKh)_{fml\text{-}b} = (Kh/T)_{soil\text{-}c}$$

where: N,S,F are the number, size, and flow-effects factor of FML holes [13-15]; K is the FML subgrade or soil layer hydraulic conductivity; h is the head above FML holes or head loss through soil layers; T is soil layer thickness; and f, for each FML and soil layer, is the total proportion of leakage not removed by downgradient LCRSs ($0 \leq f \leq 1$). For each FML (1,2,...,b): $(NSFKh)_{fml}$ estimates the flow (leakage) $[L^3/t]$ per unit area through the FML [13-15]--where F and K are for the FML subgrade in the flow direction. For each soil layer (1,2,...,c), including natural or geosynthetic clays or drainage materials: $(Kh/T)_{soil}$ estimates the flow $[L^3/t]$ per unit area using Darcy's equation. The total head loss through a barrier system, H, is the sum of head losses through each barrier component h; that is:

[A1b] $$H = h_{fml\text{-}1} + h_{soil\text{-}1} + h_{fml\text{-}2} + h_{soil\text{-}2} + \ldots + h_{fml\text{-}b} + h_{soil\text{-}c}$$

Substituting Eq A1a into the rhs of Eq A1b and solving for Qb yields Eq A1c:

[A1c] $$Qb = H\{(fNSFK)_{fml\text{-}1}^{-1} + (fK/T)_{soil\text{-}1}^{-1} + (fNSFK)_{fml\text{-}2}^{-1} + (fK/T)_{soil\text{-}2}^{-1} + \ldots + (NSFK)_{fml\text{-}b}^{-1} + (K/T)_{soil\text{-}c}^{-1}\}^{-1}$$

Eq A1c can be solved for any given barrier system. The average uniform advective flow through the barrier, V, can then be calculated from V=Qb/n, where n is the average effective porosity of the barrier system: $n = SUM[T_i]/SUM[(T/n)_i]$, $i = 1,2,\ldots,b+c$ ($n_i = 1$ for each FML).

For a barrier system having two identical composite liners and one high-permeability LCRS (giving negligible head loss) between the composite liners, Eq A1c yields Eq A1d; that is:

[A1d] $Qb = H\ NSFK\ f\ \{(1+NSFT_{cl})\ (1+f)\}^{-1}$

where: $K=K_{fml}=K_{clay}$; T_{cl} is composite liner thickness; and f is the proportion of leakage not removed by the LCRS. For high-quality (HQ) double composite liners $NSFT_{cl}<<1$; in which case Eq A1d simplifies to Eq A1e; and for HQ single composite liners ($NSFT_{cl}<<1$), Eq A1c simplifies to Eq A1f. And for single clay liners, Eq A1c simplifies to Eq A1g, where T is total barrier thickness. That is:

[A1e] $Qb = H\ NSFK\ (f/1+f)$ [HQ double composite liner]
[A1f] $Qb = H\ NSFK$ [HQ single composite liner]
[A1g] $Qb\text{-}clay = H\ K/T$ [Clay-only liner]

The FML/LCRS Factor, L, is the ratio of Qb to leakage through the same barrier without FMLs or LCRSs (clay only); that is: L=Qb/Qb-clay. In general $0 \le L \le 1$, with L=1 for clay-only barriers. For barriers having two identical HQ (high-quality: $NSFT_{cl}<<1$) composite liners, L is the ratio of Eq A1e to Eq A1g, which simplifies to Eq A1h; and for HQ single composite liners, L is estimated by Eq A1i. That is:

[A1h] $L = NSFT\ (f/1+f)$ [HQ double composite liner]
[A1i] $L = NSFT$ [HQ single composite liner]

Both L and Qb, and, therefore, V, depend on N, S, and F (the number, size, and flow factor of FML holes) which, realistically, cannot be accurately predicted--they are thus probabilistically estimated as follows, where E[] is the expected value and CV[] is the coefficient of variation. L is a random sum with holes occurring as Poisson events with a variable hole rate (per unit area), Hr, following a gamma distribution characterized by parameters E[Hr] and CV[Hr] [13-15]. The Poisson-event assumption uses the maximum entropy principle to provide a least-biased assignment of probabilities. E[L] and CV[L] can be estimated following [13-15]; if the variables are reasonably independent, E[L] and CV[L] can be estimated by Eqs A2j,k:

[A1j] $E[L] = E[Hr]\ E[S]\ E[F]\ E[T]\ E[f/1+f]$
[A1k] $CV[L] = Sqrt\{CV[Hr]^2+(CV[S]^2+1)(CV[F]^2+1)(CV[T]^2+1)(CV[f/1+f]^2+1)E[Hr]^{-1}\}$

Factor L is expected to be approximately lognormal for high-quality barriers. Variables S, F, and T are generally expected to be approximately lognormal; and variable N (although theoretically negative binomial) is also approximately lognormal. Factor L is lognormal if S, F, T and N are lognormal. Then, if L, K, i and n are lognormal, it follows that V is lognormal; in which case E[V] and CV[N] are calculated by Eqs A2l,m; that is:

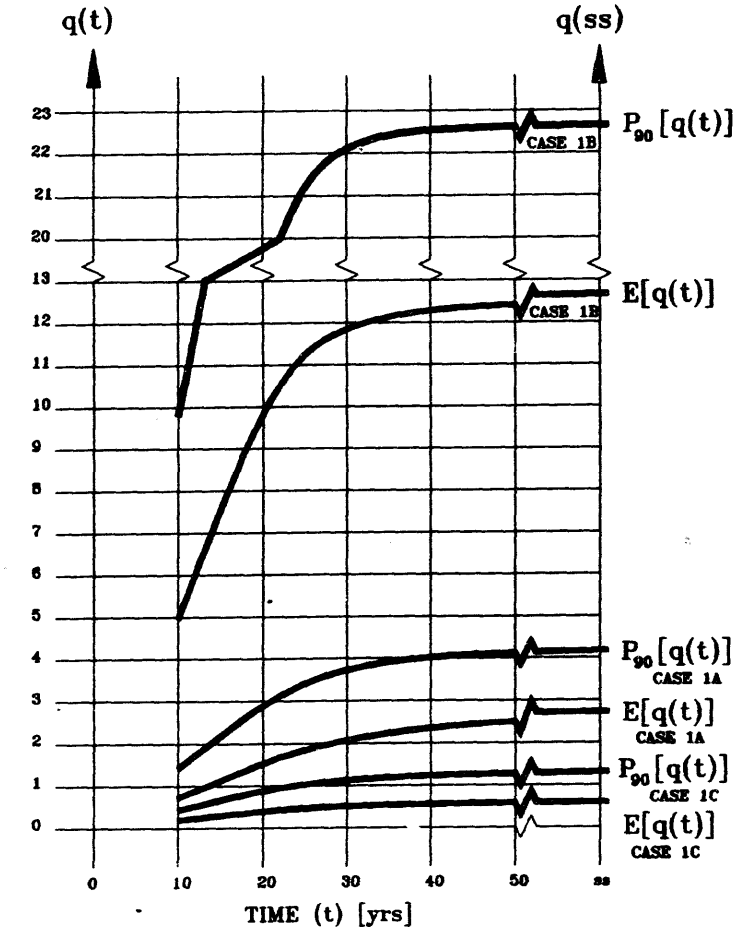
[A1l] $E[V] = E[L]\ E[K]\ E[i]\ /\ E[n]$
[A1m] $CV[V] = Sqrt\{(CV[L]^2+1)(CV[K]^2+1)(CV[i]^2+1)(CV[n]^2+1)-1\}$

Case 1. - Single Clay Liner Or Cutoff Wall Barrier

Table 1

	Case 1 (a)		Case 1 (b)		Case 1 (c)	
Inputs:	E[]	CV[]	E[]	CV[]	E[]	CV[]
T[cm]=	91	0.05	91	0.05	91	0.05
i=	0.10	0.30	2.00	0.30	-2.00	.30
n=	0.35	0.10	0.35	0.10	0.35	0.10
K[cm/sec]=	2.00E-08	1.00	2.00E-08	1.00	2.00E-08	1.00
D[cm^2/sec]=	2.00E-06	0.50	2.00E-06	0.50	2.00E-06	0.50
Outputs:						
H[cm]=	9	0.30	183	0.30	-183	0.30
L=	1.00	0.00	1.00	0.00	1.00	0.00
V[cm/sec]=	5.7E-09	1.10	1.1E-07	1.10	-1.1E-07	1.10
q(ss)=	2.73	0.41	12.65	0.65	0.59	1.42
Reliabilities:						
$R[q_L(ss)=1]$	<.10		<.10		0.85	
$R[q_L(ss)=5]$	0.96		<.10		0.99	
$R[q_L(ss)=10]$	>.99		0.46		>.99	
	Estimated Flux, q(t)[$mg/m^2/yr$]					
Time, t[yrs]	E[q(t)]	P_{90}[q(t)]	E[q(t)]	P_{90}[q(t)]	E[q(t)]	P_{90}[q(t)]
10	0.66	1.34	4.74	9.61	0.18	0.41
20	1.61	3.10	10.81	20.63	0.42	0.94
30	2.11	3.80	11.99	22.35	0.51	1.14
40	2.36	4.05	12.31	22.56	0.55	1.23
50	2.50	4.14	12.45	22.61	0.57	1.26
60	2.58	4.16	12.53	22.63	0.58	1.28
70	2.64	4.17	12.58	22.63	0.58	1.29
80	2.67	4.17	12.60	22.64	0.58	1.29
90	2.69	4.18	12.62	22.64	0.59	1.29
100	2.70	4.18	12.63	22.64	0.59	1.30
150	2.72	4.17	12.65	22.64	0.59	1.30
200	2.73	4.17	12.65	22.64	0.59	1.30
q(ss)	2.73	4.17	12.65	22.64	0.59	1.30

Figure 1



Case (a): - Low head (operating) conditions
Case (b): - High head (post-operating) conditions
Case (c): - Inward hydraulic gradient

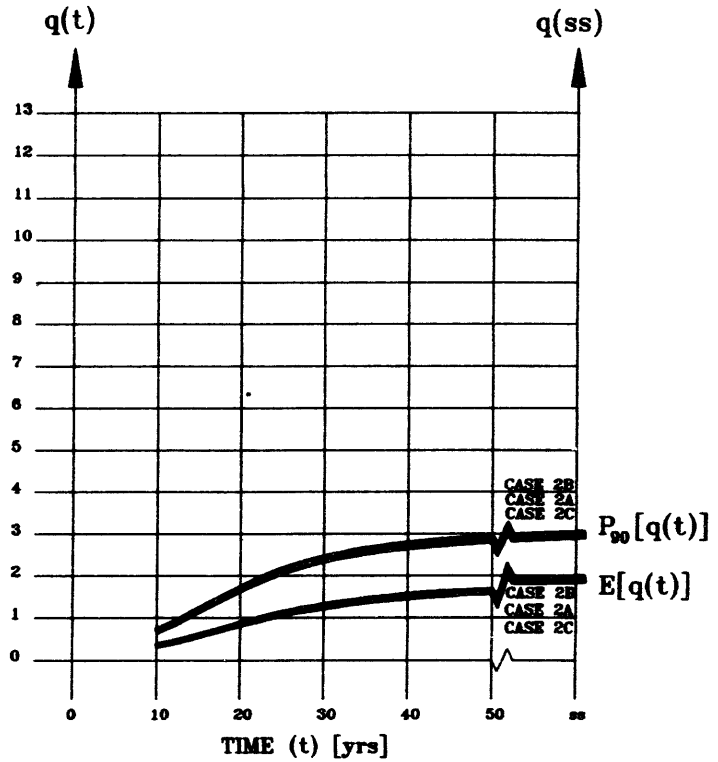
Symbols List. - E[]:Expected value; CV[]:Coefficient of variation; T:Barrier thickness; i:Hydraulic gradient through barrier; n:Porosity; K:Hydraulic conductivity; D:Effective diffusion coefficient; H:Head loss through barrier; V:Advection velocity; q(t):Predicted contaminant flux through barrier; q(ss):q(t) at steady state; q_L(ss):Specified steady state flux limit; $R[q_L(ss)]$:Reliability that $q(ss) < q_L(ss)$; P_{90}[q(t)]:q(t) with 90% probability of nonexceedance.

Case 2. - Single Composite Liner Or Cutoff Wall Barrier

Table 2

	Case 2 (a)		Case 2 (b)		Case 2 (c)	
Inputs:	E[]	CV[]	E[]	CV[]	E[]	CV[]
T[cm]=	92	0.05	92	0.05	92	0.05
S[cm]=	1.128	1.00	1.128	1.00	1.128	1.00
Hr[acre^{-1}]=	1.00	1.00	1.00	1.00	1.00	1.00
F=	2,500	0.50	2,500	0.50	2,500	1.00
i=	0.10	0.30	5.00	0.30	-2.00	0.30
n=	0.35	0.10	0.35	0.10	0.35	0.10
K[cm/sec]=	2.00E-08	1.00	2.00E-08	1.00	2.00E-08	1.00
D[cm^2/sec]=	1.57E-06	0.50	1.57E-06	0.50	1.57E-06	0.50
Outputs:						
H[cm]=	9	0.30	458	0.30	-183	0.30
L=	6.4E-03	1.87	6.4E-03	1.87	6.4E-03	2.24
V[cm/sec]=	3.7E-11	2.97	1.8E-09	2.97	-7.3E-10	3.48
q(ss)=	1.88	0.44	1.96	0.42	1.85	0.45
Reliabilities:						
R[q_L(ss)=1]	<.10		<.10		<.10	
R[q_L(ss)=5]	0.99		0.99		0.99	
R[q_L(ss)=10]	>0.99		>0.99		>0.99	
	Estimated Flux, q(t)[mg/m^2/yr]					
Time, t[yrs]	E[q(t)]	P_{90}[q(t)]	E[q(t)]	P_{90}[q(t)]	E[q(t)]	P_{90}[q(t)]
10	0.27	0.56	0.28	0.58	0.27	0.55
20	0.90	1.78	0.92	1.83	0.89	1.76
30	1.28	2.43	1.32	2.50	1.26	2.40
40	1.50	2.73	1.56	2.81	1.48	2.70
50	1.63	2.86	1.69	2.94	1.61	2.83
60	1.71	2.92	1.78	3.00	1.69	2.88
70	1.76	2.94	1.83	3.03	1.74	2.91
80	1.80	2.95	1.87	3.03	1.77	2.92
90	1.82	2.95	1.90	3.04	1.79	2.92
100	1.84	2.95	1.91	3.04	1.81	2.92
150	1.87	2.95	1.95	3.03	1.84	2.92
200	1.88	2.95	1.96	3.03	1.85	2.92
q(ss)	1.88	2.95	1.96	3.03	1.85	2.92

Figure 2



Case (a) - Low head (operating) conditions
Case (b): - High head (post-operating) conditions
Case (c): - Inward hydraulic gradient

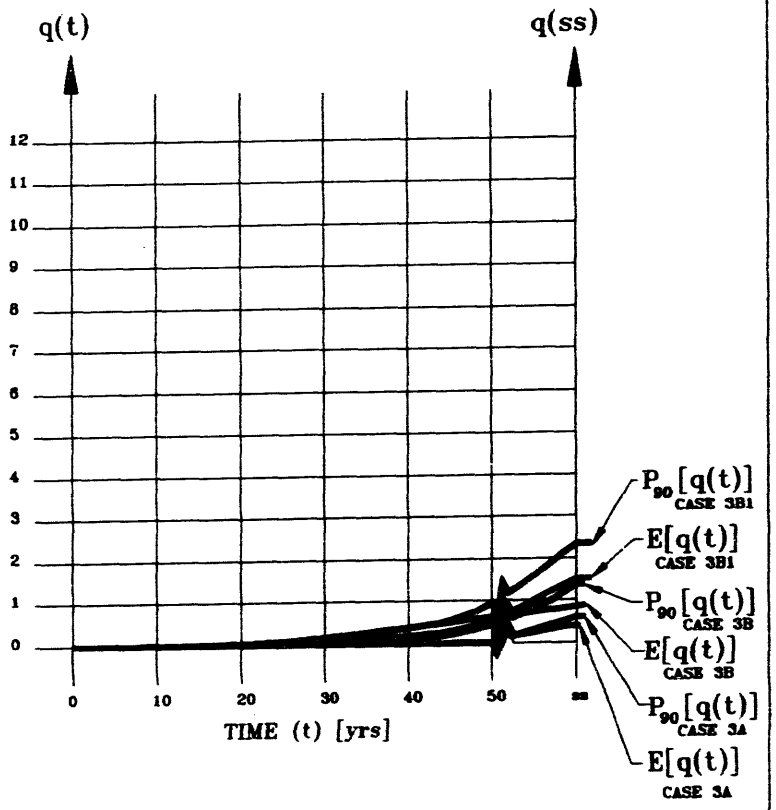
Symbols List. - E[]:Expected value; CV[]:Coefficient of variation; T:Barrier thickness; S:Size of FML holes; Hr:FML hole rate; F:FML flow factor; i:Hydraulic gradient through barrier; n:Porosity; K:Hydraulic conductivity; D:Effective diffusion coefficient; H:Head loss through barrier; L:FML/LCRS Factor; V:Advection velocity; q(t):Predicted contaminant flux through barrier; q(ss):q(t) at steady state; q_L(ss):Specified steady state flux limit; R[q_L(ss)]:Reliability that q(ss)<q_L(ss); P_{90}[q(t)]:q(t) with 90% probability of nonexceedance.

Case 3. - Composite Double Liner Barrier W/LCRS

Table 3

	Case 3 (a)		Case 3 (b)		Case 3 (b1)	
Inputs:	E[]	CV[]	E[]	CV[]	E[]	CV[]
T[cm]=	213	0.05	213	0.05	213	0.05
S[cm]=	1.128	1.00	1.128	1.00	1.128	1.00
Hr[acre^{-1}]=	1.00	1.00	1.00	1.00	10.00	1.00
F=	2,500	0.50	2,500	0.50	2,500	1.00
i=	0.04	0.30	2.15	0.30	2.15	0.30
n=	0.35	0.10	0.35	0.10	0.35	0.10
K[cm/sec]=	2.00E-08	1.00	2.00E-08	1.00	2.00E-08	1.00
D[cm^2/sec]=	8.00E-07	0.50	1.62E-06	0.50	2.00E-06	0.50
f/1+f=	0.20	0.20	0.50	0.00	0.50	0.00
Outputs:						
H[cm]=	9	0.30	458	0.30	458	0.30
L=	3.0E-03	1.90	7.4E-03	1.87	0.074	1.18
V[cm/sec]=	7.3E-12	3.02	9.1E-10	2.99	9.1E-09	2.07
q(ss)=	0.41	0.45	0.87	0.44	1.58	0.42
Reliabilities:						
R[q_L(ss)=1]	0.99		0.70		0.17	
R[q_L(ss)=5]	>0.99		>0.99		>0.99	
R[q_L(ss)=10]	>0.99		>0.99		>0.99	
	Estimated Flux, q(t)[mg/m^2/yr]					
Time, t[yrs]	E[q(t)]	P_{90}[q(t)]	E[q(t)]	P_{90}[q(t)]	E[q(t)]	P_{90}[q(t)]
10	0.00	0.00	0.00	0.00	0.00	0.00
20	0.00	0.00	0.00	0.00	0.01	0.02
30	0.00	0.00	0.02	0.04	0.07	0.15
40	0.00	0.00	0.06	0.12	0.18	0.37
50	0.00	0.01	0.11	0.23	0.30	0.62
60	0.01	0.02	0.17	0.35	0.42	0.86
70	0.02	0.03	0.23	0.47	0.54	1.09
80	0.03	0.05	0.29	0.59	0.64	1.28
90	0.04	0.08	0.34	0.69	0.74	1.45
100	0.05	0.11	0.39	0.78	0.83	1.60
150	0.12	0.25	0.57	1.09	1.14	2.04
250	0.23	0.46	0.74	1.31	1.42	2.32
500	0.35	0.63	0.85	1.37	1.56	2.42
q(ss)	0.41	0.66	0.87	1.37	1.58	2.43

Figure 3



Case (a): - Low head (operating) conditions
Case (b): - High head (post-operating) conditions
Case (b1): - Case (b) with extreme FML degradation

Symbols List. - E[]:Expected value; CV[]:Coefficient of variation; T:Barrier thickness; S:Size of FML holes; Hr:FML hole rate; F:FML flow factor; i:Hydraulic gradient through barrier; n:Porosity; K:Hydraulic conductivity; D:Effective diffusion coefficient; f:Leakage fraction not removed by LCRS; H:Head loss through barrier; L:FML/LCRS Factor; V:Advection velocity; q(t):Predicted contaminant flux through barrier; q(ss):q(t) at steady state; q_L(ss):Specified steady state flux limit; R[q_L(ss)]:Reliability that q(ss) < q_L(ss); P_{90}[q(t)]:q(t) with 90% probability of nonexceedance.

Case 4. - FML Only

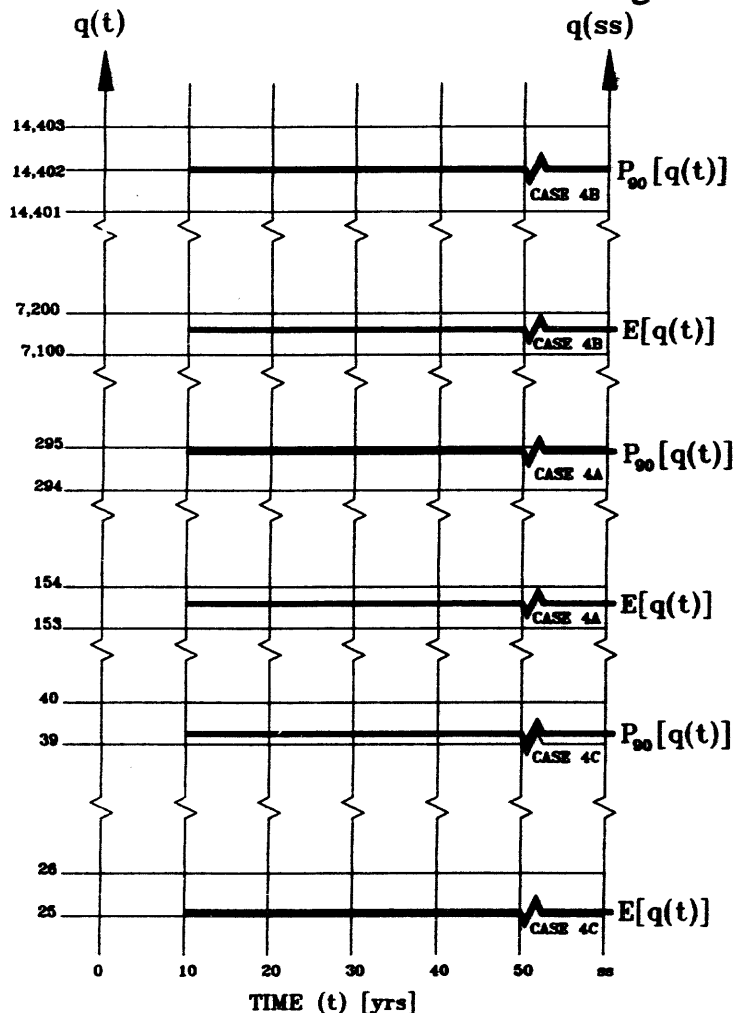
Table 4

	Case 4 (a)		Case 4 (b)		Case 4 (c)	
Inputs:	E[]	CV[]	E[]	CV[]	E[]	CV[]
T[cm]=	0.25	0.05	0.25	0.05	0.25	0.05
S[cm]=	1.128	1.00	1.128	1.00	1.128	1.00
Hr[acre^{-1}]=	1.00	1.00	1.00	1.00	1.00	1.00
F=	2,500	1.00	2,500	1.00	2,500	1.00
i=	36	0.30	1830.00	0.30	-0.01	0.30
n=	1.00	0.00	1.00	0.00	1.00	0.00
K[cm/sec]=	1.00E-03	1.00	1.00E-03	1.00	1.00E-03	1.00
D[cm^2/sec]=	2.00E-08	0.50	2.00E-08	0.50	2.00E-08	0.50
Outputs:						
H[cm]=	9	0.30	458	0.30	-0.003	0.30
L=	1.7E-05	2.24	1.7E-05	2.24	1.7E-05	2.24
V[cm/sec]=	6.4E-07	3.48	3.2E-05	3.48	-1.7E-10	3.48
q(ss)=	153.59	0.80	7,177	0.92	25.08	0.44
Reliabilities:						
R[q_L(ss)=1]	<.10		<.10		<.10	
R[q_L(ss)=5]	<.10		<.10		<.10	
R[q_L(ss)=10]	<.10		<.10		<.10	

	Estimated Flux, q(t)[mg/m^2/yr]					
Time, t[yrs]	E[q(t)]	P_{90}[q(t)]	E[q(t)]	P_{90}[q(t)]	E[q(t)]	P_{90}[q(t)]
Years						
1	153.59	294.90	7,177	14,402	25.08	39.35
q(ss)	153.59	294.90	7,177	14,402	25.08	39.35

Case (a): - Low head (operating) conditions
Case (b): - High head (post-operating) conditions
Case (c): - Inward hydraulic gradient

Figure 4



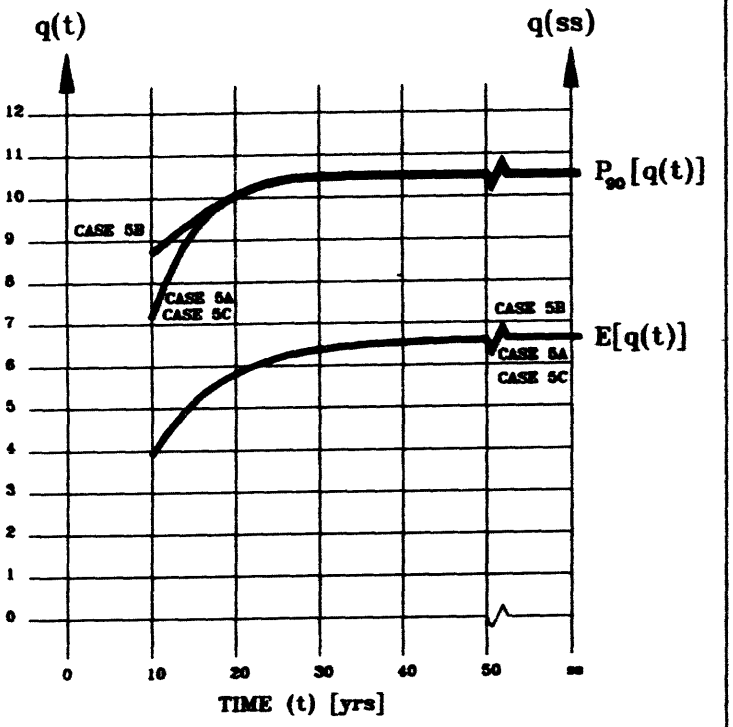
Symbols List. - E[]:Expected value; CV[]:Coefficient of variation; T:Barrier thickness; S:Size of FML holes; Hr:FML hole rate; F:FML flow factor; i:Hydraulic gradient through barrier; n:Porosity; K:Hydraulic conductivity; D:Effective diffusion coefficient; H:Head loss through barrier; L:FML/LCRS Factor; V:Advection velocity; q(t):Predicted contaminant flux through barrier; q(ss):q(t) at steady state; q_L(ss):Specified steady state flux limit; R[q_L(ss)]:Reliability that q(ss)<q_L(ss); P_{90}[q(t)]:q(t) with 90% probability of nonexceedance.

Case 5. - FML/Geosynthetic Clay

Table 5

	Case 5 (a)		Case 5 (b)		Case 5 (c)	
Inputs:	E[]	CV[]	E[]	CV[]	E[]	CV[]
T[cm]=	10.25	0.05	10.25	0.05	10.25	0.05
S[cm]=	1.128	1.00	1.128	1.00	1.128	1.00
Hr[acre^{-1}]=	1.00	1.00	1.00	1.00	1.00	1.00
F=	2,500	0.50	2,500	0.50	2,500	1.00
i=	0.91	0.30	45.70	0.30	-18.30	0.30
n=	0.36	0.10	0.36	0.10	0.36	0.10
K[cm/sec]=	1.00E-09	1.00	1.00E-09	1.00	1.00E-09	1.00
D[cm^2/sec]=	6.00E-07	0.50	6.00E-07	0.50	6.00E-07	0.50
Outputs:						
H=[cm]	9.328	0.30	468.425	0.30	-187.575	0.30
L=	7.1E-04	1.87	7.1E-04	1.87	7.1E-04	2.24
V[cm/sec]=	1.8E-12	2.99	9.1E-11	2.99	-3.6E-11	3.50
q(ss)=	6.61	0.45	6.62	0.45	6.61	0.45
Reliabilities:						
R[q_L(ss)=1]	<.10		<.10		<.10	
R[q_L(ss)=5]	0.33		0.33		0.33	
R[q_L(ss)=10]	0.88		0.88		0.88	
	Estimated Flux, q(t)[mg/m^2/yr]					
Time, t[yrs]	E[q(t)]	P_{90}[q(t)]	E[q(t)]	P_{90}[q(t)]	E[q(t)]	P_{90}[q(t)]
1	4.56	8.66	4.56	8.66	4.56	8.66
2	6.04	10.34	6.05	10.34	6.04	10.34
3	6.42	10.47	6.42	10.48	6.42	10.47
4	6.54	10.48	6.55	10.48	6.54	10.48
5	6.59	10.48	6.59	10.48	6.58	10.47
6	6.60	10.48	6.61	10.48	6.60	10.47
7	6.61	10.47	6.61	10.48	6.61	10.47
q(ss)	6.61	10.47	6.61	10.48	6.61	10.47

Figure 5

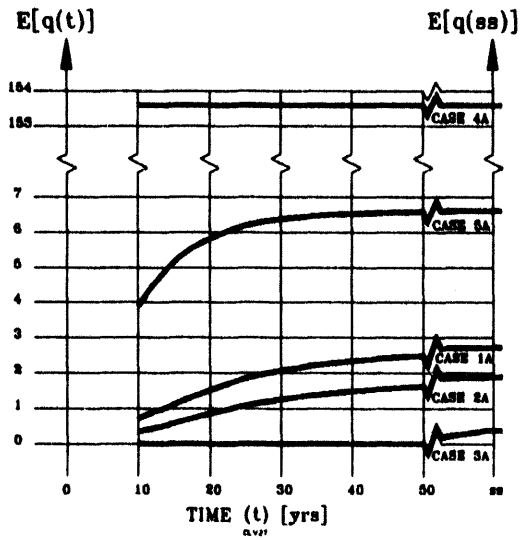


Case (a): - Low head (operating) conditions
Case (b): - High head (post-operating) conditions
Case (c): - Inward hydraulic gradient

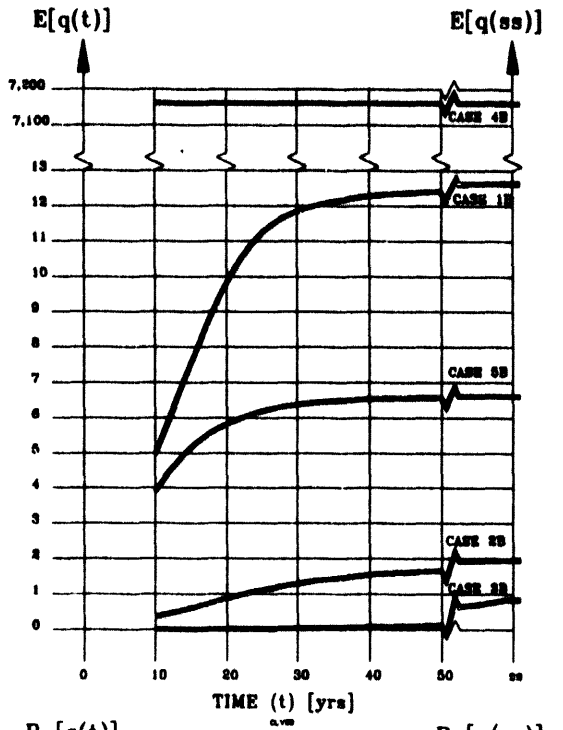
Symbols List. - E[]:Expected value; CV[]:Coefficient of variation; T:Barrier thickness; S:Size of FML holes; Hr:FML hole rate; F:FML flow factor; i:Hydraulic gradient through barrier; n:Porosity; K:Hydraulic conductivity; D:Effective diffusion coefficient; H:Head loss through barrier; L:FML/LCRS Factor; V:Advection velocity; q(t):Predicted contaminant flux through barrier; q(ss):q(t) at steady state; q_L(ss):Specified steady state flux limit; R[q_L(ss)]:Reliability that q(ss)<q_L(ss); P_{90}[q(t)]:q(t) with 90% probability of nonexceedance.

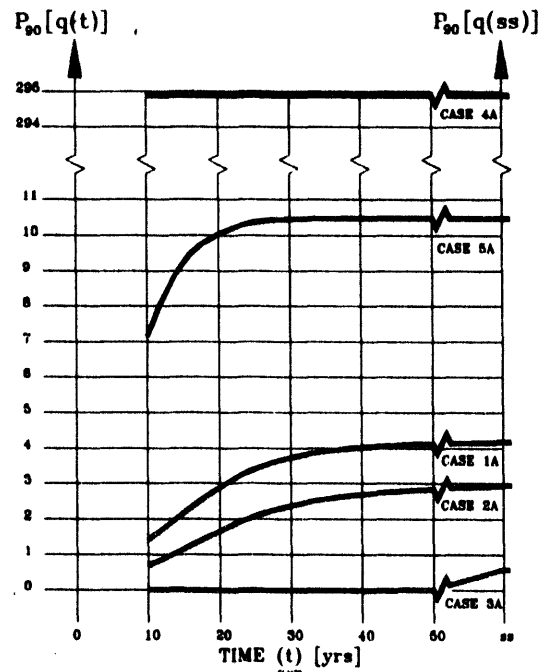
Figure 6.

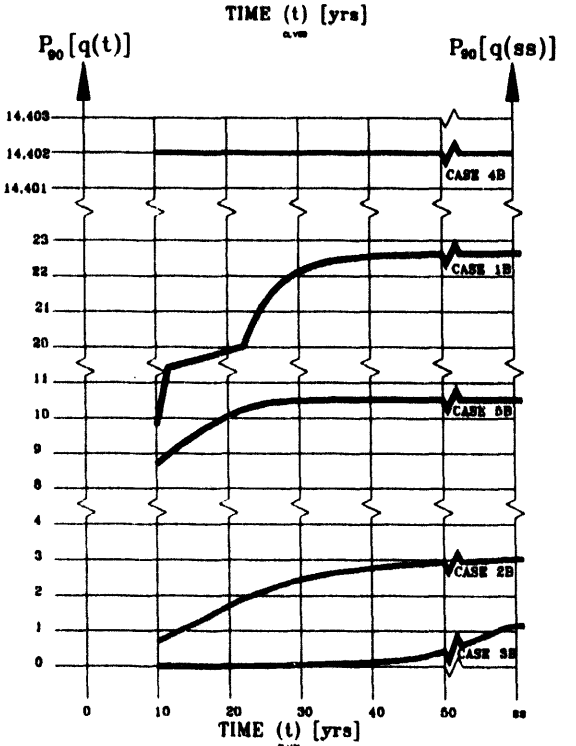
Case (a) - Low head (operating) conditions



Case (b) - High head (post-operating) conditions







SS = STEADY STATE; E[q(t)] = EXPECTED VALUES; $P_{90}[q(t)]$ = 90% NON-EXCEEDANCE VALUES
q(t) in $mg/m^2/yr$ (Ci=1 mg/L);

Hydrogeology, Waste Disposal, Science and Politics
Proceedings 30th Symposium
Engineering Geology and Geotechnical Engineering, 1994

FINITE ELEMENT ANALYSIS OF A SOIL NAILED WALL

Joseph A. Caliendo, Kevin C. Womack
Huey S. Nham, Loren R. Anderson

All - Utah State University,
Department of Civil & Environmental Engineering

ABSTRACT

Soil nails are finding increased use by Transportation Departments on widening projects where a vertical wall stabilized with nails is used to replace soil berms at bridge abutments. Soil nails provide an economic "top down" method for widening roadways beneath existing bridges.

A soil nailed wall was constructed to accommodate the widening of Interstate 5 north of Portland Oregon. The total length of the wall is 256 feet, 165 feet of which is located under an existing bridge. The height is 19 feet. Five rows of nails were installed at a horizontal spacing of 4.5 feet and a vertical spacing of 3 feet and were approximately 18 feet in length. The soil nailed wall was instrumented with slope inclinometers, strain gages, and electric load cells to measure and record lateral wall deflections and stress distribution along the nail lengths.

The finite element computer program SOILSTRUCT (Filz, Clough, and Duncan, 1990) was used to analyze the soil structure interaction of the wall/nail system. Quadrilateral elements were used to model the soil mass and hyperbolic soil parameters described the soil properties. Bar elements with interface elements modeled the nails. Both quadrilateral and beam elements were used for the wall itself. A complete report on the finite element analysis is provided by Nham, (1993). Wall deformations predicted by the finite element model compared well with the measured results.

SOIL NAILING

A complete discussion on the principals of soil nailing is provided by Elias and Juran, (1991). The soil nailing process consists of a reinforced shotcrete facing constructed incrementally from the top down. Soil nails (often referred to as "inclusions") are driven or grouted into the wall face at predetermined locations. These provide tensile, shear, and bending stress resistance. The procedure is summarized as follows:

(1) An initial unsupported cut is made.
(2) Drainage materials are provided.

(3) The exposed face is covered with reinforced shotcrete.
(4) Nails are installed at predetermined locations.
(5) Repeat steps 1-4 through the final elevation.
(6) The nails may be prestressed to a relatively low level.
(7) A cast in place or prefabricated facing may be connected to the final shotcrete face.

An increasingly popular application of soil nailing technology in the highway industry is to replace existing soil berms below bridges at the abutments thus providing additional roadway width.

CASE HISTORY DESCRIPTION

The soil nailing case history used for this study provided subsurface site parameters and wall response measurements and is well documented by Sakr and Barrows, (1991) and Dumas, (1991). The soil nailed wall was constructed to accommodate the widening of Interstate 5 (Swift-Delta Highway), north of Portland, Oregon under the existing Oregon Slough Bridge (M.P. 307.46). Figure 1 shows the relative position of the soil nailed wall and the bridge. The existing abutment is pile supported by a single row of 14 inch diameter concrete filled steel pipe piles at 4 foot 5 inch centers. Soil nails were installed between the piles. The end slope fill consisted of a fine sand with traces of silt.

The wall is located under the south end of the Oregon Slough bridge The construction process required that the widening progress from the top down. Therefore a soil nailed wall was utilized for lateral earth support. Other methods were not used because of restricted space, and economic considerations. In order to evaluate the performance of this wall, it was instrumented with slope inclinometers, strain gauges, and electric load cells to measure and record lateral wall deflections and the force distributions along the length of the nail. These measuring devices were implemented in two monitoring sections.

This paper will focus on the deflection measurements obtained at section #2 located west of the pile-supported bridge abutment. Section #1 was not analyzed with a finite element analysis because it is located adjacent to the bridge abutment, where the piles complicate the interaction of the soil nailed wall.

Soil Nailed Wall Description

The total length of the soil nailed wall is 256 feet, 165 feet of which is located under the Oregon Slough Bridge. The maximum height of the wall is 19 feet. Based on the stability analysis and physical constraints, a horizontal nail spacing of 4.5 feet and a vertical nail spacing of 3 feet were used. There were a total of 5 rows of nails. The top four rows were oriented at 15 degrees from horizontal; the bottom row was installed at 25 degrees. The nail lengths ranged from 17 feet to 18 feet. The wall geometry is shown on Figure 2.

Subsurface Conditions

The soil west of the bridge abutment near section #2 was generally loose silty fine sand with varying amounts of moisture. Large concrete pieces, rock boulders, and metal debris up to two feet in diameter were encountered during test pit excavation of the top six feet. The ground water table was located five to six feet below the bottom of the wall.

Construction Methods

The construction of the soil nailed wall consisted of the following sequence:

(1) Testing the pre-production nails to verify the Contractor's drilling procedure, the proposed maximum 5 inch diameter nail hole, and the grouting method.
(2) Excavation of the end berm in stages.
(3) Installing the steel welded wire mesh.
(4) Applying the structural shotcrete materials.
(5) Drilling nail holes with the "cased hole drilling method".
(6) Installing the epoxy-coated #9 Dywidag bars and grouting the nail holes.
(7) Placing the six inch by six inch steel bearing plate and tightening the bearing nut.
(8) Repeating step (1) through (7) for the subsequent excavation steps until the desired elevation is reached.

Instrumentation

Vibrating wire strain gauges, electric load cells, and slope inclinometers were all used on the project. The vibrating wire strain gauges were mounted in pairs and equally spaced along the length of each nail. The strain gauges were used to evaluate the axial force distribution along the length of each rows of nails. Three electric load cells were installed on the nails of rows 1, 3 and 5 to monitor nail load buildup at the nail anchorage. The ground movement in the vicinity of station two was monitored with two slope inclinometers installed 10 feet and 38 feet west of the bridge, and approximately 3.5 feet behind the wall.

FINITE ELEMENT ANALYSIS

Computer Program

The computer program SOILSTRUCT (Filz, Clough, and Duncan, 1990) was used for the finite element analysis. This program has been widely used in both academic and engineering practice to model lateral support systems. SOILSTRUCT can simulate arbitrary sequences of incremental construction and loading steps under plane strain conditions. The different functions of the program allow various Geotechnical engineering projects to be modeled. The following incremental construction steps may be simulated:

(1) Excavating.
(2) Filling.
(3) Dewatering.
(4) Installing struts, tie-backs or nails for excavation support systems.
(5) Removing excavation support systems.
(6) Applying a specified sequence of loads, such as concentrated loads, boundary pressures, and loads induced by a change in temperatures.
(7) Installing beam elements, and changing material types in a construction step.

SOILSTRUCT utilizes a hyperbolic relationship suggested by Duncan et al. (1980) to model the non-linear stress strain properties of the soils. A piece-wise linear stress-strain response is used to approximate the nonlinear stress-strain response of soils. SOILSTRUCT utilizes an incremental load analysis to create the piece-wise linear stress-strain response. The incremental process may result in a divergence from the true stress-strain curve. Chang and Duncan (1970) have indicated that the accuracy may be improved through the iterative analysis of load increment. For this process, an increment is analyzed at least two times. The modulus values are evaluated using the average values of stress from the previous increment and the first iteration during the second analysis of the load step. The SOILSTRUCT program allows the user to specify the number of iterations for each increment and the number of increments associated with each load step. During the iterations, the unload/reload modulus is used when the deviator stress decreases until the deviator stress for the current element exceeds the maximum past value.

Four different element types were used to model the soil, wall, and nails. These elements were:

(1) A two dimensional, subparametric, quadrilateral element (soil and wall).
(2) A one dimensional, two-node bar or spring element (nail).
(3) A one dimensional interface or slip element (nail/soil interface).
(4) An Euler-Bernoulli beam element (wall).

Quadrilateral Element. Doherty et al. (1969) developed a two dimensional subparametric (QM5) quadrilateral element to represent soils and some structural materials. The geometry of this element is defined by four external nodes, while the displacement functions include an internal fifth node. This fifth node improves the flexural response of the element. According to Tsui (1974), the quadrilateral element is better than a beam element when doing finite element analysis because the beam element has no thickness. Therefore, no mesh space is allocated for the actual wall location. By using a quadrilateral element to model the wall, there is no problem with incompatibility between adjacent elements since they are the same element type.

Bar Element. One dimensional bar or spring elements are used to model the behavior of braces or tiebacks. In this study, two node bar elements are used to simulate

the reinforcing nail. These bar elements are not included in the finite elements mesh initially. They are placed during the construction steps. The SOILSTRUCT user can specify a certain displacement to simulate slack in the nails prior to resisting the loads. No pre-displacement conditions were placed on the bar elements in this finite element analysis (FEA) study.

Interface Element. One dimensional interface or slip element elements were placed between the quadrilateral elements (soil) and the bar elements (nails) to permit relative movement between the two. Four nodes are used to define the element with two adjacent nodes having the same coordinates. This element possesses no thickness. Different relative movements ranging from complete slippage to no slippage can be modeled at the interface depending on the specified interface element stiffness.

Beam element. An Eulcr-Bernoulli beam element using hermite interpolation functions was utilized in place of the quadrilateral elements to model the soilcrete wall facing for the FEA. In addition to resisting axial stresses, the beam elements provide bending resistance. In SOILSTRUCT, the connection between beam elements is fixed, providing bending moment continuity between elements.

Finite Element Model. Three finite element models were used in the study. Two meshes consisted of 296 nodes and 275 elements. The third mesh had 312 nodes and 290 elements. Sixty interface elements were included in each of the meshes. The different meshes resulted from different approaches in modeling the shotcrete wall. Mesh #1 models the wall with a single column of quadrilateral elements. Mesh #2 uses beam elements; and mesh #3 contains two columns of two dimensional quadrilateral elements. Mesh #3 is shown on Figure 3.

Six bar elements are used to model one reinforcing nail. Accompanying the bar elements, twelve interface elements are placed at the soil-nail interface. No interface elements are positioned at the soil-wall interface.

Construction Steps

In order to simulate the actual construction progress of the soil nailed wall, six loading steps were applied sequentially in the finite element model. These steps are the following:

(1) Excavate the first two rows of elements as shown in Figure 3 and install the first row of nails.
(2) Excavate the next four rows of elements, and install second row of nails.
(3) Excavate the next one row of elements, and install third row of nails.
(4) Excavate the next two rows of elements, and install fourth row of nails.
(5) Excavate the next two rows of elements, and install fifth row of nails.
(6) Excavate the next row of elements to a depth of 19 feet.

All the soil elements are initially in the mesh and remain even after excavation. However, as they are excavated, SOILSTRUCT assigns them the physical properties of air (i.e weightless and no stiffness)

Wall Modeling

The shotcrete wall was represented in the finite element mesh as a single column of two dimensional quadrilateral elements (model #1), by beam elements (model #2) and by a double column of two dimensional quadrilateral elements (model #3). The wall is assumed to behave elastically and homogeneously. A Young's modulus was calculated from the familiar equation: $E = 57{,}000 \times f'_c$ where $f'_c = 3{,}000$ psi

For the beam element wall, the moment of inertia (I), cross section area (A), and height or thickness must be entered along with E. Based on an assumed wall thickness of 6 inches, an I of 216 in^4 per foot of wall was used with an area of 72 in^2 per foot of wall.

The actual Young's modulus of the third wall model must be adjusted to accommodate the two column thick model. The model Young's modulus (E_m) is obtained by first determining the model moment of inertial (I_m) based on the width and unit length of the modeled wall, then the rigidity of the model $(EI)_m$ is set equal to the rigidity of the actual wall $(EI)_a$. An E_m of 390,000 psi was used for this model.

Soil Modeling

In order to correctly model the soil response, SOILSTRUCT requires that both conventional and hyperbolic parameters be included in the input. The conventional soil strength parameters used in the actual design were used for the finite element analysis. These consist of: cohesion 100 psf, friction angle of 33°, soil unit weight of 115 pcf and a lateral earth pressure coefficient of 0.43.

The hyperbolic parameters are used to define the non-linear (i.e. hyperbolic) stress - strain response of the soil mass. These values are determined from a series of steps using data from either unconsolidated-undrained or drained triaxial tests. Detailed information for developing these parameters are provided by Duncan et al. (1980). Also shown in this reference is a compilation of hyperbolic parameters recommended when triaxial results are not available (as was the case for this study).

Nail Reinforcement Modeling

Six bar elements were used to model the reinforcing nails. The bar elements are connected end to end to form a nail. The orientation of the nails are shown on Figure 3. The top four rows of bar elements and the bottom row of bar elements are inclined at 15 degrees and 25 degrees from the horizontal respectively.

The composite grout-steel reinforcing nails are assumed to behave elastically and have perfect bonding between steel and grout. Therefore, an equivalent steel cross sectional area can be used in the finite element model. For this model, with a steel bar

area of 1 in^2 and grouting area of 19.6 in^2, an equivalent area of 3 in^2 was used for model nail. The calculations are as follows:

- $n = E_s/E_c$ = 29000000 psi/3122018.6 psi = 9.289
- $Area_s' = Area_c/n$ = (18.63 in^2)/9.289 = 2.0 in^2
- Total equivalent steel area = $Area_{bar} + Area_s'$
- Total equivalent steel area = (2.0 + 1.0)in^2 = 3.0 in^2

The stiffness (AE/L) of the actual nails are divided by the nails' spacing to accommodate the plain strain conditions. The model nail stiffness $(AE/L)_m$ is set equal to the actual nail stiffness $(AE/L)_a$. The nail stiffness that were used for the finite element analysis are shown below in table 1.

Table 1. Model bar element stiffness for the model nails (lb/ft/ft).

AE/L NAIL #1	AE/L NAIL #2	AE/L NAIL #3	AE/L NAIL #4	AE/L NAIL #5
6.787E6	6.787E6	6.445E6	6.807E6	6.458E6

Soil-Nail Interface Modeling

A total of sixty interface elements are utilized at the soil-nail interface. The interface elements are placed on the top and bottom of the bar elements, and are initially in the finite element mesh. An interface element does not have any thickness; consequently, it appears like a bar element with only two nodes.

COMPARISON OF FEA WITH FIELD RESULTS

Measured Deflections

As discussed previously, there were two monitoring stations, SD129 and SD130, at section #2 where wall displacements were measured. The displacements at different construction stages were recorded. Figure 4 shows the displacements which occurred at SD129. The maximum outward displacement of the wall occurs at the top and decreases with depth.

Predicted Results

Single Column - Quadrilateral Element Wall Model. The lateral wall displacements, at the end of each construction step, predicted by SOILSTRUCT for a wall modeled with a single column of quadrilateral elements are shown in Figure 5. Steps one to five involved excavation and installation of each sequential nail row. Step six is the final excavation.

Beam Element Model. The predicted deflection of the beam element wall model at the end of each construction step is shown on Figure 6. Steps one to five involved excavation and installation of each sequential nail row. Step six is the final excavation.

The beam elements are rigidly connected. This, combined with the outward deflection of the top of the wall and the inward pressure of the unexcavated soil at the base of the wall result in an inward (negative) displacement of the wall during the first two phases of the construction modeling. Modeling the whole shotcrete wall initially in the soil does not represent the actual condition since the shotcrete wall is constructed after the staged soil excavations. In spite of this limitation, the beam element model provides satisfactory displacement results at the end of construction. The beam elements provide flexural or bending resistance to the shotcrete wall, whereas the quadrilateral elements do not.

Double Column - Quadrilateral Element Wall Model. The predicted displacements of the double column quadrilateral element wall are shown on Figure 7. This mesh results in a smoother wall deflection as compared with the single column model.

Conclusion

The end of construction wall displacements for the three wall models are compared to the measured results (SD129 & SD130) on Figure 7. Overall, the beam elements did a better job of modeling the displaced wall (at end of construction) than did either combination of quadrilateral wall elements. The quadrilateral element wall models were much too flexible in the lower parts of the wall and provided accurate wall displacements only at the very top of the wall. The beam elements, on the other hand, modelled the stiffness of the wall extremely well indicating that the shotcrete wall had significant bending stiffness. The only exception to this is near the top of the wall where the beam element model is stiffer than the actual wall and underestimates the top of wall displacements. This is most likely due to cracking in the upper portions of the shotcrete wall, resulting in "hinges" that allows these large displacements to occur.

If SOILSTRUCT allowed for the modification of rigid beam joints to include some flexibility, and the upper two joints in this wall model were so modified, this beam model would be very capable of modeling quite accurately the displacements for the entire wall.

BIBLIOGRAPHY

Chang, C-Y. and Duncan, J.M. Nonlinear Analysis of Stress and Strain in Soil. Journal of Soil Mechanics and Foundations Division, ASCE, Vol. 96, No. SM5,; September, 1970.

Dumas, Christopher. Permanent Soil Nailed Wall I-5 Portland, Oregon. 1991; 41 p. Training Report to the Federal Highway Administration.

Duncan, J.M.; Byrne, P.; Wong K.S.; Mabry, P. Strength, Stress-Strain and Bulk Modulus Parameters For Finite Element Analyses of Stresses and Movements in Soil Masses. Geotechnical Engineering. 1980; 70 p. Department of Civil Engineering, University of California, Berkeley.

Elias V.; Juran I. Soil Nailing For Stabilization of Highway Slopes and Excavations. Federal Highway Administration, Publication # FHWA A-RD-89-193, June 1991.

Filz, G.; Clough, G. W.; Duncan, J.M. Draft User's Manual For Program Soilstruct (Isotropic) Plane Strain With Beam Element. 1990; 50 p. Virginia Polytechnic Institute and State University, Department of Civil Engineering.

Juran, I.; Elias, V.; M. ASCE. Soil Nailed Retaining Structures: Analysis of Case Histories. Geotechnical Special Publication No. 12. 232-244; 1990.

Nham, Huey S. Finite Element Analysis of a Soiled Nailed Wall and Case History Comparison. Master of Science Report. 1993;
90 p. Department of Civil and Environmental Engineering, Utah State University, Logan, Utah.

Sakr, T. C. Soil Nailing: Its Applicability To Bridge Embankment Retention. Report--Oregon Department of Transportation, Highway Division, Bridge Section. 1991; 12 p.

Tsui Y. A Fundamental Study of Tied-Back Wall Behavior. PhD Dissertation. Duke University. 1974. 258 p.

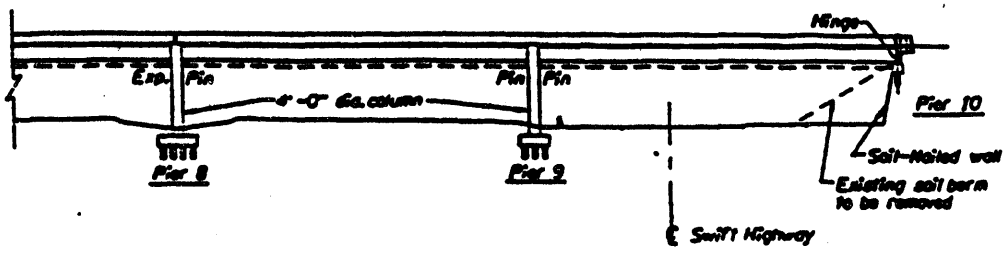


Figure 1. Oregon Slough Bridge
(Source: Sakr et al., 1991)

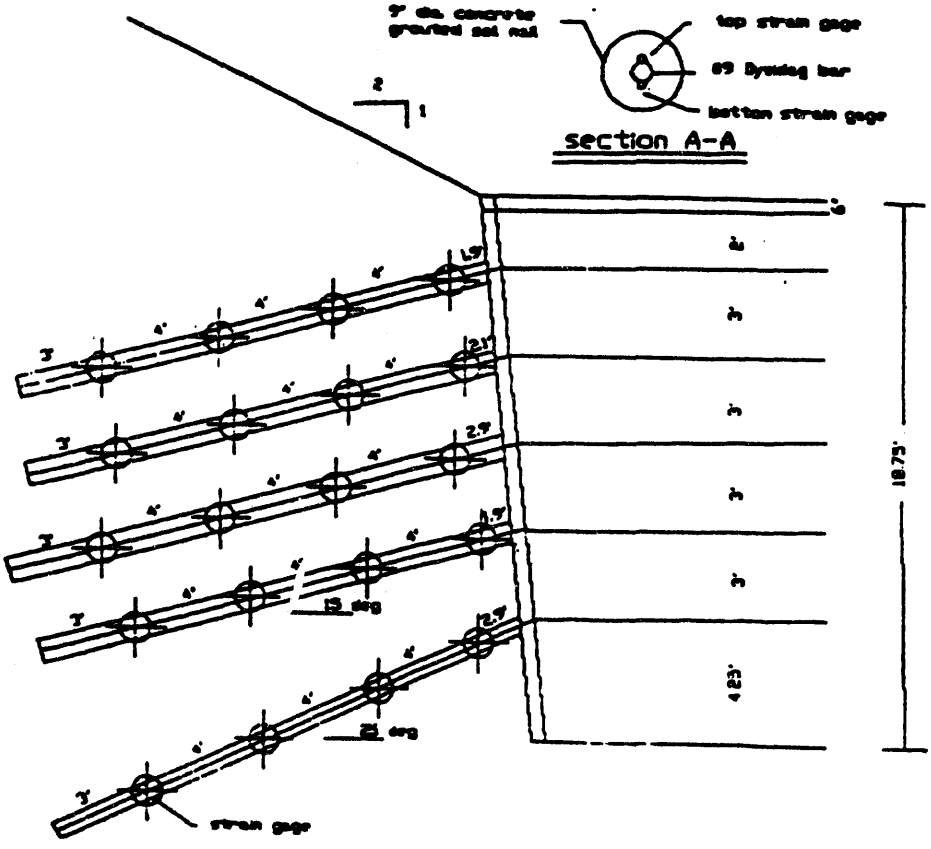


Figure 2. Soil nailed wall geometry at section #2
(Source: Sakr et al., 1991)

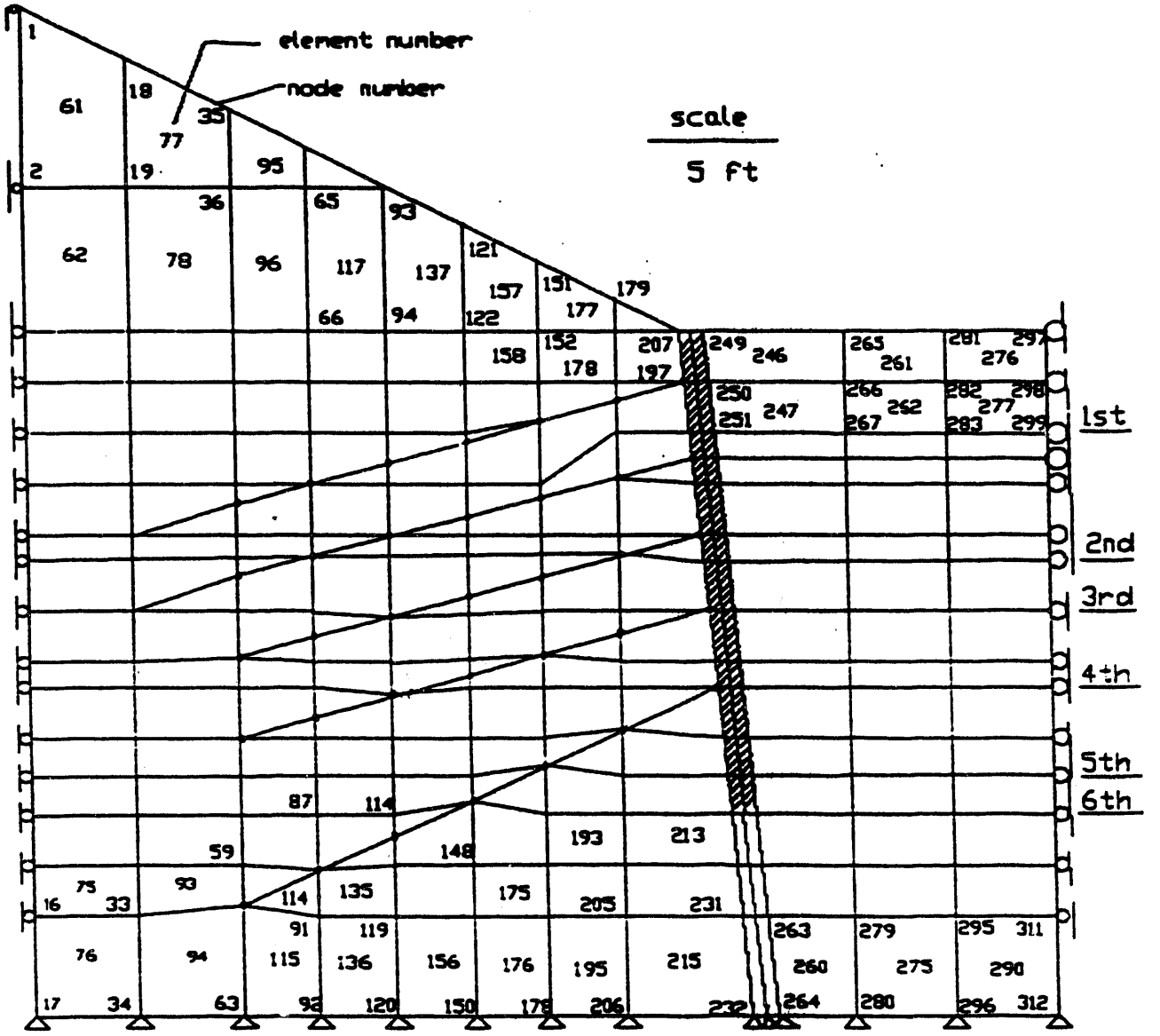


Figure 3. Finite elements mesh with two columns of quadrilateral elements representing the wall

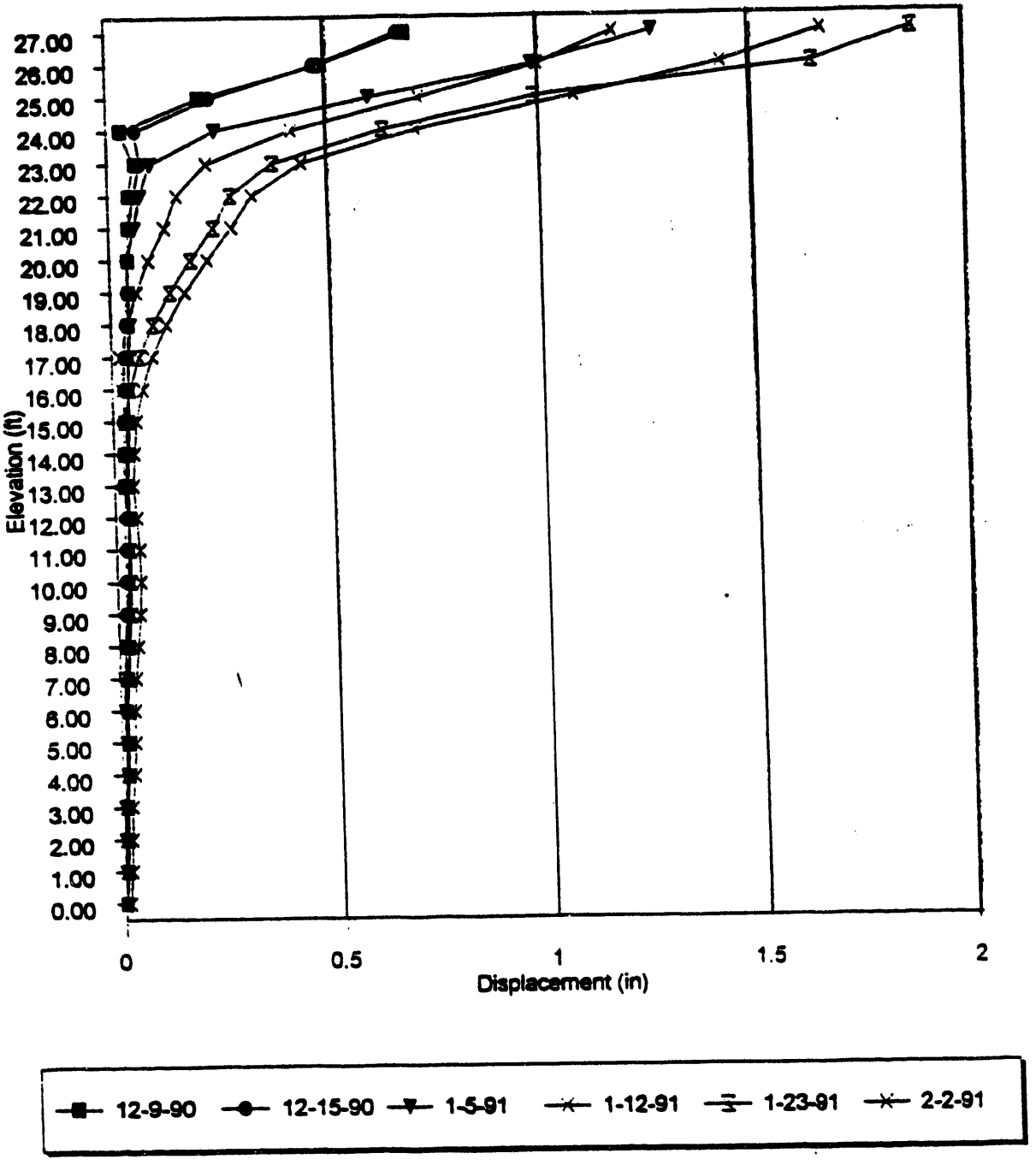


Figure 4. Measured displacements, SD129

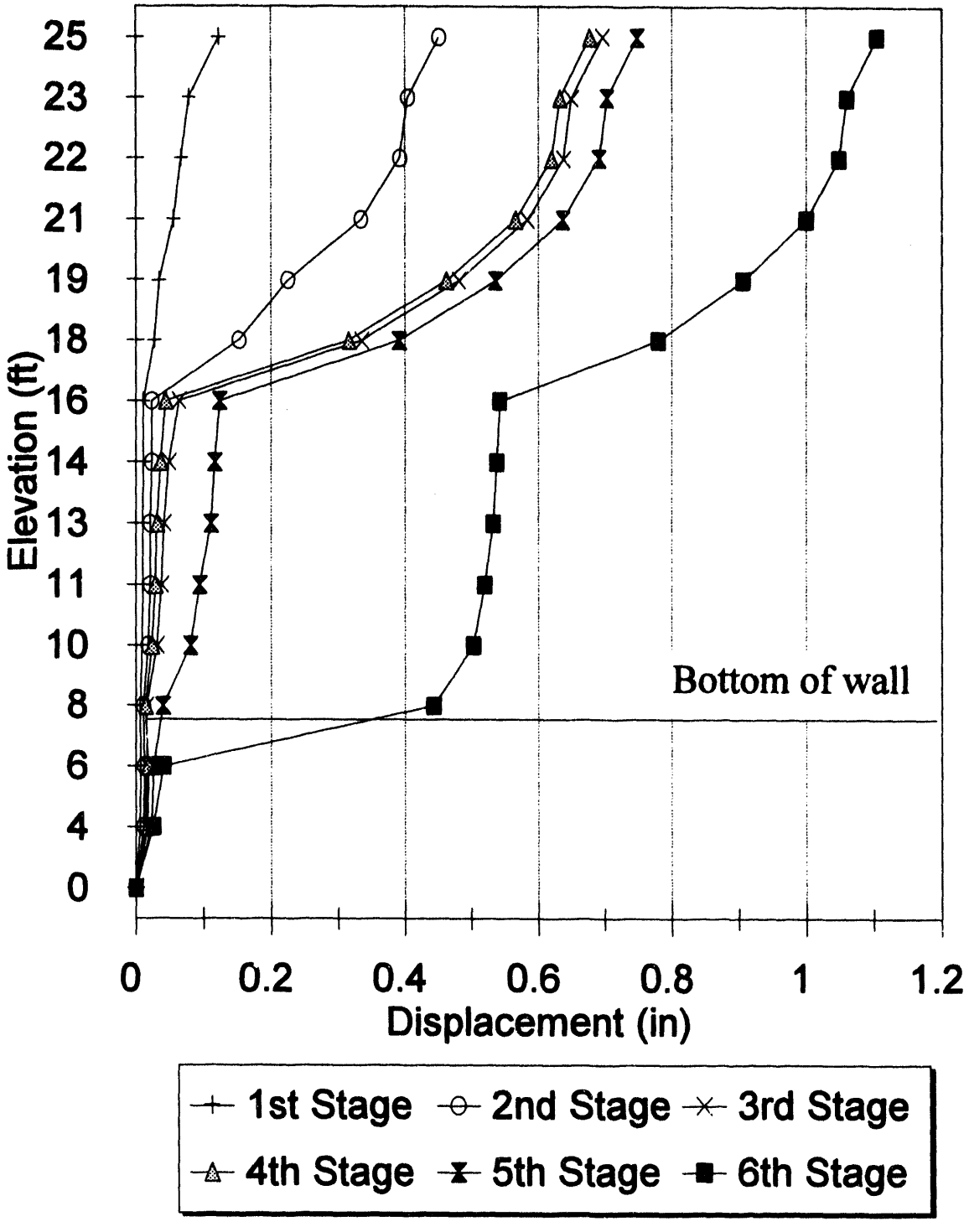


Figure 5. FEA predicted displacements for wall modeled with single quad elements

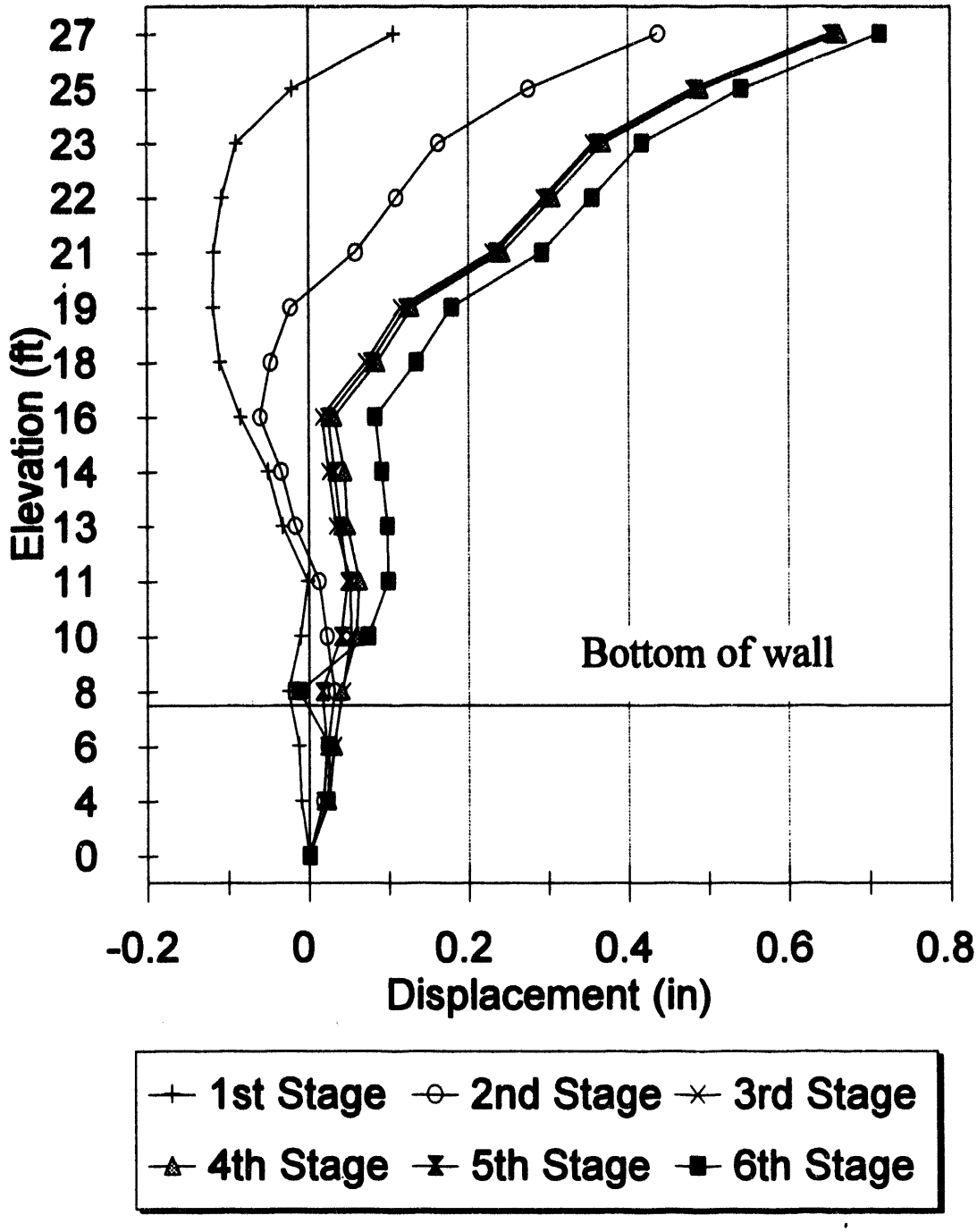


Figure 6. FEA predicted displacements for wall modeled with beam elements

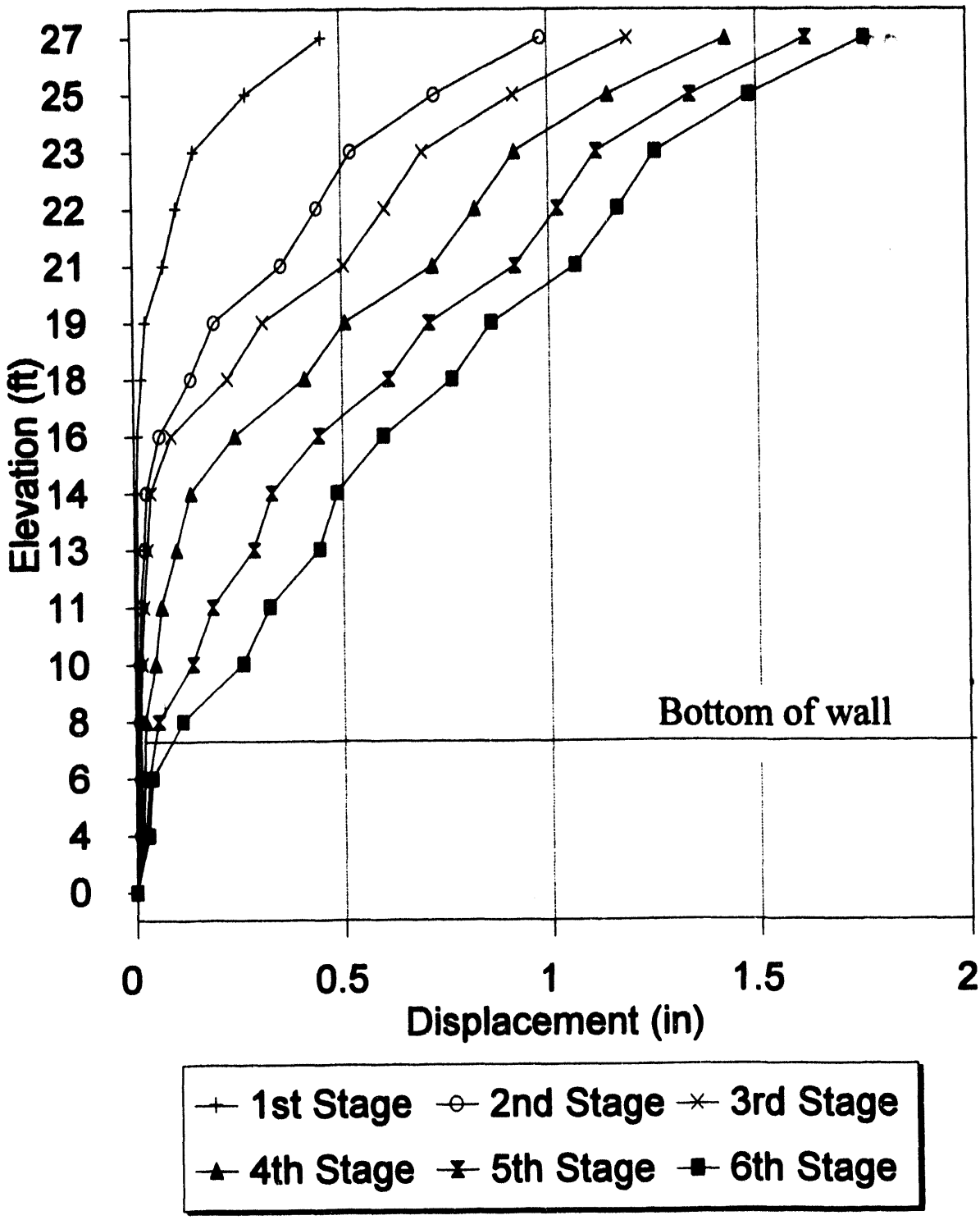


Figure 7. FEA predicted displacements for wall modeled with double quad elements

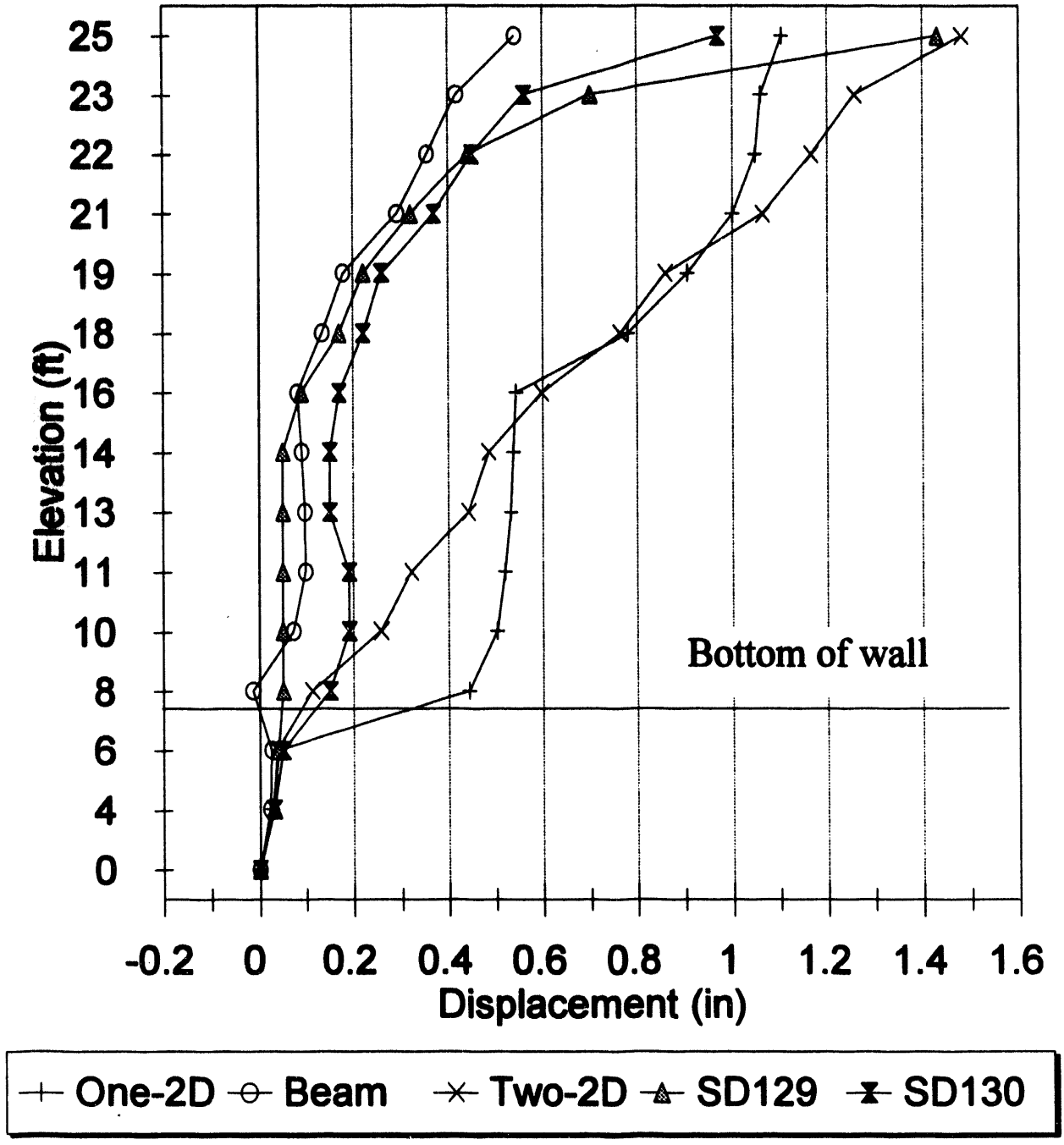


Figure 8. FEA predicted displacements vs. measured displacements, end of construction

Hydrogeology, Waste Disposal, Science and Politics
Proceedings 30th Symposium
Engineering Geology and Geotechnical Engineering, 1994

A Modified Cap Model Implemented in DYNA-3D

Isam G. Jardaneh[1], Thomas H. Fronk[2], Loren R. Anderson[3]

Abstract

In 1957, Drucker, Gibson and Henkel [1] were the first to introduce the concept of work-hardening theories of plasticity into the soil mechanics, and using the hardening cap to control dilatancy. This cap model and all of the recent ones are based on Drucker's stability postulates. Good results have been found using cap models. Most of these versions of cap models have been implemented in many specialized finite element codes, as well as general purpose finite element codes, such as DYNA-3D. A cap model is included in DYNA-3D, but there are problems modeling certain materials. The cap model is considered as a complicated material model due to the fact that it consists of three surfaces (the yield surface, the hardening cap, and the tension cutoff), which are intersecting in an nonsmooth fashion. In this paper, a modified cap model based on Hofstetter et al. 1993 [2] implemented in DYNA-3D is presented. The modified cap model incorporates a return mapping algorithm of Simo et al, 1988 [3] and Simo and Taylor, 1985 [4]. Koiter's generalized flow rule, Koiter, 1960 [5]. Kuhn-Tucker optimization conditions are also applied to the modified cap model. The Newton iteration technique for solving the nonlinear equations is used. This makes the convergence quadratic, i.e. faster and less computer time consuming. Finally, evaluation of the model is presented by comparing the results to the original DYNA-3D cap model which was developed by Simo et al, 1988 [6], and to test results.

1.0 Introduction

The cap model is based on classical incremental theory of work hardening plasticity. It was developed as part of a constitutive model to account for important characteristics of geological materials such as compaction, hardening, and failure. The cap model differs from other geological elasto-plastic models, in that the hydrostatic stresses are limited by capping the frictional failure envelope.

DiMaggio and Sandler [7] first introduced the cap model in 1971, and since then several versions of cap models have been successfully developed [8-16], as shown in Table (1). As a

[1]Research Assistant, Civil and Environmental Engineering, Utah State University, Logan, Utah.

[2]Assistant Professor, Mechanical and Aerospace Engineering, Utah State University, Logan, Utah.

[3]Professor and Department Head, Civil and Environmental Engineering, Utah State University, Logan, Utah.

Table 1 Features and Shortcomings of Cap Models.

Developers/ Year	Features	Shortcomings	Ref
DiMaggio, Sandler 1971	The first cap model, Drucker-Prager yield surface with an elliptical hardening cap.	Linear elastic. Not generalized.	[7]
Sandler, DiMaggio, and Baladi 1976	Generalized cap, nonlinear elastic, and tension behaviors are specified.	Numerical problems.	[8]
Sandler, DiMaggio, and Baladi 1976	Vertical hardening cap.	For rocks of low porosity, and loading and unloading bulk modulus are the same.	[8]
Sandler, DiMaggio, and Baron 1984	Extension of the cap model to include pore pressure and kinematic hardening effects.	Same as the original cap model.	[9]
Katona 1984	Viscoplastic type cap model.	Numerical solution problems, tension cutoff and viscous tension damage index need, and also hardening/softening function need modifications.	[10]
Resenda and Martin 1985	Drucker-Prager cap model. It may harden or soften and coupled to the yield surface.	Stability problems under certain conditions.	[11]
Faruque and Chang 1986	Same parameters for both failure surface and the yield cap.	Still under improvements.	[12]
Baladi and Schuster 1987	Cap model with strain-dependent elastic moduli.	Can't be used for all geological materials.	[13]
Faruque 1987	Cap model for plain concrete. Plain concrete failure surface including the hardening cap.	For concrete only.	[14]
Simo et al 1988	DYNA-3D cap model. Consistent numerical solution (closest- point projection), with viscoplastic extension (rate-dependent).	Doesn't work as advertised.	[6]
General Atomic 1989	Failure envelope and hardening cap are represented by on curve. Permit gradual yielding at the cap.	Still under improvements.	[15]
Abduljawwad et al 1992	Modified the original cap model to include the third invariant stress tensor and also the kinematic hardening rule.	Just appeared.	[16]

result of these investigations, more sophisticated cap models have evolved with a number of features which can be included or excluded in specific problems. These features include anistorpy, rate-dependency, pore pressure effects, and elasto-viscoplastic modelling.

The cap model has been used to study various geotechnical problems, such as ground shock effects from explosive sources, and soil-structure interactions problems, including buried pipeline, retaining walls, foundations, embankments, in situ tests, etc. Good results have been obtained using the cap model which make it well known and commonly used for solving geotechnical problems.

However, like other models, the cap model has some shortcomings such as, it is usually assumed that the isotropic model is independent of the third invariant of stress, a discontinuity is created at the intersection of the failure curve and the hardening cap, a non-continuous yield surface will cause computational difficulties, and the hardening cap is not defined in terms of both the shear and the normal plastic displacements.

In this paper a modified cap model that is implemented in DYNA-3D is presented, with its new features. Including return mapping algorithm, Koiter's generalized flow rule, Kuhn-Tucker optimization condition, and Newton iteration technique to solve nonlinear equations. Conclusion and recommendations are also presented.

2.0 Cap Model

In this section a description of the modified cap model features are presented; the cap model surfaces, Koiter's generalized flow rule applied to these surfaces, Kuhn-Tucker optimization conditions that will specify the activation of each mode, return mapping algorithm that will determine the value of the final stress for each increment, and finally, the characterization of the six different modes of this modified cap model.

2.1 Cap Model Surfaces

The surfaces of the modified model are plotted in stress space, as shown in Fig. (1) [2], in which the coordinates are the J_1 (the first invariant of the stress tensor), and $|\mathbf{s}|$ (the norm of the deviatoric stress tensor **s**). Three surfaces characterize the cap model. These are, the fixed failure envelope surface, the cap surface, and the tension cutoff surface. Details of these surfaces are presented below.

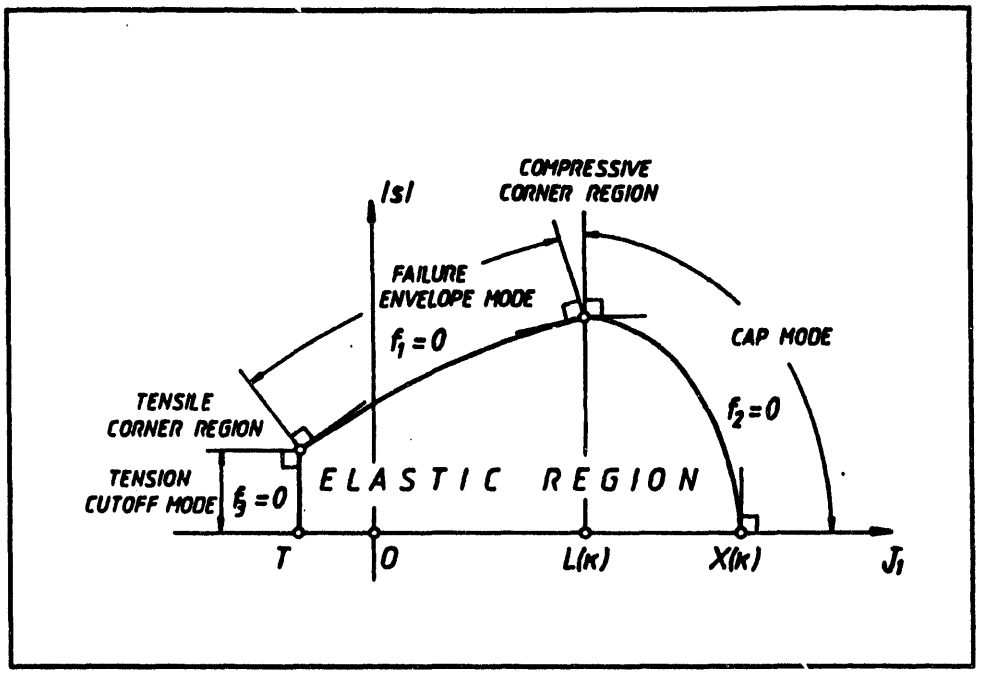


Figure 1 The Yield Surfaces of the Cap Model [2].

2.1.1 Fixed Failure Envelope Surface

The functional form of the fixed failure envelope surface is presented in the following equations:

$$f_1(\sigma) = |s| - F_e(J_1), \qquad \text{for } T \le J_1 < \kappa \tag{2.1}$$

where

$$F_e(J_1) = \alpha - \gamma \exp^{-\beta J_1} + \theta J_1 \tag{2.2}$$

where J_1 is the first invariant of the stress tensor and $|s|$ is the norm of the deviatoric stress tensor. T is a material constant referred to as the tension cutoff. κ is the hardening parameter. α, β, γ, and θ are the material parameters to be determined.

2.1.2 Hardening Caps

The functional form for representing the hardening caps are presented in the following equations:

$$f_2(\sigma,\kappa) = F_c(|s|, J_1, \kappa) - F_e(\kappa) \qquad for\ \kappa \le J_1 \le X(\kappa) \tag{2.3}$$

where

$$F_c(|s|, J_1, \kappa) = \sqrt{|s|^2 + \frac{1}{R^2}[J_1 - L(\kappa)]^2} \tag{2.4}$$

$X(\kappa)$ is the intersection point of the cap the J_1 axis. R is the shape factor which is the ratio of major to minor axes of
the ellipse. $L(\kappa)$ is the value of J_1 at the intersection of the cap and the fixed failure envelope surface. It is defined as

$$L(\kappa) = \langle \kappa \rangle = \begin{Bmatrix} \kappa & \kappa > 0 \\ 0 & \kappa \le 0. \end{Bmatrix} \tag{2.5}$$

where κ is the hardening parameter.

The point of intersection of the cap with the J_1 axis is defined as follows:

$$X(\kappa) = \kappa + R F_e(\kappa) \tag{2.6}$$

2.1.2.1 Hardening Behavior of the Cap

The parameters required for the hardening behavior of the cap are presented in the following equation:

$$\varepsilon_v^p = W(1 - \exp^{D(Z - X(\kappa))}) \tag{2.7}$$

D, W, and Z are the material parameters which govern the hardening behavior of the caps;

where W characterizes the maximum plastic volumetric strain, D denotes the total volumetric plastic strain rate which controls the initial loading moduli, and Z determines the initiation of the volumetric plastic deformation under hydrostatic loading conditions. ε_v^P is the effective volumetric plastic strain corresponding to the point X(κ), defined by integrating the following discontinuous equation

$$\dot{\varepsilon}_v^P = \begin{cases} \dot{\varepsilon}_v^P & \text{if } \dot{\varepsilon}_v^P \Rightarrow 0, \quad \text{or} \quad \kappa > 0 \quad \text{and} \quad \kappa > J_1 \\ 0 & \text{otherwise} \end{cases} \tag{2.8}$$

Where ε_v^P is the incremental plastic strain. The last equation was suggested is to avoid softening behavior, accordingly if the stress point is at the compressive corner point, movement of the cap is prevented and the model behaves as perfect plasticity.

2.1.3 Tension Cutoff Surface

The functional form of the tension cutoff is

$$f_3(\sigma) = T - J_1, \qquad \text{for} \quad J_1 = T \tag{2.9}$$

where T is as defined above, a material constant referring to the tension cutoff.

2.2 Koiter's Normality Law for Singular Yield Surfaces

Koiter, 1960 [5] proposed an associated flow rule for both elastic perfectly plastic, and work hardening materials. Singular yield surfaces with edges or corners are considered as a finite number of regular yield surface functions $f_\alpha(\sigma)$, such that the elastic domain is given by

$$f_\alpha(\sigma) < 0, \quad \text{where} \quad \alpha = 1,2,\ldots \ (\text{number of surfaces}) \tag{2.10}$$

The yielding will occur as soon as at least one of the functions $f_\alpha(\sigma)$ is equal to zero, all the other yield functions being negative (i.e., at least one yield surface is provoked).

The associated flow rule for elastic perfectly plastic materials, as proposed by Koiter, that will give the value of the plastic strain rate is as follows:

$$\dot{\varepsilon}^p = \sum_\alpha \Delta\lambda_\alpha \frac{\partial f_\alpha}{\partial \sigma} \tag{2.11}$$

where

$\Delta\lambda_\alpha = 0$ *if* $f_\alpha < 0$ *and also if* $f_\alpha = 0$, $\dot{f}_\alpha = \frac{\partial f_\alpha}{\partial \sigma}\dot{\sigma} < 0$;

$\Delta\lambda_\alpha \geq 0$ *if* $f_\alpha = 0$ *and* $\dot{f}_\alpha = 0$.

From the above equation, loading occurs if the stress rates are such that $f_\alpha>0$. While unloading occurs if $f_\alpha<0$. This will define $\Delta\lambda$ as follows: it is always non-negative and it is non-zero only if the state of stress is at the yield limit and no unloading occurs. It is noteworthy to mention that $\Delta\lambda$ is an indeterminate parameter, of dimension $(\text{time})^{-1}$. Time may be replaced by any other parameter provided it increases monotonously with time. $\Delta\lambda$ is not a material constant.

2.3 Kuhn-Tucker conditions

Plastic loading or elastic loading/unloading is formulated in Kuhn-Tucker form. The plastic strain rate is given by the associated flow rule in the form of Koiter's generalized flow rule as shown above. It is satisfied Kuhn-Tucker complementary conditions for $\alpha=1,2,...,m$:

$$\begin{aligned} \Delta\lambda_\alpha &\geq 0 \\ f_\alpha(\sigma) &\leq 0 \\ \Delta\lambda_\alpha f_\alpha(\sigma) &= 0 \\ \Delta\lambda_\alpha \dot{f}_\alpha(\sigma) &= 0 \end{aligned} \tag{2.12}$$

The last equation is known as the consistency conditions.

From the above equation, the discrete Kuhn-Tucker conditions that governs the change of the discrete consistency parameter $\Delta\lambda_{i,n+1}$ are

$$\begin{aligned} &\Delta\lambda_{i,n+1} \geq 0, \quad f_{i,n+1} \leq 0 \quad \textit{and} \\ &\Delta\lambda_{i,n+1} f_{i,n+1} = 0 \qquad i=1,2,3 \end{aligned} \tag{2.13}$$

2.4 Return Mapping Algorithm

In this model a general closest-point-projection algorithm [3,4] for multi-surface plasticity is used, which is unconditionally convergent, and is capable of accommodating an arbitrary number of yield surfaces intersecting in a nonsmooth fashion. The algorithm is basically consists of two major steps, the formulation of the elastic trial stress, also referred to an elastic predictor and the return mapping to the yield surface, which is the closest point projection of the trial stress onto the yield surface, also referred to as a plastic corrector. For multisurface plasticity, using Koiter's generalized flow rule yields the following return mapping algorithm

$$\epsilon^{P}_{n+1} = \epsilon^{P}_{n} + \Delta\,\epsilon^{P}_{n+1} = \epsilon^{P}_{n} + \sum_{i=1}^{3} \Delta\lambda_{i,n+1}\,\frac{\partial f_{i,n+1}}{\partial \sigma_{n+1}} \tag{2.14}$$

$$\sigma^{Trial}_{n+1} = C : (\epsilon_{n+1} - \epsilon^{P}_{n}) \tag{2.15}$$

$$\sigma_{n+1} = C : (\epsilon_{n+1} - \epsilon^{P}_{n+1}) = \sigma^{Trial}_{n+1} - C : \Delta\epsilon^{P}_{n+1} \tag{2.16}$$

where $\Delta\lambda = \lambda_{i,n+1}\,\Delta t$ and C is the elastic tensor.

The trial functional forms of the cap model surfaces can be calculated as follows

$$\begin{aligned} f^{Trial}_{1,n+1} &= f^{Trial}_{1,n+1}\left(|s^{Trial}_{n+1}|, J^{Trial}_{1,n+1}\right) \\ f^{Trial}_{2,n+1} &= f^{Trial}_{2,n+1}\left(|s^{Trial}_{n+1}|, J^{Trial}_{1,n+1}, \kappa_{n}\right) \\ f^{Trial}_{3,n+1} &= f^{Trial}_{3,n+1}\left(J^{Trial}_{1,n+1}\right) \end{aligned} \tag{2.17}$$

where

$$\begin{aligned} s^{Trial}_{n+1} &= 2G\left(e_{n+1} - e^{P}_{n}\right) \\ J^{Trial}_{1,n+1} &= 3K\left(\bar{J}_{1,n+1} - \bar{J}^{P}_{1,n}\right) \end{aligned} \tag{2.18}$$

where G is the shear modulus, K is the bulk modulus, e is the devaitoric strain tensor, J_1 is the volumetric strain, the subscript n+1 and n refer to the time, and the superscript P refers to the plastic component.

The final stresses are obtained from

$$\begin{aligned} s_{n+1} &= s_{n+1}^{Trial} - 2G\,\Delta e_{n+1}^{P} \\ J_{1,n+1} &= J_{1,n+1}^{Trial} - 3K\,\Delta \bar{J}_{1,n+1}^{P} \end{aligned} \tag{2.19}$$

2.5 Implementing the Cap Model

Applying the return mapping algorithm and Kuhn-Tucker conditions for multisurface plasticity, six different modes of behavior are possible.

Depending on the trial stress, Kuhn-Tucker conditions will specify the mode that is invoked. Applying return mapping algorithm the final stress can be calculated.

2.5.1 Elastic Mode

Elastic behavior occurs when the stress is within the failure envelope and deformations are recoverable. This mode is characterized by the following equation

$$f_{i,n+1}^{Trial} < 0 \rightarrow f_{i,n+1} < 0 \rightarrow \Delta\lambda_{i,n+1} = 0 \qquad i=1,2,3 \tag{2.20}$$

Various types of linear and nonlinear elastic behavior can be implemented. However, most models only allow linearly elastic behavior. For linear elastic behavior a constant bulk modulus, K, and a constant shear modulus, G, are required.

2.5.2 Failure Mode

Failure occurs when the stress point lies on the failure envelope. This mode is characterized by

$$f_{1,n+1}^{Trial} > 0,\ \Delta\lambda_{1,n+1} > 0 \ \textit{and}\ \Delta\lambda_{2,n+1} = \Delta\lambda_{3,n+1} = 0 \tag{2.21}$$

Failure envelope may be either, fixed or movable (hardening) but are generally assumed to be fixed.

2.5.3 Cap Mode

The cap mode is initiated when the stress point lies on the movable cap and pushes it outward. The motion of the cap is due to the plastic strain and models material hardening (the cap does not move during purely elastic deformation). This mode is characterized by

$$f_{2,n+1}^{Trial} > 0,\ \Delta\lambda_{2,n+1} > 0 \ and\ \Delta\lambda_{1,n+1} = \Delta\lambda_{3,n+1} = 0 \qquad (2.22)$$

Although various geometric shapes can be used for the cap, elliptical surfaces have been found acceptable for wide range of geological materials.

The compaction resulting from the associated flow rule leads to an increase in the hardening. Therefore the cap moves to the right, increasing the extent of the elastic region inside the new yield surface.

The behavior of the cap depends on whether a soil model or rock model is used.

2.5.4 Tension Cutoff Mode

This mode is characterized by

$$f_{3,n+1}^{Trial} > 0,\ \Delta\lambda_{3,n+1} > 0 \ and\ \Delta\lambda_{1,n+1} = \Delta\lambda_{2,n+1} = 0 \qquad (2.23)$$

The tension cutoff procedure may take various forms. For simplicity, the tension cutoff criterion is chosen as $J_1 = T$, in which T represents the maximum allowable hydrostatic tension.

2.5.5 Tensile Corner Mode

This mode invoke if the trial stress fall in the tension cutoff corner. This mode is characterized by

$$\Delta\lambda_{1,n+1} > 0,\ \Delta\lambda_{3,n+1} > 0 \ and\ \Delta\lambda_{2,n+1} = 0 \qquad (2.24)$$

Since both the failure envelope and the tension cutoff surfaces behave as ideal plasticity, the return stress point is the intersection of these two surfaces.

2.5.6 Compressive Corner Mode

This mode invoke if the trial stress fall within the compressive corner. This mode is characterized by

$$\Delta\lambda_{1,n+1} > 0,\ \Delta\lambda_{2,n+1} > 0 \textit{ and } \Delta\lambda_{3,n+1} = 0 \qquad (2.25)$$

In this mode the failure envelope and the cap surfaces behave ideal plasticity. Therefore the final stress point must lie at the intersection of the cap and the failure envelope.

3.0 Applications

The modified cap model has been implemented in the general purpose finite element code DYNA-3D. The Material Model Driver in DYNA-3D makes it easy to check the accuracy of new models. Uniaxial strain tests are simulated in DYNA-3D. These tests are easy to run and give a good indication of the accuracy of the model. Three geological materials have been tested using the modified cap model. The results are compared to the DYNA-3D cap model implemented by Simo et al, 1988 [6].

3.1 DYNA-3D

DYNA-3D is an explicit, nonlinear, finite element code, for analyzing the transient dynamic response of three-dimensional solids and structures. DYNA-3D offers different element formulations, and many material models to represent a wide range of material behavior. It includes the cap model to account for material hardening. However, there are concerns about the accuracy of this model.

The advantage of using general purpose codes is the versatility, the documentation, the availability, the pre- and postprocessing capabilities, and the reputation. However, the constitutive relationships of geological material mechanics are not conventional and require codes that have been written specifically for these materials to adequately describe their behavior.

The Material Model Driver is also included in DYNA-3D to allow plotting of the stress-strain response predicted by a material model under a given load path. This feature is particularly useful when fitting complex material models to experimental data, or when using a complex model for the first time. The dynamic equations of motion are not used by the Material Model Driver, and therefore the material behavior is simulated independent of inertial effects. For these reasons the LLNL version is best suited for soil and rock dynamic problems.

3.2 Uniaxial strain tests

Uniaxial strain tests are important in representing the material behavior and the construction of new models. The simple uniaxial strain test is performed by placing a cylindrical specimen in a stiff enclosure which prevents lateral strains, and measures the axial strain produced by a given loading history. Ideally, there is only one nonzero component of strain, which is the axial strain.

3.3 Examples

Geological materials of three different types are used to verify the modified cap model. Soil material [7] (MaCormick Ranch Sand), high strength concrete material [6] (TerraTek Research Dynamic Concrete Test), and rock material [17] (Limestone Rock). The parameters of the above materials are given in Table (2).

Table 2 Parameters for Uniaxial Strain Test Materials.

Soil/Rock Type [Ref]	B Ksi (MPa)	ν	α Ksi (MPa)	β 1/Ksi (1/MPa)	γ Ksi (MPa)	θ	R	D 1/Ksi (1/MPa)	W	Z Ksi (MPa)
MaCormick Ranch Sand [7]	100. (689.)	.25	.25 (1.723)	.67 (.097)	.18 (1.24)	0.0	2.5	.67 (.097)	.066	.175
TerraTek Research Dynamic Concrete Test [6]	6000 (41340)	.22	2.1 (14.47)	.30 (.0454)	1.3 (8.957)	.116	9.7	.006 (8.71E-4)	.2	56.0 (385.84)
Limestone Rock [17]	3261 (22467)	.253	100.1 (690.)	2.7E-3 (3.92E-4)	87.08 (600.)	0.0	5.5	.01 (1.45E-3)	.20	67.78 (467.)

3.4 Results

Figures (2),(3) and (4) show the comparison between the DYNA-3D cap model and the modified cap model. Figure (2) compares the MaCormick Ranch Sand sample. The axial stress vs. the axial strain is plotted. Experimental data are also shown. These data are scaled from Ref. [7]. The modified cap model fits the experimental data better especially on the hardening cap. Unloading behavior of both models are not close to the experimental data, however, the modified cap model results are closer. DYNA-3D cap model predicts the maximum axial stress better. Both models have similar initial elastic behavior, failure envelope, and tension cutoff.

Figure (3) compares the two models for the high strength concrete sample. Good agreement between the two models is shown. The maximum axial stresses are very close in both models, and also the tension cutoff values. The initial elastic and the elastic unloading behaviors of both models are similar. The failure envelope predictions are slightly different. No experimental data are available.

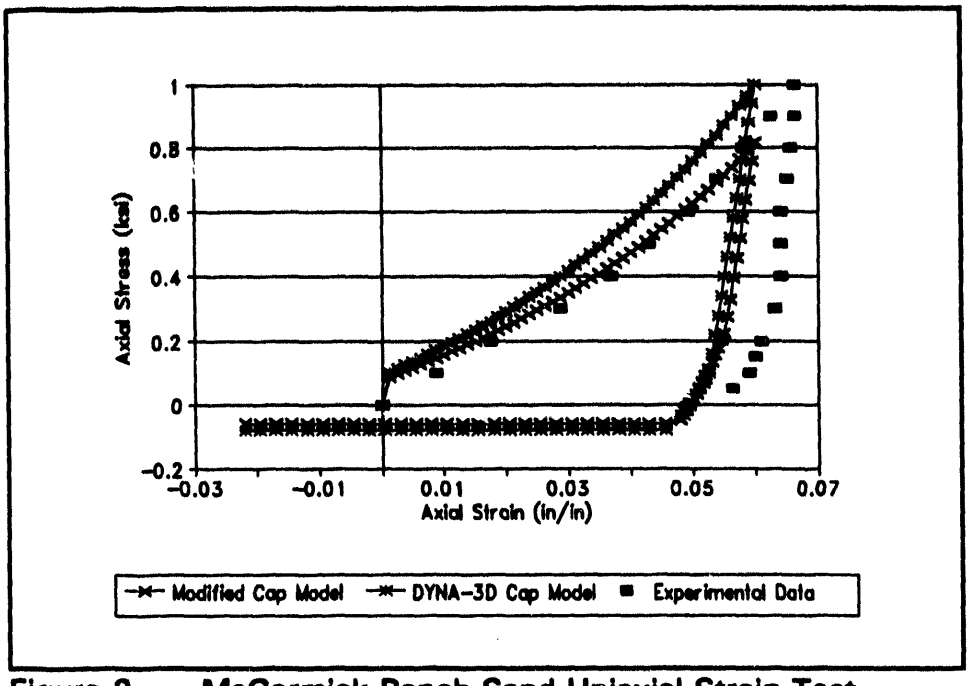


Figure 2 MaCormick Ranch Sand Uniaxial Strain Test.

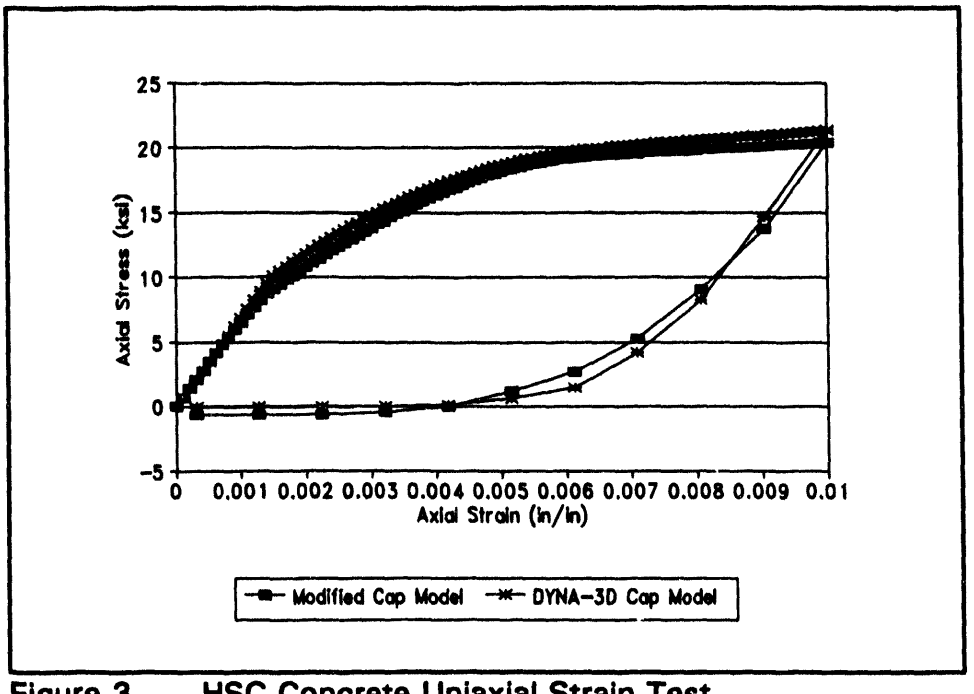


Figure 3 HSC Concrete Uniaxial Strain Test.

Figure(4) compares the limestone rock sample. It also shows good agreement between DYNA-3D cap model and the modified model. The initial elastic behavior is similar. The hardening cap behavior for the modified cap model is lower than the DYNA-3D cap model. The elastic

unloading predictions are also slightly different for both models. And the tension cutoff predictions are clearly different due to the differences in the maximum axial stress predicted. No experimental data are available.

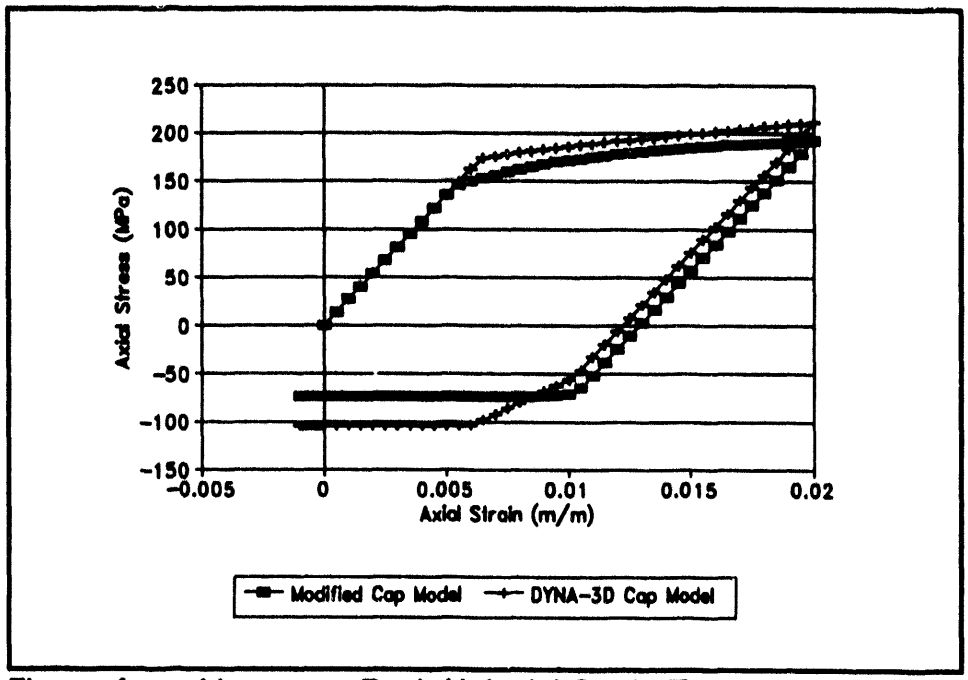


Figure 4 Limestone Rock Uniaxial Strain Test.

4.0 Conclusions and Recommendations

The following conclusions can be stated

1- Good agreement has been found between the DYNA-3D cap model and the modified cap model.
2- From the only available experimental data, the modified cap model shows a better fit of the hardening cap.
3- From a programming point of view, the modified cap model is simple and easy to follow.
4- The nonlinear equations are solved using Newton iteration method. This method converges quadratically, i.e. the modified cap model is faster.
5- New features are implemented in the modified cap model, including Koiter's generalized flow rule, Kuhn-Tucker conditions, and return mapping algorithm.

More tests and simulations using DYNA-3D and the modified cap models need to be carried out. These simulations would allow further examination of the model and verification of computer time. A dynamic compaction simulation (finite element analysis) will be modeled and tested by both models.

5.0 References

1. Drucker, D. C., Gibson, R. E., and Henkel, D. J., 1955. *Soil Mechanics and Work-Hardening Theories of Plasticity*. **Transactions ASCE**. Paper No. 2864.

2. Hofstetter, G., Simo, J. C., and Taylor, R. L., 1993. *A Modified Cap Model: Closest Point Solution Algorithms*. **Computers and Structures**. Vol. 46, No. 2, pp 203-214.

3. Simo, J. C., Kennedy, J. g., and Govindjee, S., 1988. *Non-Smooth Multisurface Plasticity and Viscoplasticity. Loading/Unloading Conditions and Numerical Algorithms*. **International Journal for Numericaland Analytical Methods in Geomechanics**. Vol. 26, pp 2161-2185.

4. Simo, J. C., and Taylor, R. L., 1985. *Consistent Tangent Operators for Rate-Independent Elastoplasticity*. **Computer Methods in Applied Mechanics and Engineering**. Vol 48, pp 101-118.

5. Koiter, W. T., 1960. *General Theorems for Elastic-Plastic Solids*. **Progress in Solid Mechanics**. Edited by Sneddon, I. N., and Hill, R., Vol. I, pp 167-218.

6. Simo, J. C., JU J.-W., Pister, K. S., and Taylor, R. L., 1988. *Assessment of Cap Model: Consistent Return Algorithms and Rate-Dependent Extension*. **Journal of Mechanical Engineering**, ASCE, Vol. 114, No. 2, February, pp 191-218.

7. DiMaggio, F. L., and Sandler, I. S., 1971. *Material Model for Granular Soils*. **Journal of Engineering Mechanics Division**, ASCE, Vol. 97, No. EM3, June, pp 935-950.

8. Sandler I. S., DiMaggio F. L., and Baladi G. I., 1976. *Generalized CAP Model for Geological Materials*. **Journal of the Geotechnical Engineering Division**, ASCE , GT7, July, pp 683-699.

9. Sandler, I. S., DiMaggio, F. L., and Baron, M. L., 1984. *An Extension of the Cap Model-Inclusion of Pore Pressure Effects and Kinematic Hardening to Represent an Anisotropic Wet Clay*. **Mechanics of Engineering Materials**. Edited by Desai, C. and Gallagher R. John Wiley and Sons Ltd.

10. Katona, M. G., 1984. *Evaluation of Viscoplastic Cap Model*, **Journal of Geotechnical Engineering**, ASCE, Vol. 110, No. 8, August, pp 1106-1125

11. Resende, L., and Martin, B., 1985. *Formulation of Drucker-Prager Cap Model*. **Journal of Mechanical Engineering**, ASCE, Vol. 111, No. 7, July, pp 855-881.

12. Faruque, M. O., and Chang, C. J., 1986. *New Cap Model for Failure and Yielding of Pressure-Sensitive Materials*. **Journal of Mechanical Engineering**, ASCE, Vol. 112, No. 10, October, pp 1041-1053.

13. Baladi, G. Y., and Schuster S. H., 1987. *A Cap Model with Strain-Dependent Elastic Moduli.* **Proceedings of the 2nd International Conference on Constitutive Laws for Engineering Materials**. Desai, C. S. et. al. (ed.), University of Arizona, Tucson, Arizona.

14. Faruque, M. O., 1987. *A Cap Type Constitutive Model for Plain Concrete.* **Proceedings of the 2nd International Conference on Constitutive Laws for Engineering Materials**. Desai, C. S. et. al. (ed.), University of Arizona, Tucson, Arizona.

15. Pelessone, D., 1989. *A Modified Formulation of the Cap Model.* Draft presented to Defence Nuclear Agency. General Atomic.

16. Abduljauwad, S. N., Al-Buraim, I., and Al-Ghanmady, H. H., 1992. *Mixed Hardening, Three-Invariants Dependent Cap Model.* **Journal of Mechanical Engineering**, ASCE, Vol. 118, No. 3, March, pp 620-637.

17. Chu, H. S., and Brandt, H., 1987. *Short Communication "Constants for an Elastic-Plastic CAP Model for Limestone".* **Int. J. Num. Analy. Meth. Geom.** Vol. 11, pp 193-202.

Hydrogeology, Waste Disposal, Science and Politics
Proceedings 30th Symposium
Engineering Geology and Geotechnical Engineering, 1994

EFFECT OF GEOGRID REINFORCEMENT ON SEEPAGE THROUGH EARTH-FILL DAM CORES

G. H. Gregory and S. Bang

Department of Civil and Environmental Engineering
South Dakota School of Mines and Technology
Rapid City, SD 57701

ABSTRACT

A conceptual model was developed to define the restrictions on soil processing and compaction, and potential seepage mechanisms related to the inclusion of geogrids in a dam core. Hydraulic conductivity tests were performed using rigid-wall permeameters. The tests covered three soil types normally used for dam cores. They included tests with and without geogrids and different levels of soil processing and compaction. Hydraulic conductivity values were slightly to moderately higher for the test specimens which included the geogrid. The test results were analyzed statistically and normalized values were used as input data for a finite element method of analysis of seepage through a hypothetical earth-fill dam core, with and without geogrids. The analysis showed an increase in phreatic surface elevation and increased flow through the dam core, however these increases were relatively small. The results of this study indicate that these increases should be in a range that can be appropriately managed and accommodated in design and construction.

INTRODUCTION

Geogrids offer a significant potential for reinforcement of earth-fill dams. Large savings in cost and construction time are possible by utilizing geogrid reinforcement to achieve steeper side slopes (and thus less fill) than for the non-reinforced cases. In cases where ideal soil materials are not available on or near the site, geogrids may allow the use of available soils, while maintaining acceptable factors of safety against the slope failures.

In order to realize the maximum practical benefit of geogrid reinforcement in dams, it will often be necessary to include geogrids in the low-permeability soil core zones. There currently exists a widespread reluctance among dam designers to penetrate the impervious core zones with geogrid materials because little information is available on the seepage effects of geogrids in such applications.

The scope of this study consisted of a laboratory testing program, statistical analysis and correlation of laboratory test results, and a finite element method (FEM) of computer analysis of seepage through a hypothetical earth-fill dam core, with and without geogrid reinforcement.

LABORATORY TESTING PROGRAM

The laboratory testing program was designed to obtain hydraulic conductivity values of the soil and the composite material consisting of the soil and the geogrid (polysoil). Three different soil samples, covering the range typically used for dam core construction, were used for laboratory testing. All references to optimum moisture content and maximum dry density are based upon standard Proctor (ASTM D 698, Ref. 1).

Previous laboratory test results of the soil samples, consisting of liquid limit and plastic limit, percent finer than number 200 mesh sieve, moisture-density relationship (ASTM D 698) are shown in Table - 1. Two of the soils classified as CH materials. One is nearer the lower end of the CH range while the other has a significantly higher plasticity index and percent finer than number 200 mesh sieve. The remaining soil classified as CL material.

TABLE 1
BULK SOIL SAMPLE PROPERTIES

Sample ID	OMC %	MDD pcf	LL	PI	(-)200 Sieve %	Group
3IB	21.1	100.2	63	43	89	CH-Fat Clay
9RT	25.5	93.4	77	52	96	CH-Fat Clay
4PT	18.9	106.4	42	25	58	CL-Sa. Lean Clay

Experimental Hydraulic Conductivity Test Parameters

The experimental hydraulic conductivity testing program with the large permeameters (model K-612 Compaction Permeameters manufactured by Soiltest® Products Division of ELE International, Inc.) was designed to compare k values of regular soil specimens, thoroughly processed and compacted using a method simulating the kneading compaction technique, with k values of polysoil specimens prepared from less-processed soil containing a geogrid and compacted using the static technique. Nine test groups were identified. These consisted of the regular soil specimens described above for each of the three bulk soil samples, and the polysoil specimens described above, for the three bulk soil samples, with geogrid oriented vertically in one group and horizontally in another (Table - 2).

All tests were performed using deaired distilled water as the permeant. Since all specimens were fully saturated during the test, the only remaining variable within each test group would be compaction density. The testing program was developed to vary the compaction density in each test group, over a range sufficiently large to determine the general effect on k values, and to facilitate the estimation of the density-k value relationship.

TABLE 2
EXPERIMENTAL HYDRAULIC CONDUCTIVITY TESTS

Test Group	Test ID	Soil ID	Test MDD%	Test Description Material-Processing-Compaction
1	HC601	3IB	102.29	Soil-Thorough-Kneading
2	HC604	4PT	102.81	Soil-Thorough-Kneading
3	HC603	9RT	95.26	Soil-Thorough-Kneading
4	HCG601	3IB	102.39	Polysoil, Geogrid Vert.-Less-Static
4	HCG605	3IB	96.21	Polysoil, Geogrid Vert.-Less-Static
4	HCG609	3IB	92.11	Polysoil, Geogrid Vert.-Less-Static
5	HCG602	4PT	98.10	Polysoil, Geogrid Vert.-Less-Static
5	HCG604	4PT	100.82	Polysoil, Geogrid Vert.-Less-Static
5	HCG608	4PT	95.99	Polysoil, Geogrid Vert.-Less-Static
6	HCG603	9RT	95.68	Polysoil, Geogrid Vert.-Less-Static
6	HGC606	9RT	92.97	Polysoil, Geogrid Vert.-Less-Static
6	HCG607	9RT	93.97	Polysoil, Geogrid Vert.-Less-Static
7	HCG6H3	3IB	97.30	Polysoil, Geogrid Horiz.-Less-Static
8	HCG6H2	4PT	101.34	Polysoil, Geogrid Horiz.-Less-Static
9	HCG6H1	9RT	94.30	Polysoil, Geogrid Horiz.-Less-Static

The soil for the polysoil specimens was prepared by manually breaking down the air-dried sample with a heavy sample cutter. This soil was less processed and the resulting specimen contained clods with a maximum size of about two inches (5 cm).

Hydraulic Conductivity Test Procedures

Hydraulic conductivity test procedures, following specimen preparation, were basically the same for both soil tests and polysoil tests. The top inlet of the permeameter was connected to the head-pressure line on the triaxial panel and a vacuum pump was connected to the bottom inlet. Saturation was started by applying deaired, distilled water under pressure at the top of the specimen and a vacuum at the base of the specimen. The head pressure ranged between 10 and 20 psi and the vacuum was approximately two to four psi, depending on the soil material type and density. The vacuum was continued for approximately one to three hours, or until water was observed seeping from the bottom of the specimen. Water under back pressure was then

applied to the bottom of the specimen and a hydraulic gradient was established across the specimen. Hydraulic gradients used in the various tests ranged from 20 to 141.

The saturation process continued until no air bubbles were observed in the back pressure line from the bottom of the specimen. Saturation was then checked by closing the valve on the back pressure line and leaving the head pressure line open. The pore pressure change on the bottom of the sample was then observed. If the pore pressure on the base of the specimen equalized with the head pressure in a few minutes, the specimen was assumed to be saturated. Each test was continued until four consecutive k-value readings had a maximum variation of 95 percent from the average of the four values for specimens with k values in the E-09 cm/sec range, or a maximum variation of 50 percent from the average of the four values for specimens with k values in the E-08 to E-06 cm/sec range.

The ratio of outflow to inflow was also required to be between 0.75 and 1.25 for each of the final four readings. The k value was then taken as the average of the four consecutive readings meeting the above criteria. A summary of the experimental hydraulic conductivity test results is presented in Table - 3.

STATISTICAL ANALYSIS AND CORRELATION

The laboratory test results from this study and the previous test results were analyzed statistically and correlated to produce normalized values for comparative purposes and for the FEM analysis. The statistical analysis included confidence interval estimation, linear regression and best-fit curve analysis. Correlations were made between the previous test results and those of this study, between various test groups in this study, and among various compacted densities within each test group.

The linear regression comparison described above for soil sample 3IB indicates a k value of 4.652E-08 cm/sec for soil (HC tests) and a k value of 5.335E-08 cm/sec for polysoil (HCG tests), at a density of 91 percent of maximum. The k values at a density of 102 percent are 2.96E-09 cm/sec and 7.88E-09 cm/sec for soil and polysoil, respectively. The linear regression comparison for soil sample 4PT indicates k values of 3.64E-08 cm/sec and 1.82E-06 cm/sec for the soil and polysoil, respectively, at a density of 91 percent of maximum. The k values at 104 percent of maximum density are 1.30E-08 cm/sec and 4.312E-07 cm/sec for the soil and polysoil, respectively. The best-fit curve comparison for soil sample 9RT indicates a k value of 4.0E-09 cm/sec for soil and a k value of 7.82E-08 cm/sec for polysoil at 93 percent density. The k values at 103 percent density are 1.4E-09 cm/sec and 3.6E-09 cm/sec for soil and polysoil, respectively. Comparisons for all three soil samples indicate a smaller difference in k values between soil and polysoil as the density increases.

The polysoil test results, with the geogrid oriented horizontally (HCGH tests), fall between the best-fit lines for soil and polysoil on each of the graphs, as expected.

FINITE ELEMENT METHOD OF SEEPAGE ANALYSIS

A program, designated as X8202 by the U.S. Army Corps of Engineers, Waterways Experiment Station, Vicksburg, Mississippi (Ref. 3 - 7) is capable of solving two dimensional

SUMMARY OF EXPERIMENTAL HYDRAULIC CONDUCTIVTIY TEST RESULTS			
Test ID	**Soil ID**	**Description**	**k - cm/sec**
HC601	3IB	Soil	3.04E-09
HC603	9RT	Soil	2.71E-09
HC604	4PT	Soil	1.52E-08
HCG601	3IB	Polysoil-Vertical	8.82E-09
HCG602	4PT	Polysoil-Vertical	8.25E-07
HCG603	9RT	Polysoil-Vertical	1.19E-08
HCG604	4PT	Polysoil-Vertical	8.77E-07
HCG605	3IB	Polysoil-Vertical	2.55E-08
HCG606	9RT	Polysoil-Vertical	7.50E-08
HCG607	9RT	Polysoil-Vertical	2.62E-08
HCG608	4PT	Polysoil-Vertical	1.42E-06
HCG609	3IB	Polysoil-Vertical	5.27E-08
HCG6H1	9RT	Polysoil-Horizontal	2.06E-08
HCG6H2	4PT	Polysoil-Horizontal	2.66E-07
HCG6H3	3IB	Polysoil-Horizontal	2.47E-08

TABLE - 3 Hydraulic Conductivity Test Results

steady-state, unconfined seepage problems without an initial estimate of the free surface and also has good graphics capabilities. The program solves the seepage problem using four-node quadrilateral elements. Following generation of the grid, the required input includes the boundary condition codes, and the known head conditions on the boundaries. The position of the free surface is found through an interpolation process between nodes with positive and negative pressure heads, and successive iterations are performed until the position of the free surface has essentially stopped moving. The coordinates of the nodes very near the free surface are temporarily adjusted to coincide with the free surface. Program output includes an echo of the input, the head at each node, percentage of available head, flow, and whether the node is above, on or below the free surface, with coordinates of those nodes on the free surface. Additional output values include the unit flow volume and the horizontal, vertical and resultant element flow velocities and direction of flow.

Grid Geometry

The finite-element grid was generated to conform to the geometry of the dam core developed in the conceptual model (Figs - 1 and 2). The grid consists of 10 elements in the horizontal direction and 17 elements in the vertical direction. The vertical spacing was selected to coincide with the polysoil strips. The grid contains 198 nodes and 170 elements, as shown in Fig - 3. The same grid was used for both the non-reinforced and reinforced cases, to prevent a bias in the FEM analysis due to a different grid geometry. For the non-reinforced case, identical k values were assigned to the thin soil layers (polysoil strips in the reinforced case) as the thicker soil layers.

Input Boundary Conditions

A datum of zero was selected at the level of the base of the core. Initial input values of total head for each node were as follows: h = 45 feet (13.7 m) on the upstream face from the head-water surface to the base; h = 45 feet (13.7 m) across the top of the truncated core; h = 5 feet (1.52 m) on the downstream face from the tail-water surface to the base; h = z on the downstream face above the tail-water surface; h = 0 along the impervious base; and h = 0 for all internal nodes.

Hydraulic Conductivity Input Values

The normalized k values from the laboratory test results were adjusted to realistic field values for use as input into the FEM program. The assigned field k values used in the computer analysis are summarized in Table - 4.

Conditions Analyzed

Nine different conditions were analyzed with the FEM program. Each of the three soil material types were analyzed for the non-reinforced case, assuming isotropic hydraulic conductivity. For the reinforced case, each soil material type was first analyzed assuming isotropic k values in the polysoil, using the higher adjusted k (HCG) values for flow parallel to the grid (assuming $k_v = k_h$). Then each soil material type was analyzed for the reinforced case assuming anisotropic hydraulic conductivity in the polysoil, and using the adjusted k_v (HCGH) and k_h (HCG) values. The soil portion of the core was assumed to have isotropic hydraulic conductivity in all analyses.

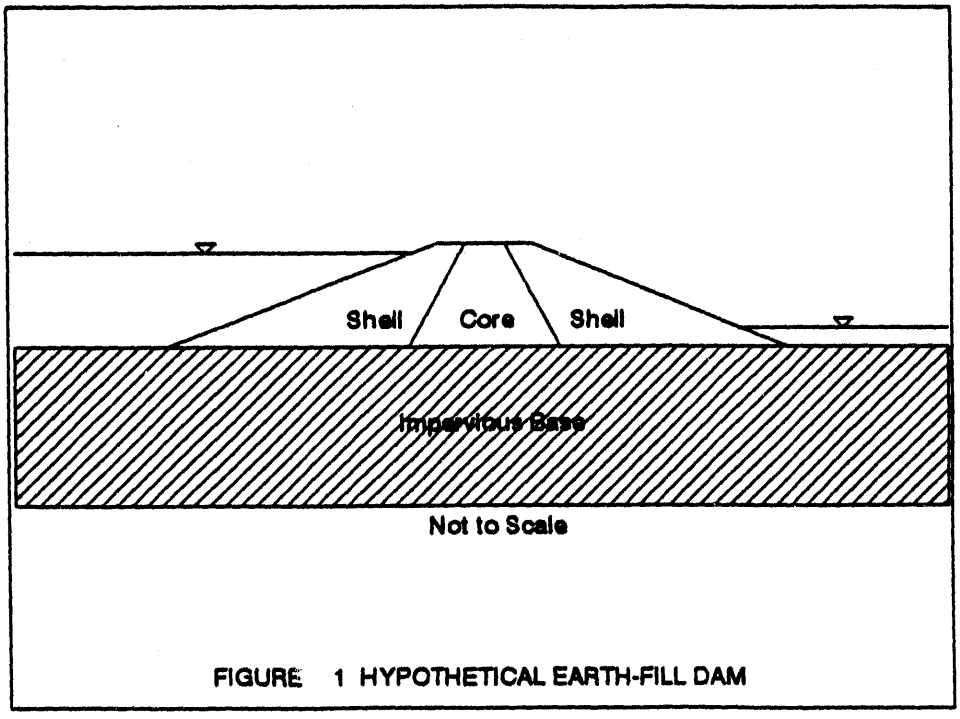


FIGURE 1 HYPOTHETICAL EARTH-FILL DAM

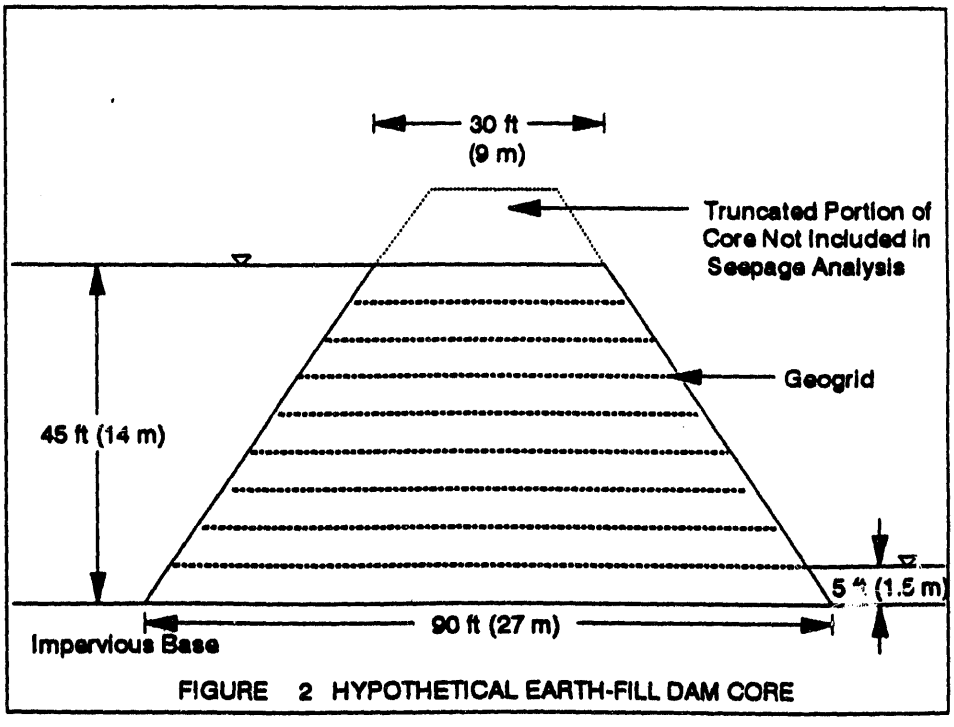


FIGURE 2 HYPOTHETICAL EARTH-FILL DAM CORE

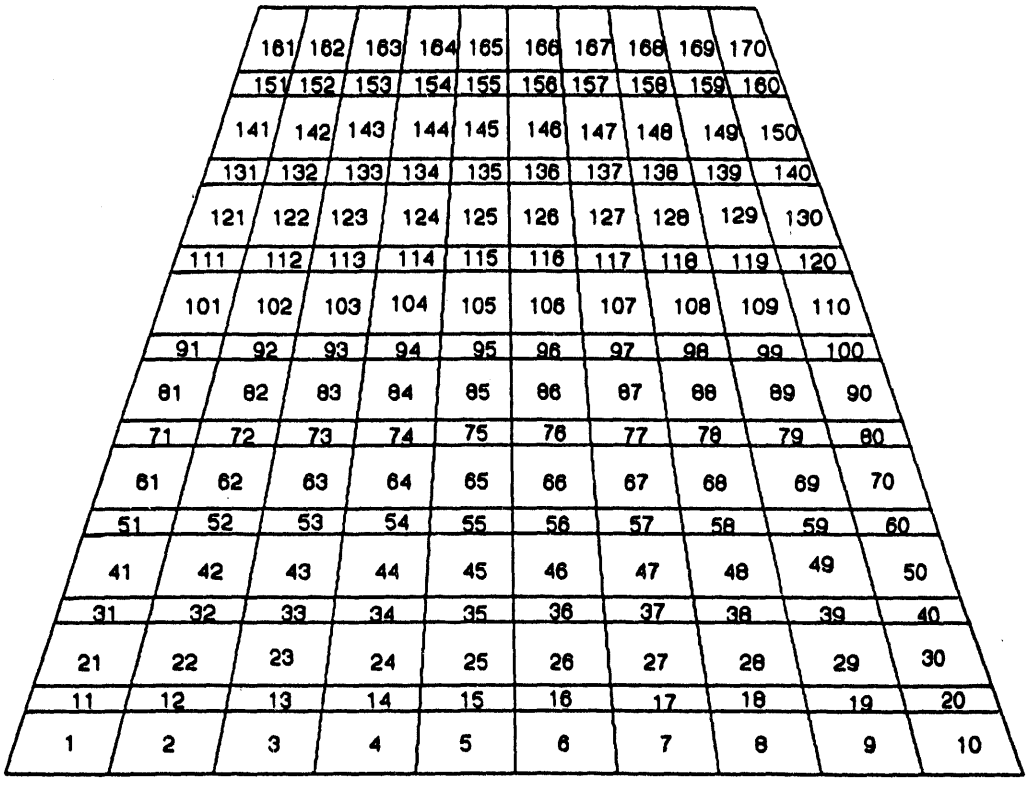


FIGURE 3 FINITE ELEMENT SOLUTION GRID

Sample ID	MDD%	Normalized Test Values (cm/sec.)	Assigned Field Value (cm/sec.)	Assigned* Field Value (ft/min.)	FS
3IB-HC	95	3.068E-08	7.000E-08	1.378E-07	2.3
3IB-HCG	95	3.681E-08	1.000E-07	1.969E-07	2.7
3IB-HCGH	95	2.209E-08	6.000E-08	1.181E-07	2.7
4PT-HC	95	2.920E-08	1.000E-07	1.969E-07	3.4
4PT-HCG	102	6.450E-07	1.000E-06	1.969E-06	1.6
4PT-HCGH	102	3.870E-07	6.000E-07	1.181E-06	1.6
9RT-HC	95	2.800E-09	1.000E-08	1.969E-08	3.6
9RT-HCG	100	5.100E-09	5.000E-08	9.843E-08	9.8
9RT-HCGH	100	3.060E-09	3.000E-08	5.906E-08	9.8

* Assigned Field Values in ft/min. Used in FEM Seepage Analyses

Table - 4 Hydraulic Conductivity Values for Analyses

Analysis Results

The results of the FEM analysis are summarized in Table - 5. The soil material type is identified by the sample ID contained in the analysis number (e.g., 3IB). The last digit in the analysis number, for each soil material type, identifies the analysis condition as follows: 1 = non-reinforced case; 2 = reinforced case with isotropic hydraulic conductivity in the polysoil; and 3 = reinforced case with anisotropic hydraulic conductivity in the polysoil. The third column contains the average flow rate for each analysis.

TABLE 5
SUMMARY OF FEM ANALYSIS RESULTS

Analysis Number	Output File Name	Ave. Flow Rate ($ft^3/min/ft^2$)	Flow Volume ($ft^3/day/1000$ ft dam)
S3IBN1	S3IBP1	2.0920E-06	68
S3IBN2	S3IBP2	2.2494E-06	76
33IBN3	S3IBP3	2.2422E-06	75
S4PTN1	S4PTP1	2.9807E-06	101
S4PTN2	S4PTP2	8.5286E-06	362
S4PTN3	S4PTP3	7.7602E-06	324
S9RTN1	S9RTP1	2.9855E-07	10
S9RTN2	S9RTP2	5.1297E-07	21
S9RTN3	S9RTP3	5.0850E-07	20

The fourth column contains the total flow quantity per day based on the height of the seepage face and assuming a dam length of 1000 feet (305 m), for illustration purposes.

Each of the nine analyses generate two plots. One plot shows the portion of the dam core below the phreatic surface and contains equipotential lines. The other plot shows the portion of the dam core below the phreatic surface and contains flow velocity vector arrows. Figs - 4 and 5 show the typical plots from the output. The plot with the equipotential lines for the reinforced case have the phreatic surface of the non-reinforced case shown with dashed lines. The dashed lines were added to the plots to facilitate comparison of the phreatic surface position for the reinforced and non-reinforced cases. The summarized FEM results in Table - 5 and the computer plots discussed above indicate only modest increases in flows and phreatic surface elevations for the reinforced cases (cases including the polysoil strips).

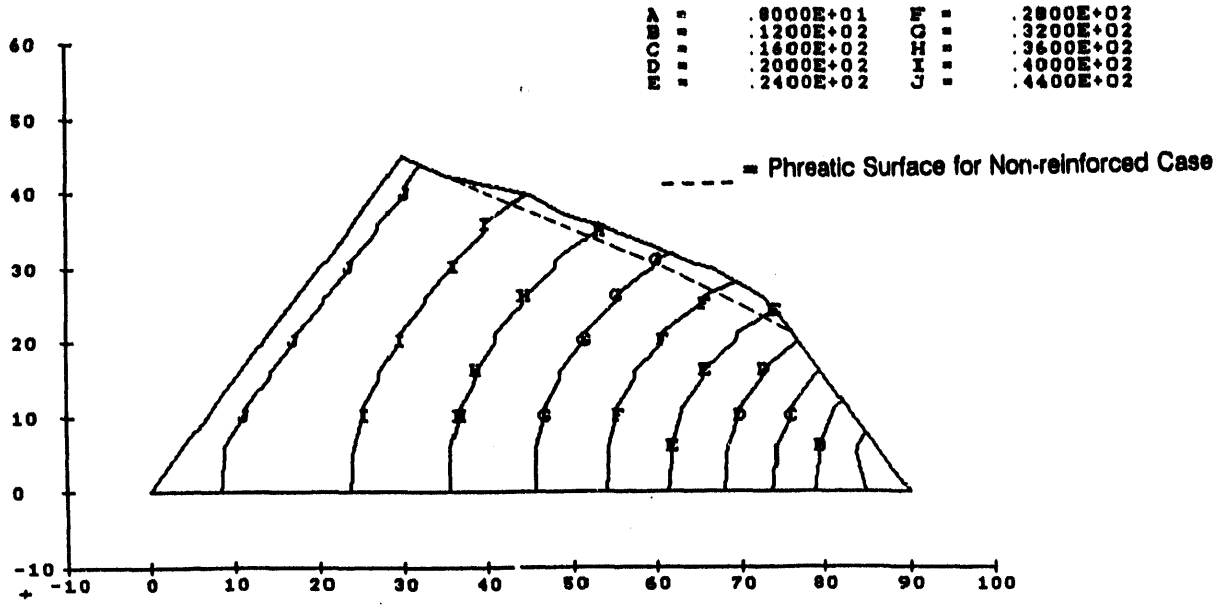


FIG - 4 Phreatic Surface and Equipotential Lines

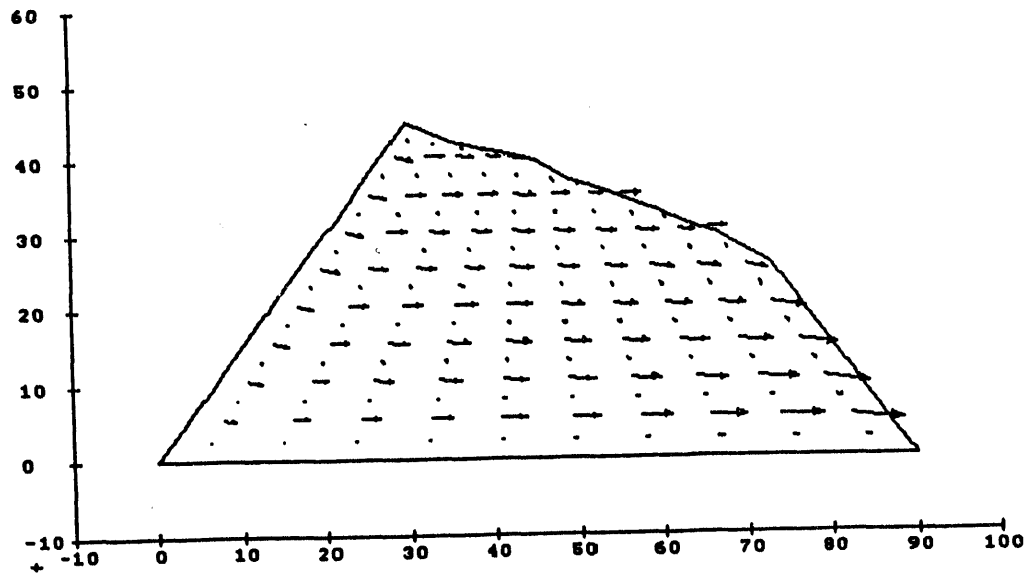


FIG - 5 Phreatic Surface and Flow - Velocity Vectors

CONCLUSIONS AND RECOMMENDATIONS

Conclusions developed during the current study include those relating to FEM analysis results and design and construction.

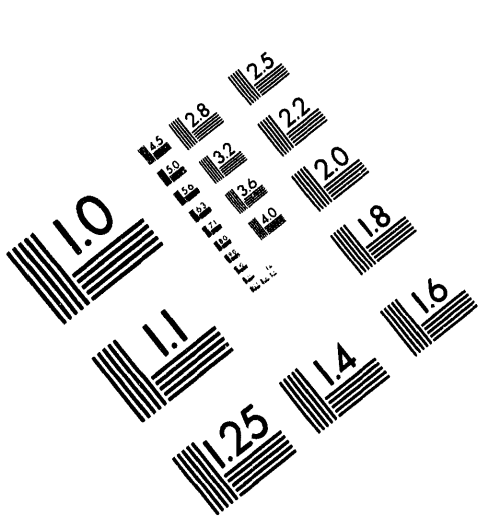
1. The increase in unit flow rates for the reinforced core with polysoil strips was a maximum of 7.5 percent for sample 3IB, 286 percent for sample 4PT, and 172 percent for sample 9RT. Although the increases may sound considerable for samples 4PT and 9RT, the actual increase in flow volumes is very modest, as shown in Table - 5, for a 1,000-foot dam length. The maximum increase in exit-seepage volume for the above configuration was 261 cubic feet per day for sample 4PT. The maximum increase for sample 3IB was eight cubic feet per day and for sample 9RT, 11 cubic feet per day. These are very modest increases. The phreatic surface configuration was virtually the same for all three analyses on sample 3IB. The maximum increase in phreatic surface elevation for sample 4PT was approximately three feet and that for sample 9RT was about 1.8 feet. The phreatic surface was virtually the same for isotropic and anisotropic hydraulic conductivity values in the polysoil, within each soil material type. Again, these increases are minimal, or modest at most.
2. The use of geogrid reinforcement through an earth-fill dam core will likely result in increased seepage through the core and a higher phreatic surface. With a well designed laboratory testing program that carefully models the field condition, the magnitude of the increased seepage and phreatic surface can be predicted. These data, with application of appropriate safety factors can be used to develop design parameters for a geogrid reinforced dam, including the core.
3. Rigid construction documents and a high level of quality control during construction will be required to produce a final product in the field that will perform as modeled in the laboratory.
4. The relatively small increases in seepage and phreatic surface rise indicated in this study, resulting from the use of geogrid reinforcement in earth-fill dam cores, should be within a range that can be appropriately managed and accommodated in design and construction.

ACKNOWLEDGEMENTS

The author wishes to gratefully acknowledge the efforts and contributions of the following individuals: Dr. James G. Collin and Mr. Ronald Anderson of Tensar Earth Technologies, Inc., who provided funding for the large permeameters used in this study, the geogrid materials for testing, and advice and technical literature; Mr. Thomas D. Baker of EMCON/Baker-Shiflett, Inc., who provided the bulk soil samples and previous laboratory test results.

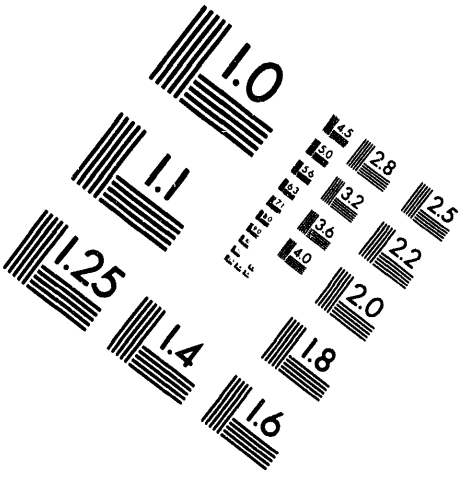
REFERENCES

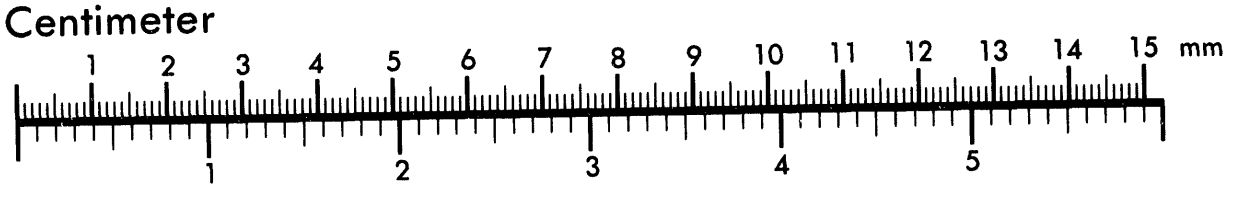
1. American Society for Testing and Materials (ASTM), 1993 Annual Book of Standards.
2. Bang, S. and Shao, L. (1993). "Analysis of Unconfined Flow with Inclined Boundaries by Finite Difference Method." *Canadian Society for Civil Engineering*, 1993 Annual Conference Proceedings, 119-128.
3. Tracy, Fred T. (1973a). "A Three-Dimensional Finite Element Program for Steady-State and Transient Seepage Problems." Miscellaneous Paper K-73-3, U.S. Army Engineer Waterways Experiment Station, Vicksburg, MS.
4. Tracy, Fred T. (1973b). "A Plane and Axisymmetric Finite Element Program for Steady-State and Transient Seepage Problems." Miscellaneous Paper K-73-4, U.S. Army Engineer Waterways Experiment Station, Vicksburg, MS.
5. Tracy, Fred T. (1977a). "An Interactive Graphics Finite Element Method Grid Generator for Two-Dimensional Problems." Miscellaneous Paper K-77-5, U.S. Army Engineer Waterways Experiment Station, Vicksburg, MS.
6. Tracy, Fred T. (1977b). "An Interactive Graphics Post-Processor for Finite Element Method Results." Miscellaneous Paper K-77-4, U.S. Army Engineer Waterways Experiment Station, Vicksburg, MS.
7. Tracy, Fred T. (1991). "Application of Finite Element, Grid Generation, and Scientific Visualization Techniques to 2-D and 3-D Seepage and Groundwater Modeling." Technical Report ITL-91-3, U.S. Army Engineer Waterways Experiment Station, Vicksburg, MS.

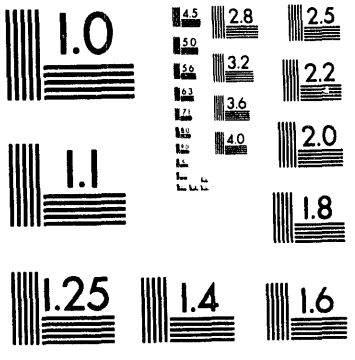


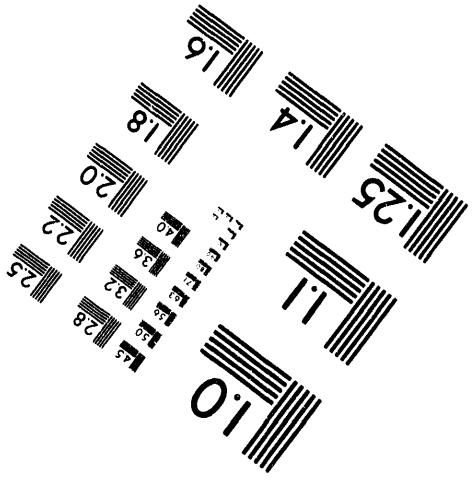


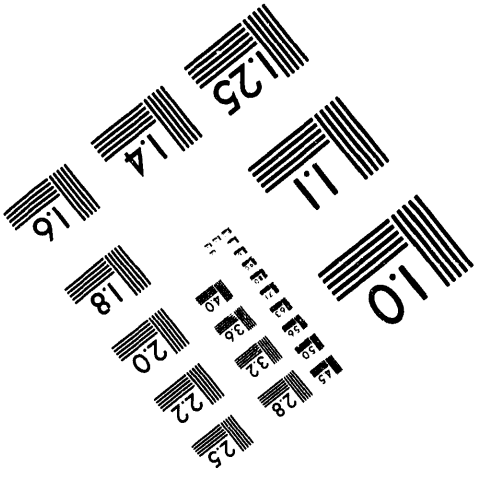
Association for Information and Image Management
1100 Wayne Avenue, Suite 1100
Silver Spring, Maryland 20910
301/587-8202











MANUFACTURED TO AIIM STANDARDS
BY APPLIED IMAGE, INC.

7 of 7

Hydrogeology, Waste Disposal, Science and Politics
Proceedings 30th Symposium
Engineering Geology and Geotechnical Engineering, 1994

DESIGN OF FLEXIBLE PAVEMENT SUBGRADES WITH GEOSYNTHETICS

G. H. Gregory and S. Bang

Department of Civil and Environmental Engineering
South Dakota School of Mines and Technology
Rapid City, SD 57701

ABSTRACT

The objective of this study is to develop design guidelines for incorporating the soil subgrade improvement functions of geosynthetics into a conventional flexible pavement design method that uses the California Bearing Ratio criteria as design input. The study incorporates a series of laboratory tests, including the standard CBR tests on weak subgrades soils and the modified CBR tests using crushed stone surcharges and geosynthetics. The laboratory CBR test results have been correlated with existing data to produce a design method that includes the effect of soil improvement due to geosynthetics. The proposed design method combines the conventional flexible pavement thickness design procedure with the geosynthetic improvement factors.

INTRODUCTION

The purpose of this study is to develop guidelines for incorporating the soil subgrade improvement functions of geotextiles and geogrids (geosynthetics) into a conventional flexible pavement design method which uses California Bearing Ratio (CBR) criteria as design input. The scope consisted of the following; (1) researching and compiling existing relevant data, (2) performing laboratory testing including series consisting of standard CBR tests on weak-subgrade soils and modified CBR tests using crushed stone surcharges and geosynthetics (geotextile only and geotextile-geogrid combination) to determine subgrade improvement factors, and (3) correlating laboratory test data with existing data combining a conventional pavement thickness design procedure with the geosynthetic improvement factors.

LABORATORY TESTING PROGRAM

The laboratory testing program was designed to provide test results which, when correlated with existing data, would indicate subgrade improvement factors for the soil-geosynthetic-pavement base interaction. The series included crushed stone, geotextile and geogrid materials. This study was, of necessity, limited in scope and multiple testing of all specimen types and combinations was not possible. However, multiple tests were performed on selected specimens and combinations to obtain an indication of the spread in test results.

CBR Soil Series

The CBR soil series was performed using two different types of soil in the "weak subgrade" range (CBR less than 10). The soils were obtained from another project source and had been previously tested in accordance with ASTM (Ref.1) procedures for classification (ASTM D 2487) and Standard Proctor density (ASTM D 698). The soil properties are summarized in Table - 1.

TABLE - 1

Sample Number	Description	Maximum Dry Density	LL	PI	-200 SIEVE
3IB	Lt. Br. Clay (CH)	100.2 pcf	63	43	89%
4PT	Br. Sa. Clay (CL)	106.4 pcf	42	25	58%

The geotextile used in the tests was Trevira® 1125. The geotextile properties were selected to meet or exceed minimum pavement design and survivability criteria (Ref. 2 and 3). The geogrid used in the tests was Tensar® BX 1200 (SS2). The Tensar BX 1200 was selected for this study because this product has performed well in numerous applicable projects and the geogrid properties meet or exceed the minimum pavement design and survivability criteria (Ref. 2 and 3).

Conventional CBR tests were performed on the two soil samples in general accordance with ASTM D 1883, except only one compactive effort and moisture content (ASTM D 698) was used in preparing the specimens. These test results were then compared to the Standard Proctor values. The compacted specimens were in the range of 95 to 100 percent of maximum dry density and optimum to plus 4 points wet of optimum moisture content. The specimens were soaked under water for a minimum of 96 hours prior to CBR testing. The CBR tests were performed with steel surcharge weight of approximately 15 pounds.

CBR test results on soil sample 3IB are presented in Fig - 1. This specimen had a CBR value of 1.81. The results on sample 4PT are presented in Fig - 2. This specimen had a CBR of 3.14. Both values were taken at a penetration of 0.1 inch. The 4PT specimen had a slightly higher CBR value (3.52) at 0.2 inch penetration.

Modified CBR Testing With Crushed Stone Surcharge

The crushed stone material used as a surcharge in CBR tests consisted of two different gradations of crushed limestone base materials. The gradations of these materials were similar to ASTM D 448, Size Number 8 (3/8 inch to No. 8 sieve) and Size Number 57 (1 inch to No. 4 sieve).

Modified CBR tests were performed on additional specimens of the two soil samples. The soil specimens were prepared and compacted in the CBR molds as described previously. The 2-inch extension collar was then placed on the mold and filled with crushed limestone. Size Number 57 was used in the lower portion of the mold and Size Number 8 was used in the upper

BEARING RATIO TEST							
PROJECT: Geosynthetics in Pavement Subgrades JOB No.:CE790-1							
LOCATION: South Dakota School of Mines and Technology							
SAMPLE No.: 3IB-1 DESCRIPTION: Lt. Br. Clay(CH)							
DATE OF TEST: 2-11-93 REMARKS:							
PENETR.	DIAL	LOAD	STRESS	CBR	SCBR	GCBR	GGCBR
Inches	.OOO1 in.	Lbs.	psi				
0.000	0.000	0.000	0.000				
0.025	3.000	24.999	8.333				
0.050	5.000	41.665	13.888				
0.075	6.000	49.998	16.666				
0.100	6.500	54.165	18.055	1.81			
0.125	7.000	58.331	19.444				
0.150	7.200	59.998	19.999				
0.175	7.500	62.498	20.833				
0.200	8.000	66.664	22.221	1.48			
0.300	9.500	79.164	26.388	1.39			
0.400	11.100	92.496	30.832	1.34			
0.500							
0.600							
0.700							
0.800							
0.900							
1.000							

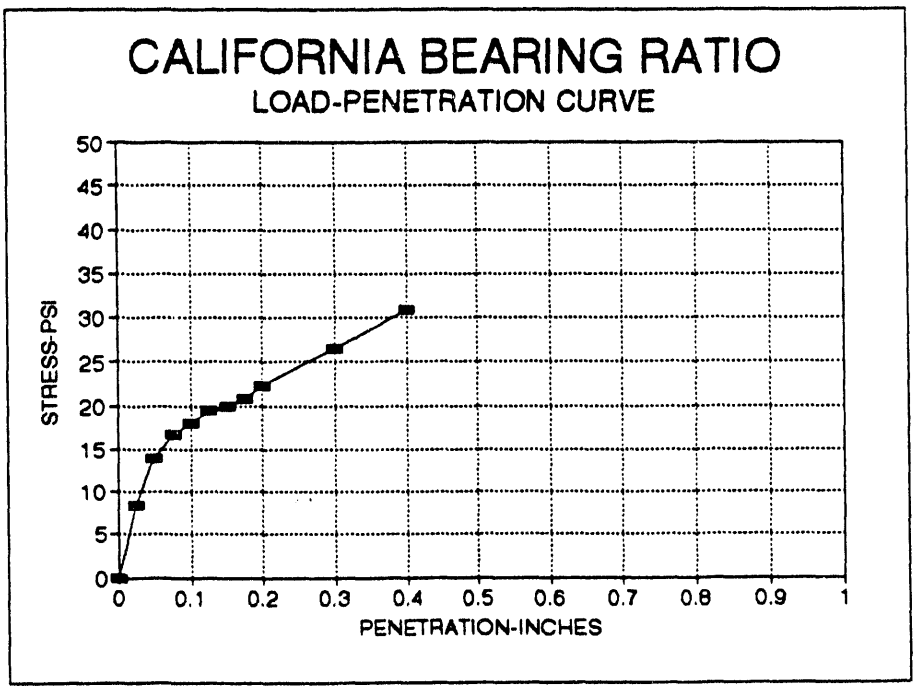


FIG - 1 CBR Test Results of 3IB Soil

BEARING RATIO TEST							
PROJECT: Geosynthetics in Pavement Subgrades JOB No.:CE790-1							
LOCATION: South Dakota School of Mines and Technology							
SAMPLE No.: 4PT-1 DESCRIPTION: Br. Sa. Clay(CL)							
DATE OF TEST: 2-11-93 REMARKS:							
PENETR.	DIAL	LOAD	STRESS	CBR	SCBR	GCBR	GGCBR
Inches	.OOO1 in.	Lbs.	psi				
0.000	0.000	0.000	0.000				
0.025	3.000	24.999	8.333				
0.050	6.000	49.998	16.666				
0.075	8.750	72.914	24.305				
0.100	11.300	94.163	31.388	3.14			
0.125	13.500	112.496	37.499				
0.150	15.500	129.162	43.054				
0.175	17.000	141.661	47.220				
0.200	19.000	158.327	52.776	3.52			
0.300	25.000	208.325	69.442	3.65			
0.400	30.000	249.990	83.330	3.62			
0.500	34.000	283.322	94.441	3.63			
0.600							
0.700							
0.800							
0.900							
1.000							

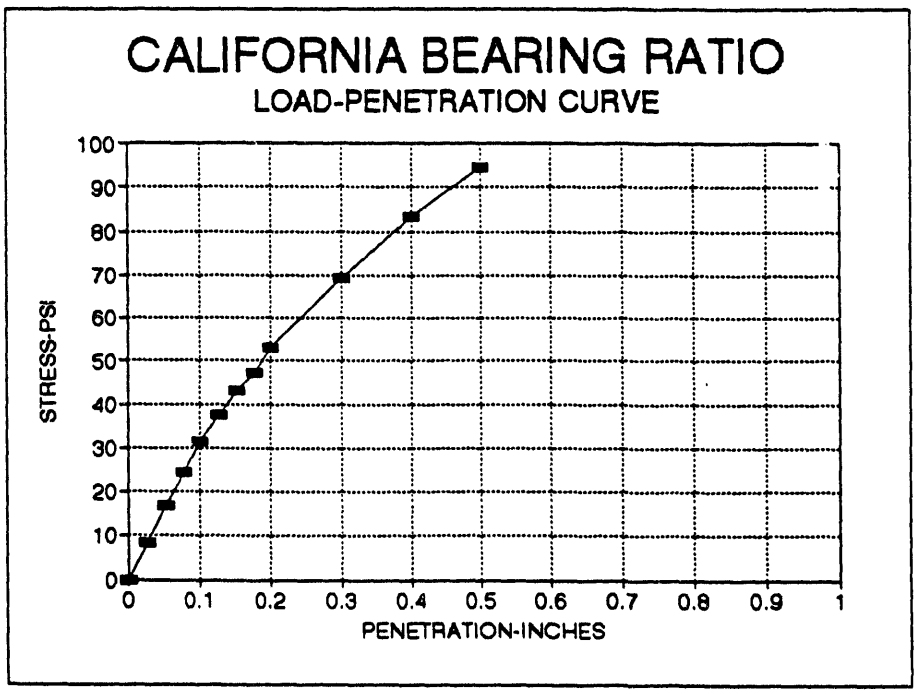


FIG - 2 CBR Test Results of 4PT Soil

portion. A 16-pound steel disc was temporarily placed on top of the crushed stone and struck with a rubber mallet to level the stone. The stone was then compacted by striking the steel disc with 40 blows with a ten-pound hammer (ASTM D 1557 type) dropping 18 inches. This compactive effort in the confined collar mold was estimated to be roughly equivalent to that which is achieved in the field with eight passes of a ten-ton vibratory roller per 6-inch lift of pavement base material. The CBR tests were then performed on the composite specimens with the piston loading applied to the crushed stone. Steel surcharge weight of approximately 15 pounds was applied to the crushed stone during the tests. The resulting CBR values are shown in Fig - 3 under the heading "SCBR."

Modified CBR Testing With Crushed Stone and Geosynthetics

Modified CBR tests were performed on additional specimens of the two soil samples including tests with geotextile only and geotextile-geogrid combination. A crushed stone surcharge was necessary for these tests as previously discussed. In all cases the geosynthetics were placed directly on the soil specimen at the bottom of the stone surcharge. Geotextile-geogrid combination tests were performed with the geogrid on top of the geotextile.

A modification to the CBR testing apparatus was necessary to accommodate the geosynthetics. In developing the geosynthetic-subgrade model, a near fully-anchored condition of the geosynthetics in the pavement structure was assumed. During the laboratory tests, a clamping device was required to anchor the geosynthetics. The clamping device was fabricated from a heavy duty PVC pipe flange assembly for a nominal 6-inch diameter pipe. The flange assembly has a bolt circle containing eight 3/4-inch diameter bolts and inner grooved compression ring. The assembly was modified to fit over the top of the basic CBR mold and to accommodate the 2-inch CBR extension collar on top. The geosynthetic materials (geotextile, geogrid or both) can be clamped in the flange assembly and then placed on top of the CBR base mold so that the geosynthetic material rests directly on the soil specimen surface. The CBR extension collar is then clamped on top of the apparatus to accommodate the crushed stone. The crushed stone for this series of tests again consisted of the Size Number 57 in the lower portion of the collar and Size Number 8 in the top portion. A schematic drawing of the modified CBR apparatus with geosynthetics in place is depicted in Fig - 4.

On the 3IB specimens, one test was performed with geotextile and three tests with geotextile-geogrid combination. On the 4PT specimen, two tests were performed with geotextile and one test with geotextile-geogrid combination. The test results are included in Fig - 3. The columns headed "GCBR" contain the test results for the tests with geotextile only and the columns headed "GGCBR" contain the test results for the geotextile-geogrid combination tests.

TEST RESULTS AND SUMMARIES

Load-Penetration Curves

The virgin stress-penetration data from the CBR tests were summarized and a composite average was obtained for each sample. These composite averages were then plotted as composite load-penetration curves for each sample material. These graphs are presented in Figs - 5 and 6. Below the 0.2-inch penetration level a distinct pattern of behavior is not evident. At

CBR SUMMARY

SAMPLE	PENET	CBR	SCBR	GCBR	GGCBR
3IB	0.10	1.81	7.50	9.40	11.90
"	0.20	-	8.33	12.00	14.13
"	"	-			15.00
"	"	-			15.44
"	0.30	-	10.09	13.16	13.95
"	"	-			15.00
"	"	-			18.90
"	0.40	-	9.42	13.04	14.35
"	"	-			15.00
"	"	-			19.34
"	0.50	-	9.51	13.46	15.38
"	"	-			15.77
"	"	-			19.07
4PT	0.10	3.14	4.92	6.90	11.80
"	"	-		7.80	
"	0.20	-	7.04	7.80	13.67
"	"	-		11.13	
"	0.30	-	8.48	9.79	14.47
"	"	-		12.89	
"	0.40	-	8.63	9.79	15.00
"	"	-		13.17	
"	0.50	-	8.76	10.38	15.77
"	"	-		14.04	

FIG - 3 CBR Summary

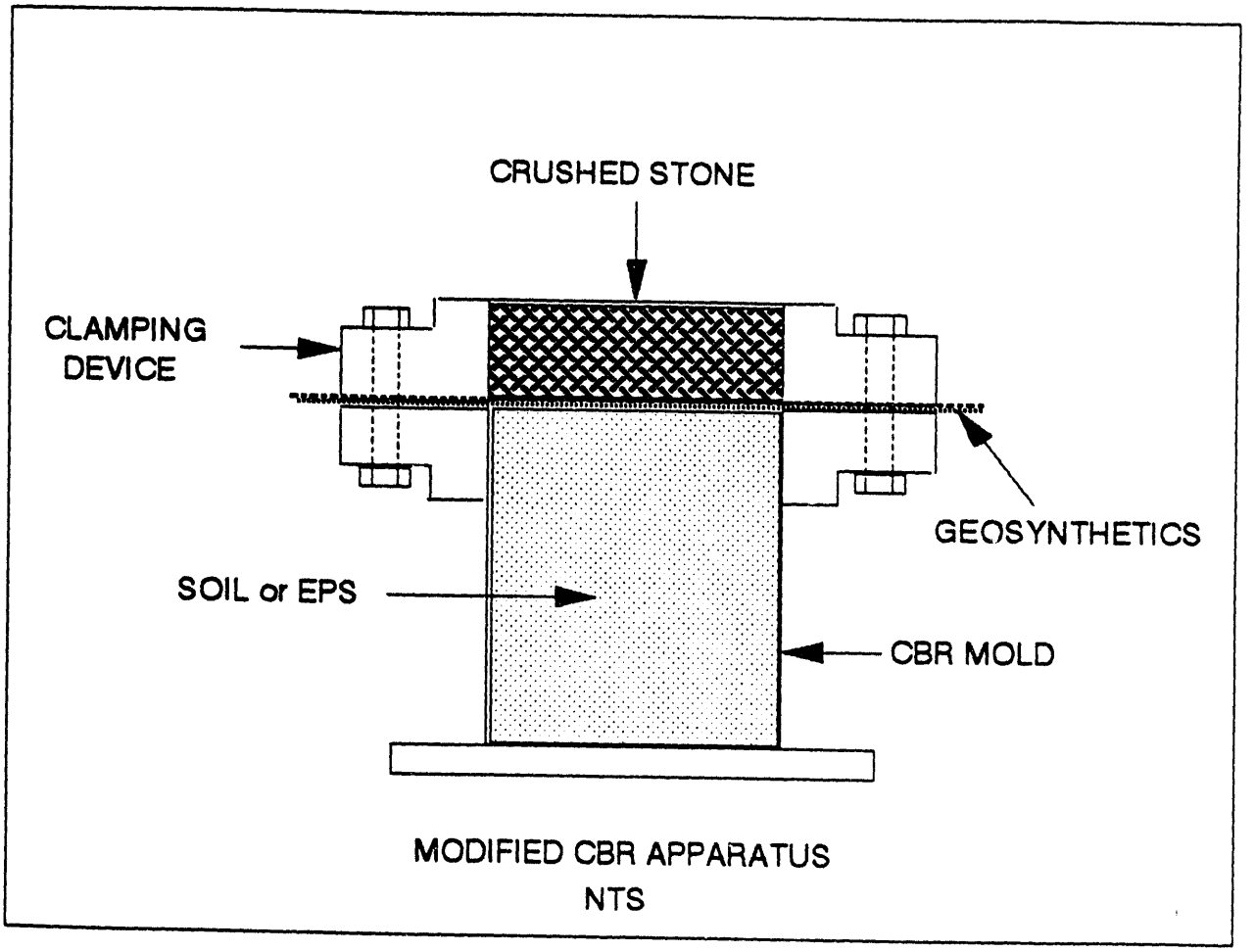


FIG - 4 Modified CBR Apparatus

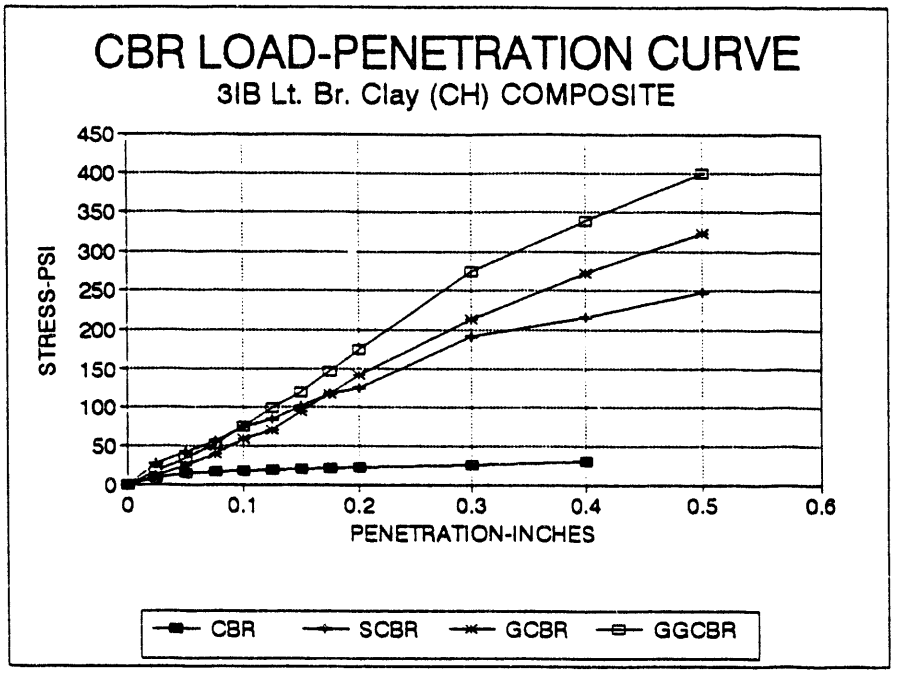


FIG - 5 Load - Penetration of 3IB Soil

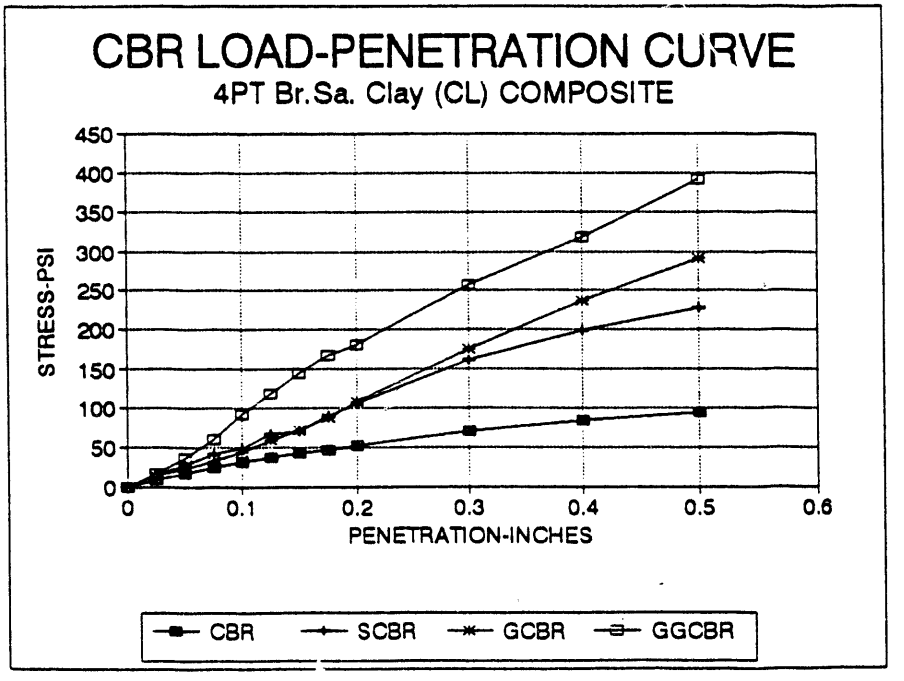


FIG - 6 Load - Penetration of 4PT Soil

and above the 0.2-inch penetration level, however, a very obvious pattern is present. An increasingly larger stress level for the same penetration is evident for the stone surcharge-only tests (SCBR), geotextile tests (GCBR), and geotextile-geogrid (GGCBR) tests, in ascending order. The only case where this is not clear at the 0.2-inch penetration is for the 4PT sample (Fig - 6), where it appears that the SCBR and GCBR curves almost coincide. However, this is partly due to the large stress-axis scale required to depict all results on the same graph. An examination of the actual stress-penetration values for the 0.2-inch penetration point will show an approximate 14 percent increase in stress value for the GCBR test over the SCBR test. Also the 4PT sample is the stronger soil and would be expected to have a higher resistance to penetration at the lower deformation than the weaker soil sample.

CBR Correlations and Summaries

The CBR values from all tests were summarized and correlated with each other for the various types of tests. A summary of CBR test results is presented in Fig - 3. The basic CBR values (CBR) were summarized and averaged only for the 0.1-inch penetration since that value represents the conventional CBR value for the basic material (soil only).

The SCBR, GCBR and GGCBR results were summarized and averaged for the 0.1, 0.2, 0.3, 0.4 and 0.5-inch penetration points. The average improvement in CBR value was then determined at each of the above penetrations between SCBR and GCBR results and between GCBR and GGCBR results. The most consistent improvement factors when considering both GCBR and GGCBR values occurred at the 0.2-inch penetration level.

GEOSYNTHETIC-SUBGRADE MODEL

The correlations and summaries of the laboratory test results discussed previously were analyzed and correlated with data from the previous study to develop the current geosynthetic subgrade model involving both geotextiles and geogrids.

Correlation With Previous Geotextile-Subgrade Model

The 1987 study (Ref. 4) involved 12 flexible pavement projects on which a geotextile was used on all or a portion of each project. All 12 pavements were constructed on relatively weak subgrade soils (CBR between 2 and 10). Actual pavement thicknesses on all projects were deficient for the traffic loads, based upon CBR values of the subgrades, without consideration of the geotextile. The portions of the projects on which a geotextile was used did not fail, even with the apparent deficiency in thickness. The portions of the projects on which a geotextile was not used all experienced significant failures within a relatively short time after being put into use. It was then postulated that the geotextile was providing a measurable improvement to the subgrade. To estimate the magnitude of the improvement, required CBR values based upon the traffic loads and actual pavement thicknesses were back-calculated. This value of required CBR was termed the "apparent CBR" of the subgrade. The difference between the actual CBR value of the subgrade and the "apparent CBR" value was the improvement factor attributed to the geotextile. Thus the apparent CBR value was designated as the geotextile-modified CBR or "GEOMOD" CBR and the improvement factor was termed the GEOMOD factor. The 12

pavement projects provided a unique opportunity to study the effects of geotextiles in flexible pavements and involved a relatively well balanced distribution of subgrade CBR values for weak soils. A model for the GEOMOD CBR was developed by plotting the subgrade CBR values versus the difference between the apparent CBR and actual CBR values. This resulted in the plotted GEOMOD CBR curve shown in Fig - 7. The curve indicates a trend toward zero improvement at a CBR value of 11 at the right hand end of the curve and a trend toward zero improvement at a CBR of zero. This curve confirmed actual experience and observations where the subgrade improvement using a geotextile is lower for very weak soils (CBR less than about 2), increases in the intermediate range (CBR of about 2 to 7) and again is lower for more competent soils (CBR of about 7 to 11). This holds true for permanent pavement structures where deformations must be limited. In temporary haul roads and similar facilities, where significant deformations are acceptable, the improvement factors would also be high in the range of CBR below 2 (but would still be zero for zero CBR).

Using the GEOMOD CBR Curve, a GEOMOD factor can be obtained for any particular subgrade between zero and 11. This GEOMOD factor is then added to the subgrade CBR to obtain the GEOMOD CBR. The GEOMOD CBR can be used in any conventional pavement thickness design procedure in lieu of the subgrade CBR. This allows conventional procedures to be used to design flexible pavements with geotextiles. The observation of numerous constructed pavement projects, designed by the author since 1987, have continued to confirm the validity of the curve.

CBR Test-GEOMOD Model Correlations

The summarized CBR test results from the current study were correlated with the GEOMOD model to establish a relationship between the GEOMOD factors from the 1987 study and the improvement factors for the geogrid observed in the CBR tests. Once this relationship was established it could be used to extrapolate GEOMOD factors for the geogrid, based upon the improvement factors for the geogrid observed in the CBR tests. This procedure could significantly mitigate the scale effects of the laboratory tests by correlations with the full-scale test projects of the 1987 study. To accomplish this correlation, the following steps were performed:

1. GEOMOD factors were determined from the mathematical model for each average conventional CBR value from the laboratory tests(samples 3IB and 4PT), at the 0.1, 0.2, 0.3, 0.4 and 0.5-inch penetration levels.
2. The above GEOMOD factors were then divided by the difference between the averages of the SCBR tests and GCBR tests at the above penetration levels. This produced a "correlation coefficient" which could be used as a multiplier to adjust the geogrid improvement factors from the laboratory tests to the full-scale field condition based on the 1987 study.

The values obtained in the above analysis, including correlation coefficients, are presented on Fig - 8.

Geotextile-Geogrid-Subgrade Model

The geotextile-geogrid-subgrade model, referred as the GEOMOD2 model, was developed in the following steps:

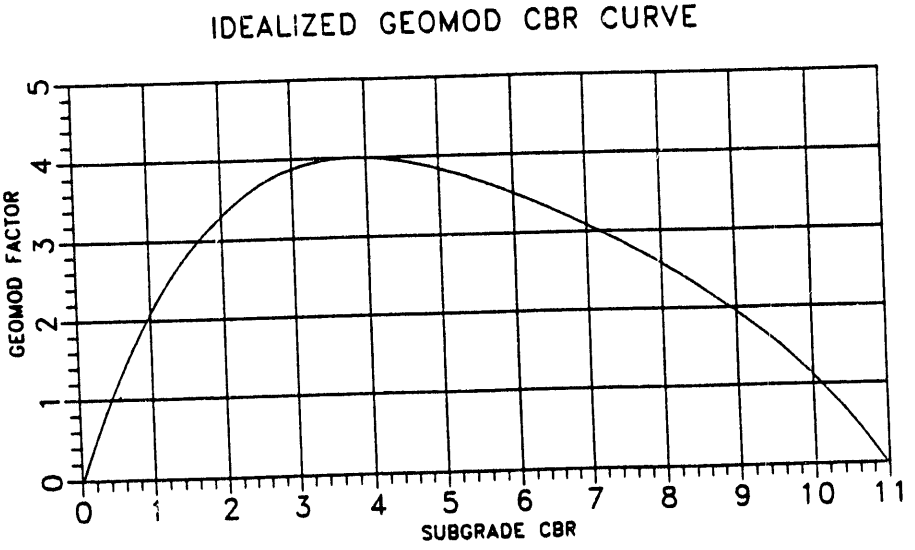


FIG - 7 GEOMOD CBR Curve

CBR CORRELATION ANALYSIS

3IB AVERAGES	1	2	3	4	5	6	7	8	9
PENET	SCBR	GCBR	GGCBR	GM FACT	(2-1)	(3-2)	(4/5)	(7*6)	(8+4)/4
0.10	7.5	9.40	11.39	3.20	1.90	1.99	1.68	3.35	2.05
0.20	8.33	12.00	14.86	3.20	3.67	2.86	0.87	2.49	1.78
0.30	10.09	13.16	15.95	3.20	3.07	2.79	1.04	2.91	1.91
0.40	9.42	13.04	16.23	3.20	3.62	3.19	0.88	2.82	1.88
0.50	9.51	13.46	16.74	3.20	3.95	3.28	0.81	2.66	1.83
4PT AVERAGES									
0.10	4.92	7.35	11.80	3.90	2.43	4.45	1.60	7.14	2.83
0.20	7.04	11.13	13.67	3.90	4.09	2.54	0.95	2.42	1.62
0.30	8.48	11.34	14.47	3.90	2.86	3.13	1.36	4.27	2.09
0.40	8.63	11.48	15.00	3.90	2.85	3.52	1.37	4.82	2.24
0.50	8.76	12.21	15.77	3.90	3.45	3.56	1.13	4.02	2.03

FIG - 8 CBR Correlation Analysis

1. The differences between the averages of the GCBR and GGCBR tests at the 0.1, 0.2, 0.3, 0.4 and 0.5-inch penetration levels were multiplied by the correlation coefficients discussed in previous section. The resulting values were the improvement factors for the geogrid adjusted to the full-scale field conditions observed in the 1987 study.
2. The above values were then added to the appropriate GEOMOD factors previously obtained for the geotextile-only condition. Each sum was then divided by the appropriate GEOMOD factor to obtain an "improvement coefficient" for the geotextile-geogrid combination, over the geotextile alone. It was found that the improvement coefficients at the 0.2-inch penetration level were the most consistent. These values had a standard deviation of 0.185 and a coefficient of variation (standard deviation ÷ mean) of 0.10.
3. The original 12 data points (GEOMOD factors) from the 1987 study, which were used to produce the GEOMOD model curve, were multiplied by the improvement coefficients at the 0.2-inch penetration level to establish 12 new extrapolated data points for the geotextile-geogrid combination. The 0,0 and 11,0 coordinates of the ends of the curve were also included in the data set.

The above analysis resulted in the new GEOMOD2 model for the geotextile-geogrid combination. The results of the analysis are also presented in Fig - 8 and a graph of the GEOMOD2 curve is included in Fig - 9.

Discussion

The GEOMOD2 model was developed from the SCBR, GCBR and GGCBR test data at the 0.2-inch penetration level. For permanent pavement structures it is necessary to establish design values at a low deformation. Larger deformation levels obviously would show a larger improvement factor for the geosynthetic materials, but would likely involve unacceptable deformations in the pavement structure. The test results indicated a significant, relatively consistent improvement factor at the 0.2-inch penetration level. This deformation is also acceptable in permanent flexible pavement structures. Accordingly, the correlated test results from the 0.2-inch penetration level were used to develop the model.

CONCLUSIONS

The following general conclusions were developed during this study:

1. Laboratory CBR tests can be used to model the effects of geosynthetic improvement of the subgrade by using a modified CBR apparatus.
2. The geosynthetic-subgrade improvement factors (GEOMOD and GEOMOD2 factors) indicate a significant improvement at the 0.2-inch penetration level. The factors at the 0.2-inch penetration level should be used in the design of permanent flexible pavements to limit deformations. Improvement factors at a higher deformation could be used for temporary facilities such as haul roads.
3. The raw geosynthetic-subgrade improvement factors from the laboratory tests with the geotextile show a larger level of improvement than that observed in the full-scale pavements in the 1987 study. This is likely due to obvious scale effects in the laboratory tests. The revised GEOMOD and GEOMOD2 factors developed in the current study were correlated with the full-scale conditions of the 1987 study to limit the scale effects of the

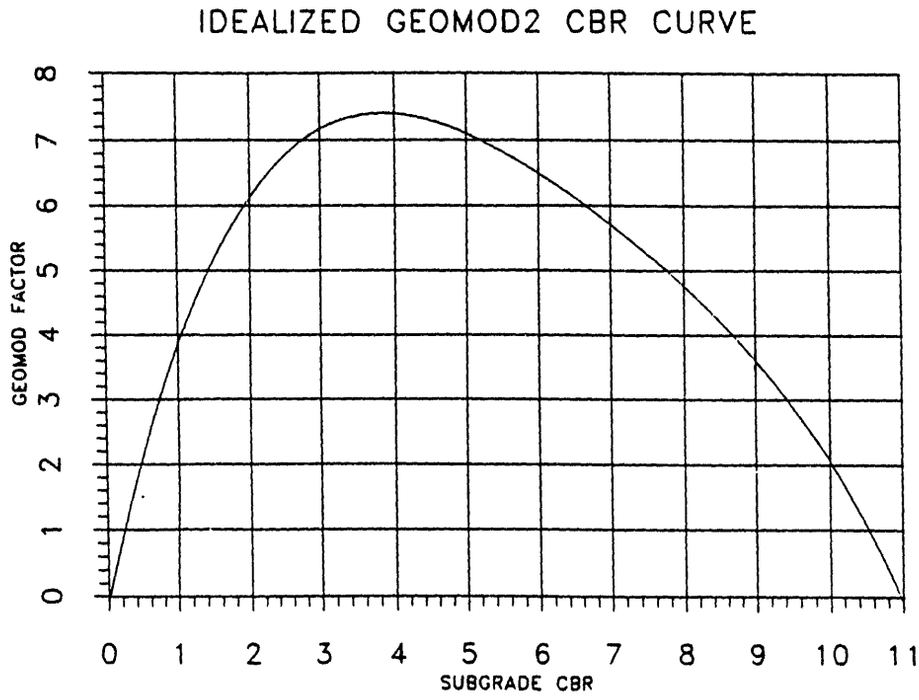


FIG - 9 GEOMOD2 CBR Curve

laboratory tests. The GEOMOD and GEOMOD2 factors should be used in design applications rather than the raw laboratory test results.

4. Conventional pavement-thickness design procedures, which use the subgrade CBR as a design basis, may be readily used to design pavements with geotextiles or geotextile-geogrid combinations by using the GEOMOD or GEOMOD2 CBR in lieu of the subgrade CBR.

ACKNOWLEDGEMENTS

The authors wishes to gratefully acknowledge the following individuals and firms who provided technical assistance, information or materials related to the current study: Mr. Ronald P. Anderson, P.E. and Tensar Earth Technologies, Inc., who provided geogrid materials for laboratory testing, and technical information; Mr. Les Neumann, P.E., Mr. Keith A. Miller and Contech Construction Products, Inc., who provided the geotextile for laboratory testing, and technical information; and Mr. Thomas D. Baker, P.E., and EMCON/Baker-Shiflett, Inc., who provided the soil samples and previous laboratory classification and Standard Proctor test results on the samples.

REFERENCES

1. American Society for Testing and Materials (ASTM), 1993 Annual Book of Standards, Volume 4.08, Soil and Rock; Dimension Stone; Geosynthetics.

2. Koerner, Robert M., Designing With Geosynthetics, Prentice-Hall, 2nd Edition, 1990.

3 Fluet, Joseph E., Jr., Editor, Geotextile Testing and the Design Engineer, ASTM STP 952.

4. Gregory, Garry H., Design of Flexible Pavements with Geotextiles, 1987. American Society of Civil Engineers, Fall Meeting, Geotechnical Session, Houston, Texas, October 2, 1987.

Hydrogeology, Waste Disposal, Science and Politics
Proceedings 30th Symposium
Engineering Geology and Geotechnical Engineering, 1994

PROPOSING AN ALTERNATIVE LINER A SUCCESSFUL EXAMPLE

Dale Ortman, P.E.
Huntingdon Chen-Northern, Inc.
P.O. Box 4699
Helena, MT 59604

ABSTRACT

The mandated Sub-Title D landfill liner design which meets the basic Sub-Title D performance requirement (no exceedance of groundwater quality standards at the landfill boundary in 30 years) specifies construction of a two foot thick clay layer with a hydraulic conductivity no greater than 10^{-7} cm/sec and a 60 mil HDPE membrane. This mandated design is easily accepted by the regulatory community but very difficult and expensive to properly construct. Fundamental problems arise constructing a clay liner that meets the 10^{-7} cm/sec hydraulic conductivity requirement and, in cold climates, protecting the clay from freeze cracking. Geosynthetic clay liners (GCL) provide a remedy to these problems but their use requires obtaining special approval for an "alternative liner" from the appropriate regulatory agency. This paper presents a simple example of an "alternative liner" proposal that has been accepted by the Montana Department of Health and Environmental Sciences for a new landfill. The arguments presented for the use of a GCL combine site-specific parameters with easily understood calculations to demonstrate compliance with the basic Sub-Title D performance requirement.

FORWARD

The intention of this presentation is to provide an example of both form and content of a successful application for an "alternative liner", therefore it is a slightly edited version of the original submittal to the regulatory agency. The specific details of the project are not important and there is no attempt to elaborate on them, instead it is hoped that the form of the developed argument will be useful to both designers and regulators when dealing with "alternative liners."

This paper attempts to show how the use of simple mathematical models may be preferable to complex analyses, providing the situation warrants their use. In most real world landfill design and permitting projects the available information, not to mention the budget, does not support the use of complex numerical modelling tools,also such approaches are often skeptically received by agencies. Therefore, when possible, it is preferable to use a more common sense approach to develop a preponderance of evidence to support the proposed alternative.

The GCL presented in this proposal is identified by brand name. This is not meant to endorse this product in favor of other GCL's available on the market. The structure of the presented proposal is applicable to all GCL's.

INTRODUCTION

The purpose of this document is to propose an alternative liner system for Cell #1 of the proposed landfill. To fulfill this purpose the following items are presented:

- Descriptions of:
  - The "standard" Subtitle D composite liner system
  - The proposed alternative composite liner system
- Excerpts from the EPA's draft "Report of Workshop on Geosynthetic Clay Liners" (Daniel & Boardman, 1992).
- An estimate of the time for leakage breakthrough for:
  - The "standard" Subtitle D composite liner system
  - The proposed alternative composite liner system
- An estimate of the amount of leakage through the liner systems for the 8 acre, Cell #1.
- An estimate of the time for leakage through the foundation soil to reach either the known water table (approximately 80 feet below the base of Cell #1) or a hypothetical water transmission zone at a lesser depth.
- An estimate of the groundwater flow velocity in the water-bearing zones beneath the site and an estimate of the time for landfill leakage to cross the landfill site boundary once it reaches the groundwater.

LINER SYSTEM DESCRIPTIONS

This section presents descriptions of:

- The "standard" Subtitle D composite liner system
- The proposed alternative composite liner system

Both the Subtitle D liner system and the proposed alternative liner system incorporate a leachate collection system that will be designed to ensure that no more than one foot (30.5 cm) of leachate head may be present on the upper high-density polyethylene (HDPE) membrane. Therefore, the following descriptions focus on the HDPE membrane and clay portions of the liner systems.

General Considerations

It is well known that the long-term performance of any well-designed liner system is a function of: (1) the construction practice used during installation, (2) the QA/QC program performed during installation, and (3) the protection provided the liner system during the operational phase of the landfill. The final design of the liner system will incorporate provisions that address all three of these vital aspects of liner design, therefore the details concerning these items are not discussed in this report. However, the bureau should be assured that the final design will include the following:

- Pre-qualification of the installer to ensure the liner is placed by an experienced constructor
- A third-party QA/QC program
- An adequate protection layer over the proposed alternative composite liner
- An operational inspection program to ensure the proposed alternative composite liner is not damaged during landfill operations.

The "Standard" Subtitle D Composite Liner System

This liner system consists of a 60 mil HDPE membrane placed over two feet of recompacted soil having a permeability of no greater than 1 x 10^{-7} cm/sec (Figure 1a)

The Proposed Alternative Composite Liner System

The proposed liner system consists of a 60 mil HDPE membrane placed over Gundseal® (Figure 1b). In addition to this basic liner configuration, the following items will be included in the final design:

- Gundseal® will have sufficient overlap of its unwelded joints to prevent thermal shrinkage from reducing the overlap distance to less than the specified length.
- Subgrade preparation for placement of the Gundseal® will include:
  - Inspection of the subgrade and removal and replacement of any sand lenses with suitable compacted clayey material.
  - Exploratory drilling of the subgrade to a depth of five feet at a suitable spacing to identify any large, near grade, sand lenses that extend beyond the cell boundary.
  - If any such sand lenses are identified, they will be further drilled to determine their extent and, depending on the site-specific condition, either:
    (1) The sand will be excavated and replaced with suitable compacted clayey material, or
    (2) A two-foot thick, recompacted soil layer having a permeability no greater than 10^{-7} cm/sec and extending ten feet outside the perimeter of the sand within the cell boundary, will be placed over the sand lens.
  - Scarification and recompaction of the upper six inches of the final subgrade to provide structural support for the liner system. This will include inspection for and removal of any oversized or sharp-edged materials in the subgrade.

EXCERPTS FROM EPA's WORKSHOP REPORT ON GEOSYNTHETIC CLAY LINERS

This section presents:

- Excerpts from the EPA's draft "Report of Workshop on Geosynthetic Clay Liners" (Daniel & Boardman, 1992).

Emphasis is added to the quoted text to highlight significant points. Explanatory notes are included where appropriate.

Page ii: ***"The information in this document . . . has been subject to the Agency's peer and administrative review and has been approved for publication as a U.S. EPA document."***

Landfill\93-3496\Liner.dwg

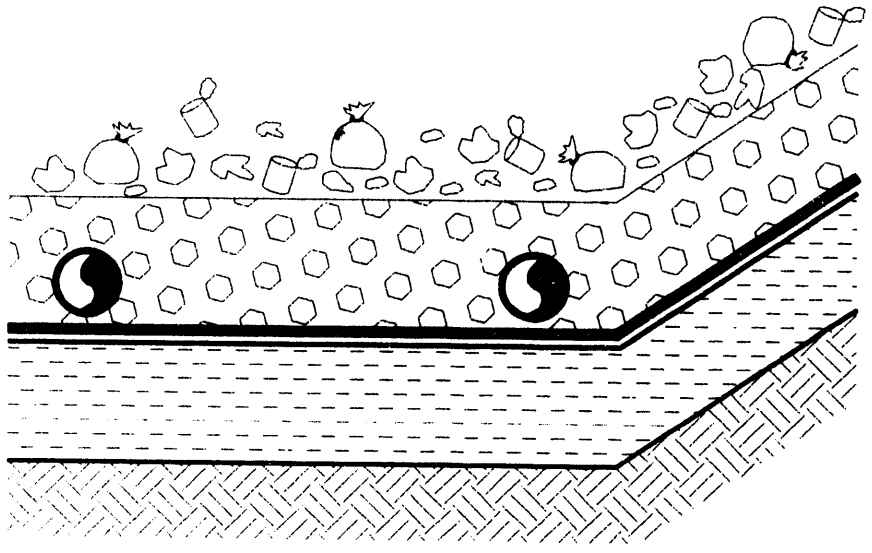


FIGURE 1a
"Standard" Subtitle D Composite Liner System

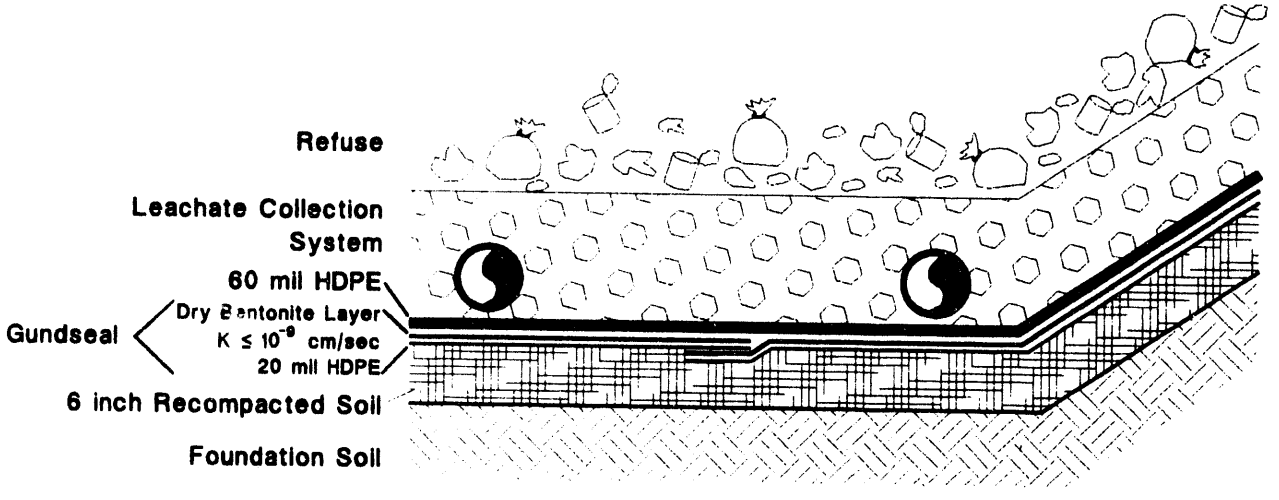


FIGURE 1b
Proposed Alternative Composite Liner System

Not to Scale

Page iv: *"A workshop was held at the Risk Reduction Engineering Laboratory in Cincinnati, Ohio, on June 9-10, 1992 to discuss geosynthetic clay liners (GCLs). The purpose of the workshop was to present and discuss the most recent information available on the use of GCLs.* ***This information will be of use to EPA program and regional officials, state regulatory officials, permit writers, and designers of waste disposal facilities."***

Page v: *"The issue of equivalency of a GCL to a CCL* (compacted clay liner) *was discussed. A number of criteria might be applied, but only a few seem truly rational.* ***Steady-state water flux and solute flux are obvious and clear criteria that should usually be part of an equivalency analysis. Other criteria can be applied but most are much less meaningful in terms of addressing regulatory compliance."***

NOTE: This report specifically addresses ***"Steady-state water flux and solute flux"*** to demonstrate the equivalency or superiority of the proposed alternative composite liner system to the "standard" Subtitle D liner.

"Finally, regulatory acceptance of GCLs was discussed. Although numerous site-specific approvals of GCLs have been given by regulatory agencies, no blanket approvals or disapprovals were identified."

Page 21-22:

"2.4.1.1 Hydraulic Conductivity"

"The hydraulic conductivity of an intact specimen of Gundseal® has been reported to be less than $4x10^{-12}$ cm/s. Researchers at the University of Texas (Daniel & Shan, 1992) and at GeoSyntec Consultants (1991) have reported that the bentonite element of Gundseal® alone has a hydraulic conductivity between $1x10^{-9}$ and $1x10^{-10}$ cm/s. ***Therefore, the 1/8 inch thick layer of bentonite, when considered by itself, is equivalent to at least twelve inches of $1x10^{-7}$ cm/s clay. The Gundseal® system, consisting of the geomembrane and the layer of bentonite, is equivalent to well over three feet of $1x10^{-7}$ cm/s clay."***

NOTE: ***"The Gundseal® system"*** only refers to the Gundseal® itself. It does not include the overlying 60 mil HDPE in the proposed alternative liner system.

"2.4.1.2 Overlapped Seams"

"When Gundseal® panels are overlapped, close contact is developed between the bentonite portion of one panel and the geomembrane portion of the other. Researchers at the University of Texas (Estornell, 1991) investigated the effectiveness of this overlap by performing large scale tests on two separate overlapping specimens. One sample had an overlap of 1.5 inches, while the other sample had an overlap of 3 inches. Two feet of gravel and one foot of water were placed over each of the specimens. ***During the five-month-long test, no outflow was noted through either of the overlapping specimens. Additional testing has been performed by***

Geosyntec Consultants (1991) and no flow was noted through the overlapped seams after one hundred hours."

NOTE: The recommended overlap for Gundseal® is 3 - 6 inches.

"2.4.1.3 Composite Action"

"The effectiveness of the overlapped seams indicates that a good composite action is formed between a geomembrane and the hydrated bentonite. Additional research at the University of Texas (Estornell, 1991) has shown that the bentonite portion of Gundseal® is able to seal off defects in an overlying geomembrane. ***At the University of Texas, slits and holes were cut into a geomembrane. This geomembrane was placed on top of the bentonite portion of Gundseal®, and the system was covered with gravel and water. These tests were performed for five months, during which time no flow was observed through the system. After five months, the tests were dismantled and the condition of the GCL was observed. Around the largest hole (3 inch diameter) in the geomembrane, only a 5 inch diameter area was wetted on the bentonite, thus indicating excellent intimate contact and composite action."***

"The effectiveness of intimate contact between Gundseal® and an overlying geomembrane was also investigated by the engineers at GeoSyntec Consultants (1991). ***Their results indicated that the hydrated bentonite can effectively seal a defect in an overlying geomembrane.*** *Water contents were taken from the bentonite portion of Gundseal® directly beneath a 0.1 mm diameter hole. The water content tests indicated a significant reduction in the water content of the bentonite radially away from the hole."*

Page 26:

"2.4.3 Conclusion"

"Research has indicated that Gundseal® is an effective replacement for clay in landfill liner systems and covers. Concern has been expressed, upon occasion, by engineers, contractors, and regulators that the thin geosynthetic clay liners, such as Gundseal®, are susceptible to damage during installation. However, the installation of geosynthetic clay liners is much easier than the construction of compacted clay liners, and when the contractors utilize the same care that is needed to install a geomembrane, an effective liner or cover system is in place and protecting the environment."

NOTE: The final design will include both pre-qualification of the installer and a third-party QA/QC program to ensure ***"the contractors utilize the same care that is needed to install a geomembrane"***. In addition, the design will incorporate both an adequate protective layer over the composite liner and an operational inspection program to ensure the proposed alternative liner system is not damaged during landfill operations.

Page 84:

"7.1 5.1 Freeze/Thaw Resistance"

"Compacted clay liners are known to be vulnerable to large increases in hydraulic conductivity from freeze/thaw. Limited laboratory data indicate that GCLs do not undergo increases in hydraulic conductivity as a result of freeze/thaw (Shan and Daniel, 1991). In addition, for those GCLs that contain a geomembrane, the geomembrane is unaffected by freeze/thaw. ***Thus, from the available data, GCLs appear to be superior to CCLs in terms of freeze/thaw resistance."***

NOTE: The site's climate is particularly conducive to freeze/thaw of liners.

"7.1.5.2. Wet/Dry Effects"

"Wetting and drying of CCLs and GCLs can cause either type of clay liner to swell or shrink. The main concern with clay liners that are wet and then dry out, is that desiccation can lead to cracking and an increase in hydraulic conductivity."

"Limited laboratory data indicate that when dry, cracked CCLs are rewetted, the clay swells and any cracks are partially closed, leading to partial recovery of the original, low hydraulic conductivity. In contrast, the available data show that the high swelling of bentonite results in full self healing and full recovery of the original, low hydraulic conductivity when dried, cracked GCLs are rewetted. In addition, for those GCLs that contain a geomembrane, the geomembrane is insensitive to wet/dry effects. ***Thus, GCLs appear to be more than equivalent to CCLs in terms of ability to self-heal if the material is wetted, dried, and then rewetted."***

Page 87-88:

"7.1.6.3 Ease of Placement or Construction"

"A GCL will always be easier to place than a CCL, unless weather conditions are adverse (e.g., constant rain), in which case even a CCL will also be difficult to construct. ***In general, GCLs are equivalent to or better than CCLs in terms of ease of placement of construction."***

"7.1.6.4 Speed of Construction"

"Geosynthetic clay liners can be placed much more quickly than CCLs. Equivalency is obvious."

"7.1.6.6 Weather Constraints"

"Compacted clay liners are difficult to construct when soils are wet, heavy precipitation is occurring, the weather is extremely dry (clay desiccates), the soil is frozen, or the temperature is below freezing. Geosynthetic clay liners are difficult to construct during precipitation. ***Weather constraints generally favor GCLs."***

"Some GCLs must be covered before they get wet. If a geomembrane will be placed over the GCL, the GCL must be covered almost immediately with the geomembrane. Additional weather constraints, e.g., wind speed, may apply to the geomembrane and, indirectly, influence the GCL. ***The fact that many GCLs must be covered before they are hydrated is a significant weather constraint for GCLs that does not exist for CCLs.*** *However, CCLs have weather constraints, too: CCLs must not be allowed to freeze or desiccate (GCLs cannot desiccate during construction because they are dry, and dry GCLs are unaffected by freezing temperatures)."*

"Equivalency in terms of weather constraints must be considered on a site-specific basis; but weather constraints generally favor GCLs over CCLs."

NOTE: The final design will include provisions requiring repair or replacement of any Gunsdeal® that is incidentally wetted prior to covering with the 60 mil HDPE.

LEAKAGE BREAKTHROUGH TIME FOR LINER SYSTEMS

This section presents:

- An estimate of the time for leakage breakthrough for:
  - The "standard" Subtitle D composite liner system
  - The proposed alternative composite liner system

Estimation of the breakthrough time for a clay liner may be calculated using the following equation developed from Darcy's Law (Tchobanoglous, et. al., 1993):

$$T = [d^2 n_e] / [k(d+h)]$$

Where:

T = Breakthrough Time (years)

d = Thickness of Clay (ft)

n_e = The Effective Porosity (n_e) of a clayey soil is considerably less than its true porosity; an average value is approximately $n_e = 0.2$ for clay soils with saturated permeabilities between 10^{-6} - 10^{-8} cm/sec (Tchobanoglous, et. al., 1993).

k = Permeability of Clay (ft/yr)

h = Head on Liner (1 ft, maximum head allowed by Subtitle D)

Assumptions in this equation are:

- The clay liner is fully saturated
- There are no macro-defects in the clay liner
- The head is constant (steady-state conditions)
- Flow is vertically downward
- There are holes in the overlying HDPE membrane

It should be noted that the theoretical "breakthrough time" is independent of the amount of flow; therefore, the number and size of defects in the overlying HDPE membrane does not influence the calculated "breakthrough time".

The "Standard" Subtitle D Composite Liner System

Using the equation given above and assuming a hole exists in the 60 mil HDPE, the breakthrough time for the standard Subtitle D liner is:

$$T = [2^2 \text{ ft} \times 0.2] / [0.103 \text{ ft/yr} \times (2 + 1)]$$

Where:

d = 2 feet

n_e = average 0.2 for clayey soil with permeability between 10^{-6} - 10^{-8} cm/sec, (Tchobanoglous, et. al., 1993)

k = 10^{-7} cm/sec = 0.103 ft/yr

Therefore:

T = 2.6 years

The Proposed Alternative Composite Liner System

Using the equation given above and assuming aligned holes exist in both the 60 mil HDPE primary liner and the 20 mil HDPE backing for the Gundseal®, the breakthrough time for the proposed alternative liner system is:

$$T = [0.01^2 \text{ ft} \times 0.2] / [0.001 \text{ ft/yr} \times (0.01 + 1)]$$

Where:

d = 0.01 feet (1/8th inch unhydrated thickness of bentonite coating = 0.01 ft)

n_e = average 0.2 for clayey soil with permeability between 10^{-6} - 10^{-8} cm/sec, (Tchobanoglous, G., Theisen, H., Vigil, S., 1993)

k = 10^{-9} cm/sec = 0.001 ft/yr

Therefore:

T = 0.02 years ≈ 1 week

The breakthrough time for the overlap seam in the Gundseal® may be estimated using the same equation by substituting the minimum overlap length (3 inches = 0.25 ft) for the clay thickness (d) and assuming the hole in the overlying 60 mil HDPE occurs exactly on the edge of the upper Gundseal® panel. For this case, the calculated breakthrough for the minimum Gundseal® overlap seam is:

$$T = [0.25^2 \text{ ft} \times 0.2] / [0.001 \text{ ft/yr} \times (0.25 + 1)]$$

Where:

d = 0.25 feet (minimum recommended overlap of 3 inches = 0.25 feet)

n_e = average 0.2 for clayey soil with permeability between 10^{-6} - 10^{-8} cm/sec, (Tchobanoglous, et. al., 1993)

k = 10^{-9} cm/sec = 0.001 ft/yr

Therefore:

T = 10 years

It should be remembered that these estimates assume: (1) the maximum allowable head exists on the liner system, (2) there is a sufficient supply of leachate to maintain this maximum head, and (3) the permeability of the bentonite layer is constant at 10^{-9} cm/sec. In reality, the laboratory testing of the Gundseal® indicates that the effective permeability of the hydrated bentonite is less than 10^{-9} cm/sec and the amount of leakage is so small that the real-world leakage is essentially immeasurable once the dry bentonite layer is hydrated (Daniel & Boardman, 1992).

AMOUNT OF LEAKAGE THROUGH LINER SYSTEMS

This section presents:

- An estimate of the amount of leakage through the liner systems for the 8 acre, Cell #1 for:
  - The "standard" Subtitle D composite liner system
  - The proposed alternative composite liner system

The amount of leakage through a composite liner is controlled by the number and size of construction defects in the membrane and the effective permeability of the underlying clay. An accepted approach to predicting the performance of a composite liner is to calculate the leakage through the expected number of holes in the upper membrane and assume this amount exits the bottom of the liner system.

The following equation has been developed by J.P Giroud for calculating the leakage through a hole in a membrane overlying a clay secondary liner; it has been accepted by the EPA in lieu of Bernouilli's Equation and has been incorporated in the recent 3.0 version of EPA's HELP model (Giroud, 1993).

$$Q = 0.21\, a^{0.1}\, h^{0.9}\, k_s^{0.74}$$

Where:

Q = Leakage Rate (m^3/sec)
a = Area of the Liner Hole (m^2)
h = Head on the Liner (m)
k_s = Saturated Permeability of the Underlying Clay (m/sec)

For predicting liner performance the following parameters have been proposed (Giroud, 1993):

- A "standard hole" is 0.2 cm in diameter; therefore the area = 3.1×10^{-6} m^2
- The number of "standard holes" per acre may be estimated based on:
  - 1 standard hole per acre if the membrane is placed by a good installer and there is a QA/QC program
  - 30 standard holes per acre if the membrane is placed by a good installer but there is no QA/QC program

Table 1 presents the results of using Giroud's equation to calculate both the annual and 30 year leakage amounts from the eight acres of Cell #1 for various combinations of "Number of Standard Holes (holes/acre)" in the membrane and "Controlling Clay Saturated Permeability (k_s)" for the underlying clay.

The final design will include pre-qualification of membrane installers to ensure a "good installer" is selected and a QA/QC program will be in force during construction of the entire liner and leachate collection system. Therefore, the leakage results for 1 standard hole per acre represent Cell #1.

TABLE 1

LEAKAGE FOR 8 ACRE CELL #1 USING GIROUD'S EQUATION[1] Q gal/yr = [0.21 $a^{0.1}$ $h^{0.9}$ $k_s^{0.74}$ m^3/sec] x 31,536,000 sec/yr x 35.3 ft^3/m^3 x 7.48 gal/ft^3 x n_h holes/acre x 8 acres				
Number of Standard Holes (holes/acre)	Controlling Clay Saturated Permeability (k_s)			
	10^{-6} cm/sec 10^{-8} m/sec	**Subtitle D** **10^{-7} cm/sec** **10^{-9} m/sec**	10^{-8} cm/sec 10^{-10} m/sec	**Alternative** **10^{-9} cm/sec** **10^{-11} m/sec**
1[2] **Good Installer with QA/QC**	1625 gal/yr 48,750 gal/30yr	**296 gal/yr** **8880 gal/30yr**	54 gal/yr 1620 gal/30yr	**10 gal/yr** **300 gal/30yr**
5	8125 gal/yr	1480 gal/yr	270 gal/yr	50 gal/yr
10	16,250 gal/yr	2960 gal/yr	540 gal/yr	100 gal/yr
20	32,500 gal/yr	5920 gal/yr	1080 gal/yr	200 gal/yr
30[2] Good Installer without QA/QC	48,750 gal/yr 1,462,5000 gal/30yr	8880 gal/yr 266,400 gal/30yr	1620 gal/yr 48,600 gal/30yr	300 gal/yr 9000 gal/30yr

a = Area of Standard Hole (3.1×10^{-6} m^2)
h = Head (0.305 m = 1 ft, Maximum Head Allowed by Subtitle D)
k_s = Saturated Permeability of Controlling Clay (m/sec)

(1) Leakage represents the amount that passes through the "standard holes" in the upper HDPE liner, assuming the underlying clay is saturated.

(2) Giroud (1993)

The "Standard" Subtitle D Composite Liner System

The standard Subtitle D composite liner system is expected to have the following leakage amounts:

- Total Annual Leakage ≈ 296 gallons
- Total 30 Year Leakage ≈ 8880 gallons

The Proposed Alternative Composite Liner System

The proposed alternative composite liner system is expected to have the following leakage amounts:

- Total Annual Leakage ≈ 10 gallons
- Total 30 Year Leakage ≈ 300 gallons

It should be noted that this estimate of total leakage through the proposed alternative liner system ignores the 20 mil HDPE membrane incorporated in the Gundseal®; the actual leakage for the proposed alternative liner system should be considerably less than that predicted by these calculations.

TIME FOR LEAKAGE TO REACH A WATER BEARING/TRANSMISSION ZONE

This section presents:

- An estimate of the time for leakage through the foundation soil to reach either the known water table (approximately 80 feet below the base of Cell #1) or a hypothetical water transmission zone at a lesser depth.

The time for the leakage through either liner system to reach a water bearing/transmission zone beneath Cell #1 may be estimated using a simple equation for seepage velocity based on Darcy's Law. The development of this simplified vertical seepage equation for any consistent set of units is as follows:

$Vs = ki/n_e$ Seepage Velocity from Darcy's Law (Cedergren, 1989)

where:

Vs = Seepage Velocity
k = Permeability of the Foundation Soil
i = Gradient (1/1 for vertical seepage)
n_e = Effective Porosity (usually less than the true porosity)

To estimate the time (T) for seepage to reach a specific depth in the foundation soil, divide the depth (d) by the seepage velocity. This results in the following equation:

$T = d/Vs$

$T = d/[(ki)/n_e]$

Therefore, the time for seepage to reach a specific depth in the foundation soil is dependent on the permeability and effective porosity of the soil. Based on the existing data, there is approximately 80 feet of primarily clayey soil from the base of Cell #1 to the known groundwater (Chen-Northern, Inc., 1990a & 1990b). This material is not fully saturated; therefore it must be determined if the controlling permeability of the soil is the saturated (k_s) or the unsaturated value (k_u).

If we assume the moisture content of the foundation soil is at or near its specific retention, then the pore volume remaining unfilled by water is the difference between its true porosity (n) and its volumetric moisture content (θ). The true porosity of clayey soils typically ranges n = 40 - 50 % and the upper limit of the typical volumetric moisture content for corresponding soils at specific retention is θ = 30 - 40 % (Vick, 1983); therefore, approximately 10 % of the foundation soil volume is empty pore space that must be filled with water to reach full saturation. The calculation for this empty pore space volume for each vertical foot of foundation underlying Cell #1 is:

$$8 \text{ acres} \times 1 \text{ vert ft} \times 43{,}560 \text{ ft}^2/\text{acre} \times 7.48 \text{ gal/ft}^3 \times 0.1 = 260{,}663 \text{ gal/vert ft}$$

By simple comparison of the estimated leakage volumes from Table 1 with the volume of fluid necessary to fully saturate just one vertical foot of the foundation beneath Cell #1, it is evident that leakage through either liner system is not sufficient to cause saturation of the foundation soil. In fact, even accepting that a leak is likely to be a localized occurrence rather than evenly distributed over the cell's area, the 2 to 3 order-of-magnitude difference between these values strongly suggests that leakage is inadequate to effectively change the moisture content of the foundation soils. Therefore, the unsaturated permeability (k_u) of the foundation soils should be the representative

permeability value.

The unsaturated permeability (k_u) of a soil is not a constant, but varies with the volumetric moisture content (θ). Although the actual value is a soil-specific parameter, it is typical that the unsaturated permeability (k_u) of a clay soil is approximately an order-of-magnitude less than its saturated permeability (k_s) (Fetter, 1980). Table 2 presents the saturated permeability values (k_s) measured for foundation materials above the groundwater (Chen-Northern, Inc.,1990a).

TABLE 2
FOUNDATION SOIL PERMEABILITY TEST RESULTS

Boring/Test Pit	Method	Direction	Material	Permeability (k) (cm/sec)
E-1D	Lab Permeameter	Vertical	Clay w/fine sand	2.2×10^{-8}
E-3	Lab Permeameter	Vertical	Sand with clay	1.0×10^{-7}
EA-1	Slug-In	Horizontal	Sand with clay/clay with fine sand	6.8×10^{-7}
EA-2	Slug-In	Horizontal	Sand with clay/clay with fine sand	1.2×10^{-7}
EA-3	Slug-In	Horizontal	Sand with clay/clay with fine sand	3.4×10^{-7}
TP-15	Dbl.Ring	Vertical	Clay with fine sand	8.8×10^{-7}
TP-18	Dbl.Ring	Vertical	Sand with clay	2.1×10^{-5}

The average of these values (Table 2), after eliminating the high and low readings, results in an average saturated permeability (k_s) of:

$$\text{Average } k_s \approx 4.24 \times 10^{-7} \text{ cm/sec} \approx 2.83 \text{ ft/yr}$$

Therefore, the corresponding average unsaturated permeability is:

$$\text{Average } k_u \approx 4.24 \times 10^{-8} \text{ cm/sec} \approx 0.283 \text{ ft/yr}$$

The effective porosity (n_e) of a clayey soil is considerably less than its true porosity; an average value is approximately $n_e = 0.2$ for clay soils with saturated permeabilities between 10^{-6} - 10^{-8} cm/sec (Tchobanoglous, et. al., 1993).

Table 3 presents the theoretical time to transmit liner leakage to various depths as a function of the controlling unsaturated permeability of the foundation soil. These estimates assume the maximum allowable head exists on the liner system and that there is a sufficient supply of leachate to maintain this maximum head. From Table 3, the time for liner leakage to reach 10 - 80 feet beneath Cell #1 is:

$$T_{10 \text{ feet}} \approx 45 \text{ years}$$
$$T_{80 \text{ feet}} \approx 364 \text{ years}$$

Therefore, it is estimated that for the proposed alternative liner system a flow of approximately 10 gallons/year may reach the known groundwater beneath Cell #1 in about 364 years.

In addition, should a hypothetical water transmission zone be encountered at a depth of 10 feet, it will take approximately 45 years for the same 10 gallons/year to pass through the foundation soil and enter this hypothetical zone. However, without an existing groundwater flux in the hypothetical zone, the amount of leakage is considered insufficient to create any measurable lateral flow of leakage from beneath Cell #1.

TABLE 3

TIME TO TRANSMIT LEAKAGE THROUGH FOUNDATION SOIL (years) USING THE SIMPLIFIED VERTICAL SEEPAGE EQUATION $T = d/[(k_u \times i)/n_e]$				
Depth of Leakage Transmission (ft)	Controlling Foundation Unsaturated Permeability (k_u)			
	10^{-6} cm/sec 6.675 ft/yr	10^{-7} cm/sec 0.678 ft/yr	**4.24 x 10^{-8} cm/sec 0.283 ft/yr**	10^{-8} cm/sec 0.068 ft/yr
10	2 yr	19 yr	**45 yr**	200 yr
20	4 yr	39 yr	**91 yr**	400 yr
30	6 yr	58 yr	**136 yr**	600 yr
40	8 yr	78 yr	**182 yr**	800 yr
50	10 yr	97 yr	**227 yr**	1000 yr
60	12 yr	117 yr	**273 yr**	1200 yr
70	14 yr	136 yr	**318 yr**	1400 yr
80	15 yr	155 yr	**364 yr**	1600 yr

T = Time of Leakage Transmission (years)
d = Depth of Leakage Transmission (ft)
k_u = Unsaturated Permeability (ft/yr)
i = Gradient (1/1 for vertical seepage)
n_e = Effective Porosity of Foundation Soil (assumed 0.2 for clayey soil with permeability between 10^{-6} - 10^{-8} cm/sec), (Tchobanoglous, et. al., 1993)

GROUNDWATER VELOCITY BENEATH THE LANDFILL SITE

This section presents:

- An estimate of the groundwater flow velocity in the water-bearing zones beneath the site and an estimate of the time for landfill leakage to cross the landfill site boundary once it reaches the groundwater.

The time for leakage to cross the unit boundary once it reaches the water bearing zone may be estimated using the same seepage velocity equation presented above. However, in this case the calculation of seepage velocity is dependent on the hydrologic parameters of the water bearing zone. Table 4 presents the existing permeability test results for the site (Chen-Northern, Inc., 1990b).

TABLE 4
WATER BEARING ZONE PERMEABILITY TEST RESULTS

Boring/ Test Pit	Method	Direction	Material	Saturated Permeability (k_s) (cm/sec)
E-1D	Slug-Copper	Horizontal	Sand/Gravel, 80'-90'	$3x10^{-4}$
E-1D	Slug-Hvorslev	Horizontal	Sand/Gravel, 80'-90'	$1x10^{-4}$
E-1D	Bailer Recovery-Cooper	Horizontal	Sand/Gravel, 80'-90'	$4.0x10^{-4}$
E-2	Slug-Cooper	Horizontal	Sand/Gravel, 85'-90'	$3x10^{-4}$
E-3	Slug-Cooper	Horizontal	Sand/Gravel, 67'-77'	$6x10^{-5}$
E-3	Bailer Recovery-Cooper	Horizontal	Sand/Gravel, 67'-77'	$4.1x10^{-5}$
E-6	Slug-Cooper	Horizontal	Sand/Gravel, 154'-164'	$8.2x10^{-6}$
E-7	Slug-Cooper	Horizontal	Sand/Gravel, 150'-160'	$2.8x10^{-3}$
E-8	Slug-Cooper	Horizontal	Sand/Gravel, 128'-134'	$3.3x10^{-4}$
E-9	Slug-Cooper	Horizontal	Sand/Gravel, 143'-157'	$3.3x10^{-4}$

The average of these values (Table 4) , after eliminating the high and low readings, results in an average saturated permeability of:

Average $k_s \approx 2.3 \times 10^{-4}$ cm/sec $\approx$ 238 ft/year

The other pertinent hydrologic parameters are:

i = 0.02 - 0.04 (Chen-Northern, Inc., 1990b)

n_e = 0.25 (assumed for Sand/Gravel with $k_s \approx 10^{-4}$ cm/sec; Note: Although Table 4 lists the material as "Sand/Gravel", there must be a fine size fraction to account for the low measured values of k_s)

Therefore, the velocity of groundwater flow beneath the site ranges:

$V_s = k_s i / n_e$

V_s = (238 ft/year x 0.02)/0.25 to (238 ft/year x 0.04)/0.25

V_s = 19 - 38 ft/year

In the vicinity of Cell #1, the general groundwater flow is toward the east unit boundary (Chen-Northern, Inc., 1990b). Table 5 indicates the range of times for the groundwater to reach the east unit boundary from various starting locations within Cell #1., the range is:

T = 3 - 37 years (depending on starting location and hydraulic gradient (i))

TABLE 5
GROUNDWATER FLOW TIMES BENEATH CELL #1

Starting Location	Distance to East Unit Boundary (ft)	Time of Groundwater Flow to East Unit Boundary (years)
West Edge of Cell #1	700 feet	18 - 37 years
Middle of Cell #1	400 feet	11 - 21 years
East Edge of Cell #1	100 feet	3 - 5 years

SUMMARY

Table 6 summarizes the significant points for comparing the performance of the "standard" Subtitle D composite liner system with the proposed alternative composite liner system. In our opinion, it not only demonstrates equivalency between the systems; it indicates the superiority of the proposed alternative composite liner.

As indicated on Table 6, the comparison of the estimated leakage through the two liners is:

- Proposed Alternative ≈ 10 gallons/year
- "Standard" Subtitle D ≈ 296 gallons/ year

Also, the estimated time for leakage to reach the unit boundary via the known groundwater flow is:

- Proposed Alternative ≈ 367 years
- "Standard" Subtitle D ≈ 370 years

In our opinion, the calculated times for leachate to reach the landfill unit boundary are essentially the same. The real difference between the liner systems is the order-of-magnitude less leakage predicted for the alternative composite liner as compared to the "standard" Subtitle D liner. In reality, as indicated by the available test work (Daniel & Boardman, 1992), the predicted leakage for the proposed alternative liner is conservatively large and any leachate penetrating the upper 60 mil HDPE should be adsorbed in hydrating the bentonite component of the Gundseal®. It should not, to any measurable extent, enter the foundation soil beneath Cell #1.

REFERENCES

Cedergren, H.R., 1989, Seepage, Drainage, and Flow Nets, Third Edition, John Wiley.

Chen-Northern, Inc., 1990a, "Hydrological Investigation Report. .", March 9, 1990.

Chen-Northern, Inc, 1990b, ". .Phase II Hydrological Investigation. .", October 26, 1990.

Daniel, D.E. & Boardman, B.T., 1992, "Report of Workshop on Geosynthetic Clay Liners", Risk Reduction Engineering Laboratory, Office of Research and Development, U.S. Environmental Protection Agency, Cincinnati, Ohio, September, 1992.

Fetter, C.W.Jr., 1980, Applied Hydrogeology, Charles E. Merrill Publishing Company.

Giroud, J.P., 1993, "Landfill Cell and Liner Design", Workshop U. of Florida, 1993.

Tchobanoglous, G., Theisen, H., Vigil, S., 1993, Integrated Solid Waste Management, Engineering Principles and Management Issues, McGraw-Hill.

Vick, S.G., 1983, Planning, Design, and Analysis of Tailings Dams, John Wiley & Sons.

TABLE 6
COMPARATIVE SUMMARY OF MAJOR ITEMS FOR THE "STANDARD" SUBTITLE D LINER AND THE PROPOSED ALTERNATIVE LINER

ITEM	"STANDARD" SUBTITLE D COMPOSITE LINER SYSTEM	PROPOSED ALTERNATIVE COMPOSITE LINER SYSTEM	COMMENTS
Total Leakage Amount	296 gallons/year 8880 gallons/30 years	10 gallons/year 300 gallons/30 years	Total leakage amount is considerably less for the alternative liner. In reality, this amount likely will be adsorbed in hydrating the bentonite and will not truly escape the liner system to any measurable extent. In addition, the estimate ignores the 20 mill HDPE underlying the bentonite.
Leakage Breakthrough Time	2.6 years	1 week (through aligned holes in both HDPE membranes) 10 years (through overlap seam assuming a hole in the upper HDPE membrane at the edge of the overlap)	The shorter leakage breakthrough time calculated for the alternative liner requires that open holes exist directly opposite each other in both membranes. An offset of only 3 inches between holes results in a breakthrough time similar to the overlap seam. Therefore, it is considered highly unlikely that the breakthrough time for the alternative liner will be truly less than for the "standard" Subtitle D system.
Time for Leakage to Reach a Water Bearing Zone	Hypothetical Water Bearing Zone @ 10 feet ~ 45 years Known Water Bearing Zone @ 80 feet ~ 364 years	Same	The known water bearing zone is at least 80 feet below the Cell #1 liner; therefore, the time for leakage to reach the existing groundwater is approximately 364 years. The estimate for the hypothetical water bearing zone at 10 feet is provided for comparison purposes; even if such a zone existed, it would take approximately 45 years for the leakage to reach it.
Time for Leakage to Cross the Unit Boundary Once It Has Reached the Groundwater	3 - 37 years depending on starting location and hydraulic gradient	Same	The general groundwater flow beneath Cell #1 is toward the eastern unit boundary with a gradient range of 0.02 - 0.04. The shortest time assumes the leak occurs at the eastern edge of Cell #1 (100 feet from the unit boundary) and has a gradient of 0.04. The longest time assumes the leak occurs at the western edge of Cell #1 (700 feet from the unit boundary) and has a gradient of 0.02.
Total Time for Leakage to Reach the Unit Boundary	Hypothetical Water Bearing Zone @ 10 feet ~ 2.6+45+3 ~ 51 years Known Water Bearing Zone @ 80 feet ~ 2.6+364+3 ~ 370 years	Hypothetical Water Bearing Zone @ 10 feet ~ 45+3 ~ 48 years Known Water Bearing Zone @ 80 feet ~ 364+3 ~ 367 years	Both estimates assume the leak is at the closest location to the unit boundary and the groundwater travel under the influence of the greatest hydraulic gradient.
Freeze/Thaw Resistance	Vulnerable to large increases in permeability from freeze/thaw	No increase in permeability from freeze/thaw	Freeze/Thaw has no effect on the alternative liner system, but will cause large increases in the permeability of the Subtitle D clay liner.
Wet/Dry Effects	Vulnerable to desiccation cracking and increase in permeability	No increase in permeability from wet/dry effects	Wet/Dry has no effect on the alternative liner system, but may cause an increase in the permeability of the Subtitle D clay liner.

Hydrogeology, Waste Disposal, Science and Politics
Proceedings 30th Symposium
Engineering Geology and Geotechnical Engineering, 1994

EVALUATION OF THE GROUND WATER RESOURCES WITHIN THE LEWISTON BASIN

Gary R. Stevens, College of Mines and Earth Resources, University of Idaho, Moscow, ID 83843

Dr. Dale Ralston, College of Mines and Earth Resources, University of Idaho, Moscow, ID 83843

ABSTRACT

The Lewiston Basin located in North Idaho covers approximately 550 square miles and includes the cities of Lewiston, Idaho and Clarkston, Washington. The deep aquifer in the Lewiston Basin has been declared a sole source aquifer. This system provides the primary water supply for the City of Clarkston Washington and a partial water supply for the City of Lewiston and the Lewiston Orchards Irrigation District. Questions have been raised relative to the maximum yield of the aquifer system with the continued growth of the area. This study addresses the hydrogeology of the basin, along with the locations and mechanisms for recharge and discharge.

The geology of the Lewiston Basin consist of Miocene-Pliocene basalt flows overlain by quaternary sediments. The basalt flows were structurally deformed during and after emplacement, thus creating a structural basin with numerous faults. The lower most basalt unit of the Lewiston Basin is the Imnaha Basalt, which is overlain by the Grande Ronde and Wanapum Basalts. The boundaries of the ground water flow system are the same as the structural basin.

The Lewiston Basin, based on static water levels, appears to have three separate aquifer systems, the sedimentary aquifer, the Wanapum Basalt aquifer and the Grande Ronde Basalt aquifers. The aquifers, composed of dipping basalt units, are most likely recharged where they intersect the Snake River in the southern part of the basin and also along a portion of the Clearwater River and its tributary creeks in the eastern part of the basin. The discharge area appears to be just west of the Snake River and Clearwater River confluence. The Grande Ronde Basalt aquifer is utilized by the cities of Lewiston and Clarkston, while the shallower sedimentary and Wanapum Basalt aquifers are used for domestic wells. Compilation and analysis of pump and water level data from the major ground water users of the Lewiston Basin from 1960 to 1993 show no apparent long term water level decline.

INTRODUCTION

Statement of Problem

The Lewiston Basin covers approximately 550 square miles and includes the Cities of Lewiston, Idaho and Clarkston, Washington (figure 1). The Lewiston Basin is a broad, shallow syncline with an axis that strikes east-west with both ends plunging towards the center of the Basin. The Snake River flows from south to north through the center of the study area (defining the Idaho-Washington border) and intersects the west flowing Clearwater River, near the northern boundary of the Lewiston Basin.

The three largest water management agencies within the Lewiston Basin are the: 1) Asotin County Public Utilities District (APUD), which serves the City of Clarkston and surrounding areas; 2) City of Lewiston; 3) Lewiston Orchards Irrigation District (LOID). The latter two agencies supply water to the City of Lewiston and vicinity. The APUD and LOID use mostly ground water for their needs while the City of Lewiston acquires almost all of its water from the Snake and Clearwater Rivers. Most of the wells were completed in the 1950s and 1960s. Other smaller public water management agencies within the study area include the Cities of Lapwai, Idaho and Asotin, Washington. The Port of Wilma along the Snake River in Idaho also has its own wells. Industry in the study area have developed their own wells; these include: the Potlatch Corporation, Blount Industries and Twin Cities foods. The United States Army Corps of Engineers manages a well that supplies water for Chief Timothy Park on the Snake River. A number of small domestic and agricultural wells are completed within the Lewiston Basin, mostly in the Lewiston Orchards and Clarkston Heights areas. Most of the shallow wells are completed in the alluvial and

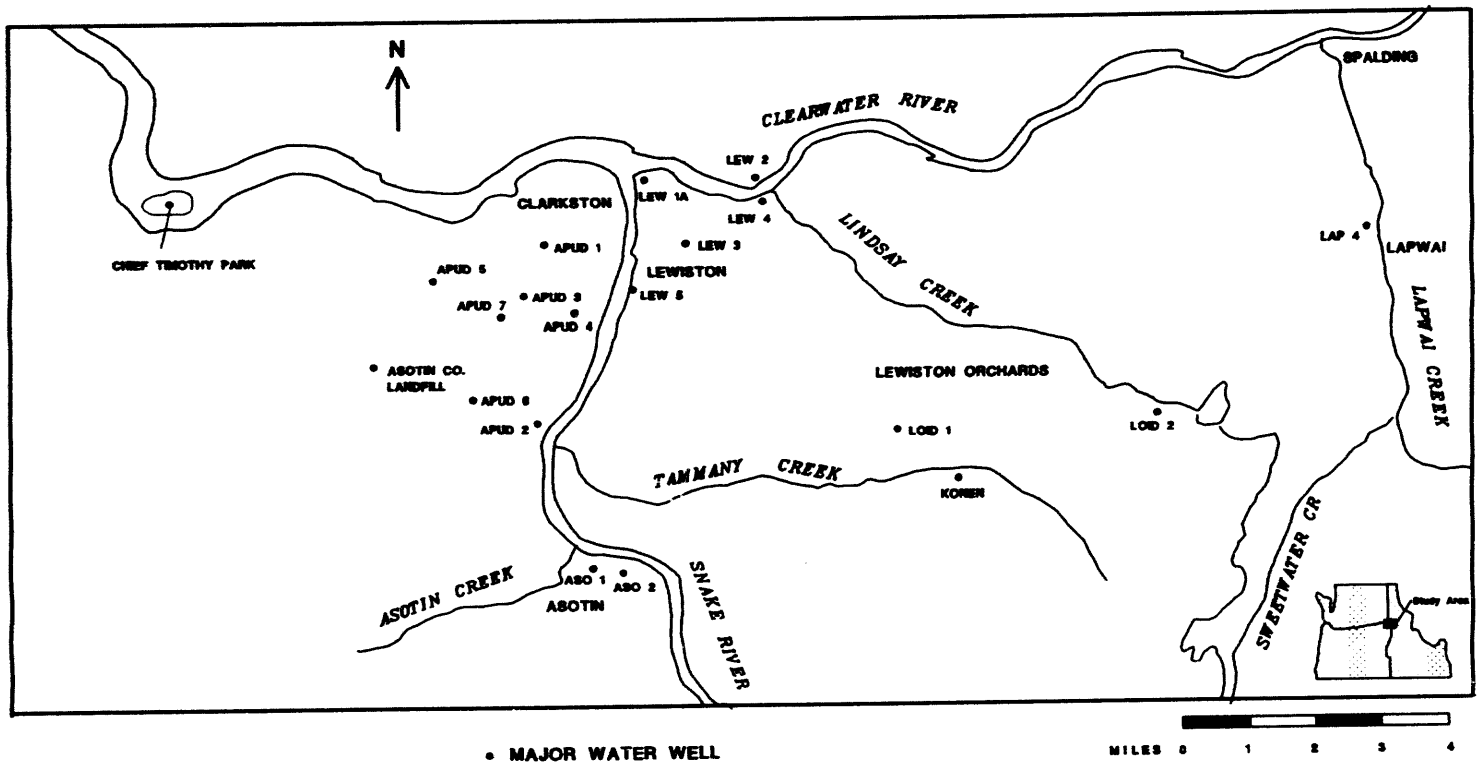


Figure 1. Location map of the Lewiston Basin study area.

shallow basalt aquifers, and the larger municipal wells are completed within deeper basalt aquifers.

Continued population and economic growth within the Lewiston Basin will necessitate greater ground water pumpage and the future construction of more production wells. This will be accelerated if the City of Lewiston partially switches away from surface water supplies.

Purpose and Objectives

The purpose of this report is to serve as a technical guide for the LOID and other water supply entities in the development of additional wells constructed into deep basalt aquifers within the Lewiston Basin. The general objectives are to 1) describe the hydrogeology of the Lewiston Basin, and 2) the potential for the additional development of high yield production wells and the impacts that future wells might have on existing wells.

Water Production Wells

All the information regarding the aquifer characteristics discussed in this report came from data on existing water wells. The discussion of where these wells are located, and the details of well construction are imperative to the description of the hydrogeology. The APUD has a total of seven wells drilled in and around the Clarkston, Washington area (see figure 1). The wells are completed with a range of depths -76 to -183 feet msl. The wells have reported yields of 1350 gpm to 4200 gpm.

The City of Lewiston has a total of five water production wells. The wells are located within and near the City of Lewiston, Idaho. The wells have depths of 460 to -5 feet msl and reported yields of 295 gpm to 1677 gpm. The City of Lewiston acquires most of its water from the Snake and Clearwater Rivers. The wells are only used during the summer months when water demands are at the peak. The two additional major wells located in the eastern portion of the Lewiston Basin, belong to the Lewiston Orchards Irrigation District. LOID wells, #1 and #2 have depths of -353 and -219 feet msl respectively. LOID #1 has a reported yield of approximately 870 gpm, and LOID #2 has reported yield of 935 gpm.

A wildcat oil well (Konen well) is located near the LOID wells. The oil well is presently used for irrigation of a parcel of farm land adjacent to the Tammney School on Waha Road in the Lewiston Orchards. The well was reported to have been drilled to a depth of approximately 3000 feet.

Other wells in the study area belong to the City of Asotin, City of Lapwai and Chief Timothy Park along the Snake River. There are a number of other small irrigation and domestic wells spread out over the study area; most of these wells are less than 500 feet deep.

HYDROGEOLOGIC SETTING

Introduction

The thickness and lateral extent of individual basalt flows, physical properties of the aquifers, and the presence of any structural deformation or lateral no-flow boundaries, all can have significant impacts on ground water flow and on water level changes related to pumping of water wells. The deeper aquifers within the Lewiston Basin are composed of a series of basalt flow contact units. The hydraulic properties and structural configuration of these units control ground water flow characteristics.

Geologic Stratigraphy

Imnaha Basalt

The Imnaha Basalt is the oldest basalt sequence of the Columbia River Basalt Group within the Lewiston Basin (see figure 2). The Imnaha Basalt, which is approximately 500 to 1000 feet thick, forms the hydrogeological basement within the Lewiston Basin.

Grande Ronde Basalt

The Grande Ronde is the most voluminous sequence of flows in the Columbia River Basalt Group, with a maximum thickness of approximately 2000 feet within the Lewiston Basin. The Grande Ronde has four alternating paleomagnetic intervals, showing remanent magnetism with both normal and reversed fields

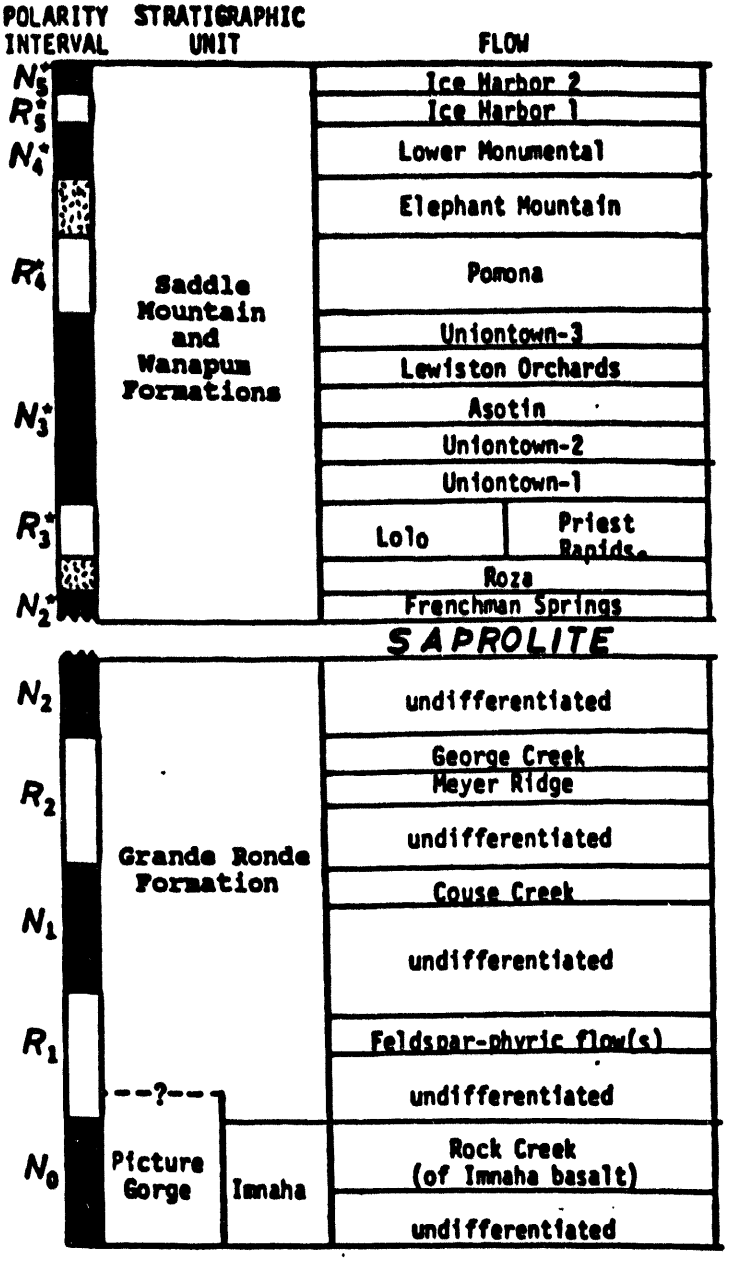


Figure 2. The basalt stratigraphy of the Colombia River Basalts within the Lewiston Basin (Camp, 1976).

(relative to the present earth magnetic field). The lowermost interval is reversed and is designated R1. This interval is overlain by the next three paleomagnetic sequences designated N1, R2 and N2 respectively. All of the basalts which overlie the N1 thicken toward the center of the basin.

Saprolite Layer

The significant period of quiescence that followed the extrusion of the Grande Ronde Basalt is expressed as a saprolite layer. The saprolite is a red-grey clay formed by weathering of the N2 basalt layer. The saprolite is widespread throughout the Lewiston Basin and forms a marker between the Grande Ronde Basalt and the overlying formations

Wanapum Basalt

The Wanapum Basalt overlies the Grande Ronde Basalt and consists of a number of flows which include from oldest to youngest: the Dodge Member, Roza Member, and two flows of the Priest Rapids Member. The most extensive of these basalts is the uppermost Priest Rapids Member which averages 150 feet through out most of the Lewiston Basin (Camp, 1976). The Priest Rapids Member overlies the saprolite everywhere except along the western boundary of the study area. The lower most Dodge Member and the middle Roza Member are not found within the Lewiston Basin, but do exist extensively elsewhere in the Clearwater Embayment.

Saddle Mountain Basalt

The Saddle Mountain Basalt consists of a number of basalt flows separated above and below by interbeds. There are a total of eight flows that consist of four different magnetic polarities. The lower five flows (Uniontown-1, Uniontown-2, Asotin, Lewiston Orchards, and Uniontown-3 flows) are laterally extensive and cover the Lewiston Basin, while the upper three (Pomona, Elephant Mountain and Lower Monumental flows) occur as intracanyon basalts. The Saddle Mountain Basalts rest upon the Sweetwater Creek Interbed, which separates it from the Priest Rapids Member. The Sweetwater Creek interbed consist of fine sands, silts clays and coarse detritus, and can be over 200 feet thick.

Quaternary Sediments

The Lewiston Basin contains a thick sequence of Quaternary stream gravels which thicken toward the present confluence of the Snake and Clearwater confluence (Kehew, 1977). The gravels are composed of basalt and basement detritus and reach a thickness of 400 feet. The gravel deposits can be found southwest of the City of Clarkston, Washington and also both north and south of the Clearwater River near Lewiston, Idaho. The gravels are most likely fluvial deposits of pleistocene age formed by the aggradation of the gravels within ancestral channels of the Snake and Clearwater Rivers.

Structural Geology

One of the most significant features of the area is the doubly plunging syncline found just south of Lewiston, Idaho and Clarkston, Washington (see figure 3). The syncline strikes east-west, with each end of the axis plunging approximately one to two degrees toward the central low point which is near the present Snake River Canyon. The limbs of the syncline dip approximately 2 degrees toward the central axis.

The northern extent of the study area is defined by the Clearwater Escarpment, which has almost 1800 feet of relief from top to bottom. At the base of the Clearwater Escarpment is the east-west striking Gaging Station Anticline, an asymmetrical anticline bounded by the Wilma fault to the south and the Vista fault to the north. The Wilma fault extends west along the Snake and Clearwater Rivers, crossing the Snake River just east of Chief Timothy Park and terminates near the western boundary of the study area. The Wilma fault is believed to be the northern major structural barrier that controls ground water flow (Cohen, 1979).

A major structure found in the southern portion of the study area is the Uniontown Anticline. The Uniontown Anticline, Lewiston Syncline and the Clearwater Escarpment are believed to be the expression of a north-south compressional regime which created the major structures of the area. The compression most likely occurred during the Miocene and was followed by subsidence of the Lewiston Basin during the Miocene-Pleistocene period. The subsidence beneath the Lewiston Basin is probably due to withdrawal of magma

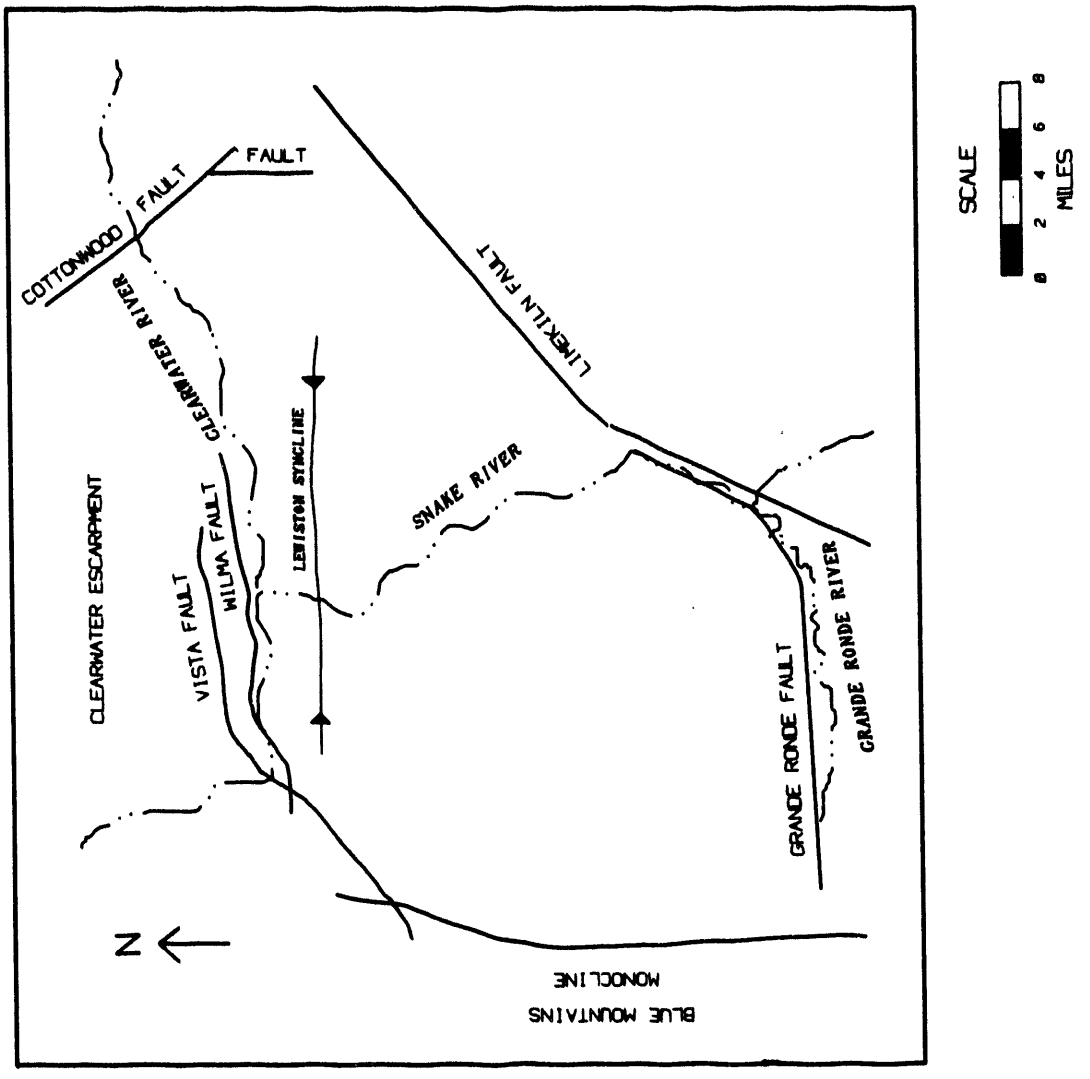


Figure 3. Structural features of the Lewiston Basin.

from reservoirs and isostatic adjustment to the load of basalt flows imposed on the crust (Bond, 1963).

The southern limit of the study area is defined by both the Limekiln Fault and the Grande Ronde Fault. The Limekiln Fault strikes northeast from the Limekiln Rapids on the Snake River to Mission Creek. The rest of the southern boundary is defined by the Grande Ronde Fault. This structural feature runs from Anatone Butte striking east-west paralleling the Grande Ronde River to an area just north of the Limekiln Rapids. At this site, it runs northeast, follows the Limekiln Fault and terminates near Captain John Rapids on the Snake River.

The western boundary is formed in part by a northeast striking fault, which intersects the Wilma Fault approximately two miles southwest of Chief Timothy Park. The southwest-northeast trending fault extends for approximately ten miles, intersecting a monocline structure that strikes north-south and dips to the east, which forms the rest of the western boundary. The eastern boundary of the study area is formed by a northwest-southeast fault that follows Cottonwood Creek.

Description of Aquifers

Introduction

Aquifers occur in all of the basalts units within the Lewiston Basin. The completed sections of the major municipal wells are for the most part limited to the R2 and N1 of the Grande Ronde Basalt; the LOID #2 well which is completed in the R1. Many of the shallow domestic wells found in Lewiston Basin are completed in the alluvium and upper basalt units.

Wanapum and Saddle Mountain Aquifers

Most of the wells completed in the Wanapum and Saddle Mountain Basalts are shallow domestic and irrigation wells. The wells have yields averaging 10 to 20 gpm. The recharge for aquifers in the Saddle Mountain and Wanapum Basalts is believed to be from irrigation and precipitation mainly in the Lewiston Orchards area in Idaho and the Clarkston Heights area in Washington (Salami, 1978). Salami (1978) also states that the Wanapum Aquifer discharges in the form of seeps and springs along the valley slopes above the Grande Ronde Basalts.

Grande Ronde Basalt Aquifers

All of the large wells in the study area are completed opposite aquifers in the Grande Ronde Basalts. Most of these wells have static water elevations near the river level elevations and have large yields (greater than 1000 gpm). The water elevation of LOID well #2 is approximately 480 feet higher than the other wells completed in the Grande Ronde Basalts. Alternative explanations for this discrepancy are presented later in the report.

PRESENTATION AND ANALYSIS OF PUMPAGE, WATER LEVEL, AND WATER QUALITY DATA.

Introduction

Pumpage and water level data from production wells provide significant information with respect to the characteristics of the ground water flow system in the study area. Correlation of water levels from area wells help identify isolated aquifers and define the ground water gradients within the aquifers. Large decreases in water levels with pumping over a number of years are indicative of the physical properties of the aquifer, particularly the presence of lateral no-flow boundaries and confining layers or that pumping is in excess of recharge. Conversely, constant water levels in the aquifers with significant pumpage usually indicate hydraulic interconnection of the aquifer with surface water systems.

Historic Pumpage and Water Level Data

Presentation of Pumpage Data

The Lewiston Orchards Irrigation District, Asotin PUD, and City of Lewiston collect the pumpage data on a daily basis. These pumpage data have been compiled on a yearly basis for the all the major municipal wells within the Lewiston Basin.

The amount of water pumped differs dramatically between the water management agencies. The user that pumps the least amount of groundwater is the City of Lewiston, with a yearly average of 2.1×10^8 gallons over the period of record. The LOID pumpage is next in magnitude with a yearly average of 4.6×10^8 gallons. The LOID pumps water for irrigation and domestic use.

The largest user of ground water within the Lewiston Basin is the APUD with a yearly average of 1.9×10^9 gallons. The APUD derives almost all of its water from ground water. The APUD provides irrigation and domestic water for the City of Clarkston and the surrounding areas.

Presentation of Water Level Data

None of the APUD wells show significant water level decline with time. The APUD wells 1,2,4,5, and City of Lewiston Wells 1A and 5 show an increase in water levels during 1975 (average of 20 feet), achieving a new equilibrium (Cohen, 1979). The new static water level is attributed to the filling of the Lower Granite Dam (Bond and Ralston, 1977). The water levels for City of Lewiston wells 1A, 2, 3, and 5 all appear to be stable with time.

Recorded static water levels for the R2-N1 basalt units within the Lewiston Basin during April of 1988 show that ground water is flowing from the south-southeast to the northwest. The ground water flow path suggests that a discharge area exists between Chief Timothy Park and the confluence of the Snake and Clearwater Rivers.

Relationship of Pumpage to Water Levels

The nature of the ground water system in the Lewiston Basin can be examined by studying the historic pumpage and temporal water level fluctuations in response to the pumpage. The primary area of pumpage in the basin is in Clarkston, centered on the APUD wells. The combined annual pumpage from these wells, plus other production wells in the basin, averaged about 2.1×10^9 gallons in the period of 1960 to 1991. The APUD wells have had no discernable pattern of water level decline over the same period. This level of pumpage with no major water level decline is possible only if the ground water system is hydraulically connected to a surface water body either in the recharge or discharge areas. The combined pumpage and water level data confirm the hypothesis that the aquifer system in the Grande Ronde Basalts is hydraulically connected to the Snake and/or the Clearwater Rivers.

The pumpage record and associated water level hydrograph for LOID well #2 show a different pattern. The pumpage from LOID well #2 has caused a significant water level decline with apparent equilibrium conditions after 1988. The pumpage/water level data show that LOID well #2 obtains water from an aquifer that is separate from other municipal production wells in the basin.

Water Chemistry

Introduction

Eight wells were sampled within the Lewiston Basin and tested for specific chemical components. The purpose of the ground water sampling project was to: 1) describe the groundwater flow paths based on the hypothesis that the chemical composition of the water will change with an increase in residence time and/or distance traveled along the flow path and 2) delineate different aquifers.

Ground water in general will evolve in basalt from a Calcium-Magnesium-Bicarbonate type to a Sodium-Potassium-Bicarbonate type (Steinkampf, 1985). The presence and distribution of ions in the ground water indicate the state of evolution.

Wells Sampled and Sampling Procedure

The wells sampled were based on a conceptual ground water flow model with recharge and discharge areas supported by static water levels and structural configuration of the basin. Relatively shallow wells were selected in hypothesized discharge and recharge areas and deeper wells were selected in the mid-portion of the ground water flow system. The specific wells selected were: LOID #1, LOID #2, City of Lapwai well #5, City of Lewiston well #5, APUD wells #2, #3 and #5, City of Asotin well #2, Chief Timothy Park well, and the Konen well.

The samples at each well were taken from water using the existing pump, and collected only after the temperature had stabilized. The temperature was noted and the pH was taken using a Hydac pH tester. The unfiltered samples were placed in plastic bottles and acidified to a pH of 2 or less with nitric acid (HNO_3). The sample bottles were stored in a cooler with ice until delivered to the lab. Holding time never exceeded eight hours for any of the samples. All of the samples were analyzed by Anatek Labs in Moscow, Idaho.

Presentation and Analysis of Water Quality Data

Each water sample was analyzed in the lab for the following parameters: Ca^{+}, Na^{+}, K^{+}, Mg^{2+}, HCO_{3-}, Cl^{-}, Fe(total), SiO_2. The anion and cation results were plotted on a Piper diagram, which shows the distribution of the major cations and anions by percent composition in miliequvalents per liter (see figure 4). The central diamond shaped diagram, shows a distinct linear distribution in relation to the Na+K and Ca+Mg content. The linear distribution extends from LOID#1 (sample 1) in the lower right with a high Na content (85%) and low Mg-Ca content, to Chief Timothy Park Well (sample 8) with a much higher Ca and Mg content (52% and 27% respectively).

Interpretation

The chemistry shows that the City of Lapwai, the City of Asotin and Chief Timothy Park wells tap ground water that is relatively younger. These wells are most likely located in recharge areas. The Lapwai and Asotin areas were postulated to be recharge sites by Cohen (1979) based on the structural settings of the basin. The Chief Timothy area probably was a regional discharge site prior to the initiation of municipal well pumping. The area is currently believed to be a recharge area because hydraulic gradients have been reversed by extensive pumping in the Clarkston area. The LOID #1 well yields ground water that is significantly older probably representing the deeper portions of the ground water flow system. The Konen well (previous oil well) shows a water chemistry characteristic of a shallower well, probably due to mixing of deep water and shallow water within the largely uncased well. LOID #2 water chemistry most likely represents ground water from a separate aquifer system, since it is completed at approximately the same depth as LOID #1.

FLOW SYSTEM DESCRIPTION

Alternative Hydrogeologic Conceptual Models

The aquifers of primary interest in this report are within the Grande Ronde basalts. The geologic, water level and water chemistry indicate that two hydraulically isolated aquifers and/or flow systems are present in the area. All of the wells except LOID #2 and the Konen well appear to penetrate a single aquifer system. The LOID #2 well and the Konen well have water level elevations that are approximately 480 feet higher than the other wells. These two wells appear to be within a different aquifer system.

Two alternative hydrogeologic conceptual models have been formulated to explain the apparent two aquifer system within the Grande Ronde basalts in the Lewiston Basin. The first conceptual model is based on horizontal stratification that isolates the two aquifers. The second conceptual model utilizes approximately vertical discontinuities to explain the water level differences. These two conceptual models are described in the following paragraphs.

First, the two separate aquifers in the Grande Ronde basalts may be correlatable to paleomagnetic sub-units of this formation. The postulated upper Grande Ronde aquifer would correlate with the N1 and R2 units and have characteristic water level elevations in the range of 720 to 740 feet. The postulated lower Grande Ronde aquifer would correlate with the R1 unit and have characteristic water level elevations of about 1,200 feet. This conceptual model is supported by the fact that the LOID #2 is the only well known to be completed in the R1 unit. However, APUD #2 (oil test well) was reported to be drilled to depths sufficient to have penetrated the R1 unit. The 1,200-foot static water level elevation for this aquifer would have produced dramatic flowing well conditions. The original records for this well do not indicate that this occurred. The APUD #2 data suggest that a continous R1 aquifer does not exist on the west side of the Snake River. Also, the discharge of water characteristics of LOID #2 (warmer temperature) has not

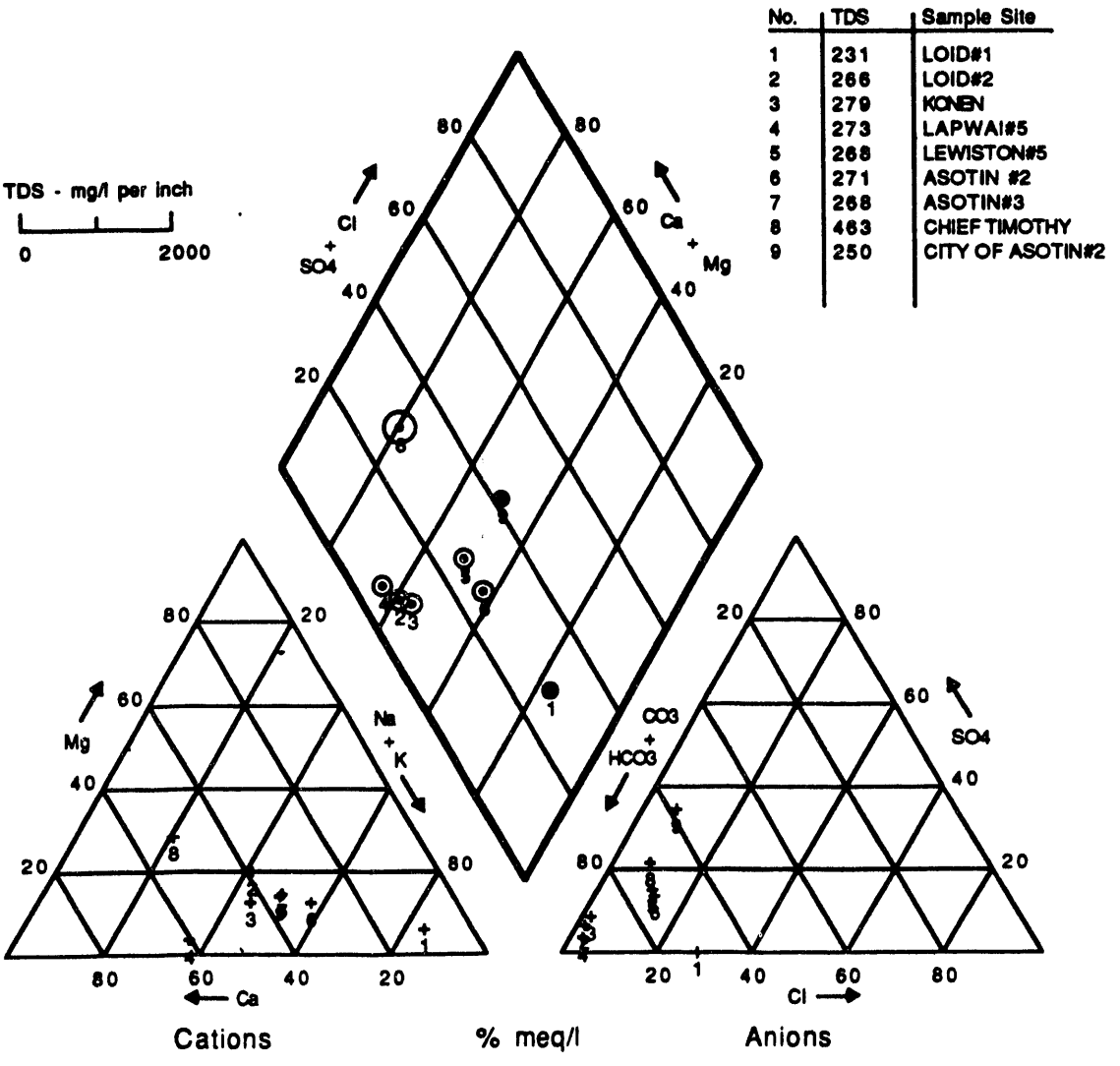


Figure 4. Piper diagrams for wells sampled in the Lewiston Basin.

been found to occur at an outcrop of the R1 unit along the Clearwater River east of the study area that is below 1,200 feet elevation or an outcrop of the R1 unit along the Snake River at an elevation of about 820 feet. The geologic, water level and water quality data indicate that separate aquifers based on paleomagnetic sub-units of the Grande Ronde basalts probably is not a valid conceptual model.

In the second conceptual model, a single aquifer in the Grande Ronde basalts is postulated to be separated into semi-isolated compartments by roughly north-south trending geologic discontinuities. One discontinuity would separate the LOID #2 and Konen wells from LOID #1 and the other wells to the west. A second discontinuity would isolate the LOID #2 area from the Lapwai Valley and Grande Ronde basalt outcrops to the east. The structural features that form the Clearwater Escarpment would bound the aquifer on the north. This conceptual model fits with all of the available hydrologic information. The western discontinuity would separate this system from interconnection with the Snake River and the water level elevations near river level. The eastern discontinuity would isolate the system from interconnection with the Clearwater River. The lack of hydraulic connection with these major surface water systems is consistent with the major water level decline experienced in LOID #2 in contrast with the relatively constant water levels in the other wells.

Description of Ground Water Flow Patterns

The recorded water levels from wells completed in the Grande Ronde formation in the Lewiston Basin (excluding the LOID #2 and Konen wells) shows a gradient toward the northwest. This ground water system probably discharged to the Snake River between the Snake and Clearwater Rivers confluence and the Chief Timothy prior to well development in the area. The location of the original discharge area is supported by early reports of lack of ice along this portion of the free flowing river (Cohen, 1979). The lack of ice would be indicative of a discharge area, where warmer ground water is discharging into the river. The present indicated direction of ground water flow probably is centered on the cone of depression created by pumpage of the APUD wells. Water quality data suggest that the Chief Timothy area now receives recharge from the Snake River; this original discharge area has been converted to a recharge area because of limited water level declines caused by pumpage.

Water chemistry data show that the areas near the Cities of Lapwai and Asotin have relatively young ground water. This supports Cohen's hypothesis that ground water recharge occurs in these areas. The water level elevations of all the Grande Ronde aquifer wells (except LOID #2 and Konen) are compatible with the elevations of the Grande Ronde outcrop areas along reaches of the Snake and Clearwater Rivers.

The static water level in the LOID #2 well (1,213 feet) is higher than the elevations of any of the identified river recharge areas. The recharge for the eastern portion of the Lewiston Basin is most likely derived from areal precipitation and possibly some contributions from along the Limekiln Fault. There is no evidence for significant ground water discharge from the portion of the Grande Ronde aquifer penetrated by the LOID #2 well.

Ground Water Equilibrium Conditions

The western portion of the Grande Ronde aquifer in the Lewiston Basin appears to be in equilibrium with the present rate of pumpage. The hydrographs of the municipal wells in this area show no long-term pattern of water level decline because of the hydraulic connection with the Snake River and possibly the Clearwater River. The rivers act as positive boundaries this limiting the water level decline in the area.

The eastern portion of the Grande Ronde aquifer in the Lewiston Basin has undergone significant historic water level decline based on records from LOID #2. At this time, the pumpage from LOID #2 apparently has been balanced by an increase in recharge and/or a decrease in discharge; the water levels in LOID #2 have been stable for about the last 5 years. The recharge and discharge characteristics and controls for the eastern portion of the Grande Ronde aquifer in which LOID #2 is completed are poorly understood.

The potential for future well development and additional pumpage from

the Grande Ronde aquifer in the Lewiston Basin is much greater in the western portion than in the eastern portion based on available hydrogeologic data. The western portion has a demonstrated hydraulic connection to major surface water systems. Additional pumpage in this area will likely be balanced by increased recharge with little change in water levels. Additional pumpage in the eastern portion of the area will likely result in additional water level decline. The recharge to this area is likely to be less then the pumpage and probably will not increase significantly with lowered water levels.

CONCLUSIONS

The Lewiston Basin is composed of a number of Miocene flood basalts which were structurally altered forming a doubly plunging syncline, which defines the Lewiston Basin. The boundaries of the basin which is delineated by a number of folds and faults, also define the boundaries of the ground water flow system.

The ground water system of the Lewiston Basin consist of aquifers in the Saddle Mountain Basalts, Wanapum Basalts, and the Grande Ronde Basalts. The Grande Ronde Basalts are the primary source of water for large municipalities within the Lewiston Basin. Most of the deep wells are completed in the R2 and N1 units and are located near or west of the Snake River. LOID well #1 which is farther east is believed to be part of this group. All of these wells have similar static water level elevations. Yields range from approximately 200 gpm to 4200 gpm. LOID well #2 is located in the eastern portion of the area and has a static water level elevation almost 450 feet higher than the other wells. The yield of this well is 1000 gpm. The LOID well #2 is hypothesized to be different from the other wells because: 1) the R1 unit is a separate aquifer relative to the R2-N1 units or 2) a lower transmissivity zone is located between LOID wells #1 and #2. The recharge regions for the aquifers of the R2-N1 and R1 units are believed to be these areas where these basalt units intersect sections of the Snake River approximately 3 to 9 miles south of Lewiston, and along portions of the Lapwai and Sweetwater creeks. The Ca^{+} and Na^{+} data show that the Chief Timothy Park, City of Lapwai, and City of Asotin wells appear to be in recharge areas.

The pre-development ground water discharge area for the Lewiston Basin appears to be a section of the Snake River between the Snake River - Clearwater River confluence and Chief Timothy Park. The discharge area was evidenced by the lowest water levels in the Lewiston Basin and reports of relatively warmer waters within this section of the Snake River. The pumping of municipal wells however, now has reversed flow to make this a recharge area. Water chemistry of the Chief Timothy Park well suggests relatively young water.

The lack of long-term water level decline in the major municipal production wells of APUD, City of Lewiston and LOID well #1 provide additional evidence for hydraulic connection to the rivers. These data indicate that additional well development is possible with little major water level decline.

REFERENCES

Bond, J.G., 1963, Geology of the Clearwater Embayment in Idaho: Ph.D. dissertation, University of Washington, Seattle, Washington, 193 p.

Bond, J.G., and D.R. Ralston, 1977, Lewiston Orchards Groundwater Potential and Well Site Location Study: Unpublished Consulting Report, Moscow, Idaho, 17p.

Camp, V.E., 1976, Petrochemical Stratigraphy and Structure of the Columbia River Basalt, Lewiston Basin Area, Idaho-Washington: Ph.D. dissertation, Washington State University, Pullman, Washington, 201 p.

Cohen, P.L., 1979, Reconnaissance Study of the "Russell" Basalt Aquifer in the Lewiston Basin of Idaho and Washington: M.S. thesis, University of Idaho, 163 p.

Kehew, A., 1977, Environmental Geology of the Lewiston and Vicinity: Ph.D. dissertation, University of Idaho, Moscow, Idaho, 210 p.

Salami, S.O., 1978, A Reconnaissance Study of the Ground Water of the Lewiston-Clarkston Area, Idaho-Washington: M.S. Thesis, University of Idaho, Moscow, Idaho, 105 p.

Steinkampf, W.C., Hearn, P.P., Bortleson, G.C., Drost, B.W., Geochemical Controls on Dissolved Sodium in Basalt Aquifers of the Columbia Plateau, Washington: U.S.G.S. Water Resources Investigations Report 84-4304, 38 p.

Hydrogeology, Waste Disposal, Science and Politics
Proceedings 30th Symposium
Engineering Geology and Geotechnical Engineering, 1994

EVALUATION OF GROUND WATER NUTRIENT LOADING TO PRIEST LAKE, BONNER COUNTY, IDAHO

K. M. Freeman and D. R. Ralston
College of Mines and Earth Resources
University of Idaho, Moscow, ID 83844-3022

INTRODUCTION

The quality of Idaho lakes is of increasing concern, particularly when related to waste disposal and land use practices within the watersheds. Priest Lake, located in northern Idaho, is one of the highest quality water bodies in Idaho. However, there are concerns about preserving the existing quality of Priest Lake. The Priest Lake Project was funded by the 1992 Idaho State Legislature with the overall objective of preserving existing water quality while allowing the continuation of nonpoint nutrient sources.

One portion of the general nutrient study of Priest Lake is determining the nutrient loading via ground water from waste disposal practices near the shore line. This portion of the study was directed by the "Groundwater/Wastewater Program Unit" of the Priest Lake Project. The stated objectives of the unit are:

> *Develop a program of groundwater sampling and/or estimation methods which would allow: 1) a lake nutrient value from groundwater, and 2) determine if generated septic effluent is percolating to potable wells, aquifers, and lake bays at unacceptable nutrient and bacteria concentrations. (IDHW-DEQ, 1993)*

Two areas of Priest Lake (Figure 1) were selected by the Groundwater/ Wastewater Program Unit as representative of the types of waste disposal practices that may impact the lake. The two study areas selected are: 1) the Kalispell Bay area and 2) the Granite Creek area. Two sewage lagoon systems in the Kalispell Bay area are septic sources of nutrients that might be tributary to the lake. The septic sources for nutrients in the Granite Creek area are on-site residential subsurface disposal systems. The Kalispell Bay area and Granite Creek area are typical of point and non-point nutrient loading sources present in the Priest Lake area.

HYDROGEOLOGIC SETTING

Introduction

Priest Lake is a glacially formed lake situated in the northwest corner of the Idaho panhandle. The rock types present in the area surrounding the lake are quartzites and argillites of the Belt Supergroup and granite of the Kaniksu Batholith. Weathering of the granite produced alluvial deposits of very coarse to fine granitic sands. Weathering of the very resistant Belt rock types produces sediments ranging in size from gravels to large cobbles. Belt rock clasts are found in the associated alluvial sands adjacent to Belt outcrops.

Kalispell Bay Area

A review of available driller's logs for wells located in the Kalispell Bay study area describe aquifer units of coarse to fine granitic alluvial sands to depths of 80 feet, which can be interbedded with thin clay layers. However, the clay layers do not appear to be stratigraphically continuous across the study area. To provide a measure of the depth to bedrock, surface resistivity surveys were performed at various locations in the area. Analysis of the surveys indicate a sediment thickness of approximately 250 feet. Field data was collected and observations made during construction of 12 shallow ground water sampling wells in the study area. Analysis of these data and observations characterize the upper 20 feet of the aquifer as a relatively homogeneous, very coarse to fine sand with occasional silt-clay lenses. From these investigations, a conceptual hydrogeological model for the Kalispell Bay area was developed. The characteristics of the conceptual model for the area are an unconfined, thick sequence of homogeneous sands averaging coarse to medium in grain size overlying an impervious granitic basement.

Granite Creek Area

Available well logs for the Granite Creek study area report the aquifer as composed of coarse to fine grained alluvial granitic sands interbedded with occasional, thin units of gravel to cobble-sized Belt clasts to depths of 70 feet. The Belt clast layers do not appear to be stratigraphically continuous through the study area, but are discrete occurrences at individual sites. A surface resistivity survey was conducted in the area to provide an estimate of the sediment thickness. Analysis of the data from the survey indicates a sediment thickness of approximately 200 feet across the area. Field data and observations collected during construction of 15 shallow ground water sampling wells determined that coarse to fine granitic sands with abundant gravel to cobble Belt clasts comprised the upper 20 feet of the alluvial sediment. Additionally, gravel to cobble Belt clasts appear as discrete but discontinuous units throughout the area. However, the occurrence of the distinct clast layers appears to decrease with depth. Through these examinations, a conceptual hydrogeologic model for the Granite creek study area was constructed. The characteristics of the conceptual model for the Granite Creek area are a thick, unconfined homogeneous aquifer composed of coarse to fine alluvial granitic sands with numerous gravel to cobble quartzite fragments overlying an impervious basement of granite and/or quartzite.

GROUND WATER FLOW SYSTEMS

Kalispell Bay Area

Preliminary evaluation of the data suggest ground water flow direction in the Kalispell Bay area is toward Priest Lake. In the western portion of Kalispell Bay there an abrupt change in topographic relief with significantly lower elevations toward the lake. In this area of lower elevation, static water levels in wells increase with increasing well depth, indicating an upward

hydraulic gradient as well as horizontal flow. In the eastern portion of the study area, water levels demonstrate strictly horizontal flow.

Granite Creek Area

In the Granite Creek study area, evaluation of the collected water level data is indicative of strictly horizontal flow towards Priest Lake. Future evaluation of the collected data will yield an estimation of ground water discharge to Priest Lake from both the Kalispell Bay and Granite Creek study areas.

GROUND WATER QUALITY

Introduction

The ground water quality of the Kalispell Bay and Granite Creek study areas was investigated with regards to nutrient enrichment of the ground water and possible contributions of nutrient through septic tank and/or sewage system percolation. A sampling program of the constructed shallow wells and selected private wells in both areas began in September of 1993. Water samples taken from these wells were analyzed for total nitrogen (NO_2 + NO_3), phosphates (ortho-P and total-P), selected cations and anions, total iron, pH, Eh, conductivity, temperature, TDS, coliform bacteria, and presence of E. coli. Chemical sampling was performed by Idaho Division of Environmental Quality and analyzed by Idaho Department of Health and Welfare. Biological samples were collected and analyzed by the Department of Microbiology, Molecular Biology, and Biochemistry at the University of Idaho. Samples were collected over two day periods during the months of September, October, and November of 1993.

Kalispell Bay Area

An analysis of the ground water quality data collected from the Kalispell Bay area indicates elevated nitrogen content in particular sites. Wells (Figure 2) K08, K09, K03, and K10, completed in the shallow portion of the aquifer system, and private wells THOMPSON and RUDIE2, completed in the deeper portion of the aquifer all exhibit elevated (>0.01 mg/L) total nitrogen content (Table 1). All anomalous wells are located in the area showing upward hydraulic gradient.

Table 1. Total Nitrogen (mg/L) for selected Kalispell Bay wells.

Well	September	October	November	Average
K08	0.064	0.056	0.064	0.061
K09	0.353	0.334	0.488	0.392
K03	0.180	0.178	0.289	0.216
K10	0.341	0.257	0.266	0.288
THOMPSON	0.170	0.146	0.167	0.161
RUDIE2	0.093	0.081	0.094	0.089

Granite Creek Area

Analysis of ground water samples collected from the Granite Creek study area indicates an elevation of total nitrogen combined with the presence of E. coli bacteria within the southern portion of the study area. Wells (Figure 3) G15, G14, G12, G02, and G11 exhibit an increase in total nitrate concentration (>0.1 mg/L) while wells G15, G14, G13, G01, G02, and G11 test positive for presence of E. coli bacteria (Table 2).

Table 2. Total Nitrogen and E. Coli presence for selected Granite Creek wells.

Well	September (mg/L)	October (mg/L)	November (mg/L)	Average (mg/L)	E. coli (+/-)*
G15	0.676	0.640	0.678	0.665	+
G14	0.233	0.261	0.282	0.259	+
G13	0.019	0.007	0.128	0.051	+
G01	0.025	0.025	0.010	0.020	+
G12	0.163	0.142	0.185	0.163	-
G02	0.252	0.110	0.102	0.155	+
G11	0.106	0.106	0.194	0.135	+

* - positive (+) indicates the presence of E. coli in the well

CONCLUSIONS

Preliminary conclusions from investigation of the Kalispell Bay and Granite Creek study areas are:

1) Both study areas demonstrate direction of ground water towards Priest Lake. The Kalispell Bay area displays horizontal ground water flow throughout the entire area with an upward hydraulic gradient over a portion of the area. The Granite Creek area displays strictly horizontal flow.
2) Both study areas contain particular sub-areas which display nutrient enrichment, particularly nitrogen, of ground water.
3) The Granite Creek study area contains a sub-area displaying both elevated nitrogen concentrations and positive tests for E. coli bacteria.

Currently, work is being performed which will provide estimation of ground water flow volume to Priest Lake from both study areas. This estimation will be used with conclusions reached from the water quality portion of the study to describe the amount of nutrient loading to Priest Lake via the ground water pathway from both study areas.

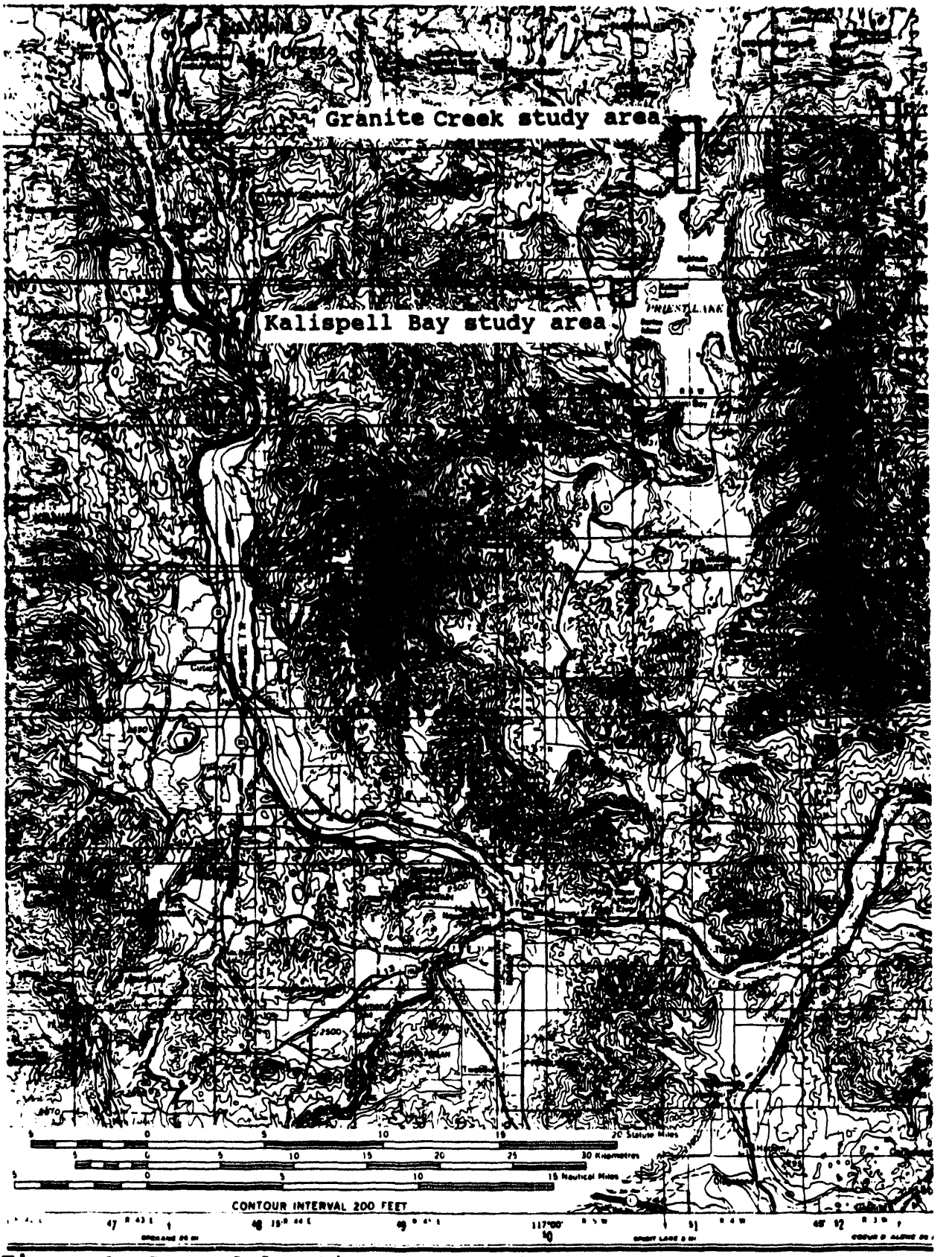


Figure 1 General location map of Priest Lake, Bonner Co., Idaho including Kalispell Bay and Granite Creek study areas.

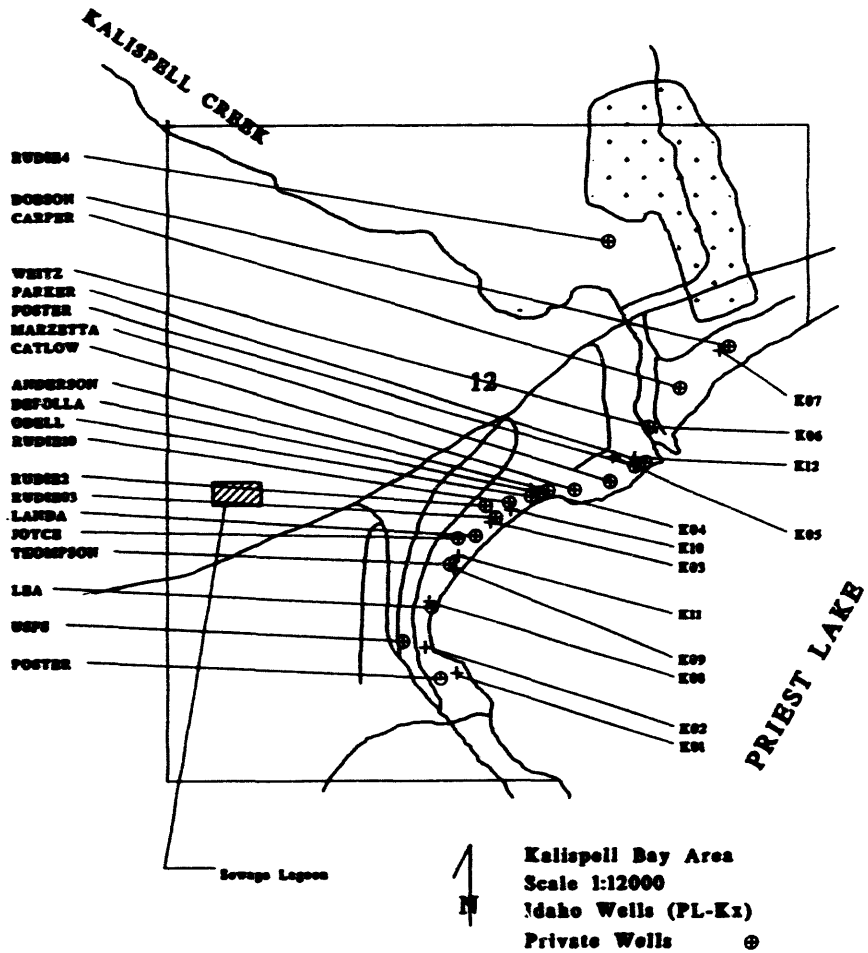


Figure 2 Well location map of the Kalispell Bay study area.

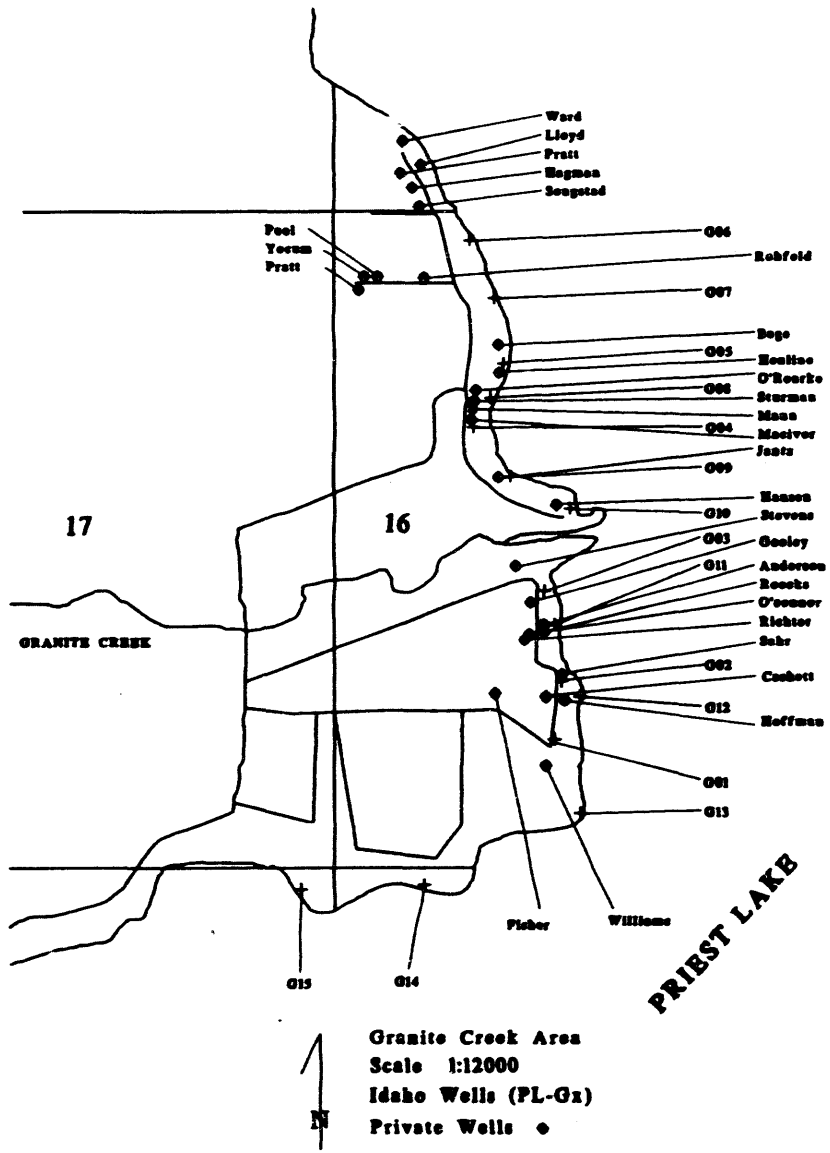


Figure 3 Well location map of Granite Creek study area.

Hydrogeology, Waste Disposal, Science and Politics
Proceedings 30th Symposium
Engineering Geology and Geotechnical Engineering, 1994

CHARACTERIZATION OF A SHALLOW CANYON AQUIFER CONTAMINATED BY MINE TAILINGS AND SUGGESTIONS FOR CONSTRUCTED WETLANDS TREATMENT

by

John C. Houck, Hydrology Graduate Students, Univ. of Idaho

and

Dr. L.L. (Roy) Mink, Director, Idaho Water Resources Research Institute (IWWRI), University of Idaho

ABSTRACT

A shallow aquifer consisting of mine tailings mixed with alluvial sediments is being investigated by the University of Idaho. The shallow aquifer is located in the lower Canyon Creek drainage in the Coeur d'Alene Mining District of northern Idaho. Canyon Creek is a major contributor of dissolved heavy metal loads to the South Fork of the Coeur d'Alene River. Problem metals include zinc, lead, and cadmium.

A total of 16 new monitoring wells were constructed in a 2.5 by .5 mile study area during summer of 1993 to map the water table configuration and collect water samples. A monitoring network of wells has been established in the Lower Canyon Creek valley which includes these 16 new monitoring wells, 5 monitoring wells installed previously, 10 domestic wells, and 7 wells located near tailing ponds.

Water quality analyses for ground and surface water samples collected during low creek flow conditions are presented along with geologic, geophysical and geohydrological information.

Creek flow measurements show that Canyon Creek gains water from the subsurface in the lower section of the study area, adjacent to and downstream from the community of Woodland Park.

The dissolved concentratins of zinc, cadmium, and lead are 33.9 mg/L, 0.26 mg/L, and 1.45 mg/L respectively for ground water sampled from recently installed shallow monitoring wells.

Two methods are proposed for consideration as methods of decreasing the input of heavy metals into Canyon Creek. These are: 1) restricting creek losses to the ground water system in the upper part of the study area and 2) construction of bench and pilot-scale anaerobic wetlands prior to large-scale constructed anaerobic wetlands.

Pages 622-636

These pages were removed at Authors' request just prior to printing.

Hydrogeology, Waste Disposal, Science and Politics
Proceedings 30th Symposium
Engineering Geology and Geotechnical Engineering, 1994

MODELING THE PULLOUT CHARACTERISTICS OF WELDED WIRE MATS EMBEDDED IN SILTY SAND

Casan L. Sampaco, Loren R. Anderson and Mark R. Nielsen

Dept. of Civil & Environmental Engineering
Utah State University, Logan, Utah 84322

ABSTRACT: This paper is an outgrowth of the on-going research on discrete finite element modeling of welded wire mesh reinforced soil structures such as the welded wire and RSE walls. The stiffness characteristics of the wire mesh-soil interfaces are modeled by a nonlinear hyperbolic relationship between the applied pullout stress and the associated mat placement. The relevant parameters are estimated from laboratory pullout tests that were conducted for welded wire mats embedded on silty sand. Since the bulk of the pullout resistance of welded wire mesh reinforcements is derived from the bearing resistance of the transverse members, an attempt is made to correlate the back-figured parameters to the number of transverse wires that constitute the test mats. This feature permits proper evaluation of actual interface parameters for the actual reinforced soil structures in which the actual lengths of the mats are longer (i.e. more transverse members) than the specimen used in the laboratory pullout tests. The resulting pullout stress-displacement formulations are then verified by comparing the predicted pullout resistance to the existing specifications and design methods for estimating the pullout capacities of grid reinforcements.

INTRODUCTION

Two general approaches are currently used in the finite element modeling of reinforced soil walls. The first approach is the composite material approach wherein the reinforced soil mass is modelled as a composite material with each element having properties representative of the composite soil and reinforcement matrix. The second approach is a discrete formulation wherein the reinforced soil mass is modelled as discrete elements that can interact with each other. Although the composite representation has been used successfully to predict stresses in a number of full scale structures, the discrete approach is considered to be more realistic and appropriate for detailed investigation of reinforced soil wall behavior because the properties and responses of the soil-reinforcement interfaces are directly quantifiable (Rowe and Ho, 1988).

The most commonly used procedure to model the relative movement of soil-reinforcement interface in the discrete finite element modeling is by the use of joint (interface) elements. In this procedure, a pair of nodes is usually introduced at the same geometric location within the structural element; one attached to the reinforcement, and the other to the soil. The nodes are linked by a pair of nonlinear springs normal and tangential to the reinforcement. The relative deformation of the soil and reinforcement prior to failure at the interface are controlled by the stiffness of these springs. The normal spring stiffness is usually assigned a very high value while the shear stiffness is usually governed by an assumed constitutive law. Many of the existing codes that were developed for finite element analysis of soil-structure interaction problems employ the hyperbolic constitutive model developed by Clough and Duncan (1971) to represent the shear stiffness of the interface (Andrawes et al, 1980; Adib et al, 1990; Seed et al, 1986; Schmertmann et al, 1989; Seed and Duncan 1984). The parameters associated with this model are usually estimated from laboratory tests that closely simulate the anticipated conditions in the field. In finite element analysis of reinforced soil walls, these parameters can be realistically estimated from pullout test results.

HYPERBOLIC MODEL FOR INTERFACE BEHAVIOR

The nonlinear, stress-dependent interface behavior was originally suggested by Clough and Duncan (1971) using a hyperbolic formulation as

$$\tau = \frac{\Delta_s}{a + b\Delta_s} \tag{1}$$

in which τ is the interface shear stress, Δ_s is the interface shear displacement, and a and b are constants which are a function of the roughness and normal stress, σ_n. Rearrangement of Eq. 1 yields the following straight line relationship:

$$\frac{\Delta_s}{\tau} = a + b\Delta_s \tag{2}$$

By plotting Δ_s/τ against Δ_s, the resulting straight line plot has a slope equal to b and an intercept of a. The reciprocal of the slope b is the asymptotic shear stress value at large displacement and is designated as τ_{ult} which is larger than the peak value τ_f, the shear strength at the interface. The relationship between τ_{ult} and τ_f is usually represented by the failure ratio, R_f defined as:

$$R_f = \frac{\tau_f}{\tau_{ult}} \tag{3}$$

The reciprocal of the coefficient a corresponds to the initial slope of shear stress-displacement curve and is designated as the initial shear stiffness K_{si}. To account for the normal stress-dependent nature of the parameter K_{si}, the empirical equation suggested by Janbu (1963) is adopted as follows:

$$K_{si} = K_j \gamma_w \left(\frac{\sigma_n}{P_a}\right)^n \tag{4}$$

in which K_j is a dimensionless stiffness number, n is the stiffness exponent, σ_n is the normal stress, P_a is the atmospheric pressure expressed in units of σ_n, and γ_w is the unit weight of water expressed in units of K_{si}. Both P_a and γ_w are introduced into the equation to permit conversion from one system of units to another more convenient. The parameters K_j and n can be determined by plotting (K_{si}/γ_w) against (σ_n/P_a) on a log-log plot such that K_j is the intercept and n is the slope of the best fit straight line.

The shear strength of the interface, τ_f is related to the normal stress, σ_n using the Mohr-Coulomb failure criterion such that

$$\tau_f = c + \sigma_n \tan\delta \tag{5}$$

where c is the interface cohesion and δ is the interface friction angle. By substituting Eqs. 3, 4 and 5 to Eq.

1, the shear stress-displacement relationship of the interface can be expressed as follows:

$$\tau = \frac{\Delta_s}{\frac{1}{K_j \gamma_w (\frac{\sigma_n}{P_a})^n} + \frac{R_f \Delta_s}{c + \sigma_n \tan\delta}} \tag{6}$$

In an incremental finite element analysis which employs the generalized Hooke's law and piecewise linear elastic algorithm, the value of the instantaneous slope of the shear stress-displacement relationship is used. The instantaneous slope, usually called the tangent stiffness value (K_{st}), can be derived by differentiating Eq. 6 with respect to Δ_s to obtain

$$K_{st} = K_{si} (1 - \frac{R_f \tau}{c + \sigma_n \tan\delta})^2 = K_j \gamma_w (\frac{\sigma_n}{P_a})^n (1 - \frac{R_f \tau}{c + \sigma_n \tan\delta})^2 \tag{7}$$

The above nonlinear formulation was developed by Clough and Duncan (1971) as an improvement to the one-dimensional linear elastic "interface element" originally developed by Goodman et al (1968). The interface element has zero thickness and essentially consists of two parallel nodal links, each controlled by a normal and a shear spring as illustrated in Fig. 1a. The properties of the interface element consist of a normal stiffness (K_n) and a tangent shear stiffness (K_{st}) which are related to the normal stress (σ_n) and shear stress (τ) acting on the element by the following equations:

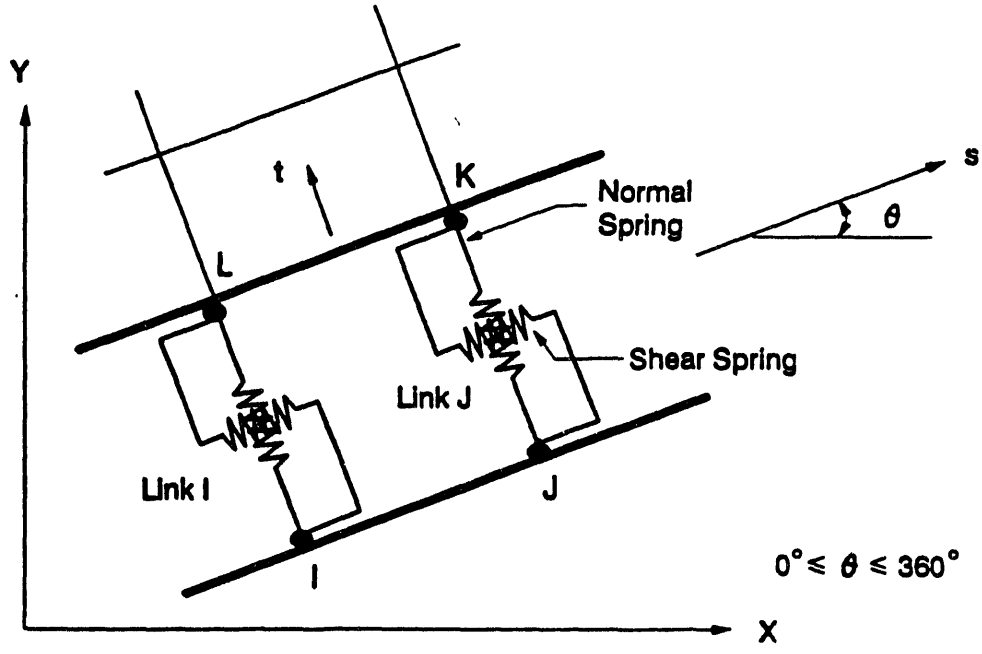
$$\sigma_n = K_n \Delta_n \tag{8}$$

$$\tau = K_{st} \Delta_s \tag{9}$$

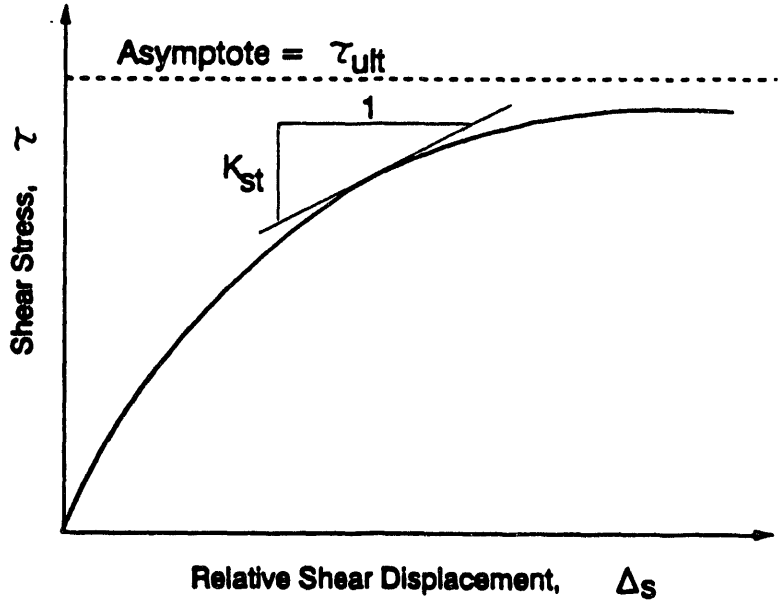
in which Δ_n is the average relative normal displacement across the element. The normal spring is assumed to be linear elastic and controls the opening and compressing of the interface element between two adjacent two-dimensional elements. During compression, overlapping of two-dimensional elements can be minimized in the analysis by using a very large value of K_n. In the case of tension loading, the normal spring stiffness is set to zero. The shear behavior of the interface described by the shear stiffness (K_{st}) can be modelled by a hyperbolic relationship (Fig. 1b) which is given by Eq. 7 for primary loading and reloading. In the case of unloading, the following equation is usually used

$$K_{st} = K_{su} \gamma_w (\frac{\sigma_n}{P_a})^n \tag{10}$$

in which K_{su} is the unloading shear spring coefficient. During shear failure or tension failure, the shear stiffness (K_{st}) value is reduced to a certain fraction of the stiffness just prior to failure (Boulanger et al, 1991).



(a) Components of an Interface Element



(b) Hyperbolic Shear Stress-Relative Shear Displacement Relationship

Fig. 1. Components of Interface Elements and Hyperbolic Shear Stress-Relative Shear Displacement Relationship (after Boulanger et al, 1991).

PULLOUT RESISTANCE EVALUATION

This section presents the three most commonly used expressions to evaluate the pullout resistance of grid reinforcements, such as the welded wire mesh. These methods are presented and adopted in this paper to validate the use of the hyperbolic relationship to model the pullout resistance of welded wire mats embedded in silty sand.

Nielsen & Anderson (1984) Empirical Equation

From the series of laboratory pullout tests that were conducted by Nielsen and Anderson (1984), prediction equations were developed based on statistical analysis to evaluate the total pullout resistance per unit width of the mat. The equations were expressed as a function of the overburden pressure, length and size of the wires, and the number of longitudinal and transverse bars that constitute the test mats. Different equations were developed for welded wire mats embedded in silty sand, washed sand and pea gravel. The pullout capacities were taken at 0.75 in. of displacement. The pullout resistance per unit width (P_r) of welded wire mats embedded on silty sand can be estimated using the equations listed below. For $N\sigma_n D_T > 113.6$ lb/ft:

$$P_r = \frac{F_t}{W} = 2143 \frac{lb}{ft} + \sigma_n D_T (\pi L_e M \tan\delta + 17.61N) \qquad (11)$$

For $N\sigma_n D_T < 113.6$ lb/ft, the following equation is recommended

$$P_r = \frac{F_t}{W} = \sigma_n D_T (\pi L_e M \tan\delta + 36.47N) \qquad (12)$$

in which σ_n is the overburden pressure (psf), D_T is the bar diameter (ft), L_e is the embedment length (ft), M is the number of longitudinal wires per unit width (ft^{-1}), W is the width of the wire mat sample (ft), tan δ is the friction factor between soil and reinforcement, and N is the number of transverse members. Equations 11 and 12 were developed on the assumption that the longitudinal and transverse members are of the same sizes.

Federal Highway Administration (Christopher et al, 1989)

Christopher et al (1989) developed a general procedure to evaluate the pullout resistance which can be applied to different soil reinforcement systems. For reinforcements capable of transmitting both frictional and passive soil resistance such as the welded wire mesh and bar mat systems, the pullout resistance per unit width of reinforcement (P_r) can be expressed as:

$$P_r = F^* \alpha \sigma_n L_e C \qquad (13)$$

where F^* is a factor that accounts for the combined effect of friction and passive (bearing) resistance, α is the scale effect correction factor and is defined as the fraction of reinforcement area that resists direct shear with the soil, σ_n is the overburden pressure, L_e is the embedment length, and c is the effective perimeter of the reinforcement which has a value of 2 for grids. The factor F^* for welded wire mesh was derived by adopting some of the experimental results reported by Nielsen and Anderson (1984). The resulting expression becomes:

$$F^* = 18.5 \frac{D_T}{S_T} + 0.475 \frac{D_L}{S_L} \qquad (14)$$

in which S_T is the spacing of transverse wires, D_L is the diameter of longitudinal members, and S_L is the lateral spacing of longitudinal wires.

AASHTO Task Force 27 Specifications

The AASHTO Task Force 27 (1990) specified that the pullout resistance evaluation for mechanically stabilized earth structures shall be based on load capacity at 0.5 in. of displacement or residual strength, whichever is less. For grid-reinforcing systems, with transverse member spacing of greater than or equal to 6 in., the pullout capacity per mat (P_p) can be evaluated as:

$$P_p = N_p z \gamma m A_b \quad (15)$$

where N_p is the passive resistance factor, z is the depth to reinforcement, γ is the unit weight of soil, m is the number of transverse bearing members behind the failure plane, and A_b is the surface area of transverse reinforcement in bearing ($A_b = D_T$ * width of mat). The passive resistance (N_p) varies from a value of 30 at the top of the wall and decreases linearly to a value of 15 at a depth of 20 ft. A constant value of 15 is used for a depth of 20 ft. and below.

LABORATORY PULLOUT TEST DATA

A total of 33 pullout tests using different sizes of welded wire mats embedded in silty sand were conducted by Nielsen and Anderson (1984) using the buried structures test facility at Utah State University. The tests were carried out using a 6 ft. wide by 5 ft. long by 4 ft. high test cell which is constructed with 12 in. reinforced concrete on three sides and steel gates closing the fourth side. Sixteen high capacity hydraulic rams which are capable of simulating up to 120 ft. of overburden pressure are used to apply normal pressure to the soil mass through a steel plate. Other details of the test cell are reported by Nielsen and Anderson (1984).

The silty sand used in the test has 40% passing sieve No. 200 and a D_{50} of 0.15 mm. Moisture-density relationship indicates a maximum dry density of 125 lb/ft^3 and an optimum water content of 9.5%. Triaxial test results yielded an angle of internal friction of 36^0 for specimens compacted at 95% relative compaction. The soils were compacted in the pullout test cell to at least 90% relative compaction density with water content near the optimum.

The welded wire mats were fabricated using two wire sizes of 1/4 in. and 3/8 in. with six longitudinal members spaced at 6 in. on centers and varying number of transverse members. The mats were laid in place as soon as the test cell was filled with compacted soil up to about 4 ft. An additional 1 ft. of soil was added to cover the mats. Two 1/2 in. thick steel plates were bolted on each side of the portion of the mat extending from the test cell and were attached to a large hydraulic ram by means of a clevis and a 3/4 in. diameter pin. The hydraulic ram was run by a hydraulic pump which was independent of the overburden hydraulic system and was capable of supplying 3000 psi pressure to the cylinder. The pullout force applied to the mats were monitored using a strain gage load cell mounted on opposite sides of the pullout rod. The displacement of the mats were measured by a dial gage mounted near the face of the mat. All the tests were run at a displacement rate of approximately 4 in/hr until the mats pulled out of the soil at a total displacement of 1 in.

ESTIMATION OF HYPERBOLIC INTERFACE PARAMETERS

Thirty-three pullout test data were analyzed to estimate the hyperbolic parameters for interface characteristics of welded wire mats embedded in silty sand. The pullout stress (τ_p) versus mat displacement (Δ_s) relationship for each normal pressure was developed by dividing the measured pullout load by twice the total plan area of the mat and plotting the results with the measured displacements. Peak values of τ_p, designated as τ_f, were then obtained from the resulting plots. The pullout stresses at 70% and 95% of the peak value were then calculated and their corresponding displacement Δ_{70} and Δ_{95} were read off from the pullout stress-displacement curves. This procedure is similar to the one suggested by Duncan et al (1980) for estimating the hyperbolic stress-strain properties of soils from triaxial test data. A plot of (Δ_s/τ_p) versus Δ_s yielded two data points and the equation of the line joining these two points was determined. The intercept of the line corresponds to the reciprocal of K_{si} while the slope represents the reciprocal of τ_{ult} as described in Eq. 2. By repeatedly doing this procedure for every normal pressure (σ_n), values of (K_{si}/γ_w) can be plotted against (σ_n/P_a) on a log-log plot to yield the shear stiffness number K_j (intercept of the best fit line) and the stiffness exponent n (slope of the best fit line). Similarly, with τ_{ult} known, values R_f for each normal pressure can be obtained using Eq. 3. Figures 2 and 3 show the typical plots of R_f and K_{si} for N = 6.

The interface friction angle (δ) for each normal pressure (σ_n) can be calculated using Eq. 5 with the cohesion c assumed equal to zero for silty sand. A plot of δ versus the log of (σ_n/P_a) gives the variation of δ with σ_n which can be expressed as:

$$\delta = \delta_o - \Delta\delta \log\left(\frac{\sigma_n}{P_a}\right) \qquad (16)$$

in which δ_o is the value of the interface friction angle (δ) at σ_n equal to P_a, and $\Delta\delta$ is the reduction in δ for an order-of-magnitude increase in σ_n. Equation 16 is a realistic expression of the interface friction angle (δ) to account for its variation with the normal pressure, which has been the trend reported by several investigators (Schlosser and Elias, 1978; Juran et al, 1988).

ANALYSES OF RESULTS

The procedure described in the preceding section was applied for all thirty-three pullout test data. Results were interpreted based on the number of transverse members contained in the mat specimen. Two wire sizes of 1/4 in. and 3/8 in. were used for the pullout tests. The mats containing 3 transverse wires have a transverse wire spacing of 24 in. while those with 4 wires have a spacing of 18 in. A transverse wire spacing of 12 in. was used for mats with 5 and 6 transverse members. Although a close similarity exists between the results of 1/4 in. and 3/8 in. wires, it is difficult to develop a general relationship that accounts for the wire diameter from a data base consisting of only two wire sizes. Thus, separate expressions were developed for each wire sizes. However, only the results of the 3/8 in. wires are presented in this study due to the quality of available data and to the space limitations of the paper.

The primary objective of the present analysis is to relate the hyperbolic interface parameters to the number of transverse members (N) by examining the estimated parameters K_j, R_f, δ, and n. Figures 4 to 7 show the plots of δ as a function of the normal pressure for different values of N. Both wire sizes (1/4 in. and 3/8 in.) displayed similar plots of decreasing δ with log (σ_n/P_a). Similar trend was observed for metallic strip reinforcements (Schlosser & Elias, 1978; Alimi et al, 1977) and for polymer geogrids (Ingold, 1983; Koerner, 1986; Rowe et al, 1985). This observation is attributed to the dilatancy behavior of dense sands in which under the effect of shear stresses mobilized at the interfaces, the granular soil in the vicinity of the reinforcement tends to dilate, but its dilatancy is restrained by the surrounding volume of soil. This restrained dilatancy

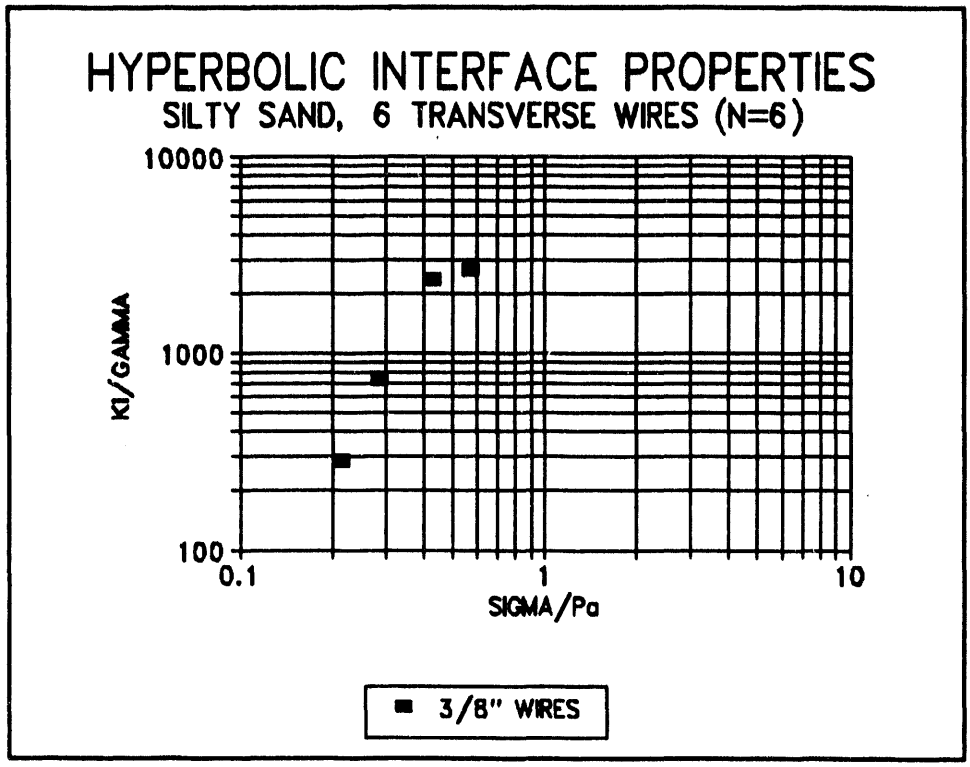


Fig. 2. Typical Plot of (K_{ni}/γ_w) and (σ_n/P_a) on a Log-Log Scale for N = 6.

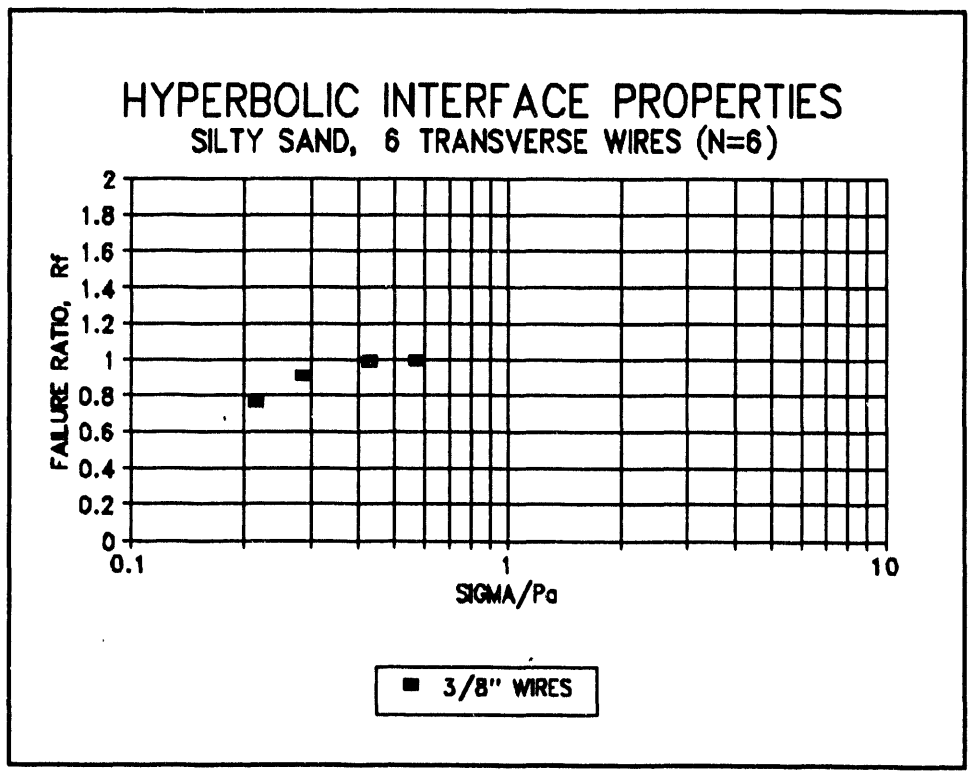


Fig. 3. Typical Plot of Failure Ratio (R_f) as a Function of log (σ_n/P_a) for N = 6.

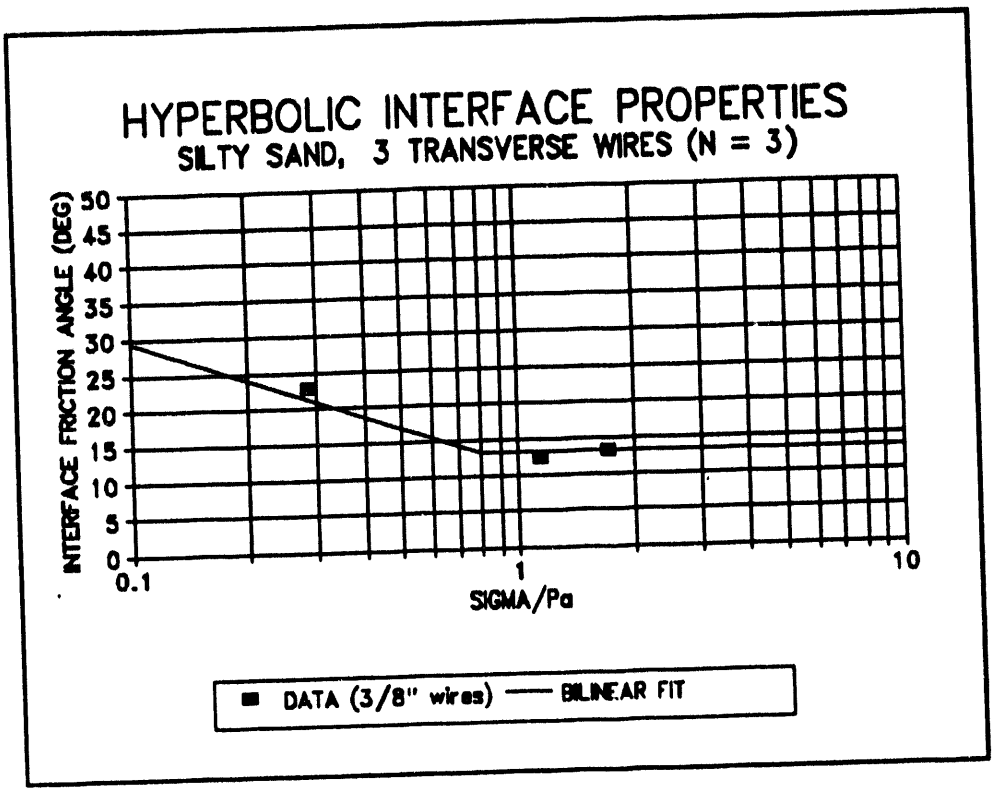


Fig. 4. Plot of Interface Friction Angle (δ) as a Function of Normal Pressure for N = 3.

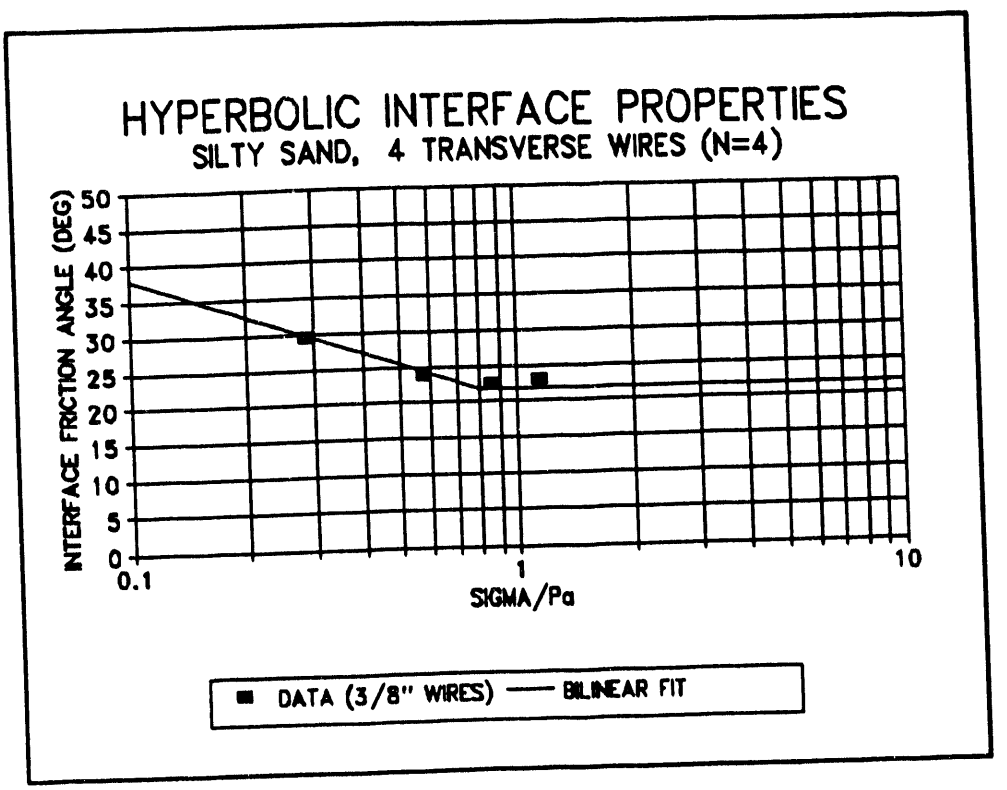


Fig. 5. Plot of Interface Friction Angle (δ) as a Function of Normal Pressure for N = 4.

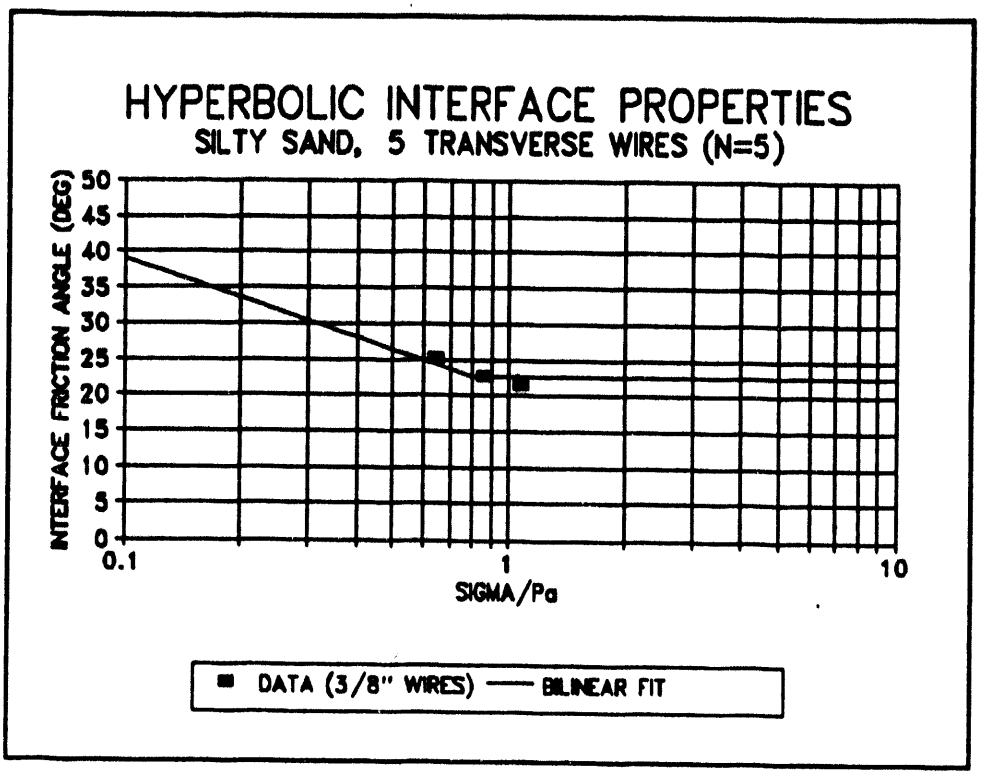


Fig. 6. Plot of Interface Friction Angle (δ) as a Function of Normal Pressure for N = 5.

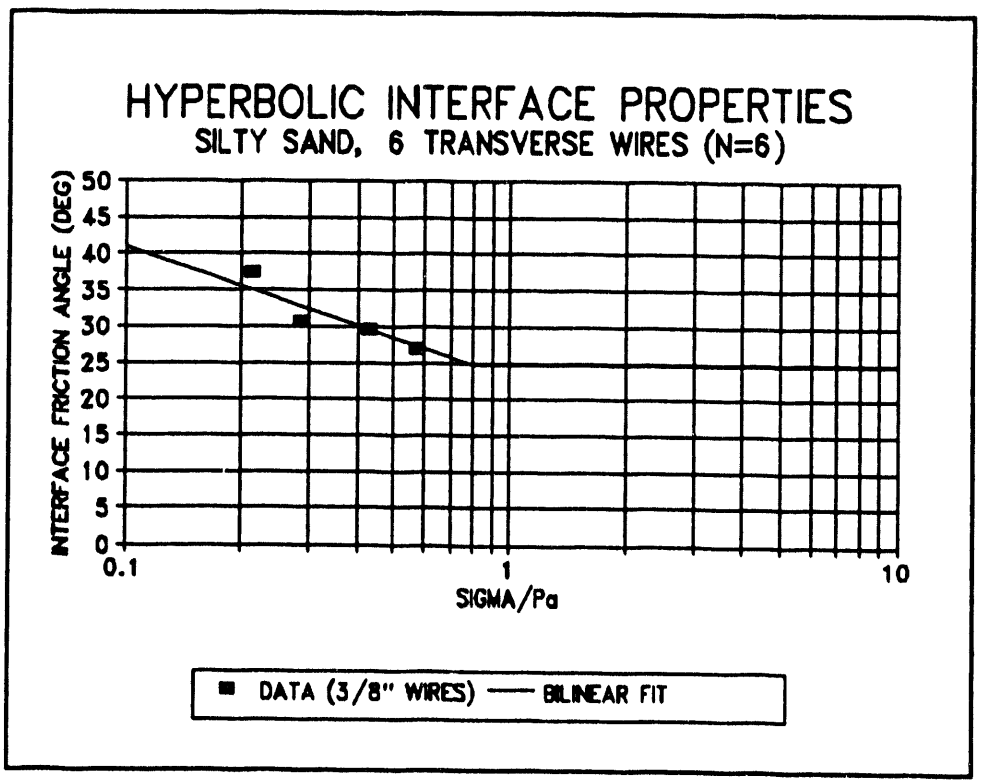


Fig. 7. Plot of Interface Friction Angle (δ) as a Function of Normal Pressure for N = 6.

results in a normal stress concentration at the soil-reinforcement interfaces, thereby increasing the pullout resistance of the inclusion (Juran et al, 1988). As a result, the apparent interface friction angle can significantly exceed the friction angle of the soil at low normal pressures. Furthermore, the effect is also highly dependent upon the surface texture of the reinforcement. Schlosser and Elias (1978) reported that ribbed strips mobilize soil-to-soil friction which in dense granular soils can result in a high dilatancy effect, whereas smooth strips mobilize soil-to-reinforcement friction resulting to a very low volume change and consequently small dilatancy effects.

Based on this premise, welded wire mesh reinforcements can result in a high dilatancy effect due to the manner in which friction is mobilized by the transverse bearing members (Peterson and Anderson, 1980). To account for this phenomenon, a bilinear relationship was fitted in the plots of Figs. 4 to 7. At a value of (σ_n/P_a) of 0.80 and lower, all points can be fitted using $\Delta\delta$ of 18° and yielded δ_o values of 11.5°, 20°, 21°, and 23° for 3, 4, 5, and 6 transverse members, respectively. A linear regression analysis yielded the following relationship with a correlation coefficient of 0.91.

$$\delta_o = 2.9° + 3.55N \tag{17}$$

in which N is the number of transverse members. The interface friction angle can, therefore, be estimated for any number of transverse wires using Eqs. 16 and 17 such that $\Delta\delta$ is equal to 18° at (σ_n/P_a) value of less than or equal to 0.80. At higher normal pressures $(\sigma_n/P_a > 0.80)$ the interface friction angle (δ) remains constant $(\Delta\delta = 0)$ at a value evaluated by Eq. 16 at $(\sigma_n/P_a) = 0.80$.

On the other hand, no definite relationships were observed from the plots of failure ratio (R_f) and stiffness exponent (n) such that simple averaging was used to obtain an R_f of 0.95 and an n value of 1.0. This process of forcing R_f and n to be constant would naturally affect the accuracy of the estimates. This was compensated by the way the values of the initial shear stiffness (K_{si}) were established. Each pullout stress-displacement data was then fitted using $R_f = 0.95$, $n = 1$, and δ calculated from Eq. 16. Adjustments were made to fit the data by varying the values of K_{si}. The new set of values of (K_{si}/γ_w) were then replotted against (σ_n/P_a) on an arithmetic scale (since $n = 1$) and the slope K_j is obtained for different values of N. Regression analysis of the interface stiffness number (K_j) versus the number of transverse members (N) yielded a correlation coefficient of 0.95 using the following relationship

$$K_j = 180 + 712N \tag{18}$$

From the empirical equations defined by Eqs. 17 and 18, a plot of the pullout load versus displacement can be made for any number of transverse members by manipulating Eq. 1. Figure 8 depicts the pullout load-displacement curves for 4 transverse wires and the corresponding hyperbolic model fit based on the equations developed in this study. The pullout resistance can also be estimated at any displacement Δ_s for any value of σ_n and N using Eq. 1. Figures 9 to 12 show the computed pullout capacities at a displacement (Δ_s) of 0.5 in. for different values of N. Also shown on the plots are the pullout resistances calculated from the equations developed by Nielsen and Anderson (1984), AASHTO Task Force 27 (1990), and Federal Highway Administration (FHWA) (Christopher et al, 1989). The measured pullout capacities at 0.5 in. of displacement are also included. It must be noted that the empirical equations developed by Nielsen and Anderson (1984) are based on 0.75 in. displacement. From these comparisons, the hyperbolic model seems to provide reasonable predictions of the pullout resistance for all values of N.

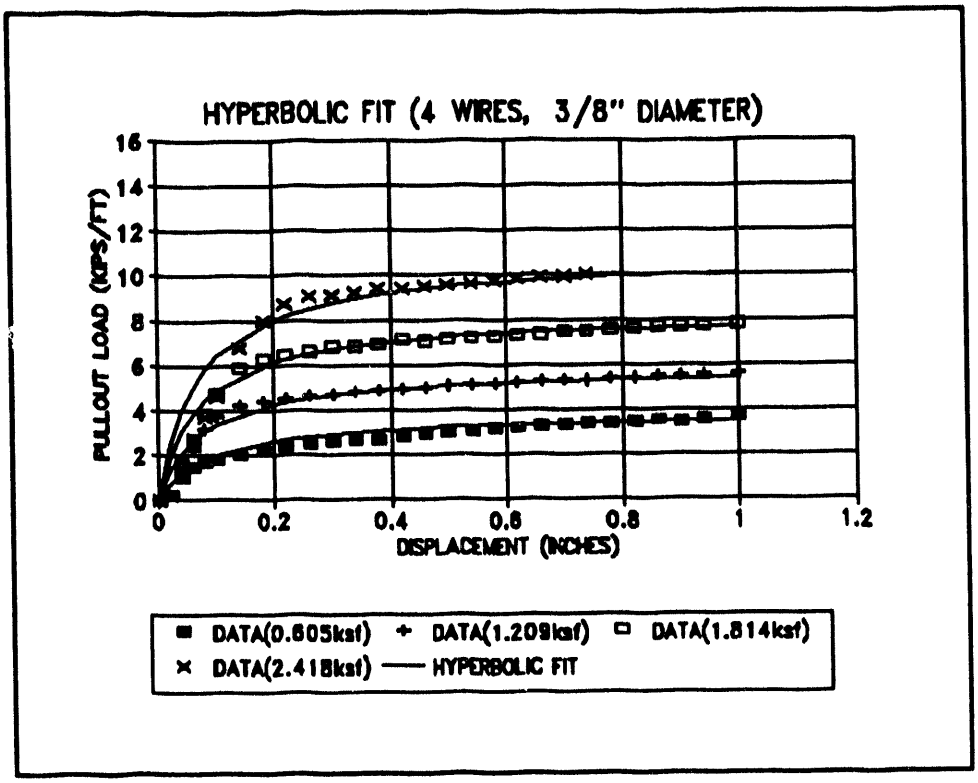


Fig. 8. Predicted and Measured Pullout Resistance-Displacement Curves for N = 4.

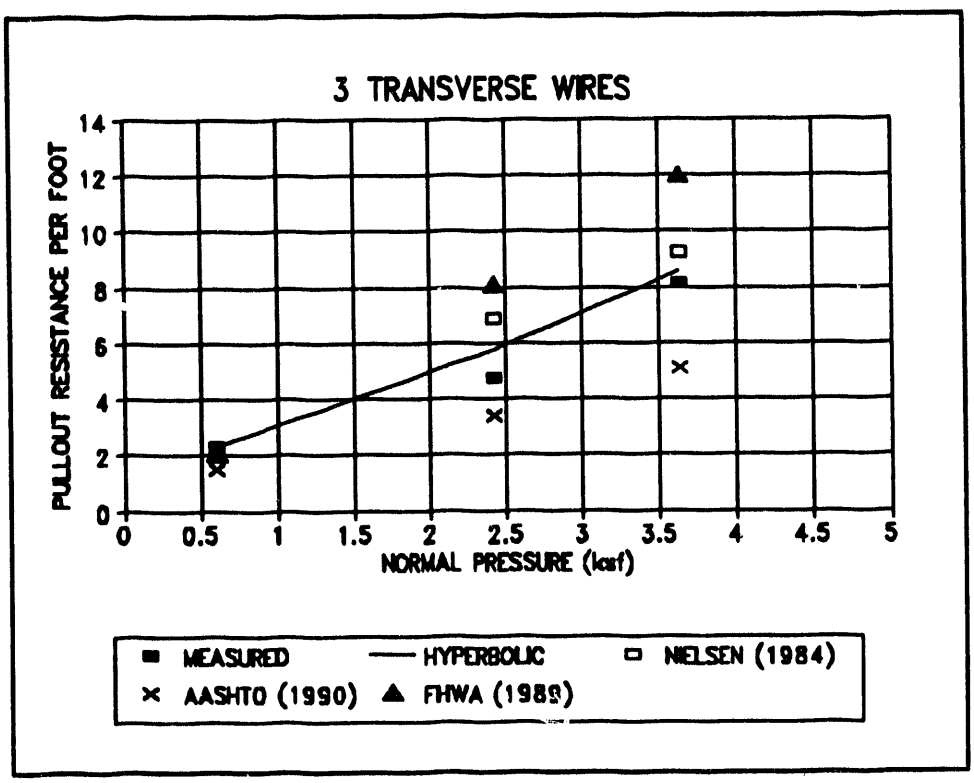


Fig. 9. Predicted and Measured Pullout Resistance at 0.5 in. Displacement for N = 3.

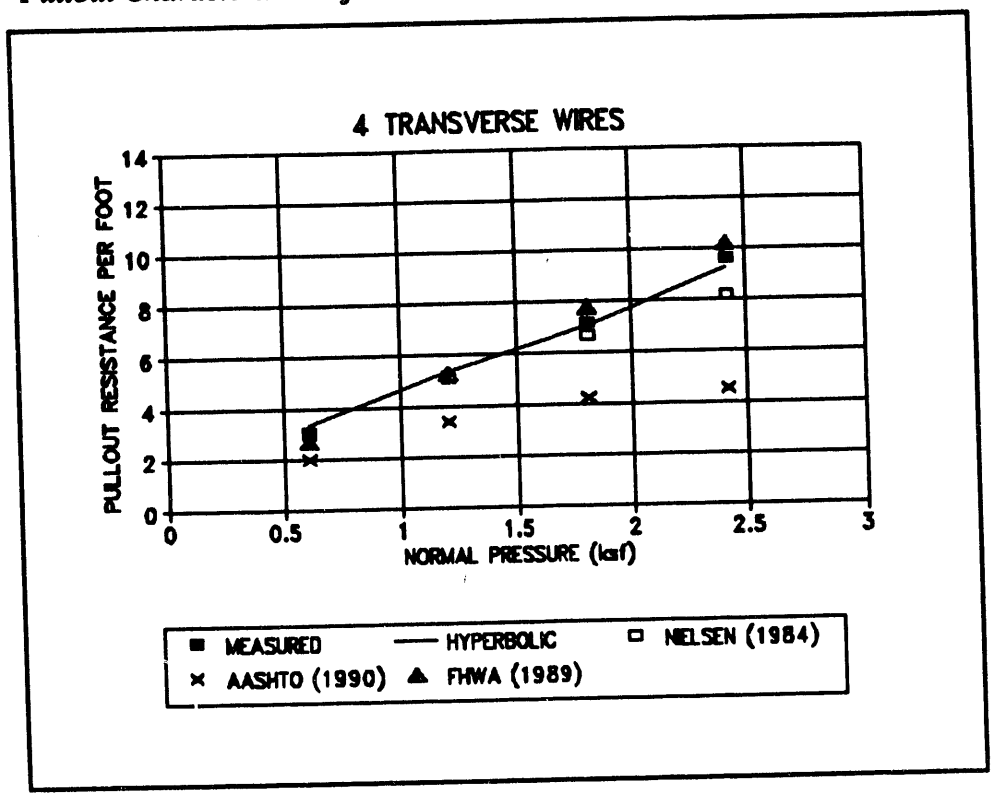


Fig. 10. Predicted and Measured Pullout Resistance at 0.5 in. Displacement for N = 4.

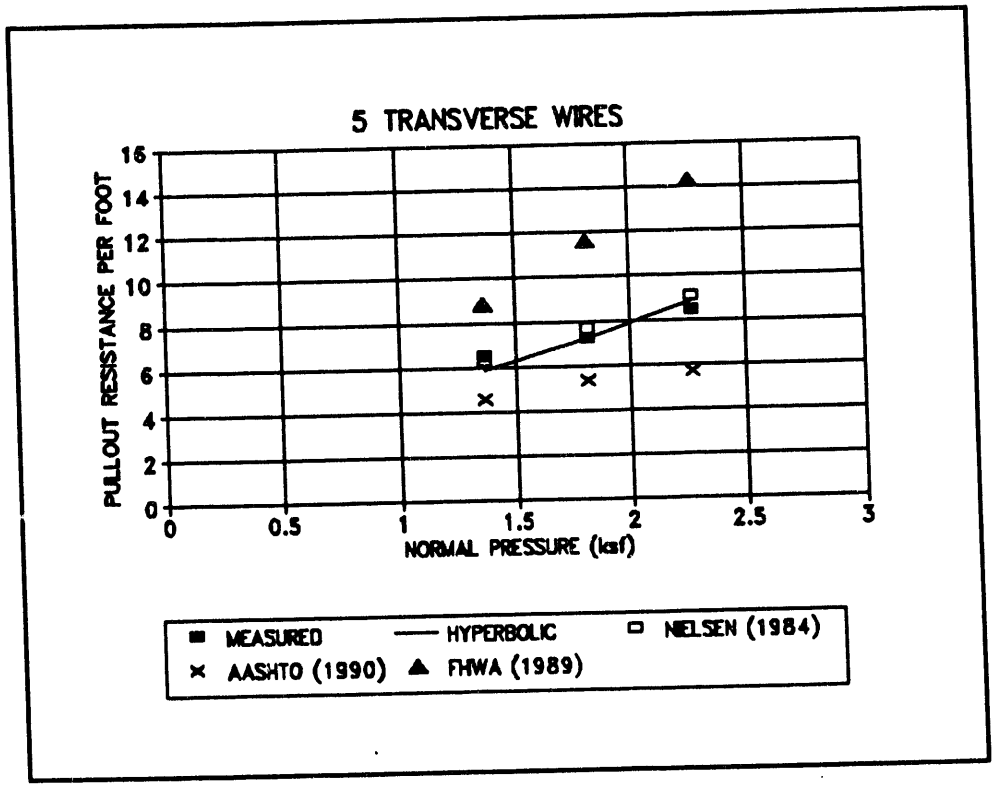


Fig. 11. Predicted and Measured Pullout Resistance at 0.5 in. Displacement for N = 5.

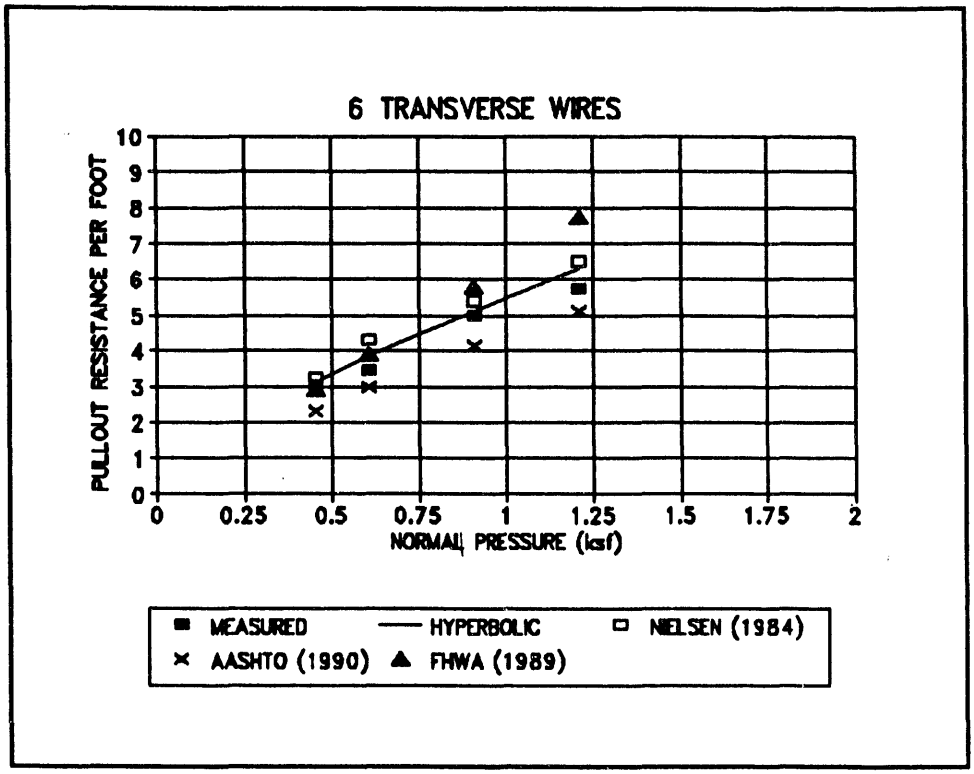


Fig. 12. Predicted and Measured Pullout Resistance at 0.5 in. Displacement for N = 6.

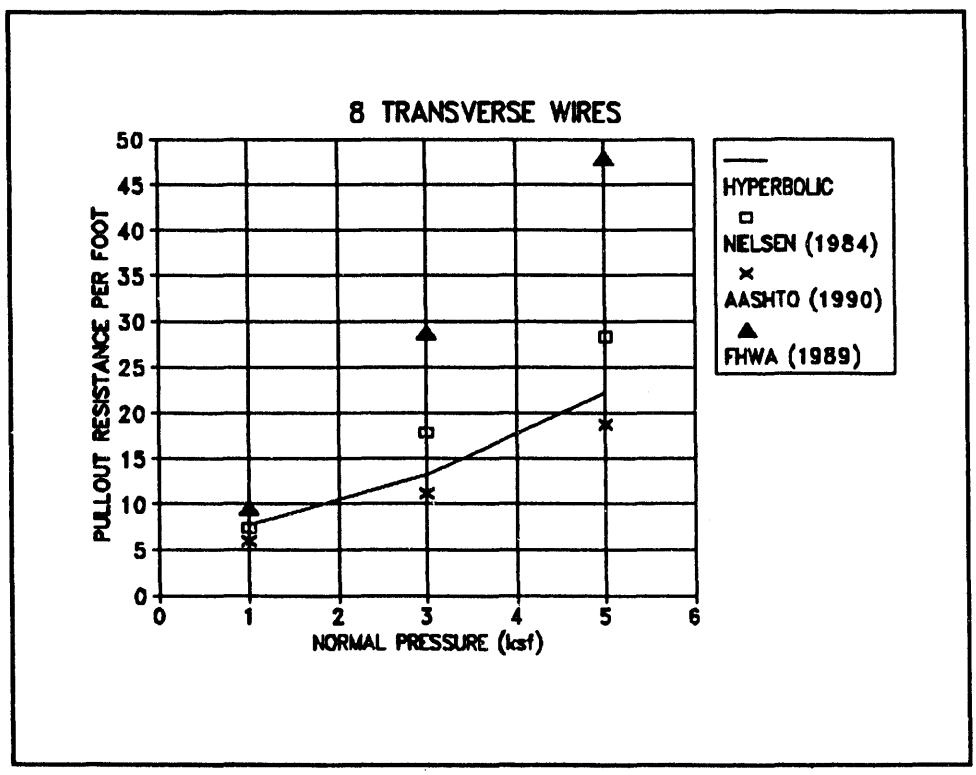


Fig. 13. Predicted Pullout Resistance for an Actual Size Mat With N = 8.

To extend the problem beyond the mat sizes studied in the laboratory pullout tests, a field mat size was chosen for analysis. A 15 ft long by 4 ft wide mat with a transverse wire spacing of 2 ft and a longitudinal wire spacing of 0.5 ft was used. This mat configuration results to 9 longitudinal and 8 transverse members with each member assumed to be 3/8 in. in diameter. Figure 13 illustrates the predicted pullout resistance using the four different methods. It is evident that the hyperbolic model can predict reasonable values of the pullout resistance which are within the range of values predicted by the existing specifications and empirical procedures.

CONCLUSIONS

The use of nonlinear hyperbolic stress-displacement relationship to model the characteristics of soil-structure interfaces seems to offer a promising application in discrete finite element modeling of reinforced soil structures. From the analyses conducted in this study, the parameters estimated from laboratory pullout tests can provide a reliable prediction of the pullout resistance which compares well with the actual measurements. The empirical equations developed in this paper to account for the number of transverse members and dilatancy effects at low normal pressures, further extended the applicability of the model to provide reasonable evaluation of the pullout resistance of full-scale reinforcing mats.

REFERENCES

Adib, M.E., Mitchell, J.K., and Christopher, B.R. (1990). "Finite Element Modeling of Reinforced Soil Walls and Embankments". Proc. Design and Performance of Earth Retaining Structures, ASCE Geotechnical Special Publication No. 25, P.C. Lambe and L.A. Hansen (eds.), pp. 409-423.

Alimi, I., Bacot, J., P. Long, N.T., and Schlosser, F. (1977). "Etude d l'adherence sol-armatures." Proc. 9th International Conference on Soil Mechanics and Foundation Engineering, Tokyo, Japan, pp. 11-14.

Andrawes, K.Z., McGown, A., Mashhour, M.M., and Wilson-Fahmy, R.F. (1980). "Tension Resistant Inclusion in Soils". Journal of Geotech. Eng'g. Div., ASCE, Vol. 106, No. GT12, pp. 1313-1326.

Boulanger, R.W., Bray, J.D., Chew, S.H., Seed, R.B., Mitchell, J.K., and Duncan, J.M. (1991). "SSCOMPPC: A Finite Element Analysis Program for Evaluation of Soil-Structure Interaction and Compaction Effects." Geotechnical Eng'g. Research Report No. UCB/GT/91-02, Dept. of Civil Eng'g., University of California, Berkeley, California.

Christopher, B.R., Gill, S.A., Giroud, J.P., Juran, I., Mitchell, J.K., Schlosser, F., and Dunnicliff, J. (1989). "Reinforced Soil Structures, Design and Construction Guidelines: Vol. 1". FHWA Report No. RD-89-043, Federal Highway Administration, Springfield, Virginia.

Clough, G.W. and Duncan, J.M. (1971). "Finite Element Analysis of a Retaining Wall Behavior". Journal of Geotech. Eng'g. Div., ASCE, Vol. 97, No. 12, pp. 1657-1673.

Collin, J.G. (1986). "Earth Wall Design". Thesis Submitted in Partial Satisfaction of the Requirements for the Degree of Doctor of Philosophy, Dept. of Civil Engineering, University of California, Berkeley, California.

Duncan, J.M., Byrne, P.M., Wong, K.S., and Mabry, P. (1980). "Strength, Stress-Strain, and Bulk Modulus Parameters for Finite Element Analysis of Stresses and Movements in Soil Masses". Report No. UCB/GT/80-01, University of California, Berkeley, California.

Goodman, R.E., Taylor, R.L., and Brekke, T.L. (1968). "A Model for the Mechanics of Jointed Rocks". Journal of the Soil Mech. and Foundations Division, Vol. 94, No. SM3, p. 637.

Ingold, T.S. (1983). "Laboratory Pull-out Testing of Grid Reinforcements in Sand." Geotechnical Testing Journal, Vol. 6, No. 3, pp. 101-111.

Janbu, N. (1963). "Soil Compressibility as Determined by Oedometer and Triaxial Tests." Proc. European Conf. on Soil Mechanics and Foundation Eng'g., Weisbaden, Germany, Vol. 1, pp. 19-25.

Juran, I., Knochenmus, G., Acar, Y.B., and Arman, A. (1988). "Pullout Response of Geotextiles and Geogrids (Synthesis of Available Experimental Data)". Geosynthetics for Soil Improvement, ASCE Geotech. Special Pub. No. 18, R.D. Holtz (ed.), pp. 92-111.

Koerner, R. (1986). "Direct Shear/Pull-Out Tests on Geogrids." Report No. 1, Department of Civil Engineering, Drexel University, Philadelphia, Pennsylvania.

Nielsen, M.R. and Anderson, L.R. (1984). "Pullout Resistance of Wire Mats Embedded in Soil". Research Report Submitted to the Hilfiker Retaining Wall Co., Dept. of Civil and Envi. Eng'g., Utah State University, Logan, Utah.

Peterson, L.M. and Anderson, L.R. (1980). "Pullout Resistance of Welded Wire Mats Embedded in Soil." Research Report Submitted to the Hilfiker Retaining Wall Company, Dept. of Civil and Environmental Eng'g., Utah State University, Logan, Utah.

Rowe, R.K., Ho, S.K., and Fisher, D.G. (1985). "Determination of Soil-Geotextile Interface Strength Properties." Second Canadian Symposium on Geotextiles, pp. 23-34.

Rowe, R.K. and Ho, S.K. (1988). "Application of Finite Element Techniques to the Analysis of Reinforced Soil Walls". The Application of Polymeric Reinforcements in Soil Retaining Structures, P.M. Jarrett and A. McGown (eds.), pp. 541-553.

Schlosser, F. and Elias, V. (1978). "Friction in Reinforced Earth." Proc. Symposium on Earth Reinforcement, ASCE, Pittsburgh.

Schmertmann, G.R., Chew, S.H. and Mitchell, J.K. (1989). "Finite Element Modeling of Reinforced Soil Wall Behavior". Rep. No. UCB/GT/89-01, Dept. of Civil Eng'g., University of California, Berkeley, California.

Seed, R.B. and Duncan, J.M. (1984). "SSCOMP: A Finite Element Analysis Program for Evaluation of Soil-Structure Interaction and Compaction Effects". Geotech. Eng'g. Research Rep. No. UCB/GT/84-02, University of California, Berkeley, California.

Seed, R.B., Collin, J.G. and Mitchell, J.K. (1986). "FEM Analysis of Compacted Reinforced Soil Walls". Proc. 2nd Intl. Symp. on Numerical Models in Geomechanics, Ghent, Belgium, pp. 553-562.

Task Force 27 (1990). "Design Guidelines for Mechanically Stabilized Earth (MSE) Walls in Permanent Applications". AASHTO-AGC-ARTBA Joint Committee, Washington, D.C.

DATE
FILMED
7/26/94
END